Oral Büyüköztürk · Mehmet Ali Taşdemir
Oğuz Güneş · Yılmaz Akkaya *Editors*

Nondestructive Testing of Materials and Structures

Proceedings of NDTMS-2011, Istanbul,
Turkey, May 15–18, 2011

Part 1

Nondestructive Testing of Materials and Structures

RILEM BOOKSERIES

Volume 6

RILEM, The International Union of Laboratories and Experts in Construction Materials, Systems and Structures, founded in 1947, is a non-governmental scientific association whose goal is to contribute to progress in the construction sciences, techniques and industries, essentially by means of the communication it fosters between research and practice. RILEM's focus is on construction materials and their use in building and civil engineering structures, covering all phases of the building process from manufacture to use and recycling of materials. More information on RILEM and its previous publications can be found on www.RILEM.net.

For further volumes:
http://www.springer.com/series/8781

Oral Büyüköztürk • Mehmet Ali Taşdemir
Oğuz Güneş • Yılmaz Akkaya

Editors

Nondestructive Testing of Materials and Structures

Proceedings of NDTMS-2011, Istanbul, Turkey,
May 15–18, 2011

Springer

Editors

Oral Büyüköztürk
Department of Civil and Environmental
Engineering
Massachusetts Institute of Technology
77 Massachusetts Avenue, Room 1-281
Cambridge, MA 02139
USA
obuyuk@mit.edu

Oğuz Güneş
Department of Civil Engineering
Çankaya University
Eskisehir Yolu, 29. km.
Ankara 06810
Turkey
ogunes@cankaya.edu.tr

Mehmet Ali Taşdemir
Department of Civil Engineering
Istanbul Technical University
ITU Ayazaga Campus
Maslak, Istanbul 34469
Turkey
tasdermirme@itu.edu.tr

Yılmaz Akkaya
Department of Civil Engineering
Istanbul Technical University
ITU Ayazaga Campus
Maslak, Istanbul 34469
Turkey
akkayayil1@itu.edu.tr

Contents

Section 2   NDT for Material and Property Characterization

Section 3   Early Age NDT of Concrete and Other Materials

Section 4   NDT for Material Characterization: Metallurgical Perspective

Section 5   NDT of Metals and Composites

Section 6   Theoretical Modeling and Simulation Studies as a Basis for NDT

Part II

Section 7   NDT of Civil Infrastructures

Section 8   Geotechnical and Geophysical Applications of NDT

Section 9   Health Monitoring of Structures

Section 10   NDT and Evaluation of Historic Buildings and Monuments

Section 11 NDT Planning, Practice, Reliability, Codes and Standards

Committee Membership

International Organizing Committee

Oral Büyüköztürk, *MIT, USA (Symposium Chair)*
Michael C. Forde, *University of Edinburgh, UK*
Christian U. Grosse, *Technical University of Munich, Germany*
Hans W. Reinhardt, *University of Stuttgart, Germany*
Mehmet A. Taşdemir, *ITU, Turkey*
Herbert Wiggenhauser, *BAM, Germany*

International Scientific Committee

D.G. Aggelis, *University of Ionnia, Greece*
C. Andrade, *IETcc_CSIC, Spain*
F. Ansari, *University of Illinois at Chicago, USA*
J.-P. Balayssac, *Université de Toulouse, France*
D. Bernal, *Northeastern University, USA*
H. Beushausen, *University of Cape Town, South Africa*
N. De Belie, *Ghent University, Belgium*
L. Binda, *Politecnico di Milano, Italy*
M. Celebi, *USGS, USA*
J.-F. Chen, *University of Edinburgh, UK*
P. Côte, *LCPC, France*
B. Drinkwater, *University of Bristol, UK*
D. Frangopol, *Lehigh University, USA*
P. Gambarova, *Politecnico di Milano, Italy*
A. Giannopoulous, *University of Edinburgh, UK*
S.D. Glaser, *University of California, Berkeley, USA*
B. Hillemeier, *Technische Universität Berlin, Germany*

N. Hoult, *Queen's University, Canada*
S. Hurlebaus, *Texas A&M University, USA*
T. Jayakumar, *IGCAR, India*
M. Krause, *BAM, Germany*
J. Krieger, *BASt, Germany*
T. Kundu, *University of Arizona, USA*
S.S. Lee, *KRISS, Korea*
C.K. Leung, *HKUST, Hong Kong*
H. Li, *Harbin Institute of Technology, China*
Z. Li, *HKUST, Hong Kong*
C. Maierhofer, *BAM, Germany*
J. Michaels, *Georgia Institute of Technology, USA*
M. Ohtsu, *Kumamoto University, Japan*
J.S. Popovics, *University of Illinois Urbana-Champaign, USA*
C.A. Prato, *National University of Cordoba, Argentina*
E. Proverbio, *University of Messina, Italy*
B. Raj, *IGCAR, India*
H.C. Rhim, *Yonsei University, Korea*
P. Rivard, *Université de Sherbrooke, Canada*
R. Roberts, *GSSI, USA*
N. Ryden, *Lund University, Sweden*
S.P. Shah, *Northwestern University, USA*
R.N. Swamy, *The University of Sheffield, UK*
K. Soga, *University of Cambridge, UK*
T. Triantafillou, *University of Patras, Greece*
T. Uhl, *AGH University of Science and Technology, Poland*
T. Vogel, *ETH Zurich, Switzerland*
G. Washer, *University of Missouri, USA*
A. Zingoni, *University of Cape Town, South Africa*

Local Organizing Committee

Oğuz Güneş, *Çankaya University, Ankara, Turkey* (Co-Chair)
Yılmaz Akkaya, *ITU, Istanbul, Turkey* (Co-Chair)
Özkan Şengül, *ITU, Istanbul, Turkey* (Secretary)
Adile Aslı Özbora, *ITU, Istanbul, Turkey*
Akın Önalp, *Istanbul Kültür University, Istanbul, Turkey*
Arda Kiremitçi, *ITU, Istanbul, Turkey*
C. Hakan Gür, *METU, Ankara, Turkey*
Cem Yalçın, *Boğaziçi University, Istanbul, Turkey*
Erhan Karaesmen, *METU, Ankara, Turkey*
Hilmi Luş, *Boğaziçi University, Istanbul, Turkey*
Ninel Alver, *Ege University, Izmir, Turkey*
Yılmaz Taptık, *ITU, Istanbul, Turkey*

Supporting Institutions and Sponsors

Organizer and Host Institutions

Istanbul Technical University (ITU), *Istanbul, Turkey* (Organizer and Host)
International Union of Laboratories and Experts in Construction Materials, Systems and Structures (RILEM), *Bagneux, France* (Co-Organizer)

Academic/Research Institutions

Massachusetts Institute of Technology (MIT), *Cambridge, MA, USA*
Federal Institute for Materials Research and Testing (BAM), *Berlin, Germany*
The University of Edinburgh, *Edinburgh, U.K.*
University of Stuttgart, *Stuttgart, Germany*
Technical University of Munich (TUM), *Munich, Germany*
Politecnico di Milano, *Milano, Italy*
Istanbul Kültür University, *Istanbul, Turkey*
Atılım University, *Ankara, Turkey*
Middle East Technical University-Welding Technology & NDT Research/Application Center, *Ankara, Turkey*
Boğaziçi University, *Istanbul, Turkey*
Çankaya University, *Ankara, Turkey*

Public Research Organizations

The Scientific and Technological Research Council of Turkey, *Ankara, Turkey*

NDT Societies

American Society for Nondestructive Testing (ASNT), *Columbus, OH, U.S.A.*
Turkish Society of Nondestructive Testing (TurkNDT), *Ankara, Turkey*

Main Sponsors

Turkish Cement Manufacturers' Association (TCMB), *Ankara, Turkey*
Turkish Ready Mix Concrete Association (THBB), *Istanbul, Turkey*
ENKA Construction and Industry. Co., Inc., *Istanbul, Turkey*
Umran Steel Pipe Inc., *Istanbul, Turkey*
YAMATA Yatırım İnşaat Turizm ve Ticaret A.Ş., *Istanbul, Turkey*
GAMA - NUROL JV, *Istanbul, Turkey*
Yapı Merkezi, *Istanbul, Turkey*

Major Sponsors

Atılım University, *Ankara, Turkey*
Istanbul Kültür University, *Istanbul, Turkey*
ISTON Istanbul Concrete Elements and Ready-Mixed Concrete Factories Co.,
Istanbul, Turkey
BASF Yapı Kimyasalları Sanayi A.Ş., *Istanbul, Turkey*
Türk Ytong Sanayi A.Ş., *Istanbul, Turkey*
Yurtiçi Kargo, *Istanbul, Turkey*
Hilti Corporation, *Schaan, Liechtenstein*
Proceq SA, *Zurich, Switzerland*
The Dynatest Group, *Glostrup, Denmark*
ÇimSA Cement Industry and Trading Co., *Istanbul, Turkey*
AkçanSA Cement Industry and Trading Co., *Istanbul, Turkey*
Istanbul Chamber of Commerce, *Istanbul, Turkey*

Preface

This two-part proceedings book comprises keynote, invited, and contributed papers presented at the International Symposium on Nondestructive Testing of Materials and Structures (NDTMS-2011), held at Istanbul Technical University (ITU), Istanbul, Turkey, on May 15–18, 2011. The concern about the deteriorating nature of the World's infrastructures, and the need for the assessment of structural materials and systems make the development and implementation of nondestructive testing (NDT) and evaluation (NDE) methodologies a necessity. Although research on NDT in engineering may have a history of more than 60 years, early developments primarily referred to metals and metal components. With the technological advances in the areas related to NDT and increasing number of engineering structures, NDT methods have also been required for the quality control and condition assessment of building structures and materials as a basis for repair, retrofit and strengthening.

Several NDT techniques which are known in metallurgy, medical diagnostics, aviation and aerospace, and geophysical applications have been adopted and further developed for use in the condition assessment of structures and construction materials. Recent advances in NDT methodologies for materials and structures combined with the increased speed and memory of computers and efficient imaging algorithms have led to the processing of measured responses from NDT to better characterize materials and determine the spatial extent of the anomalies in two or three dimensions as well as the nature of such anomalies.

Pursuant to these developments and considering the need to foster ideas and identify efficient application techniques, NDTMS-2011 at ITU has been organized. The Symposium has provided a forum of engineers, scientists, and professionals for the exchange of ideas and knowledge on NDT with applications in civil and other engineering fields. This symposium was originally conceptualized as a scientific collaboration by researchers from Massachusetts Institute of Technology, University of Stuttgart, University of Edinburgh, Technical University of Munich, German Federal Laboratory for Material Research and Testing (BAM), and Istanbul Technical University. We thank Christian U. Grosse, Hans W. Reinhardt, Michael C. Forde and Herbert Wiggenhauser for their encouragement and intellectual contributions. We also express our gratitude to Urs Meier, Dionisio Bernal, Luigia

Binda, Steven D. Glaser, and Tribikram Kundu for their support and contributions. The symposium was sponsored by a number of academic/research institutions, and technical and industrial/professional organizations. Their supports are thankfully acknowledged.

NDT/NDE is a highly multi-disciplinary field involving various scientific disciplines, innovative theoretical and experimental techniques, and advanced computational modeling and imaging. Therefore, there is a need to bridge the gaps between these various aspects, as well as the gap between the developers and the practicing engineers. It is hoped that the proceedings of this symposium will represent a unifying theme contributing to the closing of these gaps to some extent. The organizers are pleased with the overwhelming interest shown from researchers, developers and engineers in contributing to this publication. The large number of abstracts and papers received for consideration to be included in NDTMS-2011 proceedings attests to the continuing importance of the subject and the need for further developments. The proceedings included in this two-part volume comprise 175 papers contributed by 473 authors from 36 countries around the world. It is only fitting that this symposium with such multi-national representation is held in a world city, Istanbul, with its profound history and rich culture as well as unique location between two continents, Europe and Asia.

The topics of the proceedings are organized as follows: NDT methods for the characterization of materials and structures; NDT for material and property characterization; early age NDT of concrete and other materials; NDT for metallic material characterization; NDT of metals and composites; theoretical modeling and simulation studies as a basis for NDT; NDT of civil infrastructures; geotechnical and geophysical applications of NDT; health monitoring of structures; NDT and evaluation of historic buildings and monuments; NDT planning, practice, reliability, codes and standards.

A distinguishing quality of this proceedings book is that it not only captures the state of the art in NDT of materials and structures through papers by leading experts, but also provides informative descriptions of ongoing NDT research and development in diverse areas as well as field experiences by practicing engineers. Achieving this objective took much effort by all parties involved; numerous papers went through several cycles of review and revisions in the limited time available for the preparation of this book. The editors hope that the readers will benefit from this effort and will tolerate any imperfections that may remain in the book.

We would like to thank the members of the international organizing committee, local organizing committee, and the international scientific committee, for their contribution and substantial effort in the rigorous review process for the 210 submitted papers ensuring the quality of the accepted papers. We also would like to thank our students Arda Kiremitçi and Adile Aslı Özbora (ITU), Halil Ibrahim Andiç (Atılım University, Ankara), and Denvid Lau (MIT) for their assistance, positive attitude and willingness to help whenever needed. We express our appreciation to Tolga Orhon for his invaluable work in designing and managing the conference website. He volunteered his professional expertise and accommodated our needs at most critical times.

Finally, we express our most heartfelt gratitude to Oğuz Güneş for his creative ideas, his invaluable contributions and timeless efforts from the conception of the symposium to the completion of this publication. Without his efforts, initiatives, and meticulous attention to practically every detail, this book would not have been a reality.

We trust that the efforts of all those who have contributed to the International Symposium on Materials and Structures, NDTMS-2011, will be fruitful, and that, as a basic reference, this publication will contribute to the science, engineering, and practice of NDT for many years to come.

Oral Büyüköztürk   Mehmet Ali Taşdemir
MIT, Cambridge, MA, USA   *ITU, Istanbul, Turkey*

January 2011

Dedication

Professor M. Cengiz Dökmeci
Dipl.-Ing., Dr.-Ing. (ITU), Ph.D. (Cornell)

This proceedings book is dedicated to M. Cengiz Dökmeci, a research pioneer, educator, leader, and mentor in recognition of his outstanding contributions to the science of materials, continuum mechanics, and fundamental studies underpinning the development of nondestructive evaluation methods for materials and structures.

M. Cengiz Dökmeci, a native of Harput, Turkey, received his Dipl.-Ing.(Civil Engineering) and Dr.-Ing. degrees in June 1960 and March 1965, respectively, from Istanbul Technical University (ITU), and his Ph.D. degree in May 1972 from Cornell University (Ithaca, New York). His doctoral advisors were late Professor Mustafa Inan (ITU), and Professor Bruno A. Boley with whom he first worked at Columbia University, and later continued working at Cornell and Northwestern Universities. He was promoted to the rank of associate professor in 1974 and to full professor in 1980 at ITU. His mentors and co-workers included Professors Rifat Yarar (ITU), Raymond D. Mindlin and Warren P. Mason (Columbia), James A. Krumhansl (Cornell), and Liviu Librescu (Virginia Polytechnic and State University) all of whom had a profound influence on his academic life in many respects.

Dr. Dökmeci was a research fellow of the Organization of European Cooperation and Development (OECD) at ITU in 1963–1965, and a NATO postdoctoral fellow at the Massachusetts Institute of Technology (MIT) during the summer of 1976. He was a visiting scientist at MIT, University of California at Berkeley, and the University College of London in the summers of 1976 and 1982, 1977 and 1981, and 1979, respectively. He was the founding dean of the Faculty of Aeronautics and Astronautics (1983–1989) and director of the Bioengineering Research Center (1985–1987) at ITU. He was the editor-in-chief of the Bulletin of the Technical University of Istanbul (1985–1994), has been an international editorial board member of the Journal of Aircraft (AIAA) since 1987, and a reviewer for Zentralblatt für Mathematik since 1973. He has served as a recommender for the Japan Prize since 1984 and was a correspondent for the International Ship Structures Congress(ISSC) (1979–2000) and the International Council of Aeronautical Sciences (ICAS) (1987–2004). He was awarded the Encouragement Award in 1975 and the Science Award in 1985 by the Scientific and Technical Research Council of Turkey (TUBITAK). He is a member of the honor societies Sigma Xi and Phi Kappa Phi, and an honorary member of the Turkish Academy of Sciences (TUBA).

Professor Dökmeci's research has mainly dealt with structural optimization, variational principles of continuum physics, and mathematical modeling of materials and structural elements, including fully variational formulations and internal consistency of solutions. His research is distinguished as pioneering in materials and structures subjected to coupled mechanical, thermal, electric, magnetic, and moisture effects. His scientific contributions including those from his early years at Columbia, Cornell, University of California (Berkeley) and MIT have been recognized as unique in the coupled field problems of electromagnetic-acoustic discontinuous fields, high-frequency vibrations of porous piezoelectric plates, and higher order theories of piezoelectric, thermopiezoelectric, and hygrothermo-piezoelectric continua. Dr. Dökmeci's research has significantly contributed to the theoretical foundations of smart materials and nondestructive evaluation of materials and structures, crossing multi-disciplinary boundaries.

The Chair of this symposium has the privilege of having been associated with Dr. Dökmeci for many years, first at ITU and Cornell during his studies and later as a colleague and friend at MIT and beyond. Dr. Dökmeci's students and colleagues alike have a great sense of respect for his personal values and admiration for his scholarly contributions. As a mentor, Professor Dökmeci's positive influence on his students and junior colleagues through guidance and inspiration has been profound and everlasting.

Dr. Dökmeci is currently an Emeritus Professor at his alma mater, ITU, where he is active in research and teaches mechanics and applied mathematics.

Section 1
NDT Methods for the Characterization of Materials and Structures

Evolution of NDT Methods for Structures and Materials: Some Successes and Failures

C.U. Grosse

Abstract The development of techniques being used for the non-destructive evaluation of materials and structures is closely related to other disciplines. The examination of human beings in a non-destructive way for example was a goal of many generations of physicians leading to highly developed methods applied today in a routinely manner. Many techniques used in NDE have their equivalent in medical testing. Same is true for geophysics. The exploration for natural resources (e.g. gas, water, oil) and the desire to understand the structure and dynamics of the earth have been strong motors to develop sophisticated methods. It does not matter if one consider reflection seismic, seismology, vibration or electro-magnetic methods: all have their equivalent in the field of NDE of materials and structures. The paper will give some examples of these interconnections and successful adoptions. Since the characteristics of human beings, the earth and engineering structures are different these transitions are somehow limited what will be discussed as well.

Keywords Evolution • Geophysics • Medical science • Non-destructive techniques

Introduction

Probing the earth, characterising engineering materials and a medical diagnosis to identify a possible disease of a human body have several things in common and there are certainly many other fields that could be mentioned here. In all environments it is beneficial to apply non-destructive testing methods. While in geophysics there are not many other options non-destructive methods in material testing and medicine are

C.U. Grosse (✉)
Non-destructive Testing Laboratory, Center for Building Materials,
Technical University of Munich, Germany
e-mail: grosse@tum.de

always in competition with destructive or at least partial destructive techniques. Although the "subjects" are so different the techniques being used to perform the tests are similar. This is the reason why the applications have learnt from each other in many aspects and relations are present in all categories. The purpose of this paper is to reveal some of these interconnections in an exemplary way. It is certainly not possible to do this in a summarizing way and the reader could probably add more relations from his experience immediately. Since the author is more familiar with methods based on elastic wave propagation than with others this is the focus of the article.

Signals - from Magnitudes and Dimensions

It is instructive to compare signals that are related to measurements in the different applications. The analysis of acoustic emission signals for example gives usually an indication about fracture or friction processes in an object. Seismology is the science to record and interpret earthquake signals that are related to fractures of the earth's crust. Figure 1a shows an example of such an earthquake recording. As usual the earthquake signals - called seismograms - are plotted using the real time (UTC) and in this particular case about a minute of the signal is shown. In case of large earthquake signals of several minutes or even hours can be recorded. Very large earthquakes can trigger the earth to oscillate in its eigenmodes for several weeks or months.

The equivalent technique to seismology is called acoustic emission analysis. There are several applications of this technique reported being used in medical diagnoses. It is known that a bone joint in the human body can produce acoustic emissions indicating the osteoporotic disease, see Fig. 1b [1].

Figure 1c represents instead an ongoing crack in concrete. In material science it is desired to locate the cracking processes inside structures to monitor the deterioration process. Micro-cracking is usually a good indicator prior to failures.

Records in seismology are of the order minutes or hours. In medical applications or material testing they have a duration of milliseconds or seconds. The signal duration can be defined by the earliest time a signal can be discriminated from noise until it is unrecognizable again.

It can be shown that the radiation of elastic waves by the sudden release of energy caused by fractures or friction is scalable over several orders of magnitude and length. On one hand this means that the size of a crack (in terms of crack length or crack plane) is scaled to the amplitude of the acoustic emission or earthquake recording, respectively. On the other hand it was observed by Gutenberg and Richter 1954 [2] that there is a relationship between the magnitude M and total number N of earthquakes in a region (Fig. 2).

This relationship is called today the Gutenberg-Richter law:

$$\log N = a - bM \tag{1}$$
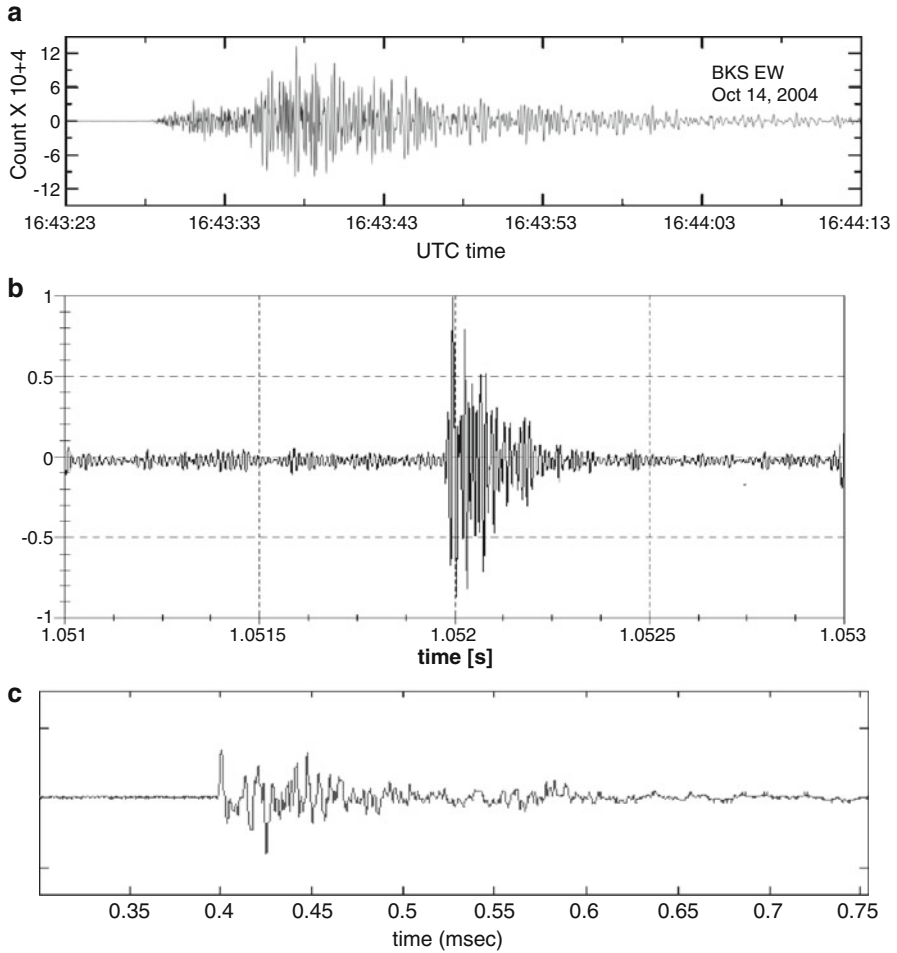
Fig. 1 a) E-W component of an regional earthquake with source-receiver distance of 50 km and magnitude 3.3. **b**) Acoustic emission induced by micro crack initiation in the compacta-spongiosa interface recorded during the in vivo monitoring of the human knee joint [1]. **c**) Acoustic emission release during fracture processes in concrete

a and b are constants with a describing the seismicity in that region - a value that varies very much from region to region. Interestingly, the b-values are between 0.8 and 1.2 and does not vary that much. A b-value of 1.0 means that for every magnitude 4.0 event there will be 10 magnitude 3.0 earthquakes and 100 magnitude 2.0 earthquakes. Several decades after Gutenberg and Richter it was proven that a similar law exists for the acoustic emission analysis of materials (Fig. 3). In recent years several papers were dealing with an improvement of the b-value analysis [4] and applications to describe the stress drop and stress redistribution in concrete [5].

Fig. 2 Frequency-magnitude
relationship
for California between
1932 and 1972 [3]
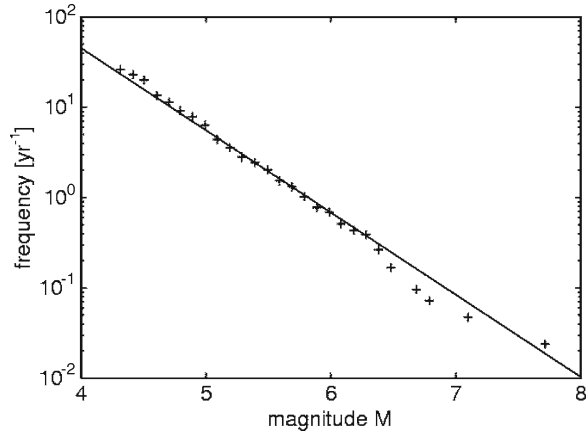
Fig. 3 Distribution
of the *I*b-Values of acoustic
emissions in concrete [4]
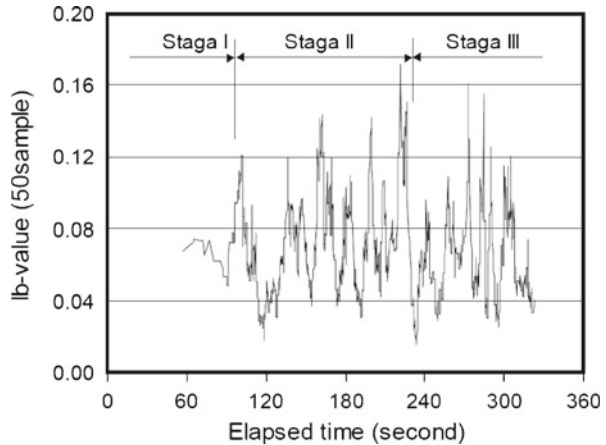
Signals - from Systems and Filters

The waveform of the earthquake signal shown in Fig. 1a is a function of the source
process caused by the earthquake itself as well as of the receiver-source distance
and the material properties along the wave path. In addition the signal can be altered
by the recording system transforming a displacement of the ground motion into
velocity or acceleration proportional equivalents or restricting the frequency
content for example. It is useful to consider all these parts of the measurement
chain separately as being "systems". As a system we indicate something that can
manipulate, change, record, or transmit signals. In this regard the concept of transfer
functions is quite powerful.
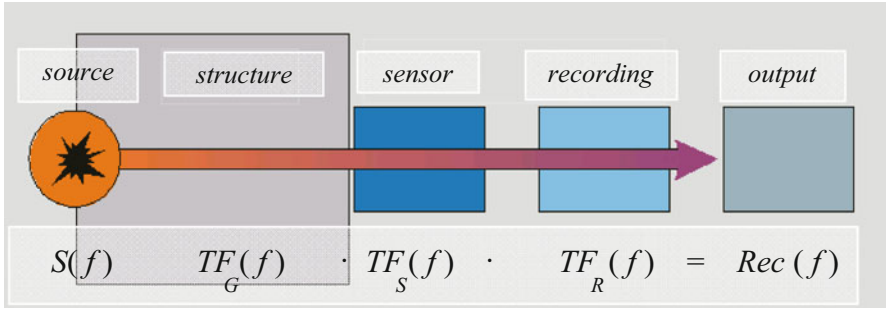
Fig. 4 Concept of transfer functions [6]

According to Fig. 4 each system is represented by its individual transfer function and the resulted post-processed recording ("output") can be seen as a convolution of all these influences onto the originating signal.

$$\text{Rec}(f) = \text{S}(f) \times \text{TF}_G(f) \times \text{TF}_S(f) \times \text{TF}_R(f) \qquad (2)$$

The "source" S can either be the acoustic emission released by a propagating crack (passive non-destructive testing techniques) or the transient pulse that is emitted by an artificial source (e.g. a piezo-electric emitter) in the frame of active ultrasound techniques. TF_G represents the Green's functions of material, TF_S describes the transfer function of the sensor and the coupling, and TF_R is the transfer function of the recording system.

The concept is valid for most (if not all) measuring techniques in non-destructive testing, medical diagnosis and geophysics. Considering a "system" in more detail it works like a filter. In the best case (that is almost never applicable) a filter has no influence to the signal.

Sensors - the Eyes and Ears

Since non-destructive testing systems as well as systems in Geophysics usually observe processes or characteristics of an object that are not visual to the human eyes nor can be recorded with other human senses the sensor system being used is of particular importance. The sensor represents a filter that can significantly influence the way we look at these processes. An ideal sensing system acts as a zero filter producing only little distortions to the data transmitting the information more or less unaltered. In the worst case the data are distorted by the sensing filter so much that the original information is completely camouflaged or even erased. The type of sensors used in non-destructive testing almost exclusively are sensors that exploit the piezoelectric effect of lead zirconate titanate (PZT). While piezoelectric sensors and their design are described in numerous books and papers (e.g. [7]) some of their
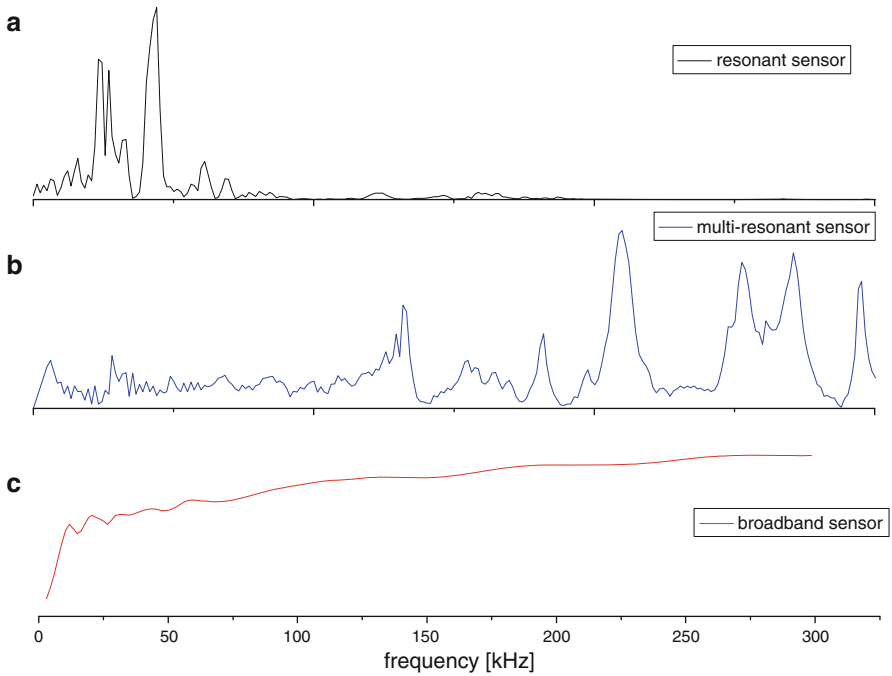
Fig. 5 Typical frequency response functions of resonance (**a**), multi-resonance (**b**) and high-fidelity broadband (**c**) piezo-electric transducers

characteristics are of particular importance for the sensitive recording of acoustic emissions (sensitivity) and the broadband analysis of signals. To enhance the detection radius of piezoelectric sensors, they are usually operated in resonance, i.e. the signals are recorded within a small frequency range due to the frequency characteristics of the transducer (Fig. 5a). The disadvantage is that a signal analysis in the frequency domain is of very limited value, because of the strong influence of the frequency transfer function of the piezo-electric sensor representing a narrow filter with non-linear amplitude response. In general, such a system can not impede the application of deconvolution techniques to reveal the source function S in Eq. (2).

Very well damped sensors, such as those used for vibration analysis, are operated outside of their resonant frequency allowing broadband analyses to be performed, but are usually less sensitive to acoustic emission signals. Progress in the development of the theory of AE has led to the need for high sensitivity, wideband displacement sensors that have a flat frequency response (i.e. the sensor gives the same response over a wide frequency range). To overcome the disadvantages of limited bandwidth transducers showing several particular resonances were developed. These sensors, which are called multi-resonance transducers (Fig. 5b), have a higher sensitivity than sensors with a backward mass used outside of their resonance frequency. However, such sensors should not be considered as high-fidelity broadband sensors
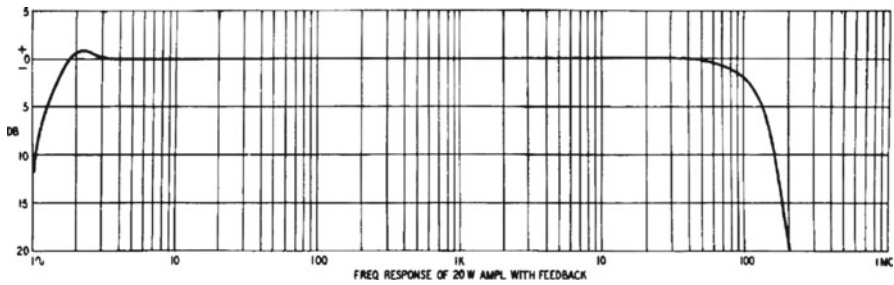
Fig. 6 Frequency response of an ideal "high-fidelity" amplifier for audiophile purposes in music reproduction [8]

and it is essential to know their frequency response function. Otherwise, signal characteristics from the source are not distinguishable from artefacts introduced by incorrect knowledge of the frequency response. A calibration of the sensors' frequency response, as well as understanding of the direction sensitivity, is important for many applications in non-destructive testing. It was a goal for many years to develop sensors for non-destructive testing purposed that exhibit a so-called high-fidelity behaviour. The problem is similar to sound systems where in the 1960ies standards were developed for music equipment (loud speaker, microphone, amplifier, vinyl and later on tape recording) to minimize the amount of noise and distortions and providing an accurate frequency response. A linear frequency response over the whole audio range (i.e. from 20 Hz to 20 kHz, Fig. 6) was essential in this context and called "high-fidelity" [8].

The instruments in Geophysics that are used to record seismic waves are either seismometers or geophones. Their frequency response is optimized for the type waves being recorded. While seismometers are usually operated in an upper frequency range of 50 to 100 Hz geophones are operated up to several hundred Hertz. While it is certainly true that all these instruments have a high-fidelity response in the mentioned frequency range the upper band limit is much lower than the one required for non-destructive testing applications. The design of modern seismometers [9] allow the geophysicists to neglect the influence of the recording system and its frequency transfer function in regard to the data analysis.

Measurement Systems - Recording Data

The setup to record data differs between geophysics, medical applications or non-destructive testing. Since the investigated object in geophysics is the earth observations are usually done on a large scale with a relative sensor position of many meters, hundreds of meters, kilometers or even hundreds of kilometers depending on the purpose of the study and the resolution required. Applications in geotechnics to
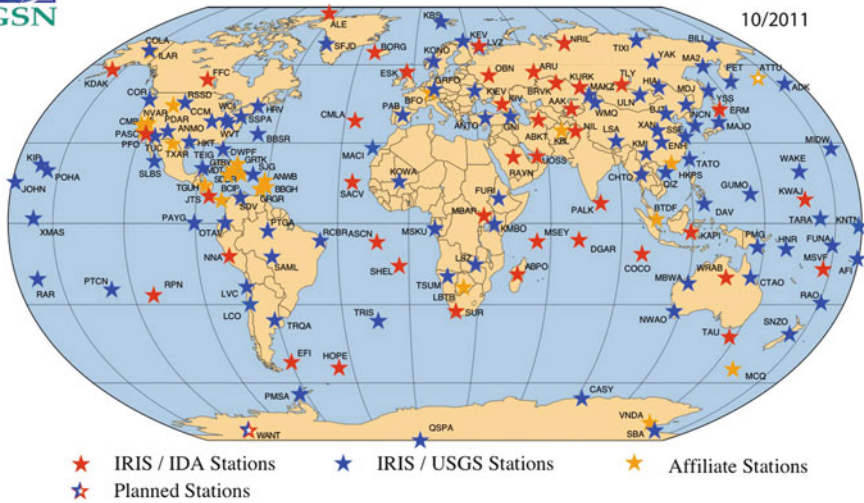
Fig. 7 Distribution of seismometers of the Global Seismographic Network (e.g. [10]). More than 150 instruments were included in this network as of September 2010. Global Seismographic Network (GSN) is a cooperative scientific facility operated jointly by the Incorporated Research Institutions for Seismology (IRIS), the US Geological Survey (USGS), and the National Science Foundation (NSF)

study for example foundations are done on a much smaller scale than investigations of global seismicity where instruments (seismometers) are used that belong to sensor networks distributed around the whole earth (Fig. 7).

Common for applications in earth science is that the sensing instruments are usually placed on the very outside of the "object" only. While the earth's diameter is about 12,700 km only the outer 10 to 12 km are directly accessible by drilling techniques. While the aperture of the geophysical sensors is so much smaller than the dimensions of the "object" almost all measurements can be considered as point measurements. Further on, techniques based on wave propagation usually deal with plane wave and far field approximations. Challenges are usually to access the best points for measurements in a region of interest and to deploy a profile (i.e. a sensor line) with enough instruments to get a good resolution.

Medical applications instead have much smaller apertures related to the dimensions of the human body. The detection range of medical applications is not varying much and is limited to millimeters up to several centimeters. Usually it is easy to access the region of interest from outside (Fig. 8). The patient can be transported to the investigation facility or can even walk in. The challenge is here to avoid unpleasant or even painful "measurements". Therefore, data acquisition have to be fast and non or minimal invasive according to Hippocrates' postulate "primum nihil nocere".

Fig. 8 Application of ultrasound testing equipment in the prenatal diagnosis

Minimal invasive techniques are often acceptable since the human body is having unique self-healing capabilities.

Regarding non-destructive testing techniques in engineering one can subdivide into methods used in a laboratory environment or in situ. Compared to the prior described applications in geosciences and medical diagnosis NDT laboratory experiments have the advantage that the object can be accessed easily plus there is often no need to be non-invasive. Challenges are related typically to the complicated material composition, the small dimensions of the targets (cracks, voids) compared to the size of heterogeneities or to the signal to noise conditions. In situ applications are very often more complicated because in addition to the afore mentioned issues geometric effects related to different structural components and coupling problems have to be considered for example. Measurements at structures like buildings, facilities or bridges are in particular challenging since they are usually large compared to the aperture of NDT signals.

The coupling problem is dominating some of the NDT techniques and this is the reason why so much effort was put into methods to speed up data acquisition and to overcome the coupling problem. Contact free techniques are the first choice among them are RADAR (Fig. 9, left) and Infrared-Thermography (Fig. 9, right). While near-field problems can be handled using for example far-field airborne RADAR [11], such problems are of less importance using IR-Thermography.

Although ultrasound is the method of choice in many applications including medical diagnosis (Fig. 8) or the inspection of welded joints, its usability at concrete structures was limited. Some new developments like air-coupled transducers (Fig. 10, left) or point-contact arrays (Fig. 10, right) are promising new techniques that will certainly be further considered.

Fig. 9 Contact-free NDT applications like Radar (left) and IR-Thermography (right) enhancing the measurement speed (right picture by courtesy of Dr. J. Frick)
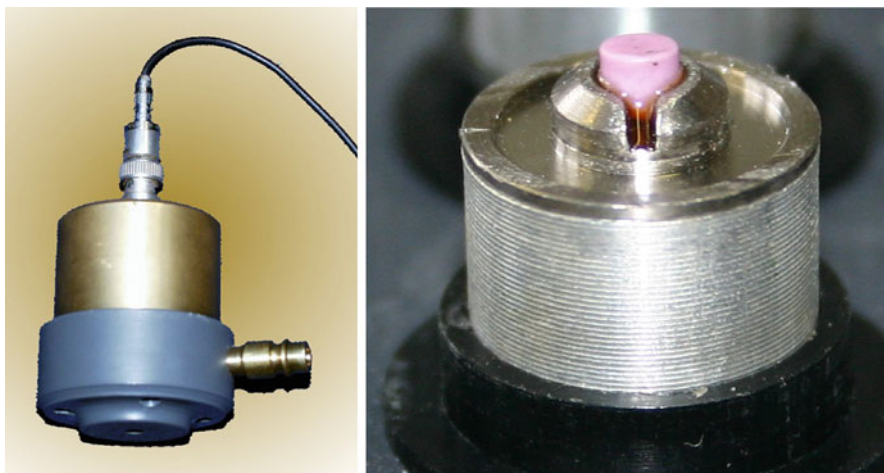
Fig. 10 Ultrasound techniques like air-coupled transducers (left) or point-contact transducers (right) are developed to speed up NDT measurements

Source Inversions - Revealing the Invisible

Passive monitoring techniques are used on all scales to reveal deteriorating processes like earthquakes or the cracking of materials or bones (Fig. 1). While the detection and localization of these processes is a basic task inversion techniques are applied to
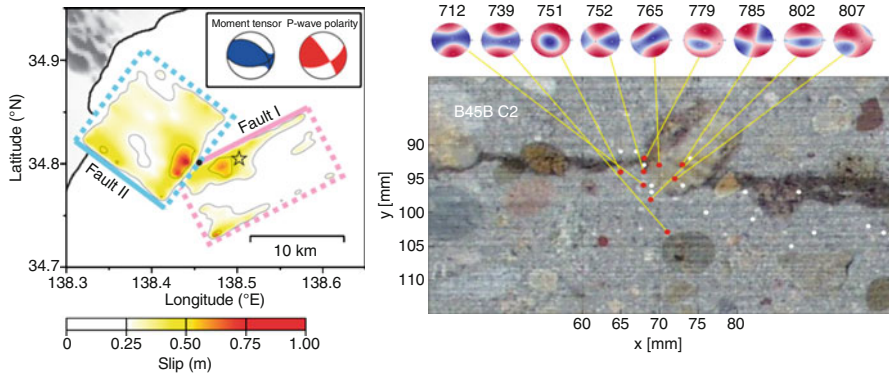
Fig. 11 Results of moment tensor inversion techniques on different scales. In seismology (left) [14] scales are usually in a range of several tenth kilometer, while in material testing (right) a millimeter scale can be applied [15]

uncover the mechanisms leading to failure. It was a goal for many scientists to develop source inversion techniques to observe the failure processes. While this was done successfully in seismology for many decades [12] applications in civil engineering are reported first in the early 1980ies [13]. There are rarely other applications showing in such a similar impressive way how successful techniques can be migrated over many scales. While the inversion of earthquakes with several 10 kilometer fault zones are recorded with seismometers located thousands of kilometers away, the propagation of microcracks in material testing is observed with acoustic emission techniques operating on the centimeter or millimeter scale. The technique used for this inversion is called moment tensor inversion (MTI). The goal of all MTI methods (either in seismology of NDT) is to use observed values of ground displacement to infer properties of the source, as characterized by the moment tensor. By using the representation theorem for seismic sources [12] and assuming a point source, the displacement field u_k recorded at a receiver k is given by:

$$u_k = G_{ki,j} M_{ij} \tag{3}$$

While M describe the moment tensor components, G are the elastodynamic Green's functions containing the propagation effects between the source and receiver (refer to TF_G in Fig. 6). This equation can be used on different scales like in seismology or material testing successfully (Fig. 11). It is remarkable that the "object" (earth/concrete specimen) is so different not only in terms of size but also in composition and that the sensing techniques are also varying a lot (see above) but obviously the principles of wave propagation are applicable on different scales and can take size effects into account.

However, the example given can also work to demonstrate differences in the described applications. While in seismology it is impossible to predict the size and location of an earthquake and therefore some luck is required to have enough instruments available in a region for high-resolution studies the situation is different in NDT. Problems are there more related to inhomogeneities and to the change

of the structural integrity (cracking) leading for example to a degradation of wave velocities throughout the observation. Green's functions can change so fast and so significantly that relative [16] or hybrid [17] moment tensor inversion methods are preferred compared to absolute methods [12]. Clusters of events in time and space are analysed with respect to the source mechanism to enable for the elimination of influences concerning variations of the Green's functions.

Data Processing - the Art of Getting the Maximum Out of Data

A pre- or post processing of measurement data is very often required. Referring to the concept of transfer functions earlier a data processing can be required to eliminate the influences of other systems (coupling, sensor characteristics, etc.) than the one under consideration (material properties, source function, etc.). Besides, it is the challenge of all applications to get the maximum of information out of the limited number of observations available. In almost all cases either the number of sensors is limited or the number of events or the time or space for further observations. To deal with these limitations scientists of all disciplines have developed methods to increase the significance of the observation for example by enhancing the signal to noise ratio. While it is impossible to describe all the different relations between data processing tools used in medicine, geophysics or NDT one example can demonstrate the cross-fertilization between.

The collection of data is very often done along lines where either several (or many) sensors are placed or where a sensor-receiver pair is moved along to perform a B-Scan (NDT) or to record a seismic section, respectively. Concerning reflection seismic profiles or B-Scans the data obtained will contain always some redundancy, e.g. by containing information of common reflectors in the depth. Methods to make advantage of this redundancy to enhance the signal to noise ratio and to determine the real depth of the reflectors are called migration techniques (time or depth migration) in geophysical prospecting. A simple way to perform such a migration is the use of common depth point techniques as illustrated in Fig. 12, left. More sophisticated techniques are the Kirchhoff migration, the Reverse Time Migration (RTM) or Gaussian Beam Migrations.

An equivalent to migration are methods called in ultrasonic applications Synthetic Aperture Focussing Techniques (SAFT) [18]. B-Scan measurements with a single transmitter-receiver pair in pulse-echo along lines can be reconstructed with SAFT algorithms (Fig. 13) enhancing the signal quality subjected to scattering or attenuation [19].

Phased array techniques in ultrasonic or RADAR NDT can be considered to be the hardware equivalent to migration and SAFT techniques. Ultrasonic phased array probes consists usually of composite crystals [20]. One can distinguish between linear, linear curved and 2D matrix composites. Instead of calculating the time delays in respect to the reflector these probes are able to steer a narrow beam
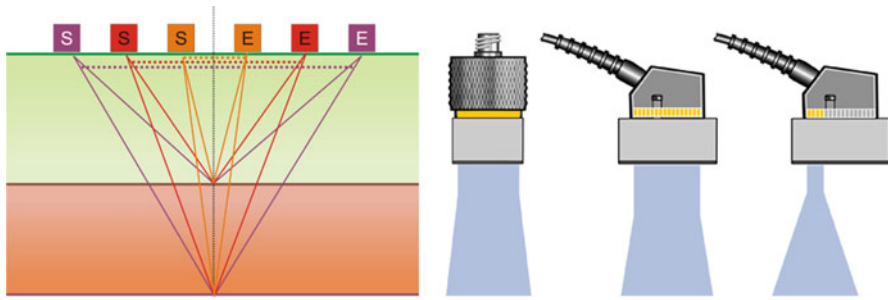
Fig. 12 Transmitter/receiver configuration (left) to perform common depth point migration in Geophysics. Comparison of the aperture of conventional and phased array transducers (right) with 16 elements (all or 4 are pulsing) - Source: Olympus
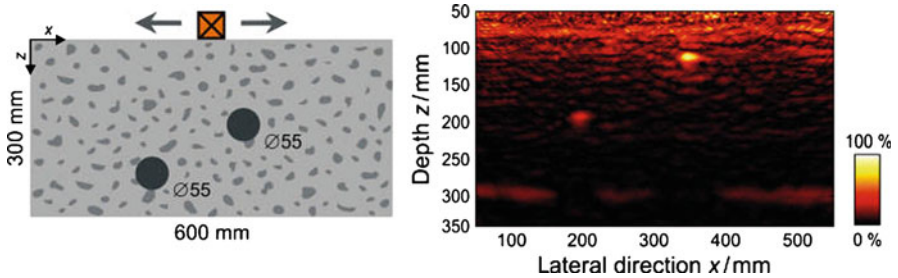
Fig. 13 Ultrasonic pulse-echo measurements at a concrete block with two inhomogeneities (left) and the SAFT reconstruction after measurement [19]

focussing to a certain depth point (Fig. 12, right). However, the physics of migration is applicable in this case as well. Successful applications are described in NDT as well as in medical imaging [21].

The applications above describe the relation between migration and phased-array techniques using active methods (reflection seismic, RADAR, ultrasonics). But also passive techniques like earthquake seismology or acoustic emission have made advantage of similar data processing techniques. The signal-to-noise ratio of an earthquake or an acoustic emission signal can be improved by stacking the coherent signals from each sensor of a dense array of transducers after correcting for the different arrival or delay times. The task of array beamforming is to find the best delay times for shifting the individual signals. In beamforming applications the user must assume that the characteristics of the waves incident on the array are relatively constant normal to their direction of propagation [22].

Under this fundamental assumption, a signal recorded by one sensor in an array (Fig. 14, left) is expected to be a time-delayed replica of a signal recorded by a neighboring sensor in that array. AE sources as well as earthquake hypocenters are usually considered point sources, so the "delayed replica" assumption is only valid
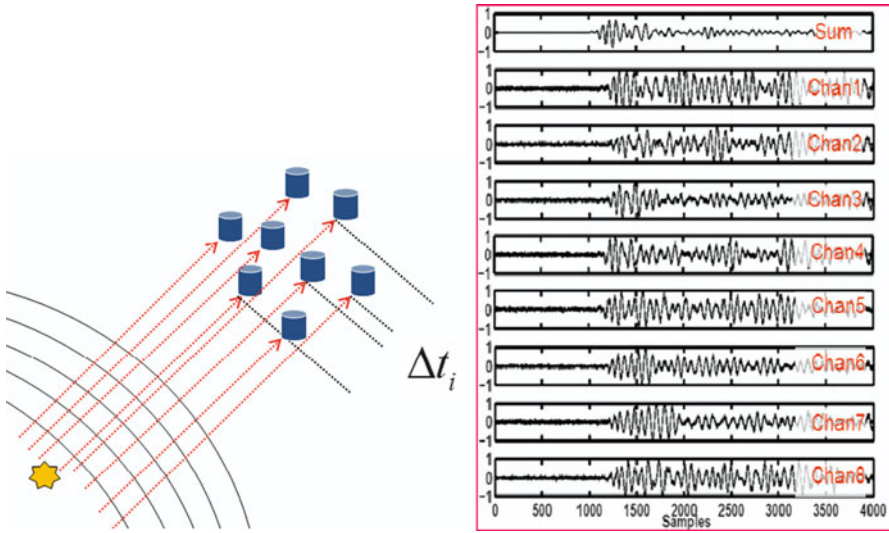
Fig. 14 Array beamforming using eight sensors (left). The corrections of the time delays Δt_i for each recording leads to a constructively summarization of the signals enhancing the signal to noise ratio and determining the azimuthal direction of the events in respect to the array center [6]

if the distance between the source and sensors is large compared to the distance between neighboring sensors. By adjusting the steering vector, and therefore changing the signal delays, the array output can be algorithmically 'steered' or 'focused' so that waves arriving from one direction and at one speed will sum constructively while waves arriving from other directions and with other velocities will destructively interfere (Fig. 14, right).

Beam forming array techniques are reported [23, 6] to be suitable for acoustic emission methods being applied to real concrete structures like bridges.

Conclusions

The basics of physical wave propagation is valid on all scales and it is fascinating to see how measurement techniques can be adopted from applications at apertures of several thousand kilometers to investigate objects in the micro and nano range. By using principally the same evaluation method one can cover several length magnitudes from 10^{-9} to 10^{8} meter. While mathematically and physically speaking there is not much of a difference in these applications in real the boundary conditions are very often the limiting factor. The concept of transfer functions (system theory) is useful to consider the influencing parts of a measuring concept individually. Accessibility, geometrical and attenuating effects as well as coupling and sensor characteristics are examples for boundary conditions controlling the proper instrumental setup and recording technique as well as the requirements for data post-processing.
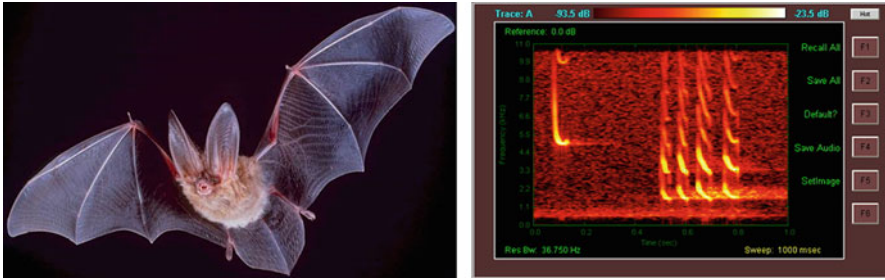
Fig. 15 A bat (left) is using ultrasound signals to navigate by using chirp frequency waveforms (right) performing real time Fourier transforms making advantage of Doppler shift techniques [26]

The transfer of techniques is stimulating all techniques like it was shown for Geophysics, medical diagnosis techniques and NDT - other areas are contributing in this scheme as well. In the past developments in Geophysics and Medicine governed the developments since the prospection of natural resources and the improvement of medical treatments were of special interest to the public. But the described cross-fertilizing process is certainly not a one-way street and several reports showed [24, 25] that application in engineering are nowadays on a very high level as well. A very stimulating condition was the fast development of micro-computers and computerized processing techniques that led to a much wider acceptance of NDT techniques. This process did not come to an end (and will probably never) since many NDT methods still wait for miniaturization of test equipment and intuitive data visualization and imaging. Handling, accuracy and reproducibility as well as redundancy by different NDT techniques are challenges for the next years.

As always in the scientific world scientists should be inspired by nature. "Systems" in biology (Fig. 15) have been developed in several thousand years to perform close to perfect. Bionics as the art to learn from biological systems will probably a key research field in future in particular also in non-destructive testing.

References

[1] Schwalbe, H.-J., Bamfaste, G., Franke, R.-P. (1999), *Non-destructive and non-invasive observation of friction and wear of human joints and of fracture initiation by acoustic emission*, Proceedings of the Institution of Mechanical Engineers, Part H: Journal of Engineering in Medicine 213 (1), 41–48.
[2] Gutenberg, B., Richter, C.F. (1954), *Seismicity of the Earth and Associated Phenomena*, 2nd ed., Princeton, N.J.: Princeton University Press, 17–19.

[3] Turcotte D.L. (1989), *A fractal approach to probabilistic seismic hazard assessment*. Tectonophysics 167 (2-4), 171–177.

[4] Shiotani, T., Yuyuma, S., Li, Z., Ohtsu, M. (2001), Application of AE improved b-value to quantitative evaluation of fracture process in concrete materials. Journal of Acoustic Emission 18, 118–133.

[5] Kurz, J.H., Finck, F., Grosse, C.U., Reinhardt, H.W. (2006), *Stress drop and stress redistribution in concrete quantified over time by the b-value analysis*. Journal of Structural Health Monitoring 5 (1), 69–81.

[6] Grosse, C., Ohtsu, M. (Eds.) (2008), *Acoustic Emission Testing in Engineering - Basics and Applications*. Heidelberg: Springer publ., 404 p.

[7] Hykes, D.L., Hedrick, W.R., Starchman, D.E. (1992), *Ultrasound Physics and Instrumentation*. Mosby-Year Book, 2. ed.

[8] Hartley, H.A. (1958), *Audio Design Handbook*. New York: Gernsback Library. p. 200.

[9] Wieland, E. (2002), *Seismic sensors and their calibration*, University of Stuttgart, Internet link, valid 7.11.2010: http://www.geophys.uni-stuttgart.de/oldwww/seismometry/man_html/index.html.

[10] Anderson, K.R., Butler, R., Berger, J., Davis, P., Derr, J., Gee, L., Hutt, C.R., Leith, W.S., Park J.J. (2007), *50 years of Global Seismic Observations*, AGU Fall Meeting Abstracts 23:1448.

[11] Yu, T.-Y., Büyüköztürk, O. (2007), *A far-field airborne radar NDT technique for detecting debonding in GFRP-retrofitted concrete structures*, NDT&E International 41, 10–24.

[12] Aki, K., Richards, P.G. (1980), *Quantitative seismology*. San Francisco: Freeman.

[13] Ohtsu, M., Ono, K. (1984), *A Generalized Theory of Acoustic Emission and Green's Functions in a Half Space*. Journal of AE 3 (1), 124–133.

[14] Aoi, S., Enescu, B., Suzuki, W., Asano, Y., Obara, K., Kunugi, T., Shiomi, K. (2010), *Stress transfer in the Tokai subduction zone from the 2009 Suruga Bay earthquake in Japan*. Nature Geoscience 3, 496–500.

[15] Grosse, C., Finck F. (2006), *Quantitative Evaluation of Fracture Processes in Concrete Using Signal-Based Acoustic Emission Techniques*. Cement and Concrete Composites 28, 330-336.

[16] Dahm, T. (1996), *Relative moment tensor inversion based on ray theory: theory and synthetic tests*. Geophysical Journal International 124, 245–257.

[17] Linzer, L.M. (2005), *A relative moment tensor inversion technique applied to seismicity induced by mining*. Rock Mechanics and Rock Engineering 38 (2), 81–104.

[18] Doctor, S.R., Hall, T.E., Reid, L.D. (1986), *SAFT - the evolution of a signal processing technology for ultrasonic testing*. NDT International 19, 163–167.

[19] Schickert, M. (2003), *Progress in Ultrasonic SAFT-Imaging of Concrete*, In: NDT-CE, Berlin: Deutsche Gesellschaft für Zerstörungsfreie Prüfung (DGZfP), BB 85-CD, 2003, V63, 11 p.

[20] Ritter, J. (1996), *Ultrasonic Phased Array probes for non-destructive examinations using composite crystal technology*, DGZfP, NDTnet - December 1996, Vol.1 No.12.

[21] Oakley, C.G. (1991), *Analysis and development of piezoelectric composites for medical ultrasound transducer applications*, PhD thesis Pennsylvania State University, PA, USA.

[22] Dudgeon, D. (1977), *Fundamentals of digital array processing*. Proceedings of the IEEE 65 (6), 898–904.

[23] McLaskey, G.C., Glaser, S.D., Grosse, C. (2010), *Beamforming array techniques for acoustic emission monitoring of large concrete structures*. Journal of Sound & Vibration 329, 2384–2394.

[24] Büyüköztürk, O. (1998), Imaging of concrete structures, NDT&E International 31 (4), 233–243.

[25] Maierhofer, C., Reinhardt, H.W., Dobmann, G. (Eds.) (2010), *Non-destructive evaluation of reinforced concrete structures*, Vol. 1 and 2, Cambridge: Woodhead Publ.

[26] Jones, G., Holderied, M.W. (2007), *Bat echolocation calls: adaptation and convergent evolution*. Proceedings of the Royal Society B-Biological Sciences 274 (1612), 905–912.

Remote Detection of Debonding in FRP-strengthened Concrete Structures Using Acoustic-Laser Technique

O. Büyüköztürk, R. Haupt, C. Tuakta and J. Chen

Abstract Fiber-reinforced polymer (FRP) strengthening and retrofitting of concrete elements, such as beams, columns, slabs, and bridge decks, have become increasingly popular. Nonetheless, rapid and reliable nondestructive testing techniques (NDT) that are capable of remotely assessing *in-situ* integrity of retrofitted systems are needed. Development of a robust NDT method that provides an accurate and remote assessment of damage and flaws underneath the FRP plates/sheets is required. In this study, a NDT based on an acoustic-laser system is proposed for remote detection of debonding in FRP-strengthened concrete structures. This technique utilizes the difference in dynamic response of the intact and the debonded regions in a FRP-strengthened concrete structure to an acoustic excitation, which is then measured using laser vibrometry. Feasibility and accuracy of the technique were investigated through a series of measurements on laboratory-sized plain, reinforced, and FRP-strengthened concrete specimens. It was shown that the difference in dynamic response could be captured by the acoustic-laser system and is in good agreement with simple calculations.

Keywords Concrete • Debonding • FRP • Laser vibrometry • NDT • Remote

Introduction

FRP-concrete interface conditions cannot be fully revealed until the FRP composite layer is removed unless the member has already been subjected to apparent damage. Partial or complete removal of the FRP composite layer for damage observation may

O. Büyüköztürk (✉) • C. Tuakta • J. Chen
Department of Civil and Environmental Engineering, MIT, Cambridge, MA, USA
e-mail: obuyuk@mit.edu

R. Haupt
MIT Lincoln Laboratory, Lexington, MA, USA

pose a danger of structural collapse. An FRP-retrofitted beam or concrete column may appear safe without showing signs of substantial damage underneath FRP composites and yet may contain severely deteriorated concrete and debonded FRP composites. A modest seismic event can cause such a scenario that significantly damages the FRP-concrete system without failure.

In order to effectively detect and characterize damages in FRP-retrofitted reinforced concrete (RC) structures, a NDT technique has to be capable of detecting the extent of concrete cracking, delamination in the interface regions, decohesion in epoxy or FRP, and sizeable voids trapped in the vicinity of interface regions. Several NDT techniques of FRP-concrete systems have been investigated, including stress wave (acoustic), infrared thermography, x-ray, and microwave (radar) techniques [1]. Acoustic emission and radar techniques have been of particular interest to researchers for possible damage detection of RC and FRP-retrofitted concrete structures tested in laboratory settings [2-7]. Limitations of many current techniques for the NDT of FRP-concrete systems include insufficient detection capability, testing equipment contact with the target, environmental conditions, and spatial resolution problems. To overcome these deficiencies, we propose to develop a non-contact and standoff acoustic-laser method for detecting such damages in FRP-concrete systems. It is anticipated that the method will be applicable to a wide variety of FRP-concrete retrofitted systems, and will represent a robust complementary capability to other rapid scanning techniques such as the microwave-based NDT.

Acoustic-Laser Technique for Damage Detection

The acoustic-laser detection technique is based on the concept that local damages, such as debonding and voids in the FRP-concrete interface region vibrate differently than intact regions. These vibration anomalies are direct functions of the damage dimensions and mechanical properties (Fig. 1). Vibration anomalies can be
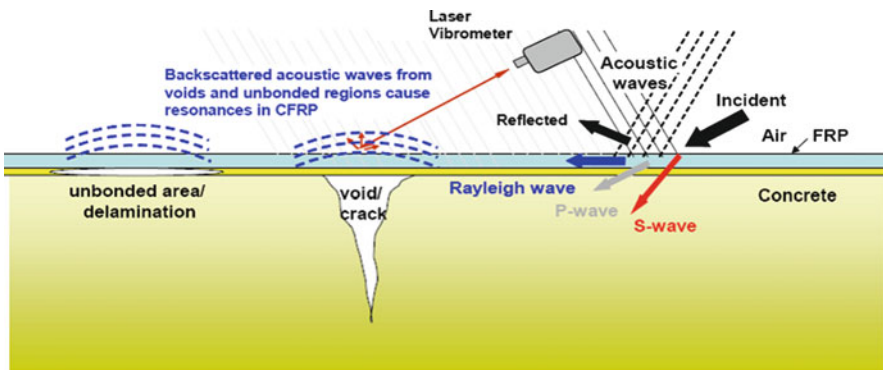
Fig. 1 Acoustic coupling to concrete structures

measured at the target surface using a laser vibrometer, and thus, target's near surface damages can be remotely detected, mapped, and quantified. The method represents a robust NDT technique well suited for thin-layered systems since debonding and voids in such systems occurring just below or within the FRP layering will interfere with acoustically induced surface waves traveling along the FRP-air interface. These discontinuities will produce vibration resonant frequencies as functions of the dimensions of the debonded region.

Acoustic source—parametric acoustic array

Parametric acoustic arrays (PAA) have been used in underwater sonar and commercial loudspeaker systems to transmit highly directional acoustic beams to targets. The PAA has two sources of sound; one source is typically ultrasound generated directly from high-frequency transducers; the other is lower frequency audible sound that is a product of the ultrasonic wave and nonlinear effects in the volume of air in front of the transducer (self-demodulation) [8]. A PAA can deliver the necessary level of acoustic power from considerable distances to localized regions of the FRP structure. To be able to detect voids of small size between FRP and concrete, the use of PAA source exhibits potential advantages of ultrasonic and high audible frequency acoustic excitation.

Vibration detection with laser doppler vibrometry

Laser vibrometry is based on the frequency modulation imparted on the laser carrier wave caused by a vibrating surface in contact with the laser beam [8]. LDV sensing of the acoustic vibration response of the FRP system offers significant advantages over contact sensors. The laser beam does not alter the target's mechanical properties, can provide location accuracies within millimeters, and can sample many points on the target rapidly, and can measure multiple target locations simultaneously with a multi-pixel vibrometer. Some commercial LDV systems are capable of sensing vibrations on targets 100-m from the laser, while custom designs can well exceed 100-m and remain eye-safe.

Experimental set-up and measurement procedure—acoustic-laser detection system

The acoustic-laser detection system was constructed from commercially available components including a 24-inch diameter Audio Spotlight Transducer (a PAA source) from Holosonics Research Labs, Inc., and a laser vibrometer from Polytec,
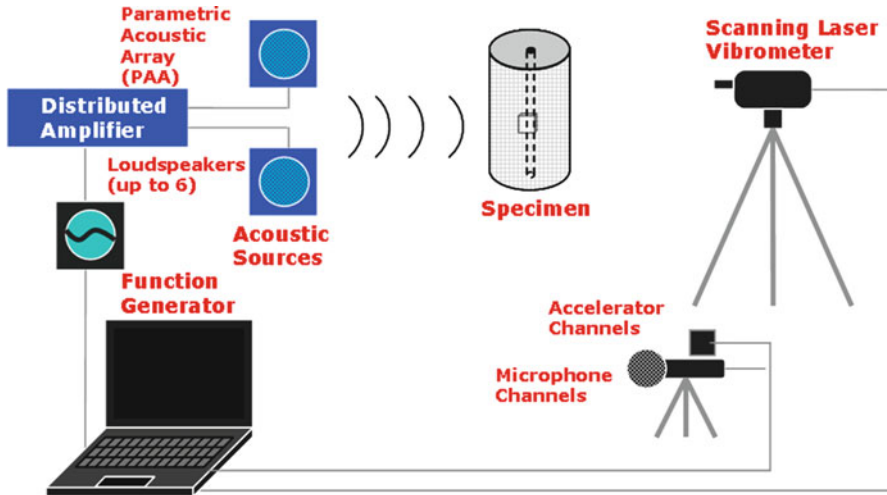
Fig. 2 Experimental setup for the acoustic-laser system

Inc., consisting of an OFV-505 optic sensor head and an OFV-5000 controller. An Earthworks 30M microphone was used to measure the acoustic wave characteristics delivered to the specimens. The PAA source was controlled by a laptop computer and generated FM linear chirps between 500-3000 Hz. Vibration response data were collected at a rate of 100 kHz using an IOtech 516E WaveBook. The measurement set-up is shown in Fig. 2.

Preliminary Study

To examine the feasibility of the acoustic-laser method, a preliminary experimental study was conducted to validate the reliability of the measurement. Two concrete cylinder specimens (30 cm height and 15 cm diameter) wrapped by GFRP sheet with artificial voids were used. Artificial voids of $1.9 \times 1.9 \times 1.9$ cm^3($0.75 \times 0.75 \times 0.75$ in^3) and $3.8 \times 3.8 \times 3.8$ cm^3($1.5 \times 1.5 \times 1.5$ in^3) cubes were introduced by inserting styrofoam pieces at the interface between concrete and the GFRP layer. Thickness of the GFRP layer was in the mm range and its Young's modulus was 148 GPa (21.465×10^6psi). The density was 1.5×10^3kg/m^3(5.4191×10^{-2}lb/in^3). Dynamic measurements were collected at MIT Lincoln Laboratory and vibration signatures were obtained as shown in Figs. 3 and 4.

Figure 3b shows the vibration velocities measured at single locations, one directly over the void (red and blue curves) and over an intact solid concrete region (black curve), as a function of acoustic excitation frequency. In Fig. 4a, b, results are shown for the loudspeaker source (a linear chirp from 50-2000 Hz) and for the PAA (a linear chirp from 2000-7000 Hz), respectively. The signature over the void exhibits larger velocity amplitudes than those of the intact region and may be useful for detecting an anomalous region in the sample. In the case of high
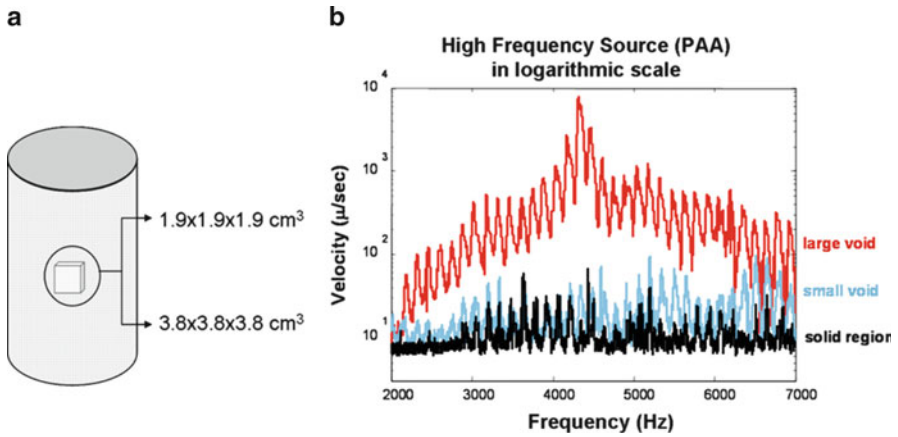
Fig. 3 GFRP-confined concrete specimen with a void (**a**) and vibration signatures of small void, large void, and solid region (**b**)
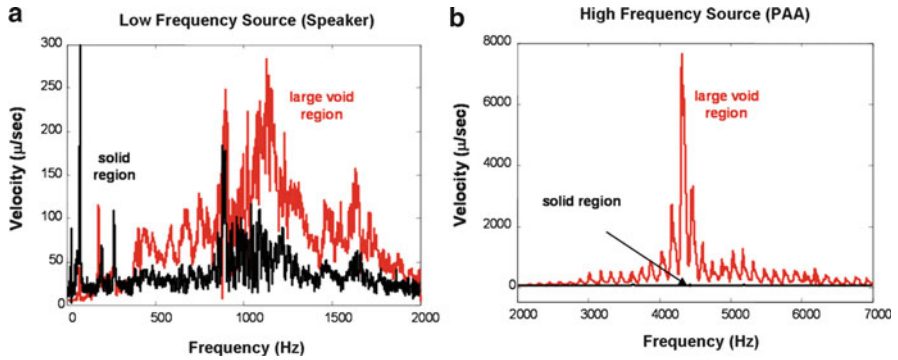
Fig. 4 Vibration signatures of a GFRP-confined concrete specimen containing a 3.8 cubic centimeter void in its surface under low (**a**) and high (**b**) frequency sources

frequency source, the larger void exhibits a distinct resonance at 4300 Hz. This is the resonance frequency of the first mode. The size of void can be inferred from the peak resonance frequency.

Assuming the GFRP layer over the defect behaved like a vibrating membrane, the resonance frequencies can be given as:

$$f = \frac{v}{2}\sqrt{\left(\frac{l}{L_x}\right)^2 + \left(\frac{m}{L_y}\right)^2} \tag{1}$$

where l and m are integers, v the speed of sound, and L_x and L_y the dimensions of the vibrating membrane. From Eqn. (1), with a speed of sound of about 340 m/s at sea level and room temperature, this gives us a fundamental frequency of 4474 Hz ($l=1$, $m=0$). This is very close to the resonance frequency of 4300 Hz measured over the void by the acoustic-laser system. The difference between these values were expected to be due to the following reasons; 1) different geometries

result in different natural frequencies; 2) actual boundary condition at the edge supports will be different from the perfectly assumed boundary condition used in analytical solution; 3) the artificial void is made of soft polymer such that the void is not air only, hence the boundary condition underneath the GFRP is different from the one used in the analytical solution. Although better theoretical prediction can be made by finite element analysis (FEA), this preliminary study exhibited the reliability of the proposed acoustic-laser method.

In addition, the distinct and large vibration resonance signatures over the area covering the voids exhibit a high signal-to-noise ratio (SNR). In our measurement example shown in Fig. 3, the SNR approached 40 dB compared to an intact region. Furthermore, the size of the damaged area can be determined from the peak resonance frequency. In these types of measurements, it is anticipated that environmental interference or "clutter" will have minimal effects. It is anticipated that delamination and flaws in the FRP materials will have the largest vibration velocity response to sound waves compared to any other structures and environment in the measurement system.

Summary and Future Work

Our preliminary work has shown that the proposed acoustic-laser technique has a potential for detection of defect in FRP-concrete structural member. The vibration signatures measured by the laser vibrometer can be used to distinguish and characterize the defect in the GFRP-confined concrete specimens. It also offers good signal-to-noise ratio, and the effect of ambient vibration on detectability is expected to be minimal. Further experimental investigations will be focused on the effect of distance between detected surface and the acoustic source, the effect of sound pressure level and frequency on detectability.

References

[1] Buyukozturk, O. (1998), *NDT&E International*, vol. 31, n. 4, pp. 233–243.
[2] Popovic, J.S. and Rose, J.L. (1994), *IEEE Transactions on Ultrasonics, Ferroeletrics, and Frequency Control*, vol. 41, pp. 140–143.
[3] Tanigawa, Y., Yamada, K., and Kiriyama, S. (1997), in Proceedings of JCI, Japan Concrete Institute, Tokyo, Japan.
[4] Mirmiran, A., Shahawy, M., and Echary, H.E. (1999), *Journal of Engineering Mechanics*, vol. 125, n. 8, pp. 899–905.
[5] Mirmiran, A. and Wei, Y. (2001), *Journal of Engineering Mechanics*, vol. 127, n. 2, pp. 126–135.
[6] Bastianini, F., Tommaso, A.D., and Pascale, G. (2001), *Composite Structures*, vol. 53, pp. 463–467.
[7] Feng, M.Q., Flaviis, F.D., and Kim, Y.J. (2002), *Journal of Engineering Mechanics*, vol. 128, n. 2, pp. 172–183.
[8] Haupt, R., and Rolt, K. (2005), *Lincoln Laboratory Journal*, vol. 15, n. 1, pp. 3–22

A Quantitative Laser Ultrasound Visualization System for Investigating the Interaction of Wedge Waves with a Defect

I.H. Liu and C.H. Yang

Abstract Machine tool blades exhibit typical wedge-shaped tips where defects are very likely to exist and call for non-destructive characterization. In order to detect the defect on the wedge tip, the interaction of wedge wave with defect characteristic needs to be investigated. Antisymmetric flexural (ASF) modes are wedge waves (WW) with their particle motion antisymmetric about the mid-plane bisecting and energy tightly confined near the wedge tip. A quantitative laser ultrasound visualization (QLUV) system which employs a pulsed laser to scan over the interested area then detected with a piezoelectric transducer. With the aid of reciprocal theorem, dynamic behaviors of ASF modes encountering a defect can be reconstructed. In this research, the QLUV system is used to evaluate the characteristic of WWs and the phenomenon of defect effect including mode conversion and the scattering intensity. With the QLUVS behaviors of ASF modes interacting with a wedge-tip-crack are characterized in a quantitative way. More complex behaviors for higher-order ASF interacting with cracks are under investigation.

Keywords Antisymmetric flexural modes • Defect detection • Laser ultrasound • Visualization • Wedge wave

Introduction

Wedge waves [1, 2], discovered in early 1970's through a numerical study, are guided acoustic waves propagating along the tip of a wedge, with energy tightly confined near the apex. ASF modes are WWs with their particle motion antisymmetric about the mid-plane bi-sectioning the apex angle. The propagation phenomena of ASF can be

I.H. Liu • C.H. Yang (✉)
Institute of Manufacturing Technology, National Taipei University of Technology, Taipei, Taiwan
e-mail: chyang@ntut.edu.tw

investigated by approximate theoretical model [3], finite-element method (FEM) [4, 5] or semi-analytical technique [6]. The propagation behavior of ASF is non-dispersive while the apex truncation is less than 10 μm, and propagates along the perfect tip without any defect. Lately, the scattering [7] while ASF propagates through a defect is discovered experimentally. Laser ultrasound generation [8] is a kind of ultrasound (UT) technique which employs the absorption and liberation remotely to generate wide bandwidth, point-wise, and nondestructive ultrasound with a high energy pulsed laser in order to apply the measurement without environment effect. The ultrasound based technique, via generating with a pulsed laser and detecting with a transducer, QLUV system is developed. The QLUV system employs the pulsed laser to scan over the interested area on the surface of an arbitrary shape of material then detects with a piezoelectric transducer. With the aid of reciprocal theorem, dynamic behaviors of wave propagation can be reconstructed. With the QLUV system, the real image of ASF propagation can be obtained and characterized.

Quantitative Laser Ultrasound Visualization System

With a scanning mechanism [9], a QLUV system is used for the visualization of ASF modes propagation along the wedge. Figure 1 shows a schematic for the experimental configuration of the QLUV system. The QLUV system includes a pulsed Nd:YAG laser, a shear transducer, a pulser-receiver, a fast rotational scanning stage, and a computer with fast A/D converter. The pulsed Nd:YAG laser (Optowave Awave1064) with a wavelength of 1064 nm, an energy of about 10 mJ, and 0.7 mm beam diameter is used for the generation of ultrasonic acoustic waves. The pulsed laser has a maximum repetition rate is up to 20 KHz. With the low energy of this laser, the surface of specimen will absorb the energy make thermal expansion without any damage called thermal elastic generation mechanism. The pulser-receiver (Panametrics 5800) is used for the detection of ultrasound with transducer. A 1 MHz shear transducer is used for detecting acoustic wave and bonded on the side and tip
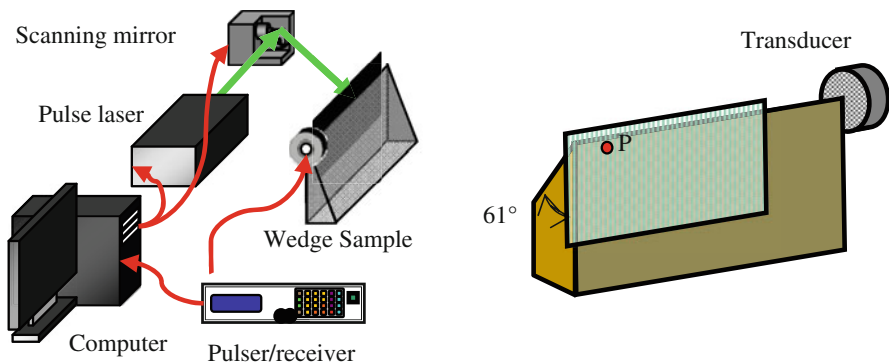
Fig. 1 A sketch for the experimental configuration of the QLUV system
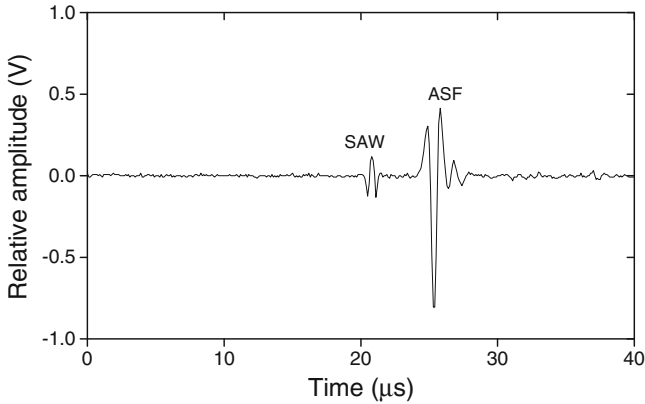
Fig. 2 The ultrasonic signal generated and detected with QLUV system at point P

where is covered the wedge tip around 3 mm depth. The scanning stage is a two axial rotational servo motor and controlled by the computer which drives two mirrors to scan the Nd:YAG laser beam on the surface area of wedge. The computer with a fast A/D converter is used for controlling the scanning stage, waveform acquisition with 2 Gs/s maximum sample rate and 500 MHz bandwidth.

With the QLUV system, an ultrasonicsignal can be generated with the pulsed laser at a desired position P located on a scanning plane. The generated ultrasonic waves are then detected with the transducer. The pulsed laser is scanned over the scanning area and the detected signals pile up into a data cube with the dimensions of (x, y, t). While the data cube is time-gated at various elapsed times, a series of pictures are created. With the aid of reciprocal theorem, these pictures represent many instantaneous frames representing wavefronts generated by the transducer and detected at the scanning area. In this way, the QLUV system is operated.

Figure 2 shows a waveform generated with the pulsed laser at point P and detected with the shear transducer. The signals designated by surface acoustic wave (SAW) and ASF correspond to surface wave and ASF mode directly reaching the transducer without reflections. With this configuration, the signal strengths of ASF modes with a signal noise ratio (SNR) of about 32 dB are apparently stronger than the SAWs with a SNR of about 18 dB.

Result and Discussion

Figure 3 shows the QLUV resolved wavefronts for the laser-generated guided waves propagating on the scanning area with elapsed time of 7.92 s. In this figure, the scanning area is below the labeled wedge tip and left edge. With the transducer located in the right corner as shown in Fig. 2, the laser generated guided waves propagate from left to right. However, while the guided waves are played back with
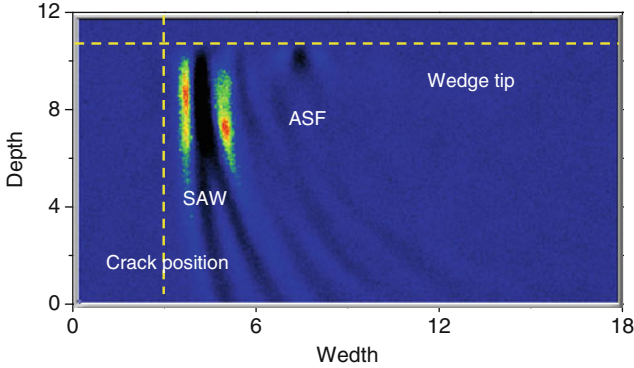
Fig. 3 The resolved wavefronts by QLUV system
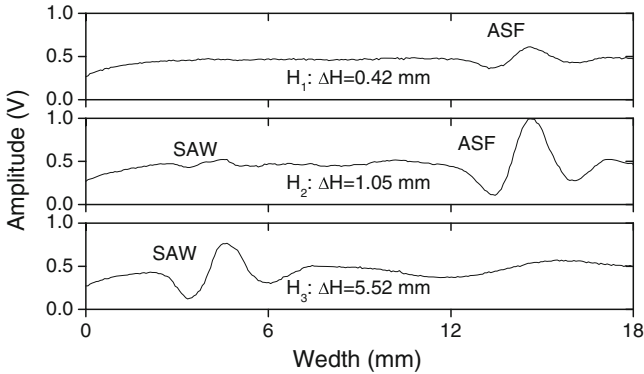
Fig. 4 Wavefronts analyzed along various horizontal cross-sections

increasing elapsed time, the guided waves show an effect of traveling from right to left. At the elapsed time of T=7.92 s in Fig. 4, the first leftward propagating wavefronts correspond to directly reaching SAW as indicated in Fig. 4. Their group velocity determined through a position-time analysis is 2934 m/s. The SAW wavefronts are slightly curved due to finite size effect of the transducer. The SAW wavefronts are always generated by the QLUV system although this research is more interested in visualizing the ASF mode.

In Fig. 3, the SAW wavefronts are followed by the slower ASF mode, which can be recognized as the A1 mode velocity of 2409 m/s. Employing the empirical formula from Lagasse, the theoretical A1 mode velocity can be determined as $V_{A1} = V_R \sin(n\theta) = 2934 \sin(61°) = 2566$ m/s, which is within 6% error compared with the measurement. Also it is found out that the energy of the A1 mode is confined near the wedge tip, while the SAW wavefronts have deeper spread.

Wavefronts in Fig. 3 can be further analyzed along various horizontal cross-sections as shown in Fig. 4 indicated as H1, H2 and H3. The horizontal line H1 is very close (0.42 mm) to the wedge tip, while H2 and H3 are 1.05 mm and 5.52 mm
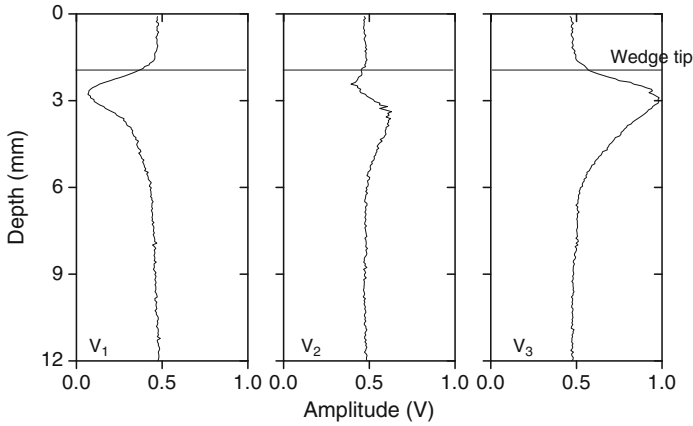
Fig. 5 The diagram of reciprocal theorem
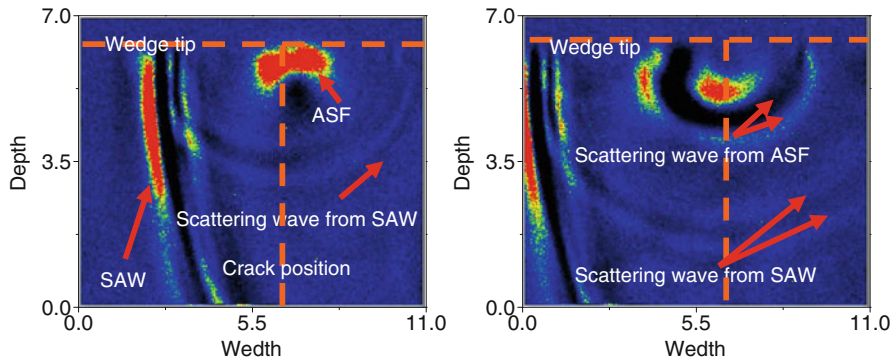
Fig. 6 The scattering waves

below the wedge tip. According to the waveform along H1 as shown in Fig. 4, the wedge tip supports only ASF mode and the wavelength of ASF is about 2.731 mm. As the horizontal cross-sections increases to H2= 1.05 mm as shown in Fig. 4, the SAW can start to exist with 19 dB signal strength difference between A1 mode. With increasing horizontal cross-sections, the existing A1 mode will be attenuated until the ΔH is increasing around to one wavelength.

In order to investigate the ASF mode shape in the vertical direction, measured amplitudes along three vertical lines denoted as V1, V2 and V3 as shown in Fig. 4 are plotted in Fig. 5. Here V1 is associated with a valley for the detected ASF contour, V2 near a central line and V3 for a peak. The particle displacement at wedge tip in Fig. 5 will not be zero, because the laser beam with finite size of 0.7 mm will still generate signals even if generation position is moving upon the tip. As indicated in Fig. 5, the particle motion of the ASF mode is localized near the wedge tip with the depth of about 3.1 mm. ASF mode shapes along V1 and V3 are similar, but 180° out of phase.

Figure 6 shows the scattering wave at different elapsed time which SAW and ASF waves propagate through the defect. According to the Fig. 6, both SAW and ASF waves propagate through the defect will centralize the energy at the corner of the defect and reconstruct a new scattering wave. These scattering waves can be formed by both SAW and ASF wave with the velocity of 2926 m/s and 2933 m/s. In addition to the scattering waves, the original wave will transmit or reflect as a SAW or ASF wave. According to the result, the scattering waves can also be recognized as surface acoustic waves.

Conclusion

In this study, a quantitative laser ultrasound visualization system (QLUV) is employed for the investigation of ASF modes interacting with defects along a wedge tip. With the QLUV system, continuous dynamic propagation behaviors of the ASF modes interacting with the defects propagating along the defected wedge tip are observed. The QLUV provides many interesting observations including reflections and transmission of ASF modes through a defect, scattering of ASF modes into surface acoustic waves radiated from a defect. Finally, mode shapes and wavelengths of ASF modes and SAW propagating in a wedge sample are also measured with the QLUV system. With the developed QLUV system, dynamic propagation natures in more complex waveguides could be explored for physical understanding and waveguide design purposes.

References

[1] Lagasse, P. E. (1972), Electron. Lett., vol.8, p. 372.
[2] Lagasse, P. E., Mason, I. M. and Ash, E. A. (1973), IEEE Trans. Son. Ultrason., vol. Su-20, no. 2, p. 143–154.
[3] McKenna, J., Boyd, G. D. and Thurston, R. N. (1974), IEEE Trans. Son. Ultrason., vol. Su-21, no. 3, p. 178–186.
[4] Yang C. H. and Tsen, C. Z. (2006), IEEE Trans. Ultrason. Ferroelectr. Freq. Control, vol. 53, no. 4, p. 754–760.
[5] Tang S. W. and Yang, C. H. (2007), Jpn. J. Appl. Phys., vol. 46, no. 9A, p. 5935–5938.
[6] Dao, C. M., Das S., Banerjee S. and Kundu T. (2009), Int. J. Solids Struct., vol. 46, p. 2486.
[7] Krylov V. V. and Reguzina, I. V. (1988), Sov. Phys. Acoust., vol. 34, no. 5, p. 546–547.
[8] White, R. M. (1963), J. Appl. Phys., vol. 34, no. 12, p. 3559–3567.
[9] Blackshire J. L. (2008), 1st International Symposium on Laser Ultrasonics: Science, Technology and Applications.

NDT of Structural Timber Members by Means of 3D Ultrasonic Imaging Techniques and Modelling

M. Krause, P.K. Chinta, K. Mayer, U.A. Effner and S. Müller

Abstract The present paper describes the development and first application of ultrasonic imaging of timber (wood) by means of reconstruction calculation (3D-SAFT; Synthetic Aperture Focusing Technique). It considers the highly anisotropic ultrasonic velocity on wood. In order to validate such techniques we report on experiments carried out on test specimens made from pine and beech. Those specimens differ for the orientations of the annual rings. For the reconstruction calculation the slowness curves of the material are considered applying the elastic constants known from the literature. The anisotropic SAFT reconstruction is calculated from measured datasets and from synthetic data resulting from EFIT modelling (EFIT: Elastodynamic Finite Integration Technique).

Keywords Modelling • Reconstruction calculation • Timber • Ultrasonic imaging • Wood

Introduction

Hidden damages on timber structures require specialized experts and sophisticated assessment tools for detecting the damage. To minimize this potential risk in the evaluation process of a structure made of wood, it is possible to use the ultrasonic echo method. As a result of the research in progress since 2002 it is possible to show that with low frequency ultrasonic echo technique different types of damages within

M. Krause (✉) • U.A. Effner • S. Müller
BAM Bundesanstalt für Materialforschung und -prüfung, Berlin
e-mail: martin.krause@bam.de

P.K. Chinta • K. Mayer
University of Kassel, Kassel, Germany

such structures can be detected [1]. In this paper we describe first applications of ultrasonic imaging techniques working for timber, which is an anisotropic material. In order to achieve this, the principle of Synthetic Aperture Focusing Technique (SAFT) is applied to the structural anatomy of wood, having orthorhombic crystal symmetry. In the first part of the article the development of SAFT for such symmetry is briefly described (based on [2]), including the consequence for the anisotropy of the ultrasonic slowness curves and group velocity. In the second part first examples of ultrasonic shear wave measurements and SAFT-evaluation are described for specimens made from beech and pine.

Development of SAFT for Orthorhombic Crystal Systems

In ultrasonic nondestructive evaluation of materials we need to understand the theory of the particle motion of the material. The motion of the particles usually depends on the applied forces, on the way they are applied and on the material properties. The elastic wave propagation of wood composites is very complex because of the crystal arrangement in wood and inconsistent material properties in different directions of the structures made of wood. But the elastic wave propagation and scattering effects in woods are efficiently realized using numerical modeling. The defects can be identified by applying the reconstruction algorithms using the elastic waves. Elastodynamic Finite Integration Technique (EFIT) 0is a numerical tool developed for the non-destructive testing of inhomogeneous isotropic and anisotropic materials. The governing equations of elastodynamics comprises of Newton-Cauchy's equation of motion are applied in order to determine the phase and group velocities using the dispersion relations (for more details see [4]).

Wood structural anatomy and group velocity

The structural anatomy of wood with the definitions of planes and its orthotropic behaviour is described e.g. in [5, 6, 7]. The crystals of a large group of wood species are orthotropic with nine independent elastic stiffness constants and show strong anisotropy. The symmetry axes are named L, T, and R: L for longitudinal (direction of growth), T and R for tangential or radial relative to the annual rings, respectively. As an example Fig. 2a) shows the RT section of a specimen glued together from small bars made of beech. One group velocity diagram of spruce wood species is shown as example in Fig. 1a. This group velocity profile is used for imaging with time domain anisotropic SAFT.

From the group velocities it is obvious that quasi pressure (qP) waves propagate fast in the direction of fibre orientation. The quasi shear qS1 and qS2 modes propagate rather slowly in the direction of fibre orientation.
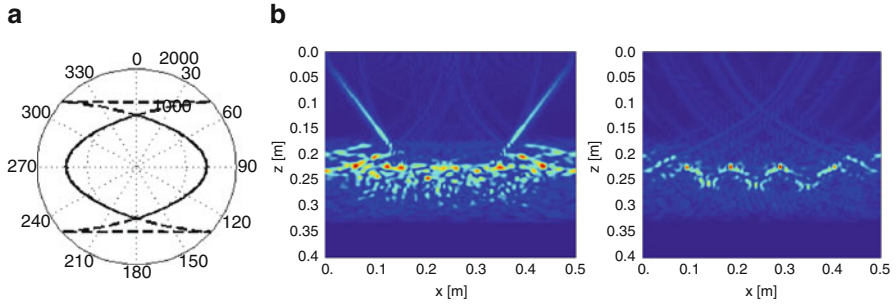
Fig. 1 Reconstruction of the scatterers. **a**) Group velocity for spruce in the RT section used in anisotropic SAFT. **b**) Left: Isotropic SAFT reconstruction with velocity 1050 m/s. Right: Reconstruction with anisotropic SAFT.
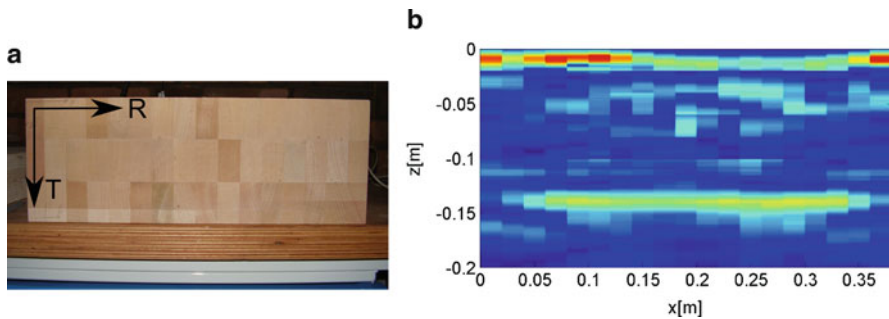
Fig. 2 Specimens glued from small bars (size about 2 x 5 x 50 cm³) using melamine resin glue, L-axis perpendicular to image plane **a**) Beech showing the RT section, **b**) Beech: anisotropic 2D SAFT reconstruction

Example of ultrasonic modelling and reconstruction: 2D-EFIT simulation and defect reconstruction in the LT-plane

The synthetic data obtained by EFIT simulation for a pulse-echo experiment is used for the reconstruction of the defects. For reconstruction with isotropic SAFT each A-scan on the measurement surface is transmitted back into the material with a circular travel time profile computed with the velocity of 1050 m/s. The result of this SAFT reconstruction is shown in Fig. 1b (left). Anisotropic SAFT in this case uses the qS1 group velocity for back propagation to obtain the reconstruction of the defects. Only the marked part of the group velocity (Fig. 1a) is used as travel time profile. With isotropic SAFT the exact focusing of the defects is not achieved. But with anisotropic SAFT all the inhomogeneities are localized at the correct positions (Fig. 1b (right)).

Test Specimens and Imaging of Back Wall Echo

For first investigations and functional tests of the new reconstruction tool two test specimens were built. The first specimen is made from beech wood and measures 49 cm x 40 cm x 14.5 cm (Fig. 2a). The second one is from pine wood with the size 50 cm x 50 cm x 7 cm. For both small bars are glued together using melamine resin glue. For initial test the orientation of the annual rings was selected in a way that the bending is as small as possible. Thus the symmetry of the specimens is quasi homogeneously anisotropic.

The thickness of beech is orientated in the direction of the T-axis. First experiments were carried out in order to image the back wall echo. They were carried out applying 50 kHz shear wave equipment which has been established for ultrasonic testing of wooden beams [1]. For the 2-dimensional anisotropic reconstruction of the measured data on the beech specimen (polarization perpendicular to the fibre direction (parallel R)) the velocity qS1 from the stiffness tensor published by Bucur [8] was used. The result is depicted in Fig. 2b. This result indicates the correct superposition of inclined ultrasonic beams during the SAFT reconstruction.

Imaging of Artificial Scatterers in the Pine Specimen

For SAFT imaging in the 2nd specimen made from pine the group velocity is presented in Fig. 3a for the R/T section, corresponding to the selected symmetry of the specimen. The velocities are applied following the stiffness tensor for pine [8] (similar to the last paragraph).
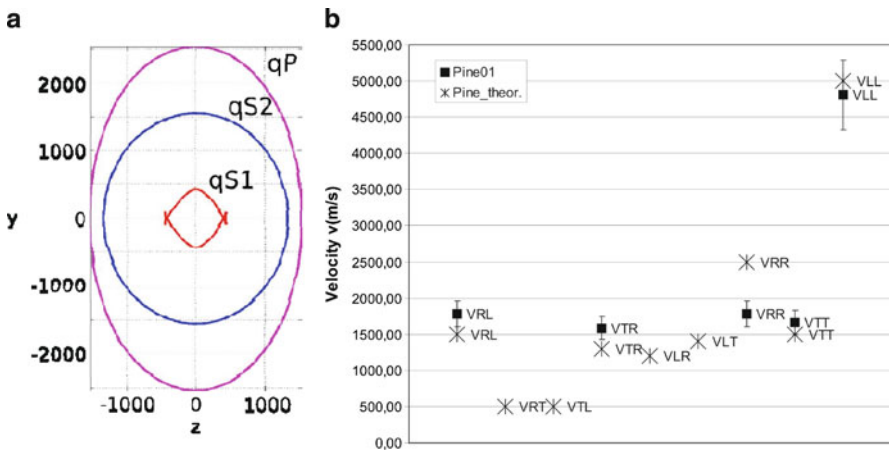
Fig. 3 a) Angle dependence of group veloc. in pine in the RT section (here yz). **b**) Comparison of velocities for pine in the axes of symmetry (first index: direction of wave propagation, 2nd index: direction of polarisation. Pine01: experiment, Pine theor.: calculated from stiffness tensor [8]
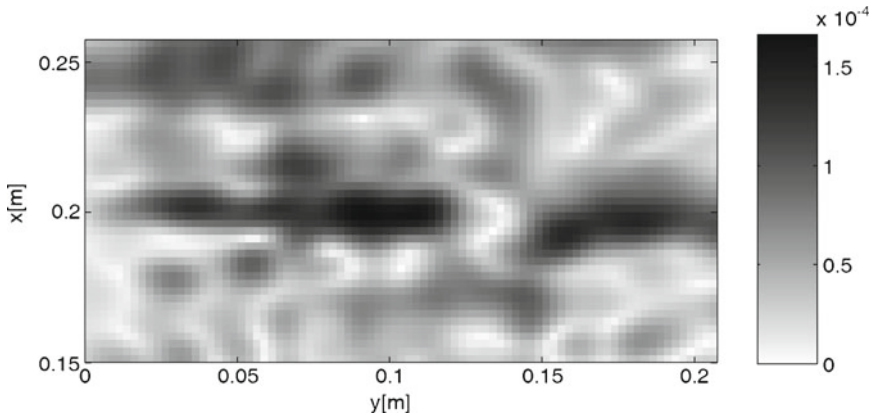
Fig. 4 Result of anisotropic SAFT reconstruction of the pine specimen with bore hole (dimensions in m). C-scan z = 0.05 m. (TL section, here xy section)

Since the experiments are carried out in the shear wave frequency range of 50 kHz, the velocities are measured for pine in through-transmission mode applying the same transducer type as used for the echo measurement. The comparison of the velocities following from the stiffness tensor to the measured velocities is presented in Fig. 3b for typical symmetry axes. For some of the small velocities the measurement in through-transmission was not successful, because faster wave modes additionally emitted by the ultrasonic transducers superimposed the onset of the wave signal.

In the following first results of 3D ultrasonic imaging by means of reconstruction calculation (3D-SAFT) are presented. The scatterer in the pine specimen was produced by drilling a bore hole parallel to the L-axis (y). Measurements were carried out with shear waves having a polarisation parallel to the L-axis in a measuring grid of 10 mm. Figure 4 shows the C-scan for z = 50 mm (TL/xy-section) obtained by anisotropic SAFT-reconstruction. The reconstructed signals from the backscatter are fitting well with the crown of the bore hole.

Conclusion

Modeling and 3D ultrasonic imaging in anisotropic wood structures is investigated and the effect of polarisation with respect to the fibre orientation is studied. In the first part the reconstruction of the defects in the homogeneous isotropic media is discussed by using artificial data obtained with elastic wave modelling (EFIT). The comparison between isotropic and anisotropic Synthetic Aperture Focusing Technique (SAFT) reconstruction is presented. Anisotropic SAFT uses the group velocity profiles computed by solving the eigenvalue problem to reconstruct the defects. The anisotropic SAFT reconstruction algorithm is able to localize defects

(realised as bore holes) in homogeneous anisotropic wood. With this technique a very good focusing of the defects can be achieved.

The presented first experiments for beech and pine specimens applying shear waves (50 kHz) demonstrate that ultrasonic echo imaging principally works with 2D and 3D-SAFT reconstruction calculation. Examples like imaging of the back wall and the location of bore holes are demonstrated. The goal of further development is a high resolution NDT testing system for quality assurance of glued and cross laminated timber.

References

[1] Hasenstab, A., Hillemeier, B., Krause, M. [2005]: *Defect Localization in Wood with Low Frequency Ultrasonic Echo Technique*. In: Proceedings of the 14th International Symposium on NDT of Wood, 02.-04.05.05, Hannover.

[2] Mayer, K., Marklein, R., Langenberg, K.J., Kreutter, T. [1990]: *Three-dimensional imaging system based on Fourier transform synthetic aperture focusing technique*. Ultrasonics V 28, pp. 241–255.

[3] Marklein, R. [1997]: *Numerische Verfahren zur Modellierung von akustischen, elektromagnetischen, elastischen und piezoelektrischen Wellenausbreitungsproblem im Zeitbereich basierend auf der Finiten Integrationstechnik*. Shaker Verlag, Aachen, Germany.

[4] Chinta, P., Mayer, K., Krause M. [2010]: *Ultraschallmodellierung und SAFT-Rekonstruktion von Fehlstellen in Holzbauteilen*. In: Berichtsband der DGZfP-Jahrestagung 2010, Erfurt, 10.-12. Mai 2010, BB 122-CD, Poster 59, 8 pages.

[5] Musgrave, M.J.P. [1970]: *Crystal Acoustics, Introduction to the study of elastic waves and vibrations in crystals*. Holden-Day, San Francisco, USA.

[6] Bucur, V. [2006]: *Acoustics of Wood*. 2nd Edition, Springer-Verlag, Berlin Heidelberg, Germany.

[7] Schubert, S. [2007]: *Acousto-Ultrasound Assessment of Inner Wood-Decay in Standing Trees: Possibilities and Limitations*. Swiss Federal Institute of Technology, Zurich, Dissertation ETH Nr. 17126, 125 pages.

[8] Bucur, V., Lanceleur, P., Roge, B. [2002]: *Acoustic properties of wood in tridimensional representation of slowness surfaces*. Ultrasonics 40, pp. 537–541.

Enhancing the Accuracy of Off-Axis Flaw Sizing and Positioning in TOFD D-scans Using Mode-Converted Waves

A. Al-Ataby and W. Al-Nuaimy

Abstract Despite the recent popularity of ultrasonic time-of-flight diffraction (TOFD) as a reliable non-destructive testing technique for the inspection of weld defects in steel structures, the critical stages of data processing and interpretation are still performed manually. This depends heavily on the skill, experience, alertness and consistency of a trained operator, and is subject to inevitable human errors due to reduced alertness arising from operator fatigue and visual strain when processing large volumes of data. This paper presents techniques developed for enhancing the accuracy of sizing and positioning of off-axis weld flaws in TOFD D-scan data as an essential stage in a comprehensive TOFD inspection and interpretation system to aid the operator by automating some aspects of the processing and interpretation. Data manipulation and post-processing techniques have been specifically developed for the sizing of off-axis weld defects in TOFD data, significantly reducing the sizing and positioning errors. The mode-converted waves are utilised to enhance positional accuracy of flaws. The results achieved so far have been promising in terms of accuracy, consistency and reliability.

Keywords Defects • Imaging • Mode-converted waves • Signal processing • Size • Time-of-flight diffraction • Ultrasonic testing • Welds

Introduction

Legacy ultrasonic inspection methods rely on the echo amplitude to size the flaw and the pulse travel time to identify the defect position and orientation [1]. These methods are based on the assumption that echoes from planar features are suitably

A. Al-Ataby (✉) • W. Al-Nuaimy
Department of Electrical Engineering and Electronics, University of Liverpool,
Brownlow Hill, L69 3GJ, Liverpool, UK
e-mail: Ali.Al-Ataby@liv.ac.uk

angled and travel back to the transducer. Though simple and inexpensive, these methods suffer from poor resolution for crack sizing when the echo may be severely attenuated because the amplitude of the reflected echo may be influenced by factors such as surface roughness, particles in the specimen, transparency and orientation of the flaw. To overcome the limitations of the pulse echo method, ultrasonic time-of-flight diffraction (TOFD) was developed. It has higher accuracy for measuring the through-wall size of crack-like defects, and can be performed in a wide range of material thicknesses. It has gained popularity because of its high probability of detection, low false call rate, portability and most importantly, its intrinsic accuracy in flaw sizing and positioning, especially in depth [1, 2].

Accurate measurement of size and position of flaws has great importance in ensuring the structural integrity of many structures by detecting the defects that could trigger failures [2, 3]. Some flaws can very quickly be enlarged by fatigue and cause a major reduction of strength leading to catastrophic failure of the structure. This failure can occur by rapid brittle fracture if these flaws exceed a certain critical size for the load applied.

Off-Axis Flaw Depth Error

In the D-scan configuration (see Fig. 1), the flaw is likely to be offset from the centre of the axis between the transmitter and receiver. However accurate the time-of-flight may be, the lateral position of the source of the echo is still unknown [3]. Consider the situation for a D-scan with the defect tip at depth d offset from the axis between the two probes by a distance X, and a transit time (neglecting probe delay) of t (Fig. 1b). The range for a signal from the defect tip is given by [2, 3]:

$$v_L t = \sqrt{(s+X)^2 + d^2} + \sqrt{(s-X)^2 + d^2} \qquad (1)$$

where v_L is the longitudinal wave velocity in the material.

The shape of the path with constant range (*i.e.*, time) is an ellipse with the index points of the two probes at its foci. Rearranging Eqn. (1), the following expression for the depth d is obtained:

$$d = \sqrt{\left(\frac{1}{4} - \frac{X^2}{v_L^2 t^2}\right)\left(v_L^2 t^2 - 4s^2\right)} \qquad (2)$$

From this equation, it is clear that if X is unknown, then d cannot be calculated. To overcome this problem, it is normal practice to perform a TOFD B-scan at the position of a detected defect to measure the depth accurately and find the offset X. Measurement errors are minimised because at some point within the B-scan the defect must lie equidistantly between the two probes. This operation requires that the operator first analyses the D-scan to find the locations of any potential flaws, and then carries out a number of supplementary B-scans to measure their depths. It is clear that this introduces further subjectivity to the operation and adds to the total

a Sample TOFD D-scan output.

b D-scan setup and configuration.
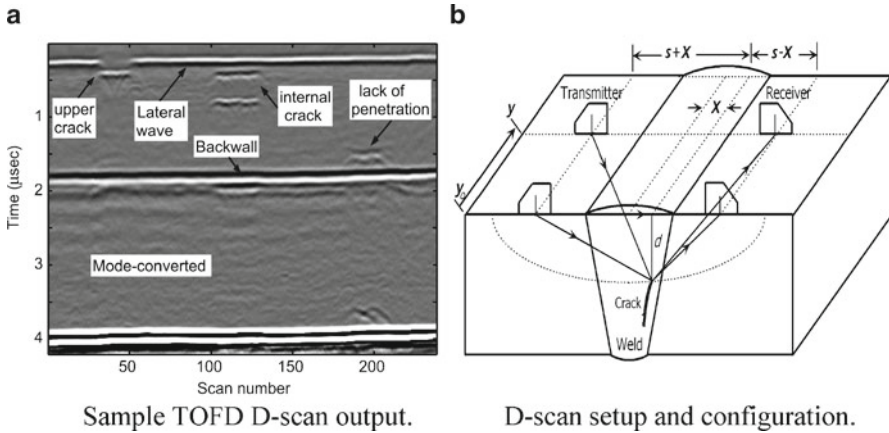
Fig. 1 D-scan and lateral flaw position

inspection time. However, this paper will show that this information can be obtained from the original D-scan.

Minimising Off-Axis Uncertainty

Although flaw sizing using TOFD in D-scanning mode is more accurate than other conventional ultrasonic techniques, the incorporated error can still be of a high order. It can be shown that this error varies with off-axis distance X and can reach 60% or higher if the flaw is located under one of the transducers (see Fig. 2) [3]. When the flaw is located in the plane normal to the inspection surface and passing through both transmitter and receiver, the transit time of the pulse is at a minimum. As the transducers move away from this position (as shown in Fig. 1b), along a scan line perpendicular to the plane of the flaw, the transit time increases resulting in arcs at the ends of the flaw record in D-scan presentation. For a flaw located at a position y_o along the weld, the shortest path of the diffracted signal when the transmitter and receiver move to position y can be shown to be [3]:

$$v_L t = \sqrt{(s+X)^2 + d^2 + (y-y_o)^2} + \sqrt{(s-X)^2 + d^2 + (y-y_o)^2} \qquad (3)$$

This equation represents the dependence of defect signature shape on the lateral offset X. Eqn. (3) is recognised as an equation of a hyperbola for variables t and y. Hence, t is at a minimum at the point where the scattering point lies in the plane defined by the two beam axes and it increases as the point moves away from that plane. It is clear that the signal loci, although hyperbolic only in the special case referred to above, is of the same general shape for all scan paths in this simple geometry. In particular, the signal loci for a scan parallel to the plane defined by the beam axes will look like hyperbolas for deep defects but will appear increasingly flattened as the defect is approached [3].

Fig. 2 Variation of depth
error with off-axis distance X
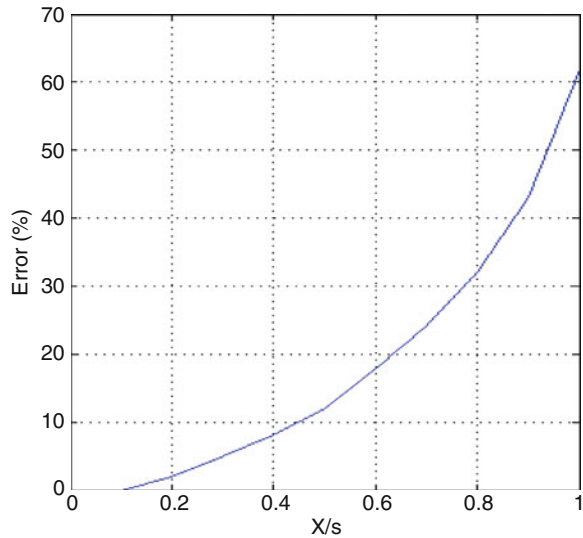
Since the shape of the arcs depends on the defect depth, the defect lateral
displacement, probe separation and direction of probe motion (see Eqn. (3)), it is
predetermined for any given depth on a B- or D-scan display. It is a simple matter
to provide a means of displaying the correct shape as a cursor on a digital display
and to move it interactively to check its fit to any suspected defect indication. For
each detected defect, the edge points of the defect signature can be determined by
a combination of 2-D alignment processing and 1-D peak tracing for each echo.
As a result, the sets of points representing the envelope of the defect echo wavefront
can be detected. They can be checked if they are arcs by identifying those with a
monotonic increase in time. These points are then modelled to fit, in a minimum mean
square error sense, a curve governed by Eqn. (3). As a result of this curve fitting
shown in Fig. 3a, not only can X be found, but also the starting point of the arcs can
be identified more accurately. This point is then used to correct the measured width
of the defect to eliminate the effect of elongation, while the estimated value of X is
then used in Eqn. (2) to correct the lateral position of the defect and, hence, minimise
the depth error [3]. Figure 3b shows a representation after using the curve fitting
method on a sample defect ($X = 6$ mm).

Mode-Converted Waves and Flaw Position Estimation

Section 3 has shown that it is possible to measure the transverse position of a defect
when performing an ultrasonic TOFD D-scan by studying how the arcs of a defect
indication vary with scan position. This information would normally be obtained only
from a B-scan image. One limitation that this method suffers from is that the value
of X can be determined accurately but it is not obvious whether this off-axis shift is
to the left or to the right of weld centreline. A method to overcome this limitation

(a) Extracting arc start point.   (b) Sample defect. $X=6$ mm.
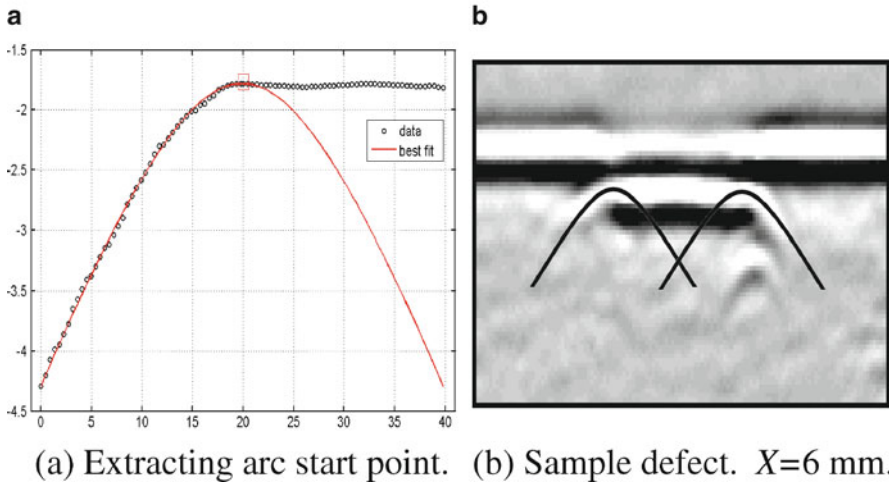
Fig. 3 Curve fitting method

is proposed here, using the mode-converted waves. Basically, each defect shows an indication in the mode-converted region of the scan that is usually more visible and indicative (because shear waves are twice as sensitive as longitudinal waves, having shorter wavelength and a lower velocity). In case of uncertainty in deciding the position of the off-axis flaw in the compression-to-shear wave region, the time of the mode-converted indications can be used. Figure 4 shows this concept. By checking the time in the mode-converted part of the D-scan display, the flaw can be determined to be closer either to the transmitter or the receiver.

Most of the equipment used for TOFD scanning can provide the facility of operating multichannel probes concurrently (called software channels). Using this feature, two channels can be defined: channel 1 with probe 1 transmitting and probe 2 receiving, and channel 2 with the arrangement reversed. As it can be seen from Fig. 4, the indication in the compression region shows almost the same position for both transmitter-receiver setups. The difference can be seen in the mode-converted region, where there are two different times (t_1 and t_2) for the same defect depending on probes setup. With reference to Fig. 4, the flaw is actually closer to R_1 in the T_1-R_1 setup (shortest time is more accurate). By utilising these observations in conjunction with the method explained in Section 3, the accuracy of the resulting sizing and positioning measurements were considerably improved.

Results

The developed procedures have been applied to 76 test plates containing 150 weld defects using TOFD system of 5 MHz and 60° probes with 100 MHz sampling frequency. The plates were of thickness between 20 to 30 mm, with different defect
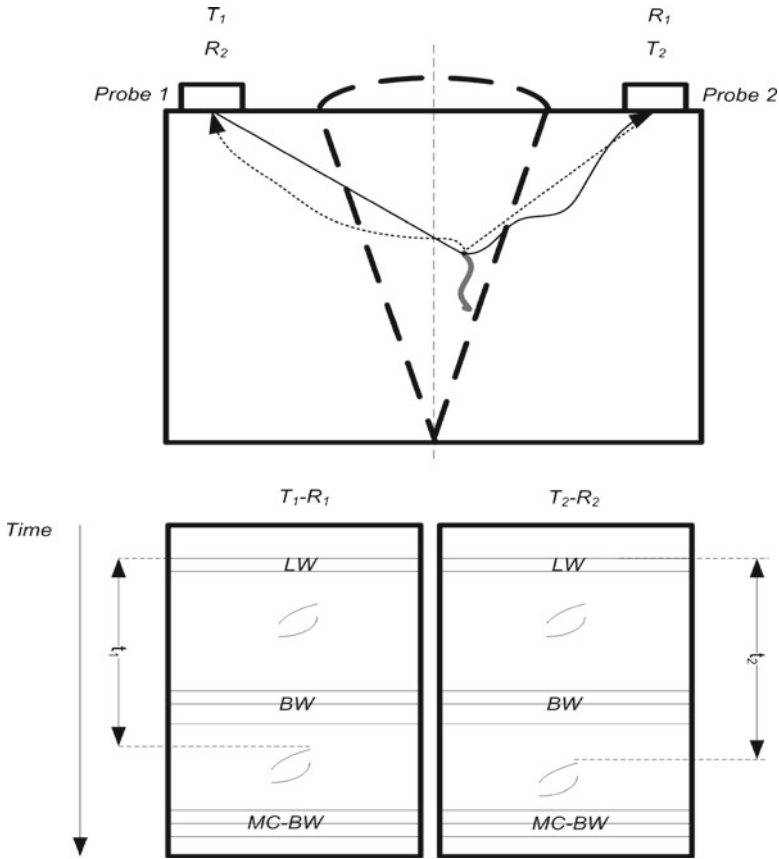
Fig. 4 The flaw is closer to R_i in T_i-R_i setup (shortest time in mode-converted)

sizes and depths. The defects have all been characterised and documented by the manufacturer of the steel plates. The majority of the achieved preliminary results are more accurate than the manual results, referring to the data sheets of the scanned plates, while only around 11% are the same as reported by a trained operator. For flaw depth, height and width measurements, the error is within ±1 mm for all defect classes except for the surface breaking crack where the error is within ±2 to ±3 mm because the flaw echo is merged with the lateral wave or backwall echo.

Conclusions

This paper has addressed the task of accurate sizing and positioning of off-axis defects in ultrasonic TOFD data as part of a comprehensive automatic interpretation aid. Data manipulation and post-processing techniques have been developed for

that specific purpose. The results obtained after using these techniques have been extremely promising in terms of speed, robustness, accuracy and reliability when dealing with highly variable data. This would make the proposed techniques suitable in situations requiring automatic near real-time processing and interpretation of large volumes of data, hence, greatly reduce human and experimental errors. The novel utilisation of the mode-converted waves in accurate sizing looks promising and is under thorough investigation to explore its potential further.

References

[1] Silk, M. (1996), *An evaluation of the performance of the TOFD technique as a means of sizing flaws*, Insight, vol. 38, no. 4, pp. 280–287.

[2] Charlesworth, J. and Temple, J. (2001), *Engineering applications of ultrasonic time-of flight diffraction*, RSP, 2nd edition.

[3] Al-Ataby, A., Zahran, O. and Al-Nuaimy, W. (2010), *Towards automatic flaw sizing using ultrasonic time-of-flight diffraction*, Insight, vol. 52, no. 7, pp. 336–371.

Time Reverse Modeling Versus Automatic Onset Detection: A Study on the Localization of Acoustic Emissions in Reinforced Concrete

G.K. Kocur, E.H. Saenger and T. Vogel

Abstract Acoustic emissions (AE) are localized using two different signal-based approaches consisting in: An iterative algorithm based on the Akaike Information Criterion (AIC) and time reverse modeling (TRM). Thereto, physical experiments (four- and three-point-bending tests) were carried out on large scale reinforced concrete (RC) slabs with the dimensions of $2620 \times 800 \times 200$ mm. AE were recorded during the entire loading history. The AE sources were localized successfully by both methods from the AE waveforms. It is the first time that time reverse modeling was used to successfully localize AE sources in RC slabs. The results of the AIC-based and TRM localization are compared and discussed.

Keywords Acoustic emission • Akaike information criterion • Elastic wave propagation • Reinforced concrete • Time reverse modeling

Introduction

Localizing acoustic emission (AE) sources in concrete structures is a demanding task due to the large amount of recorded signals and the heterogeneous material. Standard signal-based localization methods rely on the P-wave velocity and picked arrival times of the P-wave front. The most common methods are described in [1]. They include inversion techniques, such as the Moment Tensor Inversion or SiGMA (simplified Green's function for moment tensor analysis), which provide important information on the crack kinematics and fracture modes, as well as the source coordinates in 3D. The combination of two methods as suggested by [2] is particularly

G.K. Kocur (✉) • T. Vogel
Institute of Structural Engineering, ETH Zurich, Zurich, Switzerland
e-mail: kocur@ibk.baug.ethz.ch

E.H. Saenger
Geological Institute, ETH Zurich, Zurich, Switzerland

interesting. Further, the so-called Akaike Information Criterion (AIC) is used to perform automatic onset time detections (picking) [3]. Based on this criterion, AE source locations including error estimations can be determined iteratively using a high-order localization algorithm. However in some cases, noise level deviations require manual intervention, which handicaps automation. Therefore, an alternative localization method, called time reverse modeling (TRM) has been suggested [5]. Time reverse localization bypasses the picking procedure and therefore requires less user interaction. The method solves the elastodynamic equation with recorded data as an input assuming an adequate effective velocity distribution [6]. The time-reversed wavefronts propagate through the effective model and focus on the source location. The source is then localized by applying different imaging conditions. The present study aims at comparing the performance of the AIC-based iterative algorithm and TRM using AE obtained from physical experiments. The physical experiments consist of three reinforced concrete (RC) slabs with different shear reinforcements. They are loaded up to failure in four- and three-point-bending. During the entire load history piezoelectric sensors record the complete waveforms of the AEs. The source localization is performed with an automatic AIC-based algorithm and TRM. The results are compared and discussed exemplarily for one of the slabs.

Physical Experiments

The physical experiments used in this study were originally carried out for testing the performance of post-installed bounded shear reinforcement in RC slabs [7]. The RC slabs C1 to C3 (2620 × 800 × 200 mm) with variable reinforcement ratios were tested twice. After the four-point-bending test (V1), one of the supports was inverted (V2) and a three-point-bending test was performed. Within this project, the authors were invited to perform acoustic emission measurements to monitor the structural response during the entire loading process and gain additional information on the crack nucleation and formation. This study focuses on Slab C3V2. The acoustic emissions were recorded with commercial equipment (AMSY5, Vallen Systeme) by 8 piezoelectric non-resonant sensors (KSB250, Ziegler Instruments) with a range of 50-250 kHz. The sensors were arranged irregularly on the specimens' surface around the support, where the flexural cracks and the plastic hinge were expected to form. A static threshold value of 38.1 dB was used. The emphasis of the study was on recording complete waveforms for a further signal-based analysis.

Selected Signal-Based Acoustic Emission Localization in Concrete

AIC-based automatic localization

This localization procedure involves an automatic onset-time detection and is based on the arrival time of the first wave motion (P-wave) and a homogeneous velocity model. The challenge consists in determining the correct onset time for AE
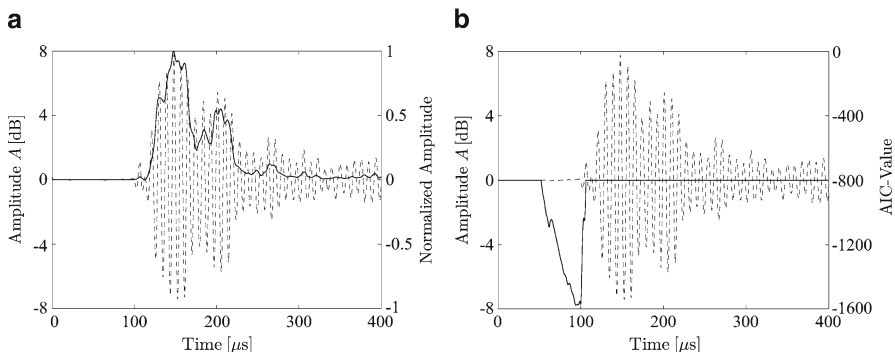
Fig. 1 (**a**) Normalized amplitude of the Hilbert envelope (solid line) and (**b**) the calculated AIC-curve (solid line) for the AE signal illustrated with the dashed lines. The onset time is the global minimum of the AIC-curve

waveforms that occur at different noise levels. The picking procedure considered to be the most efficient, relies on the AIC-values [3], where the so-called Hilbert envelope is applied to single waveforms in order to determine the partial energy content (see Fig. 1a). Further, this envelope defines the time frame within which the onset point can be found by searching the extreme values of the AIC function with respect to time (see Fig. 1b). Once the onset times of a set of AE waveforms are determined, the location of the respective AE source can be calculated iteratively [2].

The results of four AE source locations are illustrated in Fig. 2. Note that the adopted P-wave velocity $c_p = 3921$ m/s [6] underestimates the effective value due to the relatively high reinforcement ratio of Slab C3 (1.75% in x- and 0.16% in z-direction). In general it can be observed that the semi-axes of the error ellipsoids tend to be smaller for sources located in the center of the sensor-surrounding area. The semi-axis lengths are significantly larger in the direction of the y-axis in comparison to the other two directions. The reason is the close spacing of the sensors in y-direction.

Time reverse modeling

Time reverse modeling (TRM) originates from exploration geophysics where it is used to find hydrocarbon reservoirs [4]. Nowadays the method is also used for non-destructive testing problems [5]. TRM is a combined procedure which uses numerical simulations to supplement the recorded AE data. The displacement field $u_i = \mathbf{u}(\mathbf{x},t) \in \mathbb{R}^3$ is determined based on the linear, isotropic elastic wave equation

$$\rho u_{i,tt} = (\lambda + \mu)u_{k,ki} + \mu u_{i,kk}, \tag{1}$$
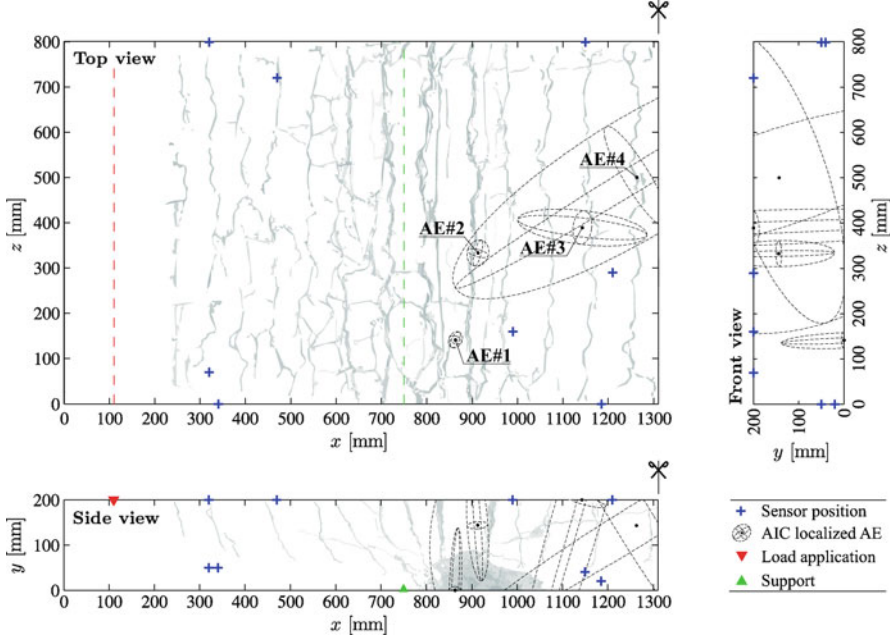
Fig. 2 Projected view of four AE sources #1 to #4 in Slab C3V2 localized based on the AIC together with the crack patterns after bending failure

with the Lamé constants λ and μ and the density ρ. The wave equation is discretized with the finite differences method. The concrete properties required for the elastic (forward) wave propagation simulations, such as c_p (P-wave velocity), c_s (S-wave velocity) and ρ (density), are approximated with a numerical concrete model with randomly distributed concrete constituents [6]. The displacements calculated at the sensor positions display the wave motion for $t \in [0;T]$, where T is the duration of the simulation. The total energy density

$$E_{tot}(\mathbf{x},t) = \max_{t \in [0;T]} \left\{ \boldsymbol{\sigma}(\mathbf{x},t) \boldsymbol{\varepsilon}(\mathbf{x},t) \right\} \tag{2}$$

is displayed by applying an imaging condition, where $\boldsymbol{\sigma}(\mathbf{x},t)$ and $\boldsymbol{\varepsilon}(\mathbf{x},t)$ represent the stress and the strain tensor, respectively. The out-coming scalar field is shown in Fig. 3. The source location is not given a priori. The information on the source location is hidden in the AE waveform, which is stored during the AE measurements. The stored waveform is time-reversed and then used as input data for the numerical (inverse) simulation to calculate the inverse displacement field $\mathbf{u}^{\mathrm{TRM}}(\mathbf{x},t) = \mathbf{u}(\mathbf{x},T\text{-}t)$. All AEs are recorded on $t \in [0;409.6]$ μs. The simulation time is extended to $t \in [0;600]$ μs to allow for sufficient interference of the inverse displacement field. The effectiveness of the TRM method is demonstrated on a concrete cuboid ($118 \times 120 \times 160$ mm) with real AE data caused by pencil-lead-break sources. In this case the location of the source signal is known a priori. The radiation patterns of the pencil-lead-break sources located close to the sensors at $[x,y,z] = [0,20,100]$ mm and
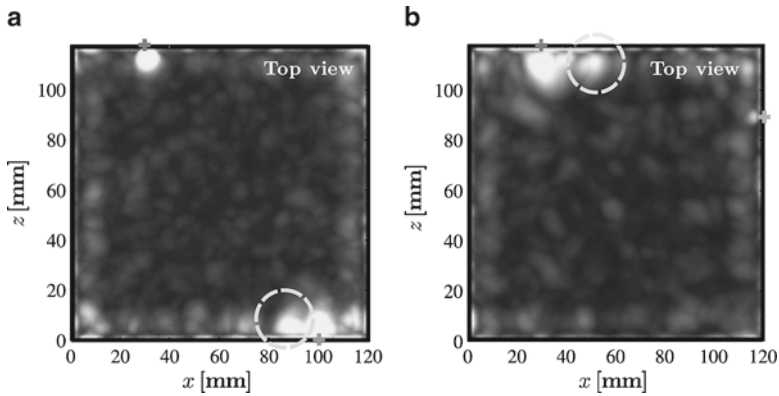
Fig. 3 (**a**) Snapshots @ $y = 20$ mm (left) and (**b**) @ $y = 25$ mm of a concrete cuboid displaying the total energy density of the out-coming scalar field. The radiation pattern of the pencil-lead-break source is well visible (dashed circle)
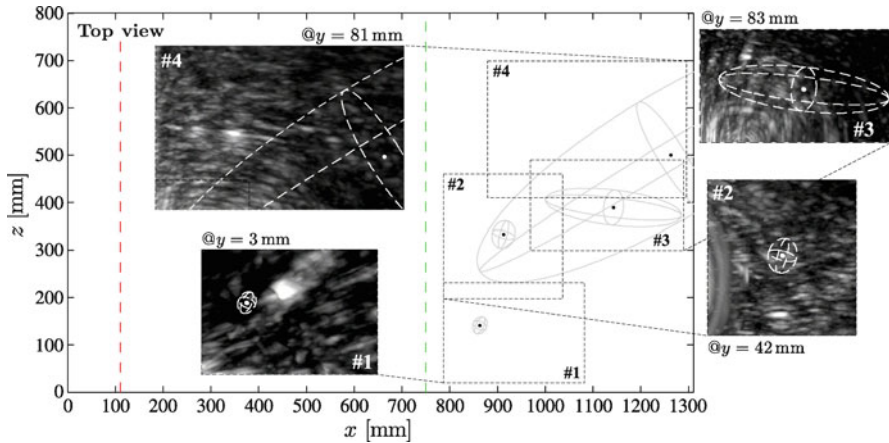
Fig. 4 AIC-based source locations (Fig. 2) together with the total energy density of the inverse displacement fields (TRM) for the AE sources #1 to #4

$[x,y,z] = [25,30,118]$ mm can be identified without doubt (see dashed circle in Fig. 3a, b). Typically, energy concentrations can always be observed at the sensor positions, represented by crosses in Fig. 3a, b, as well as some artefacts at the boarders due to remaining surface wave energy. The simulations are performed with a grid size of $\Delta h = 0.001$ m, a time increment of $\Delta t = 1.0 \times 10^{-7}$ s and a fundamental frequency of $f_{fund} = 100$ kHz.

Slab C3V2 is discretized with $1304 \times 804 \times 204$ grid points (gp) corresponding to the specimen size in mm. The effective elastic properties are assumed to be $c_{p,eff} = 3912$ m/s, $c_{s,eff} = 2272$ m/s and $\rho_{eff} = 2200$ kg/m^3 according to [6]. The input for the simulation consists in the four AE waveforms denoted #1 to #4 that have already been used for the AIC-based automatic localization. The simulation is performed separately for each set of waveforms. Figure 4 displays a top view of the

relevant detail areas where the AE sources are expected. The radiation patterns of all sources #1 to #4 can be identified as energy concentration in the enlarged dashed frames within a maximal distance of approx. 100 gp to the expected source locations (black dots with gray error ellipsoids).

Discussion and Conclusions

In general, both methods performed well. The strength of the AIC-based iterative algorithm is its adequacy for automation. Although the user has to intervene in some cases, the method is robust and reliable. The TRM does not depend on picking and no user interaction is required during the procedure. However, there is presently no automatic TRM procedure available for multiple sets of AE waveforms. The simulation requires a lot of computational time, but due to the increasing computing resources, this is a temporary obstacle. Once an automatic processing method can be developed, the TRM could be the better method.

References

[1] Grosse, C.U., Ohtsu, M. (2008), *Acoustic Emission Testing: Basics for Research – Applications in Civil Engineering; With Contributions by Numerous Experts*, Springer, Heidelberg.
[2] Schechinger, B. and Vogel, T. (2007), *Constr. Build. Mat.*, vol. 21, pp. 483–490.
[3] Kurz, J.K., Grosse, C.U. and Reinhardt, H.-W. (2007), *Ultrasonics*, vol. 43, pp. 583–546.
[4] Steiner, B., Saenger, E.H. and Schmallholz, S. (2008), *Geophys. Res. Let.*, vol. 35, L03, p. 307.
[5] Saenger, E.H., Kocur, G.K., Jud, R. and Torrilhon, M. (2011), *J. f Appl. Math. Mod.*, vol. 35, pp. 807–816.
[6] Saenger, E.H., Kocur, G.K. (2010). In: *Time Reverse Characterization of Sources in 2D and 3D Heterogeneous Media*, Proceedings of the 79th Annual International Meeting of Society of Exploration Geophysics, 4 p., Denver, USA.
[7] Ebert, B. (2010). In: *Strengthening of RC Slabs and Shells by Unilaterally Applied Shear Reinforcement*, Proceedings of the 8th fib PhD Symposium in Civil Engineering, pp. 124–138, Kgs. Lyngby, Denmark.

Use of Acoustic Emission Analysis to Evaluate the Self-Healing Capability of Concrete

K. Van Tittelboom, N. De Belie, F. Lehmann and C.U. Grosse

Abstract It has been estimated that, in Europe, 50% of the annual construction budget is spent on refurbishment and remediation of the existing structures [1]. Therefore, self-healing of concrete structures, which are very sensitive to cracking, would be highly desirable. In this research, encapsulated healing agents were embedded in the concrete matrix in order to obtain self-healing properties. Upon crack appearance, the capsules break and the healing agent is released, resulting in crack repair. The efficiency of this crack healing technique was evaluated by using acoustic emission (AE) analysis. Breakage of the capsules was proven as events with an energy higher than the energy related to concrete cracking were noticed. Upon reloading of beams with untreated cracks, fewer emissions were detected compared to beams with healed cracks. From this study it was shown that AE is a suitable technique to evaluate self-healing of cracks in concrete.

Keywords Acoustic emission analysis • Concrete • Cracking • Polyurethane • Self-healing

K. Van Tittelboom • N. De Belie (✉)
Magnel Laboratory for Concrete Research, Department of Structural Engineering,
Ghent University, Technologiepark Zwijnaarde 904, B-9052 Ghent, Belgium
e-mail: nele.debelie@UGent.be

F. Lehmann
Material Testing Institute, Department of Non-Destructive Testing and Monitoring Techniques,
Stuttgart University, Pfaffenwaldring 2b, D-70569 Stuttgart, Germany

C.U. Grosse
Non-destructive Testing Lab, Center for Building Materials, Technische Universität München,
Baumbachstr. 7, D-81245 Munich, Germany

Introduction

Concrete is used world-wide as construction material because of its excellent mechanical properties and relatively low cost. The only drawback is that concrete easily cracks because of the limited tensile strength. These cracks do not only cause high repair costs, they also endanger the durability of the structure. Aggressive substances may enter the cracks and cause concrete degradation. Due to this, cracks may grow. When the reinforcement is exposed to the environment, corrosion may originate and finally the structure may fail. Therefore, immediate and autonomous crack repair is strived for. Concrete already exhibits some natural self-healing properties as unreacted cement grains may react when coming into contact with water entering the crack [2]. This is one of the reasons why old concrete structures like the Roman Pantheon are still existing. However as 1 tonne of CO_2 is emitted during the production of 1 tonne of cement, nowadays, the dosage of cement in concrete is adapted. Due to the former cause and due to the fact that much finer cements are used, less unreacted cement is available now. Besides, the natural healing mechanism is limited to narrow cracks and is unpredictable. Therefore, research is done to improve the crack healing efficiency by encapsulating healing agents inside the concrete matrix [3, 4]. Granger et al. [5] made use of acoustic emission (AE) analysis to evaluate the natural crack healing efficiency of concrete. The promising results found by Granger et al. were the incentive to use AE in order to evaluate the crack healing ability of concrete with encapsulated healing agents.

Materials and Methods

Preparation of the specimens

Ceramic tubes, with an inner diameter of approximately 3 mm and a length of 100 mm, were used to carry the healing agent. A commercially available polyurethane-based healing agent was used to seal the cracks. This healing agent consists of two compounds, one compound is a prepolymer of polyurethane that starts foaming in moist surroundings. The second compound is an accelerator which shortens the reaction time. Half of the tubes was filled with the prepolymer and the other half was filled with a mixture of accelerator and water.

In order to protect the brittle tubes from breakage during preparation of the concrete beams, they were embedded inside mortar bars with dimensions of 20 mm x 20 mm x 120 mm. Mortar was made up of sand 0/2 (1530 kg/m³), cement CEM I 52.5 N (510 kg/m³) and water (255 kg/m³). In each mortar bar, tubes filled with the prepolymer and the accelerator were positioned next to each other.

Moulds with dimensions of 500 mm x 110 mm x 50 mm were used for preparation of four series of concrete beams. Concrete was composed of sand 0/4 (670 kg/m³), aggregates 2/8 (490 kg/m³), aggregates 8/16 (790 kg/m³), cement CEM I 52.5 N (300 kg/m³) and water (150 kg/m³). For the first three test series (reference specimens
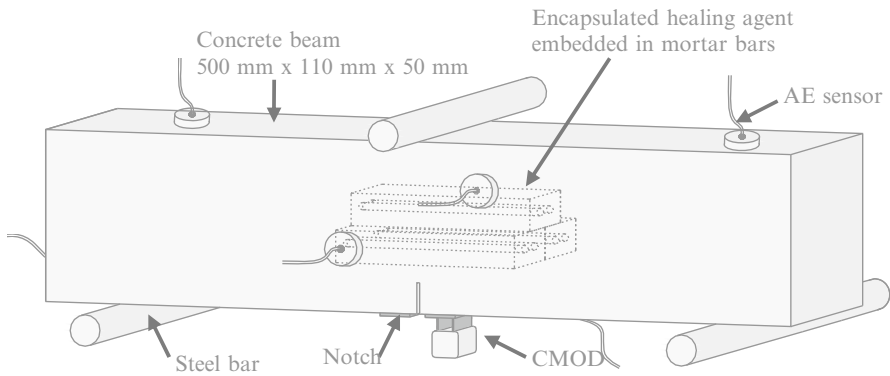
Fig. 1 Setup of the experiment showing the position of the protected ceramic tubes inside the concrete beam together with the position of some of the sensors

'REF', specimens of which cracks were treated manually with epoxy 'EPO' or polyurethane 'PUR'), standard concrete beams were prepared. When beams of the last test series (self-healing specimens with encapsulated polyurethane 'SHC_PUR') were made, the moulds were filled in several layers and the mortar bars, containing the tubular capsules, were positioned inside the beams. After casting, all moulds were placed in an air-conditioned room with a temperature of 20±2 °C and a relative humidity of 90±10 % for a period of 24 hours. After demoulding, the specimens were placed in the same room for at least 27 days. Finally, a 20 mm deep notch was sawn at the bottom, in the middle of the specimens. The design of the concrete beams with self-healing properties is shown in Fig. 1.

Creation of controlled cracks

Cracks were created by means of a crack width controlled three-point-bending test. The crack width was measured by means of a Crack Mouth Opening Displacement (CMOD) sensor, placed between two steel plates stuck on each side of the notch. The crack width was increased with a velocity of 0.5 μm/sec until a width of 300 μm was reached. At that point, the beam was unloaded giving cause to a residual crack width of about 225 μm.

During crack formation all beams were instrumented with an AE system. The instrumentation consisted of eight piezoelectric transducers (see Fig. 1) with a nominal diameter of 25 mm and a relatively flat frequency response below 1 MHz. The transducers were coupled to the concrete beams by means of hot glue. The detected signals were amplified with 54 dB gain amplifiers. The frequency range of the acquisition of wave forms was set from 1 kHz to 1 MHz. The slew rate trigger was set to 0.08 V/μs and an input range of ±5 V was chosen. The software TransOctoAE was used to record the AE signals.

Crack healing

For beams with self-healing properties, the healing mechanism was activated upon crack appearance. During crack formation, the tubes broke and both components of the healing agent were released into the crack due to capillary forces. When both components made contact, a polymerization reaction was triggered and the crack was healed. Cracks of the samples belonging to the test series 'PUR' and 'EPO' were treated immediately after crack formation with, respectively, polyurethane and epoxy. In the former case, the prepolymer was mixed with water and accelerator in the same proportions as encapsulated in the tubes, otherwise, both components of the epoxy resin were mixed according to the instructions of the provider. The cracked concrete beams were turned upside down and at the position of the crack, the sides of the beam were covered with tape. Then, the mixture was injected into the crack by means of a syringe with a needle. Injection was stopped when the crack appeared to be completely filled with healing agent.

Evaluation of the crack healing efficiency

24 hours after crack repair, the specimens were reloaded in three-point-bending in order to test the crack healing efficiency. During this reloading cycle sensors were coupled again in the same position as during crack creation.

Results and Discussion

The recorded events were filtered using the software All2SDF. A bandpass filter with a rectangular window with a lower and higher cut off frequency of 35 and 300 kHz, respectively, was used. For each event the according energy was determined and events were subdivided into seven classes based on their energy. Localization of the events was done based on the filtered signals and using the program PolarAE. The Hinckley criterion was used for automatic detection of the onset time. Subsequently, a selection of the events was made based on their energy (>1) and the number of channels used for localization (>5). All further analyses were performed onto these selected events.

In Fig. 2 the loading curves during crack creation (light grey) and reloading (dark grey) are displayed together with the emitted events (also light and dark grey). Each event is represented by means of a dot and based on their energy class they are represented in different levels.

Only for beams with encapsulated healing agent events from the highest energy level were noticed. It was thought that these events were caused by breakage of the embedded tubes as they were accompanied by drops in load and audible
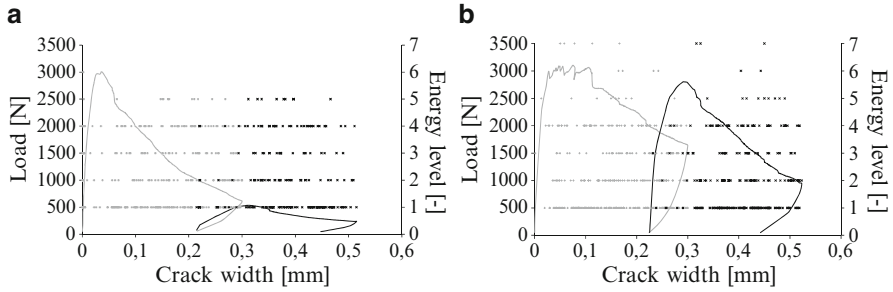
Fig. 2 Loading curve obtained during crack creation and reloading for an untreated (**a**) and autonomously healed (**b**) crack. The captured events are represented by means of dots depending on their energy level
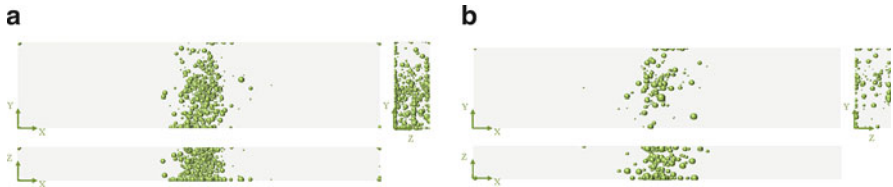
Fig. 3 Localization of the events during crack creation (**a**) and reloading (**b**), the sphere size is related to the released energy class, test specimen belonging to the test series REF

'pop' sounds. Also during reloading, the energy released for autonomously healed cracks is higher than for the other test series. This could be explained by the fact that some additional tubes broke upon reloading. This was also heard during the test and seen from the reloading curves. Due to the second release of healing agent, a second healing action may occur, as already noticed in previous experiments [6].

The position of the events was drawn on the XY, XZ and YZ plane of the beams. This was done for the loading and reloading cycle. For events with a bigger energy and thus belonging into a higher energy class bigger dots were used. It is seen in Fig. 3 that upon reloading of the beams less events were recorded. However, this is not only true for the reference beams but also for the beams from which the cracks were healed. While it was expected that more events would be captured upon reloading of the beams with healed cracks, this was not seen from these results.

The findings mentioned above could be explained by the fact that upon reloading of the beams different phases could be distinguished. In the first phase the crack just reopens for the reference beams or cracks appear in the healing agent in case of beams with healed cracks. When the crack opening, which was reached during crack creation, is reached again, new cracks start to form in the concrete matrix. This is the start of the second phase. The third phase corresponds to the moment when the adjusted crack width is reached, loading is stopped and the crack width decreases. As the second and the third phase are equal for all test series, and quite
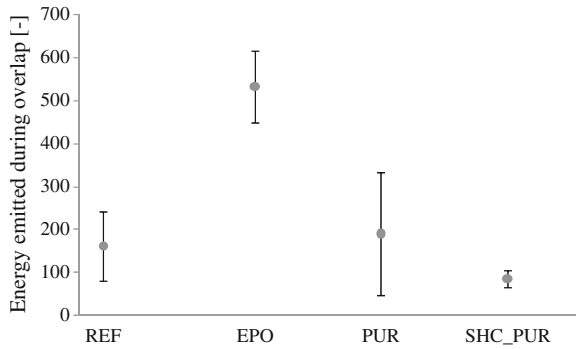
Fig. 4 Energy emitted during the first phase of reloading (this means during the overlap of pre-cracking and reloading); dots represent the mean value, error bars represent the standard error (n=5)

some events are produced during the second phase, these events may mask the differences between the first phases of the different test series.

Therefore the energy of all events which occurred during the first phase was cumulated. A significant difference was noted between the energy released for cracks manually healed with epoxy and the other test series (Fig. 4). For the specimens where the cracks were healed with polyurethane (manually or automatically) no significant difference was noted; however, from the regain in mechanical properties [7] it was seen that these cracks were healed. That no significant difference is seen by means of AE can be explained by the fact that crack formation into the polyurethane foam does not cause events with high energy.

Conclusions

From this study we can conclude that breakage of the tubes of self-healing concrete can be proven by means of AE measurements. Although self healing of cracks using PU as healing agent is not proven from the AE measurements presented in this paper, crack healing is proven in the case epoxy resin is used as healing agent. The possibility to use AE as indicator for self-healing of cracks, will therefore depend on the mechanical properties of the healing agent used.

References

[1] Cailleux, E. and Pollet, V. (2009), *Investigations on the development of self-healing properties in protective coatings for concrete and repair mortars*, Proceedings of the 2nd International Conference on Self Healing Materials, pp. 120.

[2] Neville, A. (2002, *Autogenous healing – A concrete miracle?*, Concrete International 24 (11), pp. 76–82.

[3] Li, V.C., Lim, Y.M. and Chan, Y-W. (1998), *Feasibility study of a passive smart self-healing cementitious composite*, Composites Part B: Engineering 29(6), pp. 819–827.

[4] Dry, C. and Corsaw, M. (2003), *A comparison of bending strength between adhesive and steel reinforced concrete with steel only reinforced concrete*, Cement and Concrete Research 33(11), pp. 1723–1727.

[5] Granger, S., Loukili, A., Pijaudier-Cabot, G. and Chanvillard, G. (2007), *Experimental characterization of the self-healing of cracks in an ultra high performance cementitious material: Mechanical tests and acoustic emission analysis*, Cement and Concrete Research 37(4), pp. 519–527.

[6] Van Tittelboom, K., De Belie, N., Van Loo, D. and Jacobs, P., *Self-healing efficiency of cementitious materials containing tubular capsules filled with healing agent*, submitted.

[7] Van Tittelboom, K., De Belie, N., Lehmann, F. and Grosse, C. (2010), *Towards durable concrete that repairs cracks autonomously*, Proceedings of International RILEM Conference on Use of Superabsorbent Polymers and Other New Additives in Concrete, pp. 285–292.

Identification of Tendon Ducts in Prestressed Concrete Beam by SIBIE

M. Yamada, K. Tagomori and M. Ohtsu

Abstract The impact-echo method is well-known as a non-destructive testing for concrete structures. It is based on the use of low-frequency elastic waves that propagate in concrete to determine thickness or to detect internal flaws in concrete. In this method, the presence and the locations of defects in concrete are estimated from identifying peak frequencies in the frequency spectra, which are responsible for the resonance due to time-of-flight from the defects. In practical applications, however, spectra obtained include so many peak frequencies that it is fairly difficult to identify the defects correctly. In order to improve the impact-echo method, Stack Imaging of spectral amplitudes Based on Impact Echo (SIBIE) procedure is developed as an imaging technique applied to the impact-echo data, where defects in concrete are identified visually at the cross-section. In this study, the SIBIE procedure is applied to identify grouted or ungrouted post-tensioning ducts in prestressed concrete beam. It is demonstrated that the ungrouted duct can be identified with reasonable accuracy.

Keywords Impact-echo • NDE • Prestressed concrete • SIBIE • Ungrouted tendon duct

Introduction

Stack Imaging of Spectral Amplitudes Based on Impact-Echo (SIBIE) procedure is developed to improve the impact-echo method, as the impact-echo method is well known as a non-destructive testing for concrete structures [1]. The method has been applied to thickness measurement of a slab, grouting performance and void detection in a post-tensioning tendon duct, identification of surface-opening crack depth, location of delamination and determination of material properties.

M. Yamada (✉) • K. Tagomori • M. Ohtsu
Graduate School of Science and Technology, Kumamoto University, Kumamoto, JAPAN
e-mail: 091d9112@st.kumamoto-u.ac.jp

The impact-echo method has been widely applied to identification of void in tendonducts [1, 2]. In principle, the location of void is estimated by identifying peak frequencies in the frequency spectrum. However, the frequency spectrum cannot always be interpreted successfully, because many peaks are often observed in the spectrum. Particularly, in the case of a plastic duct, it becomes more difficult to interpret the frequency spectrum due to the existence of many peaks. This is because a plastic duct has lower acoustic impedance than concrete or grout. In order to circumvent it, the SIBIE procedure is developed [3], and is applied to void detection within tendon ducts [4]. In the present paper, the effect of prestressing is examined.

Principle

Impact-echo method

The cross-section of a specimen is shown in Fig. 1. When the elastic wave is driven, the paths of the elastic wave are shown. Frequency spectrum is interpreted by Fast Fourier transform (FFT) analysis to an obtained waveform from the output point. In this spectrum, peak frequencies could be appeared at f_t and f_{void}, so calculated as,

$$f_t = C_p/2T, \tag{1}$$

$$f_{void} = C_p/2d, \tag{2}$$

where C_p = velocity of P-wave, T = plate thickness, and d = covered depth. The plate thickness and the cover depth are obtained by substituting f_t or f_{void} with C_p into these equations.

SIBIE procedure

SIBIE procedure is a post-processing technique to impact-echo data. This is an imaging technique for detected waveforms in the frequency domain. In the procedure, first, a cross-section of concrete is divided into square elements as shown in Fig. 2. Then, resonance frequencies due to reflections at each element
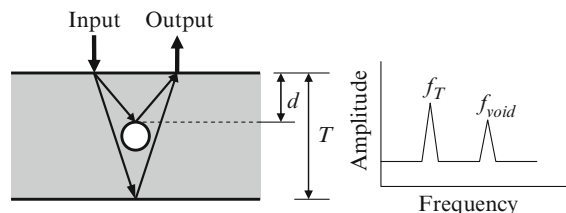
Fig. 1 Principle of void detection

Fig. 2 SIBIE imaging model
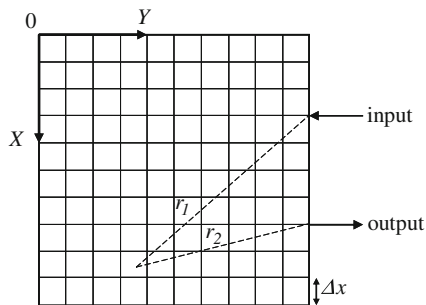
Fig. 3 Example of SIBIE result
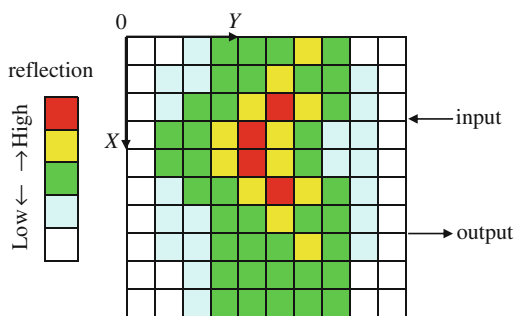
are computed. The travel distance from the input location to the output via the element is calculated [4] as,

$$R = r_1 + r_2 .\tag{3}$$

Resonance frequencies due to reflections at each element are calculated from,

$$f_R = C_p / R,\tag{4}$$

$$f_{r_2} = C_p / r_2.\tag{5}$$

Spectral amplitudes corresponding to these two resonance frequencies in the frequency spectrum are summed up. Thus, reflection intensity at each element is estimated as a stack image as shown in Fig. 3. The minimum size of the square mesh Δ for the SIBIE analysis should be approximately equal to $C_p \Delta t / 2$.

Experiments

The specimen of dimensions 250 mm × 1000 mm × 300 mm was designed. A post-tensioning tendon ducts was contained in the concrete specimen. The diameter of the polyethylene duct was 40 mm. It was located at 50 mm depth from the bottom of the specimen. The specimen is illustrated in Fig. 4. First, the duct was ungrouted and the specimen was kept un-prestressed at the measurement. Next, the specimen
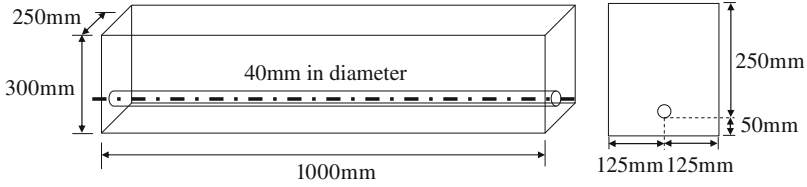
Fig. 4 Overview of the specimen

Fig. 5 Ultrasonic pulse-velocity test
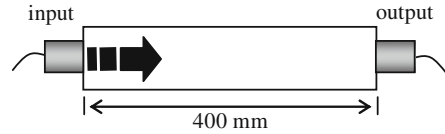
Fig. 6 Aluminum bullet
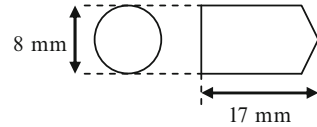
Fig. 7 Impact point
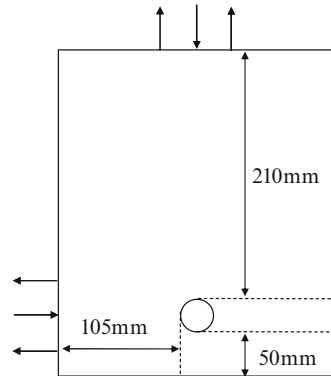
was tensioned by prestressed concrete steel bar in order to find the effect of prestressing. Finally the duct was fully grouted.

Before prestressing P-wave velocity of the test specimen was obtained as 4025 m/s by the ultrasonic pulse-velocity test. After prestressing P-wave velocity was measured as 4150 m/s. This might be the effect of stressing as well as curing. Dimensions of the specimen tested are 100 mm × 100 mm × 400 mm as shown in Fig. 5. In the impact test, the aluminum bullet of 8 mm diameter was shot by driving compressed air with 0.05 MPa pressure to generate elastic waves. Figure 6 shows the aluminum bullet. It is confirmed that the upper bound frequency due to the impact could cover up to 40 kHz, by using an accelerometer system. Fourier spectra of accelerations were analyzed by Fast Fourier Transform (FFT). Sampling time was 4 μ sec and the number of digitized data for each waveform was 2048.The locations of impact and detection are also shown in Fig. 7. Two accelerometers were placed

at the detection points to record surface motions caused by reflections of the elastic waves. Here, the interval between the impact point and the detection point was 50 mm.

Results and Discussion

The SIBIE analysis was conducted by simply adding two impact-echo results obtained from two accelerometers for each case to visually identify location of the void in a polyethylene duct. The cross-section of the concrete specimen was divided into square elements to perform the SIBIE analysis. In this study, the size of square mesh for SIBIE analysis was set to 10 mm.

SIBIE Results at un-prestressed condition

First, specimen was tested under the un-prestressed condition. The SIBIE results is given in Fig. 8, which shows a cross-section of the specimen where the ducts are located. The size of cross-section is 250 mm × 300 mm. The red color regions indicate the higher reflection due to presence of void. Open circles indicate the ducts, and the impact point and the detection points are indicated by upward
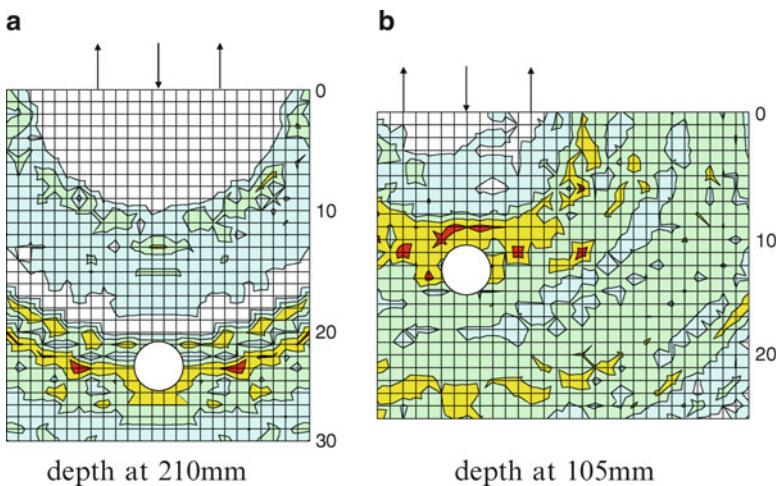
Fig. 8 SIBIE Result under un-prestressed condition
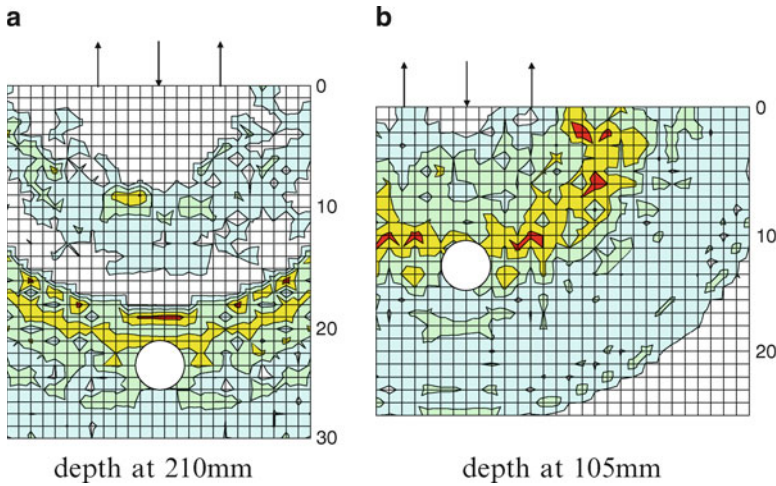
Fig. 9 SIBIE Result under prestressed condition

arrows and a downward arrow, respectively. It is clearly seen that there exists high reflection zone in front of the ungrouted ducts. There are no other high reflections observed at the cross-section.

SIBIE Results at prestressed condition

In Fig. 9, SIBIE results of the impact test for the case under the prestressed condition are shown. Red and yellow color of high reflection are clearly observed in front of the duct in both results. There are no other high reflections observed at the cross-section. There are no differences between the SIBIE result of under the un-prestressed and prestressed condition. This result implies that the prestress has little influence on the SIBIE results.

SIBIE Results at fully-grouted condition

In Fig. 10, SIBIE results of impact test for the case under the fully-grouted condition are shown. Gray circles indicate the fully grouted ducts. The high intense regions due to the plate thickness are observed at both results, however, The high intense regions can not be observed in front of the duct in both results. From this result, it is confirmed that the SIBIE procedure is available for void detection within post-tensioning tendon duct.
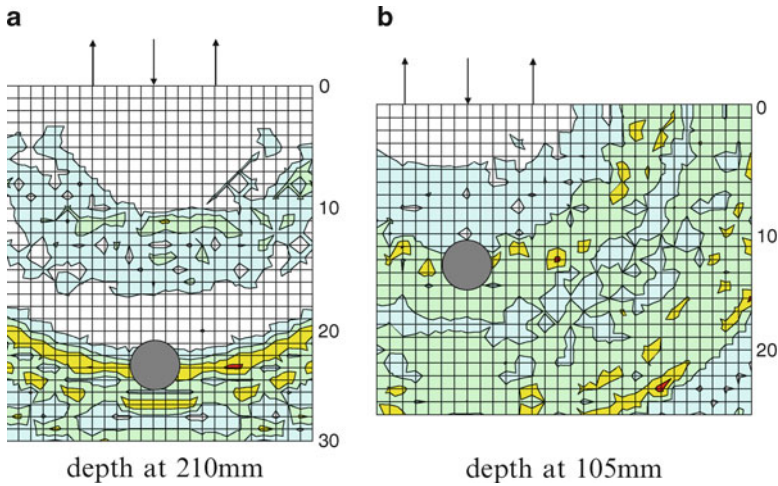
Fig. 10 SIBIE Result under fully-grouted condition

Conclusions

Results obtained are summarized as follows:

(1) It is confirmed that location of the ungrouted duct can be clearly identified using the SIBIE procedure.
(2) There are no differences in the SIBIE results for the cases with or without prestressing.
(3) The high intensty regions can not be observed in front of the duct for the fully grouted case.

Thus, it is demonstrated that the void within tendon duct can be identified with reasonable accuracy by the SIBIE procedure.

References

[1] Sansalone M.J. & Streett W.B. 1997a. Impact-echo, Ithaca, NY: Bullbrier Press.
[2] Sansalone M. 1997b. Impact-echo: The complete story, *ACI Structural Journal*, 94(6), 777–786
[3] Jaeger B.J. & Sansalone M.J. 1996. Detecting voids in grouted tendon ducts of post tensioned concrete structures using the impact-echo method, *ACI Structural Journal*, 93(4), 462–472.
[4] Ohtsu M. & Watanabe T. 2002. Stack imaging of spectral amplitudes based on impact-echo for flaw detection, *NDT&E International*, 35, 189–196.

Absolute Calibration of an Acoustic Emission Sensor

G.C. Mclaskey and S.D. Glaser

Abstract Calibrated sensors are essential for quantitative comparisons of acoustic emission source mechanics. We describe experimental techniques and mathematical models for implementation of an absolute sensor calibration scheme using glass capillary fracture and ball impact, two sources which can be easily implemented. Additionally, we describe the specific experimental procedures for absolute sensor calibration using the both the fracture of a glass capillary tube, and drop of a 0.4 mm ruby ball, as the calibration source. The mathematical formulation is based on a Green's function formalism. The Glaser-type conical piezoelectric sensor, used as an example in this study, has a noise floor of approximately 1 picometer displacement when coupled to steel. The amplitude of the sensor response is flat within 3 dB from 50 kHz to 2 MHz at a level of 0 dB relative to 1 V/nm.

Introduction

Modern studies of microseismic sources and stress wave propagation have shown that acoustic emission (AE) signals are a function of the AE source, wave propagation effects, and sensor effects [1]. These components are described schematically in Fig. 1. Typical AE analyses treat this chain of effects as a black box. While these studies are very useful for correlating counts of AE activity with other measurements and for finding the location of the AE sources within the specimen, they lack quantitative information about the amplitude and properties of the AE sources.

G.C. Mclaskey (✉) • S.D. Glaser
University of California, Berkeley
e-mail: glaser@berkeley.edu
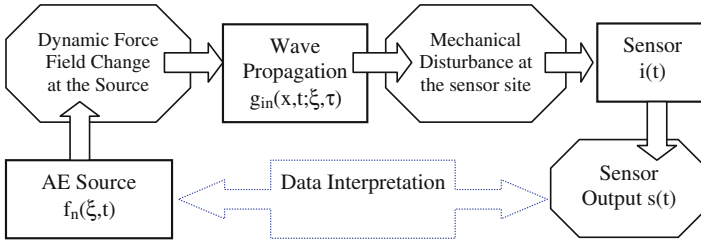
Fig. 1 Block diagram of the path linking the AE source to the sensor output

If, instead, we analyze and model the wave propagation effects and sensor response, we can quantify the time history of absolute amplitudes, orientations, and moments which generate AE. With a fully calibrated system, it is entirely possible to quantify and classify AE in much the same way as earthquakes and other seismic sources are described. This will enable AE researchers to quantitatively compare findings with others, advance our collective understanding the physics and mechanics of AE, and lead to improved AE monitoring techniques. In this paper, we present a transfer-function-type calibration scheme which relies on a Green's function formalism [2-3], and describe, in detail, the methodology used for absolute sensor calibration.

In order to calibrate an AE sensor, we must isolate the sensor's behavior. Both input and the output to the *Sensor* box, shown in Fig. 1, must be known. We must be able to calculate, or measure by some other means, the mechanical disturbance (e.g. displacement, velocity, acceleration, strain) which would exist at the sensor location. The expected disturbance is then compared with the recorded sensor output. This comparison can be achieved with a reference sensor (i.e. some other sensor which has already been absolutely calibrated) [4], but in the absence of such a sensor, we rely on known and well-characterized artificial AE sources.

Following Fig. 1, sensor output, s(t), can be represented mathematically as

$$s(t) = f_n\left(\zeta,\tau\right) * g_{in}\left(x,t;\zeta,\tau\right) * i(t) \tag{1}$$

where * represents convolution, $f_n(\xi,\tau)$ is the force acting in the n direction that the calibration source imposes on the test specimen, $g_{in}(x,t;\xi,\tau)$ is the elastodynamic Green's function which describes the displacement in the i direction at point x at time t due to a unit impulsive force at location ξ in the direction n at time τ [5], and i(t) is the instrument response function which we would like to determine.

Calibration Sources

In order to determine i(t), a known source $f_n(t)$, which produces vibrations of known amplitude and shape, is required. We must have a specimen of relatively simple geometry for which we can easily calculate the effects of wave propagation,

$g_{in}(x,t;\xi,\tau)$. Though many different mechanical, electromechanical, and thermome-chanical sources exist, this paper focuses on two simple mechanical sources, capillary fracture and ball impact. For both sources, the direction n in which the source acts is normal to the plane of the test specimen surface.

When conducting a calibration test using a glass capillary fracture source, a short (~ 2 mm) length of thin walled glass capillary tube is laid on its side and slowly loaded with a small but blunt object until it fractures. For AE tests, the capillary is typically 100 to 400 μm in diameter and breaks at a force of 5 - 25 N. When the capillary fractures, the force that was applied to the capillary unloads very rapidly. The force time history, f(t), that the capillary fracture imposes on the test specimen is known to be very nearly equal to a step function with a rise time (or unload time) of less than 100 ns [2]. This source has been used by many researchers because the force at which the fracture occurs (and therefore the amplitude of the step) can be independently measured.

For a ball impact calibration test, a ~1 mm diameter ball is dropped, the impact of which imparts an impulse-like force onto the test specimen. McLaskey and Glaser [6] verified that the collision of a small ball on a planar surface of a sufficiently thick specimen is well modeled by Hertzian impact theory for steel, glass, aluminum, and polymethlymethacrylate (PMMA) materials. The precise force time function, f(t), that the ball imparts to the test specimen can be calculated

$$
\begin{aligned}
f(t) &= f_{max} \sin\left(\pi / t_c\right)^{3/2} \quad 0 \le |t| \le t_c \\
f(t) &= 0 \qquad\qquad\qquad\quad \text{otherwise,}
\end{aligned}
\tag{2}
$$

where the time the ball spends in contact with the specimen,

$$
t_c = 4.53\left(4\rho_1(\delta_1 + \delta_2)/3\right)^{-2/5} R_1 v_0^{-1/5},
\tag{3}
$$

and the maximum force,

$$
f_{max} = 1.917\rho_1^{3/5}\left(\delta_1 + \delta_2\right)^{-2/5} R_1^2 v_0^{6/5}
\tag{4}
$$

For Equations 2 through 4, $\delta_i = (1-\mu_i^2)/(\pi E_i)$, and E and μ are the Young's modu-lus and Poisson's ratio, respectively. Subscript 1 refers to the material of the ball and subscript 2 refers to the material of the test specimen. As a rule of thumb, if the ball bounces back to only half its original height, then the peak force $f_{max1/2} \approx 0.75 f_{max}$. The change in momentum that the ball imparts to the test block can be independently calculated based on the mass of the ball and the rebound height. This change in momentum is equal to the area under the curve f(t). By using balls of various sizes and different drop heights, this source offers variability in ampli-tude and frequency content with which to test sensor linearity and bandwidth. The usable upper frequency limit for calibration by ball drop is a function of ball diameter – the smaller the ball, the first spectral zero appears at higher frequencies.
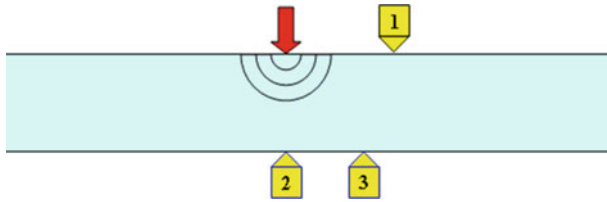
Fig. 2 Experimental setup for calibration tests

Test Geometry

The calibration tests described below were performed on a 50 mm thick steel plate, 610 mm square. Three typical sensor locations relative to the location of the calibration source are shown in Fig. 2. Location 1 is a surface location on the same side of the test block as the source where the bulk of the energy is carried by Raleigh waves, which includes motions both parallel and perpendicular to the plane of the plate. For the epicentral location 2, directly beneath the source, all displacements are in the plate normal direction, and the majority of motions are due to the P wave. Location 3 is an off-epicentral, with wave displacements at some oblique angle from the surface normal, resulting in both P waves and large S waves. By comparing and contrasting the output from sensors at the three different locations, the effects of the sensor aperture and directionality can be studied.

Greens functions for the plate geometry can be calculated analytically only for a few geometries. Other geometries require numerical models such as finite element or finite difference codes. For this work, Green's functions were calculated with a computer program [7] which uses a generalized ray theory approach.

Calibration Procedures

A set of calibration tests were performed on Glaser-type conical piezoelectric sensors in order to illustrate the method. These sensors are known to be sensitive to surface normal displacements and have an extremely flat (within 3 dB) frequency response between 20 kHz and 2 MHz [6]. While these sensors have been calibrated on many different materials, using different sources, and sensor locations, we report the details of a set of calibration tests, using both a glass capillary fracture and ball drop, performed in Location 1 with 45 mm of source-sensor separation. The signals were digitized at 10 MHz, with 16-bit dynamic bandwidth.

During the calibration test, the capillary is loaded to fracture and the corresponding AE signal, s(t), is recorded. The force on the capillary when it fractured was measured with a load cell to be 13 +/- 0.3 N. The theoretical displacements, $u(t) = f_n(\xi,\tau) * g_{in}(x,t;\xi,\tau)$ are shown in Fig. 3a. This was calculated by convolving the appropriate Greens function with a 13N step function acting normal to the plate. The Fourier transform of u(t), $U(\omega) = F_n(\xi,\omega)G_{in}(x,\varpi;\xi,\omega)$, was obtained
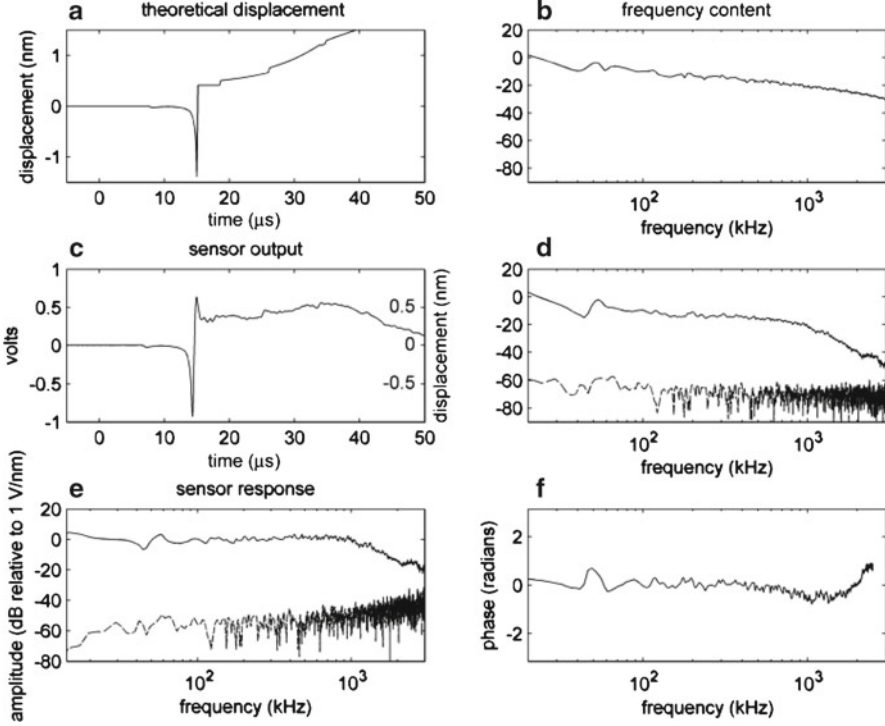
Fig. 3 (**a**), Theoretical displacements, u(t), due to a 13 N glass capillary fracture for Location 1 in the experimental arrangement shown in Fig. 2. (**b**), Amplitude of the Fourier transform of u(t). (**c**), Recorded signal, s(t), in response to the 13 N capillary fracture. (**d**), Amplitude of the Fourier transform of s(t) compared with amplitude of a noise signal (dashed line). (**e**), Amplitude of sensor response I(ω) compared with noise floor (dashed line). (**f**), Phase of I(ω)

and windowed with a Blackman Harris window. The amplitude of the Fourier transform of the theoretical signal, $|U(\omega)|$, is shown in Fig. 3b.

The AE signal, s(t), recorded from the capillary test is shown in Fig. 3c. The difference in the time histories between theory and experiment in the latter portion is due to the insensitivity of the piezo-based sensor below about 10kHz. The Fourier transform of this signal, $S(\omega) = F_n(\xi,\varpi)G_{in}(x,\omega;\xi,\varpi)I(\omega)$, was obtained with the FFT algorithm and windowed in the exact same way as u(t). The amplitude, $|S(\omega)|$, is shown in Fig. 3d. The amplitude of the Fourier transform of a sample of noise is also shown in Fig. 3d. The 400 μs noise sample is taken from the recorded AE signal prior to the first wave arrival, and it is also windowed with a Blackman Harris function.

Sensor response, I(ω), is obtained by dividing the Fourier transform of the recorded AE signal by the Fourier transform of the theoretical signal:

$$I(\omega) = \frac{S(\omega)}{U(\omega)} F_n\left(\zeta,\varpi\right)G_{in}\left(x,\omega;\zeta,\varpi\right)\frac{I(\omega)}{F_n\left(\zeta,\varpi\right)G_{in}\left(x,\omega;\zeta,\varpi\right)}. \tag{5}$$

The amplitude and phase of I(ω) are shown in Fig. 3e, f, respectively. The noise response (amplitude shown in Fig. 3e, dotted line) is calculated by dividing the Fourier transform of the noise signal by the Fourier transform of the theoretical signal. Because the recorded signal was in units of Volts and the theoretical signal was in units of nm, the sensor response will be in V/nm. The sensor amplitude response is flat within 3 dB from 20 kHz to 2 MHz at a level of 0 dB relative to 1 V/nm, therefore the sensitivity can be well approximated as 1 V/nm in this frequency range. The noise response is about -60 dB (three orders of magnitude down); the noise floor in the testing condition is approximately 1 pm.

Calibration studies have shown that while the frequency response (the shape of I(ω)) does not change dramatically when the sensor is coupled to different engineering materials, the absolute sensitivity can vary by an order of magnitude, due to the different acoustic impedance of various materials [6,8]. Thus, test results on different materials should be scaled accordingly. This calibration is only strictly valid from about 50 kHz - 2.5 MHz. Because the calculated Green's functions are for an infinite plate geometry, we only include signals recorded before reflections arrive from the side edges of the plate, which allows time windows no greater than about 400 μs to be used for calibration purposes. Below 50 kHz, less than 20 periods are captured in this 400 μs time window, therefore there is high uncertainty in spectral estimates below about 50 kHz. Above 2.5 MHz, signal to noise ratio drops below about 20 dB for the capillary fractures used in these experiments.

Conclusions

A method to absolutely calibrate AE sensors using capillary and ball-drop sources was presented. The method uses a Green's function formalism and a ray-tracing calculation of the theoretical response to these sources as the reference. A set of calibration tests were performed on Glaser-type conical sensors in order to illustrate the method. This sensor has a noise floor of approximately 1 picometer when coupled to steel, an amplitude response, flat within 3 dB from 50 kHz to 2 MHz, at 0 dB relative to 1 V/nm. The instrument response for both sources matched the theoretical expectation. Small differences seen in the results from the different calibration sources highlight deficiencies in the source models.

References

[1] Grosse, C., and Ohtsu, M. (2008). *Acoustic Emission Testing*, Springer-Verlag.
[2] Breckenridge, F., Tscheigg, C., and Greenspan, M. (1975). J. Acoust. Soc. Am. vol. 57, pp. 626–631.
[3] Hsu, N., and Breckenridge, F. (1981). Mater. Eval. vol. 39, pp. 60–68.
[4] Breckenridge, F., and Greenspan, M. (1981). J. Acoust. Soc. Am. vol. 69, pp. 1177–1185.

[5] Aki, K., and Richards, P. (1980). *Quantitative Seismology—Theory and Methods*, Freeman, San Francisco.

[6] McLaskey, G., and Glaser, S. (2010). J. Acoust. Soc. Am. vol. 128 n. 3, pp. 1087–1096

[7] Hsu, N. (1985). *Dynamic Green's functions of an infinite plate—A computer program.* Technical Report No. NBSIR 85–3234, National Bureau of Standards.

[8] Eitzen, D., and Breckenridge, F. (1987) in *Nondestructive Testing Handbook Second Edition Vol. 5: Acoustic Emission Testing.* Eds. Miller, R. K., and McIntire, P., American Society for Nondestructive Testing, pp. 121-132.

NDE with Lockin-Interferometry: Principle and Applications

G. Busse and P. Menner

Abstract Speckle-interferometric imaging is a well known method where the difference between two deformation states of an object (with and without applied load) is displayed as a fringe pattern. The standard procedure for finding hidden defects is to compare the observed fringe pattern either to the pattern that one expects or to one measured on a reference component. Observed differences are then attributed to a defect. We show how the method can be improved in terms of signal to noise ratio and resolution. The idea is to apply the modulation principle to speckle-interferometry that makes lockin-thermography superior to conventional thermography: The inspected object is periodically illuminated to induce a thermal wave and a corresponding modulation of thermal expansion while fringe images are recorded with electronic speckle pattern interferometry (ESPI) or shearography. Then, the time-dependent content of each pixel is Fourier transformed at the excitation frequency. This way the information content is compressed into local amplitude and phase of the response at this frequency. In the phase image, defects reveal themselves as deviations from a constant background and can therefore be identified easily. The signal to noise ratio is improved by up to an order of magnitude. Depth range can be adjusted by variation of the modulation frequency. This paper shows results of model samples as well as of automotive and aerospace parts.

Keywords Defect-selective imaging • Interferometric depth profiling • Lockin-ESPI • Lockin-shearography

G. Busse (✉) • P. Menner
Institute of Polymer Technology (IKT), Non-Destructive Testing (IKT-ZfP),
Stuttgart University, Pfaffenwaldring 32, 70569 Stuttgart, Germany
e-mail: gerd.busse@ikt.uni-stuttgart.de

Introduction

Shearography measures the derivative of displacement by superposing the speckle pattern of two different object states, usually caused by a short, static loading [1]. However, the depth of defects cannot be determined, and in some cases, the signal from a flaw is hidden by the large deformation of the sample itself, which reduces the probability of detection. The elimination or reduction of these drawbacks could increase the acceptance of shearography as a fast robust remote ndt method.

Methodology

Lockin shearography

Lockin shearography combines a conventional shearography setup with a dynamic excitation and a Fourier analysis. By modulating the intensity of halogen lamps, the object surface is heated periodically, thereby launching a thermal wave into the object. At thermal boundaries, the wave is reflected back to the surface where it is superposed to the initial thermal wave. This way, both local phase angle and amplitude of the modulated temperature field are modified.

The shearography sensor continuously records fringe images during the modulated excitation. After unwrapping, the image stack undergoes a pixelwise discrete Fourier transformation at the excitation frequency. This transformation extracts phase and amplitude of the modulated object displacement, thereby eliminating the dc level and condensing the image stack to only two images: the amplitude image and the phase angle image (Fig. 1). This principle of signal evaluation of an image stack is well known from optically excited lockin thermography [2-6] and was transferred to ESPI [2, 7] and to shearography [8]. In an intact sample with constant thickness, the whole object is deforming uniformly, so the thermal phase is constant.
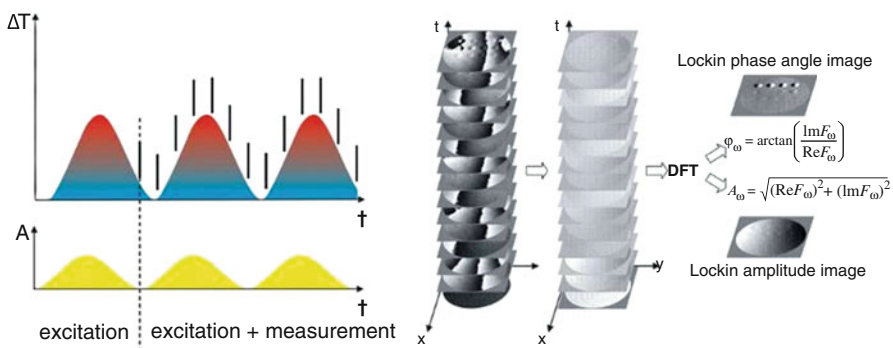
Fig. 1 Lockin shearography measurement procedure

Fig. 2 Lockin shearography system

Defects affect the local phase by reflecting the thermal wave, which makes it easy to find them. The thermal diffusion length μ depends on excitation frequency [9]:

$$\mu = \sqrt{\frac{2\alpha}{\omega}} \qquad (1)$$

with α = thermal diffusivity and ω = modulation frequency of excitation. Therefore, the depth range (which depends on μ) can be adjusted by variation of the excitation frequency to allow for depth profiling. The compression of the image stack via Fourier transformation increases the signal-to-noise ratio (SNR) since not only one image is used for data evaluation, but up to 1000 fringe images.

Experimental setup

For our lockin shearography system (Fig. 2), we use a conventional home-made out-of-plane sensor. Illumination is performed either with a DPSS laser (5W, 532nm) or an array of laser diodes (16x 80mW, 658nm). For thermal excitation, 4kW halogen lamps with lee filters are used. Data processing is performed on an nvidia GPU. The system consists of a PC with a frame grabber and a control card, a piezo amplifier, a dimmpack and a relais card, and is integrated in a flight case.

Results

CFRP plate with inserts

A CFRP sample ($450x375x5mm^3$, Fig. 3 left) with different kinds of inserts located in depths from 1.5mm to 3.5mm was tested both with conventional and lockin shearography.

In the conventional image, the teflon inserts cannot be observed at all, and some defects are difficult to detect due to the gradient caused by the deformation of the whole sample. In the Lockin phase image, almost all inserts can be detected due to the improved signal-to-noise ratio and the reduced gradient. The SNR can be enhanced by up to one order of magnitude [8], depending of the number of images.

PMMA plate with matrix of rear surface flat bottom holes

According to eq. 1, the diffusion length of a thermal wave depends on its frequency, so the depth range of the method can be adjusted. A black acrylic glass plate (140x140x3mm3, Fig. 4 bottom left) with defect sizes from 2mm to10mm and defect depths from 0.5mm to 2.5mm was inspected at various frequencies.
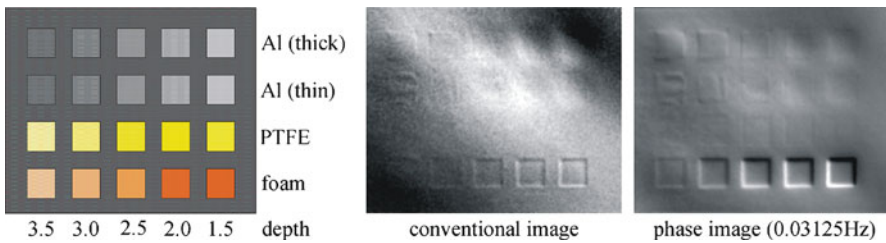
Fig. 3 CFRP plate with simulated defects (left), measured with conventional optically excited shearography (middle) and lockin shearography (right)
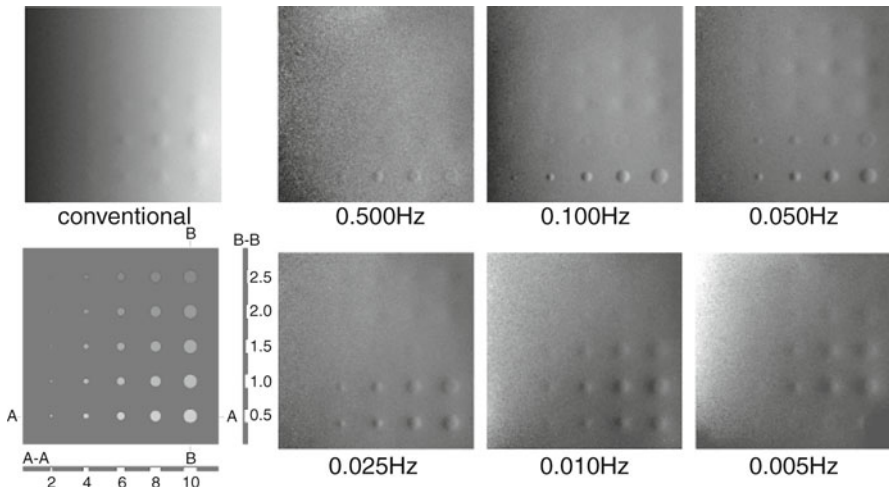
Fig. 4 PMMA plate with blind holes (bottom left), measured with conventional shearography (top left) and lockin shearography at various frequencies (right)

In the conventional shearography image, some defects are visible, but a large displacement of the whole sample can be observed as well. In the Lockin phase images, this displacement is reduced due to the narrow band Fourier filtering of the frequency-coded response, so defect detection is much easier. As the diffusion length of the thermal waves increases with decreasing frequency, more and more flat bottom holes become visible. The apparent defect size increases with larger depth and lower frequency due to lateral heat flow.

Applications

Sandwich rim of a race car

The CFRP/foam-sandwich rims shown in Fig. 5 are in-service parts from a race car built for the formula student.

The weight of these rims is half the one of rims made from aluminum, but the first series was also more sensitive to damages. Lockin shearography measurements revealed cracks in all torque arms, while conventional shearography failed due to a poor SNR and speckle decorrelation because of the necessity of a high loading (Fig. 5, see white marks).

Horizontal stabilizer of a power glider

The horizontal stabilizer (Fig. 6) of the power glider Hydrogenius which is being developed at the Institute of Aircraft Design (IFB) at the University of Stuttgart was tested to verify that the blind glueing of the cover to the spar was successful (Fig. 7).
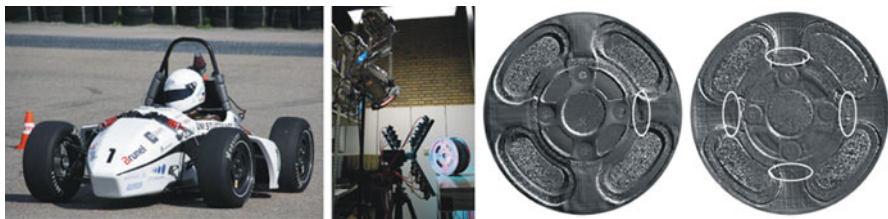
Fig. 5 CFRP/foam rim (left) during shearography testing (middle). Results of conventional shearography and lockin phase image at 0.125 Hz (right)
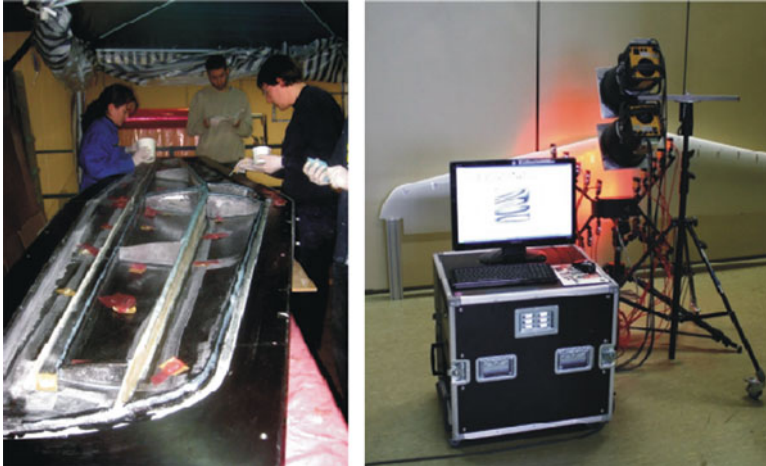
Fig. 6 Horizontal stabilizer during manufacturing (left) and lockin shearography tests with mobile setup (right)
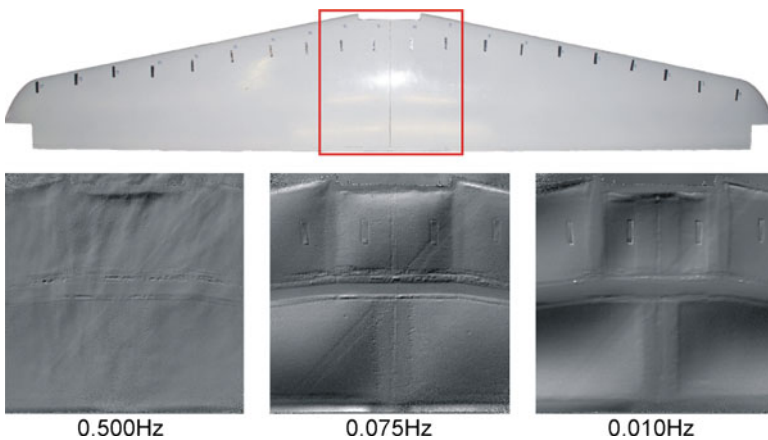
Fig. 7 Measurement field of the horizontal stabilizer (top), lockin phase images at different frequencies (bottom)

Conclusions

Conventional shearography is a fast and easy method for remote full field NDT. In combination with the lockin technique, thermal wave phase angle images are obtained that feature an increased signal-to-noise ratio, allow for depth profiling and elimination of whole body displacement effects.

References

[1] Leendertz J. A. and Butters J. N. (1973), An image-shearing speckle-pattern interferometer for measuring bending moments, Journal of Physics E: Scientific Instrument 6, pp. 1107-1110.

[2] Carlomagno G. M. and Berardi P. G. (1976), Unsteady thermotopography in non-destructive testing, Proc. 3rd Biannual Infrared Information Exchange, St. Louis/USA, pp. 33-39.

[3] Beaudoin J. L., Merienne E., Danjoux R. and Egee M. (1985), Numerical system for infrared scanners and application to the subsurface control of materials by photothermal radiometry, Infrared Technology and Applications, SPIE Vol. 590 p. 287.

[4] Kuo P. K., Feng Z. J., Ahmed T., Favro L. D., Thomas R. L. and Hartikainen J. (1987), Parallel thermal wave imaging using a vector lock-in video technique, Proc. Photoacoustic and Photothermal Phenomen, edited by P. Hess and J. Pelzl, Springer, Heidelberg, pp. 415-418.

[5] Busse G., German patent No. DE 4203272- C2, 1-3 (1992).

[6] Wu D. (1996), Lockin-Thermographie fuer die zerstoerungsfreie Werkstoff-pruefung und Werkstoffcharakterisierung, Ph.D. Thesis, University of Stuttgart.

[7] Gerhard H. and Busse G. (2003), Use of ultrasound excitation and optical lockin method for speckle interferometry deformation measurement, Proc. Nondestructive Characterisation of Materials XI, Springer-Verlag, Berlin, pp. 525-534.

[8] Gerhard H., Menner P. and Busse G. (2007), Neue Möglichkeiten und Anwendungen der Lockin-Speckle-Interferometrie für die zerstoerungsfreie Pruefung, Proc. Stuttgarter Kunststoff-Kolloquium 20, 5V3, Stuttgart, pp. 1-8.

[9] Rosencwaig A. and Gersho A. (1976), Theory of the photo-acoustic effect with solids, Journal of Applied Physics 47, pp. 64-69.

Fast Defect Shape Reconstruction Based on the Travel Time in Pulse Thermography

S. Götschel, M. Weiser, C. Maierhofer, R. Richter and M. Röllig

Abstract Pulse thermography is a non-destructive testing method based on infrared imaging of transient thermal patterns. Heating the surface of the structure under test for a short period of time generates a non-stationary temperature distribution and thus a thermal contrast between the defect and the sound material. In modern NDT, a quantitative characterization of hidden imperfections in materials is desired. In particular, defect depth and shape are of interest. The reconstruction of the defect from thermography data is a nonlinear inverse problem, and ill-posed. We propose an algorithm for the identification of subsurface defects based on the travel time of the reflected thermal pulse. Our work extends results by Lugin and Netzelmann, taking lateral thermal flows directly into account while retrieving the defect depth. This requires significantly less computational work. Quantitative information about the defect shape and depth is obtained. Application of our method to both thermography data generated by a finite element simulation and experimental heating of PVC test specimens with different defects yields good reconstruction of the actual defects.

Keywords Defect shape reconstruction • Finite element simulation • Pulsed thermography • Quantitative characterization • Thermal contrast

Introduction

Pulse thermography is a non-destructive testing method based on infrared imaging of transient thermal patterns. Heating the surface of the structure under test for a short period of time generates a non-stationary temperature distribution. The transients

S. Götschel (✉) • M. Weiser
Zuse Institute Berlin, Berlin, Germany
e-mail: goetschel@zib.de

C. Maierhofer • R. Richter • M. Röllig
Federal Institute for Materials Research and Testing, Berlin, Germany

differ for areas with defects close to the surface due to different thermal parameters. The resulting thermal contrast at the surface can be used to reconstruct the sub-surface defect [4].

Due to the governing heat equation, the estimation of the defect shape from thermography data is an ill-posed, nonlinear inverse problem. Most of the literature in pulse thermography is concerned with the reconstruction of depth, i.e. the residual wall thickness, and diameter of flat-bottom holes, for which several techniques exists. See e.g. [5] for an overview. Reconstruction of an inaccessible part of the boundary, and thus of a general defect shape, in arbitrary space dimensions was discussed in [2], where a Newton-like algorithm for matching certain weighted averages of measurement and simulation data is proposed. Starting from thermal wave theory, Lugin and Netzelmann [3] suggest a combination of 1D depth approximation and finite element simulation to reconstruct the defect shape with a fixed point iteration.

In this paper, we extend the approximation of the residual wall thickness of test specimens from [3] to 2D/3D and show reasonable reconstruction of defect shapes without using an iterative algorithm for simulated and measurement data.

Algorithm

Physical background

Consider a specimen with semi-infinite thickness exposed to a Dirac delta pulse heating. The delta pulse is equivalent to a broad spectrum of thermal waves, which are all in phase. This leads to a time-domain solution to the heat conduction problem given as

$$T(z,t) = \frac{Q}{\sqrt{4\pi\lambda\rho ct}} e^{-\frac{\rho cz^2}{4\lambda t}}, \tag{1}$$

see e.g. [1]. Here, $(z,t) \in (0,\infty)^2$ denote the spatial and temporal variable, with t being the time elapsed after the delta pulse heating with input energy density Q, and given material parameters thermal conductivity λ, specific heat capacity c and density ρ.

For an object with given finite maximum thickness, reflection and transmission occur at the interface between the backside of the object and the surroundings. For typical situations arising in pulse thermography, like the interface between metal and air, the reflection coefficient is close to one, thus transmission can be neglected. In the one-dimensional situation, this reflection leads to a temperature increase at the surface given by

$$T_+(t) = T(2z_{max}, t). \tag{2}$$
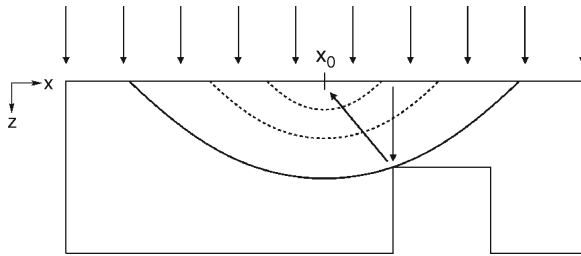
Fig. 1 Sketch of thermal wave isochrones. Reflection from all points on a parabola result in a temperature increase at x_0 at the same time. The area above the solid parabola is known to be bulk material

By considering the relative temperature increase $T_{rel}(t) = T_+(t)/T(0, t)$, the sample depth can be evaluated as

$$z_{max} = \left(-\frac{\lambda t}{\rho c} \ln T_{rel}(t) \right)^{\frac{1}{2}},$$

(3)

which is known as the echo defect shape (EDS).

In two space dimensions, due to diffuse reflection, a temperature increase at a surface point x_0 can not only be caused by a point vertically below x_0, but also by reflection at points (x, z) leading to the same travel time of the incoming and reflected thermal pulse, see Fig. 1. Points with equal travel times form parabolas.

Envelope algorithm

Assume now given surface temperatures during the cooling process for the object under inspection, $T_{obj}(x,t)$, and a reference object, $T_{ref}(x,t)$. For instance, a known defect-free area on the inspected object can be used as a reference. Taking diffuse reflection into account, instead of computing the depth at x_0 solely by Eqn. (3) the following steps are performed to reconstruct the defect shape. Note that an additional data structure is necessary, which keeps track of the estimated depth while stepping through the surface points (known as a *z-buffer* e.g. in computer graphics).

Choose tolerance τ. For every surface point x:

1. determine the relative temperature increase (also known as *relative thermal contrast*)

$$C_{rel}(x,t) = \frac{T_{obj}(x,t) - T_{ref}(x,t)}{T_{ref}(x,t)}$$

(4)

2. determine the time when the relative contrast begins to rise

$$t_* = \min\{t : C_{rel}(x,t) > \tau\} \tag{5}$$

3. compute apex coordinate

$$t_* = \left(-\frac{\lambda t_*}{\rho c} \ln \tau\right)^{\frac{1}{2}} \tag{6}$$

4. construct parabola for $x_p \in [x - 2z_*, x + 2z_*]$

$$z_p(x_p) = \frac{2z_*^2 - (x - x_p)^2}{4z_*} \tag{7}$$

5. update z-buffer for $x_p \in [x - 2z_*, x + 2z_*]$

$$z(x_p) = \max\left(z(x_p), z_p(x_p)\right) \tag{8}$$

After all surface points have been processed, $z = z(x)$ contains the reconstructed defect shape. It is the envelope of the constructed parabolas.

Results

Test specimens

To check the proposed algorithm, two PVC test specimens with triangular wedge-shaped defects were used for measurement, see Fig. 2.

Simulation

To demonstrate the effectiveness of our algorithm, we first consider simulation of several PVC test specimens. We use the semi-analytic method developed in [6] to get accurate simulation results within reasonable computing times. Figure 3 shows the reconstruction results.
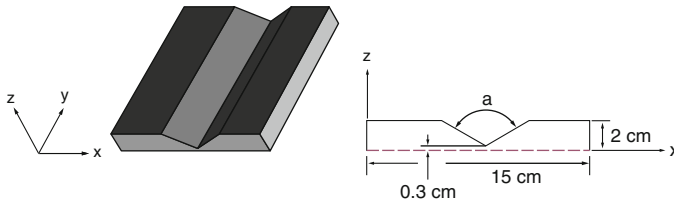
Fig. 2 Sketches of the test specimens. The angle a is 90° and 120°, respectively, for the two defect shapes. The experimentally determined material parameters are

$$\lambda = 0.213 \pm 0.020 \,{}^{W}\!/_{mK}, \; \rho = 1413.4 \pm 4 \,{}^{kg}\!/_{m^3}, \; c = 1038 \pm 40 \,{}^{J}\!/_{kgK}$$
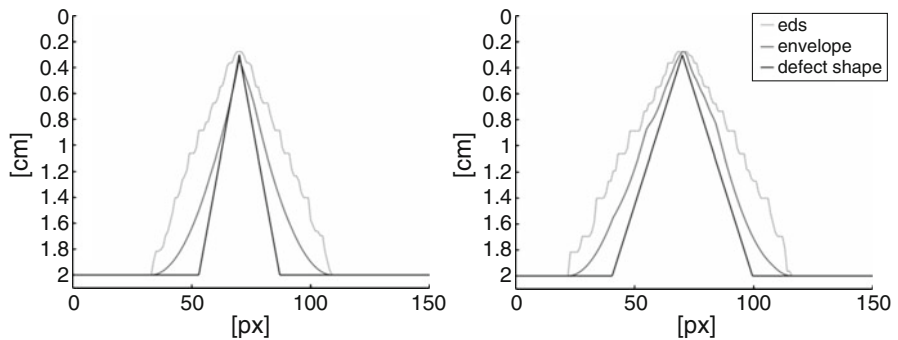
Fig. 3 Reconstruction results for the simulated 90°- (left) and 120°-triangle (right) with thresholds of 0.1. Additionally, for comparison, the echo defect shape (Eqn. (6)) is plotted

Experiments

Measurements with the described PVC test specimens were performed. The test setup is sketched in Fig. 4. The heating was performed using two flash lights with 6kJ emission energy and a flash duration of 3ms. The cooling curve was recorded with a Thermosensorik InSb 640 IR-camera. Due to noise, the data needed to be preprocessed before applying the reconstruction algorithm. The recording frequency was originally 93Hz, with an averaging in time reducing this to 1Hz. As the defect is uniform in x-direction, averaging over this coordinate was used to significantly increase the signal-to-noise ratio. For $T_{ref}(x,t)$, a point far away from the defect was chosen. Despite uneven heating, this provided better results than using an additional measurement with a defect-free sample object of the same size and material. In Fig. 5, the reconstruction results can be seen.
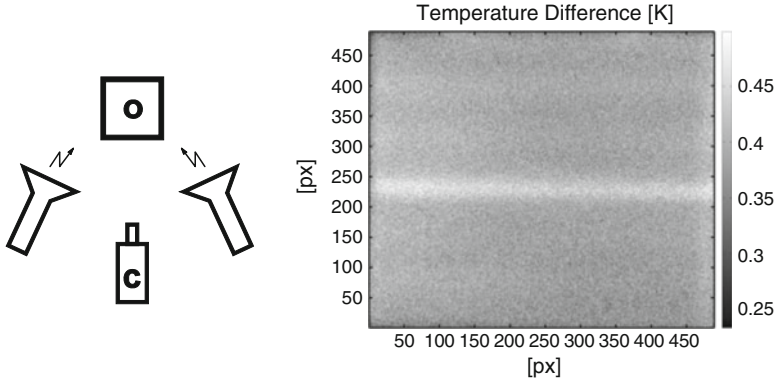
Fig. 4 Left: Sketch of the test setup. Right: surface temperature of 120°-triangle shaped defect 71.4s past heating, after subtraction of the initial temperature distribution and Gaussian smoothing with variance 0.5
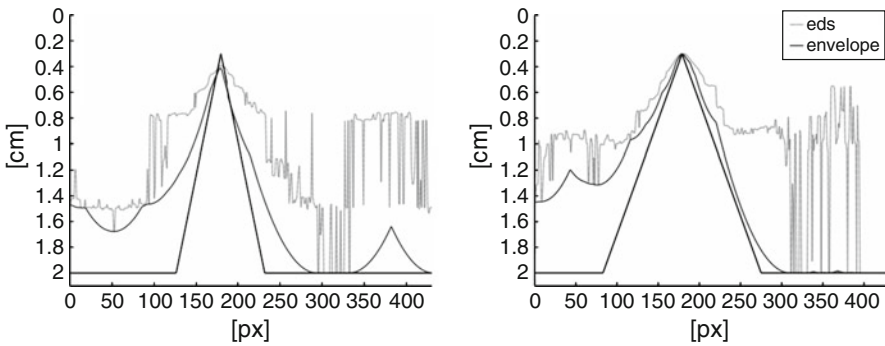
Fig. 5 Reconstruction using measurement data for the 90°-triangle shaped defect with threshold 0.025 (left), and the 120°-triangle shaped defect with threshold 0.02 (right). The dark grey line is the result of the envelope algorithm, for comparison the echo defect shape is shown in light grey. The worse reconstruction of the left side of the triangles is mainly due to uneven heating. Compared with the simulation data, the influence of noise is clearly visible

Comparison with iterative EDS

For comparison with the iterative algorithm developed in [3], Figs. 3 and 5 also show the echo defect shape used as a starting point for the iterations. To compare the final reconstruction results and runtimes, we used a simpler simulation module neglecting convection and radiation, and limited the analysis to 2D domains. As a defect shape, we used a cross section of the 120°-triangle specimen. An initial simulation with higher accuracy was used to generate the "measurement" data. Reconstruction results of the envelope algorithm and iterative EDS can be seen in Fig. 6.
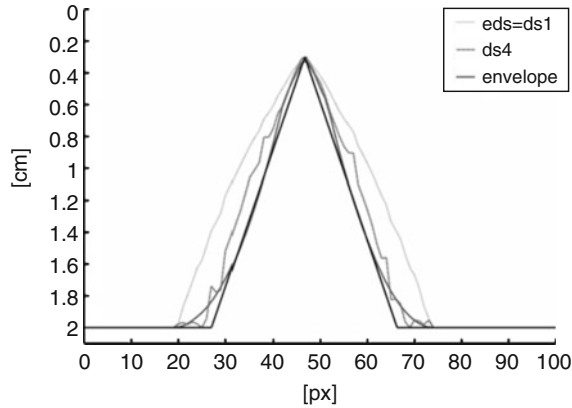
Fig. 6 Comparison with iterative approach. The solid dark grey line shows the result of the envelope algorithm with a reconstruction time of 0.06s. Also shown are the EDS (light grey) and defect shape (medium grey) after three iterations of Lugin and Netzelmanns algorithm with a total runtime (mainly consisting of time used for the simulation part, without grid generation) of about 5500s

Conclusion

Extending the echo defect shape to take lateral heat conduction directly into account is both simple and highly effective. While the envelope algorithm can be used in the same way as the echo defect shape in fixed point iteration, numerical examples indicate that the accuracy should most often be sufficient without iterative correction. This reduces the computational effort tremendously.

References

[1] Almond, D. and Patel, P. (1996), *Photothermal science and techniques*, Chapman & Hall, London
[2] Bryan, K. and Caudill, L. (2005), *Inverse Problems*, vol. 21, n. 1, p. 239–255
[3] Lugin, S. and Netzelmann, U. (2007), *NDT&E International*, vol. 40, n. 2, p. 220–228
[4] Maldague, X. (2001), *Theory and practice of infrared technology for nondestructive testing*, Wiley, New York
[5] Sun, J. G. (2005), *Journal of Heat Transfer*, vol. 128, n. 4, p. 329–338
[6] Weiser, M., Röllig, M., Arndt, R. and Erdmann, B. (2010), *Heat and Mass Transfer*, vol. 46, n. 11–12, p. 1419–1428

The Role of Infrared Thermography in NDT

C. Meola and G.M. Carlomagno

Abstract Infrared thermography (IRT) is becoming ever more popular in NonDestructive Testing (NDT) of materials and structures since it is completely noncontact and may be faster than many other techniques. In some cases, such as in the control of the envelope of a building, it is practically the unique technique, which, in one click, supplies a comprehensive image of the entire façade of the building with information about buried structures, tightness of envelope and fixtures, and presence of anomalies. The attention of this work is focused on the actual role of IRT in the NDT field. First, some basic principles of the two main techniques, which are Pulse termography (PT) and Lockin Thermography (LT) are briefly recalled and then some examples of application are presented. Such examples include laboratory tests and in situ inspections. Two types of specimens are considered: a glass fibre reinforced composite and masonry structure including different types of problems such as voids and cracks, and impact damage. Within the inspection in situ of buildings, information about the conservation state of masonry structures (overall degradation, crack network) were gained for planning of restoration.

Keywords Artworks • Composites • Infrared thermography • Lockin thermography • Masonry structures

Background

Non-destructive evaluation (NDE) is today a recurrent term in many fields from the high-tech development to the past footsteps conservation. In fact, NDE is indispensable to assure fabrication of defects-free products, but it is also necessary

C. Meola (✉) • G.M. Carlomagno
Department of Aerospace Engineering (DIAS), University of Naples Federico II,
Napoli, Italy
e-mail: carmeola@unina.it

for artefacts maintenance as well as control of the artworks conservation state. Many techniques exist and many different forms of energy are exploited for non destructive testing (NDT) and evaluation of materials and structures. Basically, no technique is able to detect every type of defects in every type of materials and thus, the most effective technique must be chosen. Sometimes, a synergic integration of techniques is compulsory.

Amongst the NDT techniques, which are today available, a key role is played by infrared thermography (IRT) [1]. IRT is completely non contact, non intrusive and relatively fast and then is gaining ever more importance. Basically, two thermographic techniques can be used: pulse thermography (PT) and lock-in thermography (LT).

PT consists simply in the stimulation of the object (under evaluation) and monitoring of its surface temperature variation during the transient heating, or cooling, phase. Heating is generally performed by lamps, flash lamps, scanning lasers, or hot air jets. Cooling can be practically attained only by cold air jets. Of course, air jets (hot or cold) can be used only on a massive surface since jet impingement may damage delicate objects, e.g., artworks. For the case of slabs, analysis with PT can be performed in two different modes: transmission and reflection. In the transmission mode, the infrared camera views the rear face, i.e. the face opposite the heating/cooling source. But, since the opposite side is not always accessible and/or available, the reflection mode, for which both heating (cooling) source and camera are positioned on the same side, is mainly applied. The thermal energy propagates by diffusion under the surface (surface losses due to radiation and convection are also present) while the infrared camera monitors the temperature variation over the viewed surface. Obviously, for a uniform surface heating, the temperature distribution is uniform in case of a homogeneous material. The presence of a defect at a certain depth interferes with the heat flow causing local surface temperature variations. The defect detection is limited by the signal-to-noise ratio (SNR) [2], or by the noise equivalent temperature difference (NETD) of the temperature detector. In addition, the surface finish is of great importance since variations in surface roughness, cleanliness, uniformity of paint and other surface conditions can cause variations in the emissivity coefficient and affect the temperature measurement. These drawbacks are overcome using lockin thermography.

The concept of lock-in thermography was first introduced by Carlomagno and Berardi [3] and later further investigated by other researchers [4-11]. It can be performed in two different modes: stimulation with a heating lamp, which is called optical lock-in thermography and abbreviated as LT, or OLT (some authors also call it modulated thermography MT) or stimulation with elastic waves and is called ultrasound lock-in thermography (ULT). In the LT, the thermographic system is coherently coupled to a thermal source which is operated in such a way that a temperature modulation results. This modulation is obtained from a non-linear electrical signal produced by the lock-in module which allows also for frequency variation. The depth range, for the amplitude image, is given by the thermal diffusion length μ which is calculated from the thermal diffusivity α and the wave frequency f:

$$\mu = \sqrt{\frac{\alpha}{\pi f}} \tag{1}$$

the depth p corresponds to 1.8μ [7-10]. The material thickness, which can be inspected, depends on the wave period (the longer the period, the deeper the penetration) and on the material properties (thermal conductivity, specific heat and density). Generally, tests start at a quite high wave frequency, at which only surface (or shallow) defects are visible, and later on, to inspect deeper layers, the frequency is decreased until the entire thickness has been traversed.

A third technique which combines the advantages of both PT and LT without sharing their drawbacks is pulse phase thermography (PPT) [12]. However, there are other techniques, which are variants of PT and LT because they include a different heating method, or a different processing algorithm. As technology evolves, new techniques may be tailored for a specific need.

Tests and Data Analysis

Both pulse and lockin techniques were used for the inspection of laboratory specimens and real structures.

Laboratory tests

Two types of specimens involving masonry and composite materials were considered for laboratory tests.

One specimen (Fig. 1a) is made of concrete (a mixture of cement, sand and water) with buried defects at depth of 1 cm, or 2 cm, respectively on left, or right, half part. Defects, in the number of 6 per part of different diameter from 1 to 10 cm, are in the form of cork diskettes and plastic bags containing an air layer to simulate presence of voids. Tests were carried out with PT and with the Flir SC6000 camera by acquiring time sequence images during both heating and cooling phases. A relief temperature

Photo   thermal image – 3D representation
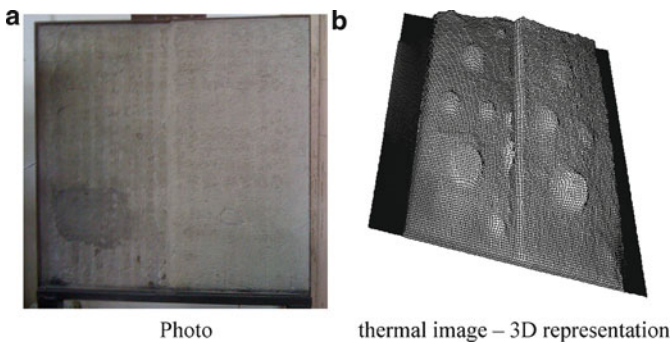
Fig. 1 Concrete specimen
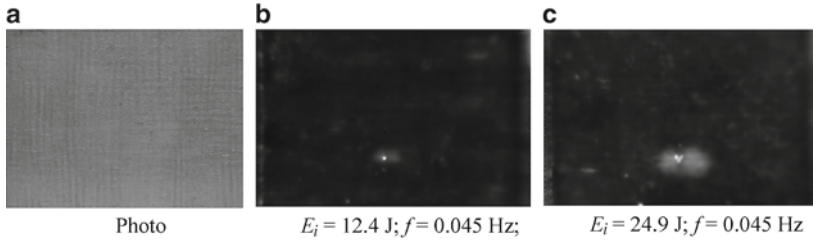
Fig. 2 GFRP specimen

map is shown in Fig. 1b; it refers to the time instant of 100 s after shutting down of the thermal stimulation source. As can be seen, defects on the left side are all well outlined; instead, in the right side some defects appear with low thermal contrast. This is due to their different thermal capacity and depth; the thickness variation between left and right parts is clearly distinguishable. It is also possible to individuate a discontinuity around the larger defect on the bottom left side which accounts for a restoration of the panel by adding new concrete (i.e., darker zone in Fig. 1a). In addition, the lighter zone, which is visible over the thinner layer at half height on the right side towards the thicker layer, is likely due to the presence of a longitudinal crack there.

A panel of a polymeric matrix reinforced with glass fibres (GFRP) was fabricated and cut into specimens 13 cm × 10 cm × 0.3 cm (Fig. 2a). These specimens were subjected to impact tests and then non-destructively inspected with lockin thermography using the Flir SC3000 camera. Phase images taken at heating frequency $f = 0.045$ Hz of two specimens impacted at $E_i = 12.4$ J and 24.9 J are respectively shown in Fig. 2b, c. The viewed surface is that opposite to the impact. In both images there is a small whiter central zone which most probably indicates cracks in the matrix and fibres rupture, while the adjacent larger area is characterized by delamination between fibres and matrix. Comparing the two images it is possible to gain information about the extension of the damaged area with in creasing the impact energy. However, varying the heating frequency f it is also possible to acquire information about the damage occurred in the different layers through the material thickness.

Tests in situ

Two examples of inspection *in situ* are herein reported which include a civil edifice and a warehouse. From the wall part shown in Fig. 3 it has been found traces of previous masonry consolidation. Both visible (a) and thermal (b) images were taken with the Flir B360 camera; due to small room, three thermal images were taken and patched up. Darker zones on the top and on the central right side account for local presence of more recent concrete, which was added during the wall restoration.

Photo   thermal images
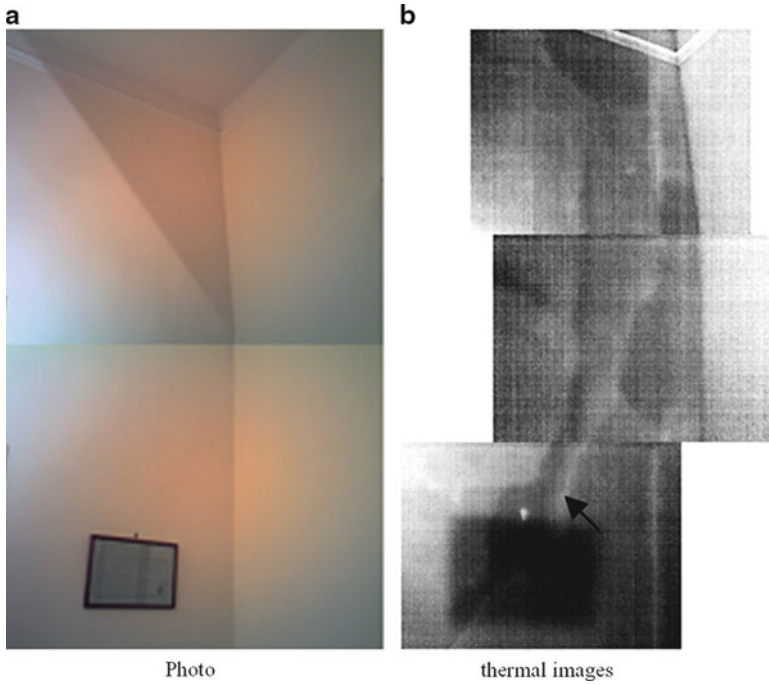
Fig. 3 An apartment wall

visible   infrared
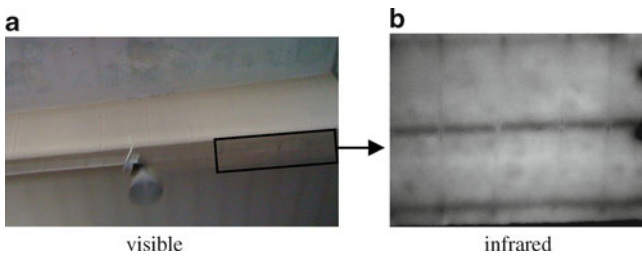
Fig. 4 Roof ferroconcrete beam

Of course the rectangular dark area in the bottom was caused by the painting there (Fig. 3a). The dark almost vertical band is produced by a duct cables, while the irregular lighter band, which is indicated by an arrow, denotes presence of a transversal fracture along the entire wall. It is possible to argue that the previous restoration was not at all successful even if no visible signs appear on the wall (Fig. 3a).

Owing to the warehouse case study, in Fig. 4b is reported a thermal image obtained through pulse thermography with the Flir SC3000 camera. This image refers to the area inside the rectangle in Fig. 4a over a roof ferroconcrete beam; the thicker dark horizontal lines representing the buried steel rods, while the vertical milder

lines indicating brackets. The beam under study is 40 cm wide (about the height of the image in Fig. 4b) and about 15 m long and it is tapered along the third dimension. The viewing distance was about 3 m. It is interesting to see that infrared thermography offers the possibility to ascertain the presence of steel bars inside ferroconcrete beams and to evaluate their diameter. This, of course, is of paramount importance since it prevents from destructive tests and is time and money saving.

Remarks

In this work, due to the space limitation, it was not possible to adequately describe the role of infrared thermography amongst the NDT techniques. It is worth noting that, with reference to the building field, the use of an infrared camera is of remarkable value and, for certain problems, represents the unique solution. In fact, it allows discovering buried anomalies for restoration planning, but also structures such as feeding and sewage pipes, electric conduits which are necessary to locate before drilling a hole in a wall to safely hanging a painting, or a cupboard. Again, it helps finding presence of moist and mold that, even not affecting the room aesthetic appearance, may produce harmful effects for human beings and for pets. A major application of an infrared imaging device to buildings is, without doubts, the home energy audit since just a simple shot allows knowing the conditions of the edifice envelope and of windows tightness.

References

[1] Meola, C. and Carlomagno, G.M. (2004) *Measurement Sci. and Technol*. vol. 15, pp. 27–58.
[2] Vavilov, V.P., Almond, D.P., Busse, G., Grinzato, E., Krapez, J.C., Maldaque, X., Marinetti, S., Peng, W., Shirayev, V. and Wu, D. (1998) In Proceedings of *QIRT 98*, pp. 43–52, Balageas, D., Busse, G. and Carlomagno, G.M. (Eds), Akademickie Centrum Graficzno-Marketingowe, Łódź, Poland.
[3] Carlomagno, G.M. and Berardi, P.G. (1976) In Proc. *III Infrared Information Exchange*, Warren, C. (Ed.), pp. 33–40. AGA, St. Louis, MO.
[4] Beaudoin, J.-L., Merienne, E., Danjoux, R. and Egee, M. (1985) In Proc. *SPIE* vol. 590, pp. 287–292.
[5] Kuo, P.K., Feng, Z.J., Ahmed, T., Favro, L.D., Thomas, R.L. and Hartikainen, J. (1987) In *Photoacoustic and Photothermal Phenomena*, Hess, P. and Pelzl, J. (Eds), pp. 415–418. Springer-Verlag, Heidelberg.
[6] Busse, G., Wu, D. and Karpen, W. (1992) *J. Appl. Phys*. vol. 71, pp. 3962–3965.
[7] Letho, A., Jaarinen, J., Tiusanen, T., Jokinen, M. and Luukkala, M. (1981) *Electronic Lett*. vol. 17, pp. 364–365.
[8] Bennett, C.A.Jr. and Patty, R.R. (1982) *Appl. Opt*. vol. 21, pp. 49–54.
[9] Busse, G. (1979) *Appl. Phys. Lett*. vol. 35, pp. 759–760.
[10] Thomas, R.L., Pouch, J.J., Wong, Y.H., Favro, L.D., Kuo, P.K. and Rosencwaig, A. (1980) *J. Appl. Phys*. vol. 51, pp. 1152–1156.
[11] Busse, G. (1982) *Appl. Opt*. vol. 21, pp. 107–110.
[12] Maldague, X. and Marinetti, S. J. (1996) *Appl. Phys*. vol. 79, pp. 2694–2698.

Industrial Applications of Dual X-ray Energy Computed Tomography (2X-CT)

T. Fuchs, P. Keßling, M. Firsching, F. Nachtrab and G. Scholz

Abstract The Fraunhofer Development Center X-ray Technology (EZRT) developed an industrial dual-energy X-ray Computed Tomography (2X-CT) system in order to obtain quantitative 3-D information on the material inside arbitrary samples. The goal was to develop an easy-to-use dual-energy solution that can be handled by the average industrial CT operator without the need for a specialist. First, an introduction is given of the physical background of the method that was realized. Also, the strengths and weaknesses thereof are discussed. Next, the results of 2X-CT measurements from different fields of investigations are presented: measurements with vegetables, e.g. potatoes or bananas, quantitative assessments of bore cores in geological applications, and studies of carbon fibre reinforced plastic (CFRP). In summary, it is shown that 2X-CT can provide accurate information about the composition of a wide range of materials and objects. On the other side, there is still the need for further optimization of X-ray parameters in order to increase quantitative accuracy, and for extending the range of materials which can be assessed by industrial 2X-CT.

Keywords Computed tomography • Dual x-ray energy • Industrial application • Material analysis • Quantitative 3-D imaging

Motivation

Dual-energy Computed Tomography is an established method in the field of medical CT to obtain quantitative information on bone mineralization or calcifications in a human patient - instead of mean attenuation coefficients or grey values only. Up to

---

T. Fuchs (✉) • P. Keßling • M. Firsching • F. Nachtrab • G. Scholz
Fraunhofer Development Center X-ray Technology EZRT,
Dr.-Mack-Str. 81, 90762 Fürth, Germany
e-mail: theobald.fuchs@iis.fraunhofer.de

now, in the field of industrial X-ray imaging dual-energy techniques have been used to solve particular problems on a case-by-case basis rather than as a standard tool.

The goal of the presented work was to develop an easy-to-use dual-energy solution that can be handled by an average industrial operator without the need for a specialist. The actual dual-energy analysis tool is called *2X-Suite* [1]. In cases where qualitative measurements are not sufficient, it provides additional quantitative information (e.g. mass density) about the sample at hand.

Theory and Method

The *2X-Suite* is based on an algorithm proposed by Heismann et al. for application in medical CT [2]. As input data this algorithm needs two CT data sets, one with a low (LE) and another with a high effective X-ray energy (HE). A first order linearization is applied to the raw data, and two volumes are reconstructed thereafter. The dual-energy analysis is done voxel by voxel, using a pre-calculated function:

$$F(Z) = \frac{\mu_{LE}}{\mu_{HE}} \tag{1}$$

$F(Z)$ accounts for the different interaction probabilities of the X-rays with the material at the low resp. high energy and therefore depends on the parameters of both measurements (such as tube voltage, filtration and detector sensitivity). As a result, two volume data sets are obtained, one giving the mass density ρ (in g/cm^3) in each voxel, the other providing the effective atomic number Z_{eff} of the material therein. Thereby every pair of measurements of the attenuation coefficient at different effective energies (μ_{LE}, μ_{HE}) is transformed to another basis, e.g. the density ρ and atomic number Z of the materials contained in the sample:

$$\begin{pmatrix} \mu_{LE}(\rho, Z) \\ \mu_{HE}(\rho, Z) \end{pmatrix} \rightarrow \begin{pmatrix} \rho(\mu_{LE}, \mu_{HE}) \\ Z(\mu_{LE}, \mu_{HE}) \end{pmatrix} \tag{2}$$

One important difference between medical and industrial CT is that the range of materials occurring in a sample is much wider in the latter case, and can cover almost the full range of chemical elements. Heismann's algorithm is limited to a range of elements from $Z = 1$ to 30, which seems very suitable for medical applications but is not enough for most industrial materials.

Therefore the possibilities of extending the afore mentioned approach to dual-energy imaging to a wider range of materials were investigated. For $Z > 30$ the function $F(Z)$ as given by Heismann is not a bijective function anymore.

By varying the parameters like e.g. the material and the beam filtration, it is possible to obtain different functions $F(Z)$, allowing the inversion of the function for different ranges of Z. Especially the influence of different detectors (exhibiting
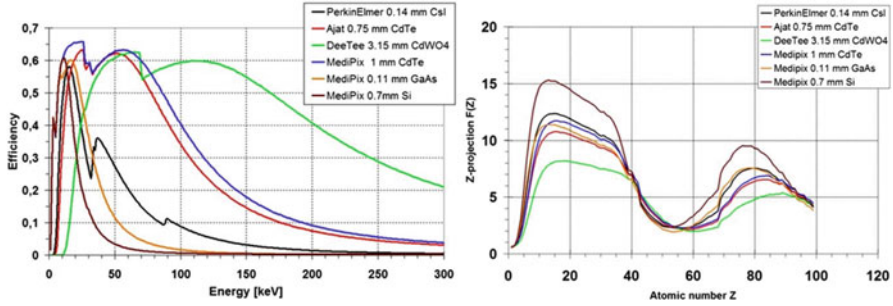
Fig. 1 Comparison of different sensor efficiencies (left) and influence of different sensor efficiencies on *F*(*Z*) (right)

different sensor sensitivities) on the *F*(*Z*) function is of note. The efficiency of several detectors was simulated using models of these detectors with the Monte-Carlo X-ray simulation tool ROSI [3]. Simulated efficiency curves and the influence of the detectors on *F*(*Z*) are shown in Fig. 1.

In addition, the projection function *F*(*Z*) is influenced by many parameters: the high- and low-energy tube voltage, filter materials and filter thicknesses for the high- and low-energy spectrum and the detector sensitivity. Thus, a database was built up including all data needed for the calculation of *F*(*Z*) like material parameters (attenuation coefficients, density), and descriptions of tubes (spectra) and detectors (spectral sensitivities). A numerical tool was implemented allowing a quick forecast of different setups and measurement situations. With these tools, the CT operator is enabled to analyze systematically the influence of the different parameters on the projection function *F*(*Z*). Having this knowledge, a projection function for a certain range of materials which shall be distinguished can be 'tailored'.

Equipment

The realized setup consists of a commercially available CT-machine which was equipped with specially chosen components and upgraded with self-developed hardware (see Fig. 2). The X-ray source is a 225 kVp minifocus tube with a maximum power of 1.8 kW. A computer-controlled filter wheel is used to automatically change filter packs to modify the spectrum. A motorized collimator is used to reduce the cone beam diameter in order to suppress scattered radiation. An accurate manipulation system is used to place the object in the beam and to rotate the object for CT data acquisition. The image is recorded using an indirectly converting flat-panel detector, the Perkin Elmer XRD 820 CN14 (200 μm pixel, 1024²) with a carbon entrance window to enhance low energy detection efficiency.

Fig. 2 Experimental setup
of the 2X-CT system
including the wheel
to remotely change
the filtration and a
multi-purpose collimator
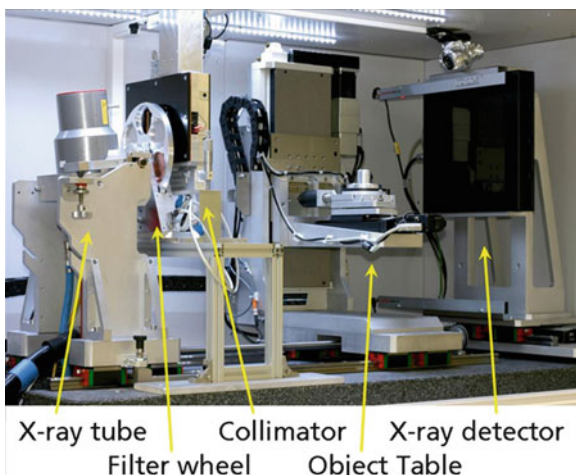
Results

Application in Biology

Figure 3 shows the measurements of a banana as an example for a dual-energy measurement with ρ-Z_{eff}-projection. It is remarkable, that the chemical composition given by Z_{eff} is very homogeneous (Fig. 4), with nearly constant values close to that of water (approx. 7). The X-ray parameters were 80 kV, 1.5 mA, and 1 mm Al, respectively 120 kV, 3.0 mA, 1 mm Cu for the LE and HE data set.

Geological Sample

Another task 2X-CT was used for is the assessment of bore cores (e.g. from sand stone or granite) to quantify mineral contents. One example is a Gneiss pebble of about 6 cm in diameter. The resulting Z_{eff} varied around 8.4, while from theoretical calculation about 11 was expected. ρ was measured as 2.6 g/cm^3 with 0.1 g/cm^3 standard deviation. The reconstructed sections (Fig. 5) show, that the metamorphit has a rough internal structure, due to the geological processes creating this kind of natural rock. Data acquisition was made with 120 kV, 0.75 mA, 2 mm Al for LE and 200 kV, 1.75 mA, 2 mm Cu for HE.
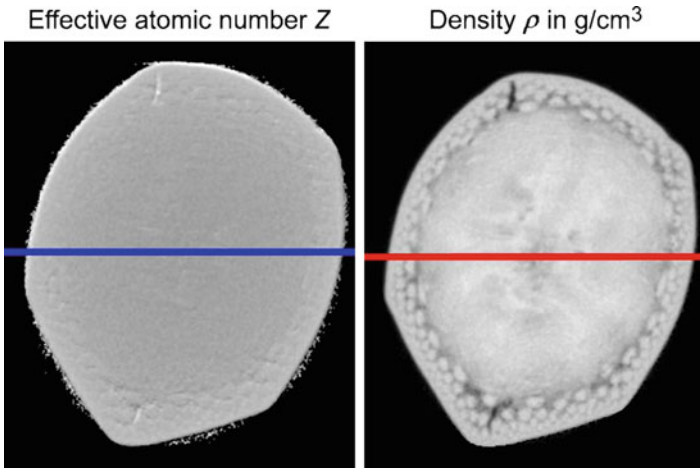
Fig. 3 Quantitative results from a 2X-CT measurement of a banana. Left: central slice showing Z_{eff}, right: corresponding distribution of mass density representing structural details inside the fruit
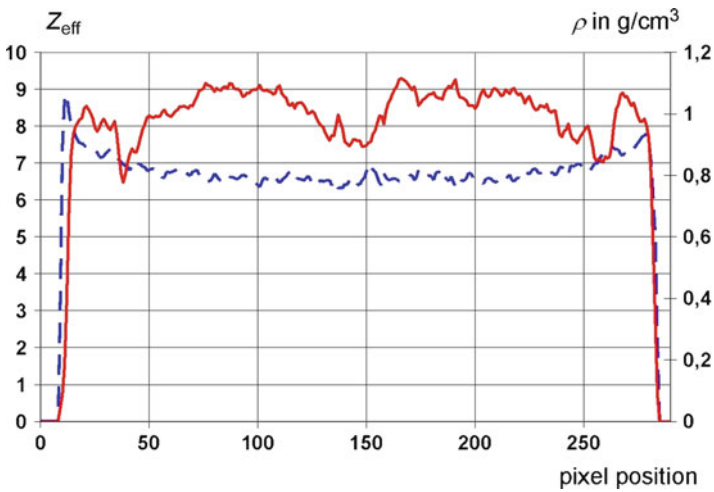
Fig. 4 Profile plots along the lines indicated in Fig. 3. Z_{eff}-values (dashed line) increase slightly towards the surface of the fruit, which is due to beam hardening. Mass density (solid line) varies strongly along the cross-section
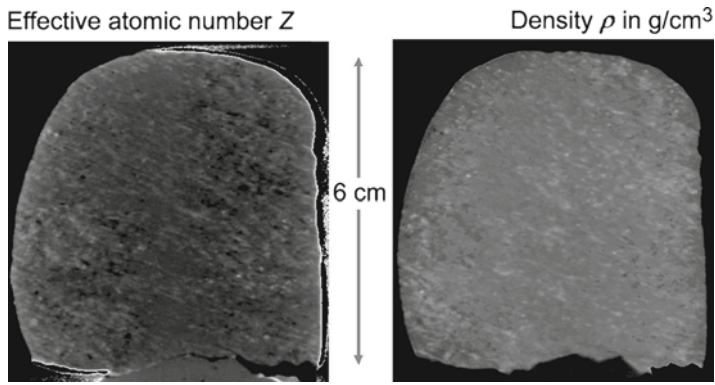
Fig. 5 Results for a Gneiss pebble. The distribution of different materials is seen in the atomic number and the density map, both generated by the 2X-CT.
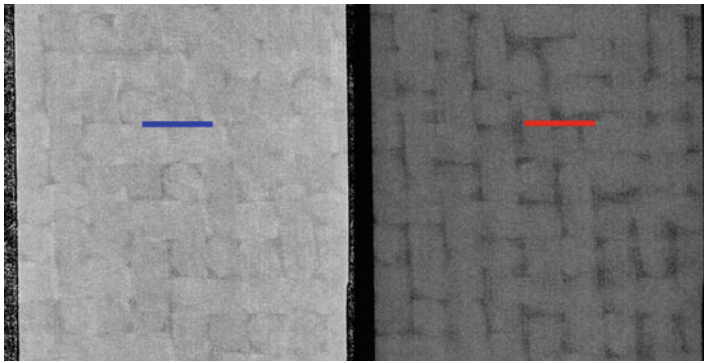
Fig. 6 2X-CT cross-sections of a CFRP sample (left: Z_{eff}, right: mass density ρ)
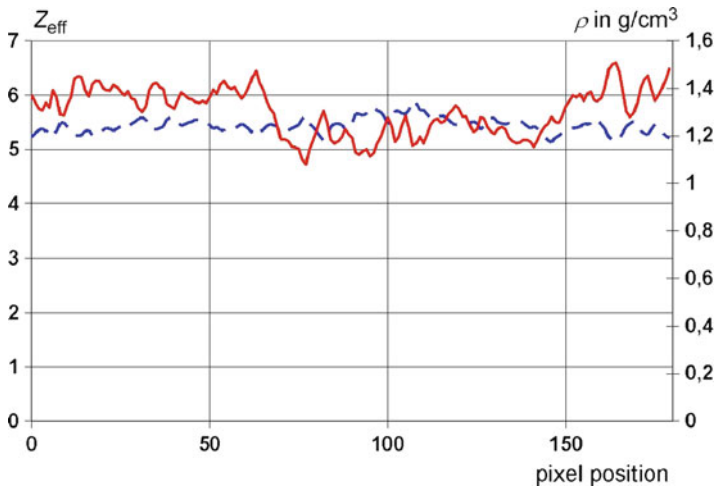
Fig. 7 Profile plots along the lines indicated in Fig. 6. Profiles correspond to the lines in the Z_{eff}-cross-section (dashed line) and mass density (solid)

Material sciences

One highly promising application of 2X-CT is the evaluation of the properties of newly developed CFRP. Fig. 6 shows the result for a CFRP sample. Data acquisition was made with 40 kV, 1 mA, 0.5 mm Al filtration for the LE-measurement and 120 kV, 0.33 mA, 0.3 mm Cu for the HE-measurement, respectively. While Z_{eff} (dashed line in Fig. 7) does not differ significantly between fiber bundles and the matrix material, the mass density changes for about 0.2 g/cm^3.

Summary

In summary, it was shown that 2X-CT provides means for quantitative assessment of materials and objects which are of interest in industrial production, science and technology. The *2X-Suite* is an easy-to-use tool, enabling 2X-CT measurements for various fields of applications in research and industry.

References

[1] Nachtrab F. et al. (2010), *NIM A*, DOI: 10.1016/j.nima.2010.06.154
[2] Heismann, B.J et al. (2003), *J. Appl. Phys*. vol. 94, pp. 2073
[3] Giersch J. et al. (2003), *NIM A* vol. 509, pp. 151 – 156

Research on Improvement of Receiving-Detecting Circuit for Digital Radiographic Systems with Advanced Spatial Resolution

V.D. Ryzhikov, O.D. Opolonin, O.K. Lysetska, S.M. Galkin, Y.F. Voronkin and V.L. Perevertaylo

Abstract   Radiographic inspection is among the most reliable methods for inspection of pipelines and metals. The worldwide trend of transition from film radiography to digital radiography requires developmentof advanceddigital radiography systems (DRS). The main task in developmentof DRS is the improvement of spatial resolution (SR). The pixel size of the X-ray film is several microns while solid-state detector pixels have dimensions of several hundred to several thousand microns. For the most common detectors of "scintillator-photodiode" (S-PD) type, it is impossible in principle to obtain the film pixel sizes. However, the detecting ability for substances that differ by their density and atomic number achieved using "scintillator-photodiode" detectors is by several orders higher. Using the known method of digital radiography with a standard experiment scheme, but with dual-energy detector arrays, this study aimed at showing that it could be possible to substantially increase the accuracy of separation of substances in the inspected object by their atomic number.The sensitivity of the method was increased by using a multi-energy approach and detectors that have substantially different sensitivity in the low- and high-energy range of the X-ray emitter spectrum. Using the developed instruments and software, dual energy CT and 3D imaging of different objects such as welding, fragment of bone and tissue, and bags containing potentially hazardous items can be performed.

Keywords   Digital • Image • Radiography • Resolution • Spatial

V.D. Ryzhikov • O.D. Opolonin • O.K. Lysetska (✉) • S.M. Galkin • Y.F. Voronkin
Institute for Scintillation Materials of STC "Institute for Single Crystals",
NAS of Ukraine, Kharkov, Ukraine
e-mail: lisetskaya@isma.kharkov.ua

V.L. Perevertaylo
Research Institute for Micro Instrument, Kiev, Ukraine

Introduction

The film radiographic inspection is limited in its ability to allow detailed evaluation of damage in materials [1-6]. Also, it is time-consuming and requires expensive materials. Recent studies show that the main direction in the development of digital radiography systems (DRS) is the improvement of spatial resolution (SR). DRS are inferior to film by their resolution, however, their contrast sensitivity is relatively much higher - 0.8-1% and 1-2%, respectively [6].

This work aimed at looking for new possibilities of improvement of SR, resolution over thickness and detection ability of DRS based on X-ray radiation detectors of "scintillator-photodiode" (S-PD) type, as well as the most efficient use of the possibilities of two- and multi-energy radiography in discerning between substances that only slightly differ in their effective atomic number (Zeff) and density.

Preliminary studies indicated two main technological problems hindering creation of S-PD detectors with improved SR [1-3,7]. One of them is preparation of scintillator arrays (assemblies) with small aperture of each scintillation element. The other is compact arrangement of pre-amplifiers (PA).

In this paper, a newly developed DRS system is introduced which involves improved PD and scintillation arrays with 32 channels on each PD, as well as an improved detector design as a system.

Design and Development of a Detector with Improved SR

The X-ray radiation detector of S-PD type comprises two main elements – a multi-channel PD and a scintillator array (assembly). Previously used design of 16- and 32-channel PD imposed limitations on the directions of PD irradiation. These detectors can be used correctly only if irradiation is normal to the plane of photosensitive elements [2,3]. In collaboration with Research Institute for Micro Instrument, Kiev, Ukraine, we have developed a new design of the 32-channel PD. Its advantages are: feature allow reaching the identity of characteristics of detector couples (high-energy and low-energy detectors, HED and LED, respectively) [4,7,8]. Furthermore, feature allows easy attachment of detectors with minimum gap between them, which is important for preserving the channel step in $0.8 \cdot 10^{-3}$m arrays. Also, the PD design ensures sufficiently large distance between the detector and the PA board, which protects the element base from effects of direct and scattered ionizing radiation. Protection of the elements of electronics is especially important when, e.g., high-energy X-ray sources (XRS) with anode voltage up to 450 keV are used [9].

Experimental samples of 1D-arrays were prepared using monolithic scintillator pieces. 32-channel scintillator assemblies made from plates had dimensions $(25.4 \times 4 \times 0.6) \cdot 10^{-3}$m, showed good uniformity of scintillation characteristics and could be precisely placed on photosensitive elements of multi-channel PD [9].

Preparation of Model Detectors and Studies
of Their Characteristics

According to the developed design documentation and technological regulations, prototypes of 32-channel X-ray radiation detectors were made (Table 1).

Topology of the detector module should allow sequential attachment of modules into a line preserving the detector step at the module junction.

DRS prototype with a receiving-detecting circuit
equipped with an array of 32-channel detectors

A DRS prototype was assembled having a receiving-detecting circuit (RDC) with an array of 32-channel detectors. External appearance of the model DRS is shown in Fig. 1. Using the model system, planar (2D) scanning of objects is possible through vertical movement of the scanning mechanism. Also, in each vertical position of the scanning mechanism, angular rotation of the object was performed at steps of $1,05 \cdot 10^{-1}$ Rad, i.e., 60 different views at 6 degree steps. Thus, using the developed software, a tomographic image of the object was obtained, which in combination with the vertical movement lead to a 3D image.

Main characteristics of the DRS prototype are specified in [9].

Table 1   The parameters of the 32-channel detector

Parameters	Data
Detector output window area	$(0.6 \times 0.6) \cdot 10^{-3}\,\mathrm{m}^2$
Detector step	$0.8 \cdot 10^{-3}\,\mathrm{m}$
Static detector current without irradiation (T=293 K, Ubias = $10 \cdot 10^{-3}$ V)	$< 20 \cdot 10^{-12}$ A
Detector signal decay after $10 \cdot 10^{-3}$ s	
CsI(Tl)	to 2% level
ZnSe(Te)	to 0,2% level
$CdWO_4$	to 0,1% level
Detector capacitance (T=293K, Ubias = $100 \cdot 10^{-3}$ V)	$< 50 \cdot 10^{-12}$ F
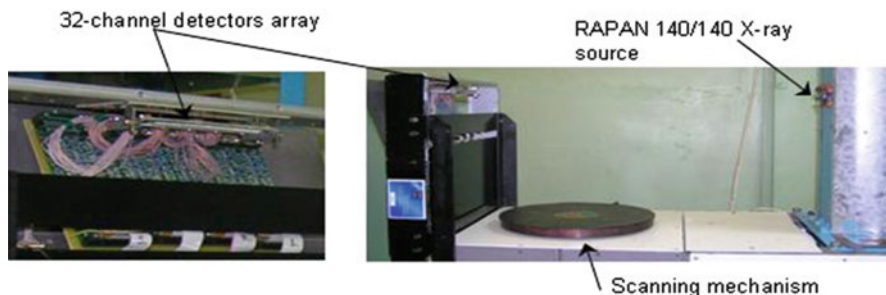
Fig. 1   DRS prototype based on RDC with an array of 32-channel detectors

Thickness of scintillation element is 1 mm   Thickness of scintillation element is 0.4 mm
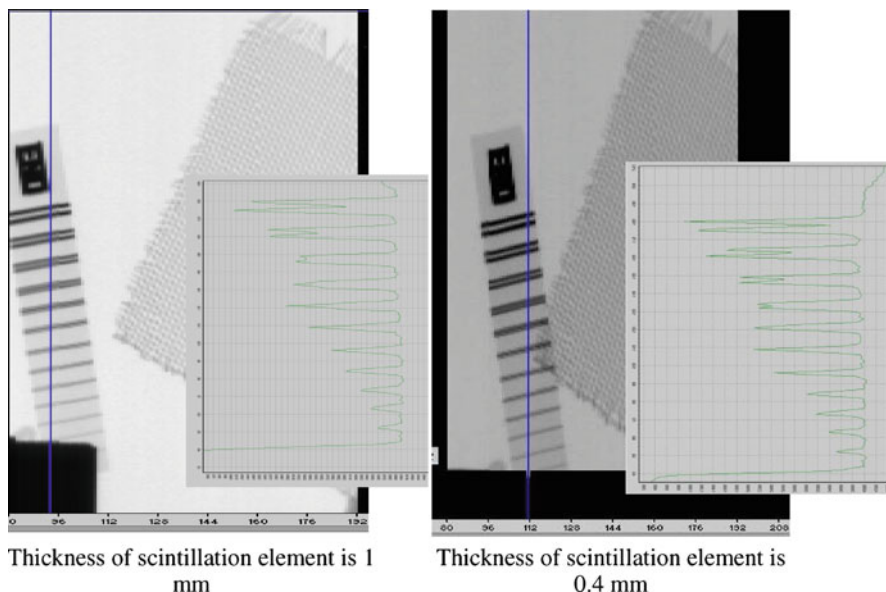
Fig. 2 Shadow X-ray image of the test object obtained using 32-channel detectors with different thickness of scintillation elements

Testing of Detector Array as Part of Model RDC

Using detectors with scintillation elements of different thickness, spatial resolution of DRS was determined using several test objects, namely, EN 462 (calibrated pairs of wires) and a brass gauze with step $1.23 \cdot 10^{-3}$ m and wire diameter $0.38 \cdot 10^{-3}$ m. For quantitative determination of the spatial resolution, an EN 462 test object (calibrated wire pairs) was used.

Using an array of detectors of new design, a shadow X-ray image of the gauze under the same conditions (anode voltage $140 \cdot 10^3$ V, magnification ≈ 2) was obtained. Comparison of these images is a clear evidence of higher spatial resolution with detectors of new design. Tests of detector arrays with different thickness of scintillation elements as part of model DRS, with obtaining images of tested objects (calibrated wire pairs), have shown that, depending upon thickness of the scintillation assembly, the spatial resolution is $1 \div 1.25$ line pairs/10^{-3} m, and detecting ability is better than $0.1 \cdot 10^{-3}$ m steel wire (Fig. 2) [9].

Conclusions

It can be concluded that X-ray detectors reported in this work can be successfully used for creation of fast DRS with improved SR. Their applications include welded joints, pipelines, fabricated metals and metalworks, as well as various objects with components made of materials with different effective atomic numbers.

An important point is the combination of principles of multi-energy X-ray measurements and (reconstruction of substance structure) and tomography (reconstruction of spatial structure). This allows creation of "multi-energy tomographs" – new instruments with unique possibilities in detection and diagnostics. It can be used in inspection systems, including anti-terrorist activities, technical diagnostics, and medicine [9].

References

[1] Ryzhikov, V.D., Opolonin O.D., Galkin S.M.(2009). In: *Hard X-Ray and Gamma-Ray Detector Physics YII*, Proceeding of SPIE Optics+Photonics (Optical Engineering + Application), vol. 7450, pp. 0J1-0J6, San Diego, California, USA.

[2] Ryzhikov, V.D., Opolonin, O.D., Kozin, D.N. (2003), *Nucl. Instr. Meth. A*, vol. 505, pp.192–199

[3] Ryzhikov, V., Kozin, D., Grynyov, B. (2003), *Nucl. Instr. Meth. A*, vol. 505, p.p. 181–184.

[4] Naydenov, S.V., Ryzhikov, V.D., Smith, C.F. (2006). In: *Hard X-Ray and Gamma-Ray Detector Physics YII*, Proceeding of SPIE Optics+Photonics (Optical Engineering + Application), vol. 6319, pp. A1–A8, San Diego, California, USA.

[5] Seminozhenko, V.P., Ryzhikov, V. D., Opolonin, A.D. (2006). In: *Hard X-Ray and Gamma-Ray Detector Physics YII*, Proceeding of SPIE Optics+Photonics (Optical Engineering + Application), vol. 6319, pp. B1–B8, San Diego, California, USA.

[6] Bavendiek, K., Ewert, U., Zscherpel, Meade, U. (2006). In: *New Digital Radiography Procedure Exceeds Film Sensitivity Considerably in Aerospace Applications*, Proceeding of the 9-th Europian Conference on NDT, vol. 2, pp. 44–48, Berlin, Germany.

[7] Grinyov, B.V., Ryzhikov, V.D., SeminozhenkoV.P. (2010). *Scintillation detectors and radiation monitoring systems on their base*, p. 342 (Eds.), Akademperiodyka, Kyiv, Ukraine.

[8] Ryzhikov, V., Grynyov, B., Opolonin, A. (2007), *Radiat. Meas*, vol. 42, pp. 915– 920

[9] Ryzhikov, V. D., Opolonin, O. D., Galkin, S. M., et al. (2010). In: *Hard X-Ray, Gamma-Ray and, Neutron Detector Physics XII*, Proceeding of SPIE Optics+Photonics (Optical Engineering + Application), vol. 7805, pp. 78051P1–P9, San Diego, California, USA.

Novel Approach for Non-Destructive Evaluation of Electrochemical Potentials in Reinforced Concrete Structures

K. Reichling and M. Raupach

Abstract Various non-destructive diagnostic tools are available for a condition assessment of reinforced concrete structures. Potential mapping is a helpful method for locating areas with a high risk of chloride induced corrosion. The influence of the reinforcement continuity was investigated by using laboratory specimens. Furthermore the potential differences were compared between a measuring setup with a reinforcement connection and by measuring with two external electrodes. In assessing the results a novel approach was developed to locate critical areas without a reinforcement connection. The results are displayed by means of vectors similar to the needle of a compass that point to the areas of high corrosion potential, enabling an easy and non-destructive assessment.

Keywords Building diagnoses • Corrosion of steel in concrete • Non-destructive testing • Potential mapping • Reinforced concrete

Introduction

Corrosion of steel in concrete induced by chlorides is one of the major reasons for the deterioration of reinforced concrete structures. Therefore it is important to survey the condition of such structures in suitable time intervals to detect and to monitor critical areas before the degradation progresses so far that a repair measure becomes uneconomical. Potential mapping is a proven method to localise areas

K. Reichling (✉) • M. Raupach
Institute of Building Materials Research, RWTH Aachen University, Germany
e-mail: reichling@ibac.rwth-aachen.de

with a high corrosion risk. To do the measurements without reinforcement connection a wireless method is developed to measure potential gradients and to locate critical areas.

Potential Mapping Without Reinforcement Connection

The most common way to map the electrochemical potentials of a reinforced concrete structure is to connect a high-resistive voltmeter to the reinforcement as well as to a reference electrode and to measure the potentials at the concrete surface vs. the reference electrode. Measuring with this setup the potential values over active areas are typically more negative compared to the nearby areas with passive reinforcement. Figure 1 shows an exemplary potential distribution over an active area.

The measurement of single potentials is not possible. Hence the potential difference is always measured as voltage between a measuring electrode vs. a reference electrode. Usually the reinforcement serves as the measuring electrode (ME) and a copper/copper sulphate electrode, which is electrolytically connected to the concrete surface (electrolyte), serves as the reference electrode (RE). The function of the RE is to provide an arbitrary zero level. Alternatively to the reinforcement a second external reference electrode can be used as ME. The absolute potential differences are the same. While performing the measurement a sufficient high electrolytic conductivity between both external electrodes is important. This measurement setup was already mentioned in [2-4].

The applicability of this method was investigated with a laboratory specimen. A reinforced concrete beam was cast with two electrically disconnected reinforcement bars. The concrete consists of an Ordinary Portland Cement (CEM I) with a w/c = 0,45 and a chloride content of 2,5 wt.-%/cement to depassivate the steel. After curing for a period of approximately two months potential measurements were carried out with different electrode combinations. One external RE ($Cu/CuSO_4$) was
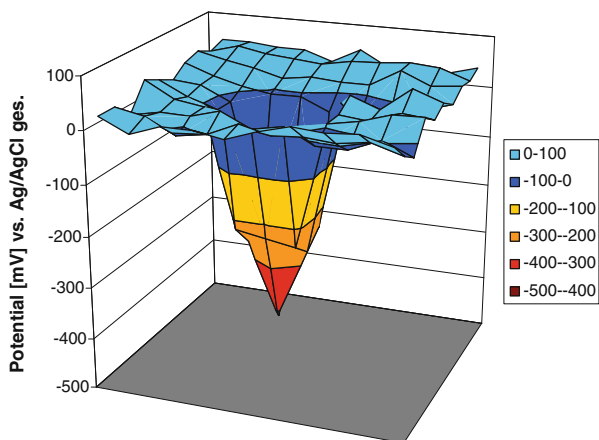
Fig. 1 Exemplary potential distribution over an active area [1]
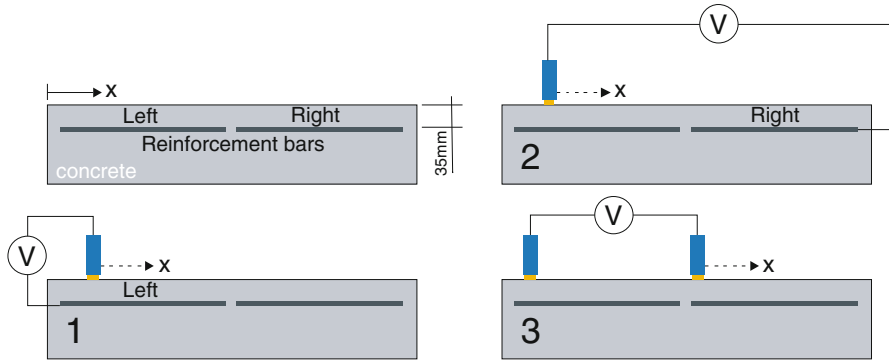
Fig. 2 Illustration of the different measuring procedures

moved in steps of 5 cm at the top of the beam. Three different electrode combinations were investigated as described below (see Fig. 2):

(1) In the first test the potentials were measured between the left reinforcement bar connected as ME vs. a moving Cu/CuSO4 electrode connected as RE.
(2) Then the test was repeated where the right reinforcement bar served as ME.
(3) Within the third test a second external reference electrode served as ME and stayed at x = 2,5 cm, while the external RE was moved in steps of 5 cm over the top of the beam.

The temporal potential changes were minimized by pre-wetting the concrete surface 30 min. before the measurement was started.

In order to compare the results, the potential differences E(x) of the tests 1 and 2 were calculated by subtracting the potential value at x = 2,5 cm ($E_{x=2,5cm}$) from the each value ($E_{x,\,measured}$) within the corresponding test. (see Eqn. (1))

$$E(x) = E_{x,measured} - E_{x=2,5cm} \tag{1}$$

The results are shown in Fig. 3. Two conclusions can be drawn. Firstly the potential differences measured with a second external electrode correspond to the values measured with a reinforcement connection. Secondly the values measured with the left reinforcement bar are similar compared to the values measured with the right reinforcement bar. All this leads to the conclusion that the potential differences can be measured by using only external electrodes. Even if single reinforcement bars are electrically (not electrolytically) disconnected, the potential differences can be measured, supposed that the electrolytic resistance between the electrodes does not influence the readings.

The distance between both electrodes should be minimised to avoid an influence of the resistance. One possible solution is to move all electrodes together. When moving two electrodes, the potential gradient can only be determined for the area along the two electrode positions. A localisation of critical spots in the nearby area can just be realised by measuring the potential difference with at least one further
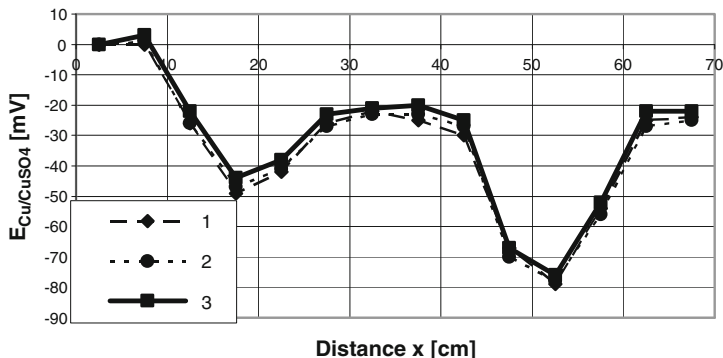
Fig. 3 Potential differences vs. $E_{Cu/CuSO4}$ (x=2,5)
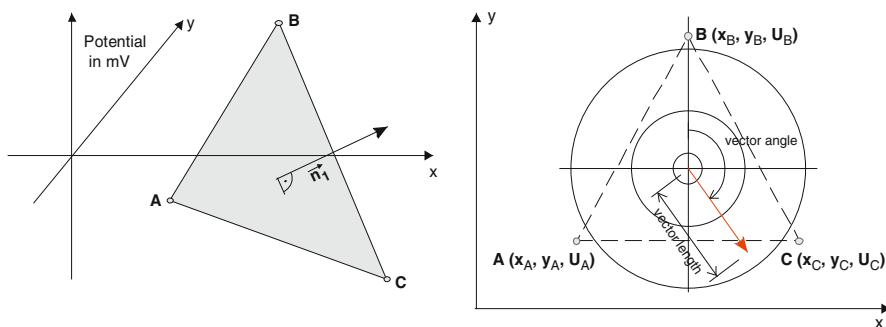
Fig. 4 Illustration of the section (left) and the corresponding results (right)

electrode. This idea led to the development of a novel method to localise critical areas without reinforcement connection during the measurement. The measurement technique is described in the following chapter.

Localisation of Critical Areas with 3 External Electrodes

The measurement setup (so-called Delta-Sensor) consists of three electrodes positioned in the shape of an equal-sided triangle. In each of the 3 corners of the triangle (A, B, C) a copper/copper sulphate electrode is situated. By means of a high resistance voltmeter the readings are taken by measuring two potential differences between the three electrodes.

With these readings and the distance between the electrodes a section in a three dimensional Cartesian coordinate system can be described mathematically (see Fig. 4). The x and y axes are parallel to the concrete surface. The potential

values are plotted in the z direction. The potential value of one point is specified to zero. The mathematical connection of the three points results in a vector space with an inclination corresponding to the potential gradient at the investigation area.

The direction of the inclination and the gradient are required to localise critical areas. To gather the gradient from the reading the unit vector normal to the vector space mentioned above and then the projection of this unit vector parallel to the concrete surface (x-y space) is determined. As result a vector length and a vector angle are calculated for each reading (see Fig. 4). The direction of this projected vector always points to the lowest potential values. The length of the vector correlates with the potential gradient. The higher the potential gradient is, the steeper the vector space is and the longer the projected vector gets.

Application of the Method on a Slab Specimen

Test measurements were carried out on a slab specimen (90 x 70 x 12 cm) to verify the method. The concrete of the specimen contained no additional chlorides and showed similar potential values over the whole surface. To induce a local potential drop an external anode (steel sample in water containing chlorides) was connected
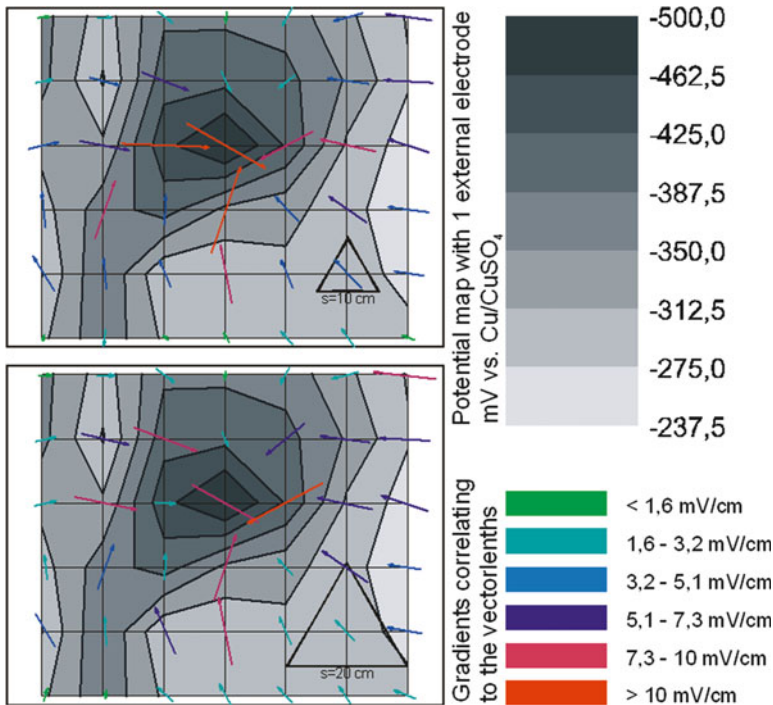
Fig. 5 Potential map and vectors for an electrode distance of 10 cm (top) and 20 cm (bottom)

electrically with the reinforcement in the slab and electrolytically with the concrete in the middle of the slab surface.

The concrete surface was pre-wetted 30 minutes before the first reading was taken. First of all a conventional potential mapping with one external electrode was carried out. Then the 3-electrode readings were taken with an electrode distance of 10 cm and 20 cm. The results are shown in Fig. 5.

The triangle in the right bottom area of the specimen shows the distances between the 3 measuring points. The vectors point more or less all to the most negative potential values. The length of the vectors also correlates well with the potential gradients. The values of the gradients correlating with the vector lengths are indicated on the right bottom side in Fig. 5. Comparing both measurements leads to the conclusion that the results are reproducible. But the readings seem to be sensitive to a discontinuous, unsymmetrical shape of the potential distribution. In this case adequate electrode sizes must be chosen to reduce this effect. Within the next steps the application of the measurement on real structures will be investigated.

Conclusions

On the basis of the discussed tests the following conclusions can be drawn:

1) Potential differences can be measured at the concrete surface by using at least 2 external electrodes without a reinforcement connection.
2) The continuity of the reinforcement is not obligatory as long as the resistivity between the electrodes does not effect the readings significantly. However continuity will be important for a successful repair by cathodic protection.
3) A 3 electrode setup allows a localisation of critical areas.
4) The results of the slab specimen verified the applicability of the method.

References

[1] DGZfP-Merkblatt; Deutsche Gesellschaft für Zerstörungsfreie Prüfung e.V.: Merkblatt B3 Elektrochemische Potentialmessungen zur Detektion von Bewehrungsstahlkorrosion. (Ausgabe April 2008) Berlin: Deutsche Gesellschaft für Zerstörungsfreie Prüfung e.V., 2008
[2] Isecke, B.: Potentialmessung zur Ermittlung von Bewehrungskorrosion. Darmstadt: Freunde des Instituts für Massivbau e.V., 1990. - In: Darmstädter Massivbau-Seminar 4 (1990), 10 Seiten
[3] Marquardt, H. ; Cziesielski, E.: Anwendung der elektrochemischen Potentialdifferenzmessung zum zerstörungsfreien Auffinden korrodierender Bewehrung im Hochbau. Berlin: Institut für Baukonstruktionen und Festigkeit Fachgebiet allgemeiner Ingenieurbau der Technischen Universität Berlin (1987)
[4] Menzel, K. ; Preusker, H.: Potentialmessung: Eine Methode zur zerstörungsfreien Feststellung von Korrosion an der Bewehrung. In: Bauingenieur 64 (1989), Nr. 4, S. 181–186

Non Destructive Monitoring of Fiber Dispersion and Flow-Induced Orientation in Self-Compacting SFRC: A Method Based on Magnetic Properties

L. Ferrara, M. Faifer, M. Muhaxheri, S. Toscani and R. Ottoboni

Abstract Steel fiber reinforced concrete (SFRC) is a composite material which is becoming more and more widely employed in building construction. The mechanical behaviour of the material and the performance of structural elements may significantly depend on the fiber dispersion and orientation with respect to the stress pattern. Non-destructive monitoring of fiber dispersion related issues hence becomes of the foremost importance in order to reliably anticipate the structural performance of elements made with fiber reinforced cementitious composites, as well as for quality control during manufacturing. In this paper a new method for the detection of fiber density and orientation is presented, which is based on the employment of a probe sensitive to the magnetic properties of the steel fibers. The presence and the relative position of steel fibers modify the flux linked by the winding of the probe thus resulting in an impedance variation. The local average concentration and orientation of the fibers can be thus assessed by measuring the variation of the probe inductance. The performance of the method has been analyzed with reference to a self-consolidating high performance fiber reinforced cementitious composite slab. Besides its good sensitivity, the method is also characterized by ease of use, since it just requires to lean the probe on the surface of the specimen, without any particular care about the coupling. This guarantees a high degree of repeatability and low uncertainty in the measurements, even, e.g. on vertical elements or slabs accessible from the bottom.

Keywords Fiber dispersion • Flow induced orientation • Magnetic probe • Monitoring • Self-compacting SFRC

L. Ferrara (✉) • M. Muhaxheri
Department of Structural Engineering, Politecnico di Milano, Italy
e-mail: liberato.ferrara@polimi.it

M. Faifer • S. Toscani • R. Ottoboni
Department of Electrical Engineering, Politecnico di Milano, Italy

Introduction

The dispersion of fibers inside a structural element has been long time recognized as a crucial issue for a safe and reliable design. A spotty dispersion of fibers can in fact affect the element load bearing capacity as well as trigger unanticipated failure mechanisms. Recently it has been shown that the synergy between the Fiber Reinforced Concrete (FRC) and the Self-Compacting Concrete (SCC) technology, due to the rheological stability of the SCC matrix, may be effective at guaranteeing a randomly uniform dispersion of the fibers within a structural element [1]. Furthermore, thanks to both the adapted rheology of the mixture and a carefully designed casting process, it is possible to orient the fibers along the direction of the casting flow [2-3], thus achieving, along the same direction, superior mechanical behaviour of the material and structural performance.

The assessment of fiber dispersion- and orientation-related issues through a non-destructive method is hence of the utmost importance in the framework of an integrated material and structure design approach. The topic has received lots of attention in the very last years and dramatic progresses also thanks to the use of highly sophisticated techniques.

Computer Axial Tomography scanning [2] is able to provide nice 3D visualization of the fiber arrangement within a specimen, but the need of a dedicated equipment (like in the case of X-rays) and software for the quantitative processing of the collected data still stands as a major drawback to a wider use of the method.

Electrical methods have been developed, based on the effects of the conductive fiber reinforcement on either the resistive [4] or the capacitive [5] behavior of the composite, as well as on the whole impedance [6]. The sensitivity of each method to either the preferential orientation of the fibers [4] or their local concentration [5], or both [6], has been shown through comparison with destructive monitoring methods [6,7]. Clearly and widely assessed quantitative correlations between non-destructive measurements and actual local fiber concentration and orientation are still lacking. The major drawbacks stand in the influence of the electrical coupling between the electrodes and the specimens, and in the sensitivity of the matrix resistivity to moisture content and gradients and to the presence of electrolytes in the pores. Measurements can be highly affected by the aforementioned artefacts.

In this paper a new method is employed, which monitors fiber dispersion and orientation through a probe sensitive to the magnetic properties of the composite. The method is based on the magnetic effects of the fibers, as a function of their concentration and relative orientation; when the probe is leant-on the element/structure surface, they cause a variation of the winding inductance. For a careful calibration of the method garnered measurements have been processed for both the local fiber concentration and orientation and correlated to the same quantities evaluated through much more time consuming destructive techniques.

Experimental Program

A High Performance Fiber Reinforced Cementitious Composite (HPFRCC) has been assumed as a reference for this study. Its mix design is shown in Table 1. Two further mixes, with either 50 kg/m³ fibers and no fibers at all (plain matrix) have been designed to the purpose of this study (Table 1). The values of the slump flow diameter, also detailed in Table 1, highlight a self-consolidating ability.

A thin slab 1 m x 0.5 m x 0.03 m thick has been cast with each of the three mixes: fresh concrete was poured at the center of one short edge and, after spreading to the whole width of the slab, completely filled the formwork by flowing parallel to the long side. A preferential orientation of the fibers along the aforementioned direction was with high probability obtained.

Fiber dispersion was monitored by means of the method detailed hereafter and according to the schematic shown in Fig. 1. For each of the 18 cells the slab was "divided" into, measurements were garnered parallel and orthogonal to the flow direction. Each slab was then cut into square tiles according to the same schematic as in Fig. 1 and destructive fiber dispersion evaluation was performed with reference to the tiles shadowed in Fig. 1. Fibers on cross section either parallel (even numbered cells) or orthogonal (odd numbered) to the flow were first counted and

Table 1 Mix design and fresh state performance of the employed HPFRCCs

Mix design (dosages in kg/m³)			
Constituent	HPFRCC 100	HPFRCC 50	HPFRCC 0
Cement type I 52.5	600	600	600
Slag	500	500	500
Water	200	200	200
Superplasticizer	33 (l/m³)	33 (l/m³)	33 (l/m³)
Sand 0-2 mm	983	1000	1017
Steel fibres (l_f = 13 mm; d_f = 0.16 mm)	100	50	0
Fresh state performance			
Slump flow diameter (mm)	750	760	775
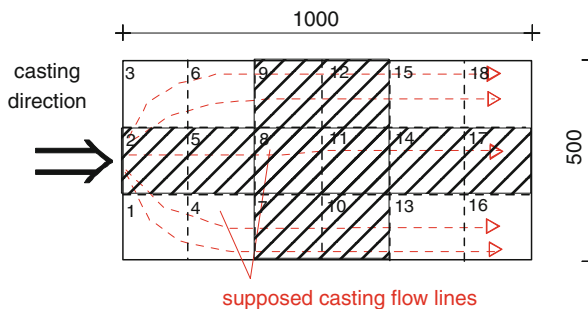
Fig. 1 Slab casting schematic and grid for magnetic measurements
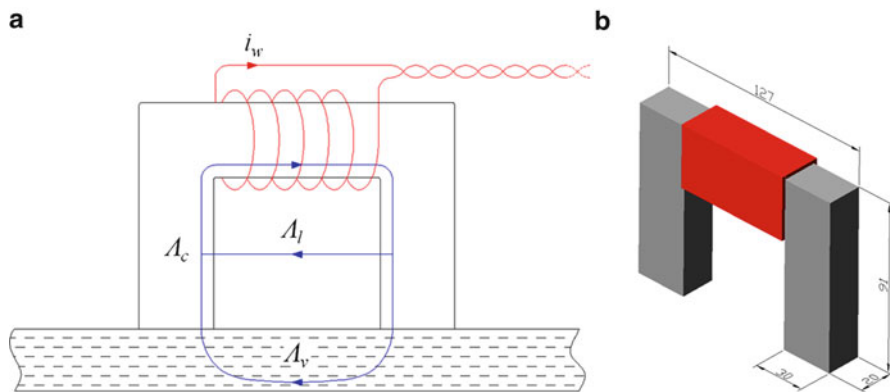
Fig. 2 Scheme of the measurement set-up (**a**) and of the magnetic probe (**b**)

related fiber orientation factor evaluated. Finally specimens were crushed and fibers separated with a magnet and weighed. Comparison with non-destructive measurements, suitably processed for fiber local concentration evaluation, allowed the reliability of the proposed method to be thoroughly assessed.

Magnetic Method: Data Acquisition and Analysis

Because of the ferromagnetic behaviour of steel fibers employed in most of FRC applications, a SFRC may be regarded as consisting of two phases with strongly different magnetic permeabilities: the cement based matrix and the fibers. Neglecting interactions between them, (thanks to the generally quite low volume fraction of the steel fibers) the effective permeability of the composite depends on the permeability of the matrix and of the fibers, on the fiber volume fraction and on their aspect ratio. The measurement of a parameter affected by the effective composite permeability can be hence used to assess both the local average concentration and preferential orientation of fibers in a FRCC specimen.

This concept has been implemented by means of the experimental set-up shown in Fig. 3: it consists of a C-shaped N87 ferrite core with a 78-turn coil wounded around it, through which carries a 100 mA sinusoidal current, providing the magnetic flux. When the magnetic core is leant against a SFRCC specimen, the magnetic flux flows also through the specimen and the impedance measured at the terminals of the equivalent electrical circuit can be expressed as:

$$Z = R_c + j\omega\left[L_l + L_v\right] \tag{1}$$

where R_c denotes the resistance of the coil and L_l and L_v respectively denote the magnetic inductance associate to a magnetic flux outside and through the specimen.
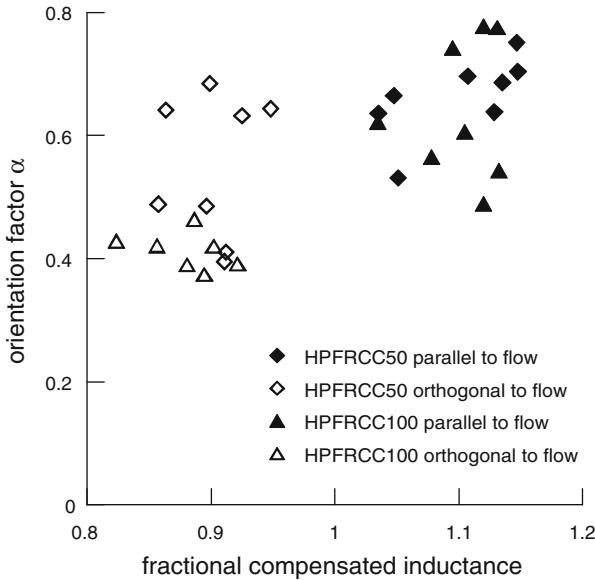
Fig. 3 Fiber orientation factor α (from destructive test) vs. fractional compensated inductance from non-destructive measurements

The inductance L_v can be split into a matrix contribution L_{v0} and an incremental contribution $\Delta L_{v,fibers}$, which depends on the fiber volume fraction and orientation and can be employed to evaluate their local concentration. This incremental contribution will be referred to as compensated inductance and was shown to be sensitive to both the nominal and local average fiber concentration and to the preferential orientation of the fibers. Whereas inductance L_v depended on the measurement frequency, compensated inductances resulted independent of it.

Quantitative assessment of local concentration of fibers, for each of the measured slab cells, was performed through the calibration of the relationship between the "nominal average compensated inductance" and the nominal fiber content in the mix. The former is defined as the average, computed over the whole slab, of the averages of the compensated inductance as measured along the four directions for each cell. By means of such a calibrated law, the average values of compensated inductance for each cell could be processed to assess whether and to what extent the local concentration of fibers differed from the assumed nominal value.

For the assessment of fiber orientation "fractional" compensated inductances along the directions parallel and orthogonal to the flow direction have been calculated:

$$f_{//} = \frac{\Delta L_{//}}{0.5\left(\Delta L_{//} + \Delta L_{\perp}\right)} \text{ and } f_{\perp} = \frac{\Delta L_{\perp}}{0.5\left(\Delta L_{//} + \Delta L_{\perp}\right)} \tag{2}$$

0.5 is the expected value in the case of perfectly in-plane isotropic dispersion.

a

3 ND = 54.	6 ND = 59.5	9 ND = 54.4 D = 56.1	12 ND = 54.7 D = 56.7	15 ND = 50.2	18 ND = 37.3
2 ND = 49.1 D = 54.1	5 ND = 57.6 D = 59.	8 ND = 53.8 D = 55.5	11 ND = 49.6 D = 52.2	14 ND = 45. D = 46.7	17 ND = 36.4
1 ND = 52.1	4 ND = 59.8	7 ND = 52.7 D = 54.9	10 ND = 49.1 D = 46.7	13 ND = 47.7	16 ND = 36.9

b

3 ND = 110.5	6 ND = 110.5	9 ND = 106.6 D = 109.9	12 ND = 103.6 D = 106.7	15 ND = 97.5	18 ND = 88.7
2 ND = 101.8 D = 119.1	5 ND = 108.7 D = 109.5	8 ND = 103.5 D = 107.8	11 ND = 100 D = 101.9	14 ND = 93.7 D = 98.2	17 ND = 79.4 D = 85
1 ND = 100.8	4 ND = 111.7	7 ND = 105.7 D = 105.6	10 ND = 99.5 D = 99.4	13 ND = 94.2	16 ND = 75.9

Fig. 4 Fiber concentration: ND vs. destructive for HPFRCC-50 **(a)** and -100 **(b)**

Method Validation: Destructive vs. Non-destructive

The number of fibers on the cross section of the 18 cells of each slab was counted, with the aid of micro-imaging techniques, either parallel or orthogonal to the casting flow direction (and hence to the preferred orientation of the fibers) respectively for even and odd numbered cells (Fig. 1). Fiber orientation factor was calculated as $\alpha = n_f \, (A_f / V_f)$, with n_{fibers} specific number of fibers on the cross section, A_f cross section area of the single fiber and V_f nominal fiber volume fraction. It can be noticed that α is reliably correlated to the fractional compensated inductance in the same direction (Fig. 3).

Local average concentration of fibers, as from specimen crushing and fiber weighing, has been finally correlated to the one estimated from non destructive measurements. Results shown in Fig. 4 highlight a reasonably homogeneous fiber dispersion inside the elements and coherent with the hypothesized casting flow kinematics. The reliability of the non destructive evaluation is also shown.

Concluding Remarks

A non-destructive method based on the magnetic properties of SFRCCs has been applied to monitor fiber dispersion and orientation in HPFRCC slabs. The results, correlated to the same quantities measured through destructive techniques, highlight the method reliability and its potential for engineering applications.

References

[1] Ferrara, L., Park, Y.D. and Shah, S.P. (2008): *ASCE J. Mat. Civil Eng.*, vol. 20, n. 7, pp. 493–501.
[2] Stahli, P., Custer, R. and van Mier, J.G.M. (2008): *Mats. Struct.*, vol. 41, n. 1, pp, 189–196.
[3] Ferrara, L., Ozyurt, N. and di Prisco, M. (2011): *Mats. Struct.*, vol. 44, n.1, pp. 109–128.

[4] Lataste, J.F., Behloul, M. and Breysse, D. (2008): *NDT & E International*, vol. 41, n. 8, pp. 638–647.
[5] Van Damme, S., Franchois, A., De Zutter, D. and Taerwe, L. (2009): *IEEE Trans. Geosci Remote Sens*, vol. 42, n. 11, pp. 2511–2521.
[6] Ozyurt, N., Woo, L.Y., Mason, T.O. and Shah, S.P. (2006): *ACI Mat. J.*, vol. 103, n. 5, pp.340–347.
[7] Barnett, S., Lataste, J.F., Parry, T., Millard, S. G. and Soutsos, M.N. (2010): *Mats. Struct.*, vol. 43, n. 7, pp. 1009–1023.

Mobile NMR – A Powerful Tool to Measure Coating Thicknesses in Concrete Buildings

J. Orlowsky

Abstract Scores of infrastructural concrete buildings possesses coating systems as protection against aggressive exposure. The functionality of these coating systems is mainly affected by the composition and thickness of there different polymeric layers. A mobile NMR sensor, the so called "NMR-MOUSE®" (Nuclear Magnetic Resonance Mobile Universal Surface Explorer, registered trademark of RWTH Aachen University), enables for the first time ever a nondestructive determination of these controlling parameters. The current results demonstrate the capability of the NMR sensor investigating different coating systems applied on concrete. Analyzing the NMR amplitude as a function of the measuring depth, the composition of the different coating layers gets visible while an accuracy of about 5 to 20 μm can be achieved for the thickness determination. Studying the influence of steel reinforcement inside the coated concrete on the NMR signal leads to a correction of the measuring field position influenced by concrete cover, steel diameter, amount and position of steel.

Keywords Coating • Coating thickness • Concrete • NMR • Nondestructive testing

Introduction

Infrastructural concrete buildings are often protected with coating systems against aggressive exposure. These coating systems assure:

- Protection of the concrete against the penetration of substances like water, chloride, carbon dioxide.

J. Orlowsky (✉)
Institute for Building Materials Research, RWTH Aachen University
e-mail: Orlowsky@ibac.rwth-aachen.de

- Drying up of the concrete due to the coating barrier for water ingress and the moisture transport out of the concrete through the coating.
- Increase of the resistance against chemical and/or mechanical attack.

The concrete-coatings usually consist of different layers of polymers or cement bonded materials. Concrete-coatings are also called "surface protection systems" in Germany.

To ensure the target functions of a surface protection system, the following aspects are important: Thickness of the different coating layers, application method of the coating materials, consideration of environmental parameters like temperature, humidity and wind and preparation of the substrate. The last three points affect the reactive hardening of the coating materials, which is directly linked to the material properties, and the adhesion between concrete and coating as well as between the different layers. The thickness of the coating layers mainly affects the durability and properties like the crack bridging of the surface protection system.

Up to now no non-destructive test-methods exist to determine:

- the whole thickness of the surface protection system as well as the thickness of the different layers,
- the water ingress through the surface protection system,
- the drying process of the concrete after application of a surface protection system,
- changes of the material due to weathering,
- quality and conformity of the applied material.

It is shown below, that the NMR-MOUSE® provides the potential to investigate these issues in a non-destructive way.

The NMR-MOUSE

NMR is a method to interrogate molecular properties of matter by irradiating atomic nuclei in a magnetic field with radio-frequency waves. There is a big variety of the conventional NMR techniques that are used for characterization of polymers. This normally requires the sample to be positioned inside the NMR probe, which is placed inside a magnet with a strong homogeneous magnetic field. In unilateral NMR the magnetic field is applied to the sample from one side, so that the sample can be arbitrarily large. A compact unilateral sensor developed for non-destructive tests of materials is the so called "NMR-MOUSE®" (Nuclear Magnetic Resonance Mobile Universal Surface Explorer, registered trademark of RWTH Aachen University) [1, 2]. The main advantage of the NMR-MOUSE® is its small size and weight.

The NMR-MOUSE consists of four permanent magnet blocks positioned on an iron yoke. Two magnets are polarized along y, and two along $-y$, producing a magnetic field B_0 above the magnet parallel to the surface of the sensor. For analysis, a radio-frequency (rf) magnetic field B_1 is applied by means of a rectangular rf coil mounted in between the magnet blocks, which is perpendicular to B_0 [2, 3].

Different types of the NMR-MOUSE are available. The types differ according to frequency, gradient, measuring depth and resolution [4]. For the investigations described in this paper the NMR-MOUSE PM 5 with a resonance frequency of 18 MHz was used. The PM 5 has a measuring field (sensitive volume) of 20 by 20 mm in the cross-section, while the thickness can be chosen between 10 and 100 µm. The NMR signal can be collected in the described sensitive volume which can be moved until a depth of 5 mm into the specimen by using a lift. At this lift the NMR sensor is mounted on a mobile plate while the specimen is placed on a fixed top plate which is parallel to the mobile plate [4].

The most important contrast parameters employed by the NMR-MOUSE are the signal amplitude corresponding to the proton density and the transverse relaxation time T_2 which relates to the molecular mobility and the effective self-diffusion coefficients of materials containing hydrogen isotopes within the sensitive volume. This information is obtained by using the Carr-Purcell-Meiboom-Gill (CPMG) pulse sequence [3]. To determine the transverse relaxation time, the decay curve measured with the CPMG sequence is fitted with an exponential function (Eq. 1). The proton density is estimated from the integration of the signal corresponding to the first part of the CPMG decay.

$$s(t) = A_0 \cdot \exp\left(\frac{1}{b} \cdot \left(\frac{-t}{T_2} \right)^{b} \right) \tag{1}$$

with amplitude A_0 [-], scaling factor b [-], time t [ms] and relaxation time T_2 [ms]

Application of the NMR-MOUSE

Thickness of coatings

Measuring the proton density in steps of 30, 50 or 100 µm allows conclusions about the composition and layer thickness of coating systems on concrete. In a first step a reference specimen consisting out of polyurethane between two glass plates was investigated (Fig. 1, left). As shown in Fig. 1, right, the proton density inside the glass is nearly zero while the polyurethane has a significant higher proton density. Due to the chosen thickness of the sensitive volume of 100 µm the resolution is about 100 µm. To determine the polyurethane thickness the measuring depth at half of the averaged maximum proton density was calculated (Fig. 1).

Table 1 gives an overview about the mean glass plate and polyurethane thickness calculated from ten profiles in each case. Sensitive volumes (similar to step sizes) of 100, 50 and 30 µm were chosen for the measurements. The standard deviation shows an increasing scatter with decreasing step sizes. An accuracy of 5 µm can be reached with a step size of 50 µm for this example.

Figure 2 shows a comparison of two coated concrete specimens with the same coating system – only the PUR top coat differs, mentioned with the number 2 or
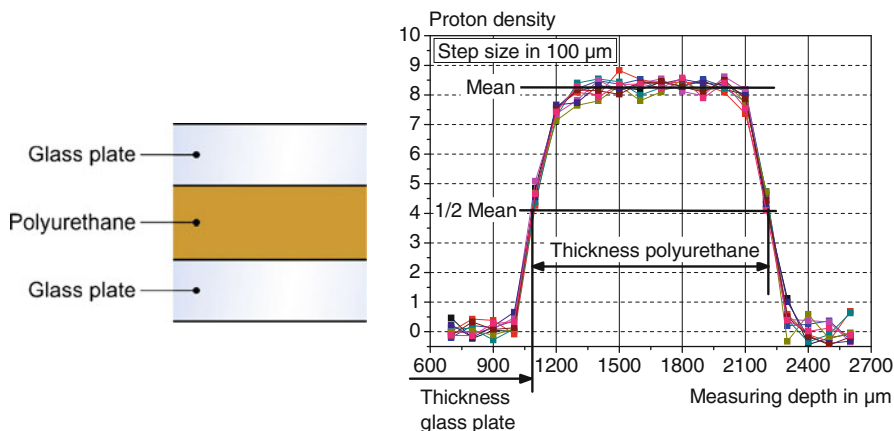
Fig. 1 Left: Draft of the specimen. Right: Proton density as function of the specimen depth

Table 1 Thickness of the glass plate and polyurethane layer depending from the step size. (Mean and standard deviation calculated from 10 profiles in each case.)

	Glass plate		Polyurethane layer	
Step size	Mean	Standard deviation	Mean	Standard deviation
μm				
100	1087	5	1122	4
50	1080	4	1130	5
30	1079	10	1121	20
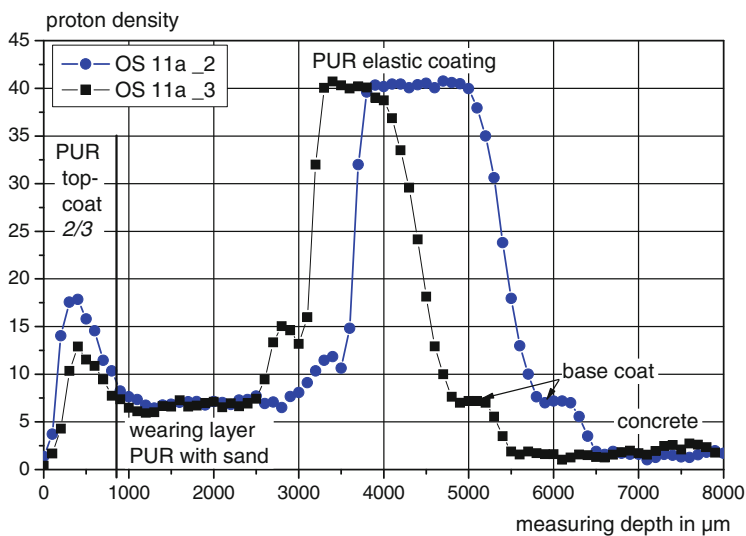
Fig. 2 Comparison of the proton density as function of the measuring depth of two specimens with similar coating systems

rather 3. This coating system consist out of a base coat, applied at the concrete surface, followed by an elastic polyurethane coat, a wearing layer out of polyurethane filled with sand and finally a top coat. Advantage of this kind of multilayer system is a high crack-bridging ability and robustness. Due to the arrangement of the specimens on the lift the measuring depth is top down. The thickness of the sensitive volume was 100 μm. The increasing polymer content leads to an increase of the proton density. This enables us to differ between the top coating, the PUR-layer with sand and the elastic coating.

Figure 2 clarifies a lower thickness of the PUR elastic coating of the specimen OS 11a_3 compared to the specimen OS 11a_2. The thickness of this layer is reduced from ~2000 μm to ~1500 μm. The thickness of the wearing layer of OS 11a_3 is also reduced in comparison to OS 11a_2. Furthermore the different materials for the top-coat can be distinguished by the changed proton density in this area. The use of same materials for the base, elastic and wearing coat is also detectable by the unchanged proton density. Consequently the NMR-MOUSE can be used as quality control for the uniformity of coatings on the construction site.

The good correlation between the measured thicknesses of the coating layers via microscope and NMR-MOUSE were shown in [3, 4].

Influence of the steel reinforcement inside the concrete on the NMR-signal

Infrastructural concrete buildings with coating systems mostly consist of steel reinforced concrete. Against concrete cover, steel diameter, amount and position of steel the NMR-signal shifts along the measuring depth and the amplitude changes. Figure 3 clarify the influence of steel bars at different distances from the NMR-sensor
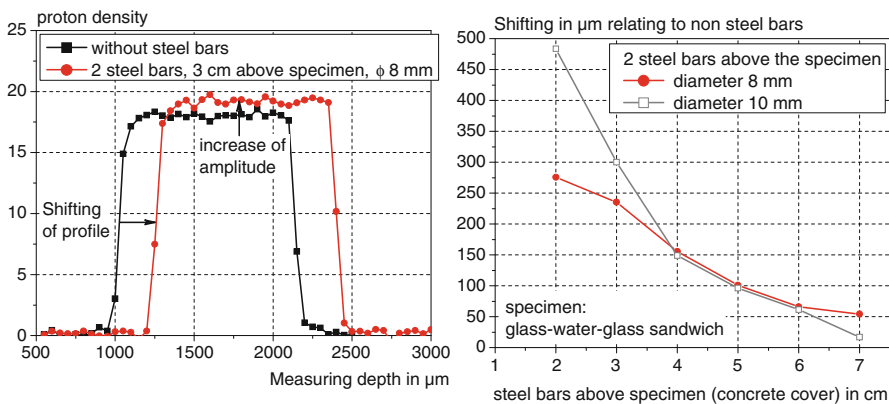
Fig. 3 Left: Changes of a glass-water-glass-profile due to steel bars 3 cm above the specimen. Right: Influence of the distance between specimen and steel bars

on the NMR-profile. The measurements were done with a glass-water-glass-specimen comparable with the sample shown in Fig. 1, left, while the reinforcement bars were positioned at a certain distance above the specimen. Due to the steel bars the NMR-signal is shifted parallel to higher measuring depth, the proton density is increased while the thickness of the water-layer keeps constant. The value of the parallel shift decreases with increasing distances between the steel bars and the NMR-sensor. An increase of the steel diameter leads to an increase of the shift.

Summary

The current results demonstrate that the NMR-MOUSE is a promising tool for non destructive testing of coatings on concrete. The thickness of the coating and its constituting layers can be measured. Furthermore, conclusions about the composition of coatings can be drawn. Realising the application of this described technique on building surfaces the influence of steel reinforcement inside the concrete has to be taken into account. Against the steel amount and distance between steel and NMR-sensor a shift of the profile as well as an increase of the proton density occurs, while the measured thicknesses keeps constant.

References

[1] Blümich, B. (2004), Essential NMR, Springer, Berlin
[2] Perlo, J., Casanova, F., Blümich, B. (2005), Profiles with microscopic resolution by single-sided NMR, *J. Magn. Reson.* 176, p. 64–70.
[3] Orlowsky, J. (2010), NMR Inspection on Concrete-Coatings, Proceedings of the 2nd International *Conference on Service Life Design for Infrastructure* (SLD), Delft, Netherland
[4] http://www.act-aachen.com/profile_MOUSE.html
[5] Orlowsky, J., Raupach, M., Baias, M., Blümich, B. (2008), Application of the NMR-Technique to Concrete Coatings, Proceedings of the 2nd International *Conference on Concrete Repair, Rehabilitation and Retrofitting* (ICCRRR), Cape Town, South Africa, p. 335–336

Innovative Sensor Technologies for Nondestructive Imaging of Concrete Structures: Novel Tools Utilising Radar and Induction Technologies

S. Korl, C. Wuersch and J. Zanona

Abstract Nondestructive testing methods in building construction and civil engineering are needed to avoid costly damages caused by cutting reinforcement during drilling and coring and to image structures for condition assessment and evaluation. In this paper, the technology and application of two of Hilti's nondestructive imaging tools are presented. The handheld wall penetrating radar system is suited to locate various objects, such as rebar, tendons, conduits, pipes, cables, voids, etc. in concrete. The radar tool comprises an antenna array for quick scanning and high data quality, real-time processing and visualisation for easy interpretation and 3D data representation available at the job-site. Furthermore, reinforcement verification, measurement of concrete coverage and statistical analysis can be performed with the Hilti Ferroscan system based on electromagnetic induction.

Keywords Electromagnetic induction • Nondestructive imaging • Reinforcement verification • Safe drilling and coring • Wall penetrating radar

Introduction

In this paper the Hilti PS 1000[*] Scanner system is introduced, which is a new ground/wall penetrating radar tool for nondestructive testing of concrete structures. The established Hilti PS 200 Ferroscan[*] is an imaging and analysis tool based on

S. Korl (✉) • C. Wuersch • J. Zanona
Hilti AG, Feldkircherstrasse 100, FL-9494 Schaan, Liechtenstein
e-mail: sascha.korl@hilti.com

electromagnetic induction. In the course of the paper the technology and application of the novel radar tool is focused on and differences to the complementary induction technology are selectively pointed out.

The paper starts with an overview, before the details of the newly developed technology are presented. Afterwards, some application examples are shown. The paper is closed with the description of the system solution and a summary and outlook.

Overview

Ease-of-use and productivity for the professional on the jobsite in building construction and civil engineering have been the major foci for development of the radar system. Figure 1 shows the radar scanner which is a self-contained tool for data acquisition, processing and visualisation.

The radar front-end comprises an antenna array of three linear polarised antennas (cf. Fig. 1). Short pulses are used as excitation signals, where each antenna is consecutively used as transmitter and all antennas are used as receivers to record the reflections from subsurface objects. In radar terminology the combined use of antennas as transmitter and receiver is called mono- and bistatic configuration. This special array configuration leads to superior separation of objects laterally and in depth. The use of each of the three antennas in monostatic and bistatic mode leads to five simultaneous radar traces.

In the Ferroscan system a transmitter coil generates a periodic electromagnetic field. A sophisticated pattern recognition algorithm deduces rebar position, embedment depth and diameter from the signals recorded by multiple coil pairs.

Fundamental differences between electromagnetic induction and radar technology are the detectability of objects of different materials and the dependency on the properties of the base material. With the induction technology only ferrous materials can be detected whereas with radar objects of different materials (such as ferrous and non-ferrous metals, water-filled pipes, voids, etc.) can be detected.
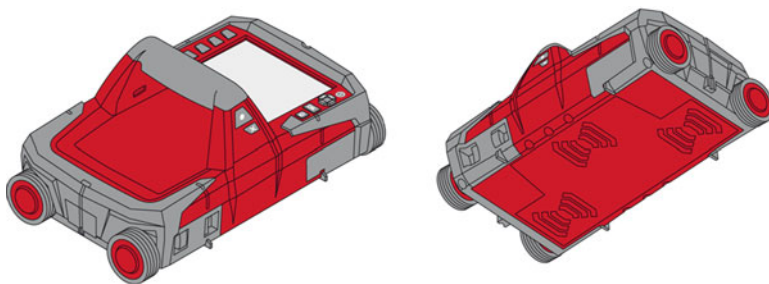
Fig. 1 The radar scanner, view from above (left) and below (right). Note the antenna array configuration on the bottom side of the scanner

Furthermore, the induction technology is independent of the base material as long as it is non-conductive whereas the depth scaling of the radar data depends on the permittivity of the base material. In addition, with the radar technology it is possible to visualise multiple layers of objects (if the mesh size is not too small).

Detailed Description

The radar scanner supports different measurement modes. First, the so called Quickscan, which acquires, processes and visualises the data in real-time. Second, Quickscan Recording, where data of scans up to 10m can be recorded and stored for later analysis and third, the Imagescan mode, which is used to analyse areas (up to 1.2x1.2m / 4x4ft). Three dimensional analysis is available for both Quickscan Recordings and Imagescans.

The emitted radar pulses spread over a wide frequency range (measured in air from 1.0 to 4.3 GHz). The lower the frequency the deeper the subsurface is penetrated and the higher the frequency, the smaller objects can be resolved.

As the radar tool is moved over the surface a measurement is taken every 5mm. An intelligent distance measuring algorithm samples the position of all four wheels and compensates for slipping, spinning or lifted wheels. At one scanner position a large number of pulses are emitted and recorded to determine the full reflection pattern of the subsurface objects. Multiple acquisitions are used to reduce the noise (which usually appears as unwanted clutter in the visualisation) in the measured data which leads to a clearer image. In the radar scanner a high pulse repetition rate is used, which allows high scanning speeds (up to 2m/s).

The recorded raw data is processed according to the processing chain as depicted in Fig. 2.

The signal acquired by the radar front-end is further conditioned by the following steps [1]:

- Correction of antenna sizes and positions;
- Background removal with automatic foreground/background detection to mask uniform structures such as the surface and possible stratifications;
- Automatic gaining to compensate the damping of the radar waves in the base material;
- Time-zero estimation (automatic recognition of the surface position) and
- Temperature compensation to allow immediate and accurate measurements directly after start-up.
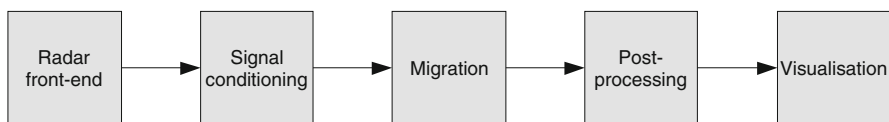
Fig. 2 Processing chain for the radar data

The central processing step is the transformation of the raw measurement data into images of objects, which is called migration. In the scanner a modified f-k migration is used [2]. The radar PC-software[†] supports also modified Kirchhoff migration [3].

Before the migrated data can be visualised it is further processed to extract the approximate shape of objects (Hilbert envelope and Isosurface computation for 3D view).

Application Examples

In the following selected application examples are shown out of the vast range of applications.

As a first example, the Quickscan mode can be utilised for quickly locating a spot to set an anchor, for instance. Figure 3 shows the application scenario and a screen copy of the scanner during real-time measurement of the horizontal direction. Another measurement for the vertical direction has to be done in addition.

As a second example, a pre-stressed concrete slab has been scanned to find a save spot for a through-penetration. It is vital for the safety of construction workers and the stability of buildings not to cut tensioning cables during drilling or coring. A 1.2x1.2m Imagescan has been made and the resulting visualisation is shown on the right-hand side of Fig. 4.

The last example demonstrates a typical application area for electromagnetic induction. In tunnels the reinforcement grid has to be covered by a minimum amount
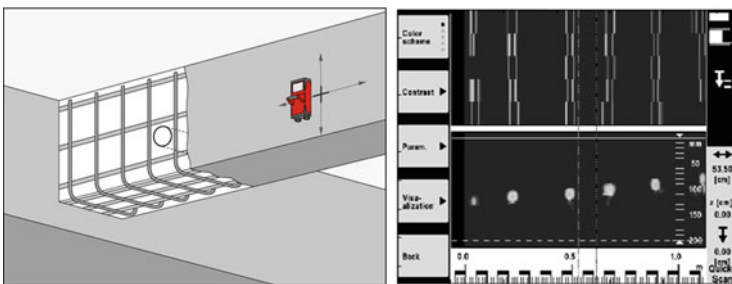
Fig. 3 A typical application of the radar scanner system: Finding save spots for drilling in beams, slabs, etc. (left) and the corresponding screen copy of the scanner in Quickscan mode (right). The upper half of the screen copy shows the top view representation, the lower half shows the corresponding cross section

---

[†]Hilti PROFIS PS 1000
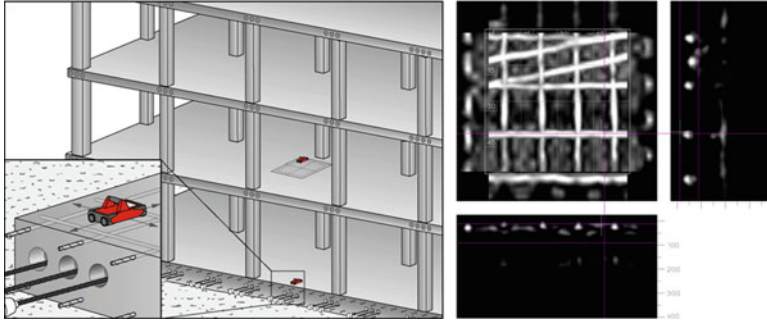
Fig. 4 In another application example an area of a pre-stressed concrete slab has been scanned to find a save spot for a through-penetration. Cutting a tensioning cable would endanger construction workers and reduce the stability of the building. The resulting Imagescan is depicted on the right-hand side; the tensioning cables underneath the first layer of reinforcement are visible as two inclined lines in the top view
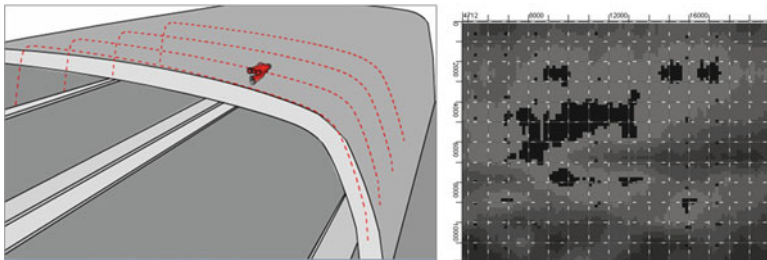
Fig. 5 Example use of magnetic induction for measurement of concrete coverage in tunnels. The right-hand image shows a map of concrete coverage (shown area approx. 12x10m). Dark colours indicate areas where the concrete coverage is too low and therefore those areas are susceptible to corrosion

of concrete to prevent corrosion. In the example a tunnel wall has been scanned with the Ferroscan and the associated software is used to generate a map of concrete coverage (cf. Fig. 5).

System Solution

The scanner itself is self-contained and can be used for data acquisition, processing and analysis. For further analysis, though, especially in full 3D, and for voluminous data storage the job-site qualified PSA 100 Monitor can be used. An example of a 3D-visualisation on the monitor is shown in Fig. 6.

If further reporting capabilities are needed, Software for standard office PCs is included in the set (Hilti PROFIS PS 1000).
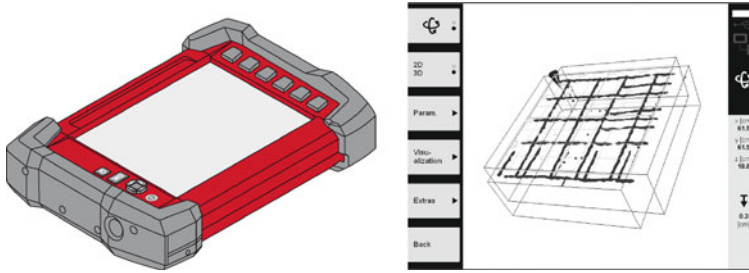
Fig. 6 The radar system consists of the radar scanner, the PSA 100 Monitor, a job-site computer for in-depth analysis and archival storage (left) and the radar PC-software for the office computer. An example of a 3D-visualisation on the monitor is shown on the right-hand side

Summary and Outlook

In this paper a glimpse onto the new radar scanner system has been given. This easy-to-use impulse radar scanner offers high productivity and good data quality through a special antenna array configuration, sophisticated real-time data processing and comprehensible visualisation to help the professional in building construction and civil engineering prevent costly damages by visualising objects of a lot of different materials. Full 3D analysis is available on the PSA 100 job-site monitor as well as on the PC software.

The Ferroscan is a complementary imaging system based on electromagnetic induction which is used for the detection of ferrous objects such as rebars with accurate estimation of rebar depth and diameter.

In future, it will be possible to combine data of both measurement principles to profit from the advantages of both technologies.

References

[1] Daniels, David J. (2004), *Ground Penetrating Radar – 2nd Edition*, IEEE.
[2] Stolt, R. H. (1978), *Migration by Fourier Transform*, Geophysics, vol. 43, n. 1, p. 23–48.
[3] Schneider, William A. (1978), *Integral Formulation for Migration in two and three Dimensions*, Geophysics, vol. 43, n. 1, p. 49–76.

Comparative Study of Nonlinear Resonance and Wave Interaction Techniques for Concrete Damage Assessment

Y. Boukari, P. Rivard, D. Bulteel, G. Balleivy and N.E. Abriak

Abstract Two nonlinear parameters extracted from different approaches have been compared on their sensitivity and reliability to detect thermal damage in concrete. One approach is based on nonlinear resonance while the other relies on wave interactions. Results show that both nonlinear parameters have a sensitivity to thermal damage of the same order of magnitude. Variations observed are much higher than in the case of linear parameters (ultrasonic pulse velocity and dynamic modulus). Coefficients of variation showed that resonance frequency technique is more reliable than wave interaction technique. However, the latter technique remains of great interest and needs further developments since it is more adapted to *in situ* measurements.

Y. Boukari
Department of Civil Engineering, Université de Sherbrooke, Sherbrooke, Canada

Univ Lille Nord de France, F-59000 Lille, France

EMDouai, MPE-GCE, F-59500 Douai, France

P. Rivard (✉) • G. Balleivy
Department of Civil Engineering, Université de Sherbrooke, Sherbrooke, Canada
e-mail: patrice.rivard@usherbrooke.ca

D. Bulteel • N.E. Abriak
Univ Lille Nord de France, F-59000 Lille, France

EMDouai, MPE-GCE, F-59500 Douai, France

Introduction

Nonlinear acoustics have generated an increasing interest over the last decade in the field of concrete damage assessment. Although the nonlinear behavior of concrete is a complex issue that has not been well understood yet, some experiments based on nonlinear acoustics have been developed in order to observe and quantify several nonlinear phenomena. These are, for instance, resonance frequency shift, higher harmonic generation or mixed frequency response [1].

The great majority of nonlinear monitoring techniques rely on two different approaches: nonlinear resonance [2] and nonlinear wave interaction [3]. Regardless the approach used and parameters analyzed, several studies have systematically shown that nonlinear parameters are more sensitive to concrete degradation than traditional linear parameters such as ultrasonic pulse velocity, resonance frequency or dynamic modulus [4-8].

This paper aims at comparing the sensitivity and reliability of nonlinear wave resonance and nonlinear wave interaction with thermal damage induced on concrete. Ultrasonic pulse velocity and dynamic modulus were also monitored as reference parameters.

Experimental

Concrete casting and degradation

Four concrete cylinders (100x200mm) were cast with a w/c ratio of 0.5 and a cement content of 420 kg/m³. The maximum size of aggregate was 20mm. After a 28-days cure in fog room, the cylinders have been kept in laboratory ambient conditions. Degradation process consisted in heating the specimens for 3 hours at 150°C and cooling them by soaking them for 15 minutes in water at room temperature. Measurements were taken after the curing period and the thermal damage.

Linear acoustics

Measurements were performed in compliance with ASTM standards to monitor ultrasonic pulse velocity (ASTM 597) and dynamic modulus of elasticity (ASTM C215-02).

Nonlinear resonance technique

Concrete cylinders were exited with pure sine waves. A series of frequency sweeping was performed around the resonance frequency of the sample, with increasing drive amplitude. The experimental device used in shown in Fig. 1.
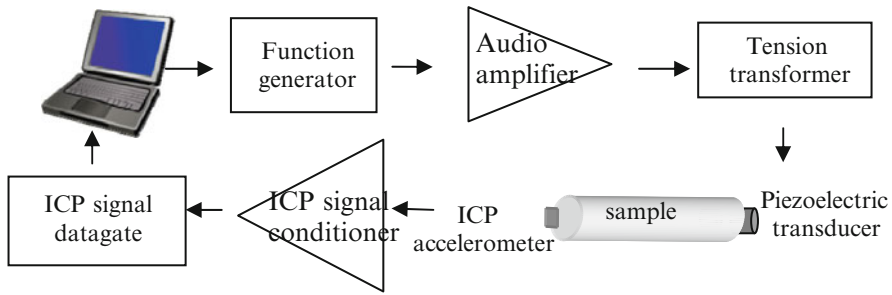
Fig. 1 Nonlinear resonance experimental device
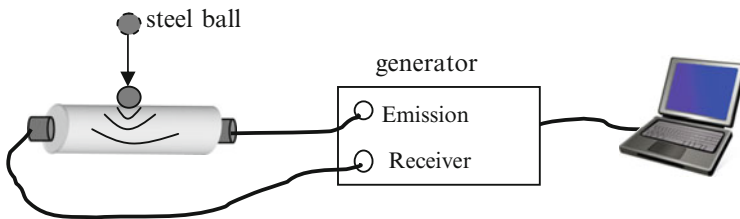
Fig. 2 Nonlinear wave interaction experimental device

The nonlinear elastic behaviour of concrete can be observed by the resonance frequency shifting towards lower values when the drive amplitude increases. Nonlinear parameter α_1 can be extracted by plotting the frequency shift vs the amplitude, as shown in Eqn. (1).

$$\frac{\Delta f}{f_0} = \alpha_1 . \Delta \varepsilon \tag{1}$$

$\Delta f = f - f_0$, f is the monitored reonance frequency and f_0 the linear resonance frequency (at lower strain), $\Delta \varepsilon$ is the strain amplitude.

Wave interaction technique

Wave interaction technique basically consists in studying the interactions between a high frequency (HF) and low frequency (LF) harmonic signals. When simultaneously transmitted trough concrete, the HF signal is amplitude modulated by the LF signal, which results in the presence of side lobes around HF on the transmitted signal spectrum.

The wave interaction technique developed for this study (*Fig. 2*) differs from classical approach by one main characteristic: the HF signal transmitted through the sample consists in a series of pulse instead of a continuous signal. A LF signal was generated by a short mechanical impact, causing cycles of opening/closing of
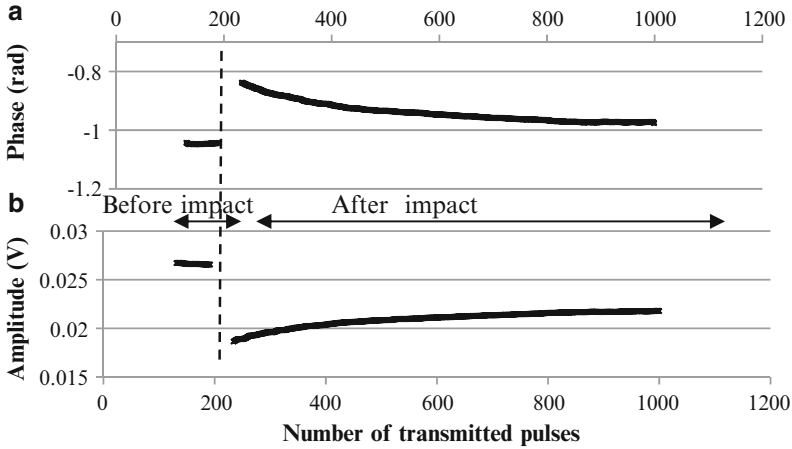
Fig. 3 Typical variation of phase (a) and amplitude (b) of the transmitted signal during wave interaction experiment

cracks within the concrete. As a result of such mechanical disturbance, the HF waves undergo a temporal delay that can be determined from a phase shift in the transmitted signal (*Fig. 3a*).

Nonlinear parameter α_2 can be extracted from this experiment by plotting the phase shift of the transmitted series of signal vs its amplitude, after the impact.

$$\alpha_2 = \left| \frac{\Delta\Phi}{\Delta A} \right| \tag{2}$$

$\Delta\varphi$ represents the phase variation of transmiited signal after the impact, ΔA its amplitude variation

Results and Discussion

Figure 4 shows the relative variations of the monitored parameters between sound and damaged concrete.

The pulse wave velocity decreased from aproximatively 4600 m/s to 4300 m/s, indicating that the induced thermal damage did not affect significantly the engineering properties of concrete. Indeed, the samples remain of good quality from a mechanical point of view.

As expected, nonlinear parameters α_1 and α_2 show a much higher sensitivity to the thermal damage with regards to linear parameters. This significant increase is associated with the formation of microcracks in the concrete, mostly at the cement-aggregate interface and in the cement paste, without any preferential direction [6]. Although they have been derived from distinct experiments, α_1 and α_2 show variations
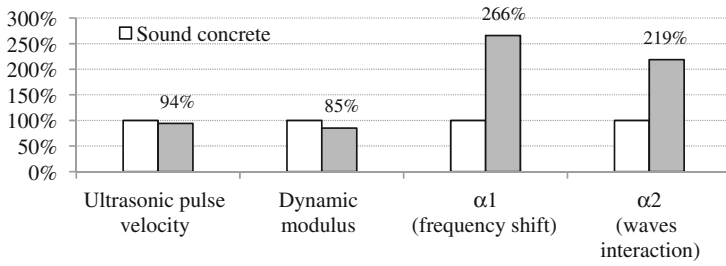
Fig. 4 Relative variations of non destructive parameters to thermal damage

Table 1 Coefficient of variation for each parameter

	Coefficient of variation (%)			
	Ultrasonic pulse velocity	Dynamic modulus	α_1	α_2
Sound concrete	1	2	5	58
Damaged concrete	2	6	20	47

of the same order of magnitude. In order to complete comparision between nonlinear methods, the coeffcients of variation are given in *Table 1*.

Table 1 shows that linear parameters are generally more stable than nonlinear parameters. The relatively high coefficients of variation of α_1 and α_2 are mainly associated with three characterisitics of experimental techniques: sensitivity, repeatability and reproductibility.

The sensitivity to microcracking of both nonlinear techniques was demonstrated. This sensitivity also includes natural heterogeneity of concrete, hence the heterogeneity between different samples. The part of the coefficients of variation that can be attributed to the heterogeneity of samples is hard to determine.

However, α_1 and α_2 have shown similar sensitivy to thermal damage in concrete, and yet the coefficients of variation for α_2 are 2 to 10 times higher than those for α_1. Conclusion can be drawn that the interaction wave technique used presents lower repeatability and reproductibility than nonlinear resonance technique. Indeed, signal processing and analysis are more complex in the case of wave interactions, although the technique used in this study allows a lighter signal processing compared with the one required for the wave modulation.

Further developments are needed to make wave interaction techniques more reliable. These developments are of great interest since wave interaction techniques are more adapted to *in situ* measurements than nonlinear resonance techniques.

The next step of development concerning this study will focus on repeatability and reproductibility of nonlinear techniques. Repeatability will be investigated by means of larger series of measurements on identical samples. Reproductibility will be investigated on the basis the water content of concrete. Indeed, water content is known to have a significant impact on nonlinearity of concrete as it changes the nature of cracks interface [9], but few data are available on this issue.

Conclusion

This study showed that both nonlinear techniques tested have a similar sensitivity to thermal damage in concrete but differ on their repeatability and reproductibility. Nonlinear resonance has proven to be more reliable since the coefficients of variation are low compared with those of interaction wave. Hence, nonlinear resonance should be used in priority to monitor limited damage in concrete, especially if a statistical number of samples cannot be available. This technique, which requires driving elements into resonance, is however very hard to perform *in situ* on large structures. Nonlinear wave interaction techniques therefore remain of major interest and need further development to improve their reliability.

References

[1] Ostrovsky, L.A. and Johnson, P., (2001), *La Rivisita del Nuovo Cimento*, vol. 24, n. 1–46.
[2] Van den Abeele, K.E.A., Carmeliet, J., Ten Cate, J.A., and Johnson, P.A., (2000), *Res. Nondestruct. Eval.*, vol. 12, n. 1, 31–42.
[3] Van den Abeele, K.E.A., Johnson, P.A., and Sutin, A., (2000), *Res. Nondestruct. Eval.*, vol. 12, n. 1, 17–30.
[4] Van Den Abeele, K. and De Visscher, J., (2000), *Cem. Concrete Res.*, vol. 30, n. 9, 1453–1464.
[5] Stauffer, J.D., Woodward, C.B., and White, K.R., (2005), *ACI Mater. J.*, vol. 102, n. 2, 118–121.
[6] Payan, C., Garnier, V., Moysan, J., and Johnson, P.A., (2007), *J. Acoust. Soc. Am.*, vol. 121, n. 4, EL125–EL130.
[7] Chen, J., Jayapalan, A.R., Kim, J.-Y., Kurtis, K.E., and Jacobs, L.J., (2010), *Cem. Concrete Res.*, vol. 40, n. 6, 914–923.
[8] Sargolzahi, M., Kodjo, S.A., Rivard, P., and Rhazi, J., (2010), *Constr. Build. Mater.*, vol. 24, n. 8, 1398–1403.
[9] Kodjo, A.S. (2008), *PhD Thesis*, Université de Sherbrooke, 127p.

Ultrasonic Signal Processing Based on the Combined Use of Empirical Mode Decomposition and Split Spectrum Processing Using the Prism Technique

S. Haddad, M. Grimes, T. Benkedidah and A. Bouhadjera

Abstract   In this work we present the application of Empirical Mode Decomposition (EMD) and Split Spectrum Processing (SSP) in non-destructive testing of materials using ultrasound. The SSP as well as the EMD technique enable to enhance target detection and the visibility of reflected echoes. The use of the EMD technique before using SSP makes the detection of any desired target-echo more flexible, when looking for a good solution to the coherent noise problem. Some types of coherent noise can be removed by frequency filtering but only provided that the amplitude spectrum of the noise does not overlap the spectrum of the desired signal. In the most practical situations, this noise may comprise refractions, multiple reflections, reflected refractions or refracted reflections, and coherent noise from grains and scatters with different sizes. The signals were obtained using a technique applied in pulse-echo mode, known as the prism technique and processed in Matlab environment. Tests carried out on trapezoidal-prism shaped specimens of mortar highlight the capability of this signal processing technique.

Keywords   Coherent noise • Empirical mode decomposition • Non-destructive testing • Prism technique • Split spectrum processing

Introduction

In ultrasonic NDT of highly scattering materials, detection of reflected echoes from defects or boundaries is difficult due to the masking effect of the structural noise. The most frequently used signal-processing method for noise reduction is

S. Haddad (✉) • M. Grimes • T. Benkedidah • A. Bouhadjera
NDT Lab, Faculty of Sciences and Technology, Jijel University, Algeria
e-mail: sof_had@yahoo.fr

time averaging but it can reduce only the incoherent content of the signal noise. This is not enough for testing concrete because the remaining noise, which is the coherent (or scattering) noise produced by backscatter of the propagating ultrasound, is still overwhelming. The reduction of the scattering noise requires a more advanced technique and the split spectrum processing (SSP) is such a technique. SSP is based on the observation that a source of scatter in the concrete reflects different echoes from different frequencies in the form of coherent noise; that is, the scattering content is highly sensitive to shifts in the operating frequency, whereas the echoes from defects and boundaries are not. In this work, SSP and empirical mode decomposition (EMD proposed by Huang et al. [1]) are used to deal with detecting complex multiple targets in ultrasonic applications. EMD is one of the most advanced concepts considered in digital signal processing and focused on processing nonlinear and nonstationary processes. In comparison with the classical Fourier analysis and wavelet algorithms, EMD has a very high extent of adaptation to processing various nonstationary signals. Furthermore, it does not impose any serious restrictions on the harmonic nature of basis functions. The key role is played by empirical mode decomposition, which allows any complicated signal to be decomposed into finite and a usually very small number of empirical modes (IMFs—Intrinsic Mode Functions), each containing information about the initial signal.

Split Spectrum Processing

Split-spectrum algorithms exploit the frequency diversity phenomenon appearing when an ultrasonic pulse is scattered by many small scatters having sizes comparable to the pulse wavelength. The combined response of all the scatters is frequency sensitive due to the different phases of every individual contribution. On the contrary, the response of an isolated reflector of enough size will be unique and so frequency insensitive. Given an operating bandwidth, the inherent idea in SS algorithms is to use a filter bank to decompose the received signal followed by a comparison of the different filter outputs, so that, broadly speaking, when all the filter outputs are similar, the presence of a true defect is enhanced, otherwise, presence of grain noise is reduced [2]. The algorithm can be described as follows: The first step involves fast Fourier transform (FFT) which gives the frequency spectrum of the received echo signal. In the second step, several filters split the signal spectrum into different narrow frequency bands. Next step, inverse FFT gives the time domain signal of each individual frequency band. Observations from each channel cover the bandwidth of the frequency spectrum of the transducer and each observation contributes to signal-to-noise improvement. Therefore, at any given time, the outputs of band pass filters can be represented as a random feature vector that contains information related to flaw and grain echoes. The signals from each individual frequency band (SSP channel) are passed into a post-detection processor. In this paper, we have employed polarity thresholding algorithm as processor, which was shown to be effective in the past applications. The PT algorithm was based on the principle that at the time instants when flaw signal is presented, the corresponding SSP data set

will not exhibit any polarity reversal since the flaw or the boundary echo will dominate the grain noise. If the data set contains only grain noise, which possesses a zero mean value, then it is likely that the data will exhibit polarity reversal. The PT output can be expressed as

$$\begin{cases} y(t) & = & \max(|\,x\,(t)\,|)\,(x\,(t) > 0 \quad or \quad x\,(t) < 0, j = 1,2,\ldots,N) \\ y(t) & = & 0(otherwise) \end{cases} \tag{1}$$

Empirical Mode Decomposition

The Empirical Mode Decomposition (EMD) is a signal processing technique capable of extracting all the oscillatory modes present in a signal at different length scales. The decomposition method [3] involves the following steps:

Step 1: Given a signal $x(n)$, finding the local maxima of the signal, all the maxima are connected by a cubic spline line as the upper envelope. Then finding the local minima of the signal, all the minima are connected by a cubic spline line as the lower envelope. The mean of the upper envelope and the lower envelope is designated as $m_1(n)$,

$$h_1(n) \;=\; x(n) - m_1(n) \tag{2}$$

If $h_1(n)$ satisfies all the requirements of the IMF, it is the first IMF.

Step 2: If $h_1(n)$ does not satisfy the conditions of the IMF, it is treated as the datum, and Step 1 is repeated. $m_{11}(n)$ is the mean of the upper and the lower envelopes of $h_1(n)$, then

$$h_{11}(n) \;=\; h_1(n) - m_{11}(n) \tag{3}$$

If $h_{11}(n)$ satisfies all the requirements of the IMF, it is the first IMF. If $h_{11}(n)$ does not satisfy all the requirements of the IMF, Step 1 is repeated continually up to k times until $h_{1k}(n)$ is an IMF, that is,

$$h_{1k}(n) \;=\; h_{1(k-1)}(n) - m_{1(k-1)}(n) \tag{4}$$

It is designated as the first IMF component $c_1(n)$ from $x(n)$, that is, $c_1(n) \;=\; h_{1k}(n)$. Then $c_1(n)$ is removed from $x(n)$ to obtain the residue $r_1(n)$, that is,

$$r_1(n) \;=\; x(n) - c_1(n) \tag{5}$$

The residue $r_1(n)$ is treated as the new datum. Then Steps 1 and 2 are repeated to obtain the second IMF $c_2(n)$. This procedure is repeated to obtain all the IMFs, and the results are

$$r_i(n) \;=\; r_{i-1}(n) - c_i(n), \qquad i = 2,3,\ldots,l. \tag{6}$$

The decomposition stops as any of the following predetermined criteria is achieved:
(1) Either the component $c_l(n)$ or the residue $r_l(n)$ becomes so small that the residue

is less than the predetermined value of the substantial consequence; (2) The residue $r_l(n)$ becomes a monotonic function from which no more IMF can be extracted. Thus, the original data are the residue plus the sum of the IMF components:

$$x(n) \; = \; r_l(n) \, + \, \sum_{i=1}^{l} c_i(n) \tag{7}$$

To guarantee that the IMF components retain enough physical sense of amplitudes and frequency modulations, a criterion for stopping the EMD process is determined by SD,

$$SD \; = \; \sum_{n=0}^{T} \frac{\left| h_{1(k-1)}(n) - h_{1k}(n) \right|^2}{h_{1(k-1)}^2(n)} \tag{8}$$

A typical value for SD can be set between 0.2 and 0.3 [1].

Combined use of EMD and SSP

Empirical Mode Decomposition is an emerging new technique of signal decomposition having many interesting properties. In particular, EMD can be applied to non-linear; nonstationary noisy signals and does not require any prior knowledge on the nature and number of modes embedded in a signal. The typical EMD application generates a number of intrinsic modes from one single signal: this makes EMD a powerful technique that can be used also when dealing with multiple targets echoes. In this paper we combined the EMD capability of extracting the oscillatory modes embedded in coherent or backscattering noise and the SSP capability of detecting multiple targets simultaneously as long as these targets have similar spectral characteristics. However, in complex and nonhomogeneous media, such as composites, concrete, etc., SSP applied over a single spectral range is less likely to detect multiple targets located in different regions. In order to improve the detection of multiple targets with different spectral and temporal characteristics using split spectrum processing, five steps need to be followed:

Step 1: Decompose the ultrasonic signal by EMD to obtain the finite IMF components;
Step 2: Apply FFT to each IMF component to obtain the frequency information;
Step 3: Calculate the energy of each IMF;
Step 4: Select IMF components that have the maximal energy;
Step 5: Apply SSP according to the selected IMF components.

Experimental Results

The experiment presented here was performed using the prism technique [4] to detect the multiple echoes reflected from a sample of a trapezoidal concrete/mortar/cement-paste prism whose dimensions are 21 x 10 x 7.4(lc=2+lm=2.2+lcp=3.2) cm
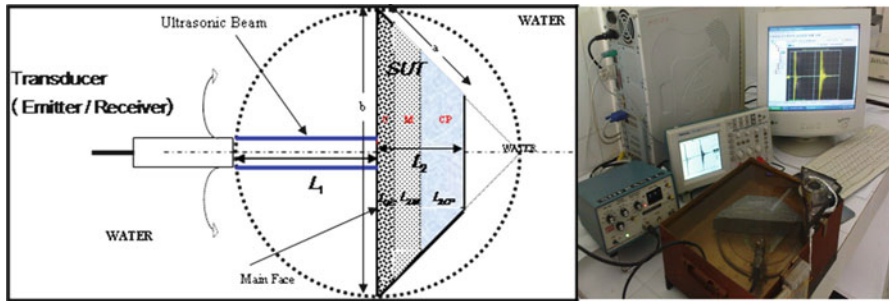
Fig. 1 General view of the measuring system

(*Fig. 1*) with 0.5 W/C ratio, 0.5 C/S ratio and 9% aggregate with 0.5 cm maximum particle size for the concrete layer, 12 days after making. Measurements were made in the pulse-echo mode in the longitudinal direction using immersion transducer with 2.25 MHz center frequency and 0.5 inch diameter. The main objective was the detection of reflected echoes from different interfaces (E1: water-concrete, E2: concrete-mortar, E3: mortar-cement paste and E4: cement paste-water). Consequently, the received signal is processed first using EMD to obtain a set of IMFs; these IMFs are used to identify the optimal frequency region(s) to perform split spectrum processing technique.

In order to extract the ultrasonic reflected echoes from the grain noise, we decomposed the received signal by EMD. Figure 2a shows the decomposition results from IMF1 to IMF3, the IMFs with high energy (E_{IMF1}=7.63, E_{IMF2}=13.19 and E_{IMF3}=2.69). Correspondingly, the Fourier transform of each IMF was plotted in Fig. 2b. It is shown that EMD acts as a set of filters and decomposes the original signal from high frequency to low frequency in their turn. It can be seen from Fig. 1a that the four ultrasonic reflected echoes are centralized in the two first IMFs. In order to enhance the detection of those echoes SSP based PT was then applied to each selected IMF. Figure 2c shows clearly the effectiveness of this method to overcome some limitations of the other signal processing techniques such as 1) partial echo overlap and 2) attenuation phenomena at high frequencies. For instance, in our experiment, we have a partial overlap between the echo reflected from the main face of the specimen (E1: echo from interface water-concrete) at 5.124×10^{-5}s and the echo reflected from the main face of the interface concrete-mortar (E2) at 5.248×10^{-5}s, the EMD extract the second one clearly in the second IMF (Fig. 2d). As a numerical example, the velocity in concrete layeris $v_{lc} = l_c / (T_{fc} / 2) = (2 \times 10^{-2} / ((5.248 \times 10^{-5} - 5.124 \times 10^{-5}) / 2) = 3226 m / s$

Conclusion

The combined use of EMD and SSP techniques for multiple targets detection has been conducted in this work. The experimental results show that this procedure is very appropriate to analyze ultrasonic signals in difficult materials (coherent noise problem,
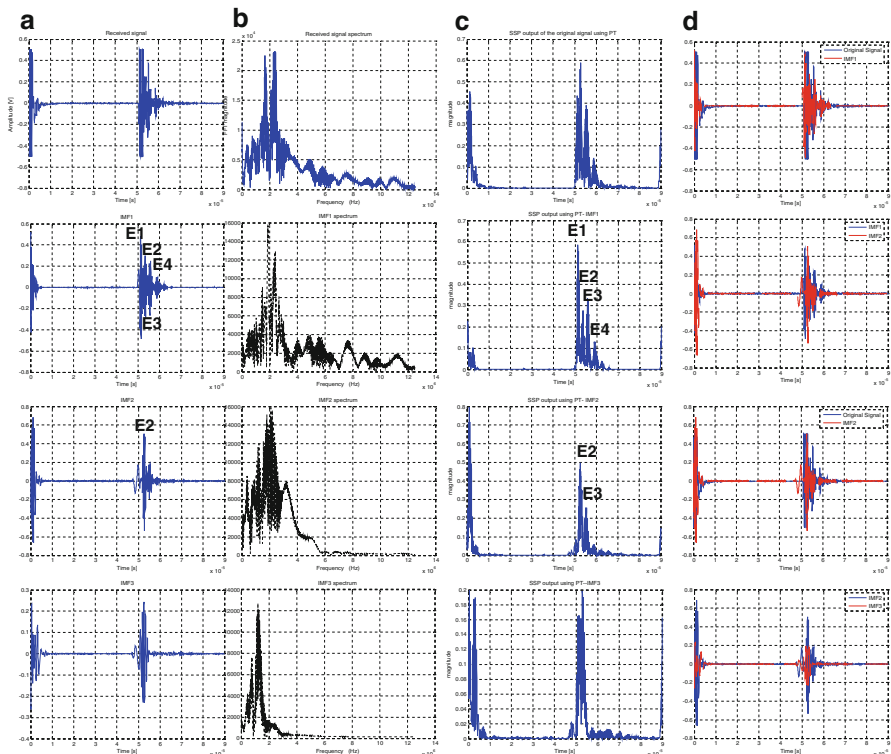
Fig. 2 a) The received signal and the three first IMFs; **b)** Their spectrums; **c)** Their SSP outputs using PT Algorithm and **d)** Comparison between IMFs

partial echo overlap). The results confirm that EMD is capable of determining the optimal spectral regions for processing and makes the application of SSP more effective. This method of detection could be further improved by selecting the right filters parameters, such as the number of bands, inspection bandwidth, bandwidth of each filter and overlap between different bands.

References

[1] Huang, N.E., Shen, Z., Long, S.R., Wu, M.L., Shih, H.H., Zheng, Q., Yen, N.C., Tung, C.C. and Liu, H.H. (1998), *The empirical mode decomposition and hilbert spectrum for nonlinear and nonstationary time series analysis*, Proc. R. Soc. London A, vol. 454, pp. 903–995.
[2] Rodríguez, A. and Vergara, L. (2009), *A new split-spectrum algorithm for dispersive materials using variable bandwidth filters*, Proc. IEEE Ultraso. Sym., pp. 710–713.
[3] Zhang, Q., Que, Pw. and Liang, W. (2008), *Applying sub-band energy extraction to noise cancellation of ultrasonic NDT signal*, J. Zhejiang Univ. Sci. A. vol. 9(8), pp. 1134–1140.
[4] Bouhadjera, A. (2005), *High frequency ultrasonic testing of young cement-based materials using the "prism technique"*, J. NDT&E Int, vol. 38, pp. 135–142.

Advancing the Rebound Hammer Method: A New Concrete Test Hammer

D. Corbett

Abstract The concrete test hammer patented by Proceq's Ernst O. Schmidt at the beginning of the 1950's is without a doubt the most widely used NDT instrument worldwide for rapid assessment of the condition of a concrete structure. Despite this fact, the validity of the method remains a hotly debated topic amongst experts in the NDT field. This is largely due to two factors; (a) since the original Proceq patent expired, there has been a proliferation of imitations with widely varying quality. Some are good, others are poor and the unreliability of the poor quality instruments has damaged the method in general; (b) the validity of the method in its primary use, i.e. for uniformity testing, is undisputed; however, incorrect use of the hammer for estimating compressive strength, (i.e. blind reliance on the manufacturer's conversion curves) is a major cause for concern amongst NDT experts. Furthermore, since its introduction, not much has been done to improve the test method itself. This paper describes how recent advances in rebound hammer technology together with extensive research into the various factors that influence the results can improve the rebound hammer method, providing users with more reliable results and reducing doubts concerning the viability of the method.

Keywords Compressive strength • Concrete • Condition assessment • Rebound hammer method • Recent advances

A New Measurement Principle

In the classical Schmidt hammer, the rebound energy is quantified by means of the distance travelled by the hammer mass. The method is strongly influenced by diverse frictional effects that increase with use and also by gravity. Both of these influences

---

D. Corbett (✉)
Proceq SA, CH-8603 Schwerzenbach, Switzerland
e-mail: David.Corbett@proceq.com
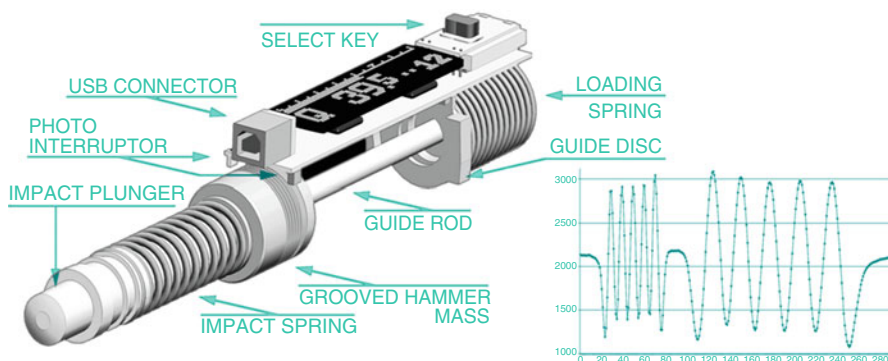
Fig. 1 Arrangement of the optical sensor relative to the hammer mass. Differential signal of the optical sensor

lead to errors if neglected, as they so often are by the user. A new measurement principle was conceived with the intention of reducing these shortcomings.

An optical method was developed for the new hammer (named SilverSchmidt) that was proven to be very robust. By cutting grooves along the circumference of the hammer mass with mechanical precision (Fig. 1), it was possible to realize a transmissive photo sensor with the following advantages:

- The received light is independent of the surface condition of the hammer mass.
- Any period corresponds to the real velocity, allowing the impact energy to be determined with an accuracy that was not previously possible.

The impact velocity and the rebound velocity are measured directly before and after the impact, practically eliminating any influence of gravity.

The SilverSchmidt produces a higher rebound value than the classical hammer. This is due to the new measurement principle and the modifications made in the hammer mass and the plunger. In order to avoid confusion, the new unit was given the name "Q", hinting that it refers to a quotient.

The Result – Does It Work Better?

In order to obtain independent validation of the SilverSchmidt, Proceq contracted the Federal Institute for Materials Research and Testing in Berlin, Germany, (BAM – Bundesanstalt für Materialforschung und –prüfung) to carry out extensive testing during October and November of 2009.

For the BAM tests, three concrete mixtures were designed using different w/c ratios and cement types, resulting in 28-day compressive strength values ranging from 10 Mpa to 100 MPa.
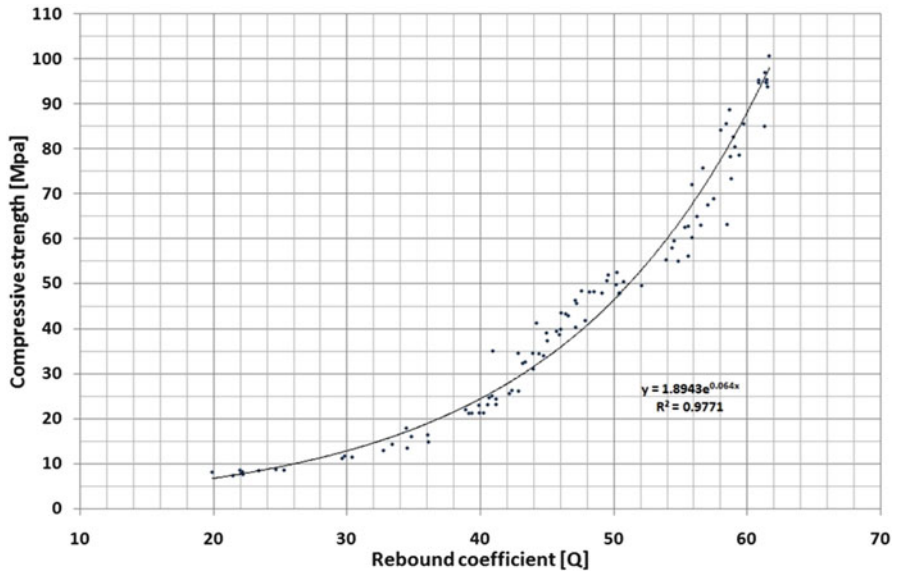
Fig. 2 BAM reference curve for SilverSchmidt ST/PC Type N

The following investigations were performed in a 28 day period on a total of 99 test cubes:

- Measurement of the dimensions and weight.
- Determination of the rebound value using five rebound hammers tests (SilverSchmidt and classical Schmidt) on the four sides of the cube in accordance with EN 12504-2.
- Determination of the compressive strength of the cube through mechanical testing in compression.

Various evaluations were made in order to fulfil the requirements of the standards DIN 1048-8, E DIN EN 13791:2008-05 and EN13791:2007:

Regression relationships between the rebound co-efficient and the compressive strength were established using the rebound hammer and compressive test data as shown in Fig. 2. The results showed conclusively that the dispersion of the SilverSchmidt was significantly lower than the classical Schmidt hammer over the entire range. The correlation coefficient using an exponential curve is 0.97 for SilverSchmidt N compared with 0.89 achieved with a classical rebound hammer, which validates the success of the new measurement principle.

Such accurate correlations are of course only possible under laboratory conditions with specific concrete mixes. For reliable in-situ estimates of compressive strength, every concrete mixture requires its own correlation curve as recommended in the major standards (e.g. ASTM C805, EN 13791). To this end, the new hammer allows both exponential curves and 3rd order polynomials to be programmed as user defined curves.
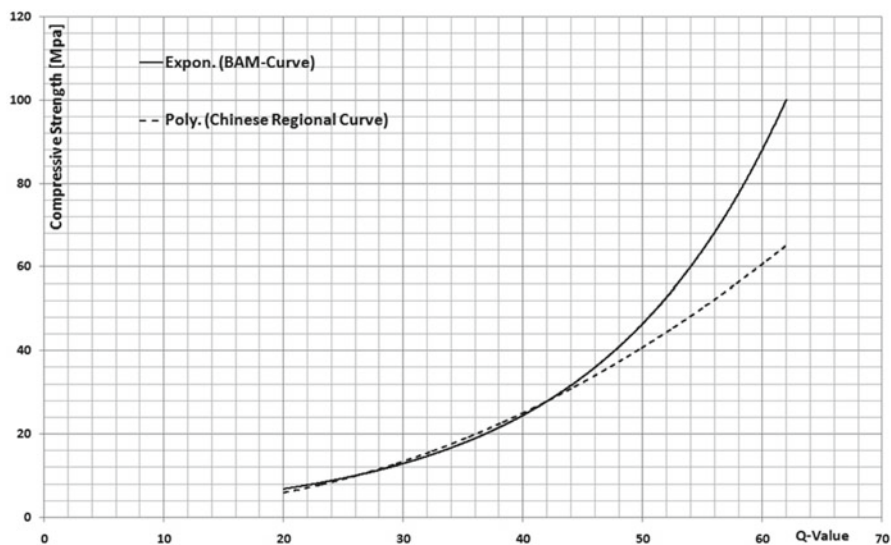
Fig. 3 Chinese Regional Curve Compared with BAM Curve

Developing Regional Curves

In certain countries or regions, the types of concrete used are less diverse and for such areas, the development of a regional curve may be desirable, or even necessary. In order to develop a curve for the Chinese market, Proceq commissioned an extensive series of tests with the Shaanxi Province Construction Science Research Institute. The testing in China was more extensive than that carried out in Germany, as the Chinese National Standard also takes into account the effects of ageing and in particular carbonation. Testing was confined to the compressive strength range covered by the Chinese standard i.e. (20 – 60 MPa) with ageing groups ranging from 7 days up to 1000 days (some of the tests are still ongoing).

Figure 3 shows that the curve obtained from the Chinese data has much lower values than the BAM curve at higher strengths. This is a good example to show that reference curves are very much dependent on the mix. Also, as stated above the Chinese data goes beyond the 28 day period.

Feedback from Field Tests

Since the launch of the new SilverSchmidt in February 2010, customer feedback has brought additional information that needs to be considered. Tests on existing structures have shown compressive strength readings significantly lower than the BAM curve, particularly in the higher range. As in the case of the Chinese data,
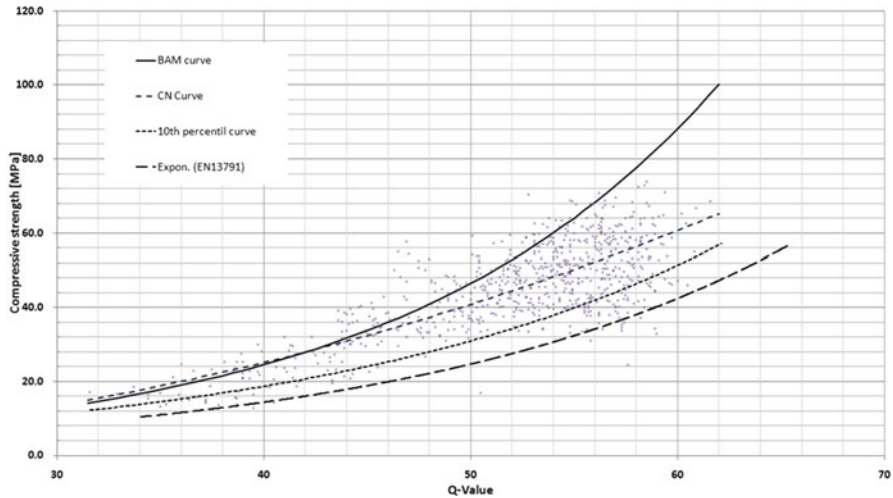
Fig. 4 Lower 10th percentile curve

this can be due to different mix design and also due to the effects of ageing, such as carbonation. It shows clearly that it is of primary importance for users to understand the basis of a manufacturer's curve. All the data collected from customers and institutions will be used to generate a lower 10th percentile curve as recommended by most major standards. The curves developed so far can be seen in Fig. 4.

Using a lower 10th percentile curve means that in 90% of the cases, a user will be underestimating the strength. This encourages the user to take core samples to shift the curve upwards if he wishes to have a better estimate. Again this is in line with the recommendations of the major standards and encourages best working practices.

The German annex to EN 13791 allows for in-situ compressive strength testing using a rebound hammer alone. The lower curve in Fig. 4 indicates the typical compressive strength that can be assigned using this method. As you can see it results in an extremely conservative estimate of the compressive strength. This is necessary however due to the nature of rebound hammer testing without a direct correlation to the specific mix under test.

Uniformity Testing

Uniformity testing remains the primary application of the rebound hammer. As stated previously, the use of a rebound hammer for uniformity testing is an undisputed method. The reason being, that it is a comparative method and the highly disputed correlation to compressive strength is therefore irrelevant. The user is looking for a pattern to identify weak points within the structure. With the SilverSchmidt, dispersion introduced by the instrument has been reduced to a minimum Fig. 5. This makes it

Diagram of series [ordered by name]
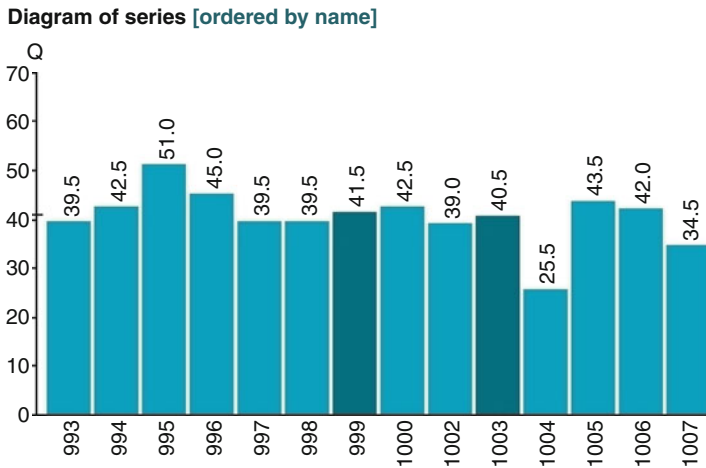
Fig. 5 Series summary presentation of uniformity test data

more suitable for accurate uniformity testing. Furthermore the possibility to review the data series on the hammer itself and on the supplied software simplifies the identification of problem areas within a structure.

Conclusions

This project has attempted to tackle well-known problems with the rebound hammer method that, despite its many detractors, remains to be the most widely used NDT method in the construction industry. The new measurement principle developed within the SilverSchmidt project reduces influences of friction and gravity and has been demonstrated to provide results with less dispersion over the entire working range. This should help reduce operator error.

The problem of incorrect use of the rebound method is a much greater challenge. While, the user interface developed for the SilverSchmidt is designed to help its correct use, manufacturers are limited in how much they can do to educate users in the correct procedures for estimating compressive strength with a rebound hammer. Ultimately, enforcement of the standards may be the only answer to this problem.

Phenomena Investigation of Guided Waves Propagation in a Multiple-Wire Cable with Gradually Increasing Cut Depths

R. Mijarez and A. Baltazar

Abstract In this study, the propagation phenomena of guided waves in a multiple-wire Aluminium Conductor Steel Reinforced (ACSR) cable with artificial cuts were investigated. A two piezoelectric transducers system, in a pitch and catch configuration, together with the wavelet transform, was employed for analyzing guided wave propagation. An ACSR cable, 0.9m in length and total diameter of 22.1mm, made of 7 steel wires and 26 aluminium wires was employed. Artificial damage was made at 0.45m from the emitter transducer; cut depth in the cable was gradually increased from 1mm to 9mm. The transducers were attached to the ends of the ACSR cable using a liquid coupling medium. A function generator was used to drive the transmitter transducer with five cycles of 500 kHz sinusoidal waves. The received guided wave signals were amplified and acquired by a digital oscilloscope that sent the data to the computer for further analysis. From this, the following conclusions were obtained: a) the modes identified using time- frequency analysis before and after the cut were $L(0,1)$ and $F(1,1)$ for steel and aluminium, respectively; b) the amplitude of the received $L(0,1)$ signals increased with the increase of the cut depth, depicting an exponential behaviour, conversely the $F(1,1)$ modes decreased, suggesting a mode conversion from $F(1,1)$ to $L(0,1)$ modes due to loosed friction contact among individual wires.

Keywords ACSR inspection • FEM analysis • Guided waves • Wavelet Transform

R. Mijarez (✉)
Instituto de Investigaciones Eléctricas, Gerencia de Control e Instrumentación,
Calle Reforma 113, Col. Palmira, C.P. 62490, Cuernavaca, Morelos, Mexico
e-mail: rmijarez@iie.org.mx

A. Baltazar
Centro de Investigacion y Estudios Avanzados del IPN, Unidad Saltillo Carretera
Saltillo-Monterrey km 13.5, C.P. 25900 Ramos Arizpe, Coahulia, Mexico

Introduction

Guided waves in rods, single wires and multiple wires have been anticipated as an attractive and effective tool for structural health monitoring of materials, since they can interrogate large structures and propagate for long distances compared with the traditional body waves [1]. The theory of wave propagation of waves in solids was developed in the 19th century; however, only just for over fifty years, the subject of wave propagation in rod and cable structures has been addressed by many investigators. Related to multi-wire problem, various experimental and theoretical techniques have been reported [2-4]. Chen et al. [2] used the Wigner-Ville transform to analyze the stress wave in order to identify the arrival time in a seven-wire steel strand. In a later study, Rizzo et al. [3] generated and detected ultrasonic waves in single wire and seven-wire cable using magnetostrictive sensors. Their research looked into the acoustoelastic effect in the cables. In another study, Rizzo et al. [3, 5] studied the wave propagation problem in seven-wire cables at the level of the individual wires. They used broadband ultrasonic transducers and time-frequency analysis based on the wavelet transform; in their research, they were capable of identifying vibration modes which propagate with minimal losses. Hagg et al. [6] presented a two-rod system in which the wave energy from an excited rod is transmitted to a neighbouring rod through friction contact. An energy-based model, to approximate the time average elastic wave power, in the two rods as a function of propagation distance was used. The model predictions were corroborated with experimental measurements and FEM simulations. Baltazar et al. [7] examined the effect of mode coupling and inter-wire mechanical contact on longitudinal modes of guided waves in a segment of an ACSR cable, making use of the Short Time Fourier Transform (STFT) and spectrograms, and correlating the spectral energy change of vibration modes to structural damage of the cable. The purpose of this work is to study the propagation phenomena of individual longitudinal and flexural guided waves modes at 500 kHz in a 0.9m ACSR cable with artificial cuts. A two piezoelectric transducers system, in a pitch and catch configuration, together with time-frequency analysis based on the wavelet transform was used to describe the propagation phenomena.

Experiments

This paper focuses on guided waves excited at 500 kHz in a multi-wire ACSR cable commonly used in power overhead transmission lines. This cable is a concentric conductor configured in strands consisting of a core of seven straight steel wires and twenty six stranded aluminium wires in two layers as illustrated in a cross-sectional view in Fig. 1a. The diameter of each aluminium and steel wire is 3.5 mm and 2.7 mm, respectively; therefore, the total diameter of the cable is approximately 22.1 mm. The length of the cable used is 0.9m. The experiment setup is depicted in Fig. 1b. A pitch and catch arrangement was applied. Two piezoelectric broadband
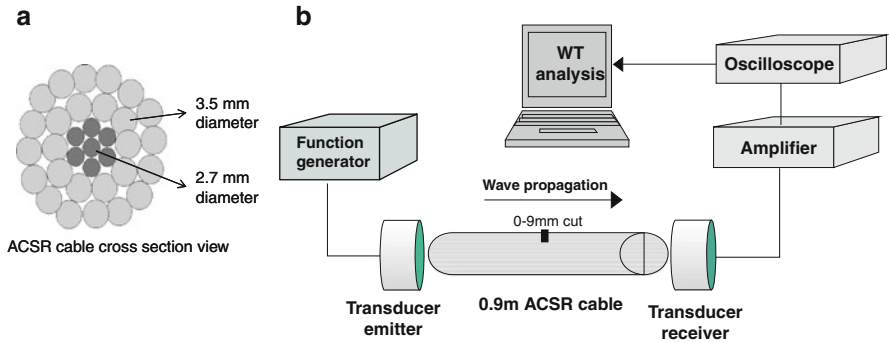
Fig. 1 **a**) Cross sectional view of the ACSR cable used; **b**) experiment setup, showing artificial damage in the middle of the ACSR cable
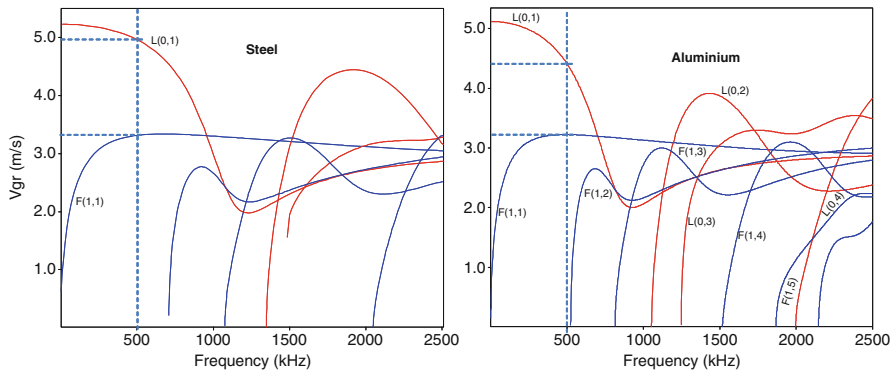
Fig. 2 a) Group velocity dispersion curve of a steel rod 2.7 mm diameter and an aluminium rod 3.5 mm diameter

transducers with a central frequency of 1 MHz and 12.7 mm in diameter were attached to the ends of the ACSR cable using a liquid coupling gel. Due to the complicated characteristics of inter-wire coupling, an analytical solution that can describe the wave propagation in these multi-wire cables does not exist. A formulation based on a Pochhammer-Chree frequency equation of a cylindrical rod has been presented [8]. Considering an isotropic homogeneous cylindrical rod, the solutions of the elastic equation of motion are known, and correspond to three types of modes: longitudinal $L(0,m)$, torsional $T(0,m)$ and flexural $F(0,m)$. By solving the equations, via the commercial package *Disperse©*, for these vibration modes with known frequencies, the dispersion curves can be obtained. The dispersion curves relate the velocity of the guided wave propagation, to the frequency of the wave and the diameter of the cylinder.

The approach taken employed individual dispersion curves of rods of aluminium and steel 3.5mm and 2.7mm of diameter, respectively. Figure 2 shows the group velocity (Vgr) dispersion curves of these rods, where it can be observed that the only

guided wave modes that could be excited below 500 kHz are the longitudinal $L(0,1)$ and the flexural F(1,1) modes. The group velocities yielded at this frequency for $L(0,1)$ in steel and aluminium are 4957.84 m/s and 4397.28 m/s, respectively, and for $F(1,1)$ are 3313.50 m/s and 3223.61 m/s, correspondently.

The function generator drives a transmitter piezoelectric transducer with five cycles of 500 kHz sinusoidal waves. Excited guided waves propagate through the cable and are sensed by the receiver transducer that converts them to electric signals via the inverse piezoelectric effect. The electric signals are amplified and acquired by a digital oscilloscope that sends the data to the computer for further analysis. Artificial damage was made at 0.45m from the emitter transducer. Cut depth in the cable was gradually increased from 1mm to 9mm.

Results

Frequency-time signal analysis

The wavelet transform (WT) addresses the general problem of time-frequency analysis and provides the means to analyse non-stationary signals [9]. In this work, the Gobor wavelet was used to identify the guided wave modes generated in the experiments and ascertain the manner they correlate with damage. Figure 3 shows
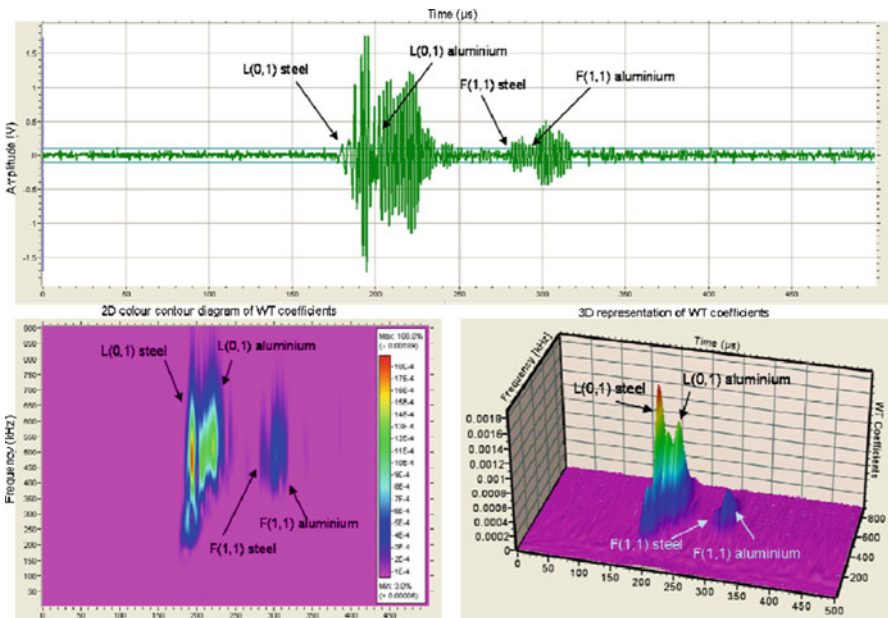
Fig. 3 Discrete wavelet transform used to estimate the TOA of the guided wave received modes in the ACSR cable without damage

Table 1 Identified guided wave modes, using the estimated TOA for calculating their *Vgr* and comparing them with the *Vgr* yielded by Disperse

Identified mode	TOA (s)	Length (m)	Calculated Vgr (m/s)	Disperse Vgr (m/s)
$L(0,1)$ steel	0.00018	0.9	5000	4957.84
$L(0,1)$ aluminium	0.00021	0.9	4285.71	4397.28
$F(1,1)$ steel	0.00028	0.9	3214.28	3313.5
$F(1,1)$ aluminium	0.000295	0.9	3050.84	3223.61

the results produced by applying the WT to the guided wave received signals without damage that allowed the signals time of arrival (TOA) estimation. Considering the 0.9m length of the ACSR cable and estimating the TOA, it was possible to recognize the excited guided wave modes. Table 1 shows the group velocities attained using the estimated TOA.

The identified received modes were predominantly $L(0,1)$, however, some energy was discerned with lower group velocities as very likely $F(1,1)$. It can be observed that $L(0,1)$ aluminium signals show more dispersion and less amplitude than the $L(0,1)$ signals of steel, which agrees with its dispersion curves. On the other hand, the $F(1,1)$ modes exhibit more energy in the aluminium.

Cut depth and amplitude behaviour

The experimental results show a relationship between the degree of damage and the received amplitude of the guided wave modes as shown in Fig. 4a. This relationship, however, exhibits that an increase in the cut depth produces an increase in amplitude of the $L(0,1)$ modes and a decrease of the $F(1,1)$. The energy augment posses an exponential tendency as shown in Fig. 4b.

Conclusions

The propagation phenomena of guided waves in a multiple-wire ACSR cable with gradually increase of artificial cuts was investigated using an ultrasonic system in a pitch and catch configuration together with the time-frequency analysis based on the WT. In this study, it was possible to identify the excited vibration modes $L(0,1)$ and $F(1,1)$ in steel and aluminium, at a frequency of 500 kHz, by estimating the TOA and calculating their group velocities, which were correlated adequately with the individual dispersion curves. Signal de-noised of guided waves using the WT related the amplitude change of guided wave modes to the degree of damage in the ACSR cable. An unusual increase in the amplitude of $L(0,1)$ modes in both materials was observed with an exponential tendency as the damage augmented; conversely, $F(1,1)$ modes decreased, suggesting a mode conversion from $F(1,1)$ to
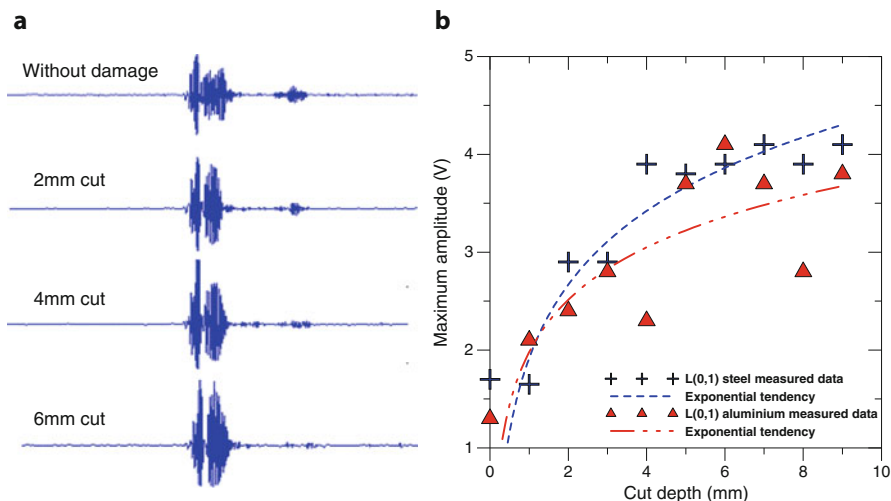
Fig. 4 a) Signal de-noised of guided waves using the WT correlating the amplitude change of vibration modes to the degree of damage in the ACSR cable; **b**) Exponential tendency of the $L(0,1)$ in steel and aluminium

$L(0,1)$ modes ascribed to a release in the degree of mechanical contact among individual wires. This study gained insight into the inter-wire coupling phenomenon of multiple-wire ACSR cables and serves as the basis for structural monitoring of $L(0,1)$ modes that could facilitate the detection of damage in early stages.

References

[1] F.K. Chang *Structural Health Monitoring: Current Status and Perspectives*, CRC Press, Lancaster, PA, (1998).

[2] H.L. Chen and Wissawapaisal, Application of Wigner-Ville Transform to evaluate tensile forces in seven-wire prestressing strands, Journal of Engineering Mechanics, 128, 1206–1214, (2002).

[3] P. Rizzo, Ultrasonic wave propagation in progressively loaded multi-wire strands, Experimental Mechanics, 46, 297–306, (2006).

[4] M.S. Wilson and S. Hurlebaus, Power Line Monitoring, Proceedings of the 2007 American Control Conference, 231–235, (2007).

[5] P. Rizzo, and F. Lanza di Scalea, Wave propagation in multi-wire strands by wavelet-based laser ultrasound, Experimental Mechanics, 44, 407–415, (2004).

[6] T. Haag · B.M. Beadle · H. Sprenger and L. Gaul, Wave-based defect detection and interwire friction modeling for overhead transmission lines, Archive of Applied Mechanics, ISSN 0939–1533, Springer Berlin / Heidelberg, vol. 79, no. 6–7, 517–528, (2009).

[7] A. Baltazar, C. Hernandez and B. Manzanares, Study of wave propagation in multiwire cable to determine structural damage, NDT&E International 43, 726–732, (2010).

[8] K.F. Graff, *Wave Motion in Elastic Solids*, Dover Publishing Inc., New York, (1975).

[9] S. Mallat, *A Wavelet Tour of Signal Processing*, Academic Press, Boston, (1998).

Use of Acoustic Emission Method for Detection of Two-Phase Flow in Service Open Type Water Pipeline

T. Suzuki, T. Naka and M. Ohtsu

Abstract Damage evaluation of a pipeline system is normally used by non-destructive testing method (i. e. elastic wave method). For effective maintenance and management of pipeline system, it is necessary to evaluate not only the degree of damage but also the water-flow conditions (i.e. gas-liquid flow). In this study, acoustic emission (AE) method was applied to be detecting a gas-liquid flow in service open type water pipeline system. Two experiments were conducted: laboratory model tests and in service open type pipeline monitoring. The results show that a gas-liquid flow conditions could be quantitatively evaluated by using AE parameters, such as AE generation behavior, average frequency and AE energy. Thus, AE monitoring is effective for qualifying the water flow conditions in an open type pipeline system.

Keywords Acoustic emission • Gas-liquid flow • Non-destructive testing • Open-type pipeline

Introduction

In service open type pipeline systems, the condition for gas-liquid flow in pipeline system is the most important function for maintenance and management [1-2]. Deterioration of open type pipeline systems often results in overt-through degradation

---

T. Suzuki (✉)
Nihon University, Fujisawa, Japan
e-mail: t.suzuki@brs.nihon-u.ac.jp

T. Naka
National Institutes for Rural Engineering, Ibaraki, Japan

M. Ohtsu
Kumamoto University, Kumamoto, Japan

of water-tightness or water leak phenomena caused by gas-liquid flow effects, such as vibration of pipe material [3-5]. For effective maintenance and management, non-destructive testing method need to be developed, because pipeline system is installed underground and the damage cannot be checked visually in service. In recent researches, it was reported that elastic wave method (e.g. acoustic emission, ultrasonic) is effective for evaluation of water-flow conditions in pipeline system [6-10]. Especially, the acoustic emission method is passive technique for detection of elastic wave from civil structures [11].

In this study, AE method is applied to be detecting a gas-liquid flow in open type pipeline system. Two experiments were conducted: laboratory model pipeline and in service open type pipeline system.

This paper reports quantitative method for evaluation of gas-liquid flow conditions in pipeline system using AE parameter analysis.

Detection of Gas-Liquid Flow in Open Type Water Pipeline

AE monitoring procedure

AE monitoring was applied to be detecting a gas-liquid flow in two experimental conditions which were laboratory model test and open type pipeline system in service. The laboratory model test was conducted to model pipeline system (Photo 1) which was made by acrylic pipe of 100mm diameter. An amount of water flow was

Photo 1 Overview of model pipeline system

Photo 2 AE monitoring condition in service pipeline

3.6 to 24.0l/sec. The water flow signals were detected by AE. AE events generated under water flow in model pipeline were counted up to end of flowing process by AE processor (SAMOS; PAC). AE sensor of 30 kHz resonance was attached at surface of the model pipeline. AE monitoring conducted with 3-channel system was employed. For event counting, the threshold level was set to 45dB, and total amplification was 60dB. In service open type pipeline (Photo 2); the water flow signals were detected same AE method in the model pipeline monitoring. This pipeline system was composed of a PC pipe of 1,350 to 1,200mm diameter, which has been used for 26 years. AE monitoring was installed on the surface of air valve, which is near the air emission point. The duration of monitoring was 30 seconds at 1monitoring site. AE hits were detected by using AE sensor (resonance frequency: approx.150kHz). To count the number of AE hits, the threshold level was set to 40-45dB, with a total 60dB gain.

Results and discussion

Detected AE waves in pipeline. The simulated flow conditions are composed 4 types (Steady flow, Stratified flow, Plug flow and Bubble flow; Fig. 1). The AE monitoring was applied to pipeline system, burst type AE waves are detected when gas-liquid flow conditions in pipeline system (Fig. 2). On the other hand, continuous AE waves of an irregular pattern are detected when water is leakage or a free water surface exists. In service open type pipeline, this structure is detected burst type AE waves.
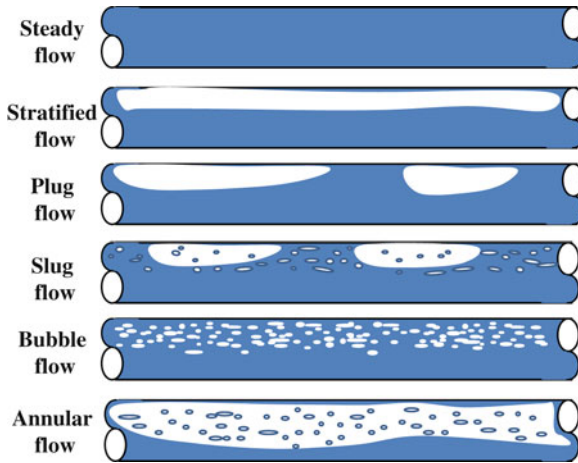
Fig. 1 Gas-liquid flow form in pipeline
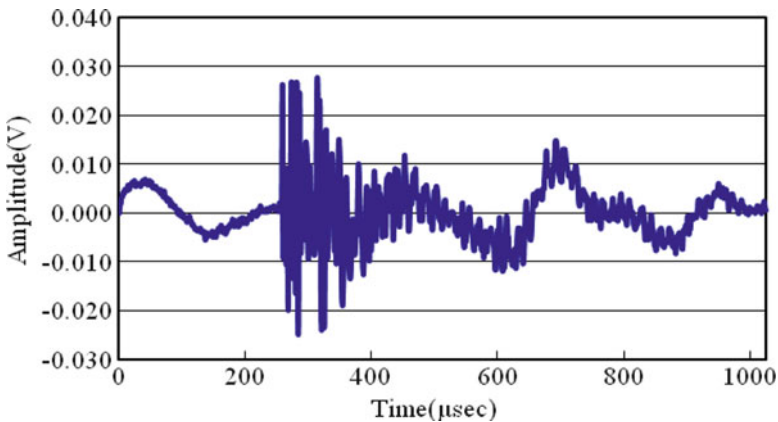
Fig. 2 Detected Waveform due to gas-liquid flow

Quantitative Evaluation of Two Phase Flow Conditions in model pipeline by AE Parameter Analysis. The gas-liquid flow characteristics in each monitoring site are evaluated by AE parameters. A typical relation between AE energy and average frequency is shown in Fig. 3. AE energy is defined as a relative value having 1000-count energy when the 10V peak value continued for 1msec. The AE energy is low at a low air mixed rate in moderl pipeline(Bubble flow>Plug flow, Stratified flow>Steady flow, Fig. 3). In air valve, results of AE monitoring are not same trend.

AE characteristics in service open type water pipeline. AE generation behavior in air emitted valve is detected 656 hits/ 300sec, which is 2.01 times higher than in the
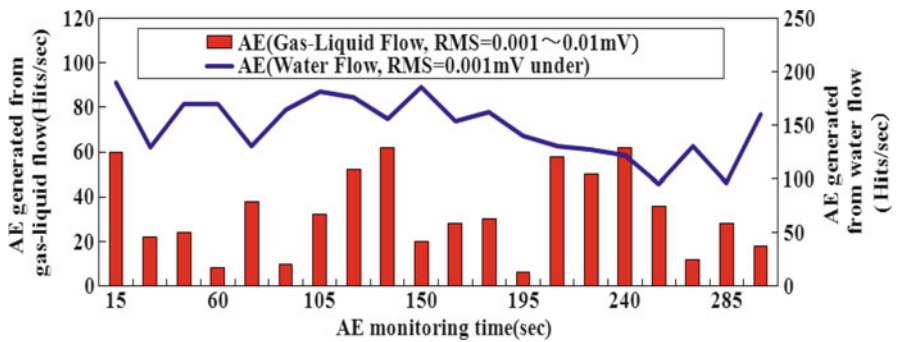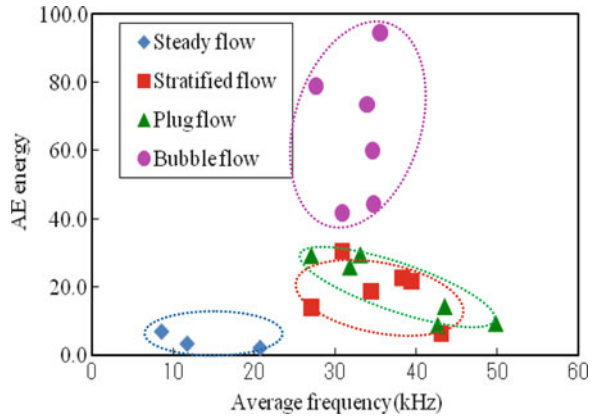
Fig. 4 AE generation behavior in service pipeline. (Monitoring site: air emitted valve)
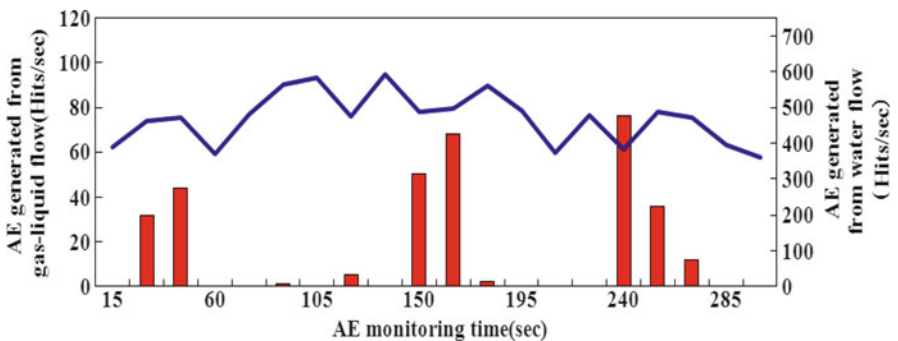
Fig. 5 AE generation behavior in service pipeline. (Monitoring site: underground line)

underground line (Figs. 4 and 5). Therefore, Calculated AE parameters are almost positively concerned with gas-liquid flow conditions in open type pipeline. Detected waves are able to be quantitatively evaluated by AE parameters, such as AE energy, average frequency and AE hit rate.

Conclusions

In this study, the acoustic emission (AE) method was applied to evaluation of gas-liquid flow in open type pipeline system. Two experiments were conducted: laboratory model tests and in service open type pipeline monitoring. The simulated flow conditions are composed 4 types in model pipeline. The burst type AE waves are detected when gas-liquid flow conditions. These detected AE waves can be quantitatively evaluated using AE parameters. As for the relationship AE hit rate, energy, average frequency and hydraulic conditions are evaluated. To conclude, evaluation of gas-liquid flow in service pipeline systems can be quantitatively evaluated through NDT monitoring using acoustic emission method.

References

[1] Nawa, N, Sonoda, K., Iwata, H. and Suzuki, T. (2002): Survey and Evaluation Method for Deteriorated Agricultural Pipeline Function, JSIDRE, Vol. 70 (12), pp. 31–36.
[2] JSMF (2004): Characteristics of Gas-liquid flow in Agricultural Pipeline, Handbook of Multiphase Flow, pp. 448–453.
[3] Suzuki, T., Ohtsu, M., Aoki, M. and Nakamura R.(2008): In-Situ Non-Destructive Monitoring of Water Flow in Damaged Agricultural Pipeline by AE, Journal of ICID, Vol. 18, pp. 73–83.
[4] Suzuki, T., Naka, T., Taruya, H. and Aoki, M. (2009): Management of Water-Tightness in Service Agricultural Pipeline System based on Non-Destructive Monitoring, The 5th Asian Regional Conference of ICID.
[5] Suzuki, T., Naka, T., Taruya, H., Tanaka, Y. and Aoki, M. (2010): Evaluation of Gas-Liquid Flow in Open Type Pipeline by Acoustic Emission, Journal of Structural Engineering, Vol. 56 A, pp. 665–670.
[6] Suzuki, T., Ikeda, Y., Tomoda, Y. and Ohtsu, M. (2004): Water-Leak Evaluation of Existing Pipeline by Acoustic Emission, Progress in Acoustic Emission, The Japanese Society for NDI, pp. 309–314.
[7] Vahaviolos, S.J., Miller, R.K., Watts, D.J., Shemyakin V.V. and Strizkov S.A. (2001): Detection and Location of Cracks and Leaks in Buried Pipelines using Acoustic Emission, Journal of Acoustic Emission, Vol. 19, pp. 172–183.
[8] Suzuki, T. and Ohtsu, M. (2005): Physical Properties of PC pipe in service for 36 years under Inner Water Pressure, JSIDRE, Vol. 235, pp. 75–76.
[9] Murakawa, H., Kimura, H., Yamanaka, G. and Aritomi, M. (2006): Measurement of Two-Phase Flow using Multi-Wave Ultrasonic (Liquid and Gas Velocity Measurement and Phase-Separation Technique using Ultrasonic Time-Domain Cross-Correlation Method), Progress in Multiphase Flow Research, Vol. 1, pp. 17–23.
[10] Matsui, G, Aizawa, T. and Morita, A. (1986): Statistical Properties of Differential Pressure Fluctuations and Flow Patterns in Horizontal Gas-Liquid Two Phase Flow (Differential Pressure between the Top and the Bottom of a Tube Cross-Section), Journal of Mechanical Engineering, Vol. 52, 478, pp. 2337–2344.
[11] JSCM B-5706 (2003): Monitoring method for active cracks in concrete by acoustic emission.

Acoustic Emission Diagnostics of Roller Bearings Damage

P. Mazal, F. Hort and F. Vlasic

Abstract This paper shows potential applications of the AE method for identification of damage at early stages in rolling bearings. The experimental part is concerned with the results of AE application during durability testing of axial and radial bearings. The recent group of experiments was carried out on durability test stations for radial bearings. Sensing of AE signal on these devices was complicated by the position of the tested bearing inside the station, making it to place the AE sensors in its direct vicinity. As a solution, waveguides were used, with one end touching the outer ring of the bearing and the other end connected to the sensor. Other sensors were placed on the surface of the testing station. Despite these complications with AE signal sensing, an optimal setting was found for the measuring chain resulting in collection of high-quality data from damaged radial bearings. Examples of basic AE signal records from rolling bearing and potentials of the new generation AE analysers are mentioned. These devices allow for continuous AE signal sensing. The results prove the AE technique enables reliable determination of running-in period, stabilised run and the prediction of the stage where surface damage forms. It is shown that the AE method can be used to predict bearing defects or can be used to complement traditional vibration bearing monitoring.

Keywords Acoustic emission • Bearing • Contact damage • Vibrodiagnostics

Introduction

Bearings diagnostics is a part of technical diagnostics; it is a discipline which deals with non-destructive and non disassembly diagnostics of technical conditions (condition monitoring). Technical diagnostics is focused on sensing damage,

---

P. Mazal (✉) • F. Hort • F. Vlasic
Brno University of Technology, Brno, Czech Republic
e-mail: mazal@fme.vutbr.cz

localizing and discovering its size, which gives evidence of the damage severity. Technical diagnostics includes detecting causes of damage inception and spreading. Various diagnostic methods are used for evaluation of the state of roller bearings: vibration measurement, stator current, shock pulse method, thermography or acoustic emission.

The acoustic emission (AE) is used in many applications, for example: detection of cracks in pressure vessels or pipelines, corrosion, initiation and growth of cracks during high cycle fatigue and many others. The AE is used also for monitoring of contact fatigue on rolling elements of bearings. Scientists often test axial low speed bearings where it is also possible to detect the location of growing defect [1], [2]. The length of bearing lifetime depends mainly on the conditions of the process. In the experimental test it is possible to artificially shorten the length of lifetime by change of shape, absence of lubricant or by increasing of the loading force. One of the main goals of simple testing of bearings on the experimental stands is subsequent disclosure and identification of damage in more complicated systems, such as for example gearboxes [3].

The Institute of Machine and Industrial Design of Brno University of Technology can contribute to disclosure of initial stadium of contact fatigue and bearings lifetime. This institution has laboratories with sophisticated stands for testing of contact fatigue of specific specimens in radial and axial directions. Furthermore these laboratories contain stands for testing of axial and radial bearings [4], [5].

Experimental Set-up

The Axmat stand (Fig. 1) was created for testing of circle specimens of various kinds of materials (steel, cast iron, plastics). The key point of the stand is shown in Fig. 1a where all of its parts are described. This figure shows also a modification which is capable of testing axial bearings. This change is possible thanks to exchangeable bush and segment, so we can test the circle specimens or axial bearings (ball bearings, roller bearing or needle bearings). The Axmat stand has also a control panel for watching the vibration level and time length of the test.

The principle of testing the materials is following: the circle specimen is put into a segment and fixed by a screw-bolt to prevent rotation. One bearing ring is put into the bush and it is fixed by a screw-bolt too. In the middle of the specimen and the bearing ring, 21 balls are embedded. The testing of axial bearing is analogical: the segment is fixed to the first bearing ring and the bush to the second ring. The snap ring is situated in the middle of the rings. The rotary base is driven by an electromotor (1380 r.p.m.) and the loading is caused by weight on the cantilever.

The stand SA 67 is used for determination of radial bearings lifetime. Figure 1b shows a scheme of the stands where the location of sensors and tested bearing is visible. The tested bearing is situated on the shaft which is driven by electromotor (2845 r.p.m.). The outer ring is bended in bush with holes for waveguides. The stand is capable to test bearings with stable flow of oil. The hydraulic piston causes the loading force on the tested bearing. The stand is equipped by five sensors in total.
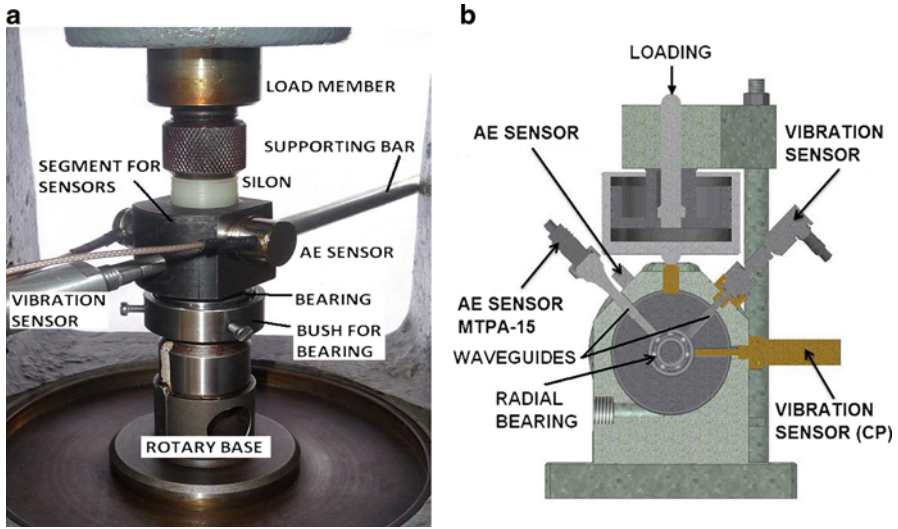
Fig. 1 Testing devices: **a**) Axmat for axial bearing tests, **b**) scheme of SA 67 station for testing of radial bearings

One of the AE sensors is placed on the waveguide and a second one is placed on the outer surface of the stand. This location is same for modern sensing of vibration signal (next two sensors). The fifth sensor is placed in horizontal direction and it is connected to a control panel. The control panel secures the vibration and temperature level of tested bearing and records the length of the measurement, too.

Used AE Testing Procedures

The AE signal is obtained from analyzers DAKEL XEDO. These are 2 and 4 channel systems with possibility to scan up to 16 free settable energy levels serving together with piezoceramic sensors for detection of AE signal from parts (bearings) under investigation. For evaluation as well as for further processing of the basic parameters of measured samples, we used the software DaeShow© which enables all basic procedures of evaluation – ring down counts, AE burst rate, summation of AE counts, RMS etc.

In a part of experiments, we had a possibility to use the new AE analyser called DAKEL IPL. It is a state-of-the-art system for continuous recording and processing of data from the acoustic emission sensors. Compared to the up to date commonly used AE analyser devices, the major advantage of the DAKEL IPL is that it is capable of continuously sampling and storing the whole AE signal for as long as there is disk space to store it. And with the currently available disks on the market having about 1 TB - we can store as long as 17 hours of 5-channel recording and

when using RAID arrays of such disks, it can be much more. The device has a total of 5 synchronous analogue input channels simultaneously and continuously sampling at 2 MHz out of which 4 channels are generally used to sample the AE signals and one additional channel can be used for synchronous monitoring of any external physical parameter that is used to excite the testing object (such as the loading force, pressure, temperature, etc.). This comes handy when you need to correlate the AE signals to some external events in time.

Examples of Experimental Results

The graph in Fig. 2 shows development of AE Counts energy levels during the first stage of loading test of radial bearing. The measurement could record up to 16 energy levels (Counts) of AE signal. Up to 0.1 day it seems like initial start-up then rise of intensity of the signal to the 0.4 day. The counts level 6 and higher are progressively rising up to 4.5 days which indicates the incipient of contact fatigue. Figure 3 shows an example of AE activity during the final stage of axial bearing durability test.
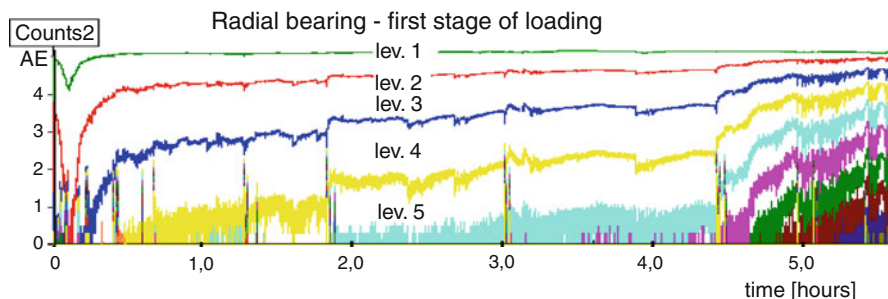
Fig. 2 Example of basic record of AE activity on all levels in first stage of loading of radial bearing
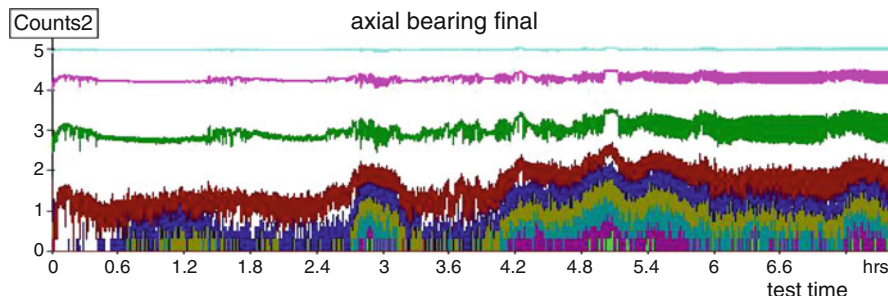
Fig. 3 Example of basic record of AE activity on all levels in the stage of propagation of contact damage of axial bearing damage – final part of the test
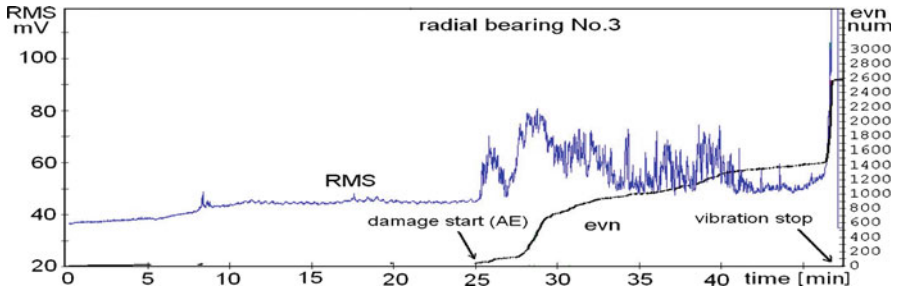
Fig. 4 RMS and events summation – short destruction test of radial bearing
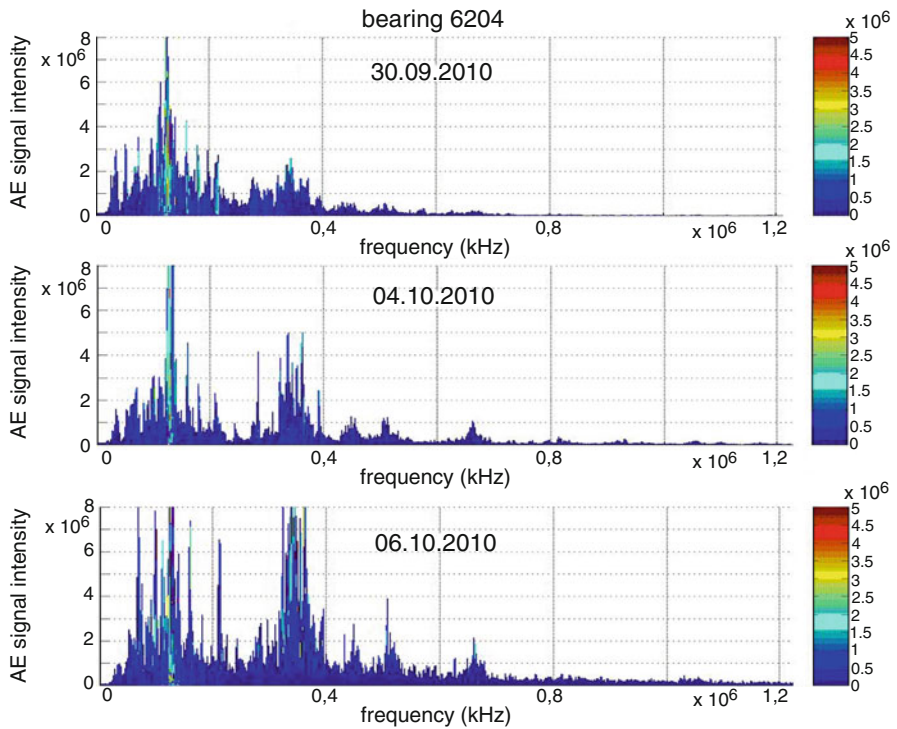
Fig. 5 Comparison of AE signal intensity in different frequencies in the starting stage of test (upper plot) and in the final stage of test (bottom) - test of radial bearing 6204

Example of the possible outputs of measurement is plotted in Fig. 4, where the values of root mean square of signal (RMS) and cumulative number of events (evn) are shown. The early identification of damage development in comparison with vibration diagnostics is clear once again. Other change is evident in the area of AE signal intensity in different frequencies (see Fig. 5). Higher frequencies were identified in the final stage of the test.

Conclusions

The situation with AE diagnostics of real bearings damage is very complicated, as the bearings are composed of many parts which are in contact and especially it is usually not possible to place the AE sensors directly on the bearing surface. For this reason, the signal contains much more undesirable disturbances, which makes adjusting of measuring chain more difficult. Nevertheless the examples shown in this paper suggest that it is possible to identify bearings with damaged parts.

Our experiments show that parameters in time domain could draw maintenances attention to main changes in the sensing part. From these graphs it is possible to consider that the amplitude of events can be one of the better characteristics to estimate the initial failures and creation of pitting. A combination of these results from time domain and frequency domain could better display which sections of mechanism are damaged. The selection of representative events is time-consuming and it requires needed experiences.

After evaluation of a number of data files, it would be possible to work out a simplified way of signal processing of selected signal characteristics that would correspond to real damage of tested bearing. This simplification would result into single-purpose analyzers that would be a part of permanent diagnostic systems used on some important bearings, e.g. in transport technology, in technological lines and energetic devices – in order to optimize intervals of planned maintenance and temporary putting out of operation connected with it (e.g. turbines mounting, rolling lines, etc.).

References

[1] Elforjani, M. and Mba, D. (2008), *J. Vibration Acoust. – Trans.of the ASME*, vol. 130, issue 4, Pages: 14, ASME, USA, ISSN 1048–9002.
[2] Rogers, L.M. (2006), *Adv. Mater. Rese.*, vol. 13–14, pages: 37 – 44, Trans. Tech. Publ., Switzerland, online at http://www.scientific.net.
[3] Tan, Ch. K. and Mba, D. (2005), *Tribol. Int.*, vol. 38, issue 5, pages: 469–480.
[4] Hort, F., Mazal, P. and Vlašic, F. (2010), In: Proceedings of the 29th Europ. Conf. on AE Testing, CD-ROM, Tscheliesnig, P.(ed), Vienna, NDTnet, ISBN: 978-3-200-01956-0.
[5] Mazal, P., Hort, F., Drab, M. and Slunecko, T. (2009), *J. Acoust. Emission*, vol. 26, pages: 189–198, AE Group Encino, USA, 2009, ISSN 0730–0050.

Wireless Sensors for Measuring Wind-Borne Pressures During Hurricanes

J.-Paul Pinelli, C. Subramanian, I. Kostanic, G. Lapilli and J. Chandiramani

Abstract A third generation of wireless sensors was developed to study wind-borne pressure variations in low-rise buildings during hurricanes. The system has the capability of measuring pressure and temperature along a roof, collecting data and sending it to a server to process and publish on the web in near real-time. Also wind speed and direction are measured by the system with the use of an anemometer. Sensors are placed inside individual custom-made plastic weatherproof cases. Small size of all components allows an aerodynamic shape, reducing the shape effect of the sensor on the flow. Low power consumption combined with Li-Ion batteries provide several days of continuous data collection. The platform created allows using almost any type of sensor via a planned expansion port. The paper presents some preliminary results.

Keywords Building • Hurricane • Pressure • Sensors • Wireless

J.-P. Pinelli (✉)
Professor of Civil Engineering, Florida Tech, Melbourne, FL, USA
e-mail: pinelli@fit.edu

C. Subramanian
Professor of Mechanical and Aerospace Engineering, Florida Tech, Melbourne, FL, USA

I. Kostanic
Associate Professor of Electrical and Computer Engineering, Florida Institute of Technology, Melbourne, FL, USA

G. Lapilli • J. Chandiramani
Research Assistant - Aerospace Engineering, Florida Tech, Melbourne, FL, USA

Introduction

The research is a continuation of previous research efforts [1, 2, 3, 4, 5] to build a third generation cost effective, versatile, reliable, and robust wireless sensor system for measuring hurricane effects on buildings, with enhanced network range and data collection capabilities.

System Description

An overview diagram of the sensor network system for the hurricane characterization is shown in Fig. 1. The network system consists of three main components; *house installation, communication network, and central server*. The *house installation* comprises a set of remote sensor units (up to 30 pressure sensors and two anemometers) that are installed on the roof of the house of interest, plus an associated base unit. The *communication network* is a cellular or satellite internet service that connects individual house installations to a central server. The *central server* processes measured data and enables a network operator to control the operation of the base and sensor units.

The base unit and the field laptop computer are placed in a weatherproof box in the vicinity of the house. The laptop is connected to the 110 VAC power supply from the house through a portable uninterrupted power supply pack for backup in case of a power outage.

Hardware

The sensors use a 48 MHz PIC18LF2553 processor and a fast serial bus speed (115,200 bps), which allows direct USB firmware updates. Every component of the new sensor circuit is in a surface mount package, which can accommodate over 40 components, including an on-board battery charger.

New features include:

- Lightweight plastic casing, sealed with standard O-ring
- More aerodynamic shape (Improved geometry and absence of exterior antenna)
- Li-Ion battery, allowing a lifetime of approximately 120 hours.
- Use of high throughput (250kbps) ZigBee transceiver.
- 12-bit A/D conversion
- Expansion port to add almost any sensor.
- PIC flashing and programming via USB port
- Fast battery charging time (6 hours full charge at 900mA – 6V)
- Improved over-the-air characteristics, with individual control on each sensor. This improves reliability, if a sensor is turned off, it does not affect the network.
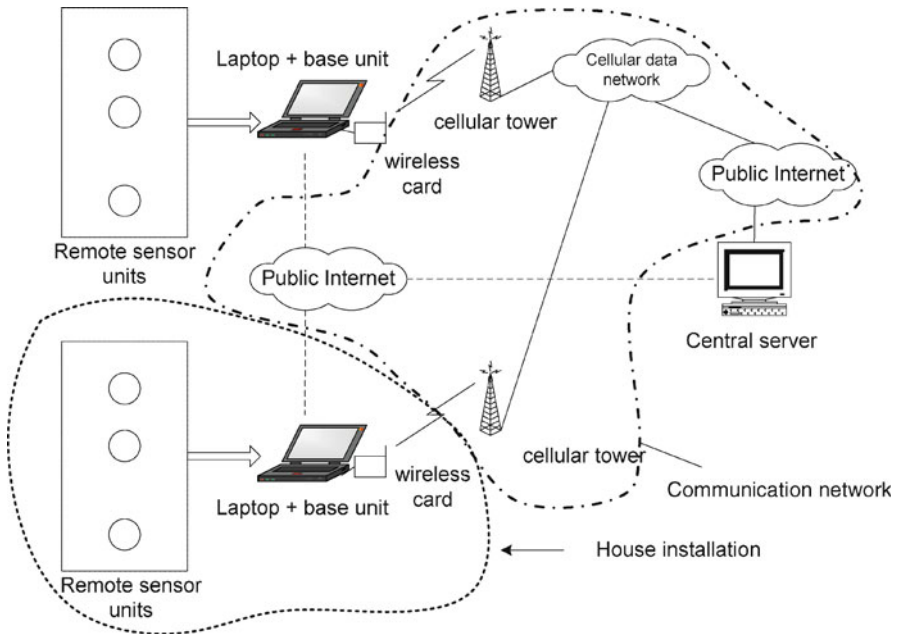
Fig. 1 General Outline of the system
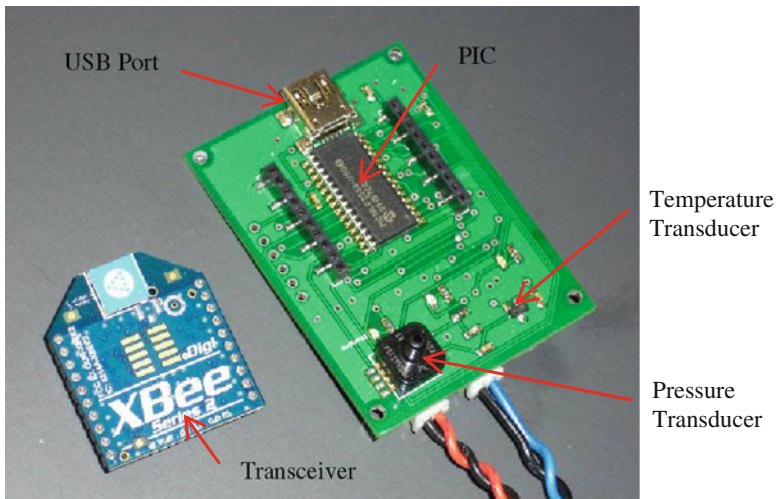
Fig. 2 Sensor and XBee transceiver

Pressure Sensor Board. The pressure transducer used is the Freestream Electronics'
MP3H6115A with case 1317A-04. The sensor board, shown in Fig. 2, was
designed to be used for many different applications. In its generic form, the
PIC18LF2553 has hookups to accommodate different inputs. In this specific

application, it measures pressure and temperature using analog sensors, sampled using the processor's onboard 12 bit A/D converter.

In addition to the binary samples representing pressure and temperature data, sensor information such as sensor type (router or endpoint), unique hardware ID, parent network address, battery level, and sequence ID is also sent. This information is used to update the GUI's (Graphical User Interface) in real time.

Anemometer. An expansion card is used to connect an RM Young's anemometer to the board. The only other board change is the firmware running on the processor. The anemometer firmware uses the ports in the expansion slot to collect data instead of the pressure and temperature sensors. Speed sampling rate is one-half the pressure sampling rate, and direction is one quarter. This is done to reduce bandwidth usage.

Measurements

A comparison between the pressure measured at the Melbourne International Airport's weather station by the National Weather Service, and the pressure recorded by the wireless system located at Florida Tech was conducted for 50 hours to evaluate the accuracy of the system (Fig. 3). Considering the fact that both measurements were taken at two different locations separated by a distance of about three kilometers, the agreement is notorious. Currently more comparisons to known references are taking place.
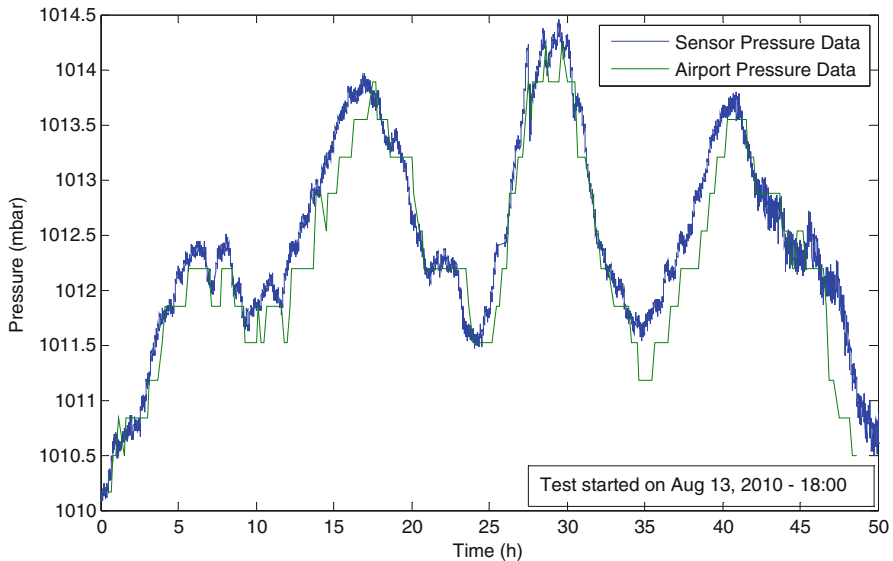
Fig. 3 50 hour comparison with MLB International Airport weather station

Fig. 4 Histogram of repeated static measurements
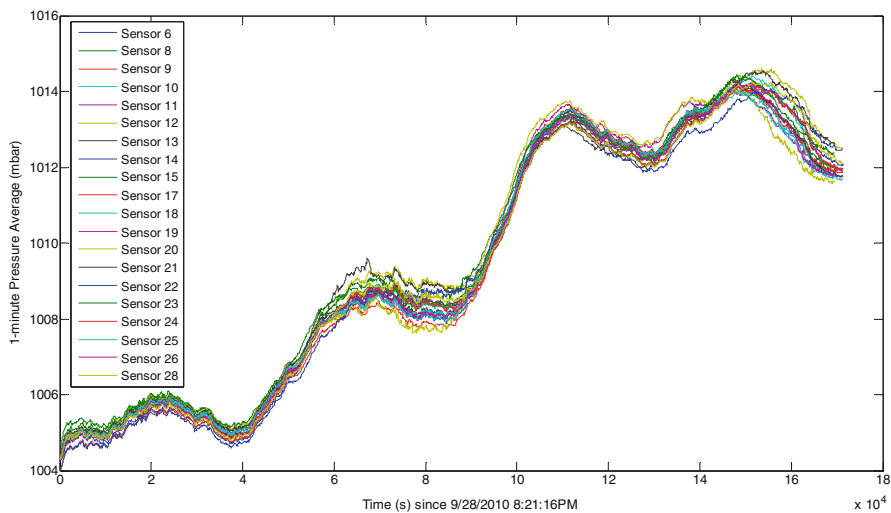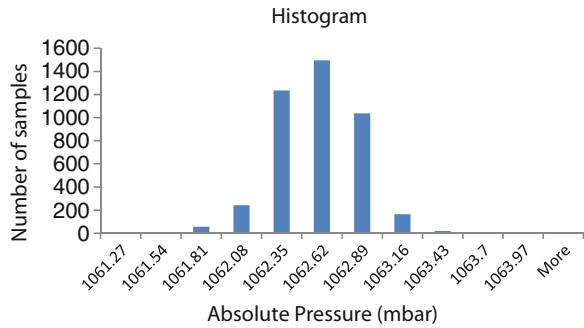
Fig. 5 Pressure history for all sensors deployed – Tropical Storm Nicole

Repeated static pressure tests at +50 mbar relative pressure (Fig. 4) show that the sensor output follows a Gaussian distribution with a standard deviation of σ = 0.2896 mbar. Therefore, considering ± 3σ we can infer with a 99.73% of reliability that the data measured is between ± 0.867 mbar.

Tropical storm nicole deployment

The system was deployed on a Satellite Beach house, in Florida during Tropical Storm Nicole in September 28th, 2010. Measurements show that the differences between sensors are never over 1mbar (Fig. 5). It is interesting to see also the increase in atmospheric pressure as the tropical depression dissipated.

Conclusions

Overall, this new generation of the sensor system resulted in major improvements, including reliability, robustness, ease of use, and expansion possibilities. In particular, speed has been doubled: the most reliable sample rate recorded is 36 samples per second for a full system of 30 sensors, while the previous generation was not exceeding 20 for the same conditions. The authors are ready to deploy 3 sets of sensors in case of a hurricane landfall in Florida. The ultimate goal is to collect data to better understand and quantify the behavior of a structure under the effects of wind.

References

[1] Michot, B.J., Full-Scale Wind Pressure Measurement Utilizing Unobtrusive Absolute Pressure Transducer Technology, M.S. Thesis, Civil Engineering Department, Clemson University, S.C., 1999
[2] Chelakara S. Subramanian, Jean-Paul Pinelli, Claudio D. Lapilli, and Larry Buist, A Wireless Multipoint Pressure Sensing System: Design and Operation, IEEE Sensors Journal, Vol. 5, No. 5, 2005
[3] Pinelli, J.-P, Subramanian, C.S., Lapilli, C., and Buist, L., "Application of a Wireless Pressure Sensing System to Coastal Wind Monitoring," Wind and Structures Journal, Vol. 8, No. 3 2005, pp 179–196
[4] Otero, C., Velazquez, A., Kostanic, I. Subramanian, C., and Pinelli, J.-P., "Real-Time Monitoring of Hurricane Winds using Wireless Sensor Technology," Journal of Computers, Vol. 4, No. 12, 2009, pp. 1275–1285.
[5] Subramanian, C.S., Lapilli, G., Kreit, F., Pinelli, J.-P; Kostanic, I., "Experimental and Computational Performance Analysis of a Multi-Sensor Wireless Network System for Hurricane Monitoring", Sensors and Transducers Journal, Vol. 10, 2011, pp. 206–244.

Overview of Fiber Optic Sensors for NDT Applications

A. Méndez and A. Csipkes

Abstract Optical fiber sensors have seen an increased acceptance as well as a widespread use for structural sensing and monitoring in civil engineering, aerospace, marine, oil & gas, composites and smart structure applications. Optical fiber sensor operation and instrumentation have become well understood and developed. Fiber sensors are attractive sensing devices for non-destructive testing (NDT) applications given their small size, lightweight and dielectric glass construction that renders them immune to electrical noise and EM interference—unlike most conventional electronic sensing systems. To date, fiber sensors have been embedded inside composite materials to determine curing, internal stresses and deformations as well as to detect the onset of cracks and damage. Surface mounted devices allow for the on-line monitoring in real time of deformations and strains in a variety of test specimens. Furthermore, some specific fiber sensor types allow for multi-point sensing at different locations using a single fiber, or even continuous, distributed sensing of temperature and strain based on Raman and Brillouin scattering systems. This paper reviews the operating principles, sensor types, benefits and applications of optical fiber sensors for non-destructive testing of materials and structures in different fields such as composites, aerospace, civil engineering, oil & gas and others.

Keywords FBG • Fiber sensor • Fiber bragg grating • Optical fiber • Optical sensor

Introduction

The field of fiber optics has undergone a tremendous growth and advancement over the past 40 years. Initially conceived as a medium to carry light and images for medical endoscopic applications, optical fibers were later proposed in the mid 1960's

A. Méndez (✉) • A. Csipkes
Micron Optics Inc., Atlanta, GA, USA
e-mail: amendez@micronoptics.com

as an adequate information-carrying medium for telecommunication applications. Ever since, optical fiber technology has been the subject of considerable research and development to the point that today light wave communication systems have become the preferred method to transmit vast amounts of data and information from one point to another. Among the reasons why optical fibers are such an attractive are their low loss, high bandwidth, EMI immunity, small size, lightweight, safety, relatively low cost, low maintenance, etc.

At the heart of this technology is the optical fiber itself. A hair-thin cylindrical filament made of glass that is able to guide light through itself by confining it within regions having different optical indices of refraction.

Optical Fiber Sensors: Operating Principle

Optical fibers are also attractive for other applications such as in sensing, control and instrumentation. In these areas, optical fibers have made a significant impact and are being the subject of substantial research over the last few years. In general, for these applications fibers are made more susceptible and sensitive to the same external mechanisms against which fibers were made to be immune for their effective operation in telecommunications. In its simplest form, an optical fiber sensor is composed of a light source, optical fiber; sensing element and a detector (see Fig. 1). The principle of operation of a fiber sensor is that the sensing elements modulates some parameter of the optical system (intensity, wavelength, polarization, phase, etc.) which gives rise to a change in the characteristics of the optical signal received at the detector.

Benefits & advantages of fiber optic sensors

Optical fiber sensors offer attractive characteristics that make them very suitable and, in some cases, the only viable sensing solution [1]. Some of the key attributes of fiber sensors are the following:

- Galvanic isolation and EM interference immunity
- Intrinsically safe
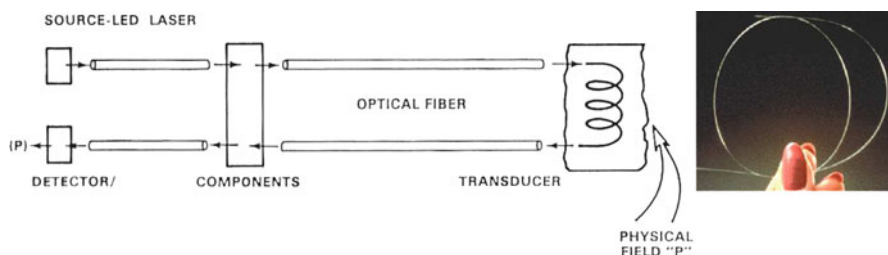
Fig. 1 Components of an optical fiber sensor

- Passive: no need for electrical power
- Possibility of remote, multiplexed operation
- Small size and lightweight
- Integrated telemetry: fiber itself is data link
- Wide bandwidth
- High sensitivity

Optical Fiber Bragg Grating Sensors

Optical fiber Bragg gratings (FBGs) are one type of fiber optic component that have—over the last few years—been used extensively for a wide variety of mechanical sensing applications [2-5] including monitoring of civil structures (highways, bridges, buildings, dams, etc.), smart manufacturing and non-destructive testing (composites, laminates, etc.), remote sensing (oil wells, power cables, pipelines, space stations, etc.), smart structures (airplane wings, ship hulls, buildings, sports equipment, etc.), as well as traditional strain, pressure and temperature sensing. The main advantage of FBGs for mechanical sensing is that these devices perform a direct transformation of the sensed parameter to optical wavelength, independent of light levels, connector or fiber losses, or other FBGs at different wavelengths. The advantages of FBGs over resistive foil strain gauges include:

- Totally passive (no resistive heating),
- Small size (can be embedded or laminated),
- Narrowband with wide wavelength operating range (can be highly multiplexed),
- Non-conductive (immune to electromagnetic interference),
- Environmentally more stable—non-corrosive

Operating principle of optical fiber bragg gratings

A fiber Bragg grating is wavelength-dependent filter/reflector formed by introducing a periodic refractive index structure, with spacing on the order of a wavelength of light, within the core of an optical fiber. Whenever a broad-spectrum light beam impinges on the grating, will have a portion of its energy transmitted through, and another reflected off as depicted in Fig. 2. The reflected light signal will be very narrow (few nm) and will be centered at the Bragg wavelength which corresponds to twice the periodic unit spacing Λ. Any change in the modal index or grating pitch of the fiber caused by strain, temperature or polarization changes will result in a Bragg wavelength shift.

FBGs are attractive for sensing applications due to the dependence of their spectral shift as a function of grating separation change with external effects. Hence, FBGs are self-referencing and absolute measuring devices for strain and/or temperature. Used in combination with opto-mechanical transducers, allow the measurement of other physical parameters such as pressure, acceleration, tilt, elongation, etc.

For example, Fig. 3 illustrates the aspect of a novel, commercial FBG strain sensor. The device is rugged and designed for use in diverse field applications.
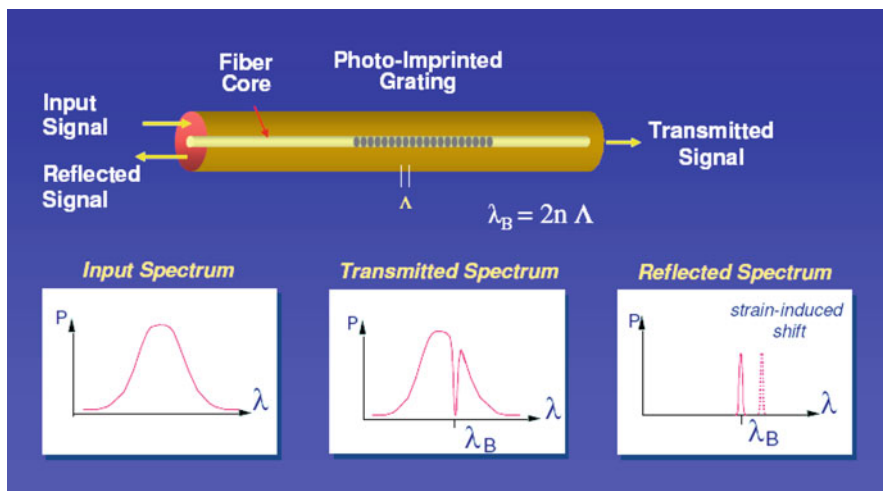
Fig. 2 Transmission and reflection spectra of a fiber Bragg grating

Fig. 3 Photograph of a commercial fiber Bragg grating strain sensor. Fiber is pre-mounted on a metallic carrier (photo courtesy of Micron Optics Inc.)

The FBG sensing element is pre-stretched and mounted on a protective metallic carrier flexure. The strain sensor can be surface mounted to test specimens of interest using epoxy bonding or spot welding techniques. This, in practice, becomes the optical fiber equivalent of a conventional foil strain gage sensor.

Applications for Non-destructive Testing

Civil structures

Since the infrastructure of civil engineering works around the world is in a state of deterioration due to aging of its materials, excessive use, overloading, weathering, lack of maintenance and proper inspection. It has become increasingly important in

the last few years to determine the safety of a structure by the non-destructive evaluation (NDE) of its strength and integrity. This assessment is essential for the repair, retrofit, rehabilitation, life extension or replacement of the structure in question. Furthermore, it would be very useful to develop means for the feedback and control of the state of health of a structure.

Optical fibers, because their small size and lightweight, offer the possibility to be embedded within cement or concrete without affecting their properties and used as sensitive, but rugged, transducers of mechanical perturbations. Given their attributes, sensors made out of optical fibers have the capability to be embedded, prior to curing, into reinforced concrete elements and structures such as buildings, bridges, dams and tanks for the NDE of structural integrity and the measurement of the internal state of stress. In other instances, sensors can simply be surface-mounted onto concrete or steel surfaces. Once installed, the fiber sensors can provide high-resolution temperature and strain measurements, detect the onset and growth of cracks, as well as to monitor creep and thermal stresses.

The fundamental applications envisioned for FOS within the field of civil engineering can be grouped into three main areas, namely:

- Structural monitoring and damage evaluation
- Experimental stress analysis
- Management and control of systems and service installations

Composites Materials

The use of optical fiber sensors embedded within composites for the measurement of internal strain and the detection of structural damage in aerospace applications has proved to be an effective non-destructive evaluation (NDE) technique and become the subject of substantial research [2, 3, 5]. Given its small size and lightweight, optical fiber sensors can be easily surface mounted or embedded into the matrix material of a composite element or structure (Fig. 4). Discrete sensors can be placed at strategic locations inside or outside the composite section under study. In the case of FBGs, a continuous fiber lead with an array of fiber gratings can be embedded into the composite material and routed around various regions of interest. This approach is particularly attractive when dealing with long sections such as airplane wings, fuselages, composite pipes, yacht masts, and many others.

Once installed, fiber optic strain sensors would allow the measurement of surface and internal strains and stresses, detect the onset and location of cracks, determine the loads acting on a given structural element, measure vibrations and determine internal pressure fluctuations in tanks and vessels, all during its installation and deployment, as well as over its entire service life. Furthermore, coupled with the use of fiber temperature sensors, it would be possible to monitor the curing process of composites and assess their residual stresses.
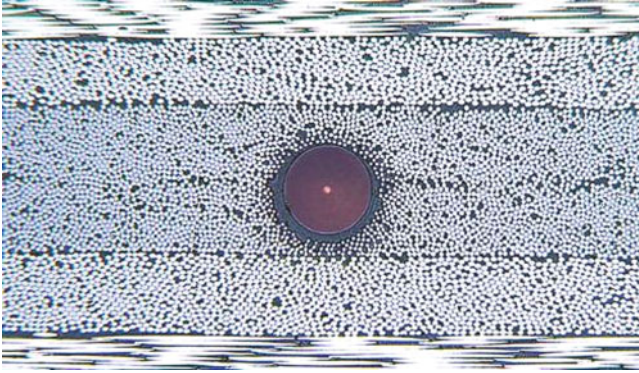
Fig. 4 Carbon Fiber Reinforced Polymer Composite with embedded fiber optic Bragg grating sensor (source: Daimler-Benz)

Conclusions

Optical fiber sensors are a practical and real sensing technology alternative to more conventional NDT techniques. Among the primary benefits for using fiber sensors are their immunity to electrical noise and EM immunity coupled with their small size that allows for direct embedment into concrete and composite materials. Sensors, interrogation instruments, and installation methods are improving, but need to continue to improve for widespread, mainstream adoption. The number of commercial companies offering fiber-optic based sensing gear is increasing as their adoption in NDT and SHM applications continues to emerge. Nowadays, fiber sensors have been used in civil engineering, aerospace, naval, geotechnical, composite, automotive, oil and gas and several other industries.

References

[1] Lopez-Higuera, J.M., *Handbook of Optical Fiber Sensing Technology*, Wiley, New York, 2002.
[2] Measures, R.M., *Structural Monitoring with Fiber Optic Technology*, Academic Press, San Diego, CA 2001.
[3] Udd, E., *Fiber Optic Smart Structures*, Wiley, New York, 1995.
[4] Ansari, F., *Applications of Fiber Optic Sensors in Engineering Mechanics*, American Society of Civil Engineers, New York, 1993.
[5] Culshaw, B., *Smart Structures and Materials*, Artech House, Neorwood, MA 1996.

Section 2
NDT for Material and Property Characterization

Evaluation of Concrete Properties by Combining NDT Methods

J.P. Balayssac, S. Laurens, D. Breysse and V. Garnier

Abstract The combination of NDT methods is currently considered as one of the more relevant way to improve the quality of the diagnosis of concrete structures. Indeed, many research actions involve the use of several families of NDT methods (ultrasonic, electromagnetic…) for the imaging of structures (voids detection, tendons and reinforcement localisation). Previous studies have shown that this approach is particularly suitable for assessing concrete properties, because concrete is a complex material in which the properties are interacting. For instance mechanical properties depend on moisture which also affects the NDT measurements. On one hand, moisture can be considered as a bias factor which affects the measurement but on the other hand, moisture has also to be considered as a durability indicator, as in such conditions the penetration of aggressive agents and the development of internal reactions is favoured. The combination of NDT methods, some being mainly sensitive to mechanical properties and others being more affected by moisture could be really relevant. Another approach concerns the assessment of chloride content which is also significantly affected by moisture. This paper will describe how the role of NDT methods regarding some concrete properties can be quantified. A specific procedure is also proposed to assess the complementarity of different NDT methods regarding the evaluation of two conjugated properties.

Keywords Combined NDT methods • Concrete • Material properties • Moisture effects

J.P. Balayssac (✉) • S. Laurens
LMDC (Laboratoire Matériaux et Durabilité des Constructions), Université de Toulouse; UPS, INSA, 135, avenue de Rangueil, F-31 077 Toulouse Cedex 04, France
e-mail: jean-paul.balayssac@insa-toulouse.fr

D. Breysse
GHYMAC Université Bordeaux 1, France

V. Garnier
LCND Université de la Méditerranée, IUT d'Aix en Provence, France

Introduction

In the field of civil engineering, nowadays, concrete structures (reinforced or prestressed) are one of the first heritage. In France, 100000 important bridges, 55 nuclear reactors, 350 hydroelectric dams and of course thousands of buildings are in service. A good knowledge of the condition of these structures is a major concern for people who are responsible of their safety. The fundamental questions which are nowadays of concern for the managers are the estimate of residual life span and the requalification of the structures. Indeed the owners are increasingly led to prolong the service life of their structures because of sustainable development and because the time required for initiating new constructions is becoming prohibitive. Such a strategy assumes that the evaluation of the residual life span of structure is possible but in reality it remains a difficult task.

Regarding the quality of concrete, even if some indicators are clearly identified and quite relevant, non destructive evaluation is still a somewhat open question. Although the sensitivity of some non destructive testing (NDT) methods versus several indicators was proved by means of laboratory investigations, the implementation of NDT on real sites is not fully achieved. The difficulty lies in the diversity of structures and building systems but also in the complexity of concrete as a material. Indeed, although NDT measurements provide information on physical properties, most of them are influenced by several indicators simultaneously. The combination of different families of NDT methods can be proposed as a solution for separating the effect of each indicator.

The aim of this paper is to present some results obtained in this context of combined use of NDT methods. An important experimental program was drawn implementing different concretes and different NDT methods (ultrasonic, electromagnetic, and electric) [1].

NDT Methods Used

Four different techniques were used, electric resistivity, radar (GPR), ultrasonic surface waves and capacitive method. The resistivity measurement was performed by using a four-probe square device developed by Lataste [2] or a Wenner probe. In the following the apparent resistivity is considered. For radar, the potential of direct wave, propagating along the air-material interface is explored. The sensitivity of this wave to both moisture and chloride content have been demonstrated by previous studies [3], [4]. Both velocity and amplitude of the direct wave are considered. The ultrasonic surface waves and particularly Rayleigh waves are relevant for the characterisation of cover concrete. In this study a specific device based on contact ultrasonic sensors developed by Piwakowski et al was used [5]. Attenuation, group velocity and phase velocity were considered. The capacitive method was developed by Dérobert et al [6] and allowed measuring the relative permittivity ε'_r of concrete.

Quality and Pertinence NDT Methods Versus Concrete Indicators

Outline of the chosen methodology; details of the program and variability assessment

An important experimental project was carried out and divided into different benchmarks. A benchmark was devoted to the simultaneous evaluation of the indicators: porosity, E-modulus, compressive strength and water content and involved 8 different concretes. For each concrete 11 slabs were prepared. Another benchmark was devised for the evaluation of chloride content: it involved 4 different concretes, two levels of salt concentration inside the interstitial solution and different saturation degrees (40, 80 and 100%) [1].

Each technique provides numerous observables, so about 50 observables were measured on each slab. Destructive tests have been performed on cores from specific specimens in order to assess the targeted indicators. Knowing the various sources of variability, during the benchmark 1, the measurement process was defined in order to quantify, for each observable, several variances:

– V1, coming from the lack of local repeatability of any measurement, at a given point.
– V2, coming from the material variability in a surface which is assumed as homogeneous. It is obtained by comparing different measurements on a same slab.
– V3, resulting from the large scale variability. It is evaluated by comparing the local representative value obtained at different points. For laboratory specimens, it is obtained by comparing values measured on 8 different slabs from the same mix.
– V4, which is the global contrast between different concretes.

Characterisation of quality and relevance of NDT methods

To qualify the quality linked to the variability of each NDT observable an index of quality (Table 1) was defined [7]:

$$IQ = -\log(V1/V3) - \log(V2/V3)$$

To be sure that the quality of the observable is good enough it must be as repeatable as possible at the scale of a homogeneous area of the material which is assumed homogeneous. With a perfect measurement the variance V2 would be null. The variance V3 is linked to the variations of the homogenised concrete in an area without any defect. The quality index is higher if the variance V3 is higher than both V1 and V2. The values of V1 and V2 have to be the lowest possible when compared to material "intrinsic variability". Of course, the higher IQ, the higher the quality of the observable. One may observe in Table 1 that the quality index is important for the

Table 1 Quality index and relevance index for different observables

Observable	IQ	IR Porosity	IR Moisture
Resistivity	2,84	1,21	1,43
Radar direct wave velocity	2,70	0,36	1,37
Radar direct wave amplitude	1,55	0,31	1,01
Phase velocity of acoustic surface waves	1,28	1,06	1,05
P-wave velocity	1,05	0,87	0,92
Surface waves attenuation	0,68	0,12	0,25
Group velocity of acoustic surface waves	0,15	0,42	0,29
Capacitive method	0,40	0,13	1,36

observables provided by the electrical resistivity. Nevertheless the ultrasonic surface waves provide the lowest quality indexes which is linked to higher variability of the measurement at the scale of the homogenised area.

The reliability of the NDT observables was assessed by means of the index of relevance IR calculated by the following relation:

$$IRi = -\log(V3/V4i)$$

V4i (V4w, V4p, V4E or V4Rc) is the variance due to contrast among the different concretes when the indicator i changes (here respectively moisture (w), porosity (p), Young modulus (E) and compressive strength (Rc). The observable is much sensitive to the indicator if this variance is high and so IRi increases.

Table 1 presents the value of IR for two indicators, moisture and porosity. The same observables than those used for the analysis of the quality index are considered. Of course the index of relevance depends on the indicator in question either moisture or porosity. The index is high for the observables provided by the resistivity technique whatever the indicator. But for the radar technique the index is high for the moisture and low for the porosity. For acoustic surface waves the relevance index is almost the same for both indicators and can be as high as for resistivity observables. The analysis of quality index and relevance index permitted to distinguish the NDT observables by discerning their differences and effectiveness and to select 18 among the 50 previously used.

Analysis of the Complementarity Among the Observables

Each observable was correlated by means of bi-linear regression to both indicators moisture and porosity. Two techniques can provide complementary information if the orientation of the planes of correlation is very different. The higher the angle of orientation, the higher the complementarity [7]. Table 2 provides the angle of orientation among different correlation planes. It is possible to remark that both surface waves and longitudinal waves don't provide complementary information since the

Table 2 Orientation angle of the correlation planes for different observables (characterisation of moisture and porosity)

	Velocity of acoustic surface waves	Velocity of longitudinal ultrasonic waves	Resistivity quadripole	Resistivity Wenner	Radar wave amplitude peak-to-peak
Velocity of acoustic surface waves	0				
Velocity of longitudinal ultrasonic waves	0.8	0			
Resistivity quadripole	82.3	82.6	0		
Resistivity Wenner	82.2	82.5	0.1	0	
Radar wave amplitude peak-to-peak	88.7	89.1	6.6	6.7	0

Table 3 Orientation angle of the correlation planes for different observables (characterisation of moisture and chloride content)

	Velocity of radar wave	Amplitude of radar wave	Resistivity quadripole	Capacitive
Velocity of radar wave	0			
Amplitude of radar wave	0.4	0		
Resistivity quadripole	0.2	0.2	0	
Capacitive	1.4	1.1	1.3	0

difference of orientation is very small. The same remark can be done between resistivity and radar measurements. On the other hand there is an important complementarity between acoustic waves and either resistivity and radar observables. Such an approach permits to quantify the real complementarity between two observables for the characterisation of two combined indicators.

We have done the same analysis for two other indicators evaluated by the other benchmark [1], i.e. both chloride content and moisture. Four observables were considered, apparent resistivity, capacitive measurement, velocity and attenuation of radar direct wave. Table 3 gives the orientation angles for the four observables considered.

In this particular situation, the angles of orientation between the correlation planes are very small. It means that all the observables are influenced in the same way by moisture and chloride content and so there is no complementarity between them.

Conclusions

The results presented in this paper are a part of a study aiming to test NDT methods for the evaluation of some properties of concrete (indicators). A wide range of NDT methods providing about 50 features (observables) were implemented on a large

number of concrete mixes by means of several benchmarks. Through an analysis of the variability at different levels, criteria for both quality and relevance of the observables provided by the NDT methods were proposed. These criteria were used to select 18 observables. Based on correlations between NDT observables and concrete indicators, a quantification of the complementarity of methods for determining two conjugated indicators was also performed. It was demonstrated that ultrasonic surface waves and resistivity or radar method are highly complementary for the conjugated evaluation of moisture and porosity. Nevertheless for the conjugated evaluation of moisture and chloride content it was not possible to find complementary NDT methods.

References

[1] J.P. Balayssac, S. Laurens, G. Arliguie, I. Fortuné, "SENSO: a french project for the evaluation of concrete structures by combining non destructive methods", *Sacomatis, RILEM conf*, 1–2 september 2008, Varenna, Italy

[2] J.F. Lataste, Evaluation Non Destructive de l'état d'endommagement des ouvrages en béton armé par mesure de résistivité électrique, PhD of University of Bordeaux I, décembre 2002 (In French)

[3] S. Laurens, J.P. Balayssac, J. Rhazi, G. Arliguie, "Influence of concrete relative humidity on the amplitude of Ground-Penetrating Radar (GPR) signal", Materials and Structures, Vol. 35, n. 248, 2002, pp 198–203

[4] G. Klysz, , J.-P. Balayssac, , "Determination of volumetric water content of concrete using ground-penetrating radar", Cement and Concrete Research, Vol. 38 n. 6, pp 783–793

[5] B. Piwakowski, P. Safinowski, "Non-destructive non-contact air-coupled concrete evaluation by an ultrasound automated device", Proceedings of 7th International Symposium of Non Destructive Testing in Civil Engineering, NDTCE'09, Nantes, 30/6-3/7 2009

[6] X. Dérobert, J. Iaquinta, G. Klysz, J.-P. Balayssac, "Use of capacitive and GPR techniques for the non-destructive evaluation of cover concrete", NDT & E International, Vol. 41 n. 1, January 2008, pp 44–52

[7] D. Breysse, M. Larget, Z.M. Sbartaï, J.F. Lataste, J.P. Balayssac, "Quality of NDT measurements and accuracy of concrete physical properties", Proceedings of 7th Int. Symp. of NDT in Civil Engineering, NDTCE'09, Nantes, 30/6-3/7 2009

Thermography and Ultrasound for Characterizing Subsurface Defects in Concrete

E.Z. Kordatos, D.V. Soulioti, M. Strantza, T.E. Matikas and D.G. Aggelis

Abstract A combination of non destructive testing (NDT) techniques is applied for subsurface damage inspection. Thermography and ultrasound are used complimentarily to detect and characterize near surface cracking. In this paper, specimens with subsurface cracks, are scanned by an infrared camera in order to indicate the position of the cracked area. For cases of small and thin cracks the cooling off curves over a specified time span are examined in order to identify the damage areas more reliably. At the specific position indicated by thermography, ultrasonic sensors are placed in order to make a more detailed assessment for the depth of the crack. Although there is no visual sign of damage, ultrasonic waves are influenced in terms of velocity and attenuation.

Keywords Elastic waves • Thermography • Subsurface damage

Introduction

Subsurface cracking in concrete may be the result of reinforcement corrosion, or delaminations between successive layers. The early detection of this kind of damage enables repair either by replacement of the surface layer or by cement injection. For this purpose suitable non destructive testing (NDT) techniques should be utilized. Thermography is established as an effective technique for investigation of civil structures. Defects or inhomogeneities which lie below the surface affect the heat transfer rate when thermal energy is propagating into or out of the structure. This can be monitored by an infrared camera and the positions of the flaws are

E.Z. Kordatos • D.V. Soulioti • M. Strantza • T.E. Matikas (✉) • D.G. Aggelis
Department of Materials Science and Engineering, University of Ioannina,
Ioannina 45110, Greece
e-mail: matikas@cc.uoi.gr

determined by the temperature variations on the surface [1,2]. When the defect is identified, another technique can be used for more accurate characterization of its depth. One of the promising techniques is ultrasound, since several wave parameters are influenced by the presence of cracks [3,4].

In this study, steel fiber reinforced concrete (SFRC) specimens with subsurface cracks were scanned by an infrared camera after being heated in an oven in order to identify the position of the subsurface crack. Consequently the specimens were examined by one-sided ultrasonic measurements and crucial parameters of wave propagation were correlated with the depth to the crack.

Materials

The specimens were made of steel fiber-reinforced concrete (SFRC). Their size was 100x100x400 mm. The fiber content was 0.5%, by volume. The specimens were tested in 4-point bending (similar to fracture toughness test [ASTM C1609/C 1609 M-05]) resulting in approximately vertical cracks which propagated from the bottom tensile surface to the top. More details on the materials and the fracture test are supplied in [5]. In total seven specimens were produced from the same mix and were loaded up to different levels of mid-span deflection, from 0.5 mm to 3 mm.

Thermography

The experimental setup consists of an infrared camera and an oven. The type of the camera was Flir T360 with a spectral range of 7.5 to 13 μm and a sensitivity of 0.06 °C at 30 °C. The infrared camera was placed at 1.6 m distance from the specimens. The thermal emissivity of concrete is 0.92 and there was no need to paint the surface. Thermographs were recorded after the specimens were heated in the oven at 90 °C for 3 h.

Results

Figure 1a show the thermograms of a typical specimen, containing a crack 12 mm below the surface. There is a distinct variation in the temperature field at the area on top of the crack. As the cracks become smaller this narrowing of the warm zone becomes less obvious, and especially for the specimen with deflection of 0.5 mm, for which the crack is approximately 28 mm away from the monitoring surface, there is no certain visible trace of the underlying damage.

As introduced in [6] a simple way to enhance the detection capability is by considering the average temperature of vertical lines, see Fig. 1b. This procedure involves calculation of the average temperature along the longitudinal axis of the specimen.
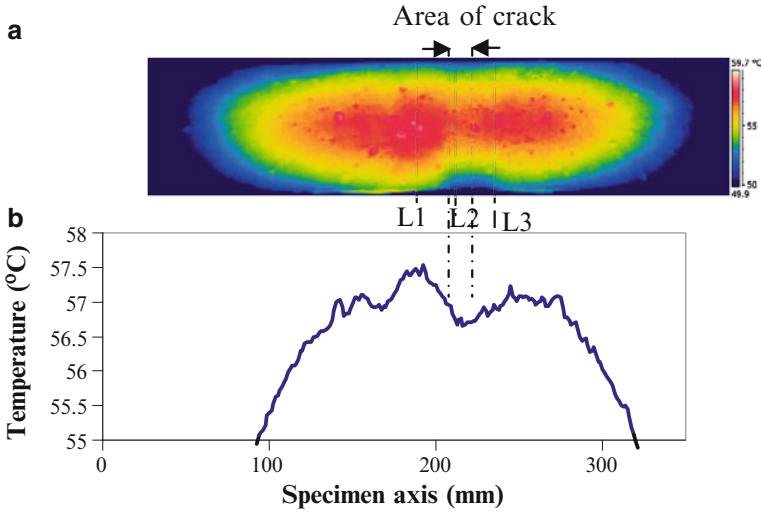
Fig. 1 (**a**) Thermograph of the specimen with mid-span deflection 2.5 mm, (**b**) average temperature along the specimen's axis

Specifically, the thermographs in this study were represented by 320x48 pixels. The average temperature of each column (e.g. Line 1 in Fig. 1a) including 48 values is depicted in Fig. 1b. It is shown that at the point of the actual crack a local minimum of the curve is exhibited, excluding the areas near the edges of the specimens which are cooling down more quickly. The above mentioned procedure enables more reliable characterization. It is mentioned that some small defects on the surface (e.g. air voids) may influence the temperature of a few pixels in the near vicinity. However, they are not enough to influence the average of 48 values of temperature from the pixels on a straight vertical line. Therefore, even slight changes of temperature due to the subsurface defect can be evaluated.

Cooling down curves

Monitoring the cooling down curve can also be studied in order to confirm or even improve the results [7]. As mentioned earlier, the subsurface defect influences the heat rate from the specimen to the environment. This has an effect not only on a specific "snapshot" of the temperature field but also on the cooling rate. Fig. 2 shows the average temperature for three vertical lines of the specimen, (L1,L2,L3, in Fig. 1) as a function of time. Line 2 is located exactly on the projection of the crack, while L1 and L3 to either sides of the crack on sound material. All of them can very well be fitted by exponential decay curves, as seen by the correlation coefficient which is almost unity. However, the exponential superscript is lower for the case of line L2 located on the crack (0.0062 compared to 0.0065 for uncracked). This is a repeatable trend especially for the initial part of the cooling stage when the
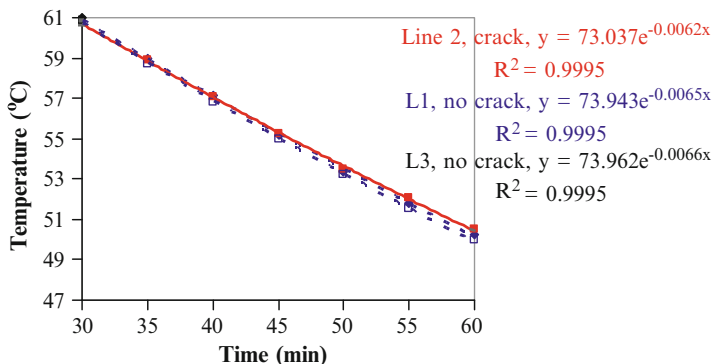
Fig. 2 Cooling down curve for cracked and uncracked areas

heat exchange is strong. This difference may be of the order of 2%, and does not crucially affect the shape of the curve; its repeatability however, makes it another descriptor to take seriously into account for subsurface damage detection. Therefore, it is suggested that calculation of the exponent of the cooling off curve for a short period of time (for this case 30 min) along the specimen's axis can indicate the position of the crack. On that position, the exponent will obtain its minimum value over the monitored surface, similarly to the minimum of the average temperature.

The above study shows that thermography is capable of identifying the location of the cracks. The use of ultrasound discussed below aims at more accurate characterization of the depth of the subsurface crack at the location pointed out by thermography. In practical application the heating will be produced by sunlight which can heat the concrete surface up to approximately 50-60 °C[1].

Ultrasound

Elastic wave parameters such as velocity and attenuation are quite sensitive to the existence of damage in the form of distributed micro-cracks, and large macroscopic voids [8].

Experimental setup

The experimental setup consists of two sensors which were placed on the intact side of the specimen at a distance of 70 mm. The excitation was conducted by pencil lead break, see Fig. 3a. The sensors were acoustic emission transducers (Physical Acoustics, PAC Pico), with broad band response from 50 kHz to 800 kHz and
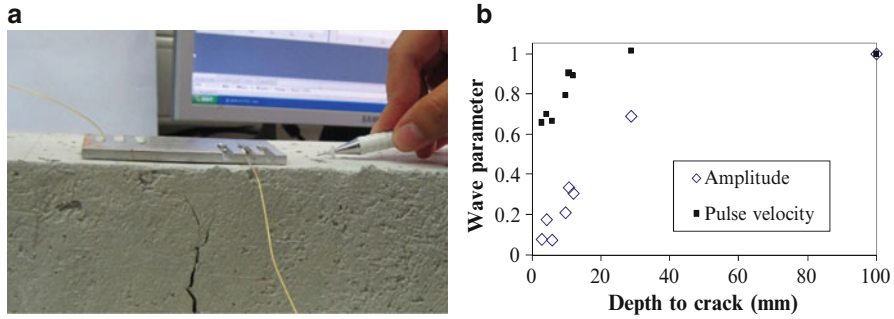
Fig. 3 (**a**) Snapshot of wave measurements, (**b**) wave parameters vs depth-to-crack

diameter of 5 mm. The sampling frequency of the acquisition board was set to 5 MHz. Wave velocity was measured by the time delay between the waveforms collected at the different sensors.

Results

Testing of specimens with different depths of damage made it possible to correlate the wave parameters with the thickness of the undamaged surface layer between the crack and the surface, apart from simply identification that has been accomplished in an earlier study [6]. Figure 3b shows the experimental results concerning velocity of the longitudinal waves for the different depths to crack. The results are normalized to the maximum which is the value on sound material (4222 m/s). It is shown that a depth of 31 mm is adequate for the longitudinal wave to propagate without velocity decrease, thus giving no warning for the underlying crack. However, as the crack closes to the surface the measured velocity drops and reaches 66% for the specimen with the largest crack (approx. 2.7 mm from the surface). It is shown that one-sided measurements of P-wave velocity will produce a noticeable decrease for damage lying down to 11 mm beneath the surface. No trace of the crack is found by P-wave velocity when the crack is located more than 20 mm deep inside the material.

A parameter that can be defined in a deterministic way is the amplitude of the wave which corresponds to the maximum voltage (V) of the received waveforms. In addition to damping and geometric spreading, another very important factor is inhomogeneity which may reflect or scatter the wave to directions other than the original. In the specific case, the subsurface crack blocks the propagation path and a portion of ultrasonic energy will not proceed to the second transducer. Therefore, the ratio of the amplitude of the second to the first receiver may well be used as a factor of transmission to correlate with the extend of damage. The results are shown again in Fig. 3b. The influence of the crack is much stronger in transmission as it is decreased to less than 10% of the transmission exhibited through sound material.

Therefore, the experimental analysis allows to conclude that the amplitude of the wave is very reliable parameter for correlation with subsurface damage, due to its high sensitivity as well as the reliability of the measurement which does not use a reference point, (sometimes difficult to be identified), and is not affected by noise, which could mask the initial arrival of the P-wave.

Conclusions

The present study deals with a methodology to detect and characterize subsurface defects in concrete. The joint use of two NDT inspection methods (thermography and ultrasound) shows promising results in terms of reliability and applicability. A basic conclusion, is that simple thermographs at approximately 60 °C reveal the existence of subsurface cracks at the depths of 11 mm. Additionally averaging of the temperature over a mesh direction enhances the characterization by the strong local minima of the curve that correspond to the crack location. The cooling down curve from approximately 60 °C to 50 °C is fitted by a lower exponential decay coefficient for the lines over the crack compared to sound material, even for the small and deep cracks (11 mm from the surface). Elastic wave parameters are sensitive to the existence of subsurface crack. Especially the amplitude changes by more than 95% for cracked material compared to the sound one. The dependence of amplitude on depth-to-crack is monotonic allowing not only damage detection, but also characterization. The work should continue in the direction of increasing the sensitivity of the methodology for detection of smaller and deeper cracks, as well as check larger specimens, in order to minimize or exclude edge effects.

References

[1] Weil, G.J. (1991). Infrared thermographic techniques. In: Handbook on Nondestructive Testing of Concrete, pp. 305–316, Malhotra V.M., Carino N.J. (eds.). CRC Press, Boca Raton, FL.
[2] Maierhofer, Ch., Brink, A., Rollig, M., Wiggenhauser, H. (2005). *Construction and Building Materials*, vol. 19, p. 731.
[3] Naik, T.R., Malhotra, V.M. (2004). The Ultrasonic Pulse Velocity Method. In: Handbook on Nondestructive Testing of Concrete, pp. 169–188, Malhotra V.M., Carino N.J. (Eds.). CRC Press, Boca Raton, FL.
[4] Aggelis, D.G., Momoki, S., Chai, H.K. (2009). *NDT & E International*, vol 42, pp.304–307.
[5] Soulioti, D.V., Barkoula, N.M., Paipetis, A., Matikas, T.E. (2011). *Strain*, 47 (Suppl. 1), pp. e535–e541.
[6] Aggelis, D.G., Kordatos, E.Z., Soulioti, D.V., Matikas, T.E. (2010). *Construction and Building Materials*, vol. 24, p. 1888.
[7] Cheng C.C., Cheng, T. M., Chiang, C.H. (2008). *Automation in Construction* vol. 18, p. 87.
[8] Aggelis, D.G, Shiotani, T., Polyzos, D. (2009). *Cement and Concrete Composites*, vol. 31, n. 1, p. 77.
[9] Qixian, L., Bungey, J.H. (1996). *Construction and Building Materials*, vol. 4, n. 10, p. 237.

Determination of the Frequency Dependent Dynamic Modulus for Asphalt Concrete Beams Using Resonant Acoustic Spectroscopy

A. Gudmarsson, N. Ryden and B. Birgisson

Abstract The objective of this paper is to study the application of resonant acoustic spectroscopy (RAS) to beam shaped asphalt concrete samples. Natural modes of vibration are generated by a small load impulse at different temperatures and an accelerometer measures the resulting acceleration through the specimen. By using the Fast Fourier Transform the obtained information is transformed to frequency domain from which the solid's damped natural frequencies can be determined. For each frequency and temperature the corresponding complex modulus is calculated using the approach of RAS. Results of the dynamic modulus from RAS are presented and compared with results of the dynamic modulus calculated according to ASTM E 1876-99 [1]. By using ASTM E 1876-99 only the fundamental frequency of each type of vibrational mode can be used. However, using RAS several resonance frequencies from the same temperature can be used in the evaluation. This opens the possibility of determining the high frequency (or the low temperature) part of the dynamic modulus mastercurve directly from RAS.

Keywords Dynamic modulus • Mastercurve • RAS • Rayleigh-Ritz • Resonance frequencies

Introduction

The dynamic modulus mastercurve is a key parameter in modern pavement design due to its ability to represent the material behavior as a function of temperature and frequency. Different non-destructive testing (NDT) methods applying seismic

A. Gudmarsson (✉) • B. Birgisson
Highway and Railway Engineering, Royal Institute of Technology,
Stockholm, Sweden
e-mail: anders.gudmarsson@byv.kth.se

N. Ryden
Engineering Geology, Lund University, Lund, Sweden

methods to determine the dynamic modulus of asphalt concrete have been presented in [2-5]. NDT in form of resonant acoustic spectroscopy (RAS) means that measurements are made to obtain the normal modes of vibration of a solid in order to determine the solids elastic properties. The resonance frequencies of a solid are a function of the geometry, boundary conditions, mass and the elastic properties of the sample. The test is simple to perform and gives significant time and cost savings compared to traditional cyclic loading tests. RAS or resonant ultrasound spectroscopy (RUS) that is widely used in other applications of engineering [6], are within the civil engineering area more known as free-free resonant column test or impact resonant test. An important difference between the methods is that RAS is based on multiple modes of vibration while the methods used in civil engineering have so far mostly been restricted to the fundamental modes of vibration [2,4]. Also, RAS is always based on numerical methods to obtain the material properties of elastic or viscoelastic objects since a complete analytical solution of the problem does not exist [6].

Resonant Acoustic Spectroscopy

The algorithms of calculating the resonance frequencies are fully described by Migliori and Sarrao [6]. Here we only present the concept of energy minimization techniques that forms the basis of RAS. We also show how it can be applied to rectangular parallelepipeds (RPPD) specimens.

By using Lagrangian mechanics Eqn. (1) and assuming simple harmonic motion for an arbitrary 3-D linear elastic body the displacements that results in the minimum solution can be found. This solution corresponds exactly to the normal modes of the body [6].

$$L = \int_V (KE - PE) dV \qquad (1)$$

KE is the kinetic energy and PE is the potential energy for a body with the volume V. To be able to evaluate the displacements numerically the Rayleigh-Ritz method is used to expand each component of the displacement (u_i) in a function (Φ_λ) according to Eqn. (2). Where $\lambda = (p,q,r)$ are positive integers and the $a_{i\lambda}$ coefficients are constants.

$$u_i = \sum_{(p,q,r)} a_{i(p,q,r)} \Phi_{(p,q,r)} = a_{i\lambda} \Phi_\lambda \qquad (2)$$

For the general case with arbitrary geometries powers of Cartesian coordinates can be chosen as the basis functions, Eqn. (3).

$$\Phi_\lambda = x^p y^q z^r \qquad (3)$$

By substituting the displacement function into the Lagrangian the following matrix equation, Eqn. (4) can be obtained.

$$L = \frac{1}{2}\omega^2 \vec{a}^T \vec{\vec{E}} \vec{a} - \frac{1}{2}\vec{a}^T \vec{\vec{\Gamma}} \vec{a} \tag{4}$$

Now considering the geometry of the RPPD specimen one can simplify the calculations of the Γ and E matrices to an analytical form Eqn. (5), where the length of the sides of the RPPD is $2d_1$, $2d_2$ and $2d_3$.

$$f(p,q,r) = \frac{8d_1^{p+1}d_2^{q+1}d_3^{r+1}}{(p+1)(q+1)(r+1)} \tag{5}$$

The natural resonance frequencies without losses are then obtained from the eigenvalues, ω^2.

Test procedure and analysis

The test set-up (see Fig. 1) includes pads of soft foam where the specimen is placed. This is assumed to fulfil the criteria of free boundary conditions [2]. A small hammer is used to excite the normal modes of vibration and a 1.5 grams miniature accelerometer (PCB model 352B10) measures the acceleration through the solid during 10 ms. The mechanical motion in the accelerometer is converted into electrical signals and stored in a computer via the PC-CARD DAS 16/16-AO from *Measurement Computing*. To determine the damped natural frequencies the Fast Fourier Transform is used to transform the data from time domain to frequency domain, see Fig. 2.

The resonance testing was performed in three different excitation directions for each temperature in order to extract as many modes of vibration as possible. A temperature chamber and a dummy specimen were used to temperate and to control the real temperature of the specimens. The specimens were tested at -10, 0, 10, 20, 25 and 30 ºC.

To solve the inverse problem and calculate the elastic parameters, the measured natural frequencies are compared with the calculated natural frequencies through an

Fig. 1 The test set-up for resonant frequency measurements
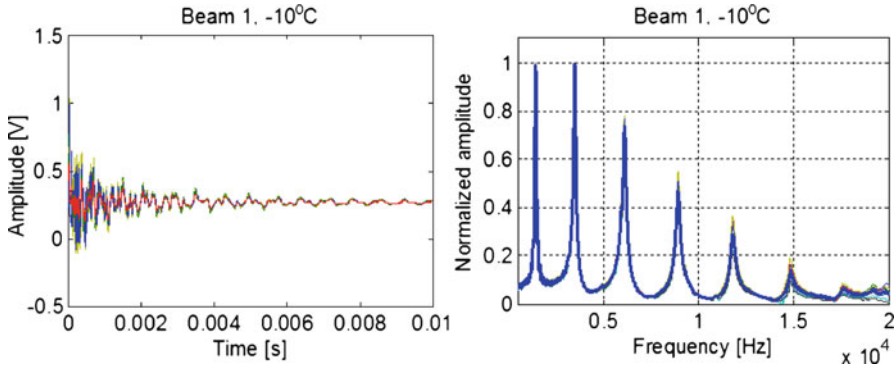
Fig. 2 Data in time domain (left) and frequency domain (right)

iterative process. The measured damped natural frequencies, f_d must therefore be converted to natural frequencies, f_n according to Eqn. (6).

$$f_n = \frac{f_d}{\sqrt{1-\zeta^2}} \tag{6}$$

The half-power bandwidth method, Eqn. (7) is used to determine the damping ratio, ζ where Δf is the width of the frequency response curve at 0,707 of the maximum amplitude.

$$\zeta = \frac{\Delta f}{2 f_d} \tag{7}$$

It should be noted that the half-power bandwidth method is applicable as long as the damping ratio does not exceed approximately 0.5 [2]. In order to obtain the elastic modulus (E) information of the Poisson's ratio (v) is needed. At this point the general form of the equation used in the Design Guide [7], Eqn. (8) has been used here as a first approximation, but with slightly modified constants.

$$v = 0.15 + \frac{0.35}{1 + e^{(-19.0 + 2.95 \times \log(E))}} \tag{8}$$

Eqn. (9) is used to determine the dynamic modulus and account for the losses that have been neglected until now.

$$|E^*| = \frac{E'}{\cos(\phi)} \tag{9}$$

Where E' is the storage modulus and ϕ is the phase angle calculated according to Eqn. (10).

$$\phi = \arctan(2\zeta) \tag{10}$$

Results

The asphalt mixture used for these tests consists of granite aggregates and unmodified binder with the penetration grade 70/100. The asphalt mixture has the gradation according to Table 1.

The mixture was compacted in a laboratory with a roller into a slab, from which three beams were sawn out. Table 2 presents the properties of each beam. It should be noted that the measured geometry is equally important as the measured resonance frequencies in RAS.

Figure 3 shows the evaluated dynamic modulus for Beam 1 from the flexural and the longitudinal modes of vibration using both RAS and ASTM E 1876-99. For each mode of vibration the temperature increases downwards according to the steps in the figure. Results show that the methods match precisely for the fundamental flexural mode of vibration. However, this is not the case for the fundamental longitudinal

Table 1 Gradation of the mix

Sieve size [mm]	0.063	0.125	0.25	0.5	1	2	4	5.6	8	11.2	16	22.4
% passing	8.9	12	16	21	28	39	50	58	70	81	98	100

Table 2 Specimen data

	Beam 1	Beam 2	Beam 3
Width [mm]	58.87	58.94	58.88
Height [mm]	58.74	58.74	58.65
Length [mm]	382.0	382.0	382.0
Mass [g]	3133	3120	3126
Density [g/cm³]	2.372	2.359	2.370
Air voids [%]	2.2	2.7	2.3
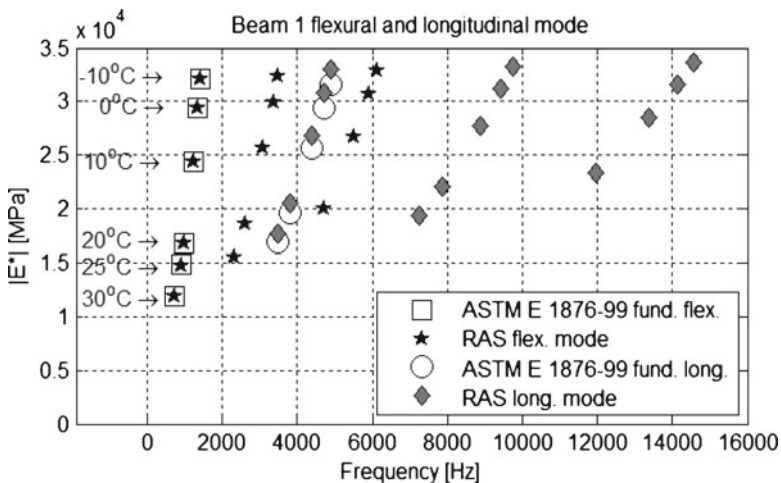
Fig. 3 The dynamic modulus for Beam 1

mode of vibration. At this point six resonance frequencies for each temperature have been successfully evaluated using RAS. Increased damping at higher temperatures has limited the number of available resonance frequencies at 25°C and 30°C. Another limiting factor for usable modes is that the mode identification becomes more difficult for higher frequencies.

Conclusions

A comparison between RAS and ASTM E 1876-99 methods indicates that the approximate formulation for the longitudinal modes of vibration in the standard test method does not provide precise results (see Fig. 3) for the geometry used in this research. For the future comparison with other standard test methods for the dynamic modulus, RAS can be used for increased accuracy and extended frequency range.

Even though six resonance frequencies have been evaluated, the data from the different temperatures have no overlap in the dynamic modulus. This means that the time-temperature superposition principle (TTSP) is not applicable to this data. The shift factors needed to determine a single mastercurve can therefore not be obtained from this data only. A solution to this is to do measurements at narrower temperature intervals to obtain the overlap. Another solution could be using the binder shift factors since previous research have shown a good agreement between binder shift factors and mix shift factors [8]. However, RAS has been successfully applied to asphalt concrete beams and it provides a promising tool for future determination of the asphalt concrete mastercurve.

References

[1] ASTM E 1876-99, Standard test method for dynamic Young's modulus, shear modulus, and Poisson's ratio by impulse excitation of vibration, American Society for Testing and Materials (ASTM).
[2] Whitmoyer, S.L., Kim, Y.R. (1994), *Journal of Testing and Evaluation*, vol. 22, n. 2, p. 139–148.
[3] Di Benedetto, H., Sauzéat, C., Sohm, J., (2009), *Road Materials and Pavement Design*, vol. 10, n. 4, p. 789–814.
[4] Ryden, N., (2009), *Determining the asphalt mastercurve from free-free resonant testing on cylindrical samples*, Proc. of the 7th Int. Symp. on Non-Destructive Testing in Civil Engineering (NDTCE'09), Ed by A. Odile and D. Xavier, June 30th – July 3rd 2009, Nantes, France.
[5] Hochuli, A.S., Sayir, M.B., Poulikakos, L.D., Partl, M.N. (2001), *Journal of the Association of Asphalt Paving Technology*, vol. 70, p. 646–674.
[6] Migliori, A., Sarrao, J.L. (1997), *Resonant Ultrasound Spectroscopy*, Wiley-Interscience Publication, New York, ISBN 0-471-12360-9.
[7] Guide for Mechanistic-Empirical Design, NCHRP, March 2004.
[8] Di Benedetto, H., Des Croix, P. (1996), *Binder-mix rheology: limits of linear domain, non linear behavior*, Eurasphalt & Eurobitume Congress, E&E.5.107, 7-10 May 1996, Strasbourg.

Assessment of Fire Damaged Concrete via the Hammer-Drill Pulse Transmission Technique

R. Felicetti

Abstract The point-by-point measurement of the resistance to hammer-drilling is a viable way to scan the steep gradients of residual mechanical properties exhibited by fire damaged concrete members. Despite the interesting pros of this technique (rapidity and immediate availability of the results), previous studies pointed out its insensitivity to low levels of damage and the significant variation that can be attributed to the coarse aggregate. In order to overcome these limitations, a renewed version has been developed, based on the continuous monitoring of two further phenomena during the drilling operation. The first observation is through acquisition of the compressive pulses generated by the hammering mechanism of the drill, which propagate along the bit shank and are partly reflected in the form of tensile stress waves. The amplitude of the reflected waves provides some meaningful information on the local acoustic impedance of the drilled material. The second observation involves measurement of the time of flight of the pulses propagating from the tip of the drill-bit to a fixed ultrasonic receiver on the surface of the member. This translates into an acoustic scan of the concrete volume enabled by the drilling process. Besides the technical challenges associated with the monitoring of these two phenomena, the paper discusses their sensitivity to fire damage and the ability to detect steep gradients in the residual material properties.

Keywords Damage • Drilling • Fire • Hardness • Waves

R. Felicetti (✉)
Dept. of Structural Engineering, Politecnico di Milano, Milano, Italy
e-mail: roberto.felicetti@polimi.it
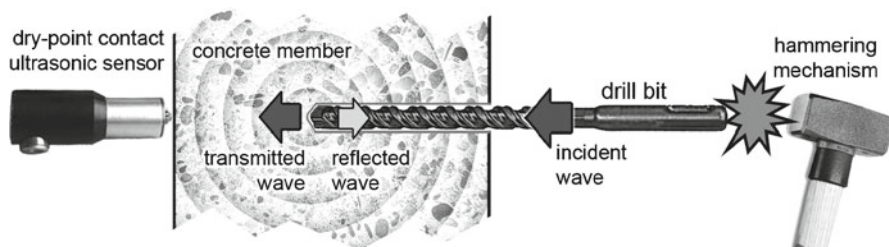
Fig. 1 Working principle of the Hammer-Drill Pulse Transmission method

Introduction

The assessment of concrete structures surviving fire is a complex problem involving different branches of expertise and distinct scales of observation, from the whole fire scenario to the local condition of the material at a point [1]. Focusing the attention on this latter aspect, the steep thermal gradients that develop as a consequence of the low thermal diffusivity lead to a strongly layered concrete cover. This applies to the residual mechanical response (compressive and tensile strength, Young's modulus, hardness) but also to a number of chemo-physical properties that are markedly affected by the exposure to high temperature (velocity and attenuation of elastic waves, density of micro-cracks, porosity, humidity, chemical composition, colour, etc.). Although this is of considerable help in ND evaluation of the material condition, not many techniques turn out to be viable in the harsh post-fire environment and precise enough to detect the damage profile at increasing depth within the cover.

In this context, the hammer-drilling resistance technique [2] stands out for its fast and easy implementation, for the immediate availability of results and for not being influenced by possible cracks or surface roughness due to spalling. So far, the most intuitive drilling resistance indicators have been considered, namely the time and work spent for a unit advance of the bit. Unfortunately, they proved to be not very responsive to fire damage, since a decrease is exhibited just for a decay of compressive strength exceeding 50% (see Fig. 5a). Moreover, the local disturbances due to the hard aggregate pebbles require to average some tests to recognize a clear trend in the material response.

To overcome these limitations, a new version of the hammer-drilling technique has been developed, taking inspiration from the Seismic While Drilling methods that are commonly used in geophysical surveys [3]. In rotary-percussive drill rigs with down-hole hammer the bit induced vibrations in both the drill string and the surrounding ground are analysed so as to reveal the layered structure of soils. In the proposed method, the propagation along the bit shank of the strong pulses generated by the drill hammering mechanism is monitored in real time. At the bit tip these are partly transmitted to the drilled member and partly reflected in the form of tensile stress waves (Fig. 1). The transmitted share of the pulses can be regarded as a measure of the local acoustic impedance of concrete and then of its soundness [4]. Moreover, the time of flight from the moving tip of the bit to an ultrasonic receiver

positioned on the surface of the structural element allows to work out a profile of the pulse velocity in the inspected volume.

The technical issues connected to the implementation of these two principles and their potential in the assessment of fire damaged concrete are discussed in the following sections.

Experimental Setup

In a former study [2] a battery hammer-drill (Hilti TE 6-A) was instrumented in order to continuously monitor the time and work per unit depth taken by the drilling operation. In this tool the electro-pneumatic hammering mechanism is based on the "flying piston", namely an unrestrained striker contained in a cylinder activated by a crankshaft (Fig. 2a). These latter exert a quick succession of vacuum and pressure on the striker on its rebounds against the rammer-bit line, leading to resonance and then considerably boosting the impact energy (~1.5 J, 80 impacts/s).

In the renewed version of this drill the strain waves propagating along the bit shank are sensed by a couple of dual-grid strain gauges arranged in a full-bridge configuration (Fig. 2b) and connected to a slip ring (Fig. 2c). This scheme strongly reduces the thermal drift due to bit heating and is little influenced by possible electrical resistance fluctuations along the signal transmission lines. The setup is completed by a wide band amplifier (Dewetron DAQP-Bridge-B, bandwidth 200 kHz) and an USB digitizer (Picoscope 3224, 2 channels, 12 bit, 5 Msample/s). The arrival of transmitted pulses at the drilled member surface is detected by a dry point contact ultrasonic transducer directly connected to the second channel of the digitizer (Acoustic Control Systems L1803, central frequency 100 kHz).

Data acquisition is performed by running two parallel tasks on a specific LabVIEW™ application. On the one side, DC voltage and current supplied by the battery, hole depth and elapsed time are measured at each turn of the motor via a multi-function card (National Instruments - DAQ Card 6036E) triggered by a photodiode. This allows to work out the feed rate and the net power consumption according to the original
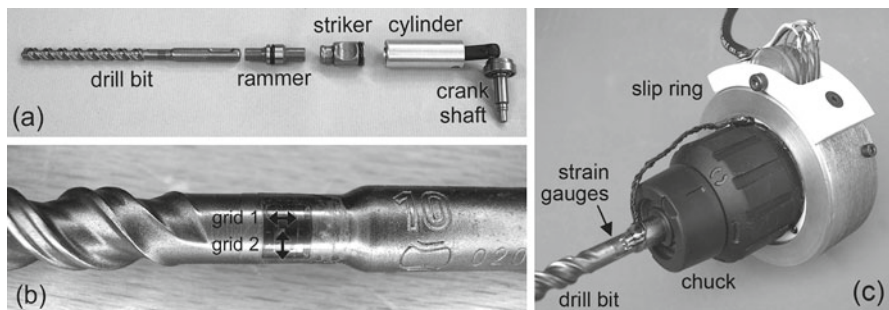
Fig. 2 (a) Components of the hammering mechanism, **(b)** dual-grid strain gauge glued on the bit shank and **(c)** modified chuck for strain signal transmission

implementation of drilling resistance technique [2]. On the other side, a data buffer from both the bit strain and the ultrasonic sensor channels is acquired at each hammer stroke (1500 samples = 300 μs). This rather intensive monitoring of the drilling process is functional to the point-by-point inspection of material response.

Calibration Tests on Uniformly Damaged Concrete

In order to ascertain the sensitivity to thermal decay of the above discussed drilling resistance indicators, a number of ordinary concrete cubes (150 mm side, average strength $f_{c,cube}$ = 52 N/mm², siliceous aggregate size = 16 mm) have been tested as they were or after being uniformly damaged by means of slow thermal cycles up to T_{max} = 200, 400, 600 and 800°C (heating rate = 0.5°C/min, 1 hour spell at T_{max}, cooling rate = 0.2°C/min, 5 cubes for each temperature). After 10 month rest in laboratory, the ultrasonic pulse velocity was measured on all samples and 3 cubes from each group were tested in compression. The remaining cubes were just clamped in the compression machine (restraining pressure ~ 7 N/mm²) and the surface hardness was measured using a type N rebound hammer. Then, the drilling resistance tests were performed taking advantage of the same restraint system (bit diameter = 10 mm, 9 holes on a 35 mm grid for each cube, Fig. 3a).

As concerns the strain waves propagating along the bit shank, the remarkable mismatch between the elastic properties of steel and thermally damaged concrete (namely their acoustic impedance) translates into a sizeable reflection of the incident wave at the bit tip (Fig. 3b). Hence, an indicator of the residual material integrity can be associated to the transmitted share of the pulse and defined as $(A_i - A_r)/A_i$, where A_i and A_r are the areas enveloped by the time plots of the incident and the
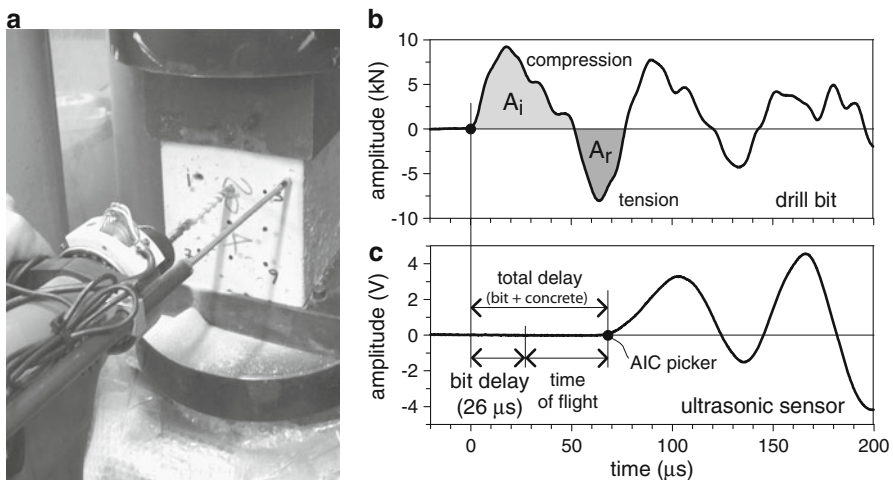
Fig. 3 a) Drilling test on a restrained concrete cube and typical waves received from **b)** the instrumented drill bit and **c)** the ultrasonic sensor
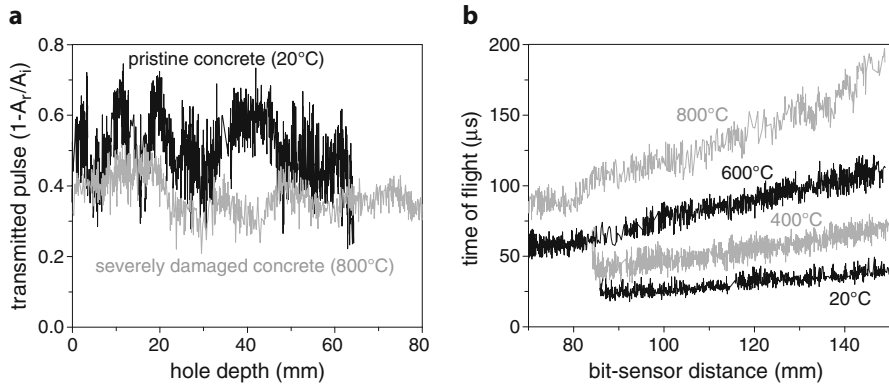
Fig. 4 a) Transmitted share and **b)** time of flight of pulses in uniformly damaged concrete cubes
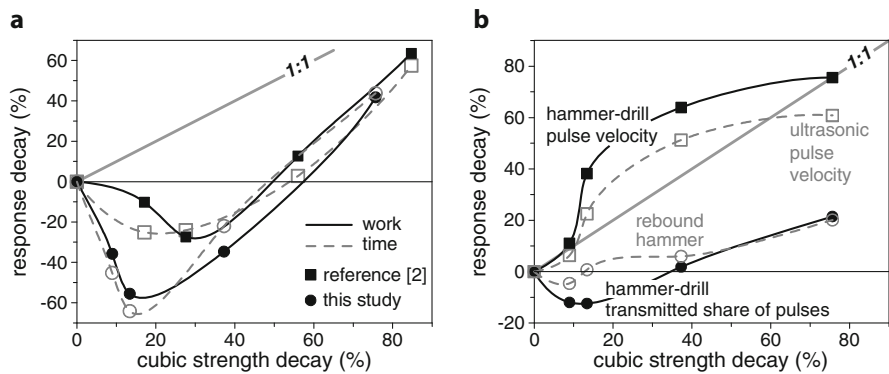
Fig. 5 Sensitivity to thermal damage of the drilling resistance indicators: **a)** time and work per unit depth; **b)** share and velocity of the transmitted pulses

reflected waves. In principle, the device can be regarded as a scanning rebound hammer, which repeatedly senses the local hardness of concrete at increasing depth. Unfortunately, as in the original Schmidt hammer, the sensitivity to thermal damage is rather poor (Fig. 5b), also in consideration of the dispersion of the results (coefficient of variation ~ 0.15) and the local influence of the coarse aggregate (Fig. 4a).

Far more promising results have been obtained from the pulse time of flight to the ultrasonic sensor. Due to the relatively slow rise of the received signal (20-60 μs to reach the first peak) a precise detection of the pulse onset was performed via an automatic time picking algorithm based on the Maeda's formulation of the Akaike Information Criterion (AIC in Fig. 3c [5]). The plots of time versus bit tip to sensor distance show a substantially linear trend (Fig. 4b), whose slope is the reciprocal of pulse velocity in the drilled material. This latter parameter proved to be very sensitive to thermal damage and in good agreement with the traditional ultrasonic

pulse velocity (Fig. 5b). The fairly low dispersion (standard deviation = 3-8 μs) with no influence of the coarse aggregate are other valuable features of the method.

The parallel acquisition of the drilling time and work confirmed their inadequacy in detecting a decay of compressive strength below 50% (Fig. 5a). The observed magnitude of the pulses (~10 kN, Fig. 3b) corroborates the negligible influence of the thrust exerted by the operator in all the hammer-drilling techniques [2].

Static Indentation Tests

As discussed, the non-monotonic response to high temperature of the drilling resistance indicators (time, work, transmitted share of pulses) is a strong limitation of this method in case of low levels of damage. In order to deepen this aspect, a series of static indentation tests was carried out on the same uniformly damaged concrete cubes intended for the calibration tests. At each temperature, the test were performed by drilling one blind hole in 4 steps, after which the hole was cleaned and a bit was inserted and loaded in three subsequent cycles (Figs. 6b). The total measured displacement was then corrected in order to account for the bit deformability (Fig. 6a). The results (Fig. 7) show the sizeable gain of stiffness exhibited by concrete exposed to 200°C, despite a 9% reduction of the residual compressive was observed. Like the other indicators (Fig. 5) a further heating up to about 500°C (strength reduction = 25%) is required to return to the original values.

Detection of Thermal Damage Gradients

To validate the proposed drilling technique in case of strongly layered materials, as is the case of fire damaged concrete, a couple of concrete panels (340 x 590 x 135 mm) were cast from the same batch as the cubes for the calibration tests. The specimens were fitted with three embedded thermocouples (two subsurface and one at mid-thick-
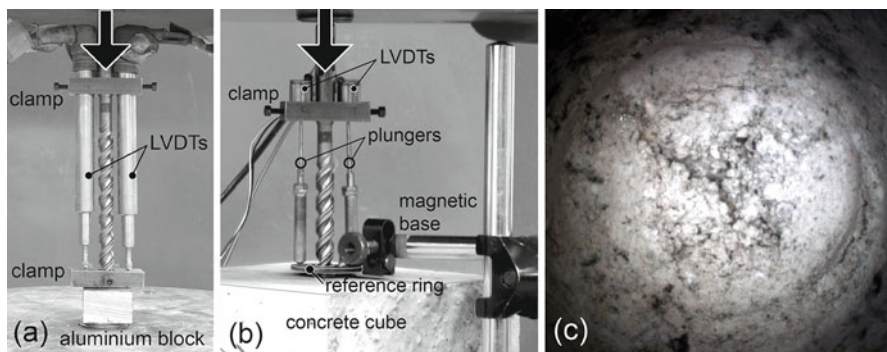
Fig. 6 Experimental setups for **a**) determining the bit stiffness and **b**) performing the indentation tests; **c**) endoscopic image of the indenter imprint
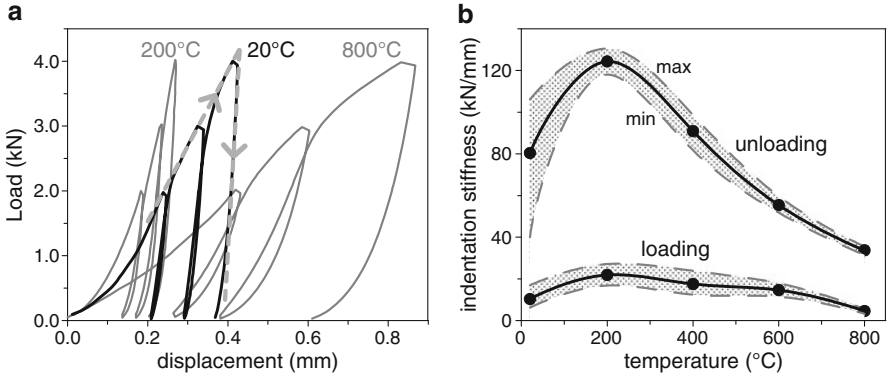
Fig. 7 a) Load-displacement curves and **b)** loading-unloading stiffness of the static indentation tests on thermally damaged concrete cubes
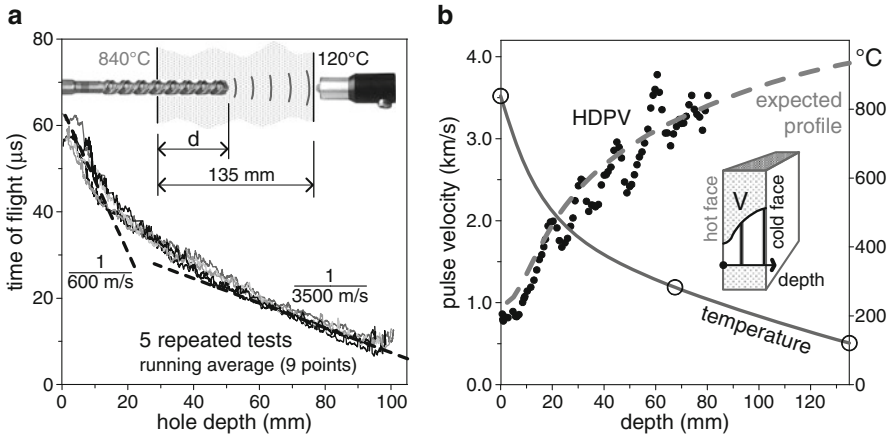
Fig. 8 a) Time of flight to the ultrasonic sensor in a thermally damaged concrete panel and **b)** profile of the Hammer-Drill Pulse Velocity through its thickness

ness) to monitor their temperature during thermal exposure. The panels were subjected to a steep gradient (up to 20°C/mm) by installing them in replacement of the door of a preheated electric furnace (T_{furn} = 880°C). The profile of the maximum experienced temperature through the thickness has been determined by modelling the thermal transient with a finite difference code so to match the experimental measurements (Fig. 8b). Based on the temperature at each point and on the calibration tests on uniformly heated cubes (residual response vs. temperature, see Fig. 5b), the expected profile of the Hammer-Drill Pulse Velocity has been also worked out for reference.

The drilling tests have been performed by clamping the panels in a stiff 5000 kN press at the same restraining pressure as before. In accordance with the indication provided by the calibration tests, the transmitted share of the hammer-drill pulses hardly gave any evidence of the damage undergone by the panels. On the contrary, meaningful information were obtained from the time of flight to the ultrasonic receiver

(Fig. 8a). The smooth transition from the initial steep reduction of arrival time in heavily damaged concrete to the final asymptotic slope in pristine concrete highlights the sensitivity and thoroughness of this method. Also the repeatability of the results is to be remarked. By differentiating these plots a profile of the residual Hammer-Drill Pulse Velocity through the thickness of the panels can be worked out (Fig. 8b). The good agreement with the expected profile confirms the reliability of this approach.

Concluding Remarks

The hammer-drilling resistance technique, albeit a fast and viable method for the assessment of fire damaged concrete structures, has the limitations of being insensitive to moderate deterioration and strongly influenced by the inherent material heterogeneity. In order to overcome these limitations, a renewed version of the method has been developed, based on the transmission of the strong pulses generated by the hammering mechanism of the drill. The main conclusions that can drawn from the results of this research programme are listed in the following.

The intensity of the transmitted pulses has a lot in common with the traditional rebound index, with the plus of being able to scan the material hardness at increasing depth. Unfortunately, the poor sensitivity to thermal damage, the sizeable influence of hard aggregate pebbles and the dispersion of the results make this parameter unsuited to the problem at issue.

On the contrary, the velocity of the transmitted pulses proved to be a repeatable and sensitive indicator of the residual condition of fire damaged concrete. Due to the relatively low frequency of the excited waves (~ 15 kHz), the method is not influenced by coarse aggregate and may be applied also to strongly damaged and rather thick members. Nonetheless, the intensive monitoring of the drilling process (10-20 pulses/mm) allows to work out a detailed profile of the velocity in the concrete cover.

Further studies are in progress, aimed at the interpretation of results in case of indirect transmission (drill and sensor on the same side), that is a relevant issue in case of single-sided access to the inspected member (e.g. walls, slabs and tunnels).

References

[1] Felicetti, R. (2007), In: *Fire Design of Concrete Structures*, Proc. Fib TG 4.3 Workshop, pp. 483–487, Rodriguez, J.P., Khoury, G.A. and Hoj N.P. (Eds).
[2] Felicetti, R. (2006), *J. Cem. Concrete. Compos.*, vol. 28, p. 321–329.
[3] Poletto F. and Miranda F. (2004), *Seismic while drilling: fundamentals of drill-bit seismic for exploration*, Elsevier, Amsterdam.
[4] Li, X., Lok, T.S., Summers, D.A., Rupert, G. and Tyler, J. (2001), *Geotech. Geol. Eng.* vol. 19, p. 119–136.
[5] Kurz, J.H., Grosse, C.U. and Reinhardt, H.-W. (2005), *Ultrasonic.*, vol. 43, p. 538–546.

Assessment of the Residual Strength of Fire-Damaged Steel-Rebars

R. Felicetti and P.G. Gambarova

Abstract Concrete structures are known to exhibit a good behaviour in fire, thanks to the low thermal diffusivity of the material, which provides an effective protection to steel reinforcement. Moreover, a significant strength recovery occurs when the bars cool down to room temperature, though this markedly depends on their metallurgical properties. Since the surviving structure is still required to bear the noticeably-higher loads assigned by the ultimate limit state, the post-fire strength of the reinforcement has to be carefully weighed up. To this purpose, two different Non-Destructive Techniques are investigated in this study. The first one is the Dynamic Hardness Test (also known as Leeb Test), which is quite sensitive to steel decay. The test can be performed onsite by means of a small specifically-designed device, provided that the surface of the bar has been smoothed prior to testing. The second technique is based on the continuous monitoring of the drilling resistance via a special setup, which allows to measure the thrust to be exerted on the bit in order to keep a constant feed rate. This latter method requires no sample preparation, but the correlation with steel decay is rather uncertain, due to the conflicting effects of the decreasing yield strength and the increasing hardening and strain capacity of fire damaged steel. The pros and cons of these two methods are discussed in the paper, in view of their practical implementation for assessing the post-fire safety of actual structures.

Keywords Damage • Drilling • Fire • Hardness • Rebars • Steel

R. Felicetti (✉) • P.G. Gambarova
Dept. of Structural Engineering, Politecnico di Milano, Milano, Italy
e-mail: roberto.felicetti@polimi.it

Introduction

Concrete structures have good chances to survive a fire, thanks to the low thermal diffusivity of the material, to the redundancy of their scheme and to the reduced level of variable loads which are likely to concur in such an exceptional event. Although the damage undergone by concrete cover is mostly irreversible and some repair measures are often needed to restore the required durability, steel rebars are expected to recover an sizeable share of their original strength when cooled down to room temperature. This recovery is critical, as the reinforcement is still required to bear the noticeably higher loads associated with the ultimate limit state. Being generally the weakest link in cross-sections designed for flexural ductility, the assessment of the residual mechanical properties of steel rebars is an important and - to authors' opinion - not adequately addressed issue in Civil Engineering.

The original strength of metals and their sensitivity to the heating/cooling cycle caused by a fire markedly depend on microstructure [1], and then on a) average size of iso-oriented crystalline regions (grains); b) number of defects at the atomic scale (dislocations); c) presence of any embedded alloying elements and d) production process (e.g. hot-rolled vs. cold-worked steel). In a recent study by the authors [2], Quenched and Self-Tempered bars (QST bars) were shown to be more sensitive to temperatures above 550°C than the "old" carbon-steel bars. On the other hand, stainless-steel exhibited a very good behaviour when the bars are hot-rolled, but the opposite was found in case of cold-worked bars.

In consideration of this wide assortment of possible material types, exposed to the highly variable heating conditions associated with real fire scenarios, fast and responsive assessment methods are needed, possibly not requiring a prior knowledge of the metallurgical properties of the examined rebars. To this purpose, two different techniques have been investigated in this study: the measurement of the dynamic hardness via a portable tester and the monitoring of the drilling resistance via an instrumented drill. The implementation and the sensitivity of these two methods are discussed in the following sections.

Steel Types and Experimental Programme

In the present study, both off-the-shelf and old high-bond bars were considered. In more details, the following reinforcement types have been investigated (Table 1):

Quenched and Self-Tempered bars (QST - Ø = 10 and 16 mm). It is presently the most extensively used reinforcing steel in Europe. The bar surface is quenched with water sprays as it exits the rolling mill, leading to a hard, tempered martensitic outer layer, and a soft, more ductile ferrite-pearlite core. In this way the average yield strength is increased while the carbon content can be kept at a rather low level, to the advantage of ductility and weldability.

Table 1 Reference strength values and ND parameters for unheated rebars

rebar type	QST 10	QST 16	MA 10	SS 12	CS 12/20
yield strength f_y (MPa)	524	529	453	701	463
Tensile strength f_t (MPa)	642	624	614	812	710
Leeb number	477	481	474	562	476
drilling thrust (N)	46.1	-	33.4	61.9	40.3
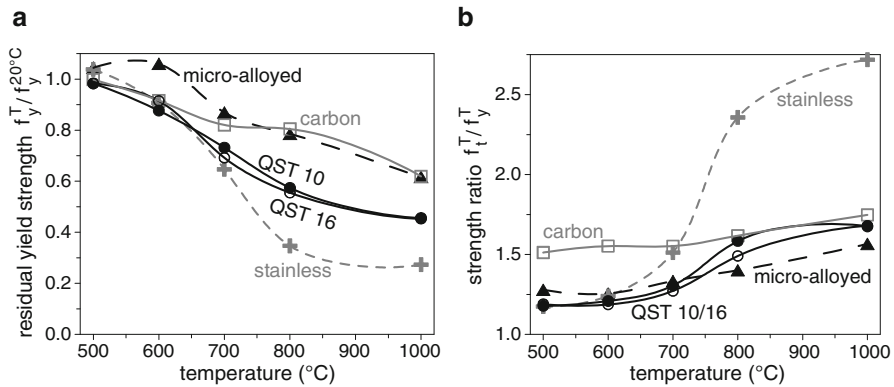
Fig. 1 Yield-strength decay and hardening growth of the investigated steels

Micro-Alloyed bars (MA - Ø = 10 mm). The mechanical properties are enhanced by incorporating alloying elements like Niobium and Vanadium in the molten metal, at increased cost but with the advantage of a homogeneous bar cross-section in terms of microstructure, strength and ductility.

Cold-worked Stainless-Steel bars (austenitic AISI 304L steel - SS - Ø = 12 mm). Corrosion resistance is achieved with chrome content exceeding 10.5% and carbon content lower than 0.07% (EN 10088-1). In spite of the higher material cost (from 4 to 8 times as much as ordinary rebars), the use of stainless steel is strategic for improving the durability of bridges, viaducts and marine structures.

Square-section, Carbon-Steel bars (CS - side = 12 and 20 mm). Currently produced in Italy in 1950-70, these bars exhibit a higher strength [2], but are more fire sensitive than old smooth hot-rolled carbon-steel bars.

All types of bars were cut in 0.6 m samples, to be tested in tension, and 0.2 m pieces for the implementation of ND techniques. The samples were heated at 3°C/min up to T_{max} = 500, 600, 700, 800 and 1000°C. The target temperature was maintained for one hour and then the samples were cooled at the same rate.

As concerns the tensile properties, two repeated tests were performed for each case, with almost identical results. All samples were unaffected by exposure up to 500°C (Fig. 1). Beyond this threshold, different decays occurred depending on the steel type, with carbon and micro-alloyed rebars exhibiting the best endurance and cold-drawn stainless-steel rebars confirming their remarkable sensitivity to high

temperature [2]. The above trends are made evident by the reduction of the residual yield strength (Fig. 1a), whereas a smoother response characterizes the tensile strength. This translates into an increasing hardening ratio f_t/f_y (Fig. 1b), which partly offsets the overall weakening of the material. It has to be remarked that at any temperature all carbon steels showed a well defined yielding point, followed by a plateau up to about 1% strain. On the contrary, stainless-steel required the introduction of a conventional proof strength (0.2% non-proportional extension).

Dynamic Hardness Tests

Hardness testing is a recognized indirect way to assess the quality of metals (tensile strength, wear resistance, ductility, etc). The principle is to indent the material surface by gradually applying an assigned force to a hard indenter (sphere, cone or pyramid) and then to measure the size or depth of the ensuing imprint. Unfortunately, the classic static methods (Brinell, Rockwell, Vickers) are generally not suited for onsite application, since they require an accurate sample preparation (roughness < 0.1-0.3 μm) and they are implemented on bench-mounted testers fitted with a precise optical measuring system.

An interesting alternative is provided by the dynamic hardness test (Leeb method), where a body fitted with a hard spherical tip (Ø = 3 mm) impacts the test surface under a spring force [3]. The impact and rebound velocities are measured at approximately 1 mm from the test surface, through the electric potential induced in a coil by a permanent magnet mounted inside the impact body (Fig. 2a). The ratio of these velocities, multiplied by a factor 1000, is defined as the Leeb hardness number. As there is no need to apply any external thrust nor to measure any imprint, the Leeb method allows to develop compact handheld devices that can be easily positioned on the tested rebar (Fig. 2b). The method still requires a smooth surface, though with less stringent limits (average roughness < 2 μm). Moreover, the sample should be firmly restrained, so to prevent any vibration during the impact, which
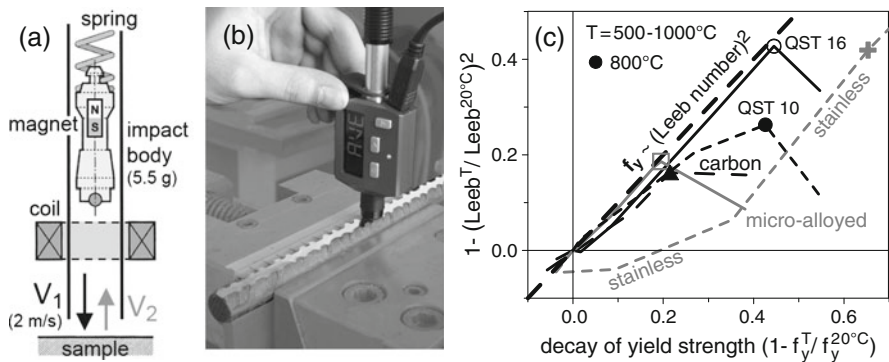
Fig. 2 **a)** Scheme of the Leeb hardness tester, **b)** handheld device (type D) and **c)** relation between the residual yield strength and the Leeb number squared

may reduce the apparent hardness of the tested material. This may be not the case of small rebars embedded in a severely damaged concrete cover.

In order to ascertain the sensitivity of this method to the strength loss exhibited by heated steels, 0.2 m rebar pieces of the types listed in Table 1 were clamped in a heavy machine vice. The top side of each sample was milled and then polished with sandpaper. About 30 tests were performed on two samples for each steel-temperature combination, with fairly repeatable results (coeff. of var. < 5%).

As regards the interpretation of the results, several studies are available in the literature, presenting either empirical, numerical or closed-form correlations with the yield strength. Among them, the linear relationship with the rebound kinetic energy (namely Leeb number squared) proposed by Stilwell and Tabor for the conical indenter (see [4]) is in good agreement with the experimental results concerning carbon steels exposed up to 800°C (Fig. 2c). At higher temperatures an increasing hardness and larger dispersion are observed, probably because of grain coarsening in the crystalline microstructure. A totally different behaviour characterizes cold-drawn stainless-steel, due to lack of a true yield point and to the remarkable strain hardening exhibited by damaged rebars (see Fig. 1b).

Drilling Resistance Tests

The continuous monitoring of drilling resistance is a promising technique for the condition assessment of construction materials, like timber, mortar, concrete and stones [5]. As for metals, the principle is to cut shavings of assigned thickness by imposing fixed rotational and feed rates, while measuring the thrust to be applied to the work-piece. This latter parameter exhibited a good correlation with the
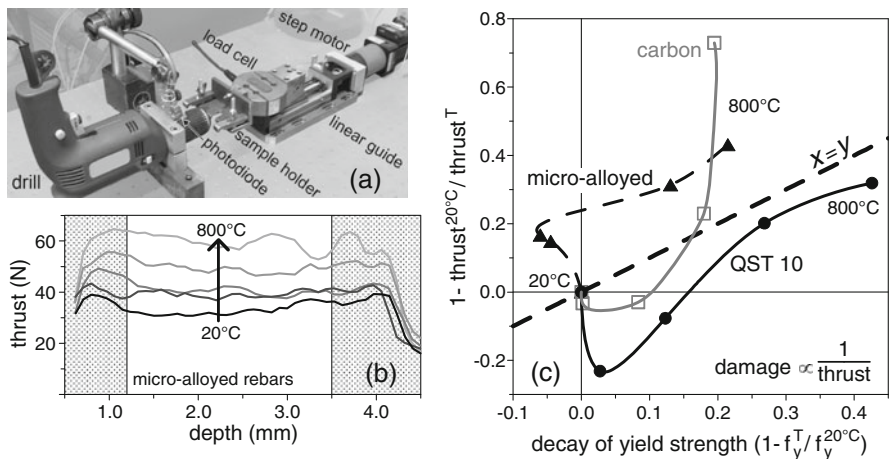
Fig. 3 a) Drilling resistance test setup, b) plots of the exerted thrust at increasing thermal damage and c) relation with the residual yield strength

Vickers hardness in the range 200-900 HV and was successfully applied to check the treatment thickness in superficially hardened steel [6].

According to the cited reference, a special setup was arranged, based on a ordinary pistol-grip drill fixed to a bench (Fig. 3a). The advance of the sample was driven by a step motor fitted with a linear guide and a load cell (0.01 mm/rev, hole depth ~ 4 mm). The tools were Titanium Carbo-Nitride coated bits (Ø = 2 mm), which proved to give repeatable results for more than 50 holes in unheated QST rebars.

Surprisingly, thermally damaged steels proved to be more difficult to drill (Fig. 3b), probably because of the increased strain capacity and the pronounced hardening behaviour. This makes the material harder to cut, to the point that drilling was not possible for carbon steels exposed to 1000°C and cold-formed stainless-steel subjected to temperatures above 500°C. Although the exerted thrust proved to be markedly affected by damage, no clear relation with the yield strength could be recognized (Fig. 3c).

Concluding Remarks

In this study two assessment methods for fire damage in steel rebars were investigated, namely the dynamic hardness and the drilling resistance tests. The main conclusions can be summarized as follows. The dynamic hardness proved to be a viable and sensitive inspection technique for the problem at issue. An easy and general relation with yield strength was found for carbon steels up to 800°C, that is the usual range for practical applications. The requirements of a smooth surface and an effective restraint of the tested rebar are the main limitations to consider in the implementation of the method. These restrictions do not apply to the drilling resistance technique, though a special tester should be developed for onsite applications. On the other hand, no simple correlation with the residual mechanical properties was found. The above results cannot be extended to cold-drawn stainless-steel, though their noticeable sensitivity to fire should be carefully weighed in the assessment of residual structural safety.

References

[1] Avner, S.H. (1974), *Introduction to Physical Metallurgy*, McGraw–Hill, New York.
[2] Felicetti, R., Gambarova, P.G. and Meda, A. (2009), *Constr. Build. Mater.*, vol. 23, n. 12, p 3546.
[3] ASTM 956 (2006), "Standard Test Method for Leeb Hardness Testing of Steel Products", ASTM Int, Philadelphia.
[4] Kohlhöfer, W. and Penny, R.K. (1995), *Int. J. Ves. Piping*, vol. 61, p. 65.
[5] Felicetti, R. (2006), *J. Cem. Concrete. Compos.*, vol. 28, p. 321.
[6] Mauvoisin, G. and Chagneau, F. (1999), *Measurement.*, vol. 25, p. 291.

Damage Assessment by Ultrasonic Images in Concrete Subjected to Freeze-Thaw Cycles

M. Molero, G. Al-Assadi, S. Aparicio, M.J. Casati and M.G. Hernández

Abstract This paper reports on damage evaluation of concrete subjected to freeze-thaw cycles using ultrasonic images. The use of automated ultrasonic inspection systems supplies velocity and attenuation maps, providing the spatial variations in velocity and attenuation in concrete specimens with high resolution. Assessment of damage in concrete specimens is conducted defining several parameters extracted from the ultrasonic images obtained before and after the freeze-thaw cycles. These parameters are related to surface scaling and internal cracking. Experimental trials were carried out using different concrete specimens with and without air-entraining agents. Comparisons between the parameters obtained from the ultrasonic images and the failure criterion defined by the standard ASTM C666/C666M-03 are performed. As a result, this work shows the feasibility of using ultrasonic images as an effective tool for evaluating freeze-thaw damage in concrete.

Keywords Concrete • Damage • Freeze-thaw cycles • Ultrasonic imaging

M. Molero
Dept of Physics, Faculty of Science, UNAM, Mexico D.F, Mexico

CAEND (CSIC-UPM), Arganda del Rey, Spain

G. Al-Assadi
Dept of Civil Engineering, Construction, ETSICCP-UPM, Spain

S. Aparicio • M.G. Hernández (✉)
CAEND (CSIC-UPM), Arganda del Rey, Spain
e-mail: margarita.gonzalez@caend.upm-csic.es

M.J. Casati
Dept of Aerospace Vehicles, EUITA-UPM, Spain

Introduction

Freeze-thaw (F-T) damage is one of the major problems of concrete in cold climates. Different standards have been developed to evaluate the resistance of concrete subjected to accelerated F-T cycles, such as UNE 12390-9 [1], ASTM C666/C666M-03 [2], Rilem TC 176-IDC [3], etc. These standards differ in the testing method and in the methodology carried out for evaluating damage. Concrete resistance to F-T damage is usually evaluated and classified depending on the type of damage, external or internal. For instance, internal damage is evaluated by ultrasonic velocity measurements, whereas external damage is monitored by the loss of mass or height [1]. Therefore, it highlights the need of developing suitable non-destructive methodologies in order to study the external damage and, if possible, both types of damage at the same time. The evaluation of concrete structures and cementitious materials by acoustic imaging seems to be an attractive solution in order to detect irregularities and defects as well as the use of the attenuation and velocity measurements at each point of the material. However, the design of equipment to generate images to evaluate the quality and deterioration degree in concrete specimens is neither direct nor obvious. Moreover, several difficulties, such as the high attenuation at the test frequencies, generally 50 to 150 kHz, or the coupling method, have limited the development of these techniques. Therefore, the above-mentioned difficulties also highlight the need for developing suitable systems for acoustic imaging to evaluate damage in concrete. The aim of this paper is to use the ultrasonic imaging system developed by this research group to evaluate the deterioration in concrete subjected to F-T cycles [4]. Two groups of concrete specimens, without and with air-entraining agents, were subjected to accelerated F-T cycles. The specimens were measured before and after the cycles by ultrasonic techniques of contact and automated inspections in immersion. Velocity and attenuation images were generated using the automated inspection system developed by the authors. From these ultrasonic images, two parameters were proposed to evaluate damage in the concrete specimens: the non-assessable area proportion, NAAP, and a weighted average velocity in terms of the NAAP. In addition, these parameters were compared with the failure criterion of the ASTM, i.e., by using the Relative Dynamic Modulus Elasticity (RDME).

Specimens, Test Modalities and Instrumentation

Two groups of seven cylindrical specimens (150x300 mm^2) were made using HA-30 concrete (see Table 1), one group without air-entraining agents (HA-30/00-0…6) and one group with air-entraining agents (HA-30/05-0…6). The materials used were Portland cement type CEM I 42.5R, normal river sand (0-5mm) and crushed limestone aggregates (5-20mm). The air-entraining agent used is Aer 5 (0.05% of cement weight).

Table 1 Mix proportions of concrete

Material	Cement (kg)	w/c ratio	Sand (kg)	Aggregates (kg)	Water (l)	Superplasticizers (%)
amount/m^3	381.1	0.5	879.99	936.4	190.55	0.60

The specimens were manufactured according to the UNE 12390-2 [5]. Subsequently, the specimens were cured in a climate chamber at 30ºC and 37% relative humidity for 28 days. These curing conditions respond to the summer conditions in Madrid (Spain) [6]. The specimens were subjected to F-T cycles according to the ASTM standard [6]. The HA-30/00-0 and HA-30/05-0 specimens acting as reference were not subjected to the process of degradation.

Ultrasonic velocity measurements by the contact method

Travel time of ultrasonic waves through the specimens was measured using commercial TICO equipment with transducers of 54 kHz emitting in longitudinal mode with a semifluid as coupling material. The measurements were made on the central point of specimens, before and after the F-T cycles. Using these measurements, the standard ASTM [2] provides a failure criterion by means of the RDME calculated as: RDME= $(V_n/V_0)^2$x100, where V_n and V_0 are the longitudinal velocity at n and 0 F-T cycles respectively. When the RDME is higher than 80%, the material is frost resistant; while in the case of values higher than 60%, it has passable frost resistance. At the lower values than 60%, the material is classified as unproven frost resistant. However, when the RDME is lower than 40%, the material is simply non-resistant to frost.

Ultrasonic radial scanning system

A radial scanning system was designed for performing automated data acquisition and imaging [4]. This system involves the use of an immersion tank and two transducers (Panametrics v413, 500 kHz) in through-transmission operation. This system allows two different motions, a rotation centered on the axis of the measuring cylinder and a movement along the specimen's height, as depicted in Fig. 1. With the rotation motion, the ultrasonic waves travel through the material along approximately two truncated-cone sections centered on a specimen diameter. Each pixel of the images generated corresponds to a diameter of a given specimen's height. The complete specimen inspection takes approximately 10 minutes with a scanning grid of 5 mm in height and a 2º diameter step. The SENDAS ultrasonic system was used to generate and receive the signals.
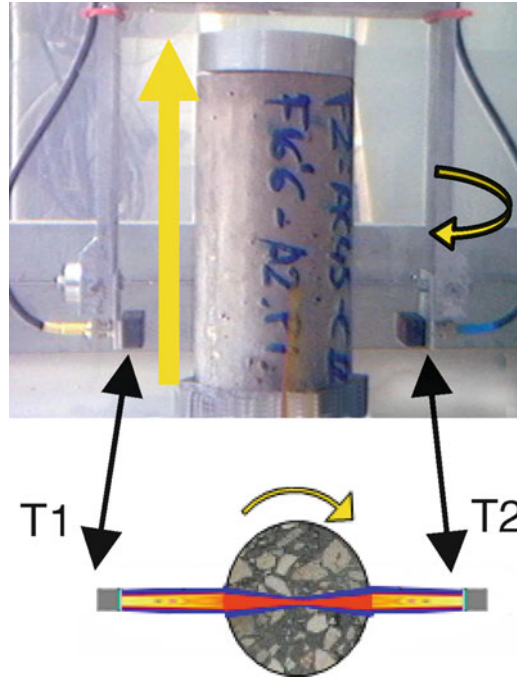
Fig. 1 Radial scanning system

Results and Discussion

The ultrasonic images before and after the F-T cycles in concrete specimens without and with air-entraining agents are shown in Figs. 2 and 3 respectively. In all images corresponding to ultrasonic inspections before the cycles, the non-uniformity of the specimens can be appreciated within the same group. From the images corresponding to the inspections after the cycles, the extension of the damaged zones can be estimated. In Fig. 2 it is observed that the attenuation significantly increases when the specimens were subjected to the F-T cycles. Therefore, there are zones where the ultrasonic waves were not able to go through, and therefore, it was not possible to measure their velocities. Moreover, in these images it can be observed that the damage was not equal in all specimens. For instance, the images corresponding to the HA-30/00-1 and HA-30/00-2 specimens showed that before the cycles they were very similar, but after the F-T cycles the damaged zones were different. It can also be seen how the damage has progressed from the parallel faces (upper and lower faces) to the center of the specimens. On the other hand, Fig. 3 shows the images of the concrete specimens with air-entraining agents. In this case, the behavior of the attenuation and the velocity is opposite to the results corresponding to the concrete specimens without air-entraining agents; the attenuation decreases
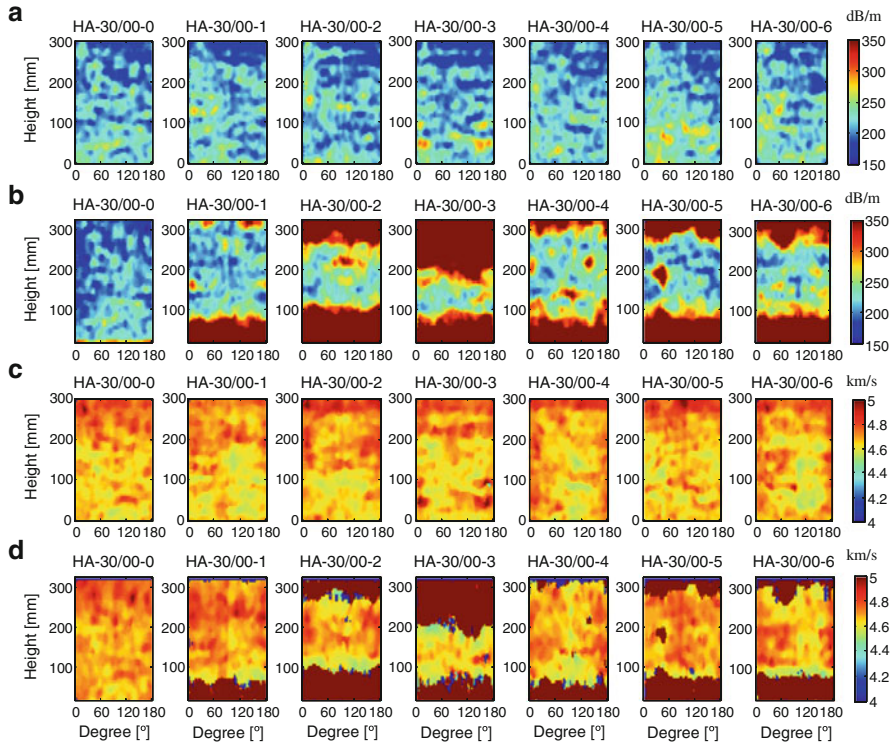
Fig. 2 Ultrasonic images for concrete specimens without air-entraining agents. Attenuation: **a)** before, **b)** after. Velocity: **c)** before and **d)** after the F-T cycle

and the velocity increases. None of the specimens was deteriorated during the cycles and it was verified the effectiveness of adding air-entraining agents to prolong the durability of the concrete.

To evaluate the deterioration degree from the ultrasonic images generated, two parameters were proposed. The first one, the Non-Assessable Area Proportion (NAAP), is defined as the area proportion where the ultrasonic signal could not travel through the specimen. The second one is a weighted average velocity in terms of the NAAP, defined as $V_{ff} = \beta \cdot V_0 \cdot NAAP + V_f \left(1 - NAAP\right)$, where β is a constant value and refers to a given failure percentage, e.g. $\beta = 0.8$. Therefore, a parameter equivalent to the RDME can be calculated, as $(V_{ff}/V_0)^2$.

Figure 4 shows a comparison between the RDME and $(V_{ff}/V_0)^2$ obtained from the automated inspections. One may observe that in either heavily-damaged or completely undamaged specimens, there were no significant differences between the results obtained with the contact measurements and the automated inspections. However, when damage is incipient (e.g. 1 and 4 specimens without air-entraining agents) the contact measurements were not able to detect or quantify it, unlike the images, which give more real and comparative information of damage produced by F-T processes.
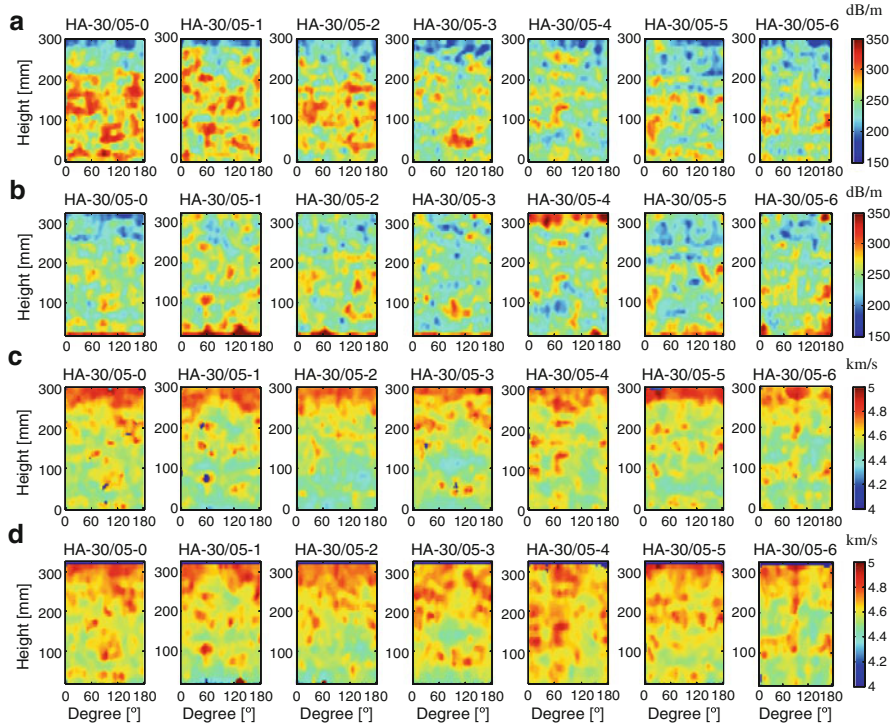
Fig. 3 Ultrasonic images for concrete specimens with air-entraining agents. Attenuation: **a)** before, **b)** after. Velocity: **c)** before and **d)** after the F-T cycle
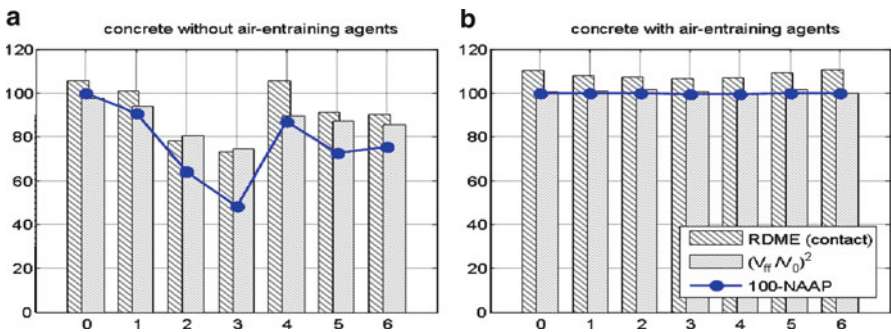
Fig. 4 Comparison between parameters extracted from contact measurements and ultrasonic images

Conclusions

The use of ultrasonic imaging as evaluation tool in concrete subjected to freeze-thawing cycles was studied. Two groups of concrete specimens, with and without air-entraining agents, were subjected to accelerated F-T cycles, and inspected before and after the cycles by using both contact and immersion ultrasonic inspections. An automated ultrasonic inspection system in immersion was used to perform precise measurements.

Velocity and attenuation images were generated with this system performing in-situ inspections. From these ultrasonic images, two parameters were proposed to evaluate the damage in the concrete specimens: the non-assessable area proportion, NAAP, and a weighted average velocity in terms of the NAAP. The results obtained in this research project suggested that NAAP is related to surface scaling as can be seen in the images, whereas the weighted average velocity is related to internal damage. Therefore, the use of the ultrasonic images provides a complete and more effective evaluation of concrete specimens. Moreover, the proposed system allows the evaluation of external and internal damage with a single automated inspection.

References

[1] UNE-CEN/TS 12390–9 (2008).
[2] ASTM C 666/C 666M – 03 (2003).
[3] Setzer M.J., Heine, P., Kasparek, S., Palecki, S., Auberg, R. Feldrappe et al. (2004), Mater. Struct. 37, pp 743–753.
[4] IMAUSHOR, Spanish Patent PCT/ES2011/070499.
[5] UNE-EN 12390–2 (2009).
[6] Al-Assadi G., Casati M.J., Fernández J., Gálvez J.C. (2008), In: Influencia de las condiciones de curado en el comportamiento del hormigón sometido a ciclos hielo-deshielo. Anales de Mecánica de la Fractura 25, pp. 629–634.

Evaluation of Temperature Influence on Ultrasound Velocity in Concrete by Coda Wave Interferometry

C. Wunderlich and E. Niederleithinger

Abstract Ultrasonic methods are valuable tools for the assessment of concrete quality and for imaging inclusions in concrete. In such applications, accurate and reliable determination of ultrasonic wave velocities as affected by various experimental and environmental factors is essential. In this research Coda Wave interferometry (CWI) was used to determine the influence of temperature (20 to 50° C) on ultrasonic wave velocity in concrete samples. A resolution of better than 10^{-2} % was achieved in the measurement of relative velocity changes. In addition the influence of sensor (transmitter and receiver) positioning errors on the results of the interferometric algorithm was evaluated. The presented results can be used to correct and refine data from monitoring systems, which may enable improved quality assessment and imaging by use of CWI.

Keywords Coda wave interferometry • Concrete • Temperature • Ultrasound • Velocity

Introduction

Ultrasonic velocity measurement is an established tool to estimate strength properties and detect damage-induced changes in materials. Temperature is known to have an influence on ultrasonic pulse velocity of solid concrete. For many applications, including the investigation of lab samples in a controlled environment, this effect seems to be negligible (e. g. in the range of 10 – 30° C according to the current DIN

C. Wunderlich (✉) • E. Niederleithinger
BAM Federal Institute for Materials Research and Testing, Division VIII.2, Berlin, Germany
e-mail: Carolin.Wunderlich@bam.de

EN 12504-4:2004 [1]. The same holds for ultrasonic echo measurements. Only if there are large temperature variations (below 0°C and in case of fire hazards) the velocity changes significantly in the type of measurements currently used (mainly time of flight). Due to water evaporation these changes are partially remanent at least if the temperature exceeds 100 °C.

Upcoming monitoring applications using ultrasonic methods do detect changes that are small by degree or spatial extension, as well as slow processes as alkali-silica reaction (ASR) require a more detailed insight into the temperature influence on velocity so to avoid misinterpretations and to correct measurements.

To detect small changes in velocity sensible evaluation methods are required. The currently used time of flight method often fails due lack of resolution in low frequency applications as well as scattering and dissipation at high frequencies [3].

The study described here had two topics: At first to evaluate the ability to measure small velocity changes induced by temperature variations and at second to check the influence of mounting and dismounting as well as misalignment of the trans-ducers on the method's result.

Coda Wave Interferometry (CWI)

In seismics the coda is defined as the long lasting wave train after a seismic event. The coda contains a notable amount of energy, but has lower amplitudes than the event itself (Fig. 1). The waves included in the coda are (at least partially) caused by multiple diffractions [4] and have travelled much longer distances than direct waves. As a result, changes in the material causing small velocity changes, which may have no visible effect on the arrival times of the direct waves (first arrivals), result in much longer time shifts in the coda (Figs. 2 and 3).

Several methods have been developed to evaluate the phase shift of coda waves and the corresponding relative velocity changes. In this research the "stretching" technique [3, 5] has been used. One of the time series is stretched (or compressed)
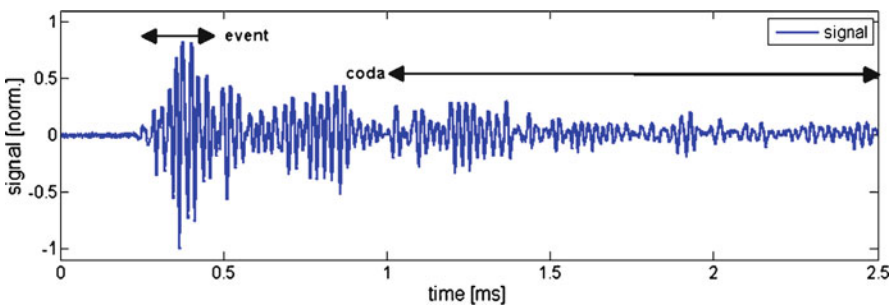
Fig. 1 Ultrasonic time series from an experiment on a concrete prism, containing event and coda
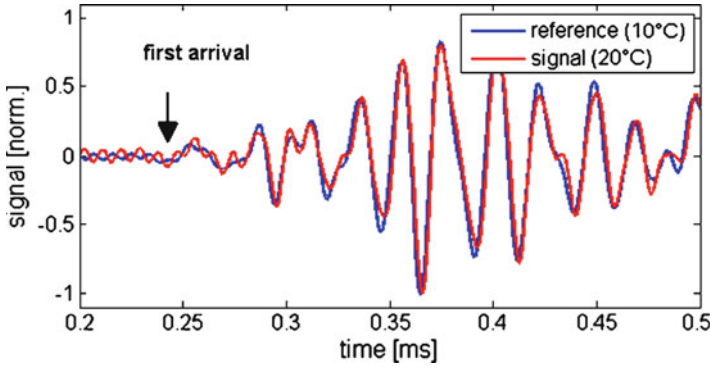
Fig. 2 Early portion of time series. No significant time shift
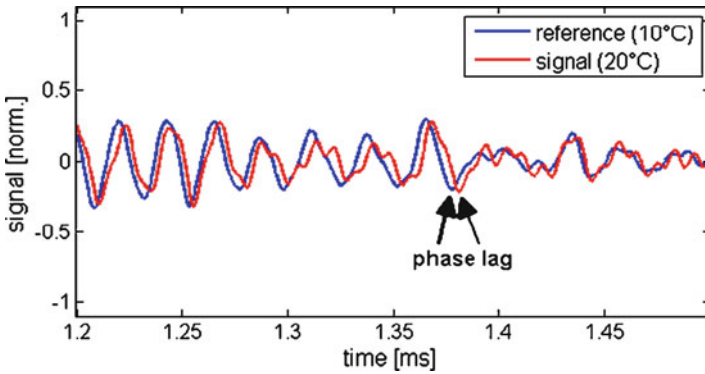
Fig. 3 Late portion of time series Significant time shift

by an assumed small relative velocity change ν until an optimum correlation of both time series is reached:

$$CC(\nu) = \frac{\int_{0}^{T} h_i(t\cdot(1-\nu))\, h_o(t)\, dt}{\sqrt{\int_{0}^{T} h_i^2(t\cdot(1-\nu))\, dt \int_{0}^{T} h_0^2(t)\, dt}} = \max. \tag{1}$$

CWI was introduced more than two decades ago to detect slight velocity changes in the earth crust due to seismic effects, mining influence or seasonal variations ([4], [5], [6]). Recently CWI was used by several researchers to detect small changes in concrete microstructure (e.g. [7], [8], [9], [10]). The influence of temperature on the results of CWI has been shown in [11]. So far CWI has been limited to the detection of bulk effects. New research has shown the possibility to locate the areas affected by changes in a concrete element [12].

Fig. 4 Ultrasonic point contact transmitter at the sample. Four positions marked. Receiver on opposite face

Experiments

For the experiments described here a simple block of concrete (CEM I 32,5R, C30/37, water cement ratio 0.52) with a size of $10 \cdot 10 \cdot 30$ cm³ was prepared. To reach a homogeneous temperature distribution the sample was put into a calibrated refrigerated incubator with forced convection (Binder KB 240) for at least 3 hours. The accuracy of the incubator temperature control was 0.2 K. After the desired temperature was reached ultrasonic transmission measurements were performed outside of the incubator using dry coupling point contact transducers (longitudinal 120 kHz and transversal waves, 55 kHz).

Custom built transmitting and receiving equipment was used for data acquisition. 32 measurements were stacked using 5 MHz sampling frequency and 2.5 ms acquisition time for A-scan recording (Fig. 1). The sensors (transmitter and receiver) were each placed on four different positions on the opposite small sides of the sample (Fig. 4), resulting in $2 \cdot 4 \cdot 4 = 32$ measurements at each temperature. The temperature was varied between 10 and 50 °C with 0.2 K steps.

Data Evaluation

The acquired data have been processed using the stretching technique described above. The results for a single heating/cooling cycle are displayed in Fig. 5. Mean values and standard deviations displayed have been calculated from 16 measurements with different transmitter/receiver positions, all referenced to their respective values at 10° C.

The step-like features and the slightly higher error bar below 20° C (room temperature) have been seen in repeated measurements, but may be due to an unknown error source in the experimental procedure. Above 20° C the velocity decreases monotonically while the temperature decreases. The change is about 3.5 % at 50° C. The error margin is less than 0.1 %.

Fig. 5 Relative velocity changes of coda data during a heating/cooling cycle (transversal transmitter/receiver)
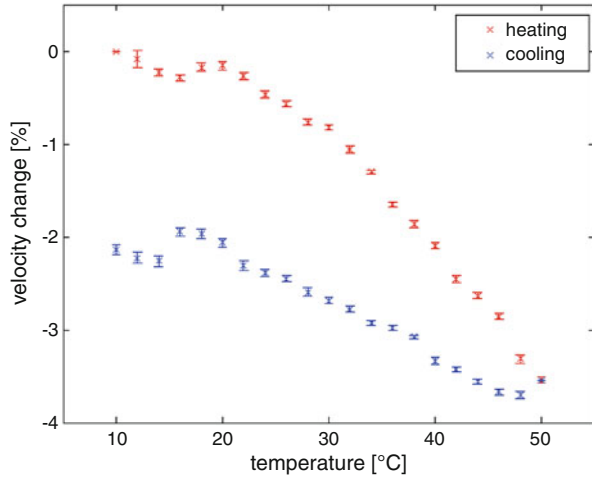
Fig. 6 Same as Fig. 5, receiver position moved compared to reference
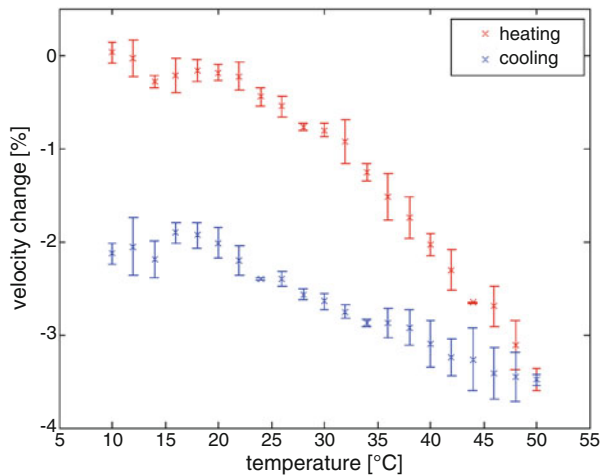
Cooling the sample down again leads to an almost linear increase of around 1.5 %. There is a remanent difference of about 2%, probably due to a loss of moisture, which was not monitored in our experiment.

Similar results have been achieved using longitudinal wave transmitters/receivers. The results show that temperature and probably also moisture have to be measured and corrected, if ultrasonic monitoring systems for concrete structures are applied.

To check the effect of erroneous sensor placement on the results of CWI the data have been reprocessed intentionally using references which have a different receiver position or even both different transmitter and receiver positions. In the former case (Fig. 6) the general shape of the curve is still clearly visible, but the error bars are (as expected) larger. Small changes in velocities, which might be of interest in practical applications might be hidden. In the latter case the standard

deviations exceed the amplitude of the velocity variation caused by the temperature (not shown here).

Conclusions and Outlook

Coda Wave Interferometry (CWI) was shown to be a valuable tool to detect small velocity changes in concrete. It might serve as a method to detect early signs of damage in laboratory or monitoring applications. CWI requires an accurate repetition of the ultrasonic measurements. Sensor misplacement leads to errors, which might hide velocity changes below 0.5 %, at least in the setup used here. In practical application the sensors should be mounted permanently, if possible.

The velocity changes due to temperature change in the range of $10 - 50°$ C are more than 3 % in the first heating cycle. There are remanent changes of about 2 % after subsequent cooling down, which might be due to moisture loss. These results call for temperature and moisture monitoring in practical ultrasonic monitoring systems to avoid misinterpretation of velocity changes.

More sophisticated experiments are required to calibrate ultrasonic monitoring systems and CWI data processing, and to allow the development of at least semi quantitative damage detection applications.

References

[1] DIN EN 12504-4: *Testing concrete in structures. Part 4: Determination of ultrasonic pulse velocity*; German version EN 12504-4:2004.

[2] Payan, C., Garnier, V., Moysan, J., & Johnson, P.A. (2007), *J. Acoust. Soc. Am.*, vol. 121, n. 4, p. EL125-EL130.

[3] Saint-Pierre, F., Rivard, P., & Ballivy, G. (2007), *Cem. Concrete. Res.*, vol. 37, p. 948–956.

[4] Snieder, R., Grêt, A., Douma, H., and Scales, J. (2002), *Science*, vol. 295, p. 2253–2255.

[5] Sens-Schönfelder, C., & Wegler, U. (2006), *Geophys. Res. Lett.*, vol. 33, p. L21302.

[6] Grêt, A., Snieder, R., & Özbay, U. (2006), *Geophys. J. Int.*, vol. 167, p. 504–508.

[7] Larose E., & Hall, S. (2009), *J. Acoust. Soc. Am.*, vol. 125, n. 4, p. 1853–1856.

[8] Stahler, S., Niederleithinger, E., Pirskawetz, S., Nowak, T.-R., & Weise, F. (2009), In: *Noise and Diuse Wavefields ' Extended Abstracts of the Neustadt Meeting*, p. 59–62, Eds.: Sens-Schonfelder, C., Ritter, J., Wegler, U., and Große, C., DGG.

[9] Niederleithinger, E., Shokouhi, P., Stähler, S., & Nowak T.-R. (2010). In: *Proceedings of ECNDT 2010*, Moscow.

[10] Zhang, Y., Abraham, O., Cottineau, L.-M., Durand, O., Larose, E., Planes, T., Le Duff, A., Lascoup, B., Tournat, V., & El Guerjouma, R. (2010), In: *37th Annual Review of Progress in Quantitative Nondestructive Evaluation*, San Diego.

[11] Larose, E., de Rosny, J., Margerin, L., Anache, D., Gouedard, P., Campillo, M., & van Tiggelen, B. (2006), *Phys. Rev. E*, vol. 73, n. 1., id. 016609.

[12] Larose, E., Planes, T., Rossetto, V., & Margerin, L. (2010), Appl. Phys. Lett., vol. 96, id. 204101.

Monitoring the Stress Level of Concrete Structures with CODA Wave Interferometry: Experimental Illustration of an Investigated Zone

Y. Zhang, O. Abraham, A. Le Duff, B. Lascoup, V. Tournat, E. Larose, T. Planes, R. El Guerjouma and O. Durand

Abstract The use of Coda Wave Interferometry (CWI) to Non Destructively assess concrete structures is an emerging topic. CWI has recently been proposed to determine the stress level of in situ pre-stressed concrete structure as well as to monitor damage of concrete material. The idea is using ultrasonic waves with a wavelength similar to the aggregate size to be in the diffusive regime, and so to probe very small changes of the material. The velocity change is of the order of 0.1% for classical concrete under a 10MPa strain which can be measured with CWI. This velocity variation can be linked to the stress level modification by Murnaghan's theory. While CODA theory and experiments are emerging in the civil engineering NDT laboratory, it becomes relevant in parallel to know what is actually the investigated zone for, *in fine*, relating the velocity changes to a given distribution of stress or damage as a function of depth in *in situ* condition. In this paper we show an experiment that illustrates the existence of an investigated zone in a concrete beam of 0.8 m x 0.2 m x 0.1 m.

Y. Zhang • O. Abraham (✉) • O. Durand
MACS Dept IFSTTAR, BP 4129, 44341 Bouguenais Cedex, France
e-mail: odile.abraham@lcpc.fr

A.L. Duff
Group ESEO, BP 30629, 49009 Angers, France

B. Lascoup
ESTACA, Laval, France

V. Tournat • R.E. Guerjouma
LAUM, CNRS, Université du Maine, Le Mans, France

E. Larose • T. Planes
LGIT, Grenoble, France

Introduction

The use of CODA wave to characterize concrete properties is an emerging topic that takes advantage of the heterogeneousness of concrete, which is opposed to classical non destructive ultrasonic techniques that use large wavelengths compare to the aggregate sizes. Indeed, in classical US survey, the heterogeneity is viewed as a drawback as attenuation is dramatically increased by scattering [1]. As a consequence, the frequencies usually remain below 100 kHz which corresponds to an average wavelength of 0.04 m for the longitudinal body wave.

For wavelengths smaller than a few centimetre, researchers have started to propose NDT techniques using either the coherent field [2-4] (eventually obtained by spatially averaging the wave field to be compared to homogenisation models [4]) or the incoherent field [5-10, 16]. In this paper we focus on the use of the incoherent field.

Our concrete specimen is a rectangular beam (0.8 m x 0.2 m x 0.1 m) and we apply on its side a compression at a series of locations along the 0.8 meter long dimension. The source and the receiver remain identical. The response of the receiver is commented in relation with the solution of a diffusion equation.

Characterization of Concrete Ultrasonic Scattering Properties

Diffusion equation

The intensity of the incoherent field is here supposed to follow a diffusion equation as a function of time [11]. The solution for a parallelepiped (in the dimensions of L, l and h) can be written as follows where t is the propagation time, (x_0, y_0, z_0) is the source position and (x,y,z) the receiver one [12]:

$$l(x,y,z,t) = l_0 \cdot e^{-\xi\tau} \quad \times \left(1 + 2\sum_{n=1}^{\infty} \cos\left(\frac{n\pi x_0}{L}\right) \cos\left(\frac{n\pi x}{L}\right) \exp\left(-D\left(\frac{n\pi}{L}\right)^2 t\right) \right)$$

$$\times \left(1 + 2\sum_{n=1}^{\infty} \cos\left(\frac{n\pi y_0}{l}\right) \cos\left(\frac{n\pi y}{l}\right) \exp\left(-D\left(\frac{n\pi}{l}\right)^2 t\right) \right) \quad (1)$$

$$\times \left(1 + 2\sum_{n=1}^{\infty} \cos\left(\frac{n\pi z_0}{h}\right) \cos\left(\frac{n\pi z}{h}\right) \exp\left(-D\left(\frac{n\pi}{h}\right)^2 t\right) \right)$$

The three parameters D, ξ, and I_0 are frequency dependent, D represents the surface travelled by unit time of the diffuse halo, ξ *represents the damping and I_0 is the intensity at source position and time origin.* Eqn. (1) is used here as a theoretical model to roughly estimate the diffusion constant D. This estimation is done by finding the optimal value of D who can fit best the theoretical curve to the experimental one.
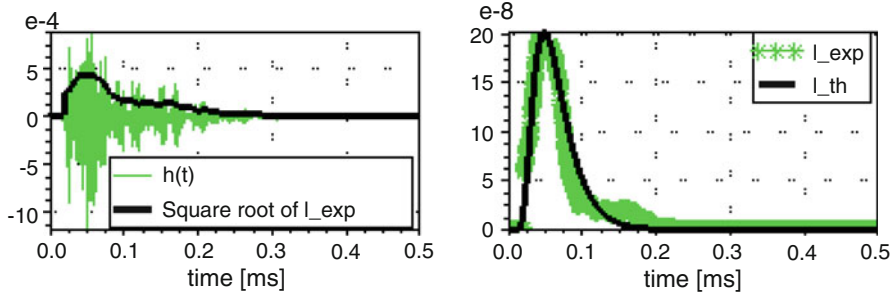
Fig. 1 *Left:* Impulse response h(t) and the square root of the experimental intensity *Right:* Experimental intensity I_exp and theoretical intensity I_th calculated from Eqn(1)

Figure 1 Left shows the impulse response and the incoherent intensity measured (in the frequency band 200 kHz→800 kHz), This intensity is compared to that computed with Eqn. (1) with D=20m^2.s^{-1}. This value is used to determine the order of magnitude of the mean free path l* [15] by using the approximation l*=3D/c, where c is the CODA transport velocity, and here chosen equal to 3000m/s. This distance can provide us a start of the time window in which we are analysing the signal.

Experimental Set-up

In order to illustrate the investigated zone we have designed an experiment where we only vary the position of the circular surface (with a diameter of 0.05m) where the compression (F) is applied. The force of this compression F is controlled by a sensor and varies from 0 kN to 12 kN in 4 steps. The maximum value for F is selected in order to remain below 30% of the compression resistance Rc.

Mechanical mock-up and transducer positions

Figure 2 Left shows a drawing of the mechanical system used to impose the load F onto the beam. Figure 2 Right shows the stress applied to the structure when d=0.16m for F=20kN. It is symmetrical around the axis of the force applied. The source and the receiver are glued 0.1m apart on the same face. The distance d, between this face and the axis of the applied load, varies along the 0.8 m dimension of the beam from 0.06 to 0.26 m. The experiment is conducted in a laboratory where the temperature is controlled. During our experiments we record the temperature and it did not vary more than ±0.2°C. The effect of temperature on coda measurements has been reported elsewhere [6,10] and we envisage to remove it using non-linear acoustics in a near future [14].
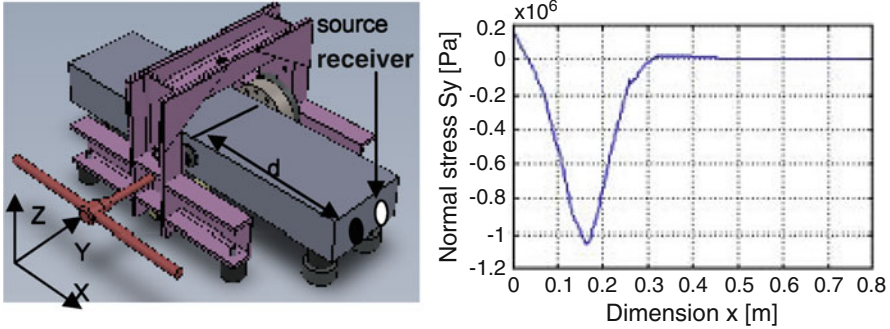
Fig. 2 *Left:* Schematic representation of the experiment *Right:* Distribution of the normal stress Sy along the axis (y=0.1m, z=0.05m) when d=0.16m

Coda Wave Interferometry

The excitation signal is a chirp in the frequency band 200 kHz-800 kHz. The largest aggregate size is 0.0125m, so that the wavelengths are comparable to the aggregate size, which will ensure the multiple diffusion requested for coda generation. All recorded signals are cross-correlated with the excitation signal to give the impulse response h(t). At each location d of the load F, a signal h_0(t) is recorded when no force (F=0 N) is applied and serves as a reference for that position. Subsequent signals for that position at other load level are stretched by an amount ε and compared to the reference h_0(t) [9,13].

The value of ε that maximizes the correlation coefficient X_d corresponds to the average velocity change (ε$_{max}$=<δv>/v) [9,13]. We also use the remnant decorrelation coefficient Kd [9] between the waveforms to present:

$$Kd = 100 \cdot \left(1 - X_d\left(e_{max}\right)\right) \text{ with } X_d\left(e\right) = \frac{\int_0^\tau h\left[t\left(1-e\right)\right] \cdot h_0\left[t\right]dt}{\sqrt{\int_0^\tau h^2\left[t\left(1-e\right)\right]dt \cdot \int_0^\tau h_0^2\left[t\right]dt}} \qquad (2)$$

Results

Varying the load at a fixed position

Figure 3 illustrates the variation of ε and Kd when the force F applied to the structure increases from 0 kN to 12 kN and then decreases to 0 kN at distance d=0.1m from the source and receiver plane. It reveals the acoustoelastic effect: the velocity is modified due to a stress level change within the structure, and CWI is sensitive enough to measure this velocity variation.
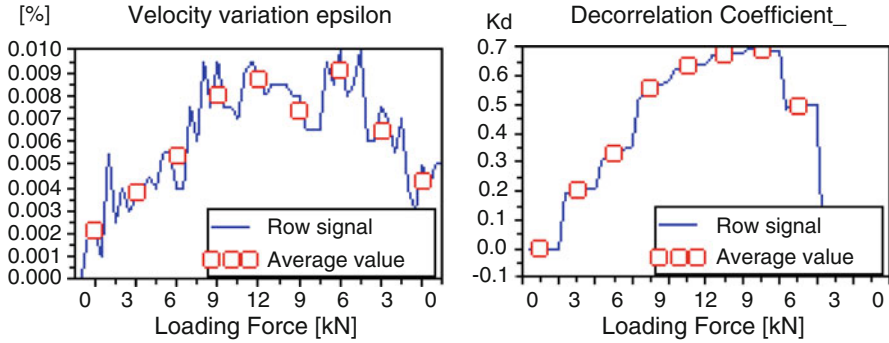
Fig. 3 *Left:* ε and *Right:* Kd when the load is located at d=0.16 m (test number n°5) and varies from 0 kN ↗ 12 kN ↘ 0 kN
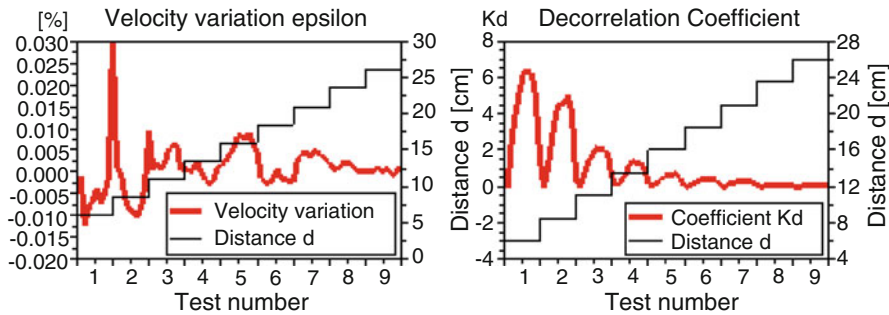
Fig. 4 *Left:* ε and *Right:* Kd when the load varies from 0 kN ↗ 12 kN ↘ 0 kN at several tests distance d

Repeating the experiment at other positions

This experiment is repeated at 8 other distances d, the values of ε and Kd are plotted on the Fig. 4. The influence on ε and Kd is, as expected, decreasing with distance d. Although the result of ε is hardly workable, the one of Kd shows a clear exponential decrease in term of distance d. This decrease is linked to the variation of the distance between a limited stressed volume and the source-receiver surface, and it indicates the existence of a zone that is investigated by the ultrasonic wave field.

Conclusions and Prospects

In this paper we have illustrated the sensitivity of coda wave to measure velocity variations in relation to stress level modification within a concrete beam. In order to illustrate the investigated zone in that beam, we have applied at different position a

load that was varied from 0 to 12 kN to remain below 30% of the compression resistance Rc. An exponential decrease of the remnant decorrelation coefficient Kd as a function of the distance d between source-receiver surface and the loading position has been observed for a given level of applied load.

References

[1] Abraham, O. and Côte, Ph. (2002), *ACI Struct. J.*, 99(3), pp. 239–247.

[2] Chaix J.-F., Garnier V., and Corneloup G. (2006), *Ultrasonics*, 44, pp. 200–210.

[3] Aggelis, D.G. and Shiotani, T. (2007), *J. Acoust. Soc. Am.*, 122(5), pp. EL151–EL157.

[4] Chekroun, M., Le Marec, L., Abraham, O., Durand, O., and Villain, G. (2009), *Ultrasonics*, 49, pp. 743–751.

[5] Payan, C. Garnier, V., Moysan J., and Johnson, P.A. (2009), *Appl. Phys. Lett.*, 94, 011904.

[6] Larose, E.J., de Rosny, J., Margerin, L., Anache, D., Gouedard, P., Campillo M., and van Tiggelen, B. (2006), *Phys. Rev. E*, 73, 016609.

[7] Larose E. and Hall, S. (2009), *J. Acoust. Soc. Am.*, 125(4), pp. 1853–1856.

[8] Lillamand I., Chaix J.-F., Ploix M.-A., and Garnier V. (2010), *NDT&E Int.*, 43, pp. 655–660.

[9] Tremblay, N., Larose, E., and Rossetto, V. (2010), *J. Acoust. Soc. Am.*, 127(3), pp. 1239–1243.

[10] Zhang, Y., Abraham, O., Larose, E., Planes, T., Le Duff, A., Lascoup, B., Tournat, V., El Guerjouma, R., Cottineau, L.M.C., and Durand, O. (2010), In: *Proceedind QNDE conference*, San Diego, USA, in press.

[11] Larose, E., Derode A., Clorennec, D., Margerin, L., and Campillo, M. (2005), *Phys. Rev. E.*, 72, 046607.

[12] Ramamoorthy, S.K., Kane, Y., Turner, J.A. (2004) *J. Acoust. Soc. Am.*, 115(2), pp. 523–744.

[13] Sens-Schönfelder, C. and Wegler, U. (2006), *Geophys Res. Lett.*, 33, L21302.

[14] Tournat, V. and Gusev, V. (2009), *Phys. Rev. E 80*, 011306.

[15] Tourin, A. Derode, A. and Fink, M. (1999), IEEE Ultrason. Symp., pp. 711–714.

[16] Bowler A.I., Drinkwater B.W., and Wilcox P.D. (2008). *AIP Confrence Proceedings*, vol. 975 pp. 648–655

Non-Destructive Measurement of Steel Fiber Dosage and Orientation in Concrete

H-Joachim Wichmann, H. Budelmann and A. Holst

Abstract Steel fiber reinforced concrete is nowadays frequently used in civil engineering and in the building industry. Apart from the general state of the concrete, the dosage and the distribution of the steel fibers are of prime importance for the quality of the structure. The current standard methods to determine the fiber dosage and the fiber orientation are complicated, time-consuming and expensive. In order to determine the steel fiber dosage in drilling cores, the samples have to be destroyed. A better non-destructive and competitive method is high in demand to supervise the steel fiber dosage not only during the production of new structures and buildings but also to examine drilling core samples from damaged structures.

Keywords Concrete durability • Electromagnetics • Monitoring • NDT/NDE • Quality control • Steel fiber reinforced concrete

During the last years, a new method to determine both the steel fiber dosage and steel fiber orientation has been developed at the Institute for Building Materials, Concrete Structures and Fire Protection (iBMB) at the University of Braunschweig. In cooperation with an industrial partner a market-ready measurement system has been produced.

The new method makes use of the magnetic induction of ferromagnetic materials. By means of a cube shaped sensor consisting of two coils samples of fresh and of hardened concrete as well as drilling core samples from existing structures can be analysed. Fresh concrete is put into a cubic container for examination. Drilling core samples taken from structures can be examined directly. In the contribution the measurement principle and sensor design as well as labmade test results and the experience of first on site-applications will be discussed.

H-J. Wichmann (✉) • H. Budelmann • A. Holst
iBMB, University of Braunschweig, Beethovenstr. 52, D-38106, Braunschweig
e-mail: h-j.wichmann@tu-bs.de

239

Basics

The magnetic properties of ferromagnetic materials in an alternating magnetic field are described by the magnetic hysteresis loop (see Fig. 1). It shows the dependency between an (externally applied) magnetic field $\vec{H}$ and the resulting magnetic flux density $\vec{B}$ for ferromagnetic and non-ferromagnetic materials.

If an alternating magnetic field is applied to a ferromagnetic material, the resulting magnetic flux density $\vec{B}$ increases non-linearly to the magnetic field strength $\vec{H}$.

During demagnetisation, the downward sloping curve does not follow the original magnetisation curve. The resulting curve for all strengths of the magnetic field is a loop in an S-shape. The slope in the zero crossing of the hysteresis curve is defined as magnetic permeability $\mu_{Rges} = \mu_r \cdot \mu_o$. Only ferromagnetic materials (iron, cobalt and nickel) have a permeability $\mu_r \gg 1$, for other materials the permeability $\mu_r \approx 1$. These materials have no hysteresis loss, so no hysteresis curve is created. The gradient of the plotted line is μ_o. Steel fiber concrete consists almost only of materials with a permeability $\mu_r \approx 1$. Only the steel fibers, mostly being made up of iron, have a permeability $\mu_r \gg 1$, so different concrete mixtures or water/cement ratios do not influence the slope of the hysteresis curve.

Measuring Principle

The dosage of steel fibers in a concrete sample can be gauged by the so-called transformer principle. Figure 2 shows the fundamental test assembly. In this case, one coil is used to excite the magnetic field and another outer coil is used to create the induced voltage U_i. The induction coil is smaller than and completely enclosed by the operating winding. A fresh or hardened concrete sample takes over the function of the core of the coil. A sine-shaped alternating current I_{err} is fed into the operating winding from the regulated generator G and the induced voltage U_i in the induction
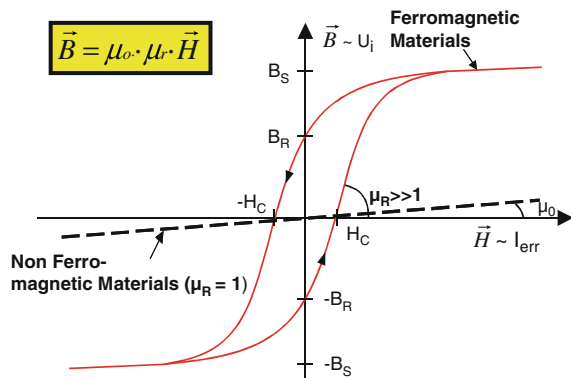
Fig. 1 Hysteresis loop

Fig. 2 Test assembly for the measurement of magnetic characteristics
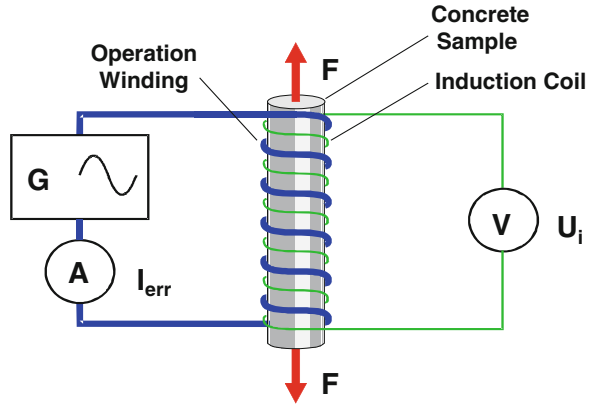
coil is gauged. The amplitude and frequency of the alternating current I_{err} are kept stable using a closed-loop control, so the induction voltage U_i is only depending on a change of the magnetic permeability (i.e. the type of steel fiber) and the amount and orientation of steel fibers in the concrete sample.

Measurement Procedure

The measurement procedure requires four single measurements. The first measurement is done using the empty sensor to determine the induction voltage of the empty sensor. For measurements with fresh concrete, the concrete is filled into a special plastic box with inner space dimensions of 15x15x15cm³. The box is put in the sensor to carry out the measurement. The measurement is repeated in all three directions in space (see Fig. 3), either turning the sample or the sensor. Samples of hardened concrete (test cubes and drilling cores) can be analyzed directly (Fig. 4).

To determine the steel fiber dosage of the sample, the average of the three measurement results is subtracted from the result of the empty sensor.

Fiber Dosage Measurement

Steel fibers are produced in many shapes and sizes. Due to different performance levels and requirements, the alloys used vary a lot. In order to determine the exact steel fiber dosage of a concrete sample, an initial calibration using calibration samples of the same steel fiber type is required.

Figure 5 shows the calibration results of five different steel fiber types. For each steel fiber type, six different test cubes with steel fiber dosages from 10-60 kg/m³

Fig. 3 Box for fresh
concrete

Fig. 4 Test Cube
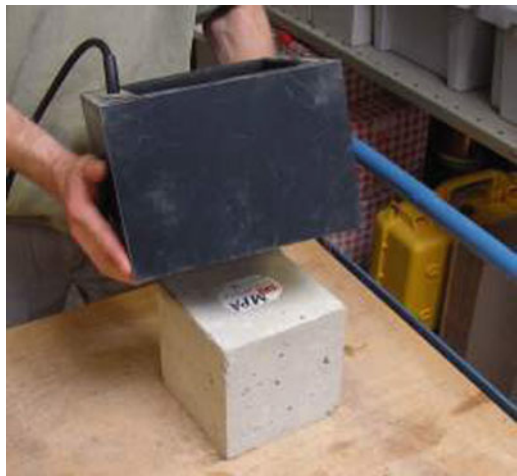
were produced and calibrated. As shown in Fig. 5, for all types the induction voltage U_i is an almost linear function of the steel fiber dosage.

The coil-sensor can also be used to examine the steel fiber dosage in drilling cores. Here too, the induction voltage is measured in the three directions in space. The volume of a 15 cm long drilling core with a diameter of 15 cm is 21% lower than the volume of a 15 cm test cube. Thus, the measurement values have to be adjusted by a correction factor. Drilling cores longer than 15 cm must be shortened. For shorter drilling cores, a correction of the measurement results is necessary.
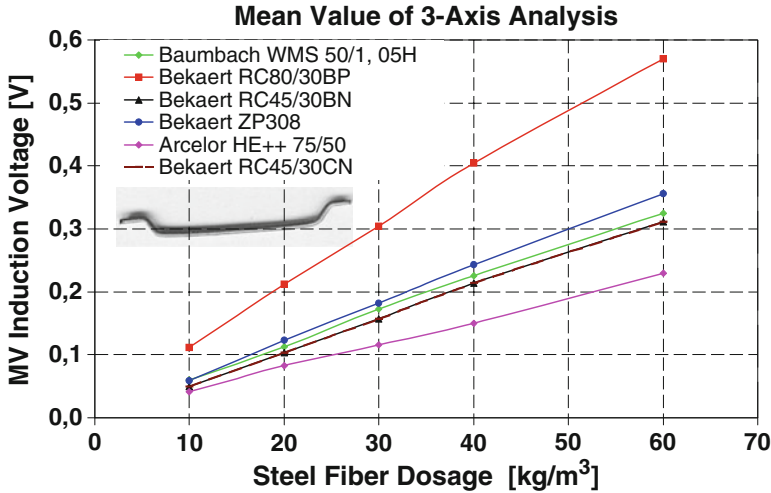
Fig. 5 Calibration diagrams of test cubes for six different steel fiber types

Steel Fiber Orientation

A steel fiber can be considered as a magnetizable rod with a preferred orientation. In a magnetic field, the rod is magnetized and tries to align tangential to the lines of the magnetic field. If all steel fibers are aligned tangential to the magnetic field, the induction voltage is at its maximum. If all steel fibers are in cross direction to the magnetic field, the induction voltage is at its minimum.

In order to determine the relation of the induction voltage U_i to the angle between steel fibers and magnetic field, different sets of 20 g steel fibers were attached on pieces of cardboard. Figure 6 shows the standardized induction voltage U_i in relation to the angle between steel fibers and magnetic field for two types of steel fibers. With increasing angle α_{ST-MF}, the induction voltage U_i decreases.

Figure 7 shows the sketch of a 4 m long concrete member, made from steel fiber-reinforced concrete. Four concrete bars (see Fig. 7, labelled 1 - 4, each bar of dimensions 72 x 12 x 12 cm³) were cut out and divided in 6 cubes of 12 cm.

The cubes were named 1.1 to 4.6, relating to the position they were taken from. The x-axis of each cube was defined as the casting direction of the concrete.

Table 1 shows the measurement results of the six cubes taken from position no. 1. For all cubes, the induction voltage in direction of the x-axis is the least of all three directions. Without calibration samples, the fiber dosage of each cube is only measured relatively to other cubes.

The percentage of each single measurement indicates the orientation of fibers in the sample. A higher percentage of measurement shows that more fibers are orientated in that direction. Or in other words: The higher output value in a single direction corresponds with a higher amount of steel fibers pointing in that direction.
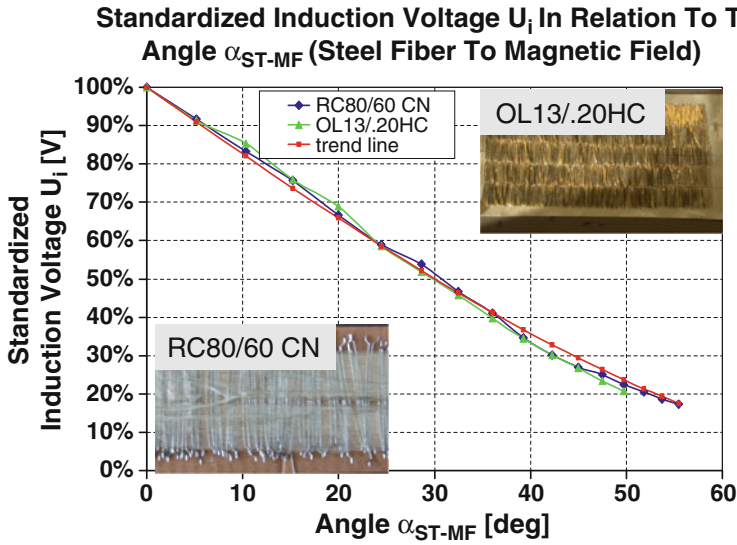
Fig. 6 Standardized induction voltage U_i in relation to the angle α_{ST-MF}
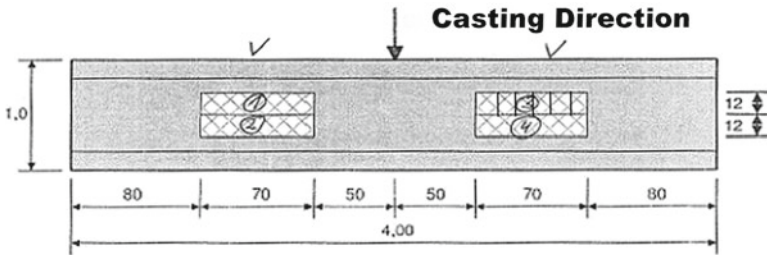
Fig. 7 Concrete member

Table 1 Fiber orientation and relative steel fiber dosage of concrete test cubes

Percentage				
Sample	x-Axis [%]	y-Axis [%]	z-Axis [%]	rel.fibre dosage [%]
1.1	16,5	31,7	51,8	107,80%
1.2	13,1	47,6	39,2	105,70%
1.3	11,9	53,1	34,9	102,70%
1.4	11,9	64,7	23,4	93,50%
1.5	15,5	59,9	24,6	93,50%
1.6	14,8	56,1	29,1	94,50%

Measurement Device

The measurement device "BSM100" was developed in a cooperation between the University of Braunschweig, Germany, and the company "Hertz Systemtechnik" in Delmenhorst, Germany and is now commercially available, [3]. Calibration data of already calibrated steel fiber types, called "fiber profiles", are already stored in the "BSM100". New user-generated "fiber profiles" can be uploaded. A separate measurement of a defined amount of fibers, attached to a special card, called "card measurement", makes it possible to compensate variations caused e. g. by differences in the chemical composition of the alloy.

References

[1] Breitenbücher, R., Rahm, H., (2009/3) *Zerstörungsfreie Bestimmung des Stahlfasergehalts und der Stahlfaserorientierung im Frisch- und Festbeton*, Beton 99(2009), 88–94
[2] Wichmann, H.-J., (2009) *Bestimmung des Fasergehaltes und der Faserorientierung im Stahlfaserbeton*, Betonbodenfachtag 2009, Betonmarketing Nord
[3] http://www.hertznet.de

Application of an Electromagnetic Method for Evaluation of Chlorine Distribution in Concrete

J. Nojima, M. Arai and T. Mizobuchi

Abstract   Presence of chloride ions in cover concrete leads to an enhanced deterioration of reinforced concrete structures. Prediction of the resultant damage in early stages of development is not possible, unless the distributions of chloride ions across the concrete section are known. This paper presents an on-going study of evaluating such distribution by a non-destructive method using electromagnetic wave. The technology is introduced in a separate paper in the symposium, shows in laboratory experiments its applicability to structures whose concrete properties are known. The ability to estimating the said distribution in cross section in existing concrete structure has been investigated in field tests and the method to be equally usable has been found by modifications of the method based on actual concrete properties in question. Once established, the method will provide a valuable means of readily collecting, not a limited and point-based data from cores, but information of area-wide chlorine ions non-destructively. This should, in turn, allow the owner of the concrete structure to identify chlorine deterioration at an early stage and to formulate effective strategies against the resultant damage.

Keywords   Chloride content • Electromagnetic wave • Estimation • Non-destructive testing • Reinforced concrete

Introduction

A definite understanding about any corrosion of reinforcement is very difficult unless corrosion induced cracks appear on the surface in marine RC structures. Thus, in order to detect chloride-induced corrosion at an early stage, chloride content

J. Nojima (✉) • M. Arai
JP Design Co., Ltd, Tokyo, Japan
e-mail: nojima@jpde.co.jp

T. Mizobuchi
Hosei University, Tokyo, Japan

within concrete needs to be investigated using cores drawn from the RC structure, and carrying out chemical analysis. On the other hand, it has been obtained from laboratory tests under limited conditions that chloride content within concrete has could be almost estimated by using electromagnetic waves as one of the non-destructive tests [1], [2].

In this report, the applicable method which is possible to estimate the chloride content included in cover concrete in the existing structures of a power plant using electromagnetic wave method which is a non-destructive testing is reported.

Outline on Measurement of Chloride Content in Concrete Using Electromagnetic Waves

Generally, it was confirmed that changes of dielectric constant in the electromagnetic waves weren't caused by differences in the chloride content in concrete. That is to say, when the electrolyte like sodium chloride exists in the concrete, it seems to be changed the electrical properties such as conductivity in comparison with the concrete without the chloride ions. Furthermore, because the amount of electrolyte varies with the difference of chloride ions concentration, the amount of electrolyte also changes depending on the moisture content in the concrete.

Figure 1 shows an example of output of the reflected waveforms at the each chloride content. As shown in Fig. 1, the amplitude decreased depending upon increasing in chloride ions concentration. Thus, as the values of the amplitude by the electromagnetic waves changed greatly the chloride ions concentration, it was
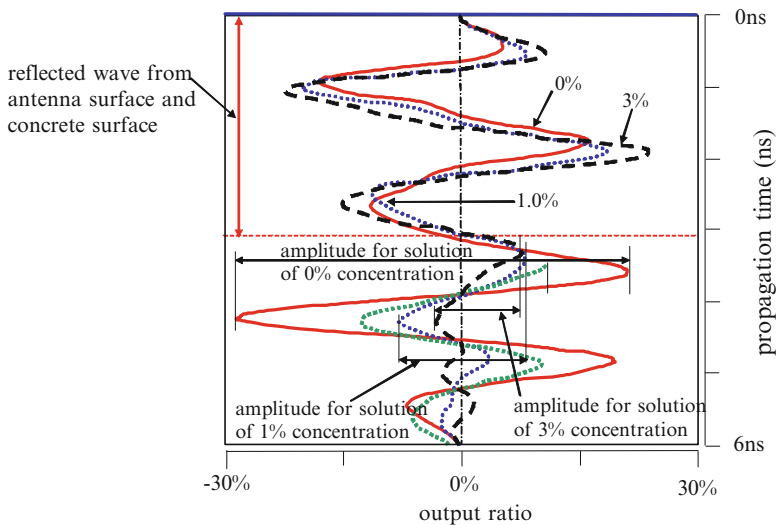
Fig. 1 Example of output of the reflected waveforms

possible to estimate the chloride ions concentration in the concrete from the values of the amplitude in the electromagnetic waves [1].

Field Investigation

Structures and location for investigation

Field investigation was carried out in the sea deck of an existing power plant. Photo 1 shows the area of investigation in the sea deck. As shown Photo 1, measurement was within 10m×10m of the upper side on the west side in the sea deck.

Details of electromagnetic wave measurement and core sampling

As shown Photo 1, measurements using the electromagnetic waves were carried out in both of Y and X directions among reinforcing bars and four core samples were drilled in order to compare with the results of measurements using the electromagnetic waves.

Measuring method

For measurement of electromagnetic waves, an antenna of about 1.0 GHz with specifications was installed on the specimen. As shown in Fig. 2, the scale of the monitor was fixed at the level of the gain of the machine when the measurement was started, and the amplitude of the reflected electromagnetic wave estimated using
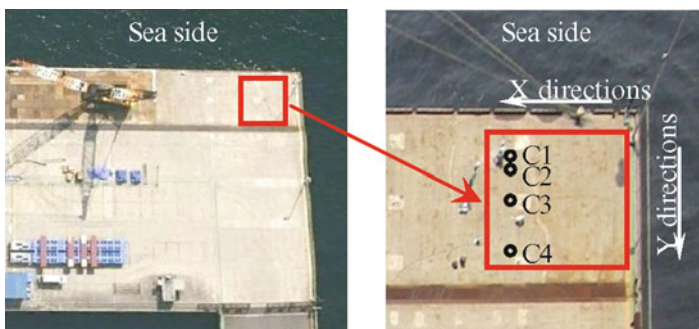
Photo 1 Area of investigation
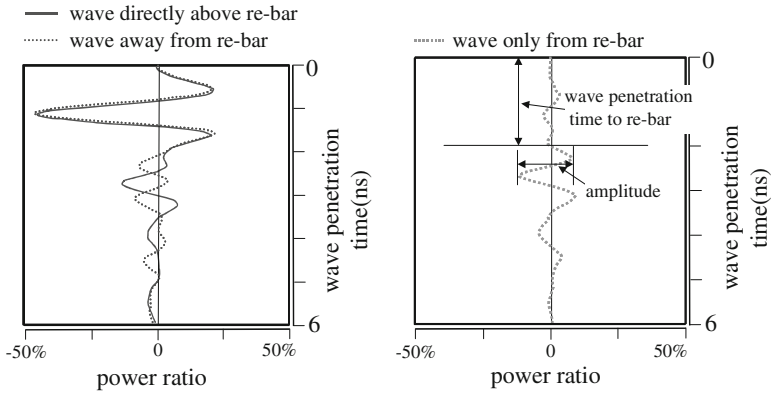
Fig. 2 Removal of reflection from re-bar

that scale (Full scale = 100%). Moreover, since the measured reflected wave contains reflected wave from reinforcing bar and reflected wave from except for reinforcing bar, the reflected waveform from except for reinforcing bar was subtracted from both the contained waveform. Thus, as shown in Fig. 2, the effect of only the presence of the reinforcement could be independently studied [3, 4].

Results of Investigation

Chemical analysis of sodium chloride in concrete

Figure 3 shows relationship between depth from the concrete surface and content of chloride ions in the four drilled core samples from the sea deck.

C1 core on the seaside contained chloride content of 5.0 kg/m³ in depth of 2cm from the surface, which is about 1.5 times higher than that for the other cores. The same content close to the surface is about 3.5 kg/m³ for other cores (C2~C4). Chloride ions have penetrated to a depth of about 4cm. Chloride content in the surface varied within 10~20 kg/m³.

Estimation of salt content by electromagnetic wave

Figure 4 shows results of chloride contents by chemical analysis each core position and the chloride content obtained from two equations using electromagnetic wave estimated from prior laboratory experiments and from the chemical analysis of cores in this investigation. The estimation of chloride content based laboratory experiments greatly varied in comparison with results of chloride contents by
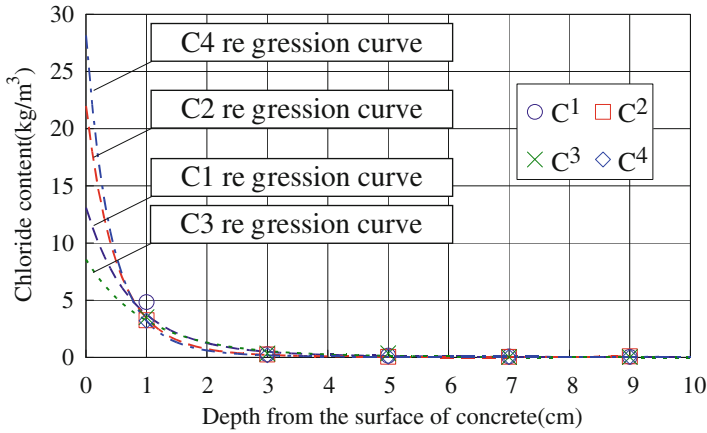
Fig. 3 Chemical analysis of sodium chloride determined for cores samples
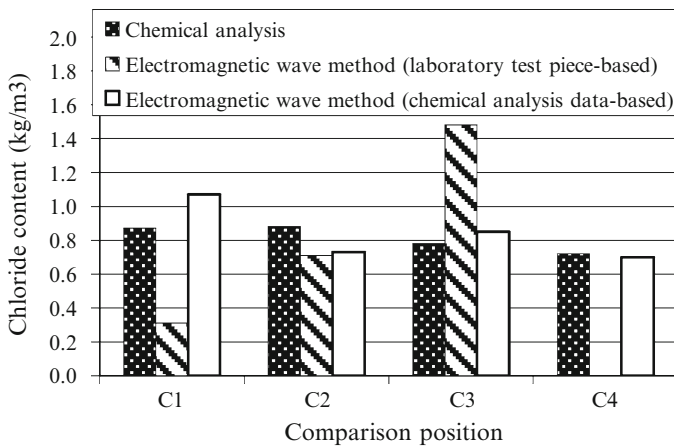
Fig. 4 Comparison of chloride content

chemical analysis because void and water content were sufficiently due to be not reflected for the estimated equation. On the other hand, by using the equation estimated by the average chloride content from the concrete surface to the reinforcing bar from the core samples, the estimated chloride content was almost equivalent to results of chloride contents by chemical analysis.

Figure 5 shows estimation map of chloride content distributions calculated from the core data from the sea deck. In this figure, height direction is the content of chloride ions. It is seemed that the content of chloride ions is high in respect of the region of seaside. This shows that the content of chloride ions of the seaward is abounding.
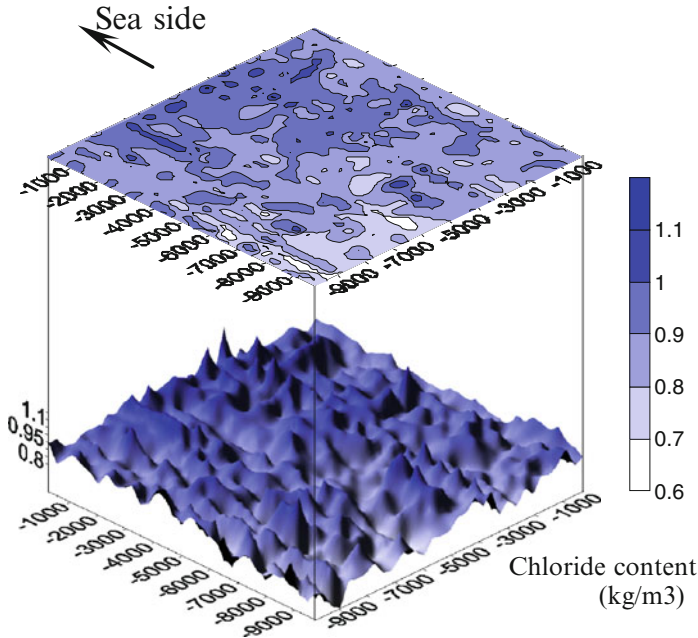
Fig. 5 Distribution of chloride content with electromagnetic wave method (chemical analysis data-based)

Conclusions

Applicability of the non-destructive using electromagnetic wave for estimation of the chloride content in concrete has been already verified in the laboratory. In present stage, it seems to be difficult that the chloride content of existing structure is estimated using the estimated equation in the laboratory. In this study, it seems to be possible to estimate chloride content in the concrete using the electromagnetic wave at the good accuracy on the basis of a limited number of cores drawn from the structure. However, as many problems have been held on application to reinforced concrete structures, further works need to be examined on influences of environmental condition, etc..

References

[1] J. Arai, T. Mizobuchi and K. Suda, *Study on Measurement of Chloride Content using Electromagnetic Wave in Reinforced Concrete Structures*, Non-Destructive Testing in Civil Engineering, 2003.09
[2] D. Hayashi, T. Mizobuchi, K. Suda and K. Yokozeki, *Experimental Study on Applicability of Measuring Method of Chloride Content using Electromagnetic Wave in Reinforced Concrete*

Structures, The Third US-Japan Symposium on Advancing Applications and Capabilities in NDE, 2005.07

[3] T. Mizobuchi, K. Yokozeki, K. Watanabe and M. Hiraishi and R. Ashizawa, *Monitoring System of Chloride Content in Cover concrete using Electromagnetic Wave and Impedance Method*, Proceedings of the 6th International Conference on Fracture Mechanics of Concrete and Concrete Structures, pp. 1865-1876, 2007.06

[4] T. Mizobuchi, K. Yokozeki and R. Ashizawa, *Applicability of Estimation of Chloride Content in Cover concrete using Electromagnetic Wave and Impedance Method*, on Site Assessment of Concrete, Masonry and Timber, 2008.09

A Study on the Variability of Electrical Resistivity of Concrete

J-F. Lataste and D. Breysse

Abstract The article presents results stemming from two French collaborative research projects (SENSO and APPLET). Electrical resistivity measurements are studied either as a tool of control of on-site structure, or as an indicator of durability. The results concern the evaluation of resistivity measurements variability at various scales. They enable to make the part between the real material information and spurious variations of various origins. We distinguish the repeatability, the reproducibility, the local variations, then, the variations on one batch, between batches and between concretes. The results show that the measurement technique is adapted to needs, and that the various variabilities remain smaller than the variations of properties looked for.

Keywords Concrete • Electrical resistivity • Measurement • Variability

Introduction

The electrical resistivity measurement on concrete is a more and more present tool in civil engineering. Electrical resistivity is sensitive to material characteristics which influence its evolution in time. Recent works [1] present the electrical resistivity as a concrete indicator of durability. The links between the electrical conduction in the concrete and its porosity or its saturation rate were experimentally studied and numerous works use this link. It can be used to estimate the transfer properties. Other applications are proposed within the framework of Non Destructive Testing.

The information contained in a measurement should be put in perspective according to the measurement variability and the material heterogeneousness.

J-F. Lataste (✉) • D. Breysse
University of Bordeaux, I2M (UMR 5295), Bordeaux, France
e-mail: jean-francois.lataste@u-bordeaux1.fr

Predictive probabilistic approaches require representative data about variability for material properties and for measurements. NDT appears as a promising tool for obtaining such information.

Electrical Resistivity Measurement Techniques

The electrical conduction through porous materials, like concrete, can be described by the empirical Archie's law, initially elaborated for rocks (see eq. (1)); with ρ_r the rock resistivity (in ohm.m), ϕ the porosity, ρ_w the interstitial fluid resistivity (in ohm.m), S the saturation rate, and a, m and n three constants linked to the material microstructures:

$$\rho_r = a.\phi^{-m}.\rho_w.s^{-n} \tag{1}$$

The value of the measured resistivity is then connected to the nature and to the volume of the fluids in concrete pores (parameters ρ_w and S of Archie's law), but also to microstructural parameters (porosity, tortuousity and pores inter-connectivity).

The resistivity measurements are done by means of a four-probes device adapted to on-site investigations. This measurement technique allows assessment of the near surface material properties. The measurement is given in terms of apparent resistivity (ρ_a in ohm.m). The square device used is characterized by a 5 cm distance between probes (a). The volume of investigation with is defined by the space between electrodes, and an investigation depth of about ½ to 1 x a.

Experimental Program

Concretes were done within the framework of the program ANR SENSO[1]. They are 9 different batches (*Table* 1). Concretes G1, G2, G3, G7 and G8 differ essentially by their water/cement ratio. The concretes G3 and G3a have the same composition and allow to study the variability between batches. Concretes G4, G5, and G6 are different regarding aggregates (size, shape and mineralogy). Every concrete series consists in 10 slabs (with dimensions 10x20x50 cm). Concretes of the SENSO program were also studied for various saturation degrees, and various chloride contents; these last results will not be presented here.

Measurements were performed within the framework of the program ANR APPLET[2], provide a second series of data. They are performed on two different concretes (*Table* 2), which were continuously poured on two construction sites, during the project. The studied samples, 40 for each mix (cylinders with 11 cm in

Table 1 Concrete mixes in SENSO French ANR project [2]

	G1	G2	G3a	G3	G7	G8	G4	G5	G6
Aggregates (type and D max)	SR 14	SR 14	SR 14	SR 14	SR 14	SR 14	SR 22	SR 14	CC 14
Cement (CEMI, 52.5N) (Kg/m 3)	405	420	370	370	320	240	370	370	370
Silica fume	Y	N	N	N	N	N	N	N	N
Water (Kg/m 3)	140	197	212	212	216	217	212	212	214
W/C	0.31	0.47	0.57	0.57	0.68	0.9	0.57	0.57	0.58
Compressive strength (Mpa)	72.9	43.3	43.5	40.5	38.3	20.2	36.6	45	38.2
Porosity (%)	12.5	14.3	15.5	16	15.9	18.1	14.2	15.2	14.9

SR: Silicceous rounded, SC: Silicceous Crushed; CC: Cakareous Crushed;

Table 2 Concrete mixes in APPLET french ANR project [3].

	A1	A2
Cement (Kg/m3)	CPA CEM I 52.5 CP 2 350	CEM III/A 52.5L LH CE PM ES
Additions	fly ashes	Calcareous fillers
Water (Kg/m3)	177	176 (193*)
W/C	0.51	0.50

* the concrete mix have been lightly modified during the project

diameter and 22 cm high) were cast at different dates. The measurements are made at 90 days. They are done on saturated samples, with the four-probes square device on the face confined by the mold (the lower face). Additional samples (20 by concrete), out of one batch, are also studied for the both mixes.

Given the differences between concretes of SENSO and APPLET programs (geometries, ages, conditioning …) only results in terms of variability will be considered.
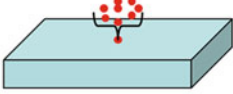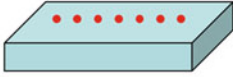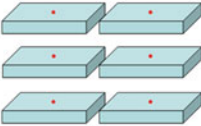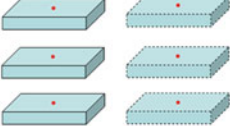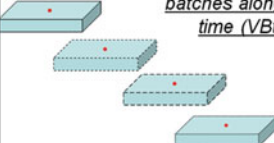
Experimental Study and Variability Scales Considered

In this study, various variabilities are considered (*Table 3*). The identification of each of them will allow estimation of the relevance of variations which can be observed between various samples, or various concretes. The measurement variability is quantified by coefficient of variation (CoV) calculated on a set of data

(1) The repeatability (noted r), which corresponds, on repeated measurements, to the variation observed with the same measurement method, by the same operator, with the same measuring instrument, to the same place, in the same conditions of use and by repeating the measurement over a short period of time. The repeatability represents the variability due to the measurement device, so called equipment.

(2) The reproducibility (noted R), which corresponds to the influence of the protocol. The reproducibility is estimated on several repeated measurements by fully repeating the protocol.

Table 3 Variability levels

(3)   The local variability (noted Vl) which results from the internal variability of the material at short distance (due to the concrete manufacturing, to the skin effect, to the spatial distribution of aggregates…). Vl is estimated by moving the device in a limited zone of supposed "homogeneous" material, that is to say without including long distance variations.

(4)   The variability in a batch (noted Vb) which corresponds to the variability measured on samples from a single batch, exposed to the same conditions during the casting.

(5)   The variability between batches (noted VB), which corresponds to the measurement variability between samples from various batches, with the same concrete composition. The composition of the concrete being in theory the same, the effects of the variations of the casting conditions and the light composition variations linked to the casting process are assessed. This variability thus allows estimation of differences between concretes stemming from the same formulation.

(5bis)   The variability between batches poured on a very long time lap (noted VBt). It will allow taking into account better, the real variability of a given concrete on a construction site.

(6)   The differences between different concretes: it is in fact the final information looked for. The range of differences between concretes must be compared to those resulting from all variabilities at different scales defined above.

The various sources of variability also cumulate, so it is expected to have a ranking for the variability levels defined: $r \leq R \leq Vl \leq Vb \leq VB \leq VBt$. When

assessing a material with NDT, the aim is to maximise the signal to noise ratio, where the signal is the real material variability and where the noise results from all variabilities at different scales.

Results and Discussion

Estimation of the variability

The measurements analysis is done at various scales: on one measurement point, on one sample, on one batch as well as by considering the various conditions of samples (different saturation rates, chloride concentrations…). It has been checked that these conditions do not change significantly the variability at various scales. Thus, results obtained in different conditions can be merged and compared. Table 4 summarizes results on local variability Vl when Table 5 provides results at different scales, provided by the two experimental programs. The average value for local variability, calculated for all concretes and all conditions (5.2% in *Table* 4), is the value given for local variability in *Table* 5.

The various variability levels are given below. We note that the CoV for repeatability (r) and reproducibility (R) values are very weak (lower than 3.2 %) and of the same order. Within the framework of APPLET project, the measurements are done in laboratory conditions (samples saturated and stored in climatic chamber before measurements, measurement at 90 days, and laboratory measurement device). In SENSO project, the measurements are done with conditions close to the on-site measurement (no temperature control …). This explains differences between the variabilities (reproducibility) obtained in both projects.

With an average of 5.2% and a range between 2.4 and 10.2%, the local variability (Vl) is slightly more important than those due to the protocol and device (r and R). It can thus be considered as a main cause of on-site "measurement noise".

Concerning the variability within (Vb) and between batches (VB), identical values indicate that properties variations within a batch are comparable to the properties variations between batches of one single concrete formulation, poured with comparable conditions (VBt). When considering variability between batches poured on a very long time lap (on one year), this variability is slightly more important.

Considering Table 4 and 5, one notes VBt >>Vl, and even VB>>Vl, whatever concretes, aggregates (shape and size), or saturation. At this stage no identification of causes of variability has been done: for a concrete, the variability between several batches (VB) is anyway higher than the effect of a single parameter of the mix.

Consequences on the quality on condition assessment

In summary, one can consider that: r and R are about 1.5 to 3% ; Vl is about 5% ; Vb, VB and VBt are about 13 to 18%. These values can help in justifying the minimum number of measurements that are required so as to identify a representative mean

Table 4 Local variability of SENSO project concretes (Vl)

CoV (%)		Local variability (VI)									Average for a Sr Given
		G1	G2	G3	G3a	G7	G8	G4	G5	G6	
Saturation rate (Sr)	0%	4.2	4.2	2.7	5.3	2.9	3.5	4.7	3.5	9.2	4.5
	40%	15.4	4.5	3.9	4.8	5.8	9.1	4.7	4.0	2.9	6.1
	60%	8.0	3.3	2.2	3.0	6.9	4.7	8.7	4.2	4.2	5.0
	80%	2.6	3.9	2.8	1.9	3.6	4.4	4.7	2.1	4.5	3.4
	100%	2.4	3.4	5.9	2.8	4.2	10.2	19.6	4.2	10.3	7.0
Average for a given mix		6.5	3.9	3.5	3.5	4.7	6.4	8.4	3.6	6.2	5.2

Table 5 Concrete electrical resistivity CoV (in %)

CoV (%)		SENSO	APPLET
repeatability	r	-	1.6
reproducibility	R	3.2	1.7
Local Variability	VI	5.2	-
Batch Variability	Vb	13.7	-
Between batches variability	VB	13.8	-
Between batches along time variability	VBt	-	18.5

value for a given (local or global) property (here representative mean resistivity ρ_m) with a given level of confidence (1 - α). Sampling statistics lead to the confidence interval I:

$$I = [-t_{1-\alpha/2} s(\rho) / \sqrt{(n-1)}, +t_{1-\alpha/2} s(\rho) / \sqrt{(n-1)},] \qquad (2)$$

where $s(\rho)$ is the empirical standard deviation, n the number of measurements $t_{1-\alpha/2}$ a function of n and α, following Student'statistics [4]. Thus, is one aims at estimating the mean resistivity at +/-x%, it comes:

$$n \geq [t_{1-\alpha/2} \, \text{cov}(\rho) / x]^2 + 1 \qquad (3)$$

Where $\text{cov}(\rho) = s/m$. *Figure* 1 shows for instance that, if cov = 15% (VB case of "global" variability), at least 9 measurements are required to obtain an estimation at +/-10% when, for cov = 5% ("local" variability) 3 measurements are enough.

These variation ranges must be put in perspective with the differences observed between concretes. When considering concretes of the SENSO project, the resistivities for saturated concrete from the 9 different mixes range from 75.5 ohm.m for G6 to 1928.0 ohm.m for G1, with a variability between-concrete being equal to 137.8 %, which is 10 times more than VB. In the same way, if one considers a given concrete and how its resistivity changes with saturation (on a range for Sr from 0 to 100 %), the mean variability between all saturation conditions is 83.1 %, which is 5 to 6 times more than VB. The two conclusions are that: (a) one knows how many measurements are required to obtain a (local or global) representative value with target accuracy; (b) one is able to make the part between this (local or global) noise and the real contrast/signal to be identified.

Fig. 1 Quality of the estimation of the average resistivity according to the number of tests and magnitude of the variability
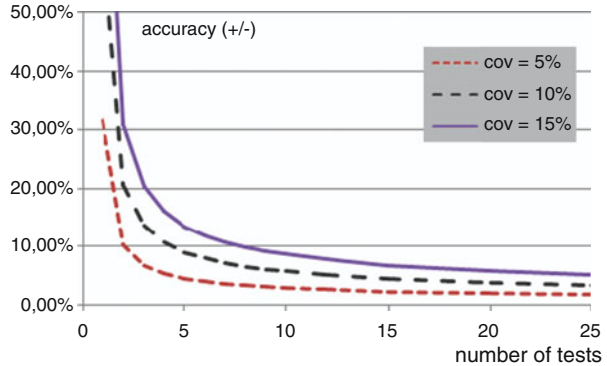
Conclusions and Perspectives

Both ANR projects illustrate the interest for electrical resistivity measurement techniques, within the framework of the management and control of the evolution of the build patrimony made of reinforced concrete.

The results aim at defining the various variability ranges for electrical resistivity, to estimate the representativeness of measurements. The measurements show that the coefficients of variation of repeatability, reproducibility and local variability remain small (about 5%). So they testify of the good quality of the measurement technique.

The results obtained on and between batches, illustrate the natural material variability connected to its manufacturing, and to its casting. This variability is intrinsic to the material and so, cannot be reduced by the measurement.

However, this material variability range remains low, with regard to the variations observed between concretes, or between different saturation conditions for one concrete. It indicates that the technique is able to distinguish various parameters which can influence material condition.

References

[1] Baroghel-Bouny V., 2004, *Conception des bétons pour une durée de vie donnée des ouvrages – indicateurs de durabilités*, AFGC, 252p.
[2] Balayssac JP., 2009, *Stratégie d'Evaluation Non destructive pour la Surveillance des Ouvrages en béton Rapport Final*, Agence Nationale pour la Recherche, 263p.
[3] Cremona Ch., 2010, *Durée de vie des ouvrages: Approche Prédictive Performantielle et probabiliste*, mémoire final de recherche, Agence Nationale pour la Recherche, 126p.
[4] Marceil J.,1992, *Aide mémoire de probabilités et statistiques*, Ed. Ellipses.

Factors Affecting the Electrical Resistivity of Concrete

O. Sengul

Abstract Field experience indicates that the traditional design methods are not effective for obtaining durable structures and performance-based methods are attaining more interest. For the production of new concrete structures in severe environments, requirements to chloride diffusivity are increasingly being used as a performance-based specification for concrete durability. As a basis for the concrete quality control during concrete construction, however, the testing of chloride diffusivity is both time-consuming and elaborate. Therefore, the relationship between chloride diffusivity and electrical resistivity should first be established. Then the chloride diffusivity can indirectly be controlled by routine-based measurements of the electrical resistivity during concrete construction. Electrical resistivity is a non-destructive testing method, which allows rapid inspection of concrete structures. Several factors affect such measurements. To provide more information about some of those factors that may affect the results and establish some simple procedures for a routine-based quality control of the electrical resistivity during concrete construction, an experimental program was carried out. The test program included different environmental conditions such as temperature and humidity as well as different concrete mixtures and factors such as binder type, and aggregate content were investigated.

O. Sengul (✉)
Istanbul Technical University, Istanbul, Turkey
e-mail: sengulozk@itu.edu.tr

Fig. 1 Relationship between
chloride diffusivity and
electrical conductivity [1]
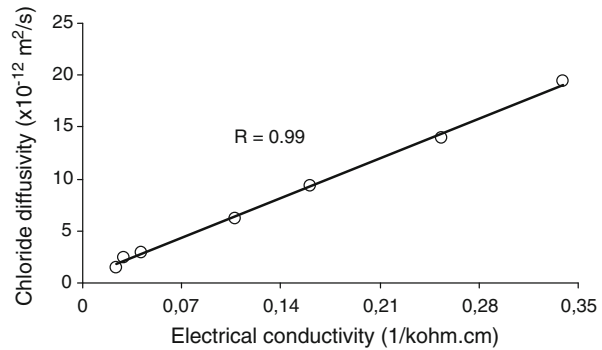
Introduction

Poor durability and thus uncontrolled and short service life is one of the main problems in reinforced concrete structures. Most of the codes in practice are based on "deem-to-satisfy rules", with limitations on the maximum water/cement ratio, minimum cement content or minimum concrete cover depth. Such design approach with respect to durability of concrete structures is mostly empirical. There is no method specified in these design codes, which can be used for the assessment of the durability performance of the structure. Low construction quality is one of the main reasons for the durability problems in concrete structures. Experience obtained from existing structures indicates that the current codes and practice do not provide a sufficiently controlled durability and performance based methods are needed. For the production of new concrete structures in severe environments, requirements to chloride diffusivity are increasingly being used as a performance based specification for concrete durability. As a basis for the concrete quality control during concrete construction, however, the testing of chloride diffusivity is both time-consuming and elaborate. Therefore, for routine quality control measures, more rapid but also reliable methods are needed. Recent studies confirm that electrical resistivity measurement is a simple, reliable and rapid test method for quality control of concrete [1]. For all porous materials, the Nernst–Einstein equation expresses the relationship between the electrical resistivity and ion diffusivity. Based on this relationship, it is possible to calculate the diffusivity of the concrete by measuring the resistivity. Figure 1 shows this relationship for a given type of concrete [1]

The electrical resistivity of the concrete is a very important material property that can be defined as the resistance of the concrete against the flow of an electrical current through the concrete. Concrete has a resistivity varying substantially depending on a number of factors. The electrical current is carried by the dissolved charged ions flowing through the pore solution in the concrete. Therefore, all the factors such as water/cement ratio, cement type, pozzolanic admixtures, and degree of hydration that are affecting the pore structure of the concrete, are also affecting the electrical resistivity of the concrete. Environmental factors such as temperature and moisture conditions can also have a large impact on the electrical resistivity of the concrete.

Although the resistivity method appears to be a very simple and convenient test method, several factors may affect the results of such testing [2]. To provide more information about some of these factors and to establish some simple procedures for a routine-based quality control of the electrical resistivity during concrete construction, an experimental program was carried out.

Experimental

Experimental program was carried out based on two series of specimens. In the first series, concretes having the same water/cement ratio of 0.45 were produced and factors such as binder type, humidity, temperature were investigated. The details of these mixtures are given elsewhere [3]. In the second series, model mixtures containing only cement paste and coarse aggregate were produced. Because these mixtures do not contain fine aggregates, it may be argued that these samples do not represent actual concrete. However, the effects of aggregate content and size can be clearly obtained on such samples. The electrical resistivities of concretes were measured by the two-electrode method using external steel plates. These measurements were applied by use of a resistance meter with a frequency of 1 kHz. To ensure proper electrical connection between the concrete and the steel plates, wet cloths were inserted in between.

Results and Discussion

Environmental conditions

Moisture content and temperature are the two environmental factors that can change significantly even in the same day. Thus, these factors may affect the resistivity results obtained. Same concrete samples were tested in; saturated – surface dry, air-dry and oven-dry conditions. Effect of moisture on resistivity is shown in Fig. 2. In addition,

Fig. 2 Effect of moisture on resistivity
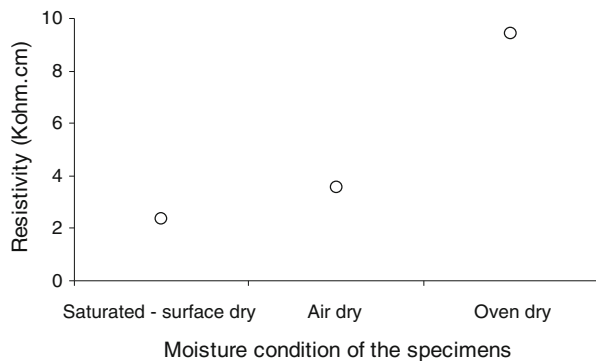
Fig. 3 Effect of temperature on resistivity
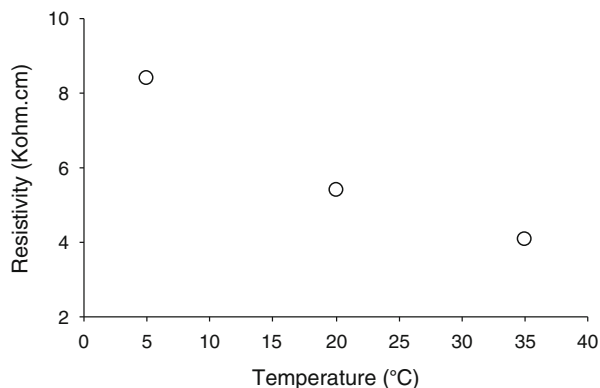
specimens were kept in water at different temperatures and tested in saturated-surface conditions. Effect of temperature on resistivity is illustrated in Fig. 3.

As seen from the figure above, moisture content of concrete substantially affects the electrical resistivity of concrete. In air-dry state, the concrete have approximately 50% higher resistivity compared to saturated condition. Since the electrical current is carried by the ions flowing through the pore solution in the concrete, higher moisture content results in easier electrical flow. Hence, the electrical resistivity observed becomes lower. However, a reduced moisture content of the concrete may significantly increase the electrical resistivity. The sensitivity of resistivity to moisture content can be utilized in a structure in order to locate areas having different moisture contents. For quality control purposes, it is important to ensure the same moisture contents in different mixtures. As seen in Fig. 3, temperature significantly affects the resistivity measured. As temperature increased, lower resistivity values are recorded. This change in resistivity may be due to ion mobility at different temperatures. To obtain reliable and comparable data, it is important that the specimens have a defined moisture condition and temperature.

Binder type

Concretes having the same mixture proportions but different binder types were tested at different ages. A natural pozzolan ground to two different finesses and a blast furnace slag was used in the concretes. The electrical resistivity results obtained are shown in Fig. 4. At the very early age, the resistivity of the concrete produced with only Portland cement was higher than the other mixtures. However, with increasing age the increase in resistivity is very limited compared to the mixtures produced with pozzolanic materials. The resistivity of the slag containing concretes increased very rapidly compared to that of the pure Portland cement, and thus by 28 days, the resistivity of the slag concrete was about three times more
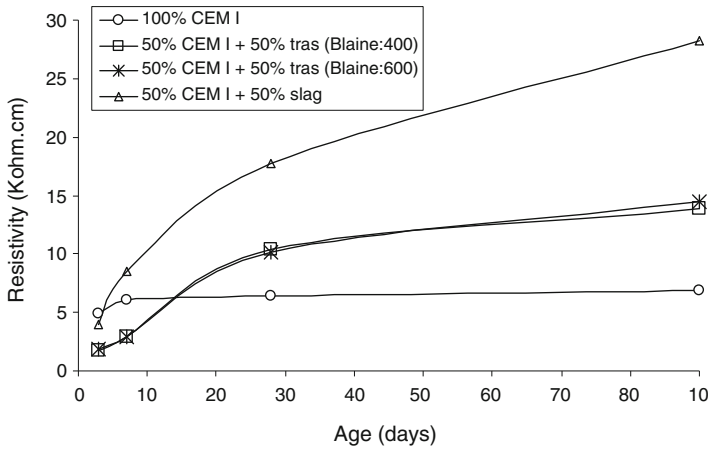
Fig. 4 Effect of binder type on resistivity

Fig. 5 Effect of aggregate size on resistivity
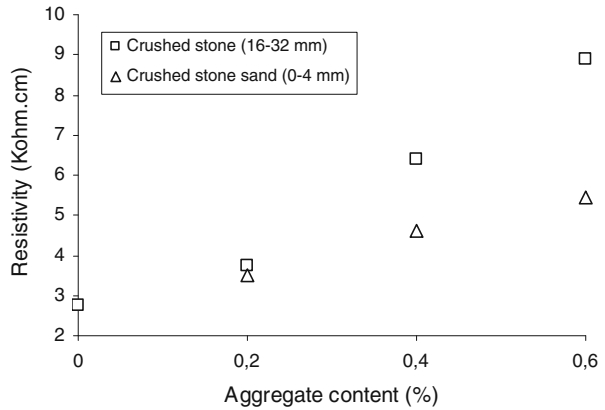
than the reference mixture, and approximately 70% more than the ones with trass. It seems that the effect of the fineness of the trass on resistivity is small. Until the age of 28 days, resistivities of mixtures with different trass finenesses were almost the same, but at 90 days, the one with finer trass had slightly higher resistivity.

Aggregate size

Figure 5 shows the effect of maximum aggregate size on resistivity. In these series, same types of crushed stone with different particle sizes were mixed with cement paste to study the effect of aggregate size. Thus, specimens with crushed stone 16-32 mm consisted of only cement paste and 16-32 mm aggregate and there is no fine aggregate in these mixtures. Aggregate content also varied in these mixtures.

Fig. 6 Effect of aggregate
type on resistivity
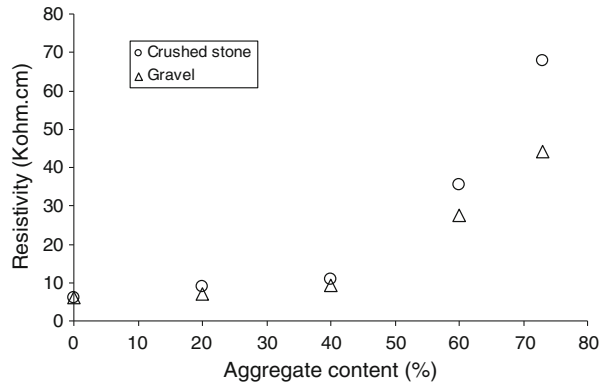
As the aggregate content increased, the resistivity also increased. For a given
aggregate content, the mixtures containing coarse aggregate of 16-32 mm had higher
resistivity compared to the ones with 0-4 mm aggregate. The interface between
cement paste and aggregate is more porous compared to bulk cement paste and due
to its higher porosity, the resistivity of this region is lower. For the same volume, the
total amount of interfacial zone is higher for fine aggregates, which may be the
reason behind the lower resistivities recorded.

Aggregate type

As seen in Fig. 6, aggregate type can also affect the resistivity of concrete. For
aggregate contents up to 40%, it seems that the resistivity is not affected much but
for higher amounts, the concretes containing gravel have lower resistivity. The
higher resistivity in the crushed stone concretes may be an indication of the better
aggregate – cement interfaces in these concretes.

Conclusions

Electrical resistivity is a convenient method for quality control purposes. Conditions
such as moisture content and temperature of concrete should be the same in all the
samples. Since mixture characteristic such as water/cement ratio, binder type or
aggregate properties can affect resistivity significantly, special attention should be
given in the comparison of different concretes.

References

[1] Sengul, O. & Gjorv, O.E. (2008), *ACI Mater. J.*, vol. 105, n. 6, p. 541.
[2] Saleem, M., Shemeem, M., Hussain, S.E., & Maslehuddin, M. (1996), *Constr. Build. Mater*, vol. 10, n. 3, p. 209.
[3] Turkoglu, A. (2010), *MSc Thesis*, ITU, Istanbul, Turkey.

A Study of the Parameters that Affect the Measurements of Superficial Electrical Resistivity of Concrete

J.W. Lencioni and M.G. de Lima

Abstract The electrical resistivity of concrete is an important property in the reinforcement corrosion kinetics, since this property and the oxygen access govern the process. Measurement of the electrical resistivity of concrete performed on the concrete surface using Wenner method (called the "superficial electrical resistivity of concrete" in Brazil) is nondestructive and can be rapidly performed in laboratory or in situ. However, this technique is not standardized in Brazil for concrete yet. There is a need to adapt test techniques and evaluation criteria established and used in other countries, with proper justification. Thus, this paper aims at quantifying and discussing some parameters that influence the measurements of superficial electrical resistivity as a contribution to the adoption of a test procedure in Brazil. Investigatins included the influence of the steel bar presence and the proximity to the edges of the concrete elements on measurements, as well as the evolution of the electrical resistivity with increasing hydration. Preliminary results show that it is necessary a minimum distance of 4 cm from the steel bar to avoid the interference of the reinforcement on the measurements; measurements made near the edges can provide more than 80% higher resistivity values; and that the electrical resistivity can increase more than 100% in 6 months due to the cement hydration process.

Keywords Concrete • Standardization • Superficial electrical resistivity • Tests

J.W. Lencioni • M.G. de Lima (✉)
Instituto Tecnológico de Aeronáutica (ITA), Brasil
e-mail: magdlima@ita.br

Introduction

The importance of studying and quantifying the apparent electrical resistivity of concrete stems from the fact that this property, together with the oxygen access to the steel bars, constitute the two principal elements that govern the electrochemical process of the reinforcement corrosion [1].

The superficial electrical resistivity of concrete can be measured by several means, but the Wenner method is the most frequently used. In this method, four equally spaced contact electrodes are placed on the concrete surface and a small AC current is applied between the outermost two electrodes. The resultant potential difference between the inner two electrodes is measured to obtain the resistivity. Measurements can be performed rapidly in laboratory or in situ using commercially available equipment in a nondestructive fashion since it is performed on the concrete surface [1].

This paper presents part of a study that is being conducted by the authors that aim at identifying and quantifying the parameters that can influence the measurements of electrical resistivity on the concrete surface. Considering the lack of a Brazilian standard to measure the superficial electrical resistivity of concrete, the authors hope that these studies will lead to the development or adoption of a measurement technique that will become a Brazilian standard.

Some Variables that Influence the Measurements of Superficial Electrical Resistivity

Presence of steel reinforcement

Previous research studies [2, 3, 4] have revealed that the electrical resistivity measurements performed over steel bars provide erroneous results. According to RILEM [4], the steel bars conduct current much better than concrete and they will disturb homogeneous current flow. When measured over the steel bars, an artificially low resistivity is typically obtained. Even if only one of the four electrodes is near a bar, current flow will be far from ideal and erroneous results may be produced. The measured resistivity may be artificially low or high, depending on which electrode is near a steel bar. To minimize this effect, none of the measuring electrodes must be placed above or near the steel bars.

The concrete geometry

The current and potential fields produced during Wenner resistivity measurement only lead to a correct value of resistivity if the measurement is performed in a semi-infinite volume of material. When the dimensions of the concrete element being

examined are large in comparison with the Wenner electrode spacing a, then the assumption of a semi-infinite geometry does not lead to significant errors. However, if the dimensions of the concrete element are relatively small, the current is constricted to flow in a different field pattern [2] and this will result in an overestimation of the resistivity of concrete. It is recommended that the contact spacing (a) does not exceed 1/4 of the concrete section dimensions. The distance of the contacts from any element edge should also be at least twice the contact spacing a, but the proximity of a contact to the end of an element can be ignored.

The cement hydration

The electrical resistivity increases with concrete age, i.e. with progress in cement hydration. Since the amount of evaporable water in a typical paste varies from about 60% by volume at the time of mixing to 20% after full hydration, the electrical conductivity of the concrete should also be a function of time [5].

Laboratory Investigation

Materials and methods

The laboratory investigations were performed on 9 concrete specimens with 25x25x65 cm dimensions, each having one 12,5 mm-diameter steel bar with 2 cm cover depth. Ready-mix concrete was used, without additives, with 351 kg of cement/m³ (Portland CP-III-RS), water cement ratio = 0,54, slump = 6 ± 1 cm, mechanically compacted, and with compressive strength (tested at 28 days) = 23,2 MPa.

Commercially available equipment was used to measure electrical resistivity on the concrete surface. This equipment was based on Wenner method, with a current of 180 µA, frequency of 72 Hz, impedance of 10 MΩ, and was able to register resistivity variations between 0 and 99 kΩ.cm ± 1 kΩ.cm; the space between the electrodes was fixed at 5 cm.

Various tests were performed to quantify the influence of the steel bar presence, the proximity to the edges, and the cement hydration process on the measurements of superficial electrical resistivity.

Influence of the steel bar presence. Measurements of the superficial electrical resistivity were performed placing the Wenner probe over and parallel to the steel bar in the specimens (one measurement performed over the steel bar and other 16 performed parallel to it). The distance from the bar was increased at 2 cm steps, as shown in Fig. 1. Specimens were 91 days old at the time of measurements.

Influence of proximity to edges. Measurements of superficial electrical resistivity were performed at 2 cm and 5 cm distance from an edge (distant from the steel bar to avoid the steel influence) on each specimen (Fig. 1), at 91 days of age. The
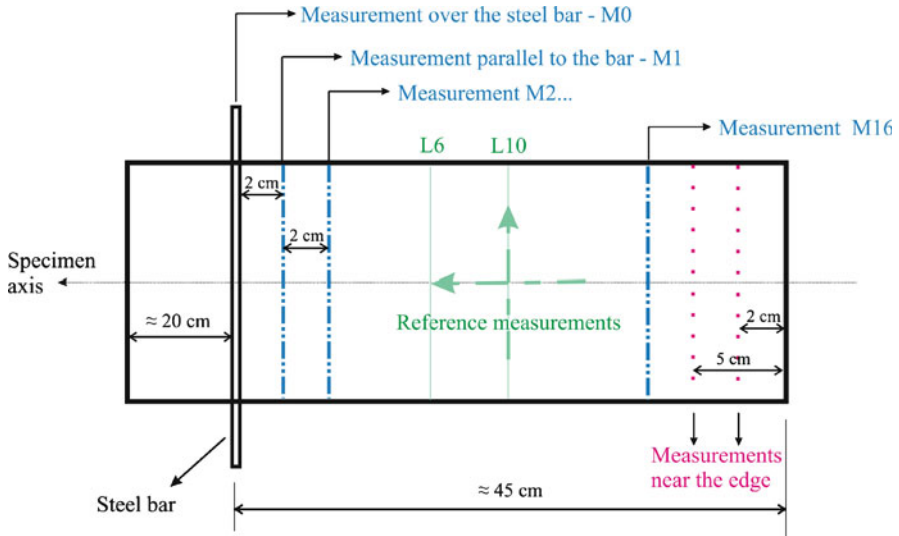
Fig. 1 Measurement locations

measured values were compared with a reference value measured for each specimen at a location with minimum influence from investigated parameters.

Influence of cement hydration. The resistivity measurements were repeated every month for 6 months to monitor the variation due to cement hydration.

Results and Discussion

Influence of the steel bar presence. Analysis of variance (ANOVA) was performed on the measured data. The analysis gave $F_0 = 32,8$ and $F_{(0,05)} = 1,67$, which showed, with a confidence level of 95%, that the presence of the steel bar influences the measurements of electrical resistivity of concrete.

Two reference measurements were performed far from the bar to minimize the influence of the steel bar (Fig. 1). The average and the standard deviation of reference resistivity values obtained for all specimens are 24,8 kΩ.cm and 1,6 kΩ.cm, respectively For each specimen, an average reference value was determined and an acceptable variation band was defined as ± *20%*. According to [4], in any set of measurements on the same concrete in the same conditions, coefficients of variation of 10% are good and 20% must be considered normal.

All resistivity values obtained over the bar and at 2 cm distance from it were out of the admissible variation band (reference value ± 20%). The values over the bar were, on the average, 50% less than the reference value, and the values at 2 cm
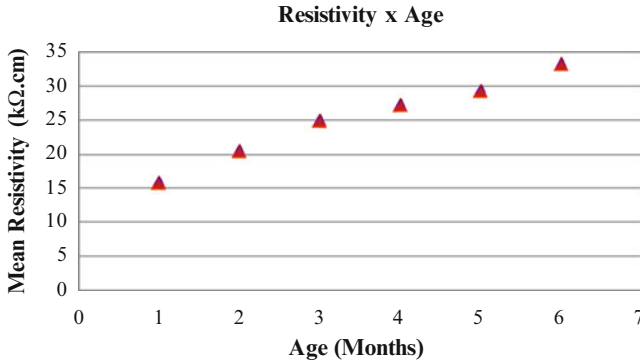
Fig. 2 Resistivity evolution to the first 6 months (mean values)

distance from the reinforcement were, on the average, 32% less than the reference value. Hence, it was experimentally verified that the measurements of superficial electrical resistivity of concrete performed over the steel bar (2 cm cover depth) and close to it (in this case, 2 cm from the 12,5 mm-diameter steel bar, at 91 days of age) are significantly influenced by the conductivity of the steel bar.

Out of all measurements performed at 4 cm distance from de rebar location, measurement from three out of nine specimens produced resistivity values that were out of the asmissible variation band. Hence, its is considered that measurements performed at a distance closer than 6 cm to the steel bar location can be influenced by the steel presence. In conclusion, it is recommended that resistivity measurements be performed at a minimum distance of 4 cm from the steel bar, preferably 6 cm, to avoid the influence of the steel bar.

Influence of proximity to edges. The measurements performed at 2 cm distance from the edges resulted in values, on the average, 87% higher than the reference value, and those performed at 7 cm distance from the edges resulted in values, on the average, 25% higher than the reference value.

These differences demonstrate the error in the resistivity values measured close the edges of concrete elements. Based on this quantitative assessment, it is recommended to keep a minimum distance of 9 cm from the edges so that no or minimum current escape from the Wenner probe takes place to result in erroneously high results. The results agreed well with the recommendation by Gowers and Millard [2] to keep a distance of *2a* from the edges of a concrete element. Considering that *a* = 5 cm in this study, *2a* = 10 cm distance recommendation agrees well with the minimum 9 cm distance recommended here.

Influence of cement hydration. The variation of the superficial electrical resistivity with time (or concrete age) due to cement hydration is clearly demonstrated in Fig. 2. At 6 months of age, the electrical resistivity of concrete increased approximately 110% in compared to that at 1 month of age.

Conclusions

Some parameters that affect the superficial electrical resistivity measurements on concrete surface were quantified and the following conclusions were drawn.

(1) The ANOVA confirmed that the steel bar presence influences the measurements of electrical resistivity on the concrete surface. A distance of 4–6 cm from the bar location is recommended to avoid the steel influence.

(2) The measured resistivity values at or closer than 7 cm distance from the edges were influenced by the current escape from the Wenner probe. It is recommended to keep a distance of *2a* from the edge to avoid this problem [2].

(3) Electrical resistivity is strongly influenced by the cement hydration process. The measured electrical resistivity increased more than 100% in 6 months. Reporting of measured values should take this fact into consideration and also report the age of concrete at the time of measurement.

(4) If the influence of various parameters on the resistivity measurements can be accurately quantified through comprehensive experimental studies, then realistic estimations of the electrical resistivity of concrete can be made even under the influence of the investigated parameters

(5) It must be noted that only one cement type was used in this study, and only one steel bar was considered. Additional studies are necessary using other cement types, other exposure conditions, and the presence of more than one bar with different bar diameters for more accurate and reliable assessment.

References

[1] Cascudo, O. (2005), In: *Concreto – Ensino, Pesquisa e Realizações*, v. 1, pp. 713-751, Ibracon, São Paulo.
[2] Gowers, K. R. and Millard, S. G. (1999), *ACI Mater. J.*, pp. 536-541.
[3] Durar. Red Tematica XV B: Durabilidade de la Armadura (1998), *Manual de Inspección y diagnostico de corrosión en estructuras de hormigón armado*, 208p.
[4] RILEM TC 154-EMC (2000), *Mater. Struct.*, vol. 33, pp. 603-611.
[5] Whittington, H. W. (1981), *Mag. of Conc. Res.*, vol. 33, n. 114, pp. 48-60.

Non-Stationary Identification of Thermal Characteristics of Building Materials

J. Vala and S. Šťastník

Abstract The pore space of building materials can act as an accumulation space, as well as a free space for liquid or gas flows. Such changes in material structure force substantial modification of its effective thermal conductivity and heat capacity. The traditional methods of stationary analysis for the thermal conductivity and calorimetric measurements for the heat capacity are often inaccurate or quite not applicable to a lot of materials of practical importance. The paper demonstrates the original non-expensive non-stationary measurement device for thermal characteristics of building materials, open to a reliable uncertainty analysis of all measurements. Its very simple structure, inspired by the "hot-wire" method, controlling the heat flux generated into a layered structure, is compensated by the non-trivial computational approach, based on the semi-analytical solution of initial and boundary value problems for corresponding differential equations of heat transfer. The numerical discretization uses the Hermite finite-element interpolation technique for the temperature field and its gradient in the Euclidean space and the Crank-Nicholson scheme in time. The required material characteristics are obtained as outputs from the least squares optimization, supported by certain iterative algorithm of the Newton type.

Keywords Building materials • Computational simulation • Heat transfer • Material characteristics • Inverse analysis

J. Vala (✉) • S. Šťastník
Brno University of Technology, Faculty of Civil Engineering, 602 00 Brno,
Veveří 95, Czech Republic
e-mail: vala.j@fce.vutbr.cz

Introduction

The complex analysis of thermomechanical behaviour of buildings requires, in addition to the evaluation of their static and dynamic response to external and internal loads, also the proper HAM ("heat, air and moisture") analysis for all load-bearing constructions, (typically porous) insulation parts and empty (partially furnished) rooms under quasi-periodic (day and year) climatic changes. Thanks to the porous material structure, liquid and gas flows are allowed in most building parts. This analysis, based on the principles of classical thermodynamics, leads to the macro-scale formulation of balance laws for mass, (linear and angular) momentum and energy (or enthalpy), exploiting available microstuctural information. Such formulation can involve even phase changes, namely those occurring in the advanced phase-change materials for insulation layers, or those driven by chemical reactions in maturing silicate mixtures, especially in early-age concrete, with the aim of controlled volume changes, preventing tensions in material and related creation of micro- and macro-fractured zones. The resulting system of partial differential (or integral) equations of evolution of unknown fields of temperature, moisture, displacements, etc., supplied by initial and boundary conditions, must be accompanied by a set of (algebraic or differential) constitutive relations. However, both its formal mathematical analysis and the design of robust and effective computational algorithms searching for sequences of approximate solutions contain a lot of open questions.

The quality of prediction of thermodynamic behaviour of materials and structures is conditioned by the realistic setting of material characteristics, coming from laboratory measurements and numerical simulations. Corresponding inverse mathematical problems are typically ill-posed and non-stable and require artificial regularization, as discussed in [5], p. 20; thus the careful arrangement of experiments under very special (but realistic) conditions is needed. We shall demonstrate that even the non-destructive identification of basic thermal characteristics of heat conduction for a building material specimen, macroscopically homogeneous and isotropic, is in general a serious problem, containing non-trivial mathematical considerations and iterative computational procedures. In this paper the least-square finite element technique for parabolic equations, introduced in [2], p. 367, will be applied; however, many alternative approaches can be found in the literature, referring to various optimizations methods – deterministic, evolutionary, stochastic, hybrid, etc.; their extensive overview is contained in [3] and [11].

The development of temperature in a material sample (as well as in whole building objects) is determined by the following characteristics, for simplicity (at least in some temperature range) considered as constants, required by most European standards: the material density ρ, the heat conductivity λ (which is important in terms of the material insulation ability) and the heat capacity c (characterizing material accumulation ability); alternatively $\kappa = \rho c$. Since ρ can be detected easily, the aim of the identification procedure is to set λ and c and to estimate the uncertainty of such setting. The stationary measurements of λ and c may not give

reliable results, especially if λ and c are time-variable, for building materials namely during hydration, moisture redistribution, etc. The non-stationary measurement equipments (rather expensive), respecting the dynamic thermal behaviour of materials, i.e. the evolution of temperature fields in time, use typically some sets of calibration materials. Both these approaches require the strict size and shape of the specimen and the laboratory measurement conditions, thus their applicability to non-classical materials is limited. The endeavour to develop some alternative non-stationary identification methods of λ and c, both in technical physics and in engineering branches (the frequency-domain method, the step-heating method, the hot-strip / hot-wire method, the infra-red photography approach, etc.) is documented in [1] and [4]. The primary and inexpensive measurement device, prepared at the Faculty of Civil Engineering of the Brno University of Technology, comes from the hot-wire method, supported by the non-trivial mathematical analysis and MATLAB-based computations.

Measurement Equipment

The announced equipment consists of the following parts: the thick polystyrene insulation Ω_0, two aluminium plates Ω_1 and Ω_2 and a material specimen Ω_3, whose thermal characteristics are a priori unknown. All Ω_i with $i \in \{0,1,2,3\}$ can be considered as domains in the Euclidean space R^3 with (sufficiently smooth) boundaries $\partial\Omega_i$; only the intersections of $\partial\Omega_i$ with $\partial\Omega_j$ for couples (i,j) from $\{(0,1), (0,2),(0,3), (1,2),(1,3)\}$ are nonempty, whereas $\partial\Omega_i$ with $i \in \{1,2,3\}$ (as inner interfaces) belong to $\partial\Omega_0$, containing (in addition to such interfaces) the complete outer boundary Γ_0 in R^3. The controlled heat fluxes are generated at Γ_1, a part of intersection of $\partial\Omega_1$ with $\partial\Omega_0$. The temperature is supposed to be constant outside the measurement system, thus also on Γ_0. The development of temperature in time is recorded simultaneously on Γ_1 and on Γ_2, a part of intersection of $\partial\Omega_2$ with $\partial\Omega_0$. Figure 1 shows the practical configuration of such measurement system at the Brno University of Technology (BUT) and a typical time progress of an experiment. Alternatively, e.g. for measurements at massive structures in situ, Ω_2 (with corresponding temperature sensors) can be removed.

The technical details of the original equipment of this type, built at BUT, has been described in [8]. However, its mathematical background by [9], based on the modified semi-analytical Fourier method of solution of a non-stationary heat equation, supplied by boundary conditions of both Dirichlet and Neumann types (similarly to [4]), did not allow to construct sufficiently simple, stable and efficient algorithm for the identification of λ and c; the practical computations are limited to the one-dimensional simplification. The revised approach, whose mathematical preliminaries are sketched in [10], tries to remove or pre-eliminate boundary conditions of Neumann type (as much as possible), to overcome above mentioned difficulties of the inverse analysis.
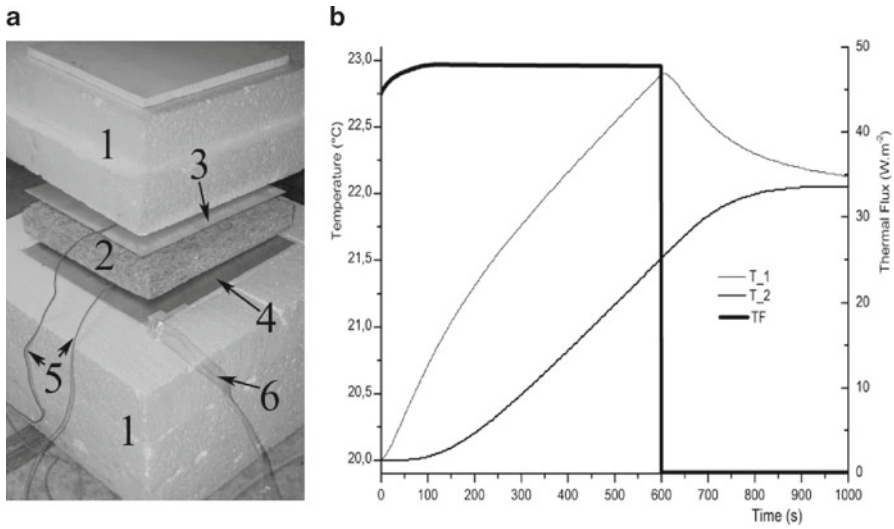
Fig. 1 (**a**) Measurement device in the Laboratory of Building Physics of BUT: 1 thermal insulation Ω_0, 2 specimen Ω_3, 3 heating plate Ω_1, 4 non-heating plate Ω_2, 5 wiring to temperature sensors, 6 wiring to heating. (**b**) Experimental porous concrete specimen: measured temperature in °C on Γ_1 (T_1) and Γ_2 (T_2), generated thermal flux in W/m² on Γ_1 (TF), both from 0 to 1000 s, heating from 0 to 600 s

Computational Support

For simplicity, following [9], let us now consider only one domain Ω in R^3 with the boundary $\partial\Omega$: on its subset Γ a Dirichlet boundary condition is prescribed for any time $t \geq 0$ in the form

$$T = T_\times$$

where the symbol $T_\times$ refers to values of temperature T recorded in time (in practice, at selected discrete times) and on the rest Θ of $\partial\Omega$ similarly a Neumann boundary condition

$$\mathrm{grad}\,T \cdot \nu = p$$

with known heat fluxes p and the outward unit normal ν to $\partial\Omega$. Introducing the notation $(.,.)$ for scalar products in the Lebesgue space $L^2(\Omega)$, analogously $\langle .,. \rangle_D$ for scalar products in $L^2(\Gamma)$ and $\langle .,. \rangle_N$ for those in $L^2(\Theta)$, the integral equation of non-stationary heat conduction, involving both boundary conditions, then reads

$$a^{-1}(\Phi, \partial T / \partial t) - B(\Phi, T) = G(\Phi) \tag{1}$$

for any Φ from the subspace of Sobolev space $W^{1,2}(\Omega)$ satisfying $\Phi=0$ on Γ. Moreover, here $a = \lambda/\kappa$, $b = 1/\lambda$ and

$$B(\Phi,T) = (div\,grad\,\Phi,T) - \langle grad\,\Phi \cdot \nu, T \rangle_N,$$

$$G(\Phi) = b\langle \Phi, p \rangle_N - \langle grad\,\Phi \cdot \nu, T_\times \rangle_D.$$

The ideal aim is to find such T in $W^{1,2}(\Omega)$ that

$$grad\,T \cdot \nu = q$$

if heat fluxes q are prescribed also on Γ. This is not a quite redundant condition because a and b, derived from λ and c, are still unknown parameters. Howewer, the realistic requirement, based on the least squares technique, is the minimization of a function

$$F(a,b) = \tfrac{1}{2}\langle bq + grad\,T(a,b)\cdot\nu, bq + grad\,T(a,b)\cdot\nu \rangle_I \qquad (2)$$

where $\langle .,. \rangle_I$ means a scalar product in the Bochner space of abstract functions $L^2(I, W^{1,2}(\Omega))$ for a finite time interval I starting from $t=0$ (in practice, its evaluation is based on the rectangular rule exploiting the discrete measurement times).

For the discretization of (1) in any time from I the Crank-Nicholson scheme is utilized. Although no explicit form of an approximate solution of (1) is available, the finite element decomposition of Ω applying cubic Hermite polynomials as basis functions enables us to evaluate (in discrete points and times) both T and grad T directly as functions of a and b; for all technical details see [9]. If Θ is empty then T in (2) depends, thanks to the missing first additive term in $G(\Phi)$ from (1), only on a, not on b, which simplifies all calculations. This can be reached also in our realistic configuration with Ω_i, $i \in \{0,1,2,3\}$, but only in the one-dimensional idealization. Having some rough estimate of a and b, we are able to minimize F from (2) using the Newton iteration algorithm. The same algorithm can be adopted, as sketched in [10], to the uncertainty analysis of identified a and b by [6] (variance-based sensitivity analysis, Sobol indices), or [11], p. 10 (probabilistic measures, Karhunen-Loève or polynomial chaos expansions) and p. 25 (Bayesian approach).

The generalization of (1), (2), etc., to a realistic geometrical measurement configuration brings some technical difficulties and formally complicated formulae, coming from the pre-elimination of interface heat fluxes from Ω_0, Ω_1 and Ω_2, but no disaster in our approach. The dependence of T on b (unlike that on a) is always linear, thus the Newton iterative solver remains effective. However, the corresponding MATLAB-based software package is still in progress. Figure 2 presents a simple numerical example, demonstrates the robustness of the iterative algorithm: even if visible differences between measured and numerically simulated heat fluxes at both Γ_1 and on Γ_2 occur, the algorithm results in the best least squares approximation due to (2).
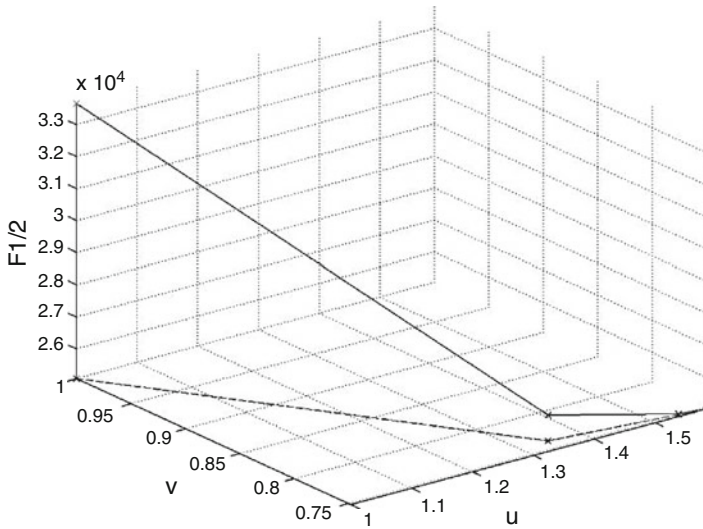
Fig. 2 Six iterative steps of least squares fitting of measured and computed heat fluxes at material interfaces for the experiment from Fig.1 b)**:** $a = 3.4 \cdot 10^{-7}\, u$ m²/s, $b = 3.5\, v$ K·m/W, initial estimate $u = v = 1$, error $F^{1/2}$ is evaluated in K·s$^{1/2}$/m by (2)

Conclusions

We have demonstrated the development of an inexpensive and robust non-destructive measurement device for basic thermal characteristics, based on the non-trivial mathematical analysis of direct and inverse heat transfer problems. The future work should pay attention namely to the uncertainty analysis and to the proper identification or suppression of influences of all physical processes active in the measurement system.

The research has been supported by the Czech research project MSM 021630511 and by the project of BUT specific research FAST-S-10-17.

References

[1] Atchonouglo, K., Banna, M, Valée, C. and Dupré, J.-C. (2008), Inverse transient heat conduction problems and identification of thermal parameters. *Heat and Mass Transfer*, vol. 45, pp. 23–29.

[2] Bochev, P.B. and Gunzburger, M.D. (2009), *Least-Squares Finite Element Methods*. Springer, New York.

[3] Colaço, M.J., Orlande, H.R.B. and Dulikravich, G.S. (2006), Inverse and optimization problems in heat transfer. *Journal of the Brazilian Society of Mechanical Sciences and Engineering*, vol. 28, pp. 1–24.

[4] Duda, P. (2003), Solution of multidimensional inverse heat conduction problem. *Heat and Mass Transfer*, vol. 40, pp. 115–122.

[5] Isakov, V. (2006), *Inverse Problems for Partial Differential Equations*. Springer, New York.

[6] Kala, Z. (2009), Sensitivity assessment of steel members under compression. *Engineering Structures*, vol. 31, pp. 1344–1348.

[7] Šťastník, S., Vala, J. and Kmínová, H. (2007), Identification of thermal technical characteristics from the measurement of non-stationary heat propagation in porous materials. *Kybernetika*, vol. 43, pp. 561–576.

[8] Šťastník, S., Vala, J. and Kmínová, H. (2006), Identification of thermal technical characteristics from the measurement of non-stationary heat propagation in porous materials. *Forum Statisticum Slovacum*, vol. 2, pp. 203–210.

[9] Vala, J. (2010), Inverse problems of heat transfer. In: *Programs and Algorithms of Numerical Mathematics*, Proceedings of 15th Seminary in Dolní Maxov (Czech Rep.). Mathematical Institute AS CR, Prague, to appear.

[10] Vala, J. (2010), Computational identification of thermal technical properties of building materials and its reliability. In*: ICNAAM 2010 – International Conference on Numerical Analysis and Applied Mathematics* in Rhodes (Greece) (Simos, T. E., Psihoyios, G. and Tsitouras, Ch., Eds.), AIP Conference Proceedings, vol. 1281, pp. 2009–2012. American Institute of Physics, Melville, New York.

[11] Zabaras, N. (2004), Inverse problems in heat transfer. In: *Handbook on Numerical Heat Transfer* (Minkowycz, W.J., Sparrow, E.M. and Murthy, J.Y., Eds.), Chap.17. Wiley, Hoboken.

Quantitative Evaluation of Thermal Diffusivity and Thickness of Mortar Cover Using Induction Thermography

T. Du, F. Brachelet, D. Defer and E. Antczak

Abstract This paper presents an inverse method used to determine the thermal diffusivity and the cover thickness of a reinforced beam. The steel reinforcement bar was heated with an induction heating device and surface temperatures were recorded with an infrared camera. Then, a numerical modelling was developed in order to simulate the surface temperature. An alternate difference implicit algorithm was used to solve the thermal transfer equation. The method was implemented in an inverse problem that leads to the identification of the thermal diffusivity and the cover thickness. A study of the sensitivity functions revealed that both parameters can be simultaneously estimated during the heating phase. The computational results are in good agreement with reference values.

Keywords Civil engineering • Concrete • Induction • Inverse method • Thermography

Introduction

Infrared thermography is a non-destructive technique widely used in NDT to detect defects in the subsurface region of materials. Active infrared techniques have been applied to civil engineering since less than 10 years with quantitative results [1]. The induction thermography is generally applied to the detection of metallic piece cracks [2] and also of CFRC broken fibres or delaminations [3]. In case of reinforced beam, induction allows to the armature heating of the beam

T. Du • F. Brachelet (✉) • D. Defer • E. Antczak
Laboratoire de Génie Civil et géo-Environnement (LGCgE), Univ Lille Nord de France,
U-Artois, FSA, Technoparc Futura, 62400 Béthune, France
e-mail: franck.brachelet@univ-artois.fr
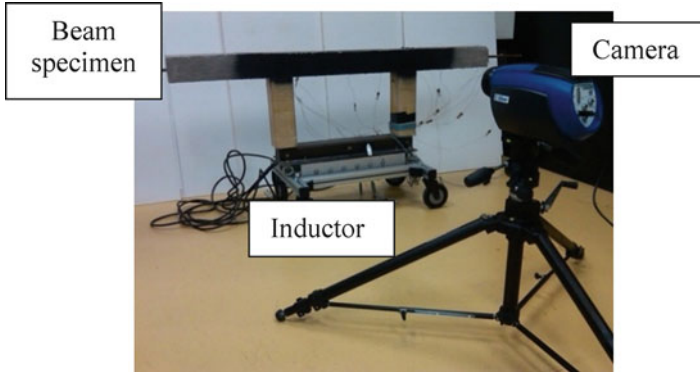
Fig. 1 Experimental set-up

without any contact. The aim of this paper is to present an active method to evaluate simultaneously thermal diffusivity and thickness of cover mortar of a beam specimen using inductive infrared thermography. The inductor supplies a square power pulse of 10 minutes duration. The diffusion of this internal dissipated heat leads to a variation of the surface temperature field which is recorded with an IR camera. Then, a numerical model is developed in order to simulate the surface temperature evolution. It is implemented in an inverse scheme that leads to both parameters identification.

Experimental Set up

The experimental set-up is shown in Fig. 1. Specimens are placed on the arms of a heating system based on an electromagnetic inductor. The IR camera is monitored by a computer. The thermograms are given by a CEDIP Silver 220 camera equipped with a 320x240 pixels InSb detector. The camera placed at a distance of 2 meters far from the system, provides a field of view of the heated area. The thermograms are recorded at a frame rate of 0.2 Hz during the warming-up and the cooling down processes during and after the induction heating.

Specimen

A 1.5 meter long mortar beam with a 0.1 meter square section has been poured. For that purpose, an ordinary mortar was designed using 450 kg/m3 of Portland

cement CEM II 32,5R and 350 kg/m3 of 0/5 mm siliceous sand with a 0.55 W/C. A 12mm diameter metallic bar, coaxial with the beam longitudinal axis was inserted as reinforcement. The mortar has been used in this first study because of its homogeneity.

Heating unit

The main advantage of the inductive heating is to be a non-contacting method. The metallic parts to be heated do not need to be connected with wires to an electric generator. The inductor has a U shape and is made with resonant LC circuit tuned at a 50 Hz frequency. The inductor coils generates a magnetic field which is closed by the metallic bar of the beam.

Numerical Method

Numerical modelling

The temperature evolution can be obtained by solving the fundamental equation [4]:

$$\frac{\partial^2 T(x,y,t)}{\partial x^2} + \frac{\partial^2 T(x,y,t)}{\partial y^2} + \frac{1}{k} g(x,y,t) = \frac{1}{\alpha} \frac{\partial T(x,y,t)}{\partial t} \tag{1}$$

Where T is the time dependent temperature at each location. k is the thermal conductivity [W.m^{-1}.K^{-1}]. g(x,y,t) is the rate of heat generation per unit volume [W.m^{-3}] and over time. α is the thermal diffusivity [m^2.s^{-1}]. It's defined as being the ratio of thermal conductivity to volumetric heat capacity (ρC_p).

In order to solve equation (1) a modelling of the beam is realised. ADI (Alternate Difference Implicit) method has been chosen. This method is assumed to be stable and substantially computer cost savings [5]. A 2D simulation of the heat transfer within the section of the beam has been carried out. Due to the two symmetry axis of the beam section only a quarter can be meshed. A schematic drawing of the meshed section of the beam is shown Fig. 2. The number of elements in the mesh is 50x50.

The modelling is completed by two kinds of boundary conditions (i.e. convection heat losses with the external environment and adiabatic conditions at the symmetry planes) see Fig. 2.

The thermophysical properties are allocated to the following domains :

For x ≤ a and y ≤ a, $\lambda=\lambda_{steel}$ and $\alpha=\alpha_{steel}$
For a < x and a < y, $\lambda=\lambda_{mortar}$ and $\alpha=\alpha_{mortar}$

Table 1 Thermophysical properties of materials used for numerical simulations

	Density [kg.m^{-3}]	λ [W.m^{-1}.K^{-1}]	C_p [J.kg^{-1}.K^{-1}]	α [m^2.s^{-1}]
Mortar	2300	1.67	800	9.07 x 10^{-7}
Rebar	7900	54	440	1.55 x 10^{-5}
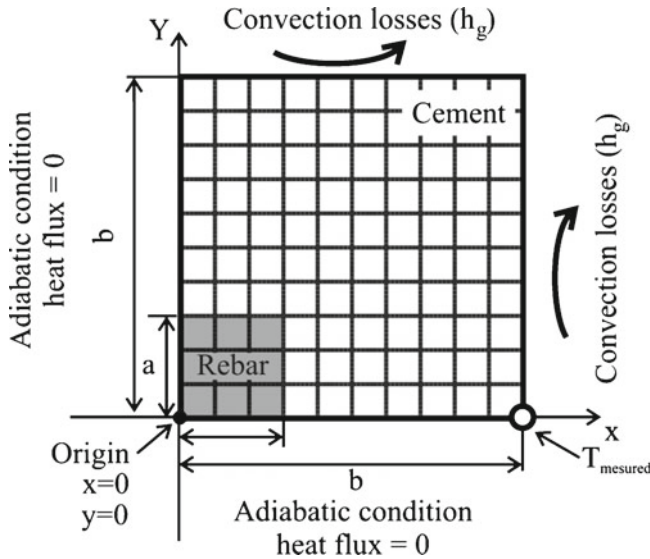
Fig. 2 Diagram of the meshing associated with the ADI method

The temperature initial condition is defined as follows:

$$\text{at } t=0s; T(x,y,0)=T_0$$

where T_0 is the ambiant temperature.

During the simulation, the heat dissipation waveform is a square pulse of unity amplitude. Due to the induction process, the real value of the dissipated power is complicated to evaluate. It is the reason why we use the linearity of thermal transfer by considering surface normalized temperature.

Inverse procedure

The first step of the inversion procedure consists in the calculation of the beam surface temperatures. Then, the simulated normalized temperature ($T_{simulated}$) is compared to the normalized experimental value measured with the infrared camera ($T_{measured}$). A error function f is expressed as being the root mean square error between measured and simulated normalized temperatures. In this case, the inversion
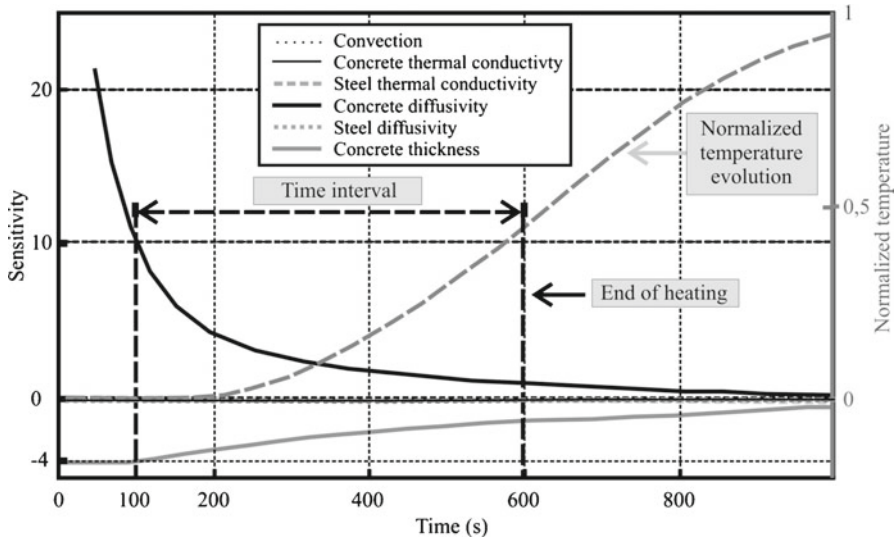
Fig. 3 Temperature sensitivity to parameter functions

procedure is an optimization process that leads to the identification of a set of parameters which allows to minimize the following function (3).

$$f\left(p_1, p_2, \cdots,\right) = \sqrt{\frac{1}{N} \sum_{i=1}^{N} \left(T_{measured}^{i} - T_{simulated}^{i}\right)^2} \rightarrow Min \tag{2}$$

The normalized temperature is a non linear function of the unknown parameters. Here, the minimization is performed using the Nelder-Mead iterative method [6].

Sensitivity study

A sensitivity study has been performed. Its purpose was to define the influence of each system parameter and to optimise the choice of the time interval to be retained for identification goal. The surface temperature sensitivity function $X_{pi}(t)$ to the parameter pi is obtained using the relation :

$$X_p(t) = \frac{\partial T(p_1, p_2, \ldots, p_n, t) / T(p_1, p_2, \ldots, p_n, t)}{\partial p_i / p_i} \tag{3}$$

Here $p_i = h_g$, λ_{mortar}, λ_{steel}, α_{mortar}, α_{steel}, and cover thickness "e"

Figure 3 shows the evolutions of temperature sensitivity functions for the first 1000s of the experimentation. Their comparative study and a complementary parameter correlation analysis inform that the thermal diffusivity and the cement thickness
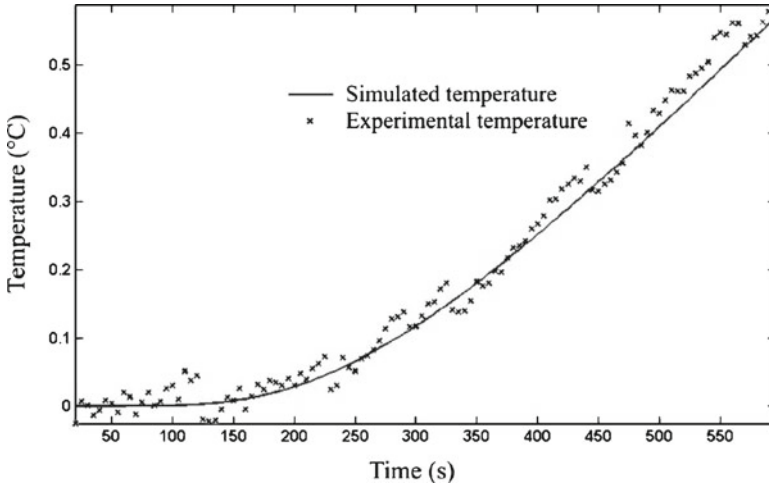
Fig. 4 Optimized and measured normalized temperatures

can be simultaneously estimated during the surface heating up phase. Thus, the [100-600s] time interval was held for this purpose.

Results and Discussion

Figure 4 shows the normalized evolution of the temperature at a point situated on the longitudinal axis of the beam surface. The simulated temperature after optimization process is superimposed. A good agreement can be observed. In this test, the thermal diffusivity and the thickness of the mortar cover are respectively $\alpha = 7.1 \times 10^{-7}$ m².s^{-1} and e= 41.8 mm. The same procedure was 10 times repeated on adjacent points of the beam axis. The mean value for the estimated thermal diffusivity is $\alpha = 7.08 \times 10^{-7}$ m².s^{-1} and the corresponding variation coefficient is 2.5%. The reference value of this parameter is $\alpha = 7.30 \times 10^{-7}$ m².s^{-1}. It has been evaluated in parallel with an improved method. The cover mortar thickness mean value is 41.3mm. In this case, the variation coefficient is less than 2%. It is in a good agreement with the theoretical value (44.0mm) if we take into account the location rebar uncertainty.

Conclusion

An inversion procedure has been carried out in order to simultaneously determine the thickness of cover mortar and its thermal diffusivity. This method is based on a finite differences modelling of a quarter of the section beam. Comparison between

experimental results and reference values shows good agreement. Further tests on concrete beams will be carried out soon. These first studies led in a laboratory should be applied to others geometries such as those encountered in civil engineering works. In future works, the thermal diffusivity variations could be correlated with the quality of concrete or pathologies.

References

[1] Wiggenhauser, H. (2002). In: *Active IR-applications in civil engineering*, Infrared Physics & Technology, Vol. 43, p. 233–238.
[2] Ostwald-Tranta, B. (2004). In: *Thermoinductive investigations of magnetic materials for surface cracks*, QIRT Journal, Vol. 1, p. 33–46.
[3] Riegert, G., Zweschper, Th., Busse, G. (2005). In: *Eddy-current lockin-thermography: method and its potential*, Journal of Physics. IV France Vol. 125, p. 587–591
[4] Necati Özişik, M. (1993). In: *Heat conduction*, 2nd Ed., Wiley, New-York.
[5] Mitchell, A., Griffith, D. F. (1980). In: *The finite difference method in partial differential equations*, p. 59–10, (Ed), John Wiley & Sons, New-York.
[6] Nelder, J., Mead, R. (1965). In: *A simplex method for function minimization*, Computer Journal, vol. 7, n 4, p. 308–313.

Three NDT Methods for the Assessment of the Concrete Permeability as a Measure of Durability

J. Adámek, V. Juranková, Z. Kadlecová and M. Stehlík

Abstract This contribution deals with the extensive measurements of the air permeability using TPT (Torrent Permeability Tester), of the water permeability by GWT (German Water Tester) and ISAT (Initial Surface Absorption Test) methods. The measurements were complemented with the determination of compressive strength. By the combination of these methods and their evaluations, it is possible to obtain the data enabling an assessment of the concrete cover quality from the viewpoint of durability on the high level of relevance.

Keywords Covercrete • Durability • Gas and liquid permeability • Pore structure

Introduction

In the last decades, the professional community has been increasingly concerned with the degradation of concrete due to the effects of harmful substances in the air, chemical substances and climatic conditions on the reinforced or prestressed concrete structures. The mentioned impact of these and a number of other influences will manifest themselves in deterioration of the surface layer after some time. The surface layer becomes a passage for the substances causing degradation of the structure. The degradation manifests itself by changing of a porous structure

J. Adámek (✉) • Z. Kadlecová • M. Stehlík
BUT, Faculty of Civil Engineering, Institute of Building Testing, Veveří 95,
602 00 Brno, Czech Republic
e-mail: adamek.j@fce.vutbr.cz

V. Juranková
BUT, Faculty of Civil Engineering, Institute of Physic, Veveří 95,
602 00 Brno, Czech Republic

of this layer, primarily causing the development of micro-cracks and later also of macro-cracks that enable the penetration of degrading substances to reinforcing steel. A number of experts agreed on the fact that the current state of the pores and cracks in the surface layer is best represented by its permeability. For measurements and evaluation of the air and water permeability various instruments were used [1]. At the Institute of Building Testing of the Faculty of Civil Engineering, BUT Brno, for more than six years there have been used a Torrent device (TPT) [2] for air permeability test, and a GWT device of the Danish company German to measure water permeability. The tests are supplemented with the Initial Surface Absorption Test, ISAT, [3] standardized in the British Standard BS 1881-208.

Experimental Procedures

Materials

A concrete mixture was composed of cement CEM I 42.5 R (430 kg), sand 0/8 mm (860 kg) and coarse aggregates 8/16 mm (910 kg). Water was dosed so the workability of fresh concrete measured by a slump test reached the value of S3 according to the Czech Code ČSN EN 206-1. Volume density of fresh concrete was 2350 kg/m^3, concrete C40/45.

Manufacturing and curing of specimens

For the tests were manufactured following specimens: cubes 150/150/150 mm, cylinders Ø 150/300 mm, prisms 100/100/400 mm and tiles 300/300/80 mm. These specimens were made for various times of actual hydration at lengths of 2, 3, 14, 28 to 90 days. Before each measurement and potentially also after it, the actual moisture content was measured with a capacity hygrometer and the specimens were also weighed. On the cubes and cylinders the volume weight and compression strength were determined in the defined times.

Research significance

The purpose of the experimental works was to obtain data about how the limited time of hydration would influence the monitored characteristics of concrete. After one day of setting and hardening in the forms covered with a sheet, the test specimens were dismantled and the hardening continued under normal laboratory conditions. It was expected that the limited time for the formation of hydration products would effect the development of the porous structures of the specimens and thus also the properties of concretes. After the defined time the prisms and tiles were given into a oven of

105°C temperature for 48 hours. After removal, the specimens were left in the laboratory condition for 2 hours, weighed and then the defined properties were tested.

It was supposed that in the hot environment without moisture, the process of hydration would almost stop and the porous structure formed until then would not basically change.

Measuring Devices

Air permeability

Air permeability was measured by a device Torrent Permeability Tester (TPT) - Fig. 1. The test consists in measuring the flow of air into the inner chamber of the TPT device. The device works in connection with the vacuum pump and creates vacuum in the specimen. The basic features of the device are a two-chamber vacuum cell and a pressure regulator that provide the air flow into the inner chamber oriented perpendicularly to the surface of the tested structure. The result of the measurement is the coefficient of air permeability k_T. 10^{-16} expressed in m². The quality class of the concrete cover from the viewpoint of durability is given in Table 1 [2].
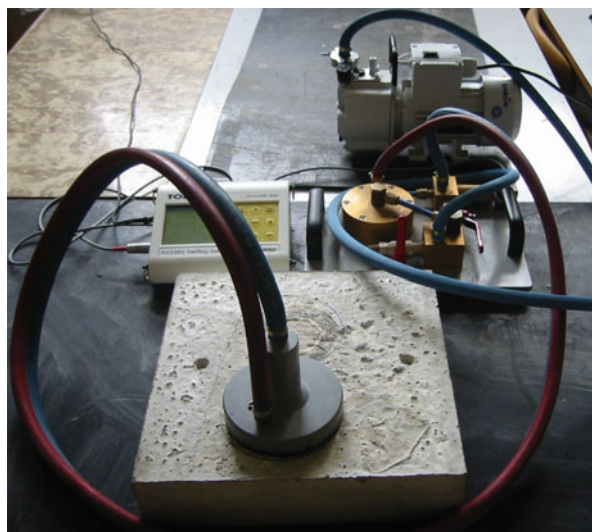
Fig. 1 Scheme of TPT device

Table 1 Classification of concrete cover [2]

Quality of covercrete	Index	k_T [10^{-16} m²]
Very bad	5	>10
Bad	4	1.0–10
Mid	3	0.1–1.0
Good	2	0.01–0.1
Very Good	1	<0.01

Water permeability

Water permeability was determined by a device GWT, which measures the amount of water absorbed by a defined surface using pressure water with an overpressure of 0.2 bar, Fig. 3 [3]. The volume of absorbed water is compensated, at the determined intervals, by the same volume of a steel spike inserted into the measuring chamber with water. Thus, a permanent water overpressure is maintained in the chamber. The test ends by taking out the whole spike and recording the time necessary for taking the spike out. On the basis of the Darcy's law, the permeability coefficient k_{LD} in mm/s was calculated and subsequently the coefficient of internal permeability k_I. 10^{-16} in m^2 was determined. The value of internal permeability of the concrete cover hereby calculated is considered, in the professional literature and in a number of European standards, as one of the basic criteria for the evaluation of concrete durability.

Initial surface absorption tester

The test is based on a similar principle as the GWT method. The concrete surface of the specimen is wetted by pressure water with an overpressure of 0.2 bar through a defined area of the chamber. The amount of water absorbed by the surface is measured after 10, 30 and 60 minutes in a gauged capillary tube placed in a horizontal position 0.2 m above the measuring chamber level (Fig. 5). The volume of water is expressed in $ml/m^2/s$ and the classification is given in Table 1.

Results

Air permeability

The values of the air permeability coefficients k_T measured in the tested time periods are shown in Fig. 2. The measurements were performed on the top surfaces of the tiles and subsequently on their bottoms. The differences were negligible. All the measurements were done after the drying up the tiles at 105 °C and subsequent tempering at 20–22 °C for two hours. Concretes older than 14 days showed almost consistent values of the coefficient k_T. The higher-order value of the air permeability coefficient of the concrete whose hydration was interrupted after 48 hours by placing the tiles in an oven is probably caused by the lack of water in the developing system of pores. Since every particles of cement are not hydrated, the porous structure is more permeable to air. The character of the pores will be different when compare with the pores of a substantially better and longer hydrated concrete.
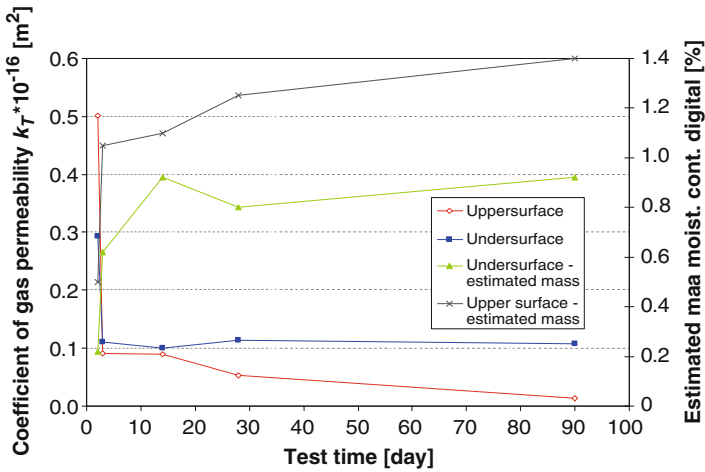
Fig. 2 Results of TPT

Fig. 3 Device GWT

Water permeability

Figure 4 shows the dependence of the water permeability coefficient on the period of concrete maturing. The course of the dependence demonstrates that also in this case the coefficients k_l were different. The difference of the porous structure manifested
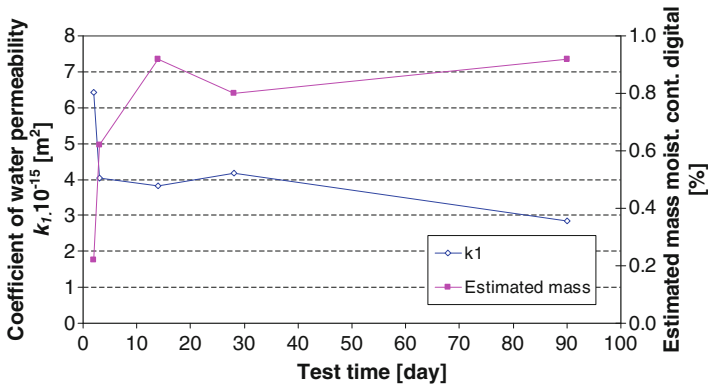
Fig. 4 Results of GWT test

Fig. 5 Device ISAT
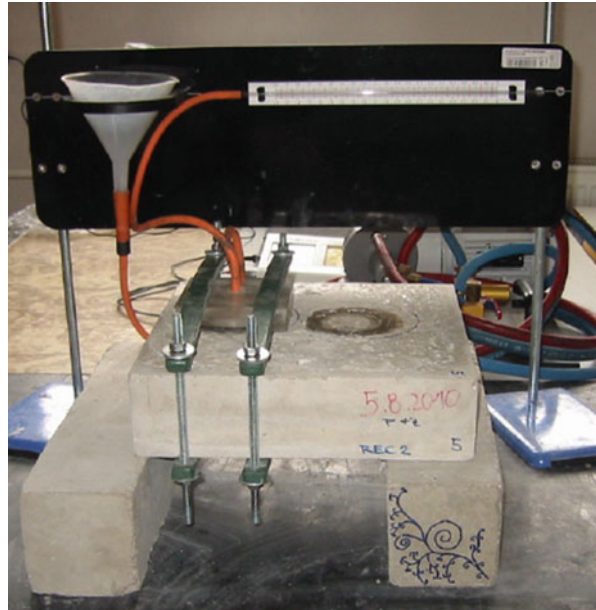
itself in the higher values of the water permeability coefficient in concretes with the interrupted hydration. However, the differences are smaller than in the tests of air permeability using TPT, since this method is of less sensitivity. In connection with durability, it is possible to apply the German standard DIN 1045 for concrete structures, which considers only the concretes with the internal permeability k_1 lower than 1.10^{-16} m2 as durable.
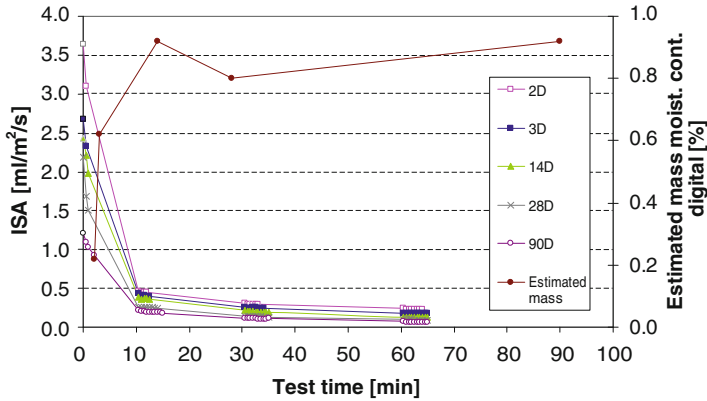
Fig. 6 Results of ISAT test

Initial surface absorption

Figure 6 shows the dependence of the amount of absorbed water on the age of evaluated concrete. The dependence trend is largely similar to the behaviour of similar dependences in the TPT and GWT tests. Table 2 shows the values of water absorption according to Levitt in the form of ISAT values and the depths of minimum reinforcement cover for an exposure of 10, 25 and 50 years, depending on the climatic conditions.

Conclusion

The presented results of air and water permeability tests (see Table 3) have proved that the water sufficiency for hydration is crucial especially in the initial stage. All the three permeability tests proved that during the setting and hardening of concrete, different porous structures with the pores of various sizes were probably developed. The TPT method proved to be the most competent because of its high sensitivity of the measurements. It was demonstrated by the intense decreasing of the coefficient k_T (Fig. 2). With the help of Table 1 it is possible to estimate the resistance of the concrete cover against the degrading effects. The size, distribution and overall volume of the pores were determined on tested concretes together with the permeability tests. The pores were evaluated by "spacing factor" method. A significant part at the permeability determination is the actual water content in the pores of concrete cover. The more the water evaporates, the higher values of permeability are measured. At present, a model for transformation of the measured values to the contractual moisture weight 3% is designed. This moisture is mostly typical at measurements "in situ".

Table 2 Classification of concrete cover by the ISAT method [4]

ISAT [ml/m²/s]			Depth of cover in mm for years to corrosion onset								
Time from start of test			10 years			25 years			50 years		
10 min	30 min	60 min	Severe	Moderate	Mild	Severe	Moderate	Mild	Severe	Moderate	Mild
0.5 ~ 0.25	0.35 ~ 0.17	0.2 ~ 0.10	10	7	5	18	15	12	25 (40*)	20 (30*)	15 (15*)
<0.25	<0.17	<0.10	6	5	4	9	7	5	12 (25*)	10 (20*)	7 (15*)

Table 3 Results of TPT, GWT and ISAT

	KAKASO			TPT				GWT		ISAT		
	KAKASO data digital	Estm ated mass moist. cont. digital		Coefficient of permeability k_T	Depth of vacuum penetration L	Conversion of k_{T3} to 3 % humdity	Quality of covering layer of concrete	Coefficient of int. permeability k_T	Acc. to DIN 1045 durable concrete?			
Age										10 min.	30 min.	60 min.
[day]	–	[%]		$*10^{-16}$ m²	[mm]	$*10^{-16}$ m²		[m²]	$k_1 < 1.0*10^{-16}$ m²	[ml/m²/s]		
2	40	0.22		5.509	97	0.502	4-bad	6.435E-15	NO	0.54	0.41	0.27
3	56	0.62		0.709	48	0.092	3-mid	4.048E-15	NO	0.41	0.19	0.17
14	69	0.92		0.534	48	0.089	3-mid	3.831E-15	NO	0.42	0.23	0.14
28	66	0.80		0.254	39	0.053	3-mid	4.185E-15	NO	0.32	0.18	0.11
90	69	0.92		0.062	19	0.014	2-good	2.858E-15	NO	0.20	0.11	0.07

References

[1] RILEM TC-116-PCD (1999), *Permeability of Concrete as a Criterion of its Durability*, Final Report, *Material and Structures*, 32, pp. 163–173.

[2] Torrent, R.J., (1992), *A Two-Chamber Vacuum Cell for Measuring the Coefficient of Permeability to Air of the Concrete Cover on Site, Materials and Structures*, 25, p. 358–365.

[3] *GWT-4000, Instruction and Maintenance Manual*, (1996), Hermann Instruments A/S, Denmark.

[4] Levitt, M., (1971), *The ISAT – A-Non-Destructive Test for the Durability of Concrete*, British Journal of N.D.T., p. 106–112.

[5] RILEM Report 40, (2007), *Non-Destructive Evaluation of the Penetrability and Thickness of the Concrete Cover*, ed. R. Torrent and L. F. Luco.

Use of Dynamic Modulus of Elasticity to Assess the Durability of Self Consolidating Concrete

N.G. Özerkan and İ.Ö. Yaman

Abstract This paper presents the effect of freezing-thawing on self consolidating concrete (SCC) that contains different percentages of fly ash (FA) and air entraining agents (AEA). The effect of freezing-thawing on concrete is assessed on the basis of the change in the dynamic modulus of elasticity. The dynamic modulus of elasticity is determined from both ultrasonic pulse velocity and resonant frequency tests. An in-house resonant frequency test apparatus was developed using an accelerometer and a data acquisition system. During the development of the test apparatus, structural eigenvalue analysis was also utilized to understand if the correct modal frequency of cylindrical test specimens is detected or not. The dynamic modulus of elasticity is then used to compute the durability factor of SCC specimens that are subjected to freezing-thawing cycles. The relationship between durability factor – FA – AEA content was evaluated, and the highest degree of reduction in durability factor was observed at mixes including maximum FA content, and no AEA and maximum AEA content. Furthermore, when FA was used in the range of certain limits, it was observed that SCC specimens were resistant to freezing-thawing cycles.

Keywords Air entraining agent • Dynamic modulus of elasticity • Fly ash • Freeze-thaw • Self consolidating concrete

N.G. Özerkan (✉)
Qatar University, Doha, Qatar
e-mail: gozde_ozerkan@yahoo.com

İ.Ö. Yaman
Middle East Technical University, Ankara, Turkey

Introduction

Self consolidated concrete (SCC) can be placed and compacted under its own weight with little or no vibration effort [1]. The main reasons for the employment of SCC and the advantages of SCC are; improving the durability of concrete, reducing the construction time and labor cost, eliminating the need for vibration, reducing the noise pollution, improving the filling capacity of high congested structural members and facilitating constructability and ensurance good structural performance [2, 3]. Although significant amount of research has been carried out regarding the fresh properties, mix design, placing methods and strength of various SCC mixes, only very limited amount of work has been done to assess the durability performance of SCC. [4–9]. By observing the reduction in its permeability, those studies have postulated that SCC has better durability properties [2, 10]. When concrete is subjected to the freezing-thawing cycles which are one of the most major durability problems, and if it is in saturated condition, those cycles lead to expansion of the water in the capillary pores of concrete and cause great internal stresses, causing a reduction in its durability. The effect of freezing-thawing on concrete is assessed on the basis of the change in the dynamic modulus of elasticity and durability factor.

The objectives of this paper were to develop a tool to determine the resonant frequency of concrete specimens which is used to non-destructively evaluate the freeze-thaw durability of concrete, and to evaluate the effectiveness of the content of the fly ash and the air entraining admixtures in the freeze-thaw durability of self consolidating concrete.

Experimental Program

Materials

Throughout the study, in all mixtures a normal Portland cement CEM I 42.5R (PC), which correspond to ASTM Type I cement and low lime fly ash (FA) was used. Crushed limestone was used as for the fine and coarse aggregate. Two types of coarse aggregate had specific gravity of 2.68 and water absorption of 0.42% and 0.52%, respectively. The fine aggregate had a specific gravity of 2.67 and water absorption of 0.75%. In all concrete mixtures, a polycarboxylic-ether type super-plasticizer with a specific gravity of 1.09 and an air entraining admixture with a specific gravity of 1.02 and pH of 10 was also used.

Mixture proportions

Within the scope of the experimental program, ten concrete mixtures were prepared. The control mixture included only the Portland cement as a binder, and named as AE0-FA0 which means that there is no air entraining agent and fly ash. The remaining

mixtures had different fly ash contents of 15%, 30% and 45% by weight of PC. For all the mixtures, the total amount of cementitious material (PC+FA) and super-plasticizer (SP) content (1.3% of cementitious materials by weight) were kept constant. However, the air entraining agent (AE) changed from 0.08% to 0.30%. As the FA and air entraining admixture interaction affected the amount of air entrainment, three levels of air entrainment were considered (none, moderate and max) defined according to added air entraining agent. According to this classification mixtures 1-4 are classified as none AE, mixtures 6, 7 and 9 are classified as moderate AE, and mixtures 5, 8 and 10 are classified as maximum AE mixes. Since the SCC characteristics such as slump flow diameter, V-funnel time were expected to be obtained, water was gradually added to the mixtures and therefore the water to cementitious ratio (w/cm) was not kept constant and changed from 0.27 to 0.33.

Freezing-thawing test

In this study, the SCC cylinder specimens were freezed and thawed in air and the temperature of the specimens was lowered from 4 to -18 °C and raised from -18 to 4 °C in 3 hours by using the climate test cabinet. The concrete specimens were removed from the cabinet at each 30 cycle to determine the relative dynamic modulus of elasticity by using the resonant frequency method. The test was continued until the relative dynamic modulus of elasticity values of the specimens reached 60% of the initial modulus or 700 cycles whichever was reached first.

In order to determine the resonant frequency of concrete specimens, a tool was developed following ASTM C 215 [11]. In the test, the accelerometer was installed to the cylinder concrete specimen with silicone coating and attached to the data acquisition system. A small diameter steel ball was used as the impact source in the test. The ball was hit onto the top surface of a cylindrical specimen, and the accelerometer measured the vertical motion. According to this setup, the data were recorded from the data acquisition system and both the amplitude-time and amplitude-frequency graphs were obtained. From the amplitude-frequency graph, the peak value which shows the resonant frequency value of the concrete specimen was obtained.

Results and Discussion

In this study, the resistance of SCC specimens to freezing-thawing was evaluated through traditional freezing-thawing test. Traditional freezing-thawing test depends on computing the durability factor obtained by measuring the resonant frequency values of the specimens from the amplitude-frequency graph. The dynamic modulus of elasticity of each concrete specimen was calculated at initial condition, and for each 30 freezing-thawing cycles. In Fig. 1, resonant frequency values of each mix for each 30 freezing-thawing cycles are given. As seen from the figure, for those
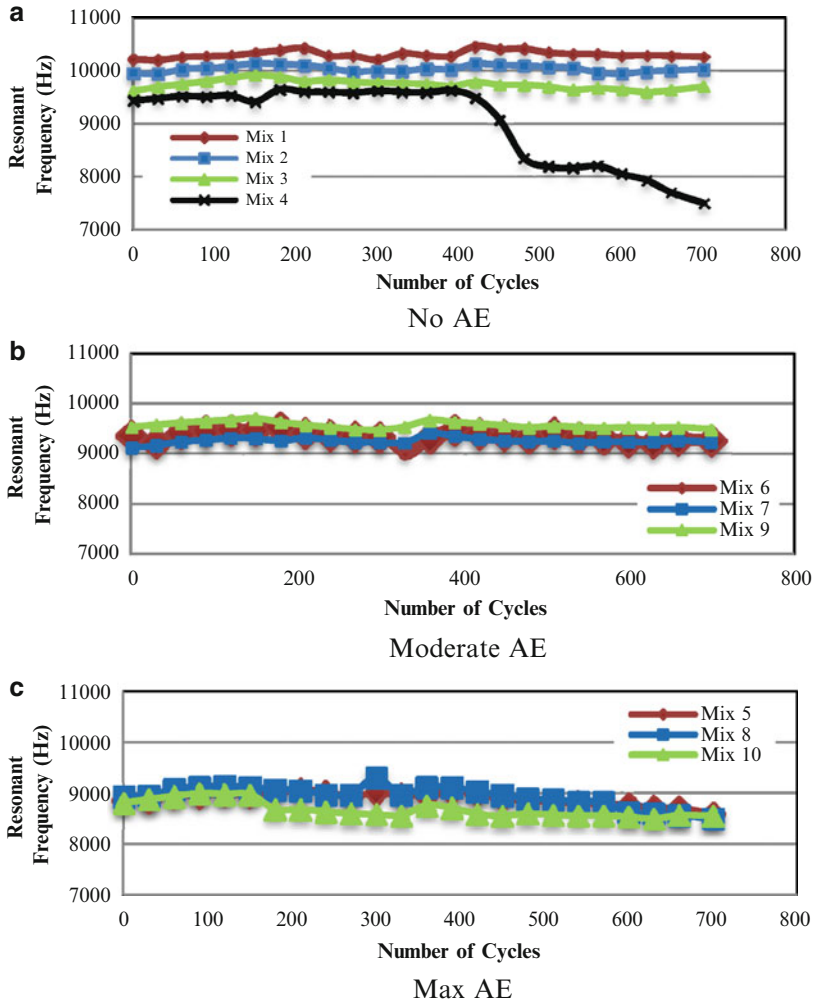
Fig. 1 Resonant Frequency Test Results

mixes that do not contain any air-entrainment the initial resonant frequency values are higher. As the air-entrainment level is increased there is a reduction in the initial resonant frequency of the concrete simply because of the increase in the porosity leading to a decrease in the modulus of elasticity. Moreover, except for the mix that does not contain any air entrainment and maximum amount of fly ash, most of the mixes are resistant to freezing and thawing cycles.

The durability factor was computed using the resonant frequency values of the specimens according to the following equation proposed by ASTM C 666 [12].

$$DF = \frac{PN}{M} \qquad (1)$$
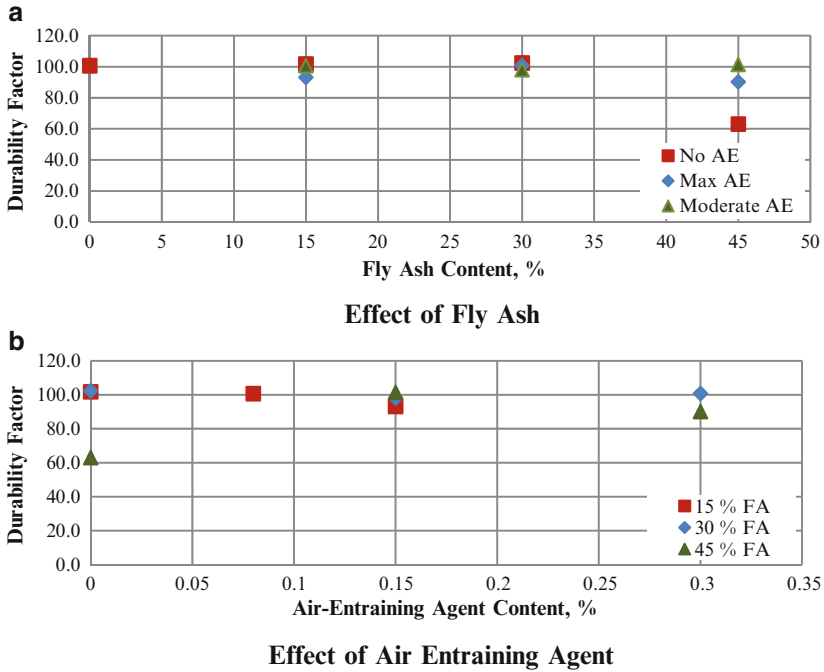
Fig. 2 The Relationship between Durability Factor and Fly Ash and Air Entraining Agent

where *DF* is the durability factor, *P* is relative dynamic modulus of elasticity at *N* cycles in % (measured at each 30 cycles), and *M* is specified number of cycles at which the exposure is to be terminated and in this study, *M* was chosen as 700 since freezing-thawing test was conducted to 700 cycles.

The relationship between durability factor and fly ash and air entraining agent content was also evaluated and it is given in Fig. 2a, b), respectively. As seen from the figure, the highest degree of reduction in durability factor was observed at mixes including maximum fly ash content, and no air entraining agent and maximum air entraining agent content. Furthermore, when fly ash was used in the range of certain limits, it was observed that SCC specimens were resistant to the freezing-thawing.

Conclusion

In this study, the effectiveness of fly ash and air entraining admixtures in the freeze-thaw resistance of self consolidating concrete was evaluated and for this purpose, durability factor of each mix was computed.

At the end of the study;

- An increase in the fly ash content decreased the effect of air entraining agent due to the unburned carbon contained in the fly ash since the unburned carbon absorbs a portion of the air entraining agent, which limits its ability for producing the needed stable air bubbles.
- The highest degree of reduction in durability factor was observed for mixes including maximum fly ash content and no air entraining agent because of the lack of a sufficient air void system and a weak microstructure before the start of freeze-thaw cycles. Additionally, when fly ash was used in the range of certain limits, it was observed that SCC specimens were resistant to the freezing-thawing cycles because of the lowered permeability properties.

References

[1] Okamura, H. and Ouchi, M. (2003), *Self compacting concrete*, Journal of Advanced Technology, Concrete Institute, Osaka, Japan, vol. 1, pp. 5–15.
[2] Kodama, Y. (1997), *Current condition of self-compaction concrete*, Cement Shimbun, Tokyo. Japan.
[3] Lachemi, M. and Bouzoubaa, N. (2001), *Self-compacting concrete incorporating high volumes of class F fly ash preliminary results*, Cement and Concrete Research, vol. 31, pp. 413–420.
[4] Ramachandran, V.S. and Beaudoin, J.J. (2001), *Handbook of analytical techniques in concrete science and technology*, Noyes Publications, New Jersey, USA.
[5] Mehta, P.K. and Monteiro, P.J.M. (1997), *Microstructure, properties and materials*, Indian Ed., Indian Concrete Institute, Chennai.
[6] Erdogan, T.Y. (2003), *Beton*, METU Press, Ankara. Turkey
[7] Basheer, L., Kropp, J. and Cleland, D.J. (2001), *Assessment of the durability of concert from its permeation properties: a review*, Construction and Building Materials, vol. 15, pp. 93–103.
[8] Zhu, W. and Bartos, P.J.M. (2002), *Permeation properties of self-compacted concrete*, Cement and Concrete Research, vol. 33, pp. 921–926.
[9] Sahmaran, M. (2006), *Self-compacting concrete with high volumes of fly ash*, PhD. Thesis, Department of Civil Engineering, METU, Ankara, Turkey.
[10] Yahia, A., Tanimura, A., Shimabukuro, A. and Shimoyama, Y. (1999), *Effect of rheological parameters on self compactibility of concrete containing various mineral admixtures*, Proceedings of the First RILEM International Symposium on self-compacting concrete, pp. 523–535, Stockholm.
[11] ASTM C 215 (2002), *Standard test method for Fundamental Transverse, Longitudinal and Torsional resonant frequencies of concrete specimens*, Annual Book of ASTM standards.
[12] ASTM C 666 (2002), *Standard test method for Resistance of concrete to rapid freezing and thawing*, Annual Book of ASTM standards.

Effect of Concrete Mixtures on Estimation of Porosity by Ultrasonic Velocity

A. Benouis and A. Grini

Abstract The most used measurement is undoubtedly the measurement of porosity accessible to water. The relationship between concrete mixtures, porosity and ultrasonic velocity of concrete samples measured by ultrasonic NDT is investigated. This experimental study is interested in the relations between the ultrasonic velocity measured by transducers of 49.5mm [1,98in.] diameter and with 54 kHz frequency. Concrete specimens (160 mm [6,3in.] diameter and 320 mm [12,6in.] height) are fabricated with concrete of seven different mixtures (various W/C and G/S ratios), which gave porosities varying between 7% and 16%. Ultrasonic velocities in concrete were measured in longitudinal direction. Finally the results showed the influence of ratio W/C, where the porosity of the concretes of a ratio W/C ≥ 0,5 have correctly estimated by ultrasonic velocity. The integration of the concretes of a lower ratio, in this relation, caused a great dispersion. Porosity estimation of concretes with a ratio W/C lower than 0,5 became specific to each ratio.

Keywords Admixture • Concrete • Correlation • Porosity • Ultrasound

Introduction

It is indicated that the ultrasonic velocity decreases and ultrasonic attenuation increases as porosity increases [1]. Hernandez et al. [2] have obtained evaluations of porosity by non destructive tests. Their evaluation is based on the micromechanical model established by Jeong and Hsu [3]. However, this model requires many

A. Benouis (✉) • A. Grini
Civil Eng. and Hydraulic Laboratory LGCH, University of Guelma, Algeria
e-mail: benouis_h@yahoo.fr

parameters, which can be unknown and the precision would require knowledge of the granulometry. Marc Goueygou [4] has also worked to connect the ultrasonic properties to the porosity and the permeability of the mortars. This study showed the difficulty to obtain precise evaluations of the ultrasonic parameters, caused by the variability of studied materials. This work focuses in measure porosity on seven concretes of different mixtures (water/cement W/C, gravels/sand G/S) to establish the influence of mixture on porosity and thereafter on the ultrasonic velocity in the concrete. Consequently to estimate concretes porosity.

Materials and Experimentation

Concrete's mixtures

The materials used for the different concretes are:

- a silicocalcareous sand rolled SCr. (0/4mm),
- two gravels crushed lime stones CC (5/15mm and 15/25mm)
- two rolled silicocalcareous gravels SCr. (5/15mm and 15/25mm)
- cement CEM II-A 42.5

Seven compositions of concrete are used in this study (table 1), while varying the gravels/sand ratios (G/S) and water/cement (W/C). The tests were carried out on cylindrical samples 16/32 [5] after curing in water for 28 days.

Measurement of ultrasonic velocities

Ultrasonic velocities were measured by an ultrasonic tester 58-E0048 (Controls mark) including transducers of 54 kHz frequency and diameter D=49.5 mm [6].

Measurement of porosity

The most-commonly used method for characterization is undoubtedly the measurement of porosity accessible to water. This simple method is used for a variety of mortar, cements pastes or concrete and is considered as the base of any microstructural characterization or evaluation of the durability properties of a material. Porosities were determined according to the procedure recommended by the AFREM [7].

Table 1 Compositions of the concretes

Concrete Composition (kg/m³)	B1	B2	B3	B4	B5	B6	B7
Sand	500	750	1000	617.31	539.39	500	500
Gravel 5/15 Cc	232	307	130	275.42	508.70	---	307
Gravel 15/25 Cc	928	613	520	899.74	524.57	---	613
Gravel 5/15 SCr	---	---	---	---	---	307	---
Gravel 15/25 SCr	---	---	---	---	---	613	---
Cement	440	440	440	350	350	440	440
Water	186	186	186	212.12	221.51	220	220
G/S	1.32	1.22	0.65	1.90	1.91	1.84	1.84
W/C	0.42	0.42	0.42	0.60	0.63	0.50	0.50
A/C	3.77	3.79	3.75	5.12	4.49	3.22	3.22
f_{c28} (MPa)	32.64±3	33.16±3.1	26.20±1.1	27.55±1.7	26.24±1.3	20.47±2.1	32.07±2.2

Results and Discussion

Ultrasonic velocities

The length of the course is thus 320 mm (sample's length) and transverse dimension is 160 mm, this is higher than the minimum value required by the standard [8]. The ultrasonic velocities were determined by measurements of the course time for a series of three samples for each mixture (Table 2). The samples remained in water until complete saturation with 20°C. That avoids the dispersion of the results caused by the variation of samples hygrometry.

Figure 1a represents the evolution of the ultrasonic velocity with ratio G/S. One may observe that this relation is very uncertain (V=172.76 G/S+ 3212.3, R^2 =0.07). The fact of considering only the concretes with a same ratio W/C led to precise this relation (V=955,28 G/S+ 2448.9, R^2 =0.85) (Fig. 1b). It can be make the same comment for the evolution of velocity with ratio W/C (Fig. 2a). The relation is precise for concretes presenting very close ratios G/S (Fig. 2b). It can be thus concluded that to estimate properties like porosity (or even strength) correlated to ultrasonic velocity through concretes it is necessary to know one of the essential mixture factors (G/S, W/C and total aggregate to cement ratio A/C).

Porosity Measurement

Three samples for each mixture were used and the porosity of the different concretes is given by Table 3.

Table 2 Ultrasonic velocity measured of the different concretes

Concrete	B1	B2	B3	B4	B5	B6	B7
G/S	1.32	1.22	0.65	1.90	1.91	1.84	1.84
W/C	0,42	0,42	0,42	0,60	0,63	0,5	0,5
V (m/s)	3842 ± 205	3459 ± 101	3093 ± 115	3264 ± 190	3145 ± 100	3792 ±24	3736 ± 77
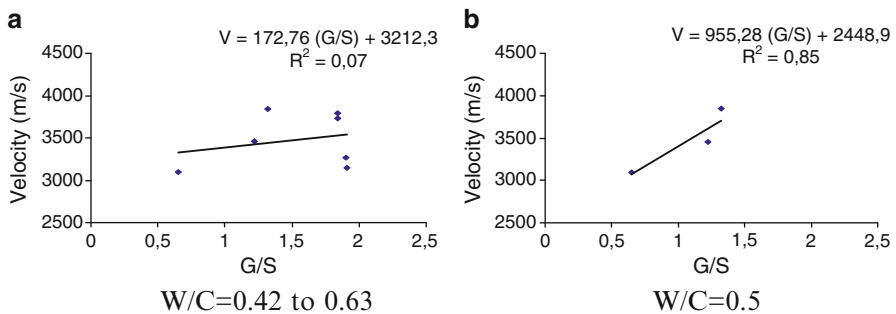
Fig. 1 Evolution of the velocity (effect of G/S)
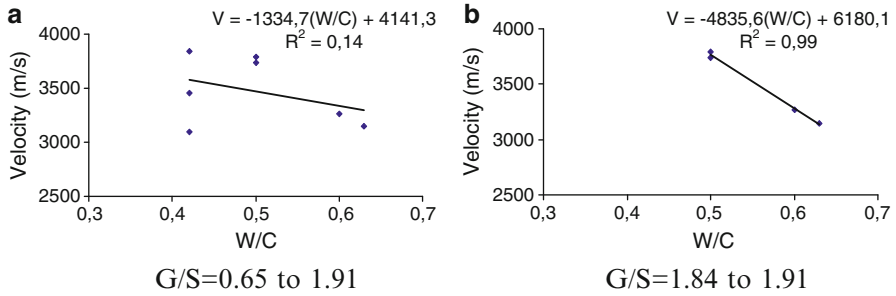
Fig. 2 Evolution of the velocity (effect of W/C)

Table 3 Porosity of concretes

Concrete	B1	B2	B3	B4	B5	B6	B7
G/S	1.32	1.22	0.65	1.90	1.91	1.84	1.84
W/C	0.42	0.42	0.42	0.60	0.63	0.50	0.50
Porosity (%)	8.42 ± 1	10.62 ± 0.4	12.12 ± 0.9	15.49 ± 0.2	16.22 ± 0.5	12.43 ± 0.8	13.06 ± 0.1

From a ratio W/C=0.42 to 0.50, there is an increase in the porosity of 27% (for a same ratio G/S). Whereas all compositions included, an increase in W/C of 50% (from 0.42 to 0.63) are reflected by an increase in the porosity of 58% (from 10.26% to 16.22%). The porosity of the concrete is deduced from the loss of the water mass after passage to the drying oven (105°C) and stabilization of the samples mass. The effect of the mixture variation on the evolution of the concretes porosity is discussed below.

Effect of the concrete mixture on porosity

One should observe that the highest values of porosity are obtained for the ratio W/C=0.63 (Table 3). The concretes B6 and B7 which present the same composition (Table 1), except for the gravel nature (peastone "silicocalcareous natural round gravel" for the B6 concrete and crushed gravel "calcareous" for the B7 concrete), present similar porosities. The porosity of the concrete B6 (12.43%) is slightly lower than that of the concrete B7 (13.06%). This minimum difference is equivalent to the variation of measurements (5%).

If the seven concretes tested are considered, it is noticed that porosity is much less influenced by G/S ratio (Fig. 3a) that by W/C ratio (Fig. 3b). Then if concretes with same W/C ratio are considered (W/C=0.42 for example), it is noted an increase in the porosity of 44% for a reduction of 50% of G/S ratio.
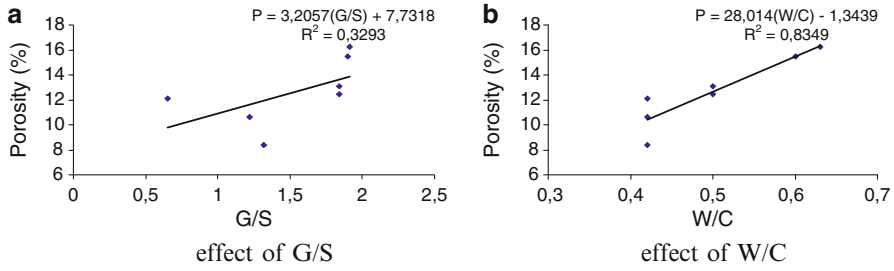
Fig. 3 Evolution of the concretes porosity with mixture
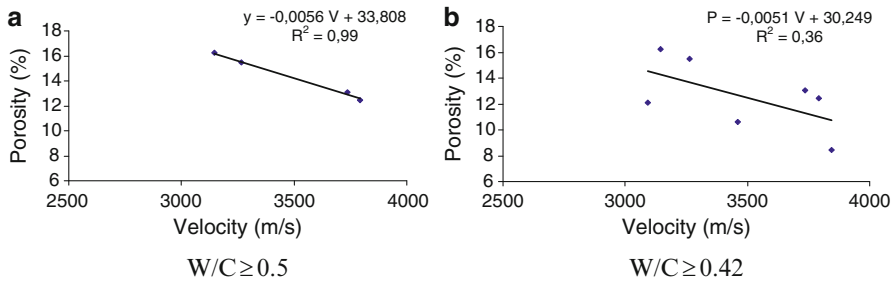
Fig. 4 Evolution of porosity with ultrasonic velocity

Relations between the ultrasonic velocity and porosity

The velocities acquired are well correlated to porosities. It should observe that correlation coefficient approach to 1 for ordinary and fluid concretes (W/C = 0.5, 0.6, 0.63) (Fig. 4a). Therefore, one may conclude that porosities can be deduced from ultrasonic velocities for concretes with a ratio W/C ≥ 0.5.

The correlations become less precise by integrating in these relations the concretes with a smaller ratio W/C (Fig. 4b). What seems to confirm the inability of the ultrasounds to qualify the high performances concretes [8]. There is a porosity non accessible to the water, which represents the unconnected pores. This porosity is much lower than the first but when the porosity accessible to water decreases (for W/C < 0.5) the relationship between the two types of porosity increases what can influence the relations "velocity – porosity". By fixing the ratio "W/C", even for values lower than 0.5 (W/C=0.42 for example), porosity of concrete can be evaluated by measuring the ultrasonic velocity. In this case, the relation becomes specific to each W/C ratio.

The regression curves for a ratio W/C=0.42 give the evolution of porosity with velocity for various G/S (Fig. 5). The increasing ratio G/S results in an increase of ultrasonic velocity and a reduction of porosity. This tendency

Fig. 5 Evolution
of porosity with ultrasonic
velocity (W/C = 0.42)

$P = -0,0049\ V + 27,523$
$R^2 = 0,99$
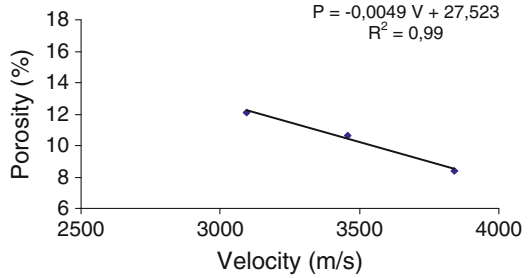
should be checked for other ratios "W/C".", the remaining concretes "W/C=0.5
and W/C=0.6" have only two ratios "G/S"" and thus do not allow to have regression
curves with two points.

Conclusion

In this study various concrete mixes have been considered in order to have different
values of the porosity. The increase of W/C or the decrease of G/S ratio led to an
increase in porosity, the nature of the gravel (B6 and B7) has a smaller influence on
porosity with a difference lower than 6% between crushed and natural round aggre-
gates for the same composition.

The relations between ultrasonic velocity and porosities of the concretes are
described by linear relations for concretes with a ratio W/C $\geq$ 0.5. They become less
precise by integrating in these relations the concretes with less W/C ratio. By fixing
the W/C ratio, even for values lower than 0.5, we can estimate porosity from veloc-
ity. This relation always remains of linear type.

Finally, one can conclude that porosity estimation can be obtained, with accept-
able accuracy, from ultrasonic velocity for ordinary or fluid concretes (W/C $\geq$ 0.5).
For the concretes with a ratio W/C < 0.5, the relation becomes specific to each W/C
and correlations are necessary for each W/C ratio.

References

[1] Ould Naffa S. et al. (2004), *Detection of chemical damage in concrete using ultrasound*,
    Ultrasonics, 40, 247–251.
[2] Hernandez M.G. et al. (2003), *Porosity estimation of concrete by ultrasonic NDT*, Ultrasonics
    38, 531–536.
[3] Jeong H., Hsu D.K. (2002), *Quantitative estimation of material properties of porous ceramics
    by means of composite micro-mechanics and ultrasonic velocity*, NDT & E Int. 29(2),
    95–101.

[4] Goueygou M. (2003), *Relationship between porosity, permeability and ultrasonic parameters in sound and damage mortar*, International symposium (NDTCE'03), Non-Detstructive Testing in Civil Engineering 2003.

[5] Norme NF EN 12390-1. (2001), *Essai pour béton durci – Partie 1: Forme, dimensions et autres exigences relatives aux éprouvettes et aux moules.* Paris: AFNOR.

[6] Controls. (2002), *Instruction manual : Ulrasonic pulse velocity tester*, Mod. 58-E0048".

[7] Afrem. (1997), Détermination de la masse volumique apparente et de la porosité accessible à l'eau : mode opératoire recommandé, *Compte rendu des journées techniques AFPC-AFREM*, Durabilité des bétons, Toulouse, 121–124.

[8] Malhotra V.M., Carino N.J. (2003), *Handbook on nondestructive testing of concrete*, Edition Eyrolles.

Nondestructive Assessment of Alkali-Silica Reaction in Concrete: A Review

F. Moradi-Marani and P. Rivard

Abstract This paper presents state-of-the-art information on the theory and application of nondestructive testing (NDT) techniques used for assessing alkali-silica reaction (ASR) in concrete. The focus is on the application of both linear and nonlinear acoustics (LA and NLA) for detecting ASR. Previous studies have shown that LA methods are less sensitive to early detection of damage in concrete and reliable interpretation of their results depends on the initial condition of the concrete. In contrast, NLA are more sensitive to early cracking and may distinguish ASR from other types of damage. The fundamental concepts of LA and NLA and their application to concrete for detecting ASR are presented with a critical review of their capabilities and limitations.

Keywords Alkali-silica reaction • Concrete • Cracking • Linear acoustics • Nonlinear acoustics

Introduction

A large number of concrete structures are affected worldwide by ASR. It is well known that ASR causes global expansion of concrete and may lead to various crack networks throughout the structure. Maintenance and rehabilitation of these structures require conducting regular and detailed assessment of the concrete conditions; and numerous methods (destructive test or DT, and nondestructive test or NDT)

F. Moradi-Marani (✉) • P. Rivard
Groupe de recherche sur l'auscultation et l'instrumentation (GRAI), Civil Engineering Department, Université de Sherbrooke, Sherbrooke, Canada J1K 2R1
e-mail: farid.moradi.marani@usherbrooke.ca

are available. DTs commonly are expensive, provided limited information, and time-consuming. For instance, for detecting propagation and intensity of ASR in a hydraulic structure, several cores should be drilled through the depth in order to have a complete view about ASR damage. NDTs have progressively been developed for concrete despite an inherently heterogeneous of this material; it is because of benefits of NDTs in comparisons with DTs [1]. Relative success in application of NDTs encourages monitoring damage mechanisms in concrete. In the following sections, a review will be provided on the research work conducted on application of NDTs, especially both LA and NLA, in early age detecting ASR and tracking its progression.

NDT and ASR

Alkali–silica reaction (ASR) is a complex reaction that altered certain forms of silica (microquartz, chalcedony, etc.) and leads to the formation of a swelling gel. This expansive product generates a crack network from the aggregates through the cement paste, reducing concrete stiffness and other mechanical properties. The gel can partially or totally filled the cracks and, therefore, influence the concrete response to external excitation, such as stress wave or vibrations.

Various NDT techniques were introduced by ACI 228.2R-98 [2] to evaluate the quality and the integrity of concrete. Among existing techniques, thermography [1], electrical resistivity [3], and acoustic-based methods (both linear and nonlinear methods) [3–16] have been mostly used to detect ASR-damage in concrete. Thermography is mostly a qualitative method and is successful for locating surface or subsurface defects (such as honeycomb or delamination) because it measures surface temperature [1]; therefore, it is not well suitable for detecting damages in depth. Electrical resistivity has been tested to assess ASR damages because ASR gels may change electrical properties of concrete; however Rivard and Saint-Pierre [3] reported no clear relation between the extent of ASR damage and electrical resistivity, mainly because, the latest parameter is highly dependent on concrete humidity. Ground penetrating radar (GPR) can be another approach for ASR monitoring; but there are two main restrictions for its application [1]: a) GPR generates pulses of electromagnetic waves and is very sensitive to dielectric constant of concrete pore water; b) in reinforced concrete, strong reflections from steel bars can obscure weaker reflections from other reflecting interfaces such as ASR microcracks. Acoustic methods, by producing stress waves in concrete, have been widely used to monitor the integrity of concrete against damage mechanisms. Linear wave attenuation and ultrasonic pulse velocity [4] are two linear acoustic (LA) methods that have been commonly used to monitor ASR. However, nonlinear approach (NLA) appeared to be more sensitive to ASR damages [5-16]; Harmonic generation, frequency modulation, and resonance frequency shift are three common methods of nonlinear acoustic.

This method has been successful in many applications, and will be discussed in the following section.

Linear and nonlinear acoustics

Acoustic methods generate mechanical elastic waves. Low amplitude waves of LA are not able to induce enough deformations in the medium that would modify the elastic properties of materials. LAs, current NDT methods widely used in the field work, are capable commonly of discriminating high levels of damage [9]. It is only after the stage when there are dense accumulations of small fractures or larger cracks, that any of the linear acoustic methods can reliably detect defects [5]. At this point, defects are usually large and significant, and it is often too late or too costly to repair the structure. In fact, concrete is a nonlinear material and damage also increases in nonlinear way; therefore LAs have not been very successful in detecting early age damage. NLAs, which have been newly run in concrete and cementitious materials, are much more sensitive to early age microdefects [14-16]. NLA methods generate relatively high amplitude waves and are capable of inducing local deformations that modify concrete mechanical properties. For instance, it causes opening/ closing of microcracks. Such defects are intrinsic (e.g. intergrain contacts) or associated with damage mechanisms [6].

The nonlinear elastic response of materials containing damage is far greater than in sound materials. Due to this nonlinearity, waves generated in concrete can distort, create accompanying harmonics, and merge with other waves of different frequency; moreover, under resonance frequency, the waves shift as a function of drive amplitude [8]. The degree of these changes in initial waves directly depends on the amplitude of wave. The nonlinear waves are not independent and their interaction produces additional frequencies. In general, linear acoustics analyzes every change in phase and/or amplitude of a signal, i.e. scattering, reflection and absorption, while the frequency is assumed to remain constant. This is different for nonlinear acoustic methods because it investigates the effect that every damage or flaw has on the modulation of the frequency of a signal sent throughout the material. Figure 1 compares the sensitivity of nonlinear and linear acoustics in a fiber-cemented slate [9] showing that NLA is more sensitive than LA.

NLA considers the nonlinearity of concrete and cement based materials much smaller than linear term; it is of order 10^{-5}-10^{-9} in dynamic experiments. These materials exhibit fast dynamic behaviors, hysteresis and end point memory effects, which have been explained by "nonlinear nonclassical effects"; and also by slow dynamic behaviors [10]. This nonclassical nonlinear behavior highly dominates the nonlinear response of concrete in the mesoscopic scale because it is a heterogeneous and microcracked material, and is described by Preisach and Mayergoyz's nonlinear hysteresis and end point memory model or P-M space [11]. In opposite of fast dynamic, which is related to decrease of the elastic modulus with increasing wave amplitude, slow dynamic relates the slow, logarithmic in time, recovery of
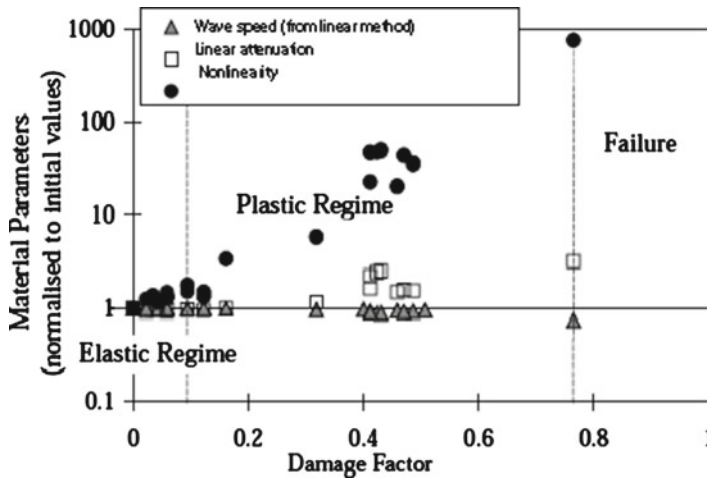
Fig. 1 Comparing sensitivity of linear parameters with nonlinear one [9]

initial elastic properties after the disturbance; it is in order of 10^3–10^4s for micro-cracked or damaged materials [12]. Kodjo [6] applied the concept of slow dynamic to detect ASR and showed that the viscoelasticity brought by ASR gel extend the time respond of material during conditioning. This time response increased from 400s for samples damaged by mechanical loading to 1400s for those damaged by ASR.

ASR Experiences with Acoustic Methods

There have been some experiences conducted to detect ASR damages by LAs in both laboratory and field experiences. The previous work by Saint-Pierre *et al*. [4] showed that the sensitivity of ultrasonic pulse velocity is too low to monitor damages created by ASR in lab samples. Instead, the results showed linear wave attenuation is more sensitive to ASR damage. In another study by Rivard & Saint-Pierre [3], similar results were observed for pulse velocity; however, the linear resonant frequency was a little more sensitive. Sargolzahi *et al*. [13] dealt with the application of both LA and NLA methods for monitoring ASR in laboratory concrete mixtures. The results showed no significance changes in pulse velocity up to expansion levels around 0.09%. However, the nonlinear frequency shift and harmonic generation increased more than 3 times and around 2 times, respectively for the same expansion levels.

Chen *et al*. [14] have used nonlinear impact resonance acoustics to show the shift in resonance frequency for mortar samples made with highly reactive aggregates. Mortar bars were excited with different energy levels of mechanical impacts in

order to have resonance frequency in different perturbation levels. The mortar bars were exposed to high alkaline solution and the measurements were continued up to 6 days. Despite early age sensitivity of nonlinear parameters to ASR expansion, no change was observed in linear parameters. In others experiences, Chen *et al*. [15, 16] used frequency modulation method to monitor early age ASR in mortar specimens. With this attempt, a high frequency and continuous sinusoidal wave was generated in the sample and then, a low frequency wave was produced by a mechanical impact. The nonlinear modulation of the two waves of different frequencies produces sidebands at the location $f_1 \pm f_2$ in the frequency domain; the results confirmed rapid changes in nonlinear parameters due to ASR progression.

Among the nonlinear acoustic techniques that appear to be promising for the detection of cracks/microcracks in concrete, only a few are applicable in both laboratory and field because their implementation is time-consuming or may cause various problems. A novel nonlinear acoustics has been used by limited literature to characterize damages associated with ASR [7]. This is a simple method that consists in quantifying the influence of an external mechanical impact on the propagation of an ultrasonic compressive wave. A sudden mechanical impact opens the microcracks and causes a reduction in the ultrasonic pulse velocity. The effect of the impact is attenuated by gradually closing the microcracks; and simultaneously the pulse velocity returns to its initial value. Kodjo et al. [7] showed there is a relation between phase variation, amplitude, and nonlinear parameter. The ultrasonic waves are modified by the mechanical excitation, leading to non linear phenomena like phase shift. The results show that the rate of change in nonlinear parameter is much higher for the ASR-damaged specimens compared with the sound specimen.

NLAs, especially the last case, reveal high potential for monitoring ASR damage in concrete. Nonlinear wave interaction, involving a mix of low and high frequencies, appears to be a good candidate for field inspection. It is worthy to consider that, alone, the high frequency waves are not applicable due to the high attenuation of these frequencies. Moreover, factors such as high density reinforcement, different levels of humidity, porosity, low frequency waves generated by a dynamic loading like traffic can influence the accuracy of the results. For instance, Payan *et al*. [8] showed nonlinear parameters decline suddenly when the water saturation increases from 0 to 20% but no significant changes were observed for water saturation from 20% to 100%. However, Kodjo found that moisture content in concrete has a strong effect on some non linear indicators, such as shift frequency and harmonic generation. This issue has to be investigated deeper.

Conclusion

Above review shows that nonlinear interaction of an elastic wave with a low frequency and high amplitude may be a good approach for nondestructive evaluation of in-service concrete structures. NLAs have already proven capability in detecting early age ASR damage by exhibiting a significant sensitivity. However, it is

necessary to understand the influence of some internal and external parameters such as presence of steel bars, external loading and stress, porosity, water saturation on the nonlinear parameters. This is the main challenge for applying nonlinear techniques for field inspections and future works would be aimed at studying the influence of some of the interfering factors in order to make NLAs applicable in the field applications.

References

[1] Carino, N.J. (2003). In: Non-destructive test methods to evaluate concrete structures, Proceedings of the 6th International Conference on Durability of Concrete (CANMET/ACI), pp. 1–78, Thessaloniki, Greece.

[2] ACI Committee 228 (2005). ACI 228.2R-98 (Reapproved 2004), Farmington Hills, MI.

[3] Rivard, P. and Saint-Pierre, F. (2009). Constr. Build. Mater., vol. 23, n. 2, p. 902.

[4] Saint-Pierre, F., Rivard, P., and Ballivy G. (2007). Cem. Concrete Res., vol 37, n. 6, p. 948.

[5] Van Hauwaert, A., Thimus, J.F., and Delannay, F. (1998). Ultrasonic., vol 36, n. 1–5, p. 209.

[6] Kodjo, A. (2008). In : Contribution à la caractérisation des bétons endommagés par des méthodes de l'acoustique non linéair. Application à la réaction alcalis-silice, Ph.D. Thesis in French - Université de Sherbrooke/Université Cergy-Pontoise, 127p.

[7] Kodjo, A.S., Rivard, P., Cohen-Tenoudji, F., and Gallias, J.L. (2009). In: "Evaluation of damages due to alkali-silica reaction with nonlinear acoustics techniques, Proceedings of Meetings on Acoustics (POMA), Acoustical Society of America Digital Library, vol. 7, n. 1, 045003-045003-10.

[8] Van Den Abeele, K.E.A., Johnson, P.A., and Sutin, A. (2000a). Res. Nondest. Eval., vol. 12, n. 1, p. 17.

[9] Van Den Abeele, K.E.A., Sutin, A., Carmeliet, J., and Johnson, P.A. (2001). NDT & E Inter. Vol. 34, n. 4, p. 239.

[10] Payan, C., Garnier, V., and Moysan, J. (2010). Cem. Concrete. Res., vol. 40, n. 3, p.473.

[11] Guyer, R.A. and Johnson, P. A. (1999). Phys. Today, vol 52, n. 4, p. 30.

[12] Delsanto, P.P. and Scalerandi, M. (2003). Phys. Rev. B, vol 68, p. 064107.

[13] Sargolzahi, M., Kodjo, S.A., Rivard, P., and Rhazi, J. (2010). Constr. Build. Mater., vol. 24, n. 8, p. 1398.

[14] Chen, J., Jayapalan, A.R., Kim, J.Y., Kurtis, K.E., and Jacobs, L.J. (2010). Cem. Concrete. Res., vol.40, n. 6, p. 914.

[15] Chen, J., Jayapalan, A.R., Kim, J.Y., Kurtis, K.E., and Jacobs, L.J. (2009). ACI Mater. J., vol. 106, n. 4, p. 340.

[16] Chen, J., Jayapalan, A.R., Kurtis, K.E., Kim, J.Y., and Jacobs, L.J. (2008). In: Ultra-accelerated assessment of alkali-silica reactivity by nonlinear ultrasonic techniques, Proceeding of 13th International Conference on Alkali-Aggregate Reaction in Concrete (ICAAR), Throndheim, Norway.

Homogeneity Detection of Fibre-Concrete Structures Using Radiographic Technique

L. Hobst, O. Anton, J. Vodicka and J. Scucka

Abstract Fibre-concrete structures have many advantages compared to standard reinforced concrete, for example, higher strength and higher tensile strength of fibre-concrete. However, fibres are often incorrectly distributed in structure during their manufacture. Wires are often clustered, which reduces the overall homogeneity as well as the quality of fibre-concrete structures. The aim of the research team of the workers from three technical universities in the Czech Republic was to develop an objective method of control that would allow establishing the homogeneity of wire distribution in finished fibre-concrete structures.

Introduction

Concretes reinforced with distributed steel reinforcements (fibres) are known as fibre-concrete. Recently, thanks to well-known physical and mechanical properties of fibre-concrete, there were very often the attempts of designers, and namely investors, to utilize this kind of materials for support structures. It has come to light

L. Hobst (✉) • O. Anton
Brno University of Technology, FAST, Veverí 95,
602 00 Brno, Czech Republic
e-mail: hobst.l@fce.vutbr.cz

J. Vodicka
Czech Technical University in Prague, FSv, Thákurova 7,
160 00 Praha, Czech Republic

J. Scucka
VSB - Technical University of Ostrava, FAST, L.Podeste 1875,
708 33 Ostrava, Czech Republic

that the applications of fibre-concrete in such structures lead to the economic success.

A homogeneous structure of fibre-concrete is one of the most important factors to secure the reliability of such fibre-concrete structures. If the homogeneity of fibre-concrete is not observed, the material has different properties in various parts of the structure (for example, tensile strength), which can lead to the defects in the structure (generation and development of cracks). The relevant lower reliability of the structure which is caused by unequal distribution of fibres (wires) in concrete volume can lead to damage of the property as well as the safety and the human lives can be jeopardized. Hence it is necessary to secure the effective control of the fibre-concrete homogeneity in ready support fibre-concrete structures.

Homogeneity of Fibre-concrete Structure

The prerequisite of the homogeneity of fibre-concrete used in support structures is to observe the principles of fibre-concrete technology. This is based on designing the proper fibre-concrete composition, where so-called aeration of aggregate mixture with fibres must be taken into account for a higher density of fibres, and furthermore, the correct procedure of production technology of fresh fibre-concrete production and the determination of the proper consolidation of concrete during concrete works of fibre-concrete structure must be considered. For the detailed description of the individual phases of fibre-concrete technology, see for example [1].

It is not difficult to assess the fibre-concrete homogeneity in fresh samples taken during concrete work. However, more complicated task is to find information about the fibre-concrete homogeneity built in the support structure. Additionally to borehole sampling and their analyses, it is necessary to find out other methods - the tests which would give the reliable information about the material homogeneity. One method which satisfies such requirements is radiography which has been developed at the laboratories of the Institute of Building Testing, Brno University of Technology, Faculty of Civil Engineering in Brno. This institute cooperates very closely in its development with the experts from the Czech Technical University in Prague and the Technical University of Ostrava.

Radiographic Control Method for Fibre-concrete Homogeneity

Radiography belongs to the non-destructive testing methods (NTM) which provide the testing of the internal material structure without its damage. This method has been successfully tested in civil engineering during radiography of reinforced concrete structures, and additionally during tendon injection control

in the structures made of pre-stressed concrete. There is an assumption that this method can be applied even for the fibre-concrete homogeneity control. Although the radiogram information capability is excellent, radiography has a number of limitations. For example, only the subjects and materials with a certain limited thickness which is dependent on the x-ray energy can be tested. Voltage of about 160 kV is used under usual conditions which can be applied for the concrete samples with a thickness of up to 100 mm. The higher thicknesses can be irradiated with a higher energy; however, the resolution of material details will be remarkably lost. Finally, the strict safety provisions must be observed during radiographic control.

Design and Production of Experimental Samples

The authors realized the experiment in which they assessed the homogeneity of fibre-concrete with respect to the fibre distribution in the volume of concrete samples. A series of concrete samples with different densities of fibres was prepared: 0.0 % (A-0-C), 0.5 % (A-1-C), 0.75 % (A-2-C), 1.0 % (A-3-C), and 1.25 % (A-4-C). The TRI-TREG fibres with a length of 50 mm were used. In total, five fibre-concrete samples were used. The samples were made in the moulds with dimensions of 300x300x150mm. Such dimensions were selected so that the samples can be handled, and at the same time, they must be sufficiently large enough to avoid so-called "wall effects" during the processing of fibres. However, such prepared and selected samples were not possible to expose directly to x-rays (due to high thicknesses). Hence, the samples were divided into smaller parts which were, additionally to radiography, subject to other non-destructive methods. Always two control plates with dimensions of 150x150x75 mm were cut for radiography. Such dimensions of the control plates can determine the fibre layout with a sufficient precision in the selected area (with dimensions of 150x150 mm and irradiated thickness of 75mm). The plates were subsequently x-rayed on radiographic films in the cassettes with voltage of 125 kV at the x-ray tube.

Even if fibre-concrete radiography was used earlier [2], an objective method should be found based on today's assessment which would be able to analyse quantitatively the radiograms much better regarding their quantity and orientation of fibres. The image processing method has appeared as a satisfactory method.

Image Analysis

The x-ray images of the test samples were digitized by means of a desk scanner which was provided with a glass lid for scanning the positive and negative films. The images with 300 dpi resolution in the TIFF format were generated which were further
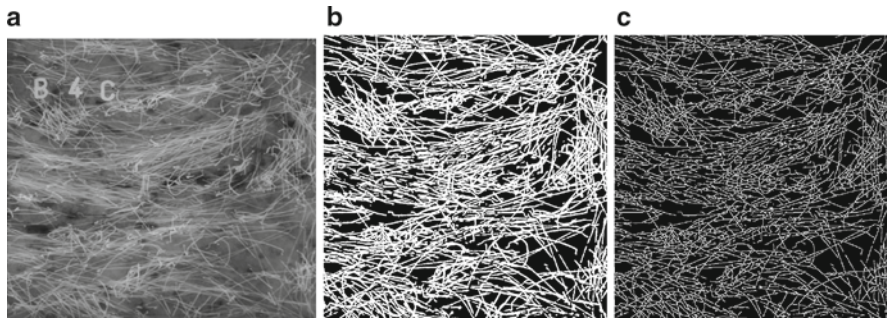
Fig. 1 The image processing for determination of the volume percentage and orientation of fibres in concrete: **a**) initial x-ray image of fibre-concrete sample, **b**) binary image (white objects of fibres on black background), **c**) central axes of fibres (line with thickness of 1 pixel)

processed by means of the Matlab Image Processing Toolbox and NIS Elements packages. The line objects (fibres) were detected in each of analyzed images (see Fig. 1a) by means of the image processing method; the image was converted by "thresholding" [3] into a binary form (white fibre objects on the black background; Fig.1b), and then, the central axes of fibres displayed as the lines with a thickness of 1 pixel (Fig. 1c) were generated. Only lines which were positioned in the directions of 0°, 45°, 90° and 135° were successively separated in the image of the central axes. The total length of lines was measured in each direction. The results of determination of the preferred fibre orientation in concrete were expressed in the rose diagrams (Fig. 2). It is obvious that the horizontal fibre orientation in the plates prefers, which is caused by intensive vibration during consolidation of the test samples.

The next parameter which can be determined by the image analysis is a volume percentage of fibres in concrete. This parameter was approximately estimated from the area percentage of fibres in the image. The area percentage was measured in the binary images (Fig. 1b). The values found are shown in Table 1. The measured value was compared with that of the calculated quantity of fibres in the control samples (150 x 150 x 75 mm), that is, 270 pieces for 0.5%, 404 pieces for 0.75 %, 540 pieces for 1.0 % and 674 pieces for 1.25 %. For comparison the results were plotted in the chart, see Fig. 3. It is evident that both curves for mass concentration from 0.00 to 0.75 % are consistent (the dependence of the area portion of fibres on the concentration corresponds to the curve of the real fibre number versus the mass concentration). If this value was exceeded the superposition of fibres displayed would occur (for the control thickness of 75 mm), and the quantity of wires in the sample cannot be simply evaluated by this method.

Conclusion

The questions of fibre-concrete homogeneity verification in support structures must be studied, and the new, more precise and simple methods should be developed than now available. A combination of radiography and the image analysis is described in
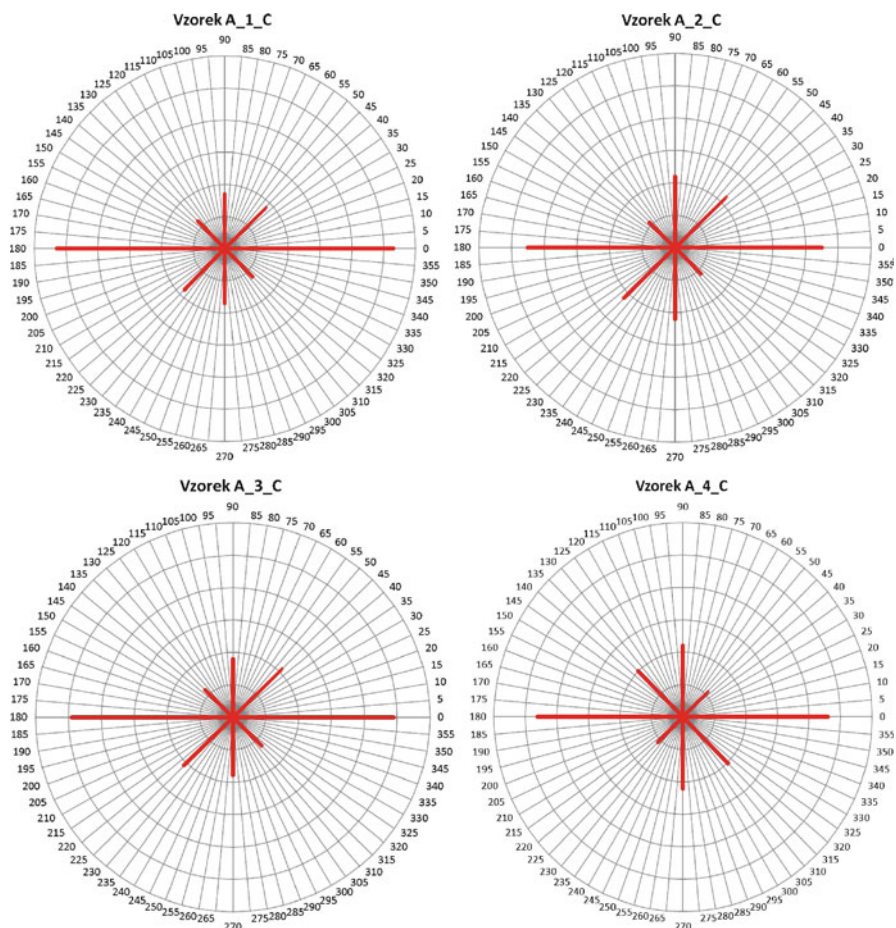
Fig. 2 The graphic representation of the preferred fibre orientation in the samples of the tested series

Table 1 The volume percentage of fibres in the concrete samples determined by the image analysis

Sample with indicated fibre concentration in [wt %]	A-0-C 0 %	A-1-C 0.5 %	A-2-C 0.75%	A-3-C 1.0%	A-4-C 1.25%
Area percentage of fibres [vol. %]	0	18	27	32	36

this contribution. Their application for homogeneity control in fibre-concrete has been tested by the authors at the present days, and according to the results obtained, this method seems to be very perspective. However, other methods are also tested which are used to test the magnetic properties of fibres. Also, the geo-radar application seems to be very perspective.
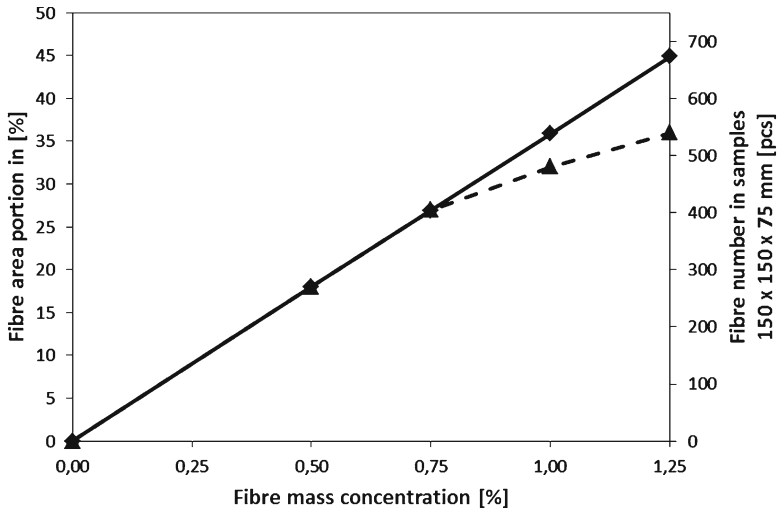
Fig. 3 The dependence of the area percentage of fibres in the image on the volume fibre concentration in fibre-concrete as well as on the real number of fibres in the control samples (150 x 150 x 75 mm)

References

[1] Barr, B.; Swamy. R.N. (Eds.): Fibre reinforced cement and concretes: recent developments. London: Spon Press. 1990. 713 p. ISBN 1851664157.
[2] Brožovský, J.; Hobst. L.Kaplan, V.: Assessment of defects in fibre-reinforced concrete of floor board (in Czech). Sanace betonových konstrukcí. 1999, vol. 7, no. 2, pp. 14–17.
[3] Gonzalez, R.C.; Woods, R.E.: Digital image processing. 3rd ed., New Jersey: Pearson Education, Inc., 2008. p. 954.

Use of Acoustic Emission Data Clustering to Identify Damage Mode in Concrete Structures

L. Calabrese, G. Campanella and E. Proverbio

Abstract Acoustic Emission (AE) technique gained increasing interest in the last two decades as monitoring methodology and as assessment tool for safety and reliability evaluation of reinforced concrete structures, historical and masonry buildings. However a widely accepted analytical instrument for AE data handling and interpretation is still missing. Cluster and discriminant analysis have been recently applied to classify AE patterns and to identify damage modes. Aim of this paper was to develop a cluster analysis procedure devoted to identify cracking mechanisms in concrete structures. Unsupervised methods, k-means as well as Principal Component Analysis and Self Organizing Map, have been used as analytical instruments. A procedure aimed to remove environmental AE noise has been also proposed.

Keywords Acoustic emission • Clustering analysis • Concrete • Damage mechanism • Deterioration

Introduction

AE techniques were recently introduced in the field of civil engineering where the development of reliable and affordable tool for monitoring and damage evaluation of reinforced concrete structures is becoming a pressing demand. Most of the analytical methodologies nowadays applied in this field derive from those ones developed for testing and evaluation of composite materials. Among others the determination of the nature of AE sources is one of the main target of AE data analysis. It is in fact realistic to consider that an AE signal contains some feature representations of the source in

L. Calabrese • G. Campanella • E. Proverbio (✉)
University of Messina, Department of Industrial Chemistry and Materials Engineering, Messina, Italy
e-mail: proverbi@ingegneria.unime.it

such a way that direct correlation exists between the damage mechanisms and the magnitude of the various AE parameters. Consequently, each signal can be considered as the acoustic signature of a damage mode. Multi-parametric analysis using many AE waveform parameters should be therefore necessary to improve the identification of damage modes.

Pattern recognition has been proposed as a suitable multi-variable technique for the classification of AE events [1]. When the type of damage mechanisms is known in advance the supervised pattern recognition is used as in the K-Nearest Neighbours method (K-NN method) [2]. The term unsupervised pattern recognition is, on the other hand, used to describe the complete methodology consisting of procedures for descriptors selection, cluster analysis and cluster validity, when no information on the attended clusters is available. A popular unsupervised clustering method is the k-means algorithm [3].

The dimension reduction of large data sets can be instead obtained by means of the Principal Component Analysis (PCA) which is a classical method of multivariate statistics [4]. PCA involves a mathematical procedure that transforms a number of possible correlated variables into a smaller number of uncorrelated variables. Neural network procedures also have been successfully adopted to numerically separate different classes of data, among other the Kohonen's Self-Organizing Map (SOM) [5]. The main characteristic of the Kohonen algorithm is its ability to develop feature maps corresponding to the distributions of vectors in the input set and to organize the data in topologically coherent maps [2]. The combination of AE multi-parametric analysis and neural networks, in the form of a Kohonen's self-organizing map, was successfully employed to discriminate signals originating from different damage types [6]. The result of the Kohonen algorithm is the so called U-matrix whose representation is a topological map showing the different classes of input signals. The 'U-matrix' shows distances between neighbouring units and thus visualizes the cluster structure of the map.

One of the main concern in the analysis of AE data is however noise removal. Environmental noise is a important aspect in the application of AE technique on real structures. AE noise could be a consequence of external acoustic sources induced for example by car traffic or electromagnetic interferences. Clustering procedures could be successfully applied in noise reduction [7].

Aim of this paper is to describe some procedures, including noise removal tools, specifically developed by the authors for AE data cluster analysis and aimed to identity different damage modes in reinforced concrete structures under loading conditions.

Experimental and results

Clustering procedures for AE signals

When large datasets of AE signals are collected it is too costly, from a hardware point of view, to record all the raw AE signals (i.e. voltage vs time history for each sensor). More commonly signals are reduced to a numbers of patterns describing the
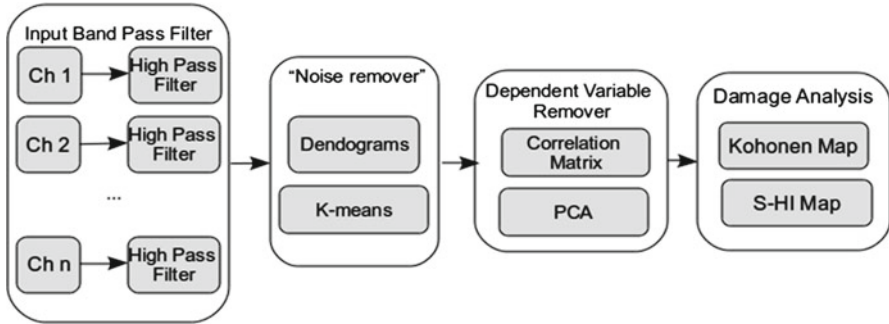
Fig. 1 Scheme of the procedure for noise removal and data clustering

signal themselves. We divided such patterns in three main groups: in the first group we considered the amplitude, counts, duration, rise-time and energy patterns that are calculated by the acquisition system from the input raw AE wave. In the second group statistical patterns calculated on the AE hits population such as historical index and severity [8], the RA value and average frequency [9] were included. The last group included variables such as time, sensor identification and external variables such as loading condition and so on.

A multi-step procedure is here described aimed to identify homogeneous clusters of AE signals to be related to specific damage conditions (e.g. tensile or shear cracking, micro cracking or macrocracking) on the basis of the adoption of a 12 variables dataset. A hardware filtering of the data was generally performed at the level of data recording in order to cut off low amplitude noise by means of a high pass filter set between 40 and 42 dB.

Then the procedure included the following steps:

- Clustering noise remover
- Dependent Variable remover
- Damage Analysis

The scheme of clustering methodology is reported in Fig. 1.

Clustering noise remover

By means of a k-means and hierarchical clustering procedure the clusters related with environmental noise, characterized by uncorrelated significant amplitude events (not removed by band pass filter) were identified. *Hierarchical clustering* refers to the formation of a recursive clustering of the data points: a partition into two clusters, each of which is itself hierarchically clustered. A dendrogram, a bi-dimensional diagram which shows the subdivisions of clusters at each successive stage of analysis, was here adopted The information were then compared with a non-hierarchical clustering approach, *k-means algorithm*, to allow a most reliable identification of

the cluster number, to identify the lack of homogeneity in the variables dispersion and to classify further noise events. The de-noised AE signals were still characterized by groups of correlated variables; to allow data comparison with different scales, logarithmic values were used instead of their natural values, afterwards a normalization procedure was applied on the data matrix.

Dependent variable remover

Aim of the third step was the reduction of the dimensionality of the data. The *principal component analysis (PCA)* is a useful procedure to retain the nature of the original variables, but to reduce their number. In a multivariate data it removes extraneous or redundant variables, which increase unproductively the dimensionality of data, to simplify the subsequent multivariate analysis. PCA, performed on the de-noised data, evidenced the relevancies and interdependencies between variables favouring the possibility to find important underlying patterns in the data. The criterion adopted in the variables reduction was connected to the evaluation of variance percentage. In our case 75% of total variance was evaluated and that led to identify only three principal components. The results were then compared with the correlation matrix to verify interdependencies between the original variables in a correlation-coefficient matrix. In the matrix all the diagonal values have a value of one because all signals are perfectly correlated with themselves. Non-diagonal values close to one indicate that the corresponding variables are highly correlated, a threshold value of 0.80 was set for this study.

Damage analysis

The remaining uncorrelated data was finally processed by the Kohonen's self-organizing map algorithm, which allowed to identify the characteristics of AE hits in specific clusters (e.g. high amplitude and low rise-time, with high load conditions) and therefore allowing to evidence a relationship between AE signals and damage mode.

Noise reduction optimization and cluster validation

In order to improve data clustering reliability and to reduce subjectivity in noise removal a modified procedure was adopted as reported in Fig. 2. In this new procedure k-mean clustering was adopted in a second time and by using the principal components resulting from PCA, instead of the original variables. The number of resulting clusters was subsequently subjected to a validation procedure [10]. Then a further noise removal step was performed to remove "noisy" cluster. In this case our aim was to remove environmental noise related to a high number of spurious events
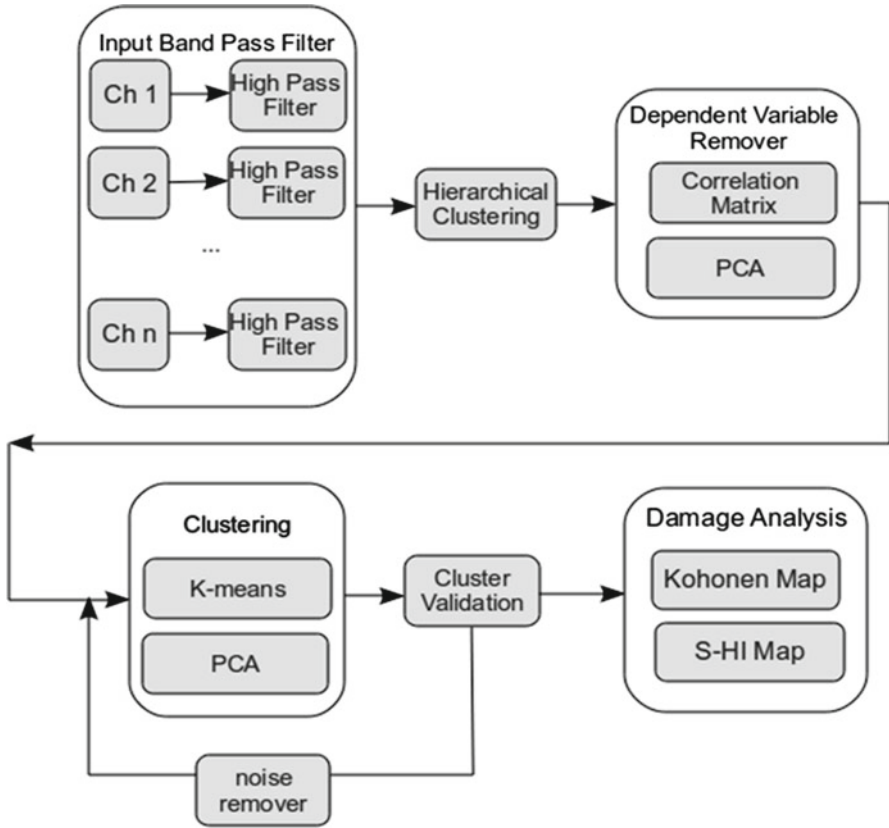
Fig. 2 Scheme of the improved procedure for noise removal, data clustering and clustering validation

recorded on daylight time, so clusters including an extremely high number of daylight events (e.g. 97-98%) were removed. Then a new PCA analysis and clustering validation was performed iteratively until no more clusters including a high number of daylight events was observed. The so filtered data were finally used as input for Kohonen's self-organizing map algorithm and for severity – historical index maps. An example of Kohonen's map obtained on AE data recorded from a post-tensioned concrete beam tested under increasing loading [11] is reported in Fig. 3.

Conclusions

Cluster analysis procedures were applied to acoustic emission technique to identify cracking modes in concrete structures under loading condition. Two different clustering procedures based on the adoption of k-means algorithm as well as Principal Component Analysis and Self Organizing Map algorithms have been proposed.
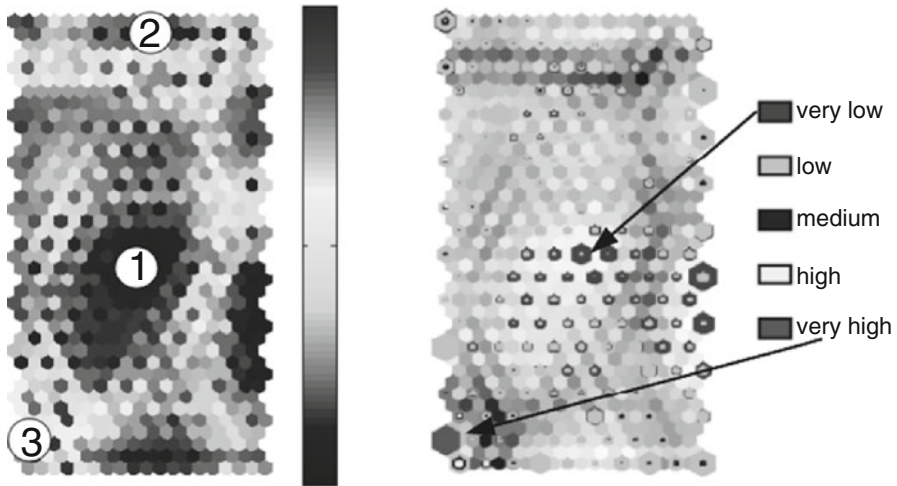
Fig. 3 U-matrix (left) as resulted from the application of SOM algorithm evidencing three clusters; energy hits map (right) which allows to identify the specific pattern of each cluster (homogeneous AE sources). Cluster 1 included very low energy hits, while in cluster 3 only high energy hits are comprised

A procedure based on cluster analysis was developed to remove AE noise signal. Results obtained up today are highly promising, even if further improvements of the algorithms and the development of a validation procedure are still required.

References

[1] Johnson M., (2002), *NDT&E Int*, vol 35, p. 367.
[2] Godin N., Huguet S., Gaertner R., Salmon L., (2004), *NDT&E Int*, vol. 37, p. 253.
[3] Likas A., Vlassis N., Verbeek J.J., (2003), *Pattern. Recogn.*, vol. 36, n. 2, p. 451.
[4] Jolliffe I.T., (2002), *Principal Component Analysis*, Springer Series in Statistics, 2nd ed., Springer, NY.
[5] Kohonen T., (1990), *P IEEE*, vol. 78, n. 9, p. 1464.
[6] de Oliveira R., Marques A.T., (2008), *Comput Struct*, vol. 86, p. 367.
[7] Emamian V., Kaveh M., Tewfik A., Shi Z., Jacobs L.J., Jarzynski J., (2003) *EURASIP J. Appl. Signal Pr*, vol. 3, p. 276.
[8] Golaski L., Gebski P., Ono K. J. (2002), *J. Acoust. Emission* vol. 20, p. 83.
[9] JCMS-IIIB5706 (2003), *Monitoring method for active cracks in concrete by acoustic emission*, Japan Construction Material Industries Federation, Tokyo.
[10] Brock G., Pihur V., Datta S. Datta S. (2008), *J. Stat. Software*, vol. 25, n. 4, p.1.
[11] Proverbio E., (2010), *Mater. and Corros.*, Vol. 61, n. 2, p.161. DOI: 10.1002/maco. 201005735

NDT of LWC with Expanded Clay

J. Brozovsky, D. Benes and J. Zach

Abstract Nowadays, light-weight concrete (LWC) is increasingly used in construction, namely LWC with aggregates of expanded clay type called Liapor. It is often necessary to perform tests for the characteristics of cast-in-place concrete during building construction as well as after the construction. One of the ways to control the quality of LWC in a structure is using non-destructive testing (NDT) methods. For compressive strength, there are reflective rebound methods and ultrasonic pulse method (UPM) which may also be used for determination of dynamic modulus of elasticity. This paper presents the results of NDT of LWC with expanded clay using above the mentioned methods and as well as the associated calibration relations. A comparison of conversion coefficients obtained from modulus of elasticity tests on normal-weight concrete (NWC) and LWC is also provided. The developed calibration relations resulted in a high degree of correlation between the NDT results and the results of compression tests on concrete specimens.

Keywords Modulus of elasticity • Nondestructive testing • Rebound hammer • Strength • Ultrasonic pulse method

Introduction

At present, use of LWC gained considerable share in the Czech construction market, mainly with regard to where LWC containing Liapor ceramic aggregates is mostly used. LWC defines as concrete featuring mass density from 800 to 2,000 kg/m³. Liapor aggregate is characterized by almost ball-shaped grain with solid sintered shell and uniformly porous center core. Aggregate strength varies generally between 0.7 and 10.0 MPa depending on its mass density and grading.

J. Brozovsky (✉) • D. Benes • J. Zach
Brno University of Technology, Brno, Czech Republic
e-mail: brozovsky.j@fce.vutbr.cz

LWC containing Liapor aggregates can achieve 5 to 60MPa compressive strength. Relatively much lower strength and mass density of the Liapor aggregates compared to those of compact aggregates defines–influence the concrete strength and modulus of elasticity which should be reflected by the NDT results.

Compressive Strength Tests on LWC Using Schmidt Impact Hammer

Impact hammers used for testing

Schmidt impact hammers type N and type L ("Original Schmidt"– spring operated hammer) with the following specifications were used. Manufacturer specifies compressive strength limits from 10 to 70MPa.

– *Schmidt impact hammer type N*. Impact energy is 2.25 J. This impact hammer is applicable for construction thickness not less than 100 mm.
– *Schmidt impact hammer type L*. impact energy is 0.75 J. This impact hammer is applicable for construction thickness not less than 60 mm.

Test procedure

Tests were conducted as follows:

– *Test equipment* conformed to CSN EN 12504-2 [6] requirements.
– *Test specimens* were 150×150×150 mm³ concrete cubes tested after 7, 14, 21, 28, 60, and 180 days of age. The specimens were stored in accordance with the related standard (t = 20 ± 2ºC, φ ≥ 95%).
– *Test surface* was dry grinded by means of abrasive stone according to CSN EN 12504-2 [6].
– *Test procedure* involved preloading of test cubes to approximately 10% of the estimated compressive strength. Two surfaces were tested using Schmidt impact hammer, taking 10 horizontal rebound readings on each surface. Acquired set of rebound values were processed to obtain a mean value under the provision that rebound values differing more that 12,5 % were omitted as described in e.g. [2].
– *Compression tests* following NDT involved loading of the test cubes to failure. Final load served for calculation of compressive strength. The $f_{c,cu}$ compressive strength test conformed to CSN EN 12390-3[5].
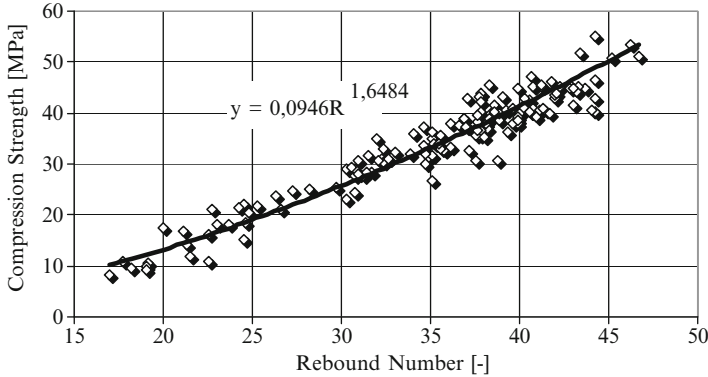
Fig. 1 LWC test results obtained using Schmidt Impact Hammer, Type N

Test Results and Calibration Relations

150 pairs of values (rebound number & compressive strength) were at hand for development of the calibration relation for Schmidt impact hammer type N, and 140 pairs of values were available for Schmidt impact hammer type L. LWC compressive strength values ranged from 7 to 51 MPa, and mass density ranged from 860 to 1,760 kg/m^3. The results obtained for Schmidt impact hammer type N are shown in Fig. 1.

Calibration relations

The results of destructive and non-destructive tests were used to develop calibration relations between compressive strength and the impact hammer value using the smallest quadrate (least square) method. The calibration coefficient, r, obtained from this method gives a quantitative indication of correlation between the compression strength and rebound number. The evaluation was based on the criteria [3] below:

– $0.5 \leq r < 0.7$: Significant correlation
– $0.7 \leq r < 0.9$: High degree of correlation
– $r \geq 0.9$: Very high dependence between variables

For practical applications, calibration relation corresponding to a correlation coefficient $r \geq 0.85$ is deemed acceptable. The developed calibrations relations are as follows:

a) Compressive strength from rebound numbers measured by the Schmidt impact hammer, type N:

– Basic curve (1), age of concrete from 7 to 180 days:

$$f_{c,N} = 0.0946R^{1.6484} \quad R \in \{17;47\} \quad r = 0.963 \tag{1}$$

– Calibration relation (2) for 7 days of concrete age:

$$f_{c,N} = 0.3171R^{1.3018} \quad R \in \{17;38\} \quad r = 0.914 \tag{2}$$

– Calibration Relations (3) for 14 days of concrete age:

$$f_{c,N} = 0.6749R^{1.0951} \quad R \in \{21;46\} \quad r = 0.916 \tag{3}$$

b) Compressive strength from rebound numbers measured by the Schmidt impact hammer, type L

– Basic curve (4) for concrete age from 7 to 180 days,

$$f_{c,L} = 0.1139R^{1.6145} \quad R \in \{16;49\} \quad r = 0.955 \tag{4}$$

where $f_{c,N/L}$ are the estimated compressive strength values obtained using rebound numbers from hammer type N/L, and R is the rebound number.

LWC Dynamic Modulus of Elasticity Measured Using Ultrasonic Pulse Velocity Method

When designing concrete structures, static modulus of elasticity of concrete is one of the significant parameters – in addition to strength. The static modulus can be determined two ways: directly from compression tests, and indirectly through NDT methods such as ultrasonic pulse velocity method or resonance method. Generally, dynamic modulus of elasticity ($E_{c,UPM}$) of common concrete is higher than its static elastic modulus (E_s) depending on concrete strength class. The dynamic modulus of elasticity can be converted to static ones through the use of reduction coefficients provided in standards such as CSN 732011[9]. Validity of the same coefficients for LWC for normal weight concrete, however, is questionable.

Dynamic modulus of elasticity of concrete specimens were determined using ultrasonic pulse velocity method in direct transmission tests. 100x100x400mm³ test specimens were used (testing according to CSN EN 12504-4[7] calculation of $E_{c,UPM}$ according to CSN 731371[8]). Following NDT, static modulus of elasticity was determined according to CSN ISO 6784[4].

We have compared E_s of $E_{c,UPM}$ ones for LWC – strength classes LC 20/22 D1.6 a LC 40/44 D1.8. Values of E_s varied between 13.6 and 22.2 GPa; values of $E_{c,UPM}$ varied between 16.4 and 24.9 GPa. In all cases, compressive strength values were between 29 and 47 MPa. The relation between the dynamic modulus of elasticity $E_{c,UPM}$ and the static modulus of elasticity E_s is obtained as follows:

$$E_s = 7.503E_{c,UPM} - 0.133E_{c,UPM}^2 - 60.786[GPa] \quad r = 0.965 \tag{5}$$
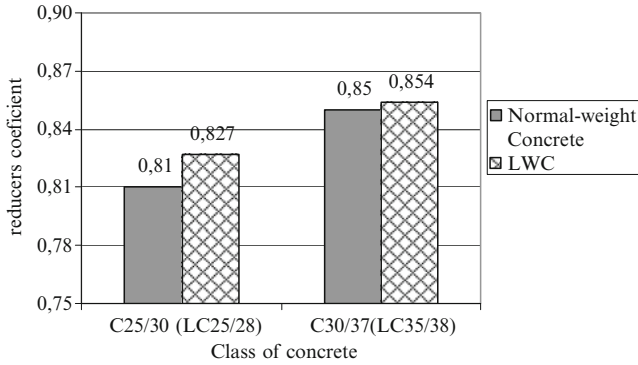
Fig. 2 Comparison of Conversion Coefficients for LWC and NWC

Figure 2 provides a comparison (two different types of NWC and LWC concrete) of coefficients for conversion of dynamic modulus from ultrasonic method to static ones as described in CSN 73 2011[9].

Discussion of Results

Impact hammer tests on LWC

The basic calibration relationship (concrete age from 7 to 180 days) in (1) for type N Schmidt impact hammer produced a correlation coefficient equal to 0.963; similarly the correlation coefficient for type L Schmidt impact hammer was 0.955. For 7 and 14 days of concrete age, the correlation coefficients are 0.914 and 0.916, respectively (Type N hammer). The fact that all correlation coefficients are higher than the minimum acceptable value i.e. 0.85, indicates that the developed relations can be used in practical applications for assessment of the LWC compressive strength using the rebound numbers obtained from testes using N/L type impact hammers

Modulus of elasticity comparison between LWC and normal-weight Concrete

Relation between dynamic modulus of elasticity as tested by ultrasonic pulse velocity method and static modulus of elasticity as determined according to CSN ISO 6784 [4] has a correlation coefficient of $r = 0.965$. Hence, the static modulus of elasticity can reliably be determined from ultrasonic pulse velocity tests.

When comparing conversion coefficients relating dynamic modulus of elasticity determined by ultrasonic pulse velocity method to the static modulus of elasticity for NWC (see CSN 73 2011[9] for appropriate values) and LWC, the differences were found to be insignificant i.e. from 0.5 to 2.1%.

Conclusions

Experimental results have proven that Schmidt impact hammer, both types N and L, can be used to determine the compressive strength of LWC containing Liapor ceramic aggregates. For practical use, the basic calibration relation is recommended. Similarly, the static modulus of elasticity can be obtained from ultrasonic pulse velocity tests for LCW using the developed calibration relations. Finally, it was found that the same conversion factors can be used to determine the static modulus from the measured dynamic modulus for both LWC and NWC.

References

[1] Drochytka R. et al. (2009), *Progressive Building Materials with Utilization of Secondary Raw Materials and their Impact on Structures Durability*. Final report of the project VVZ CEZ MSM: 0021630511, BUT Brno
[2] Brozovsky, J., Matejka, O. and Martinec, P. (2007), *Concrete Interlocking Paving Blocks Compression strenght Determination Using Non-Destructive Methods*. The e-Journal of Nondestructive Testing, vol. 12, n. 4, pp. 91–97.
[3] Janko, J. (1958), *Statistical Tables*, NČSAV, Prague.
[4] CSN ISO 6784 (1993), *Concrete-Determination of Static Modulus of Elasticity in Compression*, Czech Standards Institute, Prague.
[5] CSN EN 12390-3 (2009), *Testing hardened concrete - Part 3: Compressive Strength of Test Specimens*, Czech Standards Institute, Prague.
[6] CSN EN 12504-2 (2002), *Testing Concrete in Structures - Part 2: Non-destructive Testing - Determination of Rebound Number*, CSI, Prague
[7] CSN EN 12504-4 (2002), *Testing concrete - Part 4: Determination of ultrasonic pulse velocity* Czech Standards Institute, Prague.
[8] CSN 731371 (1982), *Method of Ultrasonic Pulse Testing of Concrete*, Czech Standards Institute, Prague.
[9] CSN 732011 (1988), *Non-destructive Testing of Concrete Structures*, Czech Standards Institute, Prague.

Evaluation of Rebound Hammer Test as a Combined Procedure Used with Drill Core Testing for Evaluation of Existing Structures

S. Yeşilmen

Abstract Rebound hammer is a non-destructive test method often used to assess the surface hardness of engineering materials. The method is used as a part of the procedure applied to evaluate existing structures. The concrete core tests are usually combined with rebound hammer tests to decrease costs and damage to the structure. Various studies attempted to establish a reliable relationship between the concrete strength and the rebound coefficient. Proposed formulas and correlation coefficients stayed reliable for narrow limits on factors like concrete age, composition, moisture content, etc. Despite the high uncertainty of the raw data the methodology remains in use. This paper presents the evaluation of rebound hammer and drill core test data from 256 different buildings in Antalya, Turkey. With uncontrolled parameters like environmental factors, age, compressive strength of concrete, the rebound hammer test results showed very little correlation with concrete core test results even for the statistically large data set.

Keywords Concrete strength • Non-destructive testing • Rebound hammer

Introduction

Nondestructive tests have become commonly used techniques to evaluate the condition of existing structures. Similar to ACI 437-R-03 code, various codes worldwide regulates the determination of in-place concrete strength by core sampling used in conjunction with a NDT technique [1]. Main use of the NDT techniques in structural evaluation is reduction in the number of core samples that need to be taken by assessing homogeneity.

S. Yeşilmen (✉)
Atilim University, Ankara, Turkey
e-mail: syesilmen@atilim.edu.tr

EN 13791 involves core testing used in conjunction with rebound hammer method or a similar NDT method for the assessment of the compressive strength of concrete [2]. Although the regulation allows other methods similar to rebound hammer; in practice core testing values are almost always matched by rebound hammer values due to its ease of use. The method simply relates energy absorbed by concrete surface to concrete strength and an empirical relation between the rebound number and concrete strength is used to estimate the actual concrete strength.

ACI 228R-1 report lists rebound hammer method as one of the least accurate methods among the major NDT methods considered [3]. The method can not be used to determine the compressive strength of concrete directly but it can provide an estimation of concrete strengths at different places in the building to be evaluated. Main factor reducing the reliability of the method is the dependence of rebound number on various factors other than concrete stiffness. Moisture condition, surface characteristics, carbonation, mix design, location of test, aggregate type, testing direction, location of reinforcement and coarse aggregates are often listed as the major parameters influencing the rebound number [1,3]. There are correction factors advised to be used in order to reduce effects of listed parameters on rebound number, however most of the above listed parameters can not be evaluated during a field study considering major limitations of budget and time.

There are a vast number of literature citing the relationship between rebound number and the compressive strength of concrete [4, 5]. Numerous equations derived addressing a number of parameters that affect rebound number, however the experiments performed could not represent the variability of the field conditions. Concrete elements in existing buildings encounter a large number of random and undocumented situations that affect to-date properties of the materials which results in uncontrolled parameters. Major uncontrolled parameters in a typical construction are quality control, curing conditions, temperature and humidity variations throughout the year, user originated undocumented loading and exposure history, etc. A laboratory testing program may not be able to be representative of the real life data even the parameter range and statistical sample size of the experimental program is extensive. A more meaningful method would be obtaining and analyzing real life data in order to set better correlation functions between rebound number and compressive strength of concrete.

In this paper a large number of building evaluations are documented and analyzed in order to establish a relationship between rebound number measurements and compressive strength values obtained from core testing. It was observed that although there is a relationship between the two measurements, variability of the data is extremely high which makes it hard to define a reliable relationship between the two.

Relation Between the Rebound Number and Core Compressive Strength

Evaluation of existing buildings are performed on buildings to grant the request of owners and/or users of the building related to building permits or when there are concerns about structural capacity of the building either due to an unusual situation

like earthquake damage or the structure is suspected to be substandard in material or construction. The evaluation can be performed by professional companies or organizations like chamber of civil engineers. The study evaluates data from both parties in the city of Antalya and covers data from 256 different buildings among which only 37 are one-storey.

Core specimens evaluated in the study are tested in uniaxial compression conforming the criteria in EN 12504-1 standards and size correction factors were applied for 93 × 93 mm specimens [6]. EN 12504-2 requires taking the median value of 10 rebound readings for each location in order to reduce the effect of localization in rebound hammer measurements [7]. Field practice is to take 3 core specimens for each storey of the building and 10 rebound hammer readings from close proximity of places where each core specimen taken. Accordingly a total of 4932 core strength values and 49320 rebound hammer values were evaluated in the study.

Proceq type N rebound hammer was used in all field measurements. Type N hammer is widely used in field applications since it is recommended for specimens with thickness' larger than 100 mm. Impact points are chosen in such a way that the distance between two consecutive points are no closer than 25 mm to each other and from the edges.

In a field investigation compressive strength values are obtained simply by reading the corresponding compressive strength values from correlation charts supplied by the producer for each equipment type. The supplier charts include adjusted curves for different directions of measurement. Measuring direction was horizontal for a greater number of data where core specimens were taken from columns and shear walls, and for a smaller number of data the hammer was directed vertically downwards where the core specimens were taken from slabs and beams. Additionally it is indicated in the correlation diagrams that, the relationships are valid for concrete specimens that are aged between 14 to 56 days. A reduction factor of 0.6 was applied to %92 of the building studied that were older than 1000 days of age to calculate the compressive strength estimated from rebound number.

It is important ot mention that due to time and budget limitations professional laboratories do not follow guidelines in relevant codes fully during field investigations. Although EN 13791 requires a more sophisticated method for the calculation of compressive strength from rebound numbers, the data presented in this study were compiled between years 2007 and 2009 when the code was not in effect. Thus compressive strength values obtained from core specimens are compared directly with the rebound numbers instead of estimated compressive strength values from rebound numbers. It was observed that correlation coefficients of regression equations observed from the latter case (i.e. relation between the compressive strength obtained from core testing and estimated compressive strength from rebound numbers) are in the same order with the case presented in Figs. 1 and 2, even after the application of correction factors.

The study used average values for three core strength measurements and measurements from three locations of rebound hammer testing for each storey of each building. From each core specimen location 10 rebound hammer readings were recorded and their median value is used to obtain the corresponding compressive strength value.
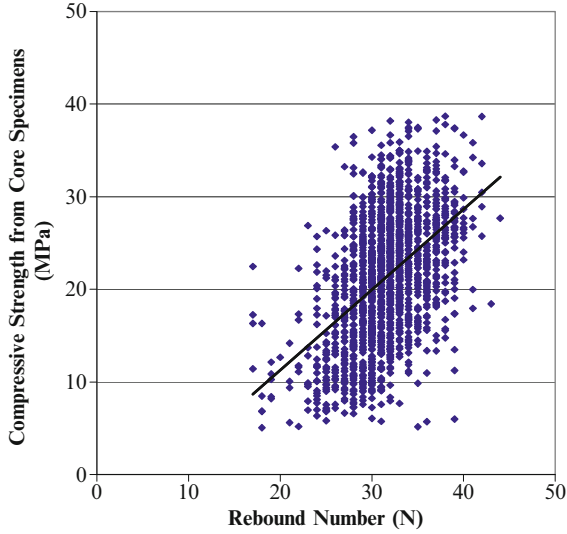
Fig. 1 Compressive strength values obtained from core specimens and rebound numbers averaged for each storey on evaluated buildings

As seen in Fig. 1 a regression analysis is performed between core strength and rebound number for each storey in 256 buildings.

Mean values for compressive strength obtained from core specimens and rebound numbers are 21.28 MPa and 32 MPa, respectively. Ranges are from 5.03 to 38.69 MPa for core data and from 15 to 46 for rebound hammer data. Various approaches are applied to determine the best fit regression line or curve, the highest coefficient of determination is obtained for Eqn. 1. Coefficient of determination r^2 is obtained as 0.233, for the best fitted model, i.e. the linear model in Eqn. 1.

$$Y = 0.8685\chi - 6.0953 \tag{1}$$

Coefficient of determination is low, which is to be expected to some extent considering variable characteristics of concrete even in the same batch [1] however the coefficient is low enough to investigate other potential reasons and question the regression relationship. The pearson coefficient of correlation of ρ is 0.47 indicating, again, that although the variation is high there is correlation between the data sets.

A second method to investigate reasons for the low coefficient of determination is to observe the residual graphs. The graph plotting residual values against y values i.e. core strength values in Fig. 2 shows a distinct linear trend which indicates the regression equation set for the relationship between the core strength and the rebound number is inadequate.
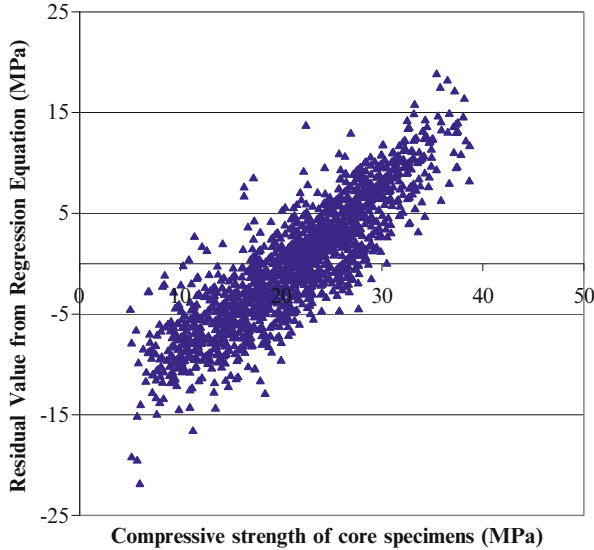
Fig. 2 Residual compressive strength values obtained from regression equation plotted against core strength averages for each storey on evaluated buildings

Discussion of Results

As mentioned in the previous section several regression equations were developed in the literature and much higher coefficient of determinations were obtained relating the strength of concrete to rebound number. Actual relationship between the two parameters is much more variable and questionable as seen from the results obtained in this study. The controlled conditions of specimens casted in laboratory with easily controlled parameters like moisture condition, age, carbonation rate, aggregate specifics does not apply to the conditions of real life. Use of rebound hammer test for the evaluation of existing buildings in conjunction with core specimen data might help to obtain the uniformity of concrete and reduce the number of core specimens to be taken to some extent. On the contrary the vast number of uncontrolled and unaccounted for parameters puts the use of rebound hammer in a controversial situation as an in-place test method along with core sampling.

The solution can either be to advise other methods over rebound hammer method for NDT tests used to complete core specimen data or to define the additional parameters affecting the relationship and oblige additional test types that will determine those parameters in the evaluation procedure. The procedures in the regulations must be critically reviewed and revised as new data becomes available.

It is expected that the use of methods mentioned in EN 13791 about the estimation of in-place strength of concrete using rebound hammer data for the field investigations have the potential to increase the accuracy of the assessments.

However the methods presented in this code are more complicated, they can be time consuming and costly which will create a resistance against its proper use considering current market conditions. Application of EN 13791 for the evaluation of the existing buildings should be followed rigorously by the relevant organizations.

Conclusion

The relationship between concrete compressive strength obtained from core specimen data and rebound numbers obtained for the same location of concrete was investigated. Data is obtained from evaluation of existing buildings by professional laboratories and laboratories of Chamber of Civil Engineers in the city of Antalya from several locations. The study put together extensive collection of real life data, as opposed to previous studies in the literature using controlled conditions of experiments comparing the same parameters.

The evaluation of existing structures is performed by inadequately inspected independent laboratories offering low prices which results in low reliability of results and minimized number and type of tests in Turkey. As the main conclusion derived from regression analysis, neither the rebound numbers nor the estimated strength from rebound number values, are representative of actual compressive strength of the concrete alone. There are other major independent factors affecting the relationship and if they are not inserted into the equation the high variability of results can mislead the involved parties.

References

[1] ACI Committee 437 (2003), 437R-03: Strength Evaluation of Existing Concrete Buildings, American Concrete Institute, Detroit, MI.
[2] British Standards Institution (2007), BS EN 13791:2007 Assessment of in-situ compressive strength in structures and precast concrete components. London, U.K.
[3] ACI Committee 228 (2003), 228.1R-03: In-Place Methods to Estimate Concrete Strength, American Concrete Institute, Detroit, MI.
[4] Leshchinsky, A. M., Yu, M. and Goncharova, A. S. (1990), *Mag. Concrete Res.*, vol. 42, n. 153, p. 245–248.
[5] Indelicato, F. (1999), *Mater. Struct.*, vol. 32, n. 219, p. 394–399.
[6] British Standards Institution (2009), BS EN 12504-1:2009 Testing concrete in structures - Part 1: Cored specimens - Taking, examining and testing in compression. London, U.K.
[7] British Standards Institution (2001), BS EN 12504-2:2001 Testing concrete in structures - Part 2: Non-destructive testing - Determination of rebound number. London, U.K.

An Experimental Study on the Evaluation of Concrete Test Results

O. Arioz, K. Kilinc, M. Tuncan, K. Ramyar and A. Tuncan

Abstract The compressive strength test applied to standard samples is one of the most important tests indicating the quality of concrete in structures. The results of the standard tests are compared with the values used in design calculations to check for specification compliance and quality assurance. Although the standard tests are well accepted by the construction industry, they may not represent the in-situ strength of concrete due to the differences between the degree of compaction and curing conditions of concrete and those of standard samples. The quality of concrete can be assessed by means of minor-destructive methods. Pull-out test is an example of minor-destructive tests. The test causes only minimal destruction to the structure and the hole is repaired easily after testing. In the present study, the results from pull-out tests, and maturity method were extensively analysed for the assessment of concrete strength.

Keywords Compressive strength • In-situ strength • Maturity • Pull-out • Standard tests

Introduction

Concrete is one of the most widely used structural material produced by mixing together aggregate, cement, water, and if necessary different types of admixtures [1-6]. One of the main characteristics of concrete is its compressive

O. Arioz • K. Kilinc (✉) • M. Tuncan • A. Tuncan
Faculty of Engineering&Architecture, Department of Civil Engineering,
Anadolu University, 26555 Eskisehir, Turkey
e-mail: kadirkilinc@anadolu.edu.tr

K. Ramyar
Faculty of Engineering, Department of Civil Engineering,
Ege University, Izmir, Turkey
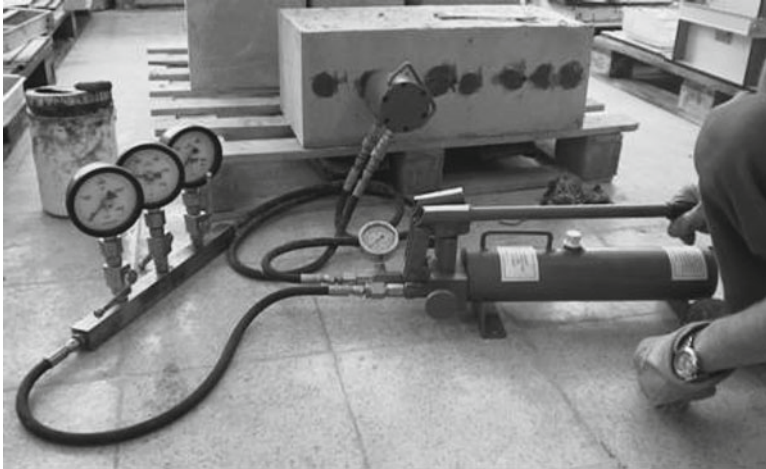
Fig. 1 Application of pull-out test

strength that is directly used in structural design calculations and also gives an idea about other important properties of concrete [1, 4]. Therefore, the quality of concrete is usually indexed by its compressive strength [7]. Different methods and techniques are utilised for the inspection and evaluation of concrete quality. Generally, standard cube and cylinder specimens are taken and tested at specified ages for the quality control of concrete cast in structures [6]. However, the standard specimens may not represent efficiently in-situ strength of concrete due to different curing and compaction. Moreover, the dimensions of the test specimen and those of the structural member are also different from each other [8-10]. Therefore, actual strength of concrete may show some differences from design strength and the uniformity may not be obtained. In such cases, the quality of concrete can be assessed by means of non-destructive and minor-destructive methods [9-20]. Pull-out test is an example of minor-destructive tests. The test leaves only a minimal destruction to the structure and the hole is repaired easily after testing.

In this experimental investigation, pull out test and maturity test were conducted on different concrete mixtures. Pull-out test is defined in ASTM C 900-01 and BS 1881: Part 207: 1992 but it is not yet included in Turkish Standards [21, 22]. Maturity method is described in ASTM 1074-87. The method is not yet involved in Turkish standards. In this investigation, hydraulic pull-out testing equipment was manufactured by supports of mechanic workshop of Anadolu University. The results of these minor-destructive tests were correlated and compared with those of compressive strength test of concrete performed on standard cube and cylinder samples. Figure 1 illustrates the manufactured pull-out equipment and the application of pull-out test in the experimental study.

Experimental Study

In this investigation, five concrete mixtures were produced using crushed limestone aggregate with four different maximum sizes. An ordinary Portland cement was used in concrete production. The maximum aggregate size was 22 mm for crushed limestone aggregate. To maintain a constant slump of 150±20 mm in all of the mixtures, a plasticizer was also used in some of the mixtures. Proportions and some properties of concrete mixtures are given in Tables 1 and 2, respectively.

By using concrete mixtures, 150 mm cube, 150x300 mm cylinder and 250x300x 650 mm beam specimens were cast and moist cured in the laboratory until testing. The cube and cylinder specimens were prepared for standard tests. Compressive strength tests were performed on cube and cylinders at specified ages. To achieve the objective of this study, a pull-out test equipment was manufactured by the support of mechanic workshop of Anadolu University. The pull-out equipment used in this study consisted of a hydraulic jack, three manometers, a reaction ring and connection hoses. The manufactured metal inserts were connected to the forms of beams before concrete casting. Pull-out tests were performed at the ages of 3, 7, and 28 days. The pull-out forces reported within this study are the average of six values. In the application of the maturity tests, a four channel maturity meter was used to measure the temperature-time developments of concrete specimens. The temperature values were recorded by maturity meter and the recording time interval was ½ hour for the first 48 hours and 1 hour thereafter. The following equation was used to calculate the maturity of the concrete samples;

$$M = \sum \left[T - \left(-10 \right) \right] \times \Delta t \tag{1}$$

Table 1 Proportions of concrete mixtures (kg/m³)

Mixture	Coarse Aggregate	Fine Aggregate	Cement	Water	Admixture
MIX-C	1034	846	315	190	-
MIX-I	1036	877	320	174	3.2
MIX-J	1043	850	360	170	3.6
MIX-K	1048	817	390	172	3.9
MIX-L	1083	640	500	200	6.0

Table 2 Some properties of concrete mixtures

Mixture	w/c ratio	Aggregate Type	Maximum Aggregate Size (mm)	28-day 150 mm Cube Compressive Strength (MPa)
MIX-C	0.60	Crushed Limestone	22	27.4
MIX-I	0.54			34.2
MIX-J	0.47			38.0
MIX-K	0.44			39.9
MIX-L	0.40			43.3

Where, M is the maturity of the concrete at a given age, T is the temperature during the specified time interval in °C, (-10) is the datum temperature in °C, and Δt is the time interval.

Results and Discussions

Pull-out tests results

The results of the pull-out tests performed on concrete mixtures MIX-I, J, K, and L are presented in Fig. 2. The relationship between the pull-out force and cube compressive strength is linear. The cube strength increases with increase in pull-out force. The regression equation and R^2 value can be seen in the figure.

Maturity tests results

Maturity tests were performed on MIX-C and MIX-L. According to the tests results presented in Fig. 3, there is no unique relationship between the maturity and the strength of concrete. It depends upon mix proportions, properties of materials used in the production of concrete, and also water/cement ratio of the mix. In the figure, the relationships found by other researchers were also depicted. It seems that the strength-maturity curve given by Gruenwald (w/c=0.51) and that found for MIX-C fit well. Similarly, the relationships between maturities and strengths of concretes are very close to each other for curve given by Gruenwald (w/c=0.36) and that found for MIX-L.
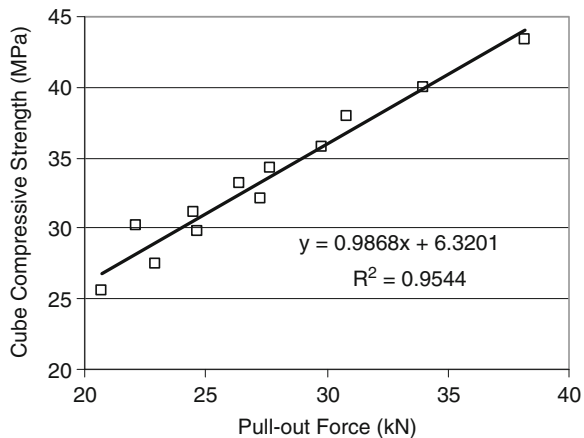
Fig. 2 Relationship between cube strength and pull-out force
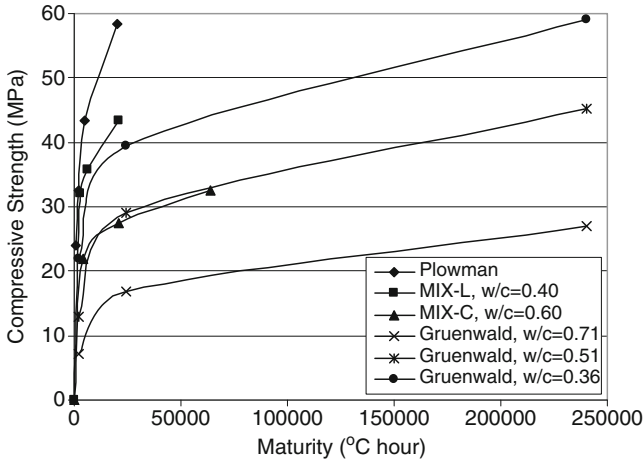
Fig. 3 Relationship between strength and maturity of concrete

Conclusions

The relationship between the pull-out force and cube compressive strength was found to be linear. The cube strength increased with increase in pull-out force. It was seen that the maturity-strength relationship depended upon mix proportions, properties of materials used in the production of concrete, and also water/cement ratio of the mix.

References

[1] Neville, A.M. (1981). *Properties of Concrete*, Pitman Books Limited, London.

[2] Mindess, S. and Young, J.F. (1981). *Concrete*, Prentice-Hall, inc, New Jersey.

[3] Troxell, G.E., Davis, H.E. and Kelly, J.W. (1968). *Composition and Properties of Concrete*, McGraw-Hill Book Company, New York.

[4] Erdogan, T.Y. (2003). *Concrete*, 1st Edition, METU Publisher, Ankara.

[5] Taylor, W.H. (1977). *Concrete Technology and Practice*, McGraw-Hill Book Company, Sydney.

[6] Arioglu, E. and Arioglu, N. (1998). *Testing of Concrete Core Samples and Evaluations*, 2nd Edition, Evrim Publisher, Istanbul.

[7] Arioz, O., Yildiz, D., Nalcaci, M., Karaesmen, E. and Erkay, C. (2004). In: *Economical aspects of concrete quality of reinforced-pre-stressed concrete structures*, Concrete 2004 Congress, pp. 131–140, Istanbul, Turkey.

[8] Chmielewski, T. and Konopka, E. (1999). *Mag. Concrete. Res.*, vol. 51, pp. 45–52.

[9] Bartlett, F.M. and Mac Gregor, J.G. (1996). *ACI Mater. J.*, vol. 93, pp. 158–168.

[10] Bungey, J.H. and Soutsos, M.N.(2001). *Const. Build. Mater.*, vol. 15, pp. 81–92.

[11] Haque, M.N. and Al-Khaiat, H.(1997). *Cem. Concrete. Comp.*, vol. 19, pp. 123–129.

[12] Abdel-Halim, M.A.H., Al-Omari, M.A. and Iskender, M.M.(1999). *Eng. Struct.*, vol. 21, pp. 497–506.

[13] Miao, B., Aitcin, P.C., Cook, W.D. and Mitchell, D. (1993). *ACI Mater. J.*, vol. 90, pp. 214–219.

[14] Franco, L., Noli, A., Degiralamo, P. and Ercolani, M. (2000). *Coast. Eng.*, vol. 40, pp. 207–219.

[15] Kenai, S. and Bahar, R. (2003). *Cem. Concrete. Comp.*, vol. 25, in press.

[16] Price, W.F. and Hynes, J.P. (1996). *Mag. Concrete. Res.*, vol. 48, pp. 189–197.

[17] Beek, V.A., Breugel, V.K. and Hilhorst, M.A. (1997). *Struct. Fault. Rep.*, vol. 2, pp. 407–414.

[18] Ohtsu, M. and Watanabe, H. (2001). *Const. Build. Mater.*, vol. 15, pp. 217–224.

[19] Zhu, W., Gibbs, J.C. and Bartos, P.J.M. (2001). *Cem. Concrete. Comp.*, vol. 23, pp. 57–64.

[20] Elverly, R.H. and Ibrahim, L.A.M. (1976). *Mag. Concrete. Res.*, vol. 28, pp. 181–90.

[21] ASTM C 900-87 (1994) (Reapproved 1993). *Standard test method for pullout strength of hardened concrete*, Annual Book of ASTM Standards.

[22] BS 1881: Part 207 (1992). *Recommendations for the assessment of concrete strength by near-to-surface tests*, British Standards.

Detection of Incipient Decay of Wood with Non- and Minor-Destructive Testing Methods

K. Frühwald, A. Hasenstab and K. Osterloh

Abstract For inspections of timber structures it is important to find defects, damages and material heterogeneities in the interior of wooden construction components. Undetected decay (especially interior rot) can result in a sudden failure of the construction. In the usual structural safety analysis of timber structures, damages and their extent are estimated by visual inspection of drilling cores and by the determination of the drilling resistance. Both reveal information only about this single point of measurement. Often repeated sampling (numerous drilling cores) becomes necessary, which still may be insufficient to assess larger buildings. The destruction from drilling cores must be considered, it´s not suitable for statically highly stressed parts (which should all be covered). In heritage-protected buildings, drilling cores and the drilling resistance method are rather limited. With the visual inspection of the drilling cores without further magnifying devices, decay can only be detected in the advanced stage. Incipient fungal attack, which already has a significant influence on the elasto-mechanical properties, can´t be detected. The drilling resistance method and drilling cores are compared with the ultrasonic echo technique with regard to their suitability for structural health monitoring of timber constructions. The low reliability of assessing the drilling cores by visual inspection for incipient fungal attack shall be improved by further non-destructive tests of the drilling cores. The applications of non- and minor-destructive test methods are considered, particularly their use in cultural timber structures.

K. Frühwald (✉)
Ostwestfalen-Lippe, University of Applied Sciences, Lemgo, Germany
e-mail: katja.fruehwald@hs-owl.de

A. Hasenstab
Ingenieurbüro Dr. Hasenstab, Augsburg, Germany

K. Osterloh
Federal Institute for Materials Research and Testing (BAM), Berlin, Germany

Keywords Drilling cores • Drilling resistance • Non destructive testing • Ultrasonic echo technique • X-ray

Introduction

After the collapse of the ice rink in Bad Reichenhall/Germany in 2006 all rinks in timber construction have to be inspected according to a decision of the Supreme Building Authority in the Bavarian State Ministry of the Interior. Almost the same took place for timber bridges in whole Germany two years later after an emergency closure of a timber bridge from red ironwood, which was extensive damaged in the main supporting structure by interior fungal infection, which was only detected by the combination of ultrasonic echo technique and the drilling resistance.

For inspections of timber structures it is important to find defects, damages and material heterogeneities in the interior of wooden construction components. Undetected, interior damages (especially interior rot, but knots an cracks as well) can result in a sudden failure of the construction. Fungal growth reduces the elasto-mechanical properties of the wood considerably; brown rot has a greater impact than white rot [i. a. 1-2]. In particular, the dynamic strength properties decrease sharply already in the early stage of infection [i. e. 3-4]. After the impact bending strength, the bending strength is influenced second most by early fungal decay [3]. With a reduction of the sample mass by 2% the strength decreases by 35% (5% reduction of sample mass → 50% strength reduction, 10% → 60%).

If timber structures recognized as cultural heritage are damaged by fungal attack, it is possible to refrain from a replacement in accordance with DIN 68800. However, no information about the remaining load bearing capacity of the damaged timber parts is currently available.

Current Capabilities of Minor- and Non-Destructive Methods

Assessing the structural safety of timber structures usually starts with estimating damages and their extent by visual inspection and picking with a hammer. Among the minor-destructive testing techniques, extraction of drilling cores, the drilling resistance and endoscopy are the most common approaches [5-6]. The disadvantages of these methods are the poor yield of information on one hand and the infliction of additional damage on the other hand. Test loading is rarely done as well as – mostly in the context of research projects – radiographic inspections, usually with X-rays [7]. Ultrasonic measurements are made since several years. The only possibility of non-destructive, large-scale, laminar measurements of all statically relevant areas is the ultrasonic echo technique, which is currently not always used for inspections of timber structures.

Ultrasonic echo measurements

The ultrasonic echo technique is based on the reflection of the acoustic waves on heterogeneities in the material, such as the rear surface of the specimen or at any other interface. So it is possible to get indirect information from the received signals about the condition of the construction element or on internal damage. The measured time of the echo signal can be converted to spatial lengths by referring to the known dimensions of the construction. The low density of wood ($\rho_{pine} << \rho_{concrete} << \rho_{steel}$) is caused by a high porosity, which requires probes with high intensity and low-frequency (50-200 kHz). A low frequency results in a small attenuation of the signal; however, the pertaining large wavelength limits size of the detectable defect accordingly.

The first successful experiments were carried out with longitudinal waves at the BAM [8]. The longitudinal wave transducers were coupled by Vaseline, ultrasonic gel and glycerine; the centre frequency was optimised at 100 kHz. Because of the radial/tangential anisotropy on longitudinal waves, transverse wave transducers were used later, which do not require a coupling agent since they are coupling by point contact, making the handling less complicated [9-10]. The centre frequency ranges from 40 kHz up to 60 kHz. The ultrasonic echo technique is currently not always used for inspections of timber structures, because many of the parameters influencing the results are currently known only partially. This requires a lot of experience with the ultrasonic echo technique and the method can therefore be used seriously only by specialists.

There is only little experience in the detection of fungal decay by ultrasonic echo with transverse waves [9, 11-12]. Near-surface damages in the area of impulse initiation show very strong damping effect. In addition to this a large number of cracks lead to additional shadowing and scattering effects. The detection of fungal decay is currently indirectly obtained by the absence of the signal.

Drilling resistance method

The drilling resistance method consists in drilling a needle into the timber with a constant feed rate. This process requires a certain power of the driving motor. The requested power consumption is high for hardwoods and low for softwoods and damaged wood. Whenever defects or cracks occur the drilling resistance drops abruptly and rises steeply after re-entry into the wood. In decomposed wood (e.g. by fungal attack) the transition from healthy to the damaged wood is smoother. Fungal growth can be detected in the wood by the drilling resistance method [i. e. 13-15]. For 10 % damage from brown rot the drilling resistance drops to 55 % and for 30 % damage to 20% of the reference value [13]. In decomposed wood the drilling resistance decreases more than the density [12]. However, the staining with the typical black to brown border lines often caused by white rot leads to a partial increase of the drilling resistance level in this area.

The drilling resistance method is minor-destructive. The drilling needle is 3 mm wide at the cutting head and leaves barely visible holes. However, this approach merely allows measurements at selective spots and thus is representative for a certain limited part of the investigated object only. The drilling resistance is mostly used in suspected areas to exclude a putative damage. In the case of a detected damage, it is usually not possible to asses the precise extend of destruction. This is particularly true for early stages of infestation because of differing mechanisms of fungal degradation. Moreover, strength characteristics of the component cannot be concluded, especially for hardwoods strength influencing grading characteristics like knots and fiber deviation are more important [i. a. 16-17].

Sampling of drilling cores

Originally, drilling cores are used for dendrochronological studies, i. e. age determination on living trees or dating of wooden constructions. Therefore the measurement of the annual ring width is done with a magnifier, a microscope or with X-ray densitometry. For the X-ray densitometry the drilling core is grinded to a flat blade, followed by extraction of resins and wood extractives. The blade is X-rayed and the density profile is determined. For a detailed description of this procedure see [18].

The drilling cores allow the determination of the tree species, the percentage of sapwood and heartwood as well as the latewood percentage, the type of wood preservative and its penetration depth and other wood-attacking constituents, the moisture content, density and compressive strength along the fiber [19-20].

Soon the drilling cores were used for the detection and analysis of damages in the interior of wooden construction components. In the usual structural safety analysis of timber structures, damages (e. g. decay) and their extent are estimated by visual inspection of the drilling cores and the remaining cross-section of the timber beam is calculated.

However, the information from the drilling cores is restricted to the pertaining measurement points. It requires of a lot of experience to conclude on the status of the whole subject. Often numerous measurement points (drilling cores) are necessary, which still may remain insufficient for larger buildings. The destruction from drilling cores (up to 30 mm diameter) must be considered which may be intolerable for statically highly stressed parts (which should all be covered). In heritage-protected buildings, drilling cores are understandably limited.

With the visual inspection of the drilling cores without further inspection devices decay can only be detected in the advanced stage. Incipient fungal attack, which already has a significant influence on the elasto-mechanical properties, cannot be detected. Decay is conjunct with a reduction of density and an increase of moisture content (both resulting in a decrease of the strength), which cannot be detected visually at least at the beginning of infestation.

Detection of Incipient Decay on Drilling Cores with Non-Destructive Methods

In the usual structural safety analysis of timber structures, damages and their extent are estimated by visual inspection, picking with a hammer, electrical moisture measurements, drilling cores and the drilling resistance. But all methods only lead to information about selected measurement points, there is no large-scale, laminar measurement of static-related areas. Often numerous measurement points (drilling cores) are necessary, which still may be insufficient for larger buildings. The destruction from drilling cores have to be considered, it may be not tolerable for statically highly stressed parts (which should all be covered). By applying the visual inspection of the drilling cores without further magnifying devices decay can only be detected in the advanced stage. Incipient fungal attack, which already has a significant influence on the elasto-mechanical properties, cannot be detected. Therefore, the methods used usually in the structural safety analysis allow only a limited assessment of the (especially interior) condition of the timber.

In a research project the problem of the low reliability of assessing the drilling cores only by visual inspection, especially for incipient fungal infection, is optimized by non- and minor-destructive testing of the drilling cores by X-ray radiation (on the ITRAX Woodscanner), neutron radiation and staining as well as destructive testing of the moisture content, density, stiffness and strength.

Incipient decay is conjunct with a reduction of density and an increase of moisture content (both resulting in a decrease of the strength), which cannot be detected visually and which is difficult to detect with the known imaging techniques (especially X-ray). So far nothing could be found in the literature about the separation of density and moisture content of wood with these imaging non-destructive testing methods. With the laminar ultrasonic echo method, (macroscopic) characteristics of wood affecting the strength and the stiffness (e. g. knots, cracks) can be detected. The results of the point wise drilling resistance method correlates with the hardness of the wood and – like for drilling cores – its density and, subsequently, the fungal infection (at microscopic level). A detection of the above mentioned structural characteristics affecting the strength is not guaranteed.

In the future, the question shall be answered whether it is possible to estimate the elasto-mechanical properties with non-destructive test methods or only an estimation of the degree of decay can be done. The relationship or difference between properties determined with non- an minor-destructive test methods and determined on core samples, on small, clear, defect free test specimens and on beams in component size with destructive testing is determined. Therefore, all influencing factors on the elasto-mechanical properties of "installed" timber were taken into account.

References

[1] Armstrong, H. F. H., Savory, J. G. (1959), *Holzforschung* vol. 13, p. 84–89.
[2] Brischke, C., Welzbacher, C. R., Huckfeldt, T. (2008), *Holz als Roh- und Werkstoff* vol. 66, n. 6, p. 433–438

[3] Wilcox, W. W. (1978), *Wood and fiber science* vol. 9, p. 252–257

[4] Glos, P. (1989), Festigkeit von Fichten-Bauholz mit Insekten- und Pilzbefall, Biegefestigkeit, In: *Holz als Roh- und Werkstoff* vol. 47, p. 329–335

[5] Wenzel, F., Kleinmanns, J. (1999), Sonderforschungsbereich 315, Historische Holztragwerke, Untersuchungen, Berechnungen und Instandsetzen. Universität Karlsruhe

[6] Bundesanstalt für Materialforschung und -prüfung (BAM) (2004), ZfPBau-Kompendium. http://www.bam.de/service/publikationen/zfp_kompendium/welcome.html

[7] Hasenstab, A., Osterloh, K., Robbel, J., Krause, M., Ewert, U., Hillemeier, B. (2004), Mobile Röntgenblitzröhre zum Auffinden von Holzschäden, In: DGZfP-Berichtsband auf CD, *DGZfP-Jahrestagung*, Plakat 15, 17.–19.05.2004, Salzburg

[8] Hasenstab, A., Rieck, C., Hillemeier, B., Krause, M. (2003), Use of low frequency Ultrasound Echo Technique to Determine Cavities in Wooden Constructions. In: Proceedings of the International Symposium Non-Destructive Testing in Civil Engineering (NDT-CE), DGZfP (Ed.), BB 85-CD, P51, 16.–19.09.2003, Berlin

[9] Hasenstab, A. (2005), Integritätsprüfung von Holz mit dem zerstörungsfreien Ultraschall-echoverfahren, Dissertation TU Berlin, www.zfp-hasenstab.de

[10] Hasenstab, A., Hillemeier, B., Krause, M. (2005), Defect localisation in wood with low frequency ultrasonic echo technique, In: Proceedings of the 14th International Symposium on Nondestructive Testing of Wood, 02.–04.05.2005, Hannover

[11] Baron, Th., Hasenstab, A., Wagenführ, A. (2008), Fäulnis in Brettschichtholz-Bindern einer Brücke mit Ultraschall-Echo lokalisieren, In: Tagungsband DGZfP-Jahrestagung, St. Gallen

[12] Baron, T. (2009), Untersuchungen an ungeschädigten und durch Pilzbefall geschädigten Nadelholzbauteilen mit ausgewählten Prüfverfahren, Dissertation an der Universität Weimar / F.A. Finger Institut

[13] Tobisch, S., Mittag, C. (1998), Zerstörungsfreie Untersuchungen von Schadphänomenen an Bauholz (1). In: *Holz-Zentralblatt* vol. 15, p. 236–238

[14] von Laar, C. (2006), Wie sicher lassen sich Holzschäden über Bohrwiderstandsmessungen ermitteln? In: *Messen und Sanieren* Heft 17

[15] Rinn, F. (1992), Chancen und Grenzen bei der Untersuchung von Konstruktionshölzern mit der Bohrwiderstandsmethode, In: *Bauen mit Holz*, Nr. 9, p. 745–748

[16] Frühwald, K. (2005), Strength Grading of Hardwoods, In: Proceedings of the 14th International Symposium on Nondestructive Testing of Wood, 02.–04.05.2005, Hannover, p. 199–210

[17] Frühwald, K., Hasenstab, A. (2009), Strength grading of hardwood with longitudinal ultrasonic waves and longitudinal vibration and locating defects in softwood and hardwood with low frequency ultrasonic echo technique, In: *Economic and Technical aspects on quality control for wood and wood products*, Proceedings of the Conference of Cost Action E53, 22.-23.10.2009, Lisbon

[18] Schweingruber, F. H. (1983), Der Jahrring. Standort, Methodik, Zeit und Klima in der Dendrochronologie, Verlag Paul Haupt, Bern, Stuttgart, 234 p.

[19] Erler, K. (1988), Bauzustandsanalyse und Beurteilung der Tragfähigkeit von Holzkonstruktionen unter besonderer Berücksichtigung der Korrosion des Holzes, Dissertation an der Ing.-Hochschule Wismar

[20] Kraft, U., Pribbenow, D. (2006), Handbuch der Holzprüfung, Verlag Bau + Technik GmbH, Düsseldorf

Coupling AE Monitoring with Discrete Element Fracture Models

E.N. Nagy, W.G. Davids and E.N. Landis

Abstract The monitoring and analysis of acoustic emissions related to fracture can be a trade-off between the simplistic yet practical empirical relationships and the more tedious yet fundamental relationships. In an intermediate area between these extremes, we are using acoustic emissions to monitor progressive fracture energy of small specimens of clear-grained wood. The wood specimens were modeled using a statistically variable lattice to represent material heterogeneity and disorder. The central hypothesis of the work is that a microfracture event captured by AE should correspond to the fracture of lattice elements in the simulation. Furthermore, the energy of the AE event should correspond to the local fracture energy released in the lattice simulation. By coupling lattice simulations with laboratory tests, we were able to establish a ratio between the cumulative fracture energy released in the simulation with the relative energy monitored by the AE system up to peak load. The magnitude of this ratio varies with failure mode, but in all cases, the shape of the cumulative AE energy captured mirrors the shape of the cumulative lattice fracture energy released. The results allow us to better match lattice element properties with the physical microstructure that the lattice elements are meant to represent.

Keywords Acoustic emission • Fracture energy • Lattice modeling • Wood • Microfracture

E.N. Nagy • W.G. Davids • E.N. Landis (✉)
University of Maine, Orono, Maine, USA
e-mail: landis@maine.edu

Introduction

The quantitative nondestructive evaluation of heterogeneous materials has been hampered by the lack of a fundamental relationship between measurable microstructural features and the effect those features have on macroscopic material properties. While linear elastic fracture mechanics provides that fundamental basis for homogeneous materials, we have yet to make such a relationship for some of our most commonly used structural materials because of the wide range of length scales over which material heterogeneities influence material strength and toughness.

In this work we address this missing quantitative microstructure-property relationship by representing the complex microstructure of a heterogeneous material with a lattice model. In the work presented here, we are representing spruce wood, but these concepts have wider application. The lattice approach allows us to represent the meso-scale physical material structure including many of the features that affect mechanical properties. As the lattice is loaded, damage can occur through the rupture of individual lattice elements. This is analogous to what occurs in the real material, where discrete microcracks occur in localized regions of the material.

The specific goal of the study presented here is to monitor acoustic emission (AE) activity in wood loaded in longitudinal tension. This AE energy release is then compared to the energy released by ruptured lattice elements in a model specimen. The hypothesis is that if the lattice is a good representation of the physical material, then the energy released by the broken lattice elements should mirror that of the AE energy monitored in laboratory specimens. This approach is relevant to nondestructive evaluation in that the lattice is a way to quantitatively relate measurable physical microstructure to bulk material performance.

Lattice Representation of Material

Lattice representations of heterogeneous materials have been applied for many years, emerging primarily from work in statistical physics [1]. The approach is that microstructural disorder can be explicitly represented both statistically and geometrically. In the case of wood, we use a 2D representation where different element types are employed to represent longitudinal and transverse directions, as well as variations in late wood and early wood. As illustrated in Fig. 1, the representation is fine enough to capture subtle variations in grain direction as well as localized irregularities in material structure. Details of the modelling approach are presented in [2,3]. A very brief summary is presented here.

The lattice representation employed here is a network of non-linear springs, each having statistically assigned strength and stiffness properties. When the model material is loaded, typically through defined displacements at certain boundaries, the "stress" is distributed through the lattice elements until the strength of a particular element is reached, and element rupture occurs. When this happens the stress is redistributed to the remaining elements. Depending on the spatial distribution of
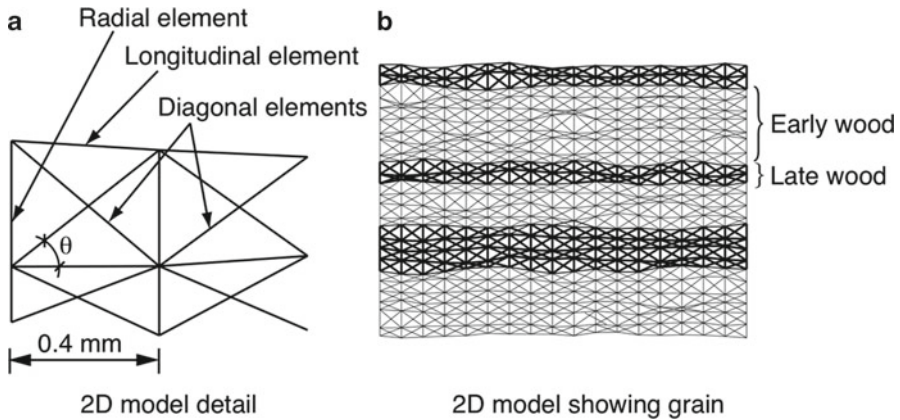
Fig. 1 Illustration of lattice representation of wood structure

element properties for the particular model, this redistribution can be stable, that is the stress redistributes in a way in which no other element strengths are exceeded, or it can be unstable, where failure of one element can lead to progressive failure in additional elements. This question of stable/unstable failure mirrors what we see in real materials.

The lattice representation affords us an interesting opportunity with respect to non-destructive evaluation. Acoustic emission monitoring has long been used to estimate the degree of progressive damage in materials and structures. In the lattice representation, a measurable amount of strain energy is released in each failed element. It is not unreasonable to conclude that this strain energy release relates to an acoustic emission from the specimen. This being the case, we should be able to run parallel laboratory tests and computer simulations where we monitor the acoustic emission activity in both laboratory and computer specimen.

Laboratory Experiments

A series of notched longitudinal (parallel to grain) dog-bone shaped tension specimens were prepared. The specimen section of interest had a 5 mm by 5 mm cross section with a nominal throat length of 48 mm. Specimens were loaded in a servo-hydraulic load frame using the output of a throat mounted clip gage for instrument control. A notch was used to force fracture to occur in a confined region.

AE activity was monitored with two broadbanded transducers connected to a full waveform acquisition system. Transducers were clamped to the specimen with a constant force, and a gel coupling agent assured good transmission of the AE signal to the transducers. Prior to acquisition, the AE signals were routed through 60 dB pre-amplifiers and were subjected to a 50 kHz high pass filter. The acquisition sampling rate was 1 MHz. The system allows continuous monitoring of AE
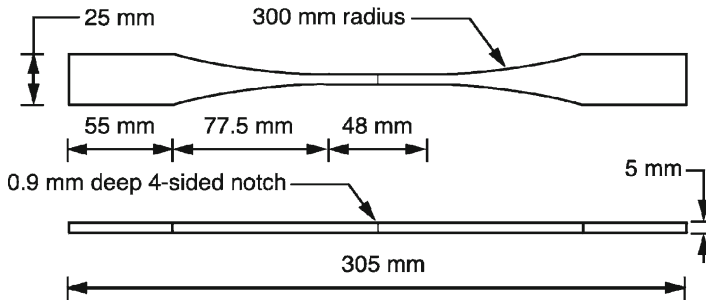
Fig. 2 Geometry of wood test specimens
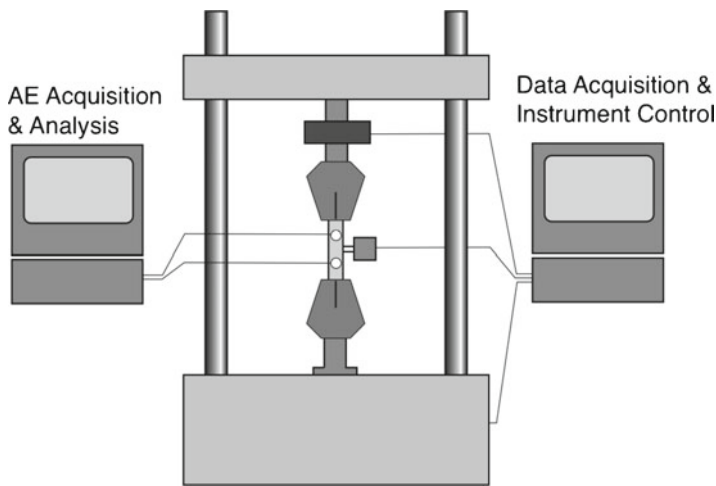
Fig. 3 Schematic illustration of experimental setup

sensors, but waveform recording occurs when the system is triggered by a signal amplitude of one tenth full scale. Each recorded event was saved as a time series with a length of 2048 points, 512 of which were pre-trigger. In addition to the AE data, load-deformation data for each specimen was recorded at a rate of 10Hz. The AE system and the load-deformation system were linked such that each recorded AE event is stamped with the current load and deformation state of the specimen.

Analysis of AE waveforms was done post test. Energy was calculated through a simplified analysis, where the AE event energy, E_{ae}, is proportional to the integral of the squared signal voltage [4]:

$$E_{ae} = \sum_i \int_{t_0}^{t} V_i(t)^2 \, dt \qquad (1)$$

In Eqn. (1) the limits of integration denote the length of the time series record, and the subscript i refers to a transducer.

Results

In the lattice simulation, the energy balance is a straightforward calculation as illustrated in Fig. 4. The total work of load can be balanced with the elastic energy of all elements, the energy dissipated by fracture, as well as the inelastic energy dissipated by plastic deformation of elements in compression. The figure illustrates how there is relatively little fracture energy released until the load in the specimen approaches peak load. At or slightly before peak we observe a rapid increase in broken elements (and therefore fracture energy release) corresponding to damage localization in the specimen.

In the laboratory specimens, isolation of energy components is more difficult. However a qualitative comparisons can be easily made as shown in Fig. 5. In this figure we see the previously mentioned rapid increase in fracture energy at or near peak load in the simulated test. In the laboratory test this rapid increase in fracture
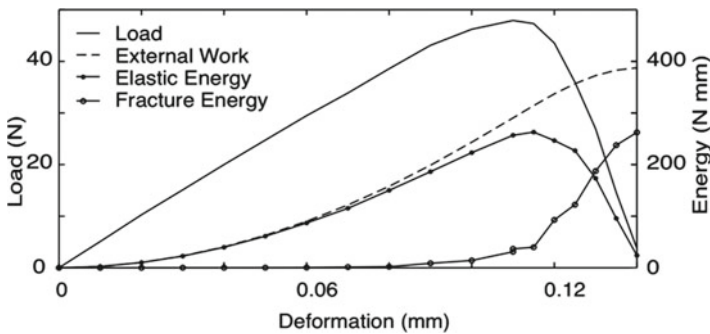
Fig. 4 Isolated energy components in simulated test
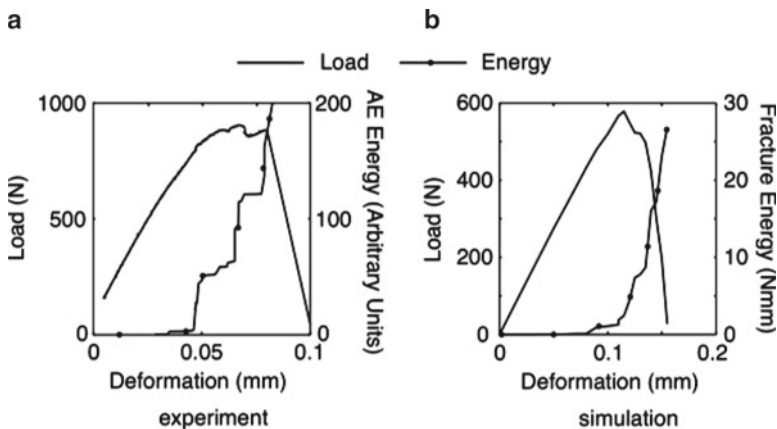
Fig. 5 Comparison of laboratory and computational tests

energy manifests itself in the form of a rapid increase in AE energy release. Very little AE activity occurs in the specimen until roughly 80% of the peak load is reached. At that point we observe a rapid burst of AE energy. This high rate of AE energy release continues past peak load through the eventual rapid unstable fracture of the specimen. This pattern parallels the observed cumulative fracture energy released by failed lattice elements.

Conclusions

While the work presented here is admittedly incremental, we offer a scenario where there is a direct and measurable link between a measurable phenomenon (acoustic emission energy) and the microstructural phenomenon (damage) that dictate residual properties. AE energy monitored in the laboratory specimens correlated well with the elastic energy released by fractured lattice elements in the computer simulation. The result supports our assertion that a lattice (or any other physically based modelling approach) offers a quantitative link between measurable microstructural features and the physical phenomena that dictate material performance.

References

[1] Herrmann, H.J., and Roux, S., eds. (1990) *Statistical Methods for the Fracture of Disordered Media* North Holland Publishers, New York.
[2] Nagy, E.N. (2010) *A Lattice model for the prediction of the mechanical properties of certain species of wood*. PhD Thesis, Dept. of Civil & Environmental Engineering, University of Maine.
[3] Nagy, E.N., Landis, E.N., and Davids, W.G. (2010) *Holzforschung*, vol. 64, p. 455.
[4] Harris, D.O. and Bell, R.L. (1977), *Exp. Mech*, vol. 17, p. 347.

Use of High Resolution Digital Images and NDT Imaging Techniques for Characterization of Timber Elements

M. Riggio, F. Prandi, R. De Amicis and M. Piazza

Abstract In this paper the combined use of high resolution images of wood texture and non destructive imaging of internal defects of wood is proposed for the characterization of structural timber on site. Experimental results are presented, based on the integrated use of digital photogrammetry, ultrasonic tomography and image analysis techniques. The implemented methodology aims at investigating the exploitation of some digital imaging techniques as complementary tools to be used during visual inspection.

Keywords Timber structures • NDT • Timber material characterization • Imaging of wood

Introduction

Visual grading criteria correlate mechanical properties of timber with visual features that can affect these properties. In order to reduce the subjectivity of the results, inspection systems, based on optical log scanning and automatic detection of defects, have been developed for the wood industry. More accurate results can be achieved if optical scanning of external features is coupled with non-destructive imaging of internal defects.

In this paper the combined use of high resolution images of wood texture and non destructive imaging of internal defects of wood is proposed for the characterization of structural timber on site. Results are presented, based on the integrated use of digital photogrammetry, ultrasonic tomography and image analysis techniques.

M. Riggio (✉) • M. Piazza
Dep. of Mech. and Struct. Engineering, University of Trento, Italy
e-mail: mariapaola.riggio@ing.unitn.it

F. Prandi • R. De Amicis
GraphiTech Foundation, Trento, Italy

The Method

The testing material

The testing material comes from the demolition of an ancient timber floor in the Belasi Castle (Trentino, Italy). A previous inspection on site was carried out on timber elements and, as it resulted from visual analysis, some of the floor beams exhibited extensive areas of decay, mostly due to insect attacks [1]. Further analysis was carried out at the Laboratory of Materials and Structural Testing of the University of Trento. The beams were cleaned up with pressurized water, in order to remove dirt and reveal the material texture on the element faces. In order to proceed to a first validation of the proposed method, a series of tests were carried out after smoothing geometrical irregularities. In this paper, results of the investigation on a timber element, 15.5x10x100 cm in size, are reported.

Sonic tomography

In the reported investigation, acoustic tomography, based on time-of flight measurements in through-transmission mode, was used for imaging internal macroscopic defects in wood.

In order to pre-evaluate the minimal size of the defects which can be detected, it is important to define the resolution of the tomography, that is limited by the applied wavelength and the distance between the sources, according to Eqn. (1):

$$D = \sqrt{d\lambda} = \sqrt{\frac{dV}{f}} \tag{1}$$

Where the wavelength is determined from the velocity *V* and frequency *f*.

The equipment used for data acquisition is a multi-channel device (TDAS 16 - Boviar s.r.l.). A 55 kHz piezoelectric transducer was used for emitting ultrasonic signals. Figure 1 illustrates the grid of the 74 independent travel time measurements for each investigated transversal section, where measurements were made on 20 points, 25 mm distant from each other. Longitudinal sections were investigated, by means of measurements made on two opposite longitudinal faces (Fig. 2).

The software used to form tomographic images optimizes the reconstruction process, comparing results from both iterative inversion algorithms and direct inversion techniques, thus permitting to reduce the influence on results of random errors in the measurement [2].

Fig. 1 Tomographic grid: transversal section [m]
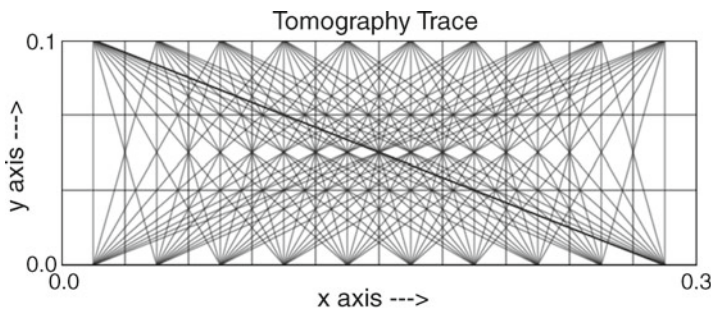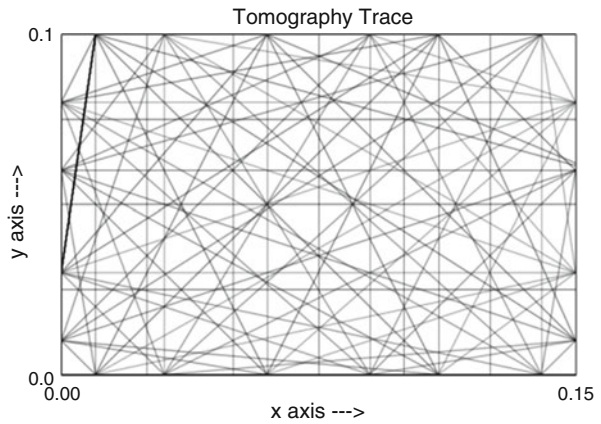
Fig. 2 Tomographic grid: longitudinal section [m]

Digital Photogrammetry

For the analysis of material features, visible on the element surface, the method of the digital photogrammetry has been adopted, which allows the reconstruction of textured three-dimensional metric models from photographic images.

The 3D coordinates of the object points can be determined knowing the exterior and interior orientation of the camera. For this purpose, a calibration process is needed (Table 1). The accuracy of the restitution depends on several factors: primarily on the scale of the photogram, secondarily on the geometry of the acquisition scheme and on the accuracy of the interior and exterior orientation [3]. Considering an acquisition scheme with the sensor parallel to the object plane, the measurement accuracy on the object plane (σ_c) is expressed by Eqn. (2):

$$\sigma_c = \pm \frac{D}{f} \sigma_{imm} \qquad (2)$$

Table 1 Nominal parameters of the camera

Camera	Hasselblad H3DII-39
Focal length [mm]	128.4282
Format size [mm] [pixels]	36.8x49 5412x7216
X Principal Point [mm]	18.9317
Y Principal Point [mm]	24.4713

Where D is the distance of the sensor from the object, f is the focal length and σ_{imm} is the measurement accuracy on the image plane, considered, approximately, equal to the pixel dimension.

High resolution images of the material texture were acquired by means of a CCD camera (Hasselblad H3DII-39) with a macro lens, of focal length 118.7 mm. The camera features Kodak's 39 megapixels sensor, measuring 36×48mm, with pixel size of 6.7 μm. The choice in using a non-metric camera was taken with the intention of developing a procedure for not expert operators. For this reason, tests described in this paper have been carried out using, for the interior orientation of the camera, the nominal parameters given by the manufacturer. These parameters have been refined during the orientation phase, the results are shown in Table 1. Of course, because of the instability of the parameters of non-metric medium format cameras, a preliminary camera calibration before each survey is recommended, if higher accuracy is required.

Close range photogrammetry basically involves the use of a network of photographs of an object taken from different angles. A series of about seventy convergent photographs, with a longitudinal coverage of 50%, in the main direction of the sample, were taken at 1 m distance from the object.

Commercial software Photomodeler® was used to extract orthographic photomaps from the acquired images of the wood surface texture. Exterior orientation parameters were calculated by means of a bundle adjustment procedure, determining the position of a series of homologous points on different images. The resulting bundle adjustment least mean square (LMS) error is equal to 1.744 pixel, which is compatible with the required accuracy. Orthophotos of each specimen face were obtained by means of a homographic transform, according to Eq. 3 (here written from X,Y-object plane to j,i-pixel image plane):

$$j = \frac{a_1 X + b_1 Y + c_1}{uX + vY + 1}; i = \frac{a_2 X + b_2 Y + c_2}{uX + vY + 1} \tag{3}$$

Where a_1, b_1, c_1, a_2, b_2, c_2, u and v are unknown transformation parameters.

Image analysis

The orthophotos representing the material texture on the element faces, were processed, with the aim of defining a procedure for the automatic/semi-automatic detection of the relevant features. On the images of the material texture, growth rings and intra-ring boundaries, knots, cavities, cracks and checks, have been analyzed and isolated by means of segmentation algorithms.
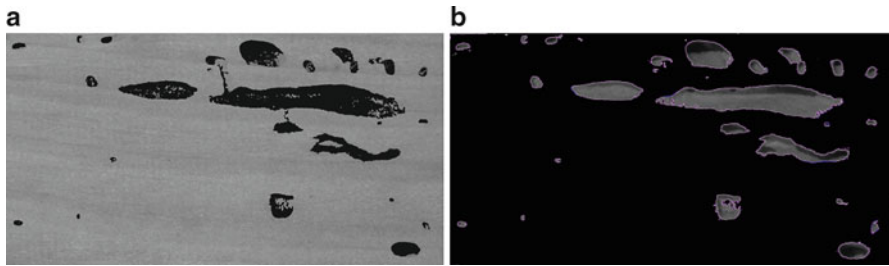
Fig. 5 Segmentation of bore-holes in wood
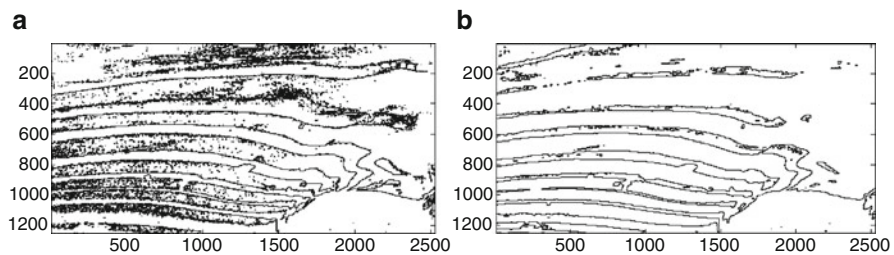
Fig. 6 Segmentation of growth layers in wood. **a**) from the original image, **b**) from the blurred image (20x10 Gaussian filter)

In [4], the core of the growth layer detection procedure is based on implementation of the morphological approach described in [5] for ring measurements. In the presented research, other standard algorithms, based on boundary detection and region growing techniques, were used for segmenting images. Region growing, based on gray-level thresholding, was adopted for the segmentation of well defined, closed regions, such as knots and bore-holes. In Fig. 5, bore-holes are detected, by segmenting directly the holes (Fig. 5a), or, conversely, the complementary surrounding areas (Fig. 5b). Boundary-based segmentation is concerned with detecting the boundary pixels of objects. A "contour following" algorithm [6], for detecting the ring boundaries has been used. Since it is based on the use of a gradient edge detector, noise from the images was preliminary removed. Results of growth layers contouring, using various kernel sizes, for Gaussian blurring, are shown in Fig. 6. As can be seen, differently filtered images give different information, in terms of boundaries' density and continuity. Further development of the research on wood images segmentation is described in [7].

Analysis of Results and Conclusions

From the presented results, difficulties in the application of ultrasonic tomography to wood, due to the natural variability, the anisotropy and the inhomogeneity of this material, are highlighted. However, accurate information of external defects can be
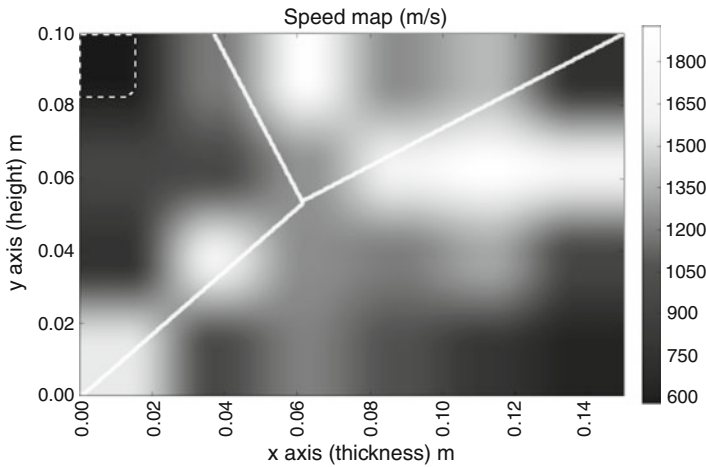
Fig. 7 Tomogram of a transversal section and, superimposed, deduced knot axes (continuous white lines) and decayed areas (white dotted line)

Table 2 Total area of each material feature (face 1)

Characteristics	Earlywood	Latewood	Knots	Checks	Decay
Area [cm2]	673	621	72	4.8	110.6
% A tot	43.42	40.07	4.66	0.31	7.14

used as indicator of internal defects and help the analyst to interpreter data from acoustic tomography. In acoustic tomography, the theoretical limit of the resolution is the wave length of the acoustic wave. With the adopted experimental setup, the calculated limit is 70÷50 mm. Nevertheless knots with diameter less than 50 mm could be detected and hypothesis of the direction of projected knots axis could be done, correlating visible knots with internal high velocity zones (Fig. 7). The presence of decay due to insect attacks is roughly estimated, correlating the position of low-velocity peripheral zone in tomograms, with the information of external decayed areas, given by the processed photographic images (Fig. 7). The checks present in the tested element were not properly detected, from tomograms.

Results of the photogrammetric analysis have been evaluated both in terms of metric accuracy and image quality. The latter aspect is related to the possibility of further processing image data for feature detection. Digital photogrammetry coupled with image analysis techniques proved to be a promising method for supporting advanced visual strength grading criteria of timber elements in service, permitting to automatically detect and quantitatively analyse relevant features.

By way of example, once images are segmented and material features are labeled, a series of proprieties of the extracted features can be calculated. In Table 2, the area of the different features is reported and the incidence of each on a single element face is represented, as a percentage of the total area.

References

[1] Piazza, M. Riggio, M. Tomasi, R. and Angeli, A. (2009). In: *Wiadomósci Konservatorskie* Proceedings of the REMO2009 Conference, vol. 26, pp. 289–298

[2] Camplani, M. Cannas, B. Carcangiu, S. Concu, G. Fanni, A. Montisci, A. and Mulas, M.L. (2008). In: *Lecture notes in Computer Science*, vol. 5073, p. 596–605, Springer, Berlin/ Heidelberg

[3] Kraus, K. (2007). *Photogrammetry. Geometry From Images and Laser Scans*. Walter de Gruyter, Berlin.

[4] De Amicis, R. Riggio, M. Girardi, G. and Piazza, M. (2011). *Computer-Aided Design*, 43, pp. 72–87

[5] Soille, P. Misson, L. (2001). *Can. J. Forest. Res*, vol. 31, pp. 1074–1083

[6] Anil, K.J. (1989). *Fundamentals of Digital Image Processing*, Prentice-Hall, Englewood Cliffs, N.J.

[7] Simões, B. Riggio, M. and De Amicis, R. (2011). *Application of image analysis for detection of wood features from NDT imaging data*. Proceedings of the 17th International Nondestructive Testing and Evaluation of Wood Symposium, Sopron, Hungary, 14–16 September, 2011

Relative Effects of Porosity and Grain Size on Ultrasonic Wave Propagation in Marbles

V. Özkan, İ.H. Sarpün and S. Tuncel

Abstract Grain size determinations by various ultrasonic techniques have been considered by several researches. Among the known methods, the ultrasonic seems to stand out because the method could be used to determine many properties of the materials. In this paper, we investigated that relative effect of porosity, mean grain size on ultrasonic velocity in marbles. We have represented ultrasonic velocity–porosity and porosity-grain size master graph. Using this graph, we have compared mean grain size of marble samples by optic microscope images. The experimental data are compared with the velocity versus porosity curves calculated according to ultrasonic methods. We see that ultrasonic velocity and porosity has showed a linear relation with the mean grain size of samples.

Keywords Marble • Mean grain size • Porosity • Ultrasounds • Ultrasonic Velocity

Introduction

Marble is a material that is constantly found in building, either for structural or decorative purposes. Marble is regarded as being the product of the metamorphism of limestone beds. Metamorphism takes place under the action of heat or pressure independently or of both heat and pressure simultaneously. It is a kind of rather hard rock consisting mainly of crystallized grains of calcite ($CaCO_3$)

V. Özkan (✉)
Physics Dept., Muş Alparslan University, 49100 Muş, TURKEY
e-mail: vozkan44@hotmail.com

İ.H. Sarpün
Physics Dept., Afyon Kocatepe University, 03100 Afyonkarahisar, TURKEY

S. Tuncel
TUBITAK Marmara Research Center, Gebze, TURKEY

or dolomite ($MaCO_3$) or a mixture of them [1-3]. The very good physical and mechanical properties of marble, such as its high resistance to abrasion, its translucence and its capability to be polished (as opposed to other type of rock materials), as well as its high strength and hardness render it one of the most widely used structural materials even today for the construction of both buildings and sculptures. Marble is no less complex; it appears to be anisotropic [4-6]. The propagation of acoustic waves through a stone material is becoming more and more important in defining its dynamic properties and therefore its mechanical behavior [7]. Ultrasonic Testing is the most preferred NDT technique for characterization of material properties. Ultrasonic testing parameters are significantly affected by changes in micro-structural or mechanical properties of materials. Some of the important metallurgical properties that have been correlated with ultrasonic testing parameters are grain size, inclusion content, elastic modulus, porosity, hardness, fracture toughness, yield strength, tensile strength, etc [8-9].

Ultrasonic testing of marbles has been examined by several researchers and all of them observed that the ultrasonic technique is suitable and accurate enough to detect chemical and structural anomalies and discontinuities in marble material [10]. One of the non-destructive physical methods with most acceptance and applications in the study of the structural characteristics and mean grain size formation marbles is by determination of the propagation velocity of ultrasonic waves [11-13]. Ultrasonic grain size determination of solid materials can be performed by several techniques which are dependent on ultrasonic quantities such as ultrasonic attenuation, ultrasonic backscattering, and velocity [14]. In this work, ultrasonic longitudinal velocity and mean grain size values of marbles, which are collected from different regions of Turkey, were compared with porosity. In addition this work shows an experimental study of these relative contributions on a set of porous marble samples.

Materials and methods

Marble samples have been collected from different regions of Turkey. Thickness of the samples was approximately 9-12 mm and their front surface is a 5×5 cm². The thickness of the samples was measured with an accuracy of 0.05 mm. Marble types have been chosen according to differences in porosity and density. Some physical and chemical properties of marble types which are obtained from the Institute of Turkish Standards are listed in Table 1.

Samples were selected according to the following two main criteria:

- Porosity of samples must be less than 0-6%.
- Density of samples must be known.

Table 1 Some physical and chemical properties of marble samples [15]

Marble Type	Hardness (Mohs)	Density (gr/cm³)	Specific weight (gr/cm³)	Elasticity Modulus (10⁴ kg/cm²)	Porosity (%)	MgO (%)	CaO (%)	Fe₂O₃ (%)	SiO₂ (%)
Eşkisehir Beige	3-5	2.71	2.74	1.90	0.49	1.39	52.09	0.33	1.89
Akşehir Black	4-5	2.66	2.69	6.09	0.40	0.49	55.40	0.30	Few
Rosso Levanto	3	2.61	2.72	5.38	3.20	26.25	13.75	9.70	28.35
Rosalia Pink	4	2.70	2.72	2.09	2.90	2.20	52.60	0.45	1.20
Denizli Travertine	4	2.50	2.72	5.38	2.30	0.31	54.55	0.32	0.26
Ameretto White	4	2.70	2.73	6.91	5.60	4.17	50.31	0.32	0.14

Table 2 Longitudinal velocity, mean grain size and porosity of marbles

Marble Names	Longitudinal Vel. (V_L - m/s)	Mean Grain Size (μm)	Porosity (%)
Eskisehir Beige	4710	43,9	0,49
Aksehir Black G	4982	54,3	0,59
Aksehir Black B	5010	55,7	0,40
Rosso Levanto	5237	65,3	3,20
Rosalia Pink	5323	68,4	2,90
Denizli Travertine	5234	77,2	2,30
Ameretto White	6248	103,1	5,60

Experiments and results

In this study, ultrasonic velocity was measured using a pulse-echo method at room temperature. Ultrasonic velocity in longitudinal and shear modes can be correlated to various material properties. The measurement involves determination of time of travel between the first and the second back-surface reflection and dividing it by the distance traveled by ultrasound. The accuracy of these measurements depends on the accuracy with which time of travel and the thickness of the component are measured. In cases, where there is access to only surface of the component (in-situ applications), velocity ratio (longitudinal to shear) serves as a useful parameter. Unlike velocity determination, which needs thickness of the component as input, velocity ratio can be found out from time of travel data alone for longitudinal and shear waves. Some of the techniques used for velocity determination are pulse echo overlap technique, pulse superposition method, sing around method and phase comparison method [16]. Porosity is a measure of the void spaces in a material, and is a fraction of the volume of voids over the total volume. Gubernatis and Domany have examined the formal structure of the multiple scattering problems and have studied the effects of distributions of pore sizes [17]. The pores are assumed to reside in an isotropic, homogeneous elastic matrix. However, the effects of grain boundary scattering in pore free materials have been considered extensively using multiple scattering, effective medium theory. The effects of pores and grains have varied depending on the internal structure of the sample, particle size and pores. Both particle size and porosity effects on ultrasonic wave propagation have been given by Thompson et al [18]. In this study, the longitudinal sound velocities was measured using a pulse-echo method at room temperature and all of the porosity was determined from precision density measurements. Both ultrasonic velocities and porosity of samples have been given in Table 2.

All graphs given below were plotted by using the values of Tables 1 and 2. In Fig. 1, the relationship between mean grain size and ultrasonic longitudinal velocity is shown. Correlation factor of this graph is 0.96799.

Graph of porosity versus longitudinal velocity is shown in Fig 2. The values show a linear relationship with a 0.93636 correlation factor.

A similar graph is given in Fig. 3 between porosity and mean grain size. This graph shows more linearity as compared to Fig. 2 which is 0.96832.

Fig. 1 The relation between mean grin size and longitudinal velocity
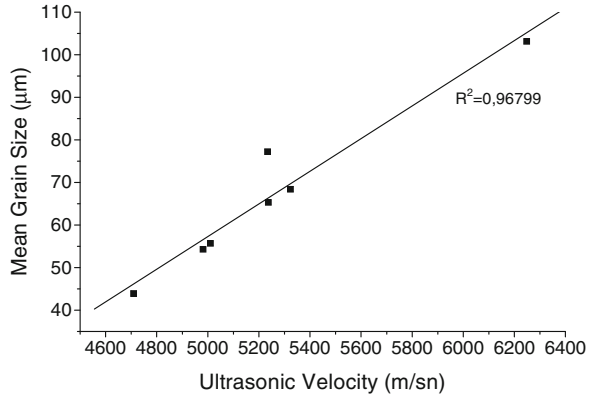
Fig. 2 The relation between porosity and longitudinal velocity
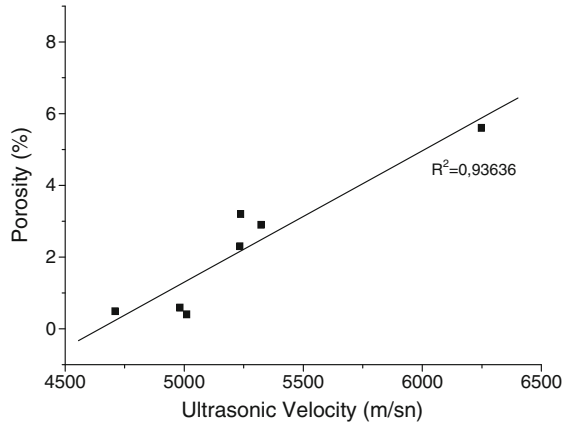
Fig. 3 The relationship between porosity and mean grain size
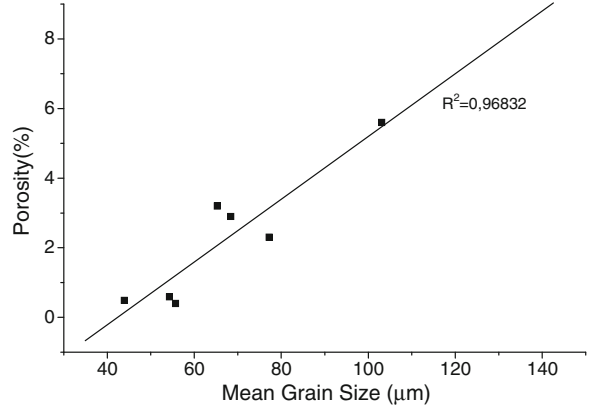
Conclusions

In this work, ultrasonic pulse-echo method has been applied to marble samples which have been collected from different regions of Turkey to determine relative effect of porosity, mean grain size and ultrasonic velocity. Our results show that the longitudinal velocity of ultrasonic wave and mean grain size of marble samples increases with increasing porosity. Additionally, progressing velocity of ultrasonic waves has been measured which has been sent to inside of samples by transducer for determining of the ultrasonic velocity. The mean grain sizes of marbles were determined using polarized light microscopy. Changing magnification values on marbles were taken suitably microscopic images. This study has shown a clear dependence of ultrasonic velocity on grain size in marble samples. It is observed that mean grain sizes increase depending on the sintered temperature. We observed that porosity is depended on a linear relation between ultrasonic velocity and mean grain size in samples. As a consequence, the theory of the effects of porosity on ultrasonic wave propagation has been showed extensively.

References

[1] Prassianakis, I.N. and Prassianakis, N.I. (2004), *"Ultrasonic testing of non–metallic materials: concrete and marble"*, Theoretical and Applied Fracture Mechanics, 42, 191–198.

[2] Prassianakis, I.N., Kourkoulis, S.K. and Vardoulakis, I. (2000), *"Marble monument examination using the NDT method of ultrasounds"*, 15th WCNDT, Roma.

[3] Rodríguez–Gordillo, J. and Sáez–Pérez, M.P. (2006), *"Effects of thermal changes on Macael marble: Experimental study"*, Construction and Building Materials, 20, 355–365.

[4] Corres, M. (1993), *From Penteli to Parthenon*, Melissa: Athens.

[5] Theocaris, P.S. and Coroneos, E. (1979), *"Experimental Study of the Stability of Parthenon"*, Publications of the Academy of Athens. 44, 1–80.

[6] Zambas, C. (1994), *"Mechanical Properties of Pentelik Marbles"*, Athens: Committee for the restoration of Parthenon Publications, Athens.

[7] Fais, S. and Casula, G. (2010), *"Application of acoustic techniques in the evaluation of heterogeneous building materials"*, NDT&E International 43, 62–69.

[8] Kumar A. (2003), *"Development, characterisation and applications of ultrasonic transducers for NDT"*, British Institute of Non-destructive Testing, 45(1), 70–72.

[9] Garnier, V., Chaix, J.F. and Payan, C. (2009), *"Improvement of new wave propagation techniques to characterize concrete"*, NDTCE'09, Non-Destructive Testing in Civil Engineering Nantes, France.

[10] Nanekar, P.P. and Shah, B.K. (2004), *"Characterization of material properties by ultrasonics"*, BARC Newsletter, 249. Founder's Day Spec. Issue.

[11] Balakrishna, S. (1959), *" Ultrasonic velocities in relation to the degree of metamorphism in limestones "*, Proceedings of Mathematical Science., 50(6), 363–365.

[12] Weiss, T., Rasolofosaon, P.N.J. and Siesgesmund, S. (2002), *" Ultrasonic wave velocities as a diagnostic tool for the quality assessment of marble"*, London Geological Society, 205, 149–164.

[13] Bellopede, R. and Manfredotti, L. (2006), *"Ultrasonic sound test on stone: comparison of indirect and direct methods under various test conditions"*, Heritage, Weathering and Conservation (HWC).

[14] Sarpün, İ.H., Tuncel, S. and Ünal, R. (2006), *"Mean Grain Size Determination in Marbles by Ultrasonic Techniques"*, ECNDT – Fr.1.7.4.

[15] Sarpün, İ.H., Kılıçkaya, M.S. and Tuncel, S. (2005), *"Mean grain size determination in marbles by ultrasonic velocity techniques "*. NDT & E International, 38, 21–5.

[16] Papadakis, E.P. (1976),*" Ultrasonic velocity and attenuation measurement methods with scientific and industrial applications"*, Physical Acoustics, 12, 277–374.

[17] Gubernatis, J.E. and Domany, E. (1983), *"Review of Progress in Quantitative Nondestructive Evaluation 2"*, D.O. Thompson and D.E. Chimenti, Eds., p. 833.

[18] Thompson R.B., Spitzig W.A. and Gray T.A. (1986), *" Relative Effects of Porosity and Grain Size on Ultrasonic Wave Propagation in Iron Compact "*, Review of Progress in Quantitative Nondestructive Evaluation, D.O. Thompson and D.E. Chimenti, Eds., Vol. 5B, 1643–1653.

Defect Detection in Porcelain Tiles Using Ultrasound

E. Eren and S. Kurama

Abstract The main point of this work is the optimization of ultrasonic methods for the non-destructive testing of sintered porcelain tiles containing defects. Zirconia and steel balls of different diameter and rubber with different thicknesses were imbedded in porcelain tile granules before pressing. After being sintered at 1473 K, the tiles were inspected using ultrasound. This method may allow defect detection using an A-scan. It can be observed that the amplitude of the back wall echo for a defective part is smaller than for a part without defects. Depending of the size, shape and position of the defect, a defect peak can be observed. An immersion pulse-echo C-scan was used to differentiate defects. The shape and place of the defects can be defined.

Keywords A-scan • C-scan • Defect • Porcelain tile • Ultrasonic

Introduction

Ultrasonic inspections measure the course of high-frequency sound waves that are introduced into the test object at various surface locations. The propagation of these electronically controlled sound pulses through the object is detected at specific points where the acoustic energy is converted back to an electronic signal [1].

E. Eren (✉)
Graniser Tile Factory, Akhisar Organize Sanayi Bölgesi, Manisa, Turkey

Anadolu University, Eskisehir, Turkey
e-mail: eeren99@gmail.com

S. Kurama
Anadolu University, Eskisehir, Turkey

Bhardwaj and et al. investigated defective ceramics. In their study, in order to determine the feasibility and detectability of defects in a non-contact ultrasonic mode, 1.5 mm diameter side drilled cylindrical holes were made in green and sintered ceramics. From their observations it is apparent that when ultrasound encounters a discontinuity in its path of propagation, the amount of energy transmitted is reduced, compared to a defect-free region [2]. Detecting delamination of green and fired ceramic tiles was achieved using ultrasonic an pulse velocity measurement [3]. High-frequency ultrasound NDE was used to locate micron-range defects, as well as to identify microstructural changes in dense armour ceramics [4]. High frequency ultrasound (80 MHz) was employed to test the valve head and valve shaft regions for volume defects. As a result, defects with dimensions down to 50 μm could be detected in the shaft [5].

In the current study, artificial defects are produced in ceramic tiles made from standard porcelain tile granules obtained from a tile company. Next, two ultrasonic methods (A- and C-scans) are used to detect different defect types within the porcelain tiles. The main aim is to observe differences at ultrasonic wave attenuation with these different defects. Therefore, the defect effect on ultrasonic wave attenuation was characterized.

Experimental Procedure

Standard porcelain tile granules were used in the preparation of samples in this study. ZrO_2 balls (4.85 mm and 2.96 mm diameter), steel balls (4 mm and 1 mm diameter) and rubber (6.8 mm diameter, 1mm and 2mm thickness) were placed in to tile 1, tile 2, tile 3, tile 4 and tile 5, respectively. Only tile1 was found to contain defects (ZrO_2 balls). Samples were prepared by the uniaxial pressing technique, in a 50 mm x 100 mm rectangular die, by applying 450 kg/cm² pressure, and then dried at 383 K. The sintering was then carried out in a laboratory kiln (Nabertherm N 20/HR) at 1473 K.

The transmission and reflection of ultrasonic waves (longitudinal waves) were performed using a contact ultrasonic transducer operating on pulse-echo mode. The centre frequency of the transducer was 5 MHz. Silicone oil was used as a couplant material. The transducer was excited by timed pulses from an ultrasonic pulser-receiver (Model 5800 Computer Controlled Pulser/Receiver, Olympus Panametrics-NDT). The amplitude of the back wall echo measurements for the ultrasonic signals was performed using a digital oscilloscope (Tektronix TDS 1012 Two Channel Digital Storage Oscilloscope).

To C-scan analyze, the Dr. Hillger USPC 3040 DAC Industrie system was used. C-scan imaging was performed on the aforementioned tiles using a 6-12 MHz longitudinal focused immersion transducer. The transducer had a diameter of 0.6 cm and a focal length of 15 cm. The tiles were placed into an immersion tank and the z-position was manually adjusted until the maximum signal was obtained. The top and bottom surface peak reflections were identified on the oscilloscope, and the

bottom surface signal was gated so that the variation of the signal could be collected as it traveled through the tile. In this technique, ultrasonic amplitude measurements were performed using a pulse-echo C-scan mode [6]. From these measurements, back wall echo graphs were drawn. The relative attenuation loss range changes from 0 dB (greatest amplitude) to – dB values (least relative amplitude). For the back wall echo the 0 dB shows 'good' or 'dense' regions.

Results and Discussion

In order to determine the feasibility and detectability of defects by a contact ultrasonic mode, defects were imbedded in sintered ceramics. Figure 1a shows a typical transmitted ultrasonic signal as a function of a defect-free part in the ZrO_2 balls containing sintered tile (tile1). The amplitude of the back wall echo is 27.2 V. Fig. 1b, c represent typical transmitted ultrasonic signals as functions of defective regions in the ZrO_2 balls containing sintered tile. There were no explicit flaw echos detected in
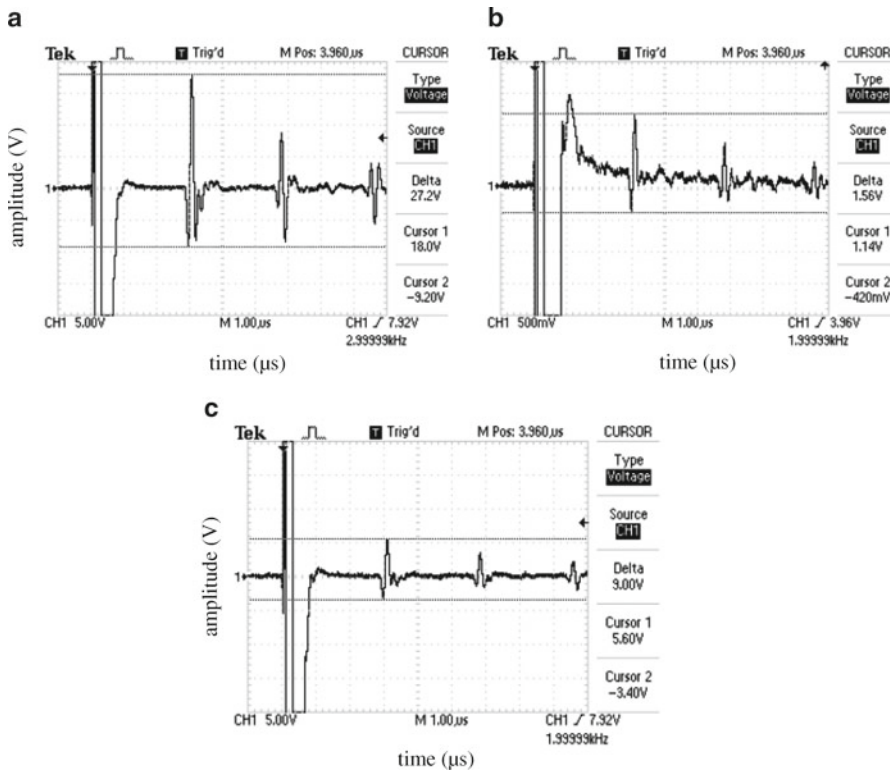
Fig. 1 A-scan displays showing amplitude of back wall echo of the defect-free part (**a**), the 4.85 mm (**b**) and the 2.96 mm (**c**) diameter ZrO_2 balls containing parts of sintered tile

Table 1 Changes in the defect-free and defective parts' back wall amplitudes

Tile	Back wall echo amplitude for defect-free part (V)	Back wall echo amplitude for defective part (V)	Change in back wall amplitude (%)
tile1 (4.85 mm dia.)	27.2	1.56	5.74
tile1 (2.96 mm dia.)	27.2	9	33.09
tile2	28	1.28	4.57
tile3	25	5.6	22.4
tile4	28.2	14	49.65
tile5	22.8	3.52	15.43
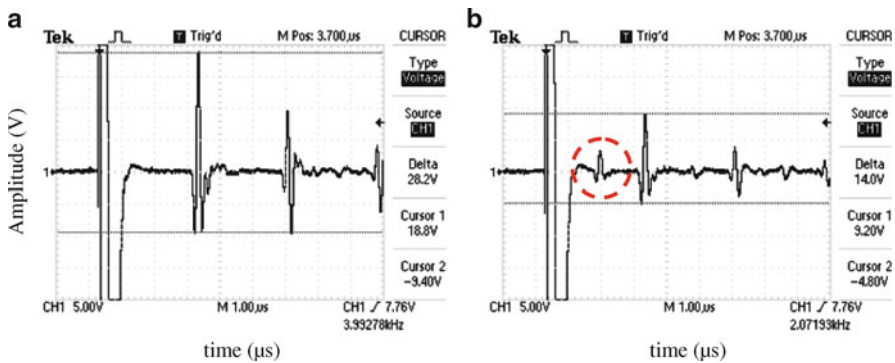
Fig. 2 A-scan displays showing amplitude of back wall echo of the defect-free part (**a**), 1 mm thickness and the 6.8 mm diameter rubber containing part (**b**) of sintered tile

the amplitude-time graphs because the balls were spherical and reflected ultrasonic signals at different angles [7]. Depending on the increased diameter of the balls, the back wall amplitude was decreased. For a 4.85 mm diameter ZrO_2 ball, the back wall amplitude was 1.56 V and the change in the back wall amplitude (back wall echo amplitude for defective part/ back wall echo amplitude for defect-free partX100) was 5.74, for a 2.96 mm diameter ZrO_2 ball, the back wall amplitude was 9 V and the change in the back wall amplitude was 33.09. This condition was valid for steel balls of different diameters embedded in tile2 and tile3. Their back wall amplitudes are given in Table 1. The steel balls were oxidized and, due to the gas-out, the back wall amplitude (%) drops are higher than for ceramic balls of larger diameter.

Figure 2a shows a typical transmitted ultrasonic signal as a function of a defect-free part in the 1 mm thick and 6.8 mm diameter rubber containing tile (tile4). Figure 2b represents a typical transmitted ultrasonic signal as a function of a defective region in this tile. The flaw is vertical to the ultrasonic signals. Thus, a flaw echo (in sphere at Fig. 2b) was also detected. The amplitude of the back wall echo amplitude decreased from 28.2 V to 14 V. When the thickness of the rubber was increased, the
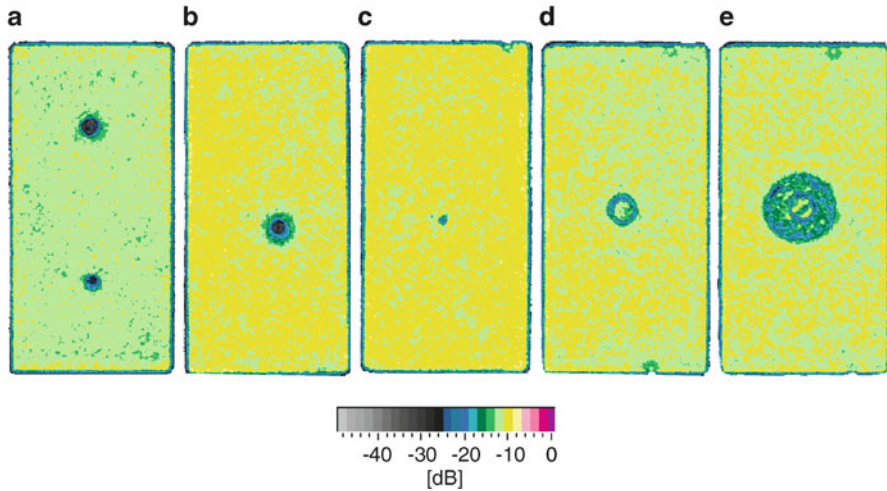
Fig. 3 C-scan displays showing (**a**) the ZrO_2 balls, (**b**) the 4 mm diameter steel ball, (**c**) the 1 mm diameter steel ball, (**d**) the 1 mm thick and 6.8 mm diameter rubber, (**e**) the 2 mm thick and 6.8 mm diameter rubber containing tiles' back wall echo images

back wall echo amplitude decreased from 22.8 V to 3.52 V. A 1mm increase in thickness decreased the back wall echo ampitude change from 49.65 % to 15.43% (Table 1).

The ZrO_2 balls and the steel ball (4 mm diameter) prevented ultrasonic signals passing completely to the back wall, increased attenuation loss (to -30dB) and could be detected in the back wall echo images (Fig. 3a, b). The steel ball (1 mm diameter) and rubbers have an attenuation loss of about – 20dB (Fig. 3c–e).

Conclusion

The detection and characterization of defects is achieved by an optimization of the use of ultrasound for non-destructive materials' characterization. By using the A-scan, different defects can be detected. The shape and size are critical factors for detection. Whereas the balls' flaw echos could not be detected, the rubbers' flaw echos were easily detected using the A-scan. Steel balls which were of smaller diameters than the ZrO_2 balls greatly decreased the back wall echo. The reason could be the difference of the ultrasonic waves propagation between metal to ceramic and ceramic to ceramic.

The defect distribution was designed as a C-scan in light of the ultrasonic-transmitted amplitudes. In other words, for an area containing a greater amount of defects, more ultrasonic waves will be deflected or scattered by the defects, resulting in the transmitted ultrasonic waves having lower amplitudes. The balls decreased

the amplitude much more than the samples perpendicular to the direction of the ultrasonic wave propagation. Both spherical and flat defects can easily be obtained using the ultrasonic C-scan. For rubber samples it is thought that a thicker sample deformed the tile and cracks occurred around the defect. To prove this, a SEM analyze should be performed.

References

[1] Grandt Jr., A.F. (2004), Fundamentals of structural integrity damage tolerant design and non-destructive evaluation, p. 341, John Wiley and Sons Inc., New Jersey.
[2] Bhardwaj, M.C., Neeson, I. and Stead, G. (2000), *NDTnet*, vol. 5, n. 6.
[3] Romagnoli, M., Burani, M., Tari, G. and Ferreira, J.M.F. (2007), *J. Eur. Ceram. Soc.*, vol. 27, n. 2–3, pp. 1631–1636.
[4] Hayes, B. (2007), *Ceram. Ind.*, vol. 157, n. 8, pp. 24–28.
[5] Netzelmann, U., Reiter, H., Shi, Y., Wang, J. and Maisl, M. (1997), *NDTnet*, vol. 2, n. 7.
[6] Kim, J. and Liaw, P.K. (1998), *JOM*, vol. 50, n. 11.
[7] Taptık, Y. (1997), Failure analysis seminar notes, p. 8.36, Kayalı, E.S., Eruslu, N., Ürgen, M., Taptık, Y., and Çimenoğlu, H. (Ed.), UCTEA Chamber of Metallurgical Engineers, Istanbul.

Characterization of Synthetic Emeralds Based on the Morphology of their Inclusions

A. Mueller, U. Hassler and J. Zaeh

Abstract The aim of the presented work was the characterization of synthetically manufactured emeralds by means of X-ray micro computed tomography (CT). As the result of the CT measurements, a three-dimensional volume representation of the gemstones became available. Three synthetic emeralds were measured containing different kinds of inclusions. For data evaluation, an image processing chain was designed, which is adapted to the particular requirements of emerald analysis. An essential aspect was the extraction of inclusions and inhomogeneities from the reconstructed volumetric data and their characterization regarding morphology. Furthermore, results of microscopic investigation of the samples have been compared to results of CT measurements demonstrating the suitability of CT for finding inclusions in emeralds.

Keywords Computed tomography • Gemstone • Image processing • Material characteristics • 3D segmentation

Manufacturing of Synthetic Emeralds

Flux-melt method. In this method, the gem-forming chemicals are dissolved in a solution of lithium molybdate. The solvent is heated in a platinum crucible to around 800°C, thereafter seed crystals of natural or synthetic beryl are given into the solution in a platinum cage. By slowly lowering the temperature the solution becomes supersaturated and crystals of synthetic emerald grow on the seeds. The process is very slow [1, 2].

A. Mueller (✉) • U. Hassler
Fraunhofer Development Center X-ray Technologies, Fuerth, Germany
e-mail: anja.mueller@iis.fraunhofer.de

J. Zaeh
Institute for Research in Applied Art, University of Applied Sciences, Duesseldorf, Germany

Hydrothermal method. The method was originally developed in 1928 by Professor Nacken for the production of quartz crystals. He successfully adapted it for the growth of emeralds. The apparatus consists of a steel autoclave lined with silver which is designed in a way so that the temperature is lower in the upper part. In this part, seeds in form of thin lamellae are placed, whereas raw material and solvent are added in the lower part. Under pressure and temperatures of about 400°C an emerald crystal grows within a few days time [3].

Experiments

Specimens

In the scope of this work three synthetic emeralds were investigated, which were manufactured using different production techniques (see Table 1). The emeralds were kindly provided by Dr. Claudio C. Milisenda from the German Foundation for Gemstone Research (Deutsche Stiftung Edelsteinforschung, DSEF).

CT setup

All of the measurements within the present study were performed at the Sub-μm CT setup of the Fraunhofer EZRT at Fuerth, which is equipped with a FeinFocus X-ray source FXE160. As X-ray detector a Hamamatsu flat panel detector C9312 was used. Table 2 lists the performed measurements along with the most important X-ray parameters. These vary slightly as the parameter set for each measurement has been optimized to the size of the measured specimen.

CT reconstructions

When examining the CT reconstructions, three major types of inclusions were found (see Fig. 1):

- Wispy veil-like inclusions: plane, extensive structures usually with higher material absorption than the surrounding emerald.
- Spiky nail-head inclusions.
- Crystal shaped inclusions.

In general it can be stated that samples 1 and 3 contained a vast number of inclusions whereas the second stone was much cleaner. The inclusions were not always homogenous, i.e. some of the inclusions consisted of both lower and higher absorbing material than the surrounding pure emerald.

Table 1 Overview of specimens

Sample ID	Producer	Method	Length / mm	Width / mm	Height / mm
1	Nacken	Hydrothermal	3.1	2.5	2.8
2	Gilson	Flux-melt	4.9	3.7	2.6
3	Linde	Hydrothermal	2.8	2.8	2.4

Table 2 Overview of measurements performed at the samples listed in Table 1

Measurement ID	Sample ID	Voltage / kV	Power / W	FDA / cm	Voxel / μm
1	1	60	4.2	21.96	1.8
2	2	60	4	21.16	2.1
3	3	60	3.8	21.96	1.7
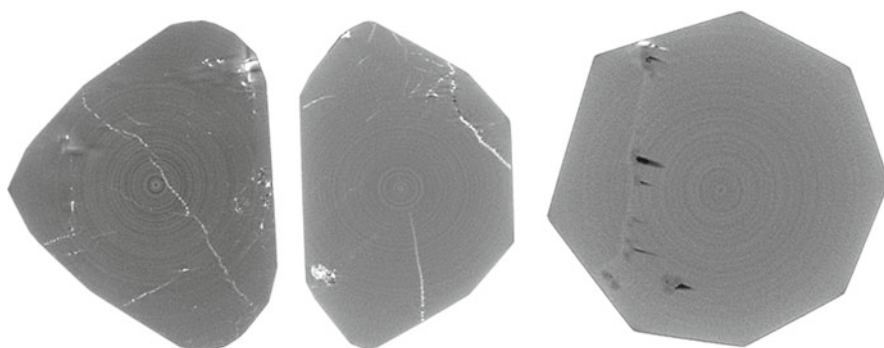
Fig. 1 Slice views of the measured gemstones (from left to right Gemstone 1, 2, 3) exhibiting different kinds of inclusions

Microscopic setup

The transparency of emeralds offers the opportunity to compare object analysis based on X-ray CT data with object analysis based on visible means. For this reason, microscopic examination of the emeralds was performed. We used a Keyence VHX 600 microscope and the integrated measurement functions to estimate sizes of inclusions. The inclusions were searched and measured manually.

Inclusion Extraction and Examination

Comparison between CT and microscopic data

The aim of the following part of the work was to ensure that computed tomography offers an appropriate mean for measurement of the relevant features. Up to now, CT has virtually not been used for the examination of gemstones. When starting to use

CT for this task, it is important to clarify if there are differences in the visibility of the inclusions with optical light versus with X-rays.

Firstly, we would like to point out the main differences between the two methods.

- *Measured property.* The microscope offers - roughly spoken - just a magnification of the normal human vision. This is in accordance to the established approval of the quality of gemstones. On the other hand, in CT reconstructions we can distinguish deviations in grey values caused by differences in material absorption.
- *Acquired data.* The microscopic setup is intended for visual inspection. Inclusions are searched for manually, the position within the object has to be estimated. In contrast, CT delivers a full 3D dataset of the entire sample, allowing for 3D positioning and measurement of inclusions. In comparison to microscopic images the noise level is much higher within the CT data.
- *Identification of materials.* Microscopic imaging does not allow for any indisputable statements regarding identification of materials. Yet it offers colour and shape information from which an experienced user can draw the corresponding conclusions. Contrariwise, CT reconstructions directly deliver information about the relative density of materials. Simulating the X-ray spectrum also enables one to estimate the corresponding physical densities of materials.

Procedure. The gemstones were first examined using the microscope. Inclusions were searched for manually, documented and measured in 2D. A sketch of the whole gemstone with the estimated position, size and colour of inclusions was worked out. Subsequently, CT scanning and 3D reconstruction was performed. Within the CT reconstructions it was intended to identify the previously specified inclusions. These were segmented and a surface description via a triangle mesh using the STL (SurfaceTesselationLanguage) data format was generated. The corresponding image processing chain is shown in Fig. 2. In this way, the digital representation of the inclusion's surface could be compared quite easily to the microscopic images.

Results

As the two measuring means do not deliver directly comparable data, the evaluation was restricted to a visual interpretation.

Gemstone 1 - Nacken. Visual inspection of CT data is normally done by scrolling axially parallel through the 3D dataset, examining 2D slices along different axes. This procedure is also supported by all important software modules in the field of industrial CT data visualisation. As inclusions are not necessarily axially parallel within the CT volume, it is often difficult to guess the actual shape of the inclusions. On the other hand, using the extracted STL data and a corresponding visualization software allowing for 3D visualization of the inclusion, the morphology can be made visible perfectly.

Gemstone 2 - Gilson. Fig. 3 shows a comparison of four inclusions of Gemstone 2 in microscopic and in CT data. It was intended to arrange the extracted STL
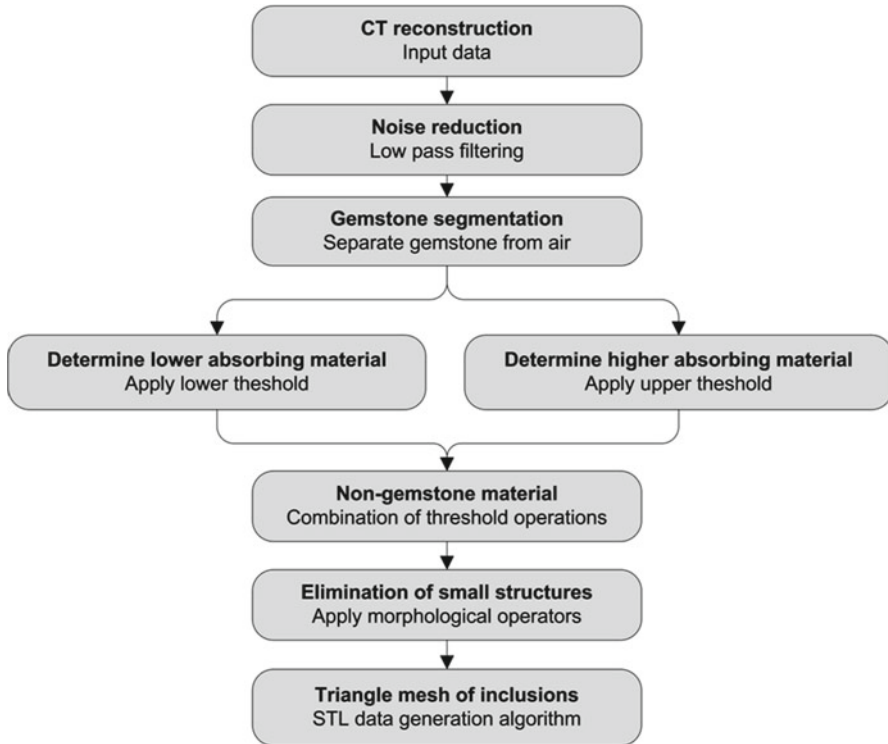
Fig. 2 Image processing chain of inclusion extraction

surface data in a corresponding way to the microscopic view. Two statements can be made. Firstly, the inclusions extracted by optical means could also be found within the CT reconstructions. Secondly, consistency of the rough shape of the inclusions can be stated for all cases, with variations in accordance of details.

Gemstone 3 - Linde. Gemstone 3 contained clearly recognisable two-phase inclusions. This was represented well in the CT reconstructions as one can see in Fig. 4 on the left. By applying the method for inclusion extraction, which was presented in the previous chapter, twice, one time for the inner and a second time for the outer structure of the inclusion, we were even able to represent two phases in the STL data set (Fig. 4, right).

Conclusion and Outlook

In the scope of this work, three synthetic emerald samples have been measured and examined by an X-ray CT setup. A comparison to microscopic investigations was performed. Inclusions could be recovered well from CT data, also ensuring accordance of morphology. Thus, the principle suitability of CT as a mean of emerald
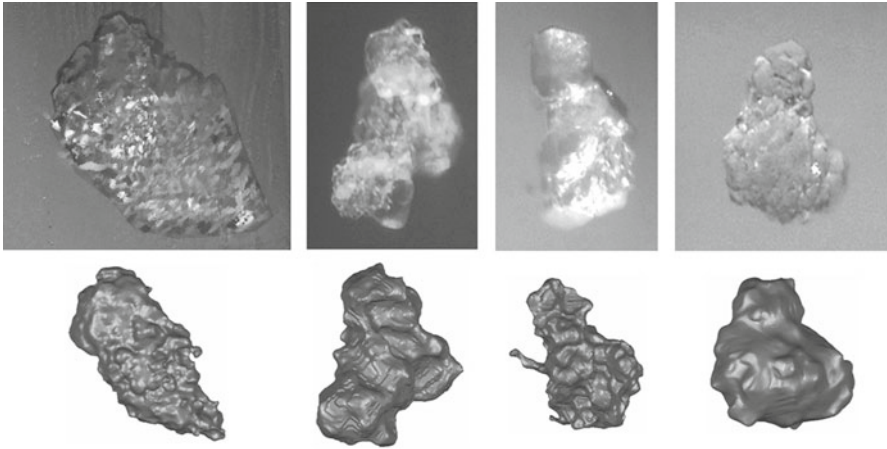
Fig. 3 Comparison between microscopic data (upper row) and rendered STL data visualisation of inclusions (lower row) in Gemstone 2. A good accordance in shape is clearly recognisable
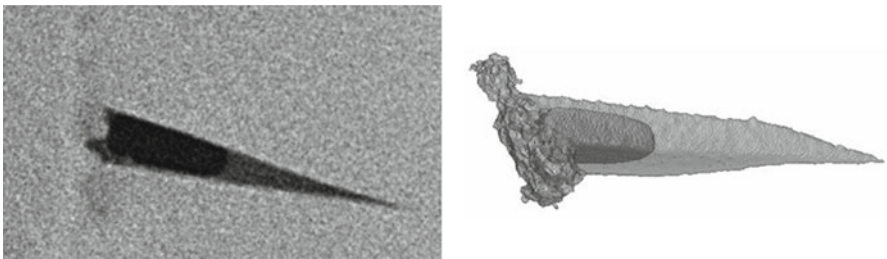
Fig. 4 Visualisation of a two-phase inclusion of Gemstone 3; left CT reconstruction slice view, right rendered STL data visualisation

investigation has been shown. Future work will on the one hand focus on further improvement of data evaluation, for example automation of inclusion extraction, characterisation based on the morphology of inclusions and material identification. On the other hand, examinations of other gemstones, for example diamonds, may be of interest.

References

[1] Eppler, W. F. (1984), *Praktische Gemmologie*, p. 180, Stuttgart: Rühle-Diebener-Verlag GmbH + Co KG.
[2] Read, Peter G. (2005), *Gemmology*, Boston: Elsevier Butterworth-Heinemann.
[3] Van Praagh, G. (1947), Synthetic Quartz Crystals, In: *Geological Magazine*, vol. 84, No. 2, pp. 98–100, Cambridge University Press.

Can Proteoglycan Change in Articular Cartilage be Detected by Ultrasound Evaluation?

I. Afara, S. Wallace, S. Singh and A. Oloyede

Abstract This paper assesses the capacity of high-frequency ultrasonic waves for detecting changes in the proteoglycan (PG) content of articular cartilage. 26 cartilage-on-bone samples were exposed to ultrasonic waves via an ultrasound transducer at a frequency of 20*MHz*. Histology and *ImageJ* processing were conducted to determine the PG content of the specimen. The ratios of the reflected signals from both the surface and the osteochondral junction (OCJ) were determined from the experimental data. The initial results show an inconsistency in the capacity of ultrasound to distinguish samples with severe proteoglycan loss (i.e. >90% PG loss) from the normal intact sample. This lack of clear distinction was also demonstrated for samples with less than 60% depletion, while there is a clear differentiation between the normal intact sample and those with 55-70% PG loss.

Keywords Articular cartilage • Proteoglycan content • Ultrasonic NDT • Reflection ratio

Introduction

Several studies have investigated the responses of articular cartilage in different physiological conditions to ultrasound wave, including the effects of surface roughening [1], collagen disruption [2, 3], proteoglycan depletion [4, 5] and naturally degenerated or osteoarthritic conditions [5, 6]. A common limitation with practically all of these studies, which are based on the analysis of reflected signals from the cartilage – bone interface, is the variabilty in the pattern of the reflected signal.

I. Afara • S. Wallace • S. Singh • A. Oloyede (✉)
School of Engineering Systems, Institute of Health and Biomedical Innovation, Faculty of Built Environment and Engineering, Queensland University of Technology, Brisbane, Australia
e-mail: k.oloyede@qut.edu.au

This inevitable and difficult to control influence is a consequence of the varying degrees of attenuation and diffraction properties of normal tissues [7] and the rough nonuniform topography of the osteochondral junction.

Another limitation of the literature material is that no study has related the ultrasound reflection patterns with quantity of proteoglycans (e.g. in a gradual depletion process), the degree of disruption of the collagen fibrillar meshwork or their combined altered osmotic state. This paper investigates the influence of the quantity of proteoglycans in the artificially degraded cartilage on the pattern of the reflected ultrasound signal relative to the ratio of the osteochondral junction to surface reflected wave proposed earlier by Brown et al [8].

Material and Methods

Sample preparation

Visually normal and intact bovine patellae, (N=6), harvested from prime oxen within 24 h of slaughter, were used in this study. The samples were wrapped in 0.15M saline soaked towels and stored at about -20°C until required for testing. Prior to testing, the intact patellae were thawed in 0.15M saline at room temperature for about 4 hours, then cartilage-on-bone blocks (n = 26, lxbxh = 7x7x5mm) were extracted from the patellae. All tests were conducted with the specimens fully submerged or hydrated in 0.15M saline.

Ultrasound echoes were taken from the saline-cartilage and cartilage-bone interfaces of all the samples. Care was taken to ensure that the tissue surface was parallel to the surface of the transducer. This is to make sure all the reflected ultrasound signal is captured by the transducer. Subsequent to ultrasound examination, the samples were treated in 1*mg/ml* of trypsin (T4667, Sigma Aldrich, Sydney, Australia) in 0.15M phosphate buffered saline at 37°C to remove proteoglycans. The proteoglycan depletion programme was performed for 4hrs, with ultrasound reflection signals obtained from the samples at 1hr intervals. This gradual progression of enzymatic action from surface to bone closely resembles the pattern of proteoglycan loss in early stage osteoarthritis which is characterised by gradual loss of proteoglycans and disruption of the collagen meshwork from the superficial zone [9] amongst others signs.

Experimental set-up

Ultrasound examinations were made at an approximate distance of 3mm from the sample surface using a 20MHz, Ø3*mm*, plane-ended contact transducer (V129, Panametric Inc., Massachusetts, USA). The experimental setup is shown in Fig. 1. The transducer was excited via a pulser/receiver that also receives the reflected
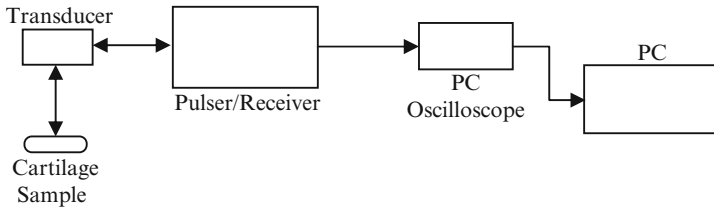
Fig. 1 Experimental setup for ultrasonic evaluation of cartilage

ultrasound echo. This was in turn connected to PC-based oscilloscope – PC 5204 (Pico technology Limited, Cambridgeshire, UK) which captures and converts the analog signal to digital in real-time and then displays it on a PC. Surface and osteochondral junction (OCJ) reflections were captured and recorded using the PicoScope 6 software (Pico technology Limited, Cambridgeshire, UK).

Histological evaluation and image analysis

Sections of each sample was excised at intervals of 1hr for histological evaluation. Subsequent to ultrasound examination, 7μm-thick sections were excised from the samples and fixed on microscopic slides. The sections were then stained with Safranin-O (which binds stoichiometrically with proteoglycans). This was followed by absorbance profiling under monochromatic light source using a Nikon Labo-Phot light microscope to obtain the micrographic images of the sections before and after staining.

Image analysis to determine the proteoglycan content was performed using *ImageJ* software version *1.44i* (Wayne Rasband, National Institute of Health, USA) according to protocols observed by Moody et al [10] and Brown et al [11]. In summary, the stained and unstained section micrographs of each sample are converted to an absorbance–depth profile. Since the light absorption is a consequence of the Safranin-O stained proteoglycans, the absorbance profile is directly related to the proteoglycan distribution and content of the sample. Using an ImageJ macro written in-house for this purpose, the proteoglycan content in the sample was calculated based on Beer Lambert's law. The proteoglycan content in the depleted sample was expressed as a percentage of the amount remaining in the tissue after depletion relative to the amount in its corresponding normal tissue.

Results

The patterns of reflections from the cartilage surface and the osteochondral junction (OCJ) between cartilage and bone were obtained for normal intact and progressively depleted samples (Fig. 2). The typical ImageJ results for the progressive removal of proteoglycans from the samples from 1 to 4 hr exposure for trypsin are
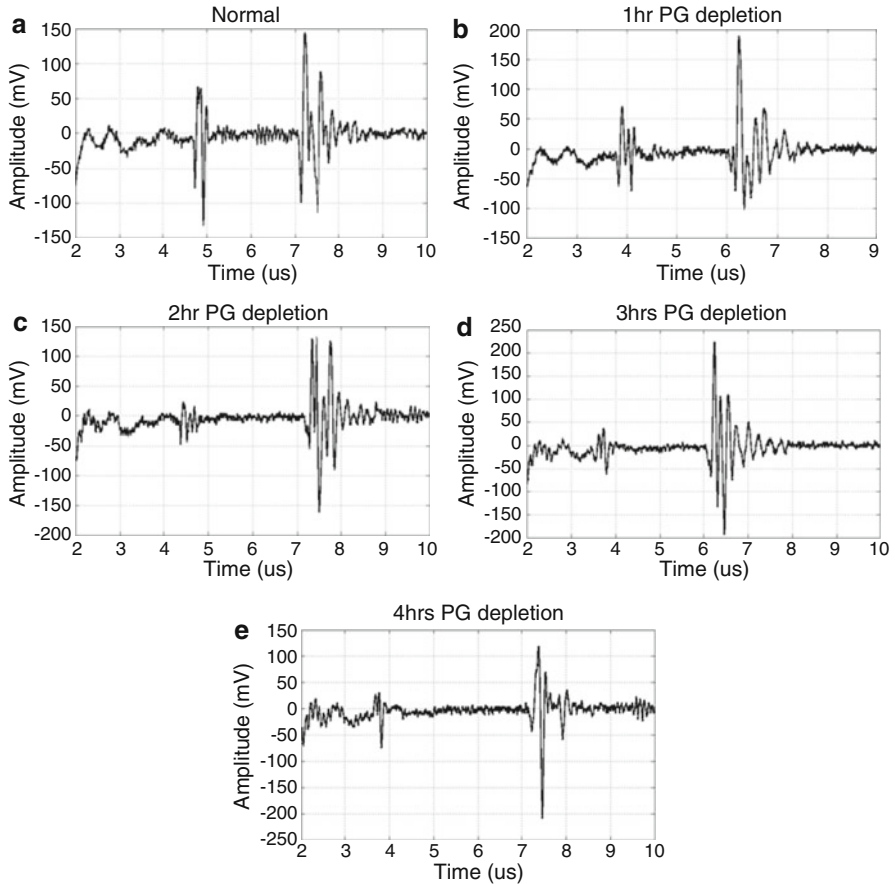
Fig. 2 Typical ultrasound signal reflection profile for (**a**) normal; (**b**) 1hr PG depleted; (**c**) 2hrs PG depleted; (**d**) 3hrs PG depleted; and (**e**) 4hrs PG depleted articular cartilage showing surface reflection (first peak) and osteochondral junction reflection (second peak)

presented in Fig. 3a. These data was used to estimate the percentage of proteoglycan that was removed from the various samples (Table 1). The reflection ratio ranged from 2.67±1.52 for normal samples to 5.11±1.65 (mean±S.D) for proteoglycan depleted samples.

The results demonstrate that there is an apparent inconsistency or discontinuity in the variation of the median values of the ratios for the surface to OCJ reflections where the ratio decreased from the normal to samples depleted for 2hrs, and then, rose for both the 3 and 4 hr enzymatically treated samples (Fig. 3b, c).

The ImageJ absorbance profile of (Fig. 3a) shows the distribution of proteoglycans from cartilage surface to bone for normal and depleted samples. A measure of the approximate proteoglycan content was obtained by calculating the area under the ImageJ absorbance curve (Fig. 3a).
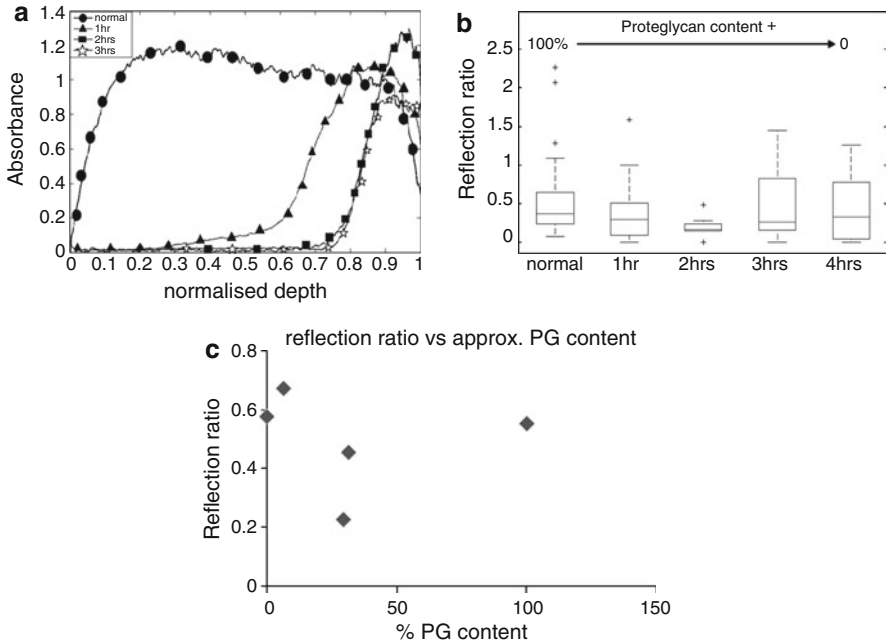
Fig. 3 (**a**) ImageJ absorbance profile for normal and depleted cartilage samples. (**b**) Boxplot of normal and proteoglycan (PG)-depleted samples. normal; 1hr group: sample with approx. 68.53% PG depletion; 2hrs group: sample with approx. 70.42% PG depletion; 3hrs group: sample with approx 93.41% PG depletion. (**c**) %Proteoglycan content versus reflection ratio

Table 1 Quantity of proteoglycan, as a percentage of total proteoglycan content of samples, removed by exposing cartilage samples to trypsin for 1 to 4 hrs, calculated as the area under the ImageJ curves in Fig. 3a

Sample	Ultrasound reflection ratio	Approximate % PG depleted
Normal	0.357±0.208	0
1hr PG depleted	0.320±0.274	68.53
2hr PG depleted	0.226±0.129	70.42
3hr PG depleted	0.425±0.327	93.41
4hr PG depleted	0.389±0.287	100

Discussion and Conclusion

This study has re-assessed the capacity of ultrasound to differentiate between normal and proteoglycan depleted articular cartilage. However, unlike the single proteoglycan depletion protocol, e.g. exposure of cartilage to a single known duration and comparing the resulting specimen to the normal, this present investigation investigates the ultrasound reflection from samples that had been subjected to progressive proteoglycan removal for 1 to 4 hrs. This provides a more comprehensive assessment of the capacity and limitation of ultrasound-based evaluation of the integrity of the cartilage matrix.

These current results (Fig. 3b, c) raise the question of the ability of the ratio of the surface-to-OCJ reflections to consistently distinguish samples with severe proteoglycan loss (i.e. >90% PG loss) from normal intact ones (Fig. 4). This lack of clear distinction was also demonstrated at <50% depletion, while there is a clear differentiation between the normal, and samples with between 55-70% of their proteoglycans removed. It should be noted that most reported data are on the comparison of cartilage that had been exposed to enzyme for about 2hrs (i.e. 55–70%) to normal specimens.

It is difficult at this stage to determine fully the reason for this inconsistency. It may be due to a limitation in the capacity of the reflection ratio for cartilage evaluation as argued above or certain issues around the enzymatic digestion of the proteoglycans. For example, in order to preserve the altered cartilage matrix and restrict the modification to that due to the enzymatic digestion only, we used a higher concentration of trypsin relative to the quantity used in for example Brown et al [8]; it probable that this type of departure from the method previously reported has an effect on our current results.

In conclusion, the reported results in this paper suggest that high frequency ultrasound method can distinguish between normal intact and degenerated articular cartilage. However, it seems that a better analysis leading to a different parameter of assessment beyond the surface-to-OCJ reflection ratio is required for consistent evaluation of cartilage health.

References

[1] Saarakkala, S., Töyräs, J., Hirvonen, J., Laasanen, M.S., Lappalainen, R., and Jurvelin, J.S., (2004), *Ultrasound Medicine Biology*, vol. 30, p. 783–792.

[2] Hattori, K., Mori, K., Habata, T., Takakura, Y., and Ikeuchi, K., (2003), *Clinical Biomechanics*, vol. 18, p. 553–557.

[3] Nieminen, H.J., Töyräs, J., Rieppo, J., Nieminen, M.T., Hirvonen, J., Korhonen, R., and Jurvelin, J.S., (2002), *Ultrasound Medicine Biology*, vol. 28, p. 519–525.

[4] Pellaumail, B., Watrin, A., Loeuille, D., Netter, P., Berger, G., Laugier, P., and Saïed, A., (2002), *Osteoarthritis Cartilage*, vol. 10, p. 535–541.

[5] Brown, C.P., Hughes, S., Crawford, R.W., and Oloyede, A., (2007), *Connective Tissue Research*, vol. 48, p. 277–285.

[6] Chérin, E., Saïed, A., Laugier, P., Netter, P., and Berger, G., (1998), *Ultrasound Medicine Biology*, vol. 24, p. 341–354.

[7] Senzig, D.A., Forster, F.K., and Olerud, J.E., (1992), *Journal of the Acoustic Society of America*, vol. 92, no. 2, p. 676–681.

[8] Brown, C.P., Hughes, S., Crawford, R.W., and Oloyede, A., (2008), *Physics in Medicine and Biology.*, vol. 53, no.15, p. 4123.

[9] Carney, S.L., Billingham, M.E.J., Muir, H., and Sandy, J.D., (1984), *Journal of Orthopaedic Research*, vol. 2, p. 201–206.

[10] Moody, H.R., Brown, C.P., Bowden, J.C., McElwain, D.L.S., Crawford, R.W., and Oloyede, A., (2006), *Journal of Anatomy*, vol. 209, p. 259–267.

[11] Brown, C.P., Moody, H.R., Crawford, R.W., and Oloyede, A., (2007), *Connective Tissue Research*, vol. 48, p. 52–61.

Near Infrared for Non-Destructive Testing of Articular Cartilage

I. Afara, T. Sahama and A. Oloyede

Abstract The concept of non-destructive testing (NDT) of materials and structures is of immense importance in engineering and medicine. Several NDT methods including electromagnetic (EM)-based e.g. X-ray and Infrared; ultrasound; and S-waves have been proposed for medical applications. This paper evaluates the viability of near infrared (NIR) spectroscopy, an EM method for rapid non-destructive evaluation of articular cartilage. Specifically, we tested the hypothesis that there is a correlation between the NIR spectrum and the physical and mechanical characteristics of articular cartilage such as thickness, stress and stiffness. Intact, visually normal cartilage-on-bone plugs from 2-3yr old bovine patellae were exposed to NIR light from a diffuse reflectance fibre-optic probe and tested mechanically to obtain their thickness, stress, and stiffness. Multivariate statistical analysis-based predictive models relating articular cartilage NIR spectra to these characterising parameters were developed. Our results show that there is a varying degree of correlation between the different parameters and the NIR spectra of the samples with R^2 varying between 65 and 93%. We therefore conclude that NIR can be used to determine, nondestructively, the physical and functional characteristics of articular cartilage.

Keywords Articular cartilage • NIR spectroscopy • Mechanical characteristics • Thickness • Predictive models

I. Afara • A. Oloyede (✉)
School of Engineering systems, Institute of Health and Biomedical Innovation,
Queensland University of Technology, Brisbane, Australia
e-mail: k.oloyede@qut.edu.au

T. Sahama
Computer Science Discipline, Faculty of Science and Technology, Queensland University
of Technology, Brisbane, Australia

Introduction

The mechanical properties of articular cartilage such as compressive stiffness have been used to assess its functional integrity in both normal and degraded conditions [1, 2]; and have been reported to successfully track changes in its structural integrity following controlled proteoglycan removal programs [3]. In addition, a number of researchers [4, 5] have suggested that an alteration of the mechanical properties in an arthritic joint may be notable before any gross morphological change is apparent. More recently, it has been noted that the mechanical stiffness of normal and degraded articular cartilage overlap to a significant degree [6]. In this paper we argue that despite this overlap, the mechanical parameter is still useful if comparison is restricted to a normal and its equivalent degraded counterpart in an evaluation process.

The accuracy of these mechanical properties is significantly dependent on an accurate determination of the tissue's thickness. This relationship between cartilage thickness and stiffness was earlier noted by Hayes et al [7]. Given that cartilage thickness is site-dependent [8], this means that it is essential to determine tissue thickness at each test site when determining sample stiffness. Furthermore, while indentation test has been widely used for in vitro [9] and in vivo [10] assessment of the functional integrity of cartilage, an accurate and non-destructive method of measuring cartilage thickness in vivo remains challenging [9], thus necessitating this research.

To this end, we hypothesize that there is a substantive degree of statistical correlation between cartilage NIR absorbance spectrum, thickness and mechanical/ functional characteristics. Near infrared spectroscopy is based on absorption of the NIR light resulting from chemical bond vibrations due to hydrogen and some light atoms. These bonds, C-H, N-H, O-H and S-H, are the predominant bond types in biological tissues like cartilage. In testing this hypothesis, we carried out experimental determination of cartilage thickness, stress-strain curves and associated parameters, and multivariate statistical (using partial least square regression - PLSR) analyses as described below.

Materials and Methods

Sample preparation

Visually normal and intact bovine patellae, (N=15), harvested from prime oxen within 24 h of slaughter, were used in this study. The samples were wrapped in 0.15M saline soaked towels and stored at about -20°C until required for testing. Prior to NIR spectroscopy, the intact patellae were thawed in 0.15M saline at room temperature for about 4 hours, then cartilage-on-bone blocks (n=173, lxbxh = 7x7x5mm) were extracted from the patellae. All tests were conducted with the specimens fully submerged or hydrated in 0.15M saline.
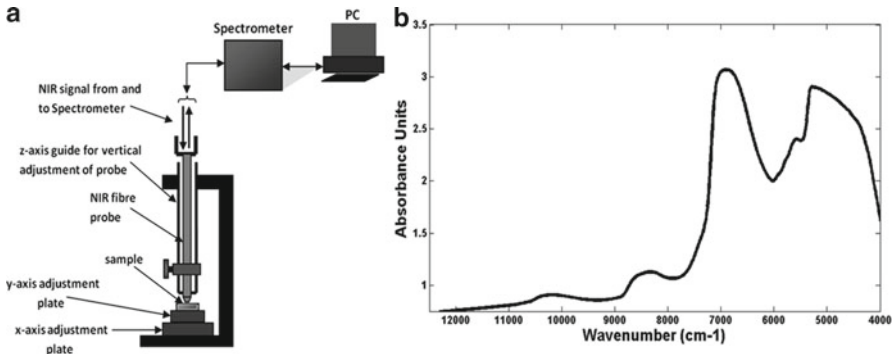
Fig. 1 (a) Experimental setup (b) Typical NIR absorbance spectrum for normal intact cartilage

NIR spectral measurement

Diffuse reflectance near infrared spectroscopy was performed using a Bruker MPA FT-NIR (Fourier Transform NIR) spectrometer (Bruker Optics, Germany). The NIR light used spans the 800 - 2500 nm wavelength region; which is the near infrared region of the electromagnetic spectrum. The probe used consisted of 100 x Ø600μm fibres, with 50 transmitting and 50 receiving NIR reflected light. Using a holder that enabled x-y adjustment of the mounted sample, the probe was lowered to the specimen surface and firmly locked in position for each measurement (Fig. 1a). After taking a reference spectrum, spectral data was obtained over the full range of the NIR spectrum (Fig. 1b), with each spectrum averaged over 64scans at 16 cm⁻¹ resolution.

Mechanical indentation test

Each specimen, already set in dental acrylic cast, was placed in a holder and subjected to compressive loading on an Instron material testing machine (Instron, Norwood, USA) to 30% strain at a loading rate of 0.5mm/min. The load was applied via a 3mm plane-ended cylindrical indenter in the centre of the sample area. After indentation, the specimen was unloaded and allowed to recover for about 2hr in saline to ensure that full thickness has been regained before further tests were carried out. The stress–strain characteristic of the specimen was obtained from the load–displacement curve and its stiffness calculated as the slope of the tangent to the curve at nominated strains corresponding to zero, shoulder and asymptotic positions of the curve.

Thickness measurement: Needle-probe method

After load-displacement tests, the indenter was changed to a "needle-probe" one and the speed of indentation was set to 10 mm/min [11]. Cartilage thickness was measured by using the load cell to sense the instant when the needle touched the articular surface and when it contacts the calcified zone. The characteristic of the curve as the needle travels from the surface to the tidemark was used to determine sample thickness. Six measurements were taken at points lying within the regions under which the NIR spectrum and mechanical characteristics were obtained.

Results and Analysis

The load–displacement curve of each sample was converted to its stress–strain characteristics using the sample thickness and indenter cross–sectional area. The stiffness at toe, shoulder and asymptote regions were calculated (Fig. 2a).

The stress values of the shoulder (σ_s) and asymptote (σ_{as}) – stress at 30% strain were also obtained for correlation with the NIR spectrum. 97 samples of the total 173 samples were subjected to needle-probe thickness measurement. A more representative value of each sample thickness was evaluated as the average of six measurements at points lying within the regions under which the NIR spectrum and mechanical characteristics were obtained. The samples' thickness value ranged from *2.422 ± 0.033* to *1.337 ± 0.055* (mean ± SD).

Using the OPUS 6.5 software (Bruker Optics, Germany), calibration and validation was performed using partial least squares (PLS) regression on the spectra with scatter correction and spectral pretreatment. The scatter correction technique employed was multiplicative scatter correction (MSC), and first derivative pretreatment was used for spectral pretreatment. Leave-one-out (LOO) cross-validation method was used in the calibration process to determine the optimal number of PLS components and to estimate the performance of the developed calibration models.

In cross-validation, calibration models are subsequently developed on parts of the data and iteratively tested (used for prediction) on other parts. Here, the model with the lowest number of components giving the highest R^2 (and possibly the lowest RMSECV) was selected. It should however be noted that the regions of the NIR spectrum that showed saturation due to O–H bond absorption of the NIR light were excluded from the analysis.

Discussion and Conclusion

Since articular cartilage is composed of constituents possessing functional groups such as C–H, O–H, N–H, and S–H which are selective absorbers of NIR radiation, an interaction between these constituents within the matrix structure and their resistance to compression may be reflected on the NIR spectrum of the tissue. Therefore, if there is
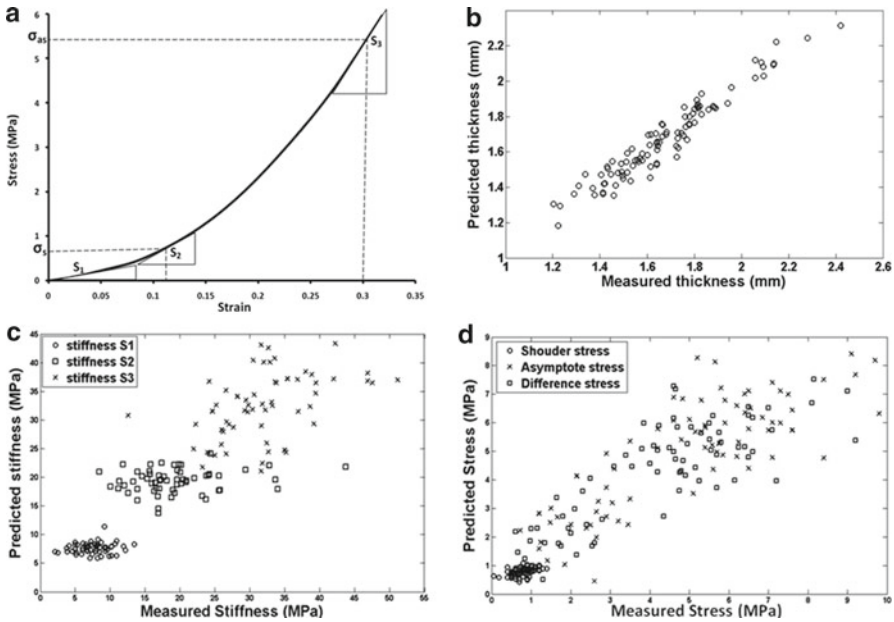
Fig. 2 (**a**) Stress-Strain characteristic of articular cartilage showing points where the stiffness values were calculated. (**b**) NIR-predicted cartilage thickness versus measured thickness. (**c**) NIR-predicted cartilage stiffness versus measured stiffness. (**d**) NIR-predicted cartilage stress versus measured stress

any linear relationship between NIR spectrum and the structure of articular cartilage, calibration equations or models could be developed to predict structure– and function–based parameters of the tissue. Consequently, partial least squares (PLS) regression analysis results, shown in Fig. 2b–d and Table 1, show that the NIR spectrum relates strongly with the tissue thickness, and is almost unrelated to its stiffness.

Indicated by the significant scatter in the stiffness calibration plot shown in Fig. 2c and the considerably low correlation coefficient (Table 1), the weak correlation between the stiffness parameters S1, S2, S3 and the NIR spectrum can be attributed to the significantly large overlap between the individual stiffness values of normal samples as observed by Brown et al [6]. Even though the current study did not consider degraded articular cartilage samples, our results confirm the hypothesis that stiffness parameters, used on their own, may not be reliable indicators of the tissue's functional viability. However, the asymptote stress (σ_{as}), and the difference in stress values ($\sigma_{as} - \sigma_s$), Fig. 2d, show better correlation with the NIR spectrum (see Table 1), relative to the stiffness parameters. This resistance to compression may be considered as a more reliable parameter for assessing the tissue's functional viability.

The NIR–thickness calibration plot, in Fig. 2b, shows a significantly high correlation (see Table 1) between the NIR spectrum and the tissue thickness. While the NIR light pathlength through biological tissues has been shown to influence the resulting absorption spectra [12], the cartilage thickness can be likened to this NIR light pathlength through the tissue.

Table 1 Physical and mechanical parameters of articular cartilage and their correlation with the NIR spectrum

	Parameters	Adjusted R^2 (%)	RMSECV
Stiffness	S1	6.219	2.41
	S2	1.305	6.25
	S3	9.822	6.67
Thickness		93.02	0.0621
Stress	σ_s	19.39	0.219
	σ_{as}	65.46	1.33
	$\sigma_{as} - \sigma_s$	66.04	1.24

These results show that the NIR spectrum of cartilage can be used to estimate both the physical and functional characteristic of the tissue. In addition to being a non-destructive, real-time and faster alternative to conventional compression test, the flexibility of NIR makes it well suited for clinical application in the assessment of joint conditions. We therefore conclude that NIR, as a non-destructive method, can be used to assess the tissue condition with respect to its physical and functional characteristics.

References

[1] Harris, E.D.J., Parker, H.G., Radin, E.L., and Krane, S.M., (1972), *Arthritis and Rheumatism*, vol. 15, p. 497–503.

[2] Kempson, G.E., Spivey, C.J., Swanson, S.A.V., and Freeman, M.A.R., (1971), *Journal of Biomechanics*, vol. 4, p. 597–609.

[3] Lyyra, T., Arokoski, J.P.A., Oksala, N., Vihko, A., Hyttinen, M., Jurvelin, J.S., and Kiviranta, I., (1999), *Physics in Medicine and Biology*, vol. 44, p. 525–535.

[4] Appleyard, R.C., Ghosh, P., and Swain, M.V., (1999), *Osteoarthritis and Cartilage*, vol. 7, p. 281–294.

[5] Arokoski, J., Jurvelin, J., Kiviranta, I., Tammi, M., and Helminen, H.J., (1994), *International Journal of Sports Medicine*, vol. 15, p. 254–260.

[6] Brown, C.P., Crawford, R.W., and Oloyede, A., (2007), *Clinical Biomechanics*, vol. 22, p. 43–848.

[7] Hayes, W.C., Keer, L.M., Herrmann, G., and Mockros, L.F., (1972), *Journal of Biomechanics*, vol. 5, p. 541–551.

[8] Li, G., Park, S.E., DeFrate, L.E., Schutzer, M.E., Ji, L., Gill, T.J., and Rubash, H.E., (2005), *Clinical Biomechanics* vol. 20, p. 736–744.

[9] Suh, J.-K.F., Youn, I., and Fu, F.U., (2001), *Journal of Biomechanics*, vol. 34, p. 1347–1353.

[10] Lyyra, T., Jurvelin, J., Pitkanen, U., Vaatainen, U., and Kiviranta, I., (1995), *Medical Engineering and Physics*, vol. 17, p. 395–399.

[11] Jurvelin, J.S., Rasanen, T., Kolmonen, P., and Lyyra, T., (1995), *Journal of Biomechanics*, vol. 28, p. 231–235.

[12] Gussakovsky, E. and Kupriyanov, V., (2008), *Applied Spectroscopy*, vol. 62, no. 6, p. 671–676.

Section 3
Early Age NDT of Concrete and Other Materials

Characterization of Fresh and Early Age Concrete Using NDT

H.W. Reinhardt

Abstract The paper reviews a few methods which are suitable for the continuous measurement of the stiffening and hardening behavior of mortar and concrete. These are the dielectric method, the nuclear magnetic resonance method, the ultrasonic methods as wave-reflection method and wave-transmission method. The first two methods detect mainly the distribution of water in the sample as function of hardening time, while the other two methods rely on the development of the mechanical properties. The measurement principles are discussed and testing devices are described.

Introduction and Motive

The knowledge of the development of concrete properties during the first hours after concreting has various aspects: the transition of a suspension into a hardened material is interesting for the materials scientist, but it has also very practical aspects such as the development of strength and the liberation of heat [1]. The setting of cement has great influence on the available duration of workability of the fresh concrete. Development of strength determines the time of stripping the formwork and the progress of slipform concreting. Heat liberation is sometimes crucial in mass concrete. The materials developer is interested in the question how new products such as additions and admixtures react together with a cement, or they develop a new binder with unknown properties.

H.W. Reinhardt (✉)
Department of Construction Materials, University of Stuttgart, Germany
e-mail: reinhardt@iwb.uni-stuttgart.de

The question arises how setting and hardening of cement paste, mortar, and concrete can be measured continuously. Continuous measurement asks for non-destructive methods. The current testing methods measure in intervals such as the Vicat needle method for cement paste [2] and the penetration resistance test for concrete [3]. These methods can be applied before the end of setting. The further hydration development is approached by other techniques such as bolt penetration, bolt extraction, and coring. All these methods do not allow continuous measurements and are partly destructive.

To follow the various stages of hydration one can utilize the chemical, electrical, physical (and mechanical) properties. Changes in hydration can be represented by the changes of these properties. Various methods are feasible. One can chemically measure the composition of the pore solution. One can use electrical methods which determine the dielectric properties, the conductivity, or the magnetic properties (NMR = nuclear magnetic resonance). One can think about the wave propagation in the setting and hardening material which is generated by ultrasound (US) or impactors (impact-echo method) or by acoustic emission. One can measure the heat of hydration and can calculate the degree of hydration as function of time. Or one can use an electron microscope, preferably an ESEM (Environmental scanning electron microscope) which allows following the progress of crystal forming. The following chapter revises some methods.

Testing Methods and Devices

Dielectric measurement [4]

Measuring principle

To translate the dielectric properties into physicochemical and engineering properties, the basics of dielectric properties should be understood [5]. Specifically, the dielectric properties of water have a special nature and water has a dominant effect on the properties of concrete.

When an electrical field is applied to a material containing ions, some ions drift through the material and discharge at the electrodes, producing conduction. Other ions, which are bound to surfaces, are not free to drift from one electrode to the other. These charges are able to oscillate back and forth under the action of an alternating field.

Polar molecules, like water are asymmetrically charged and posses a permanent dipole. When we consider a collection of molecular dipoles in thermal equilibrium, they will be ordered randomly. The polarization of this system will be zero. When a dipole is placed in an electrical field, the dipole will be orientated according to the electrical field. The orientation will not be completed at once but will take some time. When the electrical field is removed the dipoles will once again be randomly ordered. This re-orientation of dipoles, which is called relaxation, will take some time.

Fig. 1 Schematic set-up for the determination of dielectric properties of cement
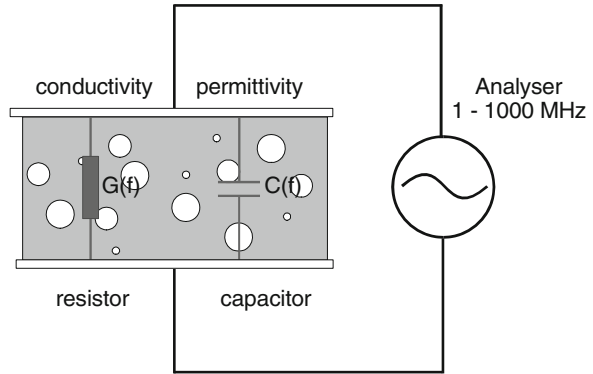
Testing the dielectric properties of cement paste

A test system for determining the dielectric properties of cement paste was developed by van Beek [5]. This system consists of the following components:

– a impedance analyser, which can generates an electrical field in the frequency range from 1 MHz to 1000 MHz
– a probe with which the electrical field can be introduced into cement paste
– a temperature logging system combined with thermocouples to determine the temperature in the specimen during hydration.

A simple dielectric model has been used in this system to calculate the permittivity and the specific conductivity for the measured data. This model consists of a parallel system with a resistor and a capacitor (Fig. 1). The relationships: capacitance – permittivity, conductivity – specific conductivity are defined as follows:

$$\varepsilon(f) = k\frac{C(f)}{\varepsilon_0} \tag{1}$$

$$\sigma(f) = kG(f) \tag{2}$$

where

f	frequency of the electrical field in Hz	k	cell constant in 1/m
ε_0	dielectric constant of the vacuum in 1/F	C	measured capacity in F
G	measured conductivity in S	ε	permittivity
σ	specific conductivity in S/m		

Before the real test starts, the calibration of this system has to be performed with water ($\varepsilon \approx 80$) and a mix of glass pearls saturated with water ($\varepsilon \approx 28$). The conductivity is varied by adding salt to these specimens. The conductivity in the specimens is measured with a conductivity meter to determine the cell constant. Once the cell
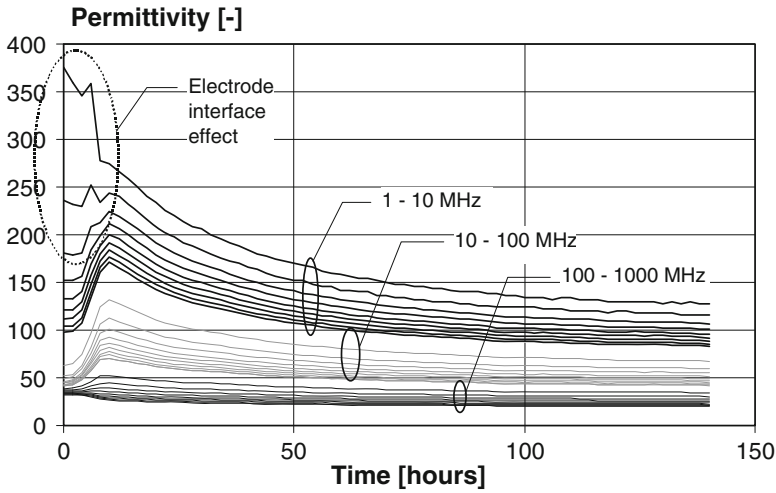
Fig. 2 Permittivity of Portland cement paste in the first 140 hours after mixing

constant of the system has been determined the dielectric properties of cement paste can be calculated from the measured capacitance and conductivity.

Dielectric properties of different types of cement at various frequencies

A number of tests were carried out by van Beek [5] to study the dielectric properties of Portland cement and blast furnace slag by using frequencies ranging from 1 to 1000 MHz. The permittivity versus time for Portland cement is shown in Fig. 2. It can be seen that at a frequency below 10 MHz the electrode interface effect strongly influence the permittivity. Portland cement reaches the maximum permittivity within about 10 hours after mixing.

The conductivity at low frequencies is mainly determined by the number of interconnected capillary pores in the cement paste. The main conducting phase in cement paste is the capillary water. The hydration products that block the pores conduct very poorly. The decrease of connectivity of the pores results in a sharp decrease in the conductivity. At higher frequencies the conductivity increases due to the dielectric losses, which, in turn, increase due to the change in the relaxation frequency. From tests it was found that the sharp decrease of the conductivity occurred due to the decrease of the amount of free water and due to the decrease of connectivity of the pores.

Dielectric properties versus degree of hydration

Since it is difficult to relate the dielectric properties to the physical state of the cement paste when the dielectric properties are presented in the time scale, the

Fig. 3 Permittivity of Portland cement paste related to the degree of hydration and volume fraction of capillary water
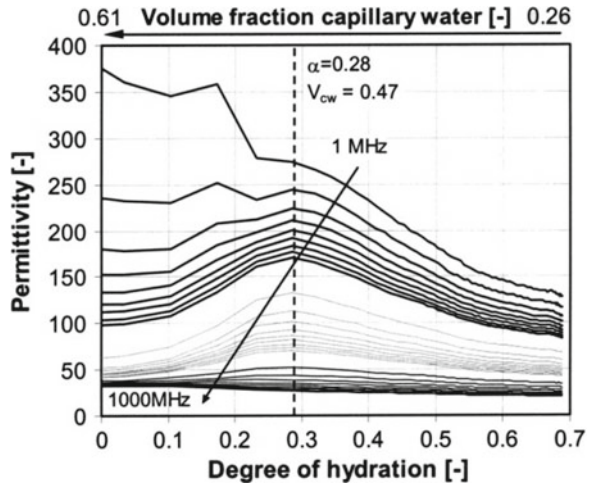
concept of the degree of hydration is introduced as an indicator of the physical state of the hydrating cement paste [6].

The dielectric properties are mainly determined by the amount of capillary water in the pore structure. The amount of capillary water in the cement paste is in turn determined by the degree of hydration and the initial amount of water. A unique relationship between degree of hydration and amount of capillary water is described by using the Powers model [7]:

$$V_{cw} = V_{cap} - V_{ec} \tag{3}$$

$$V_{cap} = \frac{wcr - 0.36\alpha}{wcr + 0.32} \tag{4}$$

$$V_{ec} = \frac{0.0575\alpha}{wcr + 0.32} \tag{5}$$

where

V_{cw}	volume fraction capillary water	wcr	water-cement ratio
V_{cap}	volume fraction capillary pores	α	degree of hydration
V_{ec}	volume fraction empty capillary pores		

For a mixture with Portland cement and a water-cement ratio 0.5, the maximum permittivity is found at a degree of hydration of 0.28 (Fig. 3). A degree of hydration of 0.28 correlates with a capillary water volume of 0.47 (from Eqs. 4 and 5). Continuous measurements have to be performed in order to follow the hydration process completely.
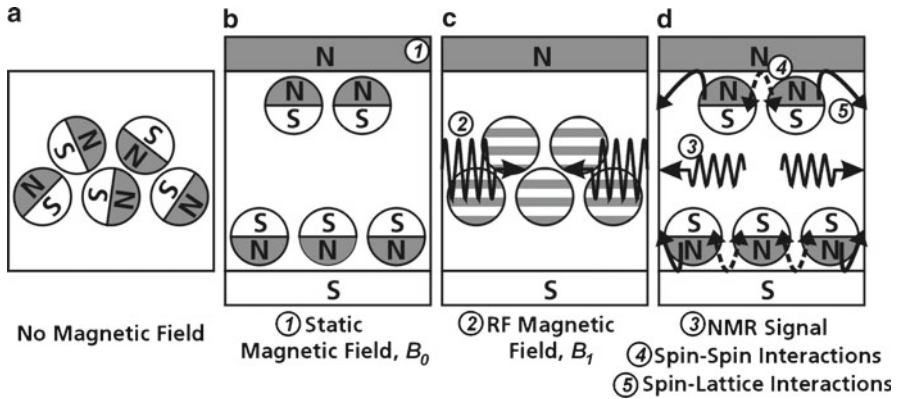
Fig. 4 Physical principle of Nuclear Magnetic Resonance

Nuclear magnetic resonance [8]

Physical principle

An atomic nucleus having an uneven number of protons and/or neutrons, as hydrogen (^{1}H) or fluorine (^{19}F), carries a nuclear magnetic dipole moment, resulting from its spin-angular momentum, comparable to a small magnetic compass needle. Without a magnetic field, the dipole moments within a specimen are randomly oriented (Fig. 4a). If the specimen is placed into a static magnetic field the magnetic moments are oriented anti-parallel or parallel (Fig. 4b). The latter is the low-energy state, leading to a slightly overbalanced population of the in-field orientation in thermal equilibrium. This excess population provides a detectable macroscopic magnetization in the specimen.

Usually, a coil of a resonant circuit generates one or more short pulses of the radio frequency field. After tuning off the pulse(s), the emitted energy is measured as an alternating voltage induced in the same coil. The amplitude of the so-called NMR spin echo signal is given by

$$S = S_0(1 - \exp(-t_r / T_1) \exp(-t_e / T_2)) \tag{6}$$

Here S_0 proportional to number of resonant nuclei in the observed specimen volume, T_1 the so-called spin-lattice or longitudinal relaxation time and T_2 is the so-called spin-spin or transversal relaxation time. t_r and t_e are variable observation times of the experiment.

Immediately after the pulse, the excess energy absorbed by the nuclear dipoles is dissipated due to interactions of the nuclei with their atomic and molecular environment (spin-lattice interactions) and interactions of the nuclei among each other (spin-spin interactions). Finally, the thermal equilibrium condition in the static magnetic field is recovered due to these interactions (see Fig. 4d). Spin-lattice and spin-spin interactions are modulated in time by molecular motion,

giving rise to the T_1- and T_2-dependencies of the NMR signal. Analyzing these relaxation processes allows to determining detailed information about molecular mobility in the specimen.

NMR methods for characterization of cement-based materials

NMR high-resolution spectroscopy

In condensed matter, the actual magnetic field B_0 and with it the Larmor frequency ω_0 on the spot of an atomic nucleus is slightly changed by its surrounding electron cloud and by adjacent neighbor atoms. Therefore, an atomic nucleus in a specific molecular environment shows up a specific Larmor frequency shifting (chemical shift). By this means, it is possible to identify and investigate the molecular environment of a nucleus, which can be the hydrogen nucleus (^1H), but also other nuclei (^{27}Al, ^{29}Si, ^{31}P). In this case the NMR frequency spectrum reveals quantitative information about the chemical composition and structure of the investigated material, for instance hydrated cement. But this NMR high-resolution spectroscopy can only be applied, if the magnetic field B_0 has a sufficient strength (about 1 Tesla and more) and its intrinsic inhomogeneity is very low (a few ppm in the sample volume).

NMR relaxometry

High-resolution as well s low-resolution NMR instruments can be applied for investigations of the hydrogen relaxation times T_1 and T_2, which is often referred as NMR relaxometry. T_1 and T_2 are extremely sensitive to dynamics of the molecular mobility in the hydrogen environment. Pure water at room temperature shows large values of both T_1 and T_2, typically in the range of seconds. These large values are related to the high degree of Brownian motion in the low-viscous liquid. Decreasing the molecular mobility, as it results from solidification or increasing viscosity, leads to a monotonous decrease in T_2 down to values between 10^{-5} and 10^{-4} s in rigid solids. In contrast T_1 first decreases and afterwards increases again, if molecular mobility is reduced. As an example, the T_2 of ice is several thousands times smaller than the T_2 of water at room temperature. Additionally, the relaxation time T_1 is strongly influenced by unpaired electrons in ions. There from, NMR relaxometry is suited to investigate processes connected with changes in molecular mobility or dissolution/precipitation of ionic compounds.

In porous building materials T_1 and T_2 will be decreased strongly with respect to that of pure water due to interactions of water with the solid matrix. It is found, that the relaxation is proportional to the surface-to-volume ratio, which is a property of the pore geometry [9]. In a material with different pore-sizes relaxometry can be used to measure nondestructively the pore-size distribution, e.g. during hydration. By means of T_1 and T_2, chemically combined water can be distinguished from water, which is physically bound to a solid surface and water, which is in the bulk liquid state. During hardening of cement stone, more and more water is chemically
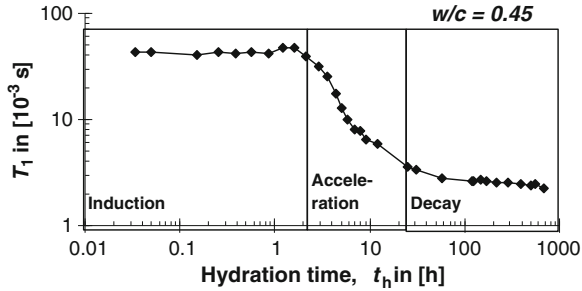
Fig. 5 Time evolution of the ^{1}H spin-lattice relaxation time T_1 in a Portland cement (PC) paste with a water-to-cement ratio of 0.45; induction, acceleration and decay period of hydration are shown (from [10])
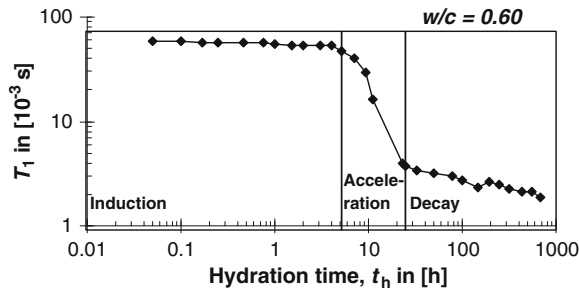
Fig. 6 Time evolution of the ^{1}H spin-lattice relaxation time T_1 in a Portland cement (PC) paste with a water-to-cement ratio of 0.60; induction, acceleration and decay period of hydration are shown (from [10])

combined in hydration products, small gel pores are developing at cost of large capillary pores. Hence, the water mobility in concrete is changing continuously, originating a pronounced effect on the relaxation times (see Figs. 5 and 6). A detailed relaxation analysis allows determining the relative portions of hydrogeneous phases in concrete, which are the chemically bound water (water of hydration) with a T_1 less than 10^{-4} s, the water in gel pores with a T_1 in the of 10^{-3} s range and the loosely bound water in capillary pores with a T_1 of about 10^{-2} s [10]. This offers the possibility to observe the development of these phases during hardening.

Ultrasound

Wave reflection method [11]

Reflection coefficient r and transmission coefficient t can directly be related to the acoustic impedances Z of the materials that form the interface. The acoustic
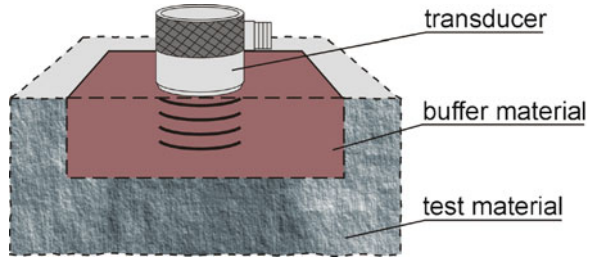
impedance is calculated as the product of the wave velocity in and the density of the material (Eq. (7)). From the acoustic impedances of the materials the coefficients r and t can be calculated with Eq. (8) and Eq. (9) [12], where Z_1 and Z_2 are the acoustic impedances of Material 1 and 2 and the wave is assumed to travel from Material 1 into Material 2.

$$Z = \rho \cdot v \tag{7}$$

$$r = \frac{Z_2 - Z_1}{Z_2 + Z_1} \tag{8}$$

$$t = \frac{2 \cdot Z_2}{Z_2 + Z_1} \tag{9}$$

If in Eq. (8) the acoustic impedance Z_2 is smaller than Z_1 the reflection coefficient r becomes negative. This negative value indicates a phase reversal of the reflected wave relative to the incident wave. Such a phase reversal occurs, when e.g. longitudinal waves are reflected at an interface of steel and hardened cement paste.

The principle of the wave reflection measurements consists of monitoring the reflection coefficient of ultrasonic waves at an interface formed by a buffer material and the cementitious material to be tested. An ultrasonic transducer is coupled to the buffer material, which in turn has to be brought in contact with the test material when it is still in liquid or unhydrated state (Fig. 7). With proceeding hydration the wave propagation properties of the test material change, which results in a variation in the reflection coefficient. The reflection coefficient is obtained from the amplitudes of successive reflections received from the interface between the buffer and the test material.

When the wave encounters the interface between the buffer and the test material, part of the wave is transmitted into the test material and part is reflected back to the transducer. The reflected waves are received by the transducer and at same time again reflected from the transducer-buffer interface into the buffer where the reflection process repeats until the waves attenuate. The described process is shown in Fig. 8, where S_T is the transducer signal transmitted into the buffer, R_1 and R_2 are the first and second reflections captured by the transducer and T_1 and T_2 are the first and second transmission into the buffer.

Fig. 8 Schematic representation of the multiple reflection and transmission process at the interface between buffer and test material [13]
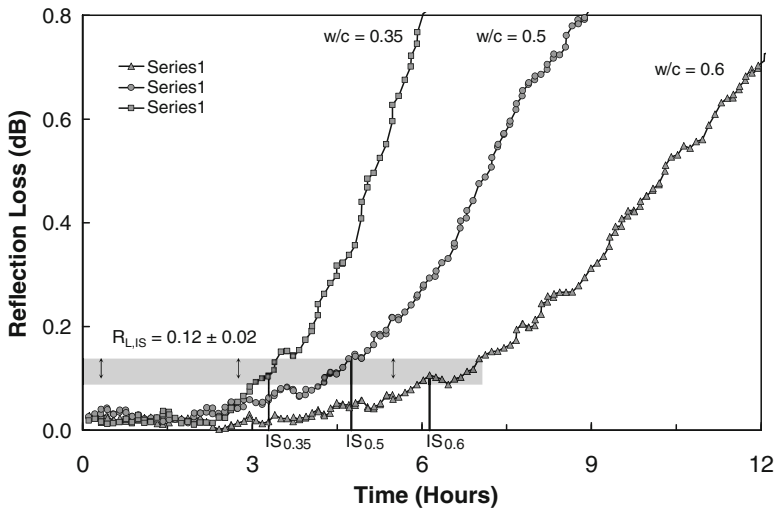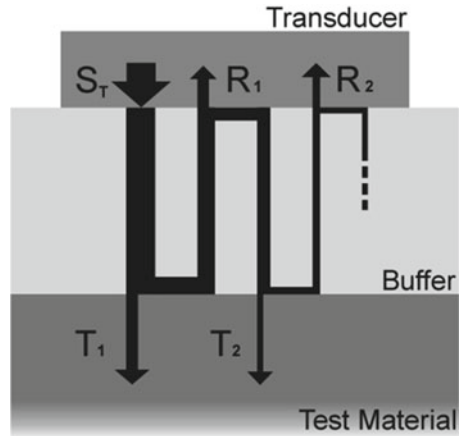
Fig. 9 Reflection loss development and initial setting time for Portland cement mortars with different w/c-ratios

Figure 9 shows a result from measurements on Portland cement. The beginning of setting has been compared with the pin penetration method. The reflection loss is a direct function of the reflection coefficient [14]. With increasing hardening time the reflection loss becomes larger since the test material gets harder.

Wave transmission method [15]

The principle of the transmission method is shown in Fig. 10. A pulse is generated at one surface of the specimen and the according wave is travelling through the
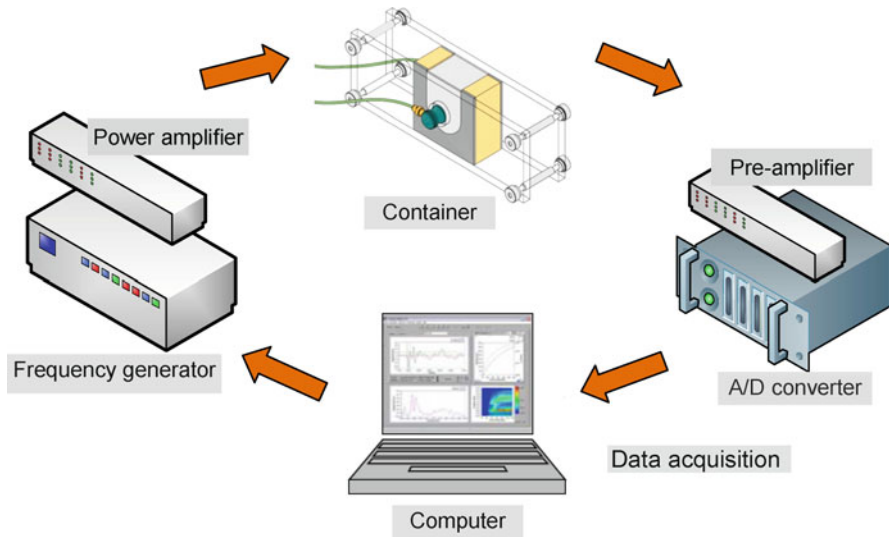
Fig. 10 Principle of US measurements based on through-transmission techniques

material and picked up at the other side. The incident pulse and the transmitted pulse are recorded, converted to a digital signal and stored in a memory for further or immediate evaluation.

At the Department of Construction Materials (IWB), University of Stuttgart, an apparatus was developed aimed at investigating the setting and hardening of cement-based materials in quality assurance. First papers on this work were published in the early 90s. In recent years, the technology has attained a good industrial standard. Proof of which, among others, is the fact that several research facilities and companies are by now successfully using the apparatus developed at the IWB.

The approach is based on the observation of waves transmitted through mortar or concrete during setting and hardening. The ultrasound wave is recorded and analyzed during the hardening of the material quasi continuously. The waveform as well as wave parameters like travel time (related to the wave velocity), amplitude (related to the wave energy) and frequency content of the signal are influenced by the elastic properties of the material. Cement based materials like concrete and mortar are changing its status from a suspension to a water saturated porous media during hardening. This change can be observed recording transient waves transmitted through the material. Usually, these transients are recorded in certain intervals to document the changes. Figure 11 demonstrates this procedure for a standard concrete mix. However, to make the changes in signal wave form during setting and hardening more obvious, all signals in this figure were normalized in respect to their amplitudes.
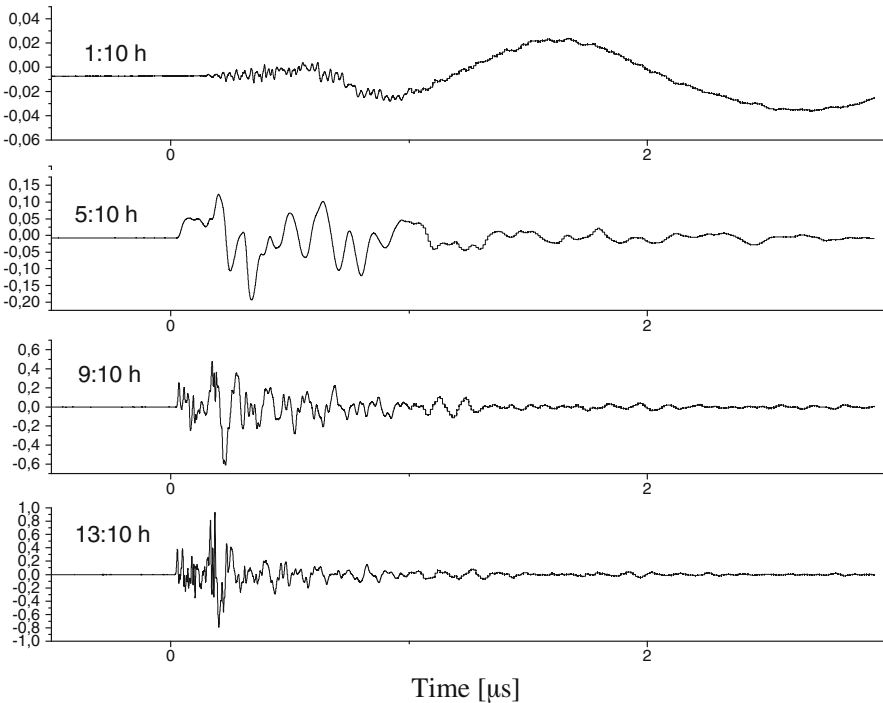
Fig. 11 Transient ultrasound waves recorded in an interval of four hours after adding water

Signals are recorded after transition through the material in a certain time interval. Picking for example the onset time of the wave arriving first at the receiver the travel time can be calculated knowing the origin time of the signal. Along with the known distance between transmitter/impactor and the receiver the wave velocity can be calculated as well. For the velocity v applies in general the well-known relationship $v = s/t$ with travel time t and travel path s. In most cases this wave is a compressional wave (being faster than other waves) and the compressional wave velocity is measured therefore.

With regard to the apparatus technology, one of the focal tasks has been the development of an easily manageable container made of PMMA for carrying out the fresh concrete measurements, which was named FreshCon-1. In parallel to this, a separate measuring setup for mortar was developed. Due to the clearly smaller aggregate diameter a much smaller container could be developed. In this way, the sample size and consequently waste could be reduced to a minimum.

There are several requirements on the container:

– the compressive pulse has to be transmitted through the mortar as directly as possible
– there should be no transmission through the container walls

Fig. 12 3D sketch of a container for concrete measurements in through-transmission
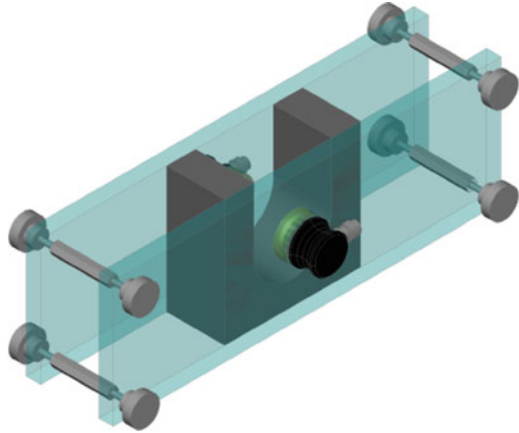
– the transducers have to be coupled as reliably as possible
– the filling, handling, mounting and demounting procedures should be as easy as possible
– the procedure should allow to receive repeatable and reproducible results
– the container should be suitable for multiple use, and finally,
– waste material should be minimized.

Figure 12 shows a container schematically which has been developed for FreshCon. The mortar or concrete is contained in the U-shaped part made of soft rubber (EPDM foam). The emitter und receiver are located in a casing in the wall. The fixation of the side walls is such that waves from the emitter do not disturb the signals which travel dietly through the concrete or mortar. The fixation is demountable for easy cleaning and calibration.

The electonic measuring device measures the emitted and received pulse. From that, the pulse velocity can be calculated. The equipment uses the longitudinal wave but the transverse wave is also possible. The result is a wave propagation velocity vs. time plot. Robeyst [17] has evaluated the energy content of the transmitted signal. He has established a relation between the energy ratio, i.e. the ratio between the measured energy during the test and the energy transmitted during the calibration of the equipment, and the initial and final set of the material as determined with the penetration test acc. to ASTM C403.

Analogously to the velocity measurement, a graph showing the change of the energy (Fig. 13).

Generally, the energy is plotted on a logarithmic scale in correspondence with the wave attenuation which is commonly expressed in dB. Generally, smoothing of the energy curves is not required to produce clear graphs.

The initial and final setting times according to the penetration resistance test [3] can also be indicated by threshold values of the ultrasonic wave energy [17].
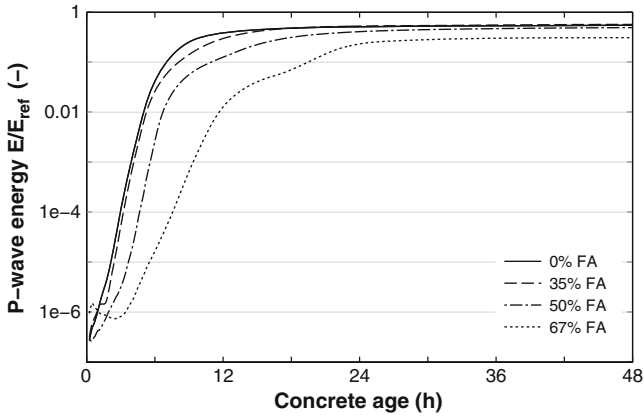
Fig. 13 Example of relative energy of concrete with fly ash over age [16]

For mortar mixtures: $t_{initial\ set}(h) = t_{E/Eref=0.02}(h)$

$t_{final\ set}(h) = t_{E/Eref=0.13}(h)$

For concrete mixtures: $t_{initial\ set}(h) = t_{E/Eref=0.02}(h)$

$t_{final\ set}(h) = t_{E/Eref=0.07}(h)$

For mixtures with OPC, an average repeatability error lower than 5% can be obtained for these threshold times.

It has been shown that the repeatability error for mixtures with ordinary portland cement is lower than 5 %.

There are several measuring methods more which are not described here, see [1], [18].

Recommendation

Up till now, there is no guideline, recommendation, or standard for the continuous measurement of setting and harderning of cementitious materials.

In order to make the techniques available for everybody RILEM has set up the TC 218-SFC "Sonic methods of quality control of fresh cementitious materials" in 2006. The aim of the technical committee is to develop recommendations for the through-transmission method, the reflection method, and the prism technique. It turned out that the preparation of a recommendation is time and labor consuming and that the small number of TC members has not the capacity to finalize all three recommendations. Therefore, it was decided to start with the recommendation for the through-transmission technique. This recommendation is ready meanwhile.

References

[1] H.W. Reinhardt and C.U. Grosse (Eds.): Advanced testing of cement based materials during setting and hardening. RILEM Report 31, 2005, 341 pp

[2] EN 196-3 Methods of testing cement - Part 3: Determination of setting times and soundness; 2009

[3] ASTM C403-08: Standard Test Method for time of setting of concrete mixtures by penetration resistance, ASTM 2009

[4] Han, Ningxu, van Beek, A., Koenders, E.A.B.: Electric methods. Chapter 3, in [1], pp 35–80

[5] Beek, A. van: Dielectric properties of young concrete – Non-destructive dielectric sensor for monitoring the strength development of young concrete, PhD Thesis, Delft University Press, 2000.

[6] Breugel, K. van: Models for prediction of microstructural development in cement-based materials. The modelling of microstructures and its potential for studying transport properties and durability. Saint-Remy-les-Chervreuse 1994, pp. 91–105

[7] Jennings, H. M., et al.: Modelling and materials science of cement-based materials, Part I –an overview. The modelling of microstructures and its potential for studying transport properties and durability, Saint-Remy-les-Chervreuse, 1994, pp. 29–62.

[8] Wolter, B., Dobmann, G., Pel, L.: Investigation of the hardening of cement-based materials with nuclear magnetic resonance (NMR). Chapter 2, in [1], pp. 13–33

[9] Valckenborg, R.M.E., Pel, L., and Kopinga, K.: Combined NMR cryoporometry and relaxometry. Journal of Physics D: Applied Physics 35 (2002), pp. 249–256

[10] Wolter, B.: Applikationsmöglichkeiten eines *H-Kernspinresonanz-Meßsystems in Aufsatztechnik für die zerstörungsfreie Charakterisierung zementöser und adhäsiv gebundener Werkstoffe, Diplomarbeit, 1995, Universität des Saarlandes

[11] Voigt, T., Subramaniam, K.V., Shah, S.P.: Monitoring the setting and hardening of cement-based materials with ultrasonic wave reflection methods. Chapter 4.2, in [1], pp. 97–141

[12] Krautkrämer, J., Krautkrämer, H.: Ultrasonic Testing of Materials. Springer Verlag, Berlin New York, 1990

[13] Voigt, T., Akkaya, Y., Shah, S.P.: Determination of early age mortar and concrete strength by ultrasonic wave reflections. ASCE Journal of Materials in Civil Engineering, vol. 15, no. 3 (2003), pp. 247–254.

[14] Voigt, T., Shah, S.P.: Properties of early-age Portland cement mortar monitored with shear wave reflection method. ACI Materials Journal 101 (2004), No. 6, pp 473–482

[15] Große, C.U. Reinhardt, H.W., Herb, A.T.: Ultrasound in through-transmission. Chapter 4.4, in [1], pp. 163–190

[16] Robeyst, N.: Monitoring setting and microstructure development in fresh concrete with the ultrasonic through-transmission method. PhD thesis, Ghent University 2009, 251 pp

[17] Robeyst, N., Grosse, C.U., De Belie, N.: Measuring the change in ultrasonic p-wave energy transmitted in fresh mortar with additives to monitor the setting. Cement and Concrete Re-search 39 No. 10 (2009), pp. 868–875.

[18] Bouhadjera, A., Bouzrira, C.: High-frequency ultrasonic testing of young cement-based materials using the ´prism technique`. NDT & E International 38 (2005), pp. 135–142

Factors Affecting the Monitoring of the Early Setting of Concrete by Ultrasonic P-Waves

N. Robeyst, C.U. Grosse and N. De Belie

Abstract Ultrasonic P-wave measurements are widely used to monitor concrete setting. Although the largest wave velocity increase occurs during setting, the earliest increase is rather caused by other factors. Air bubble migration, internal settling, formation of ettringite and early C-S-H, workability loss and thixotropy might affect the velocity change in time. Tests on mortar in which cement was replaced by bentonite, confirmed the possible influence of thixotropy on the measurements. The effect of air bubble migration, internal settling and workability loss was proven to be restricted by testing a mixture in which the cement was replaced by inert material. In a cement mixture, the precipitation of hydration products might however accelerate settling and workability loss. During cement hydration simulations, the change in porosity due to the formation of early C-S-H and ettringite was considered for the calculation of the elastic properties of the granular framework. Nevertheless, the calculated velocity hardly increased before percolation and thus could not confirm that the first velocity increase is attributed to formation of early hydration products. Thus, apart from thixotropy, none of the other factors could unarguably be indicated as the cause of early velocity increase.

Keywords Concrete • Early setting • Monitoring • P-waves • Ultrasound

N. Robeyst • N. De Belie (✉)
Magnel Laboratory for Concrete Research, Ghent University, Belgium
e-mail: Nele.DeBelie@UGent.be

C.U. Grosse
Non-destructive Testing Lab, Center for Building Materials,
Technische Universität München, Germany

a

b
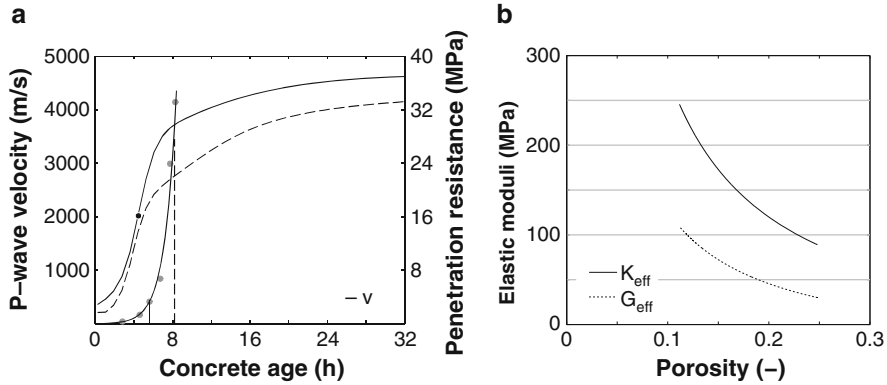
Fig. 1 (**a**) P-wave velocity of concrete (—), mortar (--) and penetration resistance (•); (**b**) Effective elastic bulk modulus K_{eff} and shear modulus G_{eff} of the solid framework vs. porosity for fresh mortar (water-to-binder w/b = 0.5)

Introduction

The setting of concrete and other cement-based materials can be measured by ultra-sonic P-wave measurements [1, 2]. The largest velocity increase occurs during set-ting, when the cement hydrates start to percolate and form complete pathways of connected particles [3]. Nevertheless, the earliest increase is rather caused by other factors than by setting. During calorimetric measurements, a clear dormant period is observed, which would also be expected during the ultrasonic measurements. In addition, comparison with the traditional penetrometer or Vicat needle, demonstrated that the P-wave velocity starts to increase before the penetration resistance starts to develop (Fig. 1a) [2]. Thus, a good identification of the factors affecting the earliest ultrasonic signals benefits the correct interpretation of the velocity curves.

Literature Review

Robeyst *et al.* [2] described fresh mortar or concrete as water-saturated porous solid. To calculate the initial velocity, the theory of Biot was applied. In this case, the wave velocity can be written as shown in Equation (1)

$$V_P^2 = \beta \cdot \frac{K + \frac{4}{3}G + \frac{K_f(K_s - K)^2}{K_f(K_s - K) + K_s(K_s - K_f)n}}{(1-n)\rho_s + n\rho_f} \tag{1}$$

with porosity n, bulk and shear modulus of the granular framework K and G and bulk modulus of the solid and fluid phase K_s and K_f. The coefficient β depends on

the frequency regime [2]. In the fresh state, the solid frame consists of packed sand and cement with a bulk modulus K of 89 MPa.

Air bubble migration

According to Ye [3], the migration of air bubbles to the surface due to bleeding contributes to the early increase in the measured ultrasonic P-wave velocity. The initial value of the ultrasonic P-wave velocity is lower than the values measured on water due to this entrapped air which decreases the bulk modulus of the fluid phase K_f significantly [2]. These air bubbles escape under the force of buoyancy when the aggregate particles move during placing and compaction. Bleeding water drags air bubbles with it. This effect is however mainly restricted to the first minutes after placing so that the corresponding air loss cannot explain the large increase in velocity. In addition, until cement setting, the smaller air bubbles dissolve into water, while larger bubbles increase in size because of air release from the saturated water. The result is an increase in air content of the concrete and a decrease of the specific area of the bubbles [4]. This process might change the tortuosity and low-frequency resonant scattering of the air bubbles. However, it has not been proven that this will increase the velocity and decrease the attenuation.

Internal settling or consolidation, and workability loss

According to [5], internal settling or consolidation causes the very early increase in P-wave velocity. Due to gravity, heavier aggregate particles tend to sink (segregation) and water appears at the surface (bleeding). Internal settling densifies the internal structure and causes a better mechanical coupling of the particles. According to Dvorkin's uncemented sand model, the effective value of the bulk and shear modulus, indicated with K_{eff} and G_{eff}, will increase with decreasing porosity according to Eq. (2) [6]. The quantities in these equations are porosity n, initial porosity n_0, bulk and shear modulus of the granular framework K and G (corresponding with n_0) and bulk and shear modulus of the solid phase K_s and G_s. Figure 1b shows the change of the effective moduli in function of the porosity for the fresh mortar mixture. According to simulations with CEMHYD3D, the porosity of a mixture with OPC decreases from 0.25 to 0.16 during the first 2 d. Although the bulk modulus of the granular framework clearly increases with decreasing porosity, the P-wave velocity is also determined by the bulk modulus of the fluid phase K_f according to Eq. (1).

Freshly mixed concrete stiffens with time even before setting. Some amount of mixing water is absorbed by the unsaturated aggregate, lost by evaporation and removed by the initial chemical reactions which cause loss of workability.

$$K_{eff}(n) = \left[\frac{n/n_0}{K + 4/3G} + \frac{1 - n/n_0}{K_s + 4/3G} \right]^{-1} - \frac{4}{3}G \tag{2a}$$

$$G_{eff}(n) = \left[\frac{n/n_0}{G + G/6 \cdot (9K + 8G)/(K + 2G)} + \frac{1 - n/n_0}{G_s + G/6 \cdot (9K + 8G)/(K + 2G)} \right]^{-1}$$
$$- \frac{G}{6}\left(\frac{9K + 8G}{K + 2G} \right) \tag{2b}$$

Ettringite and early C-S-H hydration products

According to [7], ettringite is formed during the first 3 h of cement hydration. These ettringite needles have merely a small influence on the stiffening of the cement paste. However, the P-wave velocity and energy might be strongly affected, since ettringite fills pore space. Consequently, the porosity n decreases, the bulk moduli K_{eff} and G_{eff} of the solid framework increase and the velocity increases. Kamada *et al.* [8] demonstrated for high-early strength cement that the formation of ettringite coincides with the early increase in ultrasound velocity; although ettringite formation was limited ($C_3A < 5\%$), also the earliest C-S-H hydration products can contribute to the velocity increase before setting.

Thixotropy

Some mortar mixtures exhibit thixotropic behaviour: they flow during mixing and placing, but become rigid at rest. Thixotropy is attributed to inter-particle forces. Each particle has an equilibrium position for which the potential energy due to colloidal interactions is minimum. Only particles smaller than 40 μm are influenced by potential energy effects. These particles can coagulate reversibly or permanently by combined van der Waals forces, electrostatic repulsion and steric hindrance. After placing the concrete, the reversible particle coagulation and linking will increase the velocity, before setting occurs. However, since coagulation is considered as the first step in the setting process, the distinction between thixotropic and setting behaviour might be unclear.

Materials and Methods

Specific gravity of CEM I 52.5 N, quartz and bentonite was 3.12, 2.65 and 2.15, while Blaine specific surface area amounted to 390, 355 and 810 m²/kg. Ultrasonic P-wave transmission measurements on mortar (w/b = 0.5; s/b = 3) were performed

at 20°C with the FreshCon [1], using broadband transducers with central frequency of 0.5 MHz. The velocity v is calculated and the energy E is determined by integration of squared amplitude values following the onset time. The energy ratio E/E_{ref} (E_{ref} measured on water), allows to eliminate energy loss due to divergence and reflection at interfaces. To simulate the early microstructure development, the pixel model CEMHYD3D was used [9]. The chemical reactions of the mineralogical phases are simulated by cellular automaton rules, applied iteratively to all pixels comprising the microstructure [9]. The change in P-wave velocity was calculated based on the simulated porosity change by combining Eqs. (1) and (2).

Results and Discussion

Air bubble migration, internal settling and workability loss

Internal settling and migration of air bubbles were investigated by replacing the cement by non-reactive quartz filler in a standard mortar mixture (Fig. 2).

The particle size distribution of the latter was in the same range as the cement. The velocity increased from 240 to 285 m/s during the first 48 h and to 340 m/s after 70 h due to internal settling and air bubble migration. Analogously, the energy ratio increased from $1.17 \cdot 10^{-6}$ to $5.19 \cdot 10^{-5}$ during the first 48 h and to $2.71 \cdot 10^{-4}$ after 70 h. Though the effect of internal settling and bleeding seems to be limited, this process will be accelerated in mortar by the cement hydration and coagulation. Also workability loss was partly included in the experiment since mixing water was absorbed by the unsaturated aggregate. The water reduction by initial reactions was however not incorporated and evaporation was restricted by the sealing tape.
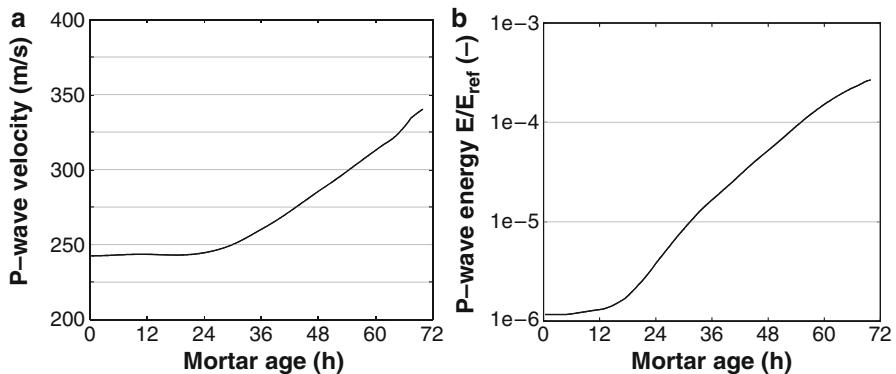
Fig. 2 Ultrasonic P-wave (**a**) velocity and (**b**) energy ratio vs. mortar age for a mortar mixture in which the cement was replaced by non-reactive quartz filler
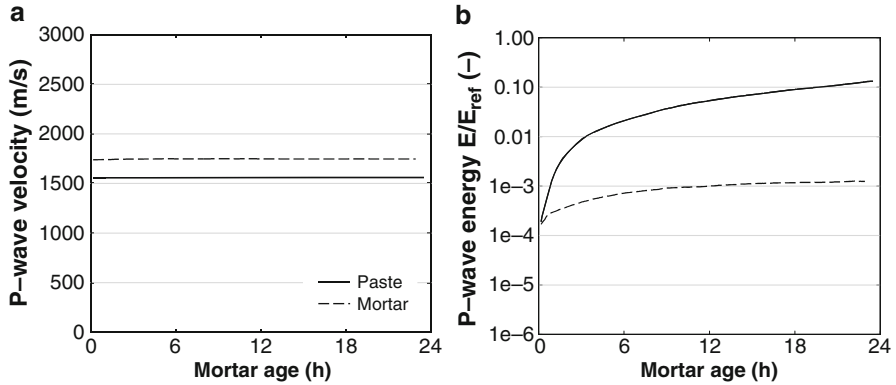
Fig. 3 Ultrasonic P-wave (**a**) velocity and (**b**) energy ratio vs. mortar age for a standard mortar mixture in which the cement was replaced by bentonite

Thixotropy

Thixotropic behaviour was simulated by testing a paste and mortar in which cement was replaced by bentonite (Fig. 3). Bentonite suspensions are thixotropic if the concentration is high enough (> 60 g/l). Due to the large specific surface area (810 m²/kg), the water demand in a betonite paste is much higher than in a cement paste. Only the results of the first 24 h are presented in Fig. 3a, but the velocity did not increase during the first 72 h in both paste and mortar sample. The initial velocity is however immediately higher than the ones measured on the actual concrete and mortar samples. Probably, the reversible structure was formed too rapidly to be captured by the measurements. A significant further increase in wave energy ratio is noticed on the paste sample, but was not reproduced with the mortar (Fig. 3b). The initial value of the energy ratio is also higher than the commonly measured values (10^{-7} to 10^{-6}).

Ettringite and early C-S-H hydration products

The hydration of the cement paste was simulated with the Cemhyd3D model. Figure 4 shows the simulated velocity increase due to formation of ettringite and early C-S-H hydration products without considering setting. The change in elastic properties of the granular framework was calculated with Eq. (2) and (1) based on the changing porosity as indicated by the Cemhyd3D simulations due to the formation of hydrates, while the particles were not assumed to be connected with each other (no setting). The presence of air still dominated the calculated velocity so that it merely increased with 50 m/s during the first 24 h.
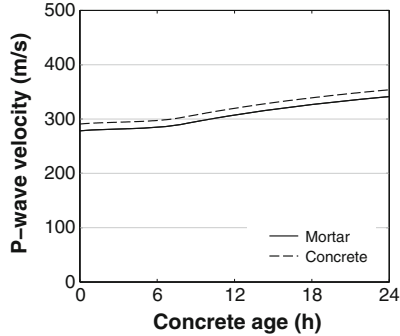
Fig. 4 Simulated velocity increase (CEMHYD3D) due to the formation of ettringite and early C-S-H hydration products without considering setting for a mortar and concrete mixture (w/b = 0.5) with OPC (CEM I 52.5)

Conclusion

Air bubble migration, internal settling and workability loss were proven to have a limited effect on the ultrasound velocity and energy. However, due to the precipitation of hydration products settling and workability loss might be accelerated. The modelled change in porosity due to formation of early C-S-H and ettringite hardly affected the calculated velocity. The possible influence of thixotropy was confirmed. However, not all concrete mixtures show thixotropic behaviour. None of the mentioned factors could unarguably be indicated as the cause of the early velocity and energy ratio increase. More likely, a combination of these factors affects the ultrasonic measurements.

References

[1] Reinhardt H.W. and Grosse C.U. (2004), *Constr Build Mater*, 18 (3) 145–154.
[2] Robeyst N., Gruyaert E., Grosse C.U., De Belie N. (2008), *Cem Concrete Res*, 38 (10) 1169–1176.
[3] Ye G. (2003), *Experimental study and numerical simulation of the development of the microstructure and permeability of cementitious materials.*, Ph.D. thesis, Technical University of Delft, p. 186.
[4] Mielenz R.C., Wolkodoff V.E., Backstrom J.E. and Flack H.L. (1958), *J ACI*, 55(5), 95–121.
[5] Voigt T., Grosse C.U., Sun Z., Shah S.P. and Reinhardt H.W. (2005), *Mater Struct*, 38 (282), 729–738.
[6] Mavko G., Mukerji T. and Dvorkin J. (2003), *The rock physics handbook - tools for seismic analysis in porous media*, Cambridge University Press, Cambridge.
[7] Scrivener K.L. (1989), *The microstructure of concrete*, in: J. Skalny (Ed.) Materials Science of Concrete, The Am Cer Soc, Westerville, pp. 127–161.
[8] Kamada T., Uchida S., Rokugo K.(2005), *J Adv Concrete Technol*, 3(3) 343–353.
[9] Bentz D. (1999), *Mater Struct*, 32, 187–195.

Automated Shear-Wave Techniques to Investigate the Setting and Hardening of Concrete in Through-Transmission

M. Krüger, C.U. Grosse and F. Lehmann

Abstract Ultrasonic methods have been developed in the past few decades to study the properties of cement based materials in fresh and hardened state. However, most of the methods consider only a certain type of ultrasonic waves. To derive elastic parameters of fresh concrete like the Poisson's ratio and elastic modules it is required to measure shear waves as well as compression waves. It is relatively much more difficult to establish a setup to transmit and record shear waves in a way that the onset of these slower waves can be detected sufficiently clear to calculate the shear velocity with the required accuracy. In this paper, an experimental setup for testing concrete with different ultrasonic waves is presented and methods for automated onset determination of p- and s-waves are described.

Keywords Concrete • Elastic properties • Hardening • Setting • Shear-waves • Ultrasound

Introduction

The properties of cement based materials in the fresh and hardening state are currently measured with rather conventional methods. Ultrasonic methods have been developed in the past using through-transmission techniques and analyzing the whole waveform. Material properties as for example the workability are investigated based on parameters like the compression velocity, the energy and the frequency content of the signals. However, to derive the Poisson's ratio of fresh

M. Krüger (✉) • F. Lehmann
Material Testing Institute, University of Stuttgart, Stuttgart, Germany
e-mail: Markus.Krueger@mpa.uni-stuttgart.de

C.U. Grosse
Center for Building Materials, Technical University of Munich, Germany
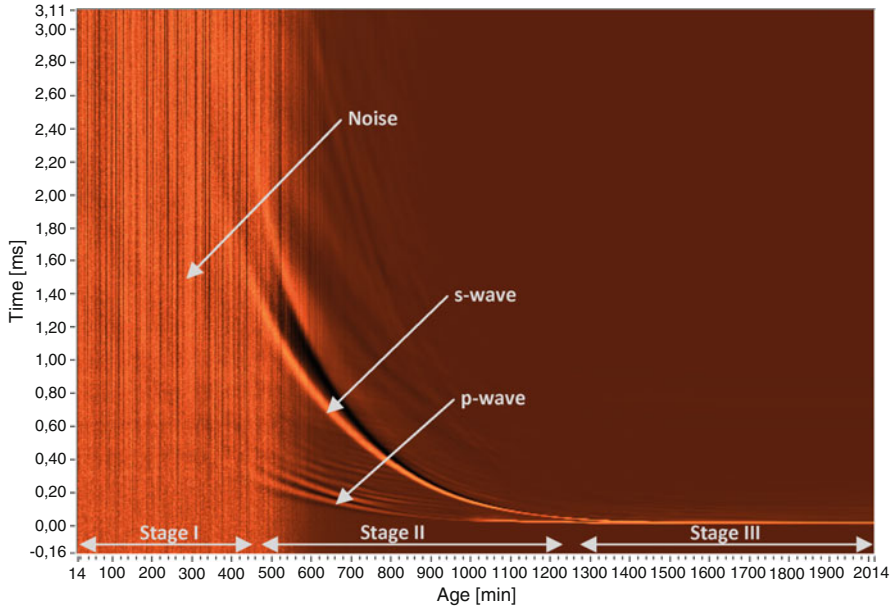
Fig. 1 Time series of normalized ultrasonic signals obtained from A-Scans of UHPC during hydration ensued setting and hardening

concrete or to get information even on the elastic modules data based on compression waves only are insufficient. It is required to obtain shear waves also [1]. It is certainly much more difficult to establish a setup to transmit and record shear waves in a way that the onset of these slower waves (compared to compression waves) can be detected as clear as necessary to calculate shear velocity values with the required accuracy.

Figure 1 shows a result from a measurement conducted with an optimized test setup as described below. It has to be noted that the setting time of the tested ultra high performance concrete (UHPC) mix is approximately 10 hours, which is quite a long time compared to ordinary concrete mixes. However, different stages during setting and hardening could be identified, that are more or less assignable to most of the ultrasonic test setups used by other researchers:

- Stage I: The signals recorded during this stage are dominated by noise, i.e. the ultrasonic signals are either not transmitted through the material or damping at this stage is too high so that the sensitivity of the receiver is not sufficient to resolute the signal. Therefore, p-wave and/or s-wave onset could not be discriminated from noise.
- Stage II: Due to large differences in the onset of the p-wave and the s-wave they could be easily identified visually. Also automated onset picker like simple threshold picker or advanced picker algorithms like the Hinkley criterion picker [2] show good results.

- Stage III: P- and s-wave velocities have reached high values. P-wave detection is still rather easy, because the p-wave is the fastest wave. However, if thickness of the tested specimen is small, dispersed p-waves might affect the s-wave, so that the simple methods for the s-wave onset detection, as mentioned to be sufficient for stage II, could not be used.

Test Setup for Simultaneous P- and S-wave Measurements

From the different stages some conclusions regarding efficient test setups can be drawn. To be able to identify signals at the very early stage it is recommended to minimize specimen thickness, while at the same time using high excitation pulse voltage. Note that the recorded signals are expected to show very low frequencies at the beginning. At later stage (stage III), due to high p- and s-wave velocities, determination of s-wave onset might be difficult. To overcome this problem greater specimen thickness might be useful. However, this has negative effect on the very early stage detectability. Thus, one has to find a suitable compromise that allow for sufficient analysis through the setting and hardening time period of interest. The test setup used for the tests is similar to that proposed by a RILEM recommendation worked out by RILEM TC 218-SFC [3]. However, instead of p-wave transducers two broadband s-wave transducers with a center frequency of 250 kHz are used. A sensor distance of 50 mm was found to be sufficient. The sensors are coupled by a thin polyimide film (d=25μm) directly through the mix to allow for best signal transmission. A detailed system description is given in Krüger [4].

Automated Determination of the P-wave Onset Time

One of the most crucial parts is to extract as accurate as possible the onset time (i.e. the arrival time) of the signal in relation to the trigger time. Therefore, onset of the signals has to be discriminated from noise. There are various possibilities to do this since there are threshold and energy based methods and auto-regressive processes (see also [2, 4]). In the following it is proposed using the AIC-Picker. Compared to a threshold picker or other simple picking algorithms the AIC-Picker is much more complicated to be handled because the picking algorithm depends on five parameters, which are further explained in the following.

The AIC-Picker for the determination of the p-wave onset is based on the Akaike Information Criterion (AIC) [6]. It was adapted to ultrasonic signals by Kurz, Grosse and Reinhardt [2]. The developed autoregressive AIC-picker first creates an envelope time function $E(t)$ via the Hilbert transform $\overline{R}(t)$ from the time signal $R(t)$ as

$$\overline{R}(t) = \frac{1}{\pi} \cdot \int_{u=-\infty}^{\infty} \frac{R(u)}{t-u} du \tag{1}$$
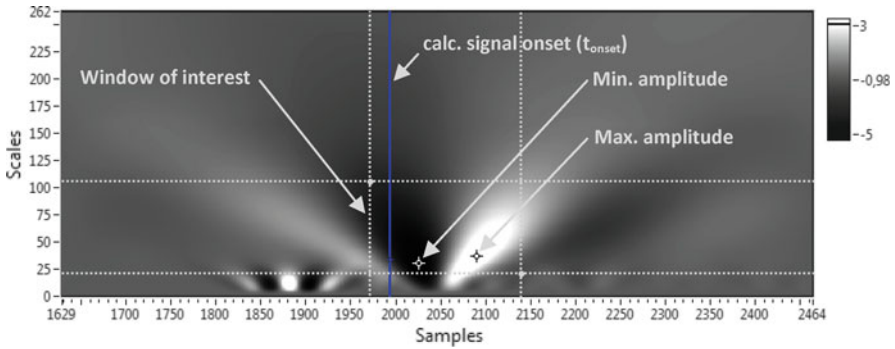
Fig. 2 Example of a wavelet graph of an ultrasonic signal

$$E(t) = \sqrt{R(t)^2 + \overline{R}(t)^2} \tag{2}$$

with time signal $R(u)$ and current timestep u. In the envelope time function, a simple threshold level could be used to pick an onset window (see Fig. 2). The size of the window is specified by the parameters *Window upper bound* and *Window lower bound.* These parameters define a number of samples before and after the located time in the envelope time function corresponding to the AIC threshold level.

The AIC function $AIC(t_w)$ could then be calculated for the selected window as

$$AIC(t_W) = t_W \cdot \log\left(var\left(R_W(t_W, 1)\right)\right) +$$
$$(T_W - t_W - 1) \cdot \log\left(var(R_W(1 + t_W, T_W))\right) \tag{3}$$

Where t_w is the time within the selected window, R_w is the time signal within the selected window, T_w is the maximum time of the selected window, $var(R_w(t_w, 1))$ is the variance of R_w from the current value of t_w and where $var(R_w(1 + t_w, T_w))$ is the variance of R_w between $1 + t_w$ and the T_w.

On the basis of this AIC function it is suggested to cut a second window in which *AIC lower bound* and *AIC upper bound* define the number of samples that where cut at the beginning and the end of the AIC function. Within the remaining window the point of the minimum could be determined, which then equals the estimated onset time of the time signal. This second cutting of the window is sometimes needed if certain noise (e.g. electromagnetic interference at the very early stage of concrete hardening) lead to multiple minima in the AIC function. Therefore, the five parameters of the AIC picking algorithm are to be set individually for different concrete mixes.

Automated Determination of the S-wave Onset Time

As discussed before, the shear wave is in certain stages affected by the faster p-wave so that its onset determination in the time signal might be inaccurate. To overcome this problem it is proposed to use frequency information to separate the p-wave

from the s-wave. A prerequisite is that main frequencies of the two waves are different for each measurement, which was found to be true for all mortar mixes tested in laboratory so far [7].

To determine the onset time of the shear wave, the time signal is transformed into a time-frequency domain by means of a continuous wavelet transform. Hereby a scalable *mother wavelet* is moved along the time axis and the correlation between the signal and the mother wavelet is calculated. This corresponds to a multiplication of the signal's Fourier transform with the scaled wavelet. Two different Mother wavelets are found to be best suited, that is the Mexican Hat (4) and the Antisymmetric (5) wavelet. They are of the form

$$\psi(x) = (x^2 - 1) \cdot e^{\frac{x^2}{2}} \tag{4}$$

$$\psi(X) = X \cdot e^{-\frac{x^2}{2}} \tag{5}$$

Analytically, the change of the mother wavelet $\psi(x)$ as governed by the chosen parameters produces a daughter wavelet

$$\psi^*(t) = \psi\left(\frac{t - \tau}{s}\right) \tag{6}$$

where τ is a parameter for shift of the wavelet along the time axis and s a scaling parameter. By choosing adequate parameters and running the transform, the calculated transform of the time signal can be plotted into a wavelet graph (see Fig. 2), that is now used for the determination for the s-wave onset.

The following calculation of the s-wave onset time mainly takes two conditions as a basis. First, it is presumed that when using shear wave transducers, the predominant part of the impulse energy is transmitted with the shear wave and not the accompanying primary wave. Furthermore, the frequency contents of shear and primary waves most likely differ from each other, as this was mentioned before. Meeting these two conditions allows an identification of the maximum and minimum value in a certain window in the wavelet graph as the extreme values of the induced shear wave (see Fig. 2). The distance on the time axis Δt between the first extreme value t_1 and the second extreme value t_2 corresponds to half the oscillation period T of the shear wave.

$$\frac{T}{2} = \Delta t = t_2 - t_1 \text{ for } t_2 > t_1 \tag{7}$$

Subtracting a quarter of an oscillation period from the time of the maximum value yields the onset time of the signal.

$$t_{onset} = t_1 - \frac{T}{4} = t_1 - \frac{\Delta t}{2} = \frac{3}{2}t_1 - \frac{1}{2}t_2 \tag{8}$$

To reduce calculation time and to avoid picking the p-wave instead of the s-wave it is recommended to reduce the wavelet window in which the extreme values are picked. This can be done by first determining a window of interest manually for one exemplary measurement. After that the wavelet of the next signal (both backward and forward calculations are possible) is calculated and new minimum and maximum amplitudes are determined within this window. The window of interest is then shifted by keeping the initial spacing parameters from the window borders to initial the minimum and maximum constant, but now rearranging the window of interest around the new determined minima and maxima. This stepwise procedure allows for a fast and reliable onset picking of the s-wave and avoids picking the p-wave, which at a later stage of hardening might become the dominant wave in the time signal.

Conclusions

The proposed test setup allows for the simultaneous measurement of p- and s-waves during setting and hardening of cementitious materials with high reproducibility. Through combined use of the AIC-picker for onset determination of the p-wave and the introduced wavelet picker for determining the s-wave onset, a practical solution for the automatic characterization of fresh cementitious materials during setting and hardening is presented. Furthermore, the developed test setup, by its ability to measure both wave velocities, enables reliable studies on elastic properties of fresh cementitious materials even before initial setting of the mix.

References

[1] Reinhardt, H.-W., Grosse, C.U., (2005). In: *Advances testing of cement based materials during setting and hardening.* RILEM Report 31. Bagneux: 2005. pp. 83–96.
[2] Kurz, J.H., Grosse, C.U. and Reinhardt, H.W. (2005), *Ultrasonics*, vol. 43, pp. 538–546.
[3] Reinhardt, H.W., Krüger, M. and Grosse, C.U., Testing of fresh concrete by ultrasound transmission. Technical Committee 218-SFC: Sonic methods for quality control of fresh cementituous materials, in preparation.
[4] Krüger, M., Lehmann, F. (2010), SmartPick – User Manual, Rev. 1.50. Smartmote.
[5] Grosse, C.U., Reinhardt, H.-W., Krüger, M. and Beutel, R. (2006), In: *Advanced testing of fresh cementitious materials*, Workshop Proceedings., Stuttgart, Aug. 2006, pp. 83–93.
[6] Akaike, H. (1974), A new look at the statistical model identification. IEEE transactions on automatic control, vol. AC-19, no. 6, 1974.
[7] Mochalska, A. (2010), Evaluation of the setting and hardening behavior of mortar mixes with shear waves. Diploma Thesis, MPA Universität Stuttgart, 2010.

Effects of Experimental Parameters in Monitoring the Hydration of Cement Mortars by Ultrasonic Testing

Ö. Kasap Keskin, İ.O. Yaman and M. Tokyay

Abstract In ultrasonic pulse velocity testing, frequency and the travel path length are important parameters that determine the attenuation rate and the influence of near-field effect. Higher frequencies and longer distances result in higher attenuation. On the other hand, smaller path lengths are not desirable due to near-field effect. This study investigated the effect of transducer frequency and the length of path used to determine ultrasonic wave velocity in monitoring the hydration process of fresh cement mortars. For this purpose, an experimental set-up was prepared to observe the ultrasonic pulse velocity (UPV) development in cement mortars during the first 24 hours after mixing. Mortar mixtures with a water/cement ratio of 0.5 were tested for 15, 10 and 5 cm travel path lengths at 54, 82 and 150 kHz frequencies. UPV curves were obtained in each test and some characteristic points on the curves were determined. The results showed that choosing the appropriate frequency and travel path distance is important in monitoring the UPV development in fresh cementitious materials.

Introduction

Wave transmission method is a popular non-destructive test method for hardened concrete which basically measures the velocities of ultrasonic waves travelling through a medium. However, many studies showed that the application of method

Ö.Kasap Keskin (✉)
Energy Efficiency Dep., Ministry of Public Works and Settlement, Ankara, Turkey
e-mail: ozlemkasap@gmail.com

İ.O. Yaman • M. Tokyay
Civil Engineering Dep., Middle East Technical University, Ankara, Turkey

in fresh cementitious materials also give reliable results to monitor the hardening and setting processes.

Ultrasonic test method was applied successfully to determine the properties of fresh cement pastes used as oil field drilling cement slurries [1-3]. Boumiz et al. [4] used a perspex mold for determining the velocity, frequency and the attenuation of longitudinal and shear waves. In cement pastes the travel distance of the waves was 1 cm, while it was 4 cm in mortars. It was revealed that the velocity of ultrasonic waves increased rapidly during setting and hardening [4]. A device for observing the change of UPV in fresh materials was developed in Stuttgart University, and was used in several investigations [5-10]. This device utilized a mold consisted of two long PMMA walls and a U-shaped rubber foam which was placed in between. The initial setting time of mortar was reported as the first maximum point in curvature of the velocity-age curve, and the final setting time was reported as the point where the UPV reached 1500 m/s [8]. Ye et al. [11] developed a microstructural model for hydration process based on the three stages observed in ultrasonic test results of concrete specimens. The steel mold had holes on two opposite walls to which the transducers were attached by PVC rings [11]. Kamada et al. [12] used a steel mold with holes on the sides in which brass plates were placed for the attachment of the transducers. The travel path distance was chosen as 35 mm so it was greater than the wavelength. According to the ultrasonic pulse velocity curves, the hydration of cement paste was divided into three stages [12]. Trtnik et al. [13] estimated the initial setting of cement pastes as the first inflection point of ultrasonic pulse velocity curves. Zhang et al. [14] divided the hydration process of pastes into four stages depending on the results of resistivity and ultrasonic tests and concluded that the ultrasonic test results were sensitive to physical change of cement paste.

Although several researches related to this subject have been carried out so far, a standard test method for the application on fresh cementitious materials has not been developed yet. In each study, the researchers used their own experimental set-up for testing the specimens. The mold material, dimension, and frequency range also vary in each study. As the material should be inside the mold during the test, the shape, size and the material of the mold may become important.

In the transducer, the pulse is generated at multiple points and during travelling they merge to form a single wave. The region behind the point where this unification occurs is known as near-field [15]. In order to have reliable data, the travel distance should be greater than the near-field zone of which length depends on the frequency and the diameter of the transducer:

$$N = (D^2 - \lambda^2)/4\lambda \tag{1}$$

where N is the near-field length, D is the diameter of the transducer and λ is the wavelength of the stress wave [15]. Therefore, as the velocity changes during hydration, near-field length also changes. The calculated values of near-field zone for two different frequency transducers which were used in this study are listed in Table 1 for different velocity levels.

Table 1 Near-field zone for different velocity levels

Frequency: 54 kHz (D=50mm)			Frequency: 150 kHz (D=25mm)		
UPV (m/s)	λ (m)	N (mm)	UPV (m/s)	λ (m)	N (mm)
2000	0.037	7.6	2000	0.013	8.8
1000	0.018	30.2	1000	$6.7*10^{-3}$	21.8
500	$9.3*10^{-3}$	65.2	500	$3.3*10^{-3}$	46.0
200	$3.7*10^{-3}$	167.8	200	$1.3*10^{-3}$	116.9

As seen from Table 1, near-field can be very large when the pulse velocity is small and the diameter of the transducer is large. However, for high velocity values, the near-field/far-field concept does not seem to cause a problem.

The aim of this study is to investigate the effect of transducer frequency and the length of path used to determine UPV in monitoring the hydration process of cement mortars. For this purpose, three different travel path lengths (15, 10 and 5 cm) with three different frequencies (54, 82 and 150 kHz) were tested by monitoring the hydration process of mortars with 0.5 water/cement ratio.

Experimental Study

The most critical problem encountered in monitoring the development of properties of fresh cementitious materials is the possibility of waves to travel through the mold instead of the hydrating material. In the literature, generally either plexiglass [5-10] or steel [11-12] molds were used.

In this study, wooden prismatic molds with a square cross-section of 150 x 150 mm were used. The path length was changed from 50 to 150 mm. Two holes were cut on two opposite sides. Two thin plexiglass sheets were placed behind the holes. The transducers were then attached to the molds by rubber bands. To determine the velocity of longitudinal waves travelling through the cement pastes, an ultrasonic apparatus and a data acquisition system were used. The sampling rate was selected as 50 MHz and kept constant during all the experiments. The details of test setup and procedure for arrival time determination were described in detail by Yaman et al. [16] and Kasap Keskin [17]. The ultrasonic wave data was collected at 15-minute time intervals during the first 24 hours. The change of ultrasonic pulse velocity during the hydration process of mortars was observed.

Test Results and Discussions

The development of UPV in mortars was monitored for the first 24 hours after mixing. The rate of UPV development (RUPV) was also determined numerically by dividing the difference in two successive UPV measurements to the time interval. A typical UPV and RUPV curves for the first 24 hours are shown in Figs. 1 and 2, respectively.

Fig. 1 Typical UPV curve
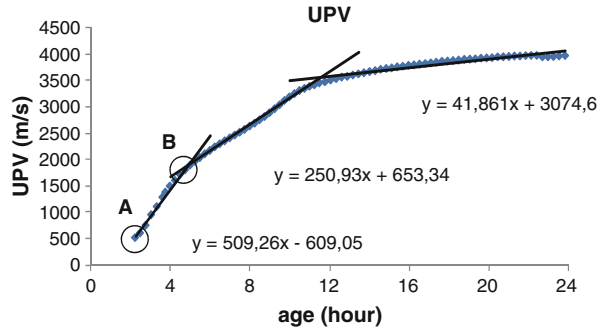
Fig. 2 Typical RUPV curve
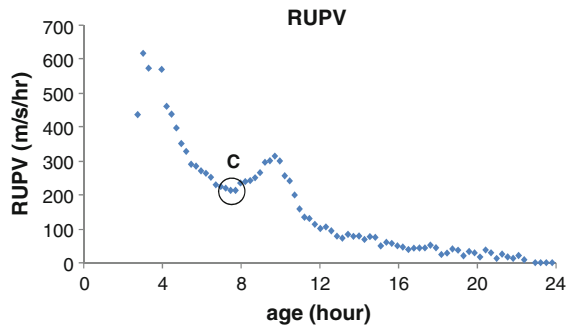
As seen in Fig. 1, UPV increases with time as the hydration proceeds within the mortar mixture, initially with a steep slope, later on with a milder slope and lastly with a mildest slope for the first 24 hours of hydration. In Fig. 2, RUPV development makes an initial peak followed by a minimum point and after a second peak it decreases approaching to zero. As a result of a comparison of UPV and RUPV curves of pastes and mortars, and the Vicat test results, the first inflection point in UPV curve (B) and the minimum point in RUPV curve (C) of mortars are chosen to be two critical points that show the physical changes in the medium [17]. The point in UPV curve where first meaningful value is obtained (A) also differs from mixture to mixture. Depending on the results obtained in [17], the effects of frequency and travel path length will be discussed by comparing these mentioned points obtained from hydrating mortar specimens.

Effect of path length and frequency range of transducers

Travel path length is important in attenuation and near-field effect points of view; such that for too long path lengths the wave can attenuate hindering reliable measurements and for too short path lengths the measurements may be taken within

Table 2 Comparison of characteristic points of UPV and RUPV curves

Frequency	54 (kHz)			82 (kHz)			150 (kHz)		
Length	15cm	10cm	5cm	15cm	10cm	5cm	15cm	10cm	5cm
t@A (h)	2.25	1.75	1.00	2.75	2.00	1.00	5	3.50	1.75
t@B (h)	4.94	4.86	4.74	5.02	5.09	4.50	*	5.07	4.48
t@C (h)	7.48	7.58	7.34	7.21	7.28	5.68	*	7.12	5.35

the near-field resulting unreliable readings. Additionally, ASTM C 597 [18] restricts the least dimension of the test object to a value greater than one wavelength.

On the other hand, frequency and wavelength are in inverse relation so that the product of the two parameters equals to wave velocity. In hydrating cementitious materials, the UPV of the medium can be measured at very low values (300-500 m/s) increasing up to about 4000-5000 m/s. Therefore, the wavelength of the ultrasonic pulse wave propagating through the medium increases with time if narrow-band transducers are used. In ultrasonic testing, the wavelength should be greater than the particle size of the medium. In fresh state the test frequency is limited by the maximum aggregate size as in the case of the hardened concrete. However, the limitation is much more severe in fresh state as the initial velocities are very low as compared to hardened case. For example, in the case of cement mortars with maximum aggregate size of 4.75 mm, the wavelength starts to be greater than the maximum aggregate size after the medium reaches a velocity level of 255 m/s for frequency of 54 kHz; while 715 m/s for frequency of 150 kHz. As a result, it could be concluded that the applied level of frequency could be quite important for low values of UPV.

In order to investigate the effect of path length and the frequency, narrow-band transducer with 54, 82 and 150 kHz frequency were applied for three travel path lengths of 15, 10 and 5 cm. The occurrence time of aforementioned characteristic points (A, B, C) obtained from UPV and RUPV curves are given for each case in Table 2.

From Table 2, it is seen that the point A is directly affected by the path length. For longer distances, due to attenuation, the initial readings can be taken at later ages. The effect of path length seems to be more severe at higher frequencies. Therefore, if high frequencies are utilized with long travel path distances, the early hydration of cementitious systems may not be monitored. On the other hand, for points B and C, the results are similar for all travel path lengths in case of 54 kHz; the results are also similar for 15 and 10 cm travel path lengths in case of 82 kHz. However, in case of 150 kHz, the results are similar to the others for 10 cm travel length, and the results are smaller for 5 cm travel path length. Therefore, it could be concluded that using very short travel path lengths is not recommended for ultrasonic testing of fresh cement mortars. This can be explained by two reasons; near-field effect and the least dimension restriction. As seen in Table 1, the near-field region is greater than 5 cm for low velocities. However, in the case of higher velocities, wavelength will start to be greater than 5 cm. As a result, it can be said that the travel path distance and the frequency range of waves should be chosen carefully for ultrasonic testing of fresh cementitious materials considering wavelength, near-field and attenuation.

Conclusions

In order to investigate the effects of travel path length and the frequency of the transducers in monitoring the hydration of fresh mortars, three different travel path lengths and three different frequencies were used when determining the UPV development. Test results showed that using high frequency transducers is not suitable for testing fresh cement mortars due to high attenuation and small wavelength which makes it difficult to distinguish the wave from electrical noise especially at the initial stages. Moreover, using short travel distance makes the measured data less reliable due to near-field effect at low velocities and due to least dimension restriction at high velocities. However, using very long travel distances especially with high frequencies is also not desirable, because due to attenuation the capturing of the ultrasonic pulses may become impossible particularly at the very early stages. Therefore, a suitable frequency range and travel distance should be chosen for the test set-up if narrow-band frequency transducers are used. Depending on the parameters used in this investigation, frequencies of 54 and 82 kHz can be used reliably for travel path lengths of 15 and 10 cm.

References

1. Keating, J., Hannant, D.J., Hibbert, A.P., (1989) *Cem. Concrete. Res.*, vol. 19, n. 4, p. 554–566
2. Sayers, C.M., Grenfell, R.L., (1993) *Ultrasonics*, vol. 31, n.3, p. 147– 153
3. D'Angelo, R., Plona, T.J., Schwartz, L.M., Coveney, P., (1995) *Adv. Cem. Based Mater.*, vol. 2, n. 1, p. 8–14
4. Boumiz, A., Vernet, C., Cohen Tenoudji, F., (1996) *Adv. Cem. Based Mater.*, vol. 3, n. 3–4, p. 94–106
5. Grosse, C.U. (2002) *Otto-Graf-Journal*, vol.13, p. 93–110
6. Grosse, C.U., Reinhardt, H.W. (2003) In: International Symposium on Non-Destructive Testing in Civil Engineering (NDT-CE), Proceedings BB 85-CD (CD-ROM), Berlin
7. Lee, H.K., Lee, K.M., Kim, Y.H., Yim, H., Bae, D.B. (2004) *Cem. Concr. Res.*, vol. 34, n. 4, p. 631–640
8. Reinhardt, H.W., Grosse, C.U. (2004) *Constr. Build. Mater.*, vol. 18, n. 3, p. 145–154
9. De Belie, N., Grosse, C.U., Kurz, J., Reinhardt, H.W. (2005) *Cem. Concrete. Res.*, vol. 35, n. 11, p. 2087–2094
10. Voigt, T., Grosse, C.U., Sun, Z., Shah, S.P., Reinhardt, H.W. (2005) *Mater. Struct.*, vol. 38, n. 8, p. 729–738
11. Ye, G., Laura, P., Breugel, K., Fraaij, A.L.A. (2004) *Cem. Concrete. Comp.*, vol. 26, n. 5, p. 491–497
12. Kamada, T., Uchida, S., Rokugo, K., (October 2005) *J. Adv. Concrete. Tech.*, vol. 3, n. 3, p. 343–353
13. Trtnik, G., Turk, G., Kavcic, F., Bosiljkov, V.B. (2008) *Cem. Concrete. Res.*, vol. 38, n. 11, p. 1336–1342
14. Zhang, J., Qin, L., Li, Z. (2009) *Mater. Struct.*, vol. 42, n. 1, p. 15–24
15. Houf, J. W., (October 2003) *The NDT Technician*, vol. 2, n. 4, (http://www.asnt.org/publications/tnt/tnt2-4/tnt2-4fyi.htm)
16. Yaman, I.O., Inci, G., Yesiller, N., Aktan, H.M. (2001) *ACI Mater. J.*, vol. 98, n. 6, p. 450–457

17. Kasap Keskin, O. (2009) *Monitoring the Development of Properties in Fresh Cement Paste and Mortar by Ultrasonic Waves*, Ph D Thesis, Civil Engineering Department, Middle East Technical University, Ankara, 170 p.
18. ASTM C 597-97 (2002) Standard Test Method for Pulse Velocity Through Concrete, *Annual Book of ASTM Standards*

Ultrasonic Monitoring of Capillary Porosity Evolution and Strength Gain in Hydrating Cement Pastes

K.V.L. Subramaniam

Abstract An ultrasonic test procedure for determining the capillary porosity in hydrating cement paste is presented. The response of hydrating cement paste through setting is monitored using horizontally polarized shear waves (SH). Changes in the ultrasonic signal through setting are related with changes in the porosity and stiffness of an equivalent water-filled poroelastic material, which provides identical acoustic impedance. The porosity obtained from the ultrasonic measurements, is identical to capillary porosity obtained from the conventional themo-gravimetric analysis. A unique relationship between capillary porosity and compressive strength is established for hydrating cement pastes.

Keywords Capillary porosity • Cement paste • Compressive strength • Hydration • Shear waves • Ultrasound

Introduction

Accurate determination of the changes in the microstructure of hydrating cement through setting, and early strength gain of the material has remained a major experimental challenge Conventional methods for probing the microstructure are not conducive to studying changes in microstructure in the first few hours after casting because (a) sample preparation procedures either alter or disturb the microstructure [1] and (b) changes in microstructure occur on a time scale that is an order of magnitude faster than the time required for sample preparation [2]. Our current understanding of changes in the microstructure during setting obtained from the computer simulation models indicates that initially starting from a weak skeleton comprised

K.V.L. Subramaniam (✉)
Department of Civil Engineering, Indian Institute of Technology, Hyderabad, INDIA
e-mail: kvls@iith.ac.in

of loosely connected cement grains within the fluid medium, the products of hydration link up to provide a continuous network of solid within the fluid filled space. The emergence of a continuous solid phase within the fluid medium has been identified as the percolation threshold [3,4]. Following percolation threshold, setting behavior is initiated in the cement paste. Through setting, as the products of hydration form within the fluid-filled spaces of cement paste, a network of pores and a pore structure develops.

The primary focus of the research presented here is to assess changes in the microstructure associated with porosity in hydrating cement paste through the setting process from ultrasonic measurements. The method measures reflection of SH waves at the surface of hydrating cement paste. A poroelastic equivalent material for hydrating cement paste is derived by matching the measured reflections response with changes in the poro-elastic parameters.

Experimental Program

The test program consisted of the following measurements: (a) ultrasonic SH wave reflection; (b) Thermogravimetric (TG) weight. Cement paste samples with water-to-cement ratios equal to 0.35, 0.45 and 0.5, were evaluated.

Ultrasonic test procedure

A schematic diagram of the experimental setup for oblique ultrasonic wave reflection measurement is shown in Fig. 1. The test probe consists of ultrasonic transducer(s) attached to a buffer plate made of fused quartz, which is in contact with the hardening cement paste. Multiple pairs of transducers (T and R) with a center frequency of 1 MHz were mounted on precisely machined faces at matched angles with respect to the vertical to generate SH waves. Wave reflection at the fused-quartz/cement paste interface was monitored at 0, 50 and 60 degree angles of incidence. The amplitude reflection factor, $r(1)$, which gives the decrease in the amplitude of a 1 MHz incident signal after reflection, was obtained using the self-compensating technique [2,5].

TG weight loss measurements

The evaporable and the non-evaporable water contents within the hydrating cement paste at different ages were measured. Weights of the samples were recorded after drying the sample at 105 °C before ramping the temperature to 1000 °C at 10 °C/minute. During the heating, the furnace was purged with nitrogen gas.
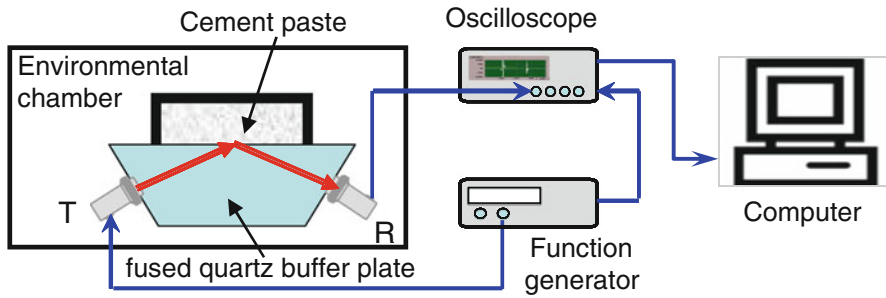
Fig. 1 Schematic Diagram of Test Setup for Ultrasonic Measurements
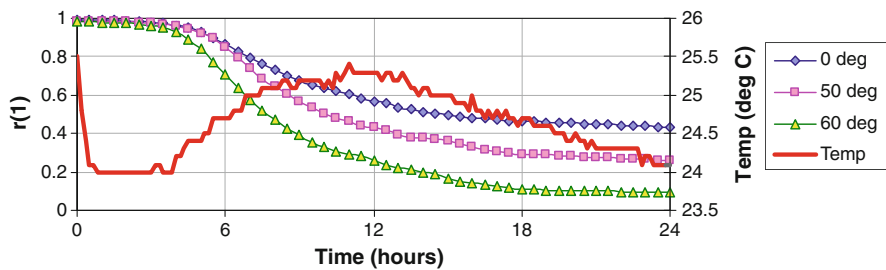
Fig. 2 Temperature and r(1) as a function of age after mixing

Analysis of Data

Changes in *r(1)* and temperature for cement paste with w/c equal to 0.5 are shown in Fig. 2. Immediately after mixing, the measured *r(1)* for the three angles of incidence are close to 1.0, suggesting that a significant portion of the incident wave energy is reflected at the quartz-cement paste interface. The increase in temperature after the dormant period signals the beginning of the acceleration stage, which is followed by the slow decrease in temperature in the deceleration stage. Starting from a gradual rate of change at the end of the dormant period, the rate of change in *r(1)*, corresponds well with the reaction rate indicated by the temperature measurements.

The measured changes in the *r(1)* can now be interpreted in terms of the expected result from the reflection of an SH wave at the interface between an elastic and a poroelastic material. In the poroelastic idealization, the hydrating cement paste is assumed to be comprised of a water-filled porous skeleton. The material of the skeleton is assumed to be homogenous and isotropic. The exact magnitude of change in amplitude of an incident SH wave *r(f)* after reflection can be obtained considering dynamic equilibrium and displacement continuity at the interface [5-7]. Changes in

the amplitude and phase of the wave following reflection from the poroelastic material can be symbolically expressed as [see Refs 5 for details]

$$R_s = r(f)e^{i\Phi} = R_s(\rho_e, E_e, \nu_e, \rho_s, \rho_f, K_f, \mu_b, \beta, \eta, a, c, \kappa, \delta_\mu) \tag{1}$$

where ρ_e, E_e, and ν_e are the density, the Young's modulus and the Poisson's ratio of the fused quartz, β is the porosity (assumed to be isotropic), ρ_s and ρ_f are the solid and fluid mass densities, respectively, η is the fluid viscosity, and κ is the coefficient of permeability of the porous frame, a is the pore diameter, c is the tortuosity coefficient, μ_b is the shear modulus of the skeletal frame (under drained conditions), K_f is the bulk modulus of the pore fluid. For the porous medium, the dynamic shear modulus of the skeletal frame is given as

$$\overline{\mu}_b = \mu_b(1 + \delta_\mu i) \tag{2}$$

where δ_μ, is the loss factor, which is usually a small number in the range of 0.11 – 0.17 [7,8]. In Equ. (2), the internal system variables of the fluid filled porous medium are shown in grey.

When applied to the case of hydrating cement paste, some simplifications can be introduced to the expression for R_s, assuming the hydrating cement paste is a water-filled porous skeleton, $K_f = 2.0 \times 10^9$ Pa, and the viscosity $\eta = 1.0 \times 10^{-3}$ Kg/ms. Further, changes in density of the hydrating cement paste with age (on account of chemical shrinkage) can be considered to produce insignificant changes in the bulk density of the material. Thus considering the hydrating cement material to be composed of two components, the porous skeleton (made up of cement grains and products of hydration) and water, a simple relation can be obtained considering

$$\rho_{bulk} = (1 - \beta)\rho_s + \beta\rho_f \tag{3}$$

where, ρ_{bulk} is the density of the cement paste. ρ_{bulk} can be considered to be constant through the hydration process. The ρ_{bulk} of cement paste samples were determined at three days of age and were found to be 1.87 g/cm³. The ρ_s, represents the effective density of the solid material, can be obtained using Equ. (6), further reducing the number of internal variables in the expressions for $r(f)$. ρ_s is the composite density of the solid made up of unhydrated cement and the hydration products. The analysis can be simplified considering inter-relations between some of the material para-meters [9]

$$c = 1 - r(1 - 1/\beta),$$

from Kozeny-Carman relation

$$\kappa(1 - \beta)^2 / \beta^3 = \kappa_0(1 - \beta_0)^2 / \beta^3 = const. \text{ and } a^2 / \kappa = a_0^2 / \kappa_0 = const. \tag{4}$$

Therefore

$$R_s = R_s(\rho_e, E_e, \nu_e, \mu_o, \beta, \delta_\mu) \tag{5}$$

The experimental data used in the optimization comprised of the *r(1)* at three different angles of incidence. The Generalized Reduced Gradient nonlinear optimization scheme was used to minimize an objective function based on squares of the differences [see ref 5 for additional details]. For the numerical inversion, the starting guess for μ_b was taken as 10^5 Pa. The range for δ_μ was initially prescribed to be within $0.01 - 0.3$. It was found that within the prescribed range, there was no influence of δ_μ on the final values of μ_b and β. The solution obtained at a given time was then used as the starting guess for the next time.

Evolution of Porosity in Hydrating Cement Paste

The porosity of cement paste obtained from the ultrasonic measurements are compared with the values obtained from TG weight loss measurements in Fig. 3. The porosity at certain degree of hydration then was calculated using the relations presented by Hansen [9] as

$$\phi(t) = \frac{\rho_{cement}(w/c) - (1.15 + 0.06\rho_{cement})\alpha_h(t)}{1 + (\rho_{cement})(W/C)} \tag{6}$$

where ρ_{cement} is the specific gravity of cement, w/c is the water to cement ratio and α_h is the degree of hydration. The porosities obtained from weight loss measurements agree well with the porosities from poro-elasticity based inversion of ultrasonic data. In addition, the values of porosity determined from TGA measurements for cement paste with w/c equal to 0.5 by Voigt [Ref 10] are also plotted in the Figure. The close agreement between the values of porosity obtained from the poro-elastic equivalent derived from wave reflection measurements and the capillary porosity calculated by applying Power's model to weight loss measurements provides
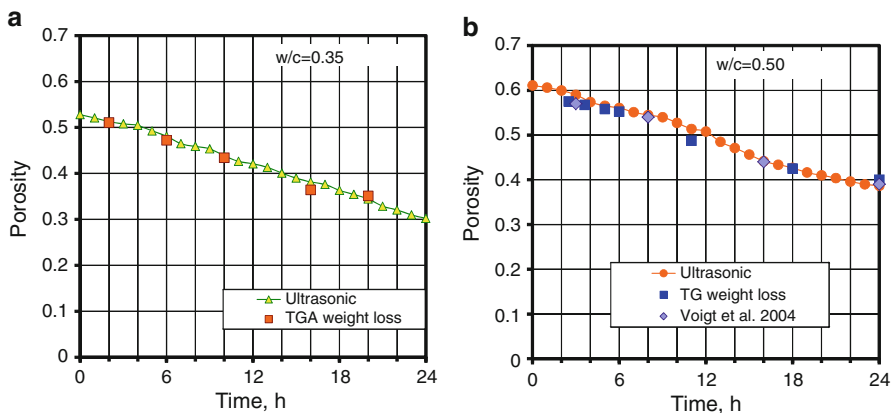
Fig. 3 Porosity from the ultrasonic measurements and the TG weight loss measurements: (**a**) w/c = 0.35; and (**b**) w/c = 0.5
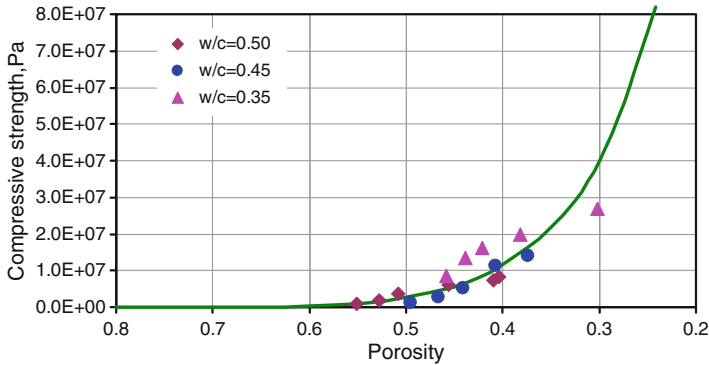
Fig. 4 Relationship between capillary porosity and compressive strength

a validation of the measured porosity. The poro-elastic equivalent for hydrating cement paste, which provides identical response for reflected ultrasonic waves, provides a realistic representation of the cement microstructure at the scale of capillary porosity. This method therefore provides a means for continuous assessment of aging cement microstructure, which can then be related to the development of macroscopic properties.

The influence of porosity on the compressive strength of cement paste is shown in Fig. 4. It can be seen that the relationship between the capillary porosity and the compressive strength is independent of the w/c ratio. This suggests that in hydrating cement paste the strength gain is controlled by the decrease in capillary porosity. While the relationship between the direct measured variable, the reflection factor (r) and the compressive strength is not unique for the different w/c ratios, there is a unique relationship between the microstructural variable derived from the reflection measurement and the compressive strength. It should be noted that the exact relationship between the capillary porosity and compressive strength will depend upon the exact composition of the cementitious material. However, the results presented in Fig. 4 suggest that for a given type of cementitious material, if the relationship between capillary porosity is established, then microstructure based tools for predicting strength gain in hydrating cement based materials can be developed.

Conclusions

An ultrasonic method for continuous, simultaneous measurement of capillary porosity of the material, with time is presented. In hydrating cement pastes, there is a unique relationship between the decrease in porosity and the increase in compressive strength, which does not depend on the w/c ratio of the paste.

References

[1] Thomas, J.J. and Jennings, H.M., 1999, Concrete Science and Engineering, vol. 1: 45–64
[2] Subramaniam, K.V. and Lee, J., 2006, *Materials and Structures*, 40 no. 3: 301-309
[3] Bentz, D.P., Garboczi, E.J. and Jensen O.M., 1999 *Cement and Concrete Research*, 29(10): 1663–1671.
[4] Ye, G. and van Breugel, K. et al. 2003, Cement and Concrete Research, vol. 33, no. 2, pp. 233–239.
[5] Wang, X. and Subramaniam, K.V., 2010, *Cement and Concrete Research*, vol. 40, no. 1, p. 33–44
[6] Wang, X., and Subramaniam, K.V., 2010, *Ultrasonics*, Vol. 50, no. 7, pp. 726–738
[7] Stoll, R. and T. Kan 1981, Journal of Acoustical Society of America, 70: 149.
[8] Berryman, J., 1980, Applied Physics Letters, 37: 382.
[9] Hansen, T. C., 1986, *Materials and Structures*, 19 no. 114: 423–436.
[10] Voigt, T., 2005, Ph.D.Thesis, University of Leipzig, Germany

Elasticity Modulus Monitoring Through an Ambient Vibration Response Method – Application to Cement Based Pastes

L. Maia, M. Azenha, R. Faria and J. Figueiras

Abstract The E-modulus of cement-based materials is a property that experiences a high rate of change at early ages, and its continuous monitoring since casting is fundamental to identify the phase transition from fluid to solid. This paper presents a study with a recently developed non-destructive method for continuous monitoring the E-modulus of cement-based materials since casting. Based on the evaluation of the first resonant frequency of a composite cantilever containing the material under testing, it is possible to detect the E-modulus growth, and also to identify the changes on its evolution due to modifications on the mix composition. Twenty one compositions are tested, encompassing cementitious pastes with five types of cement and five w/c ratios, as well as three different contents of limestone filler, fly ash, silica fume and metakaolin.

Keywords Ambient vibration response method • Cement-based pastes • Elasticity modulus monitoring

Introduction

Comprehending the E-modulus evolution is crucial to predict stresses during the hydration reaction in cement-based materials [1]. Several test methods can be used for assessing early-age E-modulus of cement-based materials, however to undertake continuous monitoring non-destructive techniques are required [2]. By using acoustic

L. Maia (✉) • R. Faria • J. Figueiras
LABEST – Laboratory for the Concrete Technology and Structural Behaviour,
Faculdade de Engenharia, Universidade do Porto, Rua Dr. Roberto Frias,
4200-465 Porto, Portugal
e-mail: dec05005@fe.up.pt

M. Azenha
ISISE – Institute for Sustainability and Innovation in Structural Engineering,
Universidade do Minho, Escola de Engenharia, Campus de Azurém,
4800-058 Guimarães, Portugal

methods non-destructive tests can be continuously performed, describing the gradual transition during the hydration reaction. Among the acoustic methods, the ultrasonic [3-6] and the resonant frequency [7] are probably the most used ones.

An alternative to the standard resonant frequency methods [7] has been recently conceived by Azenha *et al.* [8] for continuous monitoring the E-modulus evolution of cement-based materials since casting. The method consists in performing continuous modal identification of the first resonant frequency of a composite beam that contains the material under testing, and relating this resonant frequency to the evolving elasticity modulus of the tested material. The modal identification techniques are 'output-only" as they solely rely on ambient-induced vibrations as an external excitation.

Thus, this innovative method, hereinafter referred to by the acronym EMM-ARM (which stands for "Elasticity Modulus Monitoring through Ambient Response Method"), simultaneously produces information on E-modulus since casting (which was not possible with the classical resonant frequency approach) and does not require any human intervention throughout its course. Azenha *et al.* [8] initially developed the technique for the study of concrete, having noticed that the E-moduli obtained with the EMM-ARM fitted rather well the results taken from cyclic compression tests on cylinders. Soon after, a lighter setup devised for testing pastes was also developed [9], and the repeatability of the EMM-ARM was verified for two sets of cement pastes with a water to cement ratio w/c=0.50 (one using CEM I 52.5R and the other CEM IV/A 32.5R). The ability of the method for identifying dissimilar kinetics of E-modulus evolutions was further confirmed when accelerating and retarding admixtures were added to the paste compositions.

As part of a major research study on the hydration reactions of selected binders, here the EMM-ARM is applied to investigate variations on the E-modulus evolution induced by composition changes. Furthermore, this paper contributes to promote the method as an alternative non-destructive technique for continuous monitoring the E-modulus evolution in cement-based materials since casting. Six sets of pastes are experimented, in a total of twenty one mix compositions: cement pastes with different (*i*) types of cement and (*ii*) w/c ratios, with (*iii*) limestone filler, and with cement partially replaced by (*iv*) fly ash, (*v*) silica fume and (*vi*) metakaolin.

The EMM-ARM

The basic concept of the EMM-ARM is as follows: a composite cantilever is built up with an acrylic tube filled with the material to be tested, and then the first resonant frequency of the beam is identified. As the E-modulus of the tested material evolves throughout the experiment, so does the identified frequency. Just a brief outline of the overall test principle is presented herein. First, the paste to be studied is cast inside an acrylic tube, which is used as a mould. Then, both extremities of the tube are closed and the entire system is clamped on a stiff support, enduring the structural behaviour of a horizontal composite cantilever. An accelerometer is
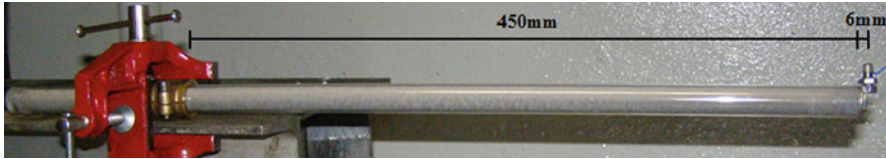
Fig. 1 Cantilever composed beam during testing
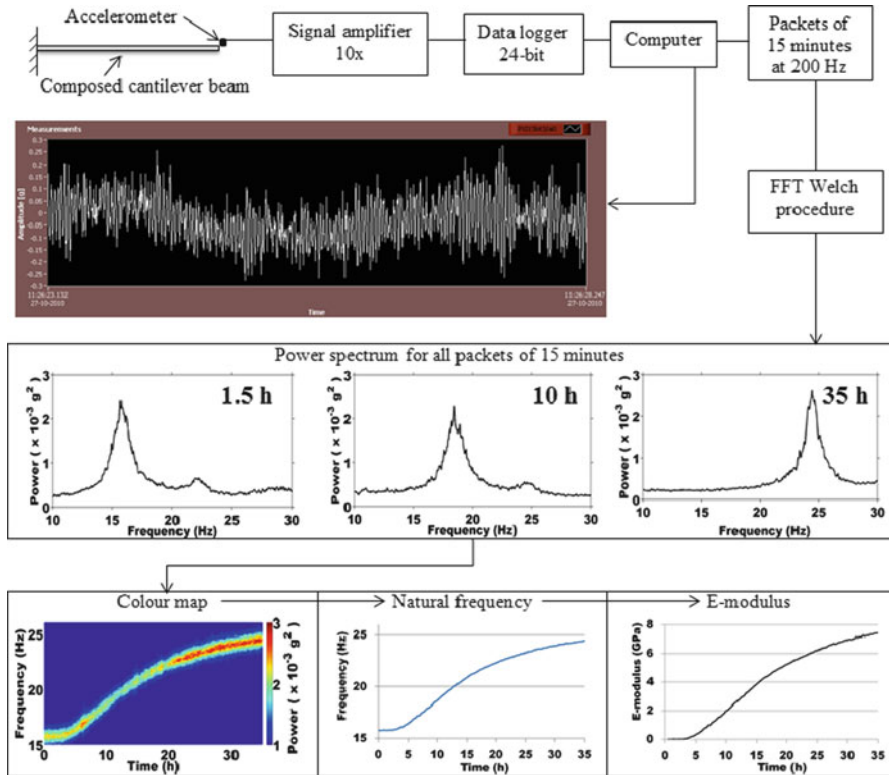
Fig. 2 Schematic set-up and data processing

placed at the free cantilever's extremity, to monitor the accelerations in the vertical direction induced by just ambient excitation (for instance: people talking/walking; machinery; vehicles passing nearby the building; room ventilation). Here, air currents from forced room ventilation were permanently used as ambient excitation. Figure 1 illustrates a sample during a test. The experiment can start as soon as all the parts are correctly placed, which usually occurs within 20 minutes after mixing the cementitious material. Figure 2 schematizes the set-up and the data processing until the plotting of the E-modulus curve. Detailed information about the set-up and the data processing is found in [8, 9].

Table 1 Mix compositions of the used pastes

Mix	Name	c (g)	f (g)	fa (g)	sf (g)	mtk (g)	w (g)
1	CEM I 42.5R	320					144
2	CEM I 52.5R	320					144
3	CEM II/A-L 42.5R	320					144
4	CEM II/B-L 32.5N	320					144
5	CEM II/B-L 32.5R (white)	320					144
6	w/c=0.50	320					160
7	w/c=0.40	320					128
8	w/c=0.35	320					112
9	w/c=0.30	320					96
10	f/c=0.15	320	48				144
11	f/c=0.30	320	96				144
12	f/c=0.45	320	144				144
13	fa/b=0.20	256		64			144
14	fa/b=0.40	192		128			144
15	fa/b=0.60	128		192			144
16	sf/b=0.05	304			16		144
17	sf/b=0.10	288			32		144
18	sf/b=0.15	272			48		144
19	mtk/b=0.05	304				16	144
20	mtk/b=0.10	288				32	144
21	mtk/b=0.15	272				48	144

Experimental Program

All the materials used for the paste mixes in the experimental program were obtained in the Portuguese market: cement (c), limestone filler (f), fly ash (fa), silica fume (sf), metakaolin (mtk) and distilled water (w). All mixes were made with 320 g of binder (b), with all other mix contents weighted according to required ratios, as shown in Table 1. Mix 1 was adopted as a reference. In mixes 6-21 cement CEM I 42.5R was used. The tests were performed in a climatic chamber at 20ºC. The maximum temperature inside samples was lower than 21ºC. Some mixes were tested twice to check repeatability.

Results

The results of the E-modulus evolutions evaluated through the EMM-ARM are reported in Fig. 3. Figure 3a shows the effect of the type of cement: the mixes with CEM I 52.5R exhibited the higher E-modulus, despite some delay at early ages in comparison to the mixes with CEM I 42.5R. In contrast the mix made with white
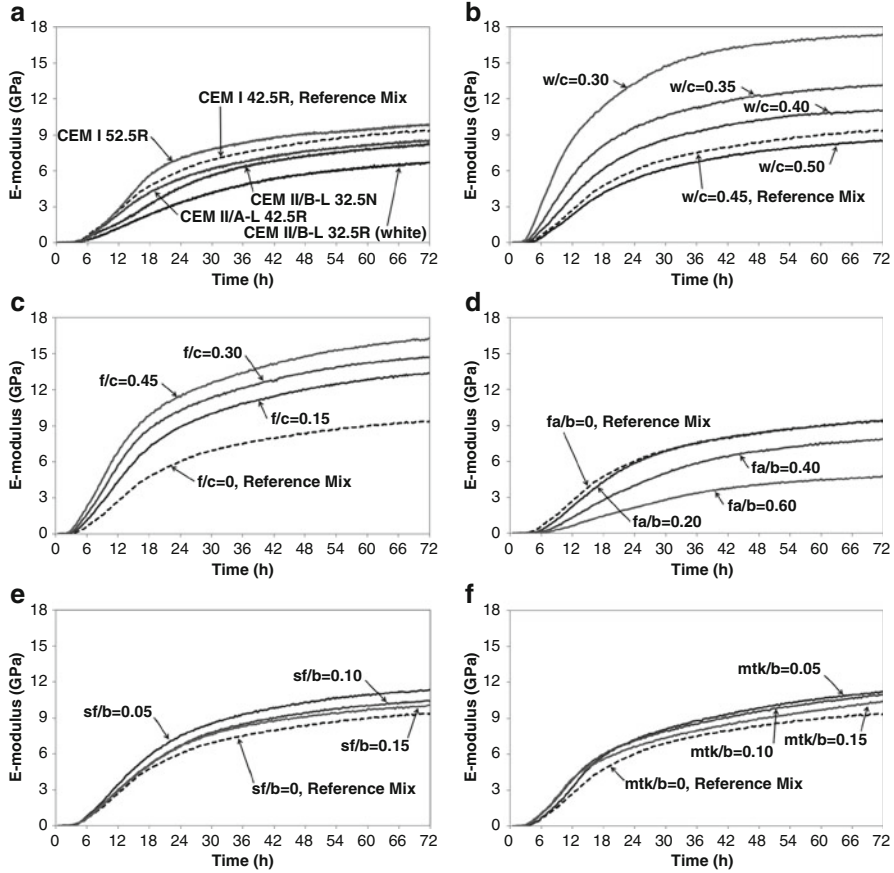
Fig. 3 E-modulus evolutions affected by: **a**) type of cement, **b**) w/c ratio, **c**) addition of limestone filler, **d**) replacement of cement by fly ash, **e**) replacement of cement by silica fume, and **f**) replacement of cement by metakaolin

cement, also with a rapid hydration rate, showed the lowest E-modulus. Figure 3b presents the effect of the w/c ratio: it is observed that the E-modulus starts sooner and is higher for mixes with lower w/c ratios.

A similar effect is reported in Fig. 3c, where the effect of the limestone content is studied. Influence of replacing cement by fly ash is illustrated in Fig. 3d: one can observe that fly ash delays and reduces the E-modulus evolution when high contents are used. The effects of replacing cement by silica fume or by metakaolin are reported in Fig. 3e, f: both additions lead to the increase of the E-modulus. However, it seems that to maximize the E-modulus low replacements are required.

Additionally, the heat generation during hydration was evaluated for all mixes using an isothermal conduction calorimeter (despite results are not presented in this paper).

When accumulated heat generation was compared to the E-modulus evolution measured with EMM-ARM it was consistently observed that the E-modulus development stars later (coherent with expectable tendencies [10]).

Final Remarks

The paper briefly describes the Elasticity Modulus Monitoring through Ambient Response Method, termed as 'EMM-ARM', which is a non-destructive technique that allows determining the evolution of the E-modulus of pastes since casting, by monitoring the change of the first natural frequency of a small composite cantilever formed by an acrylic tube filled with the cementitious material under testing. The EMM-ARM was successfully applied to the identification of the E-modulus evolutions of twenty one cementitious paste compositions. From the results it was possible to conclude that the E-modulus is very sensitive to composition modifications, especially when the water-to-powder ratio is changed.

References

[1] ACI 231R-10 (2010), *Report on Early-Age Cracking: Causes, Measurement, and Mitigation, in: Reported by ACI Committee 231*, ACI.

[2] RILEM TC-185-ATC (2005), in: H.W. Reinhardt, C.U. Grosse (Eds.), *Advanced testing of cement-based materials during setting and hardening - final report of RILEM TC 185-ATC*, RILEM Publications SARL, France.

[3] Reinhardt, H.W. and Grosse, C.U. (2004), *Construction and Building Materials*, vol. 18, n. 3, p. 145.

[4] Voigt, T. and Shah, S.P. (2004), *ACI Materials Journal*, vol. 101, n. 6, p. 473.

[5] Valic, M.I. (2000), *Cement and Concrete Research*, vol. 30, n. 10, p. 1633.

[6] Boumiz, A., Vernet, C. and Tenoudji, F.C. (1996), *Advanced Cement Based Materials*, vol. 3, n. 3-4, p. 94.

[7] ASTM C 215 (2002), *Standard test method for fundamental transverse, longitudinal, and torsional resonant frequencies of concrete specimens, American Society for Testing and Materials*, ASTM, Philadelphia.

[8] Azenha, M., Magalhães, F., Faria, R. and Cunha, A. (2010), *Cement and Concrete Research*, vol. 40, n. 7, p. 1096.

[9] Azenha, M. (2009), *Numerical simulation of the structural behaviour of concrete since its early ages*, PhD Thesis, Faculty of Engineering – University of Porto, Porto.

[10] Dehadrai, M., Sant, G., Bentz, D. and Weiss J. (2009), *Concrete International*, vol. 259, p. 66.

Characterization of Fresh Mortar with Chemical Admixtures Based on Stress Wave Dispersion

D.G. Aggelis and D. Grammenou

Abstract The performance of any concrete structure strongly depends on the quality of the fresh material used. This quality should be evaluated at an age as early as possible, even before concrete is placed in the forms. In the present paper fresh cementitious material is examined by means of ultrasonic through-transmission measurements. The frequency is varied in order to apply different wavelengths, the propagation of which is influenced in a different way by the constituent materials, e.g. air bubbles and sand grains. The wave velocity vs. frequency curves obtained for different mixes show that the existence of sand plays an important role due to interaction with different wave lengths. The effect of chemical admixtures is also examined through the release of air bubbles and the change in viscosity they impose. The possibility to characterize the effectiveness of chemical admixtures by a single measurement of dispersion is discussed.

Introduction

Concrete is the most widely used construction material. Its behaviour is time dependent since it starts as a liquid suspension of cement, sand, aggregates and air bubbles in water, while the hydration reaction transforms it into an elastic solid with load bearing capacity. It is reasonable that the quality of the fresh material, defines the performance of concrete throughout its service life. Early evaluation of the material is desired, even before it is placed in the forms, in order to eliminate

D.G. Aggelis (✉) • D. Grammenou
Department of Materials Science and Engineering, University of Ioannina, Ioannina 45110, Greece
e-mail: daggelis@cc.uoi.gr

the possibilities that the performance will be less than satisfactory. Many different approaches have been proposed for quality control of fresh concrete using stress waves [1-4]. It has been shown that material with lower water to cement ratio exhibits higher velocity and transmission [5-6], while the attenuation is governed mainly by the scattering on sand grains and air bubbles which are also responsible for velocity dependence on frequency (dispersion) [7,8].

Recent studies indicate that wave monitoring reveals the effectiveness of the type and the content of the chemical admixtures like accelerators on the setting behaviour of concrete [9]. The present study occupies with experimental measurements of wave velocity and transmission through cement paste and mortar with chemical admixture. Instead of measuring a single pulse velocity, the experiments were conducted with various pulses in order to measure wave velocities at different frequencies and exploit information on the interaction of different wavelengths with the microstructure of the cementitious material with and without superplasticizer (s/p).

Experimental Process

The experimental setup consists of a waveform generator (Tektronix AFG3102) and two piezoelectric transducers (PAC, Pico), which are placed in a plexi-glass container, as seen in Fig. 1. Between the plexi-glass plates, a U-shaped plastic plate defines the volume to be occupied by the fresh specimen (or the distance between the sensors, in this case 10 mm). The pulse from the wave generator is driven to one of the sensors acting as pulser and the received signal from the second on the opposite plate, is recorded with a sampling rate of 10 MHz.

The electric signal is sinusoidal of 10 cycles with different frequencies from 100 kHz to 1 MHz. Pulse velocity is measured by the time delay between the received signal through mortar and the electric pulse directly fed from the generator to the acquisition board, while transmittance is measured by the maximum voltage of the received waveform.
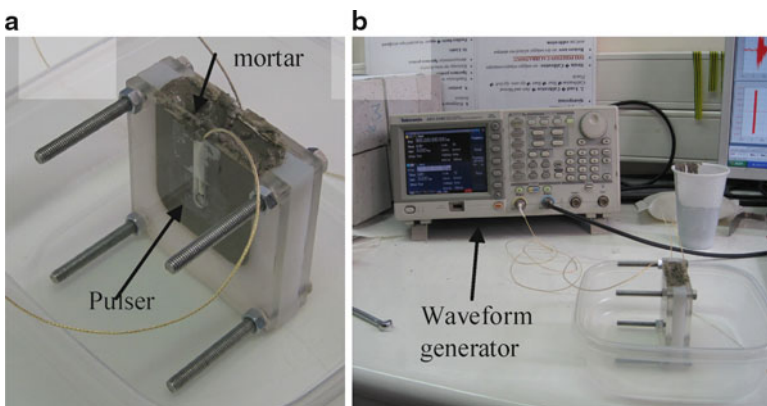
Fig. 1 (**a**) Mortar container, (**b**) Snapshot during measurement

The materials tested, were cement paste and mortar with sand to cement ratio 1 by mass. The water to cement by mass was 0.6, while super-plasticizer was added in a series of specimens in the mass content of 1% in order to examine its influence on the wave parameters. Ultrasonic measurements were conducted approximately 7 min after mixing the ingredients with water, as well as 1 hour later.

Velocity Results

In order to improve reliability 500 waveforms were stacked, typically increasing the signal to noise ratio by 60 times or more. Figure 2 shows cement paste velocity for different frequencies. Concerning plain cement paste, the velocity exhibits an increasing trend with frequency. This is typical for scattering materials, since the size of inhomogeneity exercises differential influence on different wavelengths. Measurements after 1 hr, revealed that the dispersion curve had shifted to higher levels by about 200 m/s, due to possible forming of early hydration products that increase the effective modulus of elasticity, as well as bubble migration and possible segregation. It is interesting to note the influence of superplastisizer, which results in a very smooth curve, eliminating the dispersion trends, as well as increasing the velocity level. The measurements after 1 hr do not reveal any considerable difference. The smoothness of the curve shows that any source of scattering in plain paste, does not exercise similar influence when superplasticizer is present. Therefore, it is reasonable to believe that the release of air bubbles caused by the increased workability offered by the s/p, makes the material homogeneous with a wave behaviour very similar to water, the dispersion curve of which is also shown in Fig. 2. It is also well known that s/p delays the hydration reaction and therefore, even after 1hr the velocity is still at the same levels.
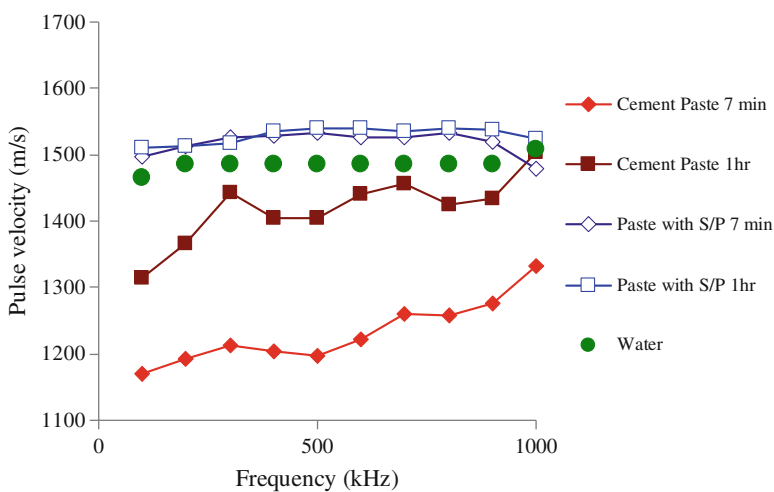
Fig. 2 Velocity vs. frequency curves for different cement pastes
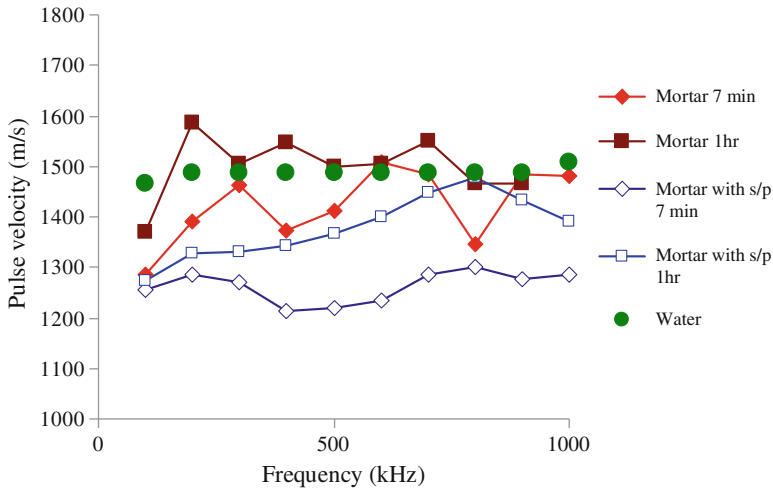
Fig. 3 Velocity vs. frequency curves for different mortar specimens

The positive influence of s/p on the velocity of paste does not apply for mortar according to the present results. Figure 3 shows the dispersion curves for mortar with and without s/p. Plain mortar exhibits higher velocity than paste, with many fluctuations as frequency increases. One hr later the velocity has increased almost for all frequencies due to setting. It is interesting that addition of s/p decreases the velocity curve, in contrary to the cement paste results. Actually the velocity curve becomes smoother but it is shifted to values less than 1300 m/s, while 1 hr later there is a considerable increase especially for higher frequencies. Considering that it is early for hydration products to be formed, this change could be due to segregation of the sand grain and/or migration of remaining air bubbles. It is mentioned that each curve comes from the average of 3 specimens.

Amplitude Results

The addition of s/p shows a greater influence on the amplitude of the transmitted waves. Since the electric excitation is constant (9 V), the amplitude of the received waves can be directly used to compare between different types of materials. Figure 4 shows the amplitude of the signals for different specimens as a function of frequency. The curve obtained for water is indicative of the sensor's frequency response, which has a maximum sensitivity at 500 kHz. The corresponding curve for plain cement paste is approximately 3 orders of magnitude lower, owing to the viscous nature of the material, as well as the presence of air bubbles. However the addition of s/p increases the transmittance to the levels of water, since it decreases the viscosity
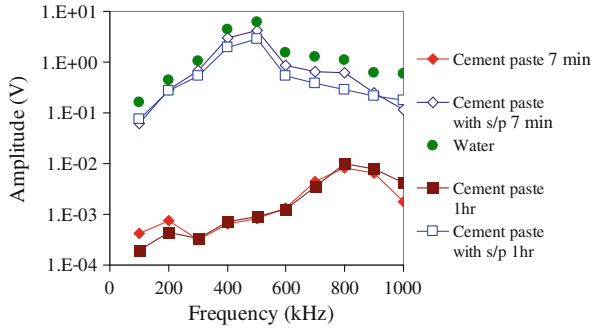
Fig. 4 Amplitude vs. frequency curves for different paste specimens

and releases the air bubbles, rendering the material more homogeneous for all applied wavelengths. It is mentioned that the wavelengths vary from approximately 1.5 mm (for 1 MHz) to 15 mm (100 kHz). One hour later no significant changes in the curves are exhibited.

One interesting qualitative characteristic of the amplitude curve is that the maximum sensitivity of the system changes with the addition of s/p. The peak frequency for plain paste is at 800 kHz, despite the sensitivity of the sensors at 500 kHz. This can be attributed to scattering on air bubbles which exhibit higher scattering attenuation at lower or moderate frequencies [10,11]. When s/p is added, the whole curve is shifted to much higher values, while its maximum is shifted to the sensors preference, due to the homogeneity of the specimen.

Specimens of paste and mortar including the same content of the s/p (1%) exhibit large difference in the transmitted amplitude, as shown in Fig. 5. The amplitude of mortar is approximately ten times lower than paste amplitude. It is concluded that sand grains are crucial in that they increase scattering attenuation directly, as well as restrain a number of air bubbles which also contribute to scattering.

Discussion and Conclusion

The aim of this study is to contribute to the understanding of the wave propagation in fresh cementitious materials. Due to their inhomogeneity, extraction of valuable information depends on the correct interpretation of the experimental results. The above measurements show that the effect of superplasticizer can be measured by ultrasound. S/p renders the material less viscous and more homogeneous due to the release of air bubbles. Therefore, the dispersion curve becomes smoother, and the dependency of velocity on frequency is diminished. The influence on transmittance is even higher, since s/p increases the amplitude by 1000 times for cement paste. The behaviour of mortar is different because the s/p is shown to decrease velocity. This should be further studied in order to be theoretically supported. It is possible,
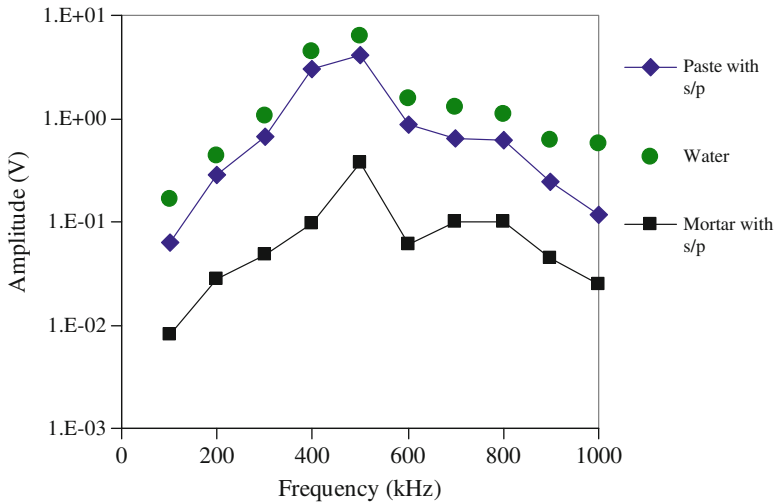
Fig. 5 Amplitude vs. frequency curves for different specimens

that microstructural effects which are present in mortar [12] are eliminated when the material becomes more workable (close to liquid) due to the addition of s/p. In any case studying dispersion and attenuation curves for different frequencies shows potential to characterize the material with one measurement a few minutes after mixing.

A next step for advancing the research is applying different contents of s/p in order to quantify the influence. In addition, different types of chemical admixtures should be studied, like air entrainment agents, accelerators and retarders.

References

[1] Popovics, S. and Popovics, J. S. (1998), *Cement Concrete Aggregates*, vol. 20, no. 2, p. 262.
[2] Valic, M. I. (2000), *Cement and Concrete Research*, vol. 30, p. 1633.
[3] Grosse, C. U. and Reinhardt, H. W. (2001), *Otto Graf Journal*, vol. 12, p. 157.
[4] Chotard, T., Gimet-Breart, N., Smith, A., Fargeot, D., Bonnet, J. P. and Gault, C. (2001), *Cement and Concrete Research*, vol. 31, p. 405.
[5] Reinhardt, H. V., Grosse, C. U. and Herb, A. T. (2000), *Materials and Structures*, vol. 33, p. 580.
[6] Arnaud, L. and Thinet, S., (2003), *Materials and Structures*, vol. 36, p. 355.
[7] Sayers, C. M. and Dahlin, A., (1993), *Advanced Cement Based Material*, vol. 1, p. 12–21.
[8] Aggelis, D. G., Philippidis, T. P. (2004), *NDT&E INT*, vol. 37, p. 617.
[9] De Belie, N., Grosse C. U., Kurz J. and Reinhardt H. W. (2005), *Cement and Concrete Research*, vol. 35, p. 2087.
[10] Temkin, S. (2000), *Journal of the Acoustical Society of America*, vol. 108, no. 1, p. 126.
[11] Aggelis, D. G., Polyzos D., Philippidis, T. P. (2005), *Journal of the Mechanics and Physics of Solids*, vol. 53, p. 857.
[12] Vavva, M. G., Protopappas, V. C., Gergidis, L. N., Charalambopoulos, A., Fotiadis, D. I., Polyzos, D., (2009), *Journal of the Acoustical Society of America*, vol. 125, no. 5, p. 3414.

Analysis of Thermal Properties of Cement Paste During Setting and Hardening

D. Mikulić, B. Milovanović and I. Gabrijel

Abstract   An experimental investigation is made in order to study changes of thermal properties of hardening cement paste. Using a hot disc principle for determination of thermal properties, specific heat capacity, effusivity and thermal conductivity are analyzed during first 4 days of hydration. Specific heat capacity value changed only slightly during hydration. Thermal conductivity decreased with the progress of hydration 20% compared to initial value. Hydration process was monitored using ultrasonic pulse velocity (UPV) test. A discussion of results is made taking into account porous nature of cement paste and transformation of liquid and hardened phases i.e. water and clinker minerals, into hardened structure.The motivation for conducted research is improvement of numerical models for calculating temperature changes in mass concrete structures using hydration dependant thermal properties. Also, another field of application could be the quality control of cement based materials.

Keywords   Cement paste • Hardening • Hydration • Porous structure • Thermal properties

Introduction

Cement hydration can be defined as a sequence of chemical reactions initiated with the contact of cement and water. Progress of hydration process reflects itself at the macro level of observation as a change of cement based material properties. Different methods of testing, like measuring of the rheological properties, strength development or heat liberation can then serve as a tool for monitoring of the hydration process.

D. Mikulić • B. Milovanović (✉) • I. Gabrijel
Faculty of Civil Engineering, Department of Materials, University of Zagreb,
Zagreb, Croatia
e-mail: bmilovanovic@grad.hr

Rate of chemical reactions significantly changes during hydration and can be divided into five stages: pre-induction, induction, acceleration, deceleration and diffusion [1, 2]. During the first few days of hydration the greatest portion of chemical reactions is finished. During that period changes of cement based material properties are also the greatest. In the early stage, hydration process is highly exothermal and generated heat may result in large temperature changes. Depending on the degree of external constraints, high tensile stresses may develop in relation to the actual tensile strength and harmful cracking is likely to appear. Temperature and stress analysis due to the hydration of concrete is highly non-linear problem because a vide variety of time-dependent boundary conditions and strongly time and temperature dependent thermal and mechanical properties of early-age concrete. In order to improve our understanding how cement based materials behave in early period of hydration it is necessary to gain more knowledge in how thermal and mechanical properties are connected to its governing process, i.e. the hydration of cement. Thermal conductivity variation during an early period of hydration is an input parameter for simulation of temperature and stress variations and evaluation of potential risk of cracking in young hardening concrete. For that reason in this paper an experimental investigation is made in order to study changes of thermal properties of cement paste during hydration. Thermal conductivity variation could also be a potential tool for monitoring of hydration process in concrete, which is a tool for estimating mechanical properties. The goal of this paper is to answer: How can changes of thermal properties of cement paste be monitored during hydration? How thermal properties are changing and how are they connected to the changes in the microstructure of cement paste?

Testing Methods Used

System for measuring thermal properties

In order to study changes of thermal properties during hydration it was necessary to use testing technique which will allow us to measure thermal properties in the small time intervals. For that purpose hot disk principle method was applied and the system used was Mathis TCi thermal conductivity analyzer (Fig. 1). Mathis TCi system is comprised of a sensor, control electronics and computer software, where the sensor employs a one-sided, interfacial heat reflectance device that applies a constant current heat source to the sample. The interfacial sensor heats the sample by approximately 1-3°C during testing, the sample absorbs some of the heat, and the rest causes a temperature rise at sensor interface. Voltage drop on spiral heater is measured. Voltage data is then translated into the effusivity value of tested material. Conductivity is then calculated from the voltage data by iterative method and specific heat capacity can be calculated if density of material is known. During testing, the sensor does not physically alter or affect the sample being tested, reducing possible contamination as much as possible. Complete testing requires only 0.8 to 5 seconds what is only a fraction of the duration needed by some traditional methods [3, 4].

Fig. 1 Mathis TCi Thermal Property Analyzer

Sensor needs to come in contact with only one side of the sample, and has the capability of "seeing through" layers into the actual sample. For example, liquid samples can be tested in plastic bags, without the thermal value of the bag skewing the results. A sample of cement paste after mixing is placed in a low density polyethylene sheet 0.025 mm thick in order to preserve sensor from coming into direct contact with fresh cement paste. Placing of the specimen in the sheet allowed a continuous measurement of thermal properties.

Description of the ultrasonic setup

Beside the thermal properties measurements hydration process was monitored using ultrasonic pulse velocity (UPV) test. An experimental setup was made so that changes of the ultrasonic pulse velocity through cement paste sample can be continuously measured during the first few days of hydration. Measuring system (Fig. 1) consists of a pulse generator which has a pulse repetition frequency of 1 pulse every 4 seconds. The pulse is converted to an ultrasonic wave through 54 kHz piezoelectric sensor. The wave is then transmitted through the material and picked up by a receiver, which is also 54 kHz piezoelectric sensor. Pulse generator is connected to a PC so that information about the speed of the ultrasonic wave is recorded. Sample of cement paste is placed in the mould after mixing and measurement is started. Results of time of flight are recorded to the computer every one minute and UPV is then calculated.

Materials and preparation of cement paste

Cement paste used is made with CEM I type cement according to European standards. Investigation is conducted on cement paste with 0.3 w/c mass ratio. The paste was mixed according to a procedure given by the standard HRN EN 196-3. Properties of cement are shown in Table 1.
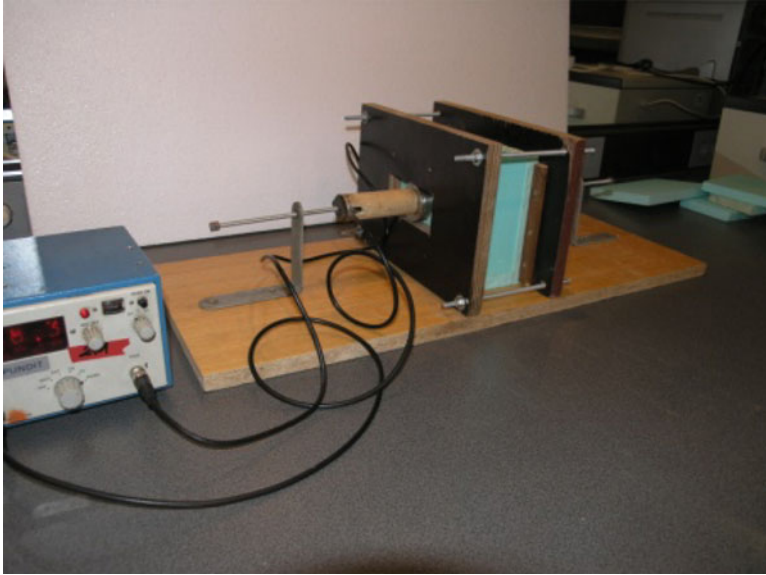
Fig. 2 Ultrasonic setup

Table 1 Properties of cement CEM I 42,5 R

Blaine (m²/kg)	Mineral composition (%)				Setting time (h) w/c ratio = 0.3	
	C_3S	C_2S	C_3A	C_4AF	Initial set	Final set
353	59.86	11.94	8.36	8.82	2.33	3.00

Analysis of Results

Development of UPV

Ultrasonic pulse velocity development can be used to describe the micro structural changes in the cement paste caused by hydration process [5, 6]. Development of the UPV can be divided into several consecutive stages. In the first stage, ultrasonic pulses transmitted through a fresh cement paste are not recorded by a measuring system, probably because of a large attenuation of the paste. After approximately 1.5 hours ultrasonic pulses are being recorded (Fig. 3). Initial UPV is at approximately 500 m/s. The reason for this low initial velocity is a large amount of very small air bubbles entrapped in the cement paste during mixing [4]. UPV has a constant increase up to about 1500 m/s which is attributed to the growth of ettringite crystals which fill out the capillary space and in that way reduce the distances
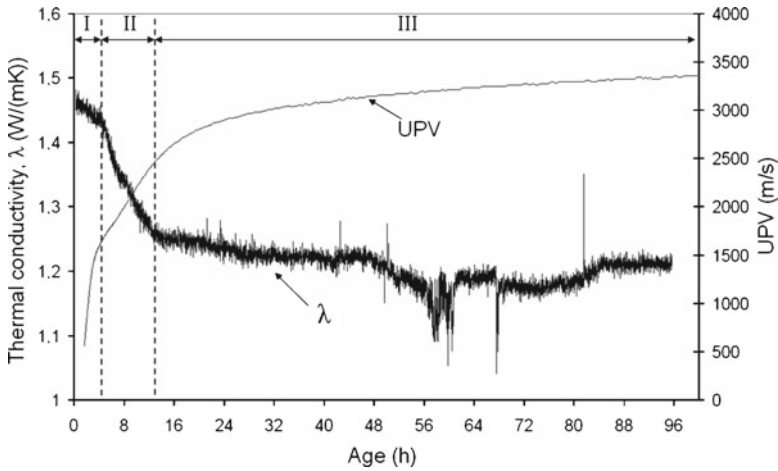
Fig. 3 Changes of the thermal conductivity and UPV of cement paste

between the cement particles. Another reason for the increase of the UPV is attributed to gravity effects and settling of cement particles which lead to improving the contact between them. It was presented by several authors [7, 8] that at the speed of ultrasonic wave of 1500 m/s cement paste, with w/c ratios varying from 0.3 to 0.6, transforms from liquid to a solid state, i.e. setting process is finished and a hardening process starts. The setting process of cement paste is caused by the increase in the connectivity of the cement particles. With the progress of hydration, connectivity increases and this causes increase of the UPV. At the same time water from capillary pores is consumed in the chemical reactions with cement and capillary spaces become partially filled with hydration products.

Development of thermal conductivity

In Fig. 3, changes of the thermal conductivity of the cement paste with a w/c ratio 0.3 are shown. Development of thermal conductivity is divided into three stages: first stage starts from the time zero (time of mixing), second stage starts approximately 4 hours after mixing and the third stage starts at the age of cement paste of 12 hours. By comparing the thermal conductivity and UPV development changes of the thermal conductivity can be connected to the micro structural changes in cement paste. In the first period, thermal conductivity decreases slightly and has a value between 1.4-1.5 W/mK. During that period mostly ettringite needles are formed in the paste. Greater decrease in thermal conductivity starts approximately at the age where UPV reaches a value of 1500 m/s so it can be attributed to the acceleration period of hydration and formation of C-S-H and CH. The value of thermal conductivity then drops to 1.2 W/mK. This can be caused by consumption of water from
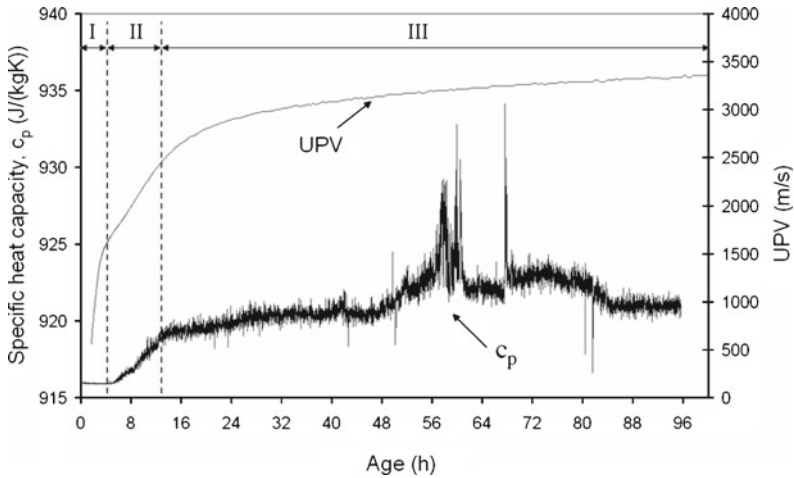
Fig. 4 Changes of the specific heat capacity and UPV of cement paste

the capillary space. Capillary spaces in the paste which are not filled with hydration products are filled with air which has a lower thermal conductivity than water. At the age of 12 hours the third stage starts. Decrease of thermal conductivity continues but the slope is very small (Fig. 3). After the age of 24 hours there are practically no changes in thermal conductivity of the cement paste.

Development of specific heat capacity

In the Fig. 4, changes of the specific heat capacity of the cement paste are shown. Changes can also be divided into three stages. In the first stage its value remains constant. In the second period heat capacity increases slightly. And in the third stage its value shows a constant slow increase. Heat capacity of the cement paste changed during hydration within the limits from 916 to 920 J/kgK. Higher values recorded during measurement in the period between 48 and 80 hours of hydration (Fig. 4) are caused by the changes in the thermal bonding between the specimen and the sensor which is changed because sensor is connected to the cement paste sample through a thin layer of low density polyethylene sheet. During measurement, the entire system is surrounded by air and if air penetrates in either of the contact surfaces it will alter (reduce) the heat flow between the sample and the sensor. Reduced heat flow will result in reduced thermal conductivity (Fig. 3) and higher specific heat capacity (Fig. 4). Penetration of air is present at every measurement but the amount of air penetrated or, in other words, surface area contaminated by the penetration of air will determine its influence on the results.

Conclusions

Presented research showed how thermal properties can be monitored continuously during hydration of cement paste by the hot disc method. Specific heat capacity value changed only slightly during hydration while thermal conductivity decreased with the progress of hydration 20% compared to initial value. Decrease of the thermal conductivity of cement paste can be attributed to the loss of water from the pore space which slows down the heat transfer within the material. Applied hot disc technique could serve in the future not only for measuring thermal properties but also as a method for monitoring hydration of cement paste. Improvement of the hot plate method can be done through enhancing the contact between sensor and the specimen to ensure stable readings through all of the hydration process.

References

[1] Taylor, H.F.W. (1990) *Cement chemistry*, Academic Press, London.
[2] Van Breugel, K. (1990) *Simulation of hydration and formation of structure in hardening cement-based materials*, Delft University Press, Delft.
[3] Ramachandran, V.S.; Paroli, R.M.; Beaudoin, J.J. and Delgado, A.A. (2002) *Handbook of thermal analysis of construction materials*, William Andrew publishing, New York.
[4] Bentz, D.P. (2007) *Transient plane source measurements of the thermal properties of hydrating cement pastes*, Materials and Structures vol. 40, pp. 1073–1080.
[5] Ye, G.; van Breugel, K. and Fraaij, A.L.A. (2003) *Experimental study and numerical simulation on the formation of microstructure in cementitious materials at early age*, Cement and Concrete Research, vol. 33 pp. 233–239.
[6] Voigt, T. and Shah, S.P. (2004). *Properties of early age Portland cement mortar monitored with shear wave reflection method*, ACI Materials Journal, vol. 101, n. 6, pp. 473–482.
[7] Trtnik, G.; Turk, G.; Kavčič, F. and Bokan Bosiljkov V. (2008) *Possibilities of using the ultrasonic wave transmission method to estimate initial setting time of cement paste*, Cement and Concrete Research vol. 38, pp. 1336–1342.
[8] Gabrijel, I. (2010) *Application of elastic waves for the determination of setting and hardening in cement composites*, Doctoral thesis, University of Zagreb, Zagreb.

Application of Ultrasonic Method for Determining Set Times of VMA Modified Cementitious Composites

S.-T. Lin and R. Huang

Abstract Viscosity modifying agent (VMA) is added to mortar to increase water retention so that more rendering plaster and tile can be installed. But, VMA would increase viscosity of pore solution to slow down water movement, and thus a dry shell may form due to evaporation. Consequently, Vicat needle test seems improper to determine set times of VMA modified mortars. The ultrasonic pulse velocities (UPV) of early-age VMA modified paste (VMA paste) are compared with Vicat test results in this paper. UPV were found to be clearly depicting the dosage effect of VMA on cement retardation, whilst Vicat test could not. Without adding VMA, initial set of Vicat test was found to be near the timing of UPV at 1420 m/s and final set was found no clear relationship with UPV values. However, with the addition of VMA, more investigations by UPV are needed before new criteria on determining both initial and final set times can be proposed.

Keywords Hydration • Isothermal calorimeter • Non-destructive test • Penetration test • Set time

Introduction

Cellulosic viscosity modifying agent (VMA), such as HPMC and MHEC have been used in the mortar industry as the water-retention agents to increase working time [1]. Yet, VMA would increase viscosity of pore solution, so the speed of water

S.-T. Lin
Tatung University, Taiwan,

Phoenix Material Technology Co., Ltd., Taiwan,

R. Huang (✉)
National Taiwan Ocean University, Keelung, Taiwan
e-mail: ranhuang@mail.ntou.edu.tw

loss to evaporation becomes greater than what inner water can supply. Thus, a dry shell may form to encapsulate wet mortar. The conventional method of determining set times of cement is Vicat needle test which defines initial set as the cement paste (paste) begins to stiffen considerably and to lose workability; final set as the paste can bear some load such as walking. The obtained times of setting are indicators for concrete works such as saw-cutting concrete pavement. However, Vicat test is sensitive to the surface drying condition, aggregate content, water-cement ratio, and types of admixture being used. Thus, it might mislead results. Therefore, ultrasonic pulse velocity (UPV), and other methods have been studied and proposed [2]. Evaporation and cement hydration changes the volume of pore solution and the pores, so as the connectivity of the cementitious hydrants [3]. The progress of connectivity of hydrants can be detected by UPV because the wave travels faster in solid medium than in liquid medium. Therefore, as cement hydrates, the strength develops so as to UPV. As a result, set times may be determined by the given UPV values [2]. This study aimed at comparing the effect of UPV method and Vicat test on the determination of set times for paste and investigating the suitable methods for the VMA pastes.

Experimental Program

Materials

Five powder type of MHEC with various molecular weights were selected as VMA. VMA powders can dissolves in water and to form viscous solution as listed in Table 1. Mixture proportions are summarized in Table 2. VMA solutions were prepared first, and then cement and VMA solutions were mixed until creamy composites were obtained.

Test method, procedure and equipment

VMA powders were mixed with water at designated ratio and their viscosities were measured using a Brookfield RVF Viscosimeter as listed in Table 2. Vicat tests were conducted following ASTM C191 Table 3. UPV tests were performed by placing fresh pastes in molds with transmitting and receiving transducers facing directly with a distance of 40 mm. The traveling time of ultrasonic wave pulse were recorded. The ultrasonic wave velocity as described in Eqn. (1).

$$V = L / T \qquad (1)$$

where V is velocity, L is distance between two transducers, T is transmitting time.

Table 1 Details of MHEC Type of VMA

Designation	Molecular weight (g/mol)	*Viscosity (cps, 20˚C, 2 wt. % solution)
4K	1 X 10^6	4000
15K	5 X 10^6	15000
30K	6 X 10^6	30000
50K	7 X 10^6	50000
100K	9 X 10^6	1000000

Table 2 Mixture proportion and viscosity of pore solution

Mixture designation	Cement	Water	VMA dosage (wt% to cement)	Viscosity of pore solution (cps, 20˚C)
Reference	100	50	0	1
4K-a	100	50	1	3100
15K-a	100	50	1	9000
30K-a	100	0	1	21000
50K-a	100	50	1	70000
100K-a	100	50	1	130000
100K-b	100	50	0.75	40000
100K-c	100	50	0.5	13000
100K-d	100	50	0.25	1000

Table 3 Summary of Vicat set times and their corresponding UPV

Mixture designation	Vicat initial set (min)	Time of UPV at 1420 m/s (U) (min)	Vicat final set (min)	UPV at Vicat final set (m/s)
Reference	433	481	508	1474
4K-a	651	1106	734	509
15K-a	768	950	821	1120
30K-a	688	1000	756	788
50K-a	652	919	737	914
100K-a	654	1105	692	402
100K-b	703	920	780	1043
100K-c	754	825	806	1361
100K-d	639	709	736	1491

Results and Discussions

Effect of solution viscosity on UPV

UPV is affected by the density and compressibility of the medium which the wave travels. UPV of tap water is 1420 m/s [4], while UPV of 1% VMA solutions were in the range of 1480-1520 m/s, regardless great differences in viscosity resulting
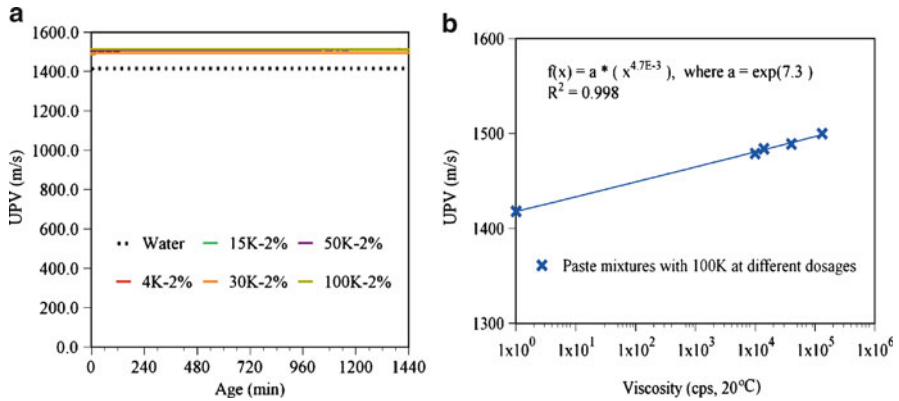
Fig. 1 (**a**) The evolution of UPV of VMA solutions with 1wt.% VMA with different molecular weight, (**b**) UPV of 100K solutions at age of 1440 min

from VMA molecular weight as exhibited in Fig. 1a. Yet, UPV of 100K-a, -b, -c, and -d solutions increased as dosages increased as shown in Fig. 1b.

Influence of VMA on the evolution of UPV of pastes

The evolution curve of UPV might be categorized into three stages: initial, acceleration, and plateau according to slope as shown in Fig. 2 [3]. UPV of paste began at the level below 400 m/s because sound traveled in the liquid where cement particles were suspended. The acceleration stage indicated that UPV increased as paste transformed from liquid phase to solid phase. When paste had become solid, UPV gradually stabilized and to form the plateau stage. The change from the initial stage to acceleration stage was at about 80 minutes for the reference paste, then, followed by an acceleration stage at the age of 1300 minutes until reaching 2500 m/s. The criteria of the initial set for the reference cement paste can be assumed when UPV is 1420 m/s. However, with VMA, the initial stage has extended to 420-540 minutes as displayed in Fig. 2a, b. This indicated that VMA retarded the setting. Moreover, by adding VMA (100K) the UPV shifted rightward as the dosage increased as shown in Fig. 2b. Nevertheless, by adding 1 wt. % of different molecular weight VMA, the UPV curves of mixtures had little fluctuation as exhibited in Fig. 2c. As a result, it might be concluded that UPV method would clearly depict the dosage effect of VMA on the setting, while Vicat test could not. To sum up, UPV showed an advantage over Vicat test on describing the dosage effect of VMA on paste setting. Concerning the correlation between UPV method and Vicat test, more investigations are needed before the new criteria can be proposed.
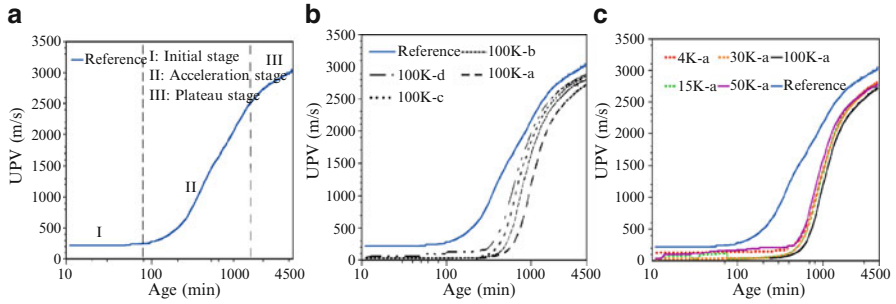
Fig. 2 (**a**) The UPV evolution of reference cement paste; 6 (**b**) Dosage effect on the evolution of UPV; 6 (**c**) Molecular weight effect on the evolution of UPV

Conclusions

Suitability of using Vicat test and UPV method on the determination of set times for the VMA paste was investigated. Following conclusions can be drawn:

1. UPV method could clearly depict the dosage effect of VMA on retarding cement setting, whilst Vicat test could not.
2. For the reference cement paste, the criteria of initial set can be assumed when UPV is 1420 m/s.

References

[1] Bayer, R., Lutz, H. (2003), *Ullmann's Encyclopedia Industry Chemical*, v. 9, p.1-26, Wiley-VCH, Germany.
[2] Lee, H. K., Lee, K. M., Kim, Y. H., Yim, H., Bae, D. B. (2004), *Cem. Concrete Res*, v. 34, n. 4, pp. 631–640.
[3] Trtnik, G., Turk, G., Kavcic, F., Bosiljkov, V.B. (2008), *Cem. Concrete Res*, v. 38, n. 11, pp. 1336–1342.
[4] http://en.wikipedia.org/wiki/Speed_of_sound

The Use of Wireless Sensor Networks to Monitor the Setting and Hardening Processes of Self-Compacting Concrete

S. Aparicio, J.V. Fuente, J. Ranz, J. Aliques, M.A.G. Izquierdo
and R. Fernández

Abstract Traditionally, the study of cementitious materials has been performed using wired sensor technologies. Because these technologies are expensive and difficult to install, the use of wireless sensor networks has gained increasing importance. In this paper, the study of setting and hardening processes for two different types of self-compacting concrete (SCC) using a wireless monitoring system is reported. The monitoring system used to perform such study consists of a wireless sensor network using Cricket motes. These motes were purchased from Crossbow Technologies. For our research, the most important capability of Cricket motes is that they host a transmitter/receiver in the ultrasonic wavelength region. For monitoring the setting and hardening processes, the velocity of the ultrasonic pulse traveling across the material was measured, along with the humidity and temperature values both inside and outside the concrete sample. Multi-hop data transmission techniques were considered to monitor the velocity data.

Several experiments were performed at the laboratory. A set of samples were manufactured with two types of SCC, in one type some portland cement was replaced by limestone filler. These specimens were exposed to different curing conditions. Although it was found that the ultrasonic acquisition was not very robust, the wireless sensor networks are an efficient technology for monitoring the early stages of self-compacting concrete.

Keywords Self-compacting concrete • Setting and hardening processes • Ultrasounds • Wireless monitoring

S. Aparicio (✉) • J. Ranz
CAEND (CSIC-UPM), Arganda del Rey, SPAIN
e-mail: sofia.aparicio@caend.upm-csic.es

J.V. Fuente • J. Aliques • R. Fernández
AIDICO, Valencia, SPAIN

M.A.G. Izquierdo
ETSIT (UPM), Madrid, SPAIN

Introduction

In the 90's, research and development of wireless sensor networks (WSN) technology with embedded sensors to monitor structures were initiated (Structural Health Monitoring, SHM). Numerous publications were dedicated to study WSN for evaluation of the structural integrity [1-2]. Promising results on the sensorization of different structures were obtained but more work is required to improve its reliability for use in the structure evaluation. An exhaustive analysis in the literature about WSN for use in the monitoring of structures can be found in [3]. In the literature many works have studied the use of the ultrasonic velocity in the monitoring of setting and hardening processes and its relationship with the temperature and the humidity measurements [4-7].

In this paper, the study of setting and hardening processes for different types of SCC using a wireless monitoring system is reported. The advantage of using low cost commercial platforms to monitor these processes is that the most interesting part occurs during the first 72 hours. Therefore the energetic needs are limited. The parameters selected are the temperature and humidity inside and outside the cementitious material, and the ultrasonic velocity through the material.

The Wireless Sensor System

The system developed by the authors is based on commercial devices which have been adapted to study the setting and hardening processes of cementitious materials. A previous version of the system was presented in [8]. The hardware platform is composed of a WSN using Cricket motes. These motes were purchased from Crossbow Technologies [9]. This platform was selected mainly because it is an open source wireless sensor platform with open access hardware and software designs. Ultrasonic velocity and temperature and humidity measurements were calculated with these motes. The mote size is 3x4x10cm.

Fig. 1 Cricket mote

Experimental

In this section the setup used in the laboratory experiments and the obtained results are presented.

Laboratory setup

The system described above was tested at the AIDICO laboratory. For that purpose, several test specimens of 0.15x0.15x0.15m size were constructed using two different dosages of SCC, reported in Table 1.

The experiment was based on a WSN composed of several Cricket motes, for measuring the ultrasonic velocity, and the temperature and humidity profiles inside and outside the specimens during the first 100 hours, approximately. One mote was configured as a base station and the remaining motes were sensorized. The temperature and humidity inside the material was monitored by sensors placed in the centre of the fresh specimens. To measure the ultrasonic pulse velocity through the material each mote was configured at the same time as transmitter and receiver of the ultrasonic pulse. The transmitter and receiver transducers were placed in opposite sides of the specimen.

Four different curing conditions (CC) were considered in this experiment. CC1 was a climatic chamber with constant conditions of 20ºC temperature and 98% relative humidity (RH). CC2 was a laboratory room with controlled temperature and RH between 20-22ºC and 50%, respectively. CC3 refers to a curing kiln with cycles of 24 hours each where the minimum temperature is approx. 22ºC and the maximum temperature of 40ºC is kept constant during 6 hours simulating the weather conditions of summer in Madrid. CC4 was performed under the same conditions as CC3 but the specimens were covered with a transparent film.

Laboratory results

In Fig. 2 the temperatures monitored for different curing conditions are shown. The mixture SCC-A reached the maximum temperature setting value in all curing

Table 1 Mix proportions of SCC used in the experiments	Kg/m³	
Material	SCC-A	SCC-B
White sand 0/4	879.9	876.1
Gravel 6/12	898.8	895.0
Cement BL I 52.5 R	387.9	231.7
Limestone filler	0.0	154.5
Superplasticizer Viscocrete 5920	4.6	3.2
Water/binder)$_{total}$ ratio	0.53	0.53
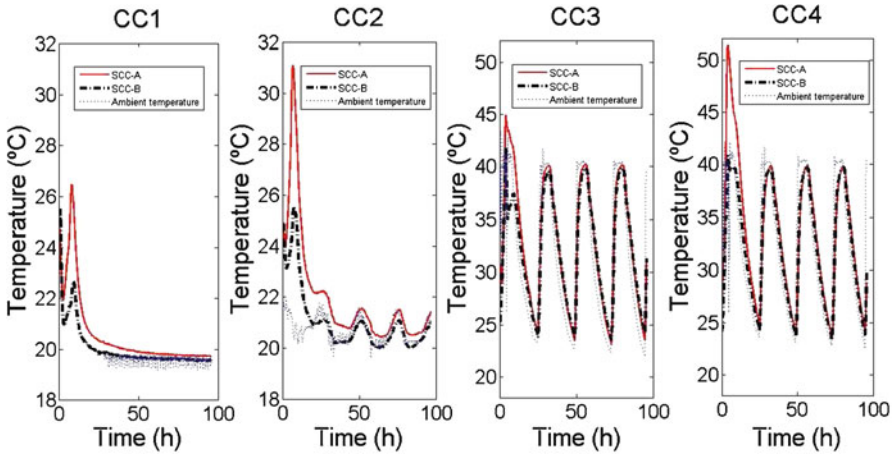
Fig. 2 Temperature results obtained for different curing conditions

conditions studied. Although, in the CC3 and CC4 curing conditions this value is reached earlier due to the high temperatures of curing. The curing at 40ºC cycles accelerates the hydration reactions of cement. The maximum temperature value measured during CC1 and CC2 conditions appears about 8 hours after making the test specimens, but during CC3 and CC4 conditions this value is measured about 4 hours after the making. As expected, the highest setting temperature value corresponds to the specimens covered by transparent film, curing conditions CC4. The ambient temperature and RH under CC1 conditions were not measured during the first 24 hours due to a problem with the sensor but they can be considered constants.

The RH results are presented in Fig. 3. Comparing the humidity values during conditions CC1 and CC2, it can be seen that the maximum temperature value is reached in CC2 because ambient humidity is lower than in CC1. In the condition CC3 it is observed that the SCC-A has less RH than the SCC-B, which may indicate that probably the different composition of these samples is responsible for a different reaction to the same ambient conditions of high temperature and absence of a cover film. Ongoing research is dedicated to study this phenomenon.

The ultrasonic velocity measurements through the material during conditions CC1, CC2 and CC3 are presented in Fig. 4. It can be seen that the velocity profiles are higher in mixture SCC-A than in mixture SCC-B.

In CC1 conditions, the ultrasonic velocity in the test specimens was measured through the mould. In the case of the SCC-A mixture an oscilloscope was used. The oscilloscope was far away from the mixture. To measure the velocity for SCC-B the mote was placed on top of the chamber and therefore the velocity measurements present electromagnetic interference. It can also be seen that after some time, the velocity values decreased due to the material retraction. In CC2 conditions, the ultrasonic velocity in the test specimens was also measured through the mould.
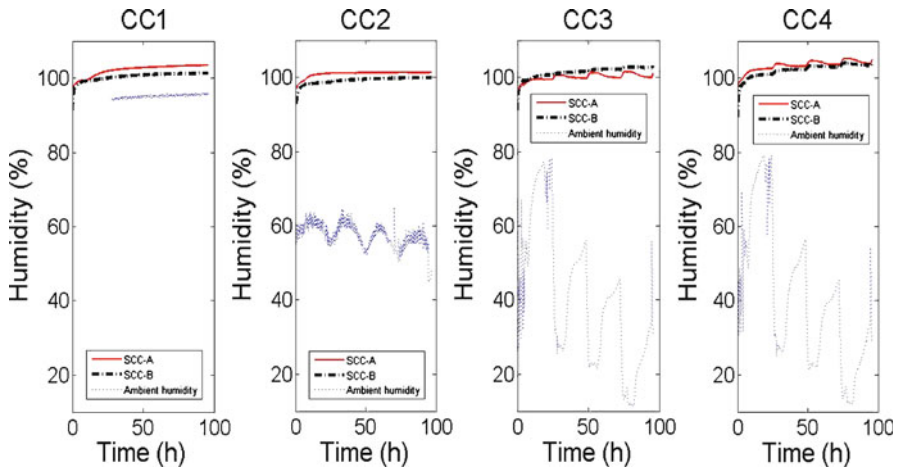
Fig. 3 Humidity results obtained for different curing conditions
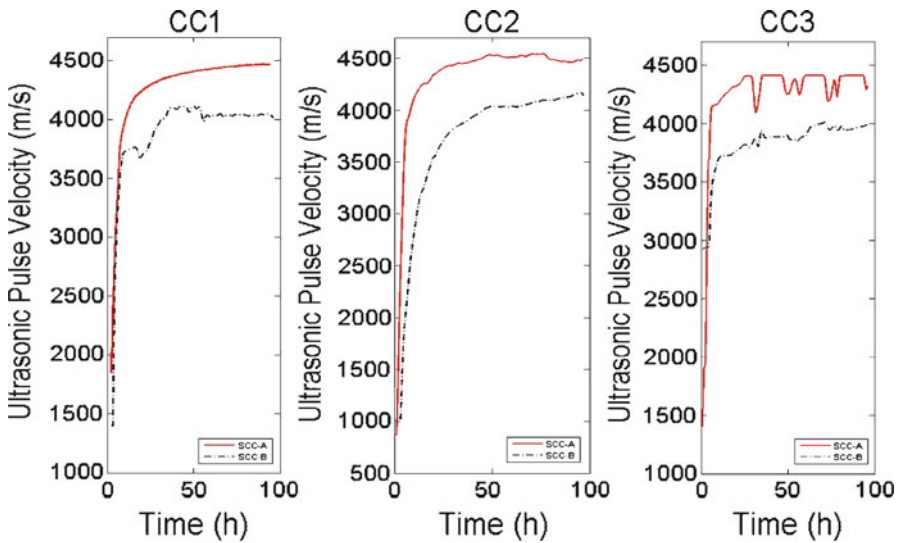
Fig. 4 Ultrasonic pulse velocity obtained for different curing conditions

In CC3 conditions, the moulds of the test specimens were removed. The motes were placed inside the curing kiln and therefore the velocity measurements also present electromagnetic interference.

The velocity data was treated using a median filter to remove spurious data due to the electromagnetic interferences and a low-pass filter to smooth the measurements. This data is presented in Fig. 4.

Conclusions

The objective of this work was to study the setting and hardening processes for two different mixtures of SCC under different curing conditions using a wireless monitoring system composed of commercial devices called Cricket motes. The WSN was in charge of the ultrasonic velocity and the temperature and humidity measurements inside and outside the material.

The system presented above was tested at the AIDICO laboratory. Several specimens were constructed using two different mixtures of SCC composed of CEM I Portland cement, in one type some portland cement was replaced by limestone filler. These specimens were exposed to different CC. Although it was found that the ultrasonic acquisition was not very robust, the WSNs are an efficient technology for monitoring the early stages of SCC. In the future, the authors will develop new prototypes to improve the ultrasonic acquisition.

References

[1] Santana-Sosa, H., Zao-Bello, S., Pérez-Álvarez, I., Raos, I., Mendieta-Otero, E. and López-Pérez, J. (2006), *European Transactions on Telecommunications (ETT)*. Vol 17, No. 6, pp. 651–657.
[2] Grosse, C.U. and Krüger, M. (2006), *NDT.net*, vol. 11, No. 1.
[3] Lynch, J.P. and Loh, K.J. (2006), The Shock and Vibration Digest, Vol. 38, No. 2, pp. 91–126.
[4] Voight, T. and Shan S.P. (2003), In: *Nondestructive Monitoring of Setting and Hardening of Portland Cement Mortar with Sonic Methods*, Proceedings of the Sixth International Symposioum on Non-Destructive Testing in Civil Engineering, Berlin, Germany.
[5] Robeyst, N., Gruyaert, E., Grosse, C.U. and De Belie, N. (2008), *Cement and Concrete Research*, 38(10), pp. 1169–1176.
[6] Öztürk, T., Kroggel, O., Grübl, P. and Popovics, J.S. (2006), *NDT & E International*, Vol. 39, no. 4, pp. 258–263.
[7] Del Río, L.M., Jiménez, A., López, F. Rosa, F.J., Rufo, M.M. and Paniagua, J.M. (2004), *Ultrasonics*, Vol. 42, no. 1–9, pp. 527–530.
[8] Aparicio, S., Molero, M., Segura, I., Anaya, J.J., Izquierdo, M.A.G., Fuente, J.V. (2010), In: *A Wireless monitoring system to study the setting and hardening processes of cementitious materials*, Proceedings of the 10th European Conference on NDT, ECNDT 2010, Volume 7, Moscow, Russia.
[9] Crossbow Technology. http://www.xbow.com/

Early-Age Ultrasonic Testing of Concrete and Shotcrete using Embedded Sensors

A. Gibson and D. Ciancio

Abstract   This paper presents the results of preliminary laboratory testing of early-age concrete properties using disposable, embedded ultrasonic sensors. These tests were carried out during the development of a field system for monitoring the early-age physical properties in concrete and shotcrete. The design is particularly suitable for applications in Fibre Reinforced Shotcrete (FRS), commonly used for ground support in underground mine tunnels in Australia, where the determination of early-age properties is critical for establishing safe re-entry times. The embedded system used in these experiments comprises a pair of piezoelectric transducers mounted to an open frame, which is designed to hold them within the concrete at a fixed offset separation. The probe is implanted at the time of placement, and connected via wire leads to an external control system. The implanted transducers are configured to excite longitudinal (P) waves, at a nominal resonance frequency of 40 kHz, and P-wave transmission is detectable soon after the initial set time. The data presented herein includes evolution of early-age P-wave velocity. This data is compared to conventional unconfined compressive strength (UCS) and dynamic (low strain) elastic modulus, as specified in ASTM C215, for equivalent batches and curing conditions. The embedded P-wave measurement is functionally equivalent to the conventional dynamic modulus testing procedure, and these results may be further used to infer UCS during the early stages of hydration. The ability to perform in-situ, real time, nondestructive testing offers significant advantages to the safe and efficient use of FRS in underground mining applications.

Keywords   Early-age • Non-destructive • P-wave • Shotcrete • Ultrasonic

A. Gibson (✉)
AG Acoustic LLC, Boulder, CO, USA
e-mail: algibson@gmail.com

D. Ciancio
School of Civil and Resource Engineering, the University of Western Australia, Perth, WA

Introduction

In recent years there has been widespread adoption of shotcrete (FRS) as a preferred material for providing ground support in underground tunneling operations within the Australian mining industry. For this application it is necessary to establish safe re-entry times, which provide sufficient curing to guarantee the integrity of the support system, while permitting operations to proceed in a timely, cost-effective manner. It is common practice in the industry to use an estimate of unconfined compressive strength of the FRS material as a proxy for the establishment of permissible re-entry time. This may be obtained by testing samples at the batching plant, or at early age using indirect *in-situ* techniques such as needle penetrometers. In this context, there is a demand for improved capabilities to track the development physical properties of the in-situ FRS material.

Ultrasonic testing methods have been applied to the measurement of physical properties in cementitious materials over the past several decades (Keating et al., 1989, Whitehurst, 1951). The main advantage of this approach being that wave velocity, itself contingent on fundamental physical properties, can be repeatedly determined in a non-destructive, economic manner on a given sample until target parameters are attained. While there is a strong positive correlation between concrete strength and P-wave velocity (C_P), several factors, including moisture content, aggregate type and content, water/cement ratio and entrained air have been shown to exert independent influences on the relationship (Bungey, 1980). Therefore, at full maturity C_P may only provide a quantitative estimate of compressive strength if calibration data is available for the specific mix design in question.

Under the assumption of a homogeneous, elastic material, C_P is related to fundamental physical properties according to Eqn. (1).

$$C_P = \sqrt{\frac{E(1-\upsilon)}{\rho(1+\upsilon)(1-2\upsilon)}} = \sqrt{\frac{M}{\rho}} \tag{1}$$

were E= Young's modulus, υ= Poisson's ratio, ρ= mass density, and M= bulk elastic modulus.

For cement based materials the above is valid for the estimation of dynamic (i.e. low strain) moduli (E_d, M_d), and wavelengths exceeding the dimensional scale of the inhomogeneties presented by aggregate, fibre reinforcement and air voids. The relationship between P-wave velocity and compressive strength is necessarily empirical. Compression wave velocity is highly sensitive to the development of material properties at early age, and increases more rapidly than compressive strength during the early stages of hydration. Previous studies have shown C_P to be a sensitive indicator of strength gain within the first 3 days, or up to 60% of 28-day strength (Pessiki and Carino, 1988). To this effect, numerous studies on the use of pulse velocity to monitor hydration in various types of cement composites have been carried out in the last decade (Boumiz et al., 1996, Chotard et al., 2001, Sayers and Grenfell, 1993, De Belie et al., 2005).

This paper presents promising results of a novel type of disposable ultrasonic sensing device, designed to be embedded into fresh FRS or concrete maretial. The purpose of the research to date has been to validate the approach of using embedded transducers for efficient, in-situ tracking of relevant physical properties.

Experimental Method and Procedures

Testing was carried out using a frame mounted transducer set, comprising a pair of 40 kHz piezo-transducers mounted at a nominal offset separation on 75mm, within an open PVC frame (Fig. 1). The probe is wired through the external surface to the test material to a control sytem that includes a high-voltage source, data acquisition system and potable PC computer. A typical dataset from this system, over the first 14 hours of curing of a concrete specimen is presented in Fig. 2. The data presented in this paper was obtained using a wet cement mortar mix, designed to simulate the properties of FRS, while allowing for the material to be cast and vibrated in 0.2x0.1m cylinders for laboratory testing and verification. The mix was alternatively prepared with and without fibre reinforcement, using both steel and synthetic fibres.

In the dataset shown in Fig. 2, there is no detectable P-wave transmission prior to 6 hours age, due to high signal attenuation in the fresh paste. First measurable transmissions coincide with the initial set time, and subsequently the P-wave velocity of the material begins to increase over the baseline value of 1480m/s (corresponding to the material's liquid phase). Velocity calculations obtained in this study are based on an initial probe calibration in water at room temperature.

The embedded velocity measurements were carried at discrete intervals during the first 48 hours of curing for each sample, and compared to traditional stiffness (not reported) and strength test results, as obtained by cylinder resonance (ASTM C-215) and unconfined compression testing.

Fig. 1 Schematic representation of the embeddable ultrasonic element
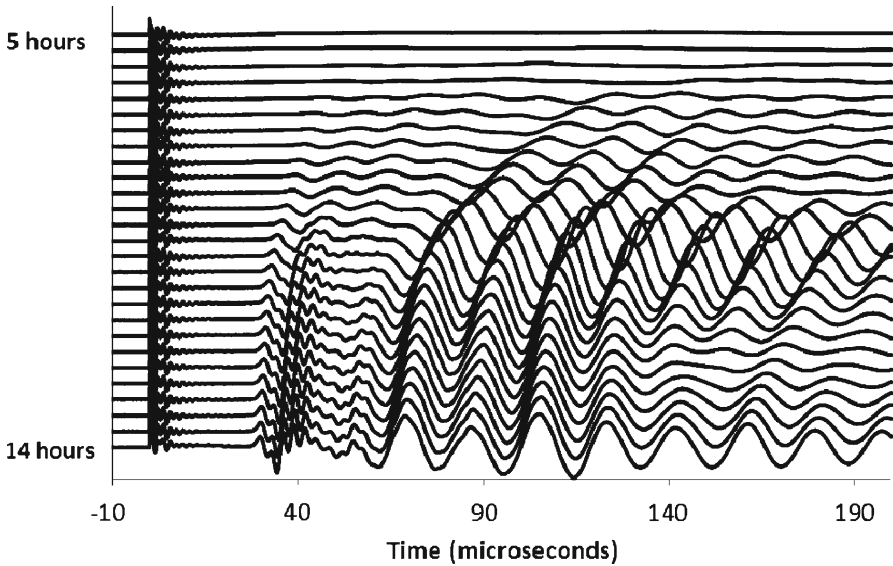
Fig. 2 Composite of ultrasonic measurements between 5 and 14 hours after mixing, showing the reduction in first arrival times, increasing transmission amplitude and development of time-frequency characteristics

Results and Analysis

Among the most relevant engineering properties to compare to the in-situ velocity measurements is unconfined compressive strength, obtained by the destructive testing of a series of concrete cylinders. Compressive strength at full maturity can be empirically calibrated to P-wave velocity, yielding a mix-specific relationship accounting for the independent influences of various factors mentioned above. However, many authors cited in this paper have determined that P-wave velocity is relevant to establishing initial set times, and tracking compressive strength at early age. (Pessiki and Carino, 1988) propose a consistent empirical relationship based on experimental data, valid for the first 3 days or up to 60% of design strength, when the strength-velocity relationship is most sensitive. The distribution of measured P-wave velocity vs. average compressive strength for samples aged between 6 and 48 hours is presented in Fig. 3, including a fitted exponential curve that would best describe the empirical velocity-strength relationship for the range of materials used.

Discussion, Conclusions & Future Work

Although the proposed use of UPV for monitoring development of material properties has received a lot of attention in the past, this paper demonstrates a novel approach of performing such measurements in-situ, using field-worthy equipment
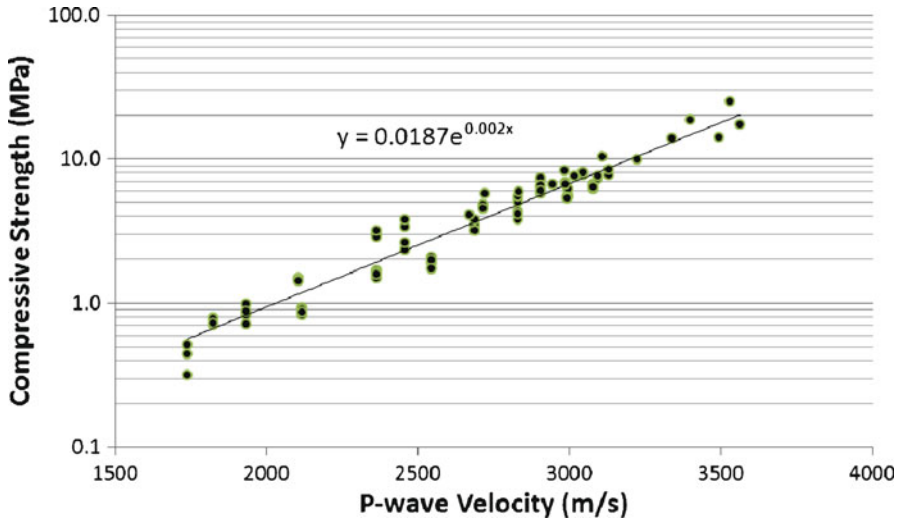
Fig. 3 Distribution of velocity vs. average compressive strength between 6 and 48 hours

and disposable ultrasonic probes. The work herein presents data derived from a prototype embedded system, which was able to detect P-wave arrivals in concrete after the initial set time, and was not adversely affected by the presence of synthetic or steel fibre reinforcement.

For the purpose of using P-wave velocity to predict early-age strength, the experimental data obtained in this study shows good correlation to the empirical relationship independently developed by other authors, for values of unconfined compressive strength higher than 4 MPa and up to 48 hours maximum curing time (the limit of this particular study).

For compressive strength values between 1 and 4 MPa, which are relevant to FRS applications, greater variability and deviation from the proposed empirical relationship was observed. It should be noted that the most significant source of statistical variability in this range is attributable to cylinder compression test results, rather than the in-situ velocity measurements.

References

[1] Bernard, E. S. (2008). Early-age load resistance of fibre reinforced shotcrete linings. *Tunnelling and Underground Space Technology*, 23, 451–460.

[2] Boumiz, A., Vernet, C. & Tenoudji, F. C. (1996). Mechanical properties of cement pastes and mortars at early ages : Evolution with time and degree of hydration. *Advanced Cement Based Materials*, 3, 94–106.

 [3] Bungey, J. H. (1980). The validity of ultrasonic pulse velocity testing of in-place concrete for strength. *NDT International*, 13, 296–300.
 [4] Chotard, T., Gimet-Breart, N., Smith, A., Fargeot, D., Bonnet, J. P. & Gault, C. (2001). Application of ultrasonic testing to describe the hydration of calcium aluminate cement at the early age. *Cement and Concrete Research*, 31, 405–412.
 [5] De Belie, N., Grosse, C. U., Kurz, J. & Reinhardt, H. W. (2005). Ultrasound monitoring of the influence of different accelerating admixtures and cement types for shotcrete on setting and hardening behaviour. *Cement and Concrete Research*, 35, 2087–2094.
 [6] Keating, J., Hannant, D. J. & Hibbert, A. P. (1989). Correlation between cube strength, ultrasonic pulse velocity and volume change for oil well cement slurries. *Cement and Concrete Research*, 19, 715–726.
 [7] Kolluru, S. V., Popovics, J. S. & Shah, S. P. (2000). Determining elastic properties of concrete using vibrational resonance frequencies of standard test cylinders. *Cement, Concrete and Aggregates*, 22, 81–89.
 [8] Pessiki, S. P. & Carino, N. J. (1988). Setting time and strength of concrete using the impact-echo method. *ACI Materials Journal*, 85, 389–399.
 [9] Reinhardt, H. W. & Grosse, C. U. (2004). Continuous monitoring of setting and hardening of mortar and concrete. *Construction and Building Materials*, 18, 145-154.
[10] Sayers, C. M. & Grenfell, R. L. (1993). Ultrasonic propagation through hydrating cements. *Ultrasonics*, 31, 147–153.
[11] Whitehurst, E. A. (1951). Soniscope Tests Concrete Structures. *Journal of the American Concrete Institute*, 47, 433–444.

Continuous Monitoring of Setting and Hardening of Epoxy Resin

S. Grammatikos, D.G. Aggelis, and A.S. Paipetis

Abstract A problem in the manufacturing of composite materials is the monitoring of the curing process in order to distinguish the different stages of the structural formation and to provide adequate conditions for proper epoxy impregnation. The method used to monitor the setting and hardening of epoxy in this study is based on ultrasonic propagation. A wave generator was connected to a sensitive broadband acoustic emission transducer in order to transmit elastic waves through the thickness of setting and hardening epoxy. The acquisition was conducted by another sensor of the same type acting as receiver. Different parameters like the wave velocity and attenuation are monitored in order to examine the rate of hardening. The changes in viscosity and elastic modulus with time can be monitored by the changes in the wave parameters. The effect of temperature is also discussed.

Keywords Attenuation • Composites • Curing • Epoxy • Wave velocity

Introduction

Curing efficiency in epoxy as well as fibre epoxy composites is of major importance in the structural integrity, particularly in the case of load bearing components, or in the case of aggressive environments. Whereas curing degree can be efficiently monitored off line using well established methods (e.g. Differential scanning calorimetry), few methods allow the on-line monitoring of curing of epoxies or epoxy based composites. A reliable method to monitor curing efficiency on line relies on the dielectric properties of the resin and their change due to the gradual immobilisation of the charge bearing particles in the epoxy system as curing is progressing [1].

S. Grammatikos • D.G. Aggelis • A.S. Paipetis (✉)
Department of Materials Science and Engineering, University of Ioannina, Ioannina 45110, Greece
e-mail: paipetis@cc.uoi.gr

In this work a novel method for curing monitoring in epoxy systems is presented base on the wave propagation properties of the time dependent solidification of the liquid epoxy.

As is well known, epoxies are moderately viscous liquids in room temperature. After mixing with the hardener there is a slight change in viscosity. If the system need to be thermally stimulated to initiate polymerisation, the viscosity is considerably reduced until, due to polymerization, macromolecules start to form. The rate of the chemical reaction is not constant with time as polymerization asymptotically reaches maximum [2]. The polymerisation rate also depends on temperature. Post curing at a higher temperature leads to increased cross linking and enhanced stiffness. The motivation for this work lies on the assumption that both viscosity and stiffness affect the wave propagation characteristics of the solidifying liquid [3].

Experimental Process

The experimental setup consists of a waveform generator (Tektronix AFG3102) and two piezoelectric transducers (PAC, Pico), which are placed in a PMMA container, as seen in Fig. 1. Between the PMMA plates, a U-shaped plastic Teflon plate defines the volume to be occupied by the fresh specimen (or the distance between the sensors, in this case 20 mm). The pulse from the wave generator is driven to one of the sensors acting as pulser and the received signal from the second on the opposite plate, is recorded with a sampling rate of 10 MHz. Initially the sensors were placed in holes specially machined in order to fit the sensors, being in direct contact with the resin. However, monitoring for long periods revealed that the transmission failed after several hours. Therefore, for the measurements presented herein, the sensors were attached on the PMMA plate using a small layer of ultrasonic gel to enhance acoustic coupling conditions.
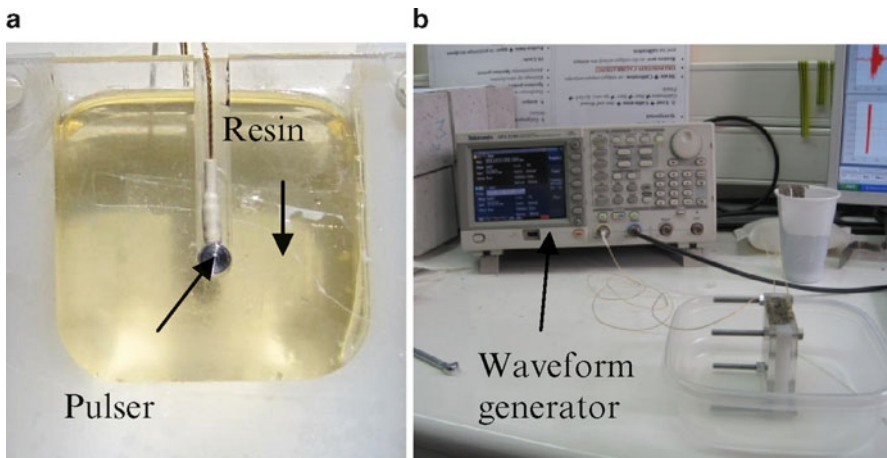
Fig. 1 (**a**) Resin container, (**b**) Snapshot during measurement

Fig. 2 (**a**) Typical electric and resin specimen waveforms. (**b**) focus on the onset of a resin waveform
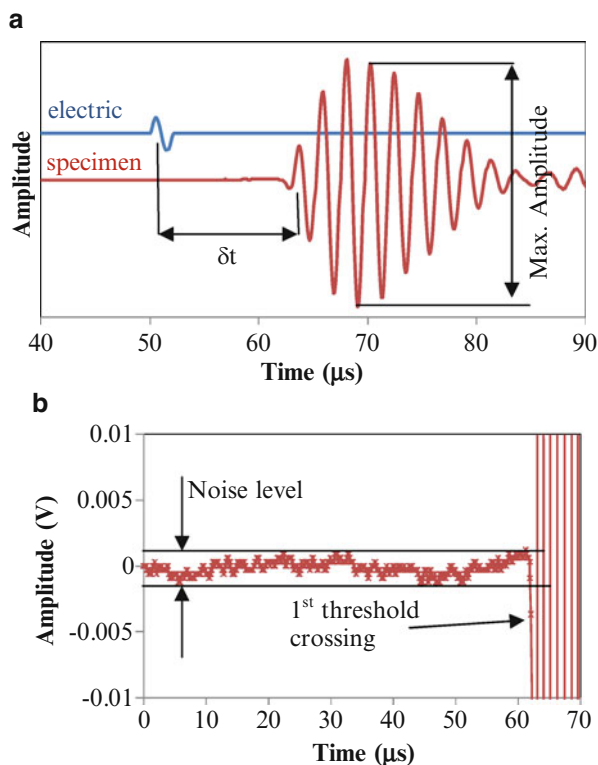
The electric signal used for excitation is 1 cycle of 500 kHz. The pulse generator produced one pulse at user defined intervals (5 min) and the received waveforms were recorded for a period of more than 15 hrs. Pulse velocity is measured by the time delay between the received signal through resin and the electric pulse directly fed from the generator to the acquisition board, while transmission is measured by the maximum voltage of the received waveform, see Fig. 2a. It is mentioned that the sensor delay effect as well as the transit time between the PMMA plates were measured separately (0.5 μs and 5.2 μs respectively) and excluded from the total transit time. A simple threshold crossing algorithm was built in Matlab environment, in order to automatically process the whole number of waveforms. The threshold was set equal to 1.2 times the maximum amplitude recorded during the 50 μs period of pre-trigger, see Fig. 2b. Due to the limited level of noise, there was no need to enhance the signal to noise ratio by stacking a number of waveforms. It is seen that the first detectable disturbance of the waveform is very close to the point picked by the algorithm, which enables reliable and automatic process of the waveforms. Considering the transit time through the plates and the resin specimen of about 15 μs, the sampling rate of 0.1 μs can results in a standard error of approximately 0.7%.

A typical commercial epoxy system (HT2 resin /HT2 hardener in a mixing ratio 100:48 per weight was used with proposed curing cycle 24h at room temperature.

Results

Figure 3a shows the pulse velocity vs. age of epoxy after mixing the two compounds. Two curves are from specimens cured in room temperature (22°C). Initial measurements show a pulse velocity of approximately 1800 m/s, which is higher than the corresponding velocity in water (1500 m/s). For a period of approximately 60 min a small decrease of velocity is recorded. Later the velocity increases steadily until about 4 h and later the velocity increase rate is slowing down. At the age of 1000 min (17 hrs) the velocity seems to converge to a value close to 3000 m/s, being increased by approximately 70% compared to the initial value just after mixing of the compounds. The two curves obtained by different specimens are almost identical, revealing that the conditions of the experiment are reliable. To test the effect of temperature, another specimen was monitored inside an oven with constant temperature of 30 °C, see also Fig. 3a. The curve is similar in shape but the final velocity is reached much earlier (approximately 400 min). Additionally, the initial period of velocity decrease is shorter and the increase of velocity thereafter is quite sharp. It is mentioned that epoxy specimens were measured some days later by contact
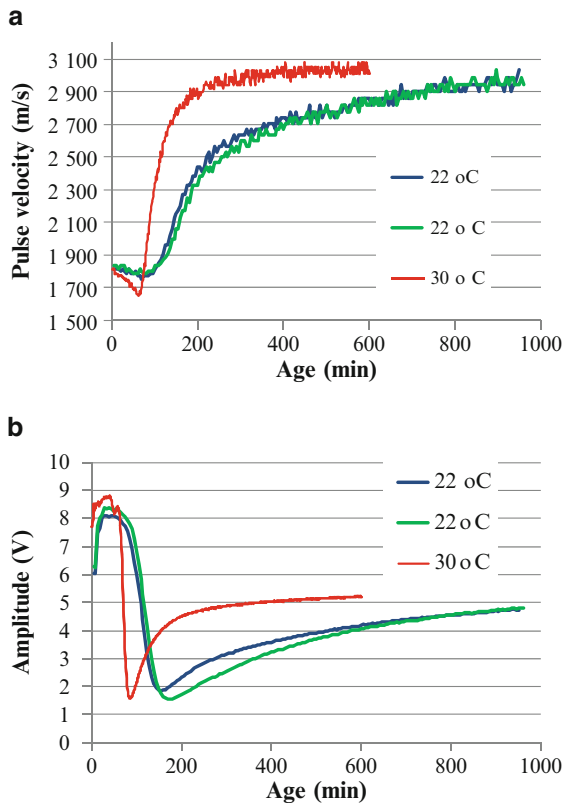
Fig. 3 (**a**) Velocity and (**b**) amplitude vs. time at different temperatures

ultrasound sensors of 5 MHz in a typical pulse-echo mode. The velocity was measured at 3130 m/s, slightly higher than the final measurement of the continuous monitoring, due to completed polymerization. The specific trends will be discussed later along with the amplitude results that follow.

Figure 3b shows the development of wave amplitude as a function of curing time. For specimens at room temperature the trend is again identical. Both specimens start at the same value and exhibit a peak in amplitude from 30 to 60 min. Afterwards the amplitude decreases rapidly to less than one third of the initial value and after the local minimum of 180 min, amplitude starts elevating slowly with decreasing rate. The specimen cured at 30 °C, starts with higher amplitude but exhibits a smaller increase during the first 30 min. Then the amplitude decreases sharply in less than the next 25 min and obtains a minimum at 86 min before increasing quickly but again with decreasing rate. It is mentioned that for the 30°C specimen, the measurements interval was reduced to 1 min in order to capture in a better detail the rapid changing trends.

Discussion

The pulse velocity increase indicates an increase of the stiffness of the material, as manifested in the attainment of structural integrity in solidifying systems. Similar curves have been obtained for fresh concrete monitoring [3]. The initial value of velocity depends on the bulk modulus of liquid epoxy, which seems to be slightly higher than that of the water (approximately 300 m/s higher). As the polymerization proceeds, the material becomes stiffer and the velocity increases. The rate of the reaction gradually slows down as polymerisation sites become scarcer. This leads to the gradual decrease in velocity change which tends asymptotically to a maximum.

Concerning the amplitude, as the mixture is a viscous liquid at room temperature the energy loss of transmitted wave is expected to be high. The polymerisation process is a typically exothermic reaction which leads to the global increase in temperature as well as a notable decrease in viscosity rendering the epoxy-hardener system close to the ideal liquid. This is manifested by the initial increase in the relative amplitude at the very initial stage of the reaction. At the same time, the polymerization and the long macromolecule chains that start to form increase the viscosity of the liquid which surpasses the aforementioned phenomenon as the two effects are superimposed. The increase in molecular weight and the viscosity gradually prevails and the transmitted amplitude starts to reduce. The amplitude continues to decrease until about 3 hrs for room temperature (85 min for 30°C). From this point onwards, the gradual stiffening of the material takes place as it is transformed from a viscous liquid to a glassy solid with increasing rigidity. As is expected, the amplitude increases similarly to velocity with decreasing rate reaching asymptotically a maximum. The two natures of the viscous fluid and the stiff solid co-exist; the fluid behaviour governs the measurements at early curing times, while at the end of the

monitoring period, the elastic material seems to be defining the ultrasonic velocity and amplitude. One characteristic moment is the amplitude minimum, which can be assumed to correspond to the point of maximum viscosity.

Conclusion

The aim of this study is to contribute to the understanding of the wave propagation in epoxy during curing, with the aim to provide an ultrasound based curing monitoring system. The nature of the material is complicated due to (a) the temperature dependent system viscosity, (b) the co-existence of both viscous fluid components with a solid phase with increasing volume fraction. Ultrasonic monitoring provides information on the rate of curing and completion of the reaction. Furthermore, combined measurements of velocity and amplitude shed light in the transformation process of epoxy allowing the study of the distinct mechanisms.

References

[1] G.M. Maistros, I.K. Partridge (1998), *Composites Part B: Engineering*, vol. 29(3), p. 245–250.
[2] W. Stark. (2010), *Polymer Testing*, vol. 29, p.723–728.
[3] N. De Belie, C. U. Grosse, J. Kurz, H.-W. Reinhardt (2005), *Cement and Concrete Research*, vol. 35, p. 2087–2094.

Section 4
NDT for Material Characterization: Metallurgical Perspective

Characterization of Steel Microstructures by Magnetic Barkhausen Noise Technique

C.H. Gür

Abstract Optimization and control of the microstructure is vital for improving performance and service life of the steel components. Development of non-destructive techniques for microstructure characterization has been a challenging task for many years. Magnetic Barkhausen Noise method is a non-destructive evaluation technique with high potential for characterization of steels. This paper summarizes the related studies performed at METU.

Introduction

The microstructure is usually determined by metallographic techniques and hardness test where certain regions of the representative samples are investigated. Since the conventional methods are destructive and time consuming, there is an industrial interest to develop nondestructive techniques capable of rapid evaluation. Magnetic Barkhausen Noise (MBN) method is applicable to ferromagnetic materials which are composed of small order magnetic regions, called domains. Each domain is spontaneously magnetized along the easy crystallographic direction, however, due to random distribution of domains the total magnetization of the material is zero. Domains are separated from each other by domain (Bloch) walls. 180° Bloch walls have greater mobility than 90° walls so their contribution to MBN is bigger [1]. If an external magnetic field is applied to a ferromagnetic substance, domains with alignments parallel or nearly paralel to the applied field vector expand and others annihilate. Saturation occurs when all magnetization vectors inside the domains align

---

C.H. Gür (✉)
Metallurgical & Materials Eng. Dept., Middle East Tech. Univ., Ankara, Turkey

Welding Technology & NDT Center, Middle East Tech. Univ., Ankara, Turkey
e-mail: chgur@metu.edu.tr

themselves in the direction of applied field by domain wall movements [2]. Under a variable external magnetic field, hysteresis cycles of ferromagnetic materials reveals discontinuous flux changes due to irreversible domain wall motion, called as Barkhausen noise. These jumps can be detected as voltage pulses induced in a pick-up coil positioned close to the surface. These signals are amplified, filtered and then processed using a computer software to characterize the samples. Grain boundaries, dislocations, second phases and impurities act as an obstacle for the movement of domain walls.

This paper summarizes the studies on grain size determination and characterization of phases in the heat-treated steels by MBN [3,4]. Details about other studies can be found elsewhere: Characterization of dual-phase steels [5]; determination of surface residual stresses in the welded steels [6] and in the shot-peened steels [7]; microstructural evolution in spheroidized steels [8]; characterization of ultra-fine grained steels [9]; investigation of the variations in microstructure and mechanical properties of dual matrix ductile iron [10]; monitoring the microstructural changes during tempering [11,12].

Case Studies

MBN measurements were performed using Rollscan/μscan 500-2. A sinusoidal cyclic magnetic field with an excitation magnetic field of 125 Hz was induced in a small volume of the specimen via a ferrite core C-coil. The signals were filtered, amplified with a gain of 50 dB, and then, analyzed using the software. The contact of the sensor was ensured by clips applying the same pressure to the samples.

Determination of average ferrite grain size in steels by MBN [3]

15x15x7 mm specimens cut from cold drawn SAE 1010 were annealed at 700°C. Table 1 gives the heat treatments and average grain sizes. All specimens are composed of dominantly ferrite, and have similar hardness values about 100 HV.

Table 1 Details of the heat treatments applied to specimens

Heating			Average Grain
Time (minute)	Temperature (°C)	Cooling	Size (μm)
20	875	Air	15
30	875	Air	18
720	700	Air	26
30	1100	Furnace	40
30	1200	Furnace	54
30	1300	Furnace	58

a

b
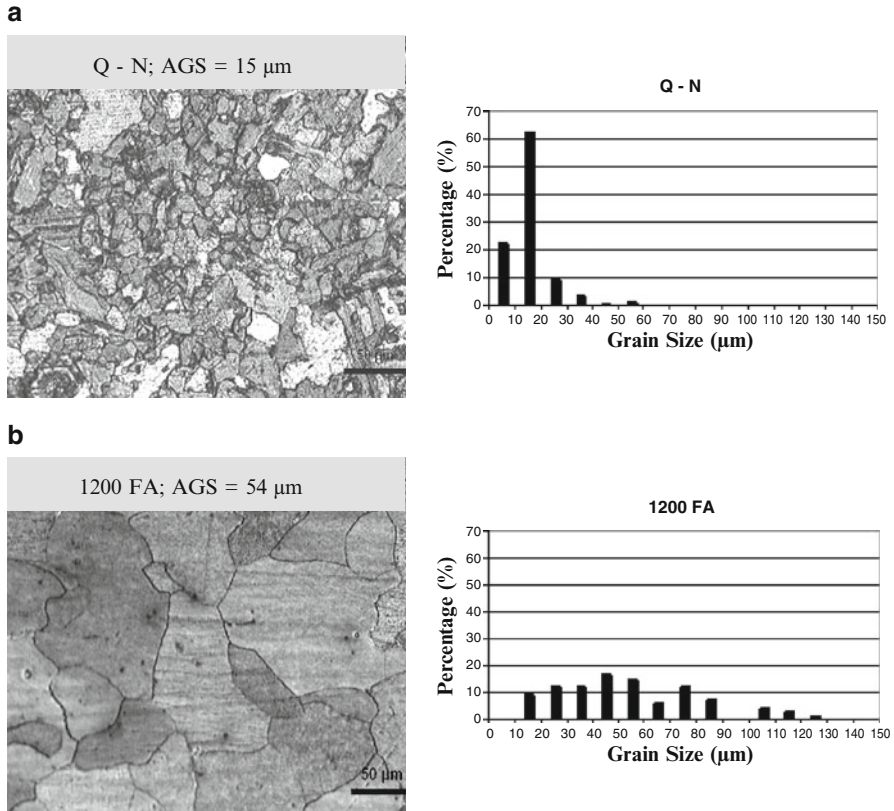
Fig. 1 Optical micrographs and grain size distribution histograms: (**a**) Q-N: quenched and normalized, (**b**) 1200 FA: furnace annealed

Figure 1 shows equiaxed ferrite grains in the micrographs and corresponding grain size distribution histograms. During cooling, the ferrite nuclei appear at the austenite grain boundaries and grow. Further growth merely thickens the grain boundary, this continues until all the austenite is transformed.

Figure 2 shows that all peak positions are near zero field strength, i.e., MBN activity occurs at early stages of magnetization in which domain nucleation is dominant. As grain size increases grain boundary area decreases that reduces the nucleation sites and makes difficult the formation of new domains. At later stages, domains grow and rotate as the material reaches magnetic saturation. With increasing grain size, the domains get larger, thus domain wall density decreases; the mean free path of domain wall motion increases, thus the field required for bulging domain walls before unpinning increases. The domain walls pinned at grain boundary can continue their motion by Barkhausen jumps generating MBN signals. Difficulties in domain nucleation, reduced number of
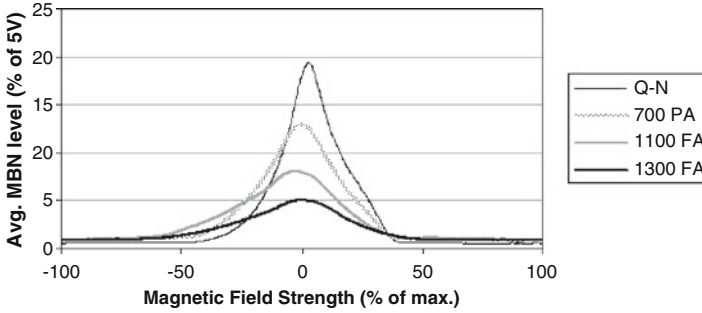
Fig. 2 MBN profiles of the specimens
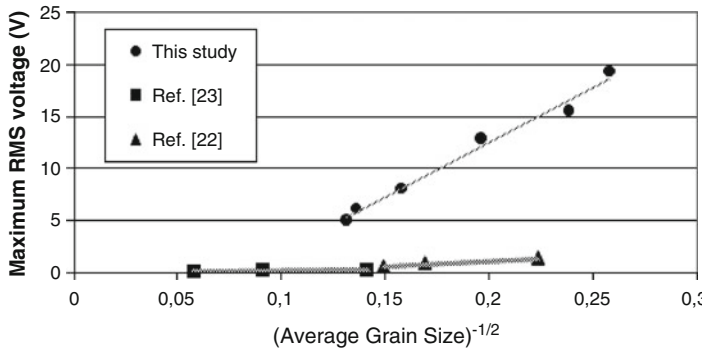
Fig. 3 Comparison of the experimental data with previous studies [15,16]

Barkhausen jumps and domain density cause low MBN activity in the coarse grained structures. A Petch like relation between RMS and AGS can be proposed [13]

$$RMS = k.(AGS)^{-0.5}$$

where "k" is a parameter independent of the grain size [14]. Figure 3 shows the correlations of various studies. The slope of the line (k) increases as impurity or C-content increases. Composition changes and the different MBN systems used in these studies are the most probable reasons for different "k" values.

Characterization of microstructures of heat treated steels [4]

5 mm-thick disk shaped samples were cut perpendicular to the rolling direction of hot-rolled SAE 1040 and SAE 4140 bars with 30 mm dia. Following the austenitization at 850°C for 30 min, they were heat treated according to the procedures in Table 2. The

Table 2 Heat treatments and corresponding microstructures

Following austenitization at 850°C/30 minutes	Microstructure
Water quenching (20°C)	Martensite
Water quenching/tempering at 600°C/2 h	Tempered martensite
Isothermal heating at 600°C/10 min /water quenching	Pearlite-ferrite (fine)
Isothermal heating at 680°C/ 1h /water quenching	Pearlite-ferrite (coarse)
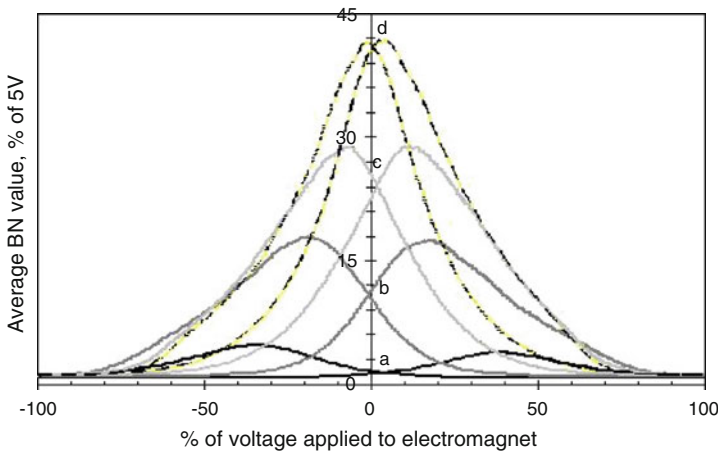
Fig. 4 The MBN fingerprints of various samples: a) Martensite, b) Tempered martensite, c) Fine pearlite-ferrite, d) Coarse pearlite-ferrite

scale was removed from the surfaces by grinding. The specimens were investigated by SEM and hardness measurements. The highest hardness, 658 HV and 674 HV, belong to the as-quenched specimens of SAE 1040 and SAE 4140, respectively. The samples consisting of coarse pearlite-ferrite have the lowest hardness, being 178 HV for SAE 1040 and 199 HV for SAE 4140.

Figure 4 shows that Martensite has the lowest peak amplitude. The peak amplitude increases subsequently for tempered martensite, fine pearlite-ferrite, and coarse pearlite-ferrite. Similarly MBN peak position shifts to lower magnetic field of excitation in the order of martensite, tempered martensite, fine pearlite-ferrite, and coarse pearlite-ferrite. The low amplitude broad peak of martensite transformed into high amplitude narrow peaks situated at a lower magnetic field for the other phases. Small martensite needles cause very small domains; the relative volume occupied by a domain wall is the largest, which increases the significance of the domain wall energy. The resistance to the domain growth is very high since the domain walls are pinned due to high dislocation density of martensite laths. The reversal of magnetization requires a strong field, displacements of the domain walls are short, and it is difficult to create new walls; therefore, the MBN peak is very weak, and situated at a relatively high magnetic field. After tempering, the magnetic structure becomes coarser, and the average

size of the domain walls increase. Since structure's resistance to the nucleation and motion of the domain walls decreases, the MBN signal amplitude increases remarkably, and the peak is situated at lower magnetic field.

There is a wider range of jump sizes in the ferritic-pearlitic samples. Pearlite consists of ferrite and cementite lamellae colonies formed along preferred crystalline directions which may facilitate the passage of a domain wall across a boundary, leading to a very large domain wall mean free path.The signal amplitude of coarse pearlite-ferrite is higher than that of fine pearlite-ferrite; coarsening causes an increase in the MBN peak amplitude. The magnetic field strength required for the movement of domain walls from pinning sites, i.e., the interfaces between proeutectoid ferrite and pearlite regions, and those between ferrite and cementite layers of pearlite, decreases remarkably.

Conclusions

Magnetic Barkhausen Noise (MBN) technique is a promising and challenging nondestructive technique for automated evaluation of microstructures in steel components in a fast and reliable manner. It has been concluded that MBN method can be utilized efficiently and effectively for evaluating the ferrite grain size; characterizing the microstructure to differentiate the phases.

References

[1] Altpeter I., Dobmann G., Kröning M., Rabung M., Szielasko S. (2009), *NDT E Int.*, vol. 42, p. 283.

[2] Jiles D. (1991), *Introduction to Magnetism and Magnetic Materials*, Chapman and Hall, London, New York.

[3] Davut K., Gür C.H., (2007), In: Proceedings of *6th Int Conf on Barkhausen Noise & Micromagnetic Testing*, pp.113-122, Valenciennes.

[4] Gür C.H., Çam I. (2007), *Mater. Charact.*, vol. 58, p. 447.

[5] Kaplan M., Gür C.H., Erdoğan M. (2007), *J. Nondestruct. Eval.,* vol. 26, p. 79.

[6] Yelbay I., Çam I., Gür C.H. (2010), *NDT E Int.*, vol. 43, p. 29.

[7] Savaş S., Gür C.H. (2010), *INSIGHT–J. Brit. Inst. NDT*, vol. 52, p. 1.

[8] Davut K., Gür C.H. (2010), *J. Nondestruct. Eval.* vol. 29, p. 241.

[9] Bayramoglu S., Gür C.H., Alexandrov I., Abramova M.M., (2010), *Mater. Sci. Eng. A*, vol. A527, p. 927.

[10] Gür C.H., Özer M., Erdoğan M., (2008), *Res. ND Eval.*, vol. 19, p. 44.

[11] Davut K., Gür C.H. (2007), *J. Nondestruct. Eval.*, vol. 26, p. 107.

[12] Gür C.H., Çam İ. (2006), *Int. J. Microstr. Mater. Prop.*, vol. 1, p. 208.

[13] Sakamoto H., Okada M., Homma M. (1987), *IEEE Trans. Mag.*, vol. MAG-23, p. 2236.

[14] Stanley J.K. (1948), *Metallurgy and Magnetism*, ASM, Cleveland, Ohio.

[15] Gatelier-Rothea C., Chicois J., Fougeres R., Fleischmann P. (1998), *Acta Mater.*, vol. 46 p. 4873.

[16] Yamaura S., Furuya Y., Watanebe T. (2001), *Acta Mater.*, p. 3019.

Magnetic NDE with Magnetic Yoke-Probe for Degradation and Mechanical Properties of Steel

H. Kikuchi, Y. Kamada, S. Kobayashi and K. Ara

Abstract Magnetic NDE techniques for an estimation of distribution of degradation in tensile-tested structural steel and for an evaluation of mechanical parameter alike hardness in low carbon steel have been developed. In order to scan magnetic properties of steel promptly, a magnetic yoke-probe having primary and secondary coils wounded around the yoke was adopted. To simplify the detection procedure, the same principle as a transformer and the impedance measurement using the secondary coil were employed. The voltage induced at and the impedance of the secondary coil decrease with the increase of applied tensile stress. As for the spatial distribution of the measured parameters, the induced voltage and the impedance at the center part of specimen which was subjected to a large stress decrease, and the area where the induced voltage and the impedance decrease becomes wider with increasing applied tensile stress. The induced voltage and the impedance decrease with increasing hardness in low carbon steel.

Keywords Degradation • Hardness • Impedance • Magnetic NDE • Magnetic yoke-probe

Introduction

Magnetic parameters have good correlations with mechanical properties such as hardness, yield stress, etc., and strongly depend on microstructures of materials. Those parameters have therefore been used for nondestructive evaluation (NDE) of mechanical properties and also for characterization of materials [1–3]. The parameters derived from a hysteresis curve of materials like coercive force and remanence are often used [4, 5]. However, a large applied magnetic field is required to obtain a hysteresis curve and it takes a much time for a measurement. Thus, a development of

H. Kikuchi (✉) • Y. Kamada • S. Kobayashi • K. Ara
Faculty of Engineering, Iwate University
e-mail: hkiku@iwate-u.ac.jp

more simple technique for magnetic NDE is desirable. To satisfy such a requirement, new magnetic NDE techniques were proposed and their applicability to an estimation of degradation in tensile-tested structural steel, and an evaluation of mechanical properties in cold-rolled low carbon steel were investigated. To scan over steels promptly with low electricity consumption, a magnetic yoke-probe having an excitation (primary) and a pickup (secondary) coils was adopted. The same principles as a transformer and the impedance measurement were employed to simplify their detection procedures.

Experimental Procedure

Specimens

The rolled steel for welded structure, SM490A, and the low carbon steel, S15C, were prepared in this study. The steel contains 0.018 wt.%C, 0.04 wt.%Si, 1.19 wt.%Mn and Fe in balance for SM490A steel and 0.16 wt.%C, 0.2 wt.%Si, 0.44 wt.%Mn and Fe in balance for S15C steel. The SM490A steels were elastically and plastically deformed with the tensile stresses of 288, 457 and 518 MPa and the applied stress was released when magnetic measurements were done. The yield strength of SM490A steel is 450 MPa and the tensile strength of that is 580 MPa. The S15C steels were annealed at 900°C for one hour, followed by air cooling and then cold-rolled with the reduction ratios of 5, 10, 20 and 40 %. The dimensions of the plates obtained from each steels are illustrated in Fig. 1.

Measurement set-up

A magnetic single-yoke, made of Fe-Si steel, having a primary and a secondary coils was adopted. The single-yoke was located on the center of a plate and a closed magnetic circuit was composed as shown in Fig. 2, where the dimension and the
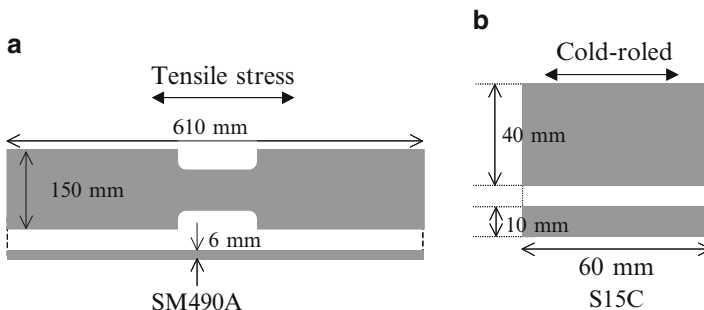
Fig. 1 The dimension of steel plates

Fig. 2 The dimension and the configuration of single-yoke
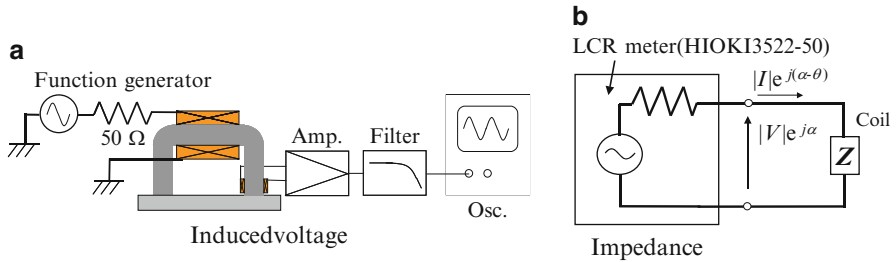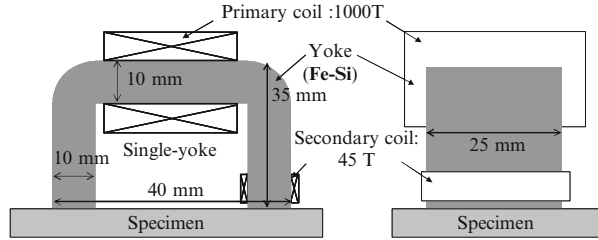
Fig. 3 Explanation of measurement systems
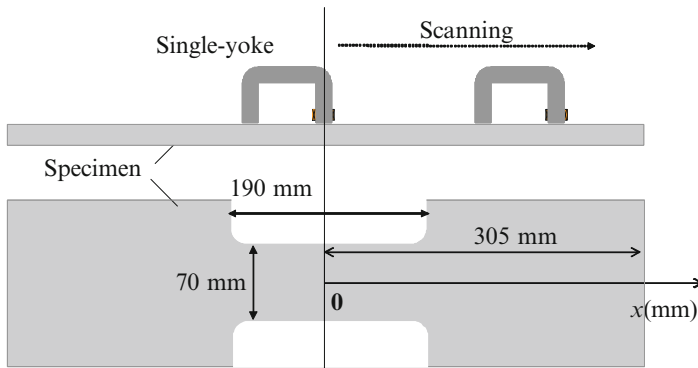
Fig. 4 Explanation for scanning single-yoke over SM490A specimen

configuration of the single-yoke are also shown. The measurement set-up for each measurement were shown in Fig. 3. When an induced voltage at the secondary coil were observed using an oscilloscope, a sinusoidal voltage of 1 Hz, 8 V was applied to the primary coil. As to impedance measurement, an impedance of the secondary coil was measured with a LCR meter (HIOKI 2250) by applying an ac current of 10 mA with a frequency range from 1 Hz to 1 kHz. Here the impedance Z, inductance L and resistance R, of the coil are the functions of initial permeability, μ_i, of the steels. The relation between Z, R and L is expressed by $Z = R + j2\pi fL$, where f is frequency. For SM490A steel plates, the single-yoke scanned over the specimens in x direction; i.e., in parallel to the length direction of the plates, as shown in Fig. 4 and distribution of induced voltage and impedance were evaluated. Here, the center of the plates is

defined as $x = 0$. In both measurements, specimens were magnetized in parallel to the direction of tensile stressed and cold-rolled. Vickers hardness of S15C steels were also evaluated by a hardness meter with a load of 500 g.

Experimental Results and Discussion

Figure 5 shows the wave profiles of the induced voltage measured at center of the plates ($x = 0$) and at edge ($x = -170$ mm) for the plates undeformed (0 MPa) and deformed with 518 MPa. There are no changes between the center and the edge part in the undeformed specimen, whereas the profile of the center becomes lower than that of the edge part in the specimen tensile stressed with 518 MPa. Figure 6 shows
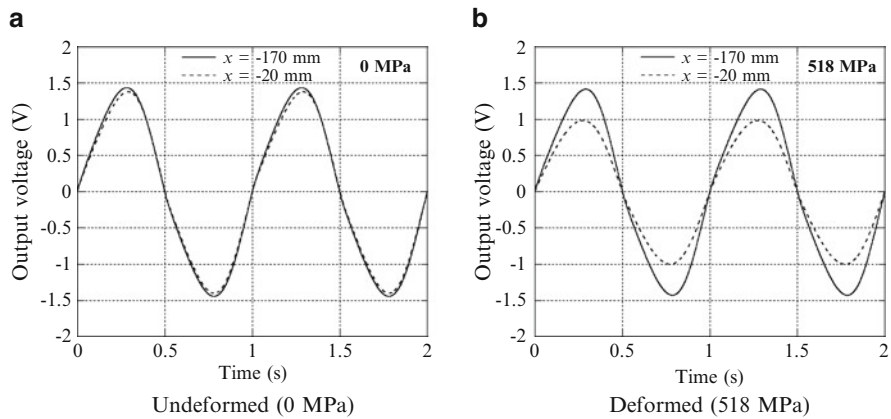
Fig. 5 Waveform of induced voltage at secondary coil
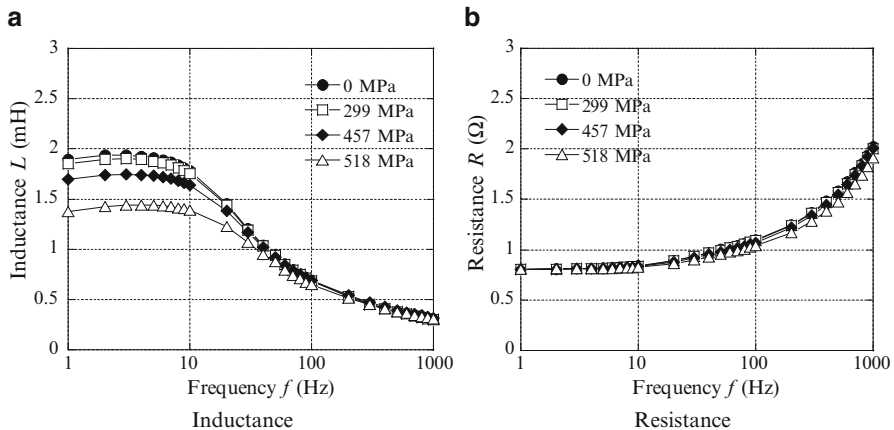
Fig. 6 Frequency dependence of impedance for SM490A steel
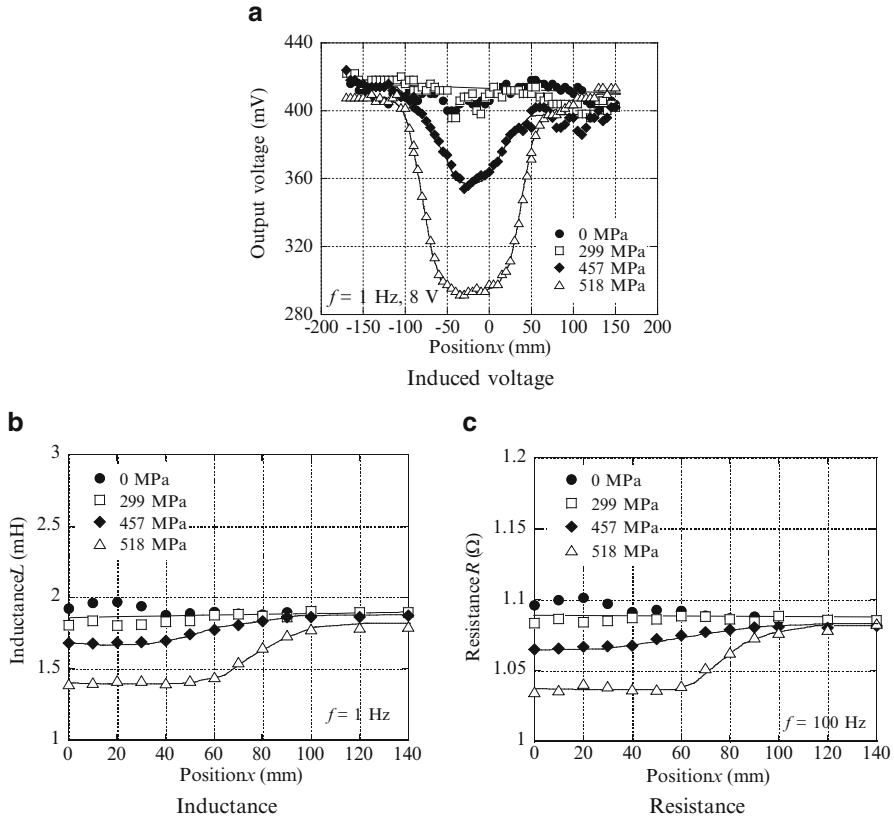
Fig. 7 Spatial distribution of magnetic parameters

the frequency dependence of the impedance for SM490A steels. The inductance is almost constant in low frequency region and then decreases due to eddy current loss with the rise in frequency, whereas the resistance is also constant up to 10 Hz, followed by its increase with upward frequency. The inductance at low frequency, for example at 1 Hz, decreases with increasing tensile stress. The inductance at higher frequency has no significant changes when the tensile stress changes. The resistance at low frequency is almost same values even if the tensile stress changes. On the other hand, the resistance at higher frequency decreases with increasing tensile stress.

Figure 7 shows the spatial distribution of measured parameters when the magnetic yoke scanned over the plates for SM490A steel. For the measurement of induced voltage, the maximum value of the profile was evaluated. For the impedance measuerment, the inductance at 1 Hz and the resistance at 100 Hz were evaluated. Both the induced voltage and the impedance at the center part decrease as the applied tensile stress increases. The value of parameters in the center of specimen decrease as compared with the values in the edge since the specimen was subjected to larger stress in the center. In addition, the area where the values of parameters decrease
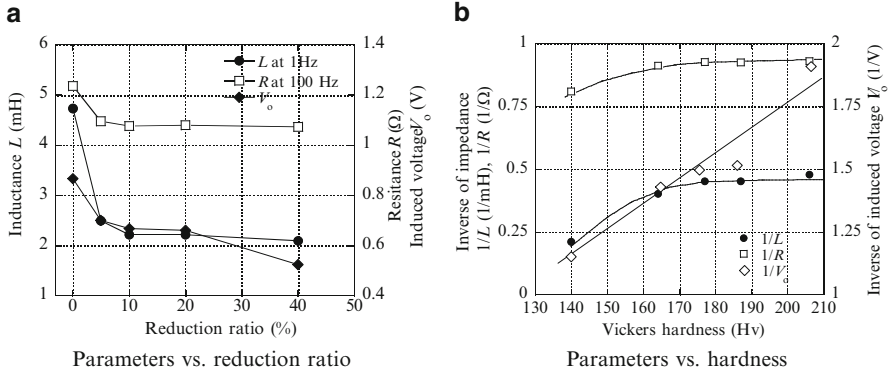
Fig. 8 Relations between induced voltage, impedance and reduction ratio, Vickers hardness

spreads with increasing applied tensile stress. These profiles of the parameters are consistent with the distribution of degradation in the materials.

Figure 8a shows the dependence of the induced voltage and the impedance on the reduction ratios for S15C steel. All parameters decrease with increasing reduction ratio. Figure 8b shows the relations between the evaluated parameters and the Vickers hardness. There are good correlations between those values.

When degradation of material progresses or hardness increases, dislocations in the material increase; dislocations increase with increasing applied tensile stress and with increasing reduction ratio. The dislocations act as pinning sites for domain wall motions. Thus domain wall motions impeded when dislocations increases; this lead a decrease in permeability of materials. The magnetic parameters is almost proportional to the permeability. Therefore, induced voltage and impedance decreases with progressing degradation and with increasing hardness. The magnetic parameters adopted here have good correlations with the distribution of degradation and the hardness. Thus results shown in this paper indicate the proposed magnetic NDE is very useful for an assessment of degradation distribution and mechanical properties of steels nondestructively.

Conclusion

A single-yoke was adopted to examine the potential of NDE by the measurement of the induced voltage at and the impedance of the secondary coil. All parameters decrease with increasing applied tensile stress and reduction ratio due to the decrease in permeability of the materials caused by the increase of dislocations. Scanning of the large plates of SM490A steel using the single-yoke was demonstrated and the evaluation of the distribution of parameters, reflects the distribution of mechanical properties, was successfully performed. For S15C steel, magnetic parameters have

good correlations with Vickers hardness. These results show the potential of NDE for the stracural component composed of ferromagnetic steels.

References

[1] Seegerw, A. Kronmüller, H. Rieger, H. and Träuble, H. (1964), *J. Appl. Phys.*, Vol. 35, pp. 740–748.
[2] Kronmüller, H. (1972), *Int. J. Nondestruct. Testing*, Vol. 3, pp. 315–350.
[3] Jiles, D.C. (1991), *Introduction to Magnetism and Magnetic Materials*, London UK, Chapman & Hail.
[4] Swartendruber, L.J. Hicho, G. E. Chopra, H.D. Leigh, S. D. Adam, G. and Tsory, E. (1997), *J. Appl. Phys.*, Vol. 81, pp. 4263–4265.
[5] Takahashi, S. Echigoya, J. and Motoki, Z. (2001), *J. Appl. Phys.*, Vol. 87 pp. 805–813.

Magnetic Inspection of Low-Carbon Steels Subjected to Plastic Deformations up to Failure

A.N. Stashkov, A.P. Nichipuruk, V.N. Kostin, M.K. Korkh, and S.A. Murikov

Abstract The possibility of magnetic inspection of plastic deformations preceding the failure of strained steel constructions was studied by locally magnetizing them with an attachable U- shaped electromagnet. Field dependences of the differential magnetic permeability of a plate made of low-carbon steel (0.09% C, 1.4-1.8% Mn) on the applied and residual stresses were determined. Critical fields of 90 and 180 degrees domain-wall motion at different deformations were calculated using a model taking into account the contribution of these domain walls to magnetization reversal processes.

Introduction

Evaluating the tension-induced plastic deformation in constructions made of low-carbon low-alloyed steels is actual problem of the magnetic evaluation of material structure. In spite of data [1] available for the analogous range of problems, the problem of low sensitivity of certain magnetic testing parameters to tensile deformations of steels close to failure remains unsolved.

As was shown in [2], the coercive force is almost unchanged at high degrees of plastic deformation. This is a reason the coercive force can't use as the testing parameter. The practical use of other characteristics of the magnetization curve and major and minor magnetic hysteresis loops is difficult owing to either absence or

A.N. Stashkov (✉) • A.P. Nichipuruk • V.N. Kostin • M.K. Korkh
Institute of Metal Physics, Ural Branch, Russian Academy of Science, Yekaterinbug, Russia
e-mail: stashkov@imp.uran.ru

S.A. Murikov
ETC «Ausferr», Magnitogorsk, Russia

imperfection of available instrumentation. It was shown in work [3] that, when studying the dependence of the differential magnetic permeability on the field, parameters of the critical fields of 90 and 180 degrees domain-wall motion can be obtained.

The sensitivity of the parameters to the magnitude and anisotropy of elastic and plastic deformations is sufficiently high. The sensitivity of these new parameters to deformations should be compared with that of earlier recommended parameters, such as the coercive force and residual induction. To locally measure these parameters, a SIMTEST small-size portable system was designed.

Thus, the aim of this investigation was a search for promising parameters for testing tensile stresses and determining the possibilities of locally measuring these parameters by attachable electromagnet with sensor system.

Experimental Work

A specimen used for the measurements was made of low-carbon steel (0.09% C, 1.4 –1.8% Mn) in the form of a plate 300 mm long, 60 mm wide, and 1.2 mm thick and had bulges at the ends, which were used to fix it in tension grips. Before the measurements, the specimen was subjected to recrystallizing annealing in a kiln at $(650\pm10)^0$ for 2 h to equilibrate the structure of the material.

In the course of the experiment, the specimen was loaded with stepwise tensile stresses and unloaded; eventually, this resulted in failure of the specimen. The unloading was performed after each loading step. The load was measured with a force-measuring sensor; the deformation was determined from the spacing between marks which were applied beforehand on the surface of the specimen. There was calculated the relative elongation equal to the ratio of the elongation to the initial spacing between the marks.

The magnetic properties of specimens were measured both under loading and after unloading. The dependence of the differential magnetic permeability on the magnetization reversing field was determined using a U-shaped attachable electromagnet with sensor system. The size of the magnetic core poles was 12 mm wide and 28 mm long. The magnetization-penetration depth of a electromagnet was about 6 mm; a fortiori, it exceeded the specimen thickness. The measuring coil was wound around the central section of the magnetic core. The structural arrangement of the measuring setup is shown in Fig. 1. The maximum magnetic field between the electromagnet pole space was ~320 A/cm. The magnetization-reversal frequency was 5 mHz; it ensured a magnetization-reversal rate of 6.4 A/(cm·s).

The measured magnitudes of the magnetizing current and signal from the coil were converted into the magnetic field strength and induction magnitudes, respectively. To do that, preliminarily, we performed a calibration. To find the permeability anisotropy, the signal was measured (using the U-shaped transducer) along two mutually perpendicular directions, namely, along and transversely to the plate.
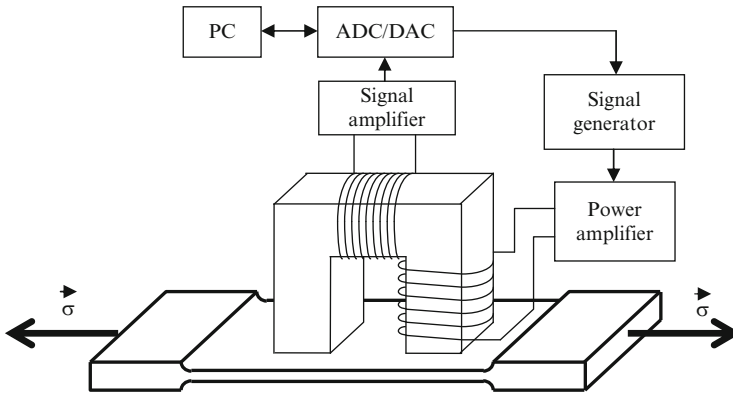
Fig. 1 Structural arrangement of the setup for measuring the differential permeability
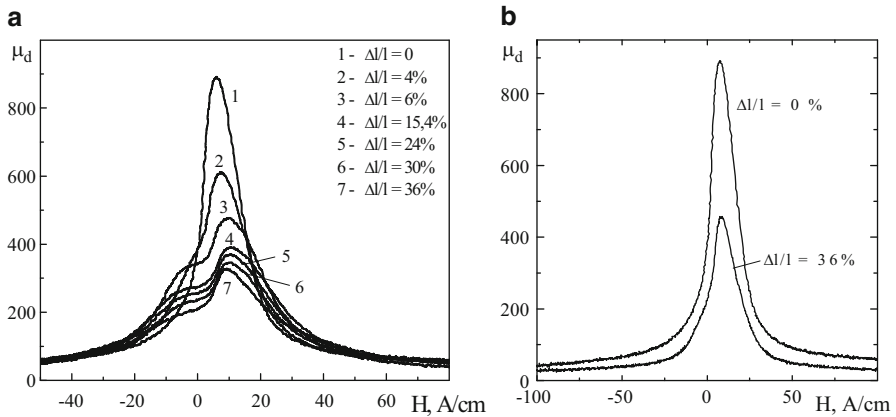
Fig. 2 Field dependences of the differential magnetic permeability measured: (**a**) along the plate after its loading to different relative-elongation magnitudes $\Delta l/l$ and unloading: (1)0, (2)4, (3)6, (4)15.4, (5)24, (6)30, and (7)36%, (**b**) transversely to the plate at $\Delta l/l=0$ and after its loading to $\Delta l/l=36\%$ and subsequent unloading

Results and Discussion

Figure 2a shows dependences of the differential magnetic permeability $\mu_d(H)$ measured after unloading the specimens at different relative elongations (up to failure at $\Delta l/l = 36\%$) on the magnetic field H. The U-shaped electromagnet was placed along the long side of specimen. In this case, the magnetization reversal is realized along the ascending branch of the hysteresis loop, i.e., from left to right. The presence of so-called "inflection" observed in a range of fields from saturation

Fig. 3 Dependences of the
critical fields of the $90^0(H_{perp})$
and $180^0(H_{para})$ domain-wall
motion and induced magnetic
anisotropy field (H_α) on the
relative elongation
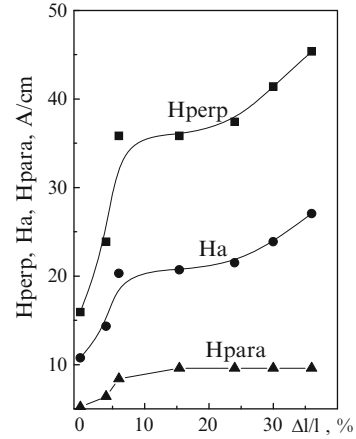
to residual induction is a typical feature of the dependences shown in Fig. 2a. As the relative elongation increases, the inflection becomes more pronounced. The existence of such an inflection is likely to be related to the fact that residual compressive stresses are induced in the plate along the loading direction after unloading the plate. Along this direction, an "easy-plane"-type magnetic texture is formed. Owing to this fact, the magnetization rotation perpendicular to the measuring direction is energetically favorable even before the reversal of the field sign; thus, an inflection is formed in the aforementioned curves. No similar effects are observed in measuring the μ_d magnitude perpendicular to the tension direction (Fig. 2b). As an example, Fig. 2b shows the initial dependence at $\Delta l/l = 0$ and the dependence measured after deformation to $\Delta l/l = 36\%$. In this case, the shape of curves at all degrees of deformation is similar to that of the initial (before loading) dependences. This confirms the conclusion on the existence of residual tensile stresses along this direction, which was inferred in [2, 4, 5], and, therefore, the existence of the "easy-axis"-type texture.

The curves measured under loading along the tension direction exhibit a similar behavior like the curves on Fig. 2b. It is obvious that, in this case, the "easy plane" texture is induced by the applied tensile stress.

Using the data obtained, the critical fields of 90 degree (H_{perp}) and 180 degree (H_{para}) domain-wall motion and induced magnetic anisotropy field H_α were calculated in terms of a model developed earlier [3]. Results of the calculations are shown in Fig. 3. It is obvious that, in contrast to H_{para}, which is proportional to the coercive force, the critical field of 90 degree domain wall motion (H_{perp}) and induced magnetic anisotropy field (H_α) are sensitive to changes in the degree of deformation of the material under study over the whole range of deformations up to specimen failure.

Conclusions

(1) The field dependences of the differential permeability measured in plastically deforming specimens during loading and after unloading are significantly different. The presence of the characteristic inflection in the curves measured after unloading indicates the appearance of the "easy-plane"-type texture in the specimen. This, in turn, is related to the presence of residual compressive stresses in the unloaded specimen along the preliminary tension direction.

(2) The critical field of 90 degree domain-wall motion H_{perp}, which is calculated from the field dependences of the differential permeability, exhibits the highest sensitivity to the relative elongation magnitude.

(3) It is possible to measure the differential permeability with a U-shaped attachable electromagnet. This will allow development of a compact measuring system.

References

[1] Ivayanagi, D. (1974), Hihakai Kensa, vol. 23, no. 3, pp. 147–154.
[2] Kuleev, V.G., Tsar'kova, T.P., and Nichipuruk, A.P. (2005), Rus. J. Nondestruct. Test., vol. 41, no. 5, pp. 285–295.
[3] Nichipuruk, A. and Rozenfel'd, E. (1997), Fiz. Met. Metalloved., vol. 84, no. 6. pp. 72–78.
[4] Abuku, S. (1977), Jpn. J. Appl. Phys., vol. 16, no. 7, pp. 1161–1170.
[5] Kuleev, V.G., Tsar'kova, T.P., and Nichipuruk, A.P. (2006), Rus. J. Nondestruct. Test., vol. 42, no. 4, pp. 261–271.

Thermography and Acoustic Emission for Monitoring the Fracture of Aluminium Plates

E.Z. Kordatos, D.G. Aggelis and T.E. Matikas

Abstract Acoustic Emission (AE) supplies information on the fracturing behavior of different materials. In this study, AE activity was recorded during fatigue experiments in metal coupons with a V-shape notch which were loaded in fatigue until final failure. AE parameters exhibit a sharp increase approximately 1000 cycles before than final failure. Therefore, the use of acoustic emission parameters is discussed both in terms of characterization of the damage mechanisms, as well as a tool for the prediction of ultimate life of the material under fatigue. Additionally, an innovative nondestructive methodology based on lock-in thermography is developed to determine the crack growth rate using thermographic mapping of the material undergoing fatigue. The thermographic results on the crack growth rate of aluminium alloys were then correlated with measurements obtained by the conventional compliance method, and found to be in agreement.

Keywords Acoustic emission • Aluminum • Fracture • Thermography

Introduction

Acoustic emission (AE) is a method widely used for real time monitoring of the structural condition of materials and structures. It utilizes the elastic energy released from any crack propagation incident which propagates in the form of stress waves and can be detected by suitable sensors [1]. High rate of incoming signals implies the existence of several active source cracks, while low or zero activity is connected to healthy material [2].

E.Z. Kordatos • D.G. Aggelis • T.E. Matikas (✉)
Department of Materials Science and Engineering, University of Ioannina,
Ioannina 45110, Greece
e-mail: matikas@cc.uoi.gr
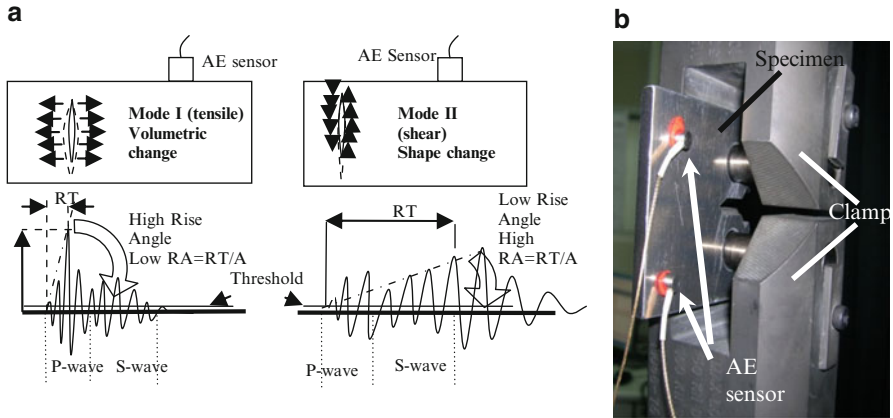
Fig. 1 (**a**) Cracking modes and corresponding AE signals, (**b**) Photograph of the sensors on the specimen

Additionally, the waveform shape depends on the cracking mode, enabling the classification of cracks in different materials [3]. Shear cracks follow tensile as the material approaches to final failure and characterization may lead to an early warning. Figure 1 shows an example of AE waveform emitted by a tensile event. The delay between the onset and the highest peak (called Rise Time, RT), is short leading to a high rise angle of the wave. In case of a shear crack the waveform exhibits much lower rise angle and frequency [4], as seen in the right of Fig. 1. Recently the shape of the initial part of the waveform is examined by the RA value which is defined as the RT over the Amplitude, A and is measured in μs/V [4].

This classification scheme has proven powerful in case of laboratory applications in concrete [5,6] while AE has also been applied in metals [7]. In this study aluminium specimens with notches were fractured in fatigue tests. Measurements of the crack propagation rate were conducted with simultaneous AE monitoring in order to correlate the parameters obtained nondestructively with mechanical results.

Infrared lock-in thermography can be used for defect detection in metal materials. The equipment is portable and can be used in the field [8]. In this paper, the fatigue crack propagation was monitored using infrared thermography and the crack-tip stress field has been mapped using thermoelasticity principles [9]. The technique is based on the fact that stresses within a solid material result in variations of the temperature. When the material is under tensile load, its temperature decreases proportionally to the load, however, when it is under compressive load its temperature increases proportionally to the load. This behavior is known as the thermoelastic effect [10]. The setup includes a radiometric camera, which measures the infrared radiation produced on the surface of the material undergoing cyclic loading, and a real-time correlator called "lock-in module", which measures the change of temperature extracting it from the noise that is specified by the thermal resolution of the camera [9]. Lock–in refers to the necessity to monitor the exact time-dependence between the output signal and the reference input signal [11]. This is done using a lock–in amplifier so that

both phase and magnitude images become available. When the material becomes deformed, a part of the energy necessary to propagate the damage is transformed into heat [12,13].The heat wave, generated by the thermo-mechanical coupling and the intrinsic dissipated energy during mechanical loading of the sample is detected by the thermal camera. In this study, the stress field has been monitored in relation to the fatigue cycles undergone by the sample.

Experimental Procedure

The material was aluminum (AA 7075). Test specimens were manufactured according to ASTM E399 - 09e1. Their size was 60x60 mm with a V-notch and a thickness of 5 mm. For the determination of the crack propagation rate (CPR) a crack opening displacement (COD) meter was fixed in the notch opening. The determination of crack propagation rate followed ASTM E647 - 08e1. The fatigue tests were conducted on an Instron machine with sinusoidal cycle of 3 Hz, while the stress ratio was set to R=0.2 and the amplitude was 4 KN. Concerning acoustic emission two piezoelectric sensors (Pico, Physical Acoustics Corp., PAC) were attached frequency bandwidth is within 50 to 800 kHz. The signals were recorded by two channels in a PCI-2 board, PAC with a sampling rate of 5 MHz. Additionally, an infrared camera (Cedip) used for lock-in thermography. The size of the area for thermographic imaging is 320x240 pixels with a resolution of 20 mK and integration time 1500μs.

Method for thermographic monitoring of fatigue crack growth

In order to determine the crack growth rate using thermographic mapping of the material undergoing fatigue a specific procedure was developed. This procedure consists in the following steps: (a) the distribution of temperature and stress on the surface of the specimen was monitored during fatigue testing using lock-in thermography. (b) Thermal images were saved as a function of testing time in the form of a movie for post-processing. (c) After the test was concluded, in post-processing mode, equally spaced reference lines of the same length were set on the thermographic image in front of the crack-starting notch (Fig. 2a).(d) Along these lines the stresses were estimated using the thermographic data for a specific fatigue cycle. The idea was based on the fact that the stress monitored at the location of a specific reference line vs. time (or fatigue cycles) would increase when the crack approaches the line (crack type I), then would attain a maximum value when the crack tip reaches that reference line at the point Y_o (crack type II), and finally would decrease when the crack has crossed that line (crack type III), as it is shown in Fig. 2a, b. (e) The stress was also monitored during the test for all fatigue cycles. Figure 2c shows the maximum values of stress along a specific reference line vs. the number of fatigue cycles. The cycle N_o for which this stress maximum occurs denotes the moment that the crack crosses that reference line, (d). This way, the points Y_o^i (points of crack crossing a reference line i) are determined, as well as the fatigue cycles N_o^i for which the crack has crossed a specific reference line i.
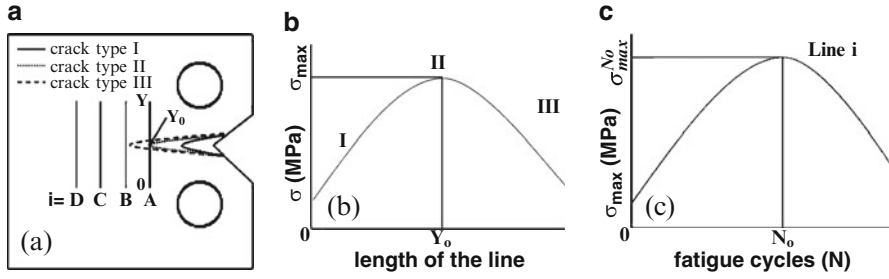
Fig. 2 Method for thermographic monitoring of fatigue crack growth
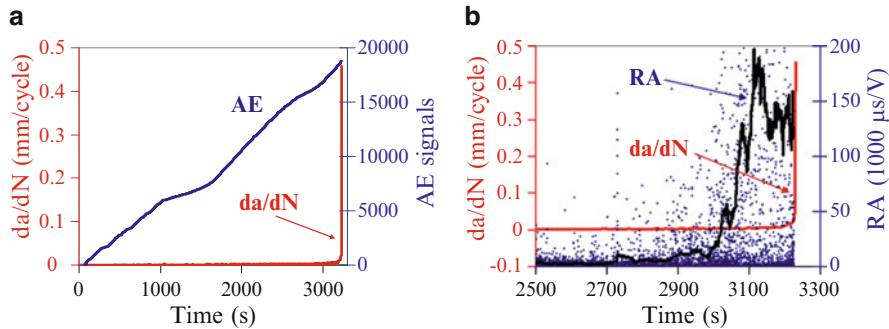
Fig. 3 Time history of CPR and cumulative AE (**a**), CPR and RA(**b**)

Results

Figure 3 shows the crack propagation rate (da/dN) as a function of time. As typically expected in metal fatigue the rate increases exponentially. The final failure of the specimen occurred at 3231 s. AE monitoring presented a more or less constant activity throughout the experiment. A typical example is again seen in Fig. 3a. AE signals are recorded shortly after the start of the test.

The AE parameters show a clear trend. Figure 3b presents the RA value of the signals. Approximately 200 to 300 s before the final fracture, the RA starts to increase sharply. The solid line stands for the moving average of the recent 150 hits, which shows an increase at 3000 s, much earlier than the specimen's fracture. As discussed above, this shift of the RA value implies also the shift between the tensile and shear fracture modes; actually this is the sequence of the cracking modes within a typical fatigue specimen of this kind. Figure 4a shows a photograph of the fracture surface after the end of the experiment. The crack propagates horizontally for approximately 20 mm away from the notch. Later, the fracture surface becomes curved. This is attributed to the local plane stress field. Due to the small thickness of the plate, the stress perpendicular to the surface (σ_z) is zero (Fig. 4b). Therefore,
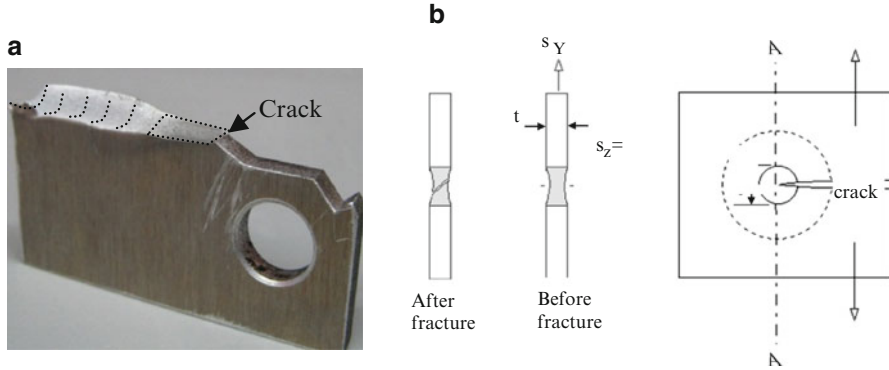
Fig. 4 (**a**) Part of the specimen after fatigue failure. (**b**) Plane stress fracture
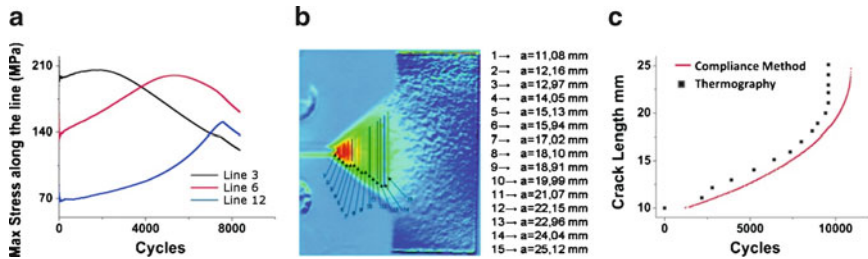
Fig. 5 (**a**) Max stress along the line vs. cycles. (**b**) Thermograph with reference lines. (**c**) Crack length vs. cycles, correlation of lock-in thermography and compliance method results

although the crack starts to propagate horizontally dictated by the notch under the application of the tensile stress (σ_Y), final fracture occurs due to the shear stresses, which are maximum at 45°. The AE behavior is repeatable for all the three specimens tested.

As to thermography, using the procedure described in the previous section, the local stress vs. time was measured along the reference lines in front of the notch. The maximum value of stress vs. the number of cycles was then plotted (Fig. 5a). As expected, Fig. 5a shows that the local stress, monitored at the location of each line, increases while the crack is approaching that line, then attains a maximum when the crack tip is crossing the line. Finally, after the crack has crossed the line, the local stress measured at the location of the line decreases. Figure 5b shows the location of reference lines. Crack growth rate was determined from the location of the lines and the cycle in which the crack reaches each line (Fig. 5c). Comparison between lock-in thermography and compliance method shows that the first can predict the crack propagation approximately 1000 cycles earlier than the latter. The results were repeatable in all specimens tested.

Conclusion

This paper presents some preliminary results on the acoustic emission and thermography monitoring during fatigue of aluminium coupons. The aim is the correlation of NDT parameters with damage accumulation and the fracture mode. Study of the AE behaviour shows that certain characteristics undergo clearly measureable changes much earlier than final fracture (approximately 1000 to 1200 cycles before final failure). The mechanism which is responsible for this change seems to be the shift between the tensile and the shear fracture modes which typically occurs in thin metal coupons with a notch. It was also demonstrated that crack growth can be monitored by the means of lock-in thermography. The results obtained using the noncontact technique showed good match with the conventional compliance method. The significant capability of this technique is the detection and monitoring of crack growth, even if it is not visible on the specimen's surface and propagates inside the material.

References

[1] Grosse, C.U., Ohtsu, M. (2008). Acoustic Emission Testing, Springer, Heidelberg.

[2] Aggelis D.G., Shiotani T., Momoki S., Hirama A. (2009). *ACI Materials Journal*., vol. 106, n. 6, p. 509–514.

[3] Anastassopoulos, A.A., Philippidis, T.P. (1994). *Journal of Acoustic Emission* vol. 13, n. (1/2), p. 11.

[4] RILEM Techincal Committee 212-ACD, (2009). (http://www.rilem.net/tcDetails.php?tc= 212-ACD).

[5] Soulioti, D.V., Barkoula, N.M., Paipetis, A.S., Matikas, T.E., Shiotani, T., Aggelis, D.G. (2009). *Construction and Building Materials*, vol. 23, p. 3532.

[6] Ohno, K., Ohtsu, M. (2010). *Construction and Building Materials*, vol. 24, p. 2339.

[7] Rousset, G., Martin, E., Lamon J., (2009). *Composite Science and Technology* vol. 69, p. 2580.

[8] Wong, B.S., Tui, C.G., Bai, W., Tan, P.H., Low, B.S. and Tan, K.S. x, (2008), *International NDT-and Condition Monitor*. 41, p. 504–509.

[9] E. Z. Kordatos; D, P. Myriounis; S, T. Hasan; T. E. Matikas, (2009), Proceedings SPIE, Vol. 7294, 72940X; doi:10.1117/12.815207.

[10] Bremond, P., Potet, P., (2001), Cedip Infrared Systems, Lock-in thermography, A tool to analyze and locate thermo-mechanical mechanism in materials and structures, Thermosence XXIII.

[11] Maldague, X.V., (2001), Theory and practice of Infrared technology for nondestructive testing. John Wiley & Sons Inc, New York.

[12] Choi, M-Y, Park, J-H, Kang, K.S., Kim, W-T., (2006), Application of Thermography to Analysis of Thermal Stress in the NDT for Compact Tensile Specimen. 12th A-PCNDT, 5th – 10th Nov Auckland, New Zealand.

[13] ASM Handbook, (1989), Nondestructive Evaluation and Quality Control Vol.17.

Nonlinear Acoustic Effect due to Evolution of a Crack and Detection of Micro-Scale Cracks in a Fatigue Process

Y-M. Cheong

Abstract Nonlinear acoustic effect is sensitive to a micro-scale crack or pre-cracking stage of the fatigue process. A resonant ultrasound spectroscopy technique was used for a diagnosis of micro-scale crack in a compact tension (CT) specimen. Information on the normalized amplitude and resonance frequency was analyzed to quantify the degree of nonlinearity and diagnose the micro-cracks. The damage produces a nonlinear stress-strain relationship and the nonlinearity can be measured by increasing excitation amplitudes. The more damage, the larger is the level of a nonlinearity, and it can be used for diagnosis of micro-cracks. The amount of nonlinearity is highly correlated to the damaged state of the material. A shift of resonance frequency as a function of driving voltage or strain is chosen as a nonlinear parameter to correlate the micro-cracks or damage. In addition amplitude of a normalized resonance pattern also reflects the nonlinearity. The normalized pattern of an intact CT specimen and cracked CT specimen were compared.

Keywords Diagnosis of micro-scaled crack • Nonlinear acoustics • Ultrasonic resonance

Introduction

The nonlinear phenomena are widely used for nondestructive testing and characterization of damages in a variety of materials because material nonlinearity is an extremely sensitive indicator of damage, fatigue and cracking [1-5]. Micro-scale cracks in a material are one of the major factors for the determination of life of a

Y-M. Cheong (✉)
Korea Atomic Energy Research Institute, Yusong P.O. Box 105, Daejeon,
305-600, Republic of Korea
e-mail: ymcheong@kaeri.re.kr

structure as well as for the structural integrity. Because of the detectability limit of current nondestructive evaluation methods, most of the cracks are detected after half of the structural life. It is now well established that material nonlinearity is an extremely sensitive indicator of damage, fatigue and cracking. Micro-scale cracks caused by materials degradation and damage will affect the resonance spectrum of a sample only very slightly and be masked by the resolution of the frequency spectrum when we use a standard linear Resonance Ultrasound Spectroscopy (RUS) analysis. The micro-scale damages, however, can produce a nonlinear stress-strain relationship, and this nonlinearity can be measured by increasing the dynamic strain i.e. excitation amplitude in a RUS device. The more damage, the larger is the level of nonlinearity, and it can be used to for the diagnosis of micro-cracks [6]. On the contrary, undamaged or intact material shows essentially linear behaviour in their resonance response. Nonlinear Resonant Ultrasound Spectroscopy (NRUS) has been applied for micro-damage assessment in the human bone [7, 8].

In this study, the feasibility of NRUS for a diagnosis of micro-cracks is investigated. A shift of resonance frequency as a function of driving voltage or strain is chosen as a nonlinear parameter to correlate the micro-cracks or damage. In addition the amplitude of normalized resonance patterns of intact sample and cracked sample were compared and analyzed.

Theory

Among the different nonlinear elastic wave spectroscopy (NEWS) techniques nonlinear ultrasonic spectroscopy (NRUS) has been successfully applied for detection and characterization of damages and cracks in bone and rock materials as well as ceramics materials [7, 8]. The elastic modulus of the material is written as follows

$$K = K_0 \left[1 + \beta\varepsilon + \delta\varepsilon^2 \right] - \alpha\left(\varepsilon, \dot{\varepsilon}\right) \tag{1}$$

where K_0 is the linear modulus, ε the strain, $\dot{\varepsilon}$ the strain rate, α the nonlinear hysteretic parameter depending on the strain derivative due to hysteresis. The nonlinear parameters β and δ describe the classical non-linear terms due to standard anharmonicity. The shift of the resonance frequency is strongly dependent on the driving amplitude and the nonlinear hysteretic behaviour proportional to dominates and the first order approximation gives

$$\frac{f_0 - f}{f_0} = \alpha\Delta\varepsilon \tag{2}$$

where f_0 is the linear resonant frequency and f the resonant frequency for an increasing driving amplitude.
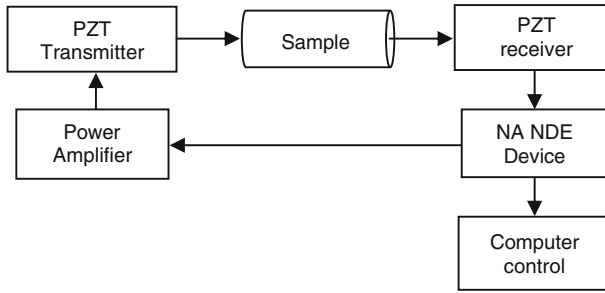
Fig. 1 Block diagram for nonlinear resonant ultrasound spectroscopy

Experimental Procedure

A fully digitized resonant ultrasound spectroscopy system was used to control the power amplifier for the excitation of the required ultrasound with a sweep function, signal processing of the received signal, shown in Fig. 1. The frequency vs. normalized amplitude is measured at the different driving voltage levels.

Standard 1/2T-1CT specimen with dimension of 63.5 mm x 61 mm x 12.72 mm was fabricated with SA508-Gr.3 material, which is used for a nuclear reactor pressure vessel. In order to fabricate a natural close crack, a fatigue test was carried out with an Instron universal test machine. The number of cycles of each step are N = 1000, 5000, 10000, 20000, 40000, 60000 and 120000 cycles with 10 Hz.

In order to shield it from vibration, temperature change, and even air flow, the sample is suspended with loops of synthetic fiber such as dental floss inside a double-wall chamber. The temperature inside the chamber was monitored with a thermocouple with a dummy specimen, shown in Fig. 2. The temperature variation was kept within ±0.10°C during data acquisition. Considering the variation of the elastic constants or acoustic wave velocity with temperature, all measured ultrasonic resonance data were compensated to the temperature of 25°C. The temperature compensation was established based on the temperature dependence of SA 508 Gr. 3 materials give by: [9]

$$\left(E = 214.54 - 0.0787T\right)\left(Gpa, T = °C\right) \tag{3}$$

The resonance frequency can be compensated as,

$$f_r^2 = K\left(214.54 - 0.0787T\right) \tag{4}$$

where $K = L / \rho = const.$ and L dimension, ρ density.

The amount of dynamic strain at the resonance was estimated and verified by a measurement by a laser Vibrometry. When the excitations were 2 ~ 10 volt, the dynamic displacement, $\Delta l = 200 ~ 600$ *nm*, can be correlated to the dynamic strain of $\varepsilon = 3.3 ~ 10.0 \times 10^{-6}$.
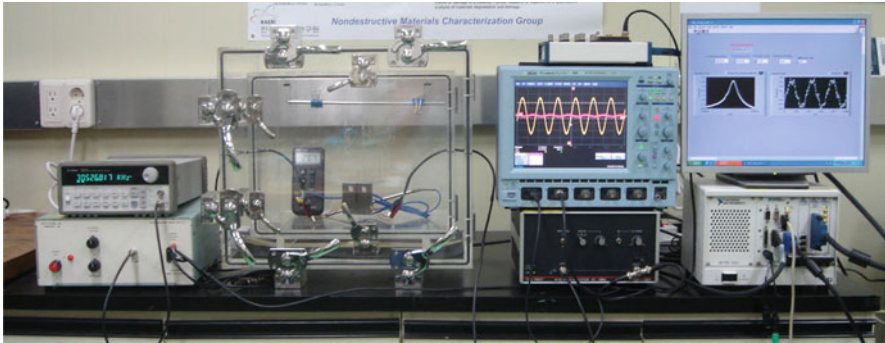
Fig. 2 Experimental setup and a chamber to maintain constant temperature and free of vibration
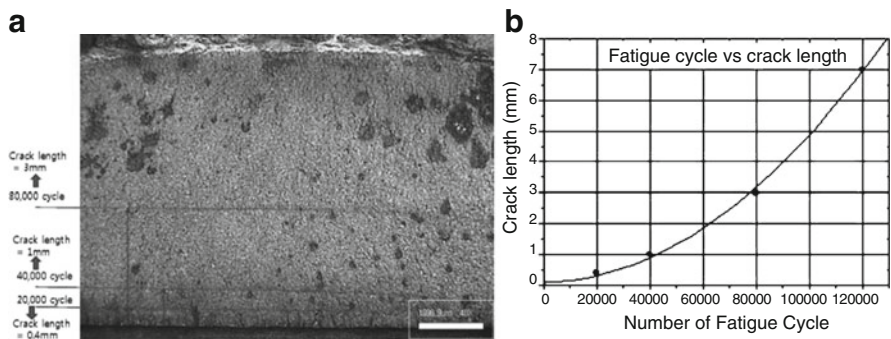
Fig. 3 (**a**) Optical image of cracked surface (**b**) Estimation of fatigue crack length at each stage of fatigue cycle

Results and Discussion

The fatigue cracks were fabricated progressively with the different fatigue cycles. The optical image of the cracked surface is shown in the Fig. 3a. Based on the heat tinted image of the crack surface, a correlation between the crack lengths and cycles is estimated and shown in the Fig. 3b, which can be consistent with Paris law.

Based on the relationship between the fatigue cycle and crack length, the nonlinear parameters were investigated. At the resonance mode, (1,3) Mode, the normalized resonance patterns of various cracked specimen with an increase of excitation amplitude from 1 volt to 160 volt are shown in Fig. 4. As the fatigue crack increases, shifting of the resonance frequency can be observed with an increase of excitation amplitudes. As the excitation voltage increases, little changes of the resonance frequency were observed at an early stage of fatigue, such as crack length of 15 μm, shown in Fig. 4a. A significant change of resonance frequency was observed from the specimen with crack length of 80 μm. It is also found that the normalized amplitude
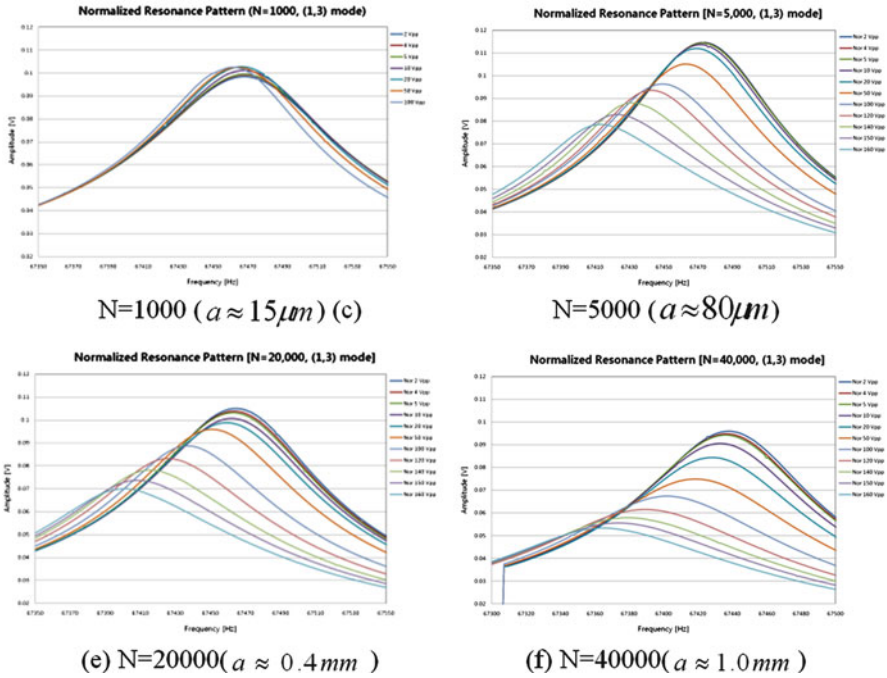
Fig. 4 Normalized resonance patterns from CT specimens with different fatigue cycles

also decreased with the crack length of 80 um (Fig. 4c) in comparison with the early stage of cracking (Fig. 4a).

The amount of resonance frequency shifts for each fatigue step, i.e. crack length is plotted in Fig. 5. It can be concluded that the amount of resonance frequency shift can be increased at the early stage of cracking, but not increased proportionally to the crack length. Therefore (1,3) resonance mode is sensitive to the early stage of crack initiation and can be used for early detection of fatigue cracks of 0.1 mm. These nonlinear parameters can be a potential tool for the early detection of micro-cracks or damage of a material.

Conclusions

A NRUS technique to diagnose the micro-cracks or damage was investigated. Two nonlinear parameters, resonance frequency shift and amplitude of normalized resonance patterns were chosen for the evaluation of fatigue cracks. The normalized resonance pattern from an intact CT specimen is exactly the same even though the driving amplitude varies, which means a linear elastic behaviour.

For the cracked specimen, the resonance frequency shifts downward and normalized resonance amplitude decreases as the excitation voltage increases. It means an
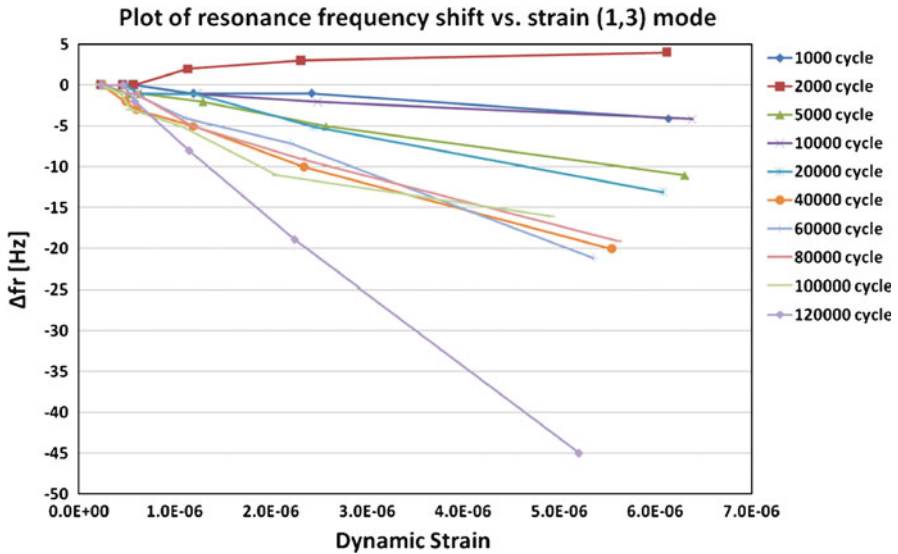
Fig. 5 Resonance frequency shift vs. dynamic strain for each fatigue steps [1,3 mode]

acoustic nonlinearity is observed from the cracked specimen. Some resonance mode is sensitive to the early stage of crack initiation and can be used for early detection of fatigue cracks of 0.1 mm.

References

[1] Johnson P. A., (1999), *Materials World, The Journal Institute Materials*, vol. 7, p. 544.
[2] Van Den Abeele K. E., Johnson P. A., and Sutin, A., (2000), *Research on Nondestructive Evaluation*, vol. 12, p. 17.
[3] Van den Abeele K. E., Carmeliet J., Tencate J. A., and Johnson P. A., (2000), *Research in Nondestructive Evaluation s*, vol. 12, p. 31.
[4] Ostrovsky L., Johnson P., (2001), *Rivista del Nuovo Cimento*, vol. 24, p. 1.
[5] Johnson P. A., Sutin A., (2005), *Journal of the Acoustical Society of America*, vol. 117, p. 124.
[6] Cheong Y. M., Alam, M. K., (2009), *Trans. Korean Nuclear Society Spring Meeting, Jeju, Korea*.
[7] Muller, M., (2006), *Ultrasonics*, vol. 44, p. 245.
[8] Muller, M., (2008), *Journal Biomechanics*, vol. 41, p. 1062.
[9] Cheong Y. M., Kim J. H., Jung H. K., and Hong H, (2001), *Trans. 2001 Spring Conf. Korean Soc. Nondestructive Testing*.

New Ultrasonic Methodology for Determining Temperature Gradient and Its Application to Heated Materials Monitoring

I. Ihara, M. Takahashi, and H. Yamada

Abstract In various fields of science and engineering, temperature measurement has become one of the most fundamental and important issues. For example, in industrial materials processing, it is required to measure the temperature gradient and its transient variation in the material being processed at high temperatures because the temperature state during processing crucially influences the quality of final products. Such temperature measurements are also required for making structural health monitoring at high temperature environments. In this work, a new ultrasonic method for monitoring temperature gradient of a material being heated or cooled is presented. The principle of the method is based on the temperature dependence of the velocity of ultrasonic wave propagating through a material. An effective analysis method coupled with a finite difference calculation is developed to determine one-dimensional temperature distributions in a heated material. To verify the practical feasibility of the method, some experiments have been made. A single side of a steel plate of 30 mm thickness is heated by contacting with a heater and subsequently cooled down by water. Ultrasonic pulse-echo measurements are performed during heating and cooling, and the measured transit time of ultrasound across the steel is used for the analysis to determine the temperature gradient in the steel. Furthermore, rapid heating by contacting with molten aluminium at 700 degree C and rapid cooling by contacting with an ice are evaluated and the transient variations of the temperature gradient in the steel have successfully been monitored.

Keywords Heated materials • Internal temperature • Surface temperature • Temperature distribution • Ultrasonic thermometry

I. Ihara (✉) • H. Yamada
Nagaoka University of Technology
e-mail: ihara@mech.nagaokaut.ac.jp

M. Takahashi
Sendai National College of Technology

Introduction

Measuring temperature has become one of the most fundamental and important issues in the fields of experimental science and engineering. In particular, in materials development and manufacturing, it is strongly required to monitor the temperature distribution and its transient variation of the material being processed at high temperatures because the temperature field in the material crucially influences the quality and productivity of final products. Thus, in-situ or in-process monitoring technique for the temperature distribution is quite beneficial not only for basic research of materials but also for developing an effective process control in materials processing. Although a conventional thermocouple technique is widely used for temperature measurements, it is not always acceptable for obtaining the spatial distribution in measurements because of difficulty of installation to materials. In addition, the thermocouple may not be appropriate for monitoring a transient variation of temperature because of its relatively slow time response in measurements. Ultrasound is expected to be an alternative for monitoring the internal temperature and its gradient in materials because of its capability to probe the interior of materials and its high sensitivity to temperature [1-6]. The advantages of using ultrasound are that it provides non-invasive measurements for internal temperatures of materials under heating or cooling. It is also attractive that ultrasound provides a faster time-response than conventional thermocouple techniques in measurements. In our previous works [7-9], effective methods consisting of an ultrasonic pulse-echo measurement and an inverse analysis were proposed and applied to some heated plates to determine the internal temperature distributions. In this work, to demonstrate the practicability of the ultrasonic method, this method has been applied to the monitoring of transient variations of temperature gradients in steels during rapid heating and cooling.

Method for Depth Profiling of Temperature

Principle of ultrasound thermometry

It is known that the velocity of ultrasonic wave propagating through a medium changes with the temperature of the medium. The principle of temperature measurement by ultrasound is based on the temperature dependence of the ultrasonic wave velocity. Assuming a one-dimensional temperature distribution in a medium, the transit time t_L of an ultrasonic pulse-echo propagating in the direction of the temperature distribution can be given by

$$t_L = 2\int_0^L \frac{1}{v(T)}dx,$$

(1)

Schematic of a
one-dimensional temperature
distribution in a material
whose single side A is heated
uniformly
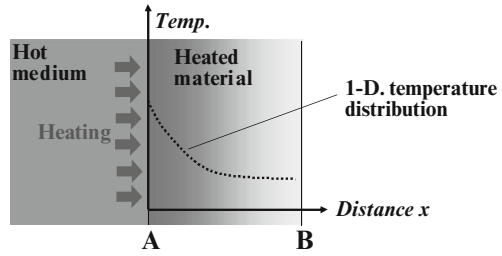
where L is the thickness of the medium, and $v(T)$ is the ultrasonic velocity which is a function of temperature T. The temperature dependence of velocity depends on the material property and may be expressed by a simple equation such as a linear or quadratic function for a certain temperature range. In general, the temperature distribution in a medium being heated can be given as a function of location x and time t. Such a temperature distribution $T(x, t)$ is subjected to the thermal boundary condition of the heated medium. Therefore, on the basis of Eqn. (1), if an appropriate inverse analysis with a certain boundary condition is properly used, it could be possible to determine the temperature distribution from the transit time t_L measured for the heated medium. In fact, such ultrasonic determination of temperature distribution of a heated silicone rubber plate was demonstrated in our previous work [7].

Ultrasound thermometry combined with finite difference calculation

Figure 1 shows a schematic of an internal temperature gradient in a material whose single side is uniformly heated or cooled. To investigate the temperature gradient, a one-dimensional unsteady heat conduction with a constant thermal diffusivity is considered. Assuming that there is no heat source in the material, the equation of heat conduction is given by [9]

$$\frac{\partial T}{\partial t} = \alpha \frac{\partial^2 T}{\partial x^2}, \tag{2}$$

where T is temperature, x is the distance from the heated or cooled surface, t is the elapsed time after the heating or cooling starts, α is the thermal diffusivity. It is known that the temperature distribution can be estimated by solving Eqn. (2) under a certain boundary condition. In actual heating processes, however, the boundary condition is not always being held stable and often being changed transiently during heating. Such boundary condition is usually difficult to know and even to measure it. Because of little knowledge about boundary condition, temperature gradient is hardly determined from Eqn. (2). This kind of problematic situation often occurs when a material is heated by contacting with a very hot medium such as a molten metal.

To overcome the problem mentioned above, an effective method for evaluating the internal temperature distribution was develped [8, 9]. The method consists of an ultrasonic pulse-echo measurement and an inverse analysis coupled with a one-dimensional finite difference calculation. The advantage of the method is that no boundary condition at the heating surface is needed. A one-dimensional finite difference model consisting of a large number of small elements and grids is used for analyzing heat conduction in a thick material. Using two information, the initial temperature distribution and the temperature dependence of the ultrasonic velocity of the material to be evaluated, the temperature distribution in the material and its temporal variation can successively be obtained as long as the transit time of ultrasound propagating in the direction of temperature gradient of the heated material, is continuously being measured and the temperature at B is being known. The detailed procedure of the method is described in Refs. [8, 9].

Experiments and Results

Slow heating and cooling

To verify the feasibility of the proposed method, internal temperature gradients of a thick steel plate are evaluated during relatively slow heating and cooling. Figure 2 shows a schematic diagram of the experimental setup used. This system provides not only ultrasonic pulse-echo measurements but also temperature distribution measurements using thermocouples, so that the validity of the ultrasonically determined temperature distribution is verified by comparing with that measured using the thermocouples. A steel plate (JIS type: SKD61) of 30 mm thickness is used as a specimen. At first, the bottom surface of the plate is heated by contacting with a heater of 200 °C for a period of about 100 s, and then the surface is cooled by water. A longitudinal ultrasonic transducer of 2 MHz is installed on the top surface of the steel plate to make pulse-echo measurements for the steel. To obtain a reference value of the temperature distribution inside the plate, five thermocouples, TC1-TC5, are inserted into the plate. In addition, an infrared radiation camera is used to measure the temperature at the top surface of the plate. Ultrasonic pulse-echo measurements are performed during the heating and cooling, and echoes reflected from the bottom surface and temperatures at each position are continuously acquired every 0.2 s with a PC based real-time acquisition system. The sampling rate of ultrasonic signal is 100 MHz. Signal fluctuation due to electrical noise in measurements is reduced by taking the average of ten ultrasonic signals. The transit time through the plate can precisely be determined from the time delay between the first and second reflected echoes, by taking a cross-correlation between them. The transit times acquired continuously during the heating and cooling are used for the inverse analysis to determine the temperature distribution and its temporal variation. The estimated temperature distributions are shown in Fig. 3, where the numbers shown in

Fig. 2 Schematic of the experimental setup
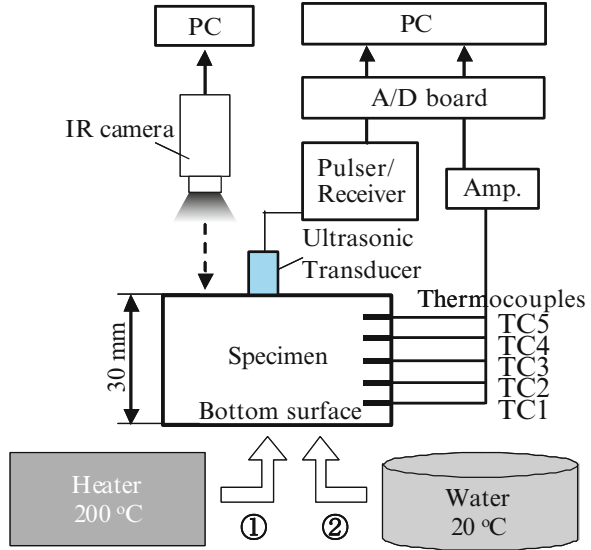
Fig. 3 Variations in temperature gradients in the steel plate with elapsed time
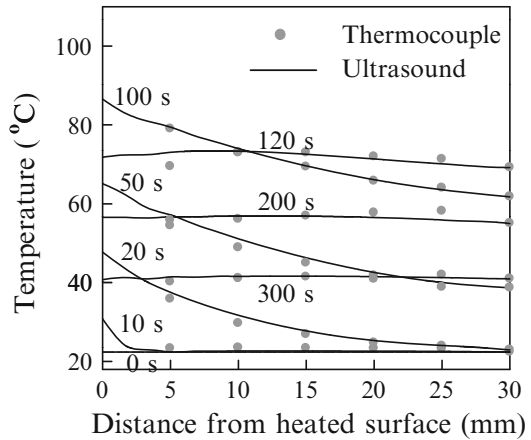
Figure 3 denotes the elapsed time after the heating starts. It is noted that the temperature dependence of the ultrasonic velocity, $v(T) = -6.036 \times 10^{-4} T^2 - 0.542T + 5931.7$ (m/s) and the initial temperature of the steel before heating, 23.3 °C, are used in the estimation. It can be seen in Fig. 3 that the temperature distribution estimated ultrasonically and its variation almost agree with those measured using thermocouples, while there are discrepancies between them in the range of high temperatures. Although the reason for the discrepancy is not clear at this moment, It is found that the proposed ultrasonic method does work properly. It is noted that it takes about 20 ms to calculate a temperature distribution at each time step from the measured ultrasonic data, which may be fast enough to make a real-time monitoring.

Fig. 4 Variations in temerature gradients of the steel during heating by molten aluminum
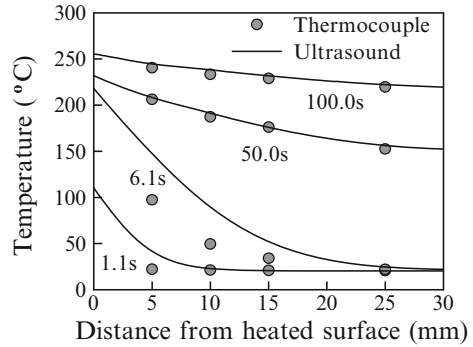
Fig. 5 Variations in temperature gradients of the steel during cooling by ice block
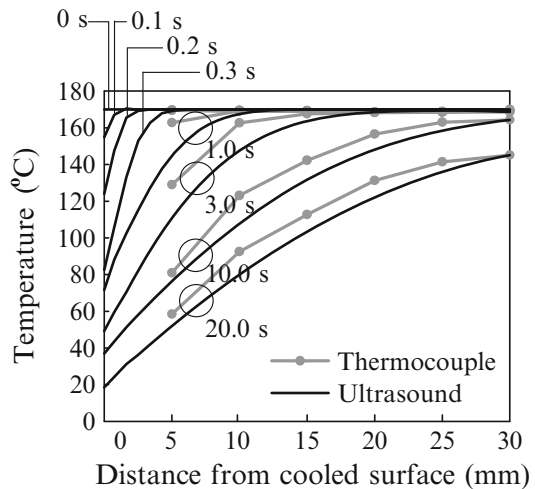
Rapid heating and cooling

The proposed method is applied to the internal temperature monitoring of the steel during rapid heating or cooling. For rapid heating the bottom of the steel plate is heated by contacting with 600 °C molten aluminium during about 100 s. For rapid cooling the bottom of the steel is cooled down by contacting with a block of ice. The experimental setup used is almost the same as that shown in Fig.2. Figures 4 and 5 are the estimated results showing the variations in the temperature gradients in the steel during heating and cooling, respectively. In the experiment with the molten alminum, the maximum temperatur of the steel surface did not reach the temperature of the molten alminum during the heating because of the heat capacity of the steel as well as the limited volume of the molten aluminum. It can be seen in each results that both temperature distributions

determined by ultrasound and using thermocouples show a similar tendency. Although there are discrepancies between ultrasound and thermocouples in early stage, this may be because of relatively slow time-response in the thermocouples measurements. The ultrasonic method is consdiered to give appropriate results because of its faster time-response to temperature change.

Conclusions

A new ultrasonic method for measuring internal temperature gradient of a heated material is proposed and its practicability is demonstrated through experiments with a steel plate under heating or cooling. Although further study is necessary to improve the robustness and accuracy in measurement, it is expected that the method will be a useful means for in-situ or on-line monitoring of transient temperature variation in materials processed at high temperatures.

References

[1] Simon, C., VanBaren, P., and Ebbini, E. (1998), *IEEE Trans. Ultrason. Ferroelectr. Freq. Control*, vol. 45, no. 4, p.1088.

[2] Chen, T. -F., Nguyen, K. -T., Wen, S. -S., and Jen, C. -K. (1999), *Meas. Sci. Technol.*, vol. 10, p. 139.

[3] Balasubramainiam, K., Shah, V. V., Costley, R. D., Boudreaux, G., and Singh, J. P. (1999), *Rev. Sci. Instrum.*, vol. 70, no. 12, p.4618.

[4] Tsai, W. -Y., Chen, H. -C., and Liao, T. -L. (2005), *Meas. Sci. Technol.*, vol. 16, p. 548.

[5] Mizutani, K., Kawabe, S., Saito, I., and Masuyama, H. (2006), *Jpn. J. Appl. Phys.*, vol. 45–5B, p. 4516.

[6] Huang, K. N., Huang, C. F., Li, Y. C., and Young, M. S. (2002), *Rev. Sci. Instrum.*, vol. 73, no. 11, p. 4022.

[7] Takahashi, M., and Ihara, I. (2008), *Jpn. J. App. Phys.*, vol. 47, p. 3894.

[8] Takahashi, M., and Ihara, I. (2008), *Mod. Phys. Lett. B*, vol. 22, no. 11, p. 971.

[9] Takahashi, M., and Ihara, I. (2009), *Jpn. J. App. Phys.*, vol. 48, no. 7, GB04.

[10] Meyers, G. E. (1971), *Analytical Methods in Conduction Heat Transfer*, McGraw-Hill, New York, p. 10.

[11] Press, W., Teukolsky, S., Vetterling, W., and Flannery, B. (2003), *Numerical Recipes in C++*, Cambridge University, New York, p. 849.

Inverse Problem for Material Analysis by Ultrasound

F. Bettayeb and M. Hakem

Abstract Internal defects detection by ultrasound non destructive testing is widely used in industry. Ultrasonic time signal data are difficult to interpret since they require continuous signal analysis for each point of the piece. Inverse problem in materials analysis puts some challenges because the composition variables are both discrete and continuous and because the engineering properties are highly nonlinear functions.

   In this paper we address the non linear features of back scatted ultrasonic waves from steel plate, for understanding its micro structural behaviour. The experiments show a challenging interface between material properties, calculations and ultrasonic wave propagation modelling.

Keywords Multiscale analysis • Structural noise • Ultrasonic NDT/NDE • Wavelet

Introduction

Due to the exact defect localization, sensitivity to inner flaw detection and identification benefit, ultrasonic testing is widely used in many material industrial inspections as austenitic steel or composite samples. Ultrasonic data are difficult to interpret since they require continuous signal analysis for each point of the inspected material. Due to the inherent inhomogeneous and anisotropy nature of these materials, ultrasonic waves undergo high acoustic attenuation and scattering effect, making data interpretation highly complex. Echoes backscattered from the front and back surface of specimen, combined with other backscattered flaws or micro-

F. Bettayeb (✉) • M. Hakem
Research Centre on welding and control. CSC, Route de Dely Brahim, Bp: 64, Chéraga, Algiers, ALGERIA
e-mail: fairouz_bettayeb@email.com

structures, are often overlapped, making flaws identification difficult. Various de-noising methods as median filtering, non-linear filtering, adaptive time-frequency filtering, correlation technique, split spectrum processing, artificial neural network, Wigner-Ville distribution, wavelet, Hilbert-Huang and others are useful, if this noise is described as a zero-mean Gaussian white noise. But if the structural noise is time invariant and slightly correlated with the signal frequency band; therefore, these methods are not very helpful. In this paper we present a new structural noise features analysis based on an energy smoothing algorithm. The new de-noising algorithm performs an accurate signal analysis as well as detection of little defects of 1mm. The following experiments obtained from structural noise signal captured from a steel plate, will give significant insights into the relationship of backscattered noise and microstructures which can help to micro structural dimension scales understanding

Theoretical Backgrounds

Estimation of a signal embedded in noise requires taking advantage of any prior information about signal and noise. Until recently, signal processing estimation was mostly Bayesian and linear. Non-linear smoothing algorithms exist in statistics, but these procedures were often ad-hoc and complex. Two statisticians, Donoho and Johnstone [1] proved that a simple thresholding algorithm in an appropriate basis can be a nearly optimal non-linear estimate. When the signal is slice smooth function, wavelet estimators have optimal properties and much lower risk [2]. In these methods the choice of threshold is a key question. Therefore, optimizing threshold and improving the computational performance of threshold estimator were the main points of many works. Wavelet theories are the most effective and promising techniques that can withdraw signal non-stable features. However, traditional wavelet analysis based attribute extraction, is complex and limited to the extracted characteristic [1-2].

Principle of wavelet for signal de-noising

If f (x) is bounded over (b_1, b_2), WTf$_\xi$ (x, a) satisfies [2]:

$$|\mathrm{WT}f_\xi(\mathrm{x,a})|\,\mathrm{Ka^a} \tag{1}$$

Then f(x) is uniformly Lipschitz a on (b_1, b_2), the constant K is depend on ξ (x). We can choose $a = 2^j$, *which* implies that:

$$|\mathrm{WT}f_\xi(\mathrm{X,a})| \leq \mathrm{K2^{ja}} \tag{2}$$

From formula (2), it can be seen that the amplitudes after wavelet transform increases with the increase of scale j for a singularity bigger than zero, the amplitudes decreases with the increase of scale j for a singularity lesser than zero, namely white noise has negative singularity. However, the coefficient of WT has positive singularity. The signal singularity and different character of noisy wavelet transform property are the main bases discriminated signal and noise among wavelet transform topic [3-4].

Wavelet threshold estimator

Ultrasonic echo-signal contaminated by noise can be expressed as [2]:

$$Y(t_i) = f(t_i) + n(t_i) \quad i = 1, 2, .., N \tag{3}$$

We consider samples of a function f that is corrupted by gauss white noise of variance σ^2. Y is the measured signal and $n = \sigma z_i$ denotes an additive noise function where z_i is a sequence of (0, 1) random variables with $\sigma > 0$. WT modulus maximum of original signal increases as level increases, so the signal can be distinguished from noise by the different trend of modulus maximum in the multi-scale space.

In a basis $B = g\{_m\}_{0 \leq m \leq n}$, a diagonal estimator of f from Y = f + n can be written [2]:

$$F^{\%} = \sum_{0 \leq m \leq n-1} d_m \left(Y_B [m] g_m \right) \tag{4}$$

Where $Y_B [m] = \langle Y, g_m \rangle$ and d_m is thresholding functions.

Threshold computation

Selected threshold T must pass the biggest level of noise. It is proved that the biggest amplitudes of noise have a higher probability which is lower than general threshold $\sigma \sqrt{2 \log N}$ where σ is noise variance. Therefore, threshold $T = \sigma \sqrt{2 \log N}$ is often selected. If signal length is identified, selecting threshold will be changed to estimate noise variance σ. If M_x is in the middle position of wavelet coefficient $\{<X, \Psi_{i, m}>\}_{0 <= m <= N/2}$ within the smallest scale of noisy signal function X it will be proved that the estimate value of noisy is $\sigma \approx median(x)$ /0.6745, where M_x is the middle value of wavelet coefficient according to the levels instead of the average value. At present, there are three frequently-used thresholding methods: hard-thresholding, soft-thresholding and semi-soft-thresholding functions

New Approach and Algorithm

In many sciences, the study of a dynamical system or signal is based on the search of the feature scale space to be used as reference for the other system measurements. Generally the scaling invariance indicates powerful data organization prevalence. This is well admitted by the multi-resolution theory, where wavelet coefficients have significant incidence for only few locations in the time scale space. I.e. the energy is mainly localized in specific frequencies and positions of the scale space. As each signal de-noising system is considered to be complex, the case of the micro structural noise can be expected as a reliable scheme of random/complex system sample. So, it can be well adapted to a chaotic dynamical system design. In this work, multi-resolution theory and chaotic dynamical system philosophy are combined. This pointed to a de-noising strategy which is only energy based method. This new filtering based wavelet and smoothing approach used in this work and pointed up in [9], allows disabling the need of threshold estimator choice; By means of noise analytical functional formulation.

In fact results denote recurrent signal distortion by discrete analysis [7-8-9] while wavelet packet analysis gives refined signal reconstruction [7]. As well as dual continuous-wavelet packet process, needs extensive data bank experiments [8-9]. Thus automatic threshold control aim recommends noise features investigation. The idea is to make approximation of the noise with a basis function. The algorithm in [9] enables as well as noise basis function identification, and filtering process without traditional thresholding rules; threshold levels are identified by wavelet energy contents. Noise energy coefficients vector is extracted from subtraction of the signal maximum energy coefficients vector. The process was used on database of 65 experimental pure ultrasonic signals.

Experiments

Steel material used in these experiments is a rich element which can undergo quenching and tempering, see chemical analyses in Table 1. Metallographic investigations reveal ferrite and pearlite structure (Fig. 1). Grain size varies between 40 and 60 μm and hardness testing gives an average value of 120 HV.

Structure noise function extracted by the above algorithm; undergoes computing mismatching and correlation process between interpolation and residuals coefficients. Results point to occurrence of quasi linear energy distribution (Fig. 2); which advise to apparent energy scales incidence of micro structural acoustic signatures. In (Fig. 3) residuals display fitting indications from first samples noise data obtained after multi-interpolation stages. This must be correlated with ultrasonic frequency band and material behavior. (Fig. 4) reveal particular residual distributions of Fourier transform noise function, after several polynomial interpolations. This will recommend relationship exploration with some material properties.

Table 1 XRF Chemical analysis	Cr	1.36%
	Ni	0.90%
	Mn	0.85%
	Si	0.52%
	Al	0.45%
	Cu	0.13%
	S	0.00218%
	Mo	0.048%
	Mg	0.04%
	Sb	0.02%
	P	0.01%
	V	0.01%
	Fe	balance
	C	0.126%
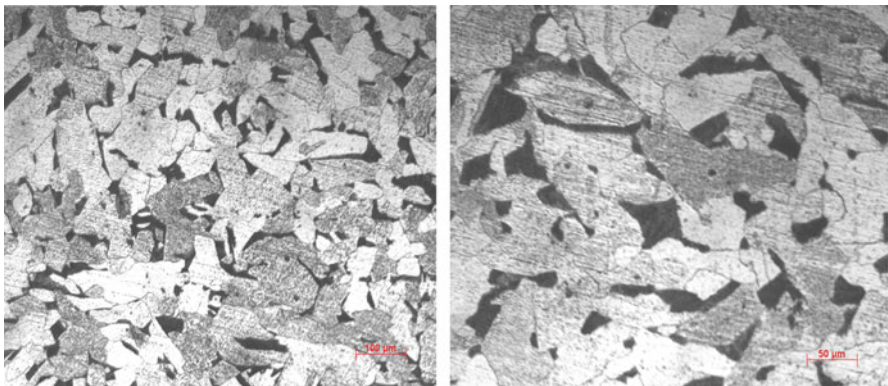
Fig. 1 Ferrite pearlite structure (X50 & X100)
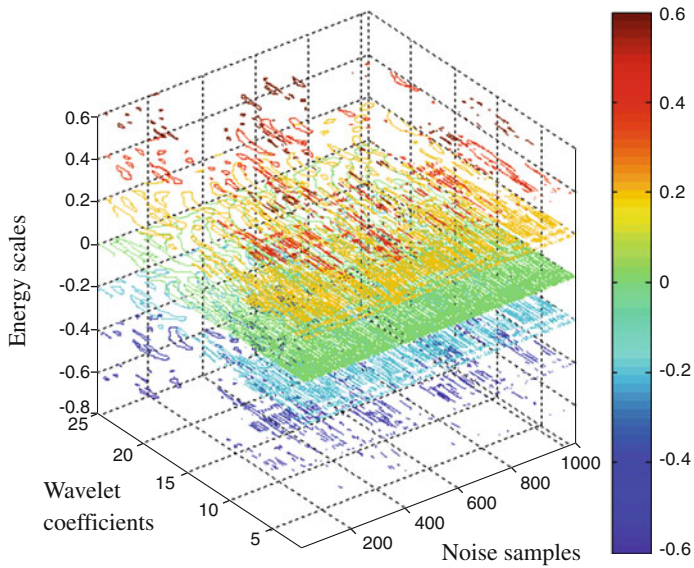
Fig. 2 Structural noise at different energy scales
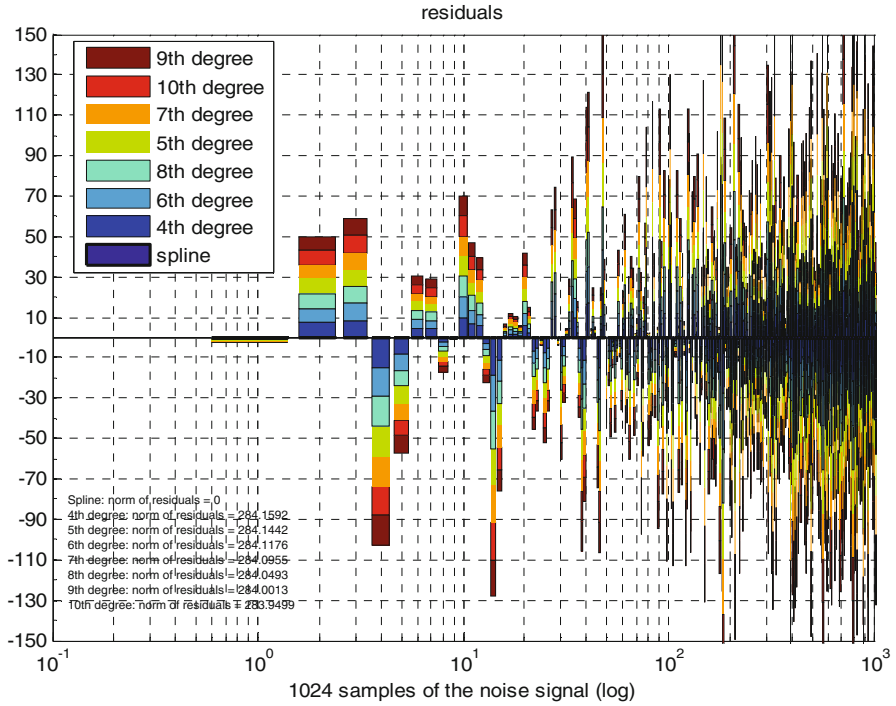
Fig. 3 Residuals of the structure noise with different interpolations
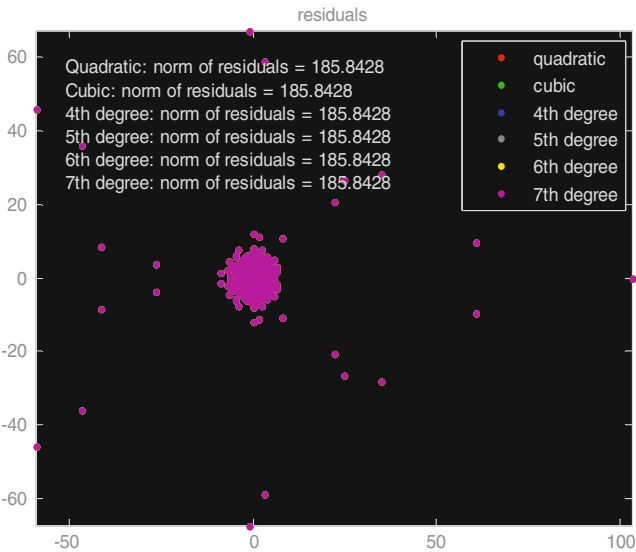
Fig. 4 Residuals of the structure noise FFT with different interpolations

Conclusions

This research indicate the well established de-noising method developed in this work; and provide us for future investigations, support for steel micro structural features testing. Experiments developed on steel samples after confirmation, could be possibly generalized to other material samples; in a prospect of an automated ultrasonic data mining system for defects acoustic signatures.

References

[1] D.L. Donoho, De-noising by soft-thresholding, IEEE Transactions on Information Theory, Vol. 41, n. 3 (1995), p. 613–627

[2] S. Mallat, A theory for multi-resolution signal decomposition: the wavelet representation. IEEE Trans. pattern analysis and machine intelligence 1989; Vol.11, n. 7 674–693.

[3] S. Mallat, A wavelet tour of signal processing, 1998, academic press, New York.

[4] P.C.Ching, H.C. So, S.Q. Wu; Wavelet de-noising and its application to time delay estimation. IEEE Transactions signal processing 1999; Vol. 47, n. 10

[5] A.R. Ferreira Da Silva, Wavelet denoising with evolutionary algorithms, Digital signal processing, Elsevier, Vol.15, n. 4: 382–399, July 2005.

[6] E. Pardo, J.L. San Emeterio, M.A. Rodriguez, A. Ramos, Noise reduction in ultrasonic NDT using undecimated wavelet transforms, Ultrasonics, Elsevier, Vol. 44, 2006, 1063–1067.

[7] F. Bettayeb, S. Aoudia, S. Haciane, "Improving the time resolution and signal noise ratio of ultrasonic testing of welds by the wavelet packet", NDT&E international, Elsevier, Vol. 38, 2005

[8] F. Bettayeb, T. Rachedi, H. Benbartaoui; An improved automated ultrasonic NDE system by wavelet and neurone networks 2004; Ultrasonics Vol. 42: 853–858

[9] F. Bettayeb, Wavelet threshold enhancement by an energetic ultrasonic signal characterization, in proceeding Acoustics'08 Paris, 2008: 2057–2060.

Use of Acoustic Emission Signal and X-ray Diffraction Analysis for Detection of Microstructural Changes in Cyclically Loaded AlMg Alloys

P. Mazal, P. Liskutin, F. Vlasic, F. Hort and J. Fiala

Abstract This paper summarizes basic experimental results of microstructural changes during high cycle fatigue loading of AlMg alloys (EN AW-6082 and EN AW-2017). These changes are detected by using of acoustic emission (AE) method. The authors targeted the main attention on more exact identification of causes of changes of AE signal activity in the stage of fatigue damage cumulation. The method of X-ray diffraction analysis of the structure is used for explanation of this phenomenon. The results of presented experimental works indicate the connections between changes of acoustic emission signal and cyclical changes of so called "mosaic blocks" of the crystal structure identified by means of X-rays diffraction during fatigue loading of material.

Keywords Acoustic emission • Crack • Damage • Fatigue • X-ray

Introduction

Al alloys present a very important group of construction materials, which are used because of their specific properties in many different industrial applications, especially in the area of transport engineering. Quite often, products made of these materials must satisfy very high requirements during long time periods. Therefore it is a must to get detailed information about their mechanical properties and the regularities of their shrinks to defect [1].

P. Mazal (✉) • P. Liskutin • F. Vlasic • F. Hort
Brno University of Technology, Brno, Czech Republic
e-mail: mazal@fme.vutbr.cz

J. Fiala
NT Center, West Bohemia University, Pilsen, Czech Republic

Table 1 Chemical composition of used Al alloys (wt %)

	Si	Fe	Cu	Mn	Mg	Cr	Zn	Ti	Al
EN AW-2017/T4	0,8	0,7	2,5	0,2	0,25	0,1	0,25	---	rest
EN AW-6082/T6	1,01	0,17	0,067	0,66	0,84	0,16	0,030	0,032	rest
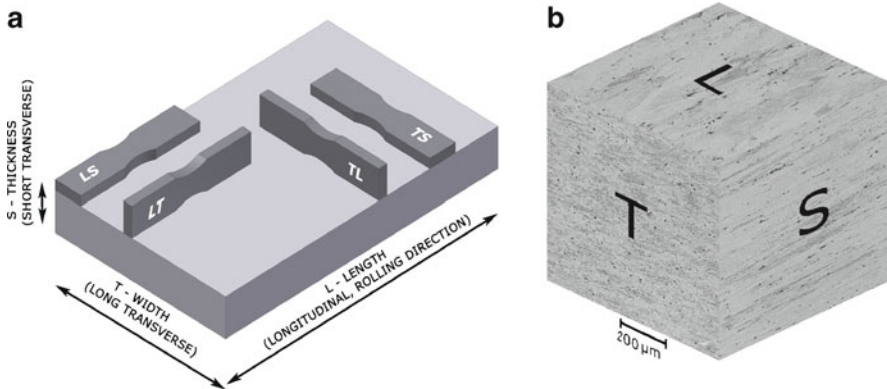
Fig. 1 Tested material: **a**) specification of structure directions, **b**) presentation of microstructural anisotropy

Al alloys EN AW-2017/T4 and EN AW-6082/T6 have been used as the experimental materials. Chemical compositions of these alloys are shown in the Table 1. Both materials have been featured by direction structural anisotropy arisen due to the extruding technology (see Fig. 1).

As to the research of fatigue damage principles, the biggest attention is paid to the description of crack initiation at this time. As to the material property evaluation it is, however, quite important to follow the processes imminently preceding the appearance of the fatigue crack. These changes take place on the microstructural level and the current investigation methods identify them only with great troubles [2].

The fatigue tests have been realised with the electroresonance testing device RUMUL Cracktronic 8204/160 working on the principle of electromagnetic resonance and loading the specimen with four point symmetric bending (R = -1). The resonance frequency of the mentioned specimens moved around 70 Hz.

Used NDT Procedures and Instrumentation

Acoustic emission method is a very valuable tool for evaluation of damage degree. This method enables monitoring of changes of damage processes directly in the course of loading cycle, which is its big advantage, compared with other

identification methods. The main problem of this method is to define the type of signal sources, of course.

X-ray diffraction analysis of loaded samples is based on the knowledge that in case of loading of wrought materials the redistribution of deformation strengthening occurs, which is caused by re-arrangement of dislocations [3, 4]. Details about this regrouping can be obtained by X-ray diffraction and by electron microscopy. The wavelength of X-rays used in such investigations is equal to the size of atom. The resolving power of X-ray diffraction is therefore much greater than the resolution of a light microscope. Due to the large penetrating power of X-rays, the X-ray diffraction gives information on a material´s volume which is greater than the volume of the material, the structure of which is seen under an electron microscope.

Acoustic emission brings information on macroscopic volumes of analyzed material, which is a big advantage when investigating structurally heterogeneous processes that occur under cyclic loading. Combining the results of the observation of AE and X-ray diffraction enables to extend our knowledge of fatigue processes.

The AE signal was taken with analyser DAKEL XEDO. It concerns 2 and 4 channel systems with possibility to scan up to 16 free settable energy levels serving together with piezoceramic sensors for detection of AE signal in material under investigation (app. 100 kHz-2000 kHz). To evaluation as well as to further processing the basic parameters measured samples, was used the software DaeShow© which enables all basic procedures of evaluation – ring down counts, AE burst rate, summation of AE counts, RMS etc.

A part of specimens were subjected to the "interrupted loading" - after fixed number of loading cycles the fatigue tests were stopped and specimens were subjected to X-ray diffraction analysis of structure of the surface (wavelength dispersive X-ray fluorescence spectrometer AXS Bruker S4 Explorer).

Experimental Results

The Fig. 2 shows examples of AE activity entries for both Al alloys. AE counts rate (level analysis) is a number of overshoots (counts–cnt) over the preset energy levels (16). The cyclic hardening (or softening) stage, rise and development of the first micro-cracks and the course of main crack propagation are registered unambiguously. It is however evident that the AE signal activity changes also in the period between these basic phases. Figure 3 shows the changes of basic parameters of AE events – peak amplitude, rise time and duration.

Classical techniques of optical observation of surface do not provide any obvious reason for this phenomenon. On the basis of analogy with other observations it is possible to expect that the reason of this AE activity can be for example the accumulation of energy sufficient for loosening of dislocations captured in structural obstacles. The reason of increased AE activity during the so called stable mode can be also the changes of material substructure – emphasizing of sub-seeds, mutual rotation of suitable areas in frame of individual seeds of material etc. can appear [4, 5].
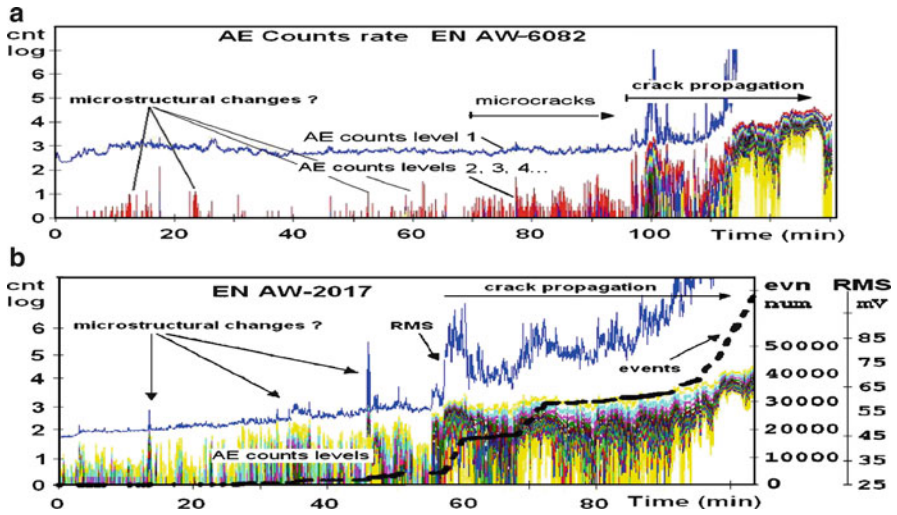
Fig. 2 Changes of AE signal parameters during the high cycle fatigue tests: **a**) EN AW-6082 - AE counts rate (level analysis), N_f app. $5,4.10^5$ cycles, **b**) EN AW-2017 - counts rate, RMS, cumul.of AE events - N_f app. $4,3.10^5$ cycles
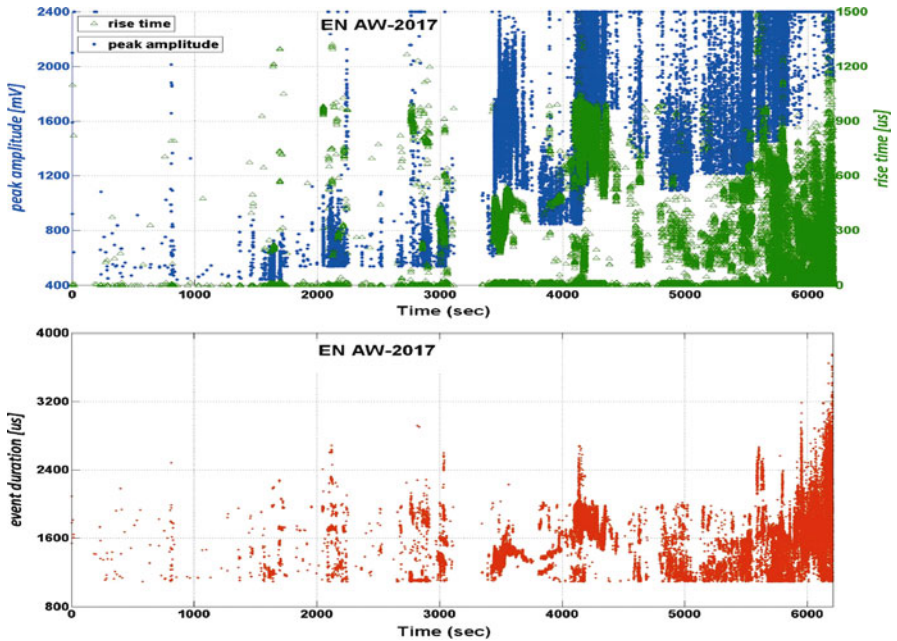
Fig. 3 Plot of changes of peak amplitude, rise time and events duration of measured AE events during the high cycle fatigue test (EN AW-2017/T4 – specimen from Fig. 2b)
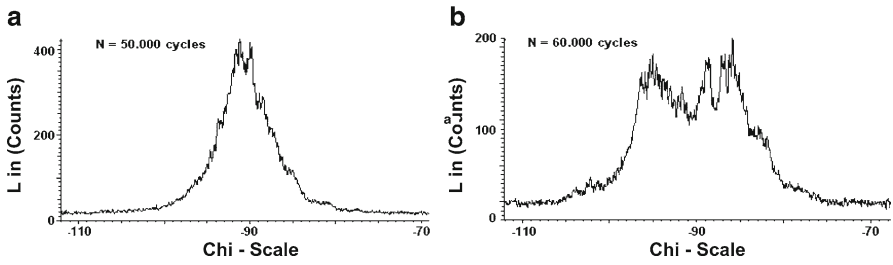
Fig. 4 Example of X-ray diffraction analysis (EN AW-2017/T4): changes of azimuth profile of the (200) Al diffraction line: **a)** test specimen TL2 after 50.000 loading cycles, **b)** results of the same test specimen after 60 000 loading cycles
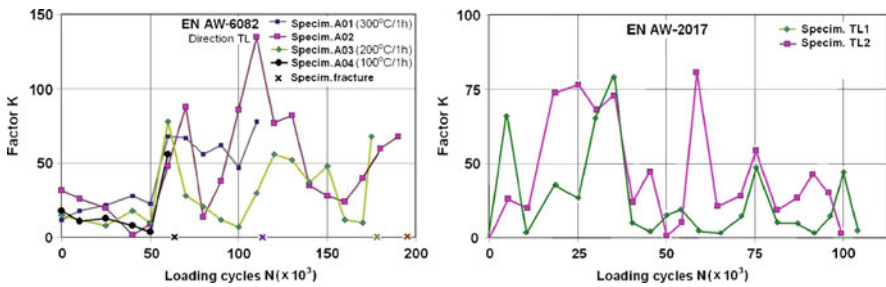
Fig. 5 Record of real change of X-ray K factor vs time of fatigue loading for EN-AW 6082 and EN AW-2017 alloys

Examples of X-ray diffraction analysis are shown on Fig. 4 (changes of azimuth profile of the (200) Al diffraction line). Figure 5 shows the records of the X-ray "K factor" changes, which were measured during fatigue tests of four samples made from EN AW-6082/T6 (with various orientation relative to forming direction) and for two samples from EN AW-2017/T4 alloys. K factor is the width of the peak of azimuth profile of diffraction line (200) alloy matrix in the half height of this peak; this coefficient represents the amount of disorientation of mosaic block structure [3]. From Fig. 5 it is seen that the cellular structure changes during the cyclic loading considerably. More detailed description of X-ray diffraction procedure is out of scope of this contribution – see [3, 4 and 5].

By X-ray examination of the aluminum alloy EN AW-6082 (4 specimens with different heat treatment) and EN AW-2017 (2 specimens), was found that the microstructure, as characterized by the proportion R of the large CSR´s (mosaic blocks, structural cells) greater than 10 μm, does change much under repeated stress [5]. In the first stage of loading, the CSR´s due to the introduced plastic strain disintegrate. As a result of this, the boundary surface of the cell aggregate extends, and, consequently, its energy finally increases enough to initiate its coarsening. The energy necessary to activate the growing of the larger blocks at the expense of the smaller

ones is supplied by further cycling. But, during this growth, paracrystalline distortions emerge, which gradually accumulate in the interior of the widening cells, raising thus their volume energy. After next fatigue loading, the energy increases to such degree that the blocks begin disintegrate a new. Due to this disintegration, the paracrystalline distortions relax and the alloy energy drops [5, 6].

Conclusion

The acoustic emission method identifies changes passing in the material mass during the damage accumulation period of the fatigue process. The results of presented experiments indicate the connections between changes of acoustic emission signal and changes of so called mosaic blocks of the crystal structure identified by means of X-rays. If these connections will be demonstrated on broader spectra of materials, then it will be possible to evaluate with acoustic emission method the scope, intensity and features of the degradation processes in the period of the fatigue crack rise as well as in the stage of damage accumulation what there was no method here up to date.

References

[1] Michna, S. et al. *Aluminium materials and technologies from A to Z*, Adin Ltd., Presov 2007, Slovakia, 620 p., ISBN 987-80-89244-18-8.
[2] Mathis, K. et al.: *Investigation of some magnesium alloys by use of the acoustic emission technique*, Material Science and Engineering A 387–389 (2004), p. 331–335.
[3] Fiala, J. et al. Monitoring of fatigue damage by X-ray diffraction and AE. *NDT Welding Bulletin Special Issue 2008*, Vol. 18, 2008, p. 11–13, ISSN 1213–3825.
[4] Fewster, P.J., Andrew N.L.: Reciprocal space mapping and ultrahigh resolution diffraction of polycrystalline materials. In: *Defect and microstructure analysis by diffraction*, Snyder R.L., Fiala, J., Bunge, H.J. (eds.), Oxford University Press, New York, 1999, p. 346–364.
[5] Fiala, J., Kolega, M.: Application of two-dimensional detectors in x-ray diffraction materials structure analysis, *Particle and Particle Systems Characterization* 22, 2005, p. 397–400.
[6] Mazal, P., Vlasic, F. Application of Selected NDT Procedures for more Detailed Identification of Crack Initiation Stage at Fatigue Tests of Al Alloys. *In: Fatigue Design*, 2009, CETIM Senlis, November 2009.

Investigating Eddy Current Response to Microstructural Changes to Determine Case Depth of Induction Hardened Parts

S. Kahrobaee and M. Kashefi Torbati

Abstract The ability to characterize hardness profile in induction hardened steel part is important from quality inspection point of view. Traditional destructive methods such as plotting hardness profile are generally time-consuming. Besides, the tests can not provide 100% quality control in a mass production line. Eddy current response of steel is sensitive to changes in microstructure of the material under investigation. So, the non-destructive method can be used in determining the depth of the hardened layer in steel parts due to the change in the microstructure from the surface to the core of the hardened part. In the present study, induction hardening technique was used to produce different case hardened depths in identical rods of CK45 carbon steel. Plotting hardness profile, effective and total case depths were determined. In order to investigate the applicability of the eddy current technique, relation between effective and total case depth and eddy current outputs (such as primary and secondary voltages and normalized impedance) were studied. High correlation coefficients of these relations indicate an acceptable level of accuracy in comparison with destructive method.

Keywords Case depth • Eddy current • Hardness profile • Induction hardening • Magnetic properties

Introduction

The Standard methods for determining case depth of induction hardened parts can be devided into following methods. The first one consists of an optical observation of the microstructure in a cross section of a sample. The difference in core microstructure (ferrite-pearlitic) from the martensitic structure at the surface can be

S. Kahrobaee • M.K. Torbati (✉)
Department of materials and metallurgical engineering, engineering faculty,
ferdowsi university of mashhad, Mashhad, Iran
e-mail: m-kashefi@um.ac.ir

used to determine case depth. The second method consists in establishing a micro-hardness profile in a cross section of the sample after polishing. The two methods are destructive and need considerable preparation and so are time-consuming and costly. Considering the advantages of non destructive methods in industrial quality control, research are focused on Non-Destructive Evaluation (NDE) of the mechanical and physical properties of materials as a substitute to destructive method which, in return, provides 100% quality control in mass production lines. Among all nondestructive methods, Eddy Current is a technique which its high sensitivity to chemical composition, microstructure and mechanical properties makes is suitable for materials characterization [1, 2].

Recently, several research have been performed to investigate electromagnetic properties of induction hardened steels. By determining magnetic hysteresis loss values, magnetic Barkhausen Noise effects [3-5] and also electrical resistivity as well as magnetic permeability [6], it was concluded that there is a difference between magnetic properties of hardened layer with the other parts of the sample. This difference is a potential of eddy current method for case depth characterization of induction hardened steel parts. In the present study relations between the eddy current equipment outputs (include primary and secondary voltages and normalized impedance) and effective and total case depths have been investigated.

Experimental Process

Nine cylindrical AISI 1045 steel rods of 30mm diameter and 150mm length were prepared for the induction hardening process. For all samples, the frequency and the power of induction hardening apparatus are fixed at 30kHz and 50kw respectively. By changing the speed of the sample in the course of passing throupth the induction coil, different case depths were produced. In order to eliminate residual stresses resulting from induction hardening treatment, all samples were put in 250°C for two hours. The case depths were determined using the hardness measurement method. Finally, the Eddy Current tests were performed on the cylindrical samples. A schematic diagram of the used Eddy Current system is shown in Figure 1. A sinusoidal current with a frequency ranging from 10 to 100Hz was applied to the coil for all
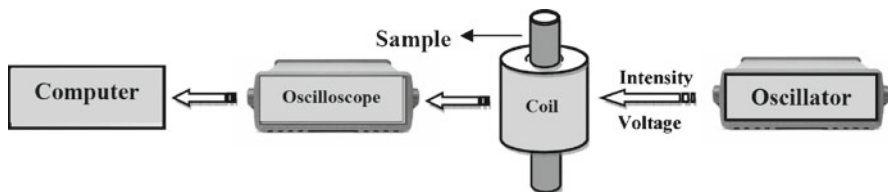
Fig. 1 General synopsis of the experimental apparatus [7]

Fig. 2 Optical microscopic image of a microstructure in a cross section of an induction hardened sample at speed of 12mm/s passing through the induction coil
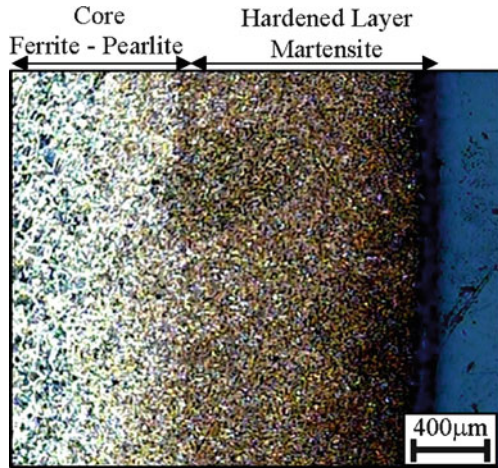
Table 1 Effective and Total Case Depth estimated from hardness measurment

The speed of the sample in the course of passing the induction coil (mm/s)	12	11	10.5	10	9	8	7.5	7	6.5
ECD(mm)	0.7	1.9	2	2.25	2.3	3.2	3.3	3.5	4.1
TCD(mm)	1.65	2.2	2.4	2.6	3.2	4	4	4.6	5.6

samples. Primary and secondary voltages and input currents were measured and the impedance of the coil was calculated.

Figure 2 indicates optical microscopic image in a cross section of an induction hardened sample at the speed of 12mm/s passing through the induction coil. As it is shown, the hardened zone with a martensitic structure at the surface is mainly darker than ferrite-pearlitic structure of the core that is not affected by the heat treatment. Effective Case Depth (ECD) and Total Case Depth (TCD) values were measured according to the International Standard ISO 3754 (Table 1).

Results and discussion

The first step for evaluation of effective and total case depth (ECD and TCD) is determination of optimum frequency. In the present study, optimum frequency has been chosen by applied regression analysis between ECD/TCD and eddy current outputs [1,2] and relations between eddy current outputs and ECD/TCD in the range of 10 to 100Hz were investigated, separately. The best correlation coefficient between these parameters was obtained at 50Hz for ECD and 25Hz for TCD, respectively. As a result, 50 and 25Hz frequencies have been used to evaluate effective and total case depth using eddy current method.
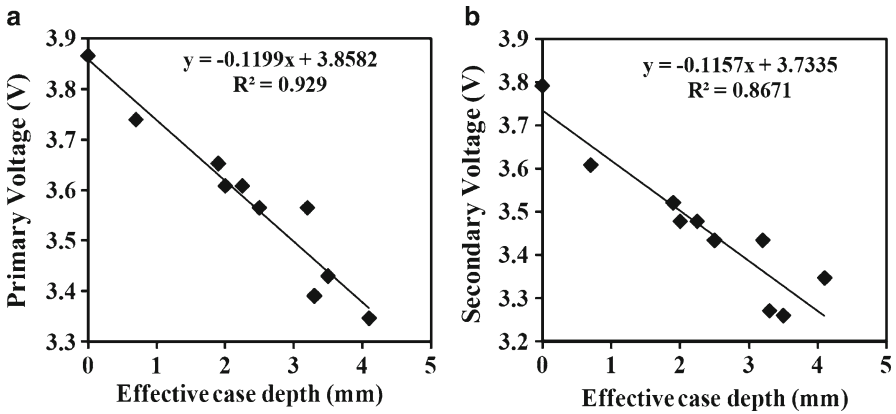
Fig. 3 Relation between ECD and **a**)Vx, **b**)Vy at 50Hz
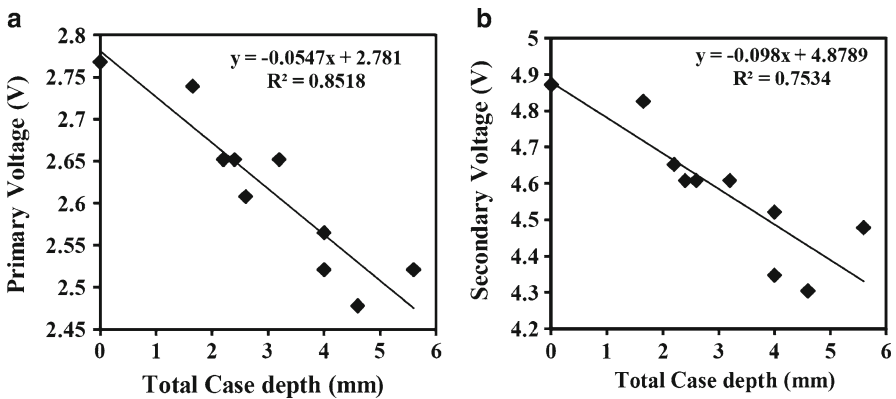
Fig. 4 Relation between TCD and **a**)Vx, **b**)Vy at 25Hz

The next step would be establish relations between effective/total case depths and eddy current equipment outputs. Figures 3 and 4 show the relationship between primary (Vx) and secondary voltage (Vy) with ECD and TCD at 50 and 25Hz frequencies. As can be seen, the maximum correlation cofficients that express the linear relationship were obtained for primary voltage. The R^2 for ECD and TCD were obtained to be 0.92 and 0.85 respectively. On the other hand, low obtained regression for secondary voltage demonstrate unreliable relationships in comparison with the primary voltage.

To find a better relationship, voltage (V) and intensity (I) of the coil were used to calculate the impedance (Z) of the coil for all samples using Eqn. (1) [1].

$$Z = V / I \tag{1}$$

The calculated impedance (Z) for each sample was divided by the impedance of the empty coil (Z_0) to make a new parameter. This parameter (Z/Z_0) is called normalized impedance [1, 2, 8].

a

b
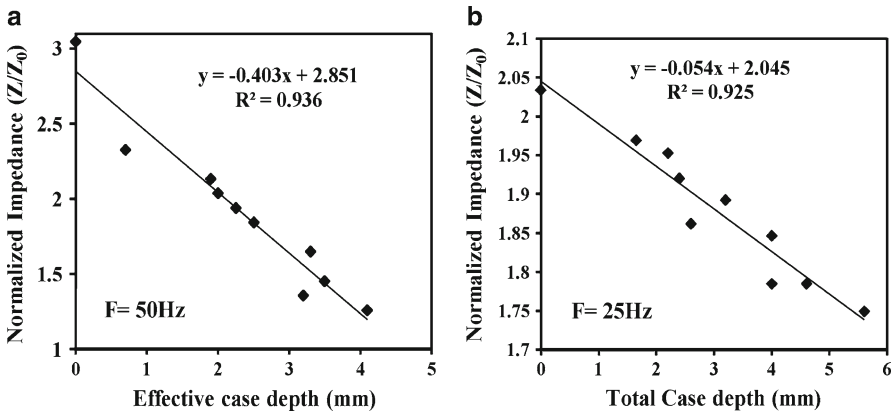
Fig. 5 Relation between normalized impedance(Z/Z_0) and **a**) ECD at 50 Hz, **b**) TCD at 25Hz

The relationship between ECD and TCD and normalized impedance (Z/Z_0)) is shown in Fig. 5. As it is seen, for determination of TCD, the best correlation coefficient was obtained for the normalized impedance ($R^2 = 0.92$) and for determination of ECD, maximum correlation coefficients were obtained for both the normalized impedance ($R^2 = 0.93$) and the primary voltage ($R^2 = 0.92$).

In the hardened layer, as a result of formation of martensitic microstructure, high dislocation density is produced due to the shear deformation of martensitic transition. This high dislocation density as well as high distortion due to the interstitial atoms embedding in crystal structure of martensite causes pinning of magnetic domain walls. As a result, less mobility of domain walls can be expected in comparison with ferrite-pearlite structure with lower dislocation density [3,5]. That is the reason that the demagnetization of martensite structure is more difficult than ferrite-pearlite one [9]. Thus, more magnetic field intensity (H) is required to overcome the obstacles against aligning the domains, and in return, more coercivity is needed. Therefore in all samples, by increasing the case depth, or in the other word martensite structure, coercivity and hysteresis loss increase and magnetic permeability (μ) decreases. These differences in magnetic properties are the main reasons for the difference in obtained responses of eddy current for samples with different case depths.

Considering Eqn. (2), it can be concluded that decreasing in μ results in decreasing of self-induction coefficient (L).

$$L = \mu N^2 A / l \qquad (2)$$

Where μ is magnetic permeability; N, number of turns round the coil; A, cross section area and l, the coil length. Finally, according to the Eqn. (3), by decreasing in magnetic permeability (μ), induction resistance (X_l) is decreased. Since in ferro-

magnetic alloys such as steel, the effect of permeability or reactance is stronger than the effect of resistance (R), impedance (Z) is decreased too (Eqn. (4)).

$$X_l = 2\pi \; f \; L \tag{3}$$

$$Z = \sqrt{X_l^2 + R^2} = V \, / \, I \tag{4}$$

According to Eqn. (4), the impedance decreases with increasing the hardened depth. Decreasing of impedance is the key factor for decreasing of output voltage of Eddy Current with increasing of hardened depth (Figs. 3, 4 and 5).

Conclusion

Based on magnetic property differences between martensitic microstructure (hardened layer) and ferrite-pearlitic microstructure (core of the sample) the eddy current method is capable of measuring effective and total case depth of induction hardened steel rods. In order to determine ECD and TCD, relations between case depth and eddy current outputs were investigated. High correlation coefficient between these relations show high success of nondestructive Eddy Current technique in determining ECD and TCD of induction hardened steel parts.

References

[1] Bray, D.E., Stanley, R.K. Nondestructive evaluation: a tool design, manufacturing and service, CRC Press, Boca Raton FL, 1997, p. 415.
[2] Hagemair, D.J. (1990), Fundamentals of Eddy Current Testing, ASNT.
[3] Zhang, C., Bowler, N., Lo, C. (2009), J. Magn. Magn. Mater., vol. 321, p. 3878.
[4] Zhu, B., Johnson, M., Jiles, D. (2000), Evaluation of Wear-Induced Material Loss in Case-Hardened Steel Using Magnetic Barkhausen Emission Measurement, IEEE Trans. Mag. vol. 36, p. 3602.
[5] Lo, C.C.H., Kinser, E.R., Melikhov, Y., Jiles, D.C. (2006), Magnetic nondestructive characterization of case depth in surface-hardened steel components. in: D.O. Thompson, D.E. Chimenti (Eds.), Review of Progress in Quantitative Nondestructive Evaluation 25B, AIP Conference Proceedings, vol. 820, p. 1253.
[6] Johnson, M., Lo, C., Hentscher, S., Kinser, E. (2005), Analysis of conductivity and permeability profiles in hardened steel. in: L. Udpa, N. Bowler (Eds.), Electromagnetic Nondestructive Evaluation (IX), IOS, Amsterdam, p. 135.
[7] Sheikhamiri, M., Kashefi, M. (2009), J. NDTE Int., vol. 42, p. 618.
[8] Shull P.J. Nondestructive evaluation: theory, techniques and applications. New York: Marcel Dekker, Inc; 2002, p.279.
[9] Rumiche, F., Indacochea, J.E., Wang, M.L. (2008), J. Mater. Eng. Perform., vol. 17, p. 586.

Surface Characterization of Carburized Steel by Eddy Current

S. Kahrobaee, M. Kashefi Torbati and M. Sheikh Amiri

Abstract In the carburizing process, it is necessary to control the surface carbon content in order to obtain desirable materials properties. Although quantometry is the most common method for determination of surface carbon content, being destructive, costly and time consuming are some disadvantages of this method. Eddy current testing has long been used as a technique for investigation of defects. However, determination of surface carbon content in carburized steels is a new application for this method which has been studied in this research. Sixteen AISI 4118 steel samples have been carburized in an enriched carbon gas carburizing furnace. Carbon potentials in the furnace were different for each sample; therefore, samples with various surface carbon contents were produced. Subsequently, the carbon content of all samples was measured using quantometry. Finally, determining the optimal frequency, eddy current testing was applied for all samples and the relationship between surface carbon content and various parameters such as normalized impedance and phase angle has been established. The study shows a good relationship between the carbon percent and phase angle can be established ($R^2=0.91$) using phase angle. Besides, the effect of temperature on the relationship was also investigated using three levels in 0, 30 and 80 °C. The formulas presented, shows improvement in corresponding corrections in experimental data.

Keywords Carburizing • Eddy current • Normalized impedance • Phase angle • Surface carbon

S. Kahrobaee • M.K. Torbati (✉) • M.S. Amiri
Department of materials and metallurgical engineering, engineering faculty,
ferdowsi university of mashhad, Mashhad, Iran
e-mail: m-kashefi@um.ac.ir

Introduction

Nowadays, application of non destructive methods is not limited to detect defects and cracks. Considering the advantages of non destructive methods in industrial quality control, in the recent years, several researches have been focused on non-destructive determining the mechanical and physical properties of materials as a substitution for destructive method which results in saving time and energy as well as providing 100% quality control in mass production lines.

Among different methods, non destructive eddy current technique has distinctive advantages. Suitable sensitivity to chemical composition, microstructure, mechanical properties and residual stress makes it a reliable alternative to conventional destructive methods [1,2].

Recently Konoplyuk [3] discovered an appropriate relation between the hardness of ductile cast iron and the output voltage of eddy current device. Uchimoto and Check [4,5] found the same relation for gray cast iron. Decarburizing depth was also studied using harmonic analysis [6] and on the base of difference in magnetic properties (magnetic relative permeability), between ferrite and pearlite phases [7]. Zergoug [8] found relation between mechanical micro-hardness and impedance variations. Rumiche et al [9] investigated the effect of microstructure on magnetic behavior of carbon steels by electromagnetic sensors and the effect of grain size on magnetic properties were investigated and proved by other researchers [10,11]. With the growing demands for nondestructive measuring of physical and mechanical properties of materials in mass production lines, there is a strong potential for research on the new applications for the nondestructive eddy current technique.

Carburizing has long been used in industry to improve surface hardness and fatigue resistance of steel parts while maintaining the toughness of the core. Proper control of surface carbon content is a major factor in performing a successful carburizing process and providing essential mechanical properties for the part. Traditionally, this has been done using costly chemical analyzing methods such as quantometry. The aim of the present research is to establish a relation between surface carbon content and the responses of the carburized part to electro–magnetic induction.

Experimental Process

The present research was conducted on AISI4118 steel. The composition of the steel is presented in Table 1.

All the samples were prepared as rod specimens with 2.5 cm in diameter and 15 cm high and were carburized at 900 °C for 7 hours in a gas carburizing furnace. The carbon potentials of the furnace were different for each sample but kept between 0.4 and 0.9. After carburizing, all samples were cooled in air and normalized using induction heating process. Short austenetizing time and, therefore, elimination of surface decarburizing was the main reason for choosing the induction heating process. Finally, surface carbon content of all samples were determined using quantometry and are displayed in Table 2.

Table 1 Chemical composition in weight percentage

C	Si	Mn	P	S	Cr	Mo	Ni	Al	Fe
0.196	0.25	0.75	0.02	0.008	0.8	0.18	0.06	0.01	Rest

Table 2 Surface carbon content of samples used in the research

Sample No.	1	2	3	4	5	6	7	8
Surface carbon (%)	0.83	0.45	0.53	0.71	0.81	0.88	0.68	0.65
Sample No.	9	10	11	12	13	14	15	16
Surface carbon (%)	0.91	0.72	0.88	0.74	0.78	0.44	0.55	0.88
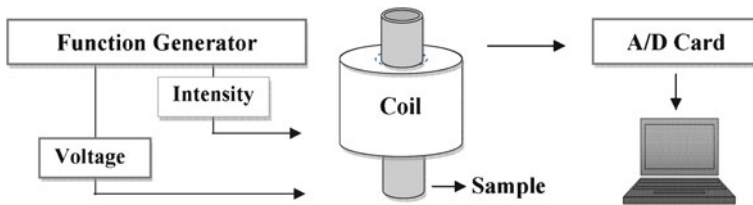
Fig. 1 General synopsis of the experimental apparatus

A sinusoidal current with a frequency ranging from 650 Hz to 4 kHz was applied to the coil for all tests. A schematic representation of the device is shown in Figure 1.

Voltage and current of the coil were measured and the impedance and phase angle of the coil were calculated for each sample.

In order to calculate the impedance (Z) and phase angle (ϕ) of the coil for all samples, voltage (V) and intensity (I) of the coil were used using Eq.(1) and (2), respectively [1].

$$Z = V / I \tag{1}$$

$$\phi = 360 \left(\Delta t / \lambda \right) \tag{2}$$

Where Δt is the time difference between two adjacent peaks and λ is the wave length. The calculated impedance (Z) for each sample was divided by the impedance of the empty coil (Z0) to make a new parameter. This parameter (Z/Z0) is called normalized impedance [1, 2, 13].

Apart from carbon content at the surface, the effect of temperature was studied using three levels; $0°C$, $30°C$ and $80°C$.

Results and Discussion

In each frequency ranging from 650 to 4000 Hz, regression analysis was applied between percentage of surface carbon content and two parameters (normalized impedance and phase angle). Eventually the correlation coefficient (R^2) was
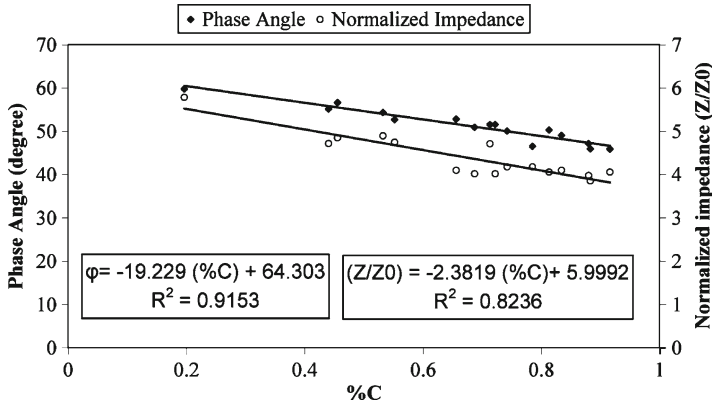
Fig. 2 Relationship between Phase angle and normalized impedance with percentage of carbon of surface at 650Hz

calculated for two above-mentioned parameters. The maximum R^2 (0.91) was observed in 650Hz frequency which indicates maximum relationship between surface carbon content and two parameters. Thus, 650Hz frequency was selected, as an optimum frequency, for all experiments in this research. The relationship between surface carbon content and normalized impedance is shown in Fig. 2 which indicates a fairly good relationship ($R^2 = 0.82$). Figure 2 also shows the best relationship, which is, between surface carbon content and phase angle (ϕ). The correlation coefficient is 0.91 at 650Hz frequency. As can be seen, in Fig. 2, Z and ϕ decrease with increase in surface carbon content. This could be due to the increase in pearlite percentage with increasing carbon content. The increase in pearlite percentage, in turn, causes an increase in the resistance (R) and a decrease in the permeability (μ) [2,12]. Keeping the relationship between μ and X in mind, the reduction of X with μ can be established [1,2].

In ferromagnetic alloys such as steel, the effect of permeability or reactance is stronger than the effect of resistance [12,2]. As a result, the impedance decreases with increasing the percentage of carbon. Because of the relationship between the phase angle and X/R ($\tan(\phi) = X/R$), the phase angle (ϕ) also decreases.

As magnetic and electrical properties of materials are strongly depend on temperature, the effect of temperature has also been studied. Figure 3 displays the influence of temperature on the output of the Eddy current evaluation used for determining the surface carbon content of the samples. The figure shows variation of evaluated carbon content at the surface for temperatures in the range of 0-80°C using Eddy current method. An increase in the temperature results in an increase in the specimen's resistance [1,13] but a small increase in the temperature does not have a noticeable effect on μ and X [1,12]. Consequently, an increase in temperature results in an increase in R without noticeable effect on X, resulting in increasing Z and decreasing ϕ.
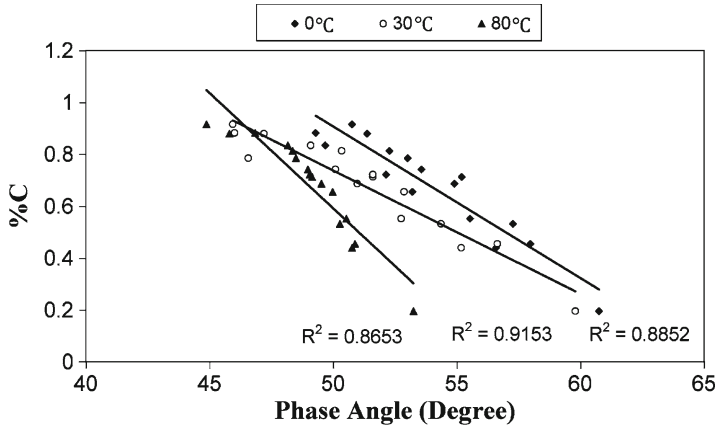
Fig. 3 Effect of temperature on the relationship between carbon surface percentage and phase angle

Equation (3) shows the corresponding temperature corrections for evaluation of the surface carbon content.

$$\%C = \left(-1E-05T^2 + 0.0008T - 0.0584\right)\varphi + \left(0.0008T^2 - 0.047T + 3.8282\right) \quad (3)$$

As a result, one has to keep in mind the temperature effect of the test and apply the corresponding corrections to the results.

Conclusion

In the present study, normalized impedance and phase angle show a strong relationship (R^2=0.91) with carbon content at the surface of carburized steel samples. The effect of temperature on the relationship was also investigated and the temperature related corrections for evaluation of the surface carbon content were calculated.

References

[1] Bray, D.E., Stanley, R.K. (1997), Nondestructive evaluation: a tool design, manufacturing and service, CRC Press, Boca Raton FL, p. 415.
[2] Hagemair, D.J. (1990), Fundamentals of Eddy Current Testing, ASNT.
[3] Konoplyuk, S., Abe, T., Uchimoto, T., Takagi, T., Kurosawa, M. (2005), J. NDT&E Int., vol. 38, p. 623.
[4] Uchimoto, T., Takagi, T., Konoplyuk, S., Abe, T., Huang, H., Kurosawa, M. (2003), J. Magn. Magn. Mater., vol. 258, p. 493.

[5] Cˇech, J. (1990), J. NDT&E Int., vol. 23, n. 2, p. 93.

[6] Mercier, D., Lesage, J., Decoopman, X., Chicot, D. (2006), J. NDT&E Int., vol. 39, p. 652.

[7] Hao, X.J., Yin, W., Strangwood, M., Peyton, A.J., Morris, P.F., Davis, C.L. (2008), Scripta Mat., n. 58, p.1033.

[8] Zergoug, M., Lebaili, S., Boudjellal, H., Benchaala, A. (2004), J. NDT&E Int., vol. 37, p. 65.

[9] Rumiche, F., Indacochea, J.E., Wang, M.L. (2008), J. Mater. Eng. Perform., vol. 17, p. 586.

[10] Degauque, J., Astie, B., Porteseil, J.L., Vergne, R. (1982), J. Magn. Magn. Mater., vol. 26, p. 261.

[11] Anglada-Rivera, J., Padovese, L.R., Capo-Sanchez, J. (2001), J. Magn. Magn. Mater., vol. 231, p. 299.

[12] Kogan, L. Kh., Nichipuruk, A. P., Gavrilova, L.D. (2006), Russ. J. Nondestruct. Test., vol. 42, n. 9 p. 616.

[13] Shull, P.J. (2002), Nondestructive evaluation: theory, techniques and applications. Marcel Dekker: New York, Inc, p.279.

Section 5
NDT of Methods and Composites

Guided Waves for Nondestructive Testing – Experiment and Analysis

T. Kundu

Abstract Use of ultrasonic waves is continuously increasing for nondestructive evaluation (NDE) and structural health monitoring (SHM) in civil, aerospace, electrical, mechanical and bioengineering applications. Between bulk waves and guided waves, the latter is becoming more popular for NDE/SHM applications because the guided waves can propagate long distances and reach difficult to access regions. Recent advances in the research related to nondestructive testing (NDT) of composites and metals are discussed in this paper. To analyze the experimental results one often needs to understand the mechanics of wave propagation in various structures. Unfortunately, only for simple structures, such as homogeneous and layered half-spaces, plates, rods and pipes, the analytical solutions are available. Complex structural geometries with internal defects are difficult to solve analytically or numerically by the popular finite element method because at high frequencies the size of the finite elements becomes prohibitively small. An alternative mesh-free technique called the distributed point source method (DPSM) is being developed for solving such problems and is discussed here in addition to the experimental results.

Keywords DPSM • Guided waves • NDT • SHM • Ultrasound

Introduction

Guided ultrasonic waves are very useful in Nondestructive Testing (NDT) applications. Their use for material inspection is increasing continuously. The reasons behind its increasing popularity are: (1) compared to the bulk waves the guided waves can propagate

---

T. Kundu (✉)
Department of Civil Engineering and Engineering Mechanics
Department of Aerospace and Mechanical Engineering,
University of Arizona, Tucson, AZ 85721, USA
e-mail: tkundu@email.arizona.edu

longer distances before they are attenuated, (2) both longitudinal and shear stresses are generated by guided waves and thus various types of defects can be detected using the combinations of normal and shear stresses, (3) guided waves propagate in different modes and by tuning the appropriate mode it is possible to image hidden defects.

Ultrasonic waves for NDT applications are often generated by ultrasonic piezoelectric transducers or piezo-ceramic patches mounted on the specimen. Piezoelectric transducers and patches are used both as transmitters to generate and as receivers to receive ultrasonic waves. Often the specimen is immersed in a fluid medium for NDT inspection because the fluid serves as a good coupling medium for ultrasonic waves. When the specimen is immersed in a fluid, the ultrasonic waves can easily travel from the transducer to the specimen through the coupling fluid. For better understanding of the experimental results and for correct interpretation of acoustic images a good understanding of the interaction between ultrasonic waves and materials is needed. For this reason a good modeling of the wave propagation in specimens of various geometry containing internal defects is necessary. These problems cannot be solved analytically. Numerical techniques like the finite element method (FEM) and boundary element method (BEM) are not very efficient for modeling high frequency ultrasonic wave propagation problems in solid structures because the required element size is too small.

An efficient semi-analytical technique called DPSM (Distributed Point Source Method) has been recently developed for this purpose and is discussed here. This technique is useful to model the stress and displacement fields generated by ultrasonic transducers of finite dimensions in the vicinity of a solid specimen when both the specimen and the transducer are immersed in a fluid. Thus DPSM numerically simulates the ultrasonic experiments. In this new era of computer technology, engineers and scientists are implementing different numerical and semi-analytical techniques to solve almost all engineering and scientific problems using high speed computers to reduce the cost and time associated with carrying out actual experiments. The FEM has gained popularity in almost all fields of engineering. However, the success of the finite element method in high frequency wave propagation problems has been limited due to the requirement of extremely small size elements. DPSM can avoid this difficulty and successfully model the ultrasonic fields in fluid and solid structures.

DPSM technique for ultrasonic field modeling was first developed by Placko and Kundu [1]. They successfully used this technique to model ultrasonic fields in a homogeneous fluid [2], non-homogeneous fluid with multiple interfaces [3], and fluid containing a cavity [4,5]. It was extended to model phased array transducers [6]. DPSM was then generalized to model stress and displacement fields near a fluid-solid interface [7], in plates with uniform and non-uniform thickness [8–10], and near cracks [11–14].

Experimental Investigation

Experimental results on a composite plate and composite-concrete interface are presented in this section to prove the superiority of the guided wave imaging technique over conventional C-scan technique that uses bulk waves.
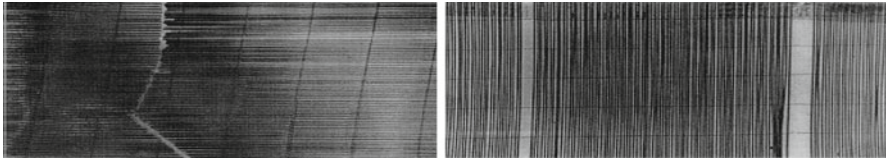
Fig. 1 Left Image: third layer of the composite plate specimen showing fibers running in the 0˚ direction are broken; right Image: fourth layer of the specimen showing some of the fibers running in the 90˚ direction are missing [15]
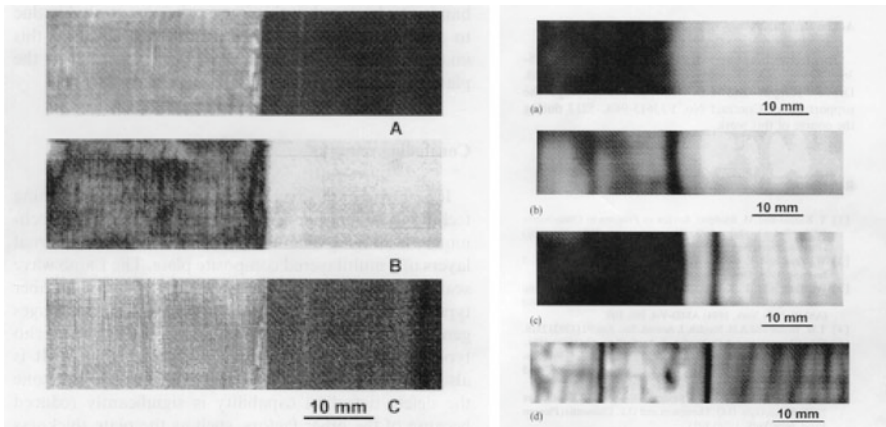
Fig. 2 Left images are generated by bulk P-waves (conventional C-scan technique); right images are generated by different Lamb wave modes [15]

Composite plate inspection

To compare guided wave and bulk wave generated ultrasonic images, a five-layered composite plate was fabricated with some internal defects [15]. Fibers in the top, bottom and middle layers run in the 0˚ direction while the second and fourth layer fibers run in the 90˚ direction. Top and bottom layers did not have any imperfection but the fibers in the middle layer were broken as shown in Fig. 1. Some fibers from the fourth layer were missing, see Fig. 1. There are no broken or missing fibers in the second layer; however during the fabrication process the left half of the second layer was not properly attached to its neighboring layer to create a delamination defect. The objective was to detect these internal defects (broken fibers in the third layer, missing fibers in the fourth layer, and delamination in the second layer) in otherwise perfect looking composite plate specimen by scanning it with the bulk P-wave (Conventional C-scan technique) and by different Lamb wave modes. Generated images are shown in Fig. 2. From this figure one can see that bulk wave images can only show the delamination defect while different Lamb mode generated images can
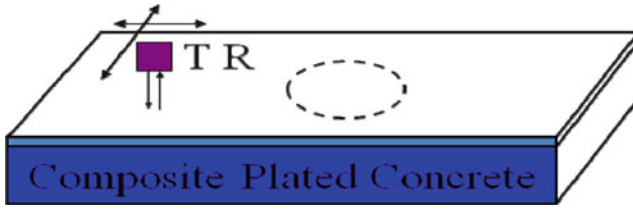
Fig. 3 Schematic of a composite plated concrete specimen with a hidden delamination defect at the interface [16]

clearly show all three types of defects. Readers are referred to [15] for more information on this composite plate inspection.

Composite-concrete interface inspection

A popular technique for strengthening old concrete structures is attaching composite plates on concrete beams and columns. If composite is properly attached then the strength of the composite wrapped structure is significantly increased. However, if there is any delamination or lack of attachment between the concrete substrate and the composite plate then its strength is reduced significantly. To compare the quality of images generated by bulk waves and guided waves, a specimen was fabricated with a debond between composite plate and concrete block as shown by the dotted line in Fig. 3. In conventional C-scan technique the ultrasonic transducer works as transmitter as well as receiver for the bulk P-wave and scans the specimen by moving parallel to the specimen, maintaining a fixed distance between the specimen and the transducer, as shown in Fig. 3 [16].

Time histories recorded over a perfectly bonded region and over the debonded or delaminated region are shown in Fig. 4. Note that the peak values for both signals are the same. This is because the signal reflected from the top surface of the composite plate is not affected by the presence of the debond. Signal arriving after the main peak is affected by the debond because the energy reflected from the interface arrives after the main peak. Ideally, the signals reflected from the top of the composite plate and from the interface should be clearly separated. However, since high frequency ultrasonic signals cannot penetrate deep inside thick composite plates that are used for civil structure rehabilitation, lower frequency (500 kHz to 1 MHz) signals were used. At this frequency signals reflected from the top and the bottom of the interface are not clearly separated as shown in Fig. 4.

Images are generated by plotting the peak signal value in the time window where reflected signal from the interface arrives but the signal reflected from the top of the composite plate does not appear. Plotting this peak value as a function of the transducer position the C-scan image is obtained. Left two images of Fig. 5 are obtained
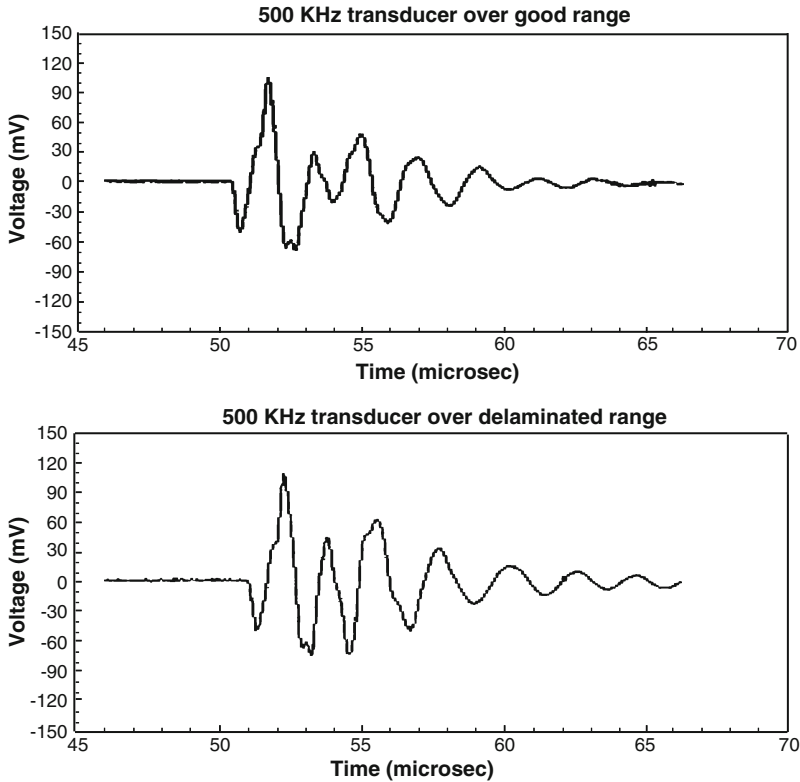
Fig. 4 Reflected (A-Scan) signals from the perfect region (top) and debonded region (bottom) of a composite plated concrete specimen shown in Fig. 3 [16]
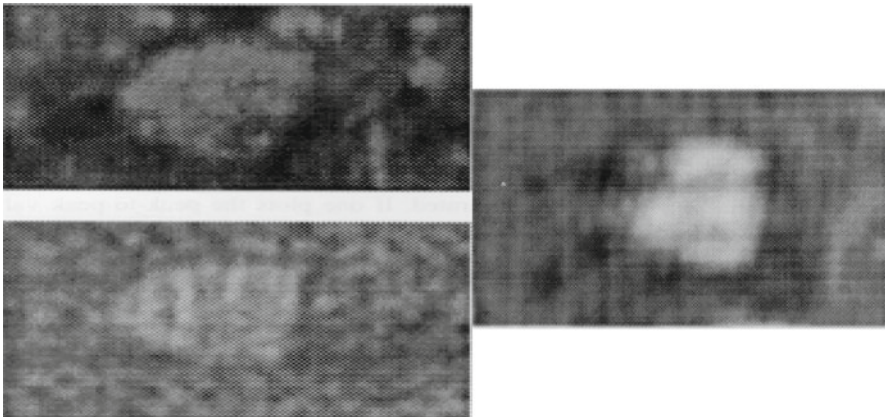
Fig. 5 Ultrasonic images of the delamination region between concrete and composite. Left two images were generated by conventional C-scan technique placing the transducer normal to the specimen as shown in Fig. 3. Top and bottom images on the left were generated by 500 kHz and 1 MHz, respectively. The right image is produced by scanning the specimen by a Lamb wave mode [16]

in this manner using 500 kHz and 1 MHz ultrasonic signals [16]. In both images the debonded region can be seen; however, the quality of the ultrasonic image is significantly improved in the right image of Fig. 5. The right image is obtained by scanning the specimen by a guided wave mode instead of the bulk P-wave. For guided wave scanning two transducers are placed in pitch-catch arrangement. The guided wave mode is generated by inclining the transmitter at a critical angle corresponding to a guided wave mode and then fine tuning the frequency to produce a strong signal at the receiver position. The generated guided wave propagates through the specimen for a short distance and then is detected by the receiver. The transmitter-receiver pair then scans the surface of the specimen to generate the acoustic image of the interface [16].

The Lamb wave inspection technique has been also used to inspect large metal plates [17, 18], metal pipes [19–21], concrete beams [22, 23] and reinforcing bars in concrete [24, 25].

Modeling

In the preceding section it is shown that guided waves are more effective in detecting and imaging internal defects. For accurate determination of their location and size it is necessary to understand the interaction between elastic waves and internal defects. Unfortunately, only for some simple defect geometries, such as circular and elliptical cracks in an infinite solid the analytical solution is available. For any other problem geometry one needs to depend on numerical or semi-analytical solutions. Finite element method (FEM) is the most popular numerical technique in engineering and science. However, in ultrasonic applications the advancement of FEM has been relatively slow for the reasons stated in Introduction. With the advancement of computation power and development of more sophisticated finite element codes, such as PZFLEX and COMSOL, specialized for handling ultrasonic problems, the FEM is becoming more popular for solving ultrasonic problems as well. It should be noted here that the FEM based ultrasonic wave propagation analyses available in the literature today are mostly confined to 2D problems [26–28]. For plane-stress, plane-strain and axi-symmetric problems FEM works very well. However, it is difficult to solve a true 3D ultrasonic problem at high frequencies by FEM even today [5].

Semi-analytical DPSM technique

The semi-analytical technique called Distributed Point Source Method (DPSM) for solving different ultrasonic problems has been discussed in various publications [1–14]. In DPSM modeling a number of point sources are placed inside the solid

Fig. 6 *M* point sources, placed at the centers of small spheres located behind the transducer face, model the transducer. Field values (pressure, velocity etc.) are comptued at *N* target points in front of the transducer [5]
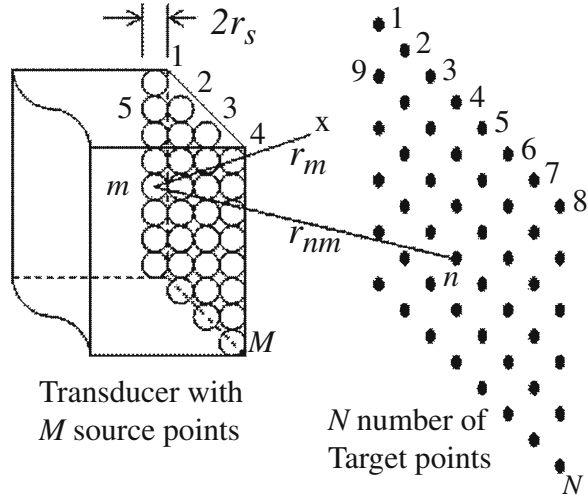
transducer slightly behind the transducer face as shown in Fig. 6 to generate the acoustic field in the fluid medium in front of the transducer face. This figure shows *M* spheres of radius r_s placed behind the transducer face. At the centers of these spheres *M* source points are placed. Therefore the point sources are located at a distance r_s behind the transducer face.

The pressure field in the fluid at point **x** at a distance r_m from the *m*-th point source of strength A_m is given by [5],

$$p_m\left(\mathbf{X}\right)= p_m\left(r_m\right)= A_m \frac{\exp\left(ik_f r_m\right)}{r_m} \tag{1}$$

By placing the point sources slightly behind the transducer face the need to compute the pressure at $r_m = 0$ is avoided. If *M* point sources model the transducer, as shown in Fig. 6, then the total pressure at point **x** is obtained from

$$p\left(\mathbf{X}\right)= \sum_{m=1}^{M} p_m\left(r_m\right)= \sum_{m=1}^{M} A_m \frac{\exp\left(ik_f r_m\right)}{r_m} \tag{2}$$

If there is an interface in front of the transducer then additional point sources should be placed on two sides of the interface. Point source strengths are obtained by satisfying the boundary and continuity conditions on the transducer surface and at the interface. Readers are referred to references [5] and [29] for detailed DPSM formulation. DPSM solutions for various ultrasonic problems are given below.

Fluid-solid interface
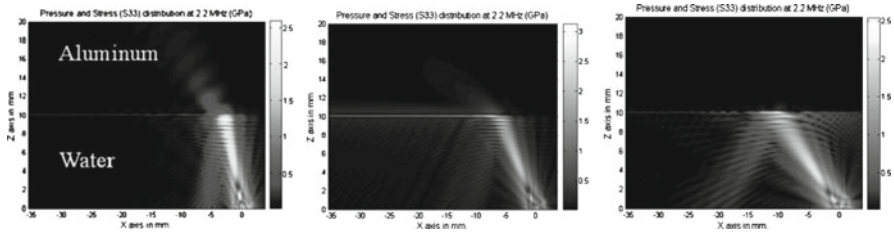
Fig. 7 An ultrasonic transducer genarating 2.25 MHz beam strikes water-aluminum interface at 15.4˚ (left), 30.4˚ (middle) and 45.4˚ (right). Note leaky Rayleigh wave generation for Rayleigh critical angle in the middle image [7]

Solid flat plate immersed in fluid
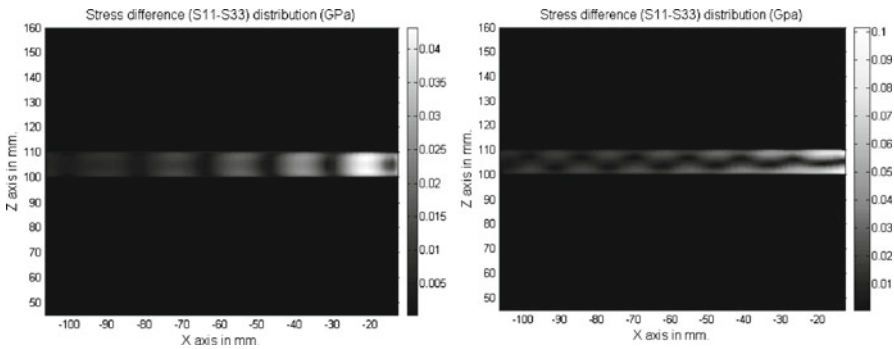
Fig. 8 A solid plate is excited by two identical ultrasonic transducers placed on two sides of the plate. Signal frequency and inclination angle of the transducers are adjusted to generate symmetric (left) and anti-symmetric (right) Lamb modes. Difference between two normal stresses (σ_{11}- σ_{33}) is plotted [8]

Solid plate containing a crack immersed in fluid
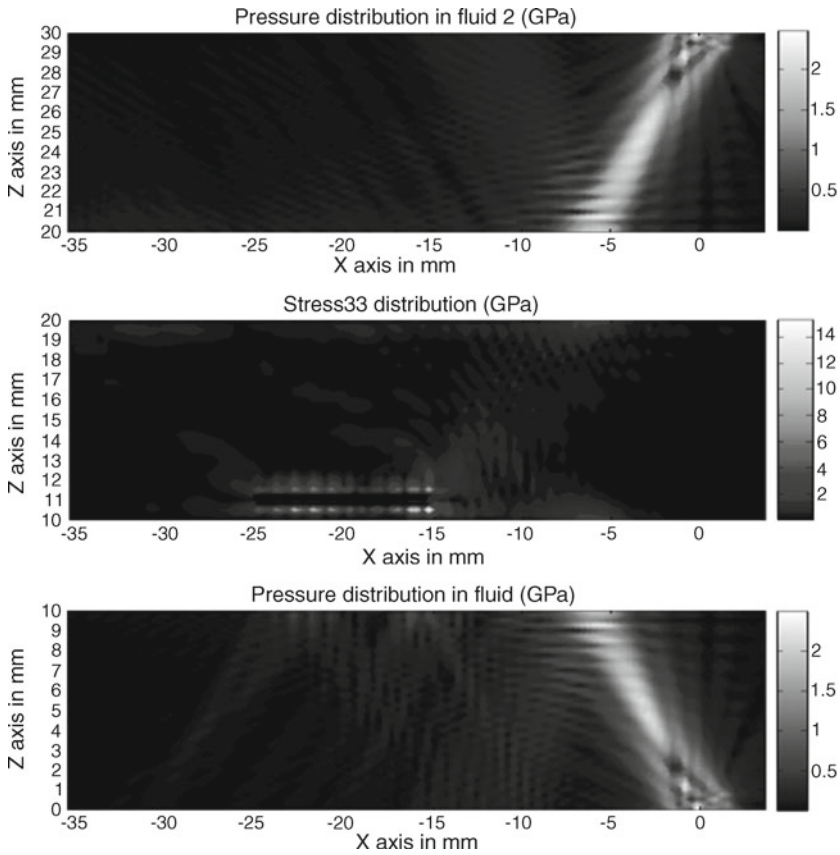
Fig. 9 A solid plate (middle image) containing a crack near the bottom surface is struck by ultrasonic beams from two sides (top and bottom) of the plate [11, 12]

Conclusions

In this paper some experimental results and semi-analytical DPSM generated results are provided. Experimental results show the advantage of using guided waves for internal defect detection. Different computed results demonstrate the flexibility of DPSM in modelling wave scattering by solid specimens and internal cracks. Interested readers are referred to a number of references provided in the text and in the figure captions for more detailed discussion and analysis.

References

[1] Placko, D. and Kundu, T. (2004), In: *Ultrasonic Nondestructive Evaluation: Engineering and Biological Material Characterization*, pp. 124-138, T. Kundu, (Ed.), CRC Press.

[2] Yanagita, T. Kundu, T. and Placko, D. (2009), *J. Acoust. Soc. Am.*, vol. 126, n. 5, p. 2331.

[3] Banerjee, S., Kundu, T. and Placko, D. (2006), *ASME J. Appl. Mech.*, vol. 73, n. 4, p. 598.

[4] Placko, D. Yanagita, T., Kabiri Rahani, E. and Kundu, T. (2010), *IEEE Trans. Ultrason. Ferro. Freq. Control*, vol. 57, n. 6, p. 1396.

[5] Kundu, T., Placko, D., Kabiri Rahani, E., Yanagita, T. and Dao, C. M., (2010), *IEEE Trans. Ultrason. Ferro. Freq. Control*, vol. 57, n. 12, p. 2795.

[6] Ahmad, R., Kundu, T. and Placko, D. (2005), *J. Acoust. Soc. Am.*, vol. 117, p. 1762.

[7] Banerjee, S., Kundu, T. and Alnuaimi, N. A. (2007), *Ultrasonics.*, vol. 46, n. 3, p. 235.

[8] Banerjee, S. and Kundu, T. (2007), *Int. J. Sol. Struct.*, vol. 44, p. 6013.

[9] Banerjee, S. and Kundu, T. (2006), J. Acoust. Soc. Am., vol. 119, n. 4, p. 2006.

[10] Das, S., Dao, C. M., Banerjee, S. and Kundu, T. (2007), *IEEE Trans. Ultrason. Ferro. Freq. Control*, vol. 54, n. 9, p. 1860.

[11] Banerjee, S. and Kundu, T. (2007), *Optical Eng.*, vol. 46, n. 5, p. 053601–1.

[12] Banerjee, S. and Kundu, T. (2008), *Wave Motion*, vol. 45, n. 5, p. 581.

[13] Das, S. and Kundu, T. (2009), *Struct. Health Monit.: Int. J.*, vol. 8, n. 5, p. 369.

[14] Shelke, A., Das, S. and Kundu, T. (2010), *Struct. Health Monit: Int. J.*, vol. 9, n. 6, p. 527.

[15] Kundu, T., Maslov, K. I., Karpur, P., Matikas, T. E. and Nicolaou, P. D. (1996), *Ultrasonics*, vol. 34, n. 1, p. 43.

[16] Kundu, T., Ehsani, M., Maslov, K. I. and Guo, D. (1999), *NDT&E Int.*, vol. 32, p. 61.

[17] Ghosh, T. and Kundu, T. (1998), *J. Acoust. Soc. Am.*, vol. 104, n. 3, p. 1498.

[18] Ghosh, T., Kundu, T. and Karpur, P. (1998), *Ultrasonics*, vol. 36, n. 7, p. 791.

[19] Guo, D. and Kundu, T. (2000), *Mat. Eval.*, vol. 58, n. 8, p. 991.

[20] Guo, D. and Kundu, T. (2001), *J. Acoust. Soc. Am.*, vol. 110, n. 1, p.303.

[21] Na, W.B. and Kundu, T. (2002), *J. Press. Vessel Technol.*, *Trans. ASME*, vol. 124, n. 2, p. 196.

[22] Jung, Y. C., Kundu, T. and Ehsani, M. R. (2001), *Mat. Eval.*, vol. 59, n. 3, p. 418.

[23] Jung, Y. C., Kundu, T. and Ehsani, M. R. (2002), *ACI Mat. J.*, vol. 99, n. 3, p. 292–299.

[24] Na, W. B., Kundu, T. and Ehsani, M. (2002), *Mat. Eval.*, vol. 60, n. 3, p. 437.

[25] Na, W. B. and Kundu, T. (2003), *J. Exp. Mech.*, vol. 43, n. 1, p. 24.

[26] Hosten, B. and Blateau, C. (2008), *J. Acoust. Soc. Am.*, vol. 123, n. 4, p. 1963.

[27] Hosten, B. and Castaings, M. (2005), *J. Acoust. Soc. Am.*, vol. 117, n. 3, p. 1108.

[28] Hosten, B. and Castaings, M. (2006), *NDT&E Int.*, vol. 39, n. 3, p. 195.

[29] Banerjee, S. and Kundu, T. (2007), In *DPSM for Model. Eng. Probl.*, pp. 143–229, D. Placko and T. Kundu (Eds.), John Wiley & Sons.

Ultrasonic Guided Waves for Hidden Damage Detection in Composite Structures: Theory and Experiments

F. Ricci, E. Monaco, S. Tancredi, L. Lecce, S. Banerjee and A.K. Mal

Abstract   In this paper the theoretical knowledge base required for the development of a reliable structural health monitoring system based on ultrasonic guided waves is considered. An exact theory is used for relatively rapid calculation of the PZT driven surface motion in a plate recorded in an ultrasonic experiment. The theoretical results are compared with those obtained from an explicit finite element code for their mutual verification, showing excellent agreement. To determine the location and the severity of a damage with a minimal operator intervention, the ultrasonic wave propagation data are analyzed using a damage index approach carefully designed to overcome the complexity and variability of the signals in the presence of damage as well as the geometric complexity of the structure.

Keywords   Composite structures • Damage detection • Guided waves • Ultrasound

Introduction

Much of Structural Health Monitoring (SHM) research is motivated by the fact that damage tolerant and fail-safe design of aircraft, aerospace and civil structures requires a substantial amount of inspection and defects-monitoring at regular

F. Ricci • E. Monaco • S. Tancredi (✉) • L. Lecce
Aerospace Engineering Department, University of Naples, "Federico II", 80125 Naples, Italy
e-mail: simone.tancredi@unina.it

S. Banerjee
Department of Civil Engineering, IIT Bombay Powai, Mumbai 400076, India

A.K. Mal
Mechanical and Aerospace Engineering Department, University of California, Los Angeles, CA 90095-1597

intervals. There is a large inventory of aircraft structures in operation throughout Europe and the world that are undergoing continuous degradation through aging. Moreover, this number is increasing by around 5% every year, resulting in significant negative impact on the economy of many nations. The degradation of defects on critical structures is controlled through careful and expensive regularly scheduled inspections in an effort to reduce their risk of failure. With the cost of scheduled but often unneeded maintenance ever increasing, intelligent, real-time monitoring of the condition of these structures is imperative to guarantee their safe and affordable continuing operation.

The ultrasonic research community has studied guided waves for the nondestructive evaluation of plate-like structures for several decades. Guided waves are created by the constructive interference of the bulk waves reflected between the surfaces of the plate; these waves have a number of characteristics that are different from those of the bulk waves. First, they are, in general, multimodal and dispersive; the particle motion (symmetric or extensional and antisymmetric or flexural) and the velocity of each mode depends upon the thickness and material properties of the plate, as well as the frequency of the excitation of the wave. Second, they can propagate a much larger distance than the bulk waves without significant decay in their amplitude. Third, and most important, they are extremely sensitive to the presence of discontinuities in their path, and carry information on certain properties of the flaws as they propagate away from the flaws.

Finally, it is relatively easy to generate and record the guided waves using (PZT) actuators and sensors that require very little power, and are therefore suitable for online structural health monitoring.

Recently, research on active health monitoring of structural components using guided waves has gained considerable interest due to advances in sensor- and hardware technologies and the increased usage of composite materials in load-carrying structural components, particularly in the aircraft industry. However, the optimum use of the favorable properties of guided waves in SHM requires a good understanding of their interaction with defects through both theoretical simulations and carefully designed experiments. While significant advances in the experimental techniques have been made in recent years, advances in the theoretical studies on the interaction problem in composite structures have been rather limited. The exact solution of three-dimensional problems consisting of undamaged multilayered, angle-ply laminates of finite thickness and large lateral dimensions subjected to various types of surface loads, has been given in [1–2].

The finite element method (FEM) is also a versatile tool to analyze this class of problems and a dynamic finite element code has been developed by NIST for the calculation of acoustic emission (AE) waveforms in isotropic and anisotropic plates [3]. Commercial finite element packages, e.g. LS DYNA, have been used extensively for large-scale simulation of impact problems in variety of structures. Although the FEA can handle complex geometries and has the capability to accommodate reflections from the lateral boundaries, it is computationally much more intensive than the analytical methods discussed above.

Numerical and Experimental Validation

In this paper, an exact theory is used for relatively rapid calculation of the PZT driven surface motion as recorded in an ultrasonic experiment. The theoretical results are compared with those obtained from an explicit finite element commercial code (LS DYNA) for their mutual verification, showing excellent agreement. Important characteristics of the ultrasonic signals recorded by the PZT patches in an experiment are carefully extracted and modeled to identify the behavior of the PZT patches used in the experiment.

The PZTs used in the experiment mostly generate and record in-plane motion in the frequency range 30÷500 kHz, that can be approximately modeled by using an in-plane point force on the surface of the plate as a source and by calculating the in-plane surface displacement at the receiver location. The combined modeling and simulation techniques of guided waves can be used for efficient and accurate predictions of the wave forms in both near and far fields for complex geometries.

The Fig. 1 shows the experimental set-up and the comparison of the results obtained from the exact theory, FE simulation and experiment. The tests were conducted on a 6061 T6 aluminum panel (0.8 m x 0.8 m x 0.001 m). Four disc-shaped piezo patches ($\varphi = 10$ mm and thickness 0.2 mm) were bonded on one surface of the plate. A predefined 4.5 cycle sinusoidal pulse of central frequency at 200 kHz in a Gaussian envelope has been used as source signal and generated by a HP/Agilent 33120A function generator wired to one of the PZTs. The response was measured by other surface-mounted PZTs located at distances of 50mm, 100mm and 200mm, respectively, from the source, and was downloaded in an HP DSO7014A 100 MHz 4 channels oscilloscope for processing. The good agreement between the exact theory results and LS DYNA simulations indicates that both methods work well for the calculation of the wave forms generated and recorded by the PZT patches in a plate. As the three curves have been normalized respect to their maximum values (first So modes), the difference in the amplitudes of the first Ao experimental and numerical modes is due to the sensitivity difference of the piezo patches in catching the symmetric and anti-symmetric motions.
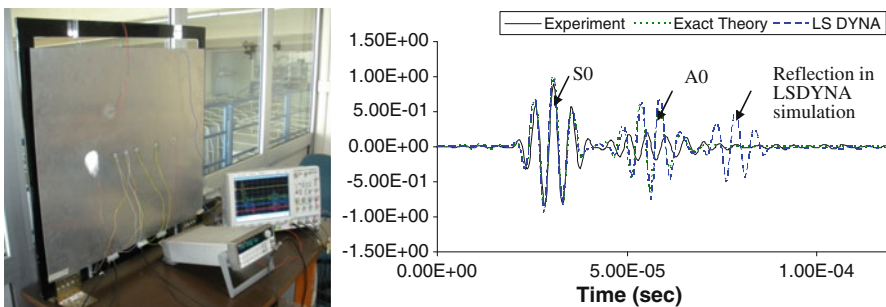
Fig. 1 Experimental set-up (left) and time histories of in-plane surface displacement at a distance of 100 mm from an in-plane point force (right)

Damage Index

To determine the location and the severity of a damage with a minimal operator intervention, the ultrasonic wave propagation data are analyzed using a damage index approach. The damage index is designed to overcome the complexity and variability of the signals in the presence of damage as well as the geometric complexity of the structure. This has been done by calculating at each acquisition point an index measuring the difference between the Fourier transforms of the wave signals collected in the two conditions (pre- and post-damage). Thus, unless the environment undergoes significant changes between the two sets of measurements (which can occur within a very short time frame), noise, in general, will have no effect on the results. The damage index vanishes if there is no change in the structure and its value increases with the severity and proximity of damage to the sensor locations. Thus if damage is initiated at a location within or near the sensor array, then its location and severity can be determined in real-time by the autonomous scheme. More details about damage index can be found in [4].

To demonstrate the effectiveness of the damage index a comparison between experimental data and numerical results is reported. The experiment involved a 300mm x 200mm x 1mm aluminum plate. A disc shaped piezoelectric patch (diameter 15.3mm and thickness 0.5m) was used as transmitter and the signal was generated by a HP/Agilent 33120A signal generator. A Polytec PSV-400 laser vibrometer was employed for the data acquisition. The damage consists of a 20 mm through-the-thickness crack at the center of the plate. The experiment was then modeled with an explicit finite element code (LS-DYNA). Figures 2 and 3 show a sketch of the aluminum plate and the experimental setup. Figures 4 and 5 show the numerical and experimental results of the spatial distribution of the damage index over the cracked plates. The experimental results locate higher values of the index near the crack location, although there is a region where the index reaches values higher than

Fig. 2 A sketch of the aluminum plate (**o** acquisition locations **O** piezo patch crack __)
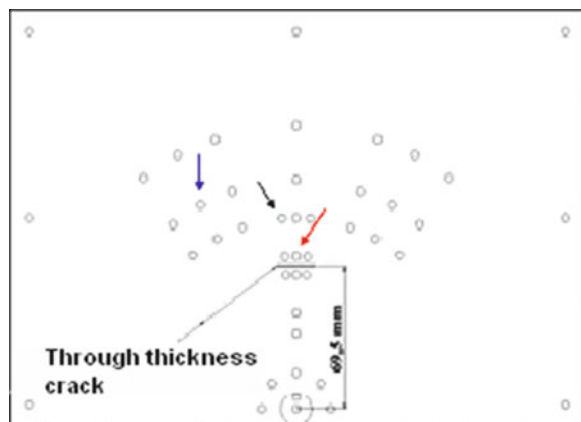
Fig. 3 The experimental set-up
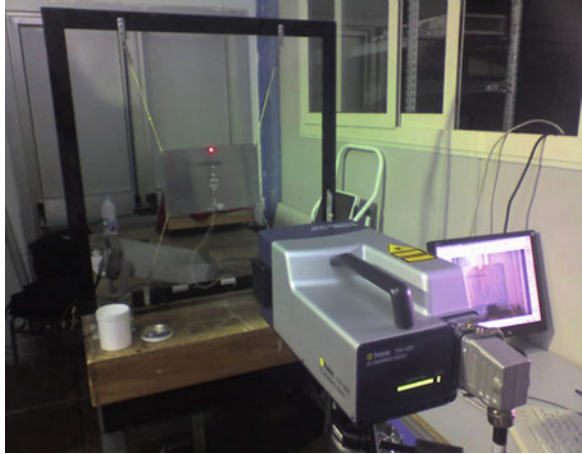
Fig. 4 Numerical (FEA) damage index calculation
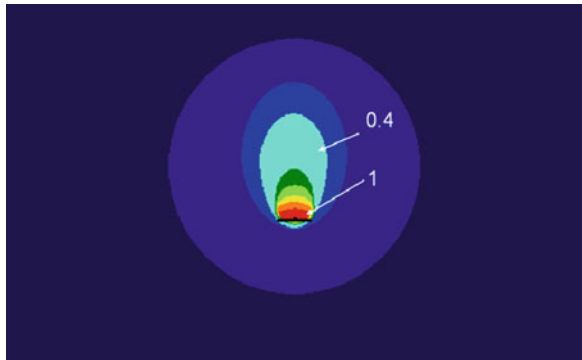
Fig. 5 Experimental damage index evaluation
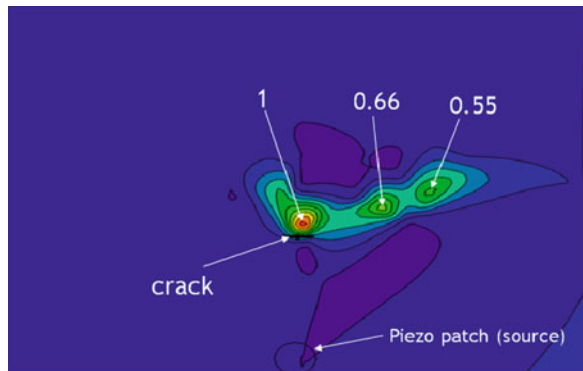
those obtained from the numerical calculations. This is probably due to a local debonding of the piezo patch from the surface of the plate which may have occurred at a certain time during the experiments.

Application to Impacted Composite Plates

An application to low velocity impact damage localization in a multi-layered composite plate is presented. The applied methodology consists in collecting signals in the pre-impact (baseline) and post-impact conditions and then analyzing them to identify the presence of hidden defects such as matrix cracks or delaminations.

A numerical calculation has been carried out for a 2.5 mm thick CFRP cross ply composite panel of dimensions (1m x 1m), for which experimental results were available. A square shaped delamination 38mm wide was simulated in the numerical model and Lamb waves analysis was carried out. The numerical analysis has been performed both for the defect free and delaminated configurations in order to determine the damage index distribution over the panel. A predefined 4.5 cycle sinusoidal pulse of central frequency at 200 kHz in a Gaussian envelope has been used as source in order to have a wavelength with the same dimension as the damage.

Although there is not any visible difference between the undamaged and damaged responses (Fig. 6), the utilization of the damage index allows a good localization of the delaminated area. As expected and shown in Fig. 7, a large area with high values of the damage index is present downstream to the damage with respect to the actuator position. The experimental validation of the impact damage localization in composite plates is currently in progress.
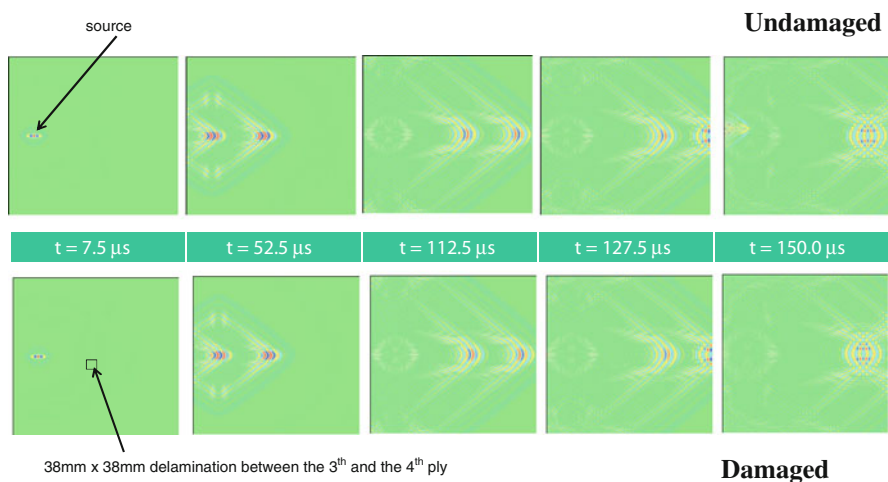
Fig. 6 Propagation of Lamb waves in damaged and undamaged condition
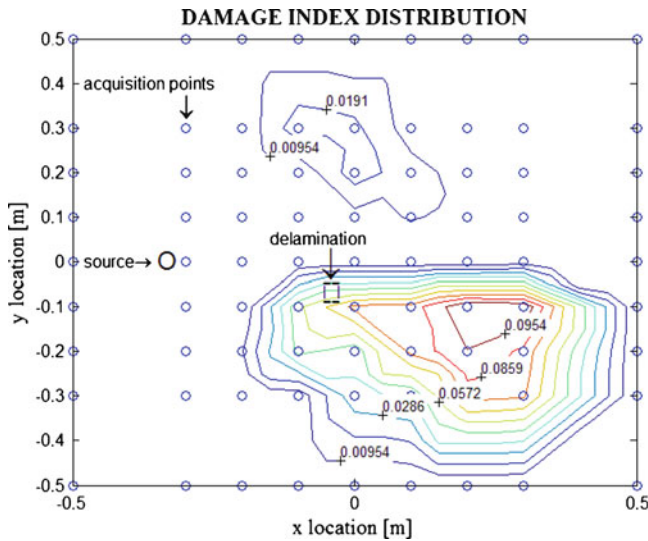
Figure 7   Damage Index from the FE results

Conclusions

Since the exact theory is computationally less expensive than the LS DYNA simulation, it can be effectively used to understand general characteristics of wave motion in simple, undamaged models of structural components. To our knowledge, theoretical solution of the class of wave interaction problems in composite structures containing hidden defects or other realistic features (e.g., stringers, joints, etc) is nonexistent, except for a few highly idealized cases [5].LS DYNA has the capability to handle models involving complex geometries containing defects and other structural anomalies. Therefore, the two methods can be combined for efficient and accurate calculation of the waveforms in plates. The applied methodology consists in collecting signals in the pre-damage (baseline) and post-damage conditions and then analyzing them to identify the presence of hidden defects in the data collected by the transducers. The algorithm developed here is shown to be capable of analyzing large amount of high frequency wave propagation to detect and localize defects in structural components without extensive manual intervention.

References

[1] Lih, S. S., and Mal, A. K. (1995). "On the accuracy of approximate plate theories for wave field calculations in composite laminates". *Wave Motion*, 21, 17–34.
[2] Banerjee, S., Prosser, W. H. and Mal, A. K. (2005). "Calculation of the response of a composite plate to localized dynamic surface loads using a new wavenumber integral method". *ASME J. Appl. Mech.*, 72 (1), 18–24.

[3] Prosser, W. H., Hamstad, M. A., Gary, J., and O'Gallagher, A. (1999). "Comparison of finite element and plate theory methods for modeling acoustic emission waveforms". *J. Nondestruct. Eval.*, 18 (3), pp. 83–90.

[4] Banerjee, S., Ricci, F., Monaco, E., Mal, A. K. (2009). "A wave propagation and vibration-based approach for damage identification in structural components", *J. Sound Vib.*, 322 (1–2), 167–183.

[5] Guo, D., Mal, A. K., and Ono, K. (1996). Wave theory of acoustic emission in composite laminates. J. *Acoust. Emission*, 14, S19–S46.

Nonlinear Ultrasound: A Novel Approach to Flaw Detection and Imaging

I. Solodov, N. Krohn and G. Busse

Abstract Conventional ultrasonic NDT equipment is normally a mono-frequency instrument which makes use of the amplitude and phase variations of the input signal due to its scattering by defects. The nonlinear approach to ultrasonic NDT (NNDT) is concerned with the nonlinear response of defects, which is related to extreme frequency changes of the original input signal. These spectral changes are caused by a high nonlinearity of micro- and macro-scale defects. In the paper, basic mechanisms responsible for frequency conversion by nonlinear defects are discussed and major features of the nonlinear spectra derived. Experimental methodologies of nonlinear scanning laser vibrometry (NSLV) and nonlinear air-coupled emission (NACE) are used to study nonlinear elastic wave-defect interactions. Applications for defect-selective imaging and NNDT are demonstrated for a series of hi-tech materials and industrial components.

Keywords Defect-selective imaging • Nonlinear air-coupled emission • Nonlinear laser vibrometry • Ultrasonic nonlinearity

Introduction

Over the last decades, an intensive world-wide study has been developed on elastic wave nonlinear phenomena and their applications in medicine, geophysics, and NDT in particular [1]. The discovery of anomalous nonlinear ultrasonic response of medical contrast agents whose local nonlinearity is enhanced due to highly nonlinear vibrations of incorporated gel bubbles made a breakthrough in medical diagnostics [2]. A two-three order of magnitude increase in local nonlinearity was also

I. Solodov (✉) • N. Krohn • G. Busse
Department of Nondestructive Testing (IKT-ZFP), Institute of Polymer Technology,
University of Stuttgart, Stuttgart, Germany
e-mail: igor.solodov@ikt.uni-stuttgart.de

revealed for damaged areas in a wide class of solid materials [3]. A physical reason for that is associated with inherently nonlinear vibrations of non-bonded contacts (contact acoustic nonlinearity, CAN [4]) due to mechanical constraint between the fragments of defects. The CAN provides a broad spectral conversion by the nonlinear defects: higher harmonics, subharmonics, combination frequencies, etc. which can be used as signatures for damage detection and imaging.

CAN Mechanisms and Manifestations

The basic mechanisms of CAN are concerned with intermittent contacting of the defect interfaces caused by an intense ultrasonic wave. This makes vibrations strongly nonlinear with a broad nonlinear spectrum localized around the defect. An overview of dynamic behaviour (as a function of strain ε in the driving wave) for nonlinear vibration modes of defects is presented in Fig. 1.

Higher harmonic (HH-) modes

The CAN mechanisms of intermittent contact between the defect fragments cause a strong time modulation of the local stiffness over the vibration period. For a normal driving traction, it causes higher contact stiffness in compression phase and lower in tension. Such "clapping" provides distortion of local vibrations in the defects driven by a harmonic wave. As a result, the vibration spectrum contains a number of both odd and even higher harmonics (HH) of the driving frequency [4]. A strong stiffness modulation in cracked defects makes CAN extremely efficient so that HH-generation develops (Fig. 1) even at low-strain excitation ($\varepsilon \sim 10^{-7}$).

Under shear traction the micro-contact interaction is determined by the nonlinearity of the friction forces. In the static friction regime, the contact stiffness
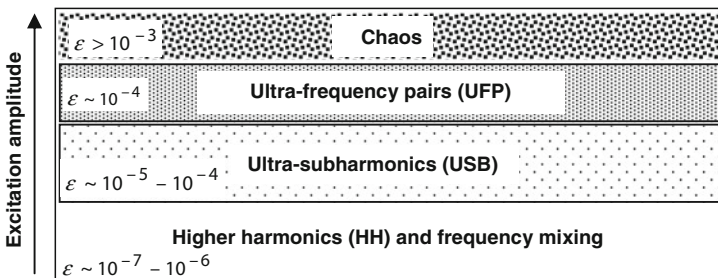
Fig. 1 Schematic diagram of nonlinear dynamics for cracked defects

modulation is caused by the interaction of the surface asperities in shear (micro-slip) which obviously causes a symmetrical distortion (rectification) of the driving vibrations and brings about odd HH generation. If the driving shear traction is beyond the static friction force, the contact surfaces start sliding ("rubbing"). The transition between stick and slide phases provides nonlinearity in vibrations with a similar symmetrical distortion and efficient odd HH generation [5].

Ultra-subharmonics (USB) and ultra-frequency pairs (UFP)

Similar to resonance behaviour of an air bubble in liquid, vibrations of a certain area of material around a cracked defect are characterized by reduced stiffness which defines a specific natural frequency ω of the nonlinear defect. The quadratic terms in defect nonlinearity provide the interaction between the natural defect vibrations and those induced by the driving wave (frequency ν) to create the combination frequencies ($\nu \pm \omega$). If $\nu = 2\omega$, the difference frequency component $\nu - \omega = \omega$ is in resonance and the output is a sub-harmonic vibration at a half of the input frequency: $\omega = \nu / 2$. Similarly, the higher-order nonlinear terms produce the spectral components of frequencies $n(\nu / 2)$ (ultra-sub-harmonics).

The spectra of nonlinear resonance are modified for driven vibrations of a more complex cracked defect represented as a set of coupled nonlinear oscillators. The lower-order nonlinear response of the two oscillators (normal frequencies ω_1, ω_2) for $\nu \approx \omega_1 + \omega_2$ contains the combination frequencies $\nu - \omega_1 \approx \omega_2$ and $\nu - \omega_2 \approx \omega_1$, respectively that provide resonance excitation of the frequency pair ω_2 and ω_1. The higher-order nonlinear terms result in generation of a line spectrum which comprises multiple ultra-frequency-pair (UFP) side-lobes around ultra-harmonics [6]. For high-amplitude excitation, the UFP bring the system to a quasi-continuous spectrum which indicates a build-up of chaotic vibrations.

Defect-Selective Imaging via NSLV

To observe the vibration spectra of defects the laser scanning vibrometry was adapted for nonlinear measurements. A piezo-stack transducer connected to CW high-power Branson PG generator was used for generation of intense flexural waves (frequencies 20 and 40 kHz, strain amplitudes up to ~10^{-3}); the out-of-plane particle velocity induces frequency modulation of the laser light reflected from the surface of the specimen. After demodulation in the controller of Polytec scanning vibrometer PSV 300 and A/D conversion, the spectrum of the vibrations (particle velocity output) is obtained over 1 MHz bandwidth by FFT in the PC-unit.

An example demonstrating the defect-selective character of the nonlinear imaging is shown in Fig. 2. The fundamental frequency (20 kHz) NSLV image of
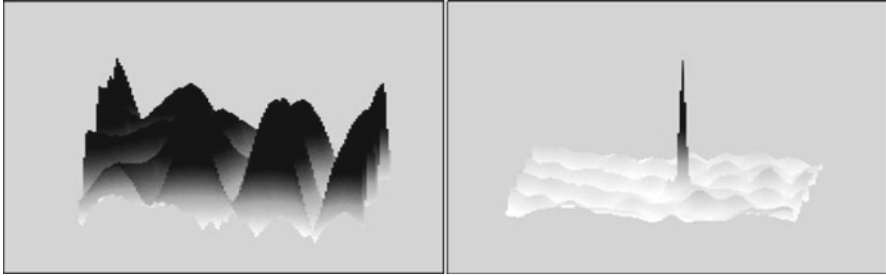
Fig. 2 Linear (left) and third harmonic (right) NSLV-images of a point impact damage in carbon-kevlar composite
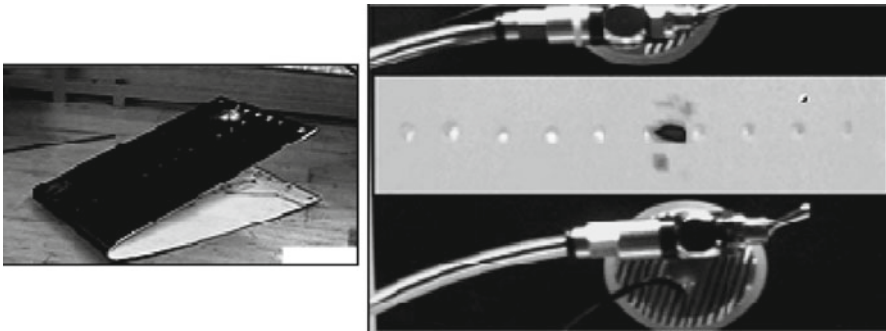
Fig. 3 Higher harmonic imaging of a fatigue crack in aviation component (left) by using excitation with portable ultrasonic transducers (right)

the damaged area in fabric carbon-kevlar fibre-reinforced composite (left) reveals a pronounced standing wave pattern in the specimen with no indication of damage. The higher harmonic image (Fig. 2, right) selectively indicates the point impact damage. The signal-to-noise ratio of the nonlinear image in Fig. 2 is about 20 dB.

Due to a relatively moderate input power required, a flexible operation in the HH-mode can be achieved even for large industrial parts by using portable ultrasonic transducers. The example in Fig. 3 shows nonlinear imaging of a fatigue crack in a riveted aviation component. The 20-kHz excitation was implemented with "dry-contact" portable piezoelectric transducers attached to the specimen by vacuum suction. The use of a pair of transducers enabled to obtain a more homogeneous driving ultrasonic field and thus to reduce the influence of the standing waves.

Figure 4 displays an example of NNDE of defects in an advanced material for aircraft industry: glass fibre reinforced aluminium laminate (Glare®). It shows the USB-NSLV images of a Glare® plate with two inserted circular Teflon-foils to simulate local delaminations. In the images, the defect can be recognized fairly well, and the quality is enhanced for the higher orders of the USB.
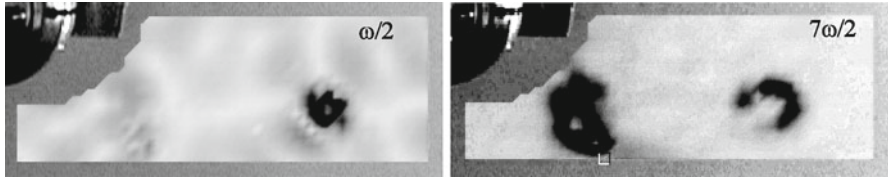
Fig. 4 USB-images of a pair of artificial delaminations in a Glare® plate
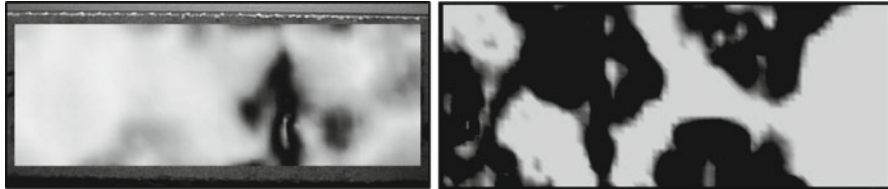
Fig. 5 NSLV imaging in GFR-concrete: USB-image of a crack (left) and UFP (30.5 kHz)-image of delamination area (dark) in GFR-concrete slab (right)

Two examples of nonlinear monitoring of macro-defects in constructional materials are shown in Fig. 5 for a slab of GFR-concrete (15x30x1.5cm). Production technology of this material often suffers from cracks and internal delaminations induced by fibre-matrix debonding. Due to a grainy structure of the fragile material, these defects include multi-contact interfaces which are highly nonlinear. The USB image in Fig. 5, left clearly visualizes a vertical surface crack.

A few cm delamination areas in the material should be considered as complicated defects with a set of characteristic frequencies. Accordingly, an efficient multiple UFP generation was measured in these areas for intense 20 kHz excitation; the 30.5 kHz UFP component image clearly indicates the delaminations (Fig. 5, right).

Imaging of Defects via NACE

Our experiments also reveal that planar defects as localized sources of nonlinear vibrations efficiently radiate nonlinear ultrasound [7] in air. This radiation can be used for detection and visualization of defects. A practical version of the NACE includes a high-frequency air-coupled (AC) transducer as a receiver of the nonlinear ultrasound activated by a low-frequency excitation. The FFT of the output signal is then applied for computer imaging of distribution of nonlinear frequency components over a specimen surface (Fig. 6).

In the experiments, the piezo-stack transducer and high-power supply (Branson Ultrasonics) provided an intense low-frequency (around 20 and 40 kHz) excitation with $\geq 10^{-6}$ strain amplitude in the source. The focused (focus spot ~2-3 mm, focus
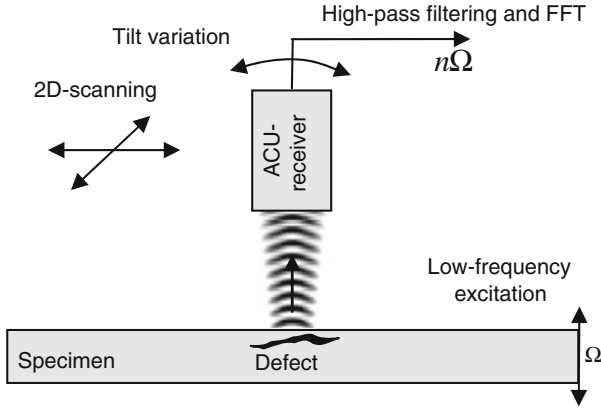
Fig. 6 Experimental set-up for imaging of defects via NACE

Fig. 7 Photo (left) and NACE image (right) of laser weld-line between steel plates
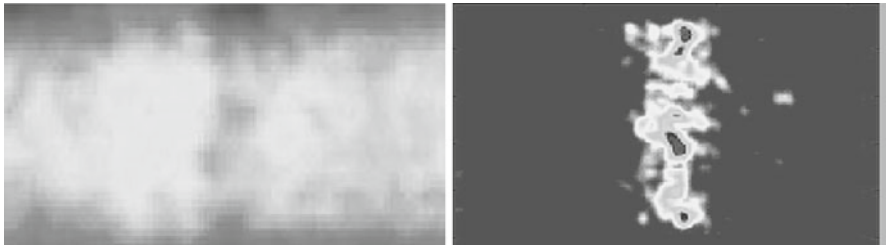
Fig. 8 NACE imaging (right) of inter-ply cracking (left) in a C/C/Si composite

distance 40 mm) AC-transducer with frequency responses centred at ~450 kHz (3 dB-bandwidth of ~20 kHz) was used as a receiver in the C-scan mode.

The NACE NDT-application was found to be particularly beneficial in metallic components where low acoustic damping facilitates the formation of standing waves which produce a strong spurious background in the NSLV. In particular, the image in Fig. 7 shows that the NACE pattern reproduces well a quality of the laser weld-line between two steel components.

The high NACE sensitivity to surface cracked defects is illustrated in Fig. 8 for sub-*mm* wide inter-ply cracking in a massive C/C/SiC-ceramic specimen (left). The

NACE image (right) reproduces a discrete structure of the edge cracking and thus demonstrates a good (mm-scale) spatial resolution.

Unlike NSLV, which analyzes the light reflected from the specimen, the NACE-imaging relies on the direct nonlinear acoustic radiation by the defects. For the weakly-focused AC-transducers with *cm*-range focus depth, the receiver is insensitive to medium scale variations of the surface profile. Our experiments show that the NACE operates well in various constructional materials (wood, concrete, metals) with raw surfaces and rugged defects in components.

Conclusions

The nonlinear vibration spectra are produced locally in the damaged area while an intact part of material outside the defects vibrates linearly, i.e. with no frequency variation in the output spectrum. This makes nonlinearity a defect-selective indicator of damage presence and development. This feature of localized nonlinearity enables 2D-imaging of the nonlinear excitations confined inside the fractured defect areas. Fortunately, this group of flaws includes the most malignant defects for material strength: micro- and macro-cracks, delaminations, debondings, impact and fatigue damages.

A number of case studies prove the applicability of nonlinear NDT and defect-selective imaging in various materials by using NSLV and NACE. Particularly successful examples include hi-tech and constructional materials: impact damage and delaminations in fibre-reinforced plastics, fatigue micro-cracking and cold work in metals, delaminations in laminates and fibre-reinforced concrete.

Unlike conventional ultrasonic testing, the NNDT provides abundant multi-frequency information on properties and location of defects. This suggests an opportunity for application of advanced data and image fusion algorithms to result in higher sensitivity and accuracy of inspection, higher reliability and quality of NDT.

References

[1] *Universality of Nonclassical Nonlinearity with Application to NDE and Ultrasonics*, Delsanto, P. (Ed.), (2006) Springer Verlag, New York, USA.

[2] Tranquart, F., Grenier, N., Eder, V., and Pourcelot, L. (1999). *Ulrasound Med. Biol.*, vol. 25, p. 889.

[3] Solodov, I. *Ultrasonics*, (1998), vol. 36, n. 1-5, p. 383.

[4] Solodov, I., Krohn, N., and Busse, G. *Ultrasonics*, (2002), vol. 40, p. 621.

[5] Pecorari, C. and Solodov, I. (2006). In: *Universality of Nonclassical Nonlinearity with Application to NDE and Ultrasonics*, pp. 307–324, Delsanto, P., (Ed.), Springer Verlag, New York, USA.

[6] Solodov, I., Wackerl, J., Pfleiderer, K., and Busse, G. (2004), *Appl. Phys. Letts.*, vol. 84, n. 26, p. 5386.

[7] Solodov, I. and Busse, G. (2007), *Appl. Phys. Letts.*, vol. 91, n. 25, p. 251910.

Evaluation of Material Degradation of Composite Laminates Using Nonlinear Lamb Wave

W. Li, Y. Cho, T. Ju, H.S. Choi, N. Kim and I. Park

Abstract This study introduces a new approach to evaluate material degradation caused by thermal fatigue in composite laminates by using nonlinear Lamb waves. The correlation between normalized nonlinear parameters and degradation states is studied. S1 Lamb mode which has phase and group matching features is chosen for the practical generation of nonlinear Lamb wave. The measured acoustics normalized nonlinearity is directly related to material degradation. It could be concluded that it is possible to use nonlinear Lamb waves to evaluate composite laminates degradation.

Keywords Composite laminates • Material degradation • Nonlinear lamb waves • Phase matching • Thermal fatigue

Introduction

Experimental research and theoretical study of Lamb wave application in composite has been addressed since the late 1980s, the exploration of Lamb wave applied in composite laminates got increasingly concern for the usually relatively small thickness

W. Li • Y. Cho (✉) • T. Ju
School of Mechanical Engineering, Pusan National University, Busan, 609-735, South Korea
e-mail: mechcyh@pusan.ac.kr

H.S. Choi
Composite R&D, Project Planning, Korean Air R&D Center, Aerospace Division, Korean Air, South Korea

N. Kim
School of Mechanical Engineering, Korean University of Technology and Education, ChungNam, 330-860, South Korea

I. Park
School of Mechanical Engineering, Seoul National University of Science and Technology, Seoul, 139-743, South Korea

compared with length of laminate-structures [1]. Material degradation is always accompanied with a certain nonlinear behavior of material properties, and ultrasonic propagation in media is directly related material properties, so nonlinear ultrasonic measurements are proposed a potential tool to characterize material degradation [2–3]. Deng and C. Pruell recently characterized the micro-structure change due to fatigue [4] or derived plasticity [5] by using nonlinear Lamb wave in metallic material. For composite laminates, the most common defects happened in the material are transverse matrix cracks, debonding and delamination, all these defects size are microscopic. Nonlinear Lamb wave should have greater potential for application in this material.

In this paper, a second harmonic generation measurement during Lamb wave propagation in composite laminates is used to evaluate the material degradation. In first section, it introduces specimens and experimental system. After testing all specimens under different thermal cycles, the correlation between material degradation degree and nonlinear parameter is found.

Specimens and Experimental System

Specimens used in this study were unidirectional and symmetric quasi-isotropic laminates, were made of carbon/epoxy laminates with stacking sequences $[0]_6$. All specimens' thickness is 1.0 mm, the dimensions were 40 mm × 40 mm as shown in Fig. 1. Thermal fatigue was imposed on specimens to fabricate degradation. The maximum and minimum temperatures of thermal cycle were respectively of 70°C and -55°C with constant cooling and heating time of 15 min. Tested specimens in this study were conducted under 0, 100, 200, 1000 thermal cycles.

Measurement of second harmonic amplitude is the goal of nonlinear ultrasonic test. Second harmonic is the wave that contains components at double frequency of
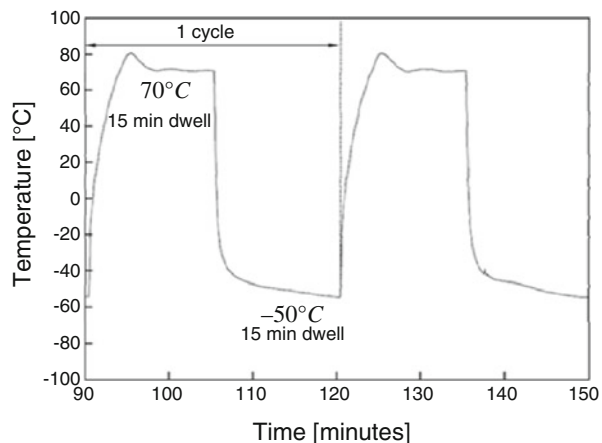
Fig. 1 Thermal fatigue cycle

the incident wave. A high voltage tone burst signal of 10 cycles at frequency of 2.25 MHz generated by the RAM-RITEC ultrasonic measurement system. A fixed pressure was loaded in the transducers through holders. The transducers are coupled to the specimen with light lubrication oil. The waveform was digitally processed using Short Time Fourier Transformation [STFT] in order to obtain the spectrogram (energy density) to represent A_1 at fundamental frequency and A_2 at the double frequency [6].

Lamb Wave Nonlinearity Measurement

S1 Lamb mode at frequency of 2.25MHz is generated. In this spectrum, at the wave velocity is 9.67km/s, (the incident angle is 16.6^0), the possible wave modes are S1 mode and A1 mode. In the experimental work, as shown in figure 2(b), the group velocity of S1mode is quite different from A1mode, so after a certain propagation distance, wave-packs of S1and A1 will separate finally. Through analysis, the S1 mode will separate singularly after 15cm propagation distance in this investigation. A singular mode S1 is selected and its higher harmonic analysis were made after 15cm.

Result and Discussion

Measured time-domain signal is processed in time–frequency domain with the short time Fourier transform(STFT) to get its spectrogram. In Fig. 3, a time domain Lamb signal includes fundamental Lamb wave(FLM) and second harmonic Lamb wave(SHLM) was processed with STFT, FLM and SHLM almost have the same
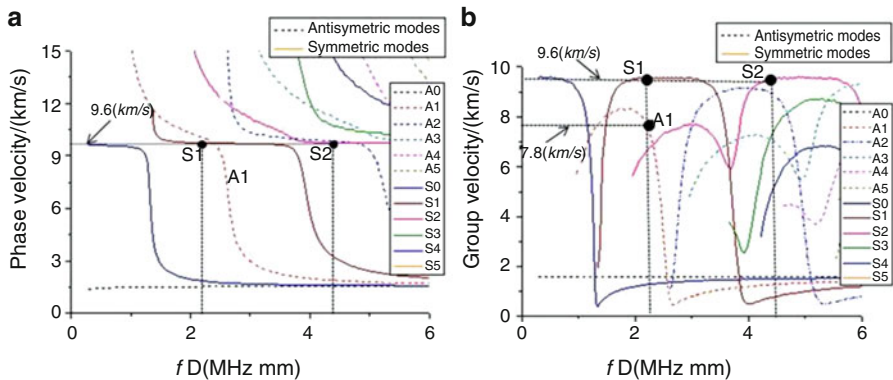
Fig. 2 Numerically calculated phase velocity (**a**) and group velocity (**b**) dispersion curves for Lamb wave in $[0]_6$ composite laminates
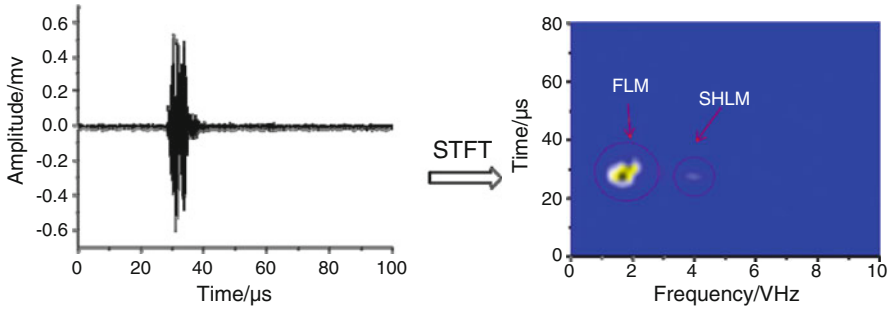
Fig. 3 (**a**) Typical time-domain signal (**b**) spectrogram resulted by STFT

Fig. 4 Normalized nonlinear parameters versus propagation distance
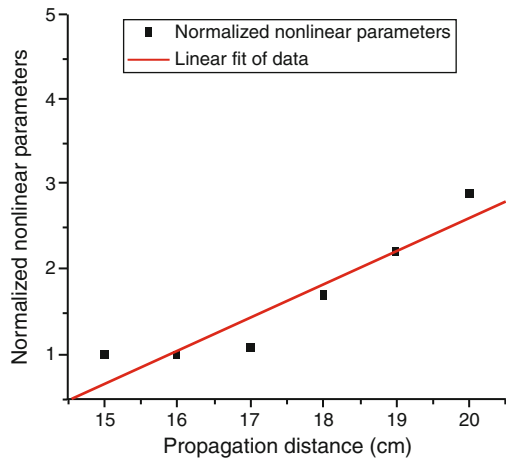
time in the spectrogram after a certain propagation distance, which means that fundamental wave and second harmonic has the same wave speed, it certifies the "phase matching" characterize of this lamb mode.

It could be found that the measured nonlinearity parameters have accumulative effect, the ratios of second harmonic amplitude and fundamental wave grow with the propagation distance as shown in Fig. 4.

The correlation of thermal cycles and normalized nonlinear parameters is studied as shown in Fig. 5, thermal fatigue will case micro-damage, As the thermal cycles increasing, the material degradation degree will become more and more serious. During the initial stage of thermal fatigue, the normalized nonlinear parameters increasing is rapid from 0 cycles to 100 cycles or 200 cycles, but much more slowly from 1000 cycles. This result has a good agreement with previous study testing metallic material using nonlinear ultrasonic. It also proves that nonlinear ultrasonic has great potential for characterizing material degradation state of composite material, especially for early stage degradation.
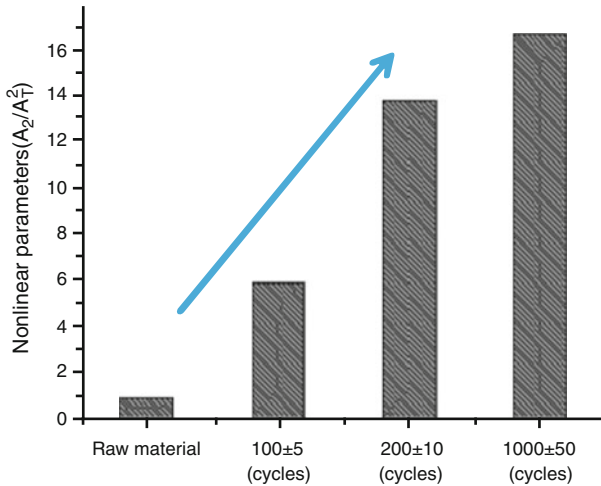
Fig. 5 Normalized nonlinear parameters versus specimens under different thermal cycles

Conclusions

The generation of second harmonic in Lamb wave propagation is considered to assess thermal fatigue damage in composite laminates. A phase matching of fundamental wave and second harmonic is required for generating accumulative second harmonic, the fundamental Lamb mode chosen in this study satisfies phase and group velocity matching, moreover, its phase velocity and group velocity are similar which has the same characterize as bulk wave. Multi-modes of wave-packet were effectively separated by group velocity delay method. It also minimized the nonlinearity from instructional system. The correlation between measured acoustics normalized nonlinearity using lamb and composite laminates thermal degradation stats shown that it is possible to use nonlinear Lamb wave to evaluate composite laminates degradation. This study develops a practical approach for applying Lamb wave to assess early degradation in composite laminates by higher harmonic generation technique.

The nonlinear vibration spectra are produced locally in the damaged area while an intact part of material outside the defects vibrates linearly, i.e. with no frequency variation in the output spectrum. This makes nonlinearity a defect-selective indicator of damage presence and development. This feature of localized nonlinearity enables 2D-imaging of the nonlinear excitations confined inside the fractured defect areas. Fortunately, this group of flaws includes the most malignant defects for material strength: micro- and macro-cracks, delaminations, debondings, impact and fatigue damages.

A number of case studies prove the applicability of nonlinear NDT and defect-selective imaging in various materials by using NSLV and NACE. Particularly successful examples include hi-tech and constructional materials: impact damage and

delaminations in fibre-reinforced plastics, fatigue micro-cracking and cold work in metals, delaminations in laminates and fibre-reinforced concrete.

Unlike conventional ultrasonic testing, the NNDT provides abundant multi-frequency information on properties and location of defects. This suggests an opportunity for application of advanced data and image fusion algorithms to result in higher sensitivity and accuracy of inspection, higher reliability and quality of NDT.

References

[1] G. Petculescu. (2008), Group Delay Measurement Using Modally Selective Lamb Wave Transducers for Detection and Sizing of Delaminations in Composites. *Smart Mater. Struct.* vol. 17, n.1, p. 15007.

[2] K-Y. Jhang. (2000), Application of Nonlinear Ultrasonic to NDT of Material Degradation. *IEEE Trans. ultrason.*, vol. 47, n. 3 p. 274–286.

[3] J.H. Cantrell. (2004), Fundamentals and Application of Nonlinear Ultrasonic Nondestructive Evaluation. In: *Ultrasonic nondestructive evaluation*, vol. 6 Buca Raton, FL: CRC press, p. 363–434. Kundu. (Ed.).

[4] M. Deng. (2006), Nonlinear Ultrasonic Lamb Wave Response to Fatigue of Solid Plates. *IEEE Ultrason. Symp.*, p. 1425–1428.

[5] C. Pruell, J.-Y. Kim, J. Qu and L.J. Jacobs. (2007), Evaluation of Plasticity Driven Material Damage using Lamb Waves. *Appl. Phys. Lett.* vol. 91, p. 231911.

[6] C. Bermes, J.-Y. Kim, J. Qu and L.J. Jacobs. (2007), Experimental Characterization of Material Nonlinearity using Lamb Waves, *Appl. Phys. Lett.* vol. 90, p. 21901.

New Opportunities in Ultrasonic Characterization of Stiffness Anisotropy in Composite Materials

I. Solodov, D. Döring, M. Rheinfurth and G. Busse

Abstract Two new ultrasonic approaches to NDT of in-plane stiffness anisotropy have been developed and applied to various composite materials. The first approach is based on polarization measurements of ultrasonic shear waves which manifest birefringence due to asymmetry of in-plane stiffness. Birefringence is applied for monitoring of fibre orientation and evaluation of in-plane stiffness anisotropy in various composites and multi-ply composite laminates. The other approach uses mode conversion of air-coupled ultrasound to zero-order plate waves for remote NDT of the in-plane stiffness anisotropy. A non-contact ultrasonic evaluation of the in-plane anisotropy of Young`s modulus is based on air-coupled measurements of the a_0-wave dispersion extrapolated to a "static" case. Depth-resolved measurements of stiffness anisotropy are demonstrated in multiple composite laminates. The methods and instrumentation developed are capable of detecting improper ply positions and orientation in composite laminates in production phase, variation in stiffness anisotropy due to material aging or damage progression in operation.

Introduction

A particular benefit of fibre-reinforced composites is concerned with flexibility in a smart material design whose elastic performance meets requirements of mechanical or thermal loading. For continuous fibre pre-preg materials, the required stiffness anisotropy and thermal expansion are obtained by a suitable orientation of fibre plies and a choice of their stacking pattern. In injection moulded short-fibre composites, fibre orientation is less

I. Solodov (✉) • D. Döring • M. Rheinfurth • G. Busse
University of Stuttgart, Institute of Polymer Technology, Department of Nondestructive Testing (IKT-ZFP), Stuttgart, Germany
e-mail: igor.solodov@ikt.uni-stuttgart.de

controllable but determined by a streamline flow direction which is quite difficult to predict or/and calculate. The recognition of fibre directions in a stack of plies, characterization of stiffness anisotropy of the ply lay-up, and monitoring of local degree of fibre orientation are the high priority tasks for composite manufacturing and applications.

Ultrasonic Birefringence for NDT of Stiffness Anisotropy

Similar to optics, the in-plane stiffness anisotropy causes an acoustic shear wave to be birefringent: to decompose into a pair of (partial) waves with different polarizations and propagation velocities [1]. The maximum wave velocity is expected when the polarization coincides with the direction of maximum stiffness. The latter can be related to fibre alignment in composites, molecular orientation in plastics, manufacturing or processing reinforcement in metals, etc. and can be identified by measuring the shear wave velocity as a function of polarization angle.

In our experiments, the 4-MHz shear wave pulses were generated and received in reflection with a piezo-transducer attached to the surface of the specimens. The wave velocity was measured as a function of polarization which was changed by azimuth rotation of the transducer. The direction of polarization corresponding to the maximum velocity reveals the predominant local orientation of reinforcement.

An example of mapping the fibre orientation in fibre-reinforced composites is shown in Fig. 1. The specimen measured is a short-glass-fibre reinforced polyurethane plate (300x200x4 mm) manufactured by the injection moulding technique. The injection direction is shown by the bold arrows on the right; the rest of the arrows indicate the local reinforcement directions measured around the group of circular obstacles in the mould. From Fig. 1, the fibre alignment is in a reasonable agreement with the expected streamline directions as one would assume for the injection moulding methodology.
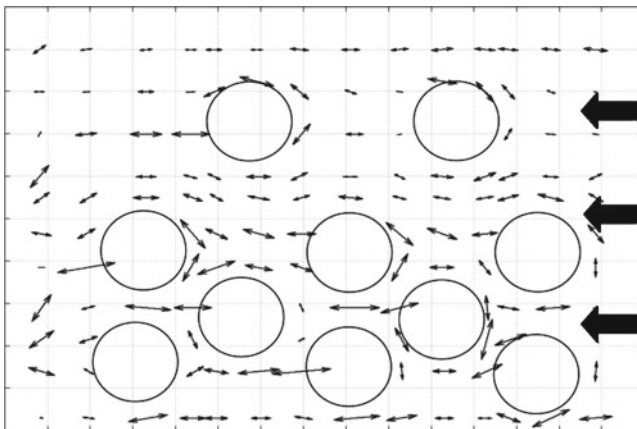
Fig. 1 Birefringence measurements of fibre orientation in an injection moulded polyurethane specimen (300x200mm)
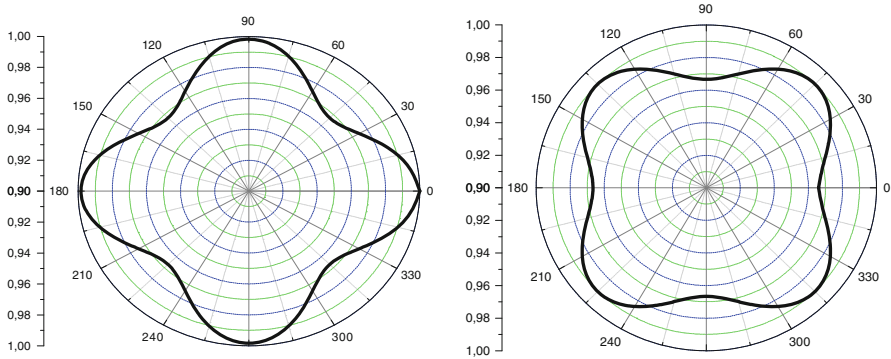
Fig. 2 Calculations of shear wave amplitude as a function of azimuth angle in "unbalanced" (0°/+45°/-45°/-90°) CFRP laminates: Left - 60 μm offset in thickness between 0° and 90° layers; right – similar offset in +45°/-45° lay-up

The partial wave approach was also applied to analysis of shear wave polarization in both transmission and reflection in composite laminates. As an example, in a (0°/+45°/-45°/-90°) laminate, the two partial waves in the external (0°) laminate acquire a phase shift and are converted into a four-partial wave field in the (+45°/-45°) layers which the 90° -ply splits into eight partial wave field. Its polarization is probed by a shear wave transducer and is shown to depend on the phase difference acquired by the partial waves in cross-plied fibre patterns. That provides a high sensitivity to any deviation from the symmetry caused either by extra plies or by the change in their alignment.

As an example, Fig. 2, left shows the results of calculations of output amplitude variations for the (0°/-90°) section of the lay-up "unbalanced" by 30° phase shift. For the birefringence in a UD-CFRP composite at low-MHz frequencies [1], this phase difference corresponds to an offset in thickness of ≈ 60 μm between the 0° and 90° layers. Such an imbalance of about a half-ply thickness is readily revealed in the deviation of the amplitude curve (Fig. 2, left).

In a similar way, a minor asymmetry in the (+45°-45°) section of the lay-up can be detected readily on the background of a symmetrical 0°-90° structure (Fig. 2, right). The ± 45° rotational turn of the amplitude curve indicates the source of the offset. The phase velocity measurements enable to quantify the inaccuracy; the "fast" polarization direction of the transducer specifies particular orientation of an extra (faulty) ply (+45° or -45°).

Remote NDT of Stiffness Anisotropy via Air-Coupled (AC)-Ultrasound

It is well-known that reflection-transmission of elastic waves at oblique incidence on a solid interface results in producing new types of waves (mode conversion). For plate-like materials in slanted AC-configurations, the mode conversion leads

to efficient excitation of flexural ($a_0 -$) waves under phase matching conditions: $\sin\theta = v_{air} / v_{a_0}$, where v_{air} is the sound velocity in air and v_{a_0} is the velocity of $a_0 -$ mode. By measuring the "resonance" angle of incidence θ, the flexural wave velocities can be determined for various propagation directions in composites [2].

In the experiments, the 50 kHz-air-coupled transducers were used to excite and receive flexural waves in the 2.5-mm UD-CFRP. The bandwidth of the transducers was broad enough to observe signal transmission in $f=(40 - 90)$ kHz frequency range. For each 10 kHz-frequency step, the θ -measurements were made and the dispersion curves of a_0 -modes obtained for 0°-, $\pm$ 45°- and 90°-propagation directions (Fig. 3, left). The dispersion curves like those obtained, are typical for the a_0-modes in both isotropic and anisotropic materials with phase velocity increase from zero to the asymptotic value of the surface wave velocity at high frequencies. However, the contribution of elastic moduli into such behaviour is too complicated to be traced analytically so that to quantify material stiffness anisotropy from the a_0-velocities in general is hardly possible.

A simplified experimental approach to evaluation of the in-plane ($x_1 x_2$) anisotropy can be based on the dispersion relation for a_0 -modes [3] valid for $f \to 0$:

$$(v_{a_0})_1 = (\pi D f)^{1/2} (E_1 / 3\rho(1 - v_{12}v_{21}))^{1/4} \tag{1}$$

Here, D is the thickness, ρ is the density of the material, and the in-plane components of Young`s modulus $E$ and Poisson`s ratios v are involved.

For CFRP, the product of v in (1) is $<< 1$ [4], so that Young`s modulus can be found as:

$$E \approx \lim_{f \to 0}[(3\rho / \pi^2 D^2)(v_{a_0}^4 / f^2)] \tag{2}$$

Figure 3, right shows the results of E evaluation from the velocity data in Fig. 3, left. A linear interpolation of the data to the "static" area $f \to 0$ yields the following values of E moduli: $E(0°) \approx 100 GPa$; $E(90°) \approx 10 GPa$; $E(45°) \approx 25 GPa$. The compliance with the literature data is mixed: $E(0°) \approx 135 GPa$; $E(90°) \approx 10 GPa$ [5].

For more precise evaluation, the velocity measurements were carried out in a wider frequency range by using the wave front imaging (WIM) methodology [6]. In the experiment, the 7mm diameter wide-band piezo-transducer (HVA B100/2, isi-sys) was attached to the surface of the 34x24x0.25 cm CFRP plate. A continuous
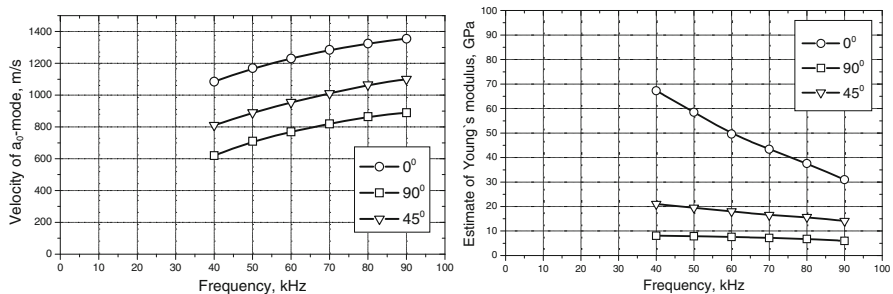
Fig. 3 Left: dispersion curves of AC- a_0 -modes in different directions of UD-CFRP; Right: values of Young`s moduli calculated from (2) for different frequencies
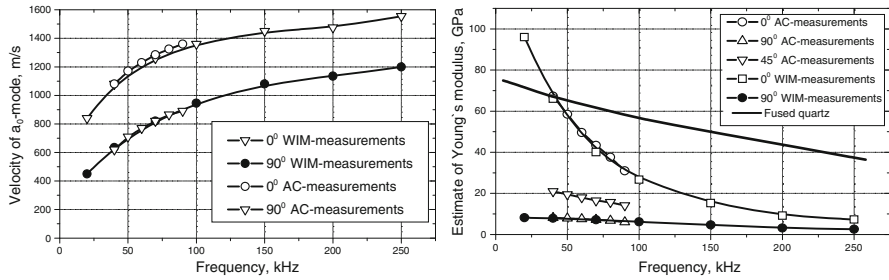
Fig. 4 Left: AC- and WIM-measurements of dispersion curves in CFRP; right: values of Young's moduli calculated from (2) for different frequencies

wave input signal of ~50 V amplitude provided efficient excitation of the a_0-mode over the frequency range (20 – 250) kHz. A Doppler-shift scanning laser vibrometer (Polytec) was used for imaging of the wave field and measurements of the wave length (and hence the wave velocity) along and across the fibre directions. The dispersion curves obtained are shown in Fig. 4, left along with the AC-data.

The results of evaluation of E moduli from these velocity data are given in Fig. 4, right. The calculations of velocities (using Disperse software) and estimations of E were also made for isotropic material (2.5 mm thick fused silica) and presented in Fig. 4. In this case, it was possible to acquire precise velocity data in a close vicinity of the zero point (down to frequency 5 kHz). The calculations showed that the ultimate precision in determining E by using relation (2) can be $\approx$ (1-2)%. The results in Fig. 4 show that for $90°$-direction the frequency dependence is close to a linear one typical for isotropic materials. Therefore a linear interpolation is justifiable in this case and can yield the values of E within 5-10% of error provided thorough velocity measurements. Along the fibre direction ($0°$), the transition to the "static" case ($f \rightarrow 0$) is strongly nonlinear. A linear interpolation of the results obtained in narrow band measurements results in 30-40% error ($E(0°) \approx 100 GPa$ from Fig. 3, right against $E(0°) \approx (135 \pm 5) GPa$ from Fig. 4, right). This conclusion seems to be also valid for the $45°$-direction: $E(45°) \approx 35 GPa$ [7].

A physical reason of E modulus to be responsible for the low-frequency velocity of the a_0-modes is concerned with particular wave field structure of this mode. At low frequencies, the axial strain dominates and runs through the whole thickness of the specimen. Such a strain naturally activates E modulus which determines the (static) bending stiffness of a plate. As the frequency increases, the wave field is "pushed out" from the interior of the material and the axial strain is diminished while the out-of-plane shear strain enhances. Material stiffness activated by the high-frequency wave is therefore close to the out-of-plane shear modulus.

Due to anti-symmetrical depth distribution of the axial strain for flexural waves in multi-ply composites, the maximum contribution to stiffness is expected from the surface plies while the role of the inner plies is diminished. This provides an opportunity for depth-resolved measurements of stiffness anisotropy in laminate composite materials.

This effect is demonstrated below for two specimens of CFRP laminates of quasi-isotropic symmetrical lay-ups (0/45/-45/90)s and (0/60/-60)s. The weighted
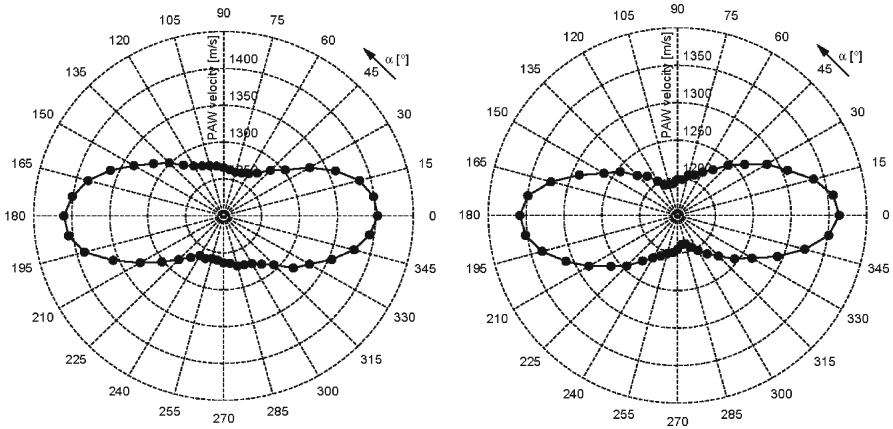
Fig. 5 AC-measurements of anisotropy of flexural wave velocity in quasi-isotropic CFRP laminates: (0/45/-45/90)s (left) and (0/60/-60)s (right)

averaging of axial stiffness with the emphasis on the outer plies ($0°$) is expected for the flexural wave propagation. The AC-measurement results (Fig. 5) confirm noticeable velocity anisotropy for both laminates. In both cases the maximum velocity is obtained for propagation along the outer $0°$–plies. The in-plane velocity anisotropy is 12% in the (0/45/-45/90)s and 14% in the (0/60/-60)s laminate.

Conclusions

A simple experimental technique, which is based on ultrasonic birefringence and uses standard ultrasonic NDT equipment is developed and applied for mapping of fibre orientation in composite materials. Remote NDT of stiffness anisotropy is demonstrated by using air-coupled ultrasound. It is shown that measurements of Young's modulus anisotropy by means of flexural waves are based on the wave structure with axial strain domination that requires different frequencies in various azimuthal directions. Inhomogeneous depth distribution of axial strain in flexural waves enables depth-resolved NDT of stiffness anisotropy in composite laminates.

References

[1] Solodov, I., Pfleiderer, K., Döring, D., and Busse, G. (2008), *Res. in NDE*, vol. 19, p. 129.
[2] Solodov, I., Stoessel, R., and Busse, G. (2004), *Res. in NDE*, vol. 15, p. 1.
[3] Haberger, C., Mann, R., and Baum, G. (1979), *Ultrasonics*, vol. 17, p. 57.
[4] Dayal, V. and Kinra, V. (1989), *J. Acoust. Soc. Am.*, vol. 85, n. 6, p. 2268.
[5] http://www.performance-composites.com/carbonfibre/mechanicalproperties_2.asp.
[6] Solodov, I., Pfleiderer, K., and Busse, G. (2005), *Materialprüfung*, vol. 47, n. 3, p. 3.
[7] http://www.tech.plym.ac.uk/sme/MATS324/MATS324A2%20E-G-nu.htm

Plate Wave Propagation as Damage Indicator in FRP Composites Under Fatigue Loading

T.T. Assimakopoulou and T.P. Philippidis

Abstract Dispersive behavior of plate waves in composite $[\pm45]_S$ Gl/Ep specimens is studied through acousto-ultrasonic measurements. Aiming to associate material damage, in this case being matrix cracking, with the propagating wave mode characteristics, acousto-ultrasonic, AU, tests are conducted in the as-received state and repeated after imposing tensile constant-amplitude cyclic loading, interrupted well before failure. Propagating plate waves are captured at several distances from the source and then processed, using two spectral techniques, in order to reconstruct segments of the dispersion curves of the orthotropic medium. Although experimental dispersion curves are in good agreement with theoretical predictions, quantitative damage assessment cannot be achieved. Limitations of the experimental procedure, as well as of the respective data processing, are commented upon. Additional tests, conducted on an isotropic aluminum specimen, are presented to enhance understanding of the complicated phenomenon.

Keywords Acousto-ultrasonics • Composites • Dispersion • Matrix cracking • Residual strength

Introduction

Propagation in waveguides is dispersive, even in non-dispersive materials. Since their laminated nature promotes their use in plate and shell structures, composites are used in a vast range of high-performance applications, including aerospace components, pipes, pressure vessels and wind turbine rotor blades.

Substantial research has been conducted on plate wave propagation, i.e. [1–3]. Wave propagation characteristics depend, among other factors, also on the elastic

---

T.T. Assimakopoulou • T.P. Philippidis (✉)

Department of Mechanical Engineering & Aeronautics, University of Patras, Greece
e-mail: philippidis@mech.upatras.gr

properties of the material. For instance, elastic moduli are proved to reduce with damage accumulation. Thus, mode propagation could provide a useful descriptor regarding strength degradation.

Measuring group and phase velocities, C_g and C_p, in the time domain is a questionable practice: for C_g estimation, a good reference point is the centroid of the pulse [4], whereas for C_p measurements an appropriate "phase point" should be selected. This could be e.g. the nth peak of the waveform or the nth zero-crossing. However, this method is susceptible to errors [5], and such problems could result in erroneous flaw location, for instance [2]. Therefore, spectral techniques are considered more appropriate for accurate C_g and C_p assessment.

Two methods are used herein to extract experimental dispersion curves. To implement the former, the propagating wave is captured at two separate distances from the source using two identical receiving sensors. The method, as suggested in [6], then uses the phase spectra of the waveforms and the distance between sensors to derive dispersion curves. The second approach is temporal localization of the signal spectral components using a time-frequency representation, TFR [7].

Experimental Procedure

Signature of propagating waves

To gain some insight on plate wave propagation in the 250x25x3.52 $[\pm 45]_S$ specimen (dimensions in mm), a couple of identical receiving sensors were placed on opposites sides of a virgin specimen (positions R_2 and R_{2B}, Fig. 1). Receivers were broadband, PAC Pico 200–750 kHz, while a Panametrics V133-RM 2.25-MHz transducer served as pulser. Transducers were strapped on the specimens using elastic tape, with grease as coupling agent. Captured signals were amplified using PAC in-line pre-amplifiers, with a gain of 40 dB and 32–1100 kHz band-pass filters. The excitation was broadband, resembling a Dirac spike, and was applied using a PAC pulse generator model C-101-HV.
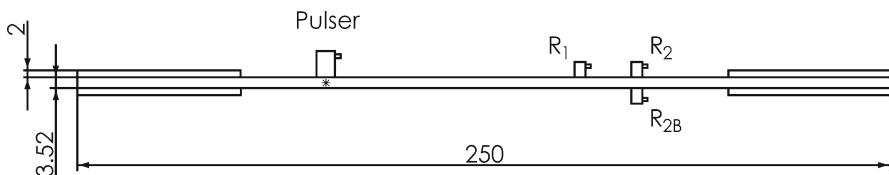
Fig. 1 Experimental set-up used either to define the signature of propagating waves (receivers R_2 and R_{2B} placed on opposite sides) or to capture a signal at two locations (receivers R_1 and R_2 placed on the same side of the $[\pm 45]_S$ specimen)

Dispersion measurements

To extract experimental dispersion curves using the method proposed in [6], the same signal is captured at two locations of known spacing (see Fig. 1, positions R_1 and R_2). Instead, no more than one waveform is required for TFR processing [8], the one used herein corresponding to location R_2. All AU measurements were conducted on virgin and then, on damaged material, using the equipment described above. More details on the entire procedure can be found in [9].

Results and Discussion

Signature of propagating waves

For a propagation distance of 120 mm, i.e. between the pulser and positions R_2 and R_{2B}, measurements are shown in Fig. 2. Due to dispersion, there is clear separation of an S and an A-mode. The S-mode travels faster and thus occupies the earliest portion of the signal whereas the A-mode is encountered at subsequent arrival times: "long" wavepaths lead to clearer separation between the propagating modes.

On the other hand, attenuation in composites is quite intense: this is seen in e.g. [2, 8], comparing signals recorded in aluminum and in composite plates. Indeed, also in the work herein, a lap from 40 to 120 mm in wavepath length proved to cause a signal amplitude reduction of more than threefold. For the S-mode in particular,
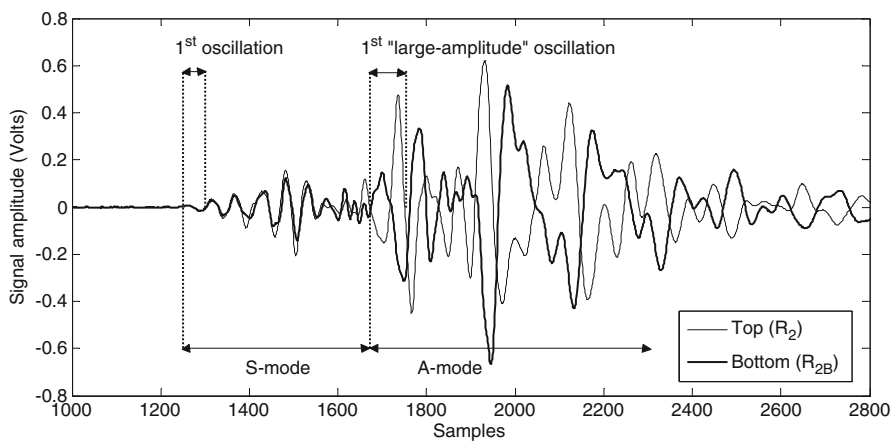
Fig. 2 Signals recorded on opposite sides of a virgin $[\pm45]_S$ specimen. Receivers placed at 120 mm from the source, positions R_2 and R_{2B}
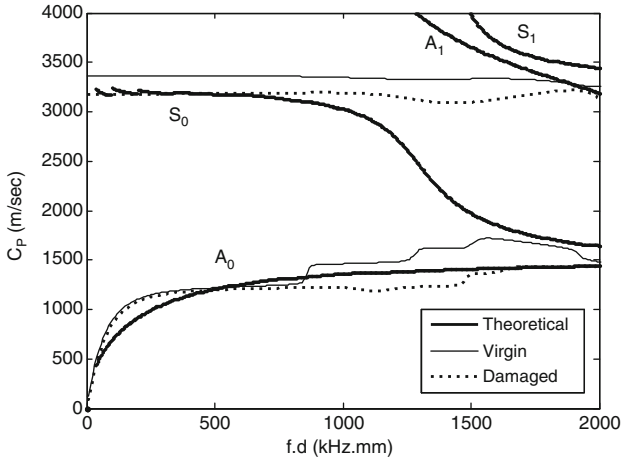
Fig. 3 Theoretical and experimental dispersion curves for a $[\pm 45]_S$ specimen

being of lower amplitude per se, this poses obvious limitations in the maximum propagation length, i.e. the location of the sensors. Therefore, although long wave-paths could cover larger areas, thus promoting rapid inspection, the respective S-mode might no longer be usable or even detectable.

Dispersion measurements in the composite

Using the phase spectra. In Fig. 3, indicative experimental dispersion curves from a specimen in the virgin and damaged state are presented. Theoretical dispersion curves, determined using in-house-developed code [10], are also demonstrated. Up to 1000 kHz·mm, the method was able to reconstruct segments of the S_0 and A_0 modes. To achieve this for each mode, particular portions of the captured signals were used: for S_0, the method was applied to the 1st oscillation of the R_1-R_2 signals (see Fig. 2), whereas for A_0 to the 1st "large-amplitude" oscillation. As expected, C_P in the damaged state is decreased. However, although this experiment is representative of a total of 16 specimens tested (see [9]), this trend could not be quantified.

Using TFR processing. Part of the S_0-mode curve could be visualised using TFR processing on the earliest arriving, low-amplitude, portion of the signals. For the waveforms captured using the R_2 sensor, 120 mm from the source, this can be seen in Fig. 4. For comparison purposes, the signals used in Figs. 3 and 4 are the same. As a result of damage, there is a slight shift downwards and to the right in the TFR of Fig. 4b, compared with the one of Fig. 4a, see arrow. Again, in the sample of 16 specimens tested in [9], no solid descriptors could be defined.
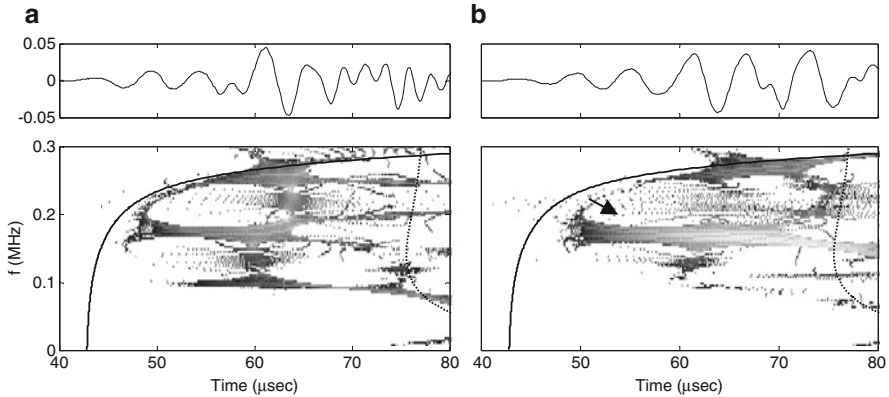
Fig. 4 TFR processing and theoretical dispersion curves for wave propagation in a $[\pm 45]_S$ specimen, (**a**) virgin state and (**b**) damaged state

Investigation of TFR processing potential: Measurements in aluminum plate

Simulation. As seen in the above, dispersion measurement in inhomogeneous and anisotropic media, such as composites, is a complicated task. To elaborate on a simpler phenomenon, the same experimental set-up was used on a 260x25x2.9 aluminum specimen (dimensions in mm).

To validate the results, wave propagation was then simulated using CyberLogic "Wave2000® Pro", a commercial package for computational ultrasonics in isotropic media [11]. Results are demonstrated in Fig. 5a for the model and Fig. 5b for the experiment. In the top sub-plot of Fig. 5a, the simulated response of both the upper and the bottom specimen surface is presented. Besides the cross-terms obscuring the TF representation, even in the simulated response, propagating modes are in tolerable agreement with the theoretical dispersion curves.

However, several issues arise regarding experimental dispersion measurements [9]. Material variation in the composite is, for example, a standard source of scatter: in a sample of 16 identical virgin specimens, the calculated C_P for mode S_0 spanned in a range as large as 500 m/sec. Second, the band-pass filtering imposed through the equipment, e.g. sensors and pre-amplifiers, limits the potential of the spectral techniques. The material per se also behaves as a low-pass filter. Third, for the method proposed in [6] in particular, minimum errors in distance measurement, i.e. the wavepath length, prove critical. In addition, as stated above, intense attenuation in the composite poses limitations regarding transducer location: with the signal reaching the remote sensor undergoing severe attenuation, there is a risk that the two waveform portions used in the implementation of [6] might not belong to the same mode.
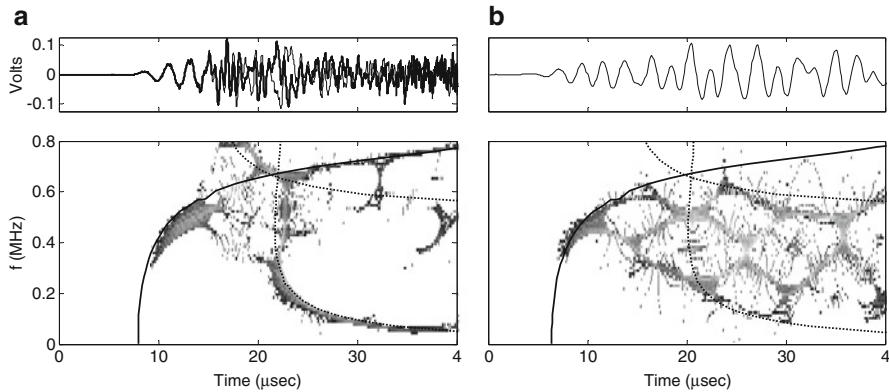
Fig. 5 TFR processing and theoretical dispersion curves for wave propagation in an aluminum specimen, (**a**) modelling and (**b**) experiment

Conclusions

Wave propagation in a $[\pm45]_S$ laminate was studied. Experimental results indicated the presence of S and A plate wave modes. Comparison of the experimental dispersion curves with the respective theoretical predictions revealed the fundamental S_0 and A_0 modes. Changes in the dispersion behavior, due to damage, were presented and studied. However, although a qualitative correlation was indeed observed between damage and modal characteristics, no appropriate descriptors could be defined: this indicated that wave propagation in anisotropic materials is perhaps too complicated. To address a simpler problem, an isotropic homogeneous material was then studied and modelled. An aluminum sheet of similar dimensions as the $[\pm45]_S$ specimen was used. Experimental and model response were compared, suggesting possible limitations of the acousto-ultrasonic technique in as simple as isotropic materials.

References

[1] Nayfeh, A. and Chimenti, D. (1989), *J. Appl. Mech.*, vol. 56, pp. 881–886.
[2] Gorman, M. (1991), *J. Acoust. Soc. Am.*, vol. 90, n. 1, pp. 358–364.
[3] Prosser, W. and Gorman, M. (1994), *J. Acoust. Soc. Am.*, vol. 96, n. 2, pp. 902–907.
[4] Wear, K. (2000), *Ultrasound Med. Biol.*, vol. 26, n. 4, pp. 641–646.
[5] Ragozzino, M. (1981), *Ultrasonics*, pp. 135–138.
[6] Sachse, W. and Pao, Y. (1978), *J. Appl. Phys.*, vol. 49, n. 8, pp. 4320–4327.
[7] Prosser, W., Seale, D. and Smith, B. (1999), *J. Acoust. Soc. Am.*, vol. 105, n. 5, pp. 2669–2676.

[8] Prosser, W., Gorman, M. and Humes, D. (1998), *J. Acoust. Emission*, vol. 17, pp. 29–36.

[9] Assimakopoulou, T. (2009), *Damage assessment in laminated composite structures using acoustic methods*, PhD Thesis, http://nemertes.lis.upatras.gr

[10] Antoniou, A., Assimakopoulou, T. and Philippidis, T. (2004), *In Proceedings of ECCM*, Rhodes, Greece.

[11] CyberLogic, inc. About Wave2000®, http://www.cyberlogic.org/about2000.html.

Monitoring of Failure of Composite Laminates using Acoustic Emission

A.S. Paipetis, N.M. Barkoula, M. Xyrafa, T.E. Matikas and D.G. Aggelis

Abstract Acoustic emission (AE) is suitable for monitoring the evolution of degradation in structural components as well as for localizing damage. In the present study acoustic emission is employed for the location and identification of the service induced damage in cross ply laminates. The sequence of the different failure mechanisms, i.e. transverse matrix cracking and the subsequent delamination propagation at the 0°/90° interface is followed closely by advanced indices which quantify the attributes of the received AE waveforms. The AE activity can be successfully correlated to the damage accumulation of the cross ply laminates, while specific acoustic emission indices proved sensitive to the various modes that evolve during loading.

Keywords Acoustic emission • Cross-ply laminates • Delamination • Transverse cracking

Introduction

Multidirectional composites are prone to various forms of damage when they are subjected to mechanical loading. This damage is different in nature to damage observed in isotropic materials in that fibrous composites inherently possess macroscopic anisotropy which, at the lamina scale is manifested as a steep property change. The typical failure behaviour of cross-ply laminates initiates with the

---

A.S. Paipetis (✉) • N.M. Barkoula • M. Xyrafa • T.E. Matikas • D.G. Aggelis
Department of Materials Science and Engineering, University of Ioannina,
Ioannina 45110, Greece
e-mail: paipetis@cc.uoi.gr

premature failure of the plies containing fibres oriented transversely to the loading axis, which is commonly known as transverse or interlaminar cracking. This failure creates the shear discontinuity at the lamina scale and the respective stress magnification which triggers all other damage mechanisms. Numerous studies have been performed to study the initiation, interaction and propagation of all involved mechanisms, and how they accumulate leading to the global failure of the composite [1].

In general, transverse cracking of the 90° creates a stress concentration at the neighbouring 0° plies. Depending on the interlaminar strength, the crack may be deflected to the 0°/90° interlaminar surface causing delamination, or altrantively cause longitudinal fibre failure of the 0° ply. Transverse cracking is typical of a mode I crack or a tensile crack, whereas delamination is typical of a mode II crack or a shear crack [2]. As is well known, there is a trade off between low interlaminar strength that favours a damage tolerant structure and high interlaminar strength that maximizes the reinforcing ability of all ply orientations. From the above postulations, it is obvious that a good knowledge of the initiation and propagation of the distinct damage mechanisms will provide an insight into the strengthening mechanisms and aid the designer towards the optimization of the interlaminar/ interfacial properties.

The Acoustic Emission (AE) technique has been employed in numerous applications for damage characterization on composite materials [3–6]. Suitable sensors are placed on the surface in order to record the transient waves (hits) generated by damage initiation and propagation inside the material. Moreover, AE has been successfully applied in cross ply composites in order to separate the acoustic activity of various damage modes in a cross ply composite [3].

Further study of the waveforms may provide in depth insight of the fracture process. The source of the AE activity is closely connected to the mode of fracture [7]. If the failure sequence is determined, it is possible to tailor the properties of the constituent phases and their interface. This may be acheived by using proper design or materials so as to optimise the resistance against the specific failure mode. As has already been mentioned, this optimisation does not necessarily coincide with maximum strength.

In the engineering field, the attributes of the AE waveforms are reported to be characteristic of the fracture mode. Shear events are characterized by longer Rise Time (RT, time delay between the first threshold crossing and the maximum peak) and usually lower peak amplitude (A, voltage of the largest cycle) than tensile events [8,9]. This is examined by the RA value which is defined as the ratio of the RT (expressed in μs) to the waveform Amplitude, A (expressed in V, see Fig. 1) [10]. It has been shown that lower RA values, indicate tensile nature of fracture events [8,9].

Experimental Process

The cross-ply laminates were fabricated by hand layup with a sequence [0°4/90°4]s, resulting in a number of 16 plies with total specimen thickness of 2 mm. The UD 220 g/m2 (Aero) unidirectional glass fibre fabric was impregnated using the HT2

Fig. 1 Typical AE waveform with basic parameters
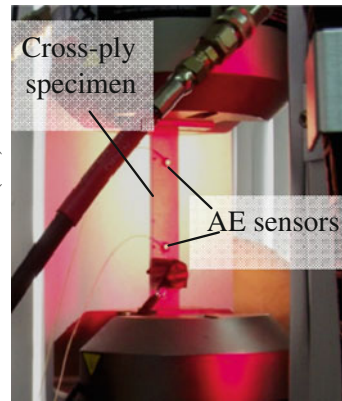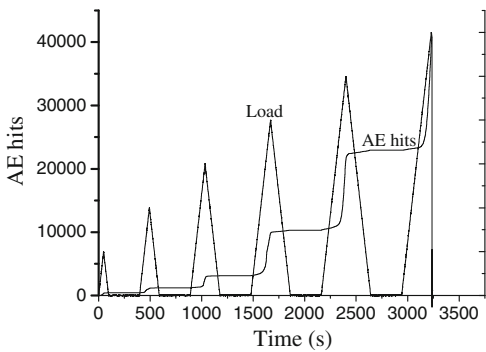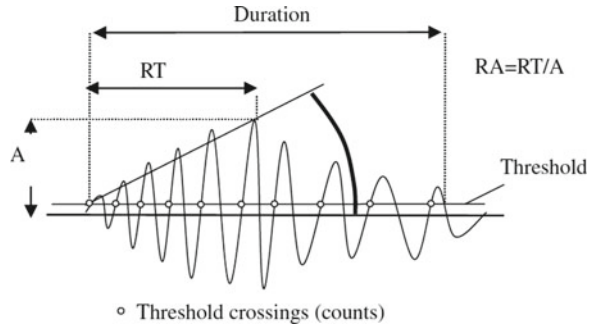
Fig. 2 (**a**) Load and cumulative AE activity history, (**b**) Snapshot during measurement

epoxy resin/ hardener matrix system (mixing ratio 100:48) manufactured by R&G Faserverbundwerkstoffe GmbH Composite Technology. A 250x250 mm² laminate was manufactured and was allowed to cure for 24 h at room temperature. Tensile specimens were subsequently cut according to the ASTM D3039 standard, at a width of 20 mm each.

The tensile specimens were loaded in load controlled tension, in a step loading mode. The loading spectrum was a saw-tooth spectrum formed from a sequence of triangular loading/unloading steps. A rate 5 kN/min was employed for both loading and unloading, as seen in Fig. 2a. The maximum load was incremented by 4 kN at each consecutive step. The step loading continued until the tensile failure of the specimen. All tensile tests were performed using an Instron Universal Testing Machine equipped with hydraulic gripping system, under load control, at controlled environmental conditions of 25 °C and 70% relative humidity.

For the purpose of the AE monitoring, two wide band AE sensors (Pico, Physical Acoustics Corp., PAC) were attached on the same side of the specimen. Electron wax as applied between the sensor and the specimen to enhance acoustic coupling, while it offered the necessary support to the sensors during the experiment. The

specific sensors were chosen over other AE transducers mainly due to their spectral response. They are sensitive to frequencies from 100 kHz up to approximately 800 kHz, with maximum sensitivity at 500 kHz. Therefore, they can capture a wide range of different sources. The distance between the two receivers was 70 mm. A snapshot during the experiment is seen in Fig. 2b

AE Results

The AE results are presented together with the load data for reference. As was expected, the RA value shift to higher levels as the load increases. This effect is pronounced as the number of steps is increasing together with the loading level. Some typical cases are presented below. Fig. 3a depicts the loading history of the 6th step corresponding roughly to the time span 2900 s to 3500 s of a single experiment. This loading step increases linearly with time until the maximum value of 24 kN and subsequently decreases linearly with the opposite rate.

On the same figure, the RA history (as a moving average of 500 values) is depicted. The first hits are recorded shortly after the application of load. Significant increase in the RA value is exhibited after a load threshold of approximately 15 kN (after 3100 s). The maximum RA value is recorded (500 μs/V) almost coincidentally with the maximum load. As the load starts to decrease, the RA rapidly falls to the initial low values of less than 1000 μs/V.

The RA for the last step until failure is shown in Fig. 3b. The RA increases in a similar way and reaches its peak value at the moment of failure. The maximum RA value of this step is distinctly higher than that of the previous step indicating that, at that point, shear failure dominates the process, or else mechanisms that relate to delamination. This behaviour is consistent for subsequent steps for all specimens studied. It may therefore be concluded that the RA value can be potentially used to
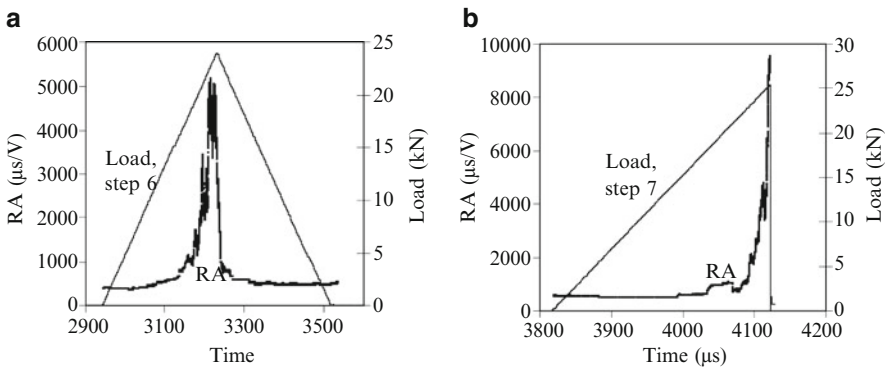
Fig. 3 Load and RA value history for successive loading steps

study the tensile to shear mode conversion in composite systems in order to tailor the interlaminar properties of the material for maximum performance.

Correlation with Mechanical Data

As the load increases, transverse matrix cracks accumulate leading to a distinct stiffness loss which is attributed to the loss of load bearing capability of the 90° plies. The transverse cracks reach the 0° ply and trigger delaminations or longitudinal fibre failures which also deteriorate the stiffness of the system. In the case of the system under investigation, the decrease is continuous for the successive steps reaching approximately 60% of the modulus measured at the first step. This degradation trend is very well correlated with the total number of AE activity recorded during each step, as seen in Fig. 4a where the measured modulus of each step E normalised by the initial modulus E_0 is depicted as a function of the total AE activity.

   This shows that each deterioration incident which contributes to the degradation of the modulus (crack or delamination) is also recorded as a part of the total AE activity, and the number of the AE hits may be used to estimate the modulus degradation or the general condition of the laminate. It is characteristic that the emissions are close to zero when the material is intact but increase to several thousands when the material has severely deteriorated. Apart from the total AE activity, specific trends are observed concerning the qualitative shape parameters of the waveforms. An example is shown in Fig. 4b which shows the correlation between the RA value and the applied load. As the load increases, matrix cracking becomes saturated and delaminations become more dominant. This is manifested by the increase of RA and shows strong correlation with the maximum applied load during each cycle.
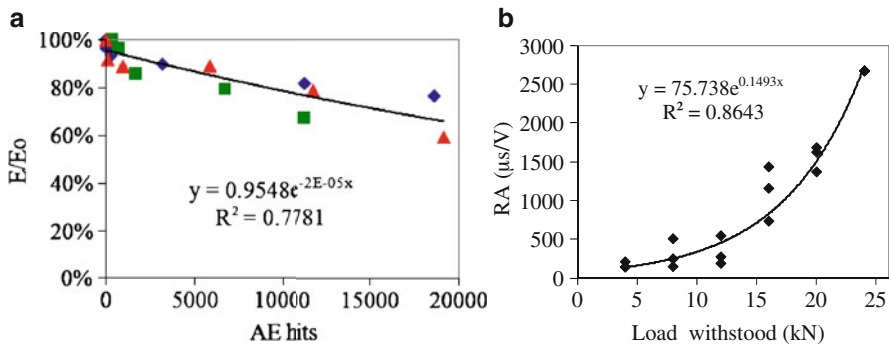
Fig. 4 Correlation between relative stiffness loss and AE hits (**a**) and between RA and maximum load for each step (**b**)

Conclusion

In this study the acoustic emission behaviour of cross-ply composite laminates is examined under triangular step loading. AE parameters like are found to follow to the damage initiation and accumulation. This is shown by the consistent increase of the RA value as the dominant failure mode changes from transverse cracking to delamination. Therefore, such parameters can act as indices associated to the damage mode conversion in composites with increasing load. Additionally AE activity and AE indices are well correlated to the modulus at each step, showing potential to estimate mechanical properties using real time AE monitoring.

References

[1] Nairn, J. and S. Hu. (1994), "Matrix microcracking", in Damage mechanics of composite materials, edited by R.B. Pipes and R. Talreja. Composite materials series, Vol. 9. Amsterdam: Elsevier.
[2] Callister D. (2000), Materials Science and Engineering, An Introduction, Wiley, New York.
[3] Katerelos, D.G., Paipetis, A.S., Loutas, T., Sotiriadis, G., Kostopoulos, V., Orgin, S. L. (2009), *Plastics, Rubber Comp.*, vol. 38, no. 6, 229.
[4] Prosser, W.H. (1992), *J. Acoust. Soc. Am.*, vol. 92, 3441.
[5] Vasudevan, N. and Shaker, A.W., (1992), *J. Acoust. Soc. Am.*, vol. 92, pp. 2964.
[6] Bentahar, M. Gouerjuma, R.E., (2009), *J. Acoust. Soc. Am.*, vol. 125, pp. EL 39.
[7] Ohtsu, M., Tomoda, Y., (2008), *ACI Mat. J.* vol. 105, no. 2, pp. 194.
[8] Shiotani, T., Ohtsu M., and Ikeda, K. (2001), *Construct. Build. Mat.*, vol. 15, no. 5-6, pp. 235.
[9] Anastassopoulos, A., Philippidis, T.P., *J. Acoust. Emission*, (1994), vol. 13, no. (1/2), pp. 11.
[10] Soulioti, D., Barkoula, N.M., Paipetis, A., Matikas, T.E., Shiotani T. and Aggelis, D.G. (2009), *Construct. Build. Mat.*, vol. 23, pp. 3532.

Acoustic Emission of Failure in Fiber-Metal Laminates

R. Kuznetsova, H. Ergun and B. Liaw

Abstract This paper studies the failure modes of Glare grades under tensile loading by means of Acoustic Emission (AE). AE transients produced by various types of microdamage, such as yielding, matrix crack initiation, matrix-fiber debonding, matrix cracking and fiber fracture, were recorded as functions of strain for various Glares and fiber orientations. Experiments showed that different microdamage mechanisms produced characteristically different AE signals which can be classified into categories based on peak amplitude and total counts parameter ranges. Moreover, it was observed that AE percent count rate is a function of the normalized strain and metal volume fraction (MVF) in similar Glare lay-ups. In addition, AE profiles were found to exhibit exponential growth behavior in the initial region of the profile and a power growth behavior after the knee point.

Keywords Acoustic emission • Failure • Fiber-metal laminates • Glare • Glass/epoxy prepreg • Tensile testing • Knee point • Metal volume fraction (MVF) • Microdamage • Stress-strain behavior

Introduction

Glass fiber reinforced laminate (Glare) is a second generation Fiber Metal Laminate (FML) developed by TU Delft team in Delft University of Technology, Netherlands in the early 1990s [1].

R. Kuznetsova
Sikorsky Aircraft

H. Ergun (✉)
Civil Eng. Faculty, Istanbul Technical University, Istanbul, Turkey,
e-mail: ergunh@itu.edu.tr

B. Liaw
CCNY, Dept. of Mechanical Eng., City University of New York, NY, USA

Numerous investigators have explored the benefits of Acoustic Emissions (AE) as a tool of non destructive testing (NDT) in composite material research [2–4]. AE cumulative profiles, usually of counts, hits, or energy parameters, provide a useful way to correlate AE activity to material and mechanical deformation parameters during testing [5–6]. This study attempts to classify AE transients of Glare, a fiber-metal laminate, based on two or more signal parameters and quantitatively relate AE damage profiles to material properties and mechanical deformation.

Material Description and Testing Procedure

Five kinds of Glare grade FML's are used in this study, which are made of continuous S-glass fiber reinforced epoxy laminae interleaved with aluminum alloy 2024-T3 sheets. The GFR epoxy laminae are made of unidirectional glass fibers embedded with FM 94 adhesive with a nominal fiber volume fraction of 59%. This prepreg is laid up in different orientations in between the aluminum alloy sheet, resulting in the different standard Glare grades as given in Table 1.

In Table 1, each individual aluminum sheet thickness in all Glare grades is 0.3mm (0.012in). The fiber orientation angles given in the prepreg stack sequence column are with respect to the loading direction. And the *m/n* configuration notation represents *n* number of fiber-reinforced epoxy laminas interleaved within *m* number of aluminum alloy layers. Metal volume fraction (MVF), which represents the relative aluminum contribution in the FML, is defined as a ratio of the sum of the aluminum layer thicknesses to the total thickness of the laminate.

Tensile tests were performed on Glares and aluminum 2024-T3 specimens using an MTS 810 universal testing machine. Displacement controlled monotonic tensile testings conducted with constant crosshead displacement rate of 2mm/min, consistent with ASTM D3039. Tests were conducted in an environmental chamber lined with acoustical foam absorber at room temperature. Rectangular specimens cut from Glare panel stock were 254mm long and 25.4mm wide. Aluminum tabs were used at the 50.8mm length gripped ends of the specimen.

Table 1 Glare grade configurations (thicknesses in mm (inches))

GLARE Type	Config. (m/n)	Prepreg Plies & Orientation	Prepreg Thickness	Total Thickness	MVF
2	3/2	$[0^\circ_2]$	0.3 (0.012)	1.4 (0.056)	0.643
2	3/2	$[90^\circ_2]$	0.3 (0.012)	1.4 (0.056)	0.643
3	3/2	$[0^\circ/90^\circ]$	0.3 (0.012)	1.4 (0.056)	0.643
5	2/1	$[0^\circ/90^\circ/90^\circ/0^\circ]$	0.6 (0.024)	1.1 (0.044)	0.545
5	3/2	$[0^\circ/90^\circ/90^\circ/0^\circ]$	0.6 (0.024)	1.9 (0.076)	0.474
5	4/3	$[0^\circ/90^\circ/90^\circ/0^\circ]$	0.6 (0.024)	2.7 (0.108)	0.444

Acoustic emission system manufactured by Physical Acoustics Corp. (PAC) with two wideband differential transducers (WD sensors), 100–1000 kHz bandwidth, were mounted on the specimen. For signal conditioning a PAC model 2/4/6 preamplifier was set to 40 dB gain and a differential input. Four-channel PAC PCI-DSP data acquisition board was used to collect AE data with a sampling rate of 10 MHz. The raw AE data was pre-processed using the AEwinPost software and MatLAB. The waveform definition parameters and standard hardware settings for both sensors were; 45dB Threshold, 40dB Pre-Amp Gain, 100kHz Lower Filter, 1000kHz Upper Filter, 10MPS Sampling Rate, 25.6μsec Pre-Trigger, 204.8μsec Length, 50μsec PDT, 150μsec HDT, 300μsec HLT. The characteristic waveform parameters; peak amplitude, signal risetime, counts, signal duration, absolute energy, hits were collected during testing.

Experimental Results and Observations

Cumulative counts

Counts parameter is used to quantify acoustic emissions due to its sensitivity to signal length and change, thus making it a good measure of AE activity [7]. From the mechanical behavior and acoustic emission response of Glare 2 3/2 [$0°_2$] (Fig.1) and those of other Glare grades (not shown), it is observed that AE damage profile
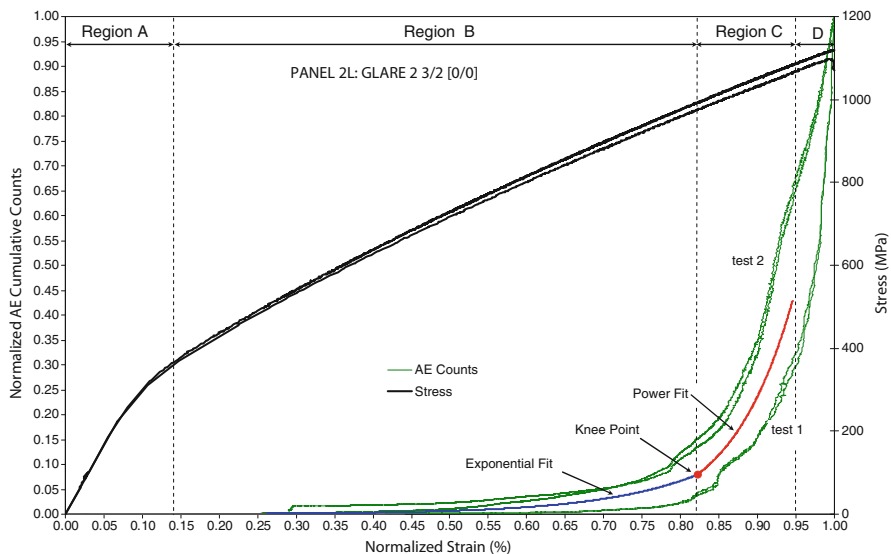
Fig. 1 Norm. AE cum. counts and stress vs. normalized strain for Glare 2 3/2 [$0°_2$]

in Glare panels, can be divided into four sections, with the exception of Glare 2 3/2 [90°_2]. The initial region A has minimal and mostly linear AE activity followed by region B, which is exponential in nature and can be represented by $Nc = Be^{\beta\varepsilon}$ where, Nc represents normalized cumulative counts and B and β are constants particular to the panel under consideration. Region B initiates around the yield stress and terminates with the knee point in the AE activity. In Section C, AE profile initiates at the knee point and proceeds to within 90%-95% of fracture strain, exhibiting power growth behavior, which can be successfully modeled by the power law $Nc = A\varepsilon^{\alpha}$ where A and α are constants particular to the panel under consideration. The last region D, spans the final 5%-10% of fracture strain, is characterized by linear growth with a steep slope preceding the final failure of the material. During this stage the AE activity is generated by the propagation of large cracks and fiber pullout in large sections along with matrix disintegration. However, after inspecting the damaged specimen delamination was not observed. The adhesion between the metal layer and the matrix is very high and remains in tact, while the matrix disintegrates in Glares [6,8].

The knee point may be defined as the location on the normalized cumulative counts profile where the exponential and power curves intersect. This point in the AE activity is significant, since, it is believed, it specifies the change from micro to macro damage modes in the material. Before the knee point the material is experiencing micro-damage mechanisms; matrix cracking, individual fiber fracture, matrix/fiber debonding and yielding. However, at the knee point the damage localizes and changes modes. Now relatively large sections of fibers are breaking, there is fiber pullout, and large cracks are propagating simultaneously disintegrating the matrix around the localized region. These macro-damage modes are responsible for the power growth evolution in AE activity.

Constant multiplier A shows a significant degree of scatter throughout the exponential regions of AE activity; constant B is close to unity ($\approx$0.88) in most Glare grades. While, the constant multipliers appear not to be related to Glare 5 grades. Exponential growth exponent, β, linearly increase, while the power growth exponent, α, exhibits a linear decrease with decreasing MVF in all Glare 5 grades. An increase in the amount of prepreg laminate present in the material should increase the rate of crack initiation and growth in an exponential manner, consistent with the theory of matrix crack saturation. Power exponent, on the other hand, decreases with increasing fiber volume present in Glare grades.

AE characteristics

The source identification and characterization of AE signals in higher Glare grades are based on aluminum and Glare 2 specimens. Counts, amplitude, and duration were chosen for classification purposes within the recorded AE parameters.

In the aluminum tests, 88% of the AE activity registered 1 count above threshold with signal duration of 1μs and a peak amplitude range between 45–50 dB which is
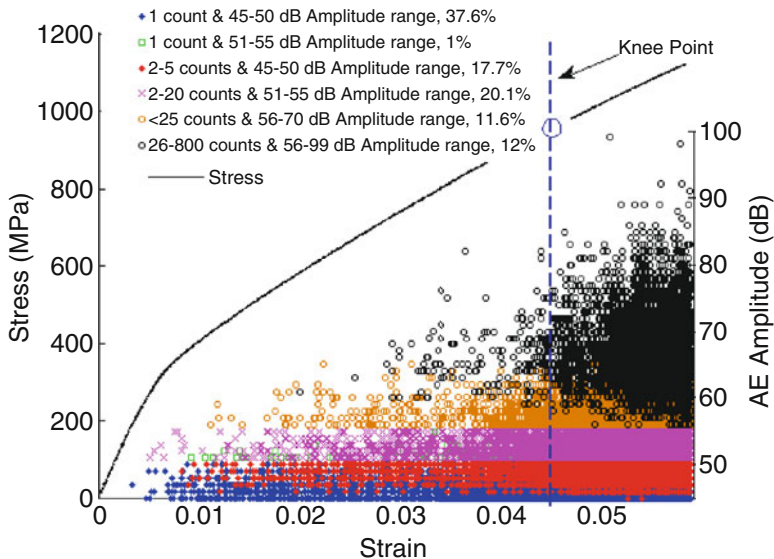
Fig. 2 Typical AE signal distribution and stress with respect to strain with average signal characteristic percent distributions of Glare 2 2/1 [$0°_2$]

attributed to the yielding micro damage mechanism. In literature, tensile testing on aluminum alloy specimens produced similar AE profiles [7–9].

It is known that the damage evolution in brittle-matrix composites consists of the matrix crack initiation followed by crack propagation and matrix-fiber debonding which ultimately leads to fiber fractures and final failure [10]. This proposed damage evolution is, by no means, clear cut and observations have shown that micro-damage modes overlap throughout the damage profile.

In examining Glare 2(3/2) [$90°_2$] tests, comparing with aluminum, 1 count & 45–50 dB AE category signals appear just before the proportional limit and there is much more AE in that category then can be generated by yielding in the aluminum layers alone. Of note, 1 count & 45–50 dB category signals generated by aluminum were predominantly 1 μs in duration, while Glare 2(3/2) [$90°_2$] produces the same signals with two distinct durations: 1 μs and 3–4 μs, thus signaling the presence of a new micro damage mechanism. Examining the location of 1 count & 45–50dB category signal initiation along the stress profile reveals that at this early stage of the profile the two dominant damage mechanisms are yielding and matrix crack initiation. Furthermore, signals with 2–5 counts & 45–50 dB characteristics have increased from 2 to 19% percent with an addition of 21% percent signals with 2–15 counts & 51–55dB characteristics. Based on these observations it can be speculated that 2–15 counts & 45–55dB signals are generated by matrix-fiber debonding.

In Glare 2 (3/2) [$0°_2$] shown in Fig. 2, the AE characteristics for yielding and matrix crack initiation deduced from the previous tests are already observed. Signals

Table 2 Signal characteristics of primary micro-damage mechanisms

Micro-damage mechanisms	Signal characteristics
Yielding in aluminum alloy	1 count & 45–50 dB (1μs)
Matrix crack initiation	1 count & 45–50 dB (3–4 μs)
Transverse matrix cracking	2–15 counts 45–55dB (5–30 μs)
Matrix cracking	2–15 counts 45–55dB (5–30 μs)
Individual fiber fracture	< 25 counts 56–70 dB (10–120 μs)

category registering 0–25 counts&56–70dB amplitudes with durations of 10–120 μs is attributed to fiber fracture, which is consistent with earlier observations in similar materials. An acoustic emission study conducted on unidirectional E-glass fiber reinforced plastic composites attributes signals with 70 μs or lower durations to individual fiber fracture [6]. The category of 2–15 counts & 45–50 dB signals produced by matrix-fiber debonding can be readily observed in Fig.2 with 2–20 counts. Also, it can be speculated that the matrix cracking micro damage mechanism, which should appear in both Glare 2(3/2) tests, takes place in the same category next to matrix-fiber debonding.

The category percent and profile distributions are similar for all higher Glare grades, except that the amount of AE increases. The identified categories of AE signal characteristics, based on counts, amplitude, and duration, of primary micro-damage mechanisms are summarized in Table 2.

Conclusion and Discussion

Different microdamage mechanisms in Glares produced characteristically different AE signals which can be classified into categories based on peak amplitude, total counts, and duration parameter ranges. It was observed that AE percent count rate is a function of the normalized strain and metal volume fraction (MVF) in similar Glare lay-ups. AE profiles were found to exhibit exponential growth behavior in the initial region of the profile and a power growth behavior after the knee point. This alteration in growth behavior is attributed to the change in damage modes from micro to macro after strain localization.

References

[1] Voselesang, L.B., Vlot, A. (2000). *J Mater Process Tech*, vol. 103, p. 1.
[2] Spanner, J.C. (1974). *Acoust. emission Tech and Appl*, Intex Pub Comp, USA.
[3] Dong, L., Mistry, J. (1998). *Compos Struct*, vol. 40, no. 1, p. 43.
[4] Huguet, S., Godin, N., Gaertner, R., Salmon, L., Villard, D. (2002). *Compos Sci Technol*, vol. 62, p. 1433.
[5] Caprino, G., Teti, R., de Iorio, I. (2005). *Compos Part B-Eng*, vol. 36, p. 365.

[6] Nayeb-Hashemi, H., Kisnomo, P., Saniei, N. (1997). *J Acoust. Emission*, vol. 15, no. 1–4, p. 33.

[7] Scott, Ian G. (1991). *Basic Acoust. Emission*, NDT monographs and tracts, vol. 6, pp. 98–107.

[8] Vlot, A., Gunnink, J.W. (2001). *Fiber Metal Laminates, an introduction*, Kluwer Academic Publishers, Dordrecht.

[9] Cousland, S., McK, S., Scala, C.M. (1983). *Mater Sci Eng*, vol. 57, p. 23.

[10] Daniel, I.M., Anastassopoulos, G. (1995). *Int J Solids Struct*, vol. 32, no. 3/4, p. 341.

NDE Using Lockin-Thermography: Principle and Recent Developments

G. Busse, A. Gleiter and C. Spiessberger

Abstract Conventional thermography provides colourful images of surface temperature fields. If the temperature on a solid surface is periodically modulated, the temperature field propagates into the inspected object as a "thermal wave". Internal reflections at thermal boundaries are superposed to the original thermal wave. They affect the signal and thereby provide information on thermal features hidden underneath the surface. This information is derived from a stack of thermographic images that are recorded when the sample is periodically excited: Along each pixel of the stack a Fourier transformation is performed of the time dependent signal at the modulation frequency. This way the information content is finally compressed into just two images one of which is the local phase shift between excitation and local thermal modulated response.

The information of such images depends both on the kind of excitation and on modulation frequency: With remote optical excitation, such images display thermal features in a depth that depends on modulation frequency. With excitation by ultrasound, the heating mechanism is local conversion of elastic energy into heat by mechanical losses, e.g. by the relative motion of boundaries in a crack. This way a crack is turned into a thermal wave transmitter. As intact material and boundaries are largely suppressed in such an image, it displays selectively defects. Data fusion of images taken at different frequencies or with different kinds of excitation allows for feature extraction and for additional information on the kind of the defects.

The techniques and their applications will be illustrated by examples that were obtained on various industry-relevant components.

Keywords Data fusion • Defect-selective imaging • Optical lockin-thermography • Ultrasound lockin-thermography

G. Busse (✉) • A. Gleiter • C. Spiessberger
A Institute of Polymer Technology (IKT), Non-Destructive Testing (IKT-ZfP),
Stuttgart University, Pfaffenwaldring 32, 70569 Stuttgart, Germany
e-mail: gerd.busse@ikt.uni-stuttgart.de

Lockin Thermography Methods

Optically activated lockin-thermography

Modulated deposition of heat is achieved e.g. by illuminating the inspected component with halogen lamps whose intensity is slowly modulated (typically at 0.1 Hz). At the same time a thermography camera records continuously images of the sample surface over several excitation periods (Fig. 1). This stack of images contains information on local phase changes and hence on thermal boundaries within the sample from which thermal waves are reflected back to the surface. This information is retrieved by applying a Fourier transformation at the frequency of modulated illumination ("lockin frequency") at each pixel to find phase and amplitude of local modulation. This way finally an amplitude and a phase image are obtained [1–5]. The Fourier transformation corresponds to a narrow band filtering with a corresponding improvement in S/N ratio. Besides the robustness of phase another advantage of Lockin-Thermography is the adjustable depth range given by the thermal diffusion length which depends on thermal diffusivity of the material and on lockin frequency. The depth range can therefore be increased by decreasing the lockin frequency.

Optically activated lockin thermography does not only reveal hidden defects but as well all other thermal features within the thermal depth range. This reduces the
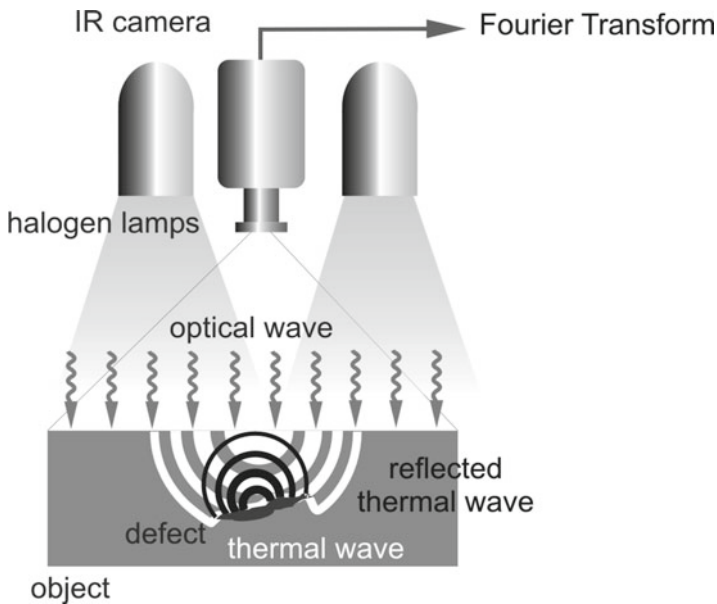
Fig. 1 Basic setup of optically activated lockin-thermography (OLT)

probability of defect detection (POD) in the presence of complicated thermal structures like in CFRP stringer panels.

Ultrasound activated lockin-thermography (ULT)

Heat can also be generated directly in damaged areas when they are exposed to powerful ultrasound excitation. Elastic energy is converted into heat mostly in areas of stress concentration and defects like cracks or delaminations [6, 7]. These heat sources can be detected by an infrared camera even in the presence of complicated intact features. Ultrasound activated thermography („ultrasound attenuation mapping") is a defect selective "dark field" NDT-technique as only defects produce a signal.

The setup for ultrasound activated lockin thermography (ULT) is similar to the one above except that the lamps are replaced by an ultrasound transducer attached to the sample. The elastic waves launched into the inspected component are amplitude modulated (again at about 0.1Hz while the carrier frequency is a couple of kHz). This results in periodical heat generation so that the defects are pulsating at the modulation (lockin) frequency and thereby emitting thermal waves [8, 9].

Ultrasound activated thermography with a fixed carrier frequency close to a resonance frequency of the sample can lead to a strong standing wave pattern which might appear as a superposed temperature pattern hiding defects. Ultrasound frequency modulation in addition to the amplitude modulation can solve this problem [10]. The frequencies causing the standing wave pattern are reduced and a more homogeneous phase image with an improved signal-to-noise ratio is achieved. Another version is burst phase ultrasound thermography (UBP) which is basically multi-frequency ULT [11]. The method is useful to detect e.g. fatigue cracks or loose rivets in structures [12].

Examples for Applications

The lockin thermography methods described above are well applicable in situations where the detection of boundaries or their changes due to damage development or processing are of interest, like in aerospace structures [13].

One example is the wing of an aircraft where the bond between the spar and the skin had to be inspected. The thin skin is made of glass fibre reinforeced plastics (GFRP). The phase angle image of OLT (Fig. 2) reveals clearly an area where bonding (black region) is insufficient. As the straight lines indicate, the bonding seam should be about 5cm wide.

Another example of technical relevance is an investigation aiming at the change of defect-induced boundaries in carbon fibre reinforced polymer (CFRP) that is afterwards transformed by heat treatment into carbon/carbon (C/C) material which
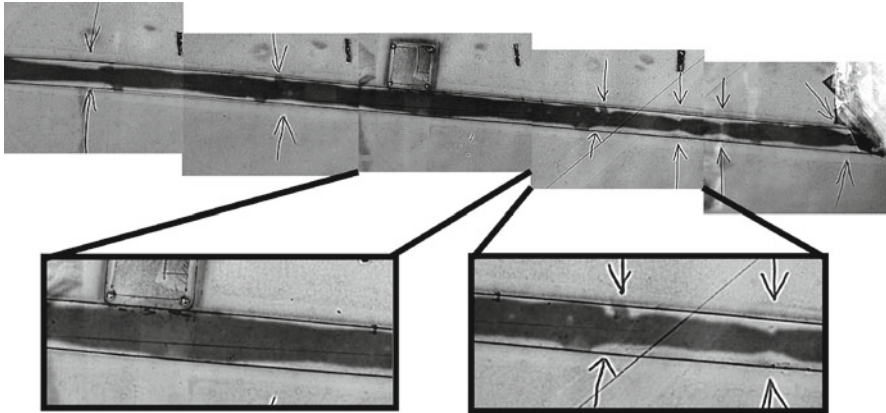
Fig. 2 OLT: Sufficient (left) and insufficient (right) bond seam in an aircraft wing (wing supplied by Sportfliegergruppe Waiblingen)
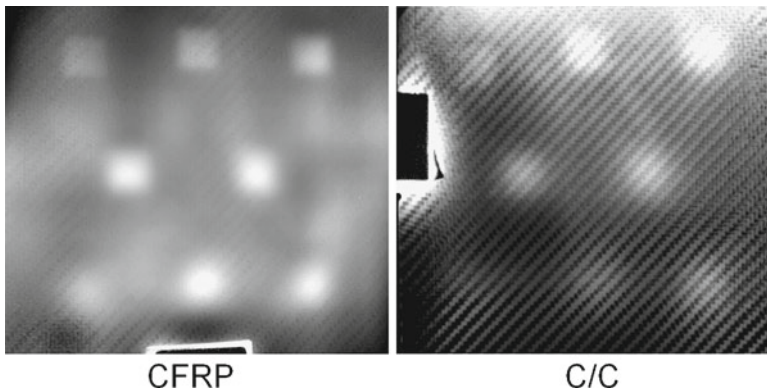
Fig. 3 OLT in transmission on CFRP and C/C-material. Sample kindly provided by Schunk Kohlenstofftechnik GmbH

is used for high temperature applications. Such a sample (sized about 20x30 cm^2) was provided with thin quadratic Teflon insert sheets in different depths of the laminate in order to simulate delaminations. The simulated defects stand out clearly in the OLT phase angle image taken in transmission at 0.1 Hz (Fig. 3). They are surprisingly still visible - though more diffuse- after heat treatment where only carbon is left of the organic material.

Another area of applications is monitoring the failure behaviour of components while they are being exposed to loads: Failure is always accompanied or initiated by boundaries, therefore their early identification and process of development is essential to understand failure processes and also as a feedback to simulation results [14, 15].

Cross Sections…

good   defective

… and UBP phase images at 0.54 Hz

good   defective
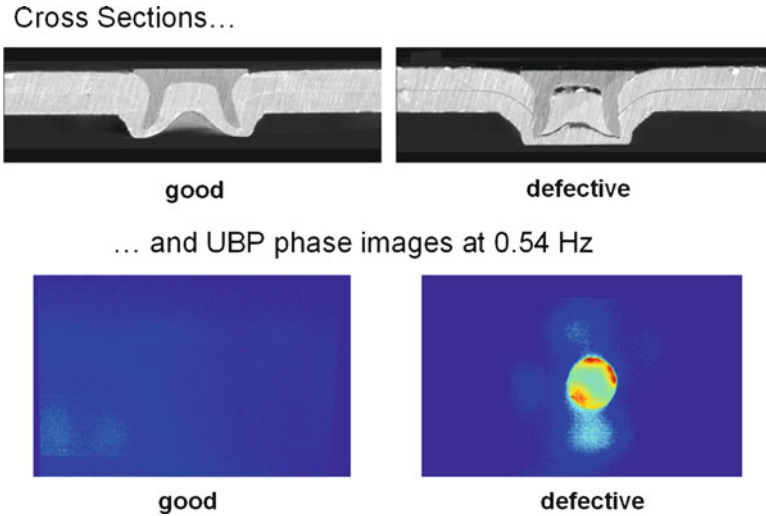
Fig. 4 UBP for finding loose rivets [11, 12]. The images show the phase lag of thermal waves at 0.54 Hz

The last example (Fig. 4) relates to the identification of loose rivets which reveal themselves when inspected with UBP due to boundary friction resulting in heat.

Conclusions

Nondestructive testing using lockin thermography is a fast and reliable method for imaging of subsurface thermal features, e.g. boundaries in all kinds of materials. As depth range is variable via modulation frequency, three dimensional information is obtained much faster than conventional methods.

References

[1] P. -E. Nordal and S. O. Kanstad, Physi. Scripta 20:659–662 (1979)
[2] G. Busse, Appl. Phys. Lett. 35:759–760 (1979)
[3] G. M. Carlomagno and P. G. Berardi, Unsteady thermotopography in non-destructive testing, Proc. 3rd Biannual Infrared Information Exchange, St. Louis/USA, 24–26. August 1976, pp. 33–39
[4] J. L. Beaudoin, E. Merienne, R. Danjoux, M. Egee, Numerical system for infrared scanners and application to the subsurface control of materials by photothermal radiometry, Infrared Technology and Applications, SPIE Vol. 590 (1985) p. 287
[5] P. K. Kuo and Z. J. Feng and T. Ahmed and L. D. Favro and R. L. Thomas and J. Hartikainen, "Parallel thermal wave imaging using a vector lockin video technique" in Photoacoustic and

Photothermal Phenomena, edited by P. Hess and J. Pelzl, Springer-Verlag, Heidelberg, pp. 415–418 (1988)

[6] R. B. Mignogna and R. E. Green and Jr. Duke and E. G. Henneke and K. L. Reifsnider, Ultrasonics 7, pp. 159–163 (1981)

[7] F. Staerk, Werkstofftechnik 13, Verlag Chemie GmbH, Weinheim, pp. 333–338 (1982).

[8] Patent DE 42 03 272 C2: Verfahren zur phasenempfindlichen Darstellung eines effektmodu-lierten Gegenstandes, IKP-ZfP (1992)

[9] J. Rantala, D. Wu and G. Busse, Research in Nondestructive Evaluation, 7:215–218 (1996)

[10] Th. Zweschper, A. Dillenz, G. Riegert D. Scherling and G. Busse, Insight Vol. 45 Nr. 3, pp. 178–182 (2003)

[11] A. Dillenz, Th. Zweschper, G. Busse: "Elastic wave burst thermography for NDE of subsurface features". Insight Vol. 42 Nr. 12, pp. 815–817 (2000)

[12] G. Riegert, Th. Zweschper, A. Dillenz, G. Busse, Inspection of rivets and cracks in metal using thermography methods. In: Balageas D., Beaudoin J.-L., Busse G., Carlomagno G. M. (ed.): Quantitative Infrared Thermography 6, Lodart S.A.: Akademickie Centrum Graficzno, pp. 293 – 298 (2002)

[13] D. Wu, A. Salerno, U. Malter, R. Aoki, R. Kochendörfer, P. K. Kächele, K. Woithe, K. Pfister, G. Busse, Inspection of aircraft structural components using lockin-thermgraphy. In: Busse, G.; Balageas, D.; Carlomagno, G.M. (Hrsg.): Quantitative infrared thermography, QIRT 96, Stuttgart, Edizione ETS, Pisa (1997), S. 251-256, ISBN 88 - 467 - 0089 – 9

[14] A. C. Orifici, R. S. Thomson, R. Degenhardt, A. Kling, K. Rohwer, and J. Bayandor, "Degradation investigation in a postbuckling composite stiffened fuselage panel", Proc. 13th International Conference of Composite Structures, Melbourne, Australia (2005)

[15] R. Degenhardt, R. Rolfes, R. Zimmermann, and K. Rohwer, "COCOMAT - Improved Material Exploitation at Safe Design of Composite Airframe Structures by Accurate Simulation of Collapse", Proc. International Conference on Buckling and Postbuckling Behaviour of Composite Laminated Shell Structures, Eilat, Israel, (2004)

Detection of Very Thin Defects in Multi-Layer Composites Made of Carbon Fibre with IR Thermography Methods

W. Swiderski

Abstract The paper presents issues related to detection of very thin defects in multi-layer composite materials based on carbon fibres. Defects that may occur in this type of multi-layer composite materials include delaminations and incomplete bonding of composite layers. Thermal non-destructive tests (NDT) have been recognised as an effective method of defect detection in multi-layer materials.

Keywords Carbon • Defect detection • Infrared thermography • Layered composites

Introduction

More and more often composite materials are used for fabrication of light-weight ballistic covers. An interest in these covers results from threats which troops participating in stabilisation missions are exposed to. Usually these troops use motor vehicles exposed to small-arms fire and mine explosions. Therefore it is necessary to provide an effective protection for these vehicles that assures an adequate safety level for their crews [1]. Composite materials feature excellent mechanical and strength-related properties, combined with a low specific weight. This combination of features actually occurs only in composites and this is the reason why their application in design of light ballistic covers, where these features are of a paramount importance, has been recently growing rapidly. One of the basic groups of reinforcement materials in

W. Swiderski (✉)
Military Institute of Armament Technology, Prymasa Wyszyńskiego7 Str.,
Poland 05-220, Zielonka
e-mail: waldemar.swiderski@wp.pl

composites are carbon fibres discovered back in 19th century. They have many technical applications including light ballistic covers where they are most often used as multi-layer composite materials constituting a structure made of several interconnected layers or many layers of carbon fibres, or in combination with other materials. Given the fact that light ballistic covers are usually several to 10-20 mm thick and are made of materials with thermo-physical properties definitely different from those of potential defects occurring in these materials, non-destructive tests using thermography methods may be an effective tool for detection of these defects.

Test Method

One of the main methods of active thermography - Pulsed Thermography (PT) [2] was used to check the effectiveness of defect detection in multi-layer carbon composites. PT is currently one of the most popular methods used in non-destructive tests of composite materials. Tests of this kind consist in use of a lamp, laser, etc. to generate a thermal exciting pulse (or series of pulses) that lasts from several milliseconds for high thermal conductivity materials (e.g. metals) to several seconds for low conductivity materials. Also a pulse that cools down the surface of the object being tested can be used (e.g. liquid nitrogen, etc.). PT can be use in both reflective and transmission method. A sequence of images (thermograms) is recorded at constant intervals between the images. Having switched the radiation source off the object under test is cooled down to the ambient temperature. In the cooling phase a temperature distribution across the surface of the object is determined and analysed. Depending on thermal properties of the material tested and defects hidden under its surface, areas of a higher or lower temperature will indicate zones where material defects might occur. Often special thermogram processing techniques need to be used to identify the defect areas. Use of the most popular optical heating (e.g. a heating lamp) is also accompanied by drawbacks of this warming mode including: 1) non-uniform heating; 2) low temperature contrast resulting from the fact that both defect areas and those not containing any defects are heated up 3) difficulties with detection of deeper defects that require larger thermal energy; however, this may result in overheating of the sample and its damage. In order to reduce effects of these shortcomings, a thermal stimulation by means of ultrasonic sound began to be used [3, 4]. First of all, ultrasounds cause a temperature increase in the fault area that significantly affects an increase of the temperature contrast value. In order to compare a possibility of increasing the probability of defect detection in multi-layer carbon composites, tests were conducted using the pulsed thermography method by means of both a heating lamp and an ultrasonic source. Figure 1 presents the set-up used for thermographic tests with ultrasonic thermal stimulation.

Fig. 1 Set-up of a stand for thermographic tests with ultrasonic sample stimulation: 1 – sample, 2 – ultrasonic stimulator, 3- IR camera
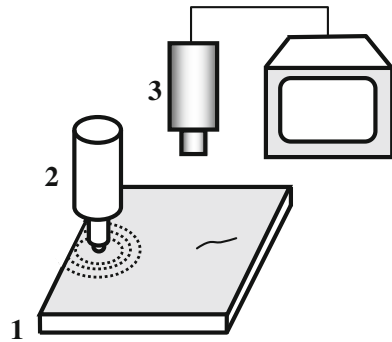
Experimental Tests

Two samples of a multi-layer carbon-fibre composite were tested in the experimental tests. Four discs of various diameters (1 to 8 mm), made of 0.1-mm thick Teflon film, simulating delamination defects (D1 to D4 at 0.6 mm depth), were introduced into the first sample that was 1 mm thick. This sample was used for comparison tests of sample thermal stimulation by means of an optical and ultrasonic pulse. A flash lamp was used as the source of the optical pulse that provided a thermal pulse (Dirac pulse) of a 3 kJ output power and duration of 1 ms. A ultrasonic pulse of frequency of 20 kHz and 300 W output power was generated by the ultrasonic generator shown in Fig.1. The ThermaCAM P65 camera (μbolometer, 320x240 pixels, 70 mK) was used for recording the changes of temperature field on the sample surface; the camera was recording sequences of thermograms (400 images in a sequence) at 25 Hz frequency.

In order to compare the defect-detection efficiency with use of various image processing algorithms used in thermographic tests, trials of another composite sample of dimensions of 100x100 mm and 5- mm thick, made of 4 layers of carbon-fibre fabric, connected with epoxy resin, were conducted. Six defects (D5 to D10) of dimensions of 5x5 mm, 10x10 mm and 10x20 mm, made of 0.1 mm thick Teflon film and simulating delaminations of the composite, were placed between the fabric layers at different depths (1.2 mm, 2.5 mm and 3.8 mm). The sample was tested by means of pulsed thermography, and the heat source was a flash lamp providing a thermal pulse (Dirac pulse) of 3 kJ output power and 2.7 ms duration. The Agema 900 LW IR camera (detector MCT, 272x136 pixels, 80 mK) was used for recording temperature changes on the sample surface.

Test Results

Several algorithms (such as Fourier transformation, normalisation, polynomial adjustment, pulsed phase thermography, principal components analysis, correlation analysis and dynamic thermal tomography) were used for analysis of the results.
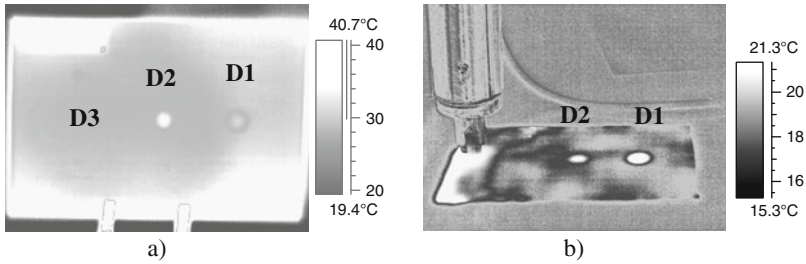
Fig. 2 Comparison of optical and ultrasonic stimulation of a 1-mm thick sample of a multi-layer carbon composite (defects are simulated by 4 Teflone inserts between the composite layers)
a – optical stimulation (maximum signal above D1defect = 1.16°C, average surplus of sample temperature 2.2°C, signal to noise ratio 18.6, temperature contrast 53%);
b – ultrasonic stimulation (maximum signal above D1 defect = 2.1°C, average surplus of sample temperature 0.6°C, signal to noise ratio 32.0, temperature contrast 580%)

These algorithms are used in thermography non-destructive testing designed for separation of signal change areas against the background of interference. Signal to noise ratio (S) [1] was used as a comparison criterion in estimation of the image processing algorithms used. Basing on the signal to noise ratio it can be estimated which algorithm is more effective in identification of areas where defects are located [5]. The signal to noise ratio is calculated basing on the following formula:

$$S = \frac{\overline{T_d} - \overline{T_{nd}}}{\sigma_{nd}} \tag{1}$$

where: $\overline{T_d}$, $\overline{T_{nd}}$ - correspondingly, average temperatures of a defected and defect-less zone; σ_{nd} – standard temperature deviation in defectless zone.

Figure 2 presents the results obtained from the comparison or optical and ultrasonic pulse stimulation of the first sample. The thermogram made by means of the optical pulse shows thermal „traces" of three defects while that obtained by means of ultrasonic pulse shows the two largest defects. Use of image processing algorithms, both the Fourier transformation and analysis of principal components, allows for locating the fourth defect (D4) with the optical stimulation of the sample (Fig. 3). Processing of thermograms obtained through ultrasonic stimulation does not allow for detection of the D3 and D4 defects by means of these algorithms (Fig. 4). Within the testing of the second sample a sequence of 400 thermograms was recorded at frequency of 25 Hz. The tests were conducted by means of both the pulse single-side pulse method (camera and stimulation source are on the same side of the sample being tested) and double-side one (camera and source are located on opposite sides of the sample). Figure 5 presents selected results obtained from the single-side method that turned out to be more effective in detection of defects in this sample. It is clearly visible that the pulsed-phased thermography method (phasogram Fig. 5b) and principal components analysis (Fig. 5c) allow for detection of all defects.
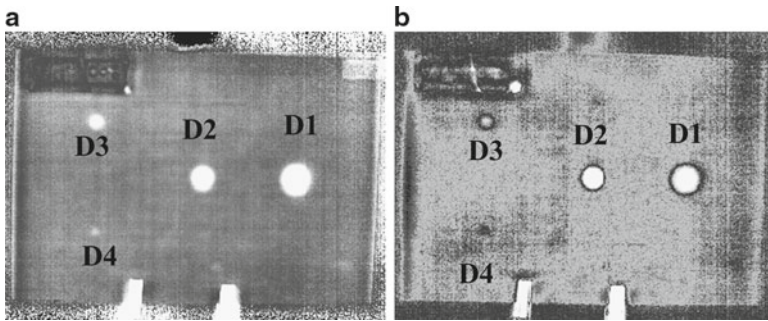
Fig. 3 Effectiveness of thermogram processing with optical sample stimulation: a - image of the Fourier transformation phase (signal to noise ratio S = 33, f=0.125 Hz) b – PCA (signal to noise ratio S = 24.6)
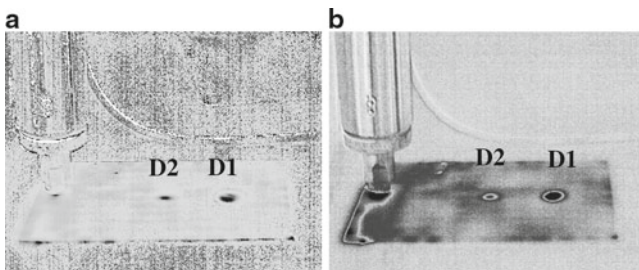
Fig. 4 Effectiveness of thermogram processing with ultrasonic stimulation: a - image of the Fourier transformation phase (signal to noise ratio S = 11.8, f=0.63 Hz) b – PCA (signal to noise ratio S = 31.7)

Conclusions

1) The comparison of the first sample stimulation by means of the optical and ultrasonic method has shown that:

   – For detected defects a value of the signal to noise ratio is higher with ultrasonic stimulation;
   – Value of the sample surface temperature in areas without any defects is much lower with the ultrasonic stimulation;
   – No small-area defects were detected by means of the ultrasonic stimulation; perhaps this was caused by a wrong selection of ultrasonic frequencies used for stimulation (this method has not been sufficiently tested yet);
   – Probably the ultrasonic stimulation can provide better results in detection of material cracks, perpendicular to its surface;
   – So far optical stimulation is more effective in delamination detecting.
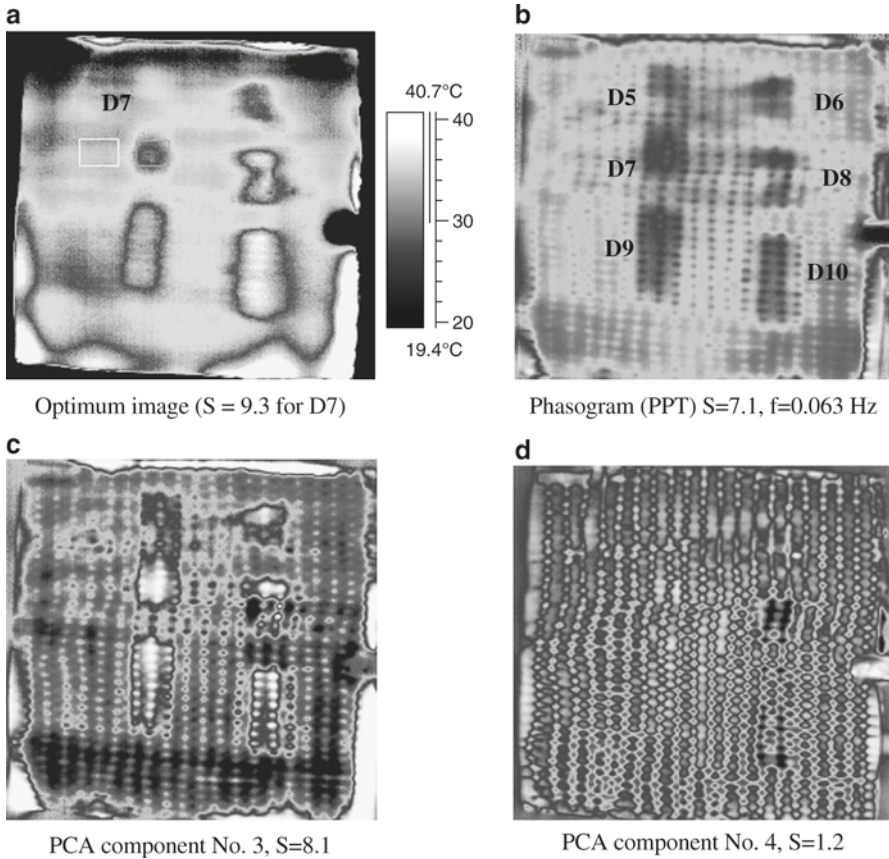
Fig. 5 Results of a carbon-fibre composite test used the pulsed thermography method (single-side method)

2) The tests of both samples shown that currently there are technical possibilities of detecting very thin defects in subsurficial layers of carbon-fibre multi-layer composites by means of IR thermography methods.
3) Temperature changes on composite surface above a defect may be relatively small; this requires use of advanced data processing methods such as pulsed phased thermography (PPT), principal component analysis (PCA) and thermal tomography.
4) Stimulation of a composite with ultrasonic pulse is a prospective method but it requires both improvement of the ultrasonic stimulator's performance (increase of output power and frequency band extension) and series of experimental efforts allowing for gaining more extensive knowledge on this.

5) The missing D3 and D4 in the results of ultrasonic excitation may result from area/position of energy input, which results in a local heating, masking the small signal amplitudes of the defects. Thus an increase of power could not solve the problem and might lead to a destruction of the sample.

References

[1] Swiderski W. (2010) *Nondestructive testing of composite materials by IR thermography methods*, Monograph, WITU, Zielonka (in Polish)

[2] Maldague X. P. V. (2001) *Theory and practice of infrared technology for nondestructive testing*, John Wiley&Sons, Inc., New York, p. 78

[3] Vavilov V. P. (2009) *IR thermography and non-destructive evaluation*, «Спектр», Moskwa, p. 544 (in Russian)

[4] Favro L. D., Han X., Ouyang Z. et al. (2000) *IR imaging of cracks excited by an ultrasonic pulse*, Proc. SPIE "Thermosense-XXII", Vol. 4020, pp. 182–185

[5] Swiderski W., Bin Umar M. Z., Ahmad I., Vavilov V. (2008) *Developing methodology of pulsed thermal NDT of composites: Step-by-step analysis of reference samples*, The e-Journal&Database of Nondestructive Testing, May Issue, pp. 1–13

A Comparison Between Optimized Active Thermography and Digital Shearography for Detection of Damage in Aerospace Composite Structures

G. De Angelis, M. Meo, D.P. Almond, S.G. Pickering and S.L. Angioni

Abstract The main goal of this research is to compare capabilities of two different Non-Destructive Testing (NDT) methods, thermosonics and digital shearography (DISH), to recognize and image back drilled hole defects. Thermosonics was optimized by varying magnitude of the heat flux, the excitation frequency, the number of excitation cycles, acquisition time, frame rate etc. DISH was optimized by investigating the test objects by dynamic loading approach in order to identify per each defect the (0 1) mode shape and the corresponding resonance frequency. In this way, whilst thermosonics provided the initial infrared imaging of the panel for a pass/fail test, DISH has been performed to provide the delamination quantitative assessment.

Keywords Delamination • Flaws assessment • Nondestructive evaluation • Shearography • Thermosonics

Introduction

In this work we report the result of thermosonics inspection and DISH optimization based on an intensive experimental study carried out by investigating two back drilled composite test plates. The optimization of thermosonics was experimentally undertaken by taking into account the period of excitation, the frequency frame rate, the position of the horn tip on the inspected surface etc. DISH methodology was used to complement thermosonics damage recognition for the assessment of both size and depth of the defects. The quantitative flaws assessment was ascertained by combining the experimental results with an optimization algorithm. Then, a new

G. De Angelis (✉)
Chemistry Department, Flight Test Center, Italian Air Force, Aeroporto De Bernardi, Pomezia (Rome), Italy
e-mail: giovanni.deangelis@aeronautica.difesa.it

M. Meo • D.P. Almond • S.G. Pickering • S.L. Angioni
Department of Mechanical Engineering, University of Bath, Bath BA27AY, UK
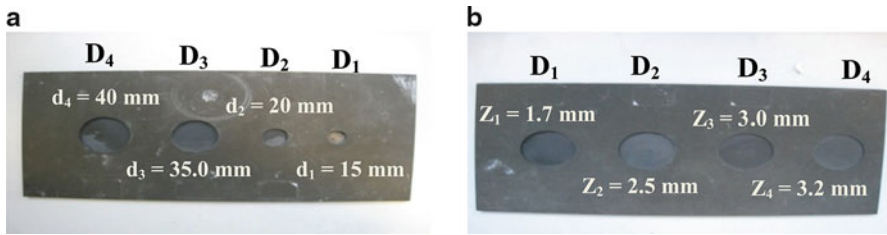
Fig. 1 CFRP laminates (**a**) CFRP$_1$ and (**b**) CFRP$_2$ made with flat bottom holes

method was undertaken to predict the range of natural frequencies to be applied for detecting defects having either variable size or depth.

Materials and Methods

Materials

Two composite fibre reinforced polymer (CFRP) test plates, Fig. 1, were manufactured with the stacking sequence $(0, \pm45, 90)_s$ with total thickness equal to four (4) mm. In the first one, Fig. 1a, four cylindrical holes (D_n) were made at around two (2) mm of depth with size (d) from 40.0 mm to 15.0 mm. For the second specimen, Fig. 1b, four cylindrical defects were created with constant size, d = 40 mm, however located at different depth (z) from 1.7 mm to 3.2 mm.

Methods

Thermosonics

The system employed in this work, Fig. 2a, comprises an ultrasonic welding horn, driven at 35 KHz, pressed against the surface of the tested object, and the small Omega™ infrared camera, used to reveal the local increase of temperature due to the rubbing between both faces of a crack when subjected to a cyclic stress induced externally [1,2]. An experimental parameter called "heating index" (HI) has been suggested as a measure of the total heating released around a crack during the period of excitation, this index is worked out by

$$HI(\tau) = \int_0^\tau e^{\tau(t-\tau)} EI(t)dt \qquad (1)$$

Where t is the time of integration, k is a decay constant estimated from the temporal decay of heating, when the excitation is switched off, and (EI) is the energy index used to weight all vibrational modes excited during the excitation burst, from the earlier to the total heating at time (τ) [3]. The experimental solution was found by
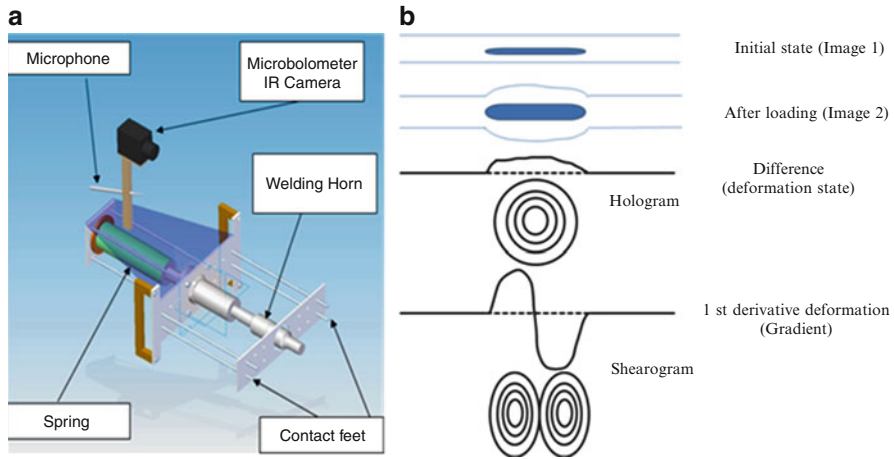
Fig. 2 (**a**) Thermosonics system. (**b**) Interpretation of shearographic results

monitoring the HI in order to verify if its value exceeds the threshold experimentally evaluated sufficient to identify the presence of cracks by a thermal image as output. The thermosonics compact system, Fig. 2a, was designed for full field inspection of the parts. Therefore, the structural response acquisition was provided by using a high frequency microphone. In the end, the short-time Fourier transform algorithm was used to analyze the vibration spectra throughout the excitation phase and from these passages the heating indices were obtained in the way indicated above.

Digital Shearography

Shearography involves the difference, Fig. 2b, of two speckle patterns, collected one before and another after the sample is deformed. Standard shearography measurements were taken for the quantitative assessment of the defect size. Therefore, the depth of the delamination was the only unknown variable. The delamination behavior under dynamic load was assumed to respond to the theory of elastic plates [4]. This simple model of circular plate, with radius (r) is basically used to simulate the deflection out-of-plane of the flaws or the bending mode excited by DISH.

This circular plate with radius (r) and thickness (h), Fig. 3, was assumed fully clamped at its border, whose dimension and thickness (h) are respectively identical to those of the region of perturbed fringe patterns recorded and to the depth (z) at which each delamination is placed [5]. From DISH measurements, the dynamic response was analyzed by recognizing for each defect the (0 1) mode shape and the corresponding resonance frequency. The numerical difference, Eqn. (2), between experimental (f_{exp}) and theoretical resonant frequencies, calculated for a circular plate clamped and free at its border, Eqn. (3), (f_n) was handled by an unconstrained

$$F_n = [f_{exp} - f_n(E_0, h_0)];$$ (2)

Fig. 3 Clamped circular plate under dynamic load (q)

Circular plate   delamination
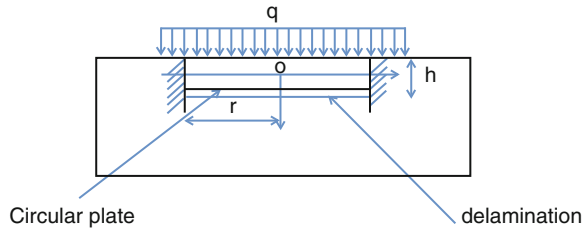
optimization algorithm written in Matlab language and based on Levenberg-Marquard coupled with the line search method [6].

$$f_n = \frac{k_n}{2\pi}\sqrt{\frac{Dg}{\omega\tau^4}}$$

(3)

Where ω is the uniform load per unit area including its own weight, r is the radius of the circular plate, k_n is a constant correlated to both resonance mode and nodal diameter [7]. This methodology of optimization involved an initial guess expressed for the unknown variables (E_0, h_0) in order to produce a sequence of improving approximations to the minimum point. The corresponding data of density, Poisson's ratio and the initial guess for Young's modulus were taken from literature [8].

NDT Results and Discussion

Thermosonics

The thermal image, related to the thermosonics inspection of the composite test plate $CFRP_2$, is shown in the Fig. 4a. The generation of heat at the defective areas was monitored for 200 frames, with a video-frame rate equal to 25 frames per second. In particular, the thermal images were collected, on the site $CFRP_2$ (d_2), for an initial pre–pulse period of excitation ranging from 0th to 50th frames, for the entire period of excitation ranging from 50th to 150th frame and during the thermal decay from 150th to 200th frames. The HI assessment was ascertained after five (5) tests and established around 3000 units hence recognized as the minimum threshold of heat for damage detection.

Digital shearography: Numerical optimization

The analysis of the obtained results, Table 1, proved, as expected, that the resonance frequency increases with the defect depths (z) or with the decrease of the defect sizes (d). In the Table 1, NDT details of the test condition on composite laminates are
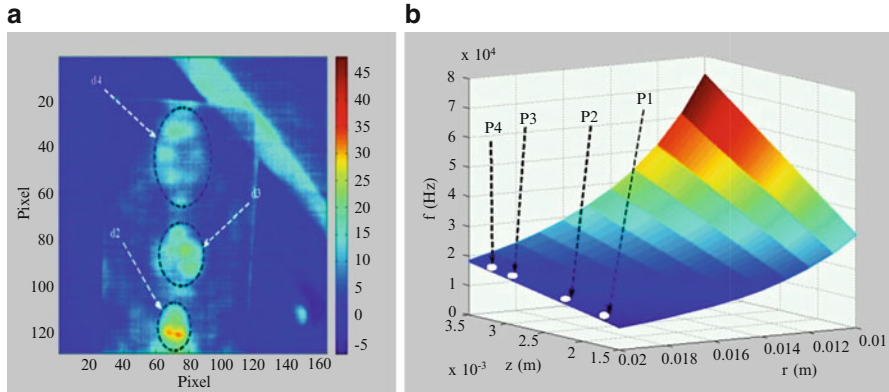
Fig. 4 (**a**) Thermal image of $CFRP_2$. (**b**) Numerical frequency for Four P_n circular defects

Table 1 Comparison between experimental size (d_{exp}), numerical depth $z(_{clamped/free})$ and both actual depths (z) and size (d), expressed in mm, for CFRP test plates

Specimen	D_n	f(KHz)	z	d	d_{exp}	$z_{Clamped}$	z_{Free}	E(GPa)
$CFRP_1$	D_4	6.85	1.70	40.0	42.0	1.40	1.80	30.00
	D_3	9.10	2.00	35.0	38.0	1.60	1.80	30.00
	D_2	32.63	2.00	20.0	22.0	1.70	1.90	37.00
$CFRP_2$	D_1	8.17	1.70	40.0	39.5	1.50	1.72	30.50
	D_2	12.50	2.50	40.0	42.0	2.25	2.70	35.00
	D_3	14.94	3.00	40.0	42.0	2.75	3.20	35.50
	D_4	16.90	3.20	40.0	42.7	3.30	3.60	38.50

reported, particularly, the defect $CFRP_1$ (d_1) was undetected. An average of the evaluated defect sizes, taken over ten observations, was compared with the real flat bottom hole sizes, Table 1. The error was estimated to be ranging from 5% to 10% for the first sample, $CFRP_1$, and less than 7% for the other laminate. Then, the flaw depths assessment was obtained by minimizing the numerical difference, Eqn. (2), between experimental and theoretical resonant frequencies. Composite test plates have a different number of plies, i.e. different bending stiffness and Poisson's ratio etc. Therefore, different values of Young's Modulus related to the equivalent circular plates approximation had to be assumed. In this way, from the numerical optimization, two variables were used: the flaw depth (z), and the Young's Modulus (E). The results, Table 1, for clamped and free mode conditions, yielded acceptable estimates of the defect depths. In the case of the composite test plate $CFRP_2$, the actual locations of the first three flat bottom holes depths were estimated with a discrepancy less than 8%.

The specimen $CFRP_1$ was manufactured with defects having different size not accurately placed at the same depth, due to manufacturing tolerance accuracy. The difference in depth and size significantly influenced the depth assessment with an error ranging from 9% to 15%. A typical numerical curve of natural frequency (f), plotted against the radius (r) of the circular defects and the flaw depths (z), is shown in the Fig. 4b.

Table 2 Comparison between experimental (f_{Exp}) and numerical frequency, expressed in (KHz), calculated assuming clamped (f) and free (f^*) mode conditions, respectively for four P_n cylindrical defects, Fig. 4b

(P_n)	f	f^*	f_{Exp}
P_4	18.60	16.68	16.90
P_3	16.00	14.45	14.94
P_2	13.10	11.84	12.50
P_1	9.90	8.10	8.17

The theoretical frequency was calculated (3) by using the defect size experimentally evaluated, the Young's Modulus (E) and the flaw depths, produced from the numerical optimization, for an equivalent circular plate clamped and free at its border. The value of the Young's Modulus was spanned between 30 GPa and 38 GPa, for circular defects with size (d) and depth (z) respectively ranging from 20 mm to 40 mm and from 1.5 mm to 3.5 mm. The experimental resonance frequencies, measured with shearography performed on the $CFRP_2$ test plate, were compared, Table 2, to those calculated for circular defects (P_n) with comparable depths and dimensions.

As shown in the Table 2, the experimental resonant frequencies (f_{exp}) were proved to be ranging from those computed assuming clamped (f) and free (f^*) mode conditions. In this way, the validity of the present methodology was demonstrated.

Conclusions

This paper presents two novel procedure, i.e. thermosonics and DISH. Thermosonics is used to provide the initial infrared imaging of flat bottom holes produced in a composite test plate. DISH is combined with a developed optimization process in order to obtain the knowledge of both size and depth of the defects. The results showed that the boundaries of the flat bottom holes, for composite test plates, can be estimated quantitatively with an accuracy of more than 90%, the error in the assessment of the flaw depths was generally less than 9%. In conclusion, Thermosonics is an intrinsically fast method of inspection. However, the technique does not offer the possibility to estimate the defect depths but provides a pass/fail test.

References

[1] Morbidini, M., Cawley, P. et al. (2006). Review of Progress in Quantitative Nondestructive Evaluation, Vols 25A and 25B **820**: 558–565.
[2] Han, X.Y., Zeng, Z. et al. (2004). Journal of Applied Physics **95**(7): 3792–3797.
[3] Polimeno, U. and Almond, D.P. (2009). ICCST7 proceedings.
[4] Reddy, J.N. (1999). "theory and analysis of elastic plates". Taylor & Francis, philadelphia, PA.

[5] Hung, Y.Y., and Ho, H.P. (2005). Mathematical Science and Engineering R 49 (61–87).
[6] Jorge Nocedal, J. and Wright, S.J. (1999). "Numerical Optimization" Springer series in Operation Research.
[7] Young, W.C., Roark, R.J., and Budynas, R.G., (2002). "Roark's Formulas for Stress & Strain". Seventh edition.
[8] Soden, P.D., Hinton, M.J. and Kaddour, A.S. (1998). Composite Science and Technology 58, (1011–1022).

Analysis of Laminar Fiber Composites with Computed Tomography Using Shape-Fitted Layers

S. Mohr and U. Hassler

Abstract Fiber composites often consist of several layers with different fiber orientations and are formed in a three-dimensional shape. For non-destructive testing of these components industrial computed tomography (CT) can be used to analyze the internal structures and to detect inhomogeneities or defects. A set of several hundred X-ray projection images is acquired from which the local attenuation coefficients of the components are reconstructed to a three-dimensional volume. Difficulties arise when the three-dimensional volume representation of a laminar component is visualized. Often these components are curved and thus it is difficult to analyze the individual layers of the laminate by scrolling through the slices of the Cartesian volume.

This presentation describes a method for the extraction of laminate layers from CT data and their subsequent evaluation. The surface of the component is described by Bézier-patches. Shifting and sampling of this surface description allows the calculation of a virtually "planar" volume. The laminate layers are aligned in parallel planes in the resulting volume and can be analyzed and visualized layer by layer. With the help of subsequent image analysis applied to each layer irregularities in the fiber layout like undulations or defects like pores and voids can be detected. The application of this method is demonstrated on a typical example.

Keywords Computed tomography • Fiber reinforced polymers • Free form surface • Image analysis • Laminate

S. Mohr (✉) • U. Hassler
Fraunhofer Institute for Integrated Circuits IIS, Development Center for X-ray Technology
EZRT, Fuerth, Germany
e-mail: stephan.mohr@iis.fraunhofer.de

Introduction

Fiber composite parts are often made up of several layers of woven or non-crimp fabrics consisting of glass- or carbon-fibers. By cutting, sewing and draping a three-dimensional shape is laid out made of several two-dimensional preform patches. In the following step, this three-dimensional shape is impregnated with a liquid resin that hardens during the so called curing step under the influence of temperature and pressure.

For purpose of quality control, non-destructive testing methods have to be applied to find possible defects. Typical defects are pores and voids on the matrix-side and undulations, broken fibers, fiber misplacements, etc on the fiber-side.

Due to the advent of flat panel detectors and increased computing speed computed tomography (CT), which is well-known as a tool in medical diagnostics, is used as a non-destructive testing method to detect these inhomogeneities and defects. Recent developments provide the possibility to use CT also as an inline testing method. This is referred to as "Inline-CT" [1]. The fast data-acquisition speed demands for an equally fast evaluation of the scanned objects. Therefore, automatic defect detection algorithms have to be used to find possible defects inside the object.

In general, the cross-sectional CT-views do not represent the object's fabric layers, thus it very difficult to analyze the object's internal structure. To solve this problem, image processing algorithms were developed [2], which offer the possibility to successively extract shape-fitted layers from the 3D volumes. Those algorithms are used in this paper as a starting point to analyze the laminar structures of fiber composites. After their application, other 2D-image processing algorithms are applied slice by slice to detect defects and inhomogeneities within individual fabric layers.

First we give a short outline of the algorithms for the extraction of shape-fitted layers. Afterwards we demonstrate the application of 2D image processing algorithms to find defects in the extracted layers. This method is shown on a CT-scan of a CFRP-clip, which is a part used for structure connecting purposes in modern aircrafts.

Extraction of the Shape Fitted Layers

Several steps are necessary for the extraction. First of all we apply binarization operators to distinguish between object and background voxels. Afterwards we detect the object's outer surface which serves as a reference layer for the extraction. Next, we sample this outer surface to determine a net of Bézier-patches [3] that mathematically describes the surface of the object. Afterwards, we evaluate the Bézier-patches to calculate the coordinates of the layer points. By subsequently sampling and shifting these layer points relatively to the reference surface along their surface normals we extract the shape-fitted layers and store them in an output volume. The best results can be achieved if the volume contains fabric layers that are parallel to the surface.
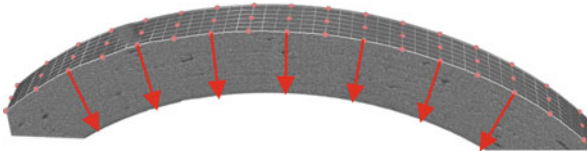
Fig. 1 Tube section with a net of Bézier-patches drawn on the object's surface

Figure 1 sketches this procedure on a three dimensional reconstructed volume of a tube section. On the surface of that section the net of Bézier-patches is drawn using the control points of the Bézier-patches and connecting lines between them. The red arrows indicate the directions of the normals along which the sampled points are moved for extracting the next object layers. Further information about this method and implementation details can be found in [2].

Analysis of the Extracted Layers

One main advantage of the extraction is that now in most cases it is possible to find defects and other inhomogeneities in the object layers by applying 2D image processing algorithms slice by slice. Without the extraction more complicated 3D image processing algorithms would have to be applied.

For the analysis of the slices we implemented two methods:

1. Calculation of statistical values of each slice
2. Defect detection using threshold binarization and median filtering

The first method provides us with statistical values which can be used to determine parameter values for detecting larger defects in each slice (e.g. by threshold binarization) whereas the second method is used to detect smaller defects which are reflected in slight grey value differences to the surrounding area. Those defects are difficult to find by simple threshold binarization.

Calculation of statistical values of each slice

Here, we calculate the mean-, the minimum-, the maximum-grey value as well as the standard deviation and the variance for each slice along an arbitrary direction. Normally, the slices have quite the same statistical values. But if there are some slices with defects like higher attenuating inclusions or lower attenuating pores and voids, in consequence these defects have an influence on the statistical values. By comparing the statistical values of slices with defects to slices without defects, those slices should be easily detectable.

Fig. 2 3D-visualization of a clip made of CFRP
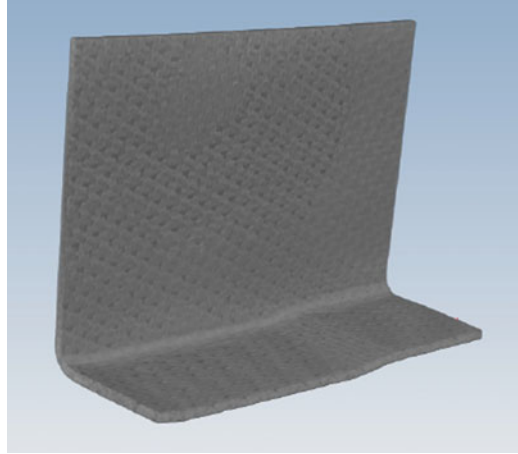
Defect detection using threshold binarization and median filtering

The median filter is an image processing operation which is often applied to remove noise in images. In our case we use the median filter to find smaller defects inside the object layers. Therefore we apply the median filter with a disc-shaped filter mask to blur the potential defect voxels. In a next step we calculate the absolute difference between the original and the filtered volume. In the resulting volume the grey value of each voxel is an indicator for the probability that this voxel can be classified as a defect voxel. A threshold can be applied to suppress voxels with a lower probability.

Example

We tested the approach described above on a CT-scan of a clip made of carbon fiber reinforced polymers (CFRP). The wall thickness of the clip was about 2.1 mm. It took 7 minutes to scan the clip with a reconstructed voxel edge length of 101 μm. In Fig. 2 a 3D-visualization of this clip is shown.

Results

The clip consists of several fabric layers and shows slight undulations on the object's surface. We defined a rectangular region where we applied the extraction algorithm first and calculated the statistical values of the extracted layers afterwards.

Figure 3 displays some slices of the extracted shape fitted layers and in Fig. 4 the statistical values for each slice are shown in a diagram. In the slices 1 to 3 some local spots with higher absorbing inclusions can be seen. This corresponds to the maximum
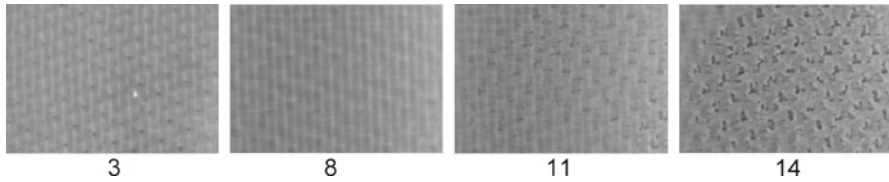
Fig. 3 Selected slices of the volume with the extracted shape fitted layers. Near the center of slice 3 a higher absorbing inclusion can be seen. Slice 8 shows a slice with only regular structures and no defects. In slice 11 some defects are already visible. Slice 14 displays a large number of defects
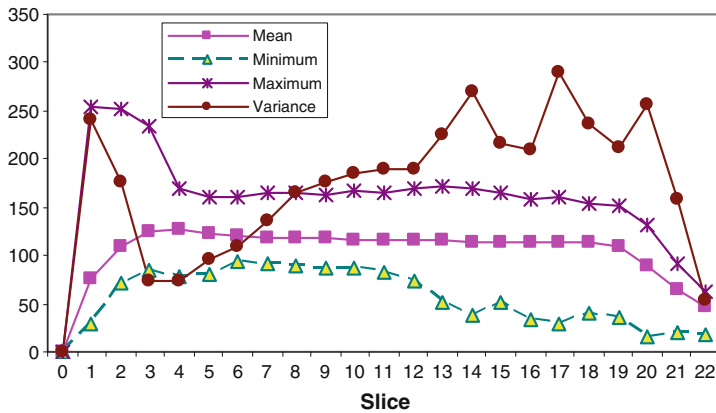
Fig. 4 Statistical values of the slices

values of these slices in the diagram. From slice 4 to 12 the mean, minimum and maximum values do not vary very much whereas the variance rises. The variance indicates that the grey value differences increase which is in this case mainly caused by the structure of the fiber layers. Then several slices are visible that show larger areas with darker grey values. This is caused by lower X-ray absorption and indicates a locally lower matrix content due to voids and pores. In the diagram those areas of lower grey values lead to a lower minimum value and to an increased variance but only a slight decrease of the mean value. A combination of the minimum and variance values may thus help for a reliable detection of layers with lower matrix impregnation.

Figures 5 and 6 show the results of the defect detection. In the left image the original slice is displayed and in the right image the defect voxels are marked with colors ranging from green over yellow to red. The colors indicate the probability that a voxel belongs to a defect. In a subsequent step adjacent defect voxels can be merged to so called blobs which represent the whole defect. For each blob characteristic features can be calculated like the size, the ratio of the diameters of the maximum inscribing sphere and the minimum covering sphere, the contrast to the surrounding area, and so on. These values can be displayed in a table and the user can filter the blobs by constraining the admissible feature values.
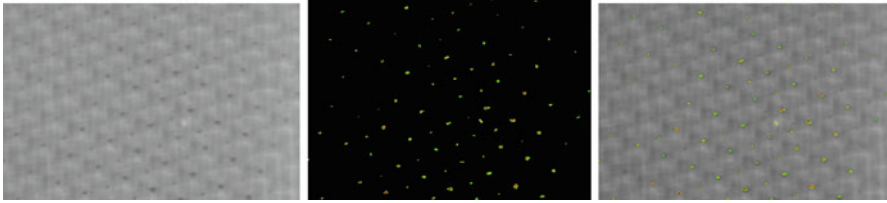
Fig. 5 Slice 7 original (left), detected defects (middle), original with detected defects as overlay (right)
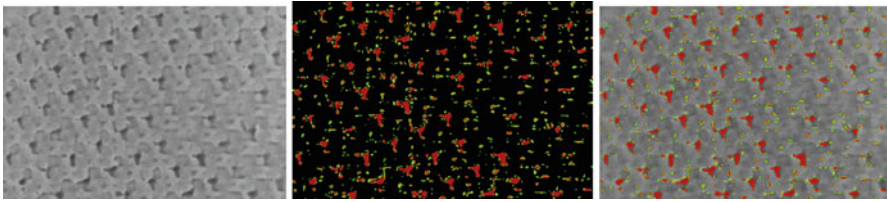
Fig. 6 Slice 17 original (left), detected defects (middle), original with detected defects as overlay (right)

Conclusion

The combination of the shape-fitted layers extraction algorithms with the 2D image processing algorithms offers good possibilities for the detection of defects in CT-scans of CFRP parts with multiple fabric layers. It was demonstrated how the object layers can be extracted from a 3D volume. Furthermore we have shown that defects in the object layers have an influence on the statistical values due to their grey value differences compared to regular structures. An example for the application of 2D image processing algorithms was given to find defects in the object structure. At the moment the best evaluation parameters for a reliable detection of all potential defects have to be determined manually. It poses a challenge for the future to determine them automatically from the CT-data.

References

[1] Oeckl, S., Eberhorn, M., Gruber, R., Bauscher, I., Wenzel, T., Gondrom, S. and Rauch, F. (2010), *Process Integrated Inspection of Castings Using Three Dimensional Computerized Tomography*, ECNDT 2010, Moscow, Russia.
[2] Mohr, S., Gayetskyy, S., Hassler, U. and Hanke, R. (2008), Extraction of shape-fitted layers from CT-data, In: *IEEE Nuclear Science Symposium Conference Record*, pp. 574–576, Dresden, Germany.
[3] Prautzsch, H., Boehm, W. and Paluszny, M. (2002), *Bézier and B-Spline Techniques*, Springer, Berlin, Germany.

Magnetic NDE Using a Double Rectangular Coil and a Hall Effect Sensor: A Simple Analysis

L. Bettaieb, H. Kokabi and M. Poloujadoff

Abstract In this paper a simple analysis and measurement device in eddy current NDE are presented. A Hall probe is associated to a double rectangular Printed Circuit Board PCB. The configurations examined involve the double coil in air and above aluminum plates, either with or without cracks of various depths. The agreement between experimental and theoretical results is very good, showing that our model accurately describes the electromagnetic fields.

Introduction

The early apparatus for Electromagnetic Non Destructive Evaluation (E-NDE) consisted of a circular probe coil whose impedance was measured all over the surface of the metal sheets to be examined [1–4]. One suggested improvement is to replace the impedance value by the resulting magnetic field as the basic signal.

Since the SQUID (Superconducting Quantum Interference Device [5–6]) is a very attractive sensor of magnetic field intensity, it has been attempted to introduce it in the vicinity of the probe coil [5–7]. But, since it is subject to saturation, investigators replaced the circular coil by a double D. In an excellent paper, Poulakis and Theodoulidis [8] have simplified the equipment by using a double rectangular printed circuit board coil and a SQUID. They have presented such a system, and given expanded analysis which is reported in [9].

L. Bettaieb • H. Kokabi (✉) • M. Poloujadoff
Université Pierre et Marie Curie (UPMC), Laboratoire d'Électronique et Électromagnétisme (L2E), 04, Place Jussieu 75252, Paris Cedex 05, France
e-mail: hamid.kokabi@upmc.fr
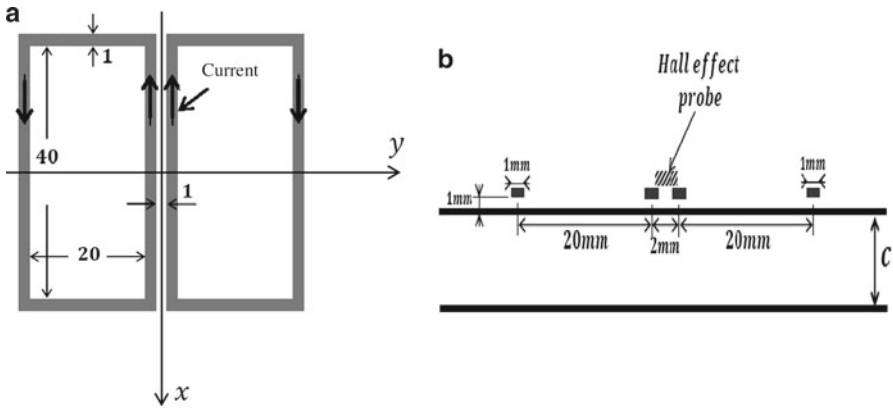
Fig. 1 (**a**) Top view of the rectangular double printed coil with arrows shown the current direction; (**b**) Side view of this coil above an aluminum plate
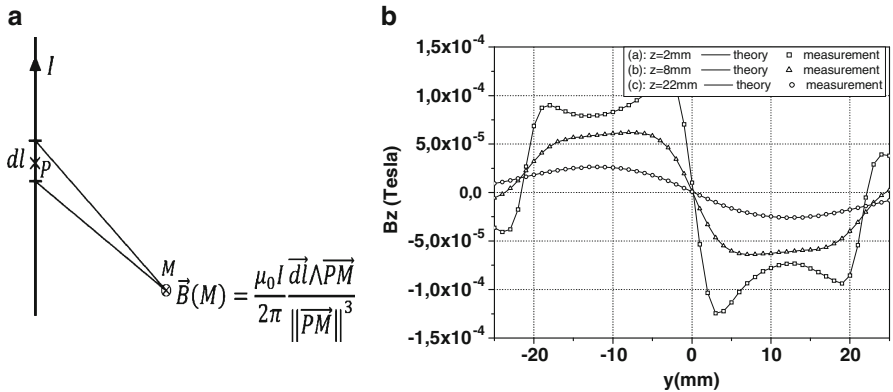
Fig. 2 (**a**) Differential element for application of Biot and Savart law; (**b**) Magnetic field evaluation and measurement for the excitation coil in air for different values of altitude z

In what follows, we present an experimental set up including a double rectangular coil where the SQUID is replaced by a Hall probe which is less sensitive, but may be installed very close to the area to be examined. And we give a simplified analytical model which is simpler than the above quoted one, without loss of accuracy.

Analysis of the Coil Field

The set up is described in Fig. 1. In Fig. 1a, a double rectangular coil printed circuit is shown. In Fig. 1b, we show a conducting plate of thickness c, and the printed circuit above it; a Hall probe is attached as shown.

We first analyze the electromagnetic field created, in free space, by a current of 1.7A flowing in the double D coil. This may be done by integrating the Biot and Savart formula (Fig. 2a) at a point M, where P is varied along the two rectangles. As for M, for the purpose of this paper, it will be varied in the plane normal to (Fig. 2b) and including Oy. We considered that, if ($\frac{L}{l} \geq 2$), it is enough to evaluate the field as if L was infinite (in [10], the authors make an analogous remark but adopt $\frac{L}{l} \geq 4$).

Therefore, the calculation of the coil field is reduced to a fourfold application of the Biot and Savart law for infinitely long conductors [11].

Those approximations have been carefully checked. In Fig. 2b, the value of the normal component of the double rectangular coil field, is described for three values (2, 8, 22mm) of the vertical distance from the double rectangular plane (current intensity being 7.7 A). This field is also measured with a Hall sensor. There is no significant difference between experimental and theoretical values.

Analysis of the Currents Induced in a Plate and of the B_z Field

Flawless plate

Assume now that the plate in Fig. 1b has a resistivity equal to 5.82 * 10^{-8} $\Omega.m$ (Aluminum AG3 at 20°C); its dimensions in the directions Ox, Oy, Oz are 110, 100, and 5mm respectively. The current in the double rectangular coil is 1.7 A (as above) and its frequency is 180Hz. The corresponding skin depth is 9.1mm, much larger than the plate thickness.

Clearly, this means that the magnetic field of the currents induced in the plate is totally negligible in comparison to the exciting field. Therefore, the plate can be viewed as shown in Fig. 3.

The vector potential is parallel to Ox, and its origin may be chosen arbitrarily. If we take this origin inside the plate, just below the geometrical center of the double rectangular coil, the *emf*'s shown in Fig. 3 will be clearly defined. Indeed, in Fig. 4, the plate is divided into $M \times N$ small elements of resistance R_{ij}, easy to evaluate. Let us call V the potential difference between the two sides of the plate An *emf* $E_{ij} = -\dfrac{dA_{ij}}{dt}$ is created along element (i, j), Aij being the potential vector created by the double rectangular coil along this element.
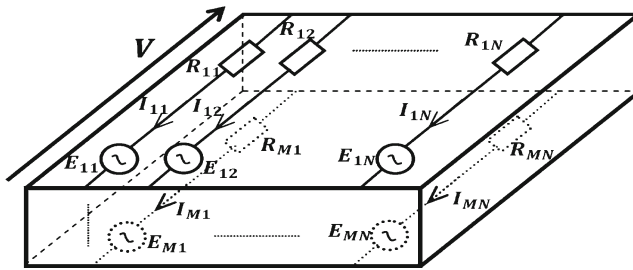
Fig. 3 Model for the evaluation of emf and currents induced inside the flawless conducting plate
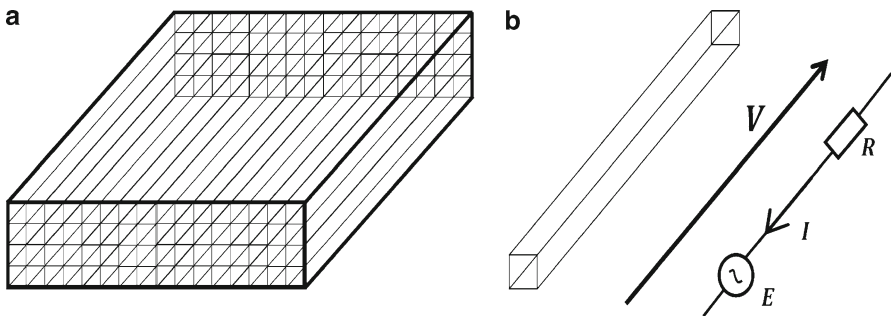
Fig. 4. (**a**) Division of a flawless plate into elements; (**b**) electrical model of one element.

The sum of the currents in the individual conductors must be zero; therefore, if the current in element (i, j) is l_{ij}, we have $M * N + 1$ equations (Eqn. (1)):

$$\begin{cases} E_{ij} - R_{ij} * I_{ij} = V \\ \qquad \Omega \\ \sum_{i,j} I_{ij} = 0 \end{cases} \qquad (1)$$

which determine V and the I_{ij}'s.

A plate with a calibrated flaw

Consider now two plates similar to the above one, but with a calibrated crack (Fig. 5). The width of the crack is $w = 1mm$, and the depths are 0.5 and $1mm$ respectively. The induced currents are described as explained in Fig. 5a, b.

The Hall effect probe has been made by "ITRAN, France". Its surface is a few mm^2, its volume is $0.001mm^3$. The white magnetic field noise is: $\dfrac{10pT}{\sqrt{Hz}}$.
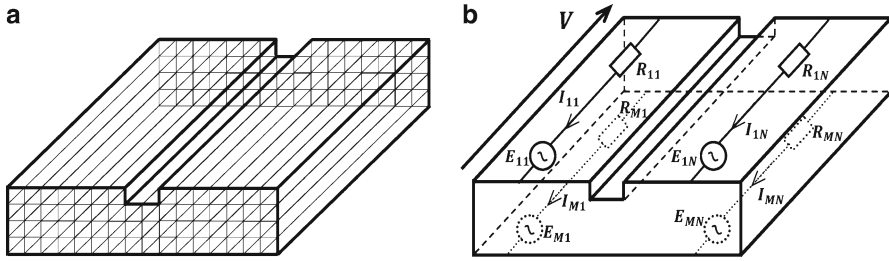
Fig. 5 Same view as in Fig. 4, but there is a calibrated crack
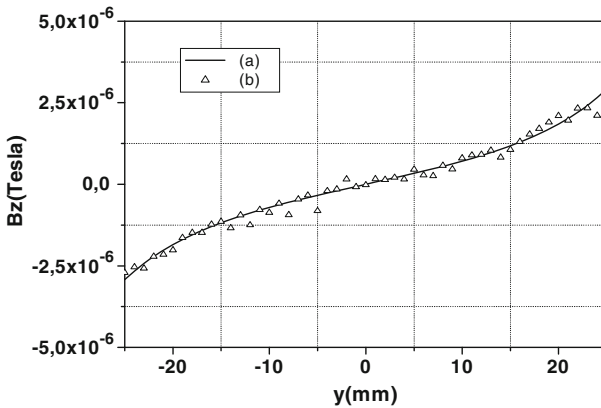
Fig. 6 Comparison of theory (**a**) and measurement (**b**) in the center of a flawless plate for y = 0

A synchronous detection set-up is used, in order to distinguish the very small signal created by the eddy currents from the much larger excitation field. Its sensitivity is $\dfrac{5mV}{\mu T}$ [12], the Hall probe sensitivity is much smaller than the SQUIDsensitivity, but it can operate very near to the center of the double rectangular coil. The active part of a SQUID is usually in a distant of more than 1cm of the same point because of the cooling dewar thickness.

At the center of the flawless plate, the theoretical and experimental values are given in Fig. 6.

When there is a calibrated crack at the center of the plate, the predicted field Bz is described in Fig. 7a for a width $w = 1mm$ and for four different depths (*depth* = 0.5, 1, 2 and 3*mm*). The corresponding measured values are described in Fig. 7b.

Conclusion

In this paper, we describe the development of a simple, but accurate, theoretical treatment of eddy current analysis of planar samples with and without flaws. We have carefully tested the computation technique by eddy current scanning experiments
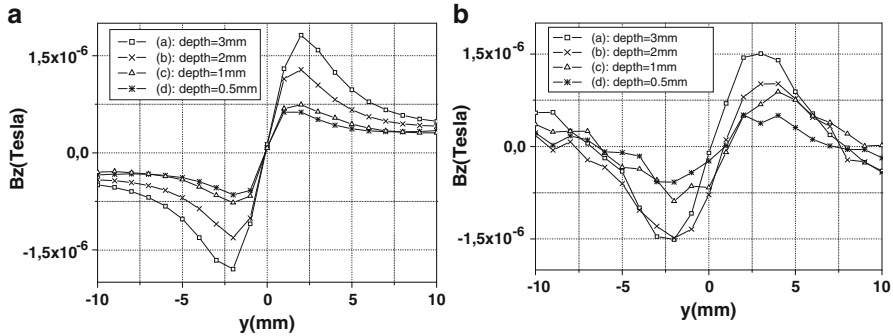
Fig. 7 Comparison of theory (**a**) and measurement (**b**) in the case of a crack in the center, for four different values of the crack depth (w = 1mm)

using a Hall probe. The agreement between experimental and theoretical results is very good, showing that our novel model-based calculations describe well the signals obtained when using a double rectangular excitation coil and a Hall effect probe.

References

[1] C. V. Dodd, and W. E. Deeds, (1969), *Integral solutions to some eddy current problems*, International Journal of Nondestructive Testing, vol. 1, pp. 29–90.

[2] S. M. Nair, and J. H. Rose, (1990), *Electromagnetic induction (eddy currents) in a conducting half-space in the absence of in homogeneities: a new formalism*, Journal of Applied Physics, vol. 68, n. 12, pp. 5995–6009.

[3] T. P. Theodoulidis, and E. E. Kriezis, (2002), *Impedance evaluation of rectangular coils for eddy current testing of planar media*, NDT&E International, vol. 35, pp. 407–414.

[4] J. R. Bowler, and T. P. Theodoulidis, (2006), *Coil impedance variation due to induced current at the edge of a conductive plate*, Journal of physics D: Applied Physics, vol. 39, pp. 2862–2868.

[5] H. Weinstock, and M. Nisenoff, (1985), *Non-destructive evaluation of metallic structures using a SQUID gradiometer*, SQUID '85, Proc. 3rd International Conference on Superconducting Quantum Devices, Hahlbohm H.D. and Lubbig H., Eds., pp. 843–847, de Gruyter, Berlin.

[6] H. Weinstock, SQUID Sensors: fundamentals, fabrications and applications, (1996), *NATO ASI series E: Applied Science*, Kluwer Academic Publishers, Dordrecht.

[7] J. Clarke, and A. I. Braginski, (2006), *The SQUID Handbook: Fundamentals and Technology of SQUIDs and SQUID Systems*, Volume I, Wiley-VCH Verlag GmbH&Co, KGaA, Weinheim.

[8] Poulakis, T. P. Theodoulidis, http://www.ndt.net/article/hsndt2007/files/Poulakis_Theodoulidis.pdf.

[9] J. R. Bowler and T. Theodoulidis, (2006), *Coil impedance variation due to induced current at the edge of a conductive plate*, Journal of Physics D: Applied Physics, vol. 39, pp. 2862–2868.

[10] M. Ya. Antimirov, A. A. Kolyshkin, and R. Vaillancourt, (1994), *Application of a perturbation to the solution of eddy current testing problems*, IEEE Transactions on Magnetics, vol. 30, n. 3, pp. 1247–1252.

[11] J. T. Conway, (2001), *Exact solutions for the magnetic fields of axisymmetric solenoids and current distributions*, IEEE Transactions on Magnetics, vol. 37, n. 4. pp. 2977–2988.

[12] P. Leroy, C. Coillot, V. Mosser, A. Roux and G. Chanteur, (2007), *Use of magnetic concentrator to highly improve the sensitivity of Hall effect sensors*, Sensor Letters, vol. 5, n. 1, pp. 162–166.

A Study of Microcracks and Delaminations in Composite Laminates

D.K. Hsu, V. Dayal, M. Gerken, A. Subramanian, K-H. Im and D.J. Barnard

Abstract With the rapid increase of composite usage on aircraft primary structures, the damage of composite laminate and its nondestructive testing are of high interest to the aerospace industry. Composite laminates, typically without reinforcement in the out-of-plane direction, are prone to impact damage. While the characteristics and the NDT of impact-induced delaminations are well known, the precursor to failure has not attracted equal attention. In this paper, we report an investigation of microcracks and delaminations in carbon composite and glass composite laminates fabricated from unidirectional and woven prepregs. Microcracks were induced by low energy impact and by thermal cycling to cryogenic temperature. The density, distribution and orientation of the microcracks caused by impact were mapped out in detail by photomicrographs. Specimens containing microcracks were then fatigued to observe the initiation and development of delaminations. With before-and-after micrographs, the changes of individual microcracks were followed and documented. The delaminations grown from microcracks in a woven glass laminate during fatigue were found to be localized, short, and tight. These "micro-delaminations" are characteristically different from the "macro-delaminations" caused by impact energy above the delamination threshold. Unlike macro-delaminations, the ultrasonic detection of micro-delamination zone has proven more challenging.

Keywords Composites • Delamination • Fatigue • Impact • Microcracks • Photomicrographs • Thermal cycling

D.K. Hsu (✉) • V. Dayal • M. Gerken • A. Subramanian • D.J. Barnard
Center for Nondestructive Evaluation, Iowa State University, Ames, Iowa, 50011, USA
e-mail: dkhsu@iastate.edu

K.-H. Im
Department of Mechanical & Automotive Engineering, Woosuk University, 490 Hujung-ri
Samrae-up Wanju-kun Jeonbuk 565-701, Korea

Introduction

The behavior of impact-induced delaminations in composite solid laminates and their nondestructive detection are well documented in the literatures. Their morphology has been modeled and experimentally verified [1,2] and their presence can be detected and imaged with ultrasonic scan [3]. The emphasis of this work is on the precursor to delamination failure, generally considered the microcrcaks of the resin matrix. The goal is to study the change of the damage morphology as the impact energy increases and exceeds the threshold for delamination. In addition, samples containing microcracks are also subjected to fatigue test to observe the evolution of the damage and the initiation of delaminations.

Experimentally, microcracks were produced in two different ways. A zone of matrix microcracking was induced by a low energy impact on a composite solid laminate. The damage zone was sectioned through the center and the edge was polished to reveal the microcracks. The sample, with one polished edge, was then fatigued to observe the changes before it failed. Microcracks were also produced by cycling the sample in and out of a cryogenic fluid (liquid nitrogen). Similarly the microcracked sample was also cut, polished, micrographed, and then fatigue tested to failure. Ultrasonic tests were carried out over the impact damage zone at different stage of the microcracking and delamination.

Results in Woven GFRP Laminate

The glass composite sample used in the experiment was a laminate of 24 woven plies. The specimen was 5.67 mm thick. The impact damage was induced by dropping a weight of 3.42 Kg with a 50 mm diameter tup from various heights. The drop tests were carried out on an Instron Dynatup 8200 impact tester, with the specimen placed on the platform over a 76mm (3") diameter hole. The threshold incident energy (mgh) for producing delamination in the specimen was approximately 11 Joules. Impacts were made at 9, 10, 11, 12, and 16 Joules and the specimen was sectioned, polished, and micrographed to document the morphology, density, and spatial distribution of the microcracks.

Microcrack density and spatial distribution

The spatial distribution of the crack density produced by impact energy of 9, 10, and 11J is shown in Fig. 1, where the numbers in the squares represent the number of cracks per square millimeter and each square in the figure was 1 mm x 1 mm. The results showed that most of the cracks were located near the back surface and slightly away from the impact point.

Number of Microcracks in 9J Sample

```
0 0 0 0 0 0 0 0 0 0 0 0 0 0 0  0 0  0 0 0 0 0  0 0 0 0 0 0 0 0 0 0 0 0 0 0
0 0 0 0 0 0 0 0 0 0 0 0 0 0 0  0 0  0 0 0 0 0  0 0 0 0 0 0 0 0 0 0 0 0 0 0
0 0 0 0 0 0 0 0 0 0 0 0 0 0 1  6 1  3 2 4 2 0  0 0 0 0 0 0 0 0 0 0 0 0 0 0
0 0 0 0 0 0 0 0 1 3 6 7 8 13 6 8 8  5 8 10 9 6 4 2 1 2 0 0 0 0 0 0 0 0 0 0
0 0 0 1 1 3 6 4 7 7 6 10 7 8 10 10 11 13 12 9 9 9 6 7 7 4 4 3 3 1 0 0 0 0 0
```
*each square represents 1 mm^2

Number of Microcracks in 10J Sample

```
0 0 0 0 0 0 0 0 0 0 0 0 0 0 0 0 0 0 0 0 0 0 0 0 0 0 0 0 0 0 0 0 0 0 0
0 0 0 0 0 0 0 0 0 0 0 0 0 0 0 0 0 0 0 0 0 0 0 0 0 0 0 0 0 0 0 0 0 0 0
0 0 0 0 0 0 0 0 0 0 0 0 2 4 3 2 0 0 0 0 3 5 2 0 1 0 0 0 0 0 0 0 0 0 0
0 0 0 0 0 0 0 0 0 1 2 8 7 9 8 6 6 5 5 3 5 6 7 6 5 4 1 0 0 0 0 0 0 0 0
0 0 0 0 0 2 2 2 5 5 4 7 4 4 6 6 5 6 8 6 7 5 5 6 9 5 5 2 3 3 3 1 1 0 0
```
*each square represents 1 mm^2

Number of Microcracks in 11J Sample

```
0 0 0 0 0 0 0 0 0 0 0 0 0 0 0 0 0 0 0 0 0 0 0 0 0 0 0 0 0 0 0 0 0 0 0
0 0 0 0 0 0 0 0 0 0 0 0 0 0 0 0 0 0 0 0 0 0 0 0 0 0 0 0 0 0 0 0 0 0 0
0 0 0 0 0 0 0 0 4 3 2 9 5 1 0 0 1 2 3 5 3 1 0 0 0 0 0 0 0 0 0 0 0 0 0
0 0 0 0 0 0 1 2 6 5 14 11 10 8 9 11 8 7 7 9 14 10 7 4 4 3 1 1 0 0 0 0 0 0 0
0 0 1 2 1 1 3 6 8 7 6 10 9 8 9 8 8 6 9 5 8 6 4 4 5 8 3 4 3 4 3 0 1 0 0
```
*each square represents 1 mm^2

Fig. 1 Spatial distribution of microcrack density produced by impact energies of 9, 10, and 11 Joules

Microcrack morphology

The microcracks produced by impact were generally tilted. Those located to the left of the impact point tilted to the right (toward the impact point) and those located to the right of the impact point tilted to the left. This behavior was also observed in impact damage above the delamination threshold where both delaminations and microcracks were present. Figure 2 shows the tilting of the microcracks in an 11J impact site.

Fatigue test of specimen with microcracks

The specimens containing microcracks induced by low energy impact were fatigued to study the evolution and development of the damage. During the fatigue test, many of the microcracks were found to grow and continue in the horizontal direction to produce "micro-delaminations". The fatigue was done using a short beam shear test fixture on a MTS machine. Figure 3 shows the comparison of a small region of a 10 Joule impact zone before and after fatigue. (The printed resolution does not allow the display of large images.) The microcracks in the two images were identical, except that some short and tight delaminations appeared after 1000 cycles of fatigue. These "micro" delaminations were much tighter and shorter than the interlaminar "macro"

Fig. 2 Microcracks in woven GFRP produced by an impact with 10 Joules of incident energy. Optical micrographs show that the microcracks (faint short fine lines) tilt toward the impact point

Fig. 3 Microcracks develop into short, tight delaminations after fatigue

delaminations caused by high energy impact. The former attenuates an ultrasonic beam only slightly, whereas the latter can efficiently block an ultrasonic beam. In a woven composite, many of the delaminations between fiber tows remain localized since their propagation became thwarted by other fiber tows. However, when the fatigue test of the sample containing the micro-delaminations continued to a higher load, the sample eventually failed after producing numerous macro-delaminations at the ply interfaces. In a laminate fabricated with unidirectional prepregs, the growth of inter-laminar delaminations during fatigue tended to propagate unimpeded.

Results in Unidirectional CFRP Laminates

In the study of carbon composite laminates, two specimens were used. A 24-ply $[0/90]_{12}$ layup was impacted at different energy to determine the delamination threshold. Another laminate with a layup of $[0_4/90_4]_s$ was cycled between room temperature and liquid nitrogen temperature to produce microcracks. The thermally cycled specimen was cut, polished, and micrographed to record the microcracks. The specimens with one polished edge were then fatigued to observe the development of the damage.

Fig. 4 Time of flight immersion C-scan image of an impact damage with almost no delamination (left, at 17 Joule) and one with extensive delamination (right, at 18.5 Joule)
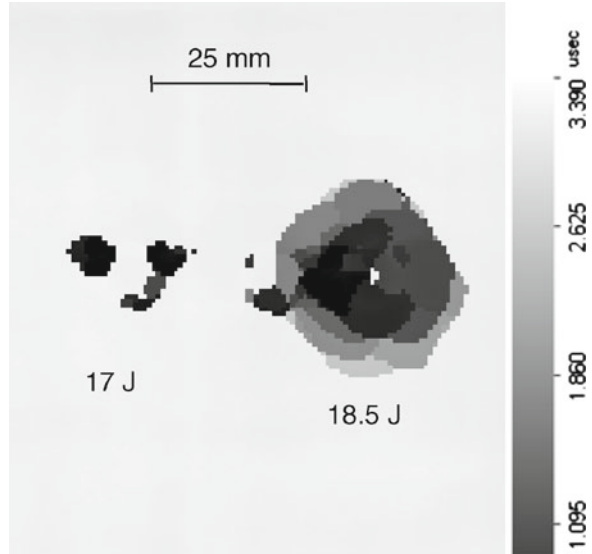
Delamination threshold in CFRP laminate

Using the same Instron impact tester, the onset of delamination of the 24-ply $[0/90]_{12}$ laminate occurred at approximately 18.5 Joules. The specimen was impacted at 15, 17, 18, 18.5, 19, and 20 Joules of incident energy and the damages were examined with contact mode ultrasonic testing and with immersion C-scan. At the energy corresponding to the onset of delamination, the changes were quite distinct. Below this energy, the damage zone was small (10 mm or less) and their effect on an ultrasonic beam was quite minimal. The back wall echo amplitude was attenuated by approximately 10%. Above the threshold energy, the diameter of the damage zone became typically 25 mm or larger and the delaminations completely blocked the back wall echo. Figure 4 shows the time-of-flight, 5 MHz pulse-echo scan image of damage below the delamination threshold (17 Joule) and damage above the threshold (18.5 Joule).

Thermally induced microcracks and fatigue test results

The 16-ply, $[0_4/90_4]_s$ CFRP laminate fabricated with unidirectional prepregs was cut into four 25mm x 140 mm strips and thermally cycled to liquid nitrogen temperature. Three of the samples produced less than 10 microcracks while one sample produced more than 50 cracks. This was consistent with the reported high variability of thermally induced cracking of CFRP [4]. On a polished edge showing the 0-degree plies on the outside, the cracks occurred in the 90-degree plies and went through the entire thickness of the stack.
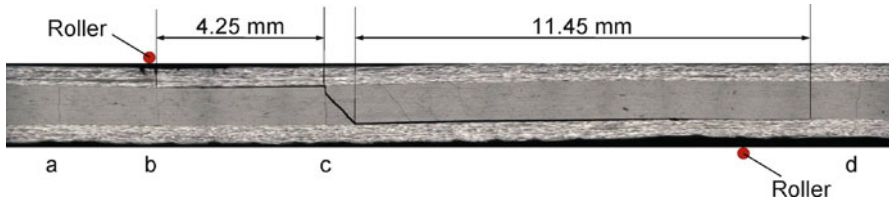
Fig. 5 Fatigue failure of a region of $[0_4/90_4]_s$ CFRP containing thermally induced microcracks (a, b, c, d). Left roller for three-point bend test is off the figure

When the samples with the thermally induced cracks were fatigue tested, they all failed catastrophically without observable precursors. Micrographs of the polished edge showed that the failure usually began under the center roller of the three-point bending test fixture as a delamination at the upper 0/90 ply interface. The delamination propagated in one direction, encountered a crack in the 90-degree plies, followed it for a short distance and then branched off at 45° and continued to propagate at the lower 0/90 interface. Figure 5 shows an example of the fatigue failure of a thermally cycled CFEP sample. This behavior of the cracks is as expected. As the crack approaches the mid-plane, the shear stresses develop and the crack propagates at 45° angle.

The fatigue behavior of the microcracks in CFRP differed greatly from that of the GFRP laminate. There were several reasons for the difference. First, the GFRP laminate consisted of woven plies while the CFRP laminate was fabricated using unidirectional prepregs. The simpler geometry of the unidirectional laminate prevented the formation of the micro-delamination precursors. Once the delamination started propagating along the 0/90 interface, there were no structural features to stop it. Secondly, the microcracks in $[0_4/90_4]_s$ were longer (through all the 90-degree plies) and were not localized like impact-induced microcracks. As this work continues, the pre-delamination impact damage in the unidirectional CFRP will be fatigued to study the evolution of the microcracks.

Conclusions

This study showed that impact damages in composite laminates were characteristically different for energies below and above the threshold for delamination. It further showed that microcracks in a woven laminate, when subjected to fatigue, led to localized micro-delaminations. Interlaminar macro-delaminations are readily detected by ultrasound, but the effect of micro-delaminations on ultrasound was more subtle.

References

[1] Gosse, J. H. and Hause, L. R. (1988), In: *Review of Progress in Quantitative NDE*, Vol. 7B, pp. 1011–1020, Thompson, D. O. and Chimenti, D. E. (Ed.), Plenum Press, New York.
[2] Freeman, S. M. (1984), In: *Composites in Manufacturing 3 Conference*, Vol. EM84-101, pp. 1–13, Society of Manufacturing Engineers, Dearborn, Michigan.
[3] Buynak, C. F. and Moran, T. J. (1987), In: *Review of Progress in Quantitative NDE*, Vol. 7B, pp. 1203–1211, Thompson, D. O. and Chimenti, D. E. (Ed.), Plenum Press, New York.
[4] Adams, D. S., Bowles, D. E., and Herakovich, C. T. (1986), *Journal of Reinforced Plastics and Composites*, Vol. 5, n. 3, pp. 152–169.

Robotic High-Speed 3D Scanner Automatically Scans Spacecraft Heat Shields

J.P. Lavelle and J.W. Steele

Abstract A novel robotic high-speed 3D scanner has been developed to demonstrate the capability of rapidly inspecting the surface of the entire Crew Exploration Vehicle (CEV) heat shield (5 meters in diameter), and its individual components. The scanner is used to measure defects (cracks, holes) in the heat shield and to see if the shield was constructed within acceptable geometrical tolerances from the design. A patented NASA 3D laser sensor is mounted onto a six-axis robot arm. The sensor uses the principle of laser triangulation and projects a laser line onto the target surface while the robot arm moves the sensor over the surface. Because of the sensor's very high 3D point generation capability and the robot arm's precise position control, scanning the entire heat shield at high-resolution takes about one hour rather than the many hours or days required by existing 3D scanning technologies.

Keywords 3D laser scanner • Heat shield • High-speed • Robot • Space craft

Introduction and Background

Successful performance of the large, hemispherical shaped heat shield on NASA's Crew Exploration Vehicle (CEV) Fig. 1 is critical for crew and vehicle survival when re-entering into the earth's atmosphere. Small surface defects such as cracks and holes, as well as out of tolerance errors in the geometrical shape generated during manufacturing can negatively affect heat shield performance. Therefore, detection, measurement, and characterization of heat shield flaws prior to final assembly and flight are critical in remediation of problems.

To meet these critical needs, a large area high-resolution 3D surface scanner has been developed as a proof of concept by NASA Ames engineers to inspect the entire

J.P. Lavelle (✉) • J.W. Steele
NASA Ames Research Center, Moffett Field Ca, USA
e-mail: joseph.p.lavelle@nasa.gov

Fig. 1 CEV crew capsule

five-meter diameter heat shield at high resolution. The scanner uses an Adept 850 Viper Robot to guide a patented NASA 3D laser sensor weighing only. 68 Kg over the heat shield at speeds of up to 150 mm/sec. It is able to achieve rapid scans with x, y, z resolutions down to .127mm because of the 3D sensor's high 3D point generation capability – 640,000 3D surface points/second. The exceptional speed and resolution of the robot scanner will enable the engineers to scan an entire heat shield at high resolution in a couple of hours rather than days.

The 3D laser sensor technology used was originally developed at NASA Ames for the hand-held Mold Impression Laser Tool (MILT) [1] to inspect space shuttle tiles, and to be used on planetary rovers to aid in navigation [2].

Software for controlling the robot, displaying and patching 3D scans in real time, zooming into and measuring defect dimensions, and providing "recession" and other kinds of analysis have been developed. or adapted from the MILT project.

This paper will begin by presenting the overall system architecture and design, then describe the essential hardware components – the robot and 3D laser sensor, followed by the PC control and analysis software, and some examples of robot scanner performance results.

System Architecture and Design

Figure 2 shows the basic components that make up the Robot Scanner and how they interact. The high-speed NASA 3D laser sensor is mounted onto a commercial six-axis robot arm – an Adept technologies Viper 850. The 3D sensor works on the principle of laser triangulation [3] with a video camera and laser line projector, and is connected to a PC via gig-ethernet. The PC initiates the 3D sensor operation through a command sequence, and receives a 3D data packet from the sensor at each camera frame during a scan. So scans consists of the control computer simultaneously commanding the robot to move over a predetermined trajectory at a given
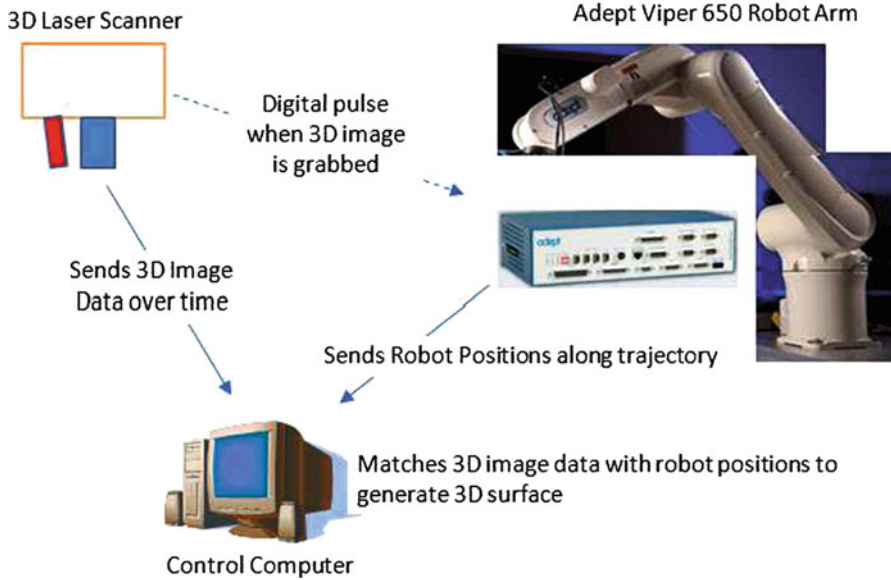
Fig. 2 System architecture

velocity while the 3D sensor begins to take frames at a set rate. During the scan, every third camera frame synch signal (214 Hz) is sent to the robot controller to latch the robot's six-axis (x, y, z, yaw, pitch, and roll) position information at that frame into the controller's memory. Using Adept's robot programming language, the position information is then sent from the robot controller box to the PC where it is matched up with the correct 3D frame data to generate a 3D surface. The custom written C++ main program running from the PC thus initiates the scan through commands to both the 3D sensor and robot, receives both 3D data from the sensor and position information from the robot, and combines 3D data and position information into a 3D image displayed on the PC monitor. Extensive display and data analysis software already written for the 3D sensor for other NASA applications has been changed and adapted for this project. A GUI (Graphical User interface) allows the user to setup both the 3D sensor and robot for a scan, initiate a scan, view the scan results in 3D, and select 3D data analysis functions to perform on the scan taken.

Hardware

High-speed 3D sensor

Components of the sensor shown in Fig. 3 include a high-speed (642 frames/sec) digital camera, a c-mount camera lens, a laser diode line generator (670nm), an electronic 3D processing subsystem, and an Ethernet communication subsystem.
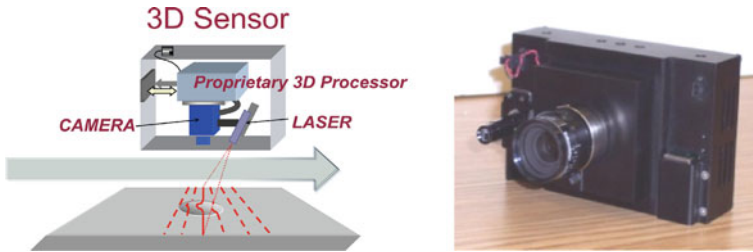
Fig. 3   Left - 3D sensor architecture drawing. Right- Photograph of sensor

As the sensor moves over the target, the camera takes frames (pictures) at constant distance intervals of the laser line reflected off of the surface. The resulting position of the laser line projected onto the sensor array determines the depth of the surface at each point along that cross section of the target. The electronics processing section processes laser line data into 3D data in real time, controls the laser and user interface and data I/O communications between the sensor and PC. During a scan, the processed data is transmitted from the instrument over gig-Ethernet or wireless 802.11g standard to the host PC.

The PC software further processes this data to create and display 3D images with range points, and calculates the depth and volume of the surface automatically.

The robot

The Robot is an Adept technologies Viper s850 model. It was chosen because of its combination of excellent position repeatability (0.030mm), good reach (854mm), the ability to read its six high-accuracy encoders a high rate (214Hz), relatively small size, and low cost. Although the robot cannot reach the five meters required to scan the entire CEV heat shield, it was intended that this system demonstrate a proof of concept for a larger system.

C++ Software

The scanner software consists of three main modules: the API (Application Programming Interface), the GUI (Graphical User Interface) shown in Fig. 4, and the MATLAB library. Our particular API is a collection of custom written classes with functions that greatly facilitate communication between the user interface GUI and the scanner hardware – the 3D sensor and Robot. There are also some data analysis functions that are packaged into a MATLAB library that the GUI also calls as appropriate.

A central function of the software are the 3D triangulation calculations, which use data from the 3D sensor and position data from the robot encoders to determine
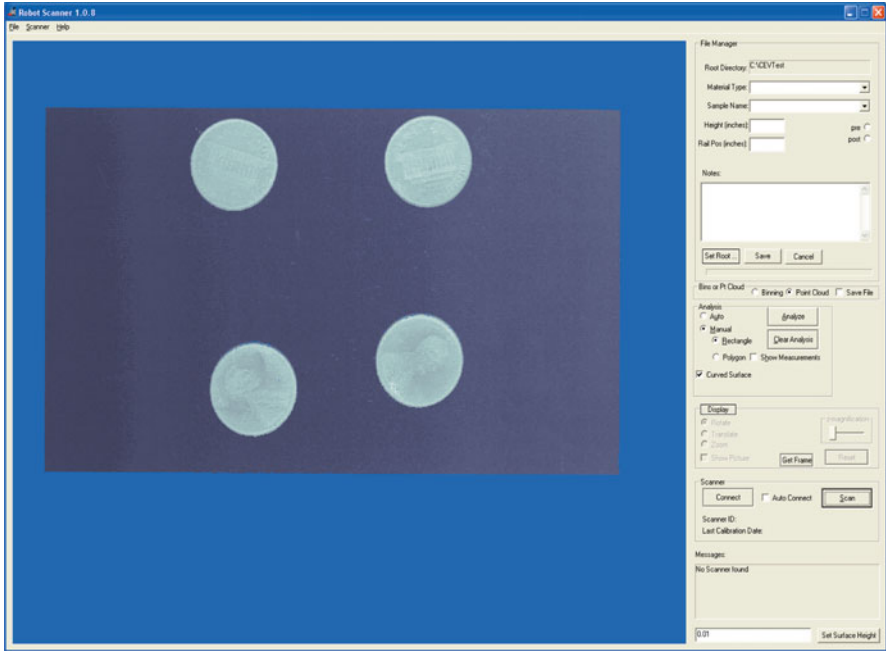
Fig. 4 Robot Scanner GUI

the 3D points of the target. Since the controller sends encoder data only at every third 3D sensor frame, the position data is interpolated for two of every three 3D data points. The triangulated surface point is calculated by applying a simple translation and tool offset for each of x, y, and z coordinate, followed by the appropriate combination of rotation matrices.

Another important software function is defect detection and analysis. A brief description of this function follows. For more detailed information on the principles and methodology of this function please see reference [4]. This function takes an input surface from the triangulated 3D points defined on an evenly spaced domain, and determines where the defects are located based on an input threshold level set by the user. Points below this threshold level are then run through a 5x5 point median filter to soften unwanted noise on the defect surfaces. A morphological operation then creates a binary map that represents each defect perimeter. This defect binary map is then sorted into individual defects by largest area/volume, and they are labeled. Finally, the maximum depth, area, width, and length of the defects are calculated and displayed in a chart with defects labeled on the 3D image.

A GUI submenu allows the user to program the robot path for the scan. Presently, this is limited to linear scans where the robot moves in a straight line over the target. However, multiple passes over the target (up to 4) can be programmed where the 3D sensor angle relative to the target can be changed. In this way targets with odd shaped holes or flaws at different angles to the surface can be accurately imaged and measured.
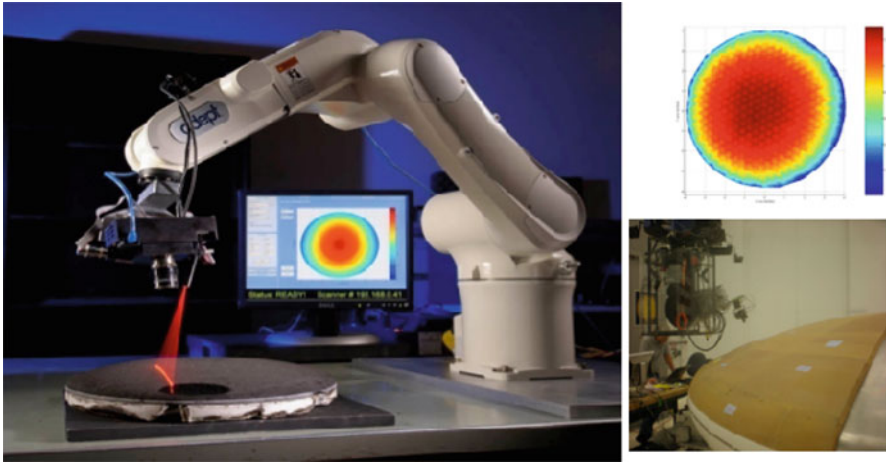
Fig. 5 Left- scanning 18-inch TPS test coupon. Right top- 3D scan results. Right bottom- Scanning five-meter CEV heat shield using KSC robot

The defect measurement software is written in a compiled version of MatLab and can be called from the GUI. Lastly, the software has a calibration function called from the GUI to assist the user in scanner calibration. It must be re-calibrated when changing robot scan height or scan Field of View.

Scan Results and Conclusion

To date only portions of the CEV heat shield have been scanned for test purposes using a large KSC robot at their facility. The Adept Robot Scanner has successfully been used to measure defects and recession in several tested Thermal Protection System (TPS) material samples (called coupons) up to eighteen inches in diameter as shown in Fig. 5. Damage and recession measurements have been taken down to .127mm resolution with robot speeds of 75mm/sec.

References

[1] Lavelle, J., and Schuet, S. (2007), In: *IV Conference Pan-American of END Proceedings*, Aerospace, 2, "A Handheld, Wireless 3D Laser Scanner for Shuttle Tile Inspection".
[2] Bualat, M., and Kuntz, C. (2005), In: *Proceedings of The 8th International Symposium on Artificial Intelligence, Robotics and Automation in Space*, "Scanning Laser Rangefinder for Accurate Arm Placement and Inspection".
[3] Girod, B., Greiner, G., and Niemann, H. (2002), *Principles of 3D Image Analysis and Synthesis*, Kluwer Academic Publishers, Dordrecht.
[4] Lavelle, J., Schuet, S., Khan, Z., Steele, J., and Deuroen, M. (2008), *MILT 3D Laser Scanner Documentation, Revision 2.6*, NASA Ames Research Center Document NASB458893A-MILT.

Inspection of Underwater Metallic Plates by means of Laser Ultrasound

P. Rizzo, E. Pistone, P. Werntges, J. Han and X. Ni

Abstract Guided Ultrasonic Waves (GUWs) are increasingly considered in the nondestructive testing of engineering systems. This paper shows a non-contact laser/immersion transducer system for the detection of damage in submerged structures. A pulsed laser was used to generate stress waves in an aluminium plate immersed in water; a pair of immersion transducers was used to detect the signals. The waveforms were processed using wavelets to extract information about the attenuation of the propagating modes. Damage was simulated by devising a notch and a circle on the face of the plate exposed to the probing system.

Keywords Gabor Wavelet Transform • Guided ultrasonic waves • Structural health monitoring • Submerged structures

Introduction

Many underwater structures are made of thin-walled metallic parts that are exposed to accidental impacts, humid and corrosive environments, or natural extremes. In recent years, the use of guided ultrasonic waves (GUWs) was proven efficient for the nondestructive testing (NDT) of waveguides. The advantage of GUW inspection is the ability to probe long lengths of waveguides, locating cracks and notches from few monitoring points, while providing full coverage of the cross section. Finally, they can travel relatively large distances with little attenuation [1–5]. Few studies presented the use of GUWs for underwater structures. Na and Kundu [6] devised an innovative transducer holder to activate flexural cylindrical waves for damage

P. Rizzo (✉) • E. Pistone • P. Werntges • X. Ni
Department of Civil and Environmental Engineering, University of Pittsburgh, U.S.A.
e-mail: pir3@pitt.edu

J. Han
Department of Civil Engineering, Hainan University, China

detection in underwater pipes. Mijarez et al. [7] developed a waterproof transmitter and a seawater-activated battery package to monitor the tubular cross-beam members of offshore steel structures.

In this paper, the ability to inspect immersed structures by means of laser-induced GUWs is discussed. We propose to exploit the optical transparency of water to induce stress waves in waveguides by means of laser pulses. The effect of water temperature on the signal-to-noise ratio (SNR) is investigated first. Then, the capability to detect damage in an immersed aluminium plate is described.

This study can put the basis for the development of a non-contact NDT system to probe large diameter pipelines that are the backbone of freshwater network, or to inspect underwater structures.

Effect of Water Temperature and Column

To investigate the effect of water on the SNR of the laser-induced stress waves two tests were performed using the setup shown in Fig. 1. A plastic pipe was bonded on the surface of an aluminium block. In the first experiment the pipe was filled with water at ambient temperature (17 °C). The water level was raised from 12.7 mm to 215.9 mm at 12.7 mm increment. For the second experiment the pipe was filled up to 50.4 mm with hot (65 °C) water and measurements were taken until the water reached the ambient temperature. The experiment then was continued by replacing the existing water with cold (6 °C) water. For both experiments, a conventional ultrasonic transducer was attached on the opposite surface of the block such as to detecting the bulk longitudinal and shear waves generated by laser pulses from a Q-switched Nd:YAG pulsed laser operating at 1064 nm.

The maximum amplitude of the time-waveforms were computed and plotted as a function of the water level (Fig. 2a) and water temperature (Fig. 2b). As the water
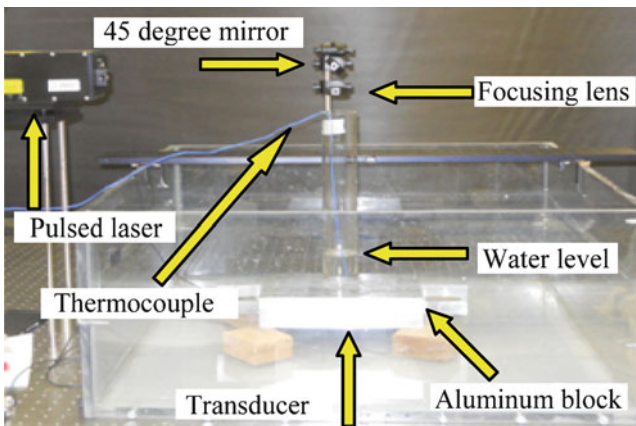
Fig. 1 Effect of water on the SNR ratio of laser-induced waves. Set-up

a

y = 0.1921e$^{-0.711x}$
R^2 = 0.9601

b

y = -3E-05x^2 + 0.0017x + 0.0721
R^2 = 0.3493
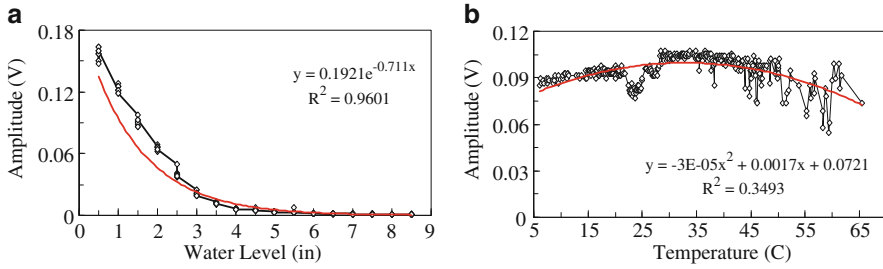
Fig. 2 Effect of the water level and water temperature on the laser-induces bulk longitudinal wave's amplitude

level increases, the maximum amplitude of the laser-induced longitudinal bulk wave decreases exponentially. This is due to light absorption in water. By observing Fig. 2b it seems that the water temperature has little or no effect on the ultrasonic energy transmitted through the bulk material.

Damage Detection

The same laser was used to illuminate the surface of a 1200 x 900 x 1.5875 mm aluminium plate immersed in water. A pair of immersion transducers (Panametrics 10 MHz/0.5in) was used as sensors. Two defects were machined on the plate. The first defect consisted of a rectangular 30 x 1.0 x 1.0 mm notch while the second defect consisted of a 4 mm diameter and 1 mm deep hole. The points on the plate were illuminated by laser pulses. The position of these points with respect to the defects and the position of the immersion transducers are schematized in Fig. 3a, b. The circular defect was aligned along the direction of point 8-sensors' pair. To increase the statistical population of the experimental data, the stress waves at each point were generated five times. A total of 50 measurements were analyzed.

Typical sensed waveforms when the laser beam was directed onto point 1 are shown in Fig. 4a, b and the corresponding scalograms extracted from the Gabor wavelet transform [8–9] are presented in Fig. c, d. Three modes are visible. The fastest mode is the first symmetric leaky Lamb wave S_0. The mode detected at about 57 microsec by transducer 1 and above 100 microsec by transducer 2 is dispersive below 400 kHz (Fig. 2d), slightly dispersive between 500 kHz and 800 kHz, and nondispersive above 800 kHz. This is the first anti-symmetric leaky Lamb wave mode A_0. Finally, the third mode, which has the largest detected amplitude, is dispersive below 600 kHz and nondispersive above 600 kHz. This mode is the quasi-Scholte mode [10].

From the scalograms' peaks amplitude, the energy transmission coefficient spectra were computed using the following equation:

$$T_{1-2}(f)[dB] = 10Log\frac{E_2(f)}{E_1(f)} \tag{1}$$
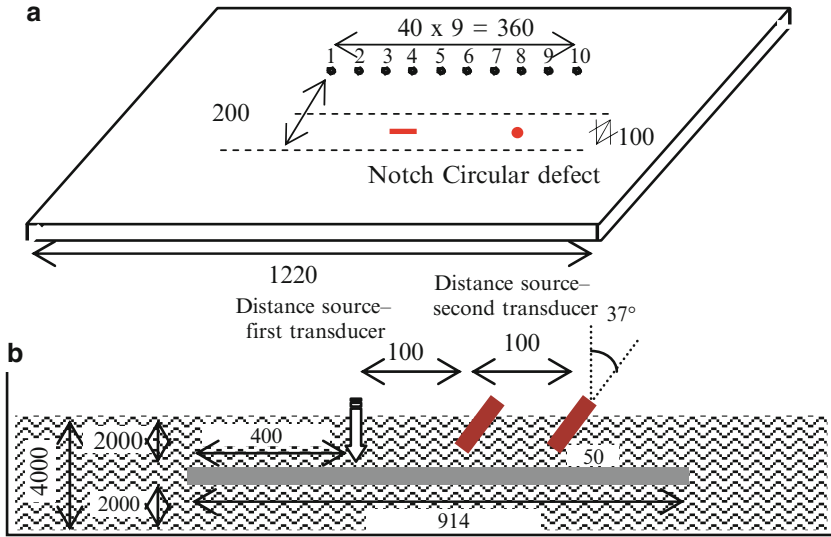
Fig. 3 (**a**) Location of the points illuminated by the laser beam with respect to the position of the defects. (**b**) Schematized side view of the plate. Dimensions in mm
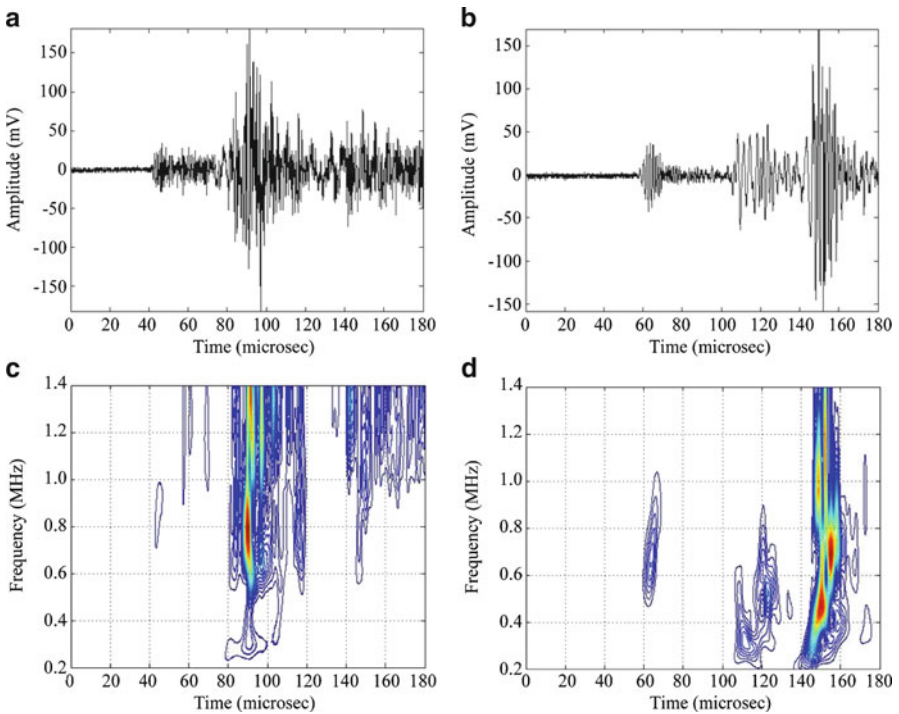
Fig. 4 Laser generated waveform along point 1. (**a**) Time waveform from immersion transducer 1, (**b**) Time waveform from immersion transducer 2. (**c**) GWT scalogram of the signal (**a**). (**d**) GWT scalogram of the signal (**b**)
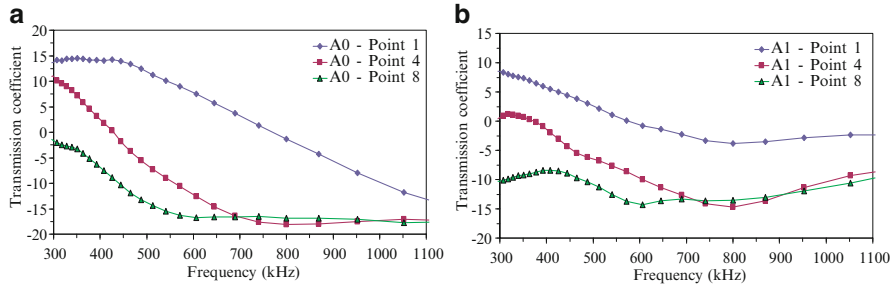
Fig. 5 Transmission coefficient at three scanning points associated with. (**a**) Anti-symmetric A_0 mode. (**b**) q-S mode. The notation A_1 in the legend here indicates the quasi-Scholte mode

where T_{1-2} is the overall transmission coefficient as a function of the frequency f from transducer 1 to transducer 2, and E_2 and E_1 are the value of the scalograms' amplitudes associated with transducer 2 and transducer 1, respectively. Dividing the transmission coefficient by the distance between the two transducers, the linear attenuation in [dB/m] can be obtained.

The transmission coefficients as a function of the propagating frequencies for modes S_0, and q-S when the waves propagated along path 1, 4, and 8 are presented in Fig. 5. Comparisons are made in terms of different path conditions, i.e. the state of damage in the plate. These differences indicate the sensitivity of an NDT strategy aimed at discriminating among the distinct cases based on transmission strength measurements. With the exception of the symmetric mode, a drop in the transmitted energy is observed when the wave propagates along the damaged path. Surprisingly, the circular defect caused larger attenuation than the notch.

By observing Fig. 5, however, it can be seen that differences in transmission strength are not uniform along the frequency spectrum considered. For instance, by looking at the outcomes from the A_0 mode, the frequency bandwidth 500-700 kHz shows a difference in transmission strength in the order of 20 dB. This difference is higher than the 5 dB difference observed in the range 300-350 kHz. When observing the response from the q-S mode a good candidate bandwidth for an ultrasonic inspection aimed at discriminating between damaged and undamaged state is $450 - 700$ kHz, where the transmission differences are in the order of 10 dB. It should also be acknowledged that the differences in the ultrasonic energy transmission between path 1 and path 4 are more uniform in the case of the q-S mode. A more detailed discussion about the results can be found in [11].

Conclusions

This paper represents the experimental phase of a project aimed at developing a new NDE technology for the inspection of immersed metallic structures. We proved that the amount of water interposed between the laser pulse and the specimen inspected

strongly affects the energy of the generated ultrasounds. In fact, we found that for a 1064nm wavelength, the amplitude of the signal quasi-exponentially decreases as the water level increases. Another important outcome is that the proposed methodology is sensitive to the presence of defects. In particular, we devised a notch and a circular hole in a submerged aluminium plate and a pair of immersion transducers was used to detect the signals. We investigated the transmission of the lowest-order, antisymmetric, symmetric leaky Lamb modes and the quasi-Scholte wave. In terms of "overall" transmission coefficients, we found that the observed modes are affected by the presence of defects because a significant drop is present in the frequency spectrum considered.

Future studies will compare the experimental results with theoretical results. First, the times of arrival presented in this paper will be compared to the values obtained from dispersion curves. Second, a numerical model will be implemented in order to validate the effectiveness of the proposed methodology.

References

[1] Achenbach, J.D. (1973), *Wave Propagation in Elastic Solids*, North-Holland, Elsevier, Amsterdam.

[2] Alleyne, D.N. and Cawley, P. (1996), *J. Nondestruct Eval.*, vol. 15, n. 1, p.11.

[3] Rose, J.L. (1999). *Ultrasonic waves in solid media*, Cambridge University Press, London.

[4] Kundu, T. (2004), *Ultrasonic Nondestructive Evaluation: Engineering and Biological Material*, CRC Press.

[5] Rizzo, P. and Lanza di Scalea F. (2007), In: *Progress in Smart Mater. and Structures Research*, Ch.8, NOVA publishers, p. 227.

[6] Na, W.B. and Kundu, T. (2002), *J. Pressure Vessel Technol.*, vol. 124, p. 196.

[7] Mijarez. R., Gaydecki, P. and Burdekin, M. (2007), *Smart Mater. Struct.*, vol. 16, p. 1857.

[8] Kim, H. and Melhem, H. (2004), *Eng. Struct.*, vol. 26, n. 3, p. 347.

[9] Lanza di Scalea, F., Rizzo, P. and Marzani, A., (2004), *J. Acoust Soc. Am.*, vol. 115, n. 1, p. 146.

[10] Cegla, F.B., Cawley, P. and Lowe, M.J.S. (2005), *J. Acoust Soc. Am.*, vol. 117, n. 3, p. 1098.

[11] Rizzo, P., Han, J. and Ni, X. (2010), *J. Intell. Mater. Syst. struct.*, vol. 21, n. 14, p. 1397–1407.

Influence of Water Flow through Pipe Networks for Damage Detection using Guided Waves

R. Ahmad and T. Kundu

Abstract Researchers have been trying to develop techniques for early forecasting of the degradation process in pipe networks. Different Non Destructive Testing Techniques are used for detecting damages in a variety of materials and structures. Guided wave technique is a suitable non-destructive technique which can be used for pipe inspection by generating cylindrical guided waves. In this research, steel pipes are inspected using cylindrical guided waves. The purpose of this paper is to investigate the influence of flowing water through the pipe on the guided wave propagation in the pipe wall. Investigations are also carried out when the pipes are in open air which gives the traction-free boundary condition. It is also investigated whether the direction of the flow influences the propagation of the guided waves. Experimental V(f) curves are extracted from the received signals for defect free and defective pipe specimens and compared to study the effect of water flow on the strength and other characteristics of various guided wave modes.

Keywords Damage detection • Guided waves • NDT • Pipe networks • Ultrasound

Introduction

Early forecasting of the degradation process caused by adverse environmental effects or mechanical damages in pipe network systems can save many catastrophic accidents. Pipes can be severely damaged and develop cracks due to natural forces like strong ground motion caused by earthquakes, underground soil and water pressure or

R. Ahmad (✉)
Department of Civil & Environmental Engineering, University of Connecticut, Storrs, CT 06226
e-mail: rahmad@engr.uconn.edu

T. Kundu
Department of Civil Engineering and Engineering Mechanics, University of Arizona,
Tucson, AZ 85721

degradation to chemical reaction. In the United States there are more than 2.0 million miles of pipelines, transporting water, oil, natural gas, hazardous materials, sewage and other hydrocarbons. According to surveys conducted by the National Safety Board and the Office of Pipeline Safety and United States Department of Transportation (US DOT), over 30 cases of fatalities and over 50 cases of injuries have occurred from 1998 to 2008 in accidents related to pipeline failures [14]. Around 166 million dollars worth of property had been damaged due to these pipeline explosions [14].

Many investigators [3, 13] used guided wave modes for detecting wall thinning defects in cylindrical pipes. Rose and coworkers [11, 12] designed a special probe which can be used both as a transmitter and a receiver during the pipe inspection. Kundu and Maslov [8] successfully used guided waves to investigate the defects in composite materials. They developed a set of ultrasonic non-destructive testing instrumentation and software. Ghosh and Kundu [4, 5] developed a transducer holder mechanism for efficient generation and reception of Lamb waves in large plates. Guo and Kundu [6, 7] designed a new transducer holder mechanism for pipe inspection using cylindrical guided waves. Na *et al.* [9, 10] experimentally generated cylindrical guided waves for detecting delaminations between steel bars and concrete interface. Ahmad and Kundu [1–2] investigated integrity of underground steel pipes using cylindrical guided waves. Ahmad developed a wavelet analysis based technique. Piezo-electric transducers were used for generating cylindrical guided waves in steel pipe walls.

Experiments

The primary objective of this paper is to investigate how cylindrical guided waves can be used effectively to detect defects in steel pipes. Another objective is to find out how the guided waves behave when the pipes are in use i.e. when water flows throgh the pipes. Experimental v(f) (voltage amplitude vs. frequency) curves are analyzed to investigate the effect of flow on the propagating modes. A specimen set, consisting of three steel pipes were fabricated. One pipe was defect-free and the other two had mechanical defects - a gouge and a dent that were artificially fabricated on the pipe. The defect covered a complete (360°) revolution. Table 1 gives all dimensions of the pipes and the defects. Table 2 shows the acoustic properties of steel – the pipe material. Figure 1 shows the schematic experimental setup including the direction of water flow through the pipes.

Table 1 Different types of pipe defects and their dimensions

		Diameter			Damage Dimension	
Type	Pipe Length (mm)	Outer (mm)	Inner (mm)	Thickness (mm)	Depth (mm) (% of thickness)	Width/ Diameter (mm)
Defect Free (Pipe A)	1200	21.4	15.6	2.9	-	-
Gouge (Pipe B)	1200	21.4	15.6	2.9	1.26 (43.4%)	5.92
Dent (Pipe C)	1200	21.4	15.6	2.9	1.41 (48.6%)	5.21

Table 2 Acoustic properties of steel

P-wave speed (km/s)	S-wave speed (km/s)	Density (gm/cc)
5.96	3.26	7.932
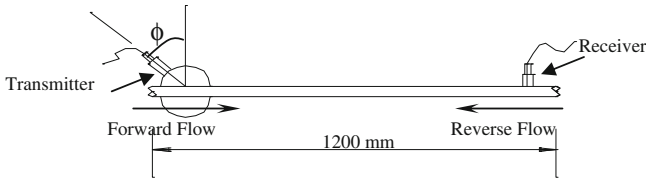
Fig. 1 Experimental setup with flow direction

Results

Guided waves are generated by piezo-electric transducers in a pitch-catch arrangement shown in Fig. 1. The purpose of this investigation is to study the effect of flowing water through the pipes on the propagating guided waves modes. It is known that generation of guided waves in pipes is very sensitive to the incident angle of the transducers. The first challenge is to find the appropriate incident angles for which strong guided waves can be generated. The incident angles of the transmitter were adjusted on trial basis to obtain strong signals. The incident angles at 28° and 57° were found to produce strong signals. V(f) curves were constructed from the received signals. Figure 2a, b show the experimental V(f) curves for incident angles of 57° and 28°, respectively when the pipes were kept in air with traction-free boundary condition. Similarly, Fig. 2c, d show the V(f) curves for incident angles of 57° and 28°, respectively when water flows through the pipes. From Fig. 2a, b it can be observed that the existence of defects affects strongly the wave propagation when the waves are generated with striking angle of 57°. The strength of the signals for the gouge and dent pipes are considerably reduced compared to the defect free pipe. In other words, the existence of defects (gouge and dent) can be easily detected when the incident angle is 57° for pipes with traction-free boundary conditions. For 28° incident angle, the dented pipe produces the strongest signal compared to the defect free and the gouged pipes. Similar V(f) curves were generated when the guided waves were produced with 57° and 28° incident angles as water was flowing through the pipes [Fig. 2c, d]. In general, the signal strengths, when water flows through the pipes, are weaker than the case when water is not flowing for all pipes (defective and defect-free). Figure 3a, b, c show comparisons of signal strengths for the conditions when the pipes are not carrying water and when water flows through it. It is interesting to see that for 28° inclination the defective pipes show stronger signals [Fig. 2b–d].
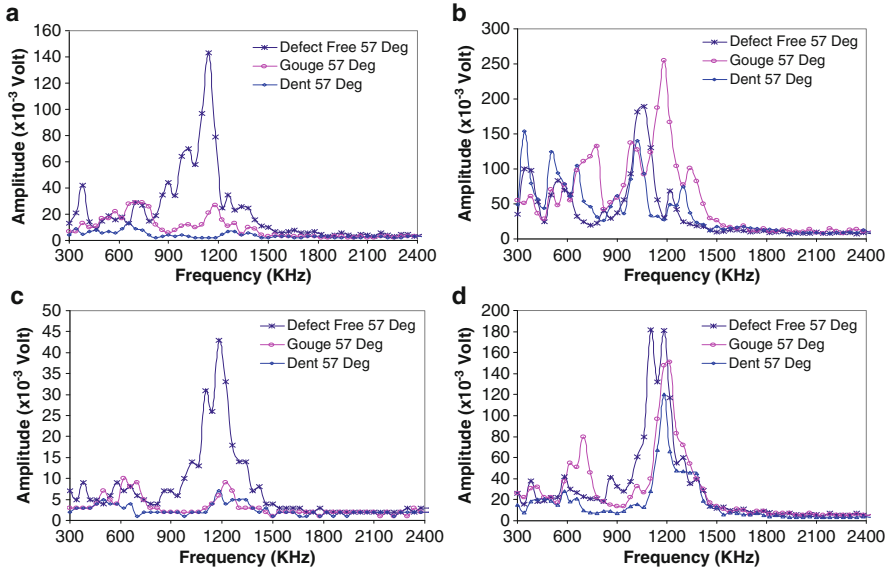
Fig. 2 Experimental V(f) curves for defect-free and defective pipes: (**a**) 57° incident angle (without water flow), (**b**) 28° incident angle (without water flow), (**c**) 57° incident angle (with water flow), (**d**) 28° incident angle (with water flow)
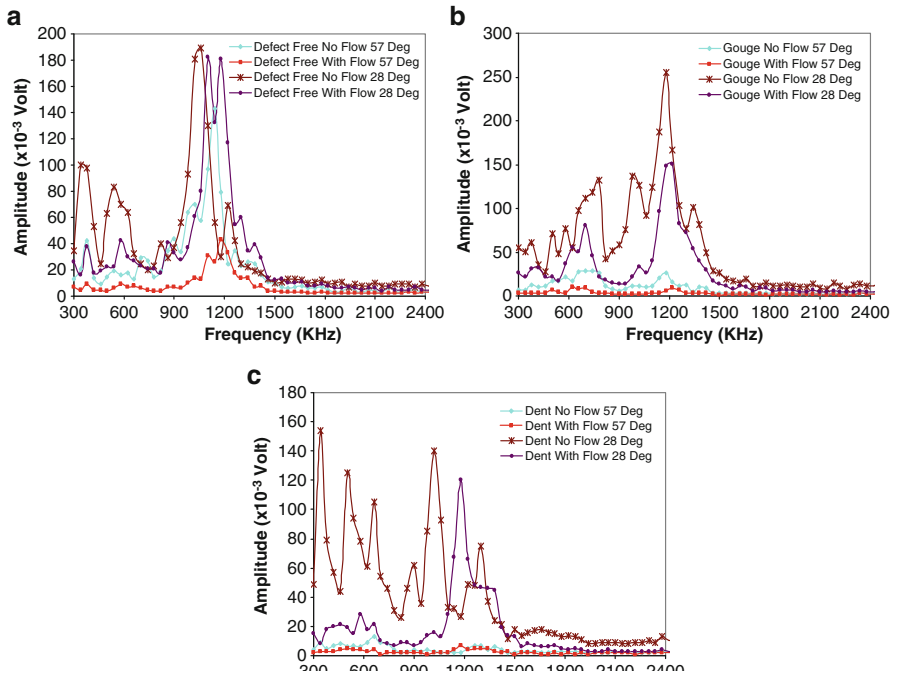
Fig. 3 Comparison of V(f) curves for pipes not carrying water and when water flows through them, (**a**) defect-free, (**b**) gouge, (**c**) dent
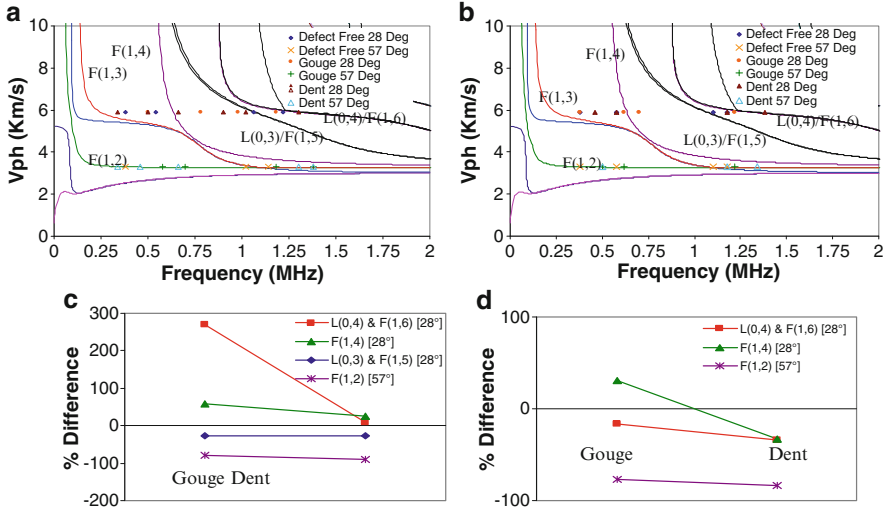
Fig. 4 Phase velocity (V_{ph}) dispersion curves plotted for identifying propagating modes, (**a**) when the pipes are kept empty, (**b**) when water flows through the pipes. Comparison of signal strengths for different propagating modes in defective pipes compared to defect-free pipes, (**c**) when the pipes are kept empty, (**d**) when water flows through the pipes

In order to identify the propagating modes through the defective and defect-free pipes, phase velocities are calculated from the peaks obtained in the V(f) curves (Fig. 2) for different incident angles. Snell's law [$v_{ph} = v_c / Sin(\theta)$] is used to calculate phase velocities, where, v_{ph} is the velocity for the wave modes and v_c is the longitudinal wave speed in the coupling medium between the transducer and the steel pipe (for plexiglass, $v_c = 2.77$ km/s). From Fig. 4a, b it can be seen that F(1,2) is the only possible mode for an incident angle of 57°. For 28° incident angle, F(1,3), F(1,4), L(0,3), L(0,4), F(1,5) and F(1,6) are strong candidates for being as propagating modes in both conditions (with or without water flow). Figure 4c, d show a comparison of strengths of the propagating modes. These figures show the difference of strength in percentile for defective pipes (gouge and dent) compared to the defect-free pipe for both without flow and with flow conditions. It can be observed that for without flow condition, F(1,4), L(0,4) and F(1,6) modes show strong propagation in a gouged pipe compared to a defect-free pipe. When water flows through the pipes, F(1,4) is the strongest mode to propagate in a gouged pipe. Figure 4c, d can help us in the selection of propagating modes for detecting defects under waterflow and no water-flow conditions.

Effect of flow direction on guided wave propagation

In another investigation, a comparison of the signal strengths for different fluid flow directions has been studied. Both forward flow and reverse flow (shown in
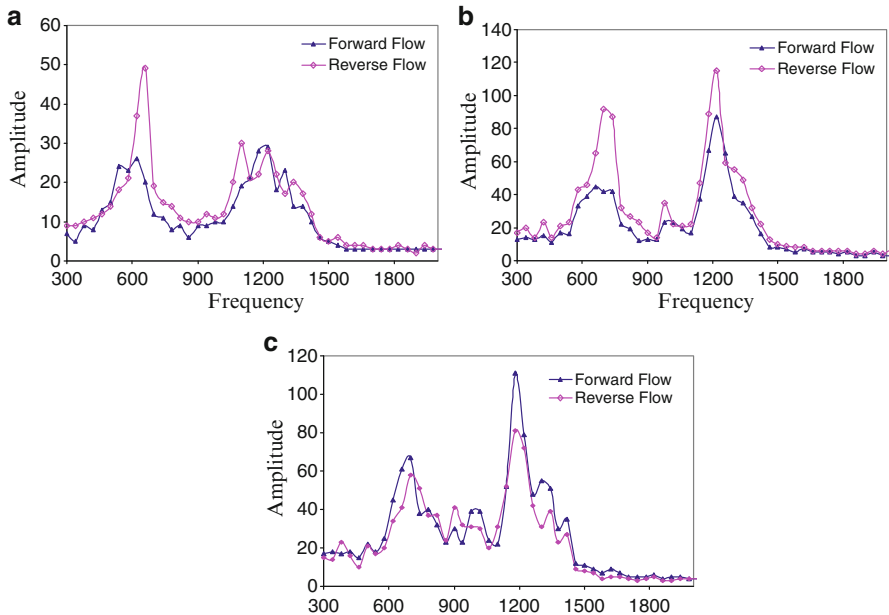
Fig. 5 Comparison of V(f) curves between the forward flow and reverse flow conditions for 38°
incident angle for (**a**) defect-free, (**b**) gouged and (**c**) dented pipes.

Fig. 5) directions are considered. In this case the incident angle was kept at 38°
where considerable deviations of the strength of the V(f) curves can be observed.
It can be seen that for defect free and the gouged pipes, reverse flow gives stronger
signals where as for the dent pipe forward flow gives stronger signal.

Conclusion

This paper investigates the effect of water flow through the pipes on the guided
wave propagation. It is shown how to select and generate an appropriate propagat-
ing guided wave mode which is effective in detecting defects in pipes.

References

[1] Ahmad, R., S. Banerjee and T. Kundu (2009) "Pipe Wall Damage Detection in Buried Pipes
    Using Guided Waves", ASME Journal of Pressure Vessel Technology, Vol. 131(1), pp.
    011501-1 to 8.

[2] Ahmad, R. and Kundu, T. (2007) "Effect of Flow Through Soil Embedded Pipes for Damage Detection using Guided Wave Techniques and Short Time Fourier Transform", Proceedings of the 6 th Int. Workshop on Structural Health Monitoring, Stanford Univ., CA, USA, Sept., 2007, Pub. DEStech Inc., Lancaster, PA, USA, Vol. 2, pp. 1676–1684.

[3] Brook, M., Ngoc, T.D.K. and Eder, J., (1990) "Ultrasonic Inspection of Stem generator Tubing by Chemical Guided Waves", Review of Progress in QNDE, Vol. 9, eds. D.O. Thomson and D.E. Chimenti, Plenum Press, New York, pp. 243–249.

[4] Ghosh, T., and Kundu, T., (1998) "A New Transducer Holder Mechanism For Efficient Generation and Reception of Lamb Modes in Large Plates", Journal of Acoustical Society of America, Vol.104(3), Pt.1, pp.1498–1502.

[5] Ghosh, T., Kundu T. and karpur, P., (1998)" Efficient Use of Lamb Modes for Detecting Defects in Large Plates", Ultrasonics, Vol. 36, pp. 791–801.

[6] Guo, D. and Kundu, T., (2000) "A New Sensor for Pipe Inspection by Lamb Waves", Materials Evaluation, Vol. 58(8), pp. 991–994.

[7] Guo, D. and Kundu, T., (2001) "A New Transducer Holder Mechanism for Pipe Inspection", Journal of the Acoustical Society of America, Vol. 110 (1), pp. 305–309.

[8] Kundu T., Maslov K., Karpur P., Matikas T. E. and Nicolauo P.D., " A Lamb Wave Scanning Approach for the Mapping of Defects in [0/9] Titanium Matrix Composites", Ultrasonics, Vol. 34, 1996, pp. 43–49.

[9] Na, W.B., and Kundu, T. (2002) "Underwater Pipe Inspection using Guided Waves", ASME Journal of Pressure Vessel Technology, Vol. 124(2), pp.196–200.

[10] Na, W.B., Kundu, T. and Ehsani, M.R., (2003) "Lamb Waves for Detecting Delamination Between Steel Bars and Concrete", Journal of Computer Aided Civil and Infrastructure Engineering, Vol. 18, pp. 57–62.

[11] Rose, J.L., Ditri, J.J., Pilarski, A., Rajana K. and Carr, F., (1994) "A Guided Wave Inspection Technique for Nuclear Steam Generator Tubing", NDT & E International, Vol. 27(6), pp. 307–316.

[12] Rose, J.L., Rajana K.M. and Carr, F.T., (1994) "Ultrasonic Guided Wave Inspection Concepts for Steam Generator Tubing", Materials Evaluation, pp. 307–316.

[13] Silk, M.G. and Bainton, K.F., (1979) " The Propagation in Metal Tubing of Ultrasonic Wave Modes Equivalent to Lamb Waves", Ultrasonics, pp.11–19.

[14] Title: Pipeline Accident Brief: Explosion, release, and ignition of natural gas, Rancho Cordova, California, December 24, 2008, NTSB Report Number: PAB-10-01, adopted on 5/18/2010.

Monitoring Hydrogen Release from 4140 Steel Using the L_{CR} Ultrasonic Technique

D.E. Bray and R.B. Griffin

Abstract Hydrogen build-up and release in steel microstructure is of considerable interest in studying the mechanical performance of the material. L_{CR} ultrasonic waves are a potential research tool that will enable the nondestructive evaluation of this reversible hydrogen buildup since their speed is affected by stress and their travel path is through affected layer just below the surface. The present study used three blocks of 4140 steel cut from a longer sample. Frequency spectrum data also were collected. The assumed model was of hydrogen occupying the vacancies in the steel block during the high temperature high-pressure period in the autoclave, and then being purged upon removal as the block contracted, creating a residual tensile stress in the surface area of the block. As the hydrogen is purged, the tensile stress should decrease. The L_{CR} results confirmed this trend, although it was more strongly seen for the 11.7 MPa (1691 psia) block. Photomicrographs confirmed no cracks in the surfaces, although there was considerable decarburization. Frequency analysis showed that the decarburization did affect the frequency spectrum but did not affect the L_{CR} wave speed.

Keywords Frequency spectrum • Hydrogen release • Photomicrographs • Steel • Ultrasound

Overview of Hydrogen Attack and Detection

The phenomenon of hydrogen induced cracking in steel components has been a serious problem in the chemical, chemical processing, hydrogen and transportation industries for a number of years. Reversible hydrogen build-up describes the initial

D.E. Bray (✉)
Don E. Bray, Inc. P. O. Box 10315, College Station, Texas 77842, USA
e-mail: debray1@brayengr.com

R.B. Griffin
Texas A&M University – Qatar Mechanical Engineering Program Doha, Qatar

Fig. 1 Schematic for L_{CR} wave
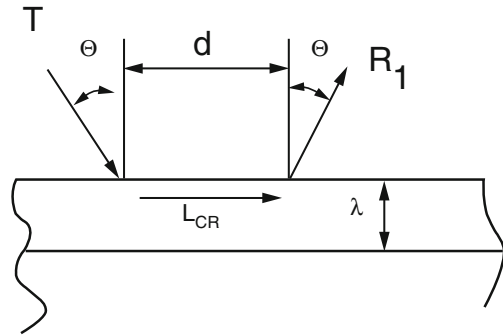
intrusion of hydrogen in the atomic structure of the metal, before any permanent distortion or cracking. This build-up increases the tensile stresses in the metal, which, unabated, leads to the onset of cracking, the effects of which cannot be reversed. Detection of hydrogen attack in this early stage could reduce failures by identifying the affected components, enabling the removal of the hydrogen and allowing the components to be returned to service. Smith et al. describes an application of an optical based electronic sensor for analyzing the hydrogen content in steels [1].

Imanaka and Suetsugu [2] studied hydrogen movement in plain carbon steel using cylindrical samples that were normalized and tempered and placed in an autoclave at temperatures 500 and 550 °C and at pressures from 19.6 MPa to 29 MPa. Application of these results would be difficult since a through transmission path often is not possible in most structures.

Principles of L_{cr} Ultrasonic Technique

The L_{CR} technique as described by Bray [3] releases a longitudinal wave travelling just beneath the surface, as shown in Fig. 1. An incident longitudinal wave is launched at transmitter T to excite the L_{CR} wave. The wave is launched at just past the first critical angle (Θ), calculated according to Snell's Law; and received at (R_1). Stress change may be measured by L_{CR} velocity change in this upper layer of the material. This layer is approximately equal to one wavelength (λ) where $\lambda = C/f$ with C = wave speed (5900 m/s) and f = frequency (5 MHz). Wavelength here is typically 1.2 mm.

The L_{CR} technique is ideally suited for research in hydrogen movement, either into or out of a material, since it investigates only the surface layer and the depth of interrogation may be changed with frequency choice.

Test Procedure

Blocks 1, 2 and 3 shown in Fig. 2 were cut from a long 4140 steel bar, 25 mm thick, and 75 mm wide. They were run separately in the autoclave. Two of the blocks were subjected to hydrogen environment (48 hours at 454 °C (850 °F) and 11.7 and 14.2 MPa
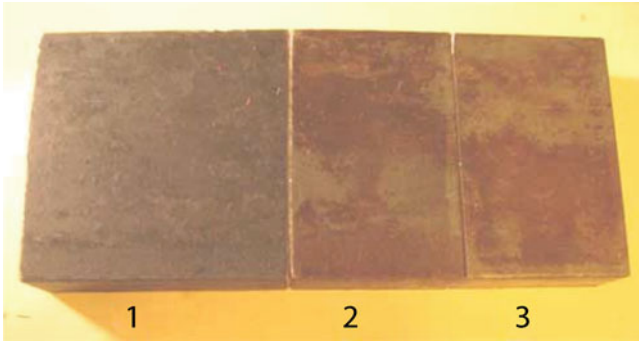
Fig. 2 Test blocks 1, 2 and 3, respectively
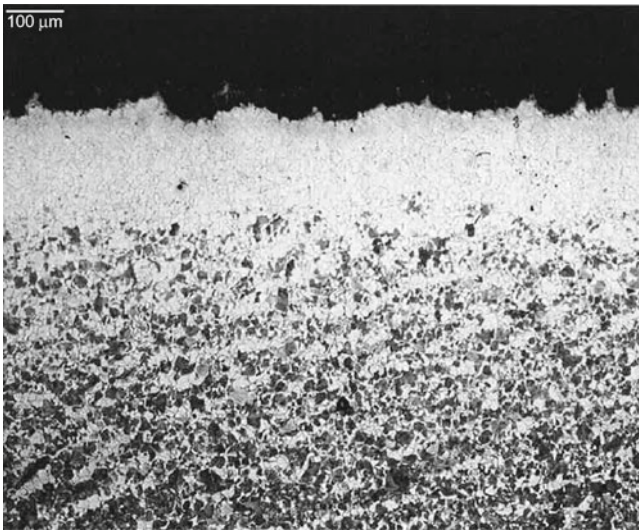
Fig. 3 *Photomicrograph of top side of Block 2*

(1691 and 2061 psia), respectively). The third block was held as a control block. After removal and cooling at 37.8°C (100°F)/hour, the blocks were analyzed using L_{CR} velocity measurements over an 80-day period. Velocities were obtained perpendicular to the rolling direction in order to have a travel path sufficiently long for the probe. Probe frequency was 5 MHz giving a wavelength of approximately 1.2 mm.

The hydrogen build-up in the samples was estimated using Fick's Second Law. Permeability of the hydrogen flowing into the blocks for our test conditions is obtained from Warren [4]. The volume of hydrogen absorption for the test conditions is estimated to be $8.64 (10)^3$ mm^3. With this, the penetration depth of the hydrogen is estimated to be 0.33 mm. While this is less than the wavelength of the L_{CR} wave, it is expected that the stress in the hydrogen buildup will be sufficiently felt.

Figure 3 shows the decarburized surface for the top side of block 2.

Results

Velocity

Velocity results are summarized from Bray and Griffin [5]. L_{CR} travel time data were taken over a two-month period with sample 2 starting 20 days after being removed from the chamber and sample 3 at 14 days after being removed. Velocities shown in Figs. 4 are differences in the velocity observed in the hydrogen-affected block and the control block (No. 1), which was never placed in a hydrogen environment. Data from block number 1 was obtained in each round of testing, assuring that all of the blocks were at the same temperature. Note that an increase in velocity difference indicates a more compressive (less tensile) change in the stress field. Typical experimental error is 0.05% or +/- 3 m/s.

The top of the block shows a definite positive trend with time, consistent with the hydrogen leaking out of the block over time, releasing the internal pressure and causing the surface stresses to become more compressive.

Block 3 velocities were approximately 20 m/s higher than those of Block 2. The trends are similar although the velocity change for block 3 was noticeable less than for block 2. It is notable that there are significant differences in the velocities of the two sides of each block. In all cases, the top side shows higher velocity change with time than the bottom side. This effect is attributed to a texture difference in the two sides, as reported by Pinault [6].
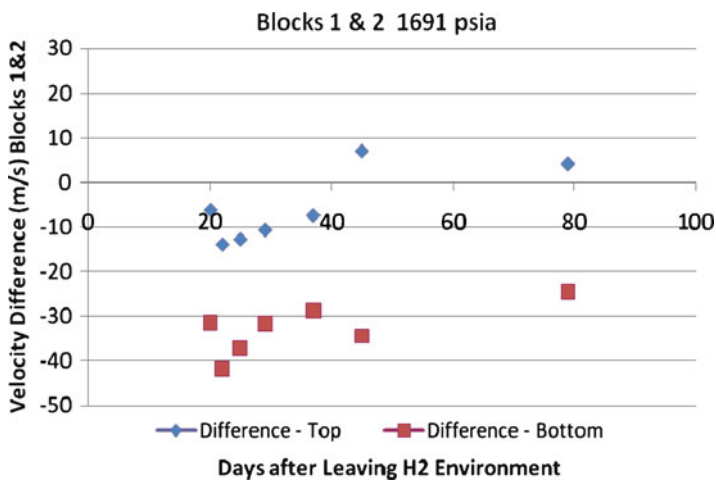
Fig. 4 Velocity difference for blocks 1 and 2
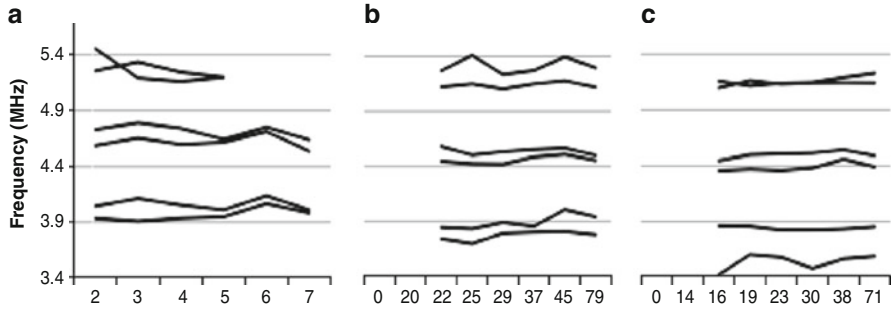
Fig. 5 Frequency spectrums for (**a**) Control Block, (**b**) Block 2 and (**c**) Block 3. Vertical axis in Freq MHz, Top, middle and lower lines - High, Peak and Low half power points, respectively. Top and bottom sides shown for each group. Horizontal axis a – Run number, b and c – Days after removal

Frequency analysis

While photomicrographs of the surfaces of the samples showed no hydrogen induced cracking, the outer 0.2 mm did show significant decarburization. Due to the thin nature of this layer, relative to the wavelength, and the fact that the remaining material is still ferrite, there was felt to be a small likelihood that the decarburization had significant effect on the velocity. Changes in the frequency characteristics of a propagating pulse are often useful in characterizing material structure changes, as might be caused by decarburization in this case. Frequency analyses are shown in Fig. 5a–c.

As expected, very little frequency variation occurs in the three components for the control block. In general, the "after autoclave" frequencies for Blocks 2 and 3 were lower for the control block, although the changes were small. No significant trend of frequency change occurred during the ultrasonic data collection, indicating no change in the properties of the blocks with time. The most significant trend was that the peak frequencies for Blocks 2 and 3 were lower, compared to the control block. Note that data from day 6 is omitted due to an apparent error. Day 7 data fell right in line with the expected trend. The conclusion here indicates a small but noticeable effect due to the different environments.

Conclusions

Information on the movement of hydrogen in and out of 4140 steel has been obtained using the L_{CR} technique. Greater movement in the early data has been observed, as well as differences in the two sides, which is related to texture. Time related effects in frequency due to decarburization were observed. The method may be useful in research studies on hydrogen and steels.

References

[1] Smith, R. D., Benson, D. K., Maroef, L., Olson, D. L., and Wilderman, T. R., (2001). Part 2:Optoelectric diffusible hydrogen sensor," http://files.aws.org/wj/supplement/Smith-Part2-05-01.pdf.

[2] Imanaka, T. and Suetsugu, J., (1995). In *Fitness for Service and Decisions for Petroleum and Chemical Equipment*, PVP-Vol 315, *Proceedings 1995 Joint ASME/JSME Pressure Vessels and Piping Conference*, Honolulu, Hawaii, pp. 507-515. The American Society of Mechanical Engineers, New York.

[3] Bray, D. E., (2001). In *Transactions of the ASME, Journal of Pressure Vessel Technology*, Vol. 124, pp. 326–335.

[4] Bray, Don E. and Richard B. Griffin, (2010). Proceedings of the 5th International Offshore Pipel. Forum IOPF 2010-6001. Houston, Texas, USA http://www.asme-ipti.org/iopf2010/

[5] Warren, D., (1987). In *Materials Performance*, January, pp. 38–48.

[6] Pinault, J. (2010). Private communication to M. Srinivasan.

Section 6
Theoretical Modeling and Simulation Studies as a Basis for NDT

Modelling of Radiographic Inspections

A. Schumm, P. Duvauchelle, V. Kaftandjian, R. Jaenisch, C. Bellon, J. Tabary, F. Mathy and S. Legoupil

Abstract Computer modelling of non-destructive testing methods has come a long way from the beginnings in the mid 90s to today. Radiographic modelling for components with higher wall thicknesses, as they are typical for nuclear applications, must include precise predictions of scattered radiation and its impact in terms of contrast reduction. Dedicated or general purpose Monte Carlo methods with the ability to calculate higher order scattering events are the state of the art for these applications. Aerospace applications, on the other hand, have stronger requirements on the modelling code's capabilities to import complex CAD geometries, and can benefit from faster analytical scatter models, limited to first or second order scattering events. Similar distinctions can be made for the various approaches proposed to accurately model geometrical and film unsharpness, film granularity, film responses, film/foil cartridges and photon noise. This article presents a state-of-the-art review of radiographic modelling from the perspective of two important application domains with very different requirements, nuclear and aerospace.

Keywords Computer modelling • FIlm • Monte-Carlo • Radiography • Selenium

A. Schumm (✉)
Electricité de France R&D, Clamart, France
e-mail: andreas.schumm@edf.fr

P. Duvauchelle • V. Kaftandjian
INSA Lyon, Lyon, France

R. Jaenisch • C. Bellon
BAM, Berlin, Germany

J. Tabary • F. Mathy
CEA-LETI MINATEC, Grenoble, France

S. Legoupil
CEA-LIST, Saclay, France

Introduction

The origins of computer modelling of radiographic inspections date back to the early 90s, with the advent of the first commercial simulation packages capable to take a real part geometry into account, and were at first limited to straight line attenuation. Since this approach neglects scattered radiation, applications were at first limited to rather thin components, as they are common in the aerospace industry.

A Radiographic Modelling Code Blueprint

A typical radiographic modelling code consists of the following components:

– a source model to generate the spectra of x-ray tubes and isotopic sources
– a ray-tracing engine able to determine ray paths in complex geometries
– a material data base containing cross section data
– a straight line attenuation model to determine the contribution of direct radiation, a scatter model, and a post-processor combining both contributions
– a film model converting radiation to an optical density

What follows is a review of the components and a discussion of the state of the art and the respective challenges in simulating the physical effects mentioned. Depending on the application domain, not all effects are equally important.

Source Modelling

The radiographic source is characterized in terms of its spectrum, activity and size/ shape. For isotopic sources, the discrete spectrum is known, and the initial activity at the time of purchase is usually provided. Some modelling codes provide means to determine current activity from radioactive decay data, which is especially important for short-lived sources like Ytterbium.

Determining spectrum and activity for x-ray tubes is considerably more complex. The coupled electrons and photons diffusion equations used to model the X-ray source are often computed using the Monte Carlo method. Instead, for the sake of simplicity and computer time saving, and at the expense of a lack of generality, one can prefer to use semi-empirical models. For instance, in SINDBAD [1] and CIVA [2], different semi-empirical models like the classical Kramer's model as well as the more recent ones described by Birch and Marshall and Tucker have been implemented, accounting for anode angle and composition, the inherent and additional filtration and the exit angle. aRTist [3] includes a model based on the angular dependent bremsstrahlung generation and the self absorption in the target. The target material can be chosen from a wide range of elemental substances and different angular

relations between target, election beam, and X-rays can be considered. The X-ray spectra model has been verified by spectral measurements in the 100 to 300 kV range and showed uncertainties less than 15%.

Geometry Representation

The ray-tracing engine's purpose is to represent the geometry, and to extract ray path and material information for the physical modelling. While nuclear applications with their rather simple geometries do not stress CAD import capabilities, an interface to a CAD system is a necessity in aerospace applications. The radiographic modelling program CIVA incorporates a CAD engine which allows seamless import of a number of commonly used CAD formats. MODERATO [4] targets the simpler nuclear applications with a library of a few parametric geometry models, from which more complex – but still rather limited - models can be constructed without particular CAD knowledge.

Scattered Radiation Models

The traditional approach to scatter modelling considers the physics of radiographic imaging as a particle transport problem, and determines the paths of a large number of photons at their propagation across the inspected part, taking due account of absorption and scattering events. The associated Monte Carlo modelling would in principle allow a complete simulation for scattered and direct radiation, but in practice is too computational expensive to be feasible for realistic configurations. Instead, the Monte-Carlo model is usually used to predict only the scattered radiation's contribution to the final image, for which a reasonable statistics can be obtained for a considerably reduced number of particles. This is possible since the scattered radiation is not sensitive to small thickness variations, allowing a computation with a coarse resolution and/or a smoothing interpolation to remove remaining noise in the image. This approach is not practicable for the direct radiation image, which must take small variations in part thickness into account, and therefore has far stricter requirements on the statistics of the Monte Carlo calculation.

Radiographic modelling codes either rely on an available general purpose Monte Carlo N-Particle solver – like Sindbad using EGS [1], or develop a customized Monte Carlo model, which is usually faster due to a tighter interface to a CAD engine. A particularly advanced example is McRay [5], which also implements pair production for high energy applications.

An alternative to the lengthy Monte Carlo calculations has been proposed by several authors [6][7] in terms of an analytical scatter model for first order scattering or semi-analytical scatter model for higher order scattering. The first order analytical models are of particular interest for aerospace and other applications where

intermediate wall thicknesses do not allow to neglect scattering altogether, but where low order scattered events dominate. Virtual X-Ray Imaging [8] (VXI, developed by INSA-CNDRI) integrates both analytical semi-analytical scatter models.

Computing analytical scattered radiation consists in calculate on the detector the contribution of scattering points inside the tested object, according to the physics laws driven by the interaction process. To perform in practice such a calculation, the algorithm is divided in two parts.

The first and crucial step of the computation is the 3D sampling of the scattering objects. Different sampling methods can be used. The geometry-based methods take into account the shape of the object only and are based on a random uniform sampling or a shape-adaptative sampling for the more sophisticated. These methods allow computing the first order only. The physics-geometric coupled methods use a simplified Monte-Carlo algorithm to provide the scattering points. This method allows computing nth order scattering.

The second step of the calculation consists in calculating the photon number arriving on each pixel of the detector after scattering from each point of the object, i.e. the 3D sampling. This step is done combining a ray-tracing algorithm and physical laws describing these phenomena. From a computing time point of view, comparing deterministic and probabilistic methods, the analytical approach allows reducing the computing duration to a few hours where Monte Carlo codes need several days, under the same conditions of noise.

Finally, one must mention the most straightforward approach of tabulated build-up factors, which are sufficient for parts with constant wall thickness, and can also be applied to parts with known wall thickness profiles by interpolation. A variation of the build-up factor approach has been implemented for central tube penetrations in aRTist. For the standard setup of tangential wall thickness measurements on tubes there is characteristic shape of distribution of scattered radiation, which can be easily parameterised. The necessary parameters have been tabulated in advance for a range of geometrical variations with the help of Monte Carlo calculations.

Combining Scattered and Direct Radiation Results

If direct and scattered radiation contributions to the radiographic image are calculated separately, a combination is necessary. In SINDBAD [9] and CIVA, this step is performed on absorbed energy images, before detector response consideration, and assumes that scattered radiation contributes only to the low frequency details of the image. Thus, the fusion involves a low pass filtering of the scattered radiation to eliminate remaining noise from the calculation with a considerably reduced number of photons, scaling to the requested exposure time, addition of both images, as well as the random generation of a realistic photon noise.

Modelling Specific Features: Image Unsharpness

Radiographic modelling has to deal with two contributions to unsharpness. Geometrical unsharpness is due to the finite size of the source, and as such can easily be taken into account by discretizing the source and adding a number of point source projections. A faster alternative consists in an analytical convolution, where a first image is simulated under the assumption of a point source, and then convolved with a X-ray spot size dependent kernel.

Intrinsical unsharpness in traditional silver film is due to electrons generated in an intensifying screen or in the film layer and propagating a small distance within the film, activating grains along their path. The distance traveled by an electron depends on its energy, which in turn depends on the incident photon's energy which produced the electron during a photoelectric absorption or a compton scattering event. As such, intrinsical unsharpness depends mainly on the source energy, and unsharpness values are tabulated for typical radiographic sources. It is customary to model intrinsical unsharpness by applying a blurring filter to the final image.

Detector Models

The last step in radiographic modelling concerns the conversion of the incoming radiation to an optical density value, or a grey value for digital detector systems. The most straightforward approach consists in providing a calibration curve, obtained experimentally for a given configuration. Moderato attempts to dispense the user of the burden of obtaining the calibration curve by deriving a 2nd order sensitivity curve from the film characterization according to the EN584 standard [10]. In this model, the film response is described by the gradient at two optical density values, and the exposure required to obtain optical density 2 above fog. A fourth parameter describes the film granularity. While this approach is convenient and allows quick comparisons between films, it implies a number of simplifying assumptions, since the characterization is obtained for an X-ray source with 220keV and standard lead screens, and cannot be easily transposed to different sources or different intensifying screen configuration.

As in SINDBAD [9], detector modelling can be envisaged in a more general way with a cascaded linear system model. In this model, the user builds its own detector by cumulating several linear processes such as amplification process, blurring process, noise process for each physical phenomenon involved in the detection. Thus, this model can be used for any kind of detector, especially for flat panel detectors, but it requires either a very good knowledge of the detector or a set of calibration measurements (MTF, electronic noise, etc.).

Conclusion

In order to obtain realistic and thus industrially usable images, particular attention has to be paid to each element of the imaging chain, in particular source size and spectrum, the different photon/matter interactions within the part to calculate scattered radiation, and the detector response, as the internal physics of the detector is often complex and determines the quality of the result.

A parametric modelling, based on the intrinsic characteristics of the detector, is often preferable in terms of processing time than a full featured Monte-Carlo simulation of the detector. Nevertheless, this approach supposes that the experimental or numerical calibrations are available to parameterize the model correctly.

State-of-the-art radiography simulators have a broad application range from training of inspection personnel to feasibility studies and optimization of testing procedures. Finally, it is important to mention the use of modelling in the scope of qualification and reliability prediction of inspection systems. Here the concept of simulation supported Probability of Detection (POD) [11] is based on recent developments in NDT modelling.

References

[1] J. Tabary, P. Hugonnard, F. Mathy, "SINDBAD : a realistic multi-purpose and scalable X-ray simulation tool for NDT applications", International Symposiun on DIR and CT, Lyon, June (2007)

[2] R. Fernandez, A. Schumm, J. Tabary, P. Hugonnard, "Simulation Studies of Radiographic inspection with CIVA", World Conference of Non Destructive Testing, Shanghai, (2008)

[3] G.-R. Jaenisch, C. Bellon, and U. Ewert, "aRTist – Analytical RT Inspection Simulation Tool for Industrial Application." Proceedings of the 17th World Conference on Non-Destructive Testing, Shanghai, China, International Committee on NDT, CDrom paper 64 (2008)

[4] A. Bonin, B. Chalmond, B. Lavayssière, "Monte Carlo simulation of industrial radiography Images and experimental designs", NDT&E International 35 (2002), pp 503–510

[5] G.-R. Jaenisch, C. Bellon, U. Samadurau, M. Zhukovskiy, S. Podoliako, "Monte Carlo Radiographic Model with CAD-based Geometry Description", Insight 48(10) (2006), pp 618–623

[6] F. Inanc, "Scattering and its role in radiography simulations", NDT&E International, Vol. 35(8), (2002), pp 581–593

[7] N. Freud, P. Duvauchelle, S. A. Pistrui-Maximean, J. -M. Létang and D. Babot "Deterministic simulation of first-order scattering in virtual X-ray imaging", NIM B, Vol. 222., (2004), pp 285–300

[8] Ph. Duvauchelle, Nicolas Freud, Valérie Kaftandjian, Daniel Babot, "A computer code to simulate X-ray imaging techniques". Nuclear Instruments and Methods in Physics Research B. (2000). pp 245–258

[9] J. Tabary, A. Glière, R. Guillemaud, P. Hugonnard, F. Mathy, "Combination of high resolution analytically computed uncollided flux images with low resolution Monte Carlo computed scattered flux images", IEEE Transactions on Nuclear Science, Vol. 51(1), pp 212–217, (2004).

[10] A. Schumm, U. Zscherpel, "Using the EN584-1 film characterization in radiographic modeling", International Symposiun on DIR and CT, Lyon, June 2007

[11] http://www.picasso-ndt.eu

Microwave Imaging of Plain and Reinforced Concrete for NDT Using Backpropagation Algorithm

O. Güneş and O. Büyüköztürk

Abstract   The focus of this paper is implementation of backpropagation algorithm as a solution for the inverse source problem for microwave imaging of plain and reinforced concrete targets for nondestructive evaluation (NDE). The data used in imaging was obtained from numerical simulation of microwave scattering by concrete targets using a finite difference-time domain (FD-TD) technique. Electromagnetic (EM) properties of concrete were obtained from previous experimental research. Simulations were performed using a Gaussian pulse wave excitation for dry concrete cylinders with and without a rebar at the center. Images reconstructed using the backpropagation algorithm showed the potential of the method for concrete NDE while drawing attention to its limitations mainly due to the linearizing assumptions in the algorithm's formulation.

Keywords   Concrete • FD-TD • Inversion • Microwave scattering • RC • Simulation

Introduction

Microwave imaging involves reconstruction of the target's representation in terms of its EM properties using the scattered fields either in transmission or reflection mode, obtained by illuminating the object from many directions or along a synthetic aperture. This is generally achieved through appropriate inversion methods which are referred to as inverse scattering methods or identification methods [1–3]. Image reconstruction can be performed using either iterative algorithms or transform-based

O. Güneş (✉)
Civil Engineering Department, Cankaya University, Ankara, Turkey
e-mail: ogunes@cankaya.edu.tr

O. Büyüköztürk
Civil and Env. Engineering Department, Massachusetts Institute of Technology, Cambridge, MA, USA

algorithms [4]. The main shortcoming of iterative algorithms is that they do not consider diffraction which can be defined as the interference effects giving rise to illumination beyond the geometrical shadow [5]. Diffraction becomes important when the dimensions of the inhomogeneities are comparable to the wavelength of the radiation which is generally the case for microwave NDE of concrete. Transform-based methods involve processing of the scattered data partially or completely in the Fourier domain depending on the algorithm. After coherently superposing multi-frequency and/or multidimensional measurement data, the object is reconstructed by an inverse Fourier transform. The advantage of transform-based algorithms is that diffraction effects can be taken into consideration. Possible disadvantages include large computation and memory requirements, difficulty in incorporating a priori information into reconstruction, and the requirement for linearizing approximations [4].

Electromagnetic Properties of Concrete

Application of microwave imaging to concrete structures requires an in depth understanding of the EM properties of concrete and how these properties affect its interaction with the EM waves. In this research, modeling of concrete targets was based on the measured EM properties of concrete by Rhim and Buyukozturk [6].

Dielectric constant and loss factor

The complex permittivity of concrete can be expressed in a dimensionless form as:

$$\varepsilon_r = \varepsilon_r^{'} - j\varepsilon_r^{''} \tag{1}$$

where the subscript r means relative to the free space permittivity. The real and imaginary parts of the relative permittivity are referred to as the dielectric constant and the loss factor, respectively. The dielectric constant provides a physical indication of how polarizable a medium is, or alternatively, how much energy is stored the medium when subjected to an electric field, while the loss factor is a measure of how lossy or dissipative a medium is to an external electric field.

Conductivity and loss tangent

The conductivity and loss tangent for concrete, classified as the derived EM properties, can be obtained from the dielectric constant and loss factor. The expression for conductivity, σ, is given by [7]:

$$\sigma = \varepsilon^{''} \omega \tag{2}$$

where ω is the angular frequency of the wave. The ratio between the imaginary and real parts of the complex permittivity is called the loss tangent, $\tan \delta$, of the medium which is a measure of how successfully the medium conducts in a dimensionless form:

$$\tan \delta = \frac{\varepsilon''}{\varepsilon'} = \frac{\sigma}{\omega \varepsilon'} \qquad (3)$$

Mathematically, a medium is called a good conductor if $\tan \delta \gg 1$ and a good insulator if the reverse is true.

## Simulation of EM Wave Propagation and Scattering

Simulation of the interaction of electromagnetic waves with a target that has known geometric and material properties is called the forward problem. A numerical simulation scheme called the finite difference-time domain (FD-TD) technique was implemented in 2-D to solve the forward problem [8,9]. FD-TD technique involves numerical solution of the Maxwell's time dependent curl equations. The constitutive relations provide the additional relationships needed between field quantities to obtain a solution. Incorporating the electromagnetic properties of the target and applying the appropriate initial and boundary conditions that satisfy Maxwell's divergence equations [7], a unique solution of the forward problem can be obtained using Maxwell's curl equations for a given excitation source.

Excitation source

A Gaussian pulse plane wave excitation was used as the incident field in the simulations. The advantage of using a Gaussian pulse is the ability to perform multi-frequency experiments simultaneously in one time domain simulation. The Gaussian pulse used in the simulations is shown in Fig. 1 in both time and frequency domains. A pulse width $T = 0.5e - 9$ (s) was chosen for the excitation source which corresponds to a maximum frequency of 1.5 GHz as shown in Fig. 1b. This frequency range is chosen for the reason that it is representative of the currently used frequency range in Civil Engineering NDE applications. A narrower pulse can be used to increase the frequency content of the incident field and the information content of the scattered fields.

Geometry and EM Properties of Concrete Targets

The concrete targets were modeled as cylindrical concrete specimens with and without a rebar at the center, assumed to be infinite in the z direction, allowing circular models in 2-D plane. The diameter of the concrete cylinder and the rebar were
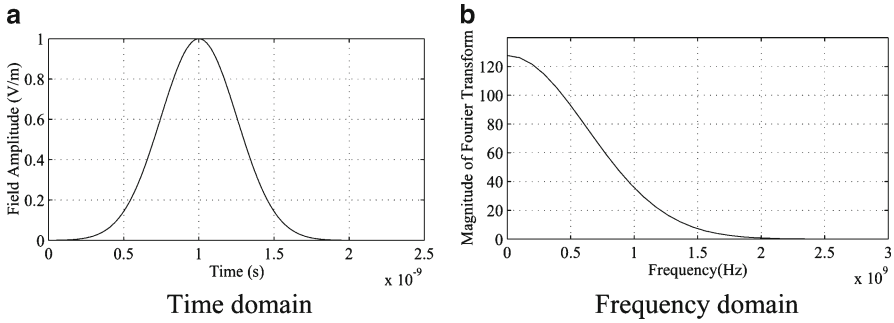
Fig. 1 The Gaussian pulse excitation in time and frequency domain
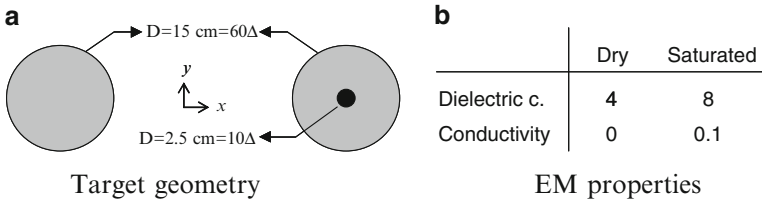
Fig. 2 Geometry and EM properties of the targets

chosen as 15 cm and 2.5 cm, respectively. The geometry and dimensions of the targets are shown in Fig. 2a. Only the results for dry condition are presented in this paper, the properties of which are shown in Fig. 2b.

FD-TD simulation results

The results of the simulations are shown in Fig. 3. It can be seen from the figure that the transmitted and reflected fields measured over a line form hyperbolic arcs as expected. Presence of rebar is clearly indicated by additional arcs.

Image Reconstruction Using Backpropagation Algorithm

The backpropagation algorithm is a solution to the inverse source problem that attempts to determine the source (target) from its radiated fields. It is based on the inhomogeneous scalar wave (Helmholtz) equation and Huygen's secondary sources principle linearized by weak scatterer approximations [1,5]. The algorithm involves backpropagation of the scattered fields measured along a measurement line (planar surface in 3-D) towards the scatterer at incremental depths to obtain an image.
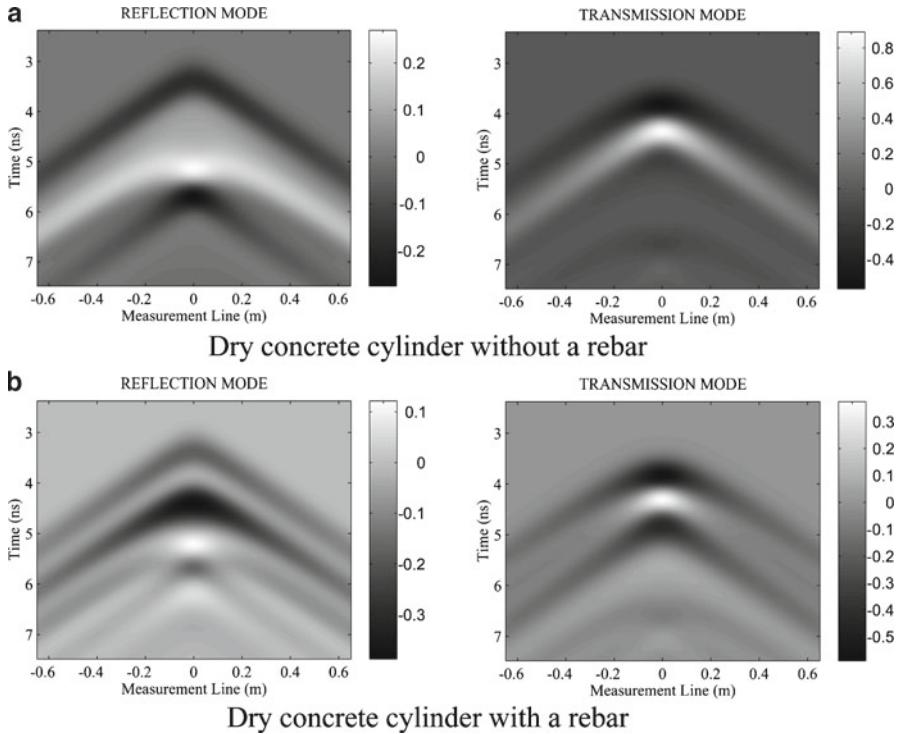
Fig. 3 Scattered fields by the dry concrete cylinders with and without a rebar

For the case of multi-frequency experiments, the procedure can be repeated for each temporal frequency (or wavelength) and superimposed since the procedure is linear. The final image is obtained by taking the inverse Fourier transforms of the superimposed fields at each depth.

Images reconstructed from the scattered fields shown in Fig. 3 by implementing the bacpropagation algorithm are shown in Fig. 4. As can be seen from the figures, the backpropagation algorithm essentially collapses the hyperbolic arcs that appear in the images of the scattered data shown in Fig. 3. A comparison of the images shows that transmission mode experiments generally result in more accurate images. Both images show the concrete cylinder. The size of the cylinder, however, generally appears larger than the actual model. The presence of the rebar resulted in a distorted image in Fig. 4b, which was expected since the rebar severely violates the linarizing (weak scatterer) approximation used in the algorithm's formulation. All the transmission images appear to be relatively insensitive to the presence of a rebar in concrete which is most probably due to the large pulse width of the incident wave resulting in low range and cross-range resolution.
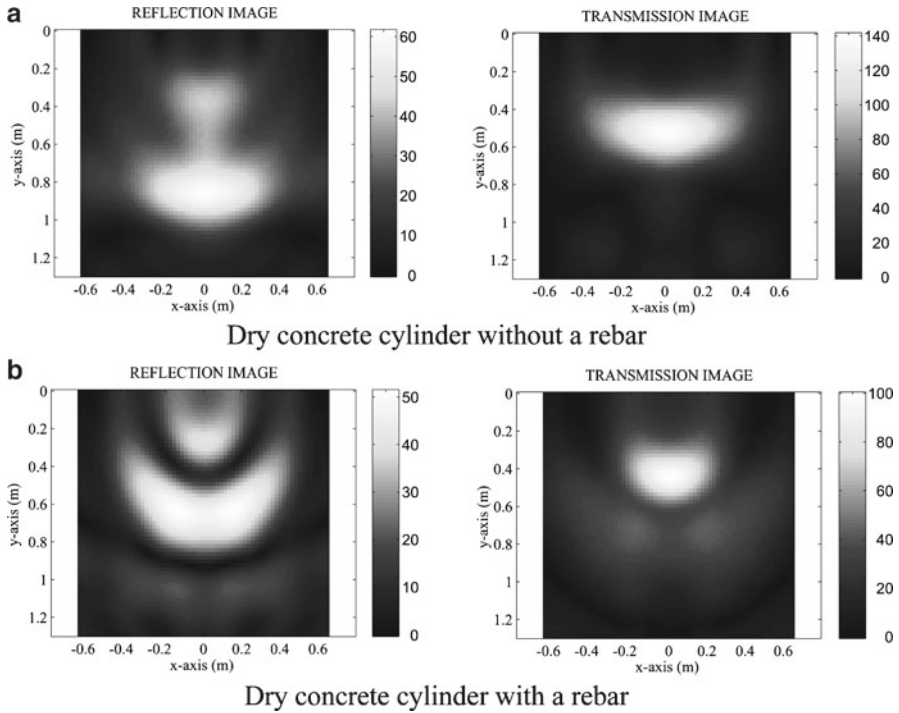
Fig. 4 Reconstructed images of dry concrete cylinders with and without a rebar

Conclusions

Based on the results of imaging applications, the following conclusions were drawn:

1. The imaging applications performed on concrete cylinders in this research were moderately successful in reconstructing the geometry of the concrete target. The reconstructed images are easier to interpret than the raw scattered data, although the size of the reconstructed image appears generally larger than the target size. In addition, presence of reinforcement in concrete may result in distortions in the reconstructed image. These limitations can be attributed to the limitations of the algorithm such as the linearizing approximations in its formulation, partial processing in the Fourier domain, and the frequency content of the source excitation.

2. The frequency content of the excitation pulse used in the simulations is representative of the frequency range currently used in civil engineering NDE applications. The imaging results show that the frequency content of the incident field must be increased in order to improve the resolution.

References

[1] Herman, G. T., Tuy, H. K. and Langenberg, K. J. (1987), and Sabatier, P. C., *Basic Methods of Tomography and Inverse Problems*, Adam Hilger, Bristol.

[2] Boerner, W.M. (1983), *Inverse Methods in Electromagnetic Imaging*, NATO ASI Series, Vol. C-143, D. Reidel Publishing Company, Dordrecht.

[3] Bertero, M. and Pike, E. R. (1992), *Inverse Problems in Scattering and Imaging*, Proc. of a NATO Adv. Res. Workshop, Cape Cod, USA.

[4] Kak, A. C. and Slaney, M. (1988), *Principles of Computerized Tomographic Imaging*, IEEE Press, New York.

[5] Cartz, L. (1995), *Nondestructive Testing*, ASM International, Materials Park OH.

[6] Rhim, H. C. and Buyukozturk, O. (1998), *ACI Mater J.*, vol. 95, n. 3, pp. 262–271.

[7] Staelin, D. H., Morgenthaler, A. W. and Kong, J. A. (1994), *Electromagnetic Waves*, Prentice Hall, Englewood Cliffs, NJ.

[8] Gunes, O. (1998), Microwave Imaging of Concrete for Nondestructive Evaluation, M.Sc. Thesis, MIT, Cambridge, MA.

[9] Li, K., Tassoudji, M. A., Shin, R. T. and Kong, J. A. (1992), *Comp. App. in Eng. Ed.*, vol. 1, n. 1, pp. 45–63.

Accuracy of Potential Mapping Assessed Through Numerical Models

S. Kessler and C. Gehlen

Abstract Potential mapping is a widely used inspection method for detection of ongoing corrosion in reinforced concrete structures. Usually based on the results from potential mappings, further inspection strategies and repair actions are scheduled. Unfortunately the probability of detection (PoD) of the method is an unknown factor. To obtain values for the PoD of potential mapping, it is necessary to compare potential measurements of reinforced structures with their true corrosion condition state. The true corrosion condition state is only identifiable by replacement of concrete cover. In general, owners will not agree to open a whole structure for evaluating the accuracy of an inspection method. Therefore, in this research, an approach based on numerical models with known condition state is pursued.

Keywords Numerical simulation • Potential mapping • Probability of detection • Qualitative inspection method

Introduction

The good quality of test results are essential for making correct decisions on maintenance planning, so their reliability for condition control methods has to be considered.

Potential mapping

Potential mapping is an effective inspection method for detecting the probability of active corroding areas in reinforced concrete structures. During potential mapping

S. Kessler (✉) • C. Gehlen
Centre for Building Materials, TU Muenchen, Germany
e-mail: Kessler@cbm.bv.tum.de
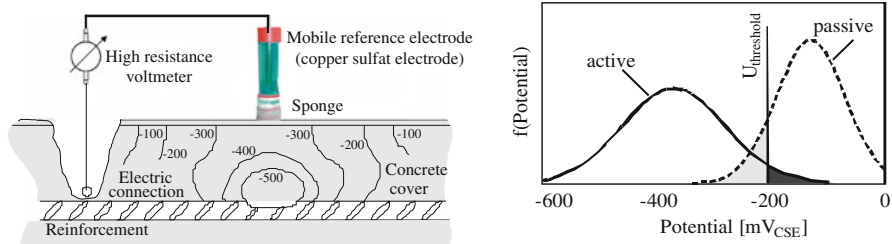
Fig. 1 Principle (left) and evaluation (right) of potential mapping

potential differences are measured between an external reference electrode and the reinforcement (*Fig. 1 left*). With grid-like displacement of the reference electrode potential differences of a whole structural element can be gathered. The detection of corroding areas is possible due to the fact that passive and active surfaces of reinforcement are different electrodes, which vary in free corrosion potential and polarisability. If conductivity and oxygen level in concrete is sufficiently high, active-passive elements will be developed and their potential differences can be measured at the concrete surface.

The aim of the evaluation of potentials is to distinguish between active and passive areas. The potentials can be divided into two probability distributions; one for active and one for passive reinforcement, with the help of frequency plot (*Fig. 1 right*). Then a threshold potential has to be defined. The values that a more negative than the threshold are assumed to belong to the corroding area.

Evaluation of the accuracy of qualitative test methods

The potential mapping measurement is a qualitative test method. This kind of measurement delivers statements with "yes" or "no" answers to the question raised: is the reinforcement corroding? The characterizing parameter to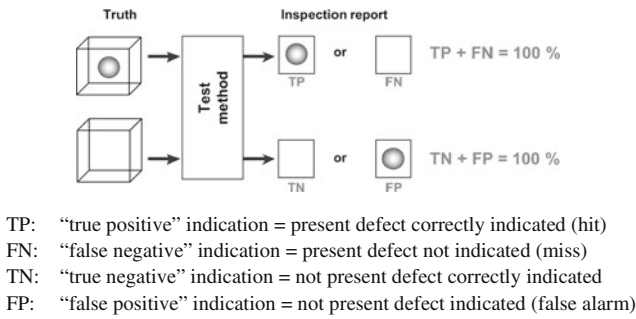 describe the accuracy of these so-called defect detection measurements is the probability of detection (PoD). Commonly, a POD curve describes the rate of detecting a defect with given defect size s (here anode area), PoD(s).

For empirical applications, the performance demonstration is suitable for evaluating the accuracy of qualitative test results. In its simplest form the approach involves the use of material samples containing known defects as a basis for studying its effects on detectability or on factors such as calibration, changes in inspection equipment or inspector training programs [1]. Primarily an unknown defect situation will be measured and afterwards the test results will be compared with the actual/real situation. Basically there are four possible

TP: "true positive" indication = present defect correctly indicated (hit)
FN: "false negative" indication = present defect not indicated (miss)
TN: "true negative" indication = not present defect correctly indicated
FP: "false positive" indication = not present defect indicated (false alarm)

Fig. 2 The four possible indications of a defect detection measurement system

indications behind such a defect detection test. These situations are explained in *Fig. 2*.

The probability of detection will be calculated as follows (Eqn.(1)):

$$\text{PoD} = \frac{\text{P(positive detected/true positive)}\,\text{Number of true positive}}{\text{Number of true positive} + \text{Number of false negative}} = \frac{\text{TP}}{\text{TP} + \text{FN}} \quad (1)$$

The higher the PoD value, the higher is the reliability of achieved satisfactory condition control. However, in order to establish a probability of detection for a special qualitative measurement under selected conditions, a large number of measurement results are needed. Not only the measurement result, but also the true value, has to be known. This is the reason, why it is costly to obtain a sufficiently accurate PoD.

Corrosion processes and the resulting potential distribution in reinforced concrete structures can be simulated numerically [2]. The advantage of such an approach is that the true corrosion condition state in the numerical model is known and the true condition state can be compared with potential distribution at the structural surface. Furthermore, other influencing factors besides anode size, such as defect orientation, environmental conditions and inspection performance, can be excluded or investigated separately.

Numerical Investigation

The present investigation has the purpose to simulate typical potential distribution of macro cell corrosion in reinforced concrete structures. The chosen numerical model has a geometry, which can be found in a lot of structures. The presented numerical calculations are realized with the Boundary Element Method software BEASY [3]. This simulation software is validated in [4].
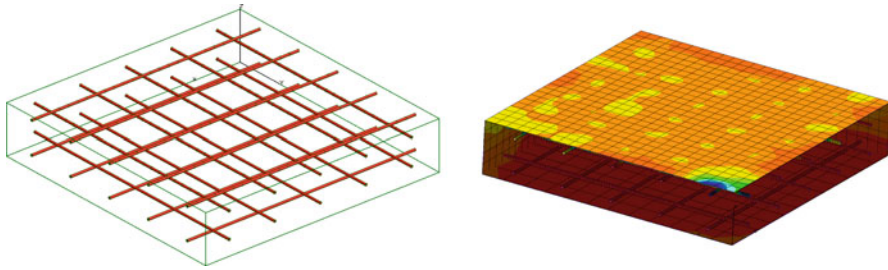
Fig. 3 Numerical model (left), numerical model with potential field (right)

Numerical model

The numerical model is a section of reinforced concrete plate. The plate dimension has to be bigger than the expansion of the macro cell element, so that at the model boundary no corrosion current takes place.

The quadratic model has a side length of 2 m. The plate contains four reinforcement layers with a diameter of 10 mm and a rod distance of 200 mm. The concrete cover is 30 mm. It is modelled only a quarter of the plate to take the advantage of the model symmetry. The numerical model is shown in *Fig. 3 (left)*.

The anode area (A1 = 3cm²; A2 = 11cm²; A3 = 24 cm²; A4 = 50cm²) is varied as well as the resistivity (R = 100, 250, 400, 550 and 700Ωm) of the concrete and the grid size (5 x 5; 15 x 15; 20 x20 cm) to analyse their influence of the PoD of potential mapping. In the evaluation of the grid size 20 x 20 cm the anodic area is situated as far as possible from the grid.

The resistivity values were chosen according to [5]. Polarization curves were taken from literature [6]. The polarization curves were determined potentiodynamically with a velocity of 1 mV/s. According to the climate of exposed structures the anodic polarization curves of 76 % relative humidity and 10°C were chosen. The cathodic polarization is dependent on the oxygen availability at the reinforcement and the oxygen availability is correlated to the humidity. Concrete is not a homogenous electrolyte and the humidity changes from place to place. So four different cathodic polarization curves (100 %, 93 %, 76 %, 66 %RH) were distributed over the numerical model. The mean driving potential averages 400 mV according to [7]. A typical solution of the numerical model is shown in *Fig. 3 (right)*.

Probability of detection

The parameter study was evaluated as follows. The elements from the surface of the model, which are situated directly above the anode, were defined as indicators of corrosion. Then the potentials from the surface was analyzed like shown in *Fig. 1 (right)* and a threshold potential $U_{threshold}$ was determined (*Fig. 4*). Based on the numerical

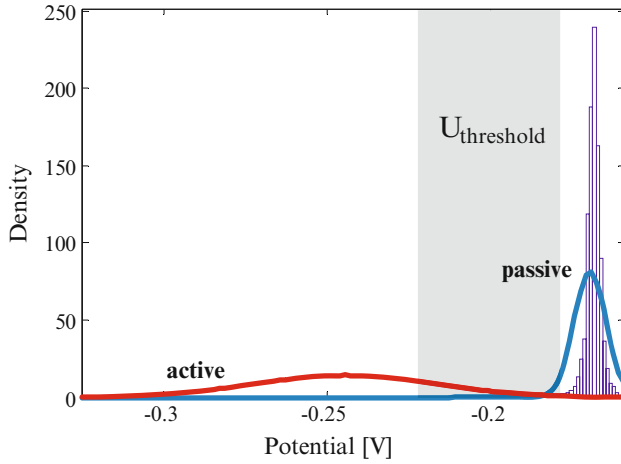**Fig. 4** Determination of $U_{threshold}$ for the parameter study of dc = 30 mm

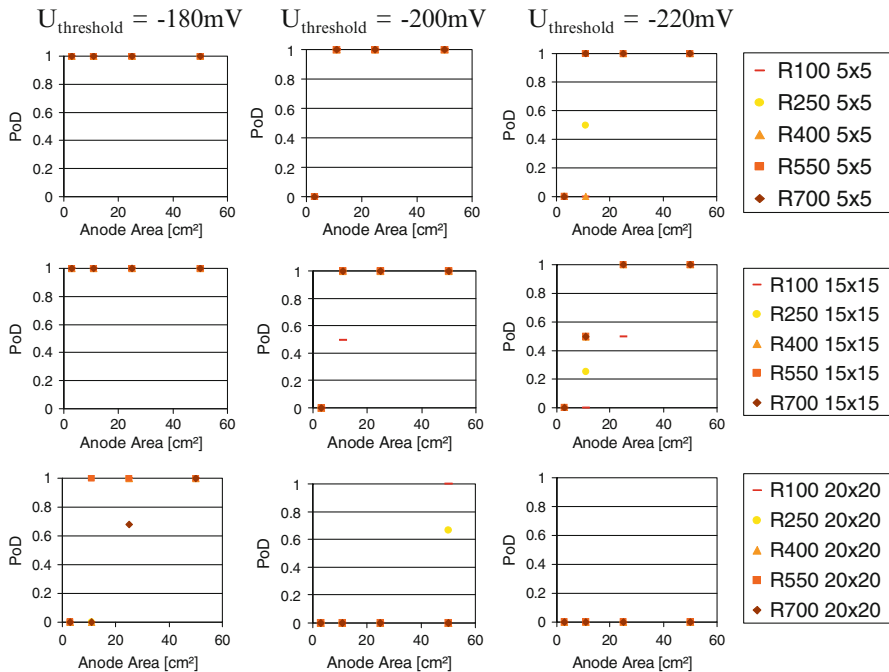**Fig. 5** PoD values in dependence of $U_{threshold}$, grid size and resistivity

results three different $U_{threshold}$.(-180, -200, -220 mV$_{SCE}$) are selected. Then the decision of the threshold potential was compared to the true state of the model. This comparison was made with each surface element depending on the chosen grid size.

Figure 5 summarises the PoD values in dependence of $U_{threshold}$ (-180, -200 and -220 mV$_{SCE}$), grid size (5 x 5; 15 x 15; 20 x20 cm) and resistivity (R = 100, 250, 400, 550 and 700Ωm).

The PoD values strongly depend on the $U_{threshold}$ and the grid size. The resistivity of the concrete has not such a big influence. With smaller grid size the PoD values increase. It is not sure to indicate anodes with a grid size of 20 x 20 cm². The guideline B3 of potential mapping recommends a standard grid size of 25 x 0.25 cm² and at most a grid size of 50 x 50 cm². In the technical bulletin of SIA grid sizes are between 15 x 15 cm² and 25 x 25 cm² for field measurements. RILEM states grid sizes of 15 x 15 cm². The results from this numerical parameter study show, that a grid size of 15 x 15 cm is reliable to detect anodic areas under the chosen boundary conditions like concrete cover 30 mm.

The highest PoD values are reached with the lowest $U_{threshold}$. But a low $U_{threshold}$ coincide with a high probability of false alarm. If $U_{threshold}$ is set too high, non-corroding areas would be repaired unnecessarily and if $U_{threshold}$ is set too negative, corroding areas would be overlooked. The $U_{threshold}$ has to be determined in consideration of the required safety level and economical aspects.

Conclusion

This paper presents a first approach to evaluate numerically the probability of detection of potential mapping in dependence of the resistivity, grid size and $U_{threshold}$. One important result is that a grid size of 15 x 15 cm is reliable to find corroding reinforcement. A grid size of 20 x 20 cm can be too large to detect small anodes. Besides $U_{threshold}$, grid size and resistivity a lot of other factors have to be investigated like the concrete cover, the rod distance, geometries (columns, walls) or carbonated layers. In the next step the PoD values has to be validated at existing concrete structures. The aim is to describe the PoD mathematically in dependence of their most influencing parameters.

References

[1] Müller, C. et al. (2004) *Determination of reliability in deminig and NDT*, NDT–Competence & Safety, MATEST, Zagreb.
[2] Warkus, J. Raupach, M. Gulikers, J. (2006) *Numerical modeling of corrosion–Theoretical backgrounds*– Materials and Corrosion, 57, No. 8.
[3] http://www.beasy.com.
[4] Kessler, S. Gehlen, C. (2010) *Potential mapping–Possibilities and limits* 8th fib PhD Symposium in Kgs. Lyngby, Denmark.

[5] Osterminski et al. (2006) *Modelling of reinforcement Corrosion– influence of measuring techniques, concrete composition, moisture and temperature on the resistivity of concrete*, EUROCORR, Maastricht.

[6] Brem, M. (2004) *Numerische Simulation der Korrosion in Stahlbetonbauteilen*, Diss. ETH Nr. 15567, Zürich.

[7] Warkus, J. Raupach, M. (2009) *Modelling of reinforcement corrosion–geometrical effects on macrocell corrosion*, Volume 61(6), p. 494–504.

[8] DGZfP Merkblatt B3 (2008) *Elektrochemische Potentialmessungen zur Detektion von Bewehrungsstahlkorrosion*, (german).

[9] Merkblatt SIA (2006) *Durchführung und Interpretation der Potentialfeldmessung an Stahlbetonbauteilen*, (german).

10] Elsener, B. et al. (2003) *Half-cell potential measurements–Potential mapping on reinforced concrete structures*, In: Materials and Structures, Vol. 36.

Model-Assisted Non-destructive Monitoring of Reinforcement Corrosion in Concrete Structures

P. Marinier and O.B. Isgor

Abstract Half-cell potential mapping is a non-destructive technique that helps predict the probability of steel corrosion in concrete. A major shortfall of this technique is that it does not give insight into the rate and the nature of corrosion. In the case of localized corrosion, the predictions of half-cell measurements can even lead to wrong interpretations of the severity of corrosion. This paper presents an inverse numerical tool that can be used to better interpret the results of half-cell potential measurements. This tool quantitatively relates the potential readings on the surface of the concrete to the rate of probable localized reinforcement corrosion, allowing engineers to gain supplementary information from half-cell tests. Numerical experiments demonstrate the potential benefits of the proposed approach when typical half-cell measurements may not be able to predict the localized corrosion mechanism.

Keywords Corrosion • Inversion • Modeling • Potential mapping • Reinforced concrete • Simulation

Background

Half-cell potential mapping is a standardized [1] non-destructive technique that is used to predict the probability of steel corrosion in reinforced concrete members. In this method, the potential difference between an external electrode located at the surface of concrete and the embedded reinforcement is measured with a high impedance voltmeter, as illustrated in Fig. 1. ASTM C876 [1] state that the more negative the measured surface potential, the greater probability of corrosion: half-cell potential measurement less than -350 mV with respect copper/copper sulfate

P. Marinier • O.B. Isgor (✉)
Dept. of Civil and Env. Eng., Carleton University, Ottawa, Canada
e-mail: oisgor@connect.carleton.ca
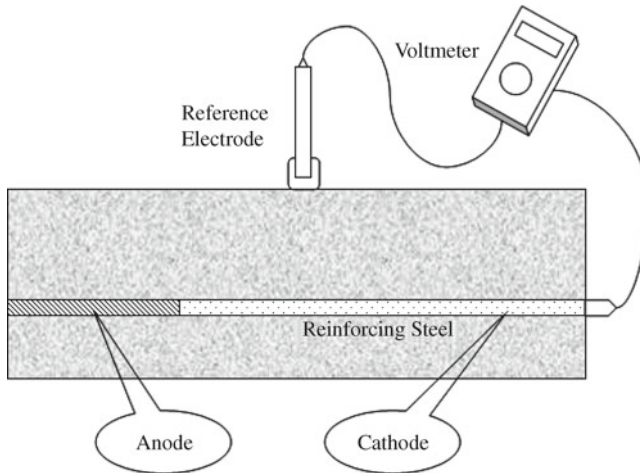
Fig. 1 Half-cell potential measurements on the surface of concrete

electrode (CSE) corresponds to 90% probability. When the measurement is greater than −200 mV (CSE) the probability is less than 10% [1].

The interpretation of the half-cell potential mapping results is a major challenge for engineers because the test results do not give any insight to the rate and type of corrosion. In the case of uniform corrosion, the potential readings at the surface of concrete are generally close to the potential at the interface of steel and concrete; however, in the case of localized pitting corrosion the measured potentials at the surface of concrete can be substantially different from those of the steel/concrete interface. This potential difference is a function of cover thickness and concrete resistivity, and increases with both.

In a recent study [2], it was shown that while carrying out half-cell measurements, potential readings should be interpreted in accordance with the resistivity of the system; otherwise, the results can be misleading. For the same corrosion rate, one can measure different potentials at the surface of concrete, corresponding to different values of resistivity, and thus have more than one probability for the same state of corrosion. The same study also showed that when the average potential at the surface of concrete is a large value (i.e. more positive) the probability of the corrosion is low as per ASTM C-876; however the rate of such a corrosion, if occurs in the form of localized corrosion, can be very high. On the other hand, if the average potential at the surface of concrete is a small value (i.e. more negative), the probability of the corrosion is higher, but such corrosion may proceed more uniformly. Accurate detection of localized corrosion, in which anode-to-cathode ratio can be small, may not be feasible with half-cell potential measurement method unless supplementary information is provided.

The main objective of this paper is to overcome these difficulties associated with half-cell mapping by presenting an inverse modelling approach that quantitatively relates the potential readings on the surface of the concrete to the rate of reinforcement corrosion, allowing the engineers to gain supplementary information from the half-cell tests, especially when localized corrosion that cannot be detected by half-cell measurements is the main mechanism of corrosion.

Forward Problem

Electrical potential distribution, ϕ, in concrete due to a corroding rebar can be determined using finite element method by solving the Laplace's equation [3]

$$\nabla^2 \phi = 0 \tag{1}$$

with the following boundary conditions defined on the anodic and cathodic surfaces of rebar:

$$\phi_a = \phi_{Fe}^\circ + \beta_a \log \frac{i_a}{i_{\circ a}} \text{ on } \Gamma_a \tag{2}$$

$$\phi_c = \phi_{O_2}^\circ + \beta_c \log \frac{i_c}{i_{oc}} - \frac{2.303 RT}{z_c F} \log \frac{i_L}{i_L - i_c} \text{ on } \Gamma_c \tag{3}$$

where ϕ_{Fe}° = standard equilibrium potential for the oxidation of iron [volts]; $\phi_{O_2}^\circ$ = standard equilibrium potential for the reduction of oxygen [volts]; β_a = anodic Tafel slope [V/dec]; β_c = cathodic Tafel slope [V/dec]; i_a = anodic current density [A/m²]; i_c = cathodic current density [A/m²]; i_{oa} = anodic exchange current density [A/m²]; i_{oc} = cathodic exchange current density [A/m²]; R = universal gas constant [≈ 8.314 J/mol.K], F = Faraday's constant [≈ 96500 C/mole], z_c = number of electrons in the reaction, T = temperature [K]; i_L = limiting current density [A/m²]. Other boundaries ($\Gamma_{ct} + \Gamma_{cs,1} + \Gamma_{cs,2}$) are have zero current fluxes shown in Fig. 2.

Current density at anodic and cathodic surfaces are calculated locally at every discretization node on the steel surface by applying the Ohm's law:

$$i = -\frac{1}{\rho} \frac{\partial \phi}{\partial n} \tag{4}$$

where i = current density [A/m²]; ρ = electrical resistivity of concrete [Ω-m]; n = direction normal to the equipotential lines. The dependence of the boundary conditions (2) and (3) on Eqn. (4) requires a non-linear solution algorithm, which is described in detail in elsewhere [2, 3].
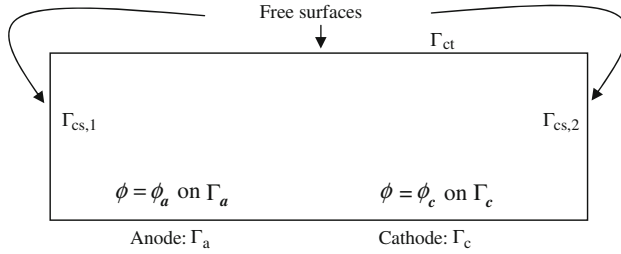
Fig. 2 Boundary conditions for the forward problem

Inverse Problem

Inverse problem is described by the identification of the anodic and cathodic boundary conditions on the rebar surface ($\Gamma_a + \Gamma_c$) from half-cell potential measurements on the concrete surface (Γ_{ct}). The inverse model requires the minimization of the cost function, J, between the measurements, ϕ_{obs}, and the predictions, ϕ_s, on the surface of the concrete such that:

$$J(\phi) = \sum_{k=1}^{N_s} \left(\phi_{obs}^k - \phi_s^k \right)^2 \quad \text{on } \Gamma_{ct} \tag{5}$$

where N_s is the number of surface nodes and k is the index for counting. Here the conjugate gradient method is used for minimization [4]. The conjugate gradient method requires the determination of the gradient of the cost function, which can be used for detecting the direction of the steepest descent towards the minimum. The gradient of the cost function is calculated as:

$$\nabla J_i = \frac{\partial J}{\partial \phi_i} = \sum_{i=k}^{N_s} \frac{\partial \phi_s^k}{\partial \phi_i} \frac{\partial J}{\partial \phi_s^k} \tag{6}$$

where $\Rightarrow$ is the nodal potentials on the rebar surface. The $\partial \phi_s^k / \partial \phi_i$ term in Eqn. (6) represent the sensitivity of the potentials on the concrete surface to the changes on the rebar surface, and can be calculated by applying perturbations on the nodes on the steel surface. $\partial J / \partial \phi_s^k$ can be obtained by taking the derivative of Eqn. (5).

The conjugate gradient method finds the potentials on the rebar surface, $\Rightarrow$, by incrementally minimizing the cost function following the steepest descent path via:

$$\phi_i^{n+1} = \phi_i^n + \alpha^n d^n \tag{7}$$

where n is the iteration step, a_n is the step size and d^n is the direction of the steepest descent. The details of the calculation of the step size and the direction of the steepest descent are not provided here, but more information can be obtained from [4].

Numerical Experiment

An identical twin experiment is presented here to demonstrate the accuracy and the efficiency of the developed inverse algorithm. The experiment involves the use of surface potentials obtained form the forward solution of a single-anode problem as observed data and finding the boundary conditions on the steel surface. The parameters for solving the forward problem are provided in Table 1. The single anode was placed in the middle of the rebar with an anode-to-cathode length ratio of 0.1, which represents localized pitting corrosion. The domain was rectangular such that the longitudinal direction to the rebar was 1200 mm and the cover of concrete was 80 mm. The domain was discretized into 20 x 2m mm square elements. The concrete resistivity was selected as 150 ohm-m. The inverse modelling iterations were carried out until the const function became smaller than 10^{-8} V^2.

Figure 3 illustrates the comparison of the inverse solution with the observed results that were obtained from the forward solution of the actual system. It is clear that inverse modelling algorithm is able to predict the location of the anode very accurately. The solution converged to the prediction show in Fig. 1 within 500 iterations; this shows the efficiency of the algorithm. However, it is expected that convergence rate will slow down and the accuracy will deteriorate as the anode-to-cathode ratio is made smaller or resistivity of the concrete is modified. Cover thickness, the domain size and the presence of multiple anodes will also affect the inverse predictions; therefore, further research on the investigation of these parameters is required. In particular, regularisation schemes will be required to overcome convergence issues and oscillations that may be encountered in the inverse solutions of complex cases.

Conclusions

An inverse modelling algorithm that quantitatively relates the potential readings on the surface of the concrete to the rate of reinforcement corrosion is presented to overcome the difficulties associated with half-cell mapping. It was demonstrated

Table 1 Input parameters of the forward solution

Parameter	Value
Standard half cell potential of *Fe* (mV ~SCE)	−780
Tafel slope of the anode, β_a (mV)	60
Anodic exchange current density, i_{oa} (A/mm^2)	187.5×10^{-12}
Standard half cell potential of oxygen (mV ~SCE)	160
Tafel slope of the cathode, β_c (mV)	160
Cathodic exchange current density, i_{oc} (A/mm^2)	6.25×10^{-12}
Temperature, T (K)	298
Limiting current density, i_L (A/mm^2)	1×10^{-6}
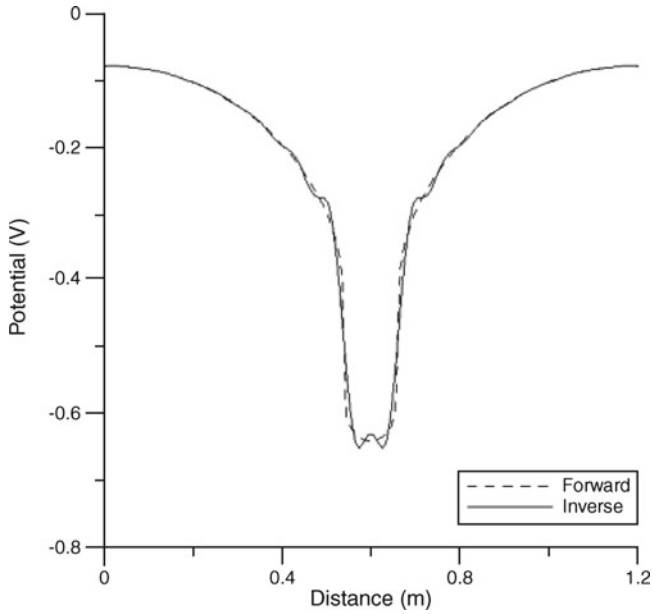
Fig. 3 Comparison of the inverse solution with the observed data

though an identical twin experiment that inverse modelling algorithm is able to predict the location of the anode very accurately.

References

[1] ASTM Standard C876 (2009), *ASTM International*, West Conshohocken, PA, USA.
[2] Pour-Ghaz, M., Isgor, O.B. and Ghods P. (2009), *ASCE Mater. J.*, vol. 21, n. 9, p. 467–675.
[3] Isgor, O.B. and Razaqpur, A.G., *Cem. Concrete Comp.*, vol. 26, n. 1, p. 57–73.
[4] Hanke M. (1995), Conjugate Gradient Type Methods for Ill-Posed Problems, Longman, ISBM: 9780582273702.

Estimation of Pre-stress in Tendons Using Elastic Wave Propagation in the Anchor Head

D.G. Aggelis, D. Kleitsa, K. Kawai and T. Shiotani

Abstract Application of pre-stress on a structure is a way to reinforce materials with low tensile strength like concrete and soil against tensile overload. After years in service, the strands may lose the pre-stress due to corrosion or other reasons endangering the whole structure. Since the strands inside the structure are not easily accessible, any inspection should be conducted on the anchor head. In this study, elastic waves are numerically applied on the anchor head. Parameters like the wave amplitude, propagation time, frequency content and others are influenced by the stress of the strand wires which affects the contact between the steel strand, and the surrounding bolt of the anchor head influencing the acoustic impedance mis-match on the interfaces. The change of contact pressure between the strands and anchor head is simulated by modifying the rigidity of a model interphase material. Therefore, an easy and fast procedure for non destructive inspection of the pre-stress load on the strands is discussed.

Keywords Anchor head • Non destructive inspection • Pre-stress • Strand wires • Ultrasound

Introduction

Millions of ground anchorages have been installed over the past decades with relatively few recorded failures. However, as permanent anchorages in service become older, the subject is of growing importance, particularly for anchorages installed more than 30 years ago, many of which have been designed with corrosion protection

D.G. Aggelis (✉) • D. Kleitsa
Department of Materials Science and Engineering, University of Ioannina, Ioannina 45110, Greece
e-mail: daggelis@cc.uoi.gr

K. Kawai • T. Shiotani
Graduate School of Engineering, Kyoto University, Kyoto 615-8540, Japan
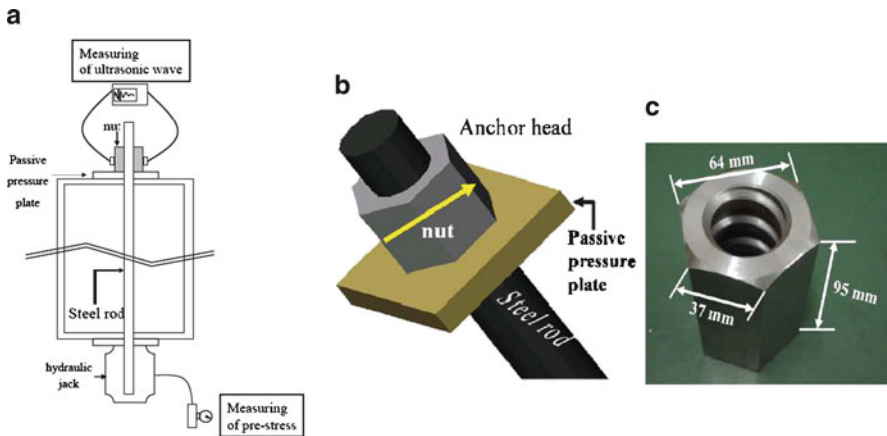
Fig. 1 (**a**) Schematic representation of pre-stress, (**b**) wave propagation in vertical direction, (**c**) details of the nut used in the anchor head

considered inadequate by today's standard. Maintenance testing involves visual survey of the physical condition of the structure and the anchorages, measurement of the overall deformation and when applicable measurement of the load of selected tendons. The method to monitor the load of a tendon is the so called "lift-off" method. However, it entails certain difficulties as it requires the anchor head to be raised by some mm using a hydraulic jack and therefore may jeopardize the safety of the structure while only specific tendons can be examined [1]. A routine, fast and easy inspection method which can confirm the satisfactory performance can extend the service life of anchored structures [2].

This study focuses on the ultrasonic method to evaluate the axial stress of the strands. The applicability of the method is examined numerically and suitable wave parameters are sought for in order to yield a robust correlation with the applied stress on the tendons. Due to the bolt geometry, as the pre-stress on the strands increases, the strand obtains stiffer contact with the bolt material of the anchor. This has an effect on the overall rigidity of the bolt. Therefore, longitudinal elastic waves are introduced in an anchor head and the time of flight, as well as the amplitude are measured for different levels of pre-stress. The experiment is numerically simulated by finite difference method software modeling the different pre-stress levels with an interphase material of varying elastic constants. A similar study was recently conducted on a different shape of anchor head [3].

Since there is no accessibility in the interior of the structure, the assessment should be conducted through the only area located in the surface, the anchor head. Fig. 1a shows the cross-section of the pre-stress structure. As the tensile load of the cables/tendons increases, the contact between the nut and the surrounding hole of the bolt becomes stiffer. At the certain cross-section of the head (see Fig. 1b) the ultrasonic monitoring can be applied. Details of the anchor bolt geometry can be seen in Fig. 1b.

Numerical Simulations

The fundamental equation governing the two-dimensional propagation of elastic waves in a perfectly elastic medium, ignoring viscous losses is seen below:

$$\rho \frac{\partial^2 u}{\partial t^2} = \mu \nabla^2 u + (\lambda + \mu) \nabla \nabla \cdot u \qquad (1)$$

where u=u(x,y,t) is the time-varying displacement vector, ρ is the mass density, λ and μ are the first and second Lame constants respectively, while t is time. The focus, from the engineering point of view is given on simulating the actual cases examined experimentally and not on the numerical method itself. However, certain prerequisites should be followed in order for the analysis to lead to reliable results. The simulations were conducted with commercially available software [4]. It operates by solving the above equation based on a method of finite differences. Equation (1) is solved with respect to the boundary conditions of the object, which include the input source that has pre-defined time-dependent displacements at a given location and a set of initial conditions. For heterogeneous media like the one studied herein, propagation in each distinct homogeneous phase is solved according to eq. (1), while the continuity conditions for stresses and strains must be satisfied on the interfaces [4].

Materials were considered elastic without viscosity components. As the stress increases in the strand, the contact at the interface between the bolt and the matrix material is enhanced. This condition is simulated by an imaginary interphase material with varying stiffness, as has been done for the case of surface cracks with faces in partial contact [5], see also Fig. 2. The minimum value for the stiffness is zero which simply means no contact between the wedge and the matrix while the maximum is the stiffness of steel as if there was no interface at all. The mechanical properties of the steel matrix, the wedge and the strand wire are equal, with Young's modulus 205 GPa, Poisson's ratio of 0.3 and density of 7800 kg/m³ resulting in a longitudinal wave velocity, C_L, of 5948 m/s. The interphase material's velocity was set to different values starting from 330 m/s which simulates the case of negligible
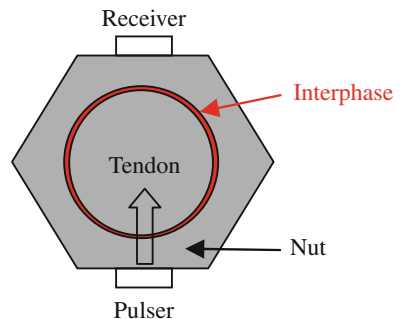

Fig. 2 Representation of the geometric model

contact. Then, by adjusting the elastic properties of the interphase, the velocity, C_L, was set to the values 1000, 2000, 3000, 4000 and 5000 m/s and 6000 m/s. The last value simulates the case in which the interphase is as rigid as the steel material itself. The geometry of the model is depicted in Fig. 2. The thickness of the interphase was 0.5 mm, being a suggestive value.

The "pulser" introduced an excitation of 1 cycle of 1 MHz vertical to the surface (longitudinal wave). The receiver provided the average vertical displacement on its whole length (10 mm).

The element size (mesh) was 0.12 mm, while considering the main frequency of 1 MHz, the wavelength is calculated to about 6 mm. This satisfies the requirement of 10 or 20 nodes per wavelength even for the case of 5 MHz that is also studied and results in reasonable accuracy [6]. The time step was 0.0167 µs, meaning that for the frequency of 1 MHz (period of 1 µs) almost 60 points were used to describe one cycle, while for the frequency of 5 MHz the number of points was 15 ensuring adequate depiction.

Results

Below one can see typical waveforms for different levels of stiffness of the interphase. The loose interphase (C_p=300 m/s) which corresponds to air exhibits considerably low amplitude, due to the strong scattering of the wavefront by the circular interphase, which acts as a hole, see Fig. 3a. As the interphase becomes stiffer, the wavefront suffers less scattering and therefore, the arrival of the wave comes with a strong peak. For the case of C_p=6000 m/s, there is no scattering because the materials (nut, interphase and tendon) are identical with properties of steel. Apart from the first strong peak, it is worth to mention that for a certain level of rigidity the first reflection becomes clear, see Fig. 3a. This reflection is not identified when the wavefront is scattered on the loose interphase and could also be used as an indicator of good contact along with other descriptors studied herein. The most common measurement in ultrasonics is the transit time which was defined by the first disturbance on the simulated waveform of the receiver. The results can be seen in Fig. 3b.

The transit time strongly depends on the interphase stiffness, see Fig. 3b. When this stiffness is near zero, the short, straight path is not available and the wave propagates on the arc of the inner hole of the nut. As the stiffness increases the straight path becomes gradually available and thus the transit time is shortened. This change of more than 1 µs, which corresponds roughly to almost 10 % can be certainly captured by any ultrasonic set up. The frequency of the pulse does not seem very influential, as both 5 MHz and 1 MHz result in quite similar curves.

As seen in Fig. 3a the amplitude of the wave front is stronger for stiff interphase. This can be observed for all applied levels of stiffness in Fig. 4a. The amplitude of the pulse is much more sensitive to the contact of the interfaces, since it increases by more than 5 times for both frequencies.

Another parameter that proved very sensitive is the accumulated amplitude line. This is calculated after rectifying the waveforms and adding the amplitude of each
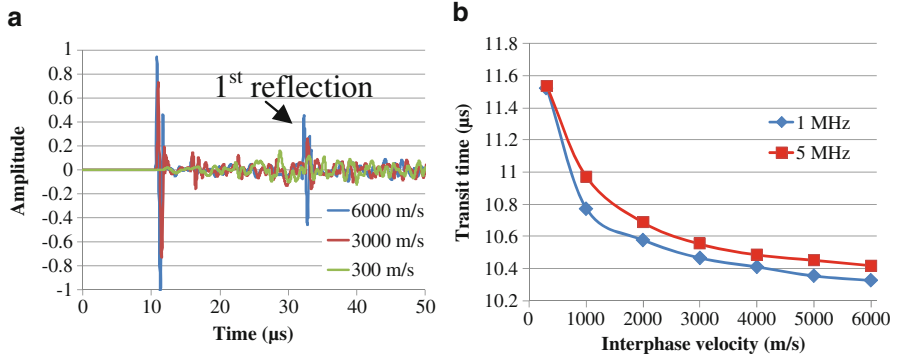
Fig. 3 (**a**) Sample waveforms for different interphases. (**b**) transit times vs. Interphase pulse velocity for two different frequencies
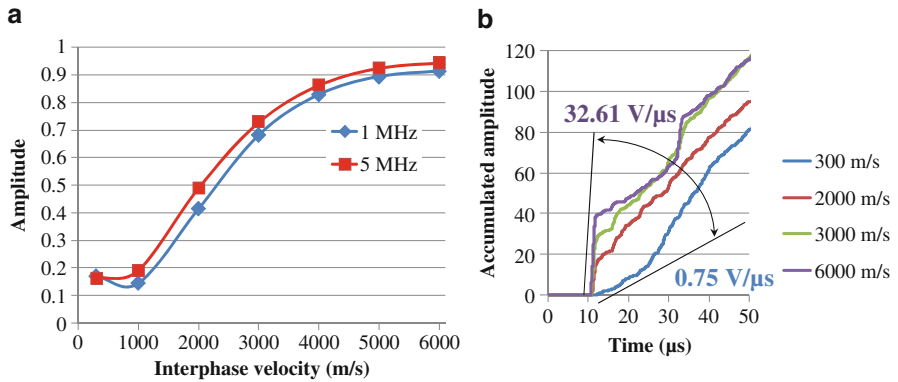
Fig. 4 (**a**) Amplitude vs. Interphase pulse velocity for two different frequencies

point to the previous [7]. It is reasonable that for the stiff interphase, where the first cycle is very strong, the initial inclination of this line is high. On the other hand for a severely scattered waveform, the energy is dispersed in a longer period of time, reducing the rate of energy at the first part. This is seen in Fig. 4b where the inclination of the accumulated amplitude increases from 0.75 V/μs to 32.61 V/μs as the interphase becomes stiffer. This parameter changes by more than 40 times, being another sensitive descriptor to characterize the contact.

Conclusions

The study presented herein concerns the non destructive evaluation of the stress in metal strand tendons. Increased pre-stress enhances the contact of the metal parts and this should have an effect on the propagation of elastic waves through the head.

Fig. 5 Experimental measurements on the anchor bolt

Numerical simulations on the exact geometry are conducted using an imaginary "interphase" material. Although this interphase does not physically exist, it is a reasonable and convenient way to simulate the change in contact between the nut and bolt interfaces. Results show a decreasing trend for transit time and an increasing one for the amplitude of the wave front as the contact pressure becomes higher. Transit time decreases by 10%, while the maximum amplitude of the received waveform increases by 5 times. The inclination of accumulated amplitude line proves even more sensitive since it increases by about 40 times. It is seen that several parameters of the waveform may be used to characterize the contact. The next step is to compare the results with experimental, which are contacted on the same geometry, see Fig. 5. Concerning simulation, further ideas include the use of shear waves which should be more sensitive to the stiffness of the interphase, while they would not be strongly affected by possible presence of grease between the nut-rod interphase.

References

[1] Littlejohn, S. (ed.) *Ground Anchorages and Anchored Structures in Service*, 4 (2007).
[2] Kawai, K., Shiotani, T., Ohtsu, H., Yanase, T., Tanaka, H., Proc. EIT-JSCE, Geotechnical Infrastructure Management, (in CD, 9) (2009).
[3] Kleitsa D., Kawai K., Shiotani T., Aggelis D.G., NDT&E Int, 43, 547 (2010).
[4] Wave2000, Cyber–Logic, Inc, New York (http://www.cyberlogic.org)
[5] Pecorari, C., *Wave Motion* 33, 259 (2001).
[6] Moser, F., Jacobs, L. J., and Qu, J., *NDT&E Int*. 32, 225 (1999).
[7] T. Shiotani and D. G. Aggelis, *Mater Struct*. 42(3), 377 (2009).

Modeling of Ultrasonic Signals Received by a Focused Circular Transducer from a Side-Drilled Hole

F. Honarvar, M.D. Khameneh, A. Yaghootian and M. Zeighami

Abstract This paper presents a model that allows us to predict the ultrasonic signal received by a focused circular transducer from a side-drilled hole (SDH). In order to develop a model for the entire ultrasonic testing system, we first need to develop models for the following three parts of the problem: 1) the ultrasonic beam field, 2) the system function, and 3) the scattered waves from the SDH. To calculate the beam field, we use the multi-Gaussian beam modeling. To model the system function, the front surface reflection signal is used as a reference reflector, and to get the scattered field, both Kirchhoff approximation and the separation of variables (SOV) method are used. By combining these three subsidiary models, we obtain a complete model for the entire ultrasonic measurement system. Experimental results are used to verify the accuracy of the developed model.

Keywords Focused transducer • Multi-Gaussian beam • Normal mode expansion • Side-drilled hole • Ultrasonic modeling

Introduction

Ultrasonic pulse-echo measurement in an immersion setup is a widely used method for testing various materials. To improve the efficiency of the test, measurements are usually done by focused ultrasonic transducers. To obtain reliable results from

F. Honarvar (✉)
NDE Lab, Faculty of Mechanical Engineering, K. N. Toosi University of Technology,
Tehran, Iran
e-mail: honarvar@mie.utoronto.ca

Department of Mechanical and Industrial Engineering, University of Toronto, Toronto,
ON, M5S 3G8, Canada

M.D. Khameneh • A. Yaghootian • M. Zeighami
NDE Lab, Faculty of Mechanical Engineering, K. N. Toosi University of Technology,
Tehran, Iran

such an ultrasonic measurement system, it is necessary to perform one or more suitable calibration processes on the system. Since side-drilled holes (SDH) are often used for calibrating ultrasonic measurement systems, it is useful to obtain a model that can predict ultrasonic pulse-echo responses from a side-drilled hole. Several ultrasonic measurement models with high computational efficiency such as multi-Gaussian beam, boundary diffraction wave, distributed point source, and Gauss-Hermite, have been recently developed for solving various ultrasonic NDE problems [1–7]. In this paper, we use the multi-Gaussian beam technique to calculate the wave profile of focused transducers. This is followed by Kirchhoff approximation and SOV method to calculate the scattering response of the side-drilled hole. We then use reference reflectors response for modeling the system function of the ultrasonic measurement system. Finally, using these ingredients, a complete model that can predict the pulse-echo signals of a focused ultrasonic transducer from a side-drilled hole is developed and compared with experiments.

Multi-Gaussian Beam Model

The multi-Gaussian beam model can describe the ultrasonic wave field of a focused circular piston transducer by superposition of a number of individual Gaussian beams with a proper set of weighting factors [8, 9]. Using an optimization method, Wen and Breazeale found ten coefficients for obtaining the multi-Gaussian beam model for a circular planar piston transducer [10]. For a circular piston transducer of radius a, the normalized velocity field on the face of the transducer is given by [8],

$$\frac{v_z(z_1 = 0, \omega)}{v_0} = \sum_{m=1}^{10} A_n . \exp\{i\omega[\mathbf{M}_n(0)]_{11} y_1^2 / 2 + i\omega[\mathbf{M}_n(0)]_{22} y_2^2 / 2\} \tag{1}$$

where $\mathbf{y}=(y_1, y_2)$ defines the transducer face, A_n and B_n are Wen and Breazeale coefficients, ω is circular frequency and v_0 is velocity at the face of transducer. For modeling of a spherically focused transducer, the Gaussian beam coefficients B_n are changed by letting $B_n \rightarrow B_n + iD_R/F$, where F is the focal length of the transducer [8]. $\mathbf{M}_n(0)$ is a 2×2 complex-valued symmetric matrix and defines phase of the multi-Gaussian beam on the face of the transducer [8],

$$\mathbf{M}_n(0) = \begin{bmatrix} iB_n / c_{p1} D_R & 0 \\ 0 & iB_n / c_{p1} D_R \end{bmatrix} \tag{2}$$

and c_{p1} is longitudinal wave speed in the first medium. $D_R = k_{p1} a^2 / 2$ is the Rayleigh distance and k_{p1} is the longitudinal wave number in the first medium. Equation (1) defines wave velocity field on the face of the transducer. To obtain a model to calculate the wave field at the distance z_1 from the transducer face, based on the propagation laws of Gaussian beams we have [8],
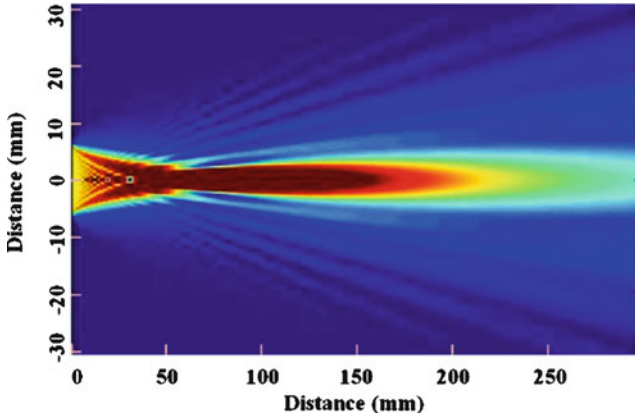
Fig. 1 Wave field of a 12.7 mm diameter focused circular transducer

$$\mathbf{v}_{z1}(\omega) / v_0 = \sum_{n=1}^{10} A_n / (1 + iz_1 B_n / D_R) . \exp\left(ik_{p1}z_1 + (ik_{p1} / 2.)\mathbf{y}^T \left[c_{p1}\mathbf{M}_n(z_1)\right]\mathbf{y}\right) \tag{3}$$

Where $\mathbf{M}_n(z_1)$ is the phase matrix at the distance z_1 from the transducer face,

$$\mathbf{M}_n(z_1) = \begin{bmatrix} (iB_n / c_{p1}D_R) / (1 + iB_n z_1 / D_R) & 0 \\ 0 & (iB_n / c_{p1}D_R) / (1 + iB_n z_1 / D_R) \end{bmatrix} \tag{4}$$

Using eqs. (3) and (4), the wave profile of the radiation field in water generated by a circular focused transducer having a diameter of 12.7 mm, focal length 50.8 mm and center frequency of 10 MHz has been calculated and is shown in Fig. 1.

The problem we are interested in is calculating the wave field around a SDH located at distance z_2 from a fluid-solid interface in a homogenous elastic solid (steel). Using the transmission laws of Gaussian beams from fluid-solid interfaces and the propagation laws of Gaussian beams, we have,

$$\frac{\mathbf{v}_{SDH}}{v_0} = \sum_{m=1}^{10} \mathbf{d}^P T_{12} \frac{A_n}{1 + [iB_n / D_R][z_1 + z_2 c_{p2} / c_{p1}]}.$$

$$.\exp\left(ik_{p1}z_1 + ik_{p2}z_2 + i\frac{k_{p1}}{2}\mathbf{Y}^T \left[c_{p1}\mathbf{M}_2^n(z_2)\right]\mathbf{Y}\right) \tag{5}$$

where $\mathbf{d}^P$ is the polarization vector for P-wave, c_{p2} and k_{p2} are longitudinal wave velocity and wave number in steel, and T_{12} is the transmission coefficient based on a velocity ratio for a planar fluid-solid interface. $\mathbf{M}_2^n(z_2)$ is the phase matrix of multi-Gaussian beam at the SDH and can be calculated from,

$$\mathbf{M}_2^n(z_2) = \begin{bmatrix} \dfrac{iB_n / c_{p1}D_R}{1+[iB_n / D_R][z_1 + z_2 c_{p2} / c_{p1}]} & 0 \\[4mm] 0 & \dfrac{iB_n / c_{p1}D_R}{1+[iB_n / D_R][z_1 + z_2 c_{p2} / c_{p1}]} \end{bmatrix} \tag{6}$$

Scattering Models

In this section, both approximate and exact characterizations of scattering responses of a SDH are modeled using Kirchhoff approximation and SOV methods. In using the Kirchhoff approximation for the side-drilled hole, any contributions from the ends of the SDH will be neglected and only the fields on the curved cylindrical surface are considered. The scattering response of a SDH of radius b and length L can be calculated by Kirchhoff approximation by using the following equation [8]:

$$\frac{A(\omega)}{L} = \frac{k_{p2}b}{2}\Big(J_1(2k_{p2}b) - iS_1(k_{p2}b)\Big) + i\frac{k_{p2}b}{\pi} \tag{7}$$

where S_1 and J_1 are the Struve and Bessel functions, respectively. Moreover, the exact scattering response of a SDH can be calculated by using the separation of variables method. In case of a longitudinal wave incidence on the SDH, the exact scattering response is given by an infinite sum of Hankel functions and complex exponential functions as follows [8],

$$\frac{A(\omega)}{L} = \frac{i}{2\pi}\sum_{n=0}^{\infty}(2-\delta_{0n})(-1)^n F_n \tag{8}$$

where

$$\delta_{0n} = \begin{cases} 1 & n = 0 \\ \\ 0 & n \neq 0 \end{cases} , F_n = 1 + \frac{C_n^{(2)}(k_p b)C_n^{(1)}(k_s b) - D_n^{(2)}(k_p b)D_n^{(1)}(k_s b)}{C_n^{(1)}(k_p b)C_n^{(1)}(k_s b) - D_n^{(1)}(k_p b)D_n^{(1)}(k_s b)}$$

$$C_n^{(i)}(x) = [n^2 + n - (k_s^2 b^2 / 2)]H_n^{(i)}(x) - (2nH_n^{(i)}(x) - xH_{n+1}^{(i)}(x))$$
$$D_n^{(i)}(x) = n(n+1)H_n^{(i)}(x) - n(2nH_n^{(i)}(x) - xH_{n+1}^{(i)}(x)) \tag{9}$$

Using eqs. (7) and (8) the approximate and exact response of a 1.5 mm diameter SDH is shown in Fig. 2.
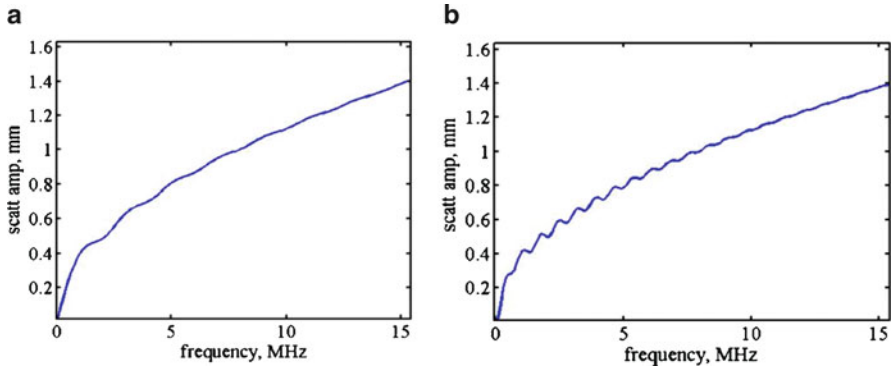
Fig. 2 Scattering response of a 1.5 mm diameter SDH (**a**) Kirchhoff approximation (**b**) separation of variables method

System Function

The system function defines the electromechanical and electrical components of the ultrasonic measurement system, including cables, transducers, pulser, and receiver. In order to calculate the system function, a reference experiment is performed under the same system setting as that of the SDH measurement. The reflection from the front surface of the specimen immersed in water, $V_R^{ref}(\omega)$, was regarded as the reference signal. Using the reference signal and its corresponding reference model, the system function can be determined by the following deconvolution procedure [8],

$$s(\omega) = \frac{V_R^{ref}(\omega)t_A^*(\omega)}{\left|t_A(\omega)\right|^2 + \varepsilon^2 \max\{\left|t_A(\omega)\right|^2\}} \tag{10}$$

Where ε is a constant which represents the noise level, ( )* denotes the complex-conjugate, and $t_A(\omega)$ is the acoustic/elastic transfer function obtained from,

$$t_A(\omega) = 2R_{12}\exp(2ik_{p1}z_1)[1 - \exp(ik_{p1}a^2/2z_1)] \times \{J_0(k_{p1}a^2/2z_1) - J_1(k_{p1}a^2/2z_1)\} \tag{11}$$

where the quantity R_{12} is the plane wave reflection coefficient at the interface.

Prediction of the SDH Signal and Comparison with Experiment

Following Ref. 8, in the frequency domain, the received voltage signal for the pulse-echo immersion setup from a side-drilled hole where the beam variations can be neglected over the cross-section of the scatterer can be written as,
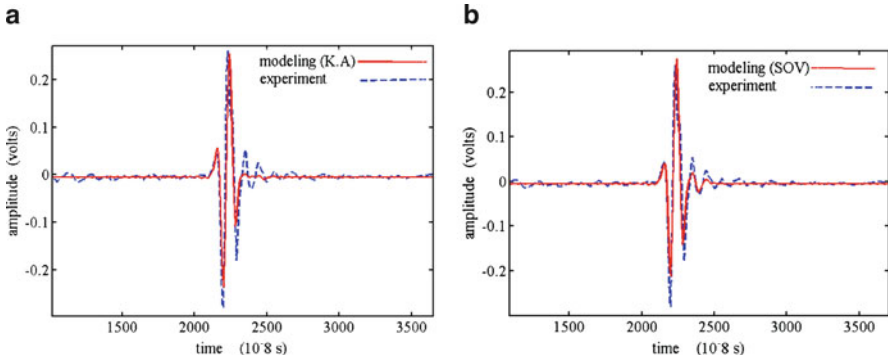
Fig. 3 Comparison between model predictions and experimental measurements. (**a**) Kirchhoff approximation and (**b**) exact separation of variables method for modeling the scattered waves

$$V_R(\omega) = \left[\int_L (\mathrm{v}_{SDH} / v_0)^2 dz \right] s(\omega) \left[\frac{A(\omega)}{L} \right] \left[\frac{4\pi}{-ik_{p2}a^2} \cdot \frac{\rho_2 c_{p2}}{\rho_1 c_{p1}} \right] \quad (12)$$

Three ingredients including the incident wave field, v_{SDH}/v_0, the system function, $s(\omega)$, and the scattered field, $A(\omega)$, were determined in the previous sections using multi-Gaussian beam model, the reference reflector model, and the Kirchhoff approximation, respectively. This general ultrasonic measurement model can predict ultrasonic signals from a SDH.

In order to validate the model, an experiment was carried out on a standard AWS calibration block. The longitudinal wave was generated by a 12.7 mm diameter focused circular transducer (focal length = 50.8 mm) having a center frequency of 10 MHz. Figure 3 shows the model predictions and the experimental signal captured by the focused circular transducer.

The early parts of the modeled signal in Fig. 3a agree very well with the experimental response. However, there are some small trailing creeping waves in the experimental signal that are not predicted by this model. This is to be expected since this model is based on the Kirchhoff approximation which neglects such creeping waves that travel around the flaw and return back to the receiver. On the other hand, as shown in Fig. 3b, more accurate results are obtained by using the SOV model for wave scattering from the SDH. The SOV method can model creeping waves and calculate the exact scattering response of a SDH.

Cross-correlation is used to measure compatibility between the two models and the experiment. Correlation coefficient between experimental and the signal estimated in Fig. 3a is 0.9085. This coefficient for the exact model estimated by the SOV model is 0.9217. This confirms the higher accuracy of the SOV technique in modeling the ultrasonic signals.

Conclusion

In this paper, we have developed an approach for modeling signals captured by focused circular ultrasonic transducers by combining some analytical methods in both beam field and scattering model calculations. The validity of the proposed model was verified by comparing the modeled and experimental signals. The cross-correlation coefficient also confirms the good agreement between model predictions and experimental measurements conducted on a SDH.

References

[1] H. J. Kim, S. J. Song and L. W. Schmerr, (2004), *J. Nondestruct. Eval.*, vol. 23, n. 1, pp. 11–19.
[2] D. Placko, T. Yanagita, E. K. Rahani and T. Kundu, (2010), *IEEE Trans. Ultra. Ferro. Freq. Cont.*, vol. 57(6), pp. 1396–1404.
[3] H. J. Kim, J. S. Park, S. J. Song and L. W. Schmerr, (2004), *J. Nondestruct. Eval.*, vol. 23 n. 3, pp. 81–93.
[4] H. J. Kim, S. J. Song and L. W. Schmerr, (2006), Ultrasonic, vol. 44, pp. 969–974.
[5] L. W. Schmerr, T. P. Lerch, and A. Sedov, (1994), *In Rev. Prog. Quant. Nondestruct. Eval., New York*, vol. 13A, pp. 69–74.
[6] S. Das, S. Banerjee, and T. Kundu, (2008), *Int. J. Solids Struct.*, vol. 45(16), pp. 4498–4508.
[7] B. P. Newberry, R. B. Thompson, and E. F. Lopes, (1987), *In Rev. Prog. Quant. Nondestruct. Eval., New York*, vol. 6A, pp. 639–647.
[8] L.W. Schmerr, and S.J. Song, (2007), In: *Ultrasonic Nondestructive Evaluation Systems: Models and Measurements*, Springer.
[9] L. W. Schmerr, (1988), In: *Fundamentals of Ultrasonic Nondestructive Evaluation–A Modeling Approach*, Plenum Press, New York and London.
[10] J. J. Wen and M. A. Breazeale, (1988), *J. Acoust. Soc. Am.*, vol. 83(5), pp 1752–1756.

A Theoretical Study on Scattering of Surface Waves by a Cavity Using the Reciprocity Theorem

H. Phan, Y. Cho and J.D. Achenbach

Abstract Scattering of surface waves by a two-dimensional cavity, which is on the free surface of an elastic half-space, is theoretically investigated in the current paper. It is shown that the expressions for the scattered field displacements are derived in an elegant approach by using the reciprocity theorem and the decomposition technique that decomposes the total field into incident and scattered fields. The displacements of the scattered field then can be analytically obtained by the reciprocity theorem. The achieved solutions are verified by the Boundary Element Method (BEM) modeling of two-dimensional wave propagation in elastic half-spaces that applies a truncation of the infinite boundary to account for the contribution of the omitted part. The comparisons of displacements are graphically displayed and show the agreements between analytical and numerical results.

Keywords Surface wave • Cavity • Half-space • Reciprocity theorem • BEM

Introduction

The studies of Rayleigh wave interaction with defects were motivated by the fact that Rayleigh waves have been used extensively in the area of nondestructive testing and evaluation to locate and size surface defects. Defects such as cracks, voids, cavities and corrosions act as the sources of acoustic scattering when illuminated by incident pulses through reflection, diffraction, and mode conversion. In the current

H. Phan • Y. Cho (✉)
School of Mechanical Engineering, Pusan National University, Busan, South Korea
e-mail: mechcyh@pusan.ac.kr

J.D. Achenbach
Northwestern University, Evanston, IL 60208, U.S.A

paper, we present a new theoretical approach to the scattering of surface waves by a two-dimensional cavity in an elastic half-space using the reciprocity theorem.

A homogeneous, isotropic, linearly elastic solid which occupies the half-space $z \geq 0$, contains a 2D cavity on the surface. The total field generated by interaction of the incident surface wave and the cavity can be expressed

$$\mathbf{u}^t = \mathbf{u}^i + \mathbf{u}^s \tag{1}$$

where $\mathbf{u}^i$ is the incident field, and $\mathbf{u}^s$ denotes the scattered field. The total field in the half-space is taken as the superposition of the specified incident field in the without-cavity half-space whose solution is well-known in several references [1] and the scattered field in the with-cavity half-space. The scattered fields due to a time-harmonic surface wave upon the cavity from far-field are investigated in this paper.

Rayleigh Waves in an Elastic Half-space

The displacements of Rayleigh waves traveling in the positive x - direction along the free surface of an elastic half-space may be written as follows [1] [2]

$$u_x = iAU^R(z)e^{i(kx-\omega t)} \tag{2}$$

$$u_z = AW^R(z)e^{i(kx-\omega t)} \tag{3}$$

where

$$U^R(z) = d_1 e^{-kpz} + d_2 e^{-kqz} \tag{4}$$

$$W^R(z) = d_3 e^{-kpz} - e^{-kqz} \tag{5}$$

The corresponding stresses of surface waves can be written as

$$\tau_{xx} = AT_{xx}^R(z)e^{i(kx-\omega t)} \tag{6}$$

$$\tau_{xz} = iAT_{xz}^R(z)e^{i(kx-\omega t)} = \tau_{zx} \tag{7}$$

$$\tau_{zz} = AT_{zz}^R(z)e^{i(kx-\omega t)} \tag{8}$$

where

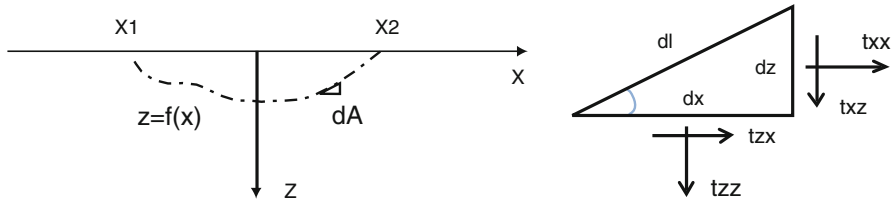$$T_{xx}^R(z) = k\mu(d_4 e^{-kpz} + d_5 e^{-kqz}) \tag{9}$$

Fig. 1 Cavity and stress analysis

$$T_{xz}^R(z) = k\mu(d_6 e^{-kpz} + d_7 e^{-kqz}) = T_{zx}^R(z) \tag{10}$$

$$T_{zz}^R(z) = k\mu(d_8 e^{-kpz} + d_9 e^{-kqz}) \tag{11}$$

Here, $d_1 - d_9$ and p, q, μ are constant depending on material property and k is wavenumber.

Consider now the boundary of the virtual cavity in a half-space

$$z = f(x) \tag{12}$$

The cavity which is smooth is shown in the Fig. 1, together with an element dA.

The horizontal and vertical force components are obtained respectively as follows

$$dQ_x = t_x d\ell = k\mu A \bar{Q}_x dx \tag{13}$$

$$dP_z = t_z d\ell = k\mu A \bar{P}_z dx \tag{14}$$

where

$$\bar{Q}_x = \left[-\left(d_4 e^{-kpf(x)} + d_5 e^{-kqf(x)}\right) f'(x) + i\left(d_6 e^{-kpf(x)} + d_7 e^{-kqf(x)}\right) \right] e^{ikx} \tag{15}$$

$$\bar{P}_z = \left[-i\left(d_6 e^{-kpf(x)} + d_7 e^{-kqf(x)}\right) f'(x) + \left(d_8 e^{-kpf(x)} + d_9 e^{-kqf(x)}\right) \right] e^{ikx} \tag{16}$$

Application of Reciprocity Theorem

Consider the point loads at (x_0, z_0) of element dA. The region V is defined by $a \le x \le b, z \ge 0$ as in Fig. 2.
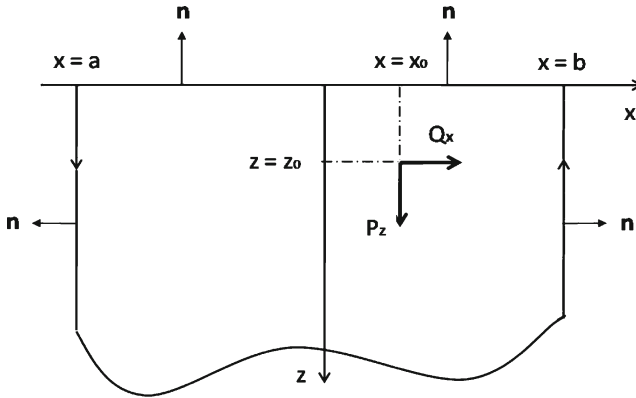
Fig. 2 Half-space subjected to two time-harmonic point loads

For state A, the body forces, including the vertical P_z and the horizontal Q_x given in (13)-(14) but with an opposite sign. The displacements and the stresses are given as

$$u_x^A(x,z) = \pm i A_{Sc}^{x_0} U^R(z) e^{\pm ik(x-x_0)}, \; u_z^A(x,z) = A_{Sc}^{x_0} W^R(z) e^{\pm ik(x-x_0)}, \tau_{xx}^A(x,z) = A_{Sc}^{x_0} T_{xx}^R(z) e^{\pm ik(x-x_0)} \quad (17)$$

$$\tau_{zx}^A(x,z) = \pm i A_{Sc}^{x_0} T_{zx}^R(z) e^{\pm ik(x-x_0)}, \tau_{xz}^A(x,z) = \pm i A_{Sc}^{x_0} T_{xz}^R(z) e^{\pm ik(x-x_0)}, \tau_{zz}^A(x,z) = A_{Sc}^{x_0} T_{zz}^R(z) e^{\pm ik(x-x_0)} \quad (18)$$

(Here, plus sign for the positive x-direction and minus sign for the negative x-direction).

For state B, the virtual wave, we select a surface wave in the positive x-direction

$$u_x^B(x,z) = i B U^R(z) e^{ikx}, u_z^B(x,z) = B W^R(z) e^{ikx}, \tau_{xx}^B(x,z) = B T_{xx}^R(z) e^{ikx} \quad (19)$$

$$\tau_{zx}^B(x,z) = i B T_{zx}^R(z) e^{ikx}, \; \tau_{xz}^B(x,z) = i B T_{xz}^R(z) e^{ikx}, \; \tau_{zz}^B(x,z) = B T_{zz}^R(z) e^{ikx} \quad (20)$$

Apply the reciprocity relation (see [1]) and note that the integrations along $x = a, 0 \le z < \infty$, and $x = b, 0 \le z < \infty$, only yield contributions from counter-propagation waves, we finally have

$$\frac{A_{Sc}^{x_0}}{A_{In}} = \frac{k}{2E} \left[-\bar{Q}_x(x_0, z_0) U^R(z_0) + i \bar{P}_z(x_0, z_0) W^R(z_0) \right] dx_0 \quad (21)$$

where

$$E = \left(\frac{d_4 d_1 - d_6 d_3}{2p} + \frac{d_4 d_2 + d_5 d_1 - d_7 d_3 + d_6}{p+q} + \frac{d_2 d_5 + d_7}{2q} \right) \quad (22)$$

We have to integrate Eq. (21) over the cavity boundary to obtain the total ratio in the positive direction

$$\frac{A_{Sc}}{A_{In}} = \int_{x_1}^{x_2} \frac{A_{Sc}^{x_0}}{A_{In}} e^{-ikx_0} = \frac{k}{2E} \int_{x_1}^{x_2} \left[-\overline{Q}_x U^R(z) + i\overline{P}_z W^R(z) \right] e^{-ikx} dx \tag{23}$$

Boundary Element Method

The Boundary Element Method (BEM) is used in this paper to obtain numerical results for comparison with the analytical solutions. Depending on the idea of Rayleigh wave correction ([3], [4]), a BEM code has been written in FORTRAN to simulate the two-dimensional scattering of surface waves by a cavity a half-space. The boundary conditions applying for the scattered field are the traction values obtained theoretically at the positions of the cavity boundary but in the opposite sign. With this idea, the problem has been solved numerically by the direct frequency domain boundary element method which allows the undamped Rayleigh waves propagating along the infinite surface to escape the computational domain without producing spurious reflections from its limits.

Example of Calculation: Scattering by a Circular Cavity

A circular cavity which has a depth D and a width $l = 2R_0$ is defined by

$$z = f(x) = \sqrt{R^2 - x^2} - z_0 \tag{24}$$

By a change of variable from x to $\overline{x} = kx$, $\overline{R} = kR, \overline{R}_0 = kR_0, \overline{D} = kD, \overline{z}_0 = kz_0$, we finally obtain the following form

$$\frac{A_{Sc}}{A_{In}} = \frac{i}{E} \int_0^{\overline{R}_0} \left(\left(d_3 d_8 - d_1 d_6 \right) e^{-2p\left(\sqrt{\overline{R}^2 - \overline{x}^2} - \overline{z}_0\right)} \right.$$

$$\left. + \left(-d_1 d_7 - d_2 d_6 - d_8 + d_3 d_9 \right) e^{-(p+q)\left(\sqrt{\overline{R}^2 - \overline{x}^2} - \overline{z}_0\right)} + \left(-d_2 d_7 - d_9 \right) e^{-2q\left(\sqrt{\overline{R}^2 - \overline{x}^2} - \overline{z}_0\right)} \right) d\overline{x}$$

$$\tag{25}$$

Keep $\overline{R}_0 / \overline{D} = 2$ while $\overline{D}$ changes from 0 to 0.8. Presented in Fig. 3b) is comparison between analytical and BEM results that shows good agreement as $kR_0 \leq 1.25$. Since $k = 2\pi / \lambda$, then $R_0 \leq 0.20\lambda$. Beyond $R_0 \approx 0.20\lambda$, the theoretical results start deviating significantly from the exact BEM results. This can be attributed to the limitations on the theoretical approach which is valid only for D, R_0 relatively small compared with wavelength λ.
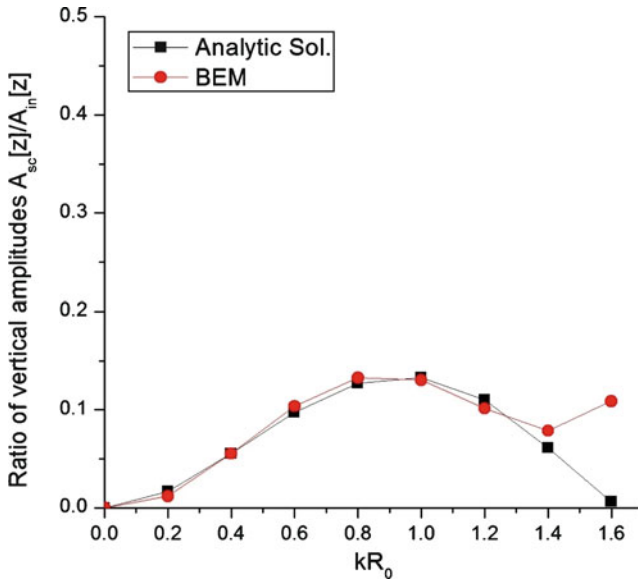
Fig. 3 Ratio of vertical amplitudes of the scattered and incident waves

Conclusion

Using the reciprocity theorem, the scattering of surface waves by a 2D cavity in a half-space could be solved in a much simpler manner to derive the ratios of the vertical displacement amplitudes of the scattered to incident surface waves in terms of dimensionless quantities $\bar{R}_0$ and $\bar{D}$. Comparisons between theoretical and BEM results are in good agreement for depth D and half of width R_0 relatively small compared with wavelength λ .

References

[1] J. D. Achenbach (2003), *Reciprocity in Elastodynamics*, Cambridge University Press, Cambridge
[2] J. D. Achenbach (1973), *Wave Propagation in Elastic Solids*, Elsevier Science, Amsterdam
[3] J. Dominguez (1993), *Boundary Elements in Dynamics*, Computational Mechanics Publications, Elsevier, Southampton
[4] I. Arias and J. D. Achenbach (2004), *Int. J. Numer. Meth. Eng.*, vol. 60, p. 1–16

Half-Space Dynamic Stiffness Models Compatible with the Thin Layer Formulation for Use in Response Analysis of Soil Profiles

M.A. Ceballos and C.A. Prato

Abstract This work presents two new wave propagation models for the half-space compatible with the thin layer formulation (TLF). The TLF is based on a polynomial expansion in the wave number κ of the exact matrix of the dynamic stiffness of a layer. The advantage of the TLF with respect to the exact model is that it allows transforming the soil profile response between wave number and spatial domains in analytical form through the decomposition of response in wave propagation modes. The expansion in κ applied to the exact matrix of the half-space does not produce a satisfactory approximation for moderate or large values of κ. Therefore, the TLF in its original form only reproduces with good accuracy the response of soil profiles composed by an assembly of layers over an infinitely stiff half-space. The proposed models eliminate such shortcomings and adequately represent the half-space stiffness in the wave number domain. The techniques used for adjustment of mechanical soil profiles generally represent the half-space through an assembly of strata with increasing thickness in depth. Such approach produces acceptable accuracy in the wave propagation velocity of the fundamental mode for normally dispersive profiles (with increasing stiffness in depth), although it generates spurious modes not related with higher propagation modes. The adjustment of mechanical parameters of inversely dispersive profiles requires an adequate approximation of the half-space dynamic behavior given the significant contribution of the higher propagation modes to the response. The proposed models are suitable for the adjustment of soil profiles with an arbitrary distribution of stiffness in depth and for evaluating the dynamic stiffness of foundations.

Keywords Half-space stiffness matrix • Modal analysis • Soil profiles • Surface waves • Thin layer formulation

M.A. Ceballos (✉) • C.A. Prato
Department of Structures, National University of Cordoba, Av. Velez Sarsfield 1611,
X5016GCA, Cordoba, Argentina
e-mail: mceballo@efn.uncor.edu

Introduction

Two new models capable of representing the dynamic behavior of the half-space located at the base of soil profiles are presented in what follows. These models allow the modal description of the spatial response of stratified soil profile through the contribution of different wave propagation modes, and are suitable for soil profiles adjustment based in multiple propagation modes analysis using multiple transducers [1]. These models could be considered a refinement of the "thin layers formulation" (TLF) presented in works of Kausel and Roësset [2–4]. In the present work only the *SV–P* wave patterns produced by axi-symmetrical vertical loads are analyzed.

Modal Description of the Half-space Flexibility

The proposed improvement to the wave propagation model is based on an approximation in two steps of the half-space dynamic flexibility through modal parameters in the wave number domain that are forced to take on the exact values for the nil wave number and, if possible, when the wave number tends to infinity. The unbounded amplitudes of the flexibility components are avoided "discounting" the exact Rayleigh wave propagation mode, which in turn is added to the modal model at the end of the approximation process. In a first step, the "remaining" flexibility is adjusted with a matrix fraction polynomial using the least square criterion. In a second step, a fine adjustment of the modal parameters through an iterative process is carried out based on gradient techniques. This procedure needs to be repeated for each value of interest of the Poisson coefficient. The use of generalized coordinates allows obtaining square matrices of modal parameters that can be transformed in physical matrices of the half-space. These matrices can then be directly assembled with the strata matrices derived with the TLF.

The dimensionless coefficients of the remaining half-space flexibility $\tilde{F}$ are fitted in the dimensionless wave number domain κ using modal analysis techniques [5–6]. The formulation may take two alternative forms depending on the application in mind, as follows:

a) κ^2 model. The flexibility is approximated using a fraction polynomial with even powers only that produces 2° order eigenvalues:

$$\tilde{F} = \left(Q_0 + \kappa^2 Q_2 + \ldots + \kappa^n Q_n + \kappa^{n+2} I\right)^{-1} \left(R_0 + \kappa^2 R_2 + \ldots + \kappa^n R_n\right) \tag{1}$$

b) κ^1 model. The flexibility is approximated using a fraction polynomial with an arithmetic progression of powers that produces 1° order eigenvalues:

$$\tilde{F} = \left(Q_0 + \kappa Q_1 + \ldots + \kappa^n Q_n + \kappa^{n+1} I\right)^{-1} \left(R_0 + \kappa R_1 + \ldots + \kappa^n R_n\right) \tag{2}$$

The κ^2 model produces half-space stiffness matrices with an identical mathematical structure to the strata matrices of the TLF. This model has as main advantage a direct assembly with the strata matrices, and allows obtaining the response in the spatial domain through analytical versions of the Hankel transform. Its main disadvantage is related with an intrinsic characteristic of the approximation in κ^2 by which it does not allow to adequately reproduce the response in the wave number domain for high values of κ. This model is suitable for the adjustment of mechanical parameters of stratified soil profiles using experimental data but is not effective for evaluation of dynamic stiffness of foundations since its approximation distorts the response at low frequencies, mainly in zones close to the applied loads.

The κ^1 model has as main advantage an adequate precision of the flexibility in the complete range of the wave number domain, and provides a convenient alternative for the dynamic analysis of foundations, even for low frequencies. Its main disadvantage is related to its incapacity to reduce the quadratic eigenvalue problem of the complete profile (layers and half-space) into a linear eigenvalue problem as in the original TLF. Therefore, it may require to use analytic expressions of the Hankel transform, not always available, in order to avoid the use of numerical integration to obtain the response in the spatial domain.

The half-space dynamic flexibility in a vertical plane XZ using the κ^1 model is expressed in function of $1°$ order eigenvalues as:

$$F = \begin{bmatrix} \Psi_x \\ \Psi_z \end{bmatrix} \left[\kappa I - K_R \right]^{-1} \begin{bmatrix} \Psi_x^T & \Psi_z^T \end{bmatrix} = \begin{bmatrix} \Psi_x (\kappa I - K_R)^{-1} \Psi_x^T & \Psi_x (\kappa I - K_R)^{-1} \Psi_z^T \\ \Psi_z (\kappa I - K_R)^{-1} \Psi_x^T & \Psi_z (\kappa I - K_R)^{-1} \Psi_z^T \end{bmatrix} \quad (3)$$

where K_R is a diagonal matrix with M eigenvalues. Ψ_x and Ψ_z are row vectors with the radial and vertical components, respectively, of the modal shapes. Since the modal matrices of the κ^2 model have identical mathematical structure to that of the TLF matrices, the dynamic flexibility can be expressed in terms of N pairs of eigenvalues as:

$$F = \begin{bmatrix} \overline{\Psi}_x & i\overline{\Psi}_x \\ \overline{\Psi}_z & -i\overline{\Psi}_z \end{bmatrix} \begin{bmatrix} \kappa I - \overline{K}_R & 0 \\ 0 & \kappa I + \overline{K}_R \end{bmatrix}^{-1} \begin{bmatrix} \overline{\Psi}_x^T & \overline{\Psi}_z^T \\ i\overline{\Psi}_x^T & -i\overline{\Psi}_z^T \end{bmatrix} \quad (4)$$

which leads to:

$$F = 2 \begin{bmatrix} \overline{\Psi}_x \overline{K}_R (\kappa^2 I - \overline{K}_R^2)^{-1} \overline{\Psi}_x^T & \kappa \overline{\Psi}_x (\kappa^2 I - \overline{K}_R^2)^{-1} \overline{\Psi}_z^T \\ \kappa \overline{\Psi}_z (\kappa^2 I - \overline{K}_R^2)^{-1} \overline{\Psi}_x^T & \overline{\Psi}_z \overline{K}_R (\kappa^2 I - \overline{K}_R^2)^{-1} \overline{\Psi}_z^T \end{bmatrix} \quad (5)$$

$$F = \begin{bmatrix} \Phi_x (\kappa^2 I - \overline{K}_R^2)^{-1} \Phi_x^T & \kappa \Phi_x \overline{K}_R^{-1} (\kappa^2 I - \overline{K}_R^2)^{-1} \Phi_z^T \\ \kappa \Phi_z \overline{K}_R^{-1} (\kappa^2 I - \overline{K}_R^2)^{-1} \Phi_x^T & \Phi_z (\kappa^2 I - \overline{K}_R^2)^{-1} \Phi_z^T \end{bmatrix} \quad (6)$$

where the relationship between the modal shapes of both models is in the form:

$$\Phi_x = \sqrt{2} \, \overline{\Psi}_x \overline{K}_R^{1/2} \qquad\qquad \Phi_z = \sqrt{2} \, \overline{\Psi}_z \overline{K}_R^{1/2} \quad (7)$$
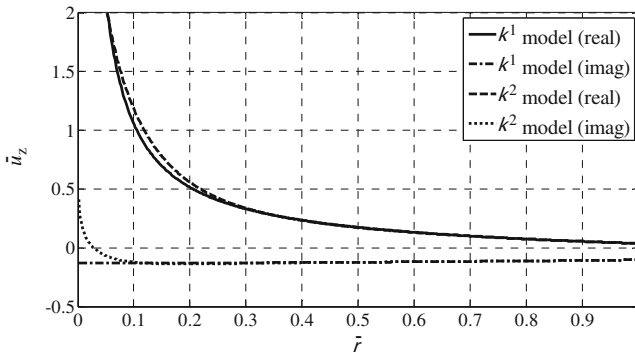
Fig. 1 Vertical displacement in the spatial domain for a vertical point load

The form of the coupling terms in Eqn. (6) is imposed during the fine adjustment step. A quantity of hysteretic material damping can be added to the profile model through its eigenvalues prior the transformation to the spatial domain:

$$\kappa_n^* = \kappa_n / (1 + i\beta) \tag{8}$$

At the same time, the addition of damping to the modal shapes of both models allows preserving the exact value of the half-space flexibility for $\kappa = 0$.

Application Cases of the Half-space Models

Some applications of the proposed half-space models are presented in this section. The κ^1 model is useful for the calculation of the dynamic stiffness of foundations although it presents a high computational cost if the analytical solutions to transform the contribution of each mode to the response are not known (numerical Hankel transforms are necessary). On the other hand, the κ^2 model is useful for the adjustment of soil profiles. Such application does not require the calculation neither of quasi-static responses nor of responses near the zone of the applied load.

Dynamic response in the half-space surface

Figure 1 shows the components of the vertical displacement produced by a vertical point load P applied on the surface of a homogeneous half-space with Poisson coefficient $\nu = 1/3$. The radial coordinate ρ and the vertical displacement u_z are converted into dimensionless parameters as follows:

$$\bar{\rho} = \omega / V_S \cdot \rho \qquad \bar{u}_z = \delta V_S^3 / (\omega P) \cdot u_z \tag{9}$$
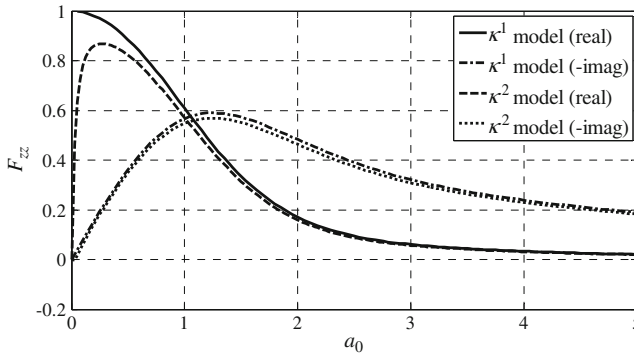
Fig. 2 Vertical dynamic flexibility of a rigid disc

where ω is the analysis frequency, V_S is the propagation velocity of shear waves and δ is the half-space density. It is observed that the κ^2 model does not adequately reproduce the response near the applied load, although the agreement significantly improves for radial coordinates greater than 0.4 where both models coincide.

Figure 2 shows the vertical dynamic flexibility F_{zz} of a rigid disc of radius R over a homogeneous half-space with Poisson coefficient $\nu = 1/3$. The ordinates are converted into dimensionless parameters using the static flexibility. The dimensionless frequency $a_0 = R / V_S \cdot \omega$ is used. It is observed that the κ^2 model does not have the capacity to reproduce the static flexibility since the flexibility components for high values of the wave number (that controls the low frequencies) asymptotically decrease with κ^2. On the other hand, these components in the κ^4 model decrease with κ just like the exact expressions.

Mechanical parameters adjustment of stratified soil profiles

The adjustment of mechanical parameters of stratified soil profiles can be carried out using the κ^2 model to obtain the response in analytical form in terms of model modal parameters. The hypothesis of considering the point vertical load applied on the surface during the tests allows calculating the axi-symmetrical vertical spatial response as:

$$u_z(\kappa) = \sum_{n=1}^{2N} \frac{\phi_{z,n}^2}{(\kappa^2 - \kappa_n^2)} \qquad \Leftrightarrow \qquad u_z(\rho) = \frac{1}{4i} \sum_{n=1}^{2N} \phi_{z,n}^2 \, H_0^{(2)}(\kappa_n \rho) \qquad (10)$$

where $H_0^{(2)}(\ldots)$ represent the Hankel function of order 0 and type 2. Care should be taken in placing the transducers sufficiently away of the applied load given that this model does not have adequate capacity to represent the response close to the applied load. The use of experimental data at low frequencies should be avoided due to the incapacity of this model to reproduce the quasi-static response. Nevertheless, this restriction does not represent a relevant practical limitation since the experimental

data presents low coherence values for low frequencies due to the energy needed to produce a response with sufficient contrast respect to the noises.

Conclusions

The adjustment of flexibility matrix coefficients of a homogeneous half-space in the wave number domain through modal parameters has led to two alternative models for the analysis of the dynamic response of stratified soil profiles. Both models can be assembled with the strata matrices of the thin layers formulation commonly used in practical cases since it allows transforming the response from the wave number domain to the spatial domain in analytical closed form. The κ^1 model is suitable for use in determining the dynamic stiffness of shallow or embedded foundations. The κ^2 model can be used with advantage in adjustment algorithms for mechanical parameters of soil profiles.

The applications presented of the proposed models show the advantages and shortcomings of both models. The main advantage of the κ^2 model is its complete compatibility with the thin layers formulation to obtain the spatial response without more precision losses than those involved in the approximation of the half-space flexibility coefficients. A disadvantage of this model is that it does not have the capacity to reproduce the response neither close the load nor for low frequencies of analysis. On the other hand, the κ^1 model adapts satisfactorily to the exact values of the half-space flexibility in the complete range of the wave number domain. Nevertheless, the analytical expressions that would allow transforming in closed form the contribution of each mode to the response between both domains are not always available.

References

[1] Ceballos, M.A. and Prato, C.A. (2011), "Experimental Estimation of Soil Profiles through Spatial Phases Analysis of Surface Waves", *Soil Dynamics and Earthquake Engineering*, vol. 31, n. 1, p. 1–104.
[2] Kausel, E. (1974), "Forced Vibrations of Circular Foundations on Layered Media", *MIT Research Report R74–11*, Cambridge, MA, U.S.A.
[3] Kausel, E. (1981), "An Explicit Solution for the Green Functions for Dynamic Loads in Layered Media", *MIT Research Rep. R81-13*, Cambridge, MA, U.S.A.
[4] Kausel, E. and Roesset, J.M. (1981), "Stiffness matrices for layered soils", *Bulletin of the Seismological Society of America*, vol. 71, n. 6, p. 1743–1761.
[5] Juang, J–.N. (1994), *Applied System Identification*, PTR Prentice-Hall Inc., NJ, U.S.A.
[6] Wolf, J.P. (1994), *Foundation Vibration Analysis Using Simple Physical Models*, PTR Prentice-Hall Inc., NJ, U.S.A.

Section 7
NDT of Civil Infrastructures

Automated NDE of Structures with Combined Methods

H. Wiggenhauser

Abstract Non-Destructive Evaluation (NDE) of structures is complex due to the uniqueness of almost all structures and their sizes. A single NDT method typically is not sufficient to meet the testing requirements, which cover different areas, such as material and structural properties. Measuring geometrical properties require other test methods than e.g. the detection of corrosion. Automation has proven to be necessary for aquiring large amounts a of high quality data in a short time. Examples of succesful method combinations from different areas of non-destructive testing in civil engineering are briefly described and their application is shown. Some of the examples also include automated inspection.

Keywords Civil engineering • NDT • Inspection • Combined methods • Automation

Introduction

Non-destructive evaluation (NDE) of structures has become a common practice in recent years. Progress in sensor development, more powerful data processing and the availability of improved software made the application and interpretation of data derived from non-destructive testing (NDT) methods easier. This is especially beneficial at the construction site for the inspection of existing structures.

NDE of concrete structures is a complex task, mainly because of the uniqueness of almost all structures, the inhomogeniety of the material and the material mix, especially in post tensioned (PT) structures. The service life of concrete structures typically exceeds the life span of the involved architects and engineers. Drawings and other data are often lost over the years. In these cases the structure must be assessed down to its last component.

H. Wiggenhauser (✉)
BAM - Federal Institute for Materials Research and Testing, Berlin, Germany
e-mail: herbert.wiggenhauser@bam.de

Single testing methods may be very powerful, but combination of methods has always been seen as the future of NDT in Civil Engineering (NDT-CE). Also automation is identified to be necessary because of the size of the structures and the need for high quality, reproducible data.

There are many examples for successful combination of NDT-CE methods, a few are highlighted in this contribution.

Visual Inspection and NDT

Visual inspection (VI) is the most commonly used inspection technique and it has proven its capability and reliability in many cases. Bridge inspection as it is mandatory in many countries is based on VI. Qualified inspectors visit the structure and follow an established procedure. Typically, there are regular inspections between in-depth inspections in pre-defined intervals (3 years in Germany and the USA) [1,2].

For in-depth inspections the inspector appraches the components of the bridge at arms length, commonly used instruments are a tapping hammer for concrete surfaces. For metal structures, additional instruments may be used, such as ultrasonic probes or eddy current to inspect bolts and other metal parts. The inspector assigns a condition rating for each bridge.

DIN-EN 1076 [1] in detail describes the inspection for bridges and other structures on federal roads in Germany. In addition EWB-PRÜF [3] provides sample cases for individual members of a structure. The overall condition rating of a structure is determined from ratings of all components of the bridge.

There are circumstances where VI is not sufficient to determine a condition. This case is regulated within the Object Oriented Damage Analysis (OSA) as described in the corresponding regulation [4]. This procedure sets a series of actions in place which is visualized in Fig. 1. Detailed studies may be used, preferably non-destructive ones in addition to VI.

This example illustrates, how VI is combined with complementary methods to reach a measurement based condition evaluation.

Tunnel Inspection (Spacetec)

Tunnels are expensive assets of any transportation infrastructure and a vital part of networks. Closure times for these bottlenecks are prohibitive under normal circumstances, any disruption of traffic may result in enormous user costs due to detours or waiting time. Inspection of tunnels is quite complicated, confined space, lighting conditions and air quality create a working environment which is unsupportive if not dangerous.

Automated tunnel inspection is an established method, carried out using a laser scanner to create an image of the tunnel surface with very good resolution (Fig. 2). At the same time, the profile of the tunnel is measured. In addition, an infrared channel can be used to get subsurface information such as the presence of moisture in the tunnel walls [5].
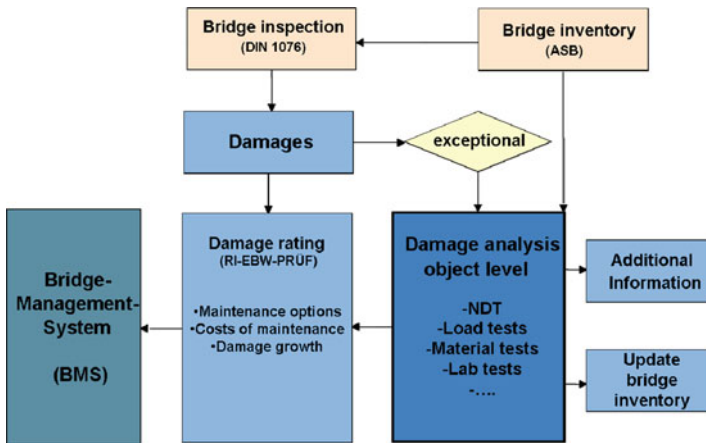
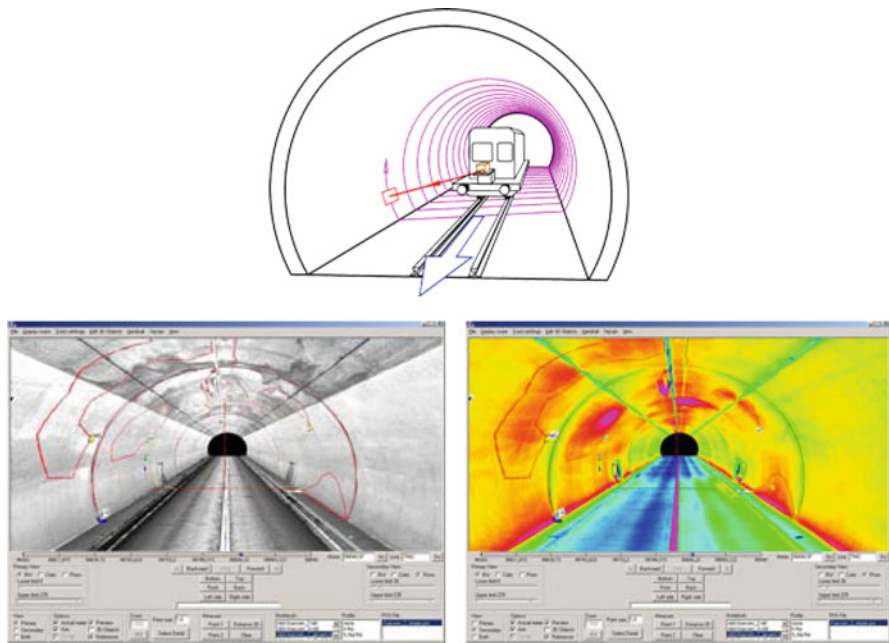**Fig. 1** OSA (Object Oriented Damage Analysis) as implemented by BASt [4]

Fig. 2 Spacetec tunnel inspection: principle of laser scanner (top) tunnel surface as measured with laser (left) thermographic image superimposed (right) [5, 6] (http://www.spacetec.de)

Virtual tunnel testing can be performed at any time based on the data from the scan through the tunnel. Combination of data recorded at different times or using complementary channels provide dedicated information to the inspector. Additional testing may be necessary if the data base is not sufficient or the interpretation needs additional support.
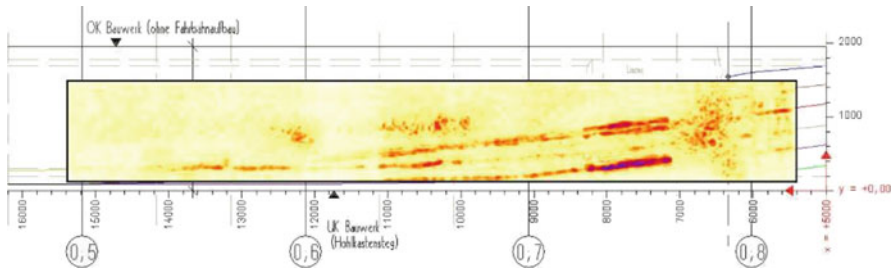
Fig. 3 Result of tendon duct inspection with GPR and Ultrasound using a scanner for automated measurements [7]

Advanced technology and computing power has been the basis for the development of this powerful testing system. The data base which is created at each scan of a tunnel enables the tunnel operator to call timely action for maintenance or rehabilitation. It also releases the inspectors largely from spending time in a unhealthy or even dangerous environment.

Tendon Duct Inspection with Ground Penetrating Radar (GPR) and Ultrasound

Post tensioned concrete structures form a large part of the infrastructure. The combination of steel and concrete has been a very successful development to meet the requirements of modern architecture and the needs of users.

The durability of PT concrete structures largely depends on the prevention of corrosion of the strands, which carry the load of the structure. Typically, the strands are inside a metallic duct, the space completely filled with cementitious material. The high pH value completely protects the steel from corrosion, any voids in the duct injection are a potential hazard. Identifying voids in tendon ducts therefore is a quality control measure to ensure the durability of the structure.

This testing task proved to be quite complex, due to the material of the components and precision required. A combination of GPR and ultrasound provides reliable results to locate ducts and closely examine the filling of the duct [7]. The use of a scanner is mandatory, to establish a precise coordinate system and to create high quality data for the large number of measurements being necessary. Figure 3 shows the result of such testing on a bridge in Vienna, where this concept was demonstrated.

GPR is used to locate the ducts, it is ideally suited for that task, because radar waves are fully reflected by metal. Acoustic waves can penetrate through the metal, the reflection carries properties of the material inside the duct. Recently, the phase of the acoustic waves reflected from the ducts is used to characterize the material interface [8].
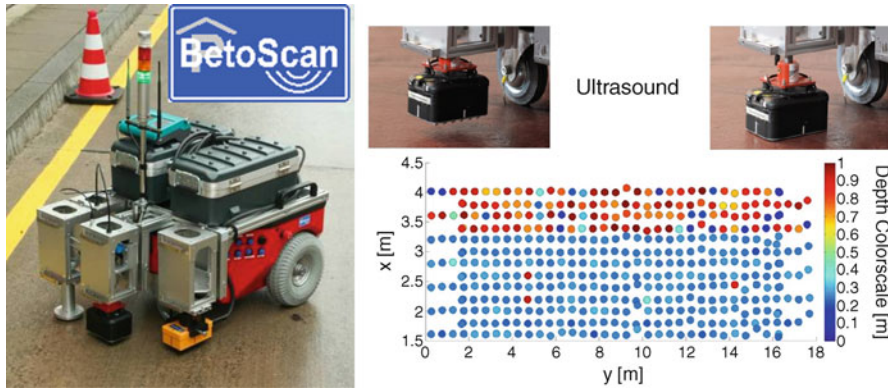
Fig. 4 Betoscan Multisensor Platform (left), result from ultrasonic thickness measurements (bottom right), and US probe lifted and in measurement position (top right)

GPR and Covermeter

Locating rebars is one of the most common testing tasks in civil engineering. There are a number of devices available for this task, from simple handheld devices to multi-probe units, some have scanning capabilities to visualize the rebars.

The testing task is to locate the rebar in its lateral position, and to determine its diameter and concrete cover. Additional layers of reinforcement may complicate this task. In such situations, the combination of GPR and a covermeter has proven to be successful. The additional information given by the covermeter supports the identification of lower lying tendom ducts [9].

Autonomous Multisensor NDT (Betoscan)

For the condition assessment of park decks, a multi sensor platform has been developed (Fig. 4). The basis is a self navigating robot, which can navigate on horizontal surfaces around obstacles within the area to be investigated. Within the *Betoscan* project, combinations of various testing systems have been tested and verified [10].

The assessment of a park deck needs complementary information about corrosion, cracks, reinforcement location, moisture, thickness of coating, chlorine content, thickness of a deck. All these parameters cannot be tested with a single probe, a variety of testing methods needs to be combined. Some of the methods require a very dense measurement grid, both for continous or point wise measurements.

The autonomous robot is equipped with a laser scanner and ultrasound sensors to identify its position and pose. Dedicated software allows to collect data from many different sensors simultaneously or in sequence.
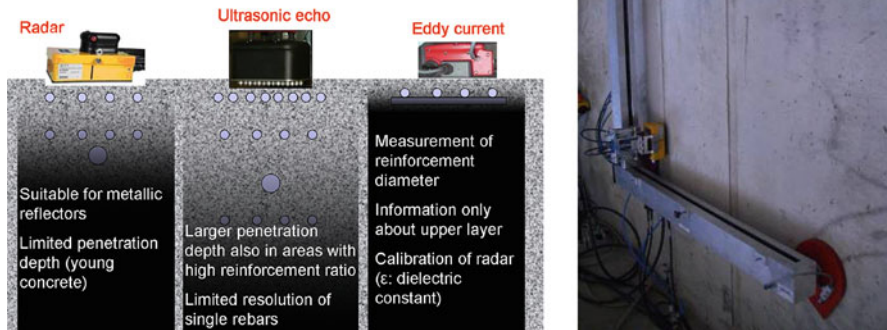
Fig. 5 OSSCAR Scanner: depth range of sensors (left), scanner mounted on bridge (right) [11]

In principle, the concept of *Betoscan* can be transferred to other horizontal surfaces, such as floors or bridge decks. It would be especially interesting for quality control after construction, to collect baseline data for subsequent assessments.

The system is especially suitable for specialized service providers offering high quality NDE. The high costs for the complete system are justified by its versatility and the large area it can test within one working day.

Scanner for Concrete Surfaces (OSSCAR)

Detailed inspection of reinforced concrete is a complex and challenging task. Best resuts have been obtained by a combination of three NDT devices: covermeter, GPR and ultrasound pulse echo. These three methods address different properties and depth ranges of the concrete under investigation.

The covermeter is best suited to locate rebars near the surface, radar can locate deeper lying reinforcement, such as tendon ducts. Ultrasound can penetrate through the metal duct and gets information about its grouting condition.

In the OSSCAR project [11] a scanner system was developed which can be used on all flat concrete surfaces (Fig. 5). Three vacuum attached legs hold a frame in place, the scanner can cover up to 0.8 m² at one position. The three sensors can be mounted very easily, and the surface can be scanned in a predefined grid. The data from all sensors can then be visualized together. This system is now comercially available and has already proven its capabilities in demonstration projects.
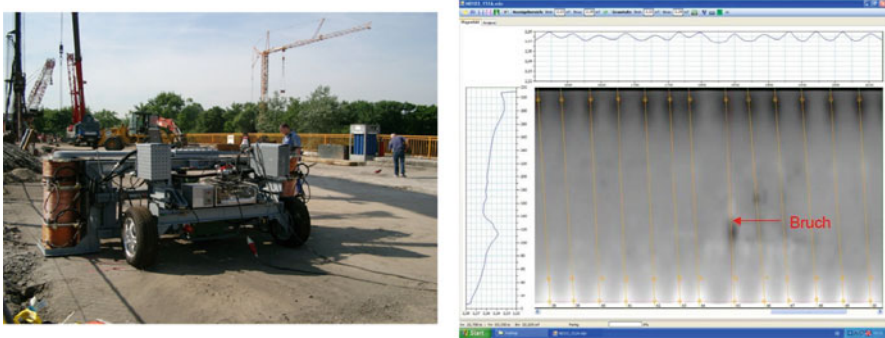
Fig. 6 Magnetic image of a bridge deck with breack detection [12]

Identification of Reinforcement Breaks with Magnetic Flux Leakage (MFL)

The breakage of a strand in a post- or pre-tensioned concrete structure can be a very serious threat to its safety. A non-destructive tesing solution has been found for this testing task, magnetic flux leackage [12, 13]. This method may identify any fissures of strands under certain conditions. Being very sensitive, this method needs to be applied with care and a good knowledge of the underlying principles.

Even early applications were based on automated measurements. Rails were used to position the magnet and the sensors to conduct the measurement. In order to be able to follow the reinforcement with the magnet, its position has to be determined. GPR is the natural choice for this task.

The power of combining two methods becomes apparent with MFL, because the localisation of tendons would otherwise be very time consuming, if not impossible. The MFL also benefits from the GPR measurements, the magnet can be guided precisely along the tendon, avoiding any disturbance that might originate from nearby other metallic elements.

Using a vary large magnet and a sensor scanner, MFL measurements can be done over large areas in very short times. Figure 6 shows the magnetic image of a bridge deck, generated from such tests.

Conclusions

Combination of NDT methods is a successful strategy to master testing tasks for NDT in civil engineering. A number of cases has been shown, where the combination has been justified and positive.

Examples for automation are less frequent, but there are many projects emerging from research with this focus. The technology becomes available and more examples can be expected in the near future.

References

[1] DIN 1076–Ingenieurbauwerke im Zuge von Straßen und Wegen; Überwachung und Prüfung, Ausgabe November (1999), Beuth Verlag Berlin

[2] M. Moore, B. Phares, D. Rolander, B. Graybeal, and G. Washer, Reliability of Visual Inspection for Highway Bridges, Volume I: Final Report, USDOT (FHWA–RD–01–020), Washington, DC, (2001)

[3] Richtlinie zur einheitlichen Erfassung, Bewertung, Aufzeichnung und Auswertung von Ergebnissen der Bauwerksprüfungen nach DIN 1076, RI-EBW-PRÜF, BMVBW (2004)

[4] Leitfaden Objektbezogene Schadensanalyse, OSA, BASt (2004)

[5] A.Wiesler, Thermografie in Tunnelbauwerken, Fachtagung Bauwerksdiagnose 23–24. Februar 2006, Berlin, Deutsche Gesellschaft für Zerstörungsfreie Prüfung, Berlin, (2006)

[6] http://www.spacetec.de

[7] D. Streicher, Ch. Kohl, H. Wiggenhauser und A. Taffe, Automatisierte zerstörungsfreie Zustandsuntersuchungen von Brückenbauwerken, Beton- und Stahlbeton 101 (2006), 5, 330–342

[8] K. Mayer, K.–J. Langenberg, M. Krause, B. Milmann and F. Mielentz, Characterization of reflector types by phase-sensitive ultrasonic data processing and imaging, Journal of nondestructive Evaluation 27 (2008), Plenum Press, 1573–4862

[9] M. Pöpel and C. Flohrer: Combination of a Covermeter with a Radar System–an Improvement of Radar Application in Civil Engineering, Int. Sympos. Non-Destructive Testing in Civil Engineering, DGZfP, Berlin (1995)

[10] K. Reichling, M. Raupach, H. Wiggenhauser, M. Stoppel, G. Dobmann and J. Kurz: BETOSCAN – Robot controlled non-destructive diagnosis of reinforced concrete decks; NDTCE `09 – 7th int. sympos. Non-Destructive Testing in Civil Engineering (Proceedings) (2009), Laboratoire Central des Ponts et Chaussées, Nantes, 425–432

[11] A. Taffe, M. Stoppel und J.H. Kurz, Bestandsaufnahme und Zustandsanalyse von Brücken und Parkhäusern mit automatisierten Verfahren, Fachtagung Bauwerksdiagnose 18–19. Februar 2010, Berlin, DGZfP, Berlin (2010)

[12] H. Scheel, B. Hillemeier, Capacity of the remanent magnetism method to detect fractures of steel in tendons embedded in prestressed concrete; NDT&E 30(4) (1997), 211–216

[13] zs of steel in tendons embedded in prestressed concrete; NDT & E International 30(4), (1997), 211–216

State of Art Image-Based Inspection Methods Used on Japanese Expressways

S. Shimeno, T. Saeki, T. Kazato and T. Sakuraba

Abstract The tunnel and bridge assets on the Japanese expressways constitute a very large sum of investment. These tunnes and bridges deteriorate quickly due to various factors such as aging,environmental exposure, and mechanical effects. The cracking of pavements constitutes serious maintenance item. Proper inspection and investigation are essential to evaluate the condition of structures and efficient non-destructive test methods are important for improved asset management. This paper presents a pavement crack investigation technology adopted automatic image processing, a damage evaluation technology for steel bridge paint which adopted analysis of digitized photos, and a crack investigation technology on tunnel concrete lining adopted laser measurement equipment which is mounted on high speed vehicles.

Keywords Flyingspot method • Genetic programming • Image processing • Japanese expressway • Morphology method

Forward

East, Central, and West Nippon Expressway Companies operate about 8,700km of toll expressways all over Japan. About two third of the expressways runs mountain sites, and the tunnel(1550tubes, 1450km) and bridge (13500bridges, 1250km) assets constitute a very large sum of investment. The assets deteriorate quickly due to various factors such as aging, environmental exposure, and mechanical effects. The cracking of pavement constitutes serious maintenance item.

S. Shimeno (✉) • T. Saeki • T. Kazato • T. Sakuraba
Nippon Expressway Research Institute Company Limited.
e-mail: s.shimeno.aa@ri-nexco.co.jp

In such condition, catching the condition of structures and pavements precisely is essential for improved asset management, and the adoption of efficient, economical inspection and investigation methods is needed. The development of non-destructive test methods in line with modification of inspection method is in progress. This paper presents a pavement crack investigation technology which adopted automatic image processing, a damage evaluation technology of steel bridge paint which adopted analysis of digitized photos, and a crack investigation technology on tunnel concrete lining which adopted laser measurement equipment on high speed vehicles.

Automatic Image Processing Technology for Pavement Cracking

The traditional methods to detect pavement cracking are visual investigation directly on the pavement surface or on the image taken from pictures. They are time and cost consuming works by skilled engineers. In order to improve this situation, the automatic image processing technology to detect and evaluate pavement cracking was developed.

The image processing method to extract cracking is as follows.

Pavements are classified into asphalt pavements and concrete pavements, and the complex image filters are designed to extract cracking on different type of pavement effectively. The tree structure of basic image processing filters is used to obtain the target image and the Genetic Programming (GP) [1] is adopted to search the proper combination of filters shown in Fig. 1.

Each grid with arbitrarily scale is divided into small areas on the image of pavement surface and the complex image filter is adopted in each area. Since the brightness on pavement surface image varies due to the distance from lights, the tone value of pavement surface image needs to be adjusted. When the noise in the pavement image is removed, subtle cracks are also removed and partially removed cracks are recovered by adoption of double resolution on the pavement images.

Since the area inside lane marking must be distinguished to adopt the image filter, the average value and standard deviation of tone value distribution on pavement images are unified in the pavement image with large difference between lane marking and pavement surface. The binarization and labeling process make lane marking distinguished from pavement surface.

The crack detection method for asphalt pavement and concrete pavement is separated and type of pavements must be identified to adopt the complex image filters. The difference of brightness on the pavement images between asphalt pavement and concrete pavement, and grooving on the concrete surface are important factors to classify the type of pavement. Therefore, two feature values, the average tone value and horizontal direction differential value are introduced to detect the type of pavement automatically shown in Fig. 2 and 99.5% of pavements are classified successfully based on the values.

The image processing methods described above are integrated and the automatic processing system including extraction of cracking and automatic calculation of crack ratio was developed.
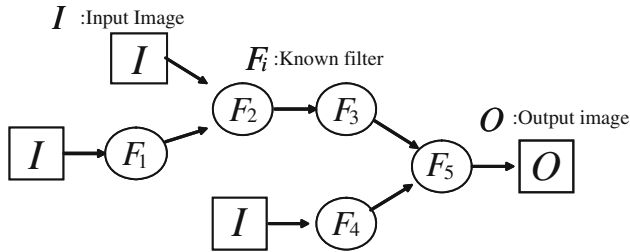
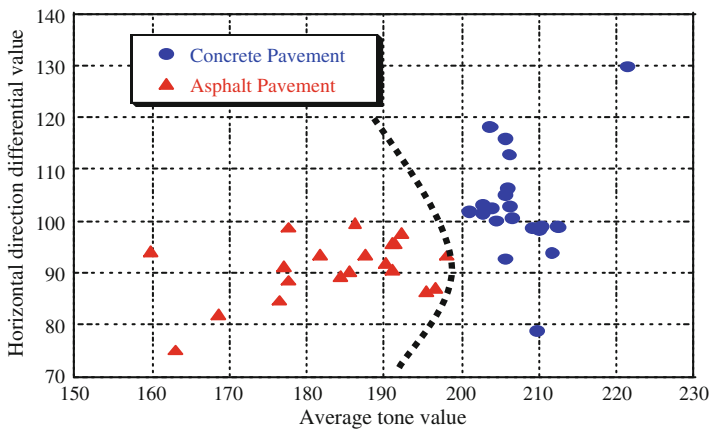**Fig. 1** Image filter with tree structure generated by GP

Fig. 2 Relation between pavement type and two feature values

Pavement type in the target area was detected and the image filters are adopted to the divided grids after the evaluation area of pavement surface inside lane markings is automatically designated. Then, the crack ratio in the each grid is calculated as follows.

First, the number of pixels with detected cracks is obtained and the ratio between the number and the total pixels is calculated in each grid.

Second,when the ratio exceeds the threshold value, statistically meaningful cracks exist in the grid and the grid is evaluated as "a damaged grid". The threshold value is the value with minimized difference of average error between the crack ratios obtained by the traditional method and developed method.

Third,crack ratio which the number of damaged grids is divived by total grid number in the pavement image is calculated.

By adopting the developed parallel image filter search system, the cracking is detected automatically in short time and the transaction time is about 180 seconds for asphalt pavement and about 100 seconds for concrete pavement.

Based on the comparison between the traditional method and developed method, the accuracy to detect cracks is 93% for asphalt pavement and 97% for concrete pavement.

Steel Bridge Paint Damage Diagnosis System (Paint View)

The repair timing of paint on steel bridges is decided by the result of visual investigation traditionally and the method causes wide distribution of the damage evaluation by inspectors and inefficient works. Therefore, the Paint View was developed for the efficient investigation and ojective evaluation of damage.

System outline is as follows. First, about 10 pictures of steel bridge paint rust condition are taken by digital camera. Then, the rust part is automatically detected by the image processing in a personal computer and the rust is coverted into numerical value to evaluate the damage objectively and quantitatively. The gray-scale morphology method is used in the image processing. The gray-scale morphology method detects relatively dark part comparing with other area like shown in Figure 3. This method enables to detect damage part precisely without being affected by weather during taking photoes and brightness of the images.

Evaluation method of damage degree is as follows. First, the diameter of rust appeared on the surface is classified and then, the damage degree is evaluated by giving weight to each classified size of rust. This idea is based on that the rust depth and area is in proportion to the size of rust on the surface. Table 1 describes the threshold value to evaluate paint damage degree on each rust diameter. This threshold value referred to "Standard Method of Evaluating Degree of Rusting on Painted Steel Surface" in ASTM [2] and was amended by digital image data of steel bridges in Japan.

The Paint View has been already introduced in the diagnosis of steel bridge paint damage and is verified to contribute the reduction of labor and time drastically.

The system also enables to judge the proper timing of paint repair and that leads to one year longer paint repair cycle compared with the result obtained by traditional visual investigation.
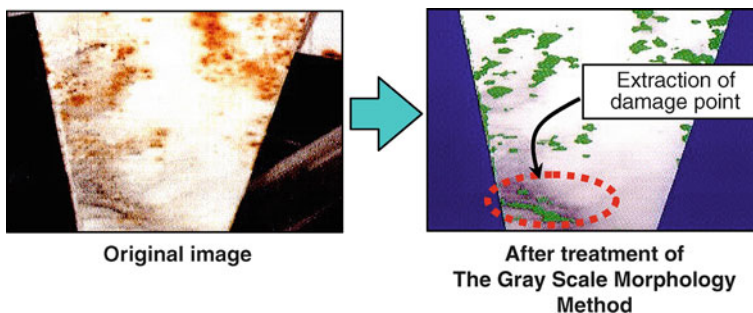

Fig. 3 Processing result of Gray-scale morphology method

Table 1 Threshold value to evaluate paint damage degree on each rust diameter

		Rust diameter (mm)					
		0.05 under	0.05~1	1~3	3~5	5~10	10 more
Rust Area (%)	0.1 under	A	B	B	B	C	C
	0.1~0.3	B	B	C	C	C	C
	0.3~0.5	C	C	C	C	C	D
	0.5~1.0	C	C	C	C	D	D
	1.0~1.5	C	C	D	D	D	D
	1.5~2.0	D	D	D	D	D	E
	2.0~5.0	D	D	D	D	E	E
	5.0 more	E	E	E	E	E	E

A good   B fair   C poor   D observation   E repaint

Crack Investigation Technology on Tunnel Concrete Lining

The traditional investigation for tunnel concrete lining is visual and sound inspection which need labor under constraints of traffic safety and cause wide distribution of the result. The argon laser-based investigation equipment on high speed vehicle show in Picture1 was developed to measure surface of concrete lining efficiently and store objective data.[3]

The measurement principle of laser-based crack investigation is called the Flyingspot method. The laser scanner on the vehicle shoots laser beams to the tunnel lining and subtle variances in luminance level of the beams reflected on the lining are detected by light sensors. The crack width is obtained after the image contrast of every beemspot is converted into numerical value and compared with standard crack width.

Printouts of images including damage part are prepared to grasp cracking condition on the concrete lining in short time. After the distortion is adjusted along with the tunnel section size and the data volume is compressed to print out the image data, cracks on the sequential images are detected by engineers and converted into electric data.

Specification of the laser-based equipment is as follows, measurement speed of vehicle: 60km/h, type of laser: argon laser, laser shooting speed: 21000 rpm, shooting angle: 120degree, number of lasers: 6, measurement interval: transverse 0.5, 1-9mm(arbitrary), longitudinal 1-9mm(arbitrary)

The accuracy of laser-based investigation is better than the traditional visual investigation judging from the result of crack density. The repeatability is also good since the error among plural measurement is about 1% at the same section.

Picture 1 Measurement by laser-based investigation vehicle
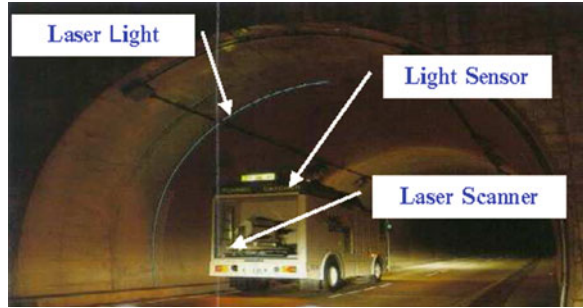
Summary

This paper presents image-based methods for the investigation on expressway structures and pavements, and they contribute efficient investigation in practice. The development of those technologies needs time, cost, and cooperation among wide range of knowledge area. Even so, huge assets in the expressways require further development of reliable non-destructive test methods for improved asset management.

References

[1] T.Nishikawa, J.Yoshida, T.Sugiyama, S.Saito, Y.Fujino (2007), *Robust Image Procesing for detection of Concrete Cracks Using a Parallel Image-Filter*, Journal of JSCE Vol. 63 No. 4, PP. 599–616

[2] ASTM, Standard method of Evaluating Degree of Rusting on Painted Steel Surface, D-610–68

[3] N.Okuno, K.Shimazu, T.Ito, K.Baba, I.Yoshitake, K.Nakagawa (2005), *High Perfprmance Investigation of Crack in Lining Concrete by Laser measurement sysytem*, Jourrnal of JSCE Vol. 67 No.788, PP. 195–200

Use of NDT in Condition Assessment of RC Buildings

A.A. Ozbora, N.U. Basar, Y. Akkaya and M.A. Tasdemir

Abstract Condition assessment and serviceability of existing reinforced concrete (RC) buildings becomes a major issue especially when substandard material and workmanship quality are used. Low quality construction materials and methods accelerate especially the corrosion of the steel reinforcement and decrease the service life of RC structures, which should maintain a service life of at least 50 years according to the EN standards. Several 40-year-old RC buildings were investigated and their serviceability condition was determined based on non-destructive testing in conjunction with semi-destructive in-situ tests. Cores were taken from the structures to determine the mechanical strength and unit weight of in-situ concrete. Microstructural studies were performed on the thin sections and plane sections to evaluate the quality of materials and methods used in the construction. Non-destructive tests such as; Schmidt hammer, impact-echo and magnetic signals were used to determine the surface hardness of concrete members, cracks and voids within the concrete, location and size of steel reinforcement throughout the structure. Extensive carbonation and high level of chlorides were measured from the cores taken. Impact-echo measurements indicated high level of deterioration of concrete and damage. It has been shown that impact-echo method could provide valuable information for the in-situ condition assessment of structures coupled with other experimental laboratory techniques.

Keywords Condition assessment • Impact-echo method • Non-destructive tests • RC structures • Serviceability

A.A. Ozbora • Y. Akkaya (✉) • M.A. Tasdemir
Istanbul Technical University, Istanbul, Turkey
e-mail: akkayayil1@itu.edu.tr

N.U. Basar
Gama-Nurol Joint Venture, Istanbul, Turkey

Introduction

Under certain circumstances, strategic structures such as; high-rise RC structures, marine structures, bridges, tunnels and historic structures that could not withstand the effects of impact and/or vibrational forces such as earthquakes, explosions or floods. The loss of adhesion between the reinforcing steel and the surrounding concrete, because of these dynamic forces, is one of the major reasons. Loss of adhesion occurs slowly in time, or it never happens at the first place because of poor compaction of concrete. Segregation of concrete and/or corrosion of the reinforcing steel are among the reasons for the loss of adhesion between the steel and the surrounding concrete.

Discontinuties in concrete members, such as segregation and steel corrosion, could be detected by non-destructive tests such as impact-echo, which uses low frequency (up to 80 kHz) sound waves [1]. Impact-echo technique is based on the use of impact-generated stress waves that propagate through the structure and are reflected by internal flaws, voids, cracks and external surfaces. Impact-echo could be used to determine the location and extent of flaws such as cracks, delaminations, voids, honeycombing and debonding in plain, reinforced and post-tensioned concrete structures, slabs, columns and beams. It could locate voids in the subgrade directly beneath slabs and pavements [2, 3] and also be used to locate cracks, voids and other defects in masonry structures where the brick or block units are bonded together with mortar. Thus, the structures in critical condition can be identified before failure, and prevention measures such as retrofitting and strengthening can be taken.

Experimental Study

Impact-echo method has been applied to existing reinforced concrete structures to assess the concrete and steel quality. For this reason, four RC buildings of 35-41 years old have been examined. During the investigations, in addition to performing non-destructive impact-echo testing, concrete cores have been taken to examine the mechanical and microstructural properties. For the assessment of mechanical properties, compressive strength tests have been performed, where microstructural properties were examined with a microscope. By means of non-destructive magnetic waves, the diameter and number of reinforced steel bars were examined. The diameter of steel bars were also measured by a calliper, where possible. Thus, it was possible to assess the quality of the materials used in the construction. The semi-destructive and non-destructive test results and analysis of a 41-year-old structure in Fatih, a district of Istanbul, is given below.

According to architectural and static design projects, the design concrete class is B160 (C14) and the class of steel is St I.

Semi-destructive methods

Five concrete cores were taken, in order to evaluate the material properties, from the structural elements which represent the structural load-bearing system. Three of these cores were used for assessing the compressive strength of the in-situ concrete and two of them were cut and polished for thin section and plane section analysis for microstructural observations. The average compressive strength of the three cores were measured as 13 MPa, where the average unit weight of the concrete was measured as 2050 kg/m^3.

The microstructure of the hardened concrete was examined with a stereo-optical microscope up to x63 magnification and a polarizing microscope with a UV-light unit up to x200 magnification.

According to the visual and microstructural observations, unwashed and unsieved sea sand was used, no particle size distribution analysis was made which caused large gaps between aggregates. Due to inadequate cement content and high water to cement ratio, concrete microstructure contained large gaps and air voids. Thus, the quality and thickness of the concrete cover was insuficient for corrosion protection. The aggregates were not fully covered with cement paste, so the bond was low and the interface was highly porous. The cement paste contained a non-uniform and heterogenous, interconnected pore system. Capillary pore system was not exhibit same quality thoughout the cross-section. High volume of capillary porosity and large gaps between the cement particles indicated that the water to cement ratio was high. Agglomerated and undispersed cement particles indicate the poor quality of mixing.

It could be concluded that concrete was not properly compacted because of the existance of high amount of entrapped air voids in the concrete. The inspections on the plane sections indicated that the entrapped air void diameters can be up to 1 cm and entrapped air void volume is around 3.1%.

These microstructural investigations indicate that the quality of the aggregates, mixing, placing and compaction of concrete was not up to the standards and specifications.

Non-destructive methods

Investigations related to steel bar quality. Within the scope of investigation of the in-situ steel bar quality, some of the first basement floor columns were scanned with Ferroscan device (Fig. 1). Number and diameter of the steel bars were measured and compared with the design project. At certain locations, concrete cover was removed and measurements were also taken with a calliper.

Investigations showed that stirrups were not placed properly. Only 6 mm-diameter stirrups were placed with 40 cm of spacing. No information was provided regarding the stirrups in the design project. The diameter of the steel bars were also different

Fig. 1 Rebar Detection
at Reinforced Elements
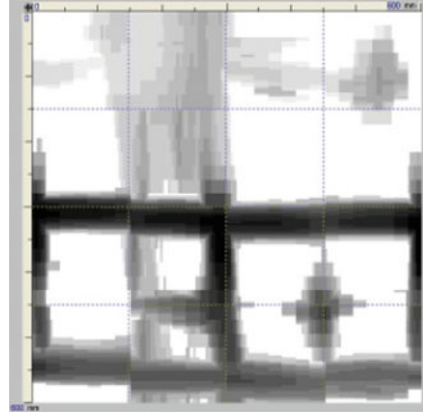
from the design project at certain locations. 10 mm-diameter steel bars were used instead of 14 mm as per the design project.

The loss in the cross-section of the steel bars due to corrosion was measured with a calliper at the first basement floor, where the corroded bars in the beams were exposed. Although, the original diameter of the lateral reinforcement was 12 mm, it was measured as 7.5 mm. The 8 mm-diameter stirrup was measured as 6.7 mm. The loss in the cross-sections of the steel bars in the columns was up to 4 mm. The loss in the stirrup diameters in the columns was up to 2 mm.

An aggresive environment for corrosion exists due to highly porous concrete cover, result of unwashed and unsieved sea sand, containing shell fragments, existence of highly carbonated zone and moisture. The examination on the thin sections indicated that the depth of carbonation was up to 4.5 cm, from the top surface.

Investigations performed at the second basement floor, which was under water flood, indicated that the concrete cover was spalled, the reinforcement of the columns were exposed and subjected to severe corrosion. At certain locations, steel bars lost their continuity, and some stirrups were completely disappeared.

Investigations with the Impact-Echo Method. The following calculations were performed within the scope of in-situ impact-echo testing:

First basement level, for 25 cm x 25 cm column:
Lateral reinforcement: 4Φ14; Stirrup: Φ8/250.

As $D/B = 1$; $\beta = 0.87$ and $Cp = 3350$ m/s therefore the calculated mode frequencies of the square column were f_1=5.8 kHz, $f_2 = 8.2$ kHz; $f_3 = 11$ kHz; $f_4 = 14.2$ kHz; $f_5 = 16.4$ kHz; $f_6 = 13.6$ kHz. The calculated thickness frequency was 5.8 kHz.

The calculated reinforcement bar frequencies: Lateral bar frequency at the front side was 33.9 kHz and stirrup frequency at the front side was 52.5 kHz. Stirrup frequency at the back side could not be determined due to the fact that $D/t < 0.3$.

In case of corrosion, the expected frequency from the lateral bars at the front side was 48.4 kHz and from the stirrup at the front side was 72.5 kHz, where, lateral reinforcement at the back side was 6.6 kHz, stirrup at the back side was 6.3 kHz.
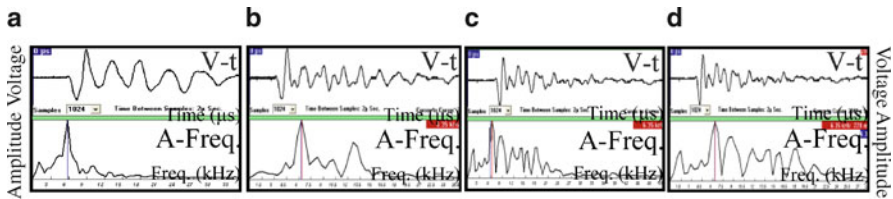
Fig. 2 Column S6 – **a**) 14 mm steel ball, **b**) 12 mm steel ball, **c**) 8 mm steel ball, **d**) 8 mm steel ball, narrowed frequency range

Representative test results are given in Fig. 2. The measured thickness frequency with all different size steel balls corresponded to the expected calculated value of 5.8 kHz. It was observed that when the diameter of the steel ball used in the Impact-echo testing, was large, the frequency range decreased and made it impossible to determine the higher frequency range of reinforcement bars. However the thickness frequency could be clearly observed with the largest ball size (Fig. 2a).

As the size of the ball decreased, the frequencies from the reinforcement bars became more visible (Fig. 2b).

In Fig. 2c, a more complex spectrum, which contained more number of higher frequencies, could be observed. When zoomed in, the reinforcement bar frequencies between 19-25 kHz could be clearly seen in Fig. 2d.

Conclusions

The investigations on the building proved that the materials and methods used in the construction were not according to the design project. Significant loss of steel bar cross section was observed, especially at the basement level, due to corrosion. Since the in-situ concrete was of poor quality, it was difficult to carry out impact-echo tests, where calculation assumptions had to be modified.

For sound elements, one dominant, single peak of P-wave was observed on the frequency spectrum, corresponding to the thickness of the element. It was possible to determine the location of the steel bars depending on the diameter of the steel ball used during the impact-echo testing. In case of damage and cracks due to the corrosion, peaks at various frequencies, due to the reflections from the cracked surfaces, were measured. A dominant frequency was not identified for damaged elements. Thus, it was possible to qualify the elements as either sound or damaged elements. The microcracked microstructure of the reinforced element caused divergence and attenuation of the elastic wave. Consequently, various frequencies with low amplitude and low energy were observed on the spectrum.

During the Impact-echo testing, it has been observed that as the steel ball diameter increased, the accuracy decreased and the contact time increased. Thus, it might be concluded that high-energy impacts could raise difficulties to identify frequencies

related to reinforcement bars and corrosion. When the contact time is long, reinforcement bar frequencies could not be observed on the spectrum and it is not possible to determine high-range mode frequencies.

It has been proved that impact-echo method can provide valuable information for the in-situ condition assessment of structures when combined with other semi-destructive test methods.

References

[1] Sansalone, M. (1997), Impact-Echo: The Complete Story, *ACI Structural Journal*, vol. 94, no. 6, p. 777–786.

[2] Carino, N. J. (2001), *The impact-echo method: an overview*, Structures Congress and Exposition 2001 Proceedings. American Society of Civil Engineers. p. 1–18, Washington, DC, Chang, P. C., (Ed.).

[3] Yikici, T. A. and Akkaya, Y. (2009), *Bond quality assessment by petrography, mechanical and nondestructive testing*, 12th Seminar on Microscopy Applied to Building Materials, Dortmund, Germany.

NDT Methods for the Assessment of Concrete Structures After Fire Exposure

E. Annerel and L. Taerwe

Abstract This paper studies the application of the Schmidt Rebound Hammer and colorimetry as tool to assess the fire damage of concrete structures. Firstly, experimental data is acquired under laboratory conditions on small specimens. Secondly, this information is used to evaluate the damage of a case study consisting of a girder exposed to a real fire. Both techniques show to be very useful in evaluating the fire damage and can provide the necessary information for a calculation of the residual load bearing capacity.

Introduction

During a fire, concrete structures behave in most cases very well [1]. It could therefore be of economic interest to repair the damaged structures, as costs for demolition and rebuilding can be avoided and the building can be reused faster. Different assessment techniques are possible to detect the internal damage [2]. In this paper the Schmidt Rebound Hammer and colorimetry are applied both at the laboratory level and in a real fire case.

E. Annerel (✉) • L. Taerwe
Department of Structural Engineering, Magnel Laboratory for Concrete Research,
Ghent University, Ghent, Belgium
e-mail: emmanuel.annerel@UGent.be

Concrete Mix

In this paper a traditional vibrated concrete with siliceous aggregates and ordinary Portland cement (TC) is studied. For 1 m³, it is composed of 640 kg sand, 525 kg gravel 2-8 mm, 700 kg gravel 8-16 mm, 350 kg cement and 165 liter water. Cubes with size 150 mm are cast and cured for 4 weeks in an air-conditioned room (RH >90%, 20±1°C), after which they are stored at 60% RH and 20±1°C for drying until further testing. The mean compressive strength at 28 days is 56.5 N/mm².

Colorimetery

At an age of 3 months, cores are drilled out of the cubes, sawn in 6 discs, polished and dried till testing time for at least two weeks at 60°C. Since this was repeated for another cube cast at a later time, a total of 24 discs were obtained. Two discs (belonging to different mixes) were heated without mechanical load at a heating rate of 30°C/min to the target temperature (till 1160°C), which was kept constant for 1h. The discs were slowly cooled in the oven, after which they were immediately tested for colour.

The colour is measured with an X-rite SP60 spectrophotometer according to the CIE Lab-colour space. In this colour system 'L*' is the lightness with values between 0 (black) and 100 (white), while 'a*' is spread between magenta (positive values) and green (negative values) and 'b*' is positioned between yellow (positive values) and blue (negative values). The coarse aggregates were masked with black ink to minimize the effect of the colourful aggregates. During heating the colour describes a path in the a*b*-colour space (Fig. 1), changing from grey at 20°C to red-pink at 300-600°C, to whitish grey at 600-900°C and buff at 900-1000°C.
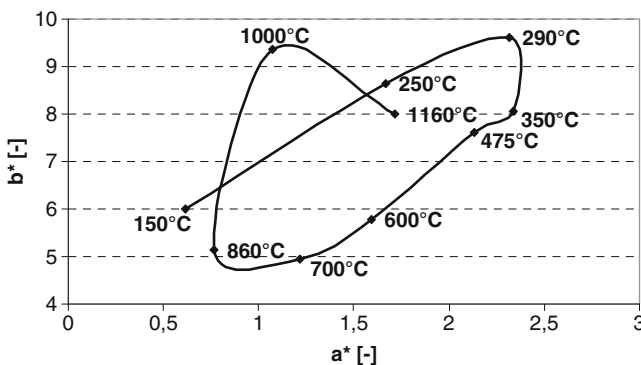

Fig. 1 Colour evolution of traditional concrete with masked aggregates

Similar colour paths can be found from cores drilled out of a heavily heated structure and cut in discs parallel to the fire exposed surface. Comparing the shape of these paths with Figure 1 results in the detection of different isotherms, such as ~300°C, ~600°C, ~800°C, ~1000°C. On the other hand, the core can also be sawn in halves along its longitudinal axis. Study of the colour changes along this longitudinal axis would only result in the detection of the 300°C isotherm, since the temperature gradient is steep at the surface layers. Based on the found isotherms, the residual load bearing capacity can be calculated with the methods given in EN 1992-1-2:2004.

Schmidt Rebound Hammer

The influence of the temperature and storage conditions after fire are tested on half TC cubes heated till uniform temperatures of up to 600°C. The specimens are allowed to cool slowly in the furnace, after which they were stored for 28 days in water or in air (60% R.H., 20±1°C). Figure 2 depicts the relative rebound index (RRI) tested immediately after cooling (0d) and after 28 days of storage, as well as the compressive strength loss measured on an additional series of heated cubes. RRI is calculated as the percentage of the rebound belonging to a target temperature after a storage period (RI_T) divided by the rebound of an unheated reference sample at the beginning of the storage period ($RI_{20°C}$).

It appears that the results at 0 days after heating are close to EN 1992-1-2:2004 and the compressive strength decay of TC cubes (except for the strength drop at about 100°C). Differences in the evolution of the surface hardness between
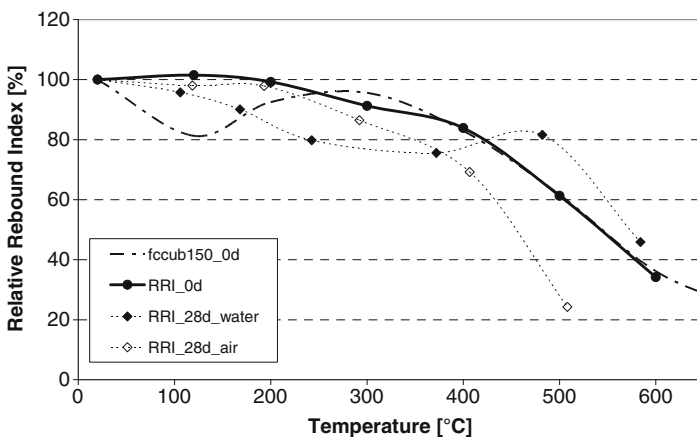

Fig. 2 Decrease of Rebound Index as function of temperature and storage conditions for traditional siliceous concrete

Fig. 3 Fire damage of roof girder

storage in water and in air are clearly visible. Below 400°C, a higher loss of Rebound Index is noticed for storage in water than in air. On the other hand, beyond 400°C, the surface hardness recovers strongly for specimens stored in water and a further decay is found for air storage. Due to atmospheric effects such as rain and sun, measurements on in-situ structures will be between the extremes as given on the graph.

Based on these results, the following criteria are formulated for the interpretation of the relative rebound index ($RI_T/RI_{20°C}$):

$RI_T/RI_{20°C} \geq 0.85$: concrete element is superficially damaged only
$0.85 \geq RI_T/RI_{20°C}$: concrete element should be further investigated

The Schmidt Rebound Hammer can be used as a valuable tool to have a first attempt of the fire damage of concrete elements. Due to its penetration depth of about 30 mm, the degradation of the concrete cover is tested. This degradation is strongly related to the remaining load bearing capacity, since it protects the reinforcement from heating.

Case Study: Fire Damage of a Girder from an Industrial Hall

Description

In 2010 an industrial hall in Belgium consisting of pretensioned roof girders with a span length of 21 meters has burnt out. The fire started in the archive located at a mezzanine, just beneath the girders.

Figure 3 shows the damage to one of the roof girders. Considering the colour change of the concrete surface, the surface temperature must have been around 900-1000°C. The roof consists of a composite concrete-steel slab, which has bent towards the fire. The concrete of the girder has spalled over a few centimetres. However, the strands are still covered with concrete and were not directly exposed

Table 1 Schmidt Rebound Hammer measurements

Test location		Direction of measurement	Average	Standard deviation	$RI_T/RI_{20°C}$ [-]
Reference girder	web	side	45.6	2.0	1.00
	flange	side	44.3	2.5	1.00
	flange	bottom	50.9	1.0	1.00
Location 1	web	side 1	36.8	1.8	0.81
	web	side 2	41.2	1.1	0.90
	flange	side 1	30.8	2.3	0.70
	flange	bottom	44.8	1.1	0.88
Location 2	web	side 2	38.0	1.4	0.83
	flange	side 2	30.0	5.7	0.59
	flange	bottom	3w9.6	1.7	0.78
Location 3	web	side 1	41.0	2.4	0.90
	flange	side 2	44.6	1.3	0.98
	flange	bottom	47.8	4.1	0.94

to the fire. Therefore, it is investigated to which extent the fire damaged has reached the reinforcement. This information is necessary for a calculation of the residual load bearing capacity of the girder.

The concrete cover of a reference girder is 36-40 mm for the stirrups and 45-50 mm for the strands when measured from the side faces. From the bottom, the cover is 39-40 mm for the strands.

Results schmidt rebound hammer

Surface hardness readings are performed along the length of the girder, as presented in Table 1. Locations 1 and 2 are situated at half span length and in the zone with severe fire damage, while location 3 is at 2.5 m of the supports and approximately 4 m from the fire. The relative rebound index is calculated by means of the measurement of a reference girder found in the neighbouring construction with similar properties. It is clear that the fire has influenced the surface hardness ($RI_T/RI_{20°C}$ < 0.85) at locations 1 and 2, while location 3 is not affected.

Results colorimetry

To know the depth of the fire damage inside the concrete, a core is drilled through the web of the exposed girder in the heavily damaged zone. The core has been exposed to fire from both sides. Damage is observed with the naked eye till a depth of 12 mm from one side and 10 mm from the other side. Based on these findings, the zone between 50 and 70 mm is assumed to be not affected by the heat and is taken as reference. From recordings with the spectrophotometer, a fire damaged zone of 25 mm from the first side and 13 mm from the other side can be
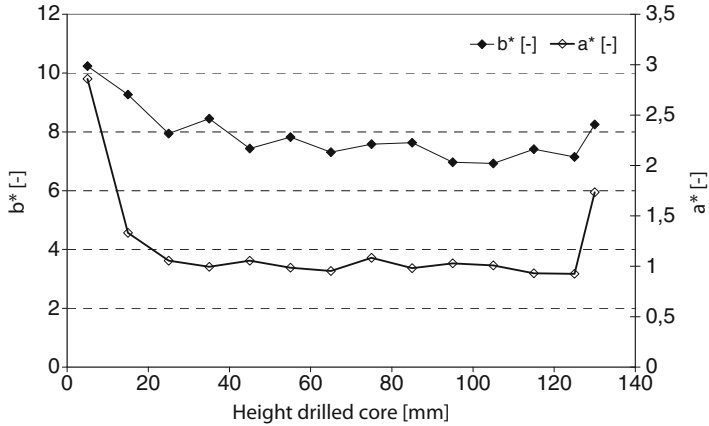
Fig. 4 Development of a* and b* over the body of the girder

detected (Fig. 4). The values near to the surface can be related to temperatures of about 300-600°C (based on Fig. 1). These depths of fire damage are below the measured concrete cover thicknesses. Therefore, the reinforcement has not been heated to critical temperatures and the load bearing capacity of the girder should be adequate.

Conclusions

– With increasing temperature, the concrete colour describes a colour path in the a*b* colour space.
– Experimental laboratory work results in a critical relative rebound index of 0.85 for siliceous concrete.
– Both techniques proved to be useful to detect the extent of fire damage of a concrete girder exposed to a natural fire.
– Although a pretensioned girder was exposed to high temperatures, the remaining bearing capacity is assumed to be sufficient since the strands are not heated.

References

[1] Taerwe, L. and Annerel, E. (2008), In: Proceedings of the 2nd International Conference on Concrete Repair, Rehabilitation, and Retrofitting (ICCRRR), pp.1061–1067, Alexander, M. et al. (Eds.), CRC Press, Cape Town.
[2] Annerel, E. and Taerwe, L. (2009), *Cem. & Concrete. Res.*, vol. 39, n. 12, p. 1239.

Damage and Defect Detection Through Infrared Thermography of Fiber Composites Applications for Strengthening of Structural Elements

L. Cantini, M. Cucchi, G. Fava and C. Poggi

Abstract Fiber Reinforced Polymer (FRP) composites are today widely used for the strengthening and seismic retrofitting of structures. The efficiency of this technology is strongly dependent on the correct positioning and bonding of the fibers on the surface of the structure to be reinforced. The connection between the surface of the substrate (concrete, masonry or steel) and the fibers is assured by the adhesives. The control of the application may be performed with different Non Destructive Evaluation (NDE) techniques but presently there are no standard procedures to assess the quality of the applications in civil engineering structures. Infrared thermography represents a valid tool for the detection and measurement of bonding defects or damage in the composite strips and can be used even for the definition of possible damage progression. The paper presents a series of results obtained using infrared thermography on masonry walls and concrete beams.

Keywords Carbon fibres • Concrete retrofitting • FRP reinforcement • NDT • Thermovision

Introduction

Fiber reinforced polymers (FRP) composites are now considered an efficient method in the strengthening of civil structures. Most of the FRP systems are applied using a wet lay-up method in which the fibers are impregnated on site. For this reasons the system can contain air voids or non uniform distributions of the epoxy resin. The performance of these applications is due not only to the quality of the materials but

---

L. Cantini • M. Cucchi • G. Fava • C. Poggi (✉)
Dept. of Structural Engineering, Politecnico di Milano, Milano, Italy
e-mail: carlo.poggi@polimi.it

mainly to the accuracy of the application and therefore to the experience of the workers. Therefore the inspection and monitoring of these applications is essential. Some national guidelines [1-3] report specific indications and acceptance criteria to assess the mechanical properties of the components of the composites (i.e. fibers and adhesives) and of the reinforcing system. Defects are an important issue that is examined by some guidelines [3, 4] that give the allowable defect size in proportion to the strengthened area. The first inspection at the end of the installation process is of primary importance for the acceptance of the strengthening. The surveyor can use different types of inspections mainly based on non-destructive evaluation (NDE) [5-10]. All the guidelines recognize that Infrared Thermography (IRT) is a possible NDE technique. IRT reveals the intensity of the infrared radiations emitted from heated surfaces at a certain time. Different materials, after heating, present different temperatures due to their different capability in transmitting and holding warmth. For this reason IRT is an effective technique for the detection of bonding defects, voids and damages and the characterization of the surface layers without a direct contact between the device and the observed area. On the other hand, in the guidelines no clear indications are given about the inspection procedure.

The present work wants to be a contribution in the definition of specifications for the use of IRT providing additional experimental data. Active thermography was applied to concrete and masonry samples while different FRP thicknesses were studied to control the efficiency of the method. In particular, debonded areas were detected from a qualitative point of view while artificial defects location and sizing were quantitatively assessed.

Experimental Tests

A series of thermographic tests was performed to verify the capabilities of IRT technique to estimate the presence of defects, their location and size.

Active IRT is based on the application of heat to a surface to generate a thermal front into the material. In this case, the heating source was applied for a period from 5 to 15 seconds using an infrared lamp positioned at a distance of about 30-40 cm from the specimen. The electric power of the lamp was 1.5 kW and the surface was equal to 0.29×0.14 m^2.

After external heating, the temperature of the sample surface during the cooling phase was recorded in real time by using a thermographic camera positioned at a distance of about 30-40 cm from the specimen. The IR camera produces images of 320×240 pixels composed of Vanadium Oxide microbolometer detectors allowing to visualize temperatures in a range from - 40°C to 500°C. The distance between the camera and the specimen was of 1.40 m, that is the standard distance used for on site tests. In the specimen, the dimension of the area analyzed by IRT was chosen to ensure an adequate image resolution for the detection of the defects.

After removal of the heating device the temperature changes, can indicate near surface inhomogeneities and the presence of defects in the structure if they give

rise to measurable temperature differences. The results are images recorded during the cooling down phase; a thermal image of the object is obtained on the basis of a color scale or a gray scale.

Description of the Specimens

The masonry-CFRP specimen consisted of a masonry wall ($25×52×102$ cm³) reinforced using unidirectional CFRP wraps. The dimensions of solid clay bricks used for the masonry wall were $250×120×55$ mm³. CFRP reinforcements were bonded on a side of the masonry wall using a thixotropic epoxy resin. The mixing ratio of the epoxy was 1:4, i.e. four parts of component A (resin) to one part of component B (hardener) by volume. Lack of bonding of the FRP to the masonry substrate was simulated by the interposition of double Teflon foils with different dimensions and geometric shapes as reported in Fig. 1. The detection of the defects was performed with 1, 2 or 3 layers of FRPs for both the specimens (Fig. 1).
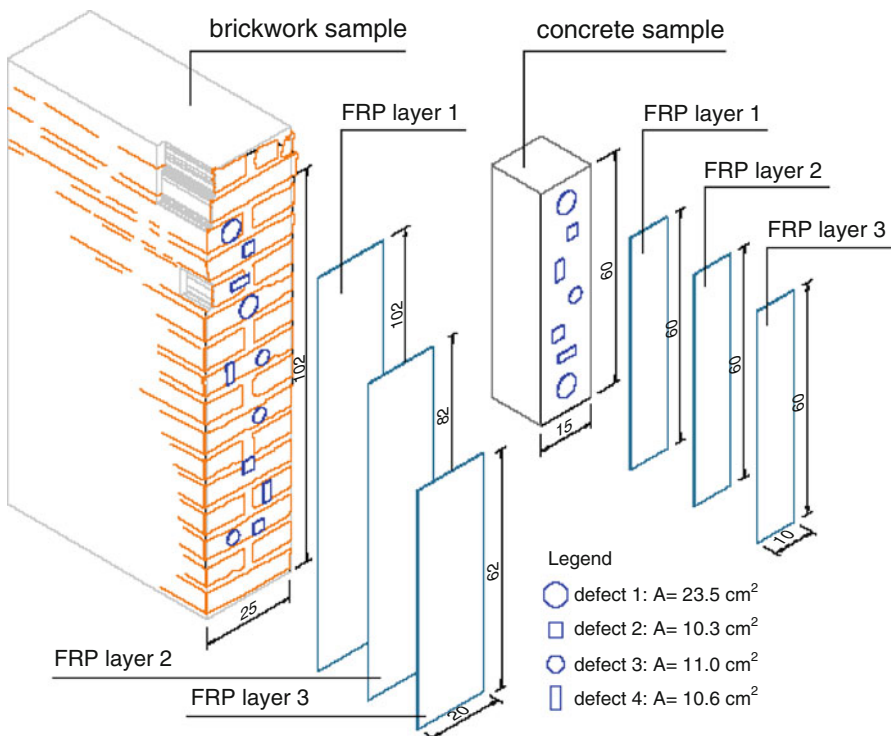
Fig. 1 Specimens and defect geometries

Table 1 Heating times used to carry out the thermographic tests in relation with the number of the FRP layers

Specimen	1 FRP layer	2 FRP layer	3 FRP layer
brickwork	5 seconds	10 seconds	15 seconds
concrete	5 seconds	5 seconds	5-10 seconds

The concrete-CFRP specimen consisted of a C25/30 concrete block (150×150× 600 mm^3) reinforced using CFRP wraps. This specimen was prepared using the same materials and procedure used in the masonry specimen.

The procedure consisted in two subsequent time periods: t_1, the heating interval and t_2 the waiting time to shoot the picture. After calibration the optimal t_1 times, reported in Table 1, were defined after calibration while the t_2 times were obtained at the beginning of the cooling phase (from 3 to 15 s after the removal of the IR lamp).

Temperature differences have peaks at the defect zone after heating, and they represent a valuable parameter for the location and sizing of the defects.

Experimental Results

The thermographic tests, carried out on brickwall and concrete samples presenting one single FRP layer provided a reasonable estimate of the presence of the artificial defects. Reliable results were also obtained in specimens reinforced with two FRP layers, except for a very limited area on the bottom of the masonry sample. In such area the position and the shape of the artificial defects were not clearly recognizable due to debonding between the first and second FRP layer. Thermal images of this area, taken at different times after the end of the heating stage show that the highest temperatures are maintained for longer periods in the debonded area. More difficulties were encountered in detecting the defects on the masonry specimen after the application of the third FRP layer, i.e., if the defect is far from the external surface, identification is more troublesome.

As shown in the thermal images reported in Figs. 2 and 3, the data elaboration permitted to optimise the temperature differences for the best identification of the position and shape of the artificial defects. During the cooling phase, the estimation of the defect dimension presented some differences from the beginning to the end of the test. The influence of the FRP thickness is evident from Fig. 3: as the number of layers increases, the differences in terms of measured defect dimensions are higher. Table 2 shows, for example, the differences between the estimated areas of 4 categories of artificial defects and the original one (see Figs. 2 and 3).

In the estimation of the defects, the error is influenced by the image resolution and by the accuracy of the operator in recognizing the borders of the defects. Besides this operation is actually time-consuming and partially influenced by the interpretation of the thermal image on the surface of the sample. To improve the
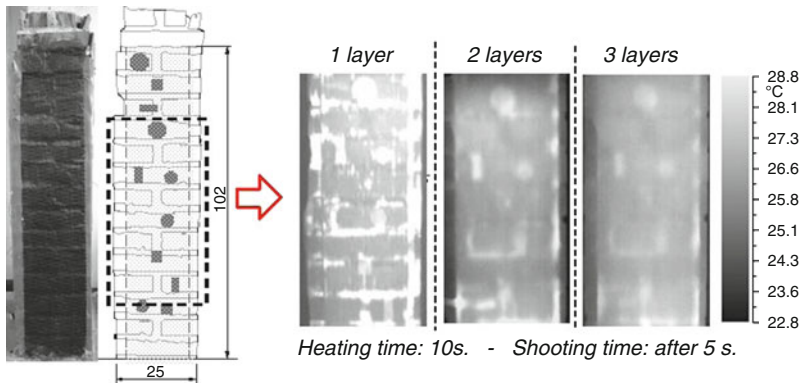
Fig. 2 Comparison between the results obtained by thermographic tests carried out on the central area of the brickwork sample with 1, 2 and 3 FRP layers
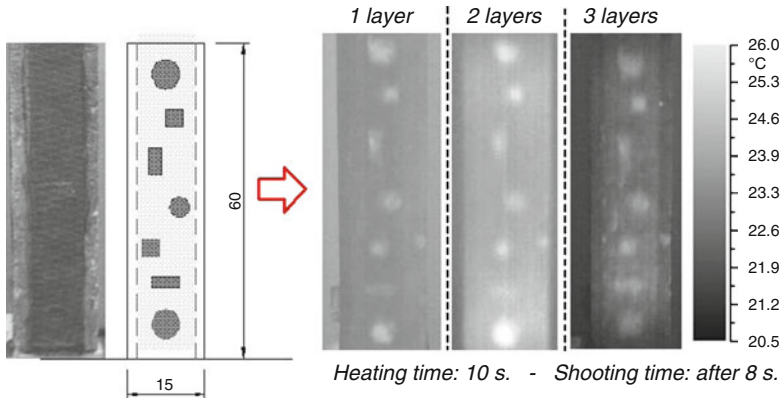
Fig. 3 Comparison between the results obtained by thermographic tests carried out on the concrete sample with 1, 2 and 3 FRP layers

Table 2 Defect areas estimation on both specimens

	Defect no.	Real shape	Real area (cm²)	Area - 1 layer (%)	Area - 2 layer (%)	Area - 3 layer (%)
masonry specimen	1	Circle A	23.5	−3.4	+8.9	+10.6
	2	Square	10.3	−5.8	−25.6	+23.3
	3	Circle B	11.0	−13.6	+3.5	+22.7
	4	Rectangle	10.6	−6.6	−5.0	+33.0
concrete specimen	1	Circle A	23.5	−10.6	−10.3	−4.3
	2	Square	10.3	−4.9	+18.3	+28.2
	3	Circle B	11.0	+2.7	+11.3	+16.4
	4	Rectangle	10.6	+17.0	+24.3	+34.0

research, authors are actually working with other routine in order to set an algorithm for the analysis of the thermographic sequence of images recorded after the test. This is based on a technique, also referred as Thermographic Signal Reconstruction (TSR). The aim is to detect during the cooling phase the best thermal image for observing the appearance of the defects and to automatically identify the shape and the area of each defect.

References

[1] ACI Committee 440. (2002), *ACI 440.2R-02-Guide for the design and construction of externally bonded FRP systems for strengthening concrete structures*, Farmington Hills, MI.

[2] CNR (National Research Council). (2004), *Guide for the Design and Construction of Externally Bonded FRP Systems for Strengthening Existing Structures*, Advisory Committee on Technical Recommendations for Construction of National Research Council, Rome, Italy.

[3] fib, (2001). *Externally bonded FRP reinforcement for RC structures* Bull. No 14, Technical Report prepared by Task Group 9.3 Lausanne.

[4] Mirmiran, A., Shawhawy, M., Nanni, A. and Kharbari, V. (2004), *Bonded Repair and Retrofit of Concrete Structures Using FRP Composites*," Report 514, National Cooperative Highway Research Program, Washington, D.C., pp. II-27 to II–28.

[5] Starnes, M., Carino, N.J. and Kausel, E.A. (2003), *Infrared thermography for nondestructive evaluation of fiber reinforced polymer composites bonded to concrete*. J Mater. Civ Eng, vol 15, n 3, pp. 5–273.

[6] Starnes, M. and Carino, N.J. (2005), *Active Infrared Thermography for NDT of Concrete Structures Strengthened with Fiber-Reinforced Polymer*. J Mater Eval, Jan. pp. 56–63.

[7] Ghosh, K.K. and Karbhari, V.M. (2006), *A critical review of infrared thermography as a method for non-destructive evaluation of FRP rehabilitated structures*. Int J Mater Prod Technol, vol. 25, n. 4, pp. 241–266.

[8] Ghosh, K.K. and Karbhari, V.M. (2010), *Use of infrared thermography for quantitative non-destructive evaluation in FRP strengthened bridge systems*. Int J Mater Prod Technol, pp.1–17.

[9] Schroeder, J.A., Ahmed, T., Chaudhryb, B. and Shepard, S. (2002), *Non-destructive testing of structural composites and adhesively bonded composite joints: pulsed thermography*, Comp A, vol. 33, n 11, pp. 1511–1517.

[10] Valluzzi, M.R., Grinzato, E., Pellegrino, C. and Modena, C. (2009), *IR thermography for interface analysis of FRP laminates externally bonded to RC beams*, Mater Struct, vol. 42, n. 1, pp. 25–34.

Thermographic Investigation of Delaminated Plaster on Concrete

R. Krankenhagen, C. Maierhofer and M. Röllig

Abstract Active thermography is sensitive to inhomogeneities at and below the surface of objects investigated. Thus, it should be useful for detecting plaster delaminations on concrete. In this paper, the results of field and laboratory investigations into plaster-covered concrete were compared. For evaluating the bonding state of the plaster it is not sufficient to study only the thermal contrasts at the surface of the investigated objects. The experimental results suggest that the overall thermal behaviour has to be considered.

Keywords Active thermography • Bonding problems • Concrete • Plaster

Introduction

Passive thermography has been successfully established as a standard quality control in civil engineering [1]. The advantages are obvious: the method is contactless, fast and easy to document. The thermographic investigation of an object during and after a heating process is called active thermography. It has much more potential than conventional passive thermography. However, up to now it is only used in a few fields of application such as aerospace and automotive industries. As a matter of principle, active thermography is very well suited to investigate quality problems in civil engineering such as delamination between different construction materials or inhomogeneities within a construction material. Especially in civil engineering, lab-based research investigations are mainly described [2, 3, 4]. Due to the fact that thermal properties of air strongly differ from those of usual building materials, thermal effects are easy to observe under laboratory conditions.

R. Krankenhagen (✉) • C. Maierhofer • M. Röllig
BAM Federal Institute for Material Research and Testing, Berlin, Germany
e-mail: rainer.krankenhagen@bam.de

The paper describes the results of thermographic investigations under field conditions and their comparison to laboratory data. Data analysis and interpretation are critically discussed.

Investigations at a Real Building Site

Sudden delaminations of plaster within the room ceilings occurred in an office building built in the 1960s during and after renovation. In some cases bigger pieces of plaster abruptly dropped. Thus, the office's owner wanted to know the scope of risks and the extent of the repair required.

The building is a reinforced concrete structure where the concrete surface was covered with cement rendering. Four room ceilings in different parts of the building have been selected for active thermography. The ceilings were heated by IR radiators or fan heaters for 10 min. This thermal activation led to an increase of the surface temperature in a range of 3 to 6 K. The thermographic recording of the cooling-down was performed over a 15-min time period. As early as during the heating phase clear temperature contrasts were observed. Fig. 1 shows a typical temperature distribution immediately after the heating. The rectangular structures visible in the upper and lower edge are the ceiling lights. The surface to be investigated is located between the lamp boxes. Similar typical pattern of increased temperature regions appeared on all investigated areas:

  (i) long and line-shaped structure vertically to the lamp boxes (D1 includes a section of this structure)
 (ii) point-shaped hot spot (marked with an arrow)
(iii) not clearly restricted areas (e.g. D2), often halo-shaped around the lines
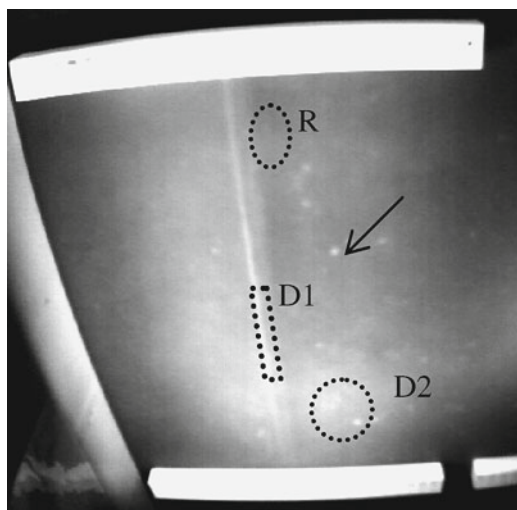
Fig. 1 Thermogram of a room ceiling (wide-angle lens), as the variation with respect to the initial state black = 2 K temperature increase white = 6 K temperature increase

Fig. 2 Temperature decay at the different regions indicated left, just after 10 min of heating
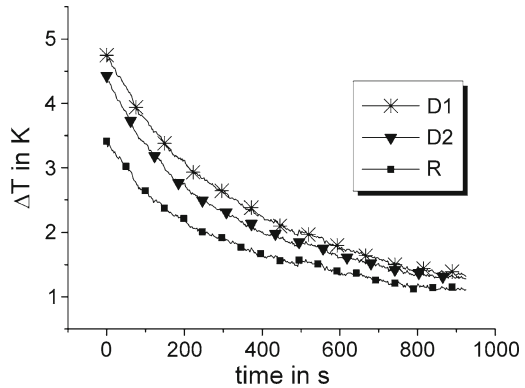
All of these structures emerge from a background showing a smaller temperature rise (3.5 K in comparison to 4.5 K at region D2). Type (ii) is probably due to small inclusions near the surface which cannot generally influence the bonding state of the plaster. Therefore, those structures will not be considered in the following. In order to evaluate the measurement data the temperature decays in different regions of the ceiling were compared with each other (Fig. 2). The shapes of curves D1 and D2 are similar and are converging with increasing time. However, the temperature at R reached a lower level, and decreases to a lesser extent. Assuming that R is a fixed bonded plaster area, the regions D1 and D2 could be interpreted as detached parts of plaster. However, there is no proof for such presumptions. In order to support the interpretation of the investigation results it was attempted to reproduce the whole measurement procedure under laboratory conditions.

Investigation Results Under Laboratory Conditions

To reproduce the thermal behaviour as precisely as possible test items have been built up using parts of the dropped pieces of plaster. The test item PAB1, shown in Fig. 3, consists of a concrete plate (30 x 30 x 5 cm), on which 4 pieces of plaster were arranged like a jigsaw puzzle. These pieces were fixed by 4 mm thick fresh mortar.

Nearly square-shaped cavities of different sizes were assembled directly below the original plaster. The remaining gaps and grooves between the pieces were filled up and smoothed with additional mortar. Finally, the surface was covered with white paint.

Figure 4 shows the obtained thermogram of the PAB1 after 10 min heating by a fan heater. The temperature increase reached was slightly smaller than on the room ceiling. Regions of increased temperature have emerged above the cavities and also on the outside edges. The cavity D1 with a lateral length of 5 cm caused an easy detectable thermal contour. In contrast, the cavity D2 has a side length of only 2.5

Fig. 3 Test item PAB1, the quadrangles indicate size and location of the covered cavities
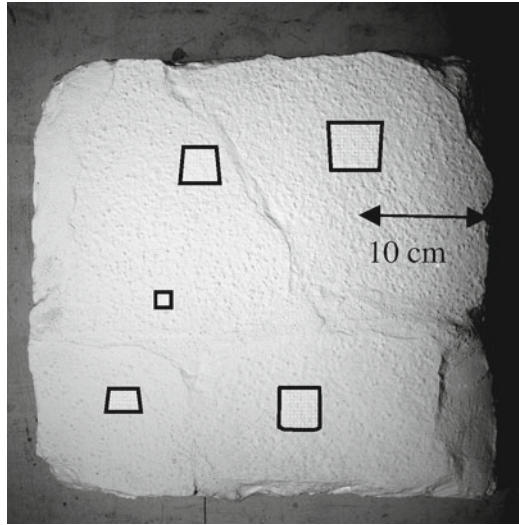
Fig. 4 Thermogram of the PAB1 after 10 min heating, displayed as variation with respect to the [black = 2.1 K temperature increase, white = 2.8 K temperature increase (temperature range saturated for contrast enhancement)]
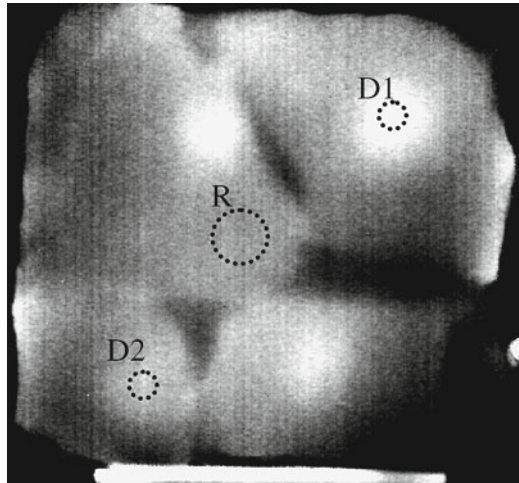
cm which corresponds approximately with the plaster thickness. This geometrical alignment is related with the well known detection limit of thermography. Therefore, the thermal contrast above D2 was rather small. Additionally to the cavities, the edges of the pieces of plaster could be observed.

By analogy with the previously described evaluation the temperature decays at two cavities are compared with that measured at a reference region R where the

Fig. 5 Temperature decays at the test item PAB1 (ROIs indicated in Figure 4) compared with the data obtained under field conditions at a room ceiling
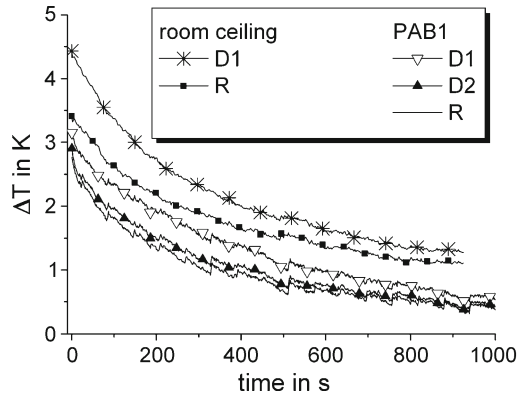
plaster piece is bonded very well. The curves in Fig. 5 are fairly similar to those given in Fig. 2. This means, in principle, that the field measurement has been reconstructed under laboratory conditions.

Discussion

A thorough inspection of the long-term region (t > 400 s) reveals an interesting detail (see Fig. 6). The temperature at the region R of the room ceiling, which was assumed to be a fixed bonded plaster area, decreases to a lesser extent in comparison to the region R of the test item with a known state of bonding. The temperature reduction is even slower than at the known cavity D1 of the test item. Thus, heat dissipation at the room ceiling had to be constrained which led to the observed retarded temperature decay. In order to figure out this effect the following possible heat loss processes has to be considered:

 i. Lateral heat conduction into unheated parts of the surface
 ii. Thermal radiation of the surface
 iii. Convection at the surface
 iv. Transversal heat conduction into the concrete body.

Due to the large temperature gradient between surface and bulk material and the high heat conductivity of plaster in comparison to that of air, process (iv) is expected to have a major influence on the cooling-down behaviour. If this assumption is true for the case considered, heat conduction from the room ceiling into the concrete structure was here disturbed. This led to a slower temperature decay compared to that observed at the test item. The reason for this disturbance could be a wide-area delamination between plaster and concrete or delaminations inside the plaster if it consists of two or more sublayers. Applying these considerations to the problem of

Fig. 6 Long-term temperature decays at the test sample PAB1 compared with the data of the region R at a room ceiling, dashed lines result from a single exponential fit
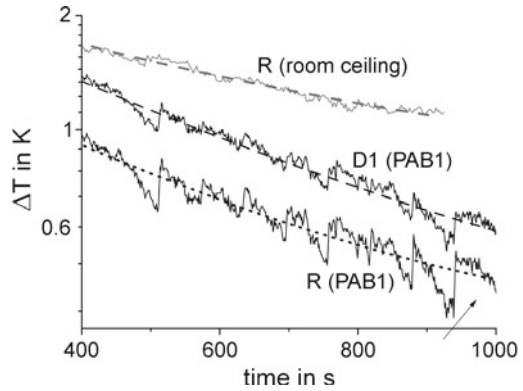
Fig. 7 Long-term temperature decay at the test sample PAB1 compared with the data of different room ceilings (only the fits are shown for clarity)
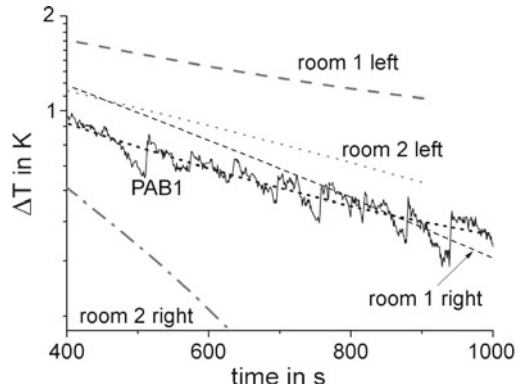
a sudden drop of delaminated plaster, thermographic data have to be evaluated for an early detection of critical delaminations in the following way:

i. Observable local thermal contrasts during or after the heating phase are due to local limited inhomogeneities inside the investigated area. This may be for example cable channels, plastered holes, local damage on the concrete surface etc. A statement concerning the stability of the plaster-concrete bond cannot be obtained in this way.

ii. Measuring the cooling-down process of the entire measurement area provides information on the dynamics of the averaged temperature decay which is mainly influenced by the degree of bond losses within the investigated area. The worse the bonding between plaster and concrete background, the slower the cooling-down of the plaster surface takes place.

To verify these findings, the long term behaviour of further room ceiling areas was compared, the result is shown in the following Fig. 7. The upper curve corresponds to the data shown before. Variations in the decay behaviour can clearly be seen. Unfortunately, there is no information about the actual bonding state of

the different investigated room ceilings. Therefore, new test items with large delaminations for non-destructive and destructive testing have to be developed. They will help to verify the findings of the paper.

Conclusions

Active thermography has been applied to non-destructive testing of the bonding state of plaster on concrete. Clearly detectable thermal signs at different room ceilings were observed, but the evaluation of the data remained ambiguous. In order to support data evaluation the field measurements were reproduced under laboratory conditions. These investigations have been carried out on test items which included original pieces of plaster. Artificial defects inside the test item were easy to detect. A direct comparison of field and laboratory measurements indicates that heat transfer at the room ceiling was reduced in one case. In view of the similar boundary conditions during all experiments it is assumed that the long term temperature decay is directly influenced by the bonding state of plaster on the concrete body.

References

[1] Kaplan, H. (2007), in *Practical applications of infrared thermal sensing and imaging equipment*, Third Edition, SPIE press, Bellingham.
[2] Maierhofer, Ch., Arndt, R., Röllig, M., Rieck, C., Walther, A., Scheel, H., and Hillemeier, B. (2006), Application of impulse-thermography for non-destructive assessment of concrete structures, *Cement and Concrete Composites*, 28, pp. 393–401.
[3] Avdelidis, N.P., Moropoulou, A., and Delegou, E.T. (2004), A thermo-graphic study for the assessment of historic structures, http://qirt.gel.ulaval.ca/archives/qirt2004/papers/054.pdf
[4] Krankenhagen, R., Kervalishvili, G.N., and Maierhofer, Ch. (2010), Influence of air gaps on the thermal behaviour of plaster-concrete-bonds, http://qirt.gel.ulaval.ca/archives/qirt2010/papers/QIRT%202010-067.pdf

Multi Layer Microwave Moisture Scans at Large Areas in Civil Engineering

A. Göller

Abstract A new mobile microwave scanner was developed for moisture mapping on large areas with high lateral resolution, working like a multidimensional microwave camera. The readings are taken position dependent in one track for three depth layers. The scan image can already be visualized with the scanner, making possible detection of moisture, water paths or similar water inclusions right at the place of measurement. Large area buildings like basement garages, indoor pools or flat roofs can be investigated quickly, simply and most of all complete.

Keywords Moisture • Microwaves • Multilayer • Non-destructive • Scanner

Basics of Microwave Moisture Measurement

Microwave moisture measurement belongs to the dielectric methods [1], that are based on the outstanding dielectric properties of water. The relative permittivity of water is about 80, for most solids like building materials it is between 3 and 6. In the microwave region the distinctive polarizability of water molecules is accompanied by strong dielectric losses, caused by bonds of water molecules under themselves. On this basis even small amounts of water can be detected well.

In addition at microwave frequencies it is possible to construct microwave antennas small enough to be handled easily, but still good focussing microwave radiation. The focussing allows penetration depths in the decimeter range, making possible true volume measurements. Such volume measurements can be combined with surface measurements using open resonators for example. This way non-destructive measurements of different depth layers of a building become feasible. Referencing

A. Göller (✉)
hf sensor GmbH, Leipzig, Germany
email: arndt_goeller@hf-sensor.de

Fig. 1 Depth gradation of different microwave moisture sensors
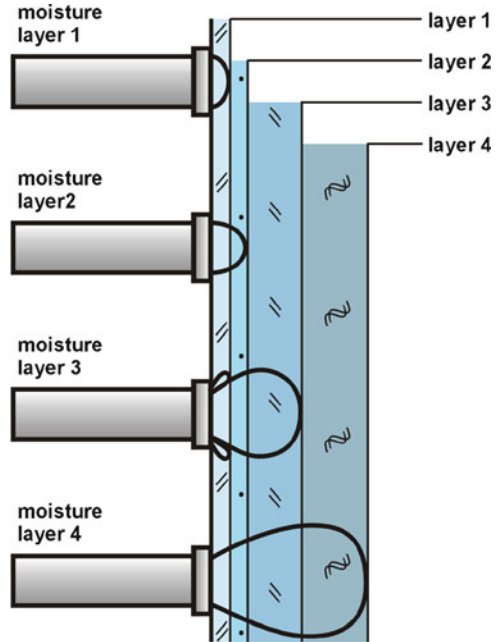
the microwave readings to standard oven drying calibration curves for absolute moisture content measurements can be won.

Single point measurements at buildings are not representative for the moisture status of the whole object. That´s why the method of moisture mapping was developped, where moisture values are taken systematically point by point. Throughout the last years microwave moisture mapping has proven to be an appropriate and simply usable tool for taking moisture distributions in buildings.

The moisture mapping ensures the statistical relevance of the results by the large number of moisture readings. Moisture maps are much more representative and meaningful than single destructive measurements, even if they are more accurate at the single point of measurement. Otherwise moisture maps deliver very descriptive moisture distributions, that help to evaluate the moisture status quite well.

The combination of surface and volume sensors gives a rough depth resolution and helps to detect moisture transport direction. Microwave sensors can be designed with different field geometries (Fig. 1), corresponding to different microwave applicators. These microwave applicators can be used in microwave sensors for different penetration depths. This leads to an expansion of the moisture mapping principle towards tomographic investigations. Currently microwave sensors for layer depths up to 3 cm, 6 cm, 10 cm, 25 cm and 80 cm are available. With these sensors a depth gradation in totally 5 steps can be carried out, whereas 4 depth steps are in the order of penetration depths that are typical for civil engineering applications.

Applications on large areas had shown that moisture mapping carried out manually is limited in terms of area size measurable and lateral resolution, leading to the

desire for an improved measuring technology with high measurement speed and enhanced lateral resolution.

Microwave Scanner

Taking position dependent moisture mappings automatically leads to a new quality and a big improvement especially for measurements at large areas or with high lateral resolution [2]. For such applications the new mobile microwave scanner can be used in terms of a multidimensionally working microwave camera. It contains an equipment carrier module as basic platform, that can work with moisture sensors of different penetration depths simultaneously, and sensors for the acquisition of position data. Up to three microwave sensors can be mounted at the scanner device.

New fast moisture probes were developed for the fast execution of microwave scans, able to guarantee a good lateral resolution even while moving the scanner. The visualization and pre-processing of scan data are carried out in the control unit, containing touchpanel and menu navigation. This makes the handling of the scanner very simple. The driving speed is very high, up to 1 m/s, making the measurement extremely fast. Even large areas of thousands of square meters are scannable in short time. The lateral resolution can be chosen between 5 cm and 200 cm.

The high lateral resolution has essential advantages. Structure details can be resolved much finer. Outliers become more articulate or can be better repressed, like reinforcement bars or single voids for example. Structure barriers in the building material can be identified much better. The influence of layer boundaries can be reduced, moisture distributions in different depths can be better identified. For the first time it`s possible to get investigations completely covering large building areas non-destructively, not possible until now with any other method.

Applications

Applications can be in all types of horizontal areas in concrete buildings or at flat roofs. Microwave scans are an excellent tool for the acquisiton of moisture distributions in large concrete buildings [3]. Using the scan data a well-defined classification of the contained images of moisture or other disturbances of the underground can be realized, as can be seen from the following two examples.

Moisture scans for leakage detection in indoor pools

Microwave scanner can be well applied in indoors swimming pools (Fig. 2). Often there are small leakages at large areas to detect, that can be buried in the underground.

Fig. 2 Microwave scanning of large area in an indoor pool

To find such leakages was very difficult until today. Before, the only ways were opening the construction or partial investigation of single components.

In this application, the surface should be dry for the measurement, but it is sufficient to whipe it dry before the measurement. The microwave scan can be carried out parallel to normal operation of the swimming pool without any problem, only the area to be measured has to be closed off before starting.

Different moisture distributions can be clearly seen from the analysis in the three depth layers surface layer (directly under the tiles), medium depth layer (down to approximately 8 cm depth) and volume layer (down to approximately 15 - 20 cm depth) Fig. 3. The surface scan with MOIST R2S Fig. 4a shows wet areas with increased moisture directly under the tiles and above the sealing. This is the normal and permissible situation in an indoor pool. The scan of mean volume layer with MOIST DS Fig. 4b shows an emerging water leakage from left to right in the middle. The scan of volume layer with MOIST PS is confirming and highlighting the water ingress from left to right in the middle section (highlighted).

Highways and streets – search for water ingress in gaps between deck slabs

Moisture scans were conducted on a German freeway with the aim to detect possible water ingresses near the gap crossings. The demand for this results from the construction of several sections of the freeway, where the interaction of stones used for

Fig. 3 Moisture scan in an indoor pool – tomographic image of 3 depth layers
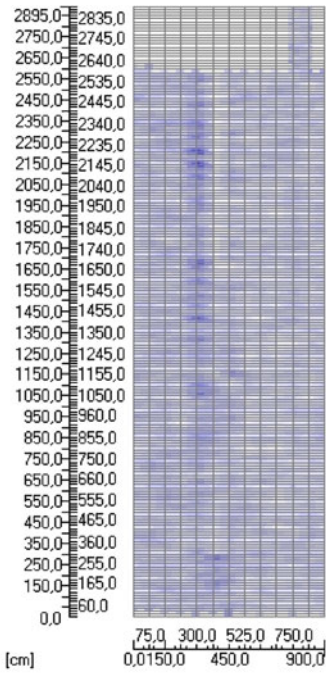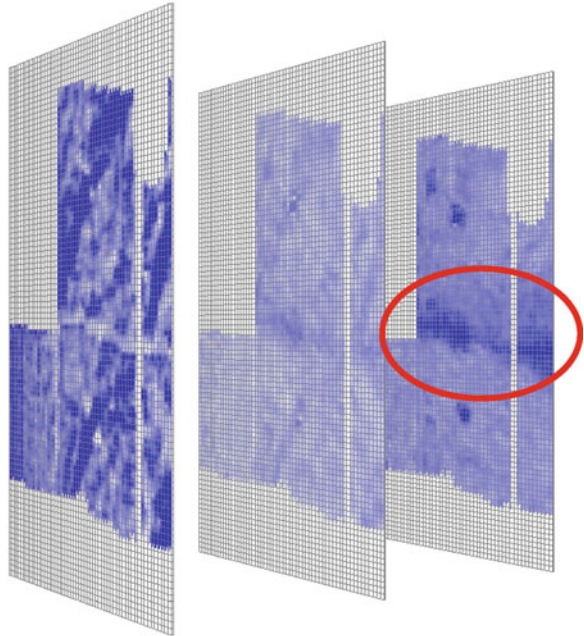
Moisture scan surface – R2S   Moisture scan middle layer – DS
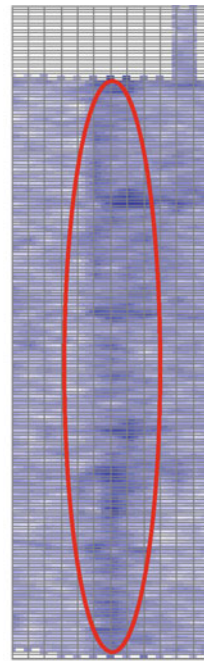
Fig. 4 Moisture scan on decking slabs of a freeway – 3 depth layers

the construction, de-icing salts used in winter and included moisture load leads to the so called Alkali-Silica reaction destroying the gaps.

Moisture load is an important parameter and could be seen with the scan measurement for the first time. As an example the scan of one section of the decking is shown here. Surface scan and volume scan show only weekly changing moisture distributions near the gaps. In contrast the scan of the middle layer is distinctive, it shows clearly shaped zones of higher moisture around the gap crossings and the transverse joints (highlighted). The moisture load in the middle layer is highest in the whole structure. The scan data can also be assigned to absolute moisture content using a special calibration curve for decking concrete.

Conclusion

MOIST SCAN is a new, very powerful instrument for fast acquisition of moisture distributions in building objects. Owing to high lateral resolution and measurement speed moisture measurements are possible in a new quality. MOIST SCAN is working comparable to a multidimensional camera and detects moisture information from different depth layers.

References

[1] Göller, A., (1997), *Proc. 9. Feuchtetag*, Weimar, MFPA Weimar
[2] Göller, A., (2005), In: *Microwave Scanning Technology for Dielectric Material Testing*, ISEMA 2005, Proc. 6th International Conference on Electromagnetic Wave Interaction with Water and Moist Substances
[3] Göller, A., (2010), In: *MOIST SCAN – Multi Layer Moisture Scans on Large Areas in Practice*, Proc. AQUAMETRY 2010, pp. 389 – 397, Kupfer, K. (Ed.), Bauhaus–Universität Weimar

Holographic Subsurface Radar as a Device for NDT of Construction Materials and Structures

S.I. Ivashov, V.V. Razevig, I.A. Vasiliev, A.V. Zhuravlev, T. Bechtel, L. Capineri, P. Falorni and T. Lu

Abstract A relatively rare type of subsurface radar – holographic radar – is described in this paper as a tool for non-destructive testing (NDT) of construction materials and structures. Its principle of operation, advantages and disadvantages are considered. Holographic subsurface radar, operating several discrete frequencies, is used to illuminate a sufficiently extensive area of a surface of opaque dialectical medium to be inspected to register interference between reflected from objects and reference waves. In a lossy media with low level of microwaves attenuation, reconstruction algorithms could be applied for obtaining the subsurface image in such a manner as in optical holography. An attempt is made to highlight significant application areas and problem cases where this type of radar could potentially be applied as a device for NDT of construction materials and structures. The paper describes results of different building surveying including objects of historical heritage. Space shuttle thermal protection system tiles were investigated in some other experiments. Each application area is illustrated by relevant data acquired in laboratory experiments or field tests.

Keywords Building surveying • Holographic subsurface radar • Inspection • Non-destructive testing • Space shuttle • Thermal protection system tiles

S.I. Ivashov (✉) • V.V. Razevig • I.A. Vasiliev • A.V. Zhuravlev
Remote Sensing Laboratory, Bauman Moscow State Technical University, Moscow, Russia
e-mail: sivashov@rslab.ru

T. Bechtel
Department of Earth & Environment, Franklin & Marshall College, Lancaster, PA, USA

L. Capineri • P. Falorni
Department of Electronics and Telecommunications, University of Florence, Italy

T. Lu
NASA Jet Propulsion Laboratory, Pasadena, CA, USA

Introduction

Nowadays infrared, acoustics or X-ray devices are most common in use for NDT diagnostics. These technologies have many advantages and find broad applications in different fields of industry [1]. Usage of one of the technology listed above depends on specific conditions of technological processes and materials.

However, demand for new NDT technologies is urgent because of progress in the industry. One of emerging technologies that is accessible now is holographic subsurface radars of the RASCAN type that are produced in lots [2]. Holographic subsurface radar, operating at one or several discrete frequencies in microwave range, is used to illuminate a sufficient area of a surface to be inspected to register the amplitude distribution of interference between signal reflected from objects beneath the surface and the reference signal. Obtained in such a manner, the dataset can be used to mathematically synthesize an effective aperture, and eventually reconstruct the subsurface image by methods analogous to those used in optical holography [3-5]. It should be noted that for many years this type of subsurface radar has been characterized as not capable of finding significant applications due to strong signal attenuation in many typical media [6]. The high attenuation also limits possibility to use reconstruction algorithm [7]. However, in the rest of this paper, an attempt is made to highlight significant application areas and problem cases where this type of radar could be used to resolve the NDT tasks.

The existing methods of non-destructive testing of structural and building materials or components have a number of disadvantages. X-ray devices, for example, require two-way approach to the observed detail. This is complicated sometimes and more often even impossible. X-ray devices are widely used in medicine, for hand-luggage control in airports and in technological processes where two-way approach to the object to be examined has no problems as a rule. Ultrasonic equipment has proved to be ineffective in media containing a great number of micro cracks and heterogeneities. Its main application is the examination of relatively homogeneous media with few defects and inclusions, for example, metal details of relatively large dimensions.

From this point of view, the microwave devices are the most promising in building diagnostics as they make possible the use of reflective sounding, i.e. transmission and reception of electromagnetic waves is performed from one side of the sounded surface. It enables to examine walls, ceilings and decorative elements and so on in ready-for-service buildings. Thus, it is possible to control the quality of their construction and repair. When using a specially designed antenna, the proposed method also makes it possible to examine corners between walls. This is hardly possible otherwise. Another advantage of radar sounding is a relatively large wavelength λ, about a few centimeters, in the used microwave range, at which there is no reflection from minor natural heterogeneities of media under investigation, for example, by cracks and small (compared to λ) technological hollows in bricks and other construction and composite materials. It is worth mentioning that subsurface radars of the RASCAN type have very low level of emission, less than 10mW that is absolutely safe for the operator.

However, taking into account that water has a very high permittivity of 80, cracks and spots filled with moisture have high contrast in microwave band [2, 7]. This effect can be used in practice. While constructing and reconstructing, concrete structures or their parts, which are under the level of the construction site ground, have to be sealed to prevent water intrusion. This type of structures includes underground garages, automobile parking places, underground pedestrian crossings, etc. This problem becomes especially actual in spring and autumn when the soil water level is high. Any crack in structures or in joints between them results in infiltration of soil water into the underground part of the construction making it unfit for service. Things become worse when the external manifestation of the infiltrated water onto the structure surface does not often coincide with the real location of the crack through which water enters the underground part of the construction. Moreover, such manifestations may be revealed after uncertain time. It makes repair and crack sealing more difficult, increases the cost and reduces the quality of work. Holographic radar may resolve some problems in this case [2].

Inspection of Construction Details and Buildings

The former Senate building, Saint-Petersburg, was being refitted for using it by the Russian Federation Constitutional court. The building was constructed by the outstanding architect Rossi in 1829–1834 and has great value for Russian culture, Fig. 1a.

In process of building's repairing, heating tubes, electricity and communication cables were fastened to metal mesh with cell of 15 by 15 cm and were laid under
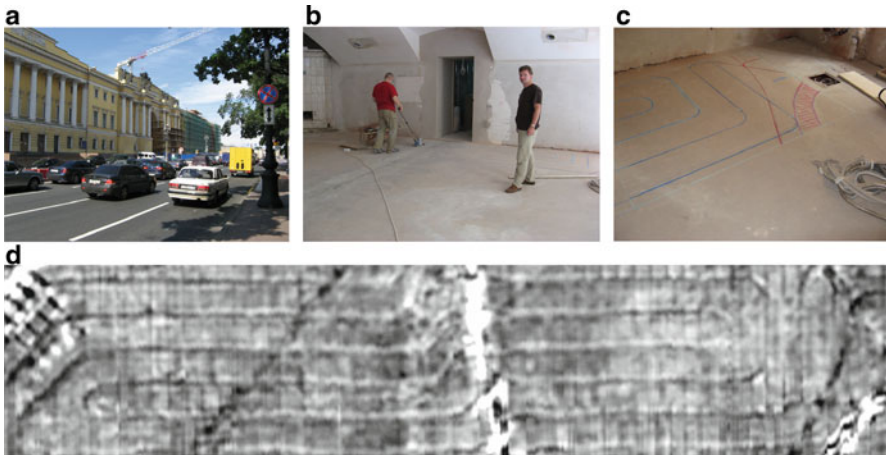
Fig. 1 **a**) the former Senate building under reconstruction **b**) floor inspection **c**) results of the inspection that were reflected by chalk on the floor surface **d**) radar image recorded by RASCAN-4/2000
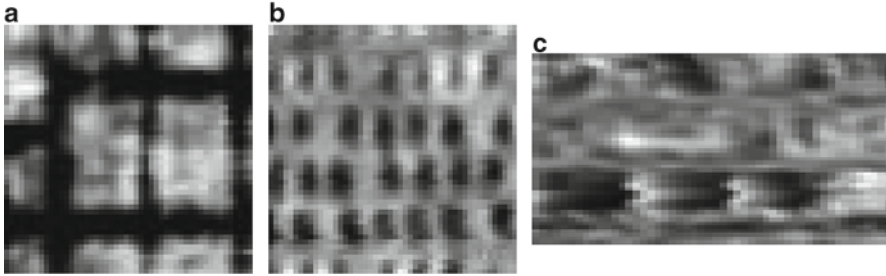
Fig. 2 Radar images of walls that made of **a**) reinforced concrete **b**) hollow slag concrete blocks **c**) brick wall covered by plaster

concrete floor. At the next step, plywood had to be nailed to the surface of the floor. There was danger to damage the tubes and cables by nails. RASCAN-4/2000 subsurface radar that operates in frequency range of 1.6 - 2.0 GHz was used to determine exact position of tubes and communications, Fig. 1b–d. To enhance the contrast of the heating tubes and cables and to reduce contrast of the metal mesh some algorithms of filtration were proposed [8].

Other examples of microwave images recorded by RASCAN-4/4000 operated in higher frequency range of 3.6 – 4.0 GHz are presented in Fig. 2a–c. The radar images depict fragments of walls that made from traditional for Russia constructional materials: a) reinforced concrete; b) hollow slag concrete blocks and c) bricks.

The reinforced concrete wall was cast in place in process of construction. Its metal bars were also welded in place. It is evident that a bar in the upper left corner for some uncertain reason was welded below of the bar's knot, Fig. 2a. Dark spots on Fig. 2b are hollows in slag concrete blocks. Each block has two hollows inside it. The last image represents brick wall covered by plaster of 1 cm thickness. It is possible to distinguish in the image the stretcher and outbond layers of bricks and grout between them. External appearance of all three walls doesn't give opportunity to form an opinion about their structure and composition because of the plaster covering. However, using RASCAN gives such possibility nondestructively.

NDT of Composite Materials

Composite materials are widespread especially in aerospace industry. Demand for new methods of diagnostics of heat protection material and tiles of spacecrafts arose after the disastrous loss of space shuttle Columbia [9]. Concerns emerged not only for diagnostics of insulation foam of hydrogen tank of the shuttle but also checking of adhesion quality of heat protection tiles that are made from quartz fibre covered by erosion-resistant coating of black or white

Fig. 3 a) aluminium plate with glue **b**) heat protection tiles scanning by RASCAN-4/4000 **c**) image of tile recorded by subsurface radar

color. Jointly with NASA JPL, some experiments related to tile diagnostics were performed earlier [10]. The purpose of the experiments was to determine whether it is possible to detect different types of de-bonding of the tiles from the underlying aluminium sheet. To verify this, parts of the sheet surface were intentionally left without glue in two round spots, Fig. 3a. Spot No. 1 did not have any filler. But spot No. 2 was filled with several drops of water that imitated the case of water infiltration under a tile at the open launching pad. Recorded images of spots without glue are distinguished from round form because of their distortion at pressing the tile into the glue, and the water. Water-filled spot No. 2 has higher contrast in comparison with spot No. 1 that is explained by water high dielectric permittivity, 80. This quality may be used for determining of water and humidity infiltration in any composite constructions even if they are laid over metallic base plate.

In media with low attenuation, it is possible to use reconstruction algorithms of recorded holograms. This improves quality of recorded images and gives possibility to measure the depth of an object under the surface [3, 4]. However, implementation of reconstruction algorithms is restricted to low attenuation media [7]. In media with high level of attenuation, radar records images that resemble shadow pictures, not holograms themselves. In this case the hologram reconstruction has no sense at all.

Conclusions

It was shown that microwave imaging by holographic subsurface radar of RASCAN-4 type may produce high resolution images of dielectric construction materials that permit to reveal the internal structure and defects. Main advantage of holographic radar is possibility to survey details with one side access in opposition to X-ray devices. The radar can be also used for diagnostics of heterogeneous media with cracks and small voids that are impossible to survey by acoustics devices. Further improvements of radar design and using higher frequency range of 15-20 GHz will give better resolution and extend fields of applications.

References

[1] *Emerging Technologies in NDT* (2008). Busse, G., Van Hemelrijck, D. and Solodov, I. (Eds.), Athanasios Anastasopoulos, CRC Press, p. 366.

[2] Ivashov, S.I., Razevig, V.V., Vasilyev, I.A., Zhuravlev, A.V., Bechtel, T.D. and Capineri, L. (2008). In: *Proceedings of the International Symposium to Commemorate the 60th Anniversary of the Invention of Holography*, pp. 183–197, Springfield, Massachusetts USA, October 27–29.

[3] Chapursky, V.V., Ivashov, S.I., Razevig, V.V., Sheyko, A.P. and Vasilyev I.A. (2002). In: *Proceedings of the Ninth International Conference on Ground Penetrating Radar*, pp. 520–526, Santa Barbara, California USA.

[4] Case, J.T., Robbins, J., Kharkovsky, S., Hepburn, F. and Zoughi, R. (2006). In: *Review of Quantitative Nondestructive Evaluation*, vol. 25, pp. 1546-1553, Thompson, D. and Chimenti D. (Eds.), American Institute of Physics.

[5] Gabor, D. (1948). In: *Nature*, vol. 161, pp. 777–778.

[6] Daniels, D.J. (1996). *Surface-penetrating Radar*, IEE. London, p. 300.

[7] Razevig, V.V., Ivashov, S.I., Vasiliev I.A., Zhuravlev A.V., Bechtel T.D. and Capineri L. (2010). In: *Proceedings of the XIII International Conference on Ground Penetrating Radar*, Lecce, Italy, pp. 657–662.

[8] Razevig V.V., Ivashov S.I., Sheyko A.P., Vasilyev I.A., Zhuravlev A.V. (2008). In: *Progress in Electromagnetics Research Letters*, vol. 1, pp. 173–79.

[9] Columbia Accident Investigation Board Report (2003), NASA, August.

[10] Ivashov, S.I., Vasiliev, I.A., Bechtel, T.D., Snapp C. (2007). In: *Progress in Electromagnetics Research Symposium*, Beijing, China, March 26-30, pp. 1816–1819.

Infrared Imaging of Roof Systems for Moisture Detection

J.S. Al-Qazweeni and H.A. Kamal

Abstract The cost of constructing roofing systems is high as they must be designed with water-proofing capability and must form thermal barriers for buildings. The traditional and inverted roof systems are typically used in Kuwait. Occasionally, due to faulty practices, incorrect materials and/or improper design, roofs fail to be water-tight and let moisture penetrated into the roofing layers causing water leakage, degradation of the roofing materials and other damages. Moisture problems in roof systems require quick action and maintenance. It is prevalent to rip off the roofing layers to detect the location and extent of damage that has been caused by moisture penetration. This method could be very costly and impractical. This paper looks into the use of Infrared Thermography as a non-destructive technique for determining water leakage in roofing systems. An experimental building unit (EBU) was constructed with six different models of roof sections on the top. For each roof section, controlled injection of moisture was performed at certain points between the roof layers to simulate the leakage process. Infrared imaging studies have shown that the technique is reasonably successful in detecting roof moisture although further evaluation and improvement of the technique was deemed necessary due to the heavy roof construction types and weather conditions in Kuwait.

Keywords Imaging • Infrared thermography • Moisture • NDT • Roof systems

Introduction

Efficient roofing systems are costly to install in most countries. They must be designed with a water-proofing capability to protect buildings and their contents as well as behaving as a thermal barrier for the comfort of the occupants and for

J.S. Al-Qazweeni (✉) • H.A. Kamal
Building and Energy Technologies Department, Kuwait Institute for Scientific Research, Kuwait
e-mail: jqazweni@kisr.edu.kw

conserving energy. In addition, roofing systems require mechanical strength to resist high wind conditions and in the case of flat roofs (predominant in Kuwait), to support pedestrian traffic and services. Finally, they must have an acceptable surface finish to maintain good appearance and serviceability functions of the building [1].

Several techniques are commonly used to detect undesired penetrated moisture in roofing systems [2, 3]. However, most of these could not be classified as non-destructive detection methods as they rely on probing at specific locations or ripping off roofing layers. On the other hand, infrared thermographic imaging has been successfully used as a non-destructive technique for moisture detection in roofing systems [4-6].

Construction methods and materials (including roofing designs) vary among countries due to changes in the environment, weather conditions and construction techniques. For efficient implementation of the technique, procedures for applying infrared technology for detection of moisture in roofing systems require advance investigation and assessment in each individual country. In this study, the main objectives are to determine the effectiveness of implementing infrared theromographic imaging as a non destructive method for moisture detection in flat roof systems and to identify its application appropriateness for the roofing systems used in Kuwait.

To properly assess the technique, experimental and analytical works were carried out in this study. The experimental work that is presented in this paper included construction of an experimental building unit (EBU) for simulating a typical room in a building. The roof of the EBU consisted of six different scaled size roof sections representing typical roofing sections used in Kuwait. Pre-determined and controlled injection thin pipes to deliver water between the roof layers were installed to simulate the leaking process into the scaled size roof sections.

The roof sections represent the typical arrangements used as roofing systems in Kuwait. Thermocouple probes were fixed between the different layers and were connected to a data acquisition system for a long term thermal monitoring. In the theoretical work, the thermocouples readings and measurements were used to produce data to be analyzed using the finite element analyses (FEA). The outcome of the FEA was used to evaluate the detrimental effect of water penetration on the thermal properties of the roofing systems.

Methodology

To achieve the objectives, an experimental and analytical work was conducted utilizing data from the experimental building unit (EBU) that was designed and constructed in an exposed location to direct natural environment (solar radiation, wind, ambient temperatures). The internal dimension of the EUB was 3 x 4.5 x 3 m and simulates a typical room in a building. Its roof was divided into six different scaled size isolated roof sections representing roofing systems typically used in Kuwait. For this purpose, six small size reinforced concrete roof slabs were precasted for each roofing system. Two of the most common types of roofing sections in Kuwait were installed. Type I, which is referred to the conventional system commonly used in hot weather area, was installed on roof sections 1, 2 and 5. Type

**Fig. 1** Installation of the six roof slab sections on the top of the EBU

Fig. 2 Installation of roof layers

II, which is referred to the inverted system commonly used in cold areas, was installed on roof sections 3, 4 and 6. Figures 1 and 2 show the installation of the six different sections of slabs placed on the EUB roof as each slab represents a complete roofing system. Efficient thermal insulation materials were installed between the boundaries of the six sections to prevent heat transfer among the sections.

Pre-determined and controlled injection points for moisture were fixed between the different roof layers to simulate the leaking process into the layers of the roof
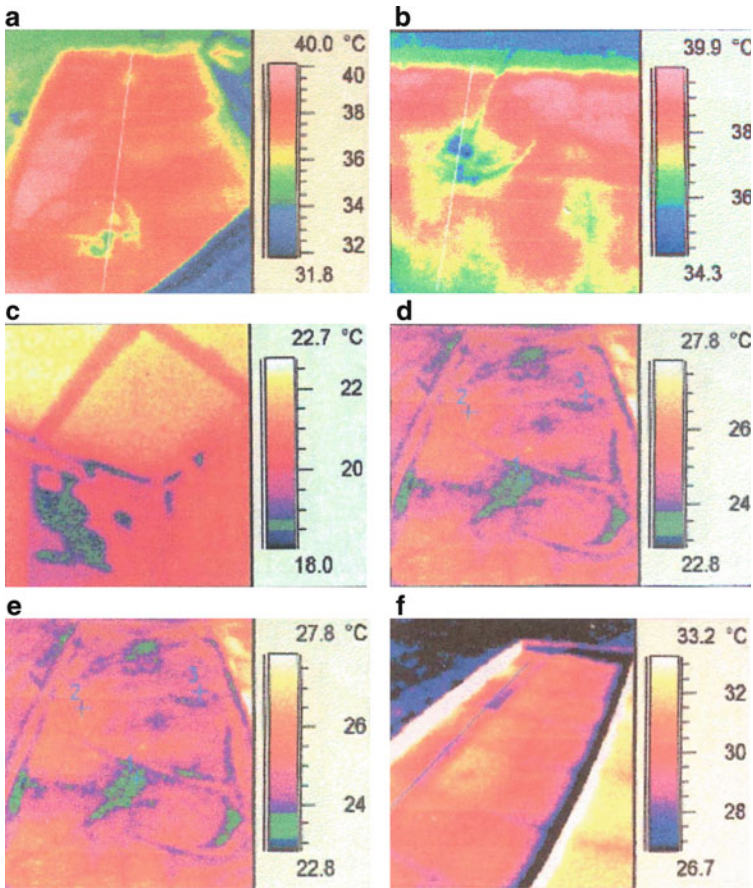
Fig. 3 Sample images taken from the EBU showing temperature variation due to water leakage

sections. From the sides of the EBU roof, a 5mm diameter pipes were embedded into the six roof systems for water injection in order to simulate water leakage by controlling the moisture location and quantity. Thermocouple probes were fixed between the layers and were connected to a data acquisition system for monitoring the thermal performance between roof layers. In the theoretical work, the thermo-couples measurements were used in the finite element analyses (FEA).

Results and Discussions

Once the construction of the EBU was completed and the roof sections were installed, controlled water quantities were injected to the middle of the roof sections and between the layers to simulate water leakage. The study was divided into two

folds, the first was to assess the capability of the infrared imagery technique to locate and detect the distribution of moisture and its intensity due to temperature variations within the roof layers due to water leakage. The second was to measure the detrimental effect of moisture on the thermal properties of the roofing system.

In this paper, the results of the images obtained from the experiments showed that the accuracy of the thermal imaging is affected by the number of layers of the roof sections. The accuracy is reduced as the layers and thickness of the roof section increases. The thermal anomalies were more obvious as the difference between the inside and the outside temperature increased. Figure 3 shows sample images taken from the inside and outside of the EBU showing the temperature variation due to water leakage. Images 3a to 3c show moisture detected in the slabs taken from the EBU inside, while images 3d to 3f taken from the outside.

By comparing the surface temperature between dry and wet areas of the roof sections, the rate of temperature change respond of wet areas is slower than dry areas. Also, wet areas store more thermal energy than dry areas. In order to efficiently apply the infrared imaging for detecting moisture of roofing systems, it is recommended to be applied in the morning or evening periods of the day as the thermal insulation is minimal. The development of infrared cameras and image processing software and algorithms may be more accurate and efficient for application in the future.

References

[1] Al-Qazweeni, J. and Abbas, M., (1994), *A Guide for Flat Roof Covering in Kuwait*, Final Report, Kuwait Institute for Scientific Research, Civil and Building Department, Kuwait.

[2] Claunch, C., (1990), *An Investigation of Using Aerial Infrared Thermography for Locating Subsurface Moisture in Built-up Roofing*, Thesis presented to the faculty of the school of systems and logistics of the US Air Force Institute of Technology, Wright-Patterson, Air Force Base, Ohio, USA. AFIT/GEM/90S-4.

[3] Dworkin, J., (1990), *The Construction Specifier*, Nov., p. 82.

[4] Jenkins, D., Knab, L., and Mathey, R., (1982), *Laboratory Studies of Infrared Thermography in Roofing Moisture Detection*, Final Report, American Society for Testing and Materials, Special Technical Publication 779, pp. 207–220.

[5] Tower, C., (1983), In: *Thermal Infrared Sensing Diagnostics (Thermosense V)*, Proceeding of The International Society for Optical Engineering (SPIE), vol. 371, pp. 174–176, Detroit, Michigan, USA.

[6] Treado, S., and Burch, D., (1982). In: *Thermosense IV*, Proceedings of the Society of Photo-Optical Engineering, vol. 313, pp. 28–34, Ottawa, Canada.

Practical Applications of Ultrasonic-Echo and Impulse Radar

Ch. Sodeikat

Abstract Determining the condition of an existing structure is a common task for engineering firms concerned with planning and consulting. In the case that reinforced concrete structures need to be repaired, the actual state must first be determined according "Instandsetzungsrichtlinie DAfStb Rili-SIB 2001". In the course of renovations and conversions, the condition of the structure must be known, which is often not the case due to a lack of planning documents. Also in many cases doubts exist as to whether the work contracted was actually carried out in full. In all of these cases one should aim to perform the tests as accurately as possible, but with minimum effort and the least possible damage to the building and inconvenience to its users. Through the development of ultrasonic echo and impulse radar methods, numerous inspection tasks have become possible, which were previously only achievable with a much larger effort and through destructive testing methods. In the following article, examples of structural investigations that were carried out using the ultrasonic echo method, the impulse radar method, or a combination of both methods, are presented and explained.

Introduction

Non-destructive testing methods (NDT methods) have been successfully used for decades in the building industry. These methods enable the survey of a structure's condition, without causing further destruction. However destructive testing methods

Ch. Sodeikat (✉)
Engineering firm Schießl Gehlen Sodeikat GmbH, Germany
e-mail: sodeikat@ib-schiessl.de

are impossible to avoid altogether. But based on the results of previously conducted non-destructive testing methods, the destructive testing methods can be implemented at specific targets and therefore limit the damage to only the necessary amount, which is better for both the property owner as well as the structure. The low-frequency ultrasonic echo method and the impulse radar make it possible today to answer questions in the assessment of concrete structures and reinforced concrete structures, which with previous NDT methods were not solvable or only solvable with restrictions. These are relevant issues in structures, which will be rebuilt, converted or repaired. Only through accurate knowledge of the current state of the existing structure and the causes of possible damage can an expert repair plan be carried out. Typical issues are finding flaws and hollow sections, determining the amount of the reinforcement and the concrete cover of deep laying reinforcement, finding the location of tendons, determining the thickness of structural components (decks, floor slabs, screeds), identifying the dimensions of inaccessible components (foundations, earth banked walls) and generally identifying the layout of the structure when plans are not available.

Ultrasonic and impulse radar are also used for controls in the context of structure monitoring and quality control for example in the acceptance of structures. Situations where these methods have been used are determining the thickness of floor slabs and screeds, foundations and tunnel linings [1].

In recent years such great success has been made in the research and development of ground-penetrating radar and ultrasonic-echo methods in terms of application, the combination of several methods and visualization that the term "transparent concrete" has been applied [2]. For an engineer it is of importance to what extent the progress of this research will migrate into daily operations and if commonly asked questions can be answered with an easily visible test and evaluation effort. The theoretical basics of measurements using ultrasound and ground-penetrating radar as well as their interpretation have been explained in detail in many technical papers, [3], [4], therefore the subsequent discussion of the measurement principles only goes so far as is necessary to understand the application examples.

Low-Frequency Ultrasonic Echo Technique

Measurement principle and multi-array test instrument

The ultrasonic echo method utilizes the fact that ultrasonic waves are reflected at the interface of discontinuities in an otherwise homogeneous material. From the elapsed time of the reflected pulse, the distance of the inhomogeneity from the probe can be determined and through scanning generally their extent can also be concluded (see Fig. 1).

Since the late 1990s, ultrasonic probes have been available which can be connected to concrete surfaces without any coupling agent. They are thus suitable for the ultrasonic echo technique, and are available as both longitudinal wave probes (pressure waves) as well as shear wave probes (transverse waves). Based on these probes a meter with probes in an array arrangement was designed, with which an
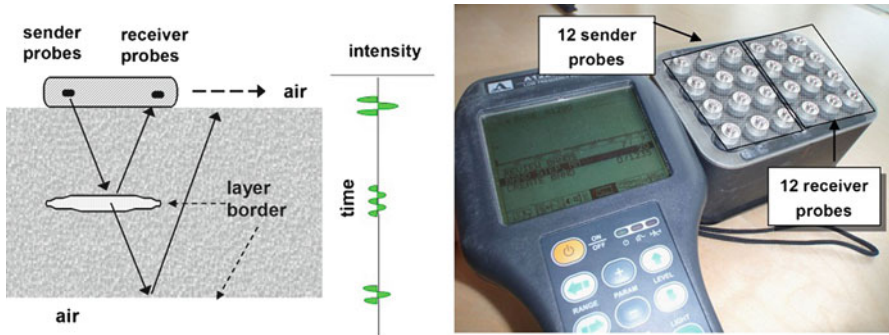
Fig. 1 left. Low-frequency Ultrasonic Echo Technique: Function principle; right: Measurement device with 24 point contact probes

examination of concrete structures up to a thickness of approx. 0.7 m is possible. With its small, robust, dust and moisture resistant design, this device is intended for construction sites. The device consists of a transmitter-receiver unit with 24 point-contact probes, which are assembled in a transmitting section and a receiving section each with 12 probes, Fig. 1 right. The battery operated control unit generates the transmission pulse and receives and stores the reflected pulses and displays them as images with their depth in millimetres on a small monochrome LCD screen. The data can be further evaluated on the PC in different scan ways.

With this instrument it is possible to solve numerous inspection tasks, which could otherwise not be solved with previous NDT methods or only at significantly higher costs. All of the following examples were conducted with the above-mentioned ultrasonic device:

– Thickness measurements of e.g. Industrial floors, screeds, ceiling systems
– Verifying the integrity of tunnel linings (lining test, see the follow practical example)
– Detecting honeycombing, voids e.g. in the base of triple walls
– Locating installation components and reinforcement elements such as central expansion joints, shear studs, conduits, hollow bodies
– Determining the location and coverage of tendons
– Under certain conditions: Investigating the grouting condition of ducts
– Given a known component thickness: Using the wave velocity to determine the E-Modulus and the compressive strength of the concrete.

Determining the thickness of a screed

Measuring task and procedure

As a result of a local screed opening in a new construction the construction manager contested that the thickness of the built in industry screed corresponds to the desired
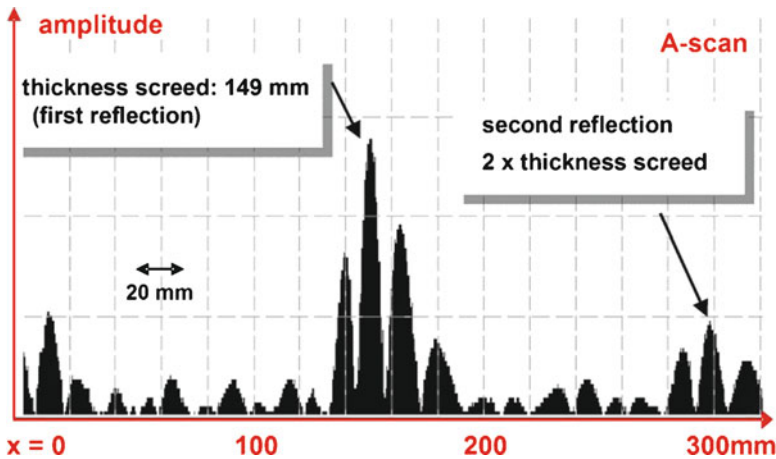
Fig. 2 Ultra-Sonic-Echo single-measurement for determining the thickness of an industrial screed; A-scan

thickness. As part of a court opinion, therefore, the thickness of the screed had to be determined everywhere. The screed was planned to be 150 mm thick. This thickness was required to avoid damage derived from the high point loading of the high rise racks. In the course of previous studies, random samples of destructive cores and sample plates were taken. At these locations the existing thickness of the concrete was known and thus the calibration of the wave velocity of the ultrasonic unit was possible. The calibration resulted in an average wave velocity of the screed of v = 2320 m / s.

Results

Based on the ultrasonic measurements, areas of the base plate could be detected where the thickness of the screed had fallen significantly under the target thickness of 150 mm. Using the ultrasonic method, locations with a thickness of approx. 110 mm were detected. A total of 100 individual measurements were carried out within one day. The measurement error of the process, determined through subsequent drilling, was less than 5%. The following figure (Fig. 2) shows the representation of corresponding A-scans (as an envelope of the signal) with a recognizable second reflection of the signal (caused by the fact that some of the transmitted signal was also reflected at the top of the screed).

Tunnel interior shell testing

Measurement task and procedure

Tunnels in Germany are primarily finished in a double wall construction with a reinforced tunnel interior shell lining in front of a plastic liner sheet. Therefore it is
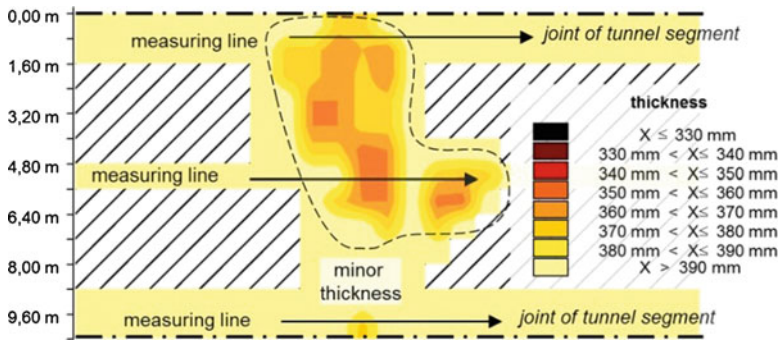
Fig. 3 Thickness distribution for one tested tunnel block (developed view)

essential for the durability of the structures constructed in this manor that the intended strength of tunnel interior shell is strictly adhered to in the tunnel roof (because the risk of defects is greatest here), otherwise the seal can lay directly on the reinforcement and (e.g. under water pressure) be perforated. So under the scope of quality protection of newly constructed traffic tunnels for federal roads, the inspection of the interior shell with a non-destructive testing method is therefore mandatory. The directive "RI-ZFP-TU" [1] of the Federal Highway Research Institute BASt regulates the implementation, documentation, evaluation and representation of non-destructive testing. The service provider must demonstrate their competence to the Federal Highway Research Institute (BASt) by testing and assessing a test specimen which is representing a part of a tunnel segment. Through this procedure, the rare cases where defects occur during concreting can be detected (Fig. 3) in order to avoid consequential damage in the tunnel sealing. The time for testing and assessing of one tunnel segment without damages is about 5 hours.

Impulse Radar Method

Measurement principle and areas of use

The radar method is based on the pulse-echo principle: for civil engineering applications a pulse generator is used to construct a very short electrical pulse (FWHM<1 ns) which is then radiated from the transmitting antenna into the material to be tested. This electromagnetic pulse is reflected at interfaces, where the dielectric characteristics of the material change, and afterwards detected by the receiving antenna. Reflections occur particularly at the surface and the back of the structures to be examined as well as at inhomogeneities in the material.

Over the last few years in the construction industry, pulse radar has become an established technique for examining road surfaces, locating reinforcement in concrete structures and particularly tendons in bridges and its use in these areas continues to grow [2, 3, 4]. The technique can also be used for detecting cavities,
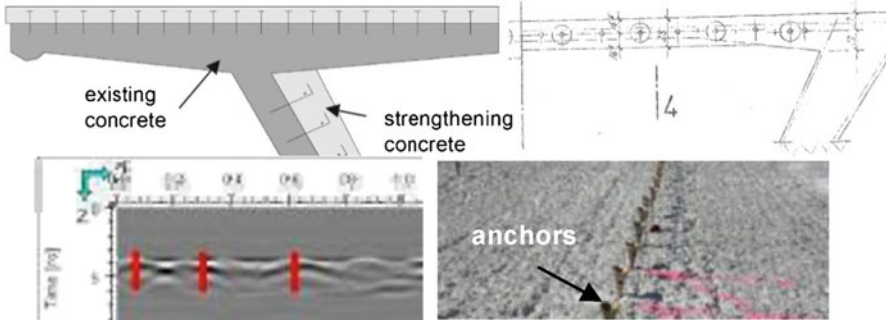
Fig. 4 Strengthening with anchored structural concrete topping

but it is not as successful since the measurements for example in concrete are strongly influenced by the location of the existing reinforcement. In the field of moisture measurement, radar is well suited for rapid and extensive tracking of moistened areas [4]; the possibilities of quantitative moisture measurements are, however, currently limited.

Location of Tendons

Structure's situation and measurement task

A common task while strengthening and repairing structures is to locate the tendons. Figure 4 (top left) shows a typical example of strengthening a bridge panel with anchored concrete topping. In order to drill the anchors without injuring the existing transverse and longitudinal prestressing, the exact location of the tendons needs to be determined. Figure 4 (top right) shows a portion of the construction plan showing the longitudinal tendons. The longitudinal tendons were built into the bridge with an intended coverage of 13 cm. After removing the top layer of concrete with hydro jetting, the designated anchors extended to the nominal depth of the longitudinal tendons. For this reason, the exact location of the tendons was determined with impulse radar.

Approach and results

Figure 4 (bottom left) shows an exemplary radar diagram marking the location of the longitudinal tendons. Overall, the positions of the longitudinal tendons were determined on 2,·18 line scans in the transverse direction. The locating of the approximately 600 transverse tendons was carried out along the bridge lengthwise in four long line scans. Once the instrument settings were optimized, the

tendons could be accurately found. The position of the tendons was charted directly onto the bridge deck. Throughout the entire work on the bridge, neither a longitudinal tendon nor one of the 600 transverse tendons was drilled. Under good conditions it is possible to measure a 100 m line scan in one day.

Conclusion

New ultrasonic echo and impulse radar devices offer numerous inspection tasks which were previously only achievable with destructive testing methods. Among others typical situations where these methods can be used are determining the thickness of floor slabs, foundations and tunnel linings, the detection of installation elements and defects like delamination, hollow zones and honeycombing.

References

[1] Bundesanstalt für Straßenwesen (2001). Richtlinie für die Anwendung der zerstörungsfreien Prüfung von Tunnel innenschalen (RI-ZFP-TU), *Verkehrsblatt-Dok. Nr. S 1050*, Verkehrsblatt-Verlag (2001).

[2] Abschlusskolloquium DFG-Forschergruppe FOR 384 (Mai 2007). Moderne ZfP bei der Bauwerkserhaltung:. *Ed. Universiy Stuttgart*.

[3] Reinhardt, H.-W. et al., (2007). Echo-Verfahren in der zerstörungsfreien Zustands untersuchung von Betonbauteilen. *Bet. Kal.*, Jahrgang 2007, issue 1, ch. V.

[4] Sodeikat, C., Dauberschmidt, C. (2008). Anwendung von Georadar und Ultraschall-Fallbeispiele aus der Praxis eines Ingenieurbüros In: *Beton- und Stahlbetonbau 103.2008)*, issue 12. pp. 819–827.

[5] Kind, T., Maierhofer, C. (2004). Das Impulsradarverfahren. In: *Bauphysik-Kalender*, ch. 2.3, pp. 333–341.

Non-Destructive Testing of Bosphorus Bridges

Y. Dost, N. Apaydın, E. Dedeoğlu, D.K. MacKenzie and O.Z. Akkol

Abstract The two suspension bridges over the Bosphorus Strait, namely Bosphorus Bridge and Fatih Sultan Mehmet (FSM) Bridge form a vitally important link for the economy of Istanbul, Turkey and the Eastern European region. On the Bosphorus Bridge, the majority of its traffic is light vehicles and over 100.000 vehicles pass a day in each direction; heavy goods vehicles were wisely banned in the 1990s following the opening of the Fatih Sultan Mehmet Bridge. This restriction on Bosphorus Bridge is intended to be maintained in future. This situation strengthens the importance of Fatih Sultan Mehmet Bridge for Turkish economy until the third bridge is constructed. The indispensable roles of these bridges necessitate safe operation throughout their lifetimes. To investigate the needs for safeguarding these long form the behaviour analysis along with general and local surveys of these structures. In the content of the studies, a variety of NDT tests were targeted at different parts of the bridge elements, and have been conducted as part of a major investigation into the bridges. The NDT tests performed included; Magnetic Flux Leakage Tests and Radiographic Tests at hanger sockets and Dye Penetrant Testing / Magnetic Particle Testing of the welding, non destructive testing on the concrete parts in anchorage rooms comprised of Schmidt Hammer Tests and Carbonation Depth Tests of concrete. The findings of these NDT tests have been also evaluated to be used in determination of remaining life of the structures together with other studies performed.

Y. Dost • N. Apaydın • E. Dedeoğlu
General Directorate of Highways - 17th Division, İstanbul, Turkey

D.K. MacKenzie
Flint and Neill, London, United Kingdom

O.Z. Akkol (✉)
Orient Research Consulting Engineers, İstanbul, Turkey
e-mail: orkunakkol@orientresearch.com

Introduction

In March 2007 Flint & Neill, in partnership with Orient Research, was contracted by the Turkish Highway General Directorate (KGM) to undertake a detailed inspection, survey and behaviour assessment of the Bosphorus and Fatih Sultan Mehmet Bridges in Istanbul [1]. The bridges are among the heaviest trafficked in the world and any further local failure might result in long term closure of one of the structures, therefore it was imperative to inspect all parts of the bridge and to use these data, along with detailed survey information, to assess the state of the bridges. A number of state of the art surveys were carried out using non destructive testing where possible to gain the greatest amount of information on the bridge. This paper details the methods used in each case.

Hanger Inspections

The hangers on the Bosphorus Bridge comprise a single 58 mm nominal diameter spiral strand, made from 168 individual wires. Each wire is a high strength, cold drawn steel element of up to 4 mm diameter. The hangers terminate in a cast socket, with a white metal or zinc socketing medium. The factory protection of the strand was to fill the strand with a bitumen based blocking compound. This was intended to prevent water and oxygen from getting into the inner lays of the hanger. Each wire was galvanised to a thickness of 200 g/m^2. For the Fatih Sultan Mehmet Bridge, the hanger wires are encased in a hard plastic sheath. This meant that visual inspection methods were not satisfactory and other non-destructive methods were needed. The authors were very reluctant to use intrusive methods that required the removal of the sheath as the reinstatement of the sheath later would not be able to be completed to the same standard as the factory installed sheath. Thus, the act of inspection to assess the state of the sheath would have been detrimental to the sheath so NDT methods were extremely important.

In order to inspect the hangers, inspection methods needed to be found that could investigate the condition of the wires both externally and internally. External inspections are relatively simple and can be conducted by eye or by remote camera; internal inspections are much more demanding. Two methods were selected; magnetic flux and X-ray.

Magnetic flux methods are used extensively in the inspection of cable systems. The system works by use of an instrument that quantitatively measures the loss of metallic cross-section area (LMA) and detects discontinuities such as
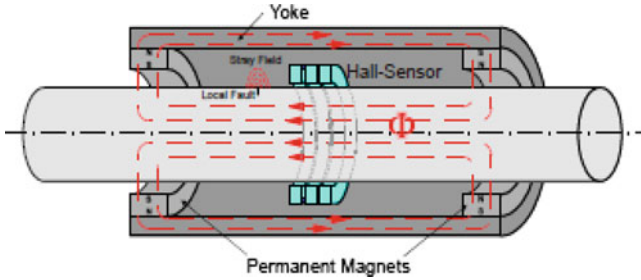
Fig. 1 Magnetic Flux Leakage Method
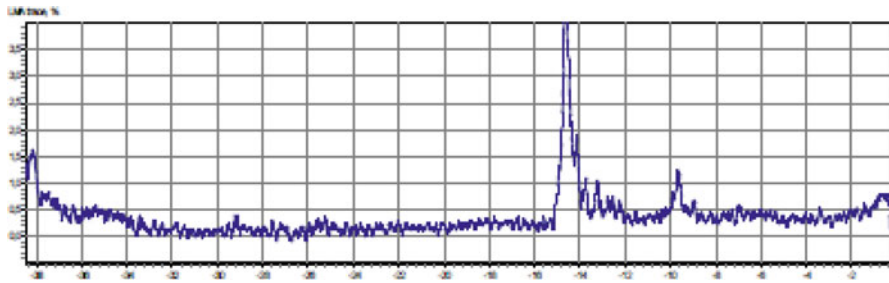
Fig. 2 Inspection record

broken wires or localized changes in rope structure (localized faults - LF). LMA is a relative measure of the amount of ferrous material loss from a location along a wire rope and is measured through comparing readings in a current point and the reference point on the rope that represents nominal metallic cross-sectional area, as measured with an instrument. LF is a discontinuity in a rope, such as a broken or damaged wire, a corrosion pit on a wire, a groove worn into a wire, or any other mechanical discontinuities that degrades the integrity of the rope, both on surface and inside the rope under test. The instrument utilizes the magnetic principle of operation. Magnetic heads magnetically saturates sections of a rope under test. Any changes in rope cross-sectional area as well as discontinuities, such as broken wires or strands, pits of corrosion etc., cause changes in leakage flux of magnetic field. These changes are detected by magnetosensitive sensors (Hall-sensors), which are placed close to the rope midway between the pole pieces of magnetic head (Fig. 1). Signals from sensors supply the basic unit where they are processed and displayed. Special software allows the transfer of this information to a computer through a serial interface which also processes the information into a readable form.

This method of inspection provides a good indication of the presence of wire breaks and loss of metallic cross sectional area, two important criteria within the assessment of the residual capacity of the hangers (Fig. 2). The results of the

inspection showed that a number of hangers on the older Bosphorus Bridge had wire breaks and that there was some metal loss in a number of the hangers. These findings demonstrate that the hangers are approaching the end of their service life and will need replacing soon. The life span of these hangers is commensurate with hangers of similar construction on other suspension bridges. For the newer Fatih Sultan Mehmet Bridge, there was no evidence of any loss of metallic cross section, nor of any wire breaks. This demonstrated that the decision to use sheathed cables was appropriate and has provided very good protection of the cables.

The draw back of this method is that the instrument cannot inspect the sockets closely. It is not possible to pass the equipment across the hanger and the significant variation in cross section shape would render any readings obtained as uninterpretable. An alternative method of X-raying the hangers was tried to determine if wire breaks could be observed directly on the film. As a trial, the equipment was set up at a position of a known broken wire to calibrate the equipment. The trial was not successful in that there was simply too much material for the X-rays to penetrate using safe radiation dosages. The sockets were even harder to X-ray owing to the thickness of the socket obscuring most of the detail. It is the author's experience from carrying out destructive testing of similar strands from a number of other bridge projects that the broken wires tend to form on the outside lays first, giving a clear indication of hanger deterioration. This, allied with knowledge gained from the magnetic flux close to the hanger, provides sufficient confidence in the assessment of the strand deterioration at the socket, although it would be beneficial to have an improved method of inspection.

There is an alternative to magnetic flux inspections that has been developed and is starting to find favour in bridge inspections. The technology, known as magneto-striction, is simpler to set up on a suspension bridge as it does not require the magnetic head to be pulled up and down the cable, as is the case with the magnetic flux method. The technology differs in that it does not use magnetic flux principles; rather it generates a guided acoustic pulse that travels up and down the strand. Where there is a defect in the rope resulting from corrosion or fatigue damage, a portion of the pulse is reflected back to the source. These reflections can be measured and quantified to determine the relative size and location of corrosion or fatigue damage on a suspender rope. The system is similarly limited in its ability to detect anomalies in the socket region, but offers an alternative means of inspection. The methodology was not available at the time of conducting the hanger inspections on Bosphorus, but could be used as a means of counterchecking results in the future.

Anchorage Inspections

A visual inspection of all the visible concrete surfaces within each of the bridge anchorages were carried out for both of the Bosphorus and Fatih Sultan Mehmet Bridges. Moreover in the Fatih Sultan Mehmet Bridge anchorage rods are partially

exposed by removing the concrete around some of the selected anchorage rods for visual inspection and carbonation tests.

The condition of the concrete surfaces was examined closely in possible locations. Any anomalies such as cracks, as well as other types of defects listed in the inspection sheet, were recorded and photographed. Additionally the deterioration locations was illustrated in the plots to supply detailed information of the damage and can provide comparison with further inspections carried out in the future. To determine the estimated strength of the concrete, the Schmidt Hammer test was adopted. The Schmidt Hammer test was applied to the surfaces where appropriate conditions were satisfied in order to obtain reliable results. Both the visual inspection and Schmidt Hammer test have indicated that the condition of the concrete was satisfactory.

In Fatih Sultan Mehmet Bridge anchorage rooms, the most conspicuous situation is the ingress of the groundwater or surface water into the anchorage chamber. This situation has been aroused during the construction of this bridge and instrumented to cover this issue. Although the instrumentation is enough, extra care is needed to be given for discharging of water.

In order to gain the maximum benefit from testing, it was decided to use an intrusive deep excavation to examine the condition of the concrete at a deeper level than just the surface. It was considered that tests on the concrete and steel surfaces will show a degree of information on the bar corrosion, but surface concrete tests are not particularly representative of deeper deterioration of the concrete. The concrete adjacent to a number of anchorage bars was removed by a percussive drill to gain access to the sides of the anchor bars in the region where they are being subjected to the greatest wetting and drying cycles and the greatest levels of oxidization. This provided the opportunity to visibly inspect the bars to observe if there had been any deterioration. The findings of the excavation have shown that there is no evidence of carbonation of the concrete or corrosion of the anchorage bars.

Steelwork Inspections

A comprehensive, principal steelwork inspection of both Bosphorus Bridges was performed for all major bridge components in order to assess the effect of corrosion and fatigue related defects. This included detailed inspections of the deck structures, towers, main cables, articulation components and anchorages of these two life-line structures.

The success of an inspection of this kind is dependant on a variety of factors. However, the most important aspect is to ensure that a robust, well organised reporting structure is adopted early in the inspection programme. This ensures that defects are recorded accurately for the purposes of assessing the structure's condition as well as ensuring a comprehensive database of known defects is formulated to act as a benchmark for future inspections. A bridge reference system was initially devised so that all bridge parts and areas could be clearly and unambiguously referenced.

A walk-through inspection of both bridges was systematically performed on all internal surfaces and joints from one end to the other. To ensure accuracy of recorded defects, random areas inside the steel box girders were independently spot checked by senior project team members.

The 100% visual inspection results of both bridge deck girders were used to select specific areas of welded steelwork that would be subject to a more detailed inspection using non-destructive testing methods. Areas that displayed a higher frequency of severe defects in particular welded joints, when compared to the rest of the bridge, were selected as this implied a higher degree of background stresses at these points in the structure. The inspection scope is huge: the length of welding present in the two suspension bridges is close to 86,000m of trough-to-deck welds in Bosphorus Bridge alone.

Magnetic Particle Inspection (MPI) was chosen over Dye Penetrant Inspection (DPI) as the preferred NDT technique on the Bosphorus Bridges. DPI employs a penetrating liquid, which is applied over the surface of the component and enters the discontinuity or crack. After the surface is cleaned of excess liquid, dye contained within surface defects is drawn to the surface using a developer, which subsequently indicates the location of any defect. It is possible for the DPI method to introduce inconsistencies on a suitably rough surface, such as a welded joint, since over-cleaning the surface can result in defective areas being overlooked while under-cleaning may result in false defect indications. By comparison, MPI is based on the principal that surface discontinuities may be detected by applying finely divided ferromagnetic particles over the surface of interest and inducing a magnetic field. Discontinuities in the magnetic field cause particles to be drawn together, which are then held by the leakage field and allow the presence of the defect to be assessed. MPI is generally the preferred technique on welded carbon steel joints due to its accuracy in determining the location of surface defects coupled with its efficiency and ease of application.

Other systems such as ultrasonic testing (UT) were also used where appropriate. In particular, transverse welds in the deck boxes were scrutinised closely to ensure that fatigue damage was not taking place in these critical details. The benefit of the UT is that it provides greater clarity of the state of the weld beneath any surface defects, but is limited in application to predominantly assessing butt welds or large fillet welds.

Conclusions

In conclusion, the methods of NDT used for the two bridges represent some of the more sophisticated methods of inspection available. The steel inspection relied on established methods so that a reliable picture could be built up of the state of the steelwork, especially the welds. The cable inspection methods were extremely

useful in identifying the extent of the corrosion in the cables and, in the case of Fatih Sultan Mehmet Bridge, confirm that the sheath protection had been a very wise design choice.

Reference

[1] Flint & Neill Partnership, (2009), *Behaviour Analysis and General and Local Technical Survey of Bosphorus and Fatih Sultan Mehmet Bridges Project*, General Directorate of Public Highways, 17th Regional Directorate, Turkey.

Non-Destructive Evaluation for Horizontal Cracks in RC Slabs of Highway Bridges Based on Analysis-Aided Impact Elastic-Wave Methods

S. Uchida, T. Kamada, T. Iwasaki and H. Tsunoda

Abstract In this study, impact elastic-wave method was performed at the bottom surface of RC slab cut from an existing highway bridges to survey horizontal cracks. Before measurements by impact elastic-wave method, impact response analysis was applied to determine elastic wave input method, elastic wave detection method and frequency analysis method. Efficiency of analysis-aided impact elastic-wave method was confirmed by drilling and observing the interior of the RC slab by a rod-shaped scanner. Evaluation results by this method are similar to those of visual inspection. Thus, the feasibility of analysis-aided impact elastic-wave method on detection of horizontal cracks in RC slabs of highway bridges was demonstrated.

Keywords Highway bridges • Horizontal cracks • Impact elastic-wave methods • Impact response analysis • RC slabs

Introduction

Recently, horizontal cracks have been found in cut cross-sections of deteriorated reinforced concrete slabs of highway bridges in Japan (see Fig. 1). The occurrence or development of horizontal cracks is very difficult to detect by visual inspection from the top or the bottom surface of RC slabs. Establishing of a non-destructive evaluation method to detect horizontal cracks has therefore been required.

S. Uchida (✉) •
Saga University, Saga, Japan
e-mail: uchida@cc.saga-u.ac.jp

T. Kamada • T. Iwasaki • H. Tsunoda
Osaka University, Osaka, Japan
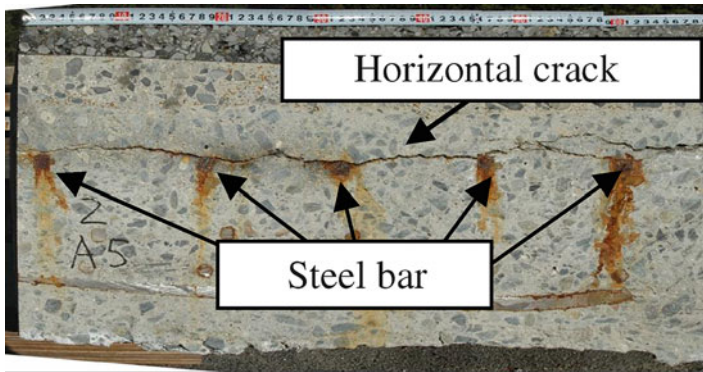
Fig. 1 Occurrence of horizontal cracks in cut cross-sections of a RC slab
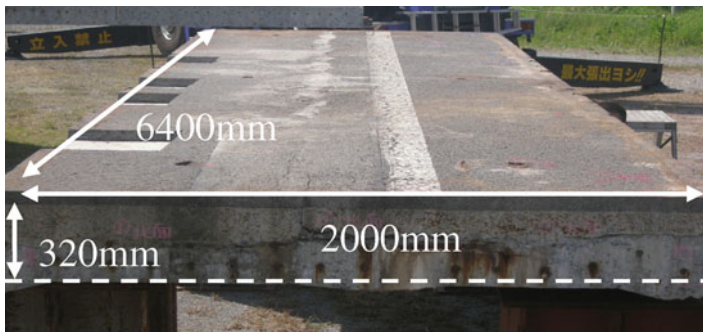
Fig. 2 Outline of a RC slab used in an existing highway bridge

In this study, impact elastic-wave method was performed at the bottom surface of a RC slab cut it out an existing highway bridge to survey horizontal cracks. Before measurements by impact elastic-wave method, impact response analysis was applied to determine elastic wave input method, elastic wave detection method and frequency analysis method. Efficiency of analysis-aided impact elastic-wave method was confirmed by drilling and observing the interior of the RC slab by a rod-shaped scanner.

Outline of a RC Slab Cut from an Existing Highway Bridge

An outline of a RC slab cut from an existing highway bridge is shown in Fig. 2. The thickness of the RC slab was increased by additionally applying SFRC of a thickness of 60 mm with an asphalt pavement of the same thickness.

Outline of the Analysis-aided Impact Elastic-wave Method

Analysis model

The width and length of the three-dimensional impact response analysis model set at 2000 mm based on the results of existing studies [1] to minimize the effects of reflection at the side surface of the model. The thickness of the slab was set at 320 mm. A disk-shaped void was placed in the model to simulate a horizontal crack. The void had a diameter of 200 mm and a thickness of 6 mm. The depth of the void was set at 60 mm, equivalent to the covering depth of the tensile reinforcement, which was considered to be the shortest distance to the depth where a horizontal crack was expected to occur. For comparison, a model with no void was also developed.

Solid elements defined by eight nodal points were adopted for the model. One side of an element had a length of approximately 10 mm. The model was supported on four sides 80 mm × 80 mm each on corner of bottom surface. As the boundary condition, the displacements at all nodal points of supporting surface were fixed. The impact force was input at a nodal point at the center of the top surface of the model. The point of output was 50 mm away from the point of input.

Selection of elastic wave input method

In order to determine elastic wave input method to evaluate both slab thickness and void depth by analysis, impact response analysis was conducted simulating the tapping with steel spheres of varying diameters. Three steel spheres of 3.2, 6.4 and 12.8 mm diameters were used. For the impact force, the waveform of half sine with duration of T_c (sec) was input. T_c was obtained by the following equation based on the results of a study of Sansalone et al [1].

$$T_c = 0.0043D \tag{1}$$

where, D is the diameter of a steel sphere (m). The maximum impact force F_{max} (N) was calculated using the following equation [2].

$$F_{max} = m\sqrt{2gH} \,/\, 0.637T_c \tag{2}$$

where, m is the mass of a steel sphere (kg), g is gravity acceleration (m/s²) and H is the drop height of a steel sphere (m).

The frequency spectra obtained by analysis are shown in Fig. 3. The arrows indicate the theoretical peak frequency corresponding to the model thickness f_T. The broken lines indicate the theoretical peak frequency corresponding to the crack depth f_d. For the frequency spectra shown in the figure, the type of output wave was acceleration and the fast Fourier transform (FFT) was adopted as the frequency analysis method. In the frequency spectrum obtained using a model with no void, a peak is
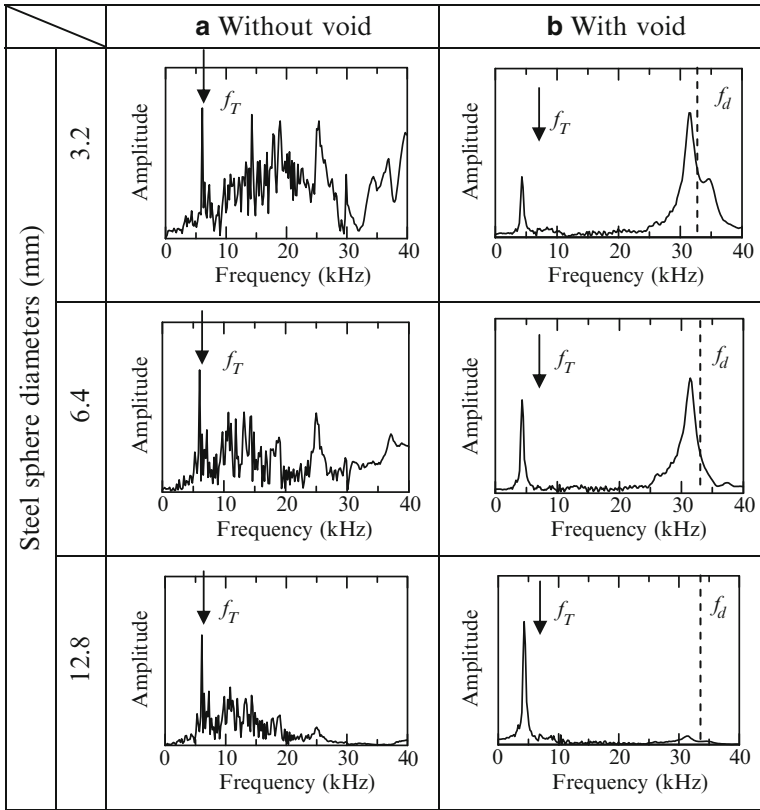
Fig. 3 Frequency spectra for different steel sphere diameters

clearly identified nearly at the position of f_T at all diameters of steel sphere. In the case of a steel sphere of 3.2 mm diameter, however, peaks also appeared at other locations that near f_T. Such peaks may be determined to be the peaks corresponding to void depth. It was considered that slab thickness could be estimated properly in cases where a steel sphere of 6.4 12.8 mm diameter was used for tapping the slab surface. On the other hand, in the frequency spectrum obtained using a model with a void, a peak is clearly identified near f_d at all diameters of steel sphere except 12.8 mm. It was concluded based on the above discussions that a steel sphere of 6.4 mm diameter is most appropriate for evaluating both slab thickness and void depth.

Selection of elastic wave detection method

In this study, waves were output as both of acceleration and displacement at measurement point. The steel sphere diameter of was set at 6.4 mm. The frequency spectra for displacement waveform obtained using models with and without void
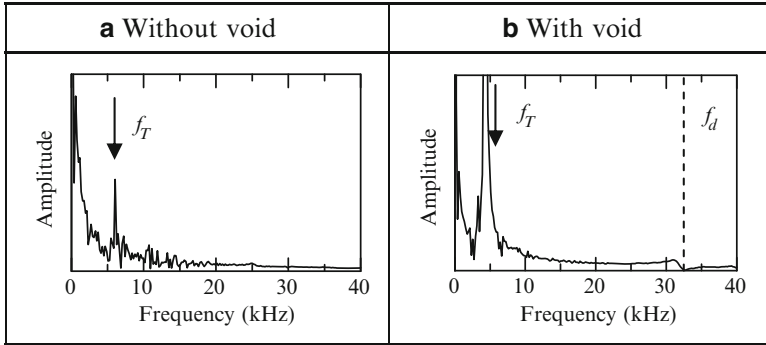
Fig. 4 Frequency spectra for displacement waveform
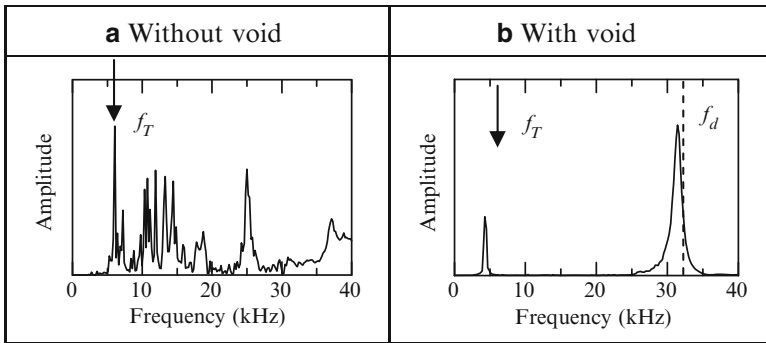
Fig. 5 Frequency spectra calculated by MEM

are shown in Fig. 4. Frequency was analyzed by FFT. The frequency spectra for acceleration waveform were shown in Fig. 3. In the frequency spectrum for displacement waveform, f_T is evidently in agreement with the peak in the frequency spectrum in the models with and without void. In the model with a void, however, peak frequency could be not confirmed near f_d in the frequency spectrum. Thus, the frequency spectrum for acceleration waveform shows that a steel sphere of 6.4 mm diameter was optimum as described earlier.

Selection of frequency analysis method

In order to investigate better frequency analysis method, different frequency analysis methods were compared using the same analysis models adopted in the previous sections. As the frequency analysis method, FFT was compared with the maximum entropy method (MEM). The results in cases where acceleration waveform was output are shown in Fig. 5. The steel sphere diameter was set at 6.4 mm. It is evident in any case that using MEM for frequency analysis resulted in a sharper peak

frequency and the level of frequency component being reduced although slightly in other frequency bandwidths than that for the peak frequency. MEM is therefore preferable to FFT (see Fig. 2) for determining the peak frequency corresponding to slab thickness and void depth.

A Case Study of Measurement of a RC Slab Cut from an Existing highway Bridge

Outline of measurement

In order to verify the validity of elastic wave input method: tapping with a steel sphere of 6.4 mm diameter, elastic wave detection method: use of acceleration waveform, and frequency analysis method: MEM, measurements were performed for a RC slab cut from an existing highway bridge shown in Fig. 2 as a case study. Measurements by the impact elastic wave method were made on the surface of concrete on the bottom surface of the slab. For receiving elastic wave, accelerometer with a response sensitivity range of 0.003 to 30 kHz was adopted. The distance between the points of elastic wave input and reception was 50 mm.

Results of measurement and discussions

Examples of characteristic frequencies obtained at several measurement points are shown in Fig. 6. The figure shows that peak in the frequency spectrum was identical to f_T at measurement point A. It therefore seems that no horizontal cracks occurred at the point. In contrast, a single peak appeared in the area of frequency higher than f_T at measurement points B and C. The peak frequency in
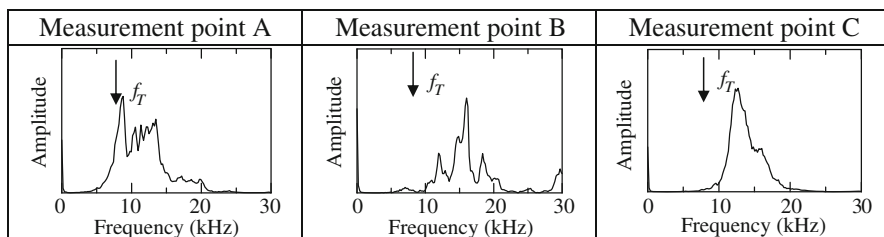
Fig. 6 Examples of frequency spectra obtained in measurement
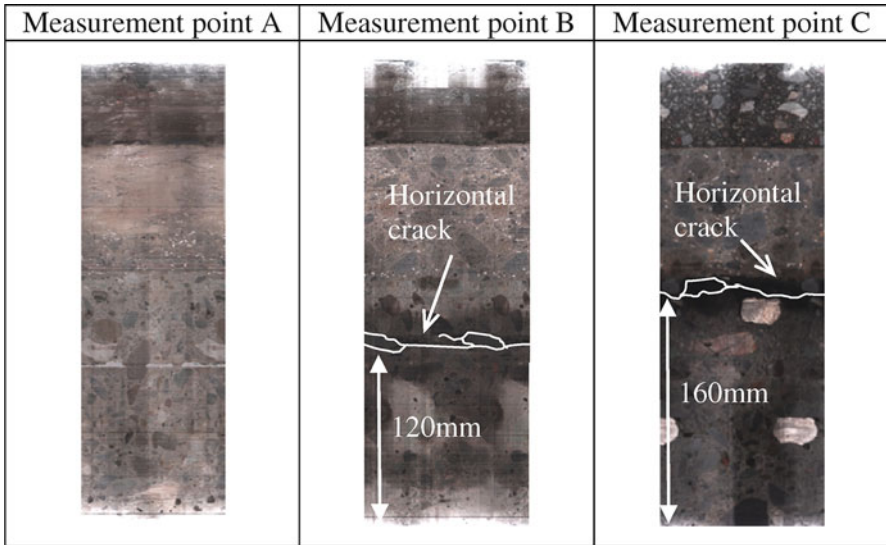
Fig. 7 Observation results by rod-shaped scanner

the frequency spectrum was 16 kHz at measurement point B and 12 kHz at C. Thus, there may be a possibility that horizontal cracks occurred at points 125 and 167 mm away from the bottom surface of the slab at measurement points B and C, respectively (C_p was 4000 m/sec). In order to verify the validity of the results of estimation by measurement, holes of 25 mm diameter were drilled at measurement points A, B and C. After the holes were drilled, rod-shaped scanners were inserted into the holes to film the internal cracks. The images obtained are shown in Fig. 7. It was thus evident that the results of estimation by the analysis-aided impact elastic-wave method were in good agreement with visual inspection results.

Conclusions

The following conclusions were obtained in this study.

(1) In order to detect horizontal cracks in RC slabs cut from an existing highway bridges, before measurements by impact elastic-wave method, a method was proposed for determining elastic wave input method, elastic wave detection method and frequency analysis method by impact response analysis.

(2) The impact elastic-wave method was applied to a RC slab using the method proposed in (1) above as a case study. As a result, it was found possible to determine where horizontal cracks occurred in the RC slab or not, or to estimate the depths of horizontal cracks.

(3) The results of non-destructive estimation by the analysis-aided impact elastic-wave method were generally in agreement with the depths of horizontal cracks measured directly in boreholes.

References

[1] Sansalone, M. and Streett, W.B. (1997). In: *Impact Echo, Nondestructive evaluation of concrete and masonry*, Bullbrier Press, Ithaca, New York.
[2] Shiratori, M., Higai, T. and Okamura, Y. (1992). Response analysis of concrete members by low impact load, Proc. of the Japan Concrete Institute, vol. 14, n. 1, pp. 679–684 (in Japanese).

Non-Destructive Testing of FRP-Structural Systems Applied to Concrete Bridges

K.C. Crawford

Abstract With the increasing application of fiber-reinforced polymer (FRP) structural systems to repair and strengthen concrete structures - in particular reinforced-concrete (RC) bridges - owners are faced with the issue of how to evaluate and predict the long-term performance of FRP systems applied to RC bridges. Methods to measure over time the performance of FRP-strengthened bridges are not fully developed. For a number of concrete bridges in the Republic of Macedonia strengthened with carbon FRP (CFRP) structural systems there is a need, ten years after application, to test and evaluate the performance of the CFRP-strengthened bridges by evaluating the tri-layer CFRP-epoxy-concrete bond. The bonding structure defines bridge load performance. For 19 bridges this involves testing the bond for over 14,000 linear meters of CFRP plates. While a number of non-destructive testing (NDT) methods to measure CFRP-concrete bond performance are used in the laboratory, an effective NDT method to evaluate in the field the bond condition of large quantities CFRP material applied to RC bridges is currently not available. This paper presents an NDT method using a mobile impact-echo device configured to generate an acoustic signal that identifies areas of CFRP material de-bonding from concrete bridge members. The NDT device is designed to test efficiently large areas of bonded CFRP plates. Identification of de-bonded areas of the CFRP-concrete bridge members will provide bonding structure data necessary to support the owner's CFRP-bridge maintenance program.

Keywords Bond • Bridges • Concrete • Debonding • FRP systems • Strengthening • Non-destructive testing • NDT • Impact-echo

K.C. Crawford (✉)
Directorate of Civil Engineering, 95th Air Base Wing, Edwards AFB, California
email: Kenneth.crawford@edwards.af.mil

Introduction

The purpose of this paper is to present a concept for the non-destructive testing of concrete bridges strengthened with FRP composite material by measuring the condition of the CFRP-concrete bonding structure. Becasue the load performance of CFRP-strengthened (CFS) RC bridges is dependent on the integrity of the CFRP-concrete (CFC) bond the objective of this approach is to identify areas of CFRP material that are de-bonding from concrete structural members. It then becomes necessary to evaluate the condition of the CFC bond and to determine how the tri-layer CFC bonding structure is performing over time under the influence of a range of deterioration factors. This paper describes an NDT method for testing the CFC bonding structure using a mobile impact-echo (hammer) device to generate low frequency acoustic pulses to detect areas of CFRP plate de-bonding from the concrete structure. The NDT concept and device presented in this paper are currently under development and will undergo field testing in late 2012, in the Republic of Macedonia, on highway bridges strengthened in 2001 with CFRP-structural systems.

In RC bridge maintenance programs, a desired objective is to maximize bridge load performance during the designed service life with a reasonable investment in maintenance and rehabilitation funds. However, for owners of CFRP-strengthened bridges a fundamental issue in bridge maintenance protocols is how to measure, maintain, and predict the performance of the CFRP-strengthened bridges at a reasonable cost. In the field there is a real-time requirement to evaluate CFS bridge load performance in relation to their original design V600 load criteria [1]. Non-destructive testing of the CFC bond with an impact-echo device is an effective method for testing the bridge CFC bonding structure to evaluate bridge load performance. For bridge maintenance programs non-destructive testing of the CFS bridges should meet the following criteria: (1) NDT testing is easy to apply; (2) the NDT device and testing methods are inexpensive; (3) the NDT procedure is capable of testing large areas of CFRP plates in reasonable time; and (4) NDT testing provides sufficient data to quantify the structural condition of the bond. Testing and measuring the condition of the CFC bonding structure is a necessary element in a comprehensive CFS bridge maintenance program to maintain CFRP-strengthened bridge load performance over time [3].

Background

In 1999, in support of the NATO peacekeeping operations in Kosovo, it became necessary to move heavy military equipment by road from Bulgaria through the Republic of Macedonia into the theater of operations. As a result, certain bridges on the movement route were overloaded above designed safety limits and required strengthening. Based on available FRP technology, recent FRP bridge strengthening experiences in Europe, and recommendations from a joint bridge survey team,

M1- Bridge B2-N
96 Plates (12cm)

M2 – Bridge B36
80 Plates (15 cm)

M2 - Bridge B22
60 Plates (15 cm)

Fig. 1 Typical slab bridges with large CFRP-plate bonded areas

consisting of the Ministry of Transportation and the Fund for National Roads in Macedonia, the Faculty of Civil Engineering of the University of Sts Cyril and Methodius in Skopje, the US Army-Europe, and NATO, the decision was made to use a CFRP-structural system to strengthen 19 of 48 slab and girder bridges (over 90 km) on the highways M2 and M1 (E-870) in northeastern Macedonia to allow the efficient movement of military heavy equipment transports (HETS). The Faculty produced the CFRP-strengthening design for the bridges using national code PBAB-87 for concrete structures (similar to ACI 318-05), national regulation for loading highway bridges with the V600 load (similar to DIN 1072), and ACI 440(2000) [1, 4]. The US Army Corps of Engineers provided design review and project oversight [2]. NATO funded the project. The 17 bridges on the M2 were strengthened from March to June 2001, and the two M1 bridges strengthened in May to July 2002. A total of 14,600 linear meters of CFRP plates in widths of 5 to 15 cm were applied to bridge girders and decks. 19 bridges, originally designed with the 1949 M-25 loading scheme, were strengthened with CFRP using the V600 load scheme, increasing the bending moment at main girder 10-meter mid-point from 75 ton-meter(tm) to 160 tm(bridge B7) and from 50 tm to 110 tm at the main girder 7-meter midpoint (bridge B18). The application of the FRP structural system produced a significant increase in the structural member bending moment and bridge loading capacity. As a consequence the CFC bonding structure is a critical element in bridge load performance and thus it becomes necessary for bridge engineers to obtain accurate data on CFC bond condition for each strengthened structural member. The bond data establishes a basis for CFS bridge maintenance programs.

Figure 1 shows examples of the numbers of CFRP plates applied to M1 and M2 bridges, with bonded areas shown in Table 1. It has been ten years since the 17 bridges on the M2 and two bridges on the M1 were strengthened, and testing of CFRP bond has not yet been performed on the bridges. The issue is this: How are the strengthened bridges currently performing, i.e. is the designed V600 load scheme still sustained by the bonded CFRP plates as originally applied to the bridges in 2001? The challenge becomes how to test and evaluate 14,000 meters of bonded CFRP plates to determine the extent of de-bonding, if any, and to measure and re-certify CFRP-strengthened bridge performance and load capacity in accordance with the original V600 design criteria.

Table 1 Area of applied CFRP plates for selected M1 and M2 bridges

Typical CFRP-Strengthened Bridges (10 of 19 CFS bridges)					CFRP Plate Length (m) and Area (m²)		
Bridge No.	Location On M2	Bridge Type	Length (m)	No. Span	Plate Length	Number Plates	Plate Area
B7	14+027	Girder	120	6	1478	72	116.1
B11	21+876	Slab	10	1	198	26	29.6
B18	38+444	Slab	36	1	218	54	32.6
B22	41+786	Slab	30	1	1308	60	196.3
B28	49+631	Girder	50	3	1210	60	100.6
B35	66+058	Girder	52	3	346	20	41.2
B36	67+409	Slab	21	2	1032	80	82.8
B37	68+452	Girder	17	1	415	36	34.4
B39	71+211	Girder	85	4	1778	48	146.2
B2-N	M1-Kum	Slab	46	4	938	96	112.5

Total CFRP Plate Area for 19 bridges: 1,318 m²

Table 1 shows the CFRP plate area per bridge for 10 of the 19 CFS bridges. The total CFRP plate area for all 19 bridges is 1,318 square meters. The issue for bridge engineers is how to evaluate the entire CFC area on 19 bridges in a timely and cost effective manner. An NDT impact-echo method is proposed in this paper as an efficient and effective solution to evaluate the CFC bond area on CFS bridges.

Concept for Non-Destructive Testing of CFRP-Concrete Bond

Of the ten NDT methods described in ACI 228 the best method for detecting flaws in bonded overlays on concrete slab structures is the impact-echo method [6]. The principle of the impact-echo technique generates a transient pulse into the CFRP-epoxy-concrete tri-layered structure such that a wave is reflected by the boundaries of the structure interfaces. The pulse produces P and S waves that propagate into the layered structure in hemispherical waveforms. The objective of using this NDT method on the CFRP plate is to accurately identify areas of de-bonding between the plate and concrete. Using the acoustic signal generated by an impact device applied to a layered bonding structure provides an effective means to detect and identify areas of voids and delaminated materials in the bonding system.

Figure 2 shows (a) the mobile impact-echo device developed to test CFRP plate bond and (b) the resulting impact-signal pattern. The four-wheel mechanical impact device consists of two 15cm cam-actuated levers with hammer pins, aligned 5 cm apart on axes A and B. Each pin is driven by an adjustable compression spring to obtain an impact force on the CFRP plate to generate optimum acoustic signal intensity. The impact of the alternating striking pins generates acoustic waves penetrating the CFRP-epoxy-concrete tri-layer bonding which in turn reflects an acoustic wave to a signal transducer (receiver). The pins are designed to strike the CFRP

Impact-echo device   Plate impact-signal pattern
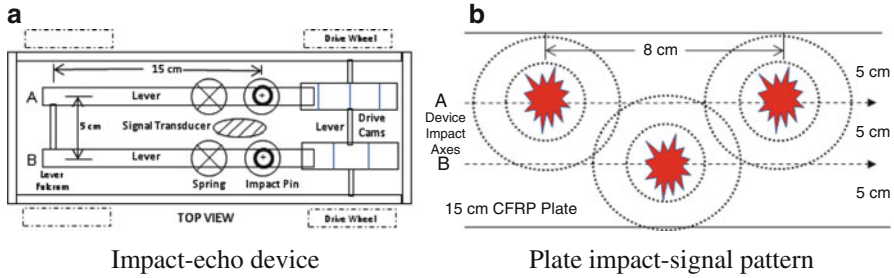
Fig. 2 (**a**) Impact-echo device (**b**) Plate impact-signal pattern

plates at four cm intervals alternately on the A and B axis. A 15cm wide CFRP plate will have 25 impacts per meter, with one impact producing a bond condition response for 600 mm^2 of CFRP plate area. The impact device is designed to strike the plate with equal force over the length of the CFRP plate generating an acoustic signal with consistent intensity for a fully bonded plate. If the CFRP plate is bonded for the length of the concrete structural member the signal frequency will be consistent, i.e. without variation over the entire length of the plate.

The frequency of the generated pulse is a function of the impact duration. A shorter duration, < 80 μs, generates a higher frequency and is suitable for detecting flaws in concrete structural members less than one meter in thickness. For the M1 and M2 bridges the desired depth of flaw detection, from the CFRP plate surface to the closest steel reinforcing in the concrete is less than 30 cm. The depth of the CFRP plate surface to the epoxy-concrete interface is less than 1.5 cm and is the focus of interest in the impact-echo NDT method proposed. Each impact signal received is logged on a data recorder. A bonded plate will generate a specific frequency, and a de-bonded plate will generate a lower frequency. The variation in received acoustic frequency will indicate a change in the CFC bond structure, i.e. potential de-bonding. As testing of the plate bond structure proceeds and different frequencies are recorded, frequency analysis of the displacement waveform (reflected pulse) is used to obtain an amplitude spectrum from the time-domain signal. The frequency of the reflected pulse is a function of wave speed and distance between the plate test surface and the internal reflecting surface, i.e. a function of the CFC bonding/de-bonding structure. As de-bonded CFRP plate areas are identified they are marked for repair and rehabilitation.

There are a number of failure modes and de-bonding mechanisms, e.g. moisture, affecting bonded CFRP plate. In work by Kotnia [7], two primary modes of bond failure occur in the plate anchorage areas and the maximum bending moment in the mid-beam region, a focus for this NDT method. In one theoretical de-bonding load model by Nigro and Savoia [5], CFRP plate width, length, thickness, and axial stiffness define the de-bonding load for a structural member. Thus a decrease in plate bonded width and length proportionally decreases CFS bridge load capacity. Control and mitigation of CFRP plate de-bonding mechanisms, especially moisture, will contribute to extended service life for CFRP-strengthened bridges.

Conclusion

Application of the impact-echo NDT method proposed in this paper to identify de-bonded CFC areas on bridge structural members will provide bridge engineers qualitative data on CFRP-concrete bond condition and the necessary input for CFRP-strengthened bridge maintenance protocols.

- For concrete bridges strengthened with CFRP-structural systems there are few practical methods available for bridge engineers to test and evaluate the condition of the bonding structure.
- The NDT method proposed in this paper using a mobile-echo device presents a means to rapidly test and evaluate large areas (long lengths) of CFRP plates applied to concrete structural members on multiple bridges.
- Recording the frequency data for the plate bond establishes a CFC-bond signature at a point in time and becomes a historical record for the condition of the CFRP-strengthened bridge and its load performance.
- Much work remains in developing effective CFRP-concrete bond test procedures in the field to the point of being useful in CFRP-bridge maintenance and performance prediction models.

CFC bond field measurements with the impact-echo device described in this paper on the 19 CFS bridges are not yet available. Field testing on a number of the CFRP-strengthened bridges on the E-870 is scheduled in the autumn of 2011.

References

[1] Crawford, K., Nikolovski, T. (2006) "The Design and Application of CFRP Composite Material to Strengthen 19 Concrete Highway Bridges in the FY Republic of Macedonia", *2nd Int'l fib Congress*, Italy, Paper n.0442

[2] Moussa, M. (2001) "Design Considerations for Bridge Strengthening Using Bonded FRP Systems", *9th Symposium of MASE*, Ohrid, Republic of Macedonia, Vol. l, p.3K-4/1-6

[3] Crawford, K. (2009) "Sustaining Long-Term Performance of Concrete Bridges Strengthened with FRP-Structural Systems", *Proceedings of the 9th FRPRCS Conference*, Sydney, Australia, p. 149

[4] ACI, "Guide for the Design and Construction of Externally Bonded FRP Systems for Strengthening Concrete Structures", *ACI No. 440.2R-02*, American Concrete Institute, Michigan USA

[5] Ferracuti B., Martinelli E., Nigro E., Savoia M. (2007) "Fracture Energy and Design Rules against FRP-Concrete Debonding", *Proceedings of the 8th FRPRCS Conference*, Patras, Greece, 16-18 July

[6] ACI, "Nondestructive Test Methods for Evaluation of Concrete Structures', ACI No. 228.2R, American Concrete Institute, Michigan, USA.

[7] Kotynia, R. (2005) "De-bonding Failures of RC Beams Strengthened with Externally Bonded Stripes", *Proceedings of Intn'l Symposium on Bond behavior of FRP in Structures*, Hong Kong, China

Inspection of Timber Bridges with Ultrasonic Echo Technique

A. Hasenstab and K. Frühwald

Abstract In timber engineering, damages, defects and inhomogenities inside wooden construction components (e. g. interior rot, knots) or at inaccessible surfaces present an important problem as they can cause sudden failure of the component or structure. For a reliable structural safety analysis using non-destructive test methods, information on the wood specie(s), wood degradation and conservation as well as the inspection of different timber grading criteria (e. g. knots, cracks, …) and their influence on the mechanical properties of in-situ, "old" timber members is essential. This paper presents an ultrasonic echo technique that makes use of transverse waves for the inspection of wooden constructions. The method was used in the inspection of numerous timber bridges. In case of missing back wall echoes during ultrasonic echo measurements, the results were complemented by the drilling resistance method. Combined use of these two methods enable evaluation of the internal structure and prediction of the remaining load bearing capacity of cross-sections. The potentials and limitations of ultrasonic methods related to the evaluation of timber structures were taken into account in the evaluations. The typical damages and their potential causes were shown for various timber bridge types. By the use of the developed method, several timber bridges were prevented from demolition.

Keywords Decay • Drilling resistance • Structural safety analysis • Timber bridges • Ultrasonic echo technique

A. Hasenstab
Ingenieurbüro Dr. Hasenstab, Augsburg, Germany
K. Frühwald (✉)
University of Applied Sciences Ostwestfalen-Lippe, Lemgo, Germany
e-mail: katja.fruehwald@hs-owl.de

Introduction

In timber engineering damages, defects and inhomogenities inside of wooden construction components (e. g. interior rot, knots) or at inaccessible surfaces present an important problem as they can cause sudden failure of the component or structure. According to the German standard regular inspections of bridges (visual inspection of the construction and of drilling cores, tapping the surface, endoscopy) are required. In 2008, a 107 m long red ironwood bridge was closed immediately, because of vast internal fungal damage of the main supporting structure (Fig. 3). It was not visible from the outside during the "normal" structural inspection, but only detected with ultrasonic echo and verified with the drilling resistance.

Non- and Minor-Destructive Test Methods

Visual inspection

Visual inspection means "viewing" at the construction to find and mark cracks, fungal decay and other damages. Usually the visual inspection is combined with tapping on the surface with a hammer to find severe fungal infection.

Ultrasonic echo technique

The ultrasonic echo technique is based on the reflection of acoustic waves on inhomogenities in the material, such as the back wall of the specimen or at any other interface. The received signals give indirect information about the condition of the construction element or internal damage. The small density of wood (ρ_{wood} $<<\rho_{concrete}<<\rho_{steel}$) is caused by a high cavity density, which demand probes with high intensity and low-frequency (50-200 kHz). A low frequency results in a small attenuation of the signal. However, it has a large wavelength which is combined with a larger minimum size of the detectable defect.

Nowadays, transverse wave transducers can be used. The transverse waves are produced by spot contact probes or an array consisting of 24 spot contact probes. The transmitting/receiving unit consists of 12 spot contact probes as transmitter and 12 probes as a receiver. This kind of probe does not need a coupling agent, so faster measurements without pollution of the measuring surface are possible. The probes are activated with a centre frequency of 55 kHz [1], which results in a wavelength of 2.5 cm (measuring direction perpendicular to the fibre with v = 1.4 km/s).

To understand the propagation of ultrasonic waves in wood, it is essential to keep in mind that wood is an anisotropic material. First experiments verifying the anisotropy of the velocity of longitudinal and transverse waves can be seen in
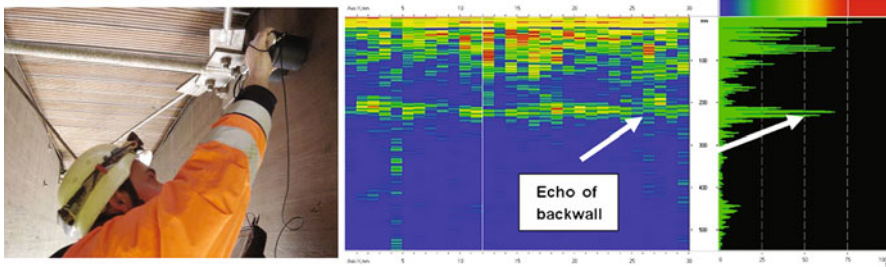
Fig. 1 Ultrasonic echo measurements of a bridge beam (centre: B-scan, right: A-scan), clear echos from the back wall → free of damage

[2-3]. If the transverse waves oscillate in the direction of the fibre, there is no radial/tangential-anisotropy (= no influence of the annual rings). The transverse waves react in wood like in a hand of spaghetti ("spaghettimodel").

Ultrasonic echo results are often represented as A-scans or B-scans. An A-scan (Fig. 1 right) shows the transit time and the intensity of the pulse. A B-scan (Fig. 1 centre) is a composite of a number of A-scans. It is a two-dimensional cross section through the specimen and shows the transit time along the line of measurement. If the measured transit time is multiplied with the known velocity of the sound wave in the material, the result is the way of flight of the sound wave. So a B-scan shows the position of inhomogenities.

Important for the practical use of the ultrasonic echo technique are its limitations: One surface of the construction has to be accessible and almost even (→ no heavy weathering, rough surface structure and not many small cracks). Inhomogenities in the interior like knots, cracks or constructive elements (e. g. screws and bolts) restrain that an echo from the back wall is received [4].

Drilling resistance method

At the drilling resistance method a drill needle is drilled into the timber with a constant feed rate. For the driving a certain power of the driving motor is required, which is high for hardwoods and low for softwoods and damaged wood. In defects or cracks the drilling resistance drops abruptly and rises steeply after re-entry into the wood. In wood with fungal decay the transition from healthy to the damaged wood is more gradual. Details about the drilling resistance are described in the paper by Fruehwald et al. of this conference and in [5]. The drilling resistance is mostly used in areas, for which there is a suspicion of damage after ultrasonic echo measurements. Under certain conditions the density can be estimated from the level of drilling resistance, but there are – especially for hardwoods – more important strength influencing grading characteristics like knots and fiber deviation [6-7].

Inspection of Timber Bridges

Types of timber bridges

Almost 40 timber bridges were inspected. All of them were only permitted for pedestrians, bicycles and horses, none of the inspected bridges was for cars or trucks. Most bridges – all smaller ones – were simple beam bridges. Some of the bigger ones are multiple span beam bridges, truss frames, kingpost trusses or arch constructions. Almost all bridges have a simple board decking because of the exclusively pedestrians use.

The load-bearing timber structure consists of solid wood, composite or glued cross-sections. Mostly European softwoods (spruce, rarely pine and larch) are used with a low (→ spruce) or medium (→ pine and larch) natural durability. Especially the glued cross-sections are only made from softwoods. Because of the higher natural durability, some bridges were made from red ironwood solid timber or composed cross-sections (composed with gate hooks).

Procedure of the timber bridge inspections

Most of the timber bridge inspections were made with a combination of visual inspection and ultrasonic echo technique (Fig. 1 left). If there is a clear echo from the back wall it can be assumed that the specimen is free of defects (Fig. 1 centre). In case of missing back wall echoes (Fig. 2 top: circle), the ultrasonic echo measurements were accompanied by the drilling resistance method (fig. 2 down).

Results and Conclusions

If the potentials and limitations of ultrasonic methods related to the evaluation of timber structures are taken into account, the ultrasonic echo technique in combination with the drilling resistance method deliver accurate view inside the internal structure of the load-bearing timber members of bridges. The remaining load bearing cross sections can be calculated. Several timber bridges were prevented from demolition.

Fungal damage in the upper part of the longitudinal and transverse beams (as shown in Fig. 2) are often due to a missing, insufficient or destroyed covering of the timber beams. For a similar reason, often the bridge bearing is destroyed due to permanent wet soil and the colum-"feets" are damaged due to vegetation (→ wood cannot dry).

In addition to the constructive wood protection either durable wood species or non-durable wood species with chemical wood protection are used. Chemical wood
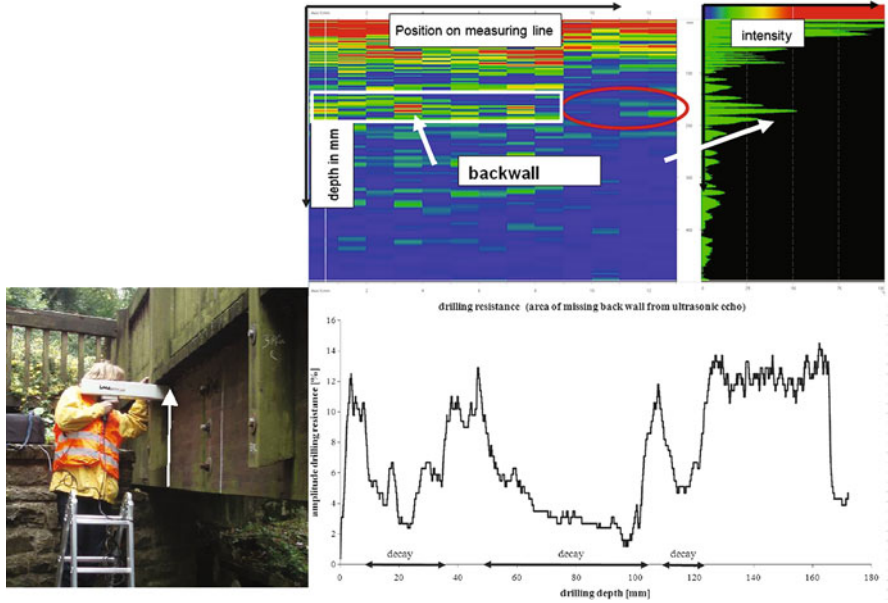
Fig. 2 Ultrasonic echo measurements of a bridge beam, left: measuring line white arrow; top centre: B-scan, lower part of the beam with clear echos from the back wall (white box), upper part of the beam no echos (circle) → measurements of the drilling resistance (left), which showed >50 % of the beam with decay

Fig. 3 left: Red ironwood timber bridge; right: Small, inconspicuous fruit bodies under a projecting cross member [8]

preservatives and the application of durable wood species are often understood equally important as the constructive wood protection or are intended to replace a properly applied constructive wood protection. For example in the 70s and 80s, small and medium dimensional tropical lumber (mainly red ironwood) was used for the construction of wooden bridges, which shows a (very) high natural durability.

Therefore it was thought that just the red ironwood guarantees the durable construction without significant wood protection. Such bridges are still made today, but in a much smaller number. However, the experience of the bridge inspections show, that without a proper, sophisticated and complete constructive wood protection durable load-bearing timber structures are not possible. The use of durable wood species or chemical wood preservative are only supplementary.

Some of the red ironwood bridges meet the expectations and are still in a perfect state, against which some are facing serious damages caused mostly by interior rot – detected with ultrasonic echo (Fig. 3). Why such damages did not occur systematically, is not fully clear yet. Part of the explanation could be, that the natural durability of red ironwood heartwood against fungi is 2v according to DIN EN 350-2:1994-10. That means, that red ironwood is permanent ("2"), but with a high degree of variability ("v").

References

[1] Shevaldykin, V., Samokrutov, A., Kozlov, V. (2003), Ultrasonic low-frequency short-pulse transducers with dry point contact. Development and application, In: Proceedings of the International Symposium Non-Destructive Testing in Civil Engineering (NDT-CE), DGZfP (Ed.), BB 85-CD, V66, September 16–19, 2003, Berlin

[2] Hasenstab, A. (2005), Integritätsprüfung von Holz mit dem zerstörungsfreien Ultraschallechoverfahren, Dissertation TU Berlin, http://www.zfp-hasenstab.de

[3] Hasenstab, A., Hillemeier, B., Krause, M. (2005), Defect localisation in wood with low frequency ultrasonic echo technique, In: Proceedings of the 14th International Symposium on Nondestructive Testing of Wood, 02.-04.05.2005, Hannover

[4] Hasenstab, A., Rieck, C., Hillemeier, B., Krause, M. (2003), Use of low frequency ultrasound echo technique to determine cavities in wooden constructions. In: Proceedings of the International Symposium Non-Destructive Testing in Civil Engineering (NDT-CE), DGZfP (Ed.), BB 85-CD, P51, 16.-19.09.2003, Berlin

[5] Baron, T. (2009), Untersuchungen an ungeschädigten und durch Pilzbefall geschädigten Nadelholzbauteilen mit ausgewählten Prüfverfahren, Dissertation an der Universität Weimar / F.A. Finger Institut

[6] Frühwald, K. (2005), strength grading of hardwoods, In: Proceedings of the 14th International Symposium on Nondestructive Testing of Wood, 02.-04.05.2005, Hannover, p. 199–210

[7] Frühwald, K., Hasenstab, A. (2009), Strength grading of hardwood with longitudinal ultrasonic waves and longitudinal vibration and locating defects in softwood and hardwood with low frequency ultrasonic echo technique, In: *Economic and Technical aspects on quality control for wood and wood products*, Proceedings of the Conference of Cost Action E53, 22.-23.10.2009, Lisbon

[8] Hasenstab, A., Mertens, M., Gunkel, O., Reher, S. (2010), Schadendetektion an hölzernen Rad- und Gehwegbrücken. In: Tagungsband der DGzfP Jahrestagung, 09.-12.05.2010, Erfurt

Acoustic Emission Monitoring of Conventionally Reinforced Concrete Highway Bridges Under Service Conditions

T. Schumacher, C. Higgins and S.C. Lovejoy

Abstract Acoustic Emission (AE) monitoring offers the unique possibility to monitor structural bridge components in real-time and detect sudden changes in the integrity of the monitored element. AE are stress waves initiated by sudden strain releases from within a solid such as crack formation and propagation, material crushing, or bond fracture of two materials in a composite due to over-loading. The present study focuses on methods for in-service monitoring of conventionally reinforced concrete (RC) bridges. Extensive laboratory experiments on two full-scale reinforced concrete bridge girders were carried out to study existing evaluation methods and to identify potential applications that will also work for in-service bridges. A novel evaluation approach based on the well-known *b*-value analysis that worked particularly well was developed and is proposed. It was found that this new method can help estimate operating load conditions and detect overloading of existing bridges. Additionally, an in-service highway bridge was monitored during structural load testing and while experiencing ambient traffic to collect real service-level AE data for comparison. Preliminary data from both the laboratory experiment as well as the in-service test are presented and compared.

Keywords Acoustic emission • Highway bridges • In-service monitoring • RC

T. Schumacher (✉)
University of Delaware, Newark, DE, USA
e-mail: schumact@udel.edu

C. Higgins
Oregon State University, Corvallis, OR, USA

S.C. Lovejoy
Oregon Department of Transportation, Salem, OR, USA

Introduction

Stuctural Health Monitoring (SHM) methods and applications have become of increasing interest due to the worldwide aging and deteriorating infrastructure network. Many bridges have reached their intended design lives of which many need to remain in service due to limited funds for repair or replacement. Tools are thus needed to permit freight mobility and operational safety. AE methods offer the opportunity to monitor and detect ongoing deterioration due to overloading or loss of structural integrity. An introduction to AE testing can be found in for example Grosse and Ohtsu [1]. RC offers some unique challenges as it is a composite material that develops cracks at service-level loads in order to engage the steel reinforcement. The current study presents experimental investigations on full-scale RC girders and a structural in-service load test on an existing bridge performed to develop AE methods that can aid in bridge maintenance and management.

Laboratory Experiment

Two full-scale reinforced concrete (RC) bridge girders were constructed and tested using an elaborate loading protocol to investigate different aspects of Acoustic Emission (AE) monitoring [2]. Incrementally increasing load amplitudes were applied to impose deterioration to the specimens as shown in Fig. 1. After each peak (OL), cyclic loads were applied until measured stresses had reached steady-state, followed by loads that are representative of in-service conditions (test trucks) to investigate the AE response. Also, the strain response from an in-service load test (presented in the subsequent section) was studied and incorporated in that an unloading effect that occurs just before the main loading was replicated as presented in [2] and is shown in Fig. 1.

The specimens comprised typical 1950s vintage details and were tested in inverted T (IT) configuration, as illustrated in Fig. 2.

The total depth was 1.22 m and the web width 0.36 m. The difference between the two specimens, named AE Specimen #1 and #2, was the following: #1 was detailed with all 6 ø 35 mm main flexural tension steel rebars spanning over the entire length of the specimen, whereas for #2 the two outer flexural tension rebars were cut-off on the south side at 2.13 m from the center line (CL). These cut-offs were common practice to optimize the steel needed to cover the flexural tension demand. The stirrup (transverse rebar) spacing was 0.31 m constant in the high shear region of interest (south side) and 0.15 m on the north side to enforce failure in the region of interest. All experiments were conducted in the Structural Laboratory at Oregon State University, USA, as presented in detail in [2]. Force was applied at mid-span through a spreader beam to load points on the specimen spaced 0.61 m apart. The spacing between the supports (span length) was 6.60 m. To minimize noise from the test frame interfering with the Acoustic Emission (AE) measurements, medium stiff neoprene strips were installed between all bearing surfaces.
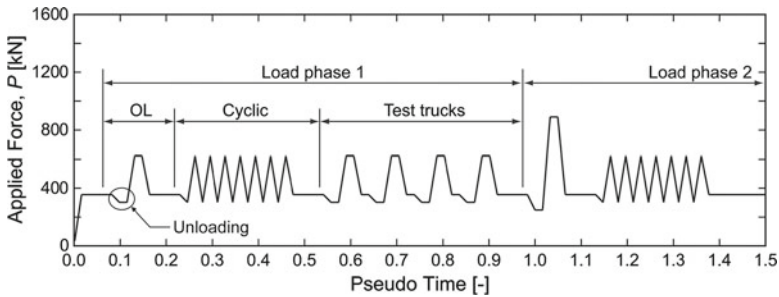
Fig. 1 Loading protocol for laboratory specimens (only beginning), adapted from [2,5]
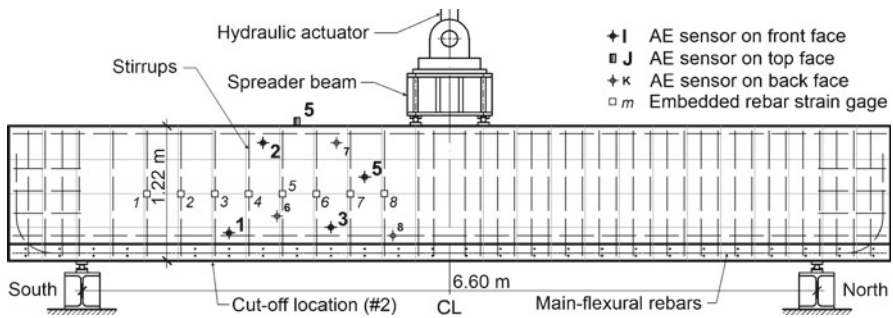
Fig. 2 Elevation view of test setup with AE sensors (typical array), adapted from [2]

Structural In-Service Load Test of a Highway Bridge

Bridge No. 7863 on Interstate Highway 5 in Oregon was constructed in 1954 as a typical reinforced concrete deck girder (RCDG) bridge. Average daily traffic in 2006 exceeded 35,000 vehicles with 10 % being heavy trucks. An elevation view of the bridge is shown in Fig. 3. The original bridge consisted of four 1.22 m deep girders with a width of 0.37 m. Over the bent caps, the girders are 1.37 m deep and 0.61 m wide. In 1995, two exterior girders were added, one on each side, and the bent caps strengthened. This was done for the following two reasons; (1) load rating indicated deficient capacity for permit loads, and (2) minor to moderate diagonal tension cracks of girders and bent caps were found near support locations.

Though scheduled for replacement, the bridge in the current condition has the structural capacity to carry all legal (including permit) loads as found with a recent load rating (July 2006) using methods presented in SPR 350 [3]. A structural in-service load test employing a commonly used 22.7 t dump truck (subsequently referred to as test truck) was used to determine service level strains on reinforcing bars and crack motions, as well as AE activity on an exterior girder of the original bridge. The load test was divided into 10 runs with the test truck on different locations relative to the instrumented girder and with different speeds. For each run, the two
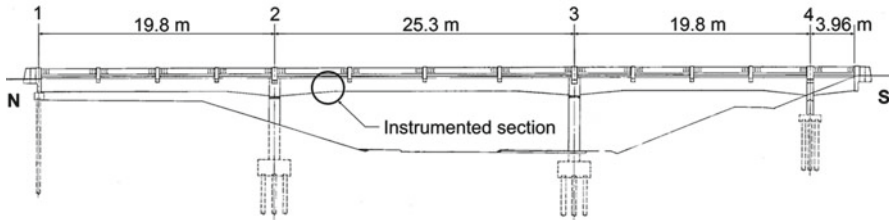
Fig. 3 Elevation view of Bridge No. 7863 on I-5, Oregon

southbound lanes were closed. In addition ambient traffic was recorded for a period of time before and after the test as presented in [4].

Data Acquisition and Presentation

In order to compare data between laboratory experiment and in-service load test, the test conditions and data acquisition settings were kept as similar as possible. The geometry of the monitored girder is virtually identical. Also, a total of eight AE sensors were deployed in a similar manner and distributed around the area of interest, i.e. where cracking was found. The same commercially available AE data acquisition system was utilized for both tests. Additional traditional measurements such as rebar strain, crack mouth opening displacement (CMOD), and applied loads (for the laboratory experiment) were recorded during the tests. In Fig. 4, typical AE hit amplitudes and rebar strain responses are shown. Figure a, b show data from the laboratory experiment (AE Specimen #2, load phase 2). The colored dots represent AE amplitudes for the different AE sensors. The strain response at stirrup 3 is shown as a green line. It can be observed that there is much higher AE activity when an overload is applied compared to a simulated service-level test truck. Also, in case of the overload (a), the strain does not return to its original position which indicates non-linear behavior and that stress redistribution has occurred.

Clearly, the strain response due to the simulated test trucks (b) is significantly lower. This is also supported by the AE response. It should be stated that the selection of stirrup 3 was based on availability. The highest strain for this example was actually found on rebar 7 and was approximately 50% higher compared to the one on rebar 3. Finally, Fig. c illustrates typical AE hit amplitude and the rebar strain responses from the in-service load test on the highway bridge. It can be observed that measured strains are noticeably lower compared to the experimental data. However, the AE response appears quite comparable to (b).

Even though looking at qualitative parameters such as AE hit amplitudes may already provide some insight in what the monitored element is experiencing, quantitative methods are eventually needed in order to estimate the impact an experienced load has. The *Minimum b-Value Analysis* proposed in [2] and presented in detail in [5] may help estimate in-service load conditions and detect overloading experienced by the
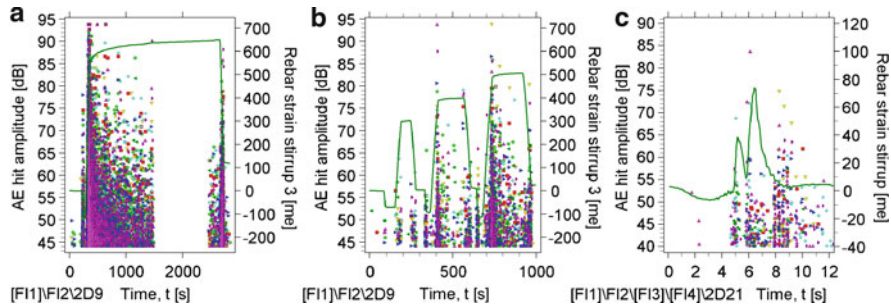
Fig. 4 Example of AE hit amplitude and rebar strain response data: (**a**) Overload applied at the beginning of load phase 2 (AE Specimen #2) (**b**) Simulated test truck (AE Specimen #2) (**c**) Test truck from in-service load test (Run 3, caused highest demand)
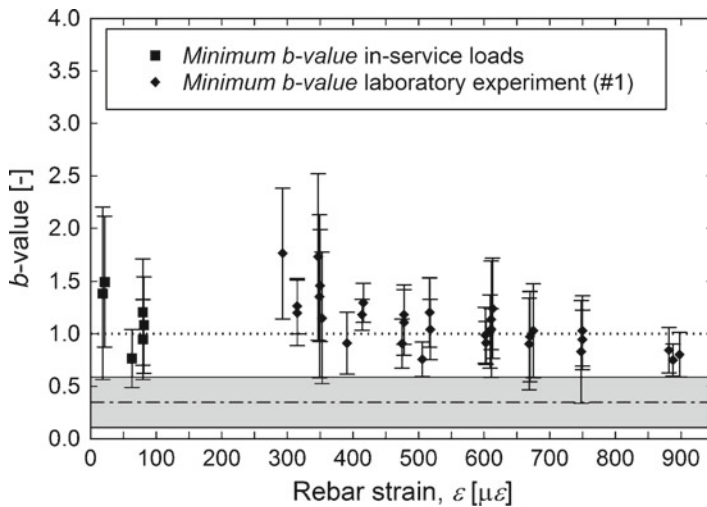
Fig. 5 Comparison of *Minimum b-Values* from laboratory and in-service test

bridge. *b*-Values represent the slope in the empirical magnitude-frequency distribution relationship originally established by Gutenberg and Richter [6] to describe earthquake populations. For AE analyses, typically AE hit amplitudes are used instead of earthquake magnitudes [7-10]. It has been widely accpeted that the change in the *b*-value may indicate a change in the structural integrity, i.e. for brittle materials the *b*-value drops when a macro-crack (localized deterioration) forms after prior existing micro-cracks have formed (distributed deterioration). The *Minimum b-Value Analysis* uses the mean of the lowest *b*-values from all deployed AE sensors over a complete load cycle as a descriptor of the impact of an experienced load [5]. Figure 5 shows a preliminary dataset comparing laboratory data (from AE Specimen #1) and the in-service load test. Error bars represent standard deviations of the different estimated *Minimum b-Values* for each load cycle.

Even though measured rebar strains are quite different in magnitude, there is an apparent trend for both datasets: *Minimum b-Values* decrease with increasing rebar strains. The shaded band represents *Minimum b-Values* that were produced during the laboratory experiment when previous maximum applied loads were exceeded, i.e. new deterioration was imposed in the structure. *Minimum b-Values* produced by service-level loads from the laboratory experiment as well as the in-service load test are well above the shaded area.

Summary

Efforts to develop AE methods to quantify the impact a passing vehicle has on an RC bridge are presented. Data from full-scale laboratory experiments as well as from an in-service bridge load test can directly be compared because the test conditions are essentially the same. From the preliminary data analysis, it was found that the simulated test trucks in the laboratory experiments and the real test trucks in the load-test produced similar *Minimum b-Values* which leads to the conclusion that the bridge did not experience deterioration during the load test. This should be expected since there are much higher loads allowed on this bridge than what was used as test truck. More detailed analysis is planned in the future.

References

[1] C. U. Grosse and M. Ohtsu, *Acoustic Emission Testing - Basics for Research-Applications in Civil Engineering*. Berlin & Heidelberg, Germany: Springer Verlag, 2008.
[2] T. Schumacher, "Acoustic Emission Techniques Applied to Conventionally Reinforced Concrete Bridge Girders," Oregon Department of Transportation (ODOT), Salem, OR, 2008.
[3] C. C. Higgins*, et al.*, "Remaining Life of Reinforced Concrete Beams with Diagonal-Tension Cracks," Oregon Department of Transportation (ODOT), Salem, OR, 2004.
[4] S. C. Lovejoy, "Development of Acoustic Emissions Testing Procedures Applicable to Convetionally Reinforced Concrete Deck Girder Bridges Subjected to Diagonal Tension Cracking," PhD Dissertation, Department of Mechanical Engineering, Oregon State University, Corvallis, OR, 2006.
[5] T. Schumacher*, et al.*, "Estimating Operating Load Conditions on Reinforced Concrete Highway Bridges with b-value Analysis from Acoustic Emission Monitoring," *Structural Health Monitoring*, vol. 10, pp. 17–32, 2011.
[6] B. Gutenberg and C. F. Richter, *Seismicity of the Earth and Associated Phenomena*. Princeton, NJ: Princeton University Press, 1949.
[7] J. H. Kurz, *et al.*, "Stress Drop and Stress Redistribution in Concrete Quantified Over Time by the b-value Analysis," *Structural Health Monitoring*, vol. 5, pp. 69–81, 2006.

[8] S. Colombo, *et al.*, "Assessing Damage of Reinforced Concrete Beam Using "b-value" Analysis of Acoustic Emission Signals," *ASCE Journal of Materials in Civil Engineering*, vol. 15, pp. 280–286, 2003.

[9] T. Shiotani, *et al.*, "Quantitative Evaluation of Fracture Processes in Concrete by the Use of Improved b-Value," presented at the Non-Destructive Testing in Civil Engineering 2000 (Seiken Symposium No. 26), Tokyo, Japan, 2000.

[10] M. V. M. S. Rao and K. J. Prasanna Lakshmi, "Analysis of b-value and Improved b-value of Acoustic Emissions Accompanying Rock Fracture," *Current Science*, vol. 89, pp. 1577–1582, 2005.

Review of NDT Assessment of Road Pavements Using GPR

C. Plati, K. Georgouli and A. Loizos

Abstract The pavement structural condition is one of the main factors to be taken into account for pavement maintenance planning. Therefore, more efficient methods for pavement monitoring and structural evaluation are required in order to ensure a good serviceability and to provide adequate maintenance solutions for the pavements. Non destructive testing (NDT) provides ideal means to test pavement structure in rapid and convenient manner, without traffic disruption and without causing any damages to the existing pavement structure. On this basis, over the past few years, Ground Penetrating Radar (GPR) technology has led to a powerful NDT technique that features several major advantages. GPR has been used successfully in a variety of pavements application such as determining layer thickness, detecting subsurface distresses, estimating moisture content, detecting voids and others. In GPR process an important parameter is the dielectric properties of road materials. This paper investigates the feasibility of GPR use in pavement assessment taking into account the sensitivity of the related results due to the variability of the materials dielectric properties.

Keywords Assessment • Dielectric properties • GPR • NDT • Pavements

Introduction

The increasing shift in resource allocation from new pavement construction to pavement rehabilitation highlights the importance of accurate and comprehensive assessment of deteriorating pavements [1]. Proper diagnosis of the root cause of a particular

C. Plati (✉) • K. Georgouli • A. Loizos
National Technical University of Athens (NTUA), Laboratory of Highway Engineering,
5, Iroon Polytechniou St., Zografou, Athens 15773, Greece
e-mail: cplati@central.ntua.gr

pavement deterioration is a critical prerequisite to the prescription of lasting, cost effective pavement rehabilitation and restoration strategies. With the advent of NDT techniques pavement engineers are able to rapidly collect extensive data [1]. GPR is a NDT, noninvasive, continuous testing, at traffic speed tool that has been used to map subsurface conditions [2]. It addresses multiple engineering aspects for geotechnical site investigation, construction and maintenance of roads/highways, bridges and airfields. The present paper investigates the feasibility of GPR use in pavements. It concerns the basic principles of the GPR technique and outlines the current applications of GPR regarding pavement evaluation.

Basic Principles of GPR Systems

GPR systems typically have the following four components: 1) a pulse generator which consists of a transmitter and a receiver, 2) an antenna enclosure which may consist of a single antenna or separate transmitting and receiving antennas, 3) a control unit and 4) a storage and display unit. For pavement evaluation purposes air coupled and ground coupled antenna systems are used. In the air coupled systems, the antennas are suspended above the pavement surface for operation at highway speeds (up to 100km/h). The greatest advantage of air coupled systems is their repeatability because antenna coupling does not change with the change in pavement properties. The drawback is that the penetration depth is limited. In the ground coupled systems, the antennas maintain contact with pavement or they are suspended just above it. The clear advantage of ground coupled systems is the better signal penetration compared to air coupled systems, although surface coupling and antenna ringing present problems which make it difficult to obtain any quantitative information from the near surface without signal processing. Another disadvantage of ground coupled systems is that the data collection speed is normally 5-30km/h and as such the survey speed is limited.

The basic principle underlying the GPR is that short electromagnetic pulses transmitted into the medium of interest are partially reflected on encountering a change in the electrical properties. The reflected energy is collected and displayed as a waveform showing amplitudes and time elapsed between wave transmission and reflection, while the transmitted part continues through the new material. This process is continued when further electrically different media are met by the transmitted signal. In the case of an asphalt pavement (Fig. 1) the observed peaks in amplitude represent the air/asphalt reflection (A_0), the asphalt/base material interface reflection (A_1) and the reflection from the base/subgrade interface (A_2). The time interval (t_1) between peaks A_0 and A_1 represents the two-way travel time through the pavement layer.

The most important electrical property affecting GPR survey results is dielectric constant and its effect on the GPR signal velocity in the material. The speed of electromagnetic waves through low-loss nonmagnetic materials such as water or soils is expressed according to Eqn. (1):

$$v = c / \sqrt{\varepsilon_r} \tag{1}$$

Fig. 1 Typical GPR reflections from a pavement system
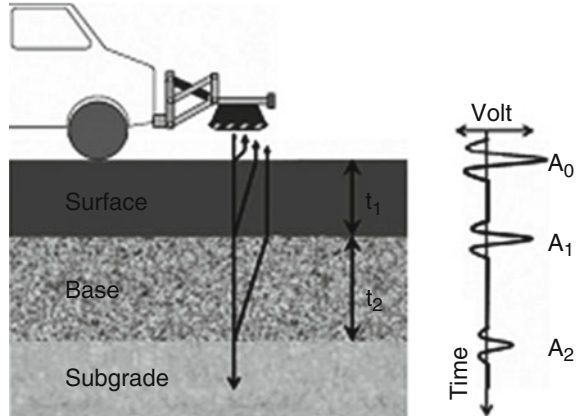
where v is the velocity of propagation of the wave (m/s), c is the velocity of an electromagnetic wave in free space ($\approx 3 \times 10^8$ m/s) and ε_r is the dielectric constant of the traveling medium. The dielectric constant of the top layer can be calculated using Eqn. (2) [3]:

$$\varepsilon_{r,1} = \left[\left(1 + A_0/A_p \right) \middle/ \left(1 - A_0/A_p \right) \right]^2 \qquad (2)$$

where $\varepsilon_{r,1}$ is the dielectric constant of the top layer, A_0 is the amplitude of the surface reflection and A_p is the amplitude of the incident GPR signal which is determined by collecting GPR data over a large scale and flat copper plate placed on the pavement surface.

Examples of Pavement Evaluation Using GPR

GPR has been explored for a variety of highway and airfield pavement applications. These have ranged from localized deterioration studies to large-scale inventories of pavement thicknesses and changes in pavement structure. As following, described.

Pavement layer thicknesses

The thickness of a pavement layer using GPR can be determined by recording the time difference between the reflected pulses from different layers and the dielectric properties of the surveyed layer. The thickness of the nth layer could be computed according to Eqn. (3) [4]:

$$d_n = \frac{c t_n}{2\sqrt{\varepsilon_{r,n}}} \qquad (3)$$

where d_n is the thickness of the *n*th layer, t_n is the electromagnetic (EM) two-way travel time through the *n*th layer as shown in Fig. 1, c is the speed of light free space ($\approx 3 \times 10^8$ m/s) and $\varepsilon_{r,n}$ is the dielectric constant of the *n*th layer.

Various researchers have investigated GPR's success in determining pavement layer thicknesses and reported varying GPR performances, depending on the structure of the surveyed site. According to several studies [5, 6] the estimation of the layer thicknesses directly from collected GPR data can be not only a sufficient but an effective procedure.

Asphalt air voids content

Measuring voids content using GPR relies on the fact that the dielectric value of the asphalt pavement is a function of volumetric proportions of the dielectric values of its components. The results obtained from a comprehensive series of field surveys, led to correlations between air void content measured with GPR technique and air void content using laboratory results [7].

Moisture

Moisture becoming trapped within the surface layer is a major cause of surface distress. According to recent studies [8], GPR can detect the presence of moisture as it will locally alter the reflection and transmission patterns in a way that can be clearly identified in the radar data. Based related studies, an expression for calculating the volumetric water content as a function of the porosity, the dielectric constants the components of the mixture and the dialectic constant obtained from the electromagnetic measurement, is given [9].

Stripping

Stripping in asphalt pavement is a moisture related mechanism that occurs in asphalt when the bond between the bitumen and the aggregate is broken, leaving an unstable lower density layer within the asphalt. The GPR technique has been widely used to detect the location and extent of stripping with varying success [10, 11]. In most cases stripping can be seen as an additional positive or negative reflection in the pavement [7].

Segregation

Segregation may be defined as a lack of homogeneity in the HMA constituents of the in-place mat of such a magnitude that there is reasonable expectation of accelerated

pavement distresses [12]. GPR offers tremendous potential to assist in monitoring the quality of a completed surfacing layer. The GPR parameter that can be used to detect these problem areas is the surface dielectric. If an asphalt surface is uniformly compacted, the surface dielectric should be constant. However, if an area of low permeability has excessive air voids this will be observable in the surface dielectric plot as a decrease in measured dielectric value [7].

Cracks and crack propagation

GPR has proven to be useful in detecting transverse cracking. The location of transverse cracks can be related to locations where the thickness of both bound and unbound layers changes quickly [4]. Most of the results for detecting cracks with GPR have not been encouraging, due to the inadequate resolution to identify vertical defects of this kind. Positive results have only been gained in cases where cracks have been large [7].

Rutting

Rutting is a localized surface depression in the wheel paths of asphalt pavement resulted from repetitive loading. GPR can be used to identify the mechanisms of rutting and identify possible corrective actions [2]. By comparing the layer thicknesses of two GPR surveys (in the wheel path and in the lane center), one can identify the layer in which the rutting has actually occurred [13].

Concluding Remarks

In the framework of not only pavement monitoring but pavement management and rehabilitation planning purposes, the use of NDT systems for pavement structure assessment and evaluation has greatly developed. GPR technology has led to a powerful NDT technique that offers arguably the most flexible technique and the ability to provide the most diverse range of information to test the pavement structure in a rapid and convenient manner. In addition, GPR data and more specific GPR thicknesses can be combined with other pavement data that can be used as input for the mechanistic analysis of pavement structure in terms of pavement adequacy. GPR can also provide a powerful tool for diagnosing current pavement problems (cracking, moisture, rutting etc.) and selecting the optimum repair technique.

References

[1] Mooney, M.A., Miller, G.A., The,Y. and Bong, W. (2000), Importance of Invasive Measures in Assessment of Existing Pavements, *Journal of Performance of Constructed Facilities*, Vol. 14, No. 4, pp. 149–154.

[2] Loken, M. (2005), *Current State of the Art and Practise of Using GPR for Minnesota Roadway Applications*, Minnesota Local Research Board, Office of Research Activities.

[3] Al-Qadi, I.L. and Lahouar, S. (2005), Measuring Layer Thicknesses with GPR – Theory to Practice, *Journal of Construction and Building Materials*, Vol. 19, pp. 763–772.

[4] Saarenketo, T. (2006), *Electrical Properties of Road Materials and Subgrade Soils and the Use of Ground Penetrating Radar in Traffic Infrastructure Surveys*, Faculty of Science, Department of Geosciences, University of Oulu.

[5] Al-Qadi, I.L., Lahouar, S. and Loulizi A. (2003), Successful Application of Ground-Penetrating Radar for Quality Assurance–Quality Control of New Pavements, *Transportation Research Record: Journal of the Transportation Research Board*, No. 1861, Transportation Research Board of the National Academies, Washington, D.C., pp. 86–97.

[6] Maser, K.R. and Scullion T. (1992), Automated Pavement Subsurface Profiling Using Radar: Case Studies of Four Experimental Field Sites, *Transportation Research Record: Journal of the Transportation Research Board*, No. 1344, Transportation Research Board of the National Academies, Washington, D.C., pp. 148–154.

[7] Saarenketo, T. and Scullion T. (1994), *Ground Penetrating Radar Applications on Roads and Highways*, Research Report 1923-2F. Texas Transportation Institute, College Station, Texas, p.36.

[8] Grote, K., Hubbard, S., Harvey, J. and Rubin, Y. (2005), Evaluation of Infiltration in Layered Pavements Using Surface GPR Reflection Techniques, *Journal of Applied Geophysics*, Vol. 57, pp. 129–153.

[9] Roth, K., Schulin, R., Fluhler, H. and Attinger, W. (1990), Calibration of Time Domain Reflectometry for Water Content Measurements Using Composite Dielectric Approach, *Water Resources Research*, Vol. 26, No. 10, pp. 2267–2273.

[10] Rmelie, E. and Scullion, T. (1997), Detecting Stripping in Asphalt Concrete Layers Using Ground Penetrating Radar, *Transportation Research Record: Journal of the Transportation Research Board*, No 1568, Transportation Research Board of the National Academies, Washington, D.C., pp 165–174.

[11] Hammons, M.I., Von Quintus, H., Geary, G.M., Wu, P.Y. and Jared, D.M. (2006), Detection of Stripping in Hot-Mix Asphalt, *Transportation Research Record: Journal of the Transportation Research Board*, No. 1949, Transportation Research Board of the National Academies, Washington, D.C., pp. 20–31.

[12] Stoup-Gardiner, M. and Brown, E.R. (2000), *Segregation in Hot-Mix Asphalt Pavements*, NCHRP Report 441, Transportation Research Board, National Research Council, Washington, D.C.

[13] Roddis, W.M.K., Maser, K.R. and Gisi, A.J. (1992), Radar Pavement Thickness Evaluation for Varying Base Conditions, *Transportation Research Record*: *Journal of the Transportation Research Board*, No. 1355, Transportation Research Board of the National Research Academies, Washington, D.C., pp. 90–98.

Condition Assessment of Mixed Paved Roads by GPR and CCR: Material Properties

C. Kaouane and M. Chouteau

Abstract Severe climatic conditions and poor methodology of maintenance and rehabilitation in Quebec make assessment survey of pavement a necessary however difficult task. In order to support prior results obtained with numerical modeling and to address optimal design of equipments, we determined physical properties of concrete, asphalt and foundation soil. These materials have been sampled from a street in the city of Montreal for which pavement had to undergo complete rehabilitation. The last complete rehabilitation of this street was done more than 30 years ago and material properties and composition were largely unknown. Before removal of pavement, we carried out a GPR survey with two distinct pairs of antennae (450MHz and 900MHz). Laboratory tests on concrete and asphalt were conducted on wet and dried samples, trying to reproduce the variability of physical properties due to changes in climatic conditions for a whole year. We measured complex dielectric constants in the range 50MHz-900MHz with a recently developed dielectric probe, and electrical resistivity using a simple laboratory system. Results show low variability of properties of asphalt depending of the saturation compared to larger variability in concrete. Finally all collected data are used as input to numerical modeling, and results compared with the survey data.

Keywords Asphalt cement • Concrete • Dielectric properties • GPR survey • Mixed pavement

C. Kaouane
École Polytechnique de Montréal, Montreal, Canada

CETE-Normandie Centre, France

M. Chouteau (✉)
École Polytechnique de Montréal, Montreal, Canada
e-mail: chouteau@geo.polymtl.ca

Introduction

In Quebec, severe climatic condition and a poor methodology of maintenance and rehabilitation make urban road network in critical condition. A lack of records on road works and the large size of the network make assessment surveys necessary. We aim to develop a reliable, quick and economical tool for assessment of road condition in order to help municipalities plan rehabilitation or reconstruction. Non Destructive Testing (NDT) methods as Capacitively-Coupled Resistivity (CCR) and Ground Penetrating Radar GPR have shown a valuable potential in Civil Engineering [1, 2]. The physical principles ruling these methods are well-known [3, 4]. However, it is common knowledge that a good interpretation of geophysical data needs additional information. Unfortunately, in our situation, detailed geotechnical structure is rarely available as well as the precise composition or age of the road materials. Mixed paved roads are made of three main layers: asphalt layer (top layer), concrete slab (middle layer) and a grade and sub-grade layer (foundation or bottom layer). The lack of structural information can be by-passed using a combination of methods like GPR and CCR [5]. Nevertheless, we need an appropriate instrumental calibration. This calibration can be done through the determination of physical properties of road materials [6]. GPR and CCR responses are both influenced by electrical properties (dielectric constant and resistivity) of materials. We present here two methods to assess a range of values for electrical properties of road materials

We first performed few GPR profiling and CCR tomography on a mixed road destined to complete rehabilitation. During the destruction of the road we sampled blocks of asphalt and concrete. Then we performed laboratory test. We assessed dielectric properties and electrical resistivity of asphalt and concrete samples. Physical properties of materials are widely dependant of water content. We carried out measurements with "wet" and "dry" samples to replicate the range of extreme moisture content found the materials when they are within the pavement. Finally, we can model the GPR data based on the lab measurements to compare with GPR survey profiles. We focus this paper on the determination of physical properties of asphalt and concrete, the subsequent validation of the results and consequences.

Laboratory Tests

Measurement systems & sample preparation

Dielectric probe

The dielectric probe have been developed at the Department of Civil Engineering of University of Sherbrooke [7]. This probe is an open-ended coaxial probe, which integrates measurements on approx. 30 cm^3 volume. This allows considering the contribution of aggregates and matrix to the dielectric properties. To reduce effects of possible anisotropy and heterogeneous distribution, we did measurements on

three faces of the blocks (at least 10 measurements per block) then we computed the mean values and the confidence interval. A Vectorial Network Analyser (VNA) generated the signal and the complex dielectric constant was measured in the 50 MHz- 900 MHz range.

Resistivity measurement system

We developed a 4-points system for resistivity measurements on asphalt and concrete cores. It consists in 2 metal plates and 2 steel band clamps. We inject a pulse current (4 sec. period) with the Syscal Jr. resistivity meter (Iris Instrument) through the metal plates and we measure the potential difference at the band clamps. Electrolytic gel is used to improve the electrical contact between the metal plates, the band clamps and the core samples.

Sample preparation

We first selected blocks after destruction of the road. As we needed flat and smooth surfaces for measurements with the dielectric probe and drill cores for the resistivity system from the same blocks, the whole process is destructive and it was done in two steps. Two kinds of measurements are done: with wet samples and dry samples. We call "wet" samples that have been immerged in water during 1 to 3 weeks. The "dry" concrete samples are oven-dried (100°C during 16 hours) while the asphalt samples are fan-dried.

Results

Dielectric properties

Results for dielectric properties are shown in Fig. 1 (asphalt) and Fig. 2 (concrete). Only data in the 200 MHz-900 MHz range are shown since some noise in the 50-200 MHz range prevented satisfactory estimates. Whatever is the wetting condition, imaginary part of the relative permittivity is always non-negligible compared to the real part. It appears that asphalt and concrete cannot probably be considered as low-loss materials here.

Electrical resistivity

We did 10 measurements for each sequence (3 cores of asphalt and 4 cores of concrete). The repeatability is excellent and the relative error small (between ±0,2% and 5%). Resistivities could be measured for wet and dry conditions for concrete but only for wet conditions for asphalt. Asphalt cores were 10 cm diameter-long and 13 cm
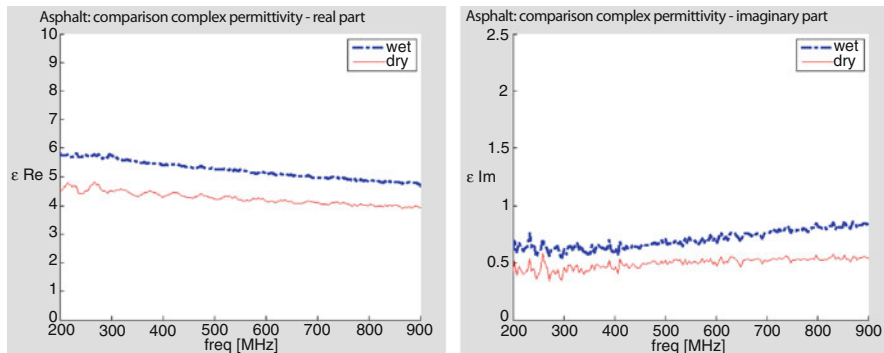
Fig. 1 Dielectric constant (real and imaginary) for dry and wet asphalt
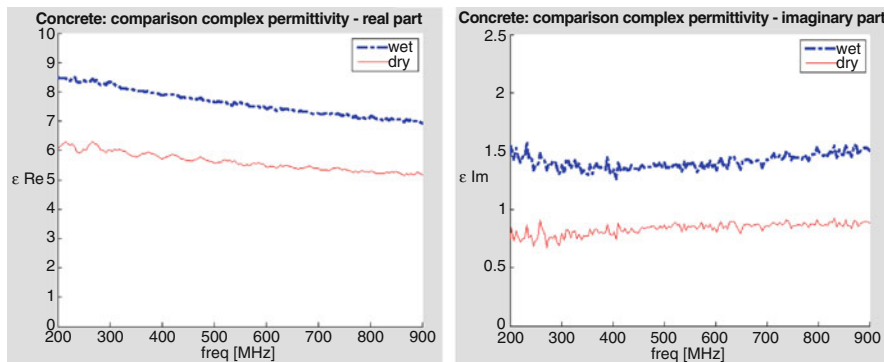
Fig. 2 Dielectric constant (real and imaginary) for dry and wet concrete

high and concrete cores were 10 cm diameter long and about 20 cm long. The injected current were generally between 0,5 mA and 1 mA for concrete and around 0,2 mA for asphalt. Finally, the resistivity (in the DC limit) of concrete in wet condition was between 145 and 275 Ω.m and between 944 Ω.m and 2630 Ω.m in dry conditions. Asphalt in wet condition showed a resistivity between 1510 and 2980 Ω.m.

Validation

We have compared the traces modelled using the GPRMax2D software with traces from our GPR street survey (Fig. 3). For the sake of demonstration here we have selected two traces from two different positions along the survey line. Radar reflections from asphalt-concrete and concrete-foundation interfaces occur at about 2 and 5 ns respectively for the field traces (2nd and 3rd in Fig. 3). The observed

Field traces with 900 MHz antennas vs Modelling 700 MHz with laboratory values
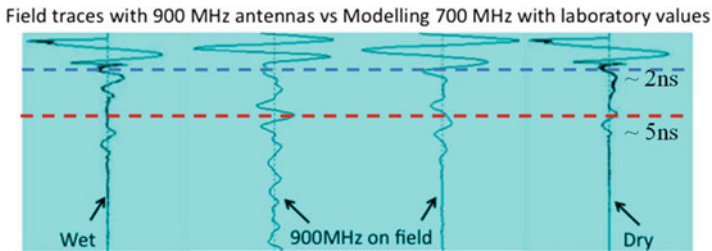
Fig. 3 Comparing modeled traces with field survey traces. The modeled traces were computed using GPRMAX2D with a layered pavement according parameters in Table 1

Table 1 Values used for modelling GPR traces. Values used for foundation were estimated from [8] and CCR soundings done in a street of Montreal

| Material | Width | Wet | | Dry | |
		Resistivity (Ω.m)	Dielectric constant	Resistivity	Dielectric constant
Asphalt	0.13 m	2000	5	5000	4
Concrete	0.17 m	200	9	1500	5
Foundation	0.50 m	20	15	50	10

center frequency on survey data (700 MHz) was used for modeling; thicknesses measured on blocks and physical properties obtained in the lab were assigned to each pavement layer. We computed the radar traces for the wet and dry conditions. We observe that survey traces correlate better with the modeled "dry" trace than the "wet" one, which is coherent with the cold period of the year (late November) the survey was performed. Note that the modeled traces were computed for average pavement geometry and electrical properties and are not specific to the survey trace location.

Discussion & Conclusion

Estimated physical properties of asphalt and concrete agree well with the published literature [6, 9-16] and with test survey traces. Considering the practical aspect of NDT on mixed pavement we can state:

1) Reflected energy from the asphalt/concrete interface are more likely to be observed when the materials are wet (Fig. 4).
2) Hence, it will probably be a preferred period for GPR surveys during the year as moisture content in road essentially depends of seasonal variations [17].

Fig. 4 Reflection coefficient for the asphalt/concrete interface
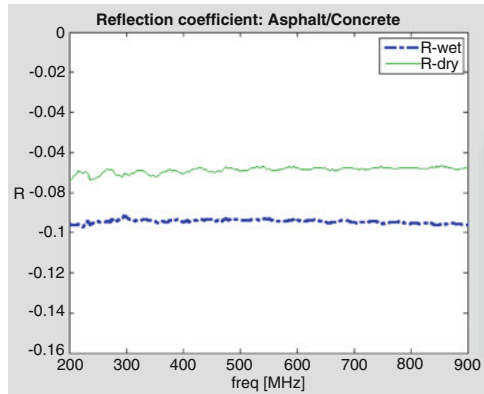
3) GPR signal will be strongly attenuated by the asphalt and the concrete layers. At 900MHz, we estimated attenuation to be about 60, 45, 115 and 60 dB/m respectively for wet and dry asphalt, and wet and dry concrete (based on data plotted in Figs. 1 and 2). CCR is more likely to allow the investigation of the foundation.

We are currently looking further to carry out a whole year investigation on an instrumented pavement site. This study will consist in combined GPR and CCR surveys associated with moisture content measurements (TDR and suction sensors). As fully automatic interpretation software for road testing is not realistic [18] we aim to provide a better interpretation of road surveys through a better knowledge of road materials characteristics and their influence on NDT.

References

[1] Chouteau, M., Vallières, S., and Toe, E. (2003), in *International Symposium of Non-Destructive Testing in Civil Engineering 2003 (NDT-CE 2003)*, Berlin, Germany, 2003.

[2] Derobert, X., Iaquinta, J., Klysz, G., and Balayssac, J.-P. (2008), *NDT and E Int.*, vol. 41, pp. 44–52.

[3] Annan, A.P. (2001), "Ground Penetrating Radar Workshop Notes".

[4] Kuras, O. (2002), "The capacitive resistivity technique for electrical imaging of the shallow subsurface" PhD thesis, University of Nottingham.

[5] Breysse, D., Klysz, G., Derobert, X., Sirieix, C., and Lataste, J.F. (2008), *Cem. Concrete. Res.*, vol. 38, pp. 783–793.

[6] Fauchard, C., Derobert, X., Cariou, J., and Cote, P. (2003), *NDT and E Int.*, vol. 36, pp. 67–75.

[7] Filali, B., Rhazi, J.E., and Ballivy, G. (2006), *Can. J. Phys.*, vol. 84, pp. 365–79.

[8] Nielsen, L., Jörgensen, N.O., and Gelting, P. (2007), *J. Appl. Geophys.*, vol. 62, pp. 1–15.

[9] Soutsos, M.N., Bungey, J.H., Millard, S.G., Shaw, M.R., and Patterson, A. (2001), *NDT & E International*, vol. 34, pp. 419–425.

[10] Robert, A. (1998), *J. Appl. Geophys.*, vol. 40, pp. 89–94.

[11] Filali, B., Boone, F., Rhazi, J., and Ballivy, G. (2008), *IEEE Trans. Microwave Theory Tech.*, vol. 56, pp. 2322–2328.

[12] Malhotra, V.M. and Carino, N.J. (1991), "Handbook on Non Destructive Testing of Concrete". Boca Raton, FL: CRC Press.

[13] Neville, A.M. (1998), "Properties of concrete", Fourth ed. Edinburgh: Longman.

[14] Jaselskis, E.J., Grigas, J., and Brilingas, A. (2003), *J. Mater. Civ. Eng.*, vol. 15, pp. 427–434.

[15] Shang, J.Q., Umana, J.A., Bartlett, F.M., and Rossiter, J.R. (1999), *J. Trans. Eng.*, vol. 125, pp. 347–356.

[16] Shao-peng, W., Lian-tong, M., Zhong-he, S., Dong-xing, X., Yong-jie, X., and Wen-feng, Y. (2002), *J. Wuhan Univ. Techno-Mater. Sci. Ed*, vol. 17, pp. 69–72.

[17] Kestler, M.A. (2003), in *Eight International Conference on Low-Volume Roads 2003, June 22, 2003 - June 25, 2003*, Reno, NV, United states, 2003, pp. 275–284.

[18] Saarenketo, T. and Scullion, T. (2000), *J. Appl. Geophys.*, vol. 43, pp. 119–138.

Portable Wireless High Power Air-coupled GPR System for Highway Inspection

W. Ren, H. Wang and C. Liu

Abstract A FCC compliant 1GHz portable wireless high power air-coupled ground penetrating radar (GPR) system has been successfully designed and implemented with the sponsorship of Texas Department of Transportation, United State. The differential transmitting pulses have 1ns pulse width and ±30V amplitude. The GPR receiver uses differential sequential sampling architecture and has 60dB dynamic range. With its high transmitting power and low-noise system design, the detecting depth of this air-coupled GPR can reach 2 meters in asphalt. The GPR data acquisition and processing software is developed. Lab tests and pavement tests were made to verify the performance. A high way survey was executed on HW69 at in Paris District northeast of Dallas, TX. The first layer dielectric constant and thickness, and other layer feature were measured. Accuracy of the GPR measurement is within −3% to +4%, comparing with the sample cores measurement.

Keywords Air-coupled • FCC compliant • High power • Low noise • Thickness measurement

Introduction

Ground Penetrating Radar (GPR) was originally developed for mapping geological features. It is now increasingly used in engineering and offers a unique non-invasive and non-destructive means for the characterizations of the subsurface and subsurface features [1].

GPR has many applications in a number of fields. The buried target can be a conductor, a dielectric or combinations of both. The surrounding host material can be soil,

W. Ren (✉) • H. Wang • C. Liu
Subsurface Sensing Lab, Department of Electrical and Computer Engineering,
University of Houston, 4800 Calhoun Rd. N308 Engr. Bldg. 1, Houston, TX, 77204 USA
e-mail: wren2@mail.uh.edu

Table 1 Characteristics of GPR systems in soil with relative dielectric constant of 9 and loss tangent of 0.1

Pulse Duration (ns)	Center Frequency (MHz)	Detecting Range (m)	Depth Resolution (m)
0.5	2000	<0.25	0.025
1	1000	<0.5	0.05
2	500	<1	0.1
4	250	<2	0.20
8	125	<4	0.4
16	63	<8	0.8
32	31	<16	1.6

earth materials, wood, rocks, ice, fresh water or manmade materials such as concrete or brick. A typical GPR achieves a range of up to a few meters, but some special systems can penetrate up to hundreds of meters or even kilometers. A few GPR systems have been operated from aircraft and from satellites to image geological features buried beneath the Saharan deserts as well as to measure the depth of the moon and features on Mars or comets. The range of the GPR in the ground is limited because of the absorption the signal undergoes, while it travels on its two-way path through the ground material. GPR works well through materials such as granite, dry sand, snow, ice and fresh water, but it will not penetrate certain clays that are high in salt content or salt water because of the high absorption of electromagnetic energy of such materials.

Different applications require different detecting ranges and depth resolutions. Typical GPR attributes are given in Table 1, assuming the target is soil with the relative dielectric constant of 9 and loss tangent of 0.1.

In this paper, a FCC compliant 1GHz high power portable wireless GPR is developed for most of the application like high speed concrete mapping, road/pavement survey, buried object mapping, construction detail mapping, etc. In these applications, it required higher resolution with respect of a certain detecting depth. So we choose 1GHz as the centre frequency. The "wireless" means the GPR has a build-in battery, and it also can send the data to the computer by wireless or wired connection by the communication subsystem, which is extremely for the operator to use.

System Design

The block diagram of the FCC compliant 1GHz portable high power wireless GPR system is shown in Fig. 1. It contains five subsystems: Transmitter, Antennas with shielding box, Sequential Sampling Head, Receiver, and Control & Communication [2, 3].

The transmitter, which is in Block 1, consists of a nanosecond pulse generator and pulse shaping and matching. The nanosecond pulse generator is based on avalanche transistor architecture [4, 5].
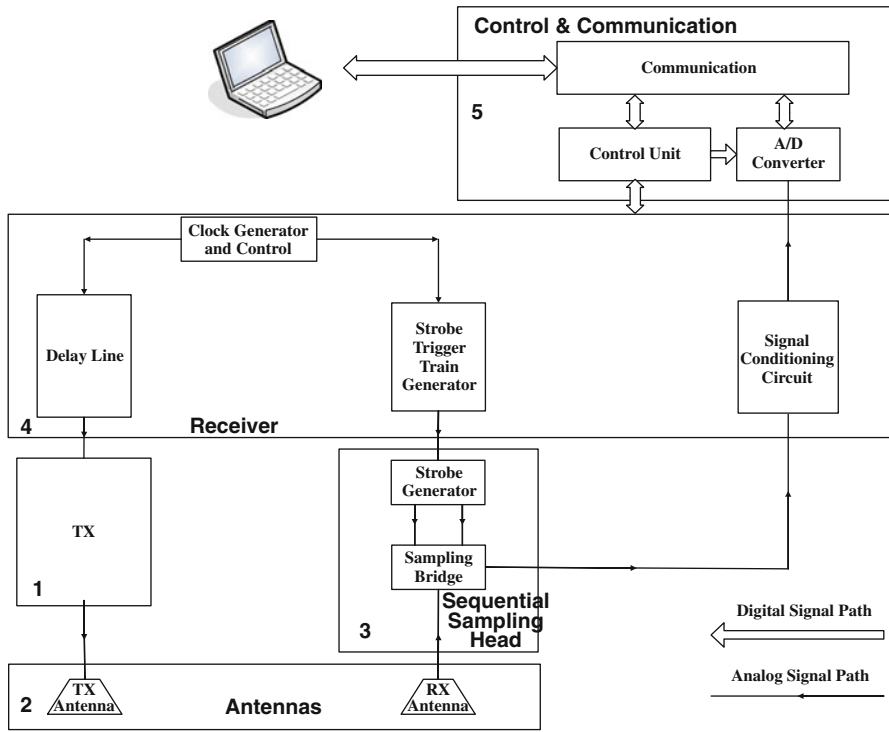
Fig. 1 The system block diagram

The shielded antenna module, which is in Block 2, consists of two antennas, shielding box and absorbers. This module is well designed and passes the FCC test.

The sampling head, which is in Block 3, consists of a strobe generator and sampling bridge. The strobe generator generates the strobe pulse train for the sampling bridge. The sampling bridge samples the received signal under the strobe pulse train, which decides the sampling position on the received signal.

The receiver, which is Block 4, consists of delay line, strobe trigger control and signal conditioning. The delay line defines the position of the sampling window. The strobe trigger train generator generates the trigger train, in which the pulse has an adjustable time delay, Δt, comparing to the previous pulse. The sample point and the window size are controlled by the control unit. The signal conditioning circuitry eliminates the noise of the sampled signal and adjusts the gain of the waveform.

The control and communication circuitry, which is in Block 5, consists of a control unit, A/D converter and communication circuitry. The control unit can read and upload all the parameters of the GPR system. The low-frequency analog signal generated by the receiver is sent to the A/D converter and converted into digital signals. The digital signals are then sent to the host computer by the communication circuitry.

System Implementation and Lab Test

Based on the block diagram shown in Fig. 1, the FCC compliant 1GHz portable GPR system is built, shown in Fig. 2. The specifications of this GPR system are shown in Table 2.

Figure 3 shows the lab verification test of the GPR. Both the waveforms recovered by the sequential sampling head, (a), and by the oscilloscope TDS3052B, (b), are shown. Those figures prove that the transmitter and sequential sampling head work well. They also prove that these GPR systems work well, and the matching for the transmitter to transmitting antenna and receiving antenna to sampling head is good for the ultra wideband.

Lab test was made to verify the function and detecting depth of the GPR system. The GPR systems are mounted on the roof of the building. We use a metal sheet as the target and move it away from the GPR system. Figure 4 shows the test results, which shows a 376 inchs detecting depth in the air. Pavement test was made in the campus of University of Houston. Figure 5 shows the pavement test result.

Field Test at Sherman HW69

A GPR test was conducted on April 14th, 2009 on HW69 in the Paris District in the northeast of Dallas. The road surface is asphalt and the layer thickness was unknown before the measurements. Both new GPR and TxDOT's old GPR systems were used independently for verification purposes. Coring was done immediately after the GPR measurement. Data was processed on site. The total measurement distance was 1 mile. The ground information is the average value of three The results is shown in Table 3.
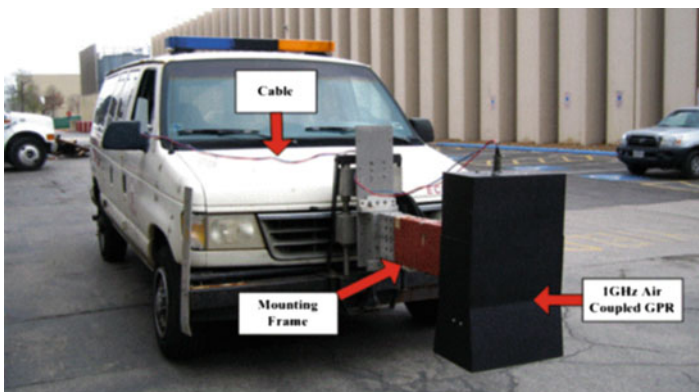
Fig. 2 1GHz Portable GPR system mounted on the vehicle

Table 2 The specifications of the 1GHz portable GPR system

Sampling Head	PRF	200kHz
	Sample Points per Cycle	Max. 4096
	Window Size	13ns to 100ns
	Strobe Pulse Rising Time	371ps
	Strobe Pulse Rising Time	334ps
	Strobe Pulse Amplitude	±7V
1GHz Transmitter	Pulse Rising Time	430ps
	Pulse Falling Time	514ps
	Pulse Width	1ns
	Pulse Amplitude	±30V
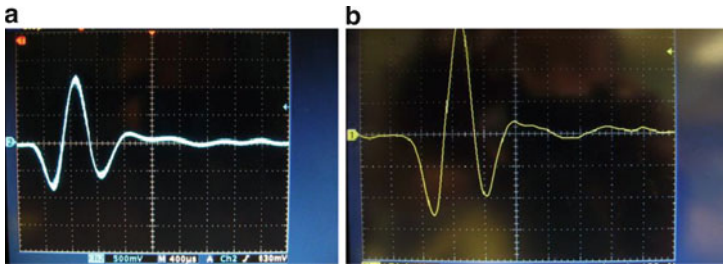
Fig. 3 Recovered waveforms of the 1GHz pulsed GPR system. (**a**), signal recovered by sampling head; (**b**), signals sampled by oscilloscope TDS3052B
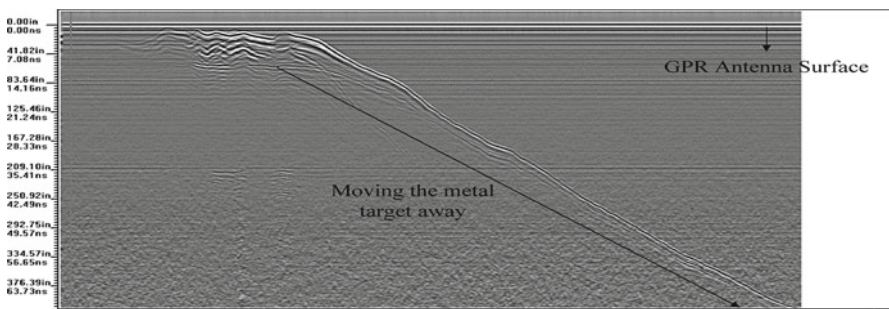
Fig. 4 1GHz GPR detecting depth test in the air
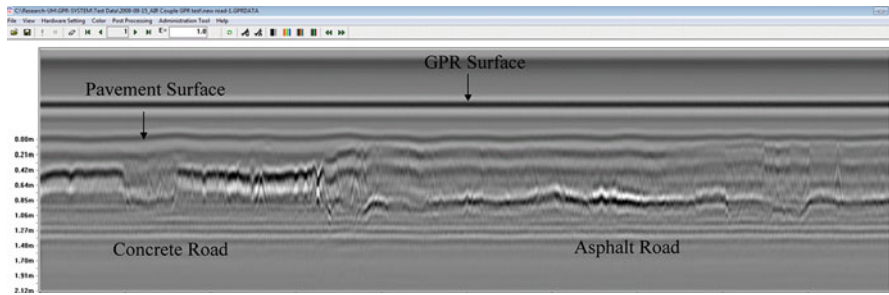
Fig. 5 1GHz GPR test through pavement

Table 3 The measurement results

#	Distance (Feet)	Top Layer Thickness GPR (in)	Core (in)	Error (in)	%	Base Layer Thickness GPR (in)	Desig (in)	Sub-Base Depth GPR (in)	Design (in)
1	450	2.6	2.67	−0.07	−2%	6.3	6	11	12
2	1170	2.9	3.00	−0.10	−3%	6.9	6	12.5	12
3	5090	2.4	2.31	+0.09	+4%	6.6	6	14.4	12
Average		2.63	2.66	-0.03	−1.1%	6.6	6	12.6	12

Conclusion

A FCC compliant 1GHz portable wireless air-coupled GPR system is designed and implemented. Both lab tests and field tests were conducted to verify the accuracy and reliability of the GPR systems. GPR field tests for the Texas Department of Transportation were conducted at Highway 69 in the Paris District. This test shows that the measurement of these GPR systems is accurate, with a -3% to +4% error, and reliable. These tests also show that the FCC compliant 1GHz air coupled GPR systems we designed has good resolution and deep detecting range. This GPR system has great potential in project evaluation and inspection.

References

[1] J. D. Taylor, (2001). *Ultra-wideband Radar Technology.*
[2] W. Ren, H. Wang, C. Guo, and R. Liu, (2009). Proceedings of 2009 5th IWAGPR, pp. 266–269.

[3] R. Liu, W. Ren, and H. Wang, (2010). In: *Implementation of an FCC Compliant Radar*, Technical Report 5-4820-01-2, TXDot.

[4] Y. Wang, C. Liu, and J. Li, (2006). In: *Comparison of three nanosecond pulse generating methods in pulse GPR applications*, Proceedings of 11th International Conference on Ground Penetrating Radar, Columbus Ohio, USA.

[5] W. B. Mitchell, (1968). In: *Avalanche transistors give fast pulse*, Electronic Design 6, pp. 202–206.

Feasibility of Detecting Debonding of Hot Mix Asphalt Layer with Nondestructive Testing

M. Celaya, F.S. Ertem, S. Nazarian and M. Saltan

Abstract Sufficient bonding between the hot mix asphalt (HMA) layers is essential to ensure the desired structural capacity of a pavement. Undetected delamination can ultimately result in the peeling of thin overlays of asphalt concrete from the surface of the roadway. Further progression of delamination may result in stripping of the lower layers due to the intrusion of moisture. Rapid nondestructive test (NDT) methods determine the existence and extent of delamination or stripping within the asphalt pavements. In this paper, several NDT procedures and/or equipment that have the potential to address the problem were identified, and their effectiveness and potential for success were evaluated. The identified NDT methods, which included the Ground Penetrating Radar, Thermography, sonic/seismic and impulse response, were evaluated on a controlled pavement section that was specifically constructed with various levels of debonding at different depths and with different asphalt mixes. Strengths and limitations of different methods are discussed in this paper.

Keywords Delamination • Ground penetrating radar • Hot mix asphalt • NDT • Sonic/seismic tests

M. Celaya • S. Nazarian
University of Texas at El Paso, El Paso, TX 79968

F.S. Ertem (✉)
Ministry of Transport and Communications, Ankara, Turkey
e-mail: selcan@mmf.sdu.edu.tr

M. Saltan
Süleyman Demirel University, Isparta, Turkey

Introduction

A poor bond between pavement layers may lead to several premature distresses of which slippage, cracking, delamination and distortion are most prominent. The delaminated layers and their associated cracks may require frequent maintenance, and may lead to premature need for major rehabilitation. For those reasons, rapid detection of delamination with NDT devices is highly desirable. In this paper, the feasibility of estimating the presence and extent of HMA delamination with four NDT methods is presented. NDT methods were evaluated on a pavement section specifically constructed to simulate different degrees of debonding. The applicability of NDT methods and their detection potentials were evaluated and summarized in this study.

NDT Methods Used in This Study

Several NDT technologies have been developed that could potentially be employed for detection of delamination within HMA layers [1]. Since most of these technologies have been developed for detecting the delamination in concrete slabs, several complications, such as thinner HMA lifts, more material heterogeneity, presence of tack coats and changes in temperature, are encountered when applying these methods to HMA. The four most promising methods are described below.

Ground Penetrating Radar (GPR): GPR uses electromagnetic pulses to characterize subsurface materials based on changes in electromagnetic properties of the layers. The application of GPR in detecting delamination has been previously found to be questionable [2]. In this study, a GSSI SIR-20 (SIRveyor), two-channel data acquisition unit, controlled by a laptop computer and a 1.5 GHz ground-coupled antenna (GSSI Model 5100) were used.

Impulse Response (IR): An impulsive loading is applied to the pavement surface with an instrumented hammer and the vertical displacement with a geophone is measured. If structural distresses are present in the form of loss of adhesion between layers, this is reflected in the dynamic response of the pavement structure. Using a simple modal analysis [3], the bonding condition of two adjacent layers can be obtained. Kruntcheva [4] successfully implemented IR for detection of debonding in controlled test sections. The equipment used in this study comprised of a 45-N hammer instrumented with a load cell and a 4.5-Hz geophone.

Ultrasonic Surface Waves (USW): USW is a seismic-based methodology, in which a dispersion curve (variation in the velocity with wavelength) is obtained. In the USW method, the surface or Rayleigh wave velocity of the top layer is measured without an inversion algorithm that can be converted to modulus [5]. This method has been successfully used to detect HMA stripping [6]. The Portable Seismic Property Analyzer (PSPA) applies the USW in real time was used in this study.

Thermography: Infrared Thermography measures temperature distributions across the surface of the pavement to detect the presence of shallow subsurface flaws in HMA.

Stroup-Gardiner [7] showed its effectiveness for large area inspections, but also its limitations. An InfraCAM™ SD from FLIR systems was used in this study.

Case Study

Ten different 2.7 m by 3 m sections were constructed (see Fig. 1a). Three transition zones were also incorporated to minimize the construction variability. The pavement cross-section consisted of a sandy-silt subgrade covered with a 200 mm thick HMA placed in three lifts. The bottom lift consisted of about 75 mm of a coarse mix whereas the middle lift consisted of 63 mm of a fine mix. The top lift of Sections 1 through 5 consisted of a coarse mix and Sections 6 through 10 a fine mix. The plan view of each section with prepared debonded areas and test locations are shown in Fig. 1b. For this study, the focus was more on the large 1.2 m by 2.7 m debonded areas. Shear tests were conducted on prepared HMA specimens to select different materials to be used as debonding agents (see [1] for details). Clay slurry, talcum powder, grease and thin paper soaked in motor oil were considered. A tack coat at a rate of 0.7 liter/m^2 was used as a control section. A severely debonded area was reproduced in the transition area by placing a 1.2 m by 1.2 m piece of thick corrugated cardboard and a thick layer
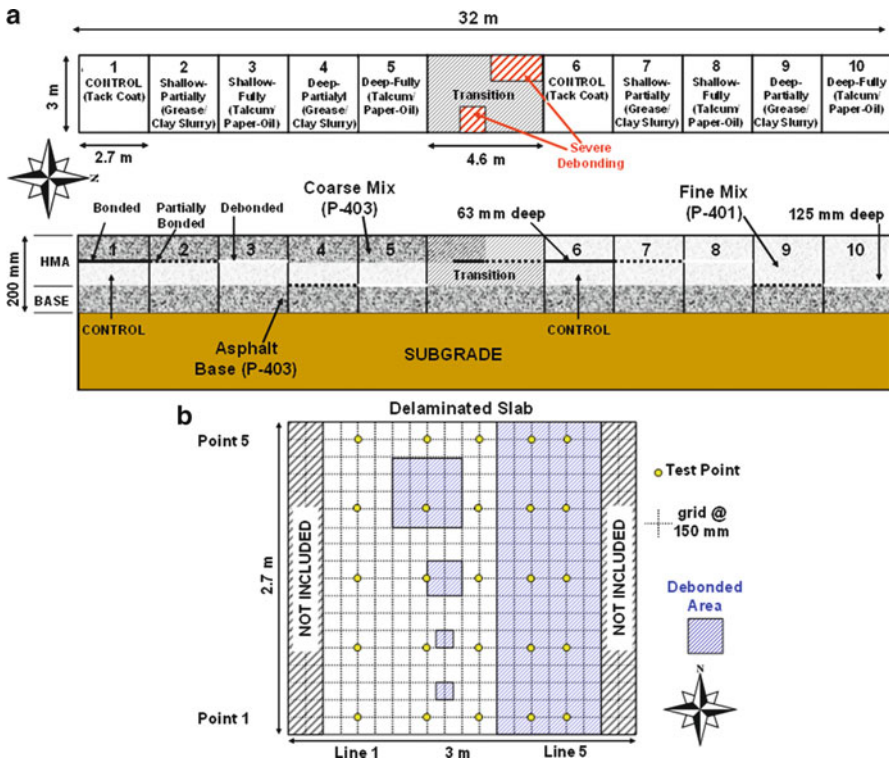
Fig. 1 Schematic of section constructed and location of test points

of clay slurry of 1.2 m by 1.8 m as shown in Fig. 1a. Shallow and deep debondings correspond to the debonding between the top two lifts (at a depth of 63 mm) and bottom two lifts (a depth of 125 mm), respectively.

Presentation of Results

Linescan with the GPR system along Line 4 (containing debonded areas) with the locations of the prepared debonding are shown in Fig. 2. The reflections from the debonded areas should easily be noticeable because of the higher reflection amplitudes. The GPR detected severely debonded area within the transition zone and some debonded areas primarily constructed on talcum powder or clay, perhaps because of the significant contrasts in their dielectric constants and HMA. This indicates that GPR may be most suitable when debonding is in severe stages or when moisture is present along the interface of the debonded layers.

The analysis of IR tests consisted of determining the frequency responses using a Fast-Fourier Transform (FFT) algorithm. The temperature-adjusted stiffnesses were compared using average stiffness and standard deviation of each control section (1 and 6) (see [1] for details). As shown in Fig. 3, most of the fully debonded regions along lines 4 and 5 were identified for both mixes. Some partially debonded areas showed indication of marginally less stiff, however some were found to be intact or substantially less stiff. Most of the intact locations (line 1 and sections 1 and 6) were identified as intact. IR seems promising for the detection of the fully-debonded areas both shallow and deep.

The PSPA USW detailed analysis can be found in Celaya et al. [1]. Dispersion curves for the intact area were fairly uniform, whereas for damaged points, a sharp decrease in modulus below the location of the damage was typically evident. As an example, dispersion curves of Line 4 along the ten sections are presented in Fig. 4 with prepared debonded areas marked when applicable. Similar to IR, average modulus and standard deviation of control sections were used to describe the effectiveness of USW. Debonded areas generally exhibited lower moduli as anticipated. However, some partially debonded sections exhibited normal moduli for both mixes. Also, deep debonding was not as well-defined as for the similar sections with coarse surface HMA.
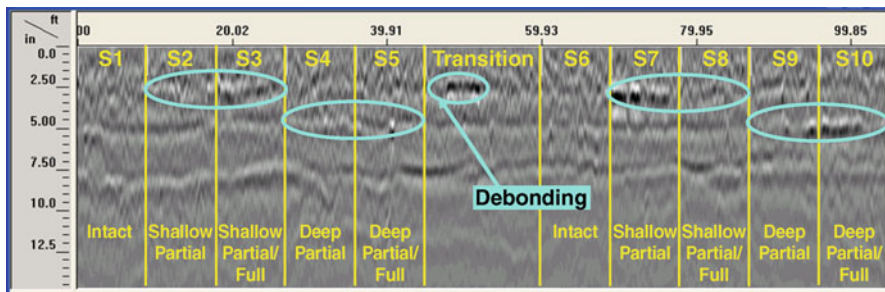
Fig. 2 Linescans with GPR along Line 4 (Debonded)

	S1, Intact					S2, Shallow Partial					S3, Shallow Partial/Full					S4, Deep Partial					S5, Deep Partial/Full				
	P1	P2	P3	P4	P5	P1	P2	P3	P4	P5	P1	P2	P3	P4	P5	P1	P2	P3	P4	P5	P1	P2	P3	P4	P5
N/A																									
Line 1	2.5	1.9	2.0	2.1	2.6	1.6	1.7	1.9	2.1	2.2	2.2	2.4	2.4	2.5	2.3	1.8	2.3	2.4	2.4	2.5	2.1	2.0	2.1	1.9	2.2
Line 2	1.9	2.0	2.0	2.1	1.9	1.9	1.8	1.8	1.6	2.3	2.1	2.1	1.9	1.6	1.6	1.9	1.6	1.6	2.0	2.3	2.0	2.0	1.7	1.7	1.7
Line 3	2.3	2.2	2.2	2.2	1.7	1.9	1.9	2.1	2.1	2.2	1.9	1.5	1.5	1.6	1.8	1.8	1.9	1.9	2.4	2.5	2.2	2.2	2.0	2.0	2.0
Line 4	2.7	2.5	1.8	2.3	2.1	2.0	1.8	2.1	2.0	1.9	1.7	1.3	1.4	0.8	1.0	1.6	1.9	2.0	2.0	2.2	2.1	1.6	1.6	1.6	1.8
Line 5	2.4	2.8	2.1	2.3	2.4	2.1	1.9	2.1	2.3	2.1	1.9	1.4	1.3	1.0	1.0	1.5	2.1	2.1	1.8	1.7	1.7	1.4	1.6	1.2	1.5
N/A																									

	S6, Intact					S7, Shallow Partial					S8, Shallow Partial/Full					S9, Deep Partial					S10, Deep Partial/Full					
	P1	P2	P3	P4	P5	P1	P2	P3	P4	P5	P1	P2	P3	P4	P5	P1	P2	P3	P4	P5	P1	P2	P3	P4	P5	
																										N/A
2.7	2.6	2.8	2.9	3.0	2.2	2.4	2.2	2.7	2.5	2.5	2.5	2.5	2.6	2.6	2.2	2.0	2.0	2.8	2.6	1.8	1.8	2.2	2.3	2.4	Line 1
2.6	2.5	2.3	2.2	2.6	2.7	2.7	2.7	2.9	2.8	2.5	1.8	2.4	1.4	1.6	2.4	2.1	2.6	2.2	2.3	2.0	2.2	2.3	1.8	2.2	Line 2
1.9	2.2	2.0	2.2	2.2	2.1	2.0	2.3	2.3	1.9	1.7	1.6	2.1	1.5	1.7	2.1	2.1	2.4	2.2	1.8	2.3	2.3	2.2	1.8	2.1	Line 3
2.2	2.3	2.3	2.1	2.1	2.0	2.2	2.4	1.8	1.6	1.7	1.8	1.7	1.4	1.5	2.1	1.7	1.8	1.5	1.3	1.6	1.6	1.3	1.7	1.8	Line 4
2.1	2.3	2.3	2.5	2.2	2.0	2.5	2.5	1.7	1.8	1.6	1.1	1.4	0.9	1.3	1.8	1.9	2.1	1.5	1.3	1.3	1.1	1.3	1.5	1.2	Line 5
																									N/A

Fig. 3 Temperature adjusted impulse response stiffnesses
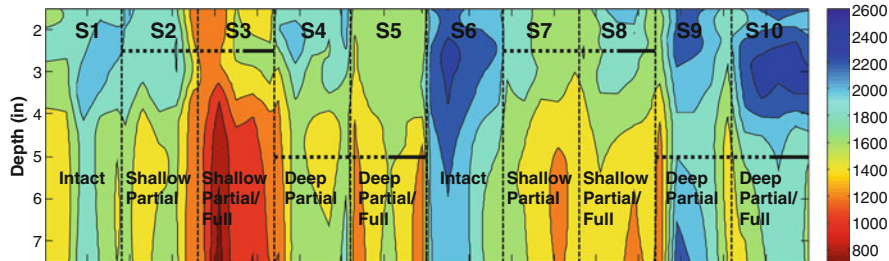
Fig. 4 Dispersion curve results for Line 4

Fig. 5 Infrared camera results on severe debonded area
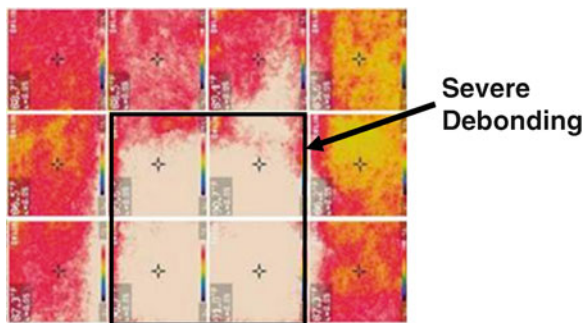
A combined image around the severely deboned area was obtained with the infrared camera as shown in Fig. 5. A passive source (sunlight) was used to create the temperature differentials. The hotter areas (depicted in white) corresponded to

Estimation of Chloride Content in Cover Concrete of Coastal Structures Using Electromagnetic Wave

T. Mizobuchi, K. Yokozeki and R. Ashizawa

Abstract Reinforcement corrosion caused by the presence of chloride ions in the neighborhood of the re-bars has been identified as one of the major causes of deterioration of concrete structures. The chlorides could find their way to concrete either as part of constituent materials when sea sand is used, or, by gradual permeation and diffusion as in the case of marine structures, etc. Thus, determination of chloride content in a concrete structure is an important part of periodic nondestructive testing carried out for structures identified to be vulnerable to chloride induced reinforcement corrosion. In this report, the applicable method which is possible to estimate the distribution of chloride content included in cover concrete in the existing structures using electromagnetic wave method which is non-destructive testing is reported.

Keywords Chloride content • Electromagnetic wave • Estimation • NDT • Reinforced concrete

Introduction

Reinforcement corrosion caused by the presence of chloride ions in the neighborhood of the re-bars has been identified as one of the major causes of deterioration of concrete structures. Especially, when cracks caused by reinforcement corrosion were generated in concrete surface, the reinforcement corrosion is accelerated. As the result, cover concrete in the RC member comes off and proof stress may be lowered with decrease in the cross section of reinforcing steel. However, a definite understanding

T. Mizobuchi (✉)
Hosei University, Tokyo, Japan
e-mail: mizobuch@hosei.ac.jp

K. Yokozeki • R. Ashizawa
Kajima Cooperation, Tokyo, Japan

about any corrosion of reinforcement is very difficult unless corrosion induced cracks appear on the surface.

In order to detect chloride-induced corrosion at an early stage, chloride content within concrete needs to be investigated using cores drawn from the RC structure, and carrying out chemical analysis. Drawing cores could be structurally unacceptable, damage the reinforcement and only very limited sampling can actually be carried out. In addition, drawing cores to estimate the chloride content in concrete could not make it possible to study the changes in chloride content over time at exactly the same place.

Thus, development of truly nondestructive tests to estimate the chloride content in concrete could make it possible to study the changes in chloride concentration over time at exactly the same place, without having to physically approach the structure, or causing any damage. Such methods would greatly improve our ability to foresee the possibility of reinforcement corrosion at early stages, and enable us to take required corrective action at an appropriate time. Then, it has been obtained from laboratory tests under limited conditions that chloride content within concrete has could be almost estimated by using electromagnetic waves as one of the nondestructive tests [1]. Though it is possible to estimate only average chloride content from the concrete surface to the reinforcing bar in case of the estimation of chloride content using the electromagnetic wave, it is not possible to estimate the distribution of chloride content from concrete surface to the reinforcing bar [2].

On the other hand, as the amplitude value of reflected wave changes for ions with the conductivity which exist in concrete, the electromagnetic wave does not always influence only to chloride ions. As various ions exist in sea water, it is necessary that various ions are investigated the degree of effect for amplitude of the electromagnetic wave.

In this report, the applicable method which is possible to estimate the distribution of chloride content included in cover concrete for RC structures using electromagnetic wave method which is non-destructive testing is reported and using water without salt, salt water of 3% concentration and artificial seawater, the results obtained from investigation on the degree of effect to the measurement of electromagnetic wave for ions permeated in the concrete is reported.

Outline of Investigation

Specimens and test method

As shown in Fig. 1, a kinds of specimen whose size was 300×200×400 mm was prepared. In the specimen, a reinforcing bar was respectively embedded from the surface to the position of 7cm. The specimens were sealed all other planes of the specimen to permeate chloride ions from a plane of the specimen. The specimens with the seal were made to penetrate in water of chloride ion concentration whose was 3%, without salt and artificial seawater. In the specimens, the measurement was started from age of 28 days. As the measuring method, drying and penetrating in three days interval were repeated about 170 cycles. The artificial seawater is the saline prepared
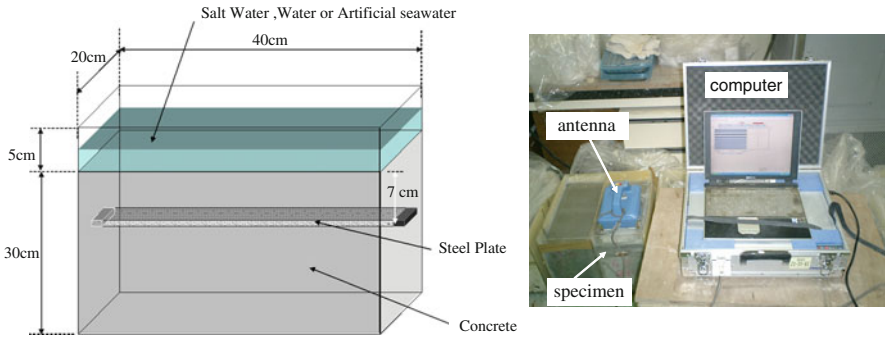
Fig. 1 Specimen and measurement setup with antenna

Table 1 Main ions included sea water

Component	Chemical formula	Solute (%)
Chloride ion	Cl^-	55.05
Sodium ion	Na^+	30.61
Sulfuric acid ion	SO_4^{2-}	7.68
Magnesium ion	Mg^{2+}	3.69
Calcium ion	Ca^{2+}	1.16
Potassium ion	K^+	1.10
Hydrogencarbonte ion	HCO_3^-	0.41
Bromide ion	Br	0.19
Bonic acid	H_3BO_3	0.07
Strortium ion	Sr^{2+}	0.03

Table 2 Specifications of electromagnetic wave measuring equipment

Item	Specifications
Radar frequencies	1.0 GHz
Measurement method	Impulse method
Transmission voltage	17Vp-p (at load 50Ω)
Horizontal resolution	80 mm

so that composition, ratio and concentration equal to sea water may be approximate. Table 1 shows the main ions which are included in the artificial seawater.

For measurement of electromagnetic waves, an antenna of about 1.0 GHz with specifications as given in Table 2 was installed on the investigation. The scale of the monitor was fixed at the level of the gain of the machine when the measurement was started, and the amplitude of the reflected electromagnetic wave estimated using that scale (Full scale = 100%). Moreover, since the reflected wave from the reinforcement and the reflected wave from concrete of part without the reinforcement are likely to interfere with the reflected wave measured in the reinforcement part, the reflected waveform of concrete of the part without the reinforcement was subtracted from the measured waveform of the reinforcement part. Thus, the effect of only the presence of the reinforcement in the part of reinforcement could be independently studied.

Table 3 Mix proportions of concrete

Type of specimen	Slump (cm)	Air content (%)	Water to cement ratio (%)	Sand content (%)	Unit quantity (kg/m³)					
					Water	Cement	Sand	Gravel	AEWRA	AEA
1	12	4.5	45.0	44.5	180	400	752	935	1.40	0.0040
2			55.0	46.5	180	327	815	935	1.15	0.0033
3			65.0	48.5	180	277	870	922	0.97	0.0028

NOTE;AEWRA:Air-Entraining and Water Reducing Agent, AEA:Air-Entraining Agent

Mix proportions

Table 3 shows the mix proportions of concrete used in casting the test specimens.

Test Results and Discussions

Effects of various ions on amplitude values

Figure 2 shows the changes in values of the amplitude of the reflected electromagnetic wave at different ages of each concrete specimen under conditions of 0.55 water-cement ratio and 7cm cover concrete. As shown Fig. 2, the amplitude of concrete specimens immersed water included chlride ions was shown smaller than ones immersed pure water. On the other hand, as changes of the amplitude values between sodium chloride aqueous solution of 3% concentration and artificial seawater were almost equivalent, it seems that effects of ions in the artificial seawater except chlride ions are small. Therefore, it seems that the amplitude values obtained from the results of measurement of electromagntic wave in existing structure are caused by chlride ions.

Estimation of chloride content using electromagnetic wave

Cores were respectively drawn from test specimen in order to analyze content of chlride ions within each specimen. Drawn core sliced in the 1cm interval was crushed, and the chemical analysis was carried out. The average chlride content in cover concrete was calcurated by the amount of chlride content from concretre surface to the position of re-bar using results of chemical analysis. Figure 3 shows the distribution of the content of chlride ions in cover concrete from results of chemical analysis. The multiple regressions were carried out in order to estimate the average content of chlride ions using the results obtained until now with the present results shown Fig. 3. As explanatory variables, water-cement ratio, amplitude values, water content, dielectric constant were used because, from past researches, it has been confirmed that water content and water-cement ratio affect the electromagnetic wave [1], [2]. Figure 4 shows the results
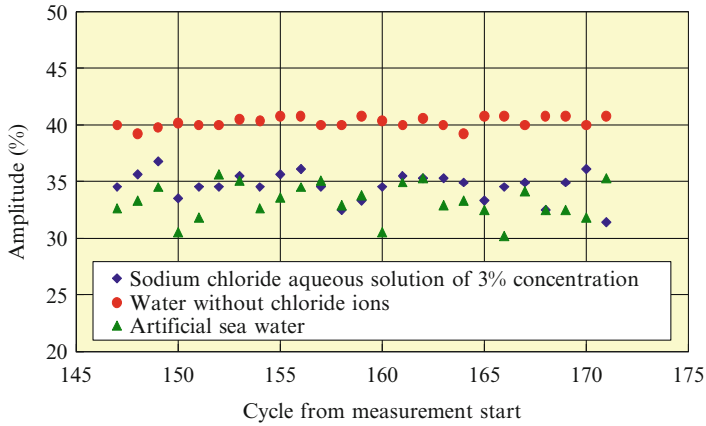
Fig. 2 Changes of amplitude of reflected electromagnetic wave
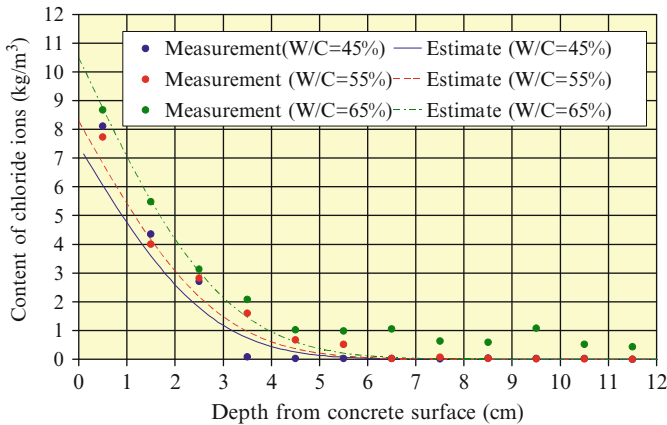
Fig. 3 Distribution of chloride content

of comparing the content of chloride ions obtained by the chemical analysis with the content of chloride ions estimated by the multiple regressions analysis. As shown Fig. 4, as the estimates were reasonably accurate, it is possible that the average content of chlride ions in cover concrete are estimated using electromagnetic wave.

Estimate of distribution curve of chloride content using electromagnetic wave

It is possible that the distribution curve of chloride content is estimated by equalizing the amount of distribution of chloride content from concrete surface to the position of re-bar calculated by chloride content in concrete surface estimated using some

Fig. 4 Estimate of content of chloride ions
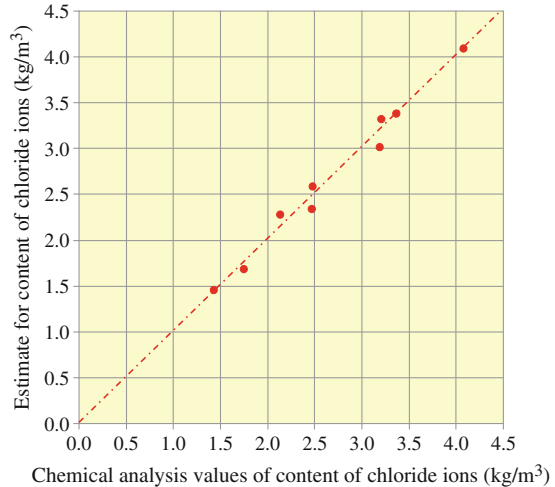
methods and the value of diffusion coefficient of chloride ions into concrete using
Fick's law of diffusion with the amount of average chlride content from concrete
surface to the position of re-bar using the electromagnetic wave. Figure 3 shows the
estimated distribution curve of chlride content compared with results of chemical
analysis at each water-cement ratio in order to verify the validity of estimated dis-
tribution of chloride content. In shown Fig. 3, the results of chemical analysis and
the estimate values were almost equivalent to the cases of both 45% and 55% water-
cement ratio. On the case of 65% water-cement ratio in which the content of chlo-
ride ions permeated over 10cm, the measurement values were not equivalent to the
estimate in the position which is deeper than 5cm from concrete surface. From these
results, it is shown that it is possible that the method for proposing in this study
using these nondestructive testing almost estimates the distribution of the content of
chloride ions.

Conclusions

The present research was carried out to investigate on effects of various ions except
chloride ion for chride content in cover concrete estimated by electromagnetic wave
using specimens immersed sodium chloride solution and artificial seawater. As the
result, it seems that it is not necessary to consider another ions except chloride ion
in the sea water in the estimation of chloride content using electromagnetic wave by
existing structure because changes of the amplitude values between sodium chlo-
ride aqueous solution of 3% concentration and artificial seawater were almost
equivalent. Furthermore, the present research was also carried out to investigate on
the applicable method which was possible to estimate the distribution of chloride

content included in cover concrete using electromagnetic wave method. As the result, using the estimated values of average content of chloride ions to the r-bar by electromagnetic wave and surface content of chloride ions, it is possible to estimate the distribution of content of chloride ions in cover concrete. However, as many problems have been held on application to reinforced concrete structures, further works need to be examined on influences of environmental condition, shape of the structure, moisture condition in concrete, etc..

References

[1] Toshiaki, M., Kosuke, Y., Kennzo, W., Masahiro, H. and Ryoichi, A. (2007). In: *Monitoring System of Chloride Content in Cover concrete using Electromagnetic Wave and Impedance Method*, Proceedings of the 6th International Conference on Fracture Mechanics of Concrete and Concrete Structures, vol. 2, pp.1865–1876, Alberto, C. (Eds.), Taylor & Francis, London.
[2] Toshiaki, M., Kosuke, Y. and Ryoichi, A. (2008). In: *Applicability of Estimation of Chloride Content in Cover concrete using Electromagnetic Wave and Impedance Method*, Proceedings of on Site Assessment of Concrete, Masonry and Timber, vol.1, pp. 463–472, L. Binda (Eds.), RILEM Publications, Bagneux.

In-Service Inspection and Structural Integrity Assessment of Atmospheric Storage Tanks

A.A. Anastasopoulos, S.E. Kattis and D.A. Kourousis

Abstract This paper presents a series of advanced inspection techniques for assessing the structural integrity of atmospheric storage tanks, in a global (floor, annular ring, shell & roof) and integrated fashion while the tank is in-service. The methods presented with sample results and advantages include floor condition assessment using Acoustic Emission, on-line tank floor annular ring corrosion evaluation using long range automated Ultrasonics and on-line tank shell or roof corrosion mapping using automated Ultrasonics C-Scan. The paper discusses means of management of the data acquired from all above techniques, according to codes and state-of-the-art risk-based inspection (RBI) programs. This is done using a combination of structural drawing software, specially designed for the needs of incorporating on stream inspection results and plant condition monitoring software.

Keywords On-line monitoring • RBI • Tank inspection • Tank maintenance

Introduction

Removal of Above Ground Storage Tanks from service for maintenance is a major inconvenience for the facility due to the downtime and the costs associated with emptying the tank, cleaning, and assessing the need for repairs, if any. In this respect, tank owners need to take educated decisions as to when is the right time to remove each tank from service without wasting money in emptying tanks in good condition or risking leaving bad tanks in service, as well as to prioritize maintenance. Assessing the tank's overall structural condition, while in service, in a fast, economic and reliable way requires the use of specialized Non Destructive Testing (NDT) techniques. For the floor, corrosion is assessed on-stream using TANKPAC™ Acoustic Emission

A.A. Anastasopoulos (✉) • S.E. Kattis • D.A. Kourousis
Envirocoustics ABEE, El. Venizelou 7 & Delfon, 14452 Metamorphosis, Athens, GREECE
e-mail: nassos@envirocoustics.gr

(AE) based technology with proven reliability. For the annular ring part, the use of specially-developed long-range Ultrasonic (UT) testing technique applied from the external of the tank, allows corrosion assessment of the outer half meter of the floor. For the wall or the roof, Automated ultrasonic corrosion mapping, using specialized, industrial robotic crawlers (LSI), performing C-Scans all the way to the top of the tank wall offers a detailed wall thickness imaging much more representative than spot UT thickness testing.

Management of the corresponding data in accordance with the code as well as with state-of-the-art RBI programs is performed with a combination of Structural Drawing Software, incorporating On Stream Inspection results, and Plant Condition Monitoring Software offering recommendations for the re-test interval or inspection based on risk-based inspection (RBI)-like matrix, taking into account individual failure mechanisms of Tank components.

On-Line Tank Floor Condition Assessment Using AE

Acoustic Emission [1] is a global NDT examination technique that can inspect entire structures in one test. For TankPac™ 100% floor testing the sensors are placed externally on the tank wall, at ~1m height from the floor detecting corrosion and potentially waves generated by the turbulent flow at a leak point [2]. Corrosion signals are generated as the scale thickens and breaks. The only requirement is that before the test, the tank remains idle with its normal product inside for max. 24h. Data collection lasts 1-3 hours and 100% of floor and annular ring are evaluated.

AE activity is evaluated using specialized software and the TankPac™ procedure. General situation ("Overall Grade") of the tank floor is classified from A (good situation), up to E (bad situation), see Fig. 1. Regions of severe corrosion are graded separately ("PLD Grade"), from 1 to 5. A "Composite Grade" is provided as a combination of the two grades (Table 1) and the time of the next inspection is proposed. If a leak is detected, recommendation is direct repair. Thus, funds and effort are directed to the tanks that most need it, saving budget by avoiding opening good tanks. TankPac™ reliability has been evaluated by independent, published studies [3], and the method is recognized by reputable international institutions [4]-[5].

On-Line Annular Ring Corrosion Evaluation with Long-Range UT

Whereas TankPac™ offers damage indications for the annular ring, in order to assess severity of damage the TALRUT™ technique was developed for assessing this area on-line without removing the tank from service!

The method uses a long-range ultrasonic technique to evaluate corrosion damage to the annular ring/floor extension and tank floor within 0.5 meter of the tank wall (Fig. 2). This method is qualitative, and gives indications and their plan position.
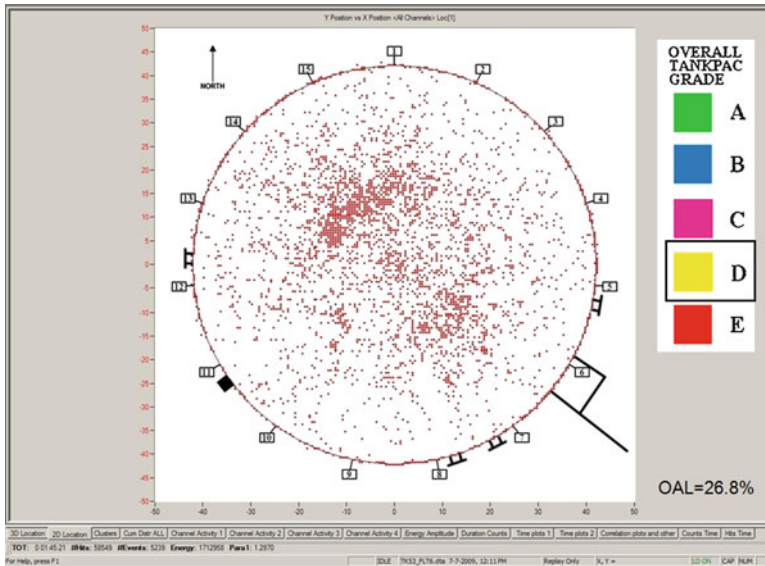
Fig. 1 Tank floor evaluation. The numbers show the angular positions of the AE sensors. Located activity from the floor is shown along with the grade for overall active damage on the floor (D)

Table 1 TankPAC™ grading system

"PLD Grade"							
	E/5	III	III	IV	IV	IV	I - No active damage, re-test in 4/5 years.
	D/4	II	III	III	IV	IV	II - Minor active damage, re-test in 2 years.
	C/3	II	II	III	III	III	III - Active damage re-test in max.1 year*
	B/2	I	I	II	II	n/a	IV - Very active damage. Re-test in 0.5 year*
None or	A/1	I	I	**II**	n/a	n/a	*or schedule for internal inspection
"Overall Grade"	----	A	B	C	D	E	n/a: Should not occur if std. threshold used

Fig. 2 Left: A TALRUT™ system in action in field. Right: Schematic representation of the principle layout of operation

Indications are compared with a test plate / calibration block in order to evaluate their severity. The standard test plate has 50% through slots at 100mm, 200mm, and 400mm from the probe (see Fig. 3 - Top), and indications are normalized and graded relative to this. A motorized crawler scanning device runs on the tank wall adjacent
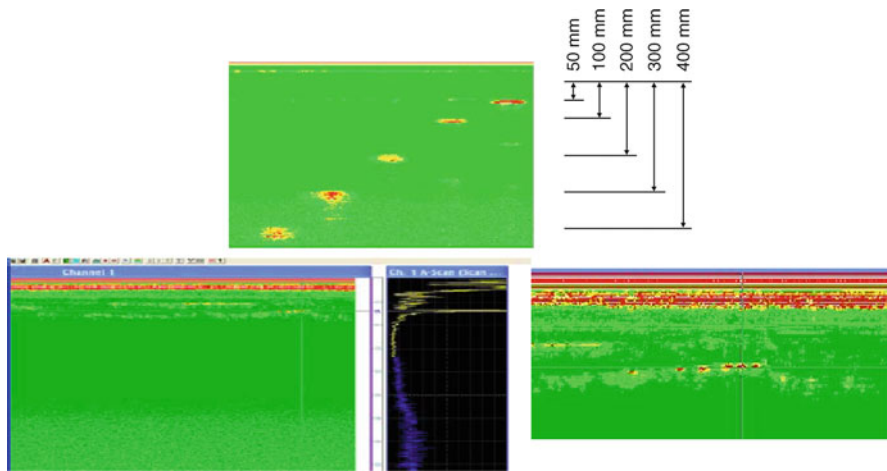
Fig. 3 Top: Reflection signals on a calibration plate. Bottom: TALRUT™ result. Left: severe pitting. Right: Close-up. Middle: Corresponding A -Scan

to the annular ring. Circumferential scan speed is ~5mm per second at 1mm resolution. Productivity of more than 40 meters per day has been achieved in the field, but this strongly depends on the condition and cleanliness of chime.

On-Line Tank Shell or Roof Corrosion Mapping Using Automated Ultrasonics C-Scan

AUT systems can sample the surface at small intervals using crawlers to mount the ultrasonic thickness probe that have magnetic wheels and can be controlled from a remote station. They can scan the entire height of the tank and produce a very detailed thickness map. The reading step is typically 10x20mm, thus the result can be hundreds of thousands of measurements. Data analysis is performed using advanced UT Imaging and Analysis software [6].

More detailed analysis of UT measurements can be performed using the Structural module of the UTIA software [6]. This module provides the user with a set of tools for easily input of common structures in refineries, such as tanks and pressure vessels. The software allows users to define the structure dimensions and all structure details and components and provides tools for painless stitching of the C-scans onto the real structure. Typical example of that representation is depicted in Fig. 4, where the UT measurements are presented on a 3D view of the tank shell. This accurate presentation of UT readings with structure allows the easily location of problematic areas. The software [6] offers further tools for examination of the structure status and compliance with regulations, for example tools for the definition of Thickness Monitoring Location (TML) (Fig. 4b). Thus, any kind of measurements (spot UT or AUT) can be calculated into the same TML over the time enabling corrosion rate calculation and remaining life estimation.
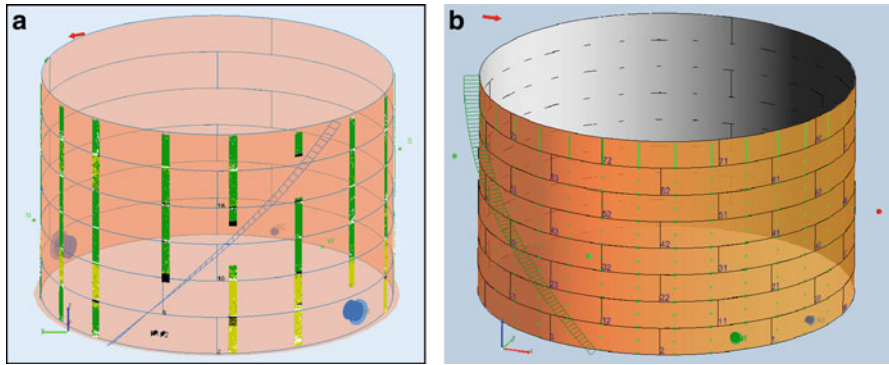
Fig. 4 (**a**) 3D presentation of Tank Shell with UT measurement. (**b**) Thickness Monitoring Location in Tank Shell (Green Points)

Cluster ID	mm²	Min	Max	Ave
1	348	5.62	8.98	7.71
2	280	6.84	8.97	8.13
3	84	7.28	8.89	8.38
4	260	4.09	8.94	7.79

Fig. 5 Details of local corrosion and clustering results

Combination of Techniques

An example of technique combination is presented below. An 85-meter diameter tank with Crude Oil content was tested using the AE TANKPAC™ methodology in June 2003. The recommendation was for re-inspection in the next 1-2 years. Also, the results indicated significant activity on the annular ring. In March 2006, the tank was opened to clean and change product. Based on TANKPAC™ test results, manual UT readings were performed. Indications of low thickness at the annular ring were observed, thus a full AUT test performed for annular plates. The results of AUT show extensive local corrosion at the annular ring caused by water seeping under the tank at certain location around its perimeter. Detailed analysis was made using the clustering module of UTIA software and accurate results of the significant thinning at annular ring were extracted (see Fig. 5).

Data Integration and Management

Data from all above techniques may be stored into an asset database for all equipment inspected and, thus, help the safety management program. The PCMS software can perform this action by storing the data into its database and its modules: Corrosion

Monitoring and RBI Calculator. The Corrosion Monitoring module allows personnel to track wall thickness. The patented risk technology analyzes reading data to recommend next inspection date and estimate retirement dates. The thickness data is put through nineteen different tests to determine the next inspection date for each Thickness Monitoring Location (TML). Automatic retiring limit (T-min) calculators are available for use at each TML. The piping T-min calculator is based on ANSI B31.3 or B31.4 standards. ASME Section VIII code is used for pressure vessels, and API 653 standard is used to calculate T-min for storage tanks. The RBI Calculator module performs the risk assessment based on the Probability of Failure and the Consequences associated with such Event. Risk management aims to calculate risk due to different failure mechanisms, evaluate risk as acceptable or not acceptable (or as Low-Medium-High) and schedule proper actions for risk reduction. In PCMS, the RBI Calculator computes risk and based on the probable damage mechanisms recommended inspection technique for each one and the date the vessel exceeds a risk threshold without inspection.

Conclusions

Assessing a tank's overall structural condition requires the use of specialized NDT techniques such as AE for floor condition assessment and advanced UT for walls and annular ring evaluation. Having in hand all above information from the tank, management of the corresponding data performed with a combination of Structural Drawing Software, and Plant Condition Monitoring Software helps the owner take educated decisions about whether to schedule maintenance or re-test based on risk-based inspection (RBI)-like matrix, significantly rationalizing relevant costs.

References

[1] ASTM E 1316-94 Standard, Definitions of Terms Relating to Acoustic Emission, (now in E 1316).
[2] Pollock, A.A., Hsu, S.-Y.S. (1982), Leak Detection Using Acoustic Emission, Journal of Acoustic Emission, Vol. 1, N 4, pp. 237–243.
[3] Van de Loo, P.J., (Shell International Oil Products BV, The Netherlands), Hermann, B., (Dow Stade, Germany) (1998), *How Reliable is Acoustic Emission (AE) Tank Testing? The Quantified Results of an AE Usergroup Correlation Study*, Proceedings of the 7th European Conference on NDT, Copenhagen, Denmark. Also available in: http://www.ndt.net/article/ecndt98/chemical/095/095.htm
[4] American Petroleum Institute (1996), *A guide to leak detection for above ground storage tanks*, API publication 334, 1st edition, STEP (Strategies for Environmental Protection) group.
[5] European Commission, Directorate General JRC, Institute for Prospective Technological Studies, European IPPC Bureau, *Reference Document on Best Available Techniques on Emissions from Storage*, 01/2005
[6] Envirocoustics ABEE, "UTIA Ultrasonic Imaging and Analysis Software Manual, Rev.2", 09/2007.

Application of Acoustic Emission to High-Voltage Electric Power Equipment Diagnostics

O.G. Santos Filho, F.S. Brasil, F.F. Silva Neto, R.C. Leite and S.L. Zaghetto

Abstract Acoustic emission has been applied in identifying evolving failures of electrical, mechanical or thermal nature in power transformers and reactors. Different kinds of failures can be identified by the characteristics of the signals received and also give the location of the source of the signals. Also, operating sequence and contact timing of on-load tap changers can be evaluated with the aid of acoustic emission. The technique has the advantage of being utilized with in-service, energized equipments, avoiding downtime to perform tests. Case studies of acoustic emission tests performed to condition monitoring of several high-voltage power transformers and reactors, rated 230 and 500 kV are presented. Results have demonstrated the effectiveness of the acoustic emission technique as a tool for the condition diagnostic of electric power equipments.

Keywords Acoustic emission • Partial discharges • Power transformers • Shunt reactors

Introduction

Power transformers and reactors represent a major part of the assets in an electric utility company. Unexpected failures in these equipments can lead to large financial and time losses. In this way, assessing their operational condition is an important issue in evaluating the risk of failure and to plan maintenance actions in the mid- and long-term.

One of the available techniques to this assessing is the Dissolved Gas Analysis (DGA), which can identify failures such as partial discharges, electric arcs and

O.G. Santos Filho (✉) • F.S. Brasil • F.F.Silva Neto • R.C. Leite
Eletronorte, Belem PA, Brazil
e-mail: oswaldo.filho@eln.gov.br

S.L. Zaghetto
Eletronorte, Brasilia DF, Brazil

overheating [1]. The energy released in these failure conditions decompose the insulating oil producing characteristic gases, such as ethane, methane, hydrogen, acetylene and others, which dissolve in the oil and can be detected by chromatographic analysis. Although DGA is a proven, low-cost and widely used technique, it is not able to give the location of the failure inside the equipment. This information can be given by the Acoustic Emission Testing which, together with the results of Dissolved Gas Analysis, and the knowledge of constructive details of the equipments, can be used in improving the quality of the diagnostic.

The sections to follow describe some constructive aspects of power transformers and reactors and discuss some failure conditions and characteristics of acoustic signals originated from them, as well as a simple description of AE testing of power transformers and reactors. Finally, two case studies of failure diagnostics in electric power equipment are presented.

Transformers and Reactors Components and Failure Mechanisms

Transformers and reactors, although having distinct functions in electric power systems, have similar constructions [2]. Power transformers are used in converting relatively low voltage, as in the output of generators to a high voltage, necessary in transporting this energy through large distances with low losses. They are based on the electromagnetic induction principle, where the energy applied to a primary coil is transferred to a secondary coil. In this process, the voltages in the coils are related as the number of turns in each of them, the inverse occurring with the currents, in order to the energy be conserved. To provide a low-reluctance path for the magnetic flux linking the primary and secondary windings, they are wound on a core of ferromagnetic material, such as silicon steel. Windings are made of high-conductivity copper conductors covered with paper and cardboard spacers, in order to ensure electric insulation and mechanical support to withstand the dynamic forces appearing under normal and abnormal operating conditions of the transformer. All these components are mounted in a steel tank filled with insulating oil. The oil serves the dual purpose of providing electric insulation and as a cooling medium to dissipate the electric and magnetic losses which are produced in the transformer in the form of heat. External heat exchangers provided with cooling fans are generally installed to improve the cooling process. Some designs include oil circulating pumps with this same objective. To provide ability to compensate for small (around +/-10%) variations in the operating voltage, there are switches (no-load or on-load tap changers) mounted internally to the transformer, selecting the adequate number of turns of the windings.

A major cause of failure in power transformer and reactors is electric insulation breakdown. Even conditions of mechanical or thermal failure can evolve to a catastrophic failure due to electric insulation breakdown. Partial discharges [3] consist of electric discharges located in a point inside a dielectric appearing when the electric field is higher than its dielectric strength. This condition generally occurs in cavities, bubbles or cracks inside the dielectrics. Although with low energy levels,

partial discharges recurrence can progressively degrade the dielectric, leading to insulation collapse and even to catastrophic failure of the equipment.

Partial discharges cause decomposition of the insulating oil, producing mainly hydrogen and other gasses, which dissolve in the oil and can be detected by gas dissolved analysis. From the acoustic point of view, partial discharges are fast phenomena, producing signals of short duration, of the order of microseconds, low energy and relatively high average frequency (100–300 kHz). [4]

On the other hand, in the electric arc situation, all the distance in a dielectric separating two conductors is crossed by an electric current. As it releases a greater amount of energy, the oil decomposition produces mainly acetylene. Acoustic signals produced by electric arcs inside transformers and reactors show lower average frequencies (typically 50–100 kHz) and longer durations than that produced by partial discharges [4].

Acoustic Emission Testing of Transformers and Reactors

Acoustic signals initiated by incipient fault conditions, such as partial discharges, electric arcs, and others, propagate through the insulating fluid and reach the metallic tank, where they are detected by piezoelectric sensors, mounted on its external surface. The acoustic emission testing of power transformers and reactors is performed with the equipment energized and under normal load [5]. It is convenient to perform the test under a time period of about 24 hours, during which the equipment undergoes all the cyclic load and voltage variations. In this way, it is possible to establish correlations between load or operating voltage levels and the acoustic activity. Acoustic sensors are properly distributed over the lateral tank walls, fixed with magnetic holders. Normally, four to six sensors installed on each wall give a good coverage for signals detection.

The characteristics of the detected acoustic signals can reveal the nature of the phenomena that originates them. As an example, a repetition rate of one hit in each power line semi-cycle, indicates that the signals are voltage-driven, as is the case of partial discharges, or current-driven, as is the case of signals generated by magnetic forces. These two phenomena can be discriminated by their frequency characteristic. As mentioned before, partial discharges are very fast phenomena, and produce signals with frequencies typically in the range of 100–300 kHz. On the other hand, signals originated due to mechanical forces, typically have average frequencies below 50 kHz. Other events, which also originate acoustic emission, such as mechanical friction, fluid flow or thermal effects do not exhibit such characteristic synchronization with the power frequency.

Case Study A : Monophase Autotransformer, 230 / 138 kV 50 MVA

This equipment, illustrated in Fig. 1, presented acetylene as result of dissolved gas analysis, suggesting evidence of internal electric arc. Due to this, it was scheduled an acoustic emission test, whose event locations are shown in Fig. 2, which represents the

Fig. 1 Monophase Autotransformer 230/138 kV, 50 MVA
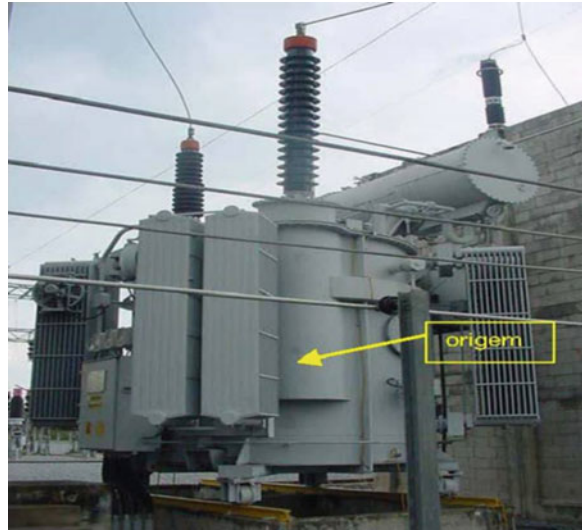
Fig. 2 Location of acoustic sources in the autotransformer
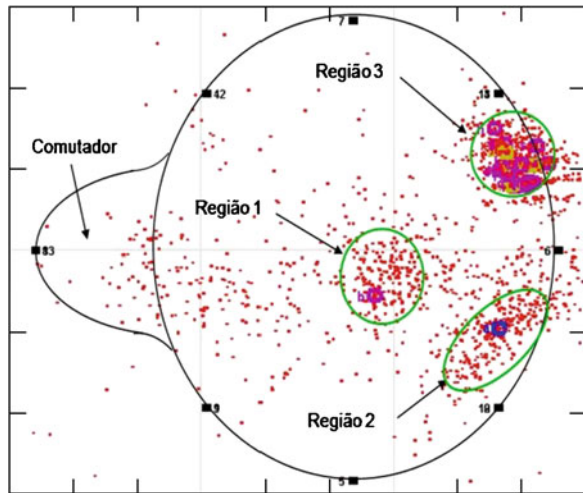
projection of the located points over an horizontal plane. In this picture, three regions are evidenced as showing relevant acoustic activity. One of them, indicated as Region 3, which showed higher activity level, is coincident with the no-load tap changer of the transformer.

A scheduled visual inspection confirmed this indication, evidencing loose parts (spacers) in this component, as shown in Figs. 3 and 4. The autotransformer was repaired in field, as well as two other similar equipments, which showed similar symptoms.
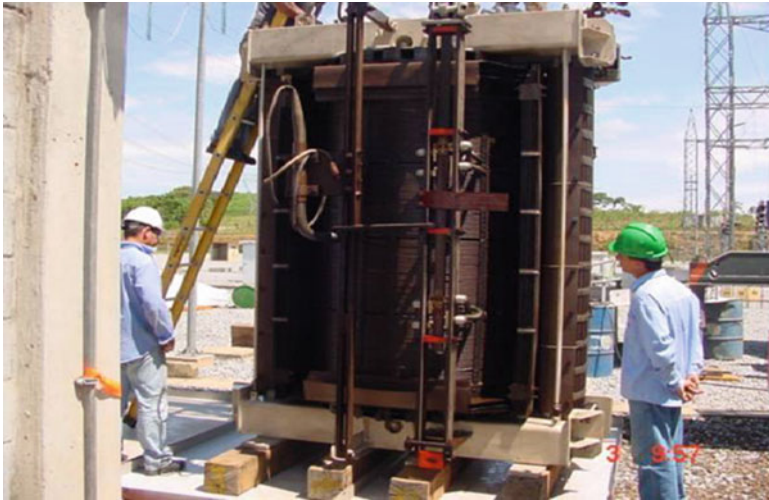
Fig. 3 Inspection of the autotransformer after removal of the tank

Fig. 4 Detail of loose parts found in the no-load tap changer
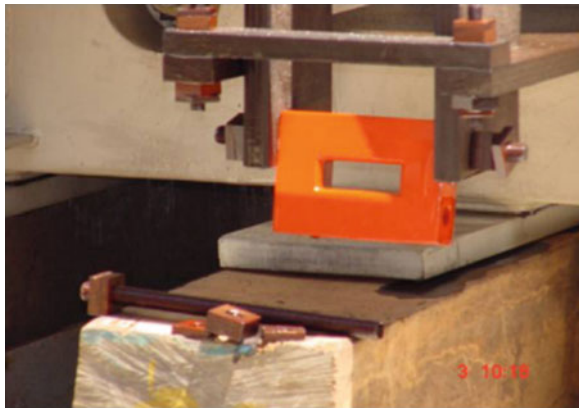
Case Study B – Single-phase 500 kV, 60 MVAR Line Reactor

In this reactor, shown in Fig. 5, an acoustic emission testing showed two regions of relevant activity, as illustrated in Fig. 6. One of them, indicated in a circle in this figure, located in the region of the high-voltage bushing, presented signals with with continuous activity and average frequency in the range of 10–30 kHz, as shown in Fig. 7, suggesting that its origin was not due to electric discharges. This diagnostic is in agreement with dissolved gas analysis, which indicated no evidence of gasses associated with electric arc or partial discharges. Nevertheless, due to the critical

Fig. 5 Single-phase reactor, rated 500 kV / 50 MVA

Fig. 6 Horizontal plane projection of located sources corresponding to acoustic activity in the reactor under test
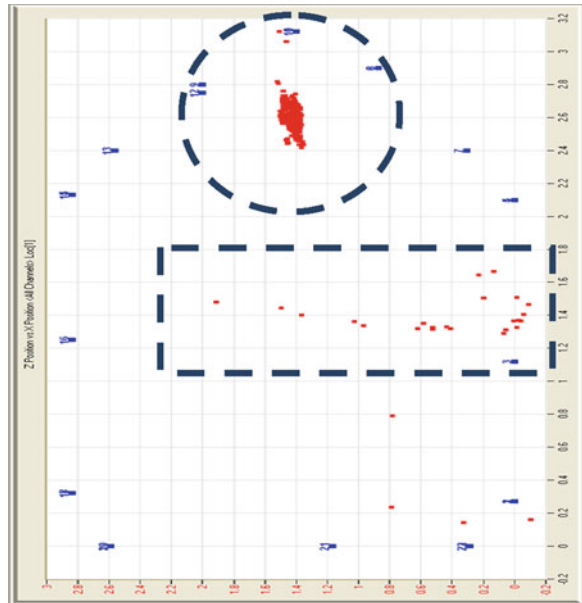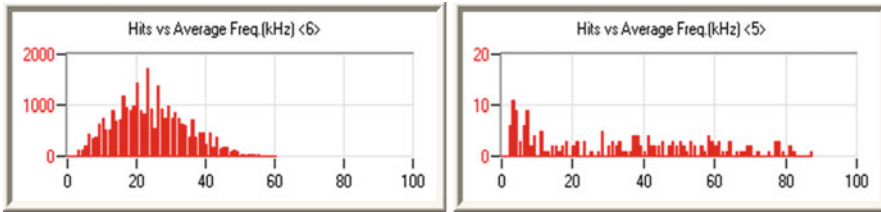
Fig. 7 Frequency distribution of the signals originated in the region under the high-voltage bushing (left) and in the center of the reactor (right)

importance of the bushing to the integrity of the reactor, it was scheduled an internal inspection/repair in this area, when the fixing structures of the lower part of the bushing were found loose and re-tightened, avoiding a dangerous evolution of the failure. Another region, indicated in the rectangle in Fig. 6, showed sporadic activity, with higher characteristic frequencies, up to 80 kHz, suggesting the presence of partial discharges. Due to the difficult access to this region and no significant presence of hydrogen dissolved in the oil, no corrective action was taken relative to this region, but the equipment has been kept in close monitoring to detect any tendency of evolution of this condition

Conclusion

Acoustic emission testing, although not yet fully disseminated in the electric power sector, has a potential to aid in assessing the operational condition of transformers and reactors. Its ability to locate the sources of acoustic signals and the possibility of performing tests with energized equipments are favorable characteristics of this method. Additionally, the characteristics of the acoustic signals, such as repetition rate, duration, average frequency can give an indication of the cause of the emissions. Used in conjunction with other techniques, such as Dissolved Gas Analysis (DGA), it can help improving the quality of the diagnostic of the equipment. Case studies have been presented, demonstrating the effectiveness in using acoustic emission to asses the condition of power transformers and reactors.

Variable propagation speed due to different materials used in the various components of these equipments can affect the determination of location of the acoustic sources. This could represent a potential use for acoustic emission tomography technique in mapping the acoustic propagation speed in the interior of the equipment under test and, consequently, the boundary between its components, allowing a better evaluation of the criticality of the failures

References

[1] IEEE Standard C57.104-1991 – *Guide for the Interpretation of Gases Generated in Oil-Immersed Transformers*

[2] HARLOW, J.H. – Electric Power Transformer Engineering, 2nd Ed. – CRC Press, 2007; ISBN 9780849391866

[3] BARTNIKAS, R. and McMahon, E.J. - Engineering Dielectrics, Volume I, Corona Measurement and Interpretation, ASTM Special Technical Publication 669, ASTM, 1979, ISBN 0-8031-0332-8

[4] TRINDADE, M.B., Menezes, R.C. and Martins, H. – Partial Discharge Detection in Power Transformes Using Acoustic Emission Technique – 15th International Symposium on High Voltage Engineering – CIGRÉ / IEEE, Ljubljana, Slovenia, 27/31 Agosto, 2007

[5] IEEE Standard C57.127-2007 - Guide for the Detection and Location of Acoustic Emissions from Partial Discharges in Oil-Immersed Power Transformers and Reactors

A De-Noising Algorithm for EMAT on Wheels

K. Yang, C. Peng, Y. Zhang, J. Peng and X. Gao

Abstract Presently electro-magnetic acoustic technology (EMAT) has been widely adopted by the China Railway High-speed (CRH). In this paper, the principle of wheels tread detection by using EMAT is introduced. To solve the noise problem existing in the detecting procedure, an integrated algorithm combining the wavelet algorithm and the phase difference algorithm is presented. Under the premise of saving the necessary signal wave, the Fast Fourier Transform based on the Blackman window is adopted to calculate the signal phase, and then the integrated algorithm is chosen to process the signals. Compared with the wavelet algorithm or the phase difference algorithm, the rate of the noised data after being processed by the integrated one is reduced by more than 45%. This algorithm will improve the waveform quality and has an enlightening function to raise the detection accuracy in the EMAT system.

Keywords EMAT application • Wavelet denoise algorithm • CRH • Phase difference • Wheel crack

Introduction

With the speed rising obviously, the risk of train is more and more high, especially after the accident of German ICE high-speed train, Government pays more attention to the wheel inspection. In recent years, China increases the train speed greatly, the safety for the wheels puts higher request. Therefore, it's urgent to accurately measure the quality condition of wheel.

Presently electro-magnetic acoustic technology (EMAT) has been widely adopted by the China Railway High-speed (CRH) to detect the cracks of wheel set. Like Fig. 1,

K. Yang (✉) • C. Peng • Y. Zhang • J. Peng • X. Gao
Opto-Electric Engineering Institute, Southwest Jiaotong University,
Chengdu, Sichuan, China
e-mail: yangkai_swjtu@163.com
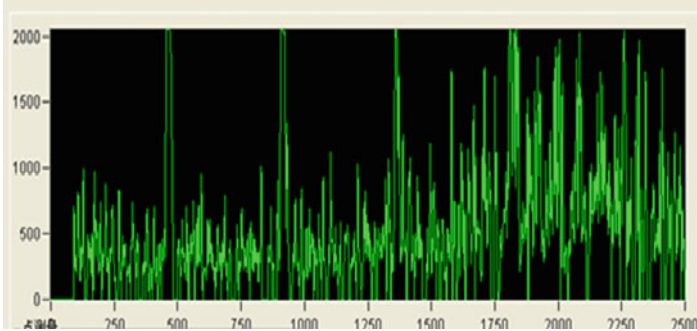
Fig. 1 EMAT signal with strong noises

but the response signals have lots of noises so that the useful signals can not be detected in such environment [1]. Although there are some research for EMAT all over the world, but lack of de-noise algorithm in practical use. The article introduces a special method to get the useful information (periodic wave and potential flaw wave) and improve the quality of signal at the same time.

Principle

The noise of EMAT system is introduced by the frequency transformer or motor of the train. Figure 1 shows the practical signals with noises. The EMAT system uses the pulse-echo principle to get the crack detection [2]. In ideal state, the pulse is emitted by the EMAT probe at the moment of the wheel is running just above the probe, the surface pulse will be propagated along the surface and near surface. When there is a crack, some part of wave energy will be reflected by side surface of crack and will be detected by the probe to produce the flaw wave (Fig. 2 E_{mn} wave); The other part of wave energy will continue propagate to produce the periodic wave (Fig. 2 RT_n wave).Compared with them, we can get the condition of the wheel surface [3].

Denoise Algorithms

The flow chart of denoise algorithm shows in Fig. 3: Firstly sampling the signals (the frequency of emit ultrasonic wave is 10MHz, the sampling rate is 400kHz) and goes to band-pass filter, then using the soft threshold wavelet-denoise method to reduce the noise, the signals is reserved by obeying the rule of certain range of difference of phase after calculating the phase of the signals. At last, the final results output through rectification for the signals of 20 points intervals.
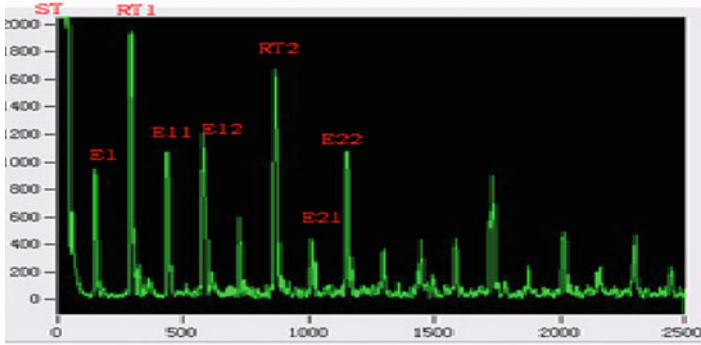
Fig. 2 Static waveform of system
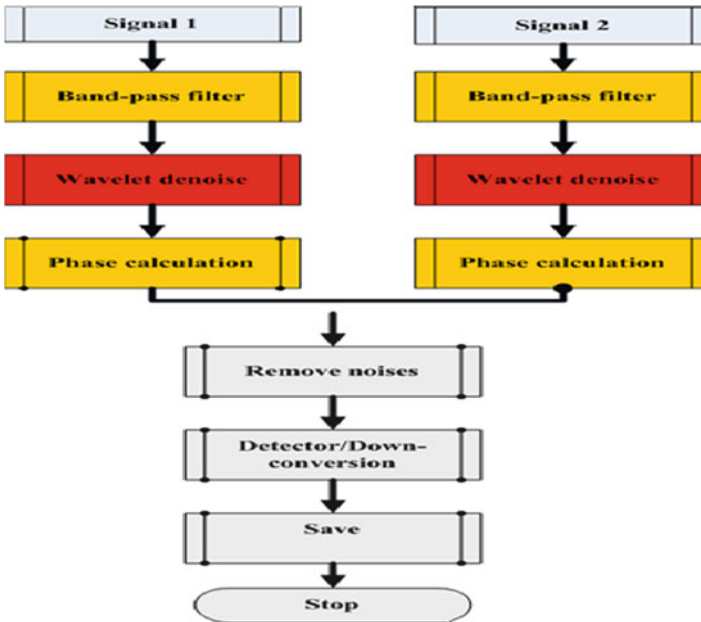
Fig. 3 Flow chart of the algorithm

For this project, the useful signals (periodic wave and potential flaw wave) represent the low frequency, the noises represent high frequency. The wavelet transform represents high frequency resolution in low frequency area, whereas high time resolution in high frequency area, so theoretically the wavelet method is suitable based on this aspect [4].
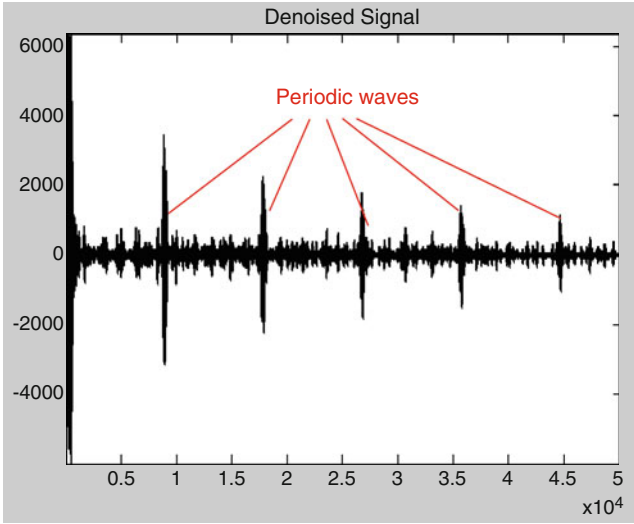
Fig. 4 Result after wavelet

Soft threshold method of wavelet denoising

Three main steps:

(a) Decomposition of signals. Select the appropriate wave function and the layer number n, then decomposes it by N layer. The noise is usually included in detailed part of high frequency area. Daubechies 3 is used in this project with 9 decomposition.

(b) Coefficient quantization. Denoise the high frequency part based on soft threshold method by choosing a threshold from 1 to n layer. The process represents formula (1): d means the final threshold of each layer, x means the coefficients of high frequency of each layer, T means the static threshold.

$$d = \begin{cases} \text{sign}(x)(|x|-T) & |x| > T, \\ 0 & |x| \leq T. \end{cases} \quad (1)$$

$T = \delta\sqrt{2\ln(N)}$, N means the length of data of each layer, δ means the standard deviation of each layer, the expression shows in formula (2)

$$\delta = \sum_{i=1}^{N} \left[x(i) - \frac{(x(1)+x(2)+\ldots+x(N))}{N} \right]^2 \quad (2)$$

(c) Reconstruction. The reconstruction will be done in each layer after wavelet-denoise soft threshold calculation. The reconstruction part will also use the reconstruction low and high-pass filter. For signals in Fig. 1, the result is shown in Fig. 4.

Compared with them, the result keep the necessary signals and eliminate most noises at the same time, so eliminate the part which don't satisfy the phase rule in next step.

DFT phase calculation based on Blackman window

The essence of applying window function is decreasing the influence of signal cutting by adding different weight at different moment. The characteristic of window is decided by the form and width. The requirement for window is: the main lobe represents as thin as possible to get peak transition region and eliminate the amplitude of largest side lobe, that is, concentrating the energy on main lobe as far as possible to decrease the ripple and increase the attenuation of stop band [5]. The Blackman window is selected through comparison.

   The core thought of DFT phase-array calculation is the relationship between two RF-coils. They differ half wavelength, which is 180 degree in phase difference conversion. Given the phase difference calculation of two period signals. Suppose they are single frequency period signals, the signal which satisfies the 180 degree phase difference will be reserved after detection, otherwise will be zero. The two input signals are both processed by wavelet denoise, the detailed steps are as follows:

(1) Estimate frequency of signals to define the sample frequency and sample time of one DFT computation. Then sample the $x_1(t)$ and $x_2(t)$, and get

$$x_1(n) = A_1\cos(\omega_0 n + \alpha_1) \tag{3}$$

And

$$x_2(n) = A_2\cos(\omega_0 n + \alpha_2) \tag{4}$$

in it,

$$\omega_0 = 2\pi f_0 \left(T_s = \frac{1}{f_0} \text{ means sample period}\right) \tag{5}$$

(2) FFT for one sequence to get the whole frequency spectrum and also get the index k of spectrum line of fundamental wave of signal by searching peaks.
(3) Apply cosine window function for $x_1(n)$ and $x_2(n)$ and use FFT to get the real and imagine part of index k of spectrum line. For $x_1(n)$, apply $w(n)$ window function and use DFT to get the real part of fundamental wave (index k of spectrum line) X_{1Rc} and imagine part X_{1Im}. The phase angle is

$$tg\theta_1 = \frac{X_{1Im}}{X_{1Rc}}. \tag{6}$$
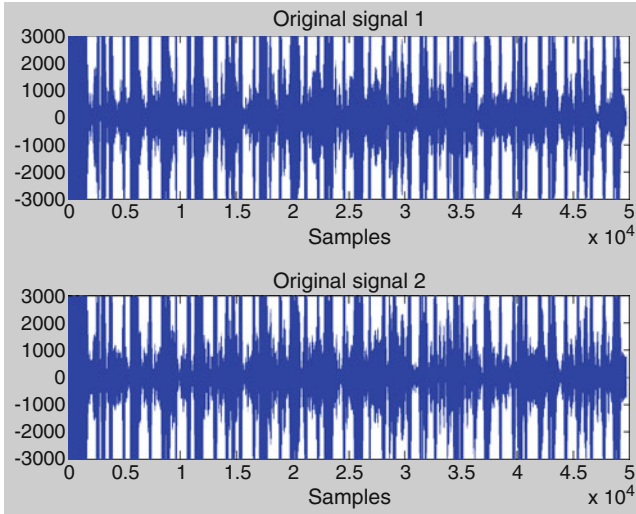
Fig. 5 Signal with flaws and noises

For $x_2(n)$ is the same, and

$$\theta = \theta_1 - \theta_2 = tg^{-1}(\frac{X_{1Im}X_{2Rc} - X_{1Rc}X_{2Im}}{X_{1Im}X_{2Rc} - X_{1Rc}X_{2Im}}) \tag{7}$$

(4) Calculate the difference of phase angle by the formula. The phase difference arithmetic can eliminate the noises after wavelet denoising method, and can get the periodic wave and potential flaw wave at the same time. The periodic wave will occur in all data, whereas the flaw wave will occur just in the wheels with defects.

Result analysis after algorithm

Figure 5 is the experiment wheels data with intense noise and in the wheel there is a crack of *40mm (length)* 10mm (width)*3mm (depth)*, the final result is shown in Fig. 6. The flaw wave shows the crack of the wheel. Figure 7 shows the result of CRH wheel in Shanghai depot, it can be seen that the wheel is in good condition in accordance with the recheck of workers. The results contain very little noise and won't influence the useful wave. From Fig. 8 it can be seen that the point number of final result is just 2500 from 50000 by sampling. Table 1 shows the effect summary comparison of single method and synthetic method; the synthetic method can get the good wave better that 95% and decrease the noise better than 45%.
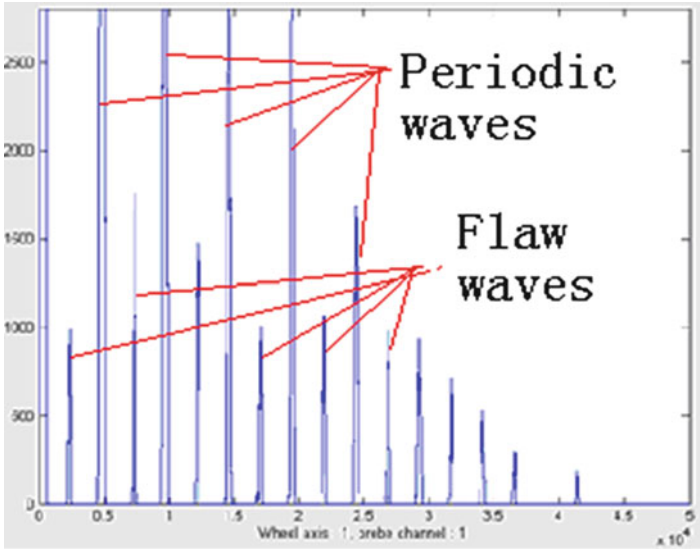
Fig. 6 Final result after processing
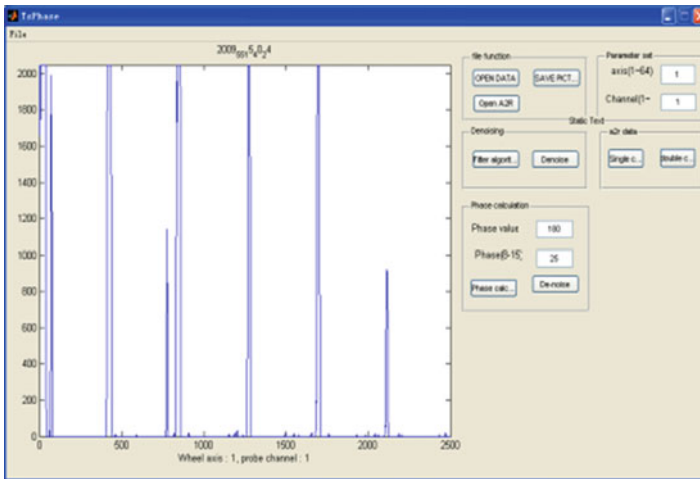
Fig. 7 Processing result of original signal

Conclusion

At present EMAT method is used to detect the wheel cracks in China, the article suggest a synthetic method with combination of wavelet and phase difference calculation to eliminate the noise, the result in lab and depot both proves effective.
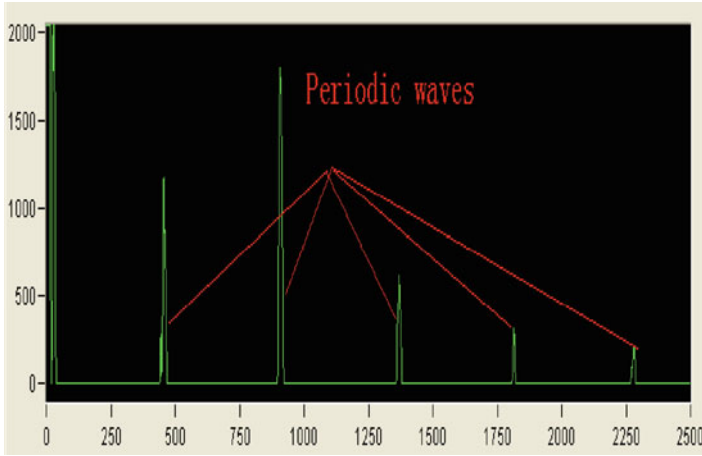
Fig. 8 Result after detection

Table 1 Compared results after three algorithms

Probe NO.	Wave condition	Phase difference	Wavelet denoise	Synthetic method
1	Good Rate	25%	47.1%	99.2%
	Noise Rate	75%	52.8%	0.8%
2	Good Rate	45%	50.6%	95.4%
	Noise Rate	55%	49.4%	3.6%

References

[1] li Jian, (2007), Application in Xian depot of Wheel set inspection system [J], Xian Railway Technology, 2007, 4:45–48

[2] Ji Huanzhong, (2000), Research on EMAT technology [J], Ma Anshan Steel Workers University Journal, 2000, 10:8–9

[3] Dai Lixin,Wangzeyong, Wangli, (2008), Application Research in Wheel Inspection of EMAT [J], Railway Quality Control, 2008, 12(36):24–26

[4] Liu Xianghong, Zhao Zhengyu, (2003), Wavelet Denoise on Terrestrial Magnetism Ripple [J], Wuhan University Journal, 2003, 10(26):630–631

[5] Cheng Peiqing, (2006), Digital Signal Processing [M], Qinghai University Press, 2006, 6:337–339

[6] Qi Guoqing, Jia Xinle, (2001), Precise Estimation Method of Sine Wave frequency and Origin Phase based on DFT [J]. Electric Journal, 2001, 29(9):1164–1167

[7] X. Jian, S. Dixon, K.T.V. Grattan, R.S. Edwards, (2006), A model for pulsed Rayleigh wave and EMAT design [J], Elsevier B.V, 2006, 48(1):296–304

Section 8
Geotechnical and Geophysical Applications of NDT

Impact Echo Q-Factor Measurements Towards Non-Destructive Quality Control of the Backfill in Segmental Lined Tunnels

N. Ryden, O. Aurell, P. Nilsson and J. Hartlén

Abstract A non-destructive method for quality control of the backfill material in segmental lined tunnels is presented in this study. The proposed method is based on the Impact Echo (IE) amplification factor (*Q*-factor). Initial results indicate that the measured IE *Q*-factor can be directly related to the quality of the backfill material. This opens up the possibility for more efficient future quality control of the backfill in segmental lined tunnels.

Keywords Impact echo • Lamb waves • Segmental lining • Surface waves

Introduction

There is a need for non-destructive quality control of the backfill behind segmental linings, typically used with shielded Tunnel Boring Machines (TBM). To secure the structural stability of the tunnel the backfill should support the lining by filling the annulus volume between the tunnel lining and the rock wall. Traditional non-destructive techniques based on radar [1] or impulse response [2] can be difficult to apply on a thick (>0.50 m) reinforced concrete lining. Destructive and time consuming proof drilling through the water tight lining is therefore still used in many cases.

The conventional Impact Echo (IE) method [3] can be used to estimate the thickness of a concrete slab or wall. In a few studies the potential of sensing the stiffness of the

N. Ryden (✉)
Engineering Geology, Lund University, Lund, Sweden
e-mail: nils.ryden@tg.lth.se

O. Aurell • P. Nilsson
Skanska-Vinci HB, Hallandsås Project, Sweden

J. Hartlén
Swedish Transport Administration, Borlänge, Sweden

material behind the concrete layer has also been pointed out [4]. Aggelis et al. [5] measured the attenuation of the IE signal in time domain and concluded that the underlying material could be "sensed" by the attenuation of the signal. Recently the same principal has been demonstrated in frequency domain using a calibrated IE spectrum [6-7].

In this study we propose an alternative method based on the Impact Echo Q-factor. By using the Q-factor (or damping ratio) instead of the amplitude there is no need to calibrate the IE spectrum with the input force from the source.

Proposed Method

In the conventional IE method [4] the resonance frequency (f_r) is measured using an impact source and one receiver close to the source (Fig. 1). The thickness (h) and compression wave velocity (V_P) of the plate is related to f_r as:

$$f_r = \frac{\beta V_P}{2h} \tag{1}$$

where β is a correction factor depending on Poisson's ratio (n) [8] ($\beta = 0.96$ is usually used for concrete). The IE resonance condition is strong and clear in a "free" good quality concrete liner element with concrete/air boundary conditions. In this case most of the seismic energy from the source is trapped in the concrete creating a clear resonant peak in the measured amplitude spectrum. Depending on the properties of the material behind the concrete (backfill) the IE resonance condition will be more or less damped due to energy loss. Figure 1 illustrates how part of the energy is transmitted into the backfill material reducing the reflected and trapped energy when the concrete is in contact with a stiff backfill material.

The quality factor (Q) of a damped oscillation is a measure of the trapped energy to the energy dissipated per cycle. This makes Q a sensitive probe of energy losses. Q can be calculated in frequency domain from f_r and the width (Δf) of the resonant peak where the amplitude is 0.707 (half-power bandwidth method) of the peak amplitude (Fig. 2).

$$Q = \frac{f_r}{\Delta f} \tag{2}$$

Eqn. 2 can be used to calculate the IE Q-factor from the measured amplitude spectrum in frequency domain. Unfortunately this property is easily masked/disturbed in reality by the arrival of direct and laterally reflected surface and body waves. We try to minimize this effect by summing several IE signals from time synchronized hammer impacts at different locations within the first nodal point of the resonance mode shape (i.e. within a radius equal to the thickness of the concrete) [9, 10]. The resulting summed time signal is then transformed to frequency domain and the IE Q-factor is calculated using Eqn. 2.
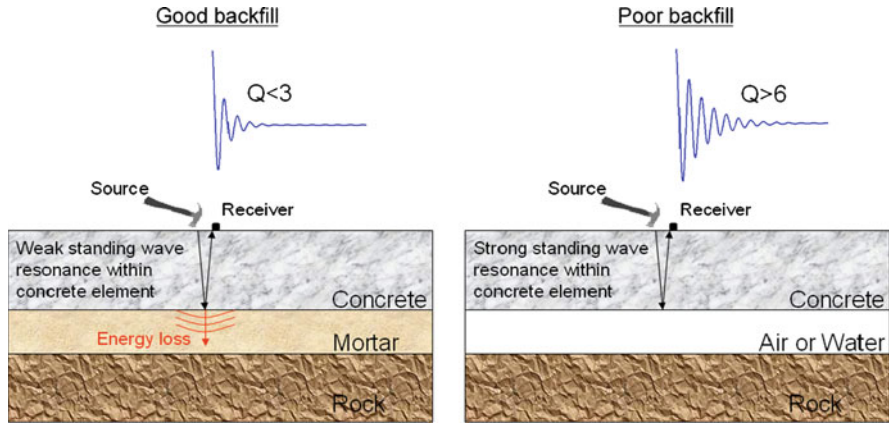
Fig. 1 Impact Echo (IE) measurement set-up on good (low *Q*-factor) and poor (high *Q*-factor) backfill material
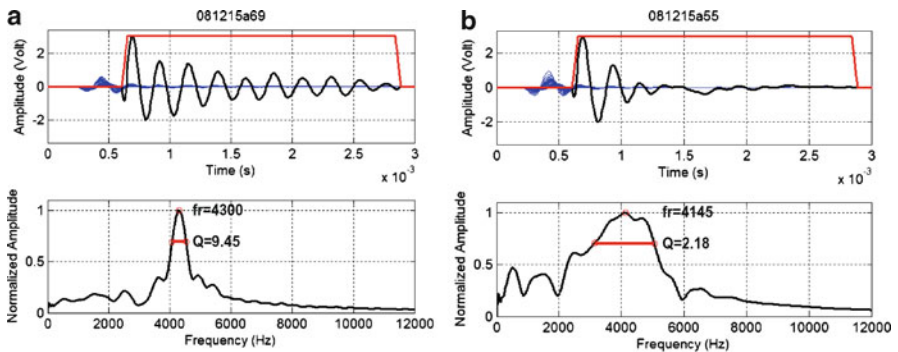
Fig. 2 Field test data in both time and frequency domain from (**a**) poor backfill (un-grouted water saturated pea gravel) and (**b**) good backfill (mortar)

Figure 2 shows two typical examples from test measurements on 0.54 m thick concrete lining elements in the Hallandsås tunnel, Sweden. Thin blue lines represent the original raw data from 40 randomly distributed impacts within 0.5 m radius from the accelerometer. The thicker black line shows the summed amplitudes from all individual signals windowed (red time window) to further suppress the influence of the direct surface wave and later arriving noise. The bottom figures show the normalized amplitude spectrum from the black summed signal. The data presented in Fig. 2a was recorded in an un-grouted section where the backfill material (nominal thickness 0.24 m) consists of water saturated pea gravel. The IE resonance peak is sharp and clear resulting in a high *Q*-factor (9.45). Figure 2b shows the same type of data recorded in a section with known good quality backfill (mortar). In this

case the IE resonance is weaker and broader resulting in a lower Q-factor (2.18). By using the Q-factor instead of the amplitude there is no need to calibrate the IE spectrum with the force from the source.

Results During Curing Backfill

Repeated measurements at the same fixed test point during curing backfill were made to further verify the application of the proposed method in the Hallandsås tunnel. In Fig. 3 time zero represents the approximate time when mortar injection started and not the exact age of the mortar or exact time when the mortar reached the test point. As expected the Q-factor (circles) starts at a high value (8-10) when the backfill is poor (water saturated pea gravel or fresh mortar). Q is then decreasing as the mortar is curing down to a low Q-factor (3–4) representing a fully backfilled state. Figure 3 shows an abrupt decrease in resonance frequency (squares) after about 5 hours indicating that the main source of reflected energy changes from the concrete/mortar interface to the deeper mortar/rock interface. However, in this case the measured Q-factor still reflects the correct status of the backfill.
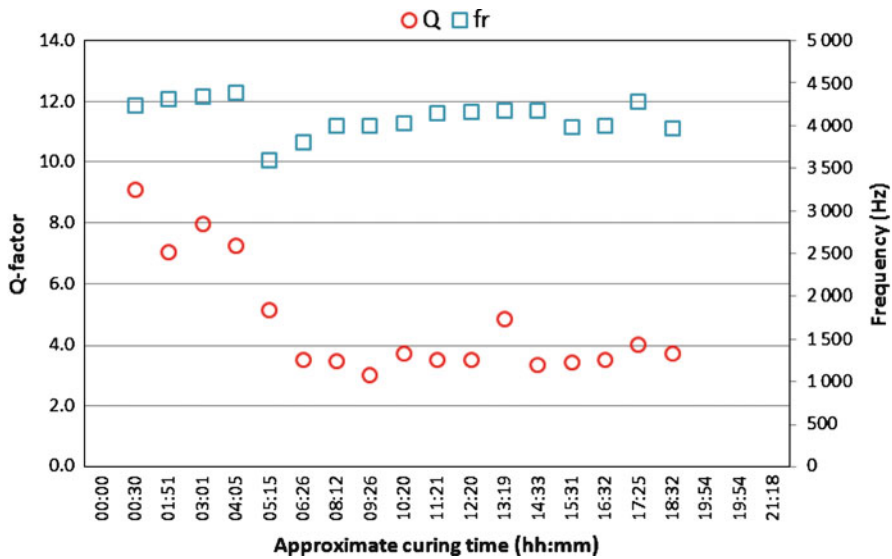
Fig. 3 Tunnel measurements at one fixed test point on a concrete liner element during curing of the backfill material. The measured Q-factor decreases with time as the backfill material becomes stiffer and stiffer

Conclusions

An alternative non-destructive method based on the amplification (Q-factor) of the IE thickness resonance mode has been proposed. Multichannel processing of signals obtained from multiple impacts close to the accelerometer is used to enhance the IE resonance peak. Initial tests indicate that the Q-factor is sensitive to the status of the backfill in segmental lined tunnels. This opens up the possibilities for more efficient future quality control of the backfill in segmental lined tunnels.

References

[1] Zhang, F., Xie, X., and Huang, H., (2009), *Tunnelling and Underground Space Technology*, vol. 5, n. 2, p. 99–108.
[2] Davisa, A.G., Lima, M.K., and Petersen, C.G., (2005), *NDT&E International*, vol. 38, p. 181–186.
[3] Sansalone, M., and Streett, W., (1997), *Impact-Echo Nondestructive Evaluation of Concrete and Masonry*. Ithaca, NY: Bullbrier Press.
[4] Popovics, J.S., and Gibson, A., (2005), Guided wave interpretation of impact-echo behavior in plates and slabs. Proceedings of McMat 2005: Joint ASME/ACE/SES Conference on Mechanics and Materials June 1–3, 2005, Baton Rouge, Louisiana, USA.
[5] Aggelis, D.G., Shiotani, T., Kasai, K., (2008), *Tunnelling and Underground Space Technology*, vol. 23, p. 629–637.
[6] Cheng, C.C., Yu, C.P., Liou, T., (2009), *NDT&E International*, vol. 42, p. 678–689.
[7] Lin, S.K., Lin, Y., Hsu, K.T., Yen, T., (2010), *NDT&E International*, vol. 43, p. 385–393.
[8] Gibson, A., and Popovics, J., (2005), *Journal of Engineering Mechanics*, ASCE, vol. 131, no. 4, p. 438–443.
[9] Ryden, N., and Park, C.B., (2006), *A Combined Multichannel Impact Echo and Surface Wave Analysis Scheme for Non-destructive Thickness and Stiffness Evaluation of Concrete Slabs*, Proceeding of the 6th International Symposium on NDT in Civil Engineering, Ed by I. Al-Qadi and G. Washer, 14–18 August 2006, Saint Louis, Missouri, United States, pp. 247–253.
[10] Ryden, N., Park, C.B., Ulriksen, P., and Miller, R.D., (2004), *Journal of Geotechnical and Geoenvironmental Engineering, ASCE*, vol. 130, no. 6, pp. 636–645.

Monitoring DC Stray Current Corrosion at Sheet Pile Structures

W.H.A. Peelen, E.A.C. Neeft, G. Leegwater, W. van Kanten-Roos and W.M.G. Courage

Abstract Steel is discarded by railway owners as a material for underground structures near railway lines, due to uncertainty over increased corrosion by DC stray currents stemming from the traction power system. This paper presents a large scale field test in which stray currents interference of a sheet pile wall was monitored in realistic conditions. The field test was representative for a sheet pile wall of 220 m length and 10 m depth. Also an anchor was incorporated. A specially designed coupon sensor was used. Measured stray current interference was very low, maximum values were found for the anchor. A conservative interpretation of the measured results showed that additional corrosion due to stray currents was smaller than 10 % of the expected natural corrosion, based on the applicable standards.

Keywords DC • Large scale field test • Monitoring • Service life design • Stray currents

Introduction

Several developments cause a large increase of the number of buried underground (sub)structures in the vicinity of railway lines in the Netherlands. Steel and concrete are the main material options. Compared to concrete, with steel potentially cheaper structures can be made, which construction causes fewer nuisances to the surrounding and the train service. Railway owners are, however, wary of accepting solutions obtaining steel near railways due to a belief that stray currents can cause significant additional corrosion and therefore loss of integrity of the structure.

Stray current is the collective term for all electrical currents running through the ground. Traction power adds significantly to the stray currents near railway lines. At present the expertise on stray current corrosion of steel structures is limited and only

W.H.A. Peelen (✉) • E.A.C. Neeft • G. Leegwater • W. van Kanten-Roos • W.M.G. Courage
TNO, P.O. Box 49, 2600AA Delft, The Netherlands
e-mail: willy.peelen@tno.nl

empirically based. Most experience is gathered in situations when large interference occurs, e.g. due to faults in the traction power systems. A European standard on; "Protection against corrosion by stray current from DC systems', EN 50162 exists [2]. Long term effects are not quantified in this standard. Very limited knowledge exists on 'normal' magnitudes of stray current interference, which can be used to account for this phenomenon in the design phase.

In this paper non destructive monitoring of stray current interference of a steel sheet pile structure in a large scale field test is described.

Stray Current Interference

In Fig. 1a schematic representation of the stray current geometry is depicted. It shows the overhead wire and the rails with in between the train. The DC Traction Power station (TPS) feeds the traction current into the overhead wires, the current runs through the electromotor of the train and returns to the TPS through the rails. A (small) part of the current leaves the rail and flows into the soil. Before it 'closes the current loop' by re-entering the TPS, it must enter the rails, since the TPS itself is not grounded. Once in the soil the stray current distributes as to minimise the total resistance. If a steel structure (including concrete reinforcement steel) is present in the soil, it constitutes a return path to the TPS, and current will enter the steel structure, flow through it and will exit at a different position(s). Since steel is a very good electrical conductor, also compared to the soil, this current can be relatively high. There were the current leaves the steel structure corrosion can be initiated and accelerated.

Field Test

Two sheet pile walls with a length and depth of 10 meter, separated roughly 220 meter from one another and connected via a cupper cable were implemented. From a stray current point of view, such a structure, in many aspects, represents a sheet
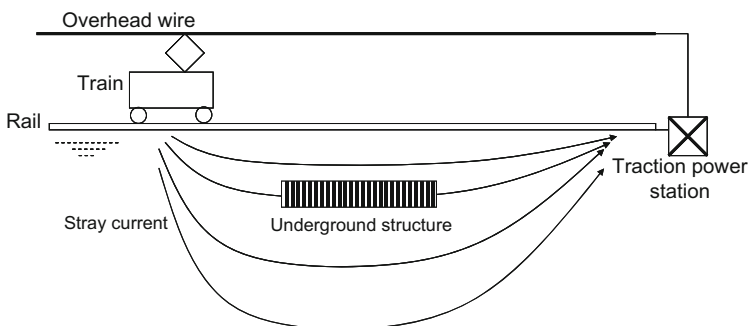
Fig. 1 Schematic representation of the stray current geometry
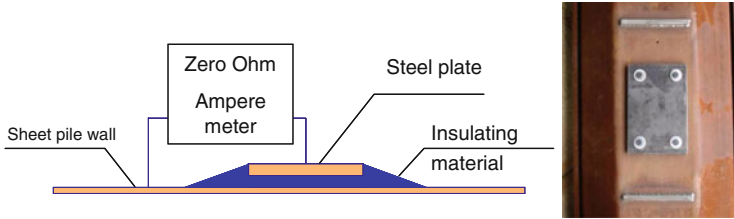
Fig. 2 Schematic representation of coupon sensor; insulating material is epoxy, steel plate is same steel as sheet pile (left), and a photograph (right)

pile wall with the same length as the distance between the two small sections. If sheet piles walls are used on a building site, usually anchors keep them in place. Therefore an anchor was incorporated in this field test. A suitable location was found next to the railway line between Leiden en Woerden, near Hazerswoude-Rijndijk. The soil type at the location is a combination of peat, clay and sand, which is representative for a corrosive soil in the Netherlands. The nearest substation is at 20 m, and there is a two tracks railway line at 11 to 15 m from the sheet piles. Thus this location represents a worst case scenario for stray current interference, for further information see [3].

Two types of sensors are used in this work; a specially developed coupon sensor for sheet piles and a so called reference electrode used to measure the electrical potential differences between the electrode and soil close to the coupon sensors. The coupon sensor, is depicted schematically in Fig. 2. A small steel plate with a known surface area of 300x200 mm^2 made of the same material as the sheet pile wall, is attached to the sheet pile avoiding metal to metal contact. The plate is electrically connected to the sheet pile wall through a Zero-ohm ampere meter. In this way, from the viewpoint of stray current interference, the plate will behave identically as the part of steel on the sheet pile which it covers, while it has become possible to measure the current entering or leaving the small steel coupon. From the surface area of the coupon and the measured current follows the averaged current density at the coupon which is representative for the current density at that position without coupon. From that the corrosion rate can be calculated [3]. Coupon size and ampere meter sensitivity and accuracy were designed such that very low stray current induced corrosion rates of 0.1 μm/year could be measured easily. Since it is mounted to the sheet pile it is installed together with the sheet pile wall without any further effort. Furthermore it is in exactly the same conditions as the sheet pile wall and its exact location is known. All these facts make this a very representative sensor.

A photograph of a sensor is shown in Fig. 2. The steel strips above and below the sensor protect it during the drilling process of the sheet pile wall from excessive forces. Material costs of the sensor are low. Drawback however is that applying the sensor to the sheet pile wall is elaborate and involves e.g. welding and isolating the coupon from the sheet pile. The Zero Ohm Ampere meter technology used is well developed and was made compatible with wireless data transport. The steel potential sensors are standard so-called reference electrodes Copper-Copper Sulfate (Cu/CuSO4).

On each sheet pile wall 12 coupon sensors and 9 reference electrodes were placed homogenously distributed over the edges of the sheet pile walls and the middle.

Results and Discussion

The monitoring system was deployed from May 2009 until March 2010. The longest period of undisturbed measuring was from September 17th 2009 until February 2nd 2010. Major problem encountered was flooding of the measuring device, which was buried in the ground above ground water level. The measurement frequency could be adjusted from the back-office and varied between every 1 sec. to every 40 sec.

A single coupon measurement over one day is shown by the red line in Fig. 3. This red line represents the raw measurement data. The black line shows the signal after post processing, in which low frequency components (means, long period trends) and high frequency contents (noise) were removed. Further post processing was performed, in which use is made of Fourier Transforms in order to identify dominant frequencies (or periods) in the signal. Doing so, a period of 30 minutes between subsequent peaks and a peak width of roughly 4 minutes could be determined, which is in accordance with the train schedule. Train passages are shown to give rise to stray current magnitudes in the order of 10 μA for this coupon location. Also the coupon sensor shows a characteristic difference between day and night period corresponding to the night period without train traffic.

In general, the values found for the sensors on the sheet piles are distinguishable but low. Relative high values are found at and near the anchor, with increasing values towards a maximum at the anchor end points.

The measured maximum values tended to fluctuate during time in a rather erratic way. This is probably due to the fact that the values are relatively small. Long term behaviour was therefore studied by obtaining the distribution of the measured maximum values. Such a graph is presented Fig. 4 for the coupon at the anchor tip. In this cumulative distribution function the empirical (measured) probability of measuring a peak current lower than a certain value is given. This distribution indicates that the probability of measuring a peak value lower than 50 μA is roughly zero. Then a steady increase in the probability of measuring peak values between 75 and 175 μA from roughly 10 to 90 % is obtained. About 10 % of the measured peak values are between 175 and 250 μA. Finally the probability to measure peak values of 250 μA or higher is roughly zero. For the other coupon similar but less distinct distributions were obtained, due to the low measured current densities.

The cumulative distribution obtained at the anchor tip, which shows largest stray current density's is used for the long term interpretation of measured results by taking the peak value at 95% as the interference measured continuously during the passage of a train and using the current train schedule, over 100 years. In this way a (very) conservative assessment of the stray current interference is obtained. Taking all peak values into account, a peak value of 196 μA represents a 95% percentile. From this value a thickness loss can be calculated of 0.2 mm in 100 years [3].
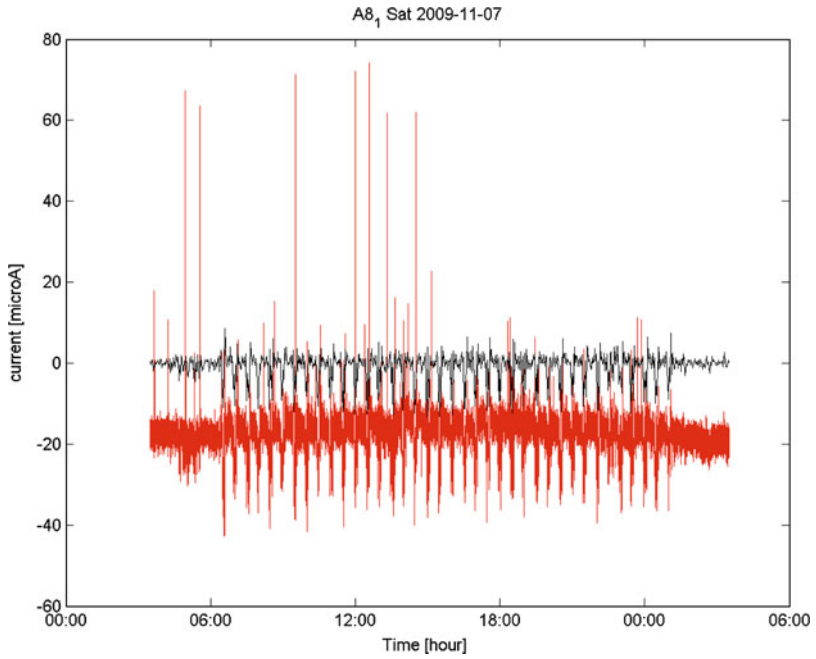
Fig. 3 Coupon signals of Saturday 2009-11-07 (red line: raw signal, black line: processed signal)
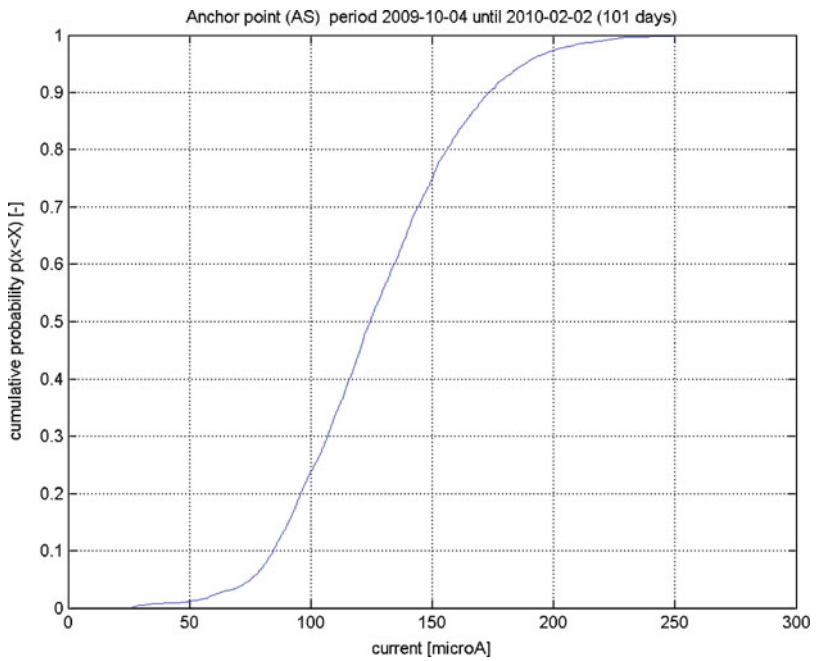
Fig. 4 Cumulative distribution functions of measured currents at the anchor endpoint, (101 days) in period Oct-4-2009 until Febr.-2-2010

The 95% percentile in natural corrosion is 3.1 mm in peat and 2.3 mm in clay using distributions for natural corrosion in 100 years [1]. Therefore the additional corrosion of 0.2 mm in 100 years, in a worse case scenario, is far smaller than the natural corrosion rates in these soils.

Conclusions

A field test in which stray current interference of a large scale sheet pile structure was monitored, was performed successfully. Additional corrosion by stray currents was successfully identified and detected using two types of sensors. The specially developed coupon sensors work properly. Low stray current induced current densities on the sheet piles were obtained, though the conditions; type of soil, sheet pile wall length, sheet pile depth and the position of the structure was optimised to obtain high current densities, i.e. relatively worst-case conditions. Under these circumstances, the additional corrosion by stray currents was determined to be less than 10% of the natural corrosion in a rather crude and conservative way.

References

[1] NEN-EN 1993–5:2008, 'Eurocode 3 – Design of steel structures–Part 5: Piling'
[2] Protection against corrosion by stray current from direct current systems EN 50162, August 2004.
[3] Peelen, W.H.A., Courage, W.M.G., Leegwater, G.A., Neeft, E.A.C., van Kanten-Roos, W., Burggraaf, H.G., TNO report TNO-034-DTM-2009-03537, 2009.

Inspection of Deteriorated Coastal Embankments Using Radar, Thermography, and Impact-Echo

C.-H. Chiang, C.-C. Cheng and K.-T. Hsu

Abstract Erosion and cavitation are threatening the structural integrity of the concrete embankment along the coast line of Taiwan. Task force is formed to investigate the embankment deterioration. Images of subsurface anomaly have been obtained based on the data coming from different techniques. The techniques applied include ground penetration radar, infrared thermography, and impact-echo method. The results are in good agreement among cross-sectional radar images, thermal images, and normalized impact-echo spectrum measurements.

Keywords Coastal embankments • Deterioration • GPR • Inspection • Impact-echo • Thermography

Introduction

Concrete embankment along the coast line may exhibit distress such as cracks, delamination, and cavities. Such deterioration is often caused by erosion of earth in the core of the embankment. The length of coast line of Taiwan is more than 1000 kilometers. Much of the coastal area is protected by concrete embankment. Local authority is concerned if embankment deterioration will worsen and structural integrity will be impaired. Task force consists of engineers and researchers have been assessing the extent of distress since 2009. Ultimate goal of such assessment is to set up a maintenance and repair plan to precede possible flooding in the coastal area of south western Taiwan.

C.-H. Chiang (✉) • C.-C. Cheng • K.-T. Hsu
Department of Construction Engineering and Center for NDT,
Chaoyang University of Technology, Wufong, Taichung, Taiwan
e-mail: chiangc@cyut.edu.tw

Cored samples may be taken for verification of areas at high risk of erosion. Such a time-consuming method may not be applicable due to its destructive nature. The task force responsible for the assessment instead selected nondestructive techniques including ground penetration radar, infrared thermography, and impact-echo method. The objective was to efficiently gather data for reliable evaluation of the deterioration. The basic principles of operation of these techniques will be introduced. Results of measurements and detail analyses will be reported in the following sections.

Inspection Techniques

Ground penetration radar, or GPR, is a device that performs line scans using electromagnetic waves of 100MHz – 2GHz in frequency. The receiving antenna picks up signals reflected from internal discontinuity. The electromagnetic waves travel in a speed of 0.06m/nsec or greater in earth or concrete. A large amount of data is thus obtained swiftly in a single scan. The scanning procedure may include multiple scanning lines for high-risk areas. The recorded data are processed online or offline such that the difference in travelling time or dielectric constant can be analyzed. A typical line scan showing reflection of an underground pipeline is given as Fig. 1. Further inspection may be performed if necessary using other techniques. Cross reference based on additional information is sometimes required for reporting severely distressed embankment sections.
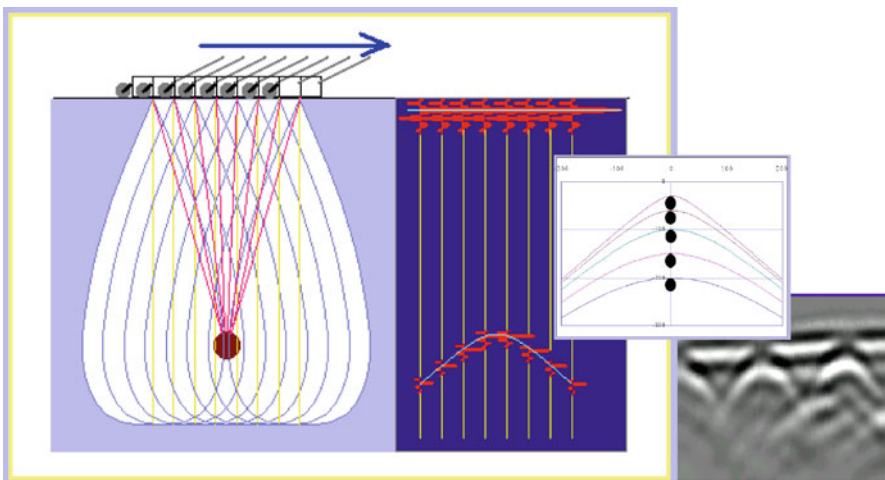
Fig. 1 GPR line scan and reflective signals (left); typical line scan of an underground pipeline (after [1])
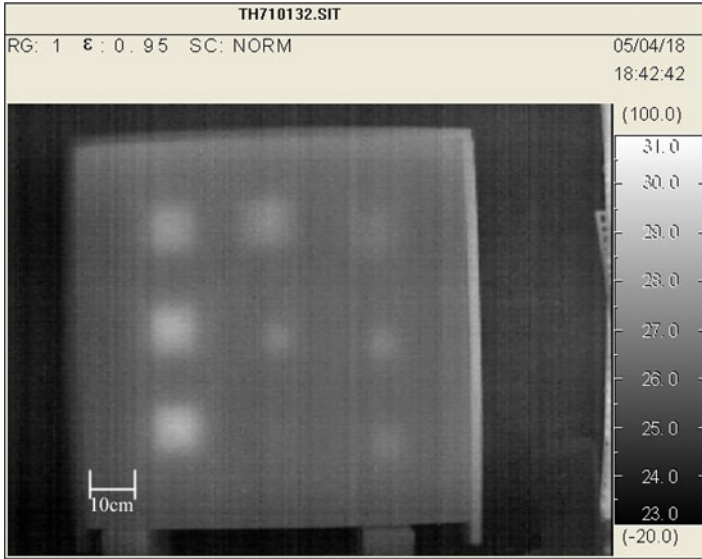
Fig. 2 Thermal image of a concrete slab with embedded defects under the surface (after [3])

Infrared thermography, or IRT, is a technique that measures surface temperature distribution using an infrared camera. Single or multiple shots are taken and stored as digital thermal images. Subsurface anomalies may be identified based on post processing of the thermal images. Environmental conditions like ambient temperature, cloud, variation in humidity and wind speed and so on can have significant effect on the results of IRT applications. Further information may have to be obtained from evaluating the temperature distribution due to non-uniform heat radiation of the surface. Concrete of invisible subsurface defects can be found in a thermal image, such as the example shown in Fig. 2.

Impact echo method improves the ultrasonic pulse velocity measurement using piezoelectric sensors to detect wave propagation triggered by an impact source. Traveling time of transmitted and reflected elastic waves can be analyzed for measurements such as the thickness of a concrete plate or the depth of a surface-opening crack. Impact force and reflected signals may also be evaluated in the frequency domain for inspection of interface properties between different materials. Response at a plate-air interface can be evaluated using the normalized impact-echo spectrum of the simulated transfer function. Cheng et al. [2] derived the following equation for the thickness amplitude of a concrete plate:

$$A_{thk} = \left(\frac{1097.5 \times (r/T)^{-0.3764}}{T^{1.25}} \right) \times \left(\frac{4000}{C_p} \right)^2 \tag{1}$$

The parameter r in eqn. (1) is the impactor–receiver distance. The plate thickness T (in mm) and the P-wave speed C_p (in m/s) are first determined using a standard impact echo measurement.

The measured thickness amplitude agrees well with that predicted by eqn. (1) at a plate-air interface, compared to a 32% difference at a plate-earth interface. Such a difference provided useful information on whether the concrete plate and the earth underneath were in good contact, as reported in the previous study [4].

Results and Analysis

Field testing for the first of the two coastal embankments under scrutiny found several critical areas of deterioration. Surface cracks and construction joints filled with water, embedded pipes, or internal voids can be detected using GPR line-scans, as illustrated by the schematic in Fig. 3. A two of 26 line-scans are assembled and shown as the GPR B-scan in Fig. 4. Another 26 line-scans are displayed as the GPR B-scan in Fig. 5. Internal voids can be identified by strong reflected signals in the GPR B-scan.

Impact-echo measurements were taken at selected spots shown also in Fig. 5. The thickness amplitudes for points A and B were within 5% from those predicted by eqn. (1). This confirmed the finding by GPR scans in which strong signals of internal voids were present. The thickness amplitudes for points C and D deviated from those predicted values by more than 29%. No GPR signals can be found there due to solid contact of the concrete and the adjacent earth.

Another example of GPR scanning results of a second embankment is given as Fig. 6. Multiple line-scan records are combined and processed to form a cross-sectional view of an area under the 30-cm-thick concrete cover. Sharp contrast, showing in black and white, is the reflection from large internal voids. The grey area of Fig. 6 is the reflected signals of the homogeneous region i.e. compacted earth.
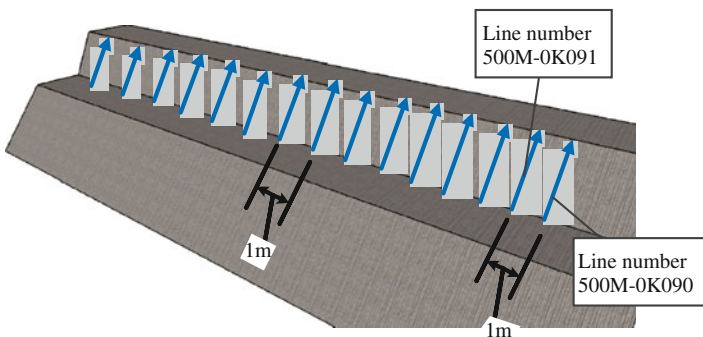
Fig. 3 GPR line scans on the side wall of the embankment are shown in blue. Antenna frequency is 500MHz
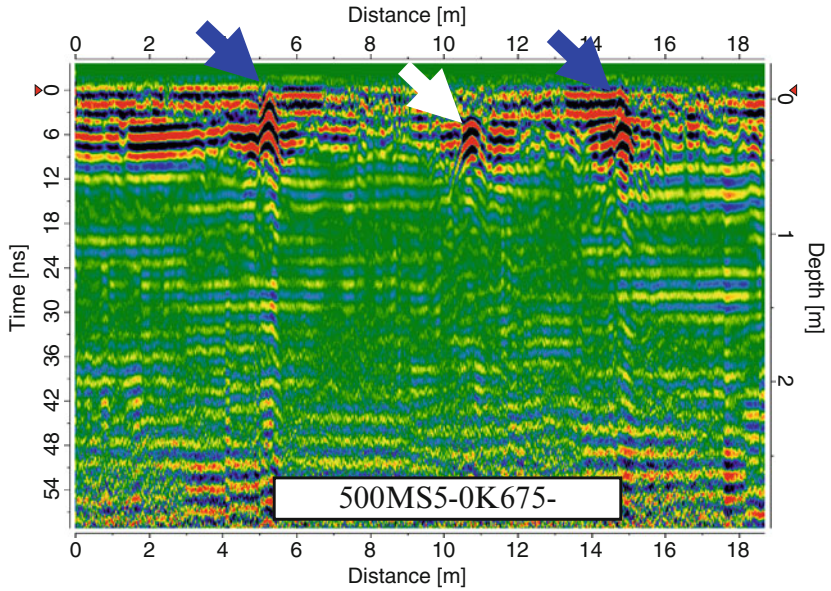
Fig. 4 A GPR B-scan of the first concrete embankment showing strong signals reflected from an internal void (white arrow) and from surface cracks (blue arrow)
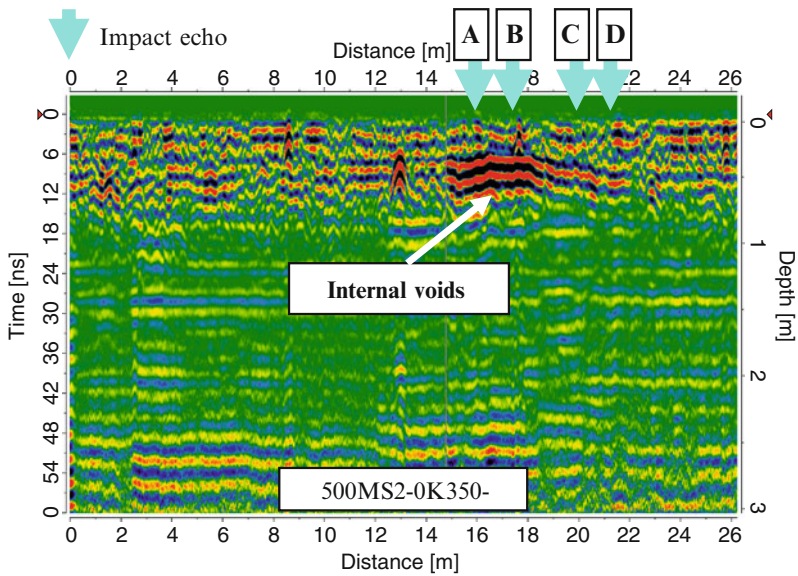
Fig. 5 A GPR B-scan of the first concrete embankment indicating strong signals reflected from internal voids. Also shown are surface points for impact echo tests
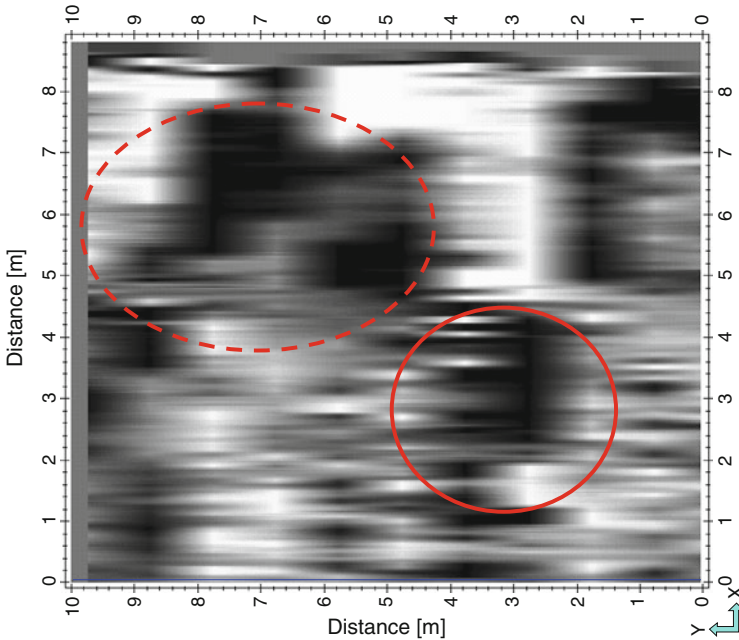
Fig. 6 A cross-sectional view of the second concrete embankment. Strong reflection from internal voids is indicated by red circles

IRT inspection was also applied to the same section of the second embankment. The infrared camera is equipped with a 320×240 sensor array having a detectable range of 8-14μm. Black and blue area near the top of Fig. 7 is the top of the embankment where strong wind was present at the time of IRT inspection. Temperature difference is 1-2°C between the right part (in green) and the left part (in brown) of the lower half of the thermal image in Fig. 7. This green area corresponds to the embankment surface above the large internal void at the right of Fig. 6. The low temperature area is associated possibly with internal erosion inside the embankment or the surface disintegration and cracks of the concrete. Much lower temperature could have been caused by the internal void had the wind found its way through the surface opening.

Concluding Remarks

Three nondestructive testing methods have been applied to the inspection of two concrete coastal embankments. GPR scans allowed effective detection of internal voids, a critical sign of erosion of earth in the core of the embankment. In many cases the GPR scans also picked up signals reflected from surface cracks or construction joints filled with water, a potential cause of erosion problems. The speed
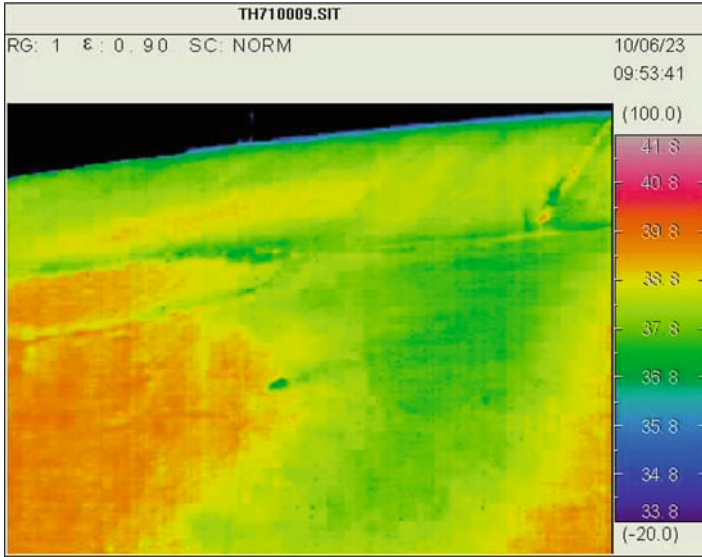
Fig. 7 Thermal image corresponding to the surface of the embankment of the same section as that shown in Fig. 6

of a GPR line scan is approximately the walking speed of the operator. This enables GPR to efficiently scan a large area in the filed inspection. Additional inspection was also performed using impact-echo and IRT. The results confirmed the findings of the GPR scans. Normalized impact-echo spectrum provided strong indication of separation between concrete and earth in erosion. Further work is in progress to enhance the contrast of thermal images due to surface and subsurface defects.

References

[1] Pei, K-C., Cheng, C-C., and Chiang, C-H. (2007) *The Magazine of the Chinese Institute of Civil and Hydraulic Engineering*, vol. 34 n.3, pp.77–92.
[2] Cheng, C-C., Yu, C-P., and Liou, T. (2009) *NDT&E International*, vol.42, pp.678–689.
[3] Cheng, C-C., Cheng, T-M., and Chiang, C-H. (2008) *Automation in Construction* vol. 18 pp.87–92.
[4] Hsu, K-T., Cheng, C-C., Lin, Y-C., and Chiang, C-H. (2010) *Concrete Technology*, vol.4 n.4, pp.23–35.

Laboratory Characterization of Mining Cemented Rockfill by NDT Methods: Experimental Set-up and Testing

C.L. Chou, M. Chouteau and M. Benzaazoua

Abstract Many types of backfill are used as supporting technique in underground mines to optimize ground control stability and to minimize environmental problem at the surface. In theory cemented rockfill can yield optimum strength resistance, yet it is the least implemented in practice due to difficulties related to laboratory analysis of coarse particles in the material. This paper focuses on finding an appropriate protocol to use nondestructive testing techniques to characterize a cement-based material and to study the evolution of the properties during a curing period of 120 days. The testing techniques are the electrical resistivity and sonic methods. The resistivity technique highlights the changes in resistivity caused by hydration processes and the bond developing between the backfill constituents. The sonic technique measures the P and S waves. Knowing the velocity of the waves, changes of the geotechnical properties can be evaluated using known relationships between velocities and mechanical properties. Overall the mechanical strength can be indirectly monitored by these two techniques. Both techniques are complementary to one another and their joint application should improve the interpretation of strength. A concrete sample was made to test these two techniques on a slightly heterogeneous material. The experiment shows that the techniques are sensitive to the physical property changes and they enable monitoring of hardening and strength development. The far-reaching outcome of this research could help assess the properties of different compositions of mining rockfills in the laboratory before using them in mines. Alternatively, these techniques may be used on other cement-based material with coarser particles.

Keywords Electrical technique • Rockfill • Monitoring • Property characterization • Sonic method

C.L. Chou (✉) • M. Chouteau
École Polytechnique de Montréal, Montréal, Canada
e-mail: lulu-catherine.chou@polymtl.ca

M. Benzaazoua
University of Quebec in Abitibi-Temiscamingue (UQAT), QC, Canada

Introduction

Underground backfill is mainly used to fill an empty stope and to act as a pillar to support the walls to prevent cave in and mine failure. There exists several types of backfill and their primary compositions are waste rock or tailing. Backfill can be combined with or without cement to achieve proper ground stability. The addition of cement, however, can neutralize or minimize the generation of acid rock drainage and decrease contamination [1]. One of the most efficient backfill is the cemented rockfill, a mixture of coarse rocks and binding agents. Rockfill is thought to have a greater strength and resistance, but because of its composition laboratory analysis is much more difficult to perform. To overcome this, two nondestructive techniques are proposed to evaluate the geotechnical properties of the cemented backfill throughout the curing time [2]. The first technique is the resistivity tomography using the Syscal Junior resistivity meter (Iris Instrument), and inversion is performed using BERT software to analyze the resistivity distribution within the sample. The second technique is the sonic velocity tomography based on measurements of time for the transmitted pulse to travel through the material; ultrasonic data are collected by two different pieces of equipment to compare results and assess their respective performance. A first data set is recorded using an impact hammer and a second data set is recorded using an ultrasonic pulse velocity (UPV) system.

To verify these techniques and to ensure a proper and efficient protocol in measuring the geophysical properties of a cemented based material, a cylindrical concrete sample is made for testing. This article is aimed specifically to validate these techniques and to discuss the results, shortcomings and possible outcomes of the protocol if apply on a cemented material composed mainly of large particles. Also, we present the correlation observed in the data obtained by both techniques.

NDT Methods

Electrical resistivity technique

Resistivity is strongly related to the content of water of the cement mixture; hence a higher degree of humidity in a cement-based material makes the material more conductive. The electrical resistivity tomography technique allows monitoring the hydration of the binding agents and water more significantly. It helps to determine when the matrix of the cement-based material is formed and the constituents are crystallized. The resistivity meter Syscal Junior R1 measures the resistance of the material at multiple positions of the sample. The electrical resistivity distribution is obtained by performing inversion using BERT software to analyze inside the material through-
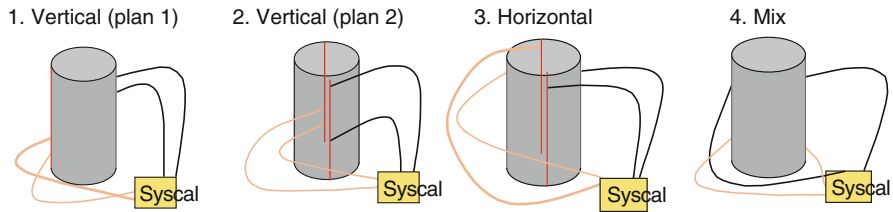
Fig. 1 Multiple electrode arrays used to map resistivity distribution within the concrete sample

out the curing period. BERT – Boundless Electrical Resistivity Tomography- is a software code designed to model the internal resistivity distribution using the finite element method [3].

Based on Ohm's law, the resistance is equal to the inverse of the current transmitted into the material over the potential difference measured. From the resistance, resistivity can be obtained through proper scaling. It is important to collect enough data in order to obtain a good resistivity distribution inside the material. Four different electrode configurations (Fig. 1) are used to maximize data measuring and to ensure an adequate amount of information is acquired.

Sonic technique

The sonic technique is a seismic method at a small scale. The basis of this technique is to send a pulse into the material, collect and analyze the signal waveform at some locations in or at the surface of the material. The compressional (P) and shear (S) waves can be determined. With the P and S waves, the mechanical properties- such as Young's modulus (E), shear modulus (G) and bulk modulus (K) - of a material can then be calculated.

For any kind of concrete mixture and at any given time during curing, the resolving velocities depend on the transmitted signal frequency and amplitude and on the sampling frequency used. A higher signal frequency yields a smaller wavelength which can greatly help the recording of P and S waves and the estimation of the time lag between the two body waves. A higher sampling frequency is suggested to decrease time picking errors. Hence to compare the frequency parameters, two sonic-ultrasonic equipments were used: an impulse force test hammer from PCB Piezotronics and an ultrasonic pulse velocity (UPV) from Olson Instruments. The impulse hammer generates a pulse and a three-directional accelerometer captures the signal. The maximum sampling frequency is 125 kHz per channel and the signal central frequency spectrum is in between 15-20 kHz. The UPV system uses two interchangeable transducers for source and receiver. The sampling rate can be up to 1 MHz for one channel, and the signal central frequency spectrum lies in between 55 and 60 kHz.

Experimental Set-Up

To evaluate and to validate these two techniques, a cylindrical 1m high 40 cm-diameter concrete sample is made. The concrete is paste filled and its mixture composed of silica fume, sand and small aggregates. A water-cement ratio of 68% is used and its density is 2382.7 kg/m^3. The sample is divided into 2 orthogonal symmetrical sectional planes, with 36 measurement positions marked by installing screws to act as electrodes (Fig. 2). Measurements were taken in a period of 120 days while the sample is stored at room temperature (~22°C) and the surface is covered to prevent drying and carbonization.

Experimental Results

Electrical resistivity technique

Figure 3 shows the resistance plots with regards to curing time for different arrays. Each graph illustrates the resistance measured by one of the four electrode configurations (Fig. 1). Each plotted curve represents a particular position of the electrodes for that configuration. The measured tomography data are input into BERT to model the electrical resistivity distribution within the sample. Figure 4 shows the internal changes throughout the 120 curing days.
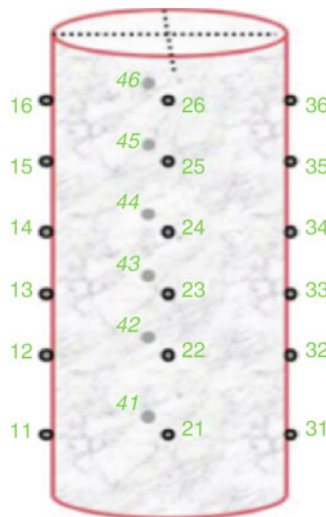
Fig. 2 NDT measurement positions over the cylindrical concrete sample
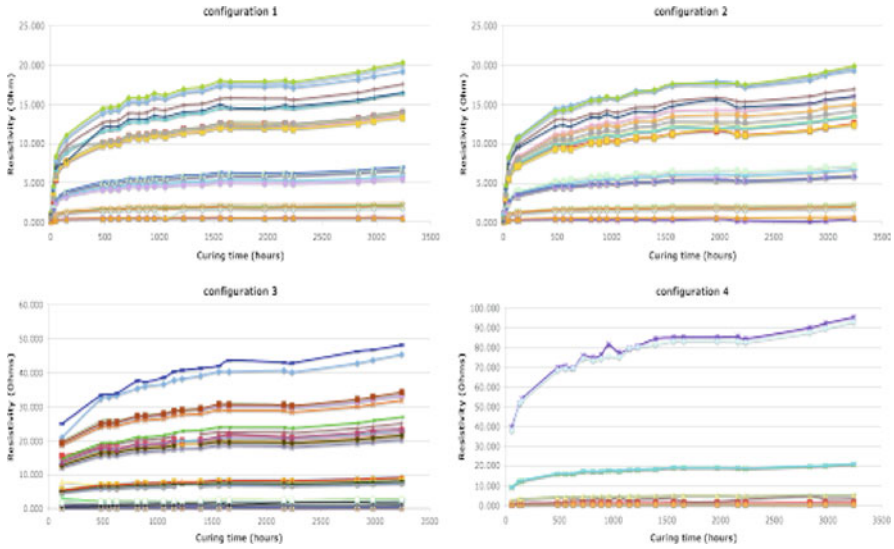
Fig. 3 Monitoring resistance (ohm) with respect to curing time (hours) for different configurations and transmitter-receiver dipoles
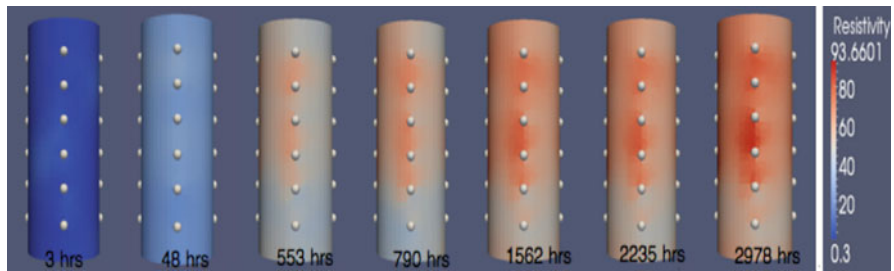
Fig. 4 Time variation of resistivity distribution within the concrete sample

Sonic technique

The impact hammer by PCB uses a simple oscilloscope display corresponding to the signals of the source (hammer) and receiver (x, y, and z components). Figure 5a illustrates a screen capture of the oscilloscope. Similarly, Fig. 5b is a display of the waveform (top) and the frequency spectrum (bottom) by the UPV system. The P and S waves can be determined visually on these waves and the coefficient of Poisson can be calculated as well as other mechanical properties, *E*, *G*, and *K*. Figure 6 shows the sonic velocities and mechanical properties with time averaged over the whole concrete sample using the dataset obtained by the PCB.
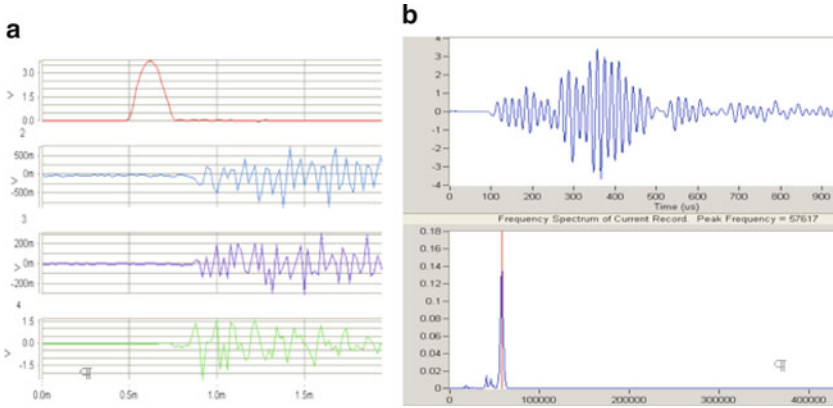
Fig. 5 Waveform display (**a**) Impact Force Test Hammer; (**b**) UPV
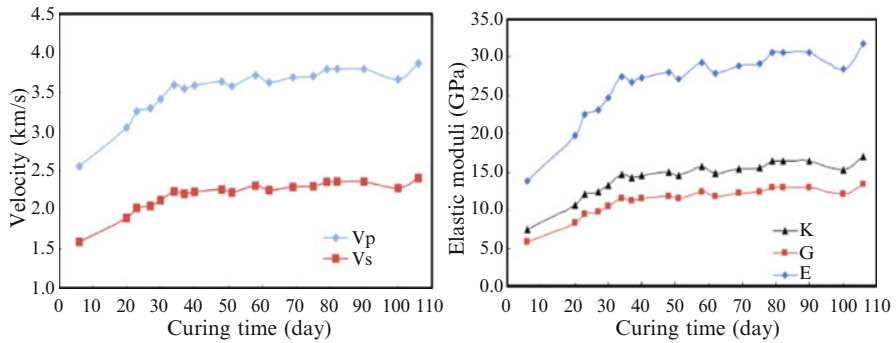
Fig. 6 Time-lapse average sonic velocities (left), and mechanical properties (right)

Discussion/Conclusion

The resistivity plots show that effective resistivity increases with time as expected and all electric dipoles behave similarly. The inversion models also agree and illustrate the material as a homogeneous solution. The hammer and accelerometer system shows that the resolution is not good enough due to noise and low frequency transmitter signal. Despite the accelerometer ability to detect transmitted signal waveform with three components, the noise level and the overlapping P and S arrivals make the picking of the first and secondary arrival time difficult (see Fig. 5a), that causes a lack of consistency and accuracy in data. With regards to the resistivity and ultrasonic tests, it is interesting to observe that results from both techniques behave similarly and should be related to similar mechanisms.

It should be noted that the final objective of the experimental set-up is to monitor the curing of cemented rockfill, a highly heterogeneous solution. It consists mainly of very coarse particles and the slurry content is about 10%. The ERT technique should be able to properly monitor the hydration of the slurry. It is also expected that the ultrasonic technique might not be as sensitive in a heterogeneous solution; Fermat's principle suggests a ray will travel through the fastest medium and rock has a higher ultrasonic velocity than cement.

References

[1] Benzaazoua, M., Marion, P., Picquet I., Bussière B., (2004). *Miner. Eng.*, vol. 17, n. 2, p. 233–243.
[2] Breysse, D., Klysz G., Dérobert X., Sirieix C., Lataste J.F., (2008). *Cem. Concrete Res.*, vol. 38, n. 6, p. 783–793.
[3] Rücker, C., Günther, T., Spitzer, K., (2006). *Geophys. J. Int.*, vol. 166, n. 2, p. 495–505.

A Case Study of the Self-Potential Method to Characterize Seepage and Earth Dam Materials

L.A. Nzumotcha Tchoumkam, M. Chouteau, B. Giroux, P. Rivard, K. Saleh and A. Côté

Abstract This paper presents a case study of the self-potential (S.P.) method applied at the junction of two embankment dams to characterize seepage. Sensitivity of the S.P. method to water runoff can be used to delineate the preferential flow paths. However S.P. can be caused by other sources, therefore only anomalies caused by water flow, described by the electrokinetic (EK) mechanism, are the targets of our study. We take advantage of the controlled progressive emptying and impounding of the upstream reservoir to monitor changes of S.P. due to changes of water flow and the displacement of materials. Also, time-lapse electrical resistivity tomography is used to control the variation of electrical conductivity of the dam material together with changes in water level. It allows for a better discrimination and interpretation of the various self-potential sources. The effective EK coupling coefficient of the dam materials was computed from the variation of potential with water level and flow rate. The S.P. monitoring allowed displaying a positive anomalous zone associated with the reservoir water level changes. It can be related to visible seepage. It is difficult to make a quantitative interpretation of the S.P. data collected at different periods of time using coupled modeling because of the poor knowledge of the hydraulic and physical properties of dam materials.

Keywords Dam • Electrokinetic • Heterogeneity • Seepage • Self-potential • Water flow

L.A.N. Tchoumkam • M. Chouteau (✉)
Ecole Polytechnique, Montréal, Canada
e-mail: chouteau@geo.polymtl.ca

B. Giroux
Institut National de la Recherche Scientifique, Québec, Canada

P. Rivard
Université de Sherbrooke, Sherbrooke, Canada

K. Saleh • A. Côté
Hydro-Québec, Varennes, Canada

Introduction

Amongst the mechanisms that cause the presence of self-potential in the ground, the electrokinetic effect is one of the most important and it could lead to the foundation of the most promising tool to detect water flow in the environment. The self-potential (S.P) method is based on the measurement of the natural electric the potential occurring within the subsurface. In the electrokinetic (EK) mechanism, an electrical current is generated in the presence of a hydraulic gradient that causes water flow in the ground. This process is expressed by the classical equation of Helmholtz-Smoluchowski [1] that relates the electrical potential gradient (ΔV) to pressure gradient (ΔP) by a cross-coupling coefficient, namely the cross-coupling EK coefficient (C). The latter depends on the microstructure of the ground.

$$\Delta V = -C.\Delta P \tag{1}$$

The EK potential has been used to investigate leakage in embankment dams. Revil and Jardani [2] give a thorough overview of the recent applications. Bolève *et al.* [3] used S.P. to detect water infiltration and seepage in an embankment dam. They were able to model quite convincingly the potential data. Limitations are illustrated in cases presented by Salmon and Johansson [4]. They show that S.P. is not applicable with the presence of highly conductive water that leads to subsurface ground soil conductivities larger than 2.5×10^{-2} S/m. The interpretation of S.P. data measured on dams is often limited because of partial knowledge of the dam construction, material heterogeneity, unknown cross-coupling coefficient for each material (cross-coupling coefficient variability) and poorly understood leakage morphology (like piping). To validate the self-potential method as a technique to locate seepage position and its importance in embankment dams, the technique was tested in the case of a complex dam structure, consisting in two dams built at different times and two reservoirs. The seepage has been monitored for some time; its approximate position and the corresponding flow rate are known. The information about its approximate position and depth were updated when injection tests were carried out to seal the leakage. However the construction of the dam is little known and does not comply with actual construction design of embankment dam. As S.P. anomalies present at the site can be generated by other mechanisms than EK, only the ones caused by EK would change with changes in water pressure gradients. A strategy was used to take advantage of the emptying and impounding of the dam reservoir to monitor S.P. variations and electrical conductivity variations.

Site Description

Dams A and B are two embankment dams located along a channel of the Saint Lawrence River upstream near the Montreal area (Canada). Built respectively in 1914 and 1971, the two dams were joined by a watertight grout curtain [5]. The grouting material
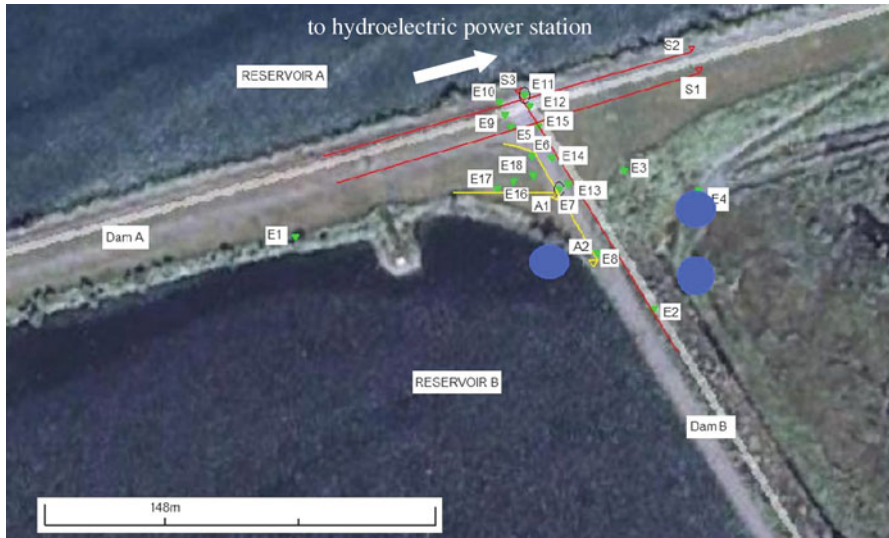
Figure 1 Survey location: junction of dam B/dam A

consisted in a mixture of cement and sand. The execution of the junction between the two dams was complex and the materials used for the junction are poorly known. The first dam (A) was built to supply water to a power station located east of the site. Dam B was built for environmental purposes. Seepage flow measurements were taken downstream of dam B, east of E2. The flow rate values were around 3 l/s in 1972, increased up to 200 l/s in spring 2009 and decreased considerably to 10 l/s in spring 2010 after grout injection. Seepage flows had been observed when the reservoir B is empty. The flows measured during emptying and impounding of reservoir B (before 2010) showed the same trend. Throughout the emptying of reservoir B in fall 2009, the flow rate decreased almost linearly with decrease in water level for the first two meters. Then, it remained constant whatever the water level until it reached the shallowest water level of the reservoir. In spring 2010, the flow rate remained constant with the variation of water level of the reservoir. This change was related to grout injection used to clog seepage. Figure 1 shows the junction of two dams with the position of DC resistivity profiling (S1, S2, S3, A1 and A2), the positions of electrodes (E1 to E18) and the visible seepages (in blue) during the emptying and the filling of the dam B reservoir.

Test and Methodology

To display the EK effect at the junction of the two dams, S.P. measurements have been conducted during the controlled emptying and impounding of reservoir B, over four successive days. They have been complemented with two electrical resistance tomography (ERT) profiles taken during the same period of time. Acquisition of S.P.

data was carried out at ground surface between roving electrodes and a reference electrode (namely E1 in Fig. 1). Eighteen non-polarizable electrodes were carefully installed to insure a good coupling with the ground. The electrodes were installed into holes with smooth bottoms, stabilized with sand and covered with a plastic cap at the top of the hole to prevent possible effects caused by showers, wind gusts or small animals. Tests were made to check that the measured voltages resulted from self-potential phenomenon and not from electrode wear, desaturation, poor coupling or high telluric noise. Electrodes were checked first by installing all of them on a small area at one site before and after the surveys, and measuring their potential differences. Measurements of S.P. were also performed with two parallel electrodes at every electrode site before beginning our survey. The potential data were referred to electrode (E1). At each electrode location, five S.P. values were measured using a SAS1000 Terrameter (ABEM) by integrating potential in windows of 20 milliseconds for 4 seconds total. The electrical resistance tomography (ERT) profiles were carried out using dipole-dipole and Wenner arrays, with spacing varying from two to four meters between the electrodes. Measures for each profile have been taken once per day; changes in water level (high and low) were approximately five meters.

Results

S.P. variations recorded with decrease of water level in the reservoir B for the first two meters showed the same trend as the distribution of the seepage flow rate during the emptying of the reservoir. In Fig. 2, the flow rate measured at downstream dam B is plotted against water level for four different time periods (two emptying, fall 2008 and 2009, and two impounding, spring 2009 and spring 2010). In the first part of the flow rate curve (level above 33.5 m; for measures before 2010), a linear relationship is found between the flow rate and the decreased water head in the reservoir, in accordance with Darcy's Law. This linear relationship between flow rate and water level, also observed for the S.P. variations with water level, was used to estimate an effective cross-coupling coefficient at each measurement site. Below 33.5 m, the flow rate became independent of the water level. The later seems to point at a constant seepage of about 22 l/s coming from elsewhere. It also indicates that the main seepage in dam B comes from a vertical location corresponding to level 33.5 m. In spring 2010, the S.P. data seemed to be independent on water level. Figure 2 shows the S.P. data observed for two electrodes (E7 and E8) plotted against water level at four different time periods. The error bars show data standard deviation. Electrodes E7 and E8 were in the vicinity of the junction between the two dams.

The mapping of the total potential during emptying of the reservoir showed an upstream voltage low [6]. To lay emphasis on electrokinetic mechanism, the total potential at each water level in the reservoir was subtracted from the background potential. The background potential corresponds to S.P. value recorded for low flow rate (below 33.5m). The level of water for the background potential was 31.9 m in fall 2009. A positive anomaly appears in the vicinity of dam B in fall 2009. It also
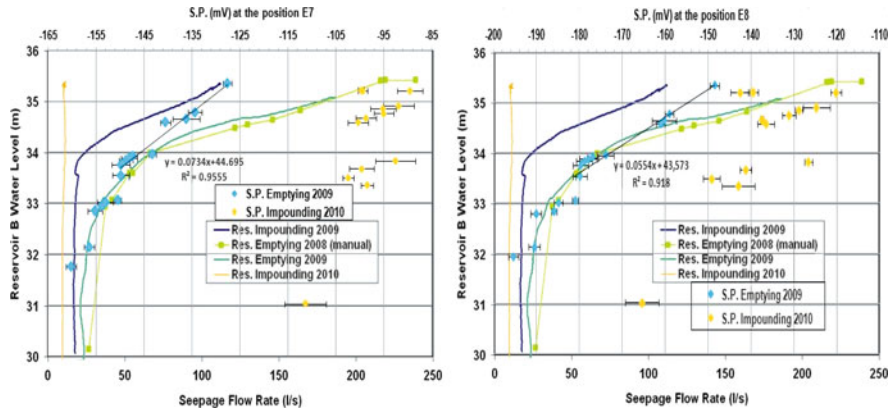
Fig. 2 Seepage flow-rate recorded at dam junction [5] at four different periods

appears that the more the hydraulic gradient increases the more the gradient of potential decreases.

Time-lapse inversion was also performed between the first ERT data (water level ~ 34.65 m) and the latest (water level ~ 31.97 m). It indicates a variation of the resistivity in some places [6]. Of particular interest is the resistive anomaly found at location E8 (in the vicinity of dam B; see Fig. 1): it is at the approximate water level 33.7 m, the level for which the main seepage appears to stop.

Discussion

The S.P. data collected before the emptying of reservoir B shows anomalies consistent with a seepage for which the upstream inlet is located between electrodes E7 and E8 (see Fig. 1). We must be very careful to jump to conclusions since S.P. anomalies on the dam can be caused by other sources. Only anomalies caused by EK would be flow pressure dependant. Therefore, noting changes of S.P. anomalies with changes in water level is a definitive way to display seepage. As the water level decreases, pressure and seepage flow rate should decrease accordingly and maximum potential differences between seepage inlet and outlet should also decrease. However, the gradient of potential related to the experiment carried out in the fall of 2009 decreased with an increase of hydraulic or pressure gradient. It did not agree with theory as expected. Three scenarios were proposed: flow path may be from reservoir A to reservoir B (see Fig. 1), EK coupling coefficient may be positive, the change in the electrically conductive water body upstream in reservoir B may have altered the expected S.P. response.

Effective coupling coefficients measured on the dam (4 - 18 mV/m) appear somewhat larger than the one noted by Suski *et al.* [7] for sand (2.8-3.8 mV/m). However, the coupling coefficients depend on the dam material as well as on the water conductivity and temperature. At the time of the survey in fall 2009, the water temperature was 8°C and its conductivity 1.94×10^{-2} S/m.

Conclusion

Time-lapse S.P. measurements during emptying of the dam reservoir B allowed mapping an S.P. positive anomaly possibly related to seepage. Effective EK coupling coefficients were estimated during emptying and could be used to predict S.P. anomaly with pressure gradient (or water level). Injection used before impounding in 2010 changed the temporal and spatial distribution of potential. Using difference between total potential and background potential was another way to discriminate self-potential sources. But gradient potential and pressure gradient moved in opposite direction. Lab experiments and more fieldwork are underway to estimate the EK cross-coupling coefficient, to model the S.P. data with a variation of electrical conductivity of the water in order to confirm the proposed interpretation.

References

[1] Ogilvy, A.A., Ayed, M.A., and Bogoslovsky, V.A. (1969). *Geophysical Prospecting*, 17, 36–62.
[2] Révil, A., and Jardani, A. (2009). In *Proceedings of SAGEEP*, vol 22, 795–800.
[3] Bolève, A., Révil, A., Janod, F., Mattiuzzo, J., and Fry, J.-J. (2009). *Near Surface Geophysics*, 7, 447–462.
[4] Salmon, G., and Johansson, S. (2003). In *Procs. International Symposium on Major Challenges in Tailings Dams, 71st Annual Meeting of the International Commission on Large Dams (ICOLD)*, 15 June 2003, Montreal, Canada, 275–289.
[5] Côté, A., Smith, M., and Saleh, K. (2009). *Report J-4042-01-001-001*; Hydro-Québec, Montréal, 90 p.
[6] Linda Armelle, N.T., Michel, C., Bernard, G., Patrice, R., Kaveh, S., and Alain, C. (2010). In *Proceedings of the 23rdSAGEEP Symposium*, 23, 118–125.
[7] Suski, B., Rizzo, E., and Révil, A. (2004). *Vadose Zone Journal*, 3, 1193–1199.

Microgravity Application for Detection of Underground Cavities in a Desert Karst Terrain

H.A. Kamal, M.F. Taha and S.A. Al-Sanad

Abstract A number of sinkholes were detected in a residential area located close to the northeast coastal side of the Arabian Peninsula. The sinkholes occurred suddenly with different sizes and a maximum depth of 31 m. Comprehensive investigation studies were conducted for understanding the causes of the sinkhole occurrence and to recommend remedial measures. Microgravity survey method was used for geophysical investigation of the area to detect subsurface cavities. The validity of the microgravity survey was confirmed after applying a drilling program. After 15 years, another microgravity survey was conducted in selected locations of the same residential area for the purpose of verifying the current underground status and assessing its development. In this paper, the nature of the desert Karst terrain under study is described. The results of the two microgravity surveys are presented. The results confirmed the capability of the microgravity method to detect density anomalies and ground disturbances. The maps showed evolution of the anomalies in some locations within the studied area.

Keywords Cavity • Detection • Geophysics • Microgravity • Sinkhole • Subsurface

Introduction

A residential area was developed around 30 years ago in a desert terrain located in the northeast coastal side of the Arabian Peninsula consisting of approximately 2500 housing units and including community services. After eight years of construction, four major ground subsidence occurred in the form of sinkholes (SH1 through SH4). The events caused destruction of property and threatened human lives. An immediate action was taken by the government to evacuate and fence the affected area consider-

H.A. Kamal (✉) • M.F. Taha • S.A. Al-Sanad
Building and Energy Technologies Department, Kuwait Institute for Scientific Research, Kuwait
e-mail: hkamal@kisr.edu.kw

Fig. 1 Sinkhole locations and distribution

Table 1 Ground Subsidence Records

Sinkhole#	Location (Sector)	Date of occurrence	Diameter/ length (m)	Width (m)	Depth (m)	
SH1	A1	April 1988	15.0	-	31.0	OLD
SH2	A1	April 1988	4.0	-	7.0	
SH3	A1	October 1988	7.0	-	9.0	
SH4	A1	June 1989	8.0	2.0	1.4	
SH5	A1	June 2004	4.8	2.6	0.83	NEW
SH6	A1	June 2004	1.5	-	0.54	
SH7	A1	June 2004	5.6	5.0	0.4	
SH8	A6	July 2004	7.0	-	6.0	

ing it as a high risk area [1]. After fifteen years, four new sinkholes were observed during a recent investigation program. The first two sinkholes (SH5 & SH6) recorded in the evacuated area, while sinkhole SH7 occurred at its northeast corner, under the footing of high voltage tower. Sinkhole SH8 occurred in Sector A6. Figure 1 shows locations and distribution of the occurred sinkholes. More information on the sinkholes including location, dimension, and present condition is listed in Table 1.

Description of the Investigation Programs

Upon the occurrence of the sinkholes, several investigation programs were conducted with the direct association of Kuwait Institute for Scientific Research (KISR). The results revealed that the geological profile is made of sandy overburden soil

Fig. 2 Site measurement using gravimeter equipment

uncomfortably overlaying Karst limestone bedrock. The cause of the sinkholes was attributed to the dissolution of the limestone bedrock and the subsequent raveling of the overburden soil cover. The affected area is located at the north-eastern edge of the Arabian Peninsula and bordered by the Arabian Gulf in the East. It is characterized by a typical desert environment with gentle ground slopes from about 270 m above sea level in the extreme south-western corner of the country towards the lowlands in the northeast [2, 3].

As part of the investigation programs, geophysical survey was carried out to investigate the existence of underground cavities and their lateral extent. Three techniques were initially applied: resistivity, seismic cross-hole shooting and gravimetric measurements. The resistivity technique was ineffective due to the presence of electrical services, bitumen or concrete surfaces and the possible presence of a dry saline crust at various depths. The seismic cross-hole shooting was expensive, and the resolution to be poor at the depth of the limestone bedrock layer. The gravimetric testing (Microgravity method) was selected as it proved dependable, non-destructive and risk free, Fig. 2. The survey results were represented in contour maps delineating anomalies varying from negative to positive values. The negative values interpreted as low density subsurface layers and the possibility of existence of cavities. As the contour numbers increase into the positive numbers, the possibility of cavities existence is reduced.

The geotechnical investigation was also carried out in the investigation program by drilling boreholes to depths reaching the limestone bedrock layer, up to the depth of 85 m. The geological profile of the area consists of 31 m to 39 m of overburden comprising of dense to very dense sand, which is underlain by limestone bedrock formation [4]. The soil-rock interface contains dark chert nodules and sandstone. The groundwater table was around the soil-rock interface level. From the drilling records, the cavities were encountered at several depths at the limestone formation.

Microgravity Survey

Theoretical concept

The principal of any gravity survey is to identify areas of contrasting density by surface measurements of the disturbance produced in the earth's gravitational field. The gravitational field is a function of: distance from the centre of the earth, centrifugal acceleration due to the earth's rotation, and distribution of the mass which is controlled by changes in the density of rocks in the earth. The theory of gravity is formulated in Newton's law. This law states that a force (F) exerted on a mass (m_2) by a mass (m_1) is directly proportional to the product of the masses and is inversely proportional to the square of the distance between the centers of the masses. The unit is commonly called a gal. The survey method involves measuring the very small differences in gravitational force field, which are a function of the gravitational acceleration due to the sum of the attraction of the Earth's mass and the effects of its rotation. Full color residual anomaly maps are then produced, where the mass deficiencies indicated by negative residual anomalies.

Results of the first microgravity survey (1989)

The first microgravity survey was carried out in the area after the occurrence of the sinkholes in 1989. The survey covered the whole residential area, sectors A1 to A6. The microgravity survey produced contour maps delimiting the existence and extension of underground cavities, which were due to Karstic formations, in relation to known ground subsidence. For the microgravity stations, a mesh of 12x12 m reduced to 5x5 m and 3x3 m in critical areas were measured. Figure 3 shows the residual map for the whole affected area and the colors indicate the density level based on the anomaly value. Figure 4 indicates the extent and location of the underground cavities (voids) inside the evacuated area. The sudden drop of the drilling heads during the drilling program proved the existence of the cavities. Accordingly, the highest risk area is determined to be within the first three sinkholes in sector A1.

Results of the second microgravity survey (2004)

After fifteen years, the second microgravity survey was carried out in 2004 covering the evacuated area and its vicinity. The main purpose of the second survey was to confirm the existence and update the status and development of previous anomalies within the residential area. The survey emphasized on the highest risk area
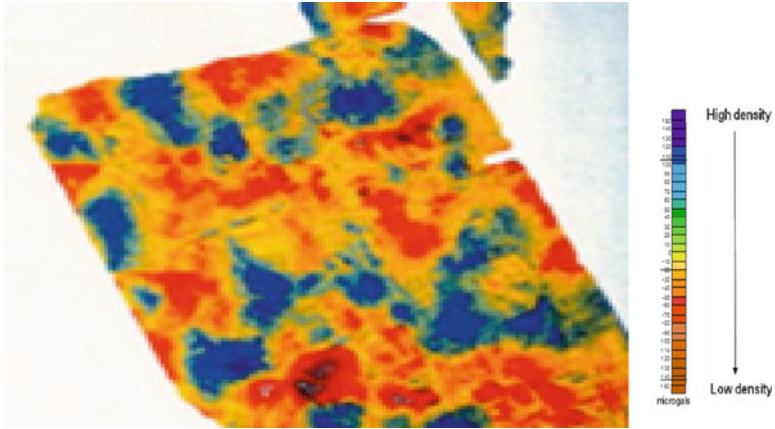
Fig. 3 Residual map for the whole area, first microgravity survey
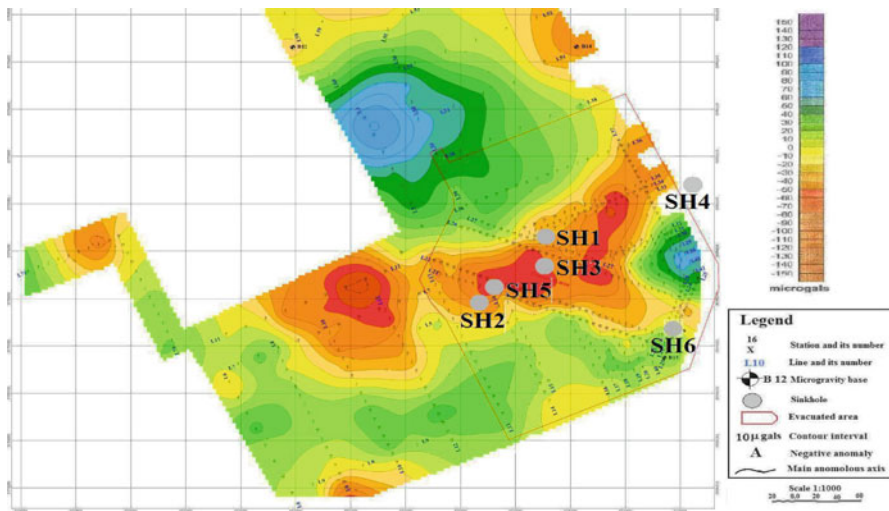
Fig. 4 Residual map for sector A1, first microgravity survey

specified in the first survey in sector A1 and other selected locations within the affected residential area. Around 1000 microgravity stations were measured with a mesh of 10x10 m reduced to 5x5 m in critical areas. The residual map for sector A1 from the second survey is shown in Fig. 5, which detects the extent and distribution of underground cavities. The existence and evolution of the anomalies from the first survey is confirmed.
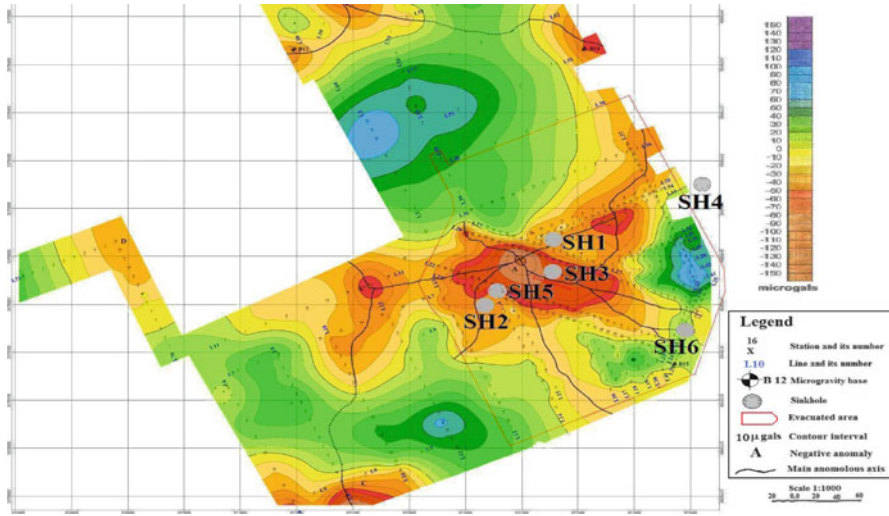
Fig. 5 Residual map for sector A1, second microgravity survey

Comparison between the microgravity surveys

In order to assess the current condition of the underground cavities, its evolution and development, the results for the residual anomalies map of the two previous surveys were compared. Residual maps represent the density variation within the clastic soil sediments and the underlying limestone bedrock in terms of low positive and negative anomalies depending upon the geological conditions. By comparing the two residual maps, the anomaly values indicate the evolving nature of the Karst cavities or loose sand lenses for some locations within the fenced zone in sector A1. It is clear from the colors and the contour lines that the anomaly values around SH3 and SH5 has increased and extended. Therefore, the risk is increased in this area while this area was not occupied. The information was sufficient for the government officials to decide on urgent treatment of this area.

Conclusions

Two microgravity surveys were conducted in a residential area affected by ground surface subsidence to detect underground Karst cavities. The time difference between the two surveys was fifteen years. The same method and professional experiences were used for the purpose of accurate comparison. The second survey detected the same general anomalies known from the first survey. Extension in size and amplitude of the anomalies were observed. The affected area is considered to be under an

increasing risk of sinkhole development, although no residential activities took place. Survey results have shown that the microgravity method is a consistent and reliable technique for detecting the existence, location, and extent of Karst cavities.

References

[1] Al-Rifaiy, I. (1990), *Quarterly Journal of Engineering Geology*, London, vol. 23, p. 337.
[2] Burdon, D., and Al Sharhan, A. (1968), *Journal of Hydrology*, vol. 6, p. 385.
[3] Mukhopadhyaya, A., Al-Sulaimi, J., Al-Awadi, E., and Al-Ruwaih, F. (1996), *Earth Science Review*, vol. 40, p. 259.
[4] Kamal, H., El-Hawary, M., Abdullah, W., Abduljaleel, A., Taha, M., Karam, H., Abdul-Salam, S., Al-Sanad, S., Abbas, M., Al-Shatti, F., Al-Elaj, M., Al-Arbied, A., and Al-Furaih, R. (2007), *Preparation of Tender Documents, Supervision of Implementation and Evaluation of Treatment Measures of the Pilot Area of Al-Dhahar-Phase II*, Final Report, KISR, Kuwait.

Section 9
Health Monitoring of Structures

20 Years of Experience with Structural Health Monitoring of Objects with CFRP Components

U. Meier, R. Brönnimann, P. Anderegg and G.P. Terrasi

Abstract The application of carbon fiber reinforced polymers (CFRP) in bridge construction was before 1991 unknown. Therefore the bridge owners did not want to rely only on the laboratory experiments made in the 1980ties. They asked for structural health monitoring. This was also in the interest of the involved R&D community. The used devices range from "old fashioned" demec gauges for off-line measurements to classical foil resistance strain gauges, self-sensing systems for unidirectional CFRP wires, and also sophisticated integrated fiber optical sensors with Bragg gratings. In the most important applications different independent systems were used in parallel. Twenty years are for devices which are exposed to outdoor weathering a fairly demanding time span. Therefore the surprisingly high reliability of most of these systems is a largely appreciated result. Applications on post-tensioned reinforced concrete bridges, stay cables, and pretensioned powerline pylons will be discussed.

Keywords CFRP-gauge • CFRP-tendon • Demac gauge • Fiber optical sensor • Long-term reliability

Motivation

During the 1980ties visions have been developed for long span lightweight bridges made of carbon fiber reinforced polymers (CFRP) [1]. Also since about that time corrosion on suspender-, main- and stay- steel cables of suspended bridges are seriously bothering bridge owners [2]. Additionally fatigue is a severe problem in the

U. Meier (✉) • R. Brönnimann • P. Anderegg • G.P. Terrasi
Empa, Swiss Federal Laboratories for Materials Science and Technology
CH 8600 Dübendorf, Switzerland
e-mail: urs.meier@empa.ch

cases of suspender- and stay- steel cables since such tendons are in use. In many cases also post- and pre-tensioning elements as well as classical reinforcing bars are concerned. Therefore some institutions in Europe, USA, Canada and Japan proposed the use of non-metallic tendons and reinforcing bars. Some few bridge owners and responsible authorities were willing to support the application of FRPs (Fiber Reinforced Polymers) however only under the condition that the long term behaviour of concerned structures was going to be monitored.

Case Studies

Mechanical strain gauge system

The mechanical strain gauge system, often called "demec gauge", was developed as a reliable and accurate way of taking strain measurements at different points on a structure using a single instrument. Empa scientists are using this kind of devices in the laboratories and on construction sites since about one hundred years. The system consists of an invar main beam with two conical locating points, one fixed and the other pivoting on a special knife edge. The points locate in pre-drilled stainless steel discs which are attached to the structure with adhesive. The movement of the pivoting point is to day measured by a photoelectric incremental length measuring device [3] which is attached to a base plate on the invar beam. Design is such that thermal movement within the instrument is negligible. It has a digital readout of 0.001 mm resolution and can be connected wireless to a lap top computer. The mechanical strain gauge system is ideal for use on many types of structure for strain measurement and crack monitoring. The gauge length in all cases discussed in the following sections is 200 mm.

Case Ibach Bridge   The Ibach Bridge was world's first bridge being post-strengthened with carbon fiber reinforced polymer (CFRP) strips. It is located near Lucerne/Switzerland. It crosses over the National Highway A2 (connecting Germany with Italy) and the Emme and Reuss rivers. The bridge is designed as a continuous beam structure with 7 spans and a total length of 228 m. In the span which crosses the six lanes of A2 a post-tensioning cable in a web was accidentally cut. The repair work was undertaken in the summer of 1991. Three CFRP strips with a total mass of 6.5 kg were bonded to the soffit of the bridge girder replacing the cut steel cable. In order to have obtained the same results with steel plates, 175 kg would have been necessary. Results of loading tests show that experimentally measured strains agree with the calculated values. For the loading test and the long term strain monitoring program 32 as called "demec points" (pre-drilled stainless steel discs) have been attached to the soffit of the bridge girder with adhesive. Eight gauge lengths were on concrete and the other eight pair wise in parallel on one of the three CFRP strips. During the last twenty years one "demec point" that means one of sixteen gauge

Fig. 1 View from underneath the Oberriet Bridge with the laterally post-strengthened concrete deck with CFRP strips (black)

Fig. 2 Measuring points for long term strain measurement on and beside the CFRP strips. Gauge length (arrow): 200 mm

lengths was lost due to adhesive failure of a point on concrete. The principle of interpretation of the results of the long term strain measurement is explained in the following section. Until now (twenty years) the CFRP post-strengthening technique performed perfectly.

Case Oberriet Bridge The two-lane bridge, build in 1963, crossing the border between Switzerland and Austria, links Oberriet to Meiningen. It crosses the river Rhine in 3 spans, 35 - 45 - 35 m as continuous steel/concrete composite girder (Fig. 1). Thorough investigations had shown that beside regular maintenance the concrete bridge deck was in need of transversal strengthening. This was obviously due to the fact that in 1963 the deck was designed for the standard 140 kN truck load. In 1996 this standard truck load was 280 kN for this type of bridge. A total of 160 CFRP strips, each 80 mm wide, 1.2 mm thick and 4.2 m long were applied to the soffit of the deck with a spacing of 75 cm. The project is described in more detail in [4]. A typical arrangement of "demec points" is shown in Fig. 2.
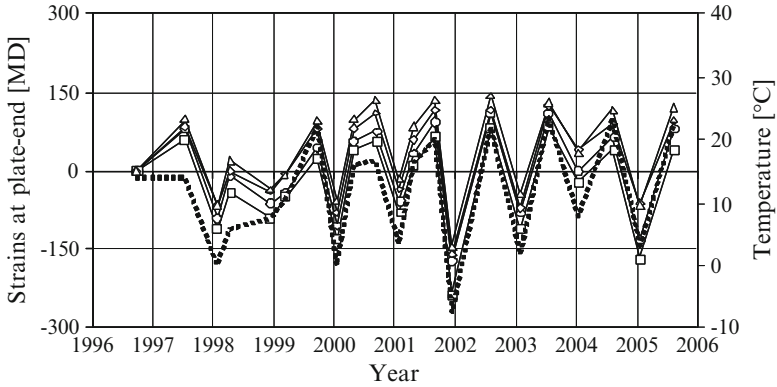
Fig. 3 Typical results of strain measurement over a period of 10 years. The dashed line corresponds to the temperature. The solid lines connecting circles, triangles and squares correspond to strains. Note: MD = micro strains; 1000 MD = 10/00

The change in strain as shown in Fig. 3 is due to change in temperature from summer to winter. As long as the strain lines proceed parallel there is perfect composite action between the concrete soffit and the CFRP strips. In general there is a good correspondence of the strain with the temperature as can be expected. These results are fully satisfactory.

Case Historic Covered Wooden Bridge in Sins This covered wooden bridge, constructed in 1807, crosses the Reuss River and consists of two spans, each of 30.8 m length. Problems arose with the crossbeams. Under the permissible load of 200 kN per vehicle the oak beams exhibited excessive deflections. To limit these deflections the beams subjected to the highest loads were successfully stiffened in 1992 with CFRP strips having a longitudinal modulus of elasticity of 300 GPa (Torayca M46 carbon fiber). Similar to Ibach- and Obberriet Bridge demec points have been installed on the CFRP strips and on the wooden crossbeams. In contrast to the RC Oberriet Bridge where the temperatures had a strong influence on the strains, the temperature has almost no influence on the strains in the wooden bridge. The results show that the strong influence factor is humidity. A good correspondence between the strains and humidity cycle can be observed (for details see [5]).

Conclusions for the Mechanical Strain Gauge System Within the three projects described above a total of 156 demec points have been installed during a time period of 14 to 20 years. Only one single point failed. Using the described configurations all possible kinds of drifts become for the applications discussed negligible. The long term reliability of the mechanical strain gauge system used to monitor the behaviour

of the externally bonded CFRP strips was instrumental to build up confidence into this novel CFRP strengthening technique.

Coin tapping technique to detect delaminations

ASTM D4580 is proposing among others an electro-mechanical sounding procedure with an electric powered tapping device for the detection of delaminations of concrete overlays on bridge decks. For CFRP strips externally bonded to concrete, wood or metals the coin tapping technique is by far sufficient. It involves striking the CFRP strip with a large coin. Areas where delaminations have occurred have an audible acoustic response that contains different frequencies than areas where the adhesion is perfect. This process is subjective, but it has been proved to be very effective and efficient since 1982. Coin tapping is also used extensively at present to detect the debonding of honeycomb structures in aircraft industry.

Replica technique

Beside the long term behaviour of the adherence of externally bonded CFRP strips also the outdoor weathering behaviour of the CFRP strips had been doubted. Therefore a surface monitoring was needed. When it is not possible to put specimens into the scanning electron microscope (SEM), the replica technique can be employed to examine surface features [6]. Replicas may be negative (single stage) or positive (double stage). The procedure is the following: wet a strip of cellulose acetate replicating tape with acetone and apply it with light pressure to the CFRP strip. After it dries completely, strip it from the substrate, turn the replica over and tape it to a glass slide. Afterwards sputter the replicas with gold and examine it by a SEM.

In the case of the CFRP strips of the Ibach Bridge this technique with negative replicas has been used. At the same time when the CFRP strips had been installed on Ibach Bridge in summer 1991 the same type of strips had been placed on inclined racks oriented at the sun. These racks are at an angle of 45 degrees in the southerly direction on a roof of the Empa laboratories in Dubendorf. Figure 4 (CFRP strip from the soffit of Ibach Bridge) shows the fiber-print on the outermost layer of EP matrix which has been pulled off by the replica technique. The visual and light microscopic inspection revealed not any damage due to outdoor weathering. In Fig. 5 with the same type of CFRP strip, however exposed to the sun, the situation is different. Contrary to Fig. 4 fibers and UV-degraded epoxy matrix have been pulled off.

Fig. 4 SEM image of negative replica of surface of CFRP strip after 18 years of outdoor-weathering under the soffit of the Ibach Bridge
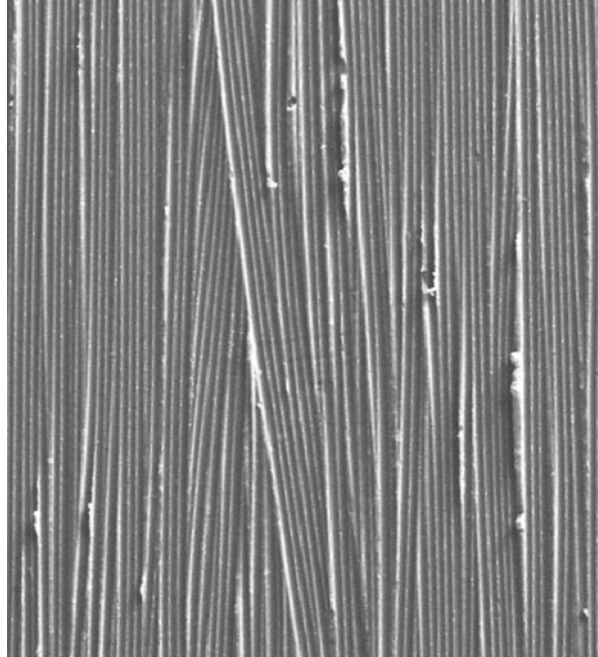
Fig. 5 SEM image of negative replica of surface of CFRP strip after 18 years of outdoor-weathering exposed to the sun on a inclined rack
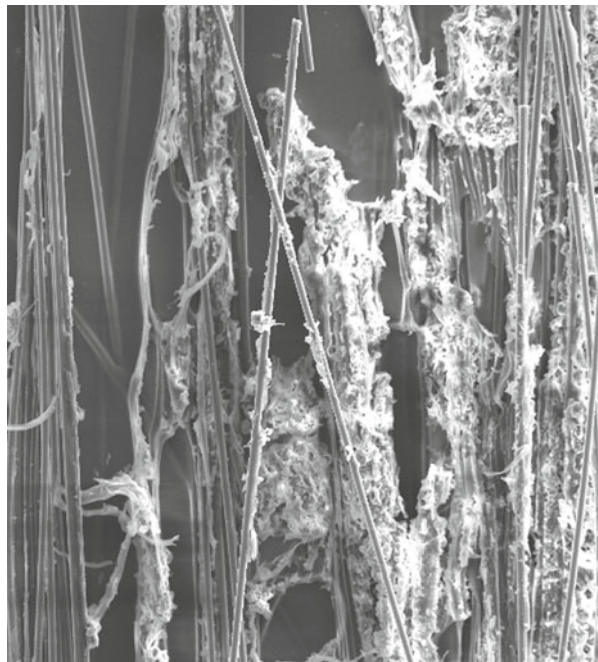
Fiber bragg grating (FBG) sensors and resistive Strain gauges (RSG)

Introduction   Resistive foil strain gauges (RSG) are state-of-the-art in experimental mechanics since more than fifty years. They have also been used fairly often in structural health monitoring. Fiber optic sensors are potentially very well suited for such applications. Measurable variables are mainly temperature, electrical current, strain and pressure. Optical fibers and sensors are often promoted to work in electromagnetic fields, at high temperature and humidity, or in aggressive chemical environment. Especially fiber Bragg grating (FBG) sensors have been demonstrated to operate in applications from airplanes to civil infrastructure like dams and bridges. The following sections are mainly based on [7].

CFRP cables   The key problem facing the application of CFRP cables and thus the impediment to their widespread use in the future is how to anchor them. The outstanding mechanical properties of CFRP wires are only valid in the longitudinal direction. The lateral properties including interlaminar shear are relatively poor. This makes it very difficult to anchor CFRP wire bundles and obtain the full static and fatigue strength. The Empa has been developing CFRP cables using a conical resin-cast termination. The evaluation of the casting material to fill the space between the cone of the termination and the CFRP wires was the key to the problem. This casting material, also called load transfer media (LTM) has to satisfy multiple requirements: (i) The load should be transferred without reduction of the high long time static and fatigue strength of the CFRP wires due to the connection. (ii) Galvanic corrosion between the CFRP wires and the steel cone of the termination must be avoided. It would harm the steel cone. Therefore the LTM must be an electrical insulator.

The conical shape inside the socket provides the necessary radial pressure to increase the interlaminar shear strength of the CFRP wires. The concept is demonstrated in the Fig. 6a, b using for this example a one-wire-system. If the LTM over the whole length of the sockets is a highly filled epoxy resin there will be a high shear stress concentration at the beginning of the termination on the surface of the CFRP wire (Fig. 6a). This shear peak causes pullout or tensile failure far below the strength of the CFRP wire. One could avoid this shear peak by the use of an unfilled soft resin. However this would cause creep and an early stress-rupture. The best design is shown in Fig. 6b. The LTM is a gradient material. At the load side of the termination the modulus of elasticity is low and continuously increases until reaching a maximum. The LTM is composed of aluminium oxide ceramic (Al_2O_3) granules with a typical diameter of 2 millimetres. All granules have the same size. To get a low modulus of the LTM the granules are coated with a thick layer of epoxy resin and cured before application (Fig. 7, left, top). Hence shrinkage can be avoided later in the socket. To obtain a medium modulus the granules are coated with a thin layer.

Figures 6a and b Stress
build-up in LTM
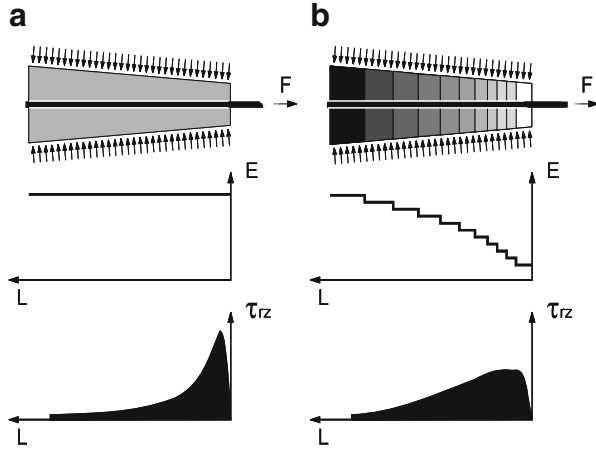
Fig. 7 Gradient anchorage
system for CFRP wires
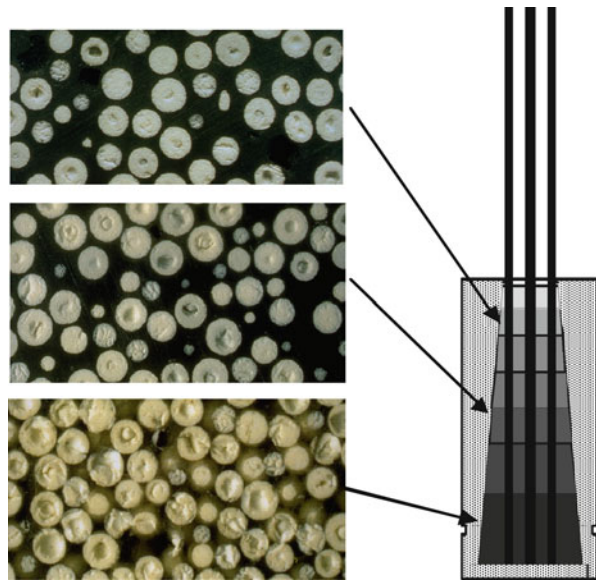
To reach a high modulus the granules are filled into the socket without any coating
(Fig. 7 left, bottom). With this method the modulus of the LTM can be designed
tailor-made. The holes between the granules are after all filled by vacuum-assisted
resin transfer molding with epoxy resin [8].
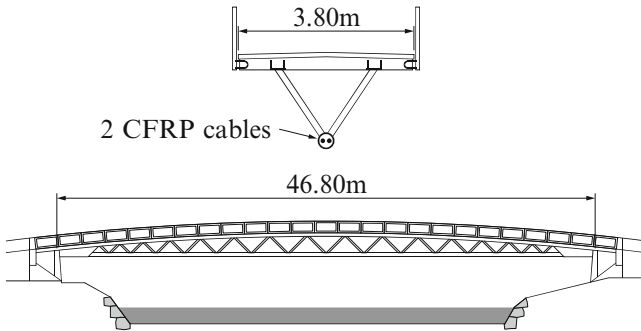
Fig. 8 Bridge over the River Kleine Emme with CFRP bottom chord and FOS

Fig. 9 SEM: CFRP wire
with a Bragg grating sensor,
Ø 100 μm
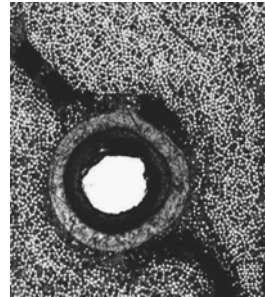
Bridge over the Kleine Emme The bicycle and pedestrian single span bridge over the River "Kleine Emme" near Lucerne (Fig. 8) was built in October 1998. The bridge deck is 3.8 m wide, 47 m long and is designed for the maximum load of emergency vehicles. The superstructure is a space truss of steel pipes in composite action with the steel rebar reinforced concrete deck. The bottom chord, a tube of 323-mm diameter, was post-tensioned with 2 CFRP cables inside the tube. Each cable was built up with 91 pultruded CFRP wires of 5-mm diameter. The post-tensioning force of each cable is 2.4 MN. Therefore the CFRP wires are loaded with a sustained stress of 1350 MPa corresponding to approximately 8000μm/m.

This project saw the first ever use of CFRP wires with integrated fiber optic Bragg gratings (FBGs) for this kind of application. They have been directly embedded during the pultrusion process in the middle of the CFRP wires (Fig. 9). This procedure allows placing FBGs not only in the free span of the wires but also in the zone of the anchor head with the critical strain decay [9]. The continuous monitoring and optimization of future production processes for high-grade CFRP wires will obviate the need for time-consuming final quality assurance checks. Where the projected application requires incorporation of sensors into the CFRP wires, these may

Fig. 10 Strain signals from
Bragg grating during
pultrusion of 5 mm CFRP
wires
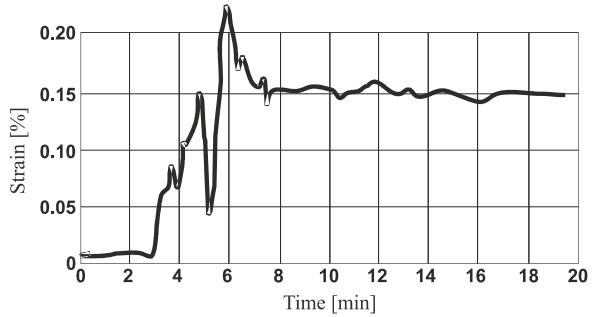
Fig. 11 Temperature signals
during pultrusion
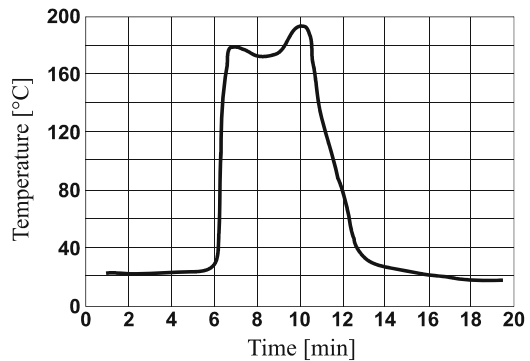
be integrated at the production stage for process monitoring. The strain (Fig. 10) and temperature (Fig. 11) signals from the sensors were monitored and analyzed already during production.

The two parallel-wire bundles were assembled in Dubendorf by Empa and BBR, wound onto 2.5-m-diameter reels and transported to the bridge site in Emmen. Each cable has four active CFRP wires and a dummy wire with several embedded FBGs. Since October 1998 these cables have tensioned the bottom chord of the new bridge over the River Kleine Emme. The sensors used for process monitoring during production now serve to monitor cable strain and thus the post-tensioning force in the bottom chord. The measured values spread with time inside a band of about 100μm/m. The temporal variation is mainly due to temperature changes. The sensor system showed early failures. Eight FBG failed out of a total number of 21, all of them in the free span (high strain) of the same cable. It is assumed that the failures can be attributed to break of FBGs and slippage of FBGs due to poor embedding, high fiber stress inside the CFRP wire and slippage due to voids and poor interface adhesion, respectively. These failures can be considered as early failures in the first four years. Such failures typically occur at the beginning of the so called bath-tube curve (failure rate versus time, with early failure period, constant failure rate, and wear out period). The steady state failure rate is assumed

Fig. 12 Strain inside gradient anchorage system
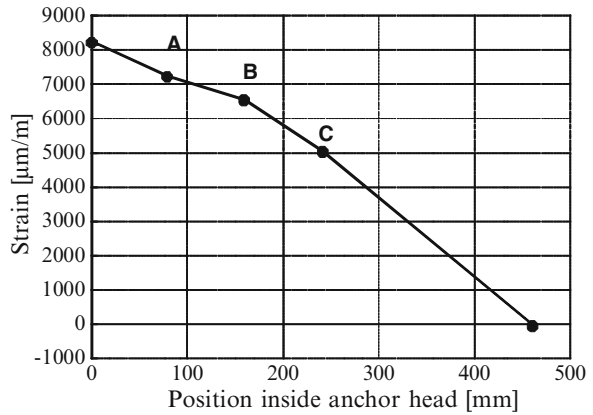
Fig. 13 Cable stayed Stork Bridge in Winterthur crossing 18 tracks of the Swiss Railways

to be much lower - at least one or two orders of magnitude. Fiber Bragg grating (FBG) sensors made it for the first time possible to monitor the strain along the CFRP wires within the gradient anchorage system (Fig. 12). None of those FBGs failed.

Stork Bridge   The Stork Bridge in Winterthur, erected in 1996, is situated over the 18 tracks of the railroad station in Winterthur and has a central A-frame tower supporting two approximately equal spans of 63 and 61 meters (Fig. 13). The cables converge at the tower top are rigidly anchored into a box anchorage at the apex of the A-frame. The superstructure has two principal longitudinal girders (HEM 550, Fe E 460) spaced at 8 m and supporting a reinforced concrete slab. At the anchorage points of the stay cables, there are cross girders (IPE 550, E 355). Longitudinal

Fig. 14 CFRP Cables
(Parallel Wire Bundles) with
241 wires and a load-bearing
capacity of 12 MN
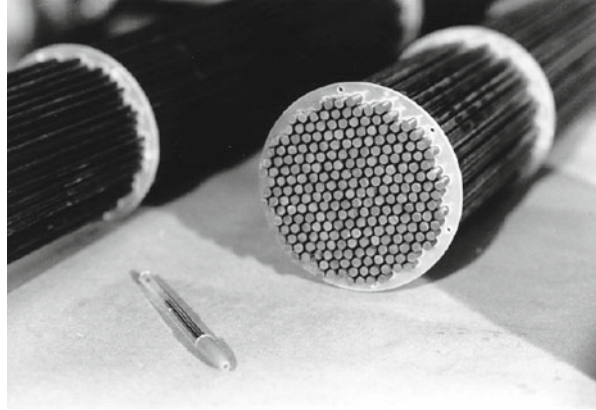
girders and concrete slabs are connected with shear bolts and work as composite girder system.

The CFRP cable type used for the Stork Bridge (Fig. 14) consists of 241 wires each with a diameter of 5 mm. This cable type was in the laboratory subjected to a load three times greater than the permissible load of the bridge for more than 10 million load cycles. This corresponds to a performance several times greater than that which can be expected during the life cycle of the bridge. The gradient anchorage system [8] is the same like for the Kleine Emme Bridge.

The strain of the CFRP cables was measured using sensing systems based on fiber optic Bragg gratings (FBGs) and electrical resistance strain gauges (RSGs) due to their high resolution, low drift, and high reliability [10]. The redundant use of sensors not only increases the reliability of the measurements but also allows drawing conclusions about the actual reliability and measurement uncertainty of the sensing systems. In conjunction with the applications, also appropriate sensor lifetime testing is performed.

In the application Stork Bridge FBGs were surface adhered to loaded wires and to dummy wires used for temperature compensation. Some FBGs were pre-strained on dummy wires (not loaded) to a level of 2500 μm/m to monitor creep due to delamination of the fiber coating or the epoxy adhesive. The working load on the regular CFRP wires is moderate and corresponds to an average strain of about 1200 μm/m. The sensor system is operational since April 1996 without any reliability problems. Important information about the reliability of the fiber optical monitoring data on the Stork Bridge can be derived from the FBGs on the so-called dummy wires. Four of the seven FBGs per cable are installed on not loaded wires for both, temperature compensation and creep monitoring. The temporal strain evolution of the pre-strained FBGs corresponds to that of the un-strained FBGs. In any case of slippage or creep the pre-strained FBGs would show a negative drift tendency. This result confirms the fault-free operation.

Fig. 15 Cross section of CFRP-cable with positions of FBG sensors
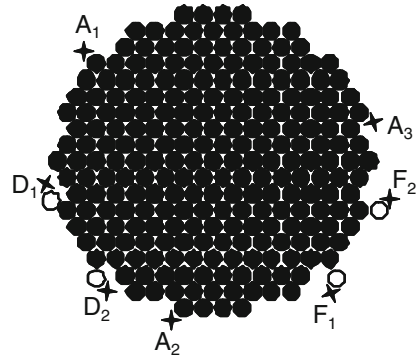
Fig. 16 Meander structure of sensor fiber accessible from both sides

● CFRP wire loaded

○ CFRP wire not loaded

✦ FBG
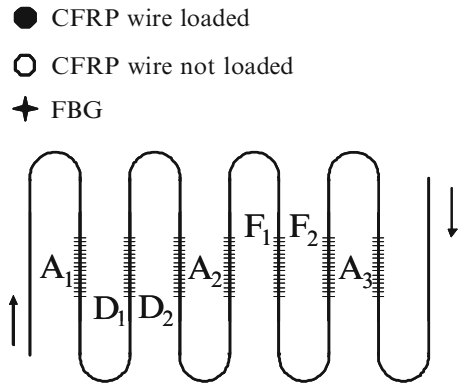
For each monitored cable a fiber with seven FBG was used as shown in Figs. 15 and 16. The fiber sensors were adhered with epoxy adhesive to the surfaces of the CFRP wires. Only the FBG A1, A2 and A3, are used to record strain of the cable. The others are attached to unstrained CFRP wires and serve for compensation and self monitoring as explained above. The FBG D1 and D2 are attached unstrained to the wires whereas F1 and F2 are adhered in a pre-strained state. Besides sporadic FBG measurements the cables are monitored continuously with resistive strain gauges (RSG). In Fig. 17 the comparison of FBG (filled markers) and RSG (open markers) measurements for a period of fourteen years are shown. The change of the measurements due to environmental conditions is synchronous. The difference between FBG and RSG measurements increases at a rate of about 4μm/m/year. The RSG measurements have a slightly higher resolution, however, the FBG have in this case better stability over time and the increasing difference can be attributed mainly to the RSG system [7]. In case of the Stork Bridge the best suited epoxy adhesive (out of selected samples) was identified by an accelerated aging test [11]. However,
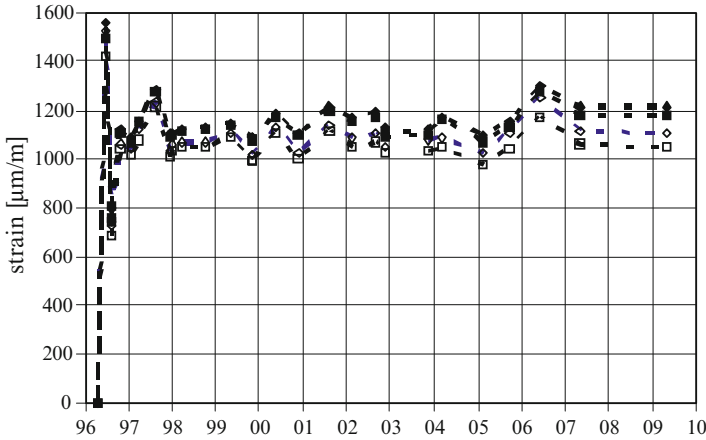
Fig. 17 Strain measured with FBG and RSG on the Stork Bridge
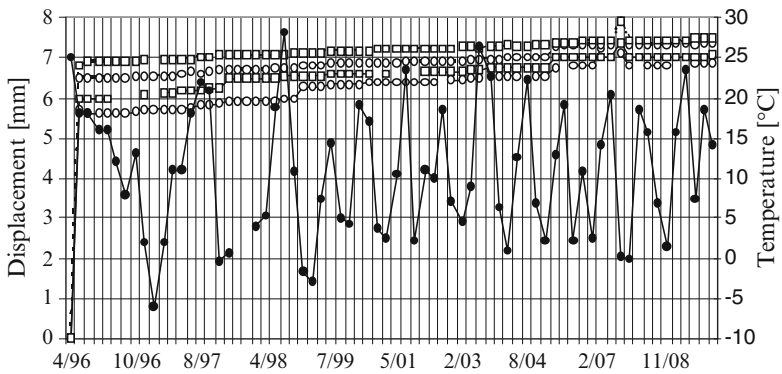
Fig. 18 Relative displacements (open markers) between the four anchorage cones of the terminations and the load transfer media (LTM) and temperature (filled markers) versus time

any documented field behaviour at that time was not known. Of 14 FBG 10 are strained and did not fail during 14 years. So far none of the FBG failed.

The most important measurements are those of the relative displacement between the anchorage cones of the terminations [8] and the load transfer media (LTM). As expected there is a relative displacement due to creep in function of time. However all displacement curves show clear signs of levelling out. These results (Fig. 18) are fully matching the earlier high expectations.

In the case of the Stork Bridge in 1996 a total of 22 RSGs have been installed. Four of them failed within 14 years. There is a high probability that three of the four RSGs failed due to a lightning strike.

Conclusions The two investigated examples of Kleine Emme and Stork Bridge have shown a large contrast in reliability parameters and therefore the suitability of such non-repairable systems for monitoring or safety purposes is questionable. No failure occurred in nearly 200 cumulated FBG operation years at the Stork Bridge while at the bridge over the Kleine Emme 8 of 21 FBG failed in 180 cumulated FBG operation years. This does not indicate an intrinsic problem of the fiber system because the same fiber and FGB were used at both locations. Main differences however exist in the details of implementation and the applied strain on the FBGs. In the case of Kleine Emme Bridge the FBGs were embedded into the wires within an experimental industrial pultrusion process. Pre-damage was possible. It was the first application of this kind. No practical experience was available. The strains are as high as ~8000 μm/m. In the case of the Stork Bridge the attachment of the FBGs was controlled, without pre-damage, with a highly established method similar like with conventional RSGs. The strains were below 3000 μm/m. Therefore, in order to achieve useful levels of reliability over decades, only well established and controllable methods for the attachment of the FBGs should be used and strain should be kept as low as feasible. As shown for the Stork Bridge, high reliability over decades can be achieved by a combination of hardware redundancy, redundancy in the measurement process, i.e. light access from both sides of the fiber system, and reliable components.

Self-sensing system for unidirectional CFRP wires

Already in 1969 single carbon fibres have been strained and their electrical resistance monitored continuously [12]. On straining, the resistance of the fibers increased. There was no detectable hysteresis when the strain was cycled and no permanent change in resistance. The fractional change in resistance of a fiber versus strain graphs showed a small initial curvature followed by a long straight region. It has been shown [13] that the crystallites in carbon fibers become more highly oriented when the fiber is strained. The graphite crystallite has marked electrical anisotropy, the resistivity parallel to the c axis being of the order of 10^3 times the resistivity perpendicular to the c axis; consequently any reorientation during straining will have a marked influence on the electrical resistance of fibres. Carbon fiber reinforced polymers are composed of the electric conductive carbon fibers and the matrix polymer, which is an insulator. Self-sensing systems have been reported utilizing the change of electric resistance of unidirectional CFRP laminates due to breakage of fibres during loading. The following sections discuss an application of the electrical resistivity for SHM on highly pre-stressed unidirectional CFRP wires.

The future for sustainable high performance precast concrete elements looks very bright. An important key technology might be the spun concrete pre-stressed
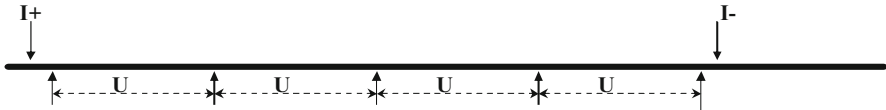
Fig. 19 Principle for the strain measurement on CFRP the CFRP wires

with wires of unidirectional CFRP. An example of this novel technique is the described precast spun concrete pylon for overhead power lines. One fundamental long-term aspect that had to be assessed for validating this novel technique is the loss of pre-stressing force in the CFRP wires due to creep of the concrete and potentially due to loss of bond between the CFRP wires and the surrounding high strength concrete. By the way: the stress relaxation of the CFRP wires themselves is negligible.

In 1994 Empa initiated a R&D project in co-operation with the SACAC Company, which is producing prefabricated concrete elements. One aim of this project was to investigate the structural principles of pre-stressed CFRP reinforcement and high strength concrete for the production of tubular bending elements like pylons [14]. A first full-scale field project was started in the year 2000. The Power Companies of North-Eastern Switzerland (NOK) decided to install a pylon of this type for the first time in a high-voltage power line [15]. A 27 m high pylon was produced for this project using an adapted pre-tensioning-spinning process [14]. The conical pylon had an external diameter of 847 mm at the bottom and 529 mm at the tip with an average wall thickness of 48 mm. The pylon weighed just 6'000 kg. This corresponds to a weight reduction of 40% in comparison to a traditional steel-reinforced concrete pylon for the same application. A centric overall initial pre-stressing of 1.0 MN was produced via 40 CFRP pre-stressing wires of 5.0 mm diameter. After initial pre-stress losses the following stresses were observed: 1'100 MPa on the CFRP wires, -7.5 MPa on high strength concrete at the foot and -13.8 MPa at the tip of the pylon. A rolltruded CFRP tape (0.5…1 mm thick, 13 mm wide) was helically wound around the pre-stressing tendons serving as shear reinforcement.

Figure 19 shows the measurement principle of the self-sensing system. A current is guided through the CFRP wires with contacts at the positions I+ and I-. Several electrical connections allow the measurement of the voltage drop along the wires. After painting epoxy-based silver paint on the locally polished wire contact surfaces, the silver paint dried and conventional lead wires of copper were placed on the electrodes. Silver paint was used here again for fixing the wires at the silver paste electrodes. After this, the electrodes were covered with epoxy resin and finally with a sealing compound to protect them. The system is equivalent to a four wire resistivity measurement. Low resistance values and high temperature dependence of the resistivity are main obstacles. The resistance per section is around 0.8Ω. The monitoring system is solar powered and therefore only an excitation current of 100 mA was used resulting in a voltage drop of only 80mV. A strain of 1 μm/m corresponds to a voltage change of about 0.2 μV. To improve resolution
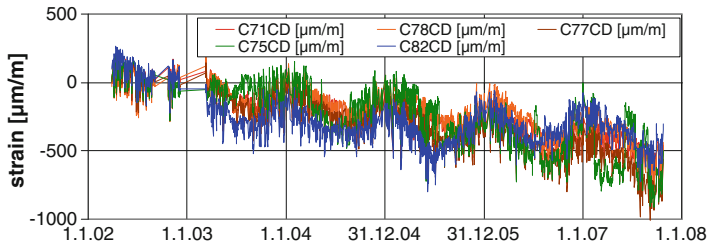
Fig. 20 Strain vs. time for 5 CFRP wires in the zone of the fixture of the pylon

and also to compensate thermo electrical voltages, the current was reversed continuously and long integration times were used and a high stability current source was constructed with a short time stability of a few ppm. Also the temperature has strong influence on the measurement. The temperature coefficient of resistivity is around -430ppm/K corresponding to an apparent strain of ca. -200μm/m/K. To compensate temperature effects a dummy tendon was installed inside the pylon. Another challenge was to assemble the tendons in a way the contacts could survive the harsh production process (centrifugal casting of the concrete) and that the contacts were not sheared off in operation.

The pylon is monitored remotely since its installation in 2001. It is an autonomous monitoring system built around a low power single board computer (SBC) running Linux. The sensing system comprises eight monitored CFRP wires each with four measurement sections (Fig. 19), nine temperature, one humidity, four conventional resistance strain gauges and means to check the battery voltage and the solar panel current. The main components for the measurement system are a 24 bit ADC (analog to digital converter), a precision current source and some sixty bistable, dual contact, low thermal voltage relays. The relays connect the various sources to the ADC and also the current source to one of the monitored CFRP wires. Measurements are performed at regular intervals and the results are stored. Via a cellular phone, it is possible not only to download the stored data, but also to completely control the Linux system via remote login. The system can also be programmed to send status reports and alerts by SMS either automatically or as a response. The complete system consumes less than 10 W and runs on a battery charged by a solar panel.

Each of the monitored CFRP wires of the pylon has four monitored sections of 0.8 m. In Fig. 20 the measurement results of five wires in the fixture section are given. The main problem is to make adequate temperature compensation because the compensation wire is located inside the pylon hanging in the in air and not being integrated in the wall, therefore having different temperatures. To alleviate the situation only measurements taken around four o'clock in the morning are shown when the temperature distribution is expected to be homogeneous. Considering seasonal changes, a decrease of the wire's pre-strain of about 500 μm/m over five years can be observed. Detailed information is presented in [16, 17].

Conclusions

The application of carbon fiber reinforced polymers (CFRP) in construction, especially in post-strengthening and rehabilitation is well known and mostly accepted today. Without successful performance monitoring on CFRP pilot projects with the means of the structural health monitoring this would not have been possible. As has been shown these means contain not only sophisticated tools like fiber optical sensors but also proven old fashioned devices similar to demec gauges.

References

[1] Meier, U. (1987), *Proc. Instn. Mech. Engrs. IMechE.*, vol. 201B2, p. 73–78.

[2] Hamilton, III H. R., Breen, J. E. and Al-Rashid Nasser, I. (1995), *Stay Cable Survey*. Report Phil M. Ferguson Structural Engineering Laboratory, Department of Civil Engineering, The University of Texas at Austin, USA.

[3] Nelle, G. (1985), Photoelectric Incremental Length or Angle Measuring Device, US Patent number 4, p. 519–707.

[4] Meier, U. (2000), *Appl. Comp. Mater.*, vol. 7, p. 75–94.

[5] Czaderski, C. and Meier U. (1969). In Proceedings 2nd International fib Congress, Naples, Italy, Vol. 2, p. 110–112.

[6] Ladd, M. W. (1973), The electron microscope handbook, Ladd Research Industries, p. 18–30.

[7] Brönnimann, R., Held, M. and Nellen, Ph. M. (2006), *Reliability, availability, and maintainability considerations for fiber optical sensor applications*, Proceedings of SPIE, the International Society for Optical Engineering, vol. 6167, p. 61671B.1-61671B.15.

[8] Meier, U., Kim, P. and Meier, H. (1998), "Anchorage device for high-performance fiber composite cables", US Patent 5713169.

[9] Brönnimann, R., Nellen, P. M., Sennhauser, U. (1999), *J. Intell. Mater. Syste. Struct.*, vol. 10, No. 4, p. 322–9.

[10] Anderegg, P., Brönnimann, R., Nellen, Ph.N., Sennhauser, U. (2002), *Reliable long-term monitoring of CFRP cables in bridges*, Proceedings of 1st International Workshop on Structural Health Monitoring of Innovative Civil Engi-neering Structures, ISIS, Winnipeg, Canada, 75–83.

[11] Sennhauser, U., Brönnimann, R., Nellen, P. M., 1996 Reliability modeling and testing of optical FBG sensors for strain measurements, SPIE 2839, p. 64–75.

[12] Conor, P. C. and Owston, C. N. (1969), *Nature*, vol. 223, p. 1146–1147.

[13] Curtis, G. J., Milne, J. M., and Reynolds, W. N. (1968), *Nature*, vol. 220, p. 1024.

[14] Terrasi, G. P. (1998), Mit Kohlenstoffasern vorgespannte Schleuderbeton-rohre. Ph.D. Thesis, Department of Civil Engineering, ETH Zurich.

[15] Terrasi, G. P, Bättig, G., Brönnimann, R. (2001), In: *University of Cambridge, FRPRCS 5. Non-metallic (FRP) reinforcement for concrete structures, Cambridge UK*, p. 1103–1112.

[16] Brönnimann, R. and Terrasi, G. P. (2009), Strain Monitoring by Resistance Measurement of Carbon Fiber Prestressing Tendons in Filigree High Performance Concrete Elements, In: *4th International Conference on Structural Health Monitoring on Intelligent Infrastructure (SHMII-4)*, p. 57.

[17] Terrasi, G. P., Brönnimann, R. and Bättig, G. (2011), CFRP Tendon Prestress Monitoring by Resistance Measurement in a Spun Concrete Powerline Pylon, in: *First Middle East Conference on Smart Monitoring, Assessment and Rehabilitation of Civil Structures, SMAR American University in Dubai (AUD)*, in print.

Review of a Null Space Strategy for Damage Localization

D. Bernal

Abstract The damage localization strategy reviewed here rests on the fact that stress fields that can be computed from the kernel of changes in transfer matrices are identically zero over the subset of the domain where damage (reductions in stiffness) have taken place. Damage can be located, therefore, by extracting these loads and inspecting the associated stress fields. In structures identified from output signals it is not possible to compute changes in transfer matrices but the methodology can be used by replacing the transfer matrix change with a surrogate that shares the same null space. The paper reviews the essential theory and discusses the issues that arise when the strategy is applied in practice.

Keywords Damage localization • Damage Locating Vector • DDLV • DLV • System identification

Introduction

A model updating approach to damage characterization proves difficult because the free parameter space needed given all the possible damage scenarios is usually large and the formulation proves ill-conditioned. The key to resolving this difficulty resides in decoupling damage localization from quantification and finding ways to solve the localization problem without the need to explicitly select a free parameter space. The null space strategy reviewed in this paper has been developed in a sequence of papers over the last decade [1-5] and is based on the idea that damage

D. Bernal (✉)
Civil and Environmental Engineering Department, Center for Digital Signal Processing, Northeastern University, Boston 02115
e-mail: bernal@neu.edu

can be located by inspecting stress fields induced by loads for which the response is unaffected by the damage; a key result being a proof that when equal response is realized the stress field is identically zero over the damaged region. Stripped to the bone the methodology contains two parts: 1) extraction of the appropriate loads and 2) calculation of the associated stress fields. For the strategy to be meaningful it is necessary that the excitations used to locate the damage be obtained in a data-driven fashion, which implies that only excitations defined in sensor coordinates are of interest. The damage locating excitations have been designated as Damage Locating Vectors (DLV), when they are static, and dynamic DLVs, or dDLVs, otherwise.

Damage Locating Vector Approach (DLV)

Let the structure have m sensors and the flexibility matrix defined in the coordinate of these sensors for the R (reference) and the D (damaged) states be F_R and F_D. Assume that there is a load distribution ℓ for which displacements at the measured coordinates are identical in the R and the D states, namely

$$F_R \ell = \Delta \tag{1}$$

$$F_D \ell = \Delta \tag{2}$$

Subtracting eq.2 from eq.1 one has

$$\left(F_D - F_R\right)\ell = DF \cdot \ell = 0 \tag{3}$$

which shows that the necessary and sufficient condition for the loads ℓ to exist is that the change in the flexibility matrix be rank deficient.

Theorem: Provided that the changes between the states R and the D are all reductions (or increases) in stiffness the stress field due to ℓ is identically zero over the damaged part of the domain.

Proof: Assume the domain is divided into two parts Ω_U and Ω_D in such a way that in the damaged state all the damage is contained within Ω_D. Let the stress field due to the vector ℓ acting on the reference state over these two regions be σ_1 and σ_2. Assuming linear behavior the stress and the strain tensors are related by some matrix E and one can write

$$U_R = \frac{1}{2}\int_{\Omega_U} \varepsilon_1^T E_1 \varepsilon_1 dV + \frac{1}{2}\int_{\Omega_D} \varepsilon_2^T E_2 \varepsilon_2 dV \tag{4}$$

where U_R is the strain energy and typically $E_1 = E_2$ in the R state; needless to say, the matrix E can be a function of the spatial coordinates. Applying the principle of virtual work and restricting the virtual displacements to variations that are zero at the location of the sensors (where the loads ℓ are acting) one has

$$\delta(U) = 0 \tag{5}$$

Namely, at equilibrium the strain energy is stationary with respect to any variation in the strain field that integrates to zero at the loaded points. Recognizing that the strain energy in the R and D states are the same (since the loaded points move identically) and that the stationary point is a minimum, one can write

$$\frac{1}{2}\int_{\Omega_U}\varepsilon_1^T E_1 \varepsilon_1 dV + \frac{1}{2}\int_{\Omega_D}\varepsilon_2^T E_{2d}\varepsilon_2 dV \geq \frac{1}{2}\int_{\Omega_U}\varepsilon_1^T E_1\varepsilon_1 dV + \frac{1}{2}\int_{\Omega_D}\varepsilon_2^T E_2 \varepsilon_2 dV \tag{6}$$

where the subscript d in the strain to stress E_2 of the left side indicates that these are the values in the damaged condition. From eq.6 it follows that

$$\int_{\Omega_D}\varepsilon_2^T E_{2d}\varepsilon_2 dV \geq \int_{\Omega_D}\varepsilon_2^T E_2\varepsilon_2 dV \tag{7}$$

Accepting that the damage can be parameterized as

$$E_{2d} = \alpha_{x,y,z} E_2 \tag{8}$$

where $\alpha_{x,y,z}$ is a scalar function of spatial position one has

$$\int_{\Omega_D}\alpha_{x,y,z}\varepsilon_2^T E_2\varepsilon_2 dV \geq \int_{\Omega_D}\varepsilon_2^T E_2\varepsilon_2 dV \tag{9}$$

which can only be satisfied if $\alpha > 1$ at some points (since the expressions are quadratic forms) of if $\varepsilon_2 = 0$, in which case both sides equal zero. Since we operate under the premise that damage does not increase the stiffness one conclude that the only alternative is that for the vector ℓ the strain field is zero over Ω_D.

Resolution

Let there be a grid of points placed throughout the structure so instead of a continuous stress field we can refer to stresses at n points. Let σ_j be the stress at the jth point (potentially multi-valued) and let b_1 b_2,.. b_m be the collection of values due to unit loads acting at coordinates, 1,2,..m. Since the structure is linear for any given loading in sensor coordinates, p, the stresses are

$$\begin{bmatrix} b_1 & . & b_r \\ & & \\ & & \\ & & \\ & & \end{bmatrix}\left\{ p \right\} = \left\{ \begin{matrix} \sigma_1 \\ \sigma_2 \\ . \\ . \\ \sigma_n \end{matrix} \right\} \tag{10}$$

Let the rows in eq.10 be organized such that the points affected by the damage appear at the top of the *rhs* vector. If the change in the flexibility matrix proves rank deficient there is at least one vector *p* for which

$$\begin{bmatrix} b_T \\ b_B \end{bmatrix} \{\ell\} = \begin{Bmatrix} 0 \\ \overline{\sigma}_2 \end{Bmatrix} \tag{11}$$

where we've taken $p = \ell$ and $\overline{\sigma}_2$ is the vector that has all the undamaged points in the discretization. From the top partition of eq.11 one can see that ℓ is in the null of b_T and from the bottom partition one has

$$\overline{\sigma}_2 = b_B \ell \tag{12}$$

Any region of the structure where the entries in $\overline{\sigma}_2$ are zero cannot be theoretically separated from the actual damage by changes in flexibility. Examination shows that the spatial resolution limit is not dependent on the structural discretization but it may depend on the sensor arrangement.

Damage parameterization and rank deficiency

To illustrate how parameterization of the damage (in simulations) can affect results consider a simple beam with 4 equally spaced sensors in the transverse direction as depicted in Fig.1a. Let there be two damage locations, centered at 29.5% and 69.5% of the length from the left support, each one having a length of 1% of the total span. If the damage is modeled as distributed there are no perfect DLVs because the change in the flexibility is full rank. The singular values of DF, normalized to a maximum of one, prove to {1, 0.077, 0.00002, 0.00001}. One notes, however, that the last two singular values are very small, suggesting that there are two "near" DLV vectors. This is, of course, the case since modeling the damage as the appearance of a spring makes the change in flexibility rank two and there are two perfect DLV's. The moment diagram for the last two singular vectors treated as loads (in the distributed damage case) are shown in Fig.1b, c as can be seen, the inflection points are located at the center of the damaged locations.

Implementation

Since one cannot get exact changes in flexibility from data and there is generally model error in the computation of the stress fields the DLV localization has to be carried out using finite thresholds. Practical implementation requires the following decisions: 1) which singular values are small enough to treat the associated vectors as DLVs, 2) how should stress fields from multiple DLVs be combined and 3) when
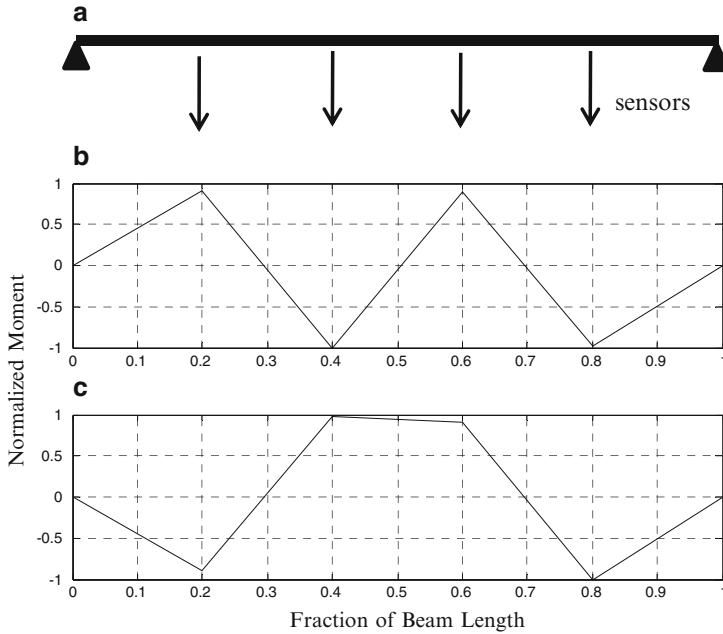
Fig. 1 DLV localization of damage – damage is 10% reduction of EI on two sections of 1% of the beam length centered at 0.295 and 0.695; (**a**) location of sensors, (**b**) from 3ʳᵈ singular vector (**c**) from 4ᵗʰ singular vector

is a stress sufficiently low to be treated as effectively zero. The procedure developed in [1] can be summarized as follows:

1. For each one of the *rhs* singular vector of DF compute the stress field. Convert the stresses over each finite element into a characterizing stress. The characterizing stress should be such that a zero value implies zero strain energy in the element and is otherwise positive. Designate the maximum characterizing stress for load vector j as c_j. Normalize the characterizing stress distribution to a maximum of unity and designate this as the normalized stress index *nsi*.

2. For each of the *rhs* singular vectors compute the product $c_j \sqrt{s_j}$. Compute the normalized value of the previous product by dividing each value by the largest value for any singular vector and designate this normalize index as *svn*, namely

$$svn_j = \sqrt{\frac{s_j c_j^2}{s_q c_q^2}} \qquad (13)$$

where the subscript q in the denominator refers to the largest value of the product. Potential DLV vectors are those with $svn \leq 0.2$.

3. Compute the weighted stress index for every element as follows

$$\text{WSI} = \frac{\sum_{i=1}^{ndlv} \dfrac{\{nsi\}_i}{\overline{svn}_i}}{ndlv} \tag{14}$$

where $\overline{svn} = \max(svn, 0.015)$ and *ndlv* is the number of DLV vectors. Take the set of potentially damaged elements as those for which WSI <1.

Dynamic Damage Locating Vector Approach (dDLV)

Writing the input output relations in the Laplace domain for the R and the D states and postulating that the loading leads to identical response, one gets, after subtracting

$$\begin{bmatrix} \Delta G_{m,r} & \Delta G_{m,\bar{r}} \\ \Delta G_{\bar{m},r} & \Delta G_{\bar{m},\bar{r}} \end{bmatrix} \begin{Bmatrix} \ell(s) \\ 0 \end{Bmatrix} = \begin{Bmatrix} 0 \\ 0 \end{Bmatrix} \tag{15}$$

where the columns are re-order so the coordinates with inputs appear first in the input vector. The notation used in eq.15 is *m* and *r* for measured output and input coordinates and the same variables with a supra-bar for the unmeasured partitions. It is shown in [2] that if there is at least one collocation the dDLV vectors (in the Laplace domain) can be computed from the null space of $\Delta G_{m,r}$ (which is available from the identification). Time domain dDLVs are computationally expensive but their evaluation can be avoided by operating entirely in the Laplace domain. In particular, a dDLV vector in the s-domain can be applied to the structure (in the s-domain) and the resulting complex stress fields used to determine the position of the damage. Specifically, with the measured coordinates appearing first it can be shown that a static load that induces a stress field that is zero over the damage is

$$L(s) = K \cdot \left[Ms^2 + Cs + K \right]^{-1} \begin{Bmatrix} \ell(s) \\ 0 \end{Bmatrix} \tag{16}$$

Implementation

The approach taken in [2] to decide on the existence of dDLVs is to make the decision on the basis of whether there are DLVs at s = 0. In other words, if the check for the existence of DLVs is positive then it is assumed that there are dDLVs. The approach is theoretically consistent because when the flexibility is rank deficient

there is a guarantee that the change in the transfer matrix is also rank deficient (provided that there are only changes in stiffness).

Stochastic DLV Approach (SDLV)

Due to space limitations we outline only the extension of the DLV approach to the stochastic case, i.e, the SDLV approach. The extension of the dDLV scheme to the SdDLV approach follows essentially the same logic and can be found in [3]. The input to state and state to output description of a linear time invariant system can be written as

$$\dot{x}(t) = A_c x(t) + B_c u(t) \tag{17}$$

$$y(t) = C_c x(t) + D_c u(t) \tag{18}$$

where the matrices $\{A_c, B_c, C_c \text{ and } D_c\}$ are the transition, the input to state, state to output and direct transmission matrices. It can be shown that the flexibility matrix (at the sensors) can be expressed as a function of the realization matrices and the result is

$$F = -C_c A_c^{-(1+p)} B_c \tag{19}$$

where $p = 0, 1$ or 2 when the measured output is displacement, velocity or acceleration, respectively. When a system is identified from operational loads the matrices B_c and D_c are undetermined so the flexibility at the sensors cannot be computed using eq.19. The key to the extension developed in [3] lies in the fact that the B_c matrix associated with a collocated input distribution can be shown to satisfy

$$HB_c = LD_c \tag{20}$$

where

$$H = \begin{bmatrix} C_c A_c^{1-p} \\ C_c A_c^{-p} \end{bmatrix} B_c \quad \text{and} \quad L = \begin{bmatrix} I \\ 0 \end{bmatrix} \tag{21a,b}$$

from where

$$B_c = H^{-*} L D_c + \text{Null}(H).v \tag{22}$$

where v is an arbitrary vector of appropriate dimension and the -* stands for pseudo-inversion. Assuming that the identified order is restricted to no more than twice the number of sensors the matrix H is expected to be full rank and the second term on the rhs of eq.22 vanishes. Accepting the truncation imposed by the limit on the order one gets, from eqs.19 and 22

$$F \cong RD_c \tag{23}$$

where

$$R = -C_c A_c^{1-p} H^{-*} L \tag{24}$$

therefore,

$$DF \cong (R_D - R_R)D_{cR} + R_D \delta D_c \tag{25}$$

In eq.25 δD_c is the change in the direct transmission from the reference to the damaged state. This matrix is identically zero when there is no truncation because the D_c matrix does not depend on the stiffness but it is not exactly zero in the truncated case. In any case, it is reasonable to expect that δD_c is small and neglecting it one gets

$$DF \cong \Delta R \cdot D_{cR} \tag{26}$$

and since DF and D_{cR} are symmetric one has

$$DF \cong D_{cR} \cdot \Delta R^T \tag{27}$$

which shows, since D_{cR} is full rank, that the null space of DF and ΔR^T coincide. It is possible, therefore, to replace the change in flexibility with the transpose of the change in R.

SDLV Approach Using Normal Mode Data

The expressions based on the state space formulation can be transformed to the conventional modal domain without difficulty. All that is required is to replace the matrices A and C with

$$A = \begin{bmatrix} \omega i & 0 \\ 0 & -\omega i \end{bmatrix} \tag{28}$$

$$C = [\psi\ \psi] \tag{29}$$

where ψ are the arbitrarily normalized modes at whatever sensor locations are available and ω are the undamped frequencies in the same order.

Example

Consider a uniform 3 story shear building having masses equal to unity and interstory stiffness equal to 100 in some consistent set of units. There are two sensors measuring acceleration in levels #2 and #3. Damage is simulated as 10% loss of

stiffness in the stiffness of level#1. We use this simple academic example to illustrate the SDLV with the normal mode equations. To consider truncation we assume that the third vibration mode could not be identified. The arbitrarily scaled identified modes and frequencies are:

$$\psi_R = \begin{bmatrix} 1 & -0.555 \\ 1.247 & 1 \end{bmatrix} \quad \omega_R = \{4.45 \quad 12.47\}$$

$$\psi_D = \begin{bmatrix} 1 & -0.504 \\ 1.230 & 1.007 \end{bmatrix} \quad \omega_D = \{4.32 \quad 12.25\}$$

Substituting into eqs.28 and 29 and the results into eq.24 one finds that the difference in the R matrices is

$$\Delta R = 10^{-3} \begin{bmatrix} 3.233 & 0.0678 \\ 3.233 & 0.0678 \end{bmatrix}$$

The singular value decomposition of the transpose of ΔR is found to have a small singular value having the associated singular vector $\ell = \{-0.707 \quad 0.707\}^T$ which leads to the characterizing stress (normalized story shears) $nsi = \{1 \quad 0 \quad 0\}^T$ indicating that there is no damage on the 3rd level and there is some change in either level #1 or #2 or both. Further discrimination with changes in flexibility is, of course, not possible.

Concluding Comments

The main source of difficulty in the null space localization strategy stems from limitations on the accuracy with which the changes in flexibility or transfer matrices can be computed from data. Success demands that there be a null space in the (albeit unknown) exact problem and on whether the "quasi null space" of the truncated change has a strong projection in it. The previous assertion suggests that damage is more easily localized when the true null space is multidimensional because in this case it is "easier" for the vector from the approximate change (in flexibility or transfer matrix) to have a strong projection. The most recent contribution to the null space localization scheme, not described in this paper, considers the case where the change in the transfer matrix proves to be full rank so the standard dDLV approach cannot be used. The idea explored is the fact that rank deficiency is realized at the transmission zeros and that the kernel at these points often contains localization information. The details of this last contribution can be found in [5].

References

[1] Bernal D. (2002). "Load vectors for damage localization", *J. Eng. Mech. ASCE*, Vol.128, n. 1, p. 7–14.

[2] Bernal D. (2007). "Localization of damage from the null space of changes in the transfer matrix", *J. Amer. Inst. Aerosp. Aeronaut. (AIAA)*, Vol.45, n. 2, p. 374–381.

[3] Bernal D. (2006). "Flexibility-based damage localization from stochastic realization results", *J. Eng. Mech. ASCE*, Vol.132, p. 651–658.

[4] Bernal D. (2010). "Load vectors for damage localization in systems identified from operational loads", *J. Eng. Mech. ASCE*, Vol.136, n. 1, p. 31–39.

[5] Bernal D. (2009). "Damage localization from transmission zeros of delta systems", *J. Eng. Mech. ASCE*, Vol.135, n. 2, p. 93–99.

Embedded NDT with Piezoelectric Wafer Active Sensors

V. Giurgiutiu

Abstract Piezoelectric wafer active sensors (PWAS) are lightweight and inexpensive enablers for a large class of embedded NDT applications such as structural health monitoring (SHM). After a brief review of PWAS physical principles and basic modeling, the paper considers several ultrasonics SHM methods such as: (a) embedded guided-wave ultrasonics, i.e., pitch-catch, pulse-echo, phased arrays; (b) high-frequency modal sensing, i.e., the electro-mechanical (E/M) impedance method; (c) passive detection, i.e., acoustic emission and impact detection. Recent developments in PWAS phased arrays are presented and discussed. The paper ends with conclusions and suggestions for further work to achieve the full potential of this promising new technology.

Keywords Embedded guided-wave ultrasonics • Modal sensing • Passive detection • PWAS • SHM

Introduction

The mounting costs of maintaining our aging infrastructure and the associated safety issues are a growing national concern. Over 27% of our nation's bridges are structurally deficient or functionally obsolete [1]. Deadly accidents due to deficient transportation infrastructure are still marring our everyday life. In response to these growing concerns, structural health monitoring (SHM) sets forth to determine the health of a structure by monitoring a set of structural sensors and assessing the remaining useful life and the need for structural actions. Built-in SHM system capable of detecting

V. Giurgiutiu (✉)
Univ. of South Carolina, Columbia, SC 29208, USA
e-mail: victorg@sc.edu

and quantifying damage would increase the operational safety and reliability, would conceivably reduce the number of unscheduled repairs, and would bring down maintenance cost. SHM sensors should be able to actively monitor the structure and find out its state of health, its remaining life, and the effective margin of safety. Two SHM sensing principles can be considered: (a) passive SHM sensing, in which the damage of the structure is inferred from the changes in load and strain distributions measured by the sensors; and (b) active SHM sensing, in which the damage is sensed by active interrogation of the structure with elastic waves. The active SHM technology is currently applied to aircraft, land vehicles, ships, and civil engineering structures.

A large number of nondestructive evaluation (NDE), nondestructive testing (NDT) and nondestructive inspection (NDI) techniques for identifying local damage and detect incipient failure in critical structures exist. Among them, ultrasonic inspection is well established and has been used in the engineering community for several decades [2][3]. Ultrasonic NDE methods rely on elastic wave propagation, reflection, and scatter within the material. They try to identify the wavefield disturbances due to local damage and flaws. Ultrasonic testing involves one or more of the following measurements: time of flight (wave transit or delay), path length, frequency, phase angle, amplitude, acoustic impedance, angle of wave deflection (reflection and refraction), etc.

Conventional ultrasonic methods include the pulse-echo, the pitch-catch (or pulse-transmission), and the pulse-resonance techniques. A piezoelectric ultrasonic probe placed on the structural surface induces ultrasonic waves in the material. Contact between the transducer and the structure is obtained by using special coupling gels. Depending on the incidence of the transducer with respect to the structural surface, the waves created in the structures may be pressure (P), shear (S), or a combination of the two. P-waves are best suited for through-the-thickness detection and for the inspection of massive parts. They are very effective in detecting anomalies along the sound path. In the pulse-echo method, defects are detected in the form of additional echoes. In the pitch-catch method, wave dispersion and attenuation due to diffused damage in the material is used as a flaw indicator. Multi-element phased-array transducers, which can steer the ultrasonic beam electronically, have found extensive use in the inspection of massive parts and in medical ultrasound.

For the inspection of thin-wall structures, such as sheet-metal constructions, airframes, large containers, pipes, or tubes, an alternate inspection method utilizing guided waves (e.g., Rayleigh waves, Lamb waves, Love waves, Stonley waves, etc.) may be more appropriate. Guided waves travel long distances in thin-wall shell structures or 1-D members such as rails, rods, cables, etc. These waves can be generated using conventional ultrasonic transducers and wedge couplers, provided the angle of the coupler is sufficiently large to trigger mode conversion. Alternatively, they can be generated by comb transducers. Guided waves are being used to detect cracks, inclusions, and disbonds in thin-wall metallic and composite structures. Lamb waves are appropriate for thin plate and shell structures, while Rayleigh waves are more useful for the detection of surface defects.

Active SHM resembles ultrasonic NDE because it utilizes ultrasonic waves which interact with the structure and detect damage in much the same way that conventional ultrasonic NDE does. One active SHM method employs piezoelectric wafer active sensors (PWAS), which send and receive ultrasonic Lamb waves and determine the presence of cracks, delaminations, disbonds, and corrosion. Two approaches are being considered: (a) traveling waves; and (b) standing waves. For this reason, active SHM can be also viewed as embedded NDE, i.e., an NDE method that utilizes embedded transducers that are permanently attached to the structure and can be interrogated on demand. Embedded nondestructive evaluation (e-NDE) is an emerging technology that will allow the transition of the conventional ultrasonic NDE methods to embedded applications in active SHM systems [4]. Viewing active SHM from the embedded NDE viewpoint allows one to draw on the experience already developed in the NDE field and to transition it into SHM applications.

Piezoelectric Wafer Active Sensors

Piezoelectric wafer active sensors (PWAS) couple the electrical and mechanical effects (mechanical strain, S_{ij}, mechanical stress, T_{kl}, electrical field, E_k, and electrical displacement, D_j) through the tensorial piezoelectric equations

$$S_{ij} = s_{ijkl}^E T_{kl} + d_{kij} E_k$$
$$D_j = d_{jkl} T_{kl} + \varepsilon_{jk}^T E_k$$

(1)

where, s_{ijkl}^E is the mechanical compliance of the material measured at zero electric field ($E = 0$), ε_{jk}^T is the dielectric permittivity measured at zero mechanical stress ($T = 0$), and d_{kij} represents the piezoelectric coupling effect. PWAS utilize the d_{31} coupling between in-plane strains, S_1, S_2, and transverse electric field, E_3. PWAS are transducers are different from conventional ultrasonic transducers because [5]:

1. PWAS are firmly coupled with the structure through an adhesive bonding, whereas conventional ultrasonic transducers are weakly coupled through gel, water, or air.
2. PWAS are **non-resonant devices** that can be tuned selectively into several guided-wave modes, whereas conventional ultrasonic transducers are single-resonance devices.
3. Because PWAS are small, lightweight, and inexpensive they can be deployed in large quantities on the structure, which is not practical with conventional ultrasonic transducers, which are relatively bulky and expensive.

By using Lamb waves in a thin-wall structure, one can detect structural anomaly, i.e., cracks, corrosions, delaminations, and other damage.
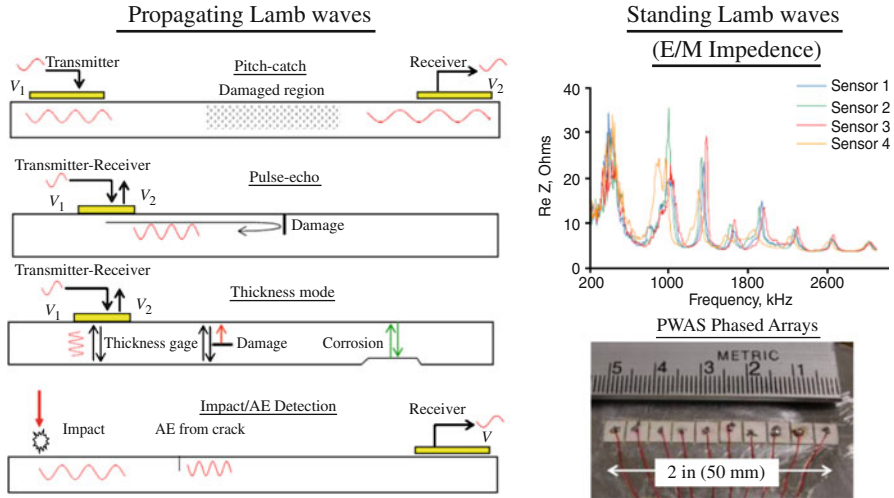
Fig. 1 PWAS used for embedded NDE include propagating Lamb waves, standing Lamb waves (electromechanical impedance) and phased arrays [4]

PWAS transducers act as both transmitters and receivers of Lamb waves traveling through the structure (*Fig.* 1). Upon excitation with an electric signal, the PWAS transmitter generates Lamb waves in a thin-wall structure. The generated Lamb waves travel through the structure and are reflected or diffracted by the structural boundaries, discontinuities, and damage. The reflected or diffracted waves arrive at the PWAS receiver where they are transformed into electric signals. PWAS transducers can serve several purposes [5]:

(a) high-bandwidth strain sensors;
(b) high-bandwidth wave exciters and receivers;
(c) resonators;
(d) embedded modal sensors using the electromechanical (E/M) impedance

By application types, PWAS transducers can be used for (i) active sensing of far-field damage using pulse-echo, pitch-catch, and phased-array methods, (ii) active sensing of near-field damage using high-frequency E/M impedance method and thickness-gage mode, and (iii) passive sensing of damage-generating events through detection of low-velocity impacts and acoustic emission at the tip of advancing cracks [4]. The main advantage of PWAS over conventional ultrasonic probes is in their small size, lightweight, low profile, and low cost. In spite of their small size, PWAS are able to replicate many of the functions performed by conventional ultrasonic probes.

An example of damage detection using PWAS phased arrays is given in *Fig.* 2, which shows that broadside and offside cracks can be independently identified with scanning beams emitting from a central location. The experimental setup consisted
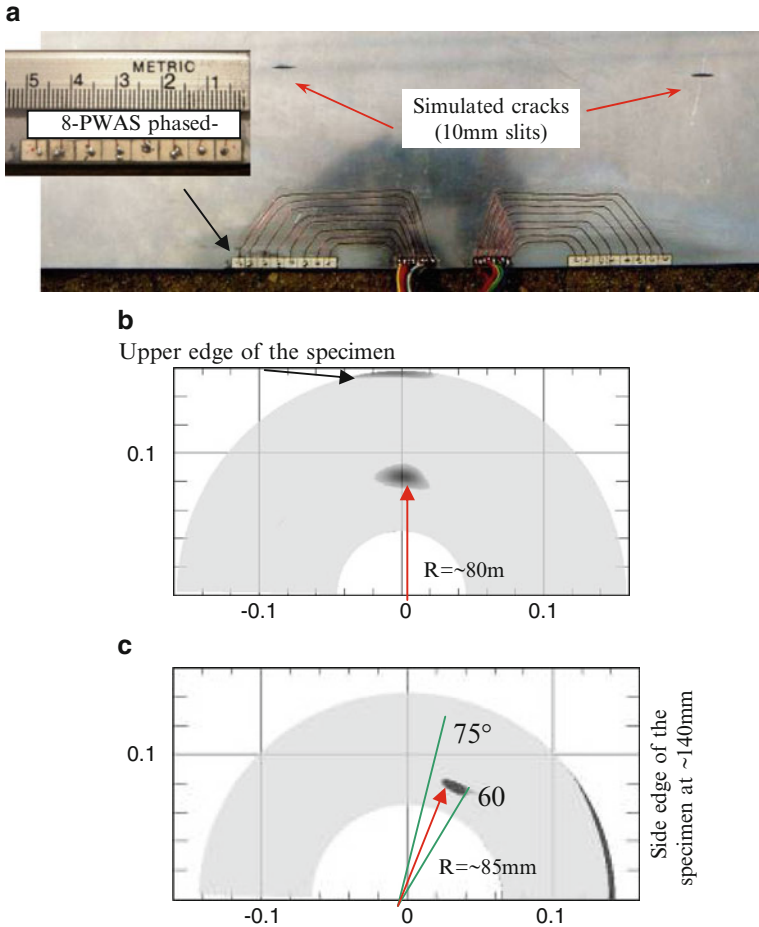
Fig. 2 Crack-detection in a thin plate using two piezoelectric wafer active sensors (PWAS) phased arrays: (**a**) test setup; (**b**) broadside crack imaging; (**c**) offside crack imaging

of a 2-mm thick aluminum alloy plate $\sim 400 \, \text{mm} \times 150 \, \text{mm}$ in size. Two hair-line through the thickness slits were cut in the plate to represent two separte cracks (*Fig.* 2a). The separate PWAS phased arrays were permanently installed on the plate, one directly under one crack (broadside location) and the other diagonally to the left of the other crack (offside location). Previous work on this topic [6] has indicated that an offside crack are more difficult to detect with a phased array because the ultrasonic beam hits obliquely and hence does not generate a specular reflection like in the case of a broadside crack. For this reason, the ultrasonic signal received back from an offside crack is much weaker than that received from a broad-side crack because it mostly represents the effect of scatter and secondary generation from the tip stress singularities. In the present experiment, we were able to detect the broadside and the offside cracks with almost equal accuracy (*Fig.* 2b, c).

Examination of *Fig.* 2b indicates that the echo image of the broadside crack is well defined at 80-mm radius and 90-deg azimuth. In addition, the upper side of the *Fig.* 2b image shows a shadow due to reflections from the upper edge of the specimen. (This shadow could be eliminated through reduction of the upper limit of the inspection radius, but we left it in in the spirit of full disclosure of our results.). Examination of *Fig.* 2c indicates that the echo fo the offside crack is well defined at 85-mm radius and azimuth delimiters $60° - 75°$. The shadow at the right extreme of the image represents the side reflection from the edge of the specimen located at ~140 mm. An implementation of these principles to crack detection and crack growth monitoring during a fatigue test is described in [7].

Conclusions

Piezoelectric wafer active sensors (PWAS) are a promising technology for achieving embedded NDE, because they are small-cost unobtrusive light-weight transducers that can be permanently attached to the structure and left in place for long-term monitoring. Although PWAS transducers have been successfully used in laboratory tests, several fundamental challenges still exist in the implementation of PWAS transducers in actual SHM, such as (a) acheiving predictable and controlled durability of PWAS transducers under environmental attacks and mechanical fatigue loading; (b) developing predictive simulation of PWAS electroacoustic interaction with the structural substrate to achieve optimal damage detection; (c) design and analysis for low-power low-voltage wireless interrogation.

References

[1] ASCE, "Report Card for America's Infrastructure", American Society of Civil Engineers, website http://www.asce.org/reportcard/2005/index.cfm
[2] Krautkramer, J.; Krautkramer, H. (1990) *Ultrasonic Testing of Materials*, Springer Verlag, 1990
[3] Kundu, T. (Ed.) (2007) *Advanced Ultrasonic Methods for Material and Structure Inspection*, ISTA Pub., London, UK, 2007
[4] Giurgiutiu, V.; Cuc, A. (2005) "Embedded Nondestructive Evaluation for Structural Health Monitoring, Damage Detection, and Failure Prevention", *Shock and Vibration Digest*, Sage Pub., London Vol. 37, No. 2, pp. 83–105, March 2005
[5] Giurgiutiu, V. (2008) *Structural Health Monitoring with Piezoelectric Wafer Active Sensors*, Elsevier Academic Press, 760 pages, ISBN 978-0120887606, 2008
[6] Giurgiutiu, V.; Bao, J. (2004) "Embedded-Ultrasonics Structural Radar for In-Situ Structural Health Monitoring of Thin-Wall Structures", *Structural Health Monitoring – an International Journal*, Vol. 3, N 2, June 2004, pp. 121–140
[7] Giurgiutiu, V.; Yu, L.; Kendall, J.; Jenkins, C. (2000) "In situ Imaging of Crack Growth with Piezoelectric Wafer Active Sensors", *AIAA Journal*, Vol. 45, No. 11, pp. 2758–2769, Nov. 2007

Rapid Identification of Critical Structural Components to Inspect or Monitor After an Extreme Event

D. Saydam and D.M. Frangopol

Abstract Nondestructive evaluation techniques can be used for condition assessment of structures after an extreme event such as earthquake or blast in order to obtain information about the overall integrity of the structure. The aim of this study is to present an approach for rapid identification of the critical components to inspect or monitor after an extreme event. The methodology is based on reliability importance of components within a system. The importance ranking of components is different under various loading conditions. The methodology is illustrated by using a truss bridge under blast. The critical components for condition assessment are identified.

Keywords Bridges • Reliability importance factor • Structural health monitoring • Sudden local damage

Introduction

Difficulties arise in assessment and prediction of structural performance because of the complexity and high uncertainty of the deterioration and damage processes. Accurate assessment and prediction of structural performance require the knowledge of several disciplines such as strength of materials, structural analysis, structural reliability, and advanced modelling techniques of structural damage. Integration of inspection and monitoring data into this task is a promising and increasing trend. However, inspection and monitoring activities come with additional cost. These activities have to be planned attentively in order to minimize the cost and maximize

D. Saydam • D.M. Frangopol (✉)
Department of Civil and Environmental Engineering, ATLSS Engineering Research Center, Lehigh University, Bethlehem, PA 18015, USA
e-mail: dan.frangopol@lehigh.edu

the benefits. Several researchers focused on optimal scheduling of inspection and structural health monitoring activities considering life-cycle performance of structures [1, 2]. Identification of the optimum locations of sensors for monitoring structures has been studied using optimization algorithms to maximize probability of damage detection [3]. Furthermore, the optimum locations of sensors were identified by formulating a multi-objective optimization problem to minimize the cost of sensors and the uncertainty associated with the measurement [4]. However, the application of these methods may be computationally expensive and time consuming if the purpose is to find the critical components of a structure to perform a condition assessment after an extreme event.

The purpose of this paper is to present methodology for rapid identification of the critical components of a structural system to inspect or monitor after an extreme event. The methodology is based on reliability importance of each component within a system. Reliability importance of components based on structural health monitoring data was used for optimal planning of long-term monitoring of structures [1]. In this paper, structural analysis is used to obtain the reliability importance factor of components. The methodology considers the extreme loading case in service and the abnormal loading condition. A numerical example consisting of a truss bridge subjected to blast loading is used to illustrate the approach. Significant failure modes of the structure are identified and incremental loading method [5] is used to derive the limit state equations for the system reliability analysis. The critical members are identified for blast and vehicle loading.

Methodology

The limit state equations defining the failure criteria of components and systems are required for reliability analysis of structural systems. These limit state equations vary under different loading conditions. Once the loading conditions are identified, the system resistance should be defined in terms of component resistances. The steps of the proposed methodology to identify critical components of a system for different loading conditions are illustrated in Fig. 1.

In reality, the resources for assessment of the structural condition may be limited to inspect or monitor most of the components within a structure. Therefore, the limited resources should be allocated on most critical components. Ranking components due to reliability importance accounts for the uncertainties associated with resistance and loading as well as the distribution of the load among the components. The most critical elements under an abnormal loading condition should be compared/combined with the most critical elements under extreme conditions of service loading. This is due to the fact that a structure which survived an abnormal event but still in service will be subjected to further loading. A damage which is not detected may cause unexpected consequences when combined with the effect of deterioration later.
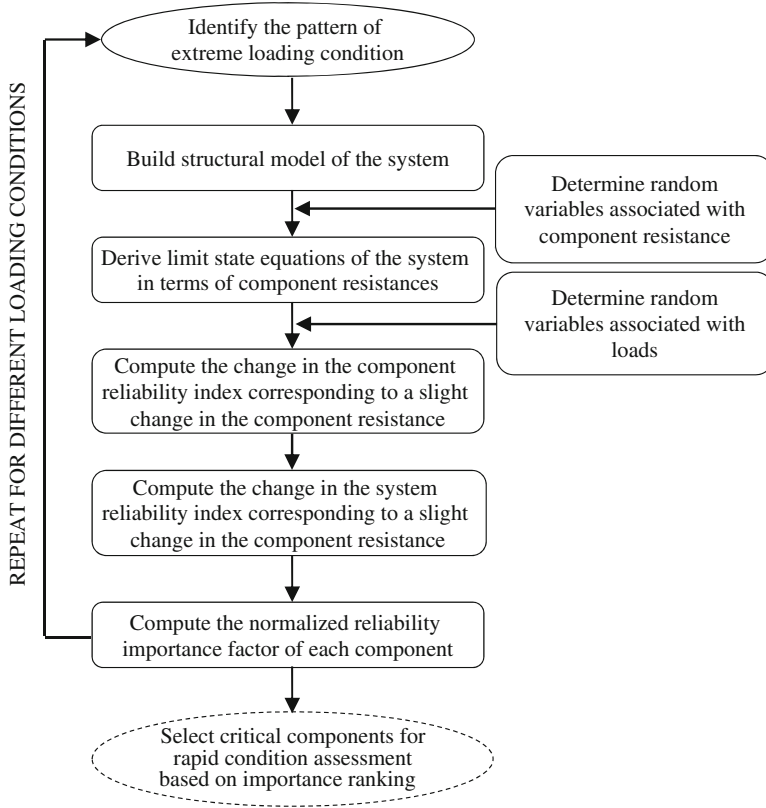
Fig. 1 Steps of the proposed methodology

Reliability Importance Factor

The components within a structural system have different levels of contribution to the reliability of the system. Reliability importance factor (*RIF*) is a performance indicator regarding the impact of each component on the system reliability. It depends on several factors such as correlation between component resistances, stiffness sharing factor of each component, component reliability level, member post-failure behavior, system failure criterion and system topology [6].

Usually, system performance is assessed by combining performance of components using series-parallel models. In a series system, the component with the lowest reliability level has the highest impact on the system reliability. The *RIF* of a component is defined as the gradient of system reliability with respect to the component reliability as

$$RIF_i = \partial \beta_{system} \ / \ \partial \beta_i \tag{1}$$

where RIF_i is the reliability importance factor of component i, β_{system} is the system reliability index, and β_i is the component reliability index. In this paper, the RIFs are computed by changing the component resistance very slightly and observing the change in system and component reliability indices. When the reliability indices of the system and the component are functions of only the component resistances, the chain rule can be applied as

$$RIF_i = \frac{\partial \beta_{system}}{\partial R_i} \cdot \frac{\partial R_i}{\partial \beta_i} \approx \left(\frac{\Delta \beta_{system}}{\Delta R_i} \right) \bigg/ \left(\frac{\Delta \beta_i}{\Delta R_i} \right) \tag{2}$$

where R_i is the resistance of component i. The normalized reliability importance factor ($NRIF$) is defined as

$$NRIF_i = RIF_i \bigg/ \sum_{j=1}^{n} RIF_i \tag{3}$$

where $NRIF_i$ is the normalized reliability importance factor of component i, n is the number of components in the system, and $0 \leq NRIF_i \leq 1.0$.

Numerical Example

The critical components of a truss bridge superstructure subjected to blast loading underneath are identified using the proposed methodology. The geometry, loading pattern of extreme vehicle load and member ID numbers of the steel truss bridge are presented in Fig. 2. The uncertainty of the system is due to the resistance of each member and the applied load. The material behavior of steel members is assumed ductile with yield strength lognormally distributed, having mean value of 248.2 MPa in tension and 124.1 MPa in compression in order to account for instability. The coefficient of variation is assumed 0.10. Additional information about the structure can be found in [7].

An explosion is assumed to happen at 4.5 m below the mid-point of the structure. The equivalent static blast pressure caused by an amount of 22.7 kg of trinitrotoluene (TNT) explosive over the bottom surface of the deck is computed [8, 9]. In order to calculate the nodal forces, these pressures are integrated over the tributary area of each node. The loading pattern considered for the blast loading is illustrated in Fig. 3.

A total number of 46 most significant failure modes are considered for each loading case. The limit state equations corresponding to each of the failure modes are derived using the incremental loading method [5]. The mean values and coefficients of variation of loads S and Q are assumed as 213.5 kN, 422.6 kN, 0.2 and 0.2, respectively. The structural analyses of the truss required in this procedure are performed using software OpenSEES [10] and reliability analyses are performed using software CALREL [11].
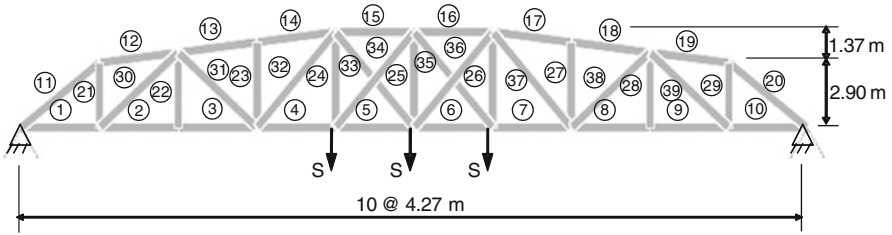
Fig. 2 Geometry, loading and member ID numbers of truss bridge
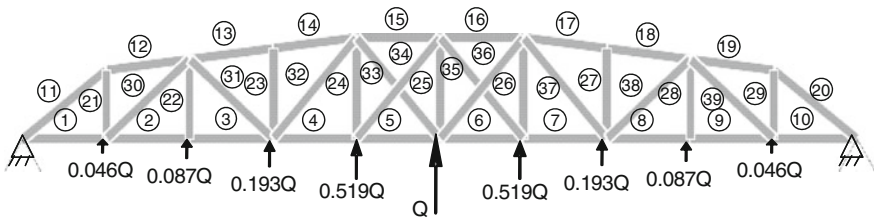
Fig. 3 Loading pattern considered for explosion under the structure

The critical components and their *NRIF*s under blast and vehicle loading are presented in *Table 1*. The most critical components for blast loading are 31, 38, 21 and 29 while components 14, 17, 13 and 18 are most critical for vehicle loading. The selection of which components to monitor depends on the number of components planned to monitor with the available budget. For instance if the budget is limited to 8 components it may be reasonable to focus on components 31, 38, 21, 29, 14, 17, 13 and 18 since there is a significant reduction in *NRIF* for blast loading after first 4 components. If 12 components are to be monitored, the additional components can be 30, 39, 15 and 16. It is worthy to note that, components 15 and 16 are selected instead of components 24 and 26 since they are critical for both blast loading and vehicle loading.

Conclusions and Recommendations

In this paper, a methodology for rapid identification of the critical components within a structural system to inspect or monitor after an extreme event is presented. Reliability importance factors are used to identify the importance ranking of components within the system. A numerical example consists of a truss bridge subjected to blast loading is analyzed under vehicle loading and blast loading separately and most critical components are identified for each case. The results indicate the importance of accounting for the vehicle loading case in addition to

Table 1 Critical components and *NRIF*s

Blast Loading		Vehicle loading	
Component ID	*NRIF*	Component ID	*NRIF*
31 and 38	0.2982	14 and 17	0.1529
21 and 29	0.1435	13 and 18	0.1516
24 and 26	0.0191	30 and 39	0.1137
14 and 17	0.0113	15 and 16	0.0656
13 and 18	0.0112	32 and 37	0.0116
15 and 16	0.0094	34 and 35	0.0034

the blast loading. A further study can focus on generalizing the selection procedure by considering a weighted average of *NRIF*s and validation of the weighting factors for loading cases.

References

[1] Kim, S. and Frangopol, D. M. (2010), *Prob. Eng. Mech.*, vol. 25, n. 1, p. 86.
[2] Kim, S. and Frangopol, D. M. (2011), *Prob. Eng. Mech.*, vol. 26, n. 2, p. 308.
[3] Rus, G., Lee, S.-Y., Gallego, R. and Park, T.-H. (2006), In: Proceedings of the Third European Workshop: Structural Health Monitoring, pp. 563, DEStech Publications.
[4] Azarbayejani, M. (2009), Ph.D. Dissertation, The University of New Mexico, Albuquerque, New Mexico.
[5] Rashedi, M. R. and Moses, F. (1988), *J. Strurt. Eng.*, vol. 114, n. 2, p. 292.
[6] Gharaibeh, E. S., Frangopol, D. M. and Onoufriou, T. (2002), *Comput. Struct.*, vol. 80, n. 12, p. 1113.
[7] Saydam, D. and Frangopol, D. M. (2010), In: Proceedings of Fifth International Conference on Bridge Maintenance, Safety and Management, IABMAS 2010, Frangopol, D. M. et al. (Eds.), CD-ROM, p. 3529–3536, CRC Press, London.
[8] Anwarul, I. and Yazdani, N. (2008), *Eng. Struct.*, vol. 30, n. 2, p. 1922.
[9] U.S. Department of Defense (2008), In: Unified Facilities Criteria, UFC 3-340-02.
[10] Mazzoni, S., McKenna, F., Scott, M. H. and Fenves G. L. (2006), OpenSees Command Language Manual. Dep. of Civil Eng., U. of California, Berkeley, CA.
[11] Liu, P. L., Lin, H. Z. and Der Kiureghian, A. (1989), Rep. No. UCB/SEMM-89/18, Dep. of Civil Eng., U. of California, Berkeley, CA.

A Fast Automated Impact Hammer Test Method for Modal Parameter Extraction: Implementation on a Composite Bridge Beam

D. Tirelli and I. Vadillo

Abstract The experimental modal properties of sub-structures of larger civil engineering structures are rarely measured on-site. In fact, usually, their dynamic characteristics are only evaluated numerically. There are a number of reasons for the lack of experimental verifications, but most probably these are due to the time and cost required to obtain the experimental modal parameters accurately within the context of challenging environmental on-site conditions. For smaller civil engineering structures, experimental dynamic testing significantly increases the overheads of the overall cost of the construction. This paper presents a dynamic identification method based only on experimental and statistical procedures, which highlights and solves some of the practical aspects of experimental identification, allowing extraction of the main modal properties speedily with a reduced cost of human resources and instrumentation. The methodology is described using as an example a composite bridge-beam, made of concrete and fibre-reinforced composite material, which constitutes the first composite bridge applied on a motorway in Europe. The use of the reciprocity of the transfer functions combined with some self-checks of the measurements is shown to be an efficient way to speed up the signal processing, without reducing the accuracy of the results. The Impact Hammer test method described here, uses a list of functions developed as a MATLAB toolbox, and is part of the SERIES project.

Keywords Carbon fibre beam • Coherence • Experimental data • Modal extraction • Transfer function

D. Tirelli (✉) • I. Vadillo
ELSA* Laboratory, European Commission, Ispra, Italy
e-mail: daniel.tirelli@jrc.ec.europa.eu

*European Laboratory for Structural Assessment

Introduction

Impact hammer methods in the last decades were not currently used for civil structure due to the low level of energy induced by the impact. Now with the transducers accuracy and adequate signal processing, small and medium structures could be investigated more easily. The FIHT (Fast Impacts Hammer Testing) developed here for the project SERIES (Seismic Engineering Research Infrastructures for European Synergies) gives a solution to find quickly and at low cost the main dynamical properties of structures of medium size.

The method doesn't substitute specific and expensive commercial tools, but gives an efficient support, to most of the needs in the dynamic field in civil engineering laboratories, because of its high degree of automation of the procedures. A structure of the ELSA laboratory is taken for example to illustrate the method. It is a fraction of a bridge deck composed of fibre composite beam of 13 meters long, built for the European project named PROMETEO [1].

Description of the Method (FIHT) Used on a Structural Element

FIHT method compared to conventional impact hammer methods

The Impact hammer testing method is already well known. The main difference between the FIHT and the classical hammer impact method, for the hardware part is the extensive use of the reciprocity of the transfer function. In this way, the number of output transducers is substituted by the impact positions. As the number of positions is not limited, the mode shapes could be designed accurately. As the number of output could be reduced to one, then the calibration test is not required. These two differences shorten drastically the experimental task.

With this fast testing procedure an important number of transfer function (FRF) could be recorded. With a great number of data, statistic procedures, used here intensively, work rather well. An automatic acceptance of the measurements (an important help to the user) is achieved by processing the coherence functions. The automatism processes are inserted mainly on the FRF noise level and on the coherence threshold value. Both are defined, by default, from dynamic testing of more than 30 different kinds of structures, and materials for civil engineering. Modal extraction is performed by the following rules. The damping and frequency values are extracted by the half power band method interpolated, and magnitude balanced, only on the number of higher peaks requested and detected automatically.
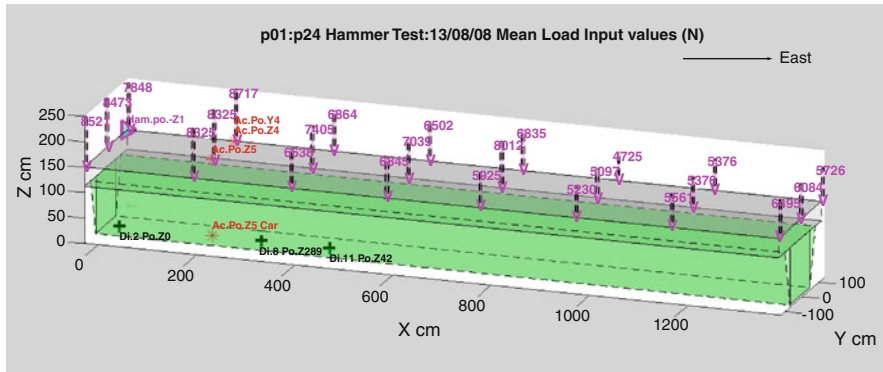
Fig. 1 Structure design with the output transducers (black+ =disp. red*=Acc.) and map of the positions tested with the mean force of 5 impacts (Arrows)

One of the main limitations of the method could be the incapacity of the modal extraction procedure, based on the peak peaking method, to isolate modes very closed, leading to operational deflection shapes instead of pure mode shapes.

Structural example

The example of structure describes here, was built for testing (static tests) the ultimate capacities of a materials combination (reinforced concrete glass fiber for the deck, and carbon fiber for the beam) used for a real bridge in Asturias (Spain). At this aim displacement transducers were already present on the structure and some of them (3) were therefore taken for output transducers for a cross-check with the dynamic analysis.

Here, the number of output signals was of seven, even theoretically, only one is sufficient. They are divided in 3 displacements and 4 accelerations shown in the *Figure* 1. Displacements, force and three accelerations were measured in the vertical direction and one acceleration in the horizontal one. The impacts were distributed on a regular mesh of 24 positions on the deck. As the method uses one output, it is necessary to choose a position not close to the nodes of the modes expected. The numerical dynamic analysis, and analytical results already performed before the tests, even not perfect, can help to find the best position which is a crucial point for the method as also mentioned by the authors [2] in their automated method of model extraction. In our case the request was to find the first 6 bending modes of the deck. An approximate analytical behaviour of the deck has shown that 1.9 m from the side is one of the best possible output positions. If all the transducers coordinates (+ Hammer impacts positions) are inserted before the beginning of the tests, then the figure is updated automatically.

We remind that the property of reciprocity of the transfer function allows making the measurements separately. The noise is removed by the impacts repetition. The

reciprocity is available only if the impacts induce very small level of strain or displacement to remain in the elastic field, and if the impacts are not too much different. The material and structure must have linear dynamic behavior, for the generated strains, which is the case of most of the new structures built actually. It is less true in the case of masonry and still worst in the case of old structures.

In the experimental task, the main shortening is brought by the property of reciprocity, as the installation of new transducers is globally long and because the number of transducers is often limited.

Each position corresponds for the modal shapes to the nodes of a mesh where the FRFs are measured. As explained before, it is of crucial importance to define the best position of the output transducer, in some cases, it is preferable to use a 2nd or a 3rd output transducers, to avoid some mistakes in the modes definition. We can note on the *Fig.* 1 that each mean impact force is reported automatically on the structure, to visualize quickly, possible irregularities in the input map.

As the main aim of the tests is to obtain the modal shapes of the structure tested, one of the limitations of the method actually is the representation of the shapes in the 3 directions coupled, as the software is still not achieved. They are obtained in each direction at each time.

It should be noted that the application of the method in this case involved processing of a number of signals equal to: (24 positions) x (5 means) x (7 outputs) = 960 signals. Without the help of the FIHT method it should have been a very long process.

Signal Processing

To understand the automated signal processing, a view of the main operations between the recorded signals (1st column) to the final results (last column), is displayed in *Fig.* 2. It shows that for each of the P (FRFs) points of the structure tested, at least 2 signals (1 input + 1 output) is measured N times (N=4 to 10). The total number of signals is then equal to (2*N*P) for each output transducer (120 in our case). One of the novelties in the FIHT method is that the FRFs, automatically calculated, are filtered because only the three first magnitude orders will be post-processed. In this way the coherence function is not biased by low signal/noise ratio. With this last operation, the coherence function could be represented in a very compact form, instead of showing one by one the traditional coherence in between 0 to 1, we display the histogram of the values of the filtered coherence for all the output channels together.

In *Fig.* 3, it is shown one of the Filtered Coherence Histogram (FCH) for impacts at the same position and for all the output channels (each colour). The shapes and the values of the histograms must respect some criteria (exponential shape + mean value > 0.7) to allow the post processing to continue in an automatic way. The next step of signal processing is the modal parameter extraction executed with a fast
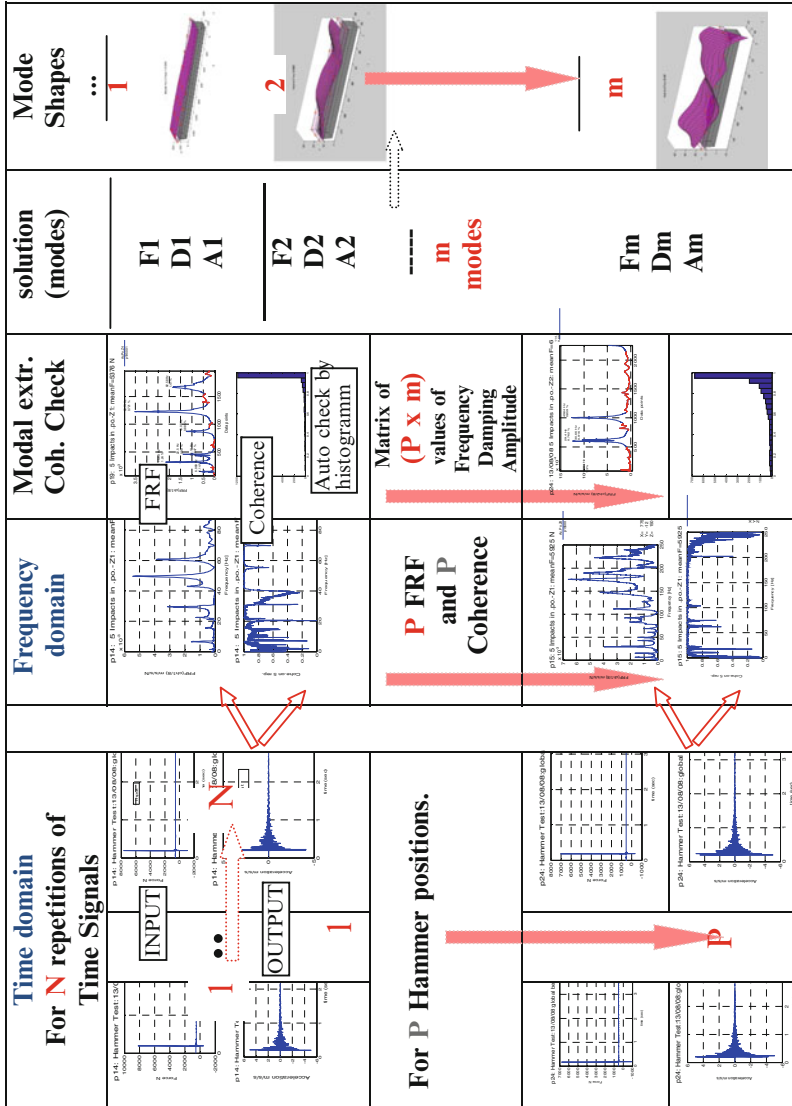
Fig. 2 General schema of signal processing and modal extraction by the Fast Impact Hammer Testing (FIHT)
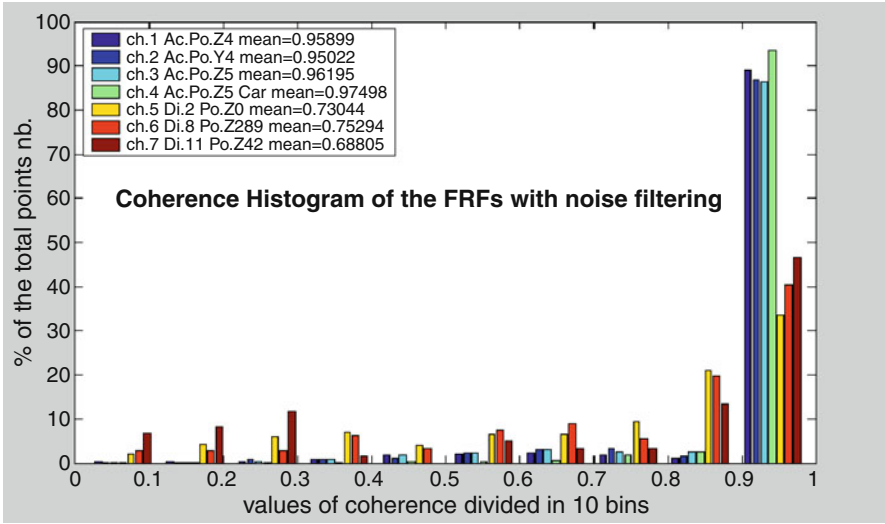
Fig. 3 Coherence histogram of 7 (colors) different outputs and from 5 impacts at the same position

modified peak picking method, which identifies the N requested main modes present in each of the P FRFs. Then (NxP) values of frequency, damping and amplitude are stored in matrix of P lines and N columns. Statistic processes applied to the frequency matrix gives the statistic solutions which are the m (m could be different from N) values of frequency, damping, amplitude and frequency dispersion. The modal shapes are then represented by the 3d surfaces measured and interpolated by a regular mesh, using the Delaunay triangulation.

The final results are illustrated in *Fig.* 4 which enables to understand which level of accuracy we can reach with the FIHT method. Bending, torsion, flapping, support characteristics and real boundaries conditions are, in effect, visible by the mode shapes representation even some of the different types of modes are strongly coupled (of only 0.3 Hz. in such case).

Conclusion

The Fast Impact Hammer Testing method built for modal testing and described by the example herein, have proved to be very efficient in time saving, at different levels of the process without neglecting the accuracy. The method has been used with success, on real structure. The main achievements in the FIHT method are for the experimental part the use of the reciprocity of the transfer functions. For the signal processing, it is mainly the display of coherence histograms coupled to the FRF filtering and mapping, which introduces a novelty in the field. Finally the
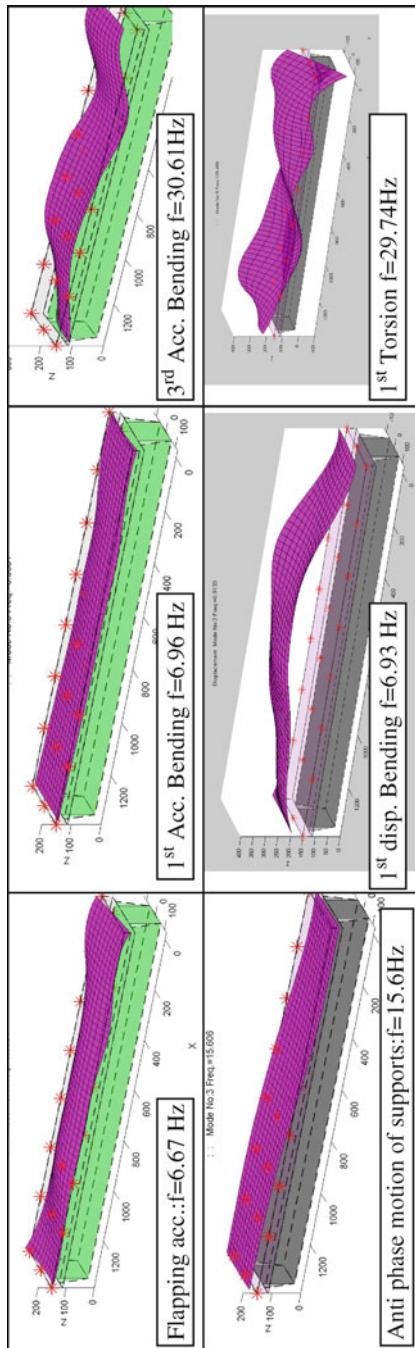
Fig. 4 Examples of exp. mode shapes from Acc. (line above), from Disp (line below)

modal extraction is eased by an automatic picking and identification of the modes. Statistic procedures applied to the identified modes gives accurate results in a very short time. This set of improvements, enables a practical use of the FIHT method by civil engineers.

References

[1] M. Poljanšek, G. Bof, P. Capéran, J. Esteves, E. Gutiérrez, O. Hubert, R. Kiefer, D. Tirelli, B. Viaccoz, A. Zorzan, (2009). *Report on Testing and Analysis of PROMETEO Fibre Reinforced Composite Bridge Beam*. Limited Distribution PUBSY JRC54320.
[2] C. Rainieri and G. Fabbrocino, (2010). *Mechanical Systems and Signal Processing*, vol 24, n 3, pp 678–695.

Case Studies of Structural Health Monitoring of Bridges

I. Harik and A. Peiris

Abstract Structural Health Monitoring of a number of bridges in Kentucky has proven to be an economical and effective method for extending the life of bridges and for providing the tools for immediate response and decision making. Three bridges are highlighted in this paper. The first bridge is on I-65 in Louisville where instrumentation that continuously monitors the bridge, permitted the design of an economical retrofit. The second bridge is on I-64 over US 60 where instrumentation continuously monitors the bridge for possible impact on the girders resulting from over the height limit trucks. The third bridge is on US 41 North over the Ohio River where instrumentation has been placed on the bridge piers to monitor for barge impact. For the I-64 and US 41 bridges, and in the case of an incident, selected personnel are notified via text messages on their cell phones along with e-mail messages. The messages identify the type of incident and its severity, and list the web site where the incident can be viewed along with data from the instrumentation on the bridge. Decisions can be made in minutes in regard to the course of action.

Keywords Bridges • Damage • Deterioration • Instrumentation • Response • Retrofit • SHM

Introduction

Structural Health Monitoring (SHM) of bridges has become extremely popular throughout the past decade. The monitoring enables engineers to identify damages to bridge structures which could be material and/or geometrical. Recent technological

I. Harik (✉) • A. Peiris
University of Kentucky, Lexington, Kentucky, USA
e-mail: iharik@engr.uky.edu

advances facilitate the usage of more complex and accurate systems for evaluating the performance of both existing and new bridges.

Depending on the desired final outcome, monitoring of bridges fall into three main categories: (i) Short-term monitoring, (ii) Long-term monitoring, and (iii) Extreme event monitoring. Short-term monitoring is carried out usually on bridges with suspected damage or deterioration in order to evaluate the degree of damage and possibly identify a practical retrofit measure. The same monitoring can be performed following repairs to evaluate the effectiveness of the repair technique. Long-term monitoring is carried out to identify behavior, loading patterns and deterioration rates, obtain data for possible future repairs and maintenance, evaluate operational safety, research and improve bridge designs, and identify possible damages following extreme events such as earthquakes. Extreme event monitoring may or may not gather information at regular time intervals as the other two categories. This type of monitoring is specially designed to identify events such as collisions or blasts at critical locations, and severe movements arising from phenomena such as earthquakes or hurricanes. This paper presents three case studies of SHM of bridges in Kentucky.

Bridge on I-65 in Louisville

The bridge on I-65 in Louisville utilized short-term monitoring where instrumentation, that continuously monitor the bridge, permitted the design of an economical retrofit [1]. The bridge is on interstate-65 (I-65) which travels in a north-south direction through the city of Louisville. The damaged section of I-65 is a parallel-bridge; each bridge carries three lanes of traffic in either northbound or southbound direction. Several elevated spans of the expressway were observed to have cracking in some of the precast prestressed concrete girders. The cracking was particularly
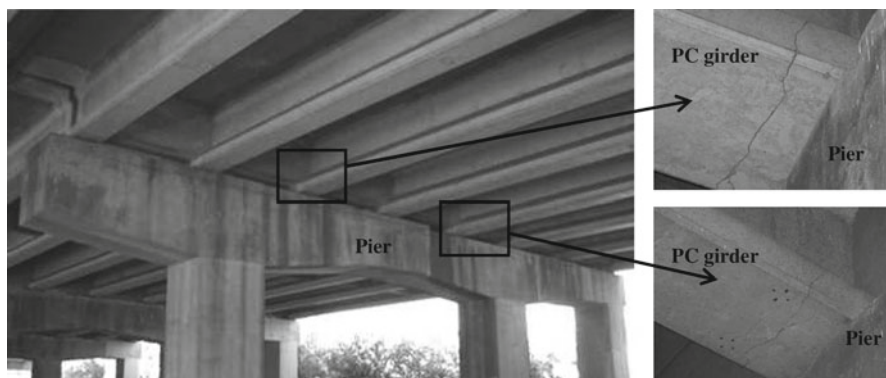
Fig. 1 Cracks in the prestressed concrete girders
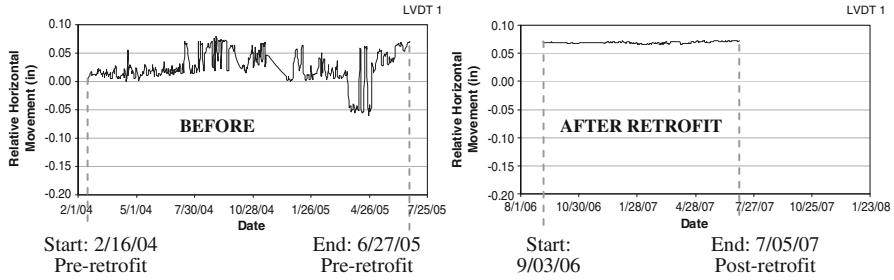
Fig. 2 Relative horizontal movement measured before and after retrofit

prevalent near or at fixed end locations where translational movement in the bridge direction is restricted (Fig. 1). The project aimed to repair, strengthen and restore the capacity of the damaged prestressed concrete girders using carbon fiber reinforced polymer (CFRP) sheets.

To investigate the liveliness of the cracks, two girders were instrumented with linear variable displacement transducers (LVDTs) in the horizontal and vertical directions to measure the respective movements. The instrumentation was installed on February 16, 2004, and the movement and temperature measured until June 27, 2005. The recoded data was used to design the retrofit measures, and once the repair was complete the LVDTs were attached again to evaluate the effectiveness of the retrofit. The monitoring confirmed that the horizontal movement was significantly reduced due to the retrofit (Fig. 2), while in the vertical direction the retrofit had stopped the vertical movement from increasing further.

Bridge on I-64 over US60

A combination of long term and extreme event monitoring is in place at the bridge on I-64 over US 60, in Franklin County, Kentucky [2]. The instrumentation continuously monitors the bridge for possible impact on the girders resulting from over the height limit trucks. The parallel bridges (Fig. 3), Eastbound and Westbound, are of composite steel-concrete type, with an overall length of 90 m. The 190 mm thick concrete deck of the bridge is supported by six continuous plate girders of varying-and-constant depth type.

The underside of an exterior girder, which has the least height-to-ground distance, of the eastbound bridge has shown signs of impact. It is suspected that the impact is caused by certain truck types traversing on the eastbound route of US 60 beneath the bridge. Remote sensing technology, that can monitor the behavior and response of the I-64 Bridges over US60 from potential impact, was set up at various locations on the bridge. The data is to be transmitted to a computer at the University of Kentucky to be analyzed, compared, and viewed, in elapsed or real time.
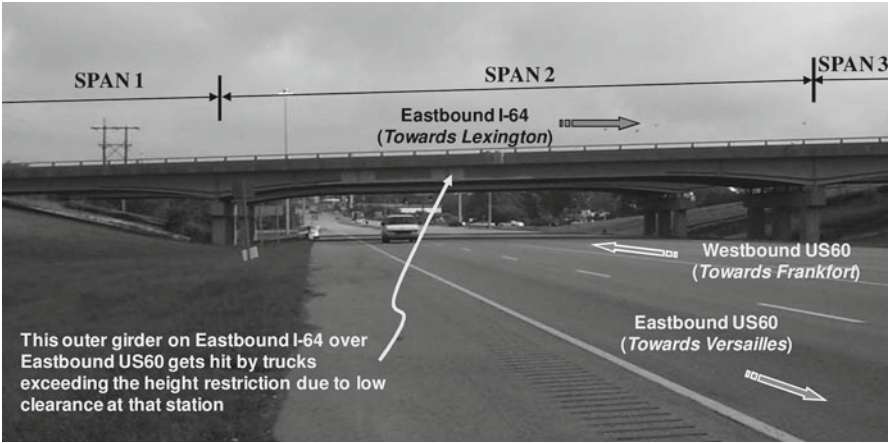
Fig. 3 I-64 over US60 parallel bridges
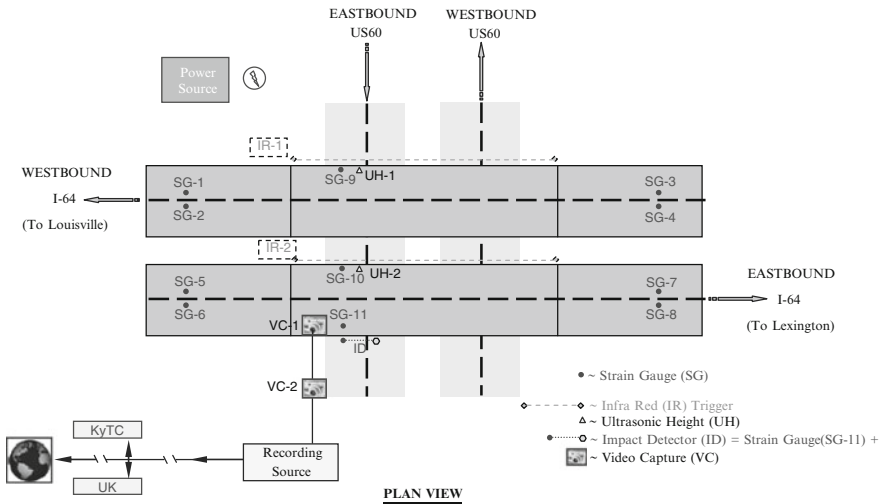
Fig. 4 Gauge layout of I-64 Bridge over US60

Remote sensing technology was implemented to both westbound and eastbound bridges that are parallel to each other. Due to the similar nature of both bridges in terms of dimensions and expected loading, the effects from the potential impact on the eastbound bridge (i.e., the subject) can therefore be compared to the westbound bridge (i.e., the base).

The different devices that are being employed in this project are shown in Fig. 4. These include strain gauges, temperature gauges, infrared sensors, ultrasonic height

detectors, accelerometer, and video cameras. Eleven locations are implemented with strain and temperature gauges (indicated as SG-#). The infrared sensors (IR-1 and IR-2) serve as a detector of trucks that would result in an impact to Girder 1 in the eastbound I-64 Bridge. When the infrared mechanism is interrupted, the sensor will simultaneously trigger its adjacent ultrasonic height detector (UH) and video camera (VC) to measure the truck height and to capture images of the truck, respectively. The accelerometer is coupled with SG-11 to form Impact Detector (ID), as shown in Fig. 4. The unit is continuously operational in order to take measurements of acceleration and vibration, whether Girder 1 in the eastbound I-64 bridge is impacted or not.

Bridge on US41 North over Ohio River

The third bridge is on US 41 North over the Ohio River where instrumentation has been placed on the bridge piers to monitor for possible barge impact. Barges are the primary means of transportation on the Ohio river to transport and receive goods. The US41 Northbound (US41N) bridge over the Ohio river in Henderson County, Kentucky, is a cantilever through-truss bridge. The total length of the bridge including approach spans is 1950 m. The plan and elevation of the main bridge are shown in Fig. 5.

The US41N Bridge was instrumented with sensing technology to monitor the piers from afar for impact from a barge or barge flotilla. The basic instrumentaion used in this project for detecting and measuring impacts is the accelerometer. Accelerometers were mounted on the top of Piers B, C, and D. In addition, linear variable displacement transducers (LVDTs) were also mounted at the expansion bearings on top of Pier B. Various acceleration and displacement limits or thresholds were set to identify 'severe' and/or 'critical' impacts. A 'severe' impact is defined as the limit or threshold of impact that would cause 'possible' damage to the piers in question. A 'critical' impact is defined as the limit or threshold of impact that would not only cause damage to the pier, but the type of impact that would also require the closure of the bridge for further inspection. The 'critical' and 'severe' impacts are defined for each structure based on limits for displacement at epansion joints and/or acceleration and/or strain measurements.

Once impacts have been identified, the system automatically proceeds to notify related personnel members in the Transportation Operation Center in the Kentucky Transportation Cabinet, the US Coast Guard and other selected personnel. The information regarding the degree of impact is transmitted via text message, email and internet uploads. Information such as impacted pier, date and time, type of impact ('severe' or 'critical') will be sent, while the notified personnel should be able to visit a web site to view in real time the two expansion supports at top of Pier B, the eastern faces of Piers B, C and D, and the surrounding areas of Piers B, C and D. Video and/or photographic records is to be stored for at least 10 minutes prior to the event and 10 minutes following the event.
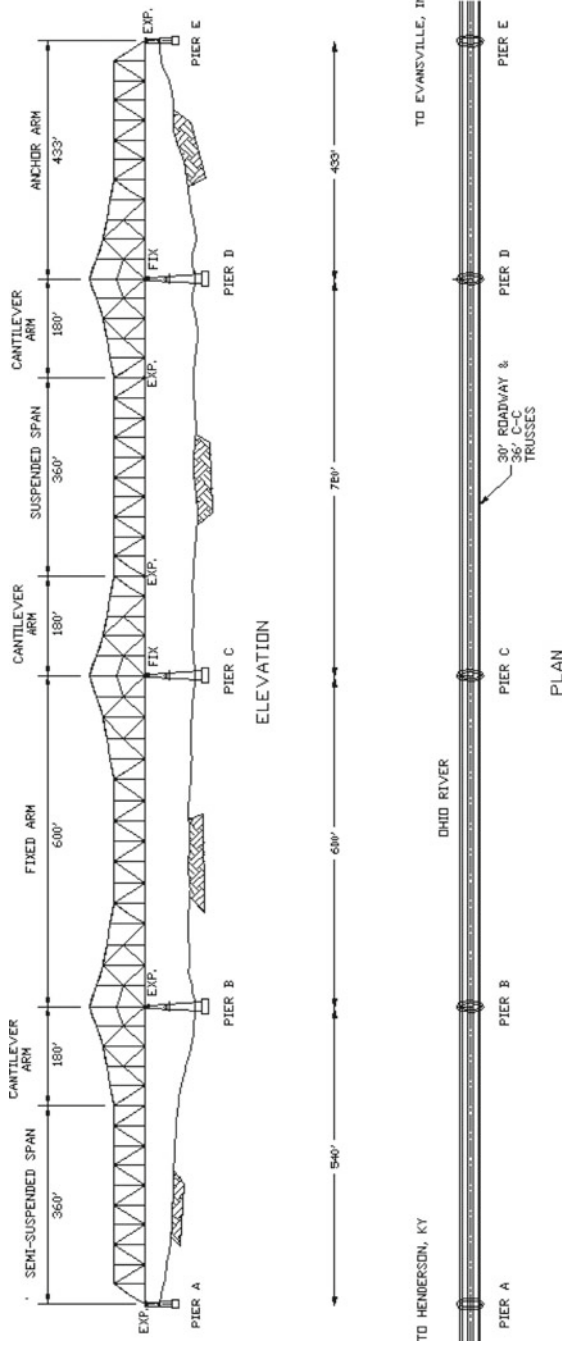
Fig. 5 US41 North over Ohio River

Typical data collected includes acceleration, displacement, and visual (video and still) records. A plot of the time history for the accelerations and displacements immediately prior to (~ 2 to 5 seconds) and following the impact (~15 to 30 seconds) as well as maximum hourly acceleration and displacement data should be accessible through the web site. If 'critical' impacts have been detected, the bridge will be closed automatically by a system set up in the process. The system contains a gate, similar to the ones employed at a railroad crossing, and flashing light warning and turning away any traffic. The bridge will remain closed until inspection has been performed and bridge is clear of no further danger.

Conclusions

Structural Health Monitoring of three bridges in Kentucky was highlighted in this paper. The short term monitoring of the bridge on I-65 in Louisville enabled researchers to quantify the degree of movement in the damaged spans, which, aided in determining the best retrofit measure. Further monitoring after the repair assisted in evaluating the effectiveness of the retrofit.

Before SHM was implemented at the I-64 Bridge over US60 and US41N Bridge over the Ohio River, damage due to impacts went unnoticed until periodic bridge inspections or until collisions were reported and Transportation personnel were deployed to evaluate the damage. Inspecting large bridges over waterways like the US41N Bridge after every impact is costly as well as time consuming. Identifying damage and being able to quantify the damage in real-time significantly improves the capability of avoiding catastrophic failures. The SHM carried out on bridges in Kentucky has proven to be an economical and effective method for extending the life of bridges and for providing the tools for immediate response and decision making. The life extension is a result of the immediate response to events and identification of any damage requiring retrofit.

References

[1] Choo, C.C. and Harik, I.E. (to be published in 2011), Repair of I-65 Expressway Bridges using Carbon Fiber Reinforced Polymer (CFRP) Composites, Kentucky Transportation Center, University of Kentucky.
[2] Harik, I.E., Choo, C.C., Peiris, A. and Eaton, D. (2011), Implementation of Remote Sensing Technology on the I-64 over US60 Bridge, KTC-11-01/SPR260-03-1F, Kentucky Transportation Center, University of Kentucky.

Long-term Data Intensive Wireless Structural Monitoring: Three Years of Experiences on the Stork Bridge

G. Feltrin, O. Saukh, R. Bischoff and J. Meyer

Abstract In the last decade, wireless sensor networks have become an intensively investigated tool for monitoring applications. Many field experiments with short-term deployments demonstrated their advantages. Very little, however, is known about the performance of wireless sensor network in mid- and long-term deployments. This paper reports about the experiences in developing, deploying and maintaining a wireless monitoring system on a cable stay bridge.

Keywords Real-world deployment • Reliability • SHM • Wireless sensor networks

Introduction

Wireless sensor networks (WSNs) are evolving to a new generation of cost-effective and easy to install monitoring tools. There are many papers describing short-term outdoor installations of wireless monitoring systems but only few long-term deployments have been reported [1-3]. However, many challenges arise when trying to set-up a WSN for a long-term operation. Firstly, system stability (hardware and software) is very important and can only be proven with time. Secondly, constantly changing environment conditions make it difficult to use indoor system test results to estimate and predict outdoor system performance. Finally, electromagnetic interference and varying weather conditions affects the performance of the basic

G. Feltrin (✉) • R. Bischoff • J. Meyer
Empa, Swiss Federal Laboratories for Materials Science and Technology,
Duebendorf, Switzerland
e-mail: glauco.feltrin@empa.ch

O. Saukh
ETHZ, Swiss Federal Institute of Technology, Zurich, Switzerland

algorithms (routing and time synchronization) and, as a result, influences the network reliability and lifetime.

This paper reports about the experiences with the wireless monitoring system deployed on the Stork Bridge in Winterthur, Switzerland, in November 2006. The main purpose of this deployment was to test the system performance and data quality against pricey conventional systems, to gain real-world experience in operating wireless monitoring systems, and to assure its stable long-term operation on a real test object under real world conditions.

System Overview

The monitoring system comprised six sensor nodes C1 to C6 (Figure 1a) attached to six cable stays of the Stork Bridge and a base station located in a technician room under the bridge deck. The base station had a root node C0 linked to a serial port and establishes an Internet connection via a UMTS link. The data were stored in a database on a server, located at the Empa campus.

The sensor nodes were based on the Tmote Sky hardware platform. Vibrations of cable stays were measured with a MEMS accelerometer that was attached to the base of the node housing, which was in turn fixed to a cable stay 3 meters above the bridge deck (Fig. 1b). Each sensor node was also equipped with a digital temperature and humidity sensor and an embedded internal voltage sensor. All hardware components were placed inside an aluminium housing that contained two 1.5V and 16'500 mAh batteries providing a maximal supply voltage of 3V.

Initially, the monitoring software was based on the TinyOS version 1.x/ Boomerang developed by Sentilla Corporation (formerly Moteiv). The software
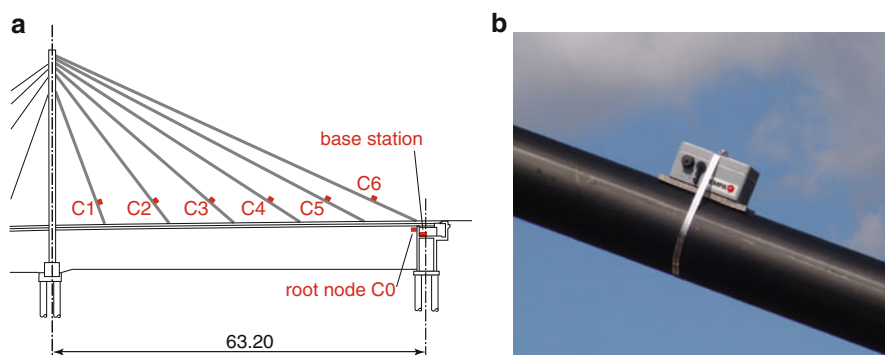
Fig. 1 (**a**) Monitoring set-up. (**b**) Node mounted on a cable

included a time synchronization protocol that periodically synchronizes the clocks of all nodes to the local clock of the root node C0. The task scheduler allowed the registration of various sensing tasks in global time. More details about the hard- and software are reported in [4].

The monitoring system used several energy saving mechanisms: (i) the system was composed of low power hardware components; (ii) the radio operates at a low duty cycle; (iii) data reduction algorithms was used to minimize the number of bytes that need to be transmitted to the base station. Particularly, acceleration time series were pre-processed at every sensor node by extracting the natural frequencies of each cable stay. Then only several values had to be transmitted to the base station. The initially used natural frequency estimation algorithm and its thorough evaluation are detailed in [5].

Initial Challenges

The wireless SHM system deployment started like most deployments on an office table which served as a smooth transition from a piece of code to a running system on the Stork Bridge. As part of the preparation, the system was previously tested on the cable stays of our laboratory bridge located in the testing hall at Empa [5].

The system was deployed at the Stork Bridge on November 30, 2006. The duty cycle of the radio, the most power consuming component, was set to 40%. The system performed quite well for four days until it suddenly crashed for an unknown reason (Fig. 2a). The total reception rate is defined as the ratio of data that successfully reached the base station to the total number of generated data. The experiment was restarted on December 18, 2006, but the high performance of the first four days was never reached again. Since the voltage threshold ensuring correct working of a node was 2.4V, on January 15, 2007, the nodes got new batteries since the supply voltages of most of the nodes had dropped to 2.5V (Fig. 2b). The test was completed
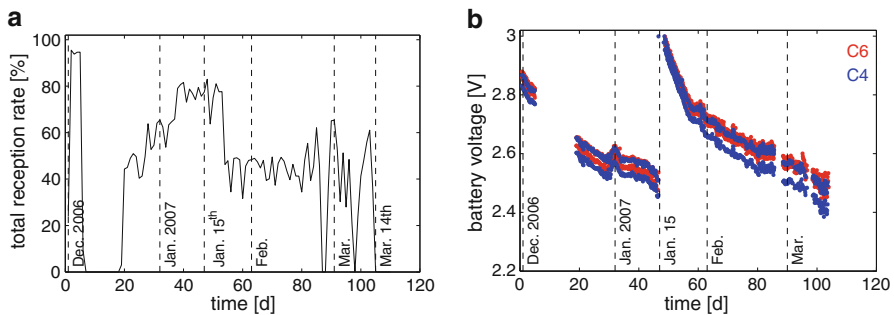
Figure 2 (**a**) Total reception rate. (**b**) Battery voltage

on March 14, 2007, after 3.5 months. The mean total reception rate was 43% which means that on average less than half of the nodes were working correctly. The actual network lifetime was around 60 days (Fig. 2b). The double-line voltage graph occurred, because the voltage measurement was made when the radio was on and the power demand produced a voltage drop. Since the measurements were not synchronized to radio duty-cycle, some measurements were taken when the radio was on and some when it was off.

This test period was characterized by many spontaneous breakdowns and resurrections of nodes and failures of the base station, which forced us to focus the future efforts on the system performance. We still do not have explanations for most failures of this early deployment stage. Furthermore, we observed that the routing changed on average every 6 minutes which was somehow surprising for such a small network.

Struggling for Reliability and Lifetime

Because of the frequent breakdowns and resurrections of individual sensor nodes, several watchdogs were added. A function of a watchdog is to recognize abnormal node states and, as a reaction, to reboot the node. The implemented watchdogs checked that (i) a missing interrupt from a malfunctioning sensor does not hang the complete system in a waiting state, (ii) a processing algorithm generates a completion event within 10 seconds, and (iii) the time synchronization algorithm initiated a reboot in case the node failed to synchronize with the master clock within 10 minutes. Furthermore, the nodes were automatically rebooted every 24 hours to prevent timer overflow problems.

In this test period three experiments were performed with the goal to test the reliability and lifetime. The radio duty cycle was progressively reduced from 10% to 3%. The sampling rates of the measurement tasks were changed to 2 minutes and later to 5 minutes. Figure 3a displays the total reception rate of the last experiment which started on December 20, 2007, and lasted for 200 days. The average total reception rate could be increased to 73% which represented a significant improvement with respect to the first test period. This improvement was achieved with a reduction of radio duty cycle from 40% to 3%. Nevertheless, the system performance was still unsatisfactory. However, not all data loss was due to the problems with the WSN. Periodic base station breakdowns and resurrections in the deployment history were related to hang ups of the UMTS link or breakdowns of the serial connection with node C0. Beside software problems, the performance was also affected by hardware problems: The nodes C3 and C4 had to be replaced because we discovered water inside their boxes and the electronics was completely wet. This problem was solved by providing the boxes with desiccant gel. Human mistakes contributed also to reduce the performance: After server updates by the IT-department of Empa, the logging application was accidentally not started, old batteries were replaced with even older batteries etc.
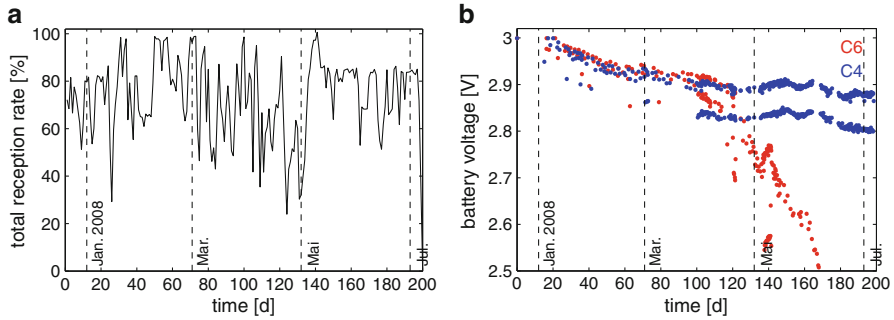
Fig. 3 (**a**) Total reception rate. (**b**) Battery voltage

According to Fig. 3b, which displays the battery voltages of the nodes C4 and C6, the voltage drop of the node C4 was 0.2V in 200 days. This figure suggests a life-time of approximately 600 days. This lifetime, however, can only be achieved if a node performs properly. In fact, as displayed in Fig. 3b, the node C6 started to consume much more power when its performance dropped, whereas its power consumption in the precedent time period was equal to those of the node C4.

Towards a Stable System

After having struggled for nearly two years without being able to achieve a high reliability we decided to redesign and re-implement the node software. The software was updated to TinyOS 2.x, which uses a new routing protocol (collection tree protocol (CTP) instead of MintRoute) and a new low power listening MAC protocol. Furthermore, the previously activated watchdogs were eliminated.

The first test with the new software period started on November 6th 2008 and lasted for 197 days. The node software redesign had a beneficial effect on the performance of the network, whose average total reception rate increased to 87%. The new software had also the effect to significantly stabilize the routing since routing changes decreased by an order of magnitude.

Before launching a new test, the old algorithm for computing the natural frequencies was replaced with a Fast Fourier Transform (FFT) algorithm since code optimization to reduce the code size and, as a consequence, to increase the usable data size. This algorithm was also much faster taking only 1 second to complete [6]. Furthermore, a detailed analysis of the results of the last test period revealed that a software mistake of the scheduler produced task scheduling interrupts lasting for 36 hours or multiple of this time period.

Figure 4 displays the reception rates of the natural frequency, temperature and supply voltage measurements of a test that started on January 16, 2010, and lasted for 60 days. The reception rates were most of the time very close to 100%. Nevertheless, three crises are still identifiable. Two of them were concerning to

Fig. 4 (**a**) Reception rates of
frequency, temperature and
battery voltage
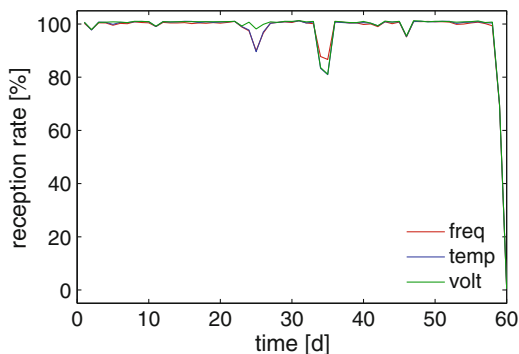
problems with the base station. The average reception rates over the test period were
better than 98%. Finally, the reason for the breakdowns of the serial connection
between base station and root node C0 could be identified. It was related to a bad
synchronization of the serial connection due to temperature effect on the clock of
the Tmote Sky hardware platform.

Conclusions

It took three years to set up a well functioning system on the Stork Bridge. Lazy
policy was applied to update the system and to fix errors, which meant that each
improvement was made for a specific reason. The decentralized and cooperative
nature of WSNs made it extremely difficult to definitively identify sources of failure.
Thus, the strength of WSNs turned out to be a severe drawback when trying to
debug and fix flaws. Although many experienced failures can still not be fully
explained, the main reason of the poor performance was the interconnection between
the different processes that was created by the time synchronization and the long
execution time of the initial data processing algorithm. Nevertheless, the good final
performance demonstrates that WSNs can be successfully applied in data intensive
long-term monitoring.

References

[1] Stoianov, I., Nachman, L., Madden, S., and Tokmouline, T. (2007) In: Proceedings of the 6th
International Conference on Information Processing in Sensor Networks (IPSN'07),
Cambridge, Massachusetts, U.S.A.

[2] Ming, X., Yabo, D., Dongming, L., Ping, X., and Gang, L. (2008) In: Proceedings of the 2008 IEEE International Symposium on Parallel and Distributed Processing with Applications, Sydney, Australia.

[3] Hoult, N.A., Fidler, P.R.A., Hill, P.G., and Middleton, C.R. (2010) *Journal of Bridge Engineering*, vol. 15, n. 2, pp. 153–159.

[4] Feltrin, G., Meyer, J., Bischoff, R., and Motavalli, M. (2010) *Structure and Infrastructure Engineering*, vol. 6, n. 5, pp. 535–548.

[5] Feltrin, G., Meyer, J., and Bischoff, R. (2006) In: Proceedings of the Third International Conference on Bridge Maintenance, Safety and Management (IABMAS'06), Porto, Portugal.

[6] Feltrin, G., Meyer, J., Bischoff, R., and Motavalli, M. (2009) In: Proceedings of the 4th International Conference on Structural Health Monitoring on Intelligent Infrastructure (SHMII-4), Zurich, Switzerland.

Identification of Structural Changes on a Movable Bridge

F.N. Catbas, M. Gul and H.B. Gokce

Abstract Movable bridges are unique structures in terms of their design, operation and maintenance. Florida has the highest number of bascule type movable bridges in the United States. According to Florida Department of Transportation (FDOT) engineers, movable bridges maintenance cost is considerably higher than that of a fixed bridge because of the problems encountered due to their proximity to waterways and special operational demands. Therefore, Structural Health Monitoring (SHM) can be used to track and evaluate incidents, anomalies, damage and deterioration in movable bridges. In this study, two most critical structural problems of a pilot movable bridge are monitored and evaluated by using a correlation based data analysis method. It is shown that the proposed methodology can be used to monitor the structural condition of the movable bridges effectively using traffic induced strain data.

Keywords Bascule • Bridge • Maintenance • Monitoring • Movable • SHM • Structural damage

Introduction

A large number of movable bridges, which are commonly used over the waterways, are owned and operated by the Florida Department of Transportation (FDOT) in United States. Movable bridges are complex structures utilizing machinery to open a portion of the bridge allowing for the passage of waterborne traffic. The majority of the movable bridges in Florida are of the bascule type, having interior spans called "leaves" that rotate upward and away from the centerline of the waterway thus providing a clear passage. Movable bridges also present significant drawbacks

F.N. Catbas (✉) • M. Gul • H.B. Gokce
Department of Civil, Environmental and Construction Engineering, University of Central Florida, Orlando, Florida, USA
e-mail: catbas@mail.ucf.edu

and problems associated with the operation and performance. According to FDOT officials, movable bridge rehabilitation and maintenance costs are about 100 times more than fixed type bridges. Deterioration is a concern since they are located over waterways, and often close to a coast with conditions suitable for corrosion that cause section losses. Maintenance costs associated with the operation system and mechanical parts require special expertise, and may cause extensive repair work that can cause an unexpected failure of bridge operation. Some early movable bridge examples in the US can be found but these publications give more details about the movable bridge types and their construction methodologies. A recent study about movable bridges can be found in [1]. Structural health monitoring can be considered as a promising approach to continuously monitor the structural, mechanical and even electrical components of a movable bridge mainly for bridge maintenance and predicting possible problems in advance. A monitoring system is an excellent tool for real-time asset management by infrastructure owners. Infrastructure owners may use flags and warnings as a mechanism to monitor/assess maintenance performance. The data may be used by the contractors in scheduling preventive maintenance to maximize the service life of the equipment and the structure. In this study, two main maintenance problems which are identified using the inspection reports will be discussed. Identification of these problems is achieved with the help of SHM.

Theory and Methodology

Collecting statistical information such as maximum, minimum, mean, standard deviation and correlation coefficients is an important step to deal with large amounts of data coming from long term monitoring applications. These preliminary statistical analyses offer an understanding of the data behaviour and thereby help to interpret the data more effectively. Consequently, statistical information collection from sensor channels can be employed for structural damage identification. In this study, correlation of the strain channels is employed for damage identification as a methodology. Cross correlation coefficient, which is a measure of similarity of two data sets in vector form, is a value between -1 and +1. Having similar behaviour in data sets gives higher correlation while low correlation indicates either low or no correlated response. The scatter plots shown in Fig. 1 illustrate the cross correlation between
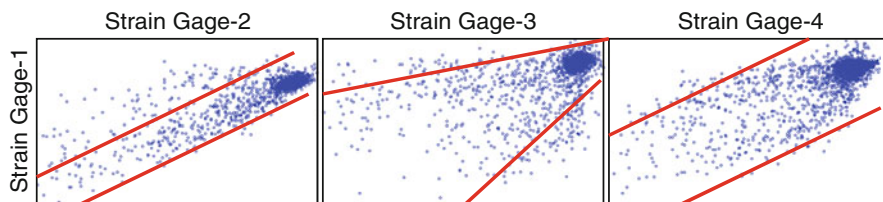
Fig. 1 Scatter plots of strain channels

two data sets. A closely bounded scatter plot indicates a high correlation, whereas the opposite means a low correlation. In these plots, bounded areas are also shown to give a better idea about the correlations. In light of this information, the authors decided to investigate the possible change in the correlation coefficients due to structural changes on a movable bridge for damage identification. The methodology can be summarized as follows: (1) Strain data is collected for the healthy and damaged cases. (2) A low-pass filter is used to eliminate the dynamic effects of the traffic in the strain data. (3) Correlation coefficient between two strain channels is tracked to see the changes before, during and after damage.

Representative Bridge and Monitoring System

In this section, the authors briefly present the monitoring design and implementation on a representative bridge (Fig. 2) in Florida. The selected representative movable span is the west-bound span of two parallel spans on Sunrise Boulevard Bridge (SBB) in Ft. Lauderdale. This span was constructed in 1989. It has double bascule leaves, with a total span length of 35.7 m, width of 16.3 m, carrying three traffic lanes. The bridge opens around 10-15 times a day.

The instrumentation plan is designed to monitor the most critical structural, mechanical and electrical components. The current installation consists of an array of 162 sensors which add up to 200+ channels. The monitored structural components include main girders, floor beams, stringers and live load shoes. As for the mechanical and electrical components, gear box, shafts, open gear, rack and pinion,

Fig. 2 Sunrise Boulevard Bridge (SBB)
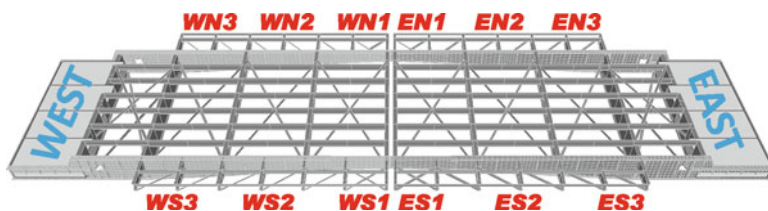
Fig. 3 Dynamic strain gage locations on SBB

trunnions and electrical motor are monitored with various sensors. In addition, a weather station is also installed to monitor and correlate the environmental factors. It should be noted only 12 Hitec-weldable-dynamic strain gages have been deployed for this study. These strain gages are placed on bottom flanges of the main girders with a data collection rate of 250Hz. The locations for the strain gages and corresponding nomenclatures are given in Fig. 3 For example, WN refers to West North and ES refers to East South. Three pre-scheduled 5 minute time slots (morning, early and late afternoons), corresponding to peak hours of operation, are selected for daily data collection. More details about the Sunrise Boulevard Bridge and instrumentation can be found in [2].

Structural Changes

The Live Load Shoe (LLS) are the support locations of the main girders when the bridge is in closed position (Fig. 4) If misaligned or improperly balanced, the bridge may not fully sit on the LLS. In that case, the dead load and traffic load are transferred to the gears and shafts, which cause damage to mechanical assemblies. Small gaps also lead the girders to pound on the live load shoes, which results in further misalignment, additional stresses, fatigue damage, and excessive wear. The Span Locks (SL) are used to connect the tip ends of two cantilever bascule leaves; therefore, both leaves are forced to deflect equally (Fig. 5). Consequently, this situation prevents a discontinuity in the deck during the operational traffic. The main concern for the span locks is that the coupling has to be loose enough to allow a proper opening operation, but at the same time, the gap between the bar and the receiver has to be small enough to ensure the adequate connection with minimal bouncing while vehicles cross from one leaf to the other. This is achieved by placing metallic sheets (or shims) to adjust the spacing.

The two structural damage scenarios for this study are LLS shim removal and Span Lock (SL) shim removal, which were identified using the inspection reports of movable bridges in Florida. A combined damage scenario was also applied to the structure. First, the West South LLS shims were removed, then the West South SL

Fig. 4 Live Load Shoe and shim removal

Fig. 5 Span Lock and shim removal

shims were removed for the combined damage scenario, and finally the LLS shims were installed again to see only the SL effect on the structure. In all cases the removed shims created a gap around 3.2 mm up to 4.8 mm.

Results

In this section, the results from the correlation studies are presented. These results are generated based on 35 different data sets before, during and after damage. First, 10 data sets were collected in 10 days to obtain the baseline level of the correlation coefficients before damage. Then, 15 data sets were collected (5 data sets for each structural change) on same day due to time consideration to illustrate the during damage correlation coefficient. Finally, 10 more data sets were collected in 10 day period to see whether the correlation coefficients are coming back to their original level after repair. Figure 6 shows the correlation coefficient change between the ES3 and WS3 strain gages during these tests. As seen from this plot, the correlation coefficients before damage cases are around -0.8, during LLS and LLS+SL damage cases are around -0.3. No significant change is observed between the first and second damage case. On the other hand, for the SL damage case the
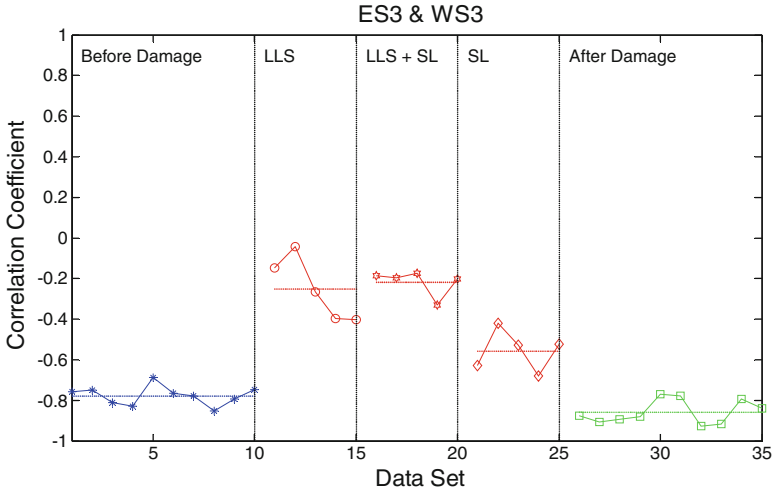
Fig. 6 Correlation change between ES3 and WS3
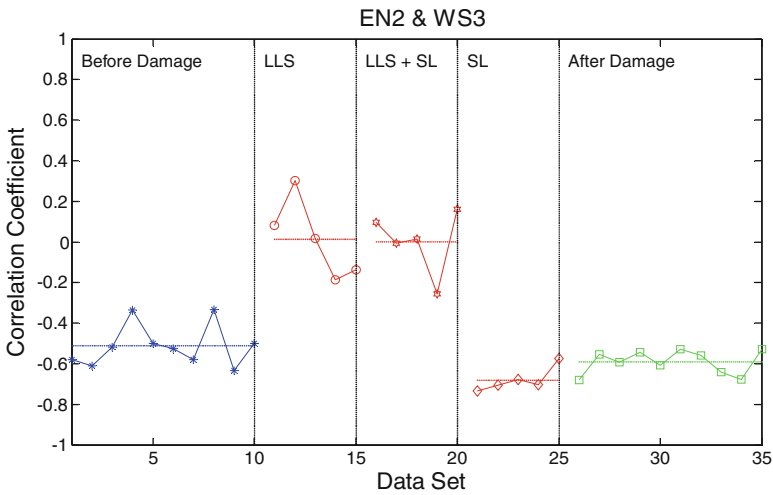
Fig. 7 Correlation change between EN2 and WS3

correlation coefficients are becoming around -0.5 and after damage these coefficients come back to the -0.8 level again but this time with a less standard deviation. The reason behind this is the significant effect of the maintenance. The trends of the correlation coefficients are also tracked for different strain gages. For example, correlation coefficient change between EN2 and WS3 can be seen in Fig. 7. Note that although the effect of the LLS damage on the correlation

coefficients is apparent in both plots, the SL damage is more visible in Fig. 6. The variations of the correlation coefficients are higher for the tip locations (WN1 and WS1) of the movable bridge because the levels of strains in these locations are lower than the other locations.

Conclusions

Based on the results summarized above, it is seen that this new and effective methodology can help track and detect the illustrated structural changes by means of correlation analysis of the traffic induced strain data. In addition, this approach can indicate the effectiveness of maintenance procedures, as it is shown that the level of correlation comes back to its original level prior to damage. This method is advantageous since it is appropriate for automation, it does not require knowledge about the traffic loading, it allows handling of large amounts of data and the results are easy to interpret. This approach is expected to help the bridge engineers and maintenance personnel to reduce the number of maintenance visits by giving early warnings about condition of the bridge.

References

[1] Wallner, M., and Pircher M. (2007), Kinematics of Movable Bridges. *ASCE Journal of Bridge Engineering*, vol.12, n. 2, p.147
[2] Catbas, F.N., Gul, M., Zaurin, R., Gokce, H.B., Terrell, T., Dumlupinar, T., and Maier, D. (2010), Long Term Bridge Maintenance Monitoring Demonstration on a Movable Bridge, submitted to Florida Department of Transportation (http://www.dot.state.fl.u...mary_STR/FDOT_BD548-23.pdf).

Experiences with Real-Life Fiber Optic Bridge Monitoring Installations

T. Graver, A. Mendez and K. Chandler

Abstract We present a brief overview of real-life bridge structural health monitoring (SHM) installations using fiber Bragg grating sensing technology. We review and describe the associated successes, challenges and lessons learned for SHM projects. In general, project successes are coupled to improved sensing tools: better sensor packages, simpler and less expensive instrumentation, improved installation techniques, and more efficient data analysis tools. Some shortcomings are the direct result or poor project planning and communications. Particular attention is given to the benefits and economics of instrumenting civil structures – when and how it pays.

Keywords Bridge monitoring • Fiber optics • Sensor integration • Structural health monitoring

Introduction

Over the last few years, fiber optic sensors (FOS) have seen increased acceptance and widespread use for industrial sensing and structural health monitoring (SHM) applications in composites, civil engineering, aerospace, marine, oil & gas, and defence. Given their EM immunity, intrinsic safety, small size & weight, and capability to perform multi-point and multi-parameter sensing remotely make of FOS an attractive, flexible, reliable and unique sensing solution. One of the most common applications is for strain/stress sensing, but a variety of other parameters such as temperature, pressure, magnetic field, voltage, chemical species and others, can also be measured using them. And, nowadays, a variety of rugged sensors and interrogation

T. Graver • A. Mendez (✉)
Micron Optics Inc., Atlanta, GA, USA
e-mail: amendez@micronoptics.com

K. Chandler
Chandler Monitoring Systems Inc., Lawrenceville, GA, USA

instruments are commercially available—offering attractive performance, ease of installation, reliability and reasonable pricing.

The technical requirements imposed by many SHM applications combined with the increased demand for practical, reliable, field-portable and low cost equipment to perform on-line measurements, has led to a new wave of commercial product and a push for the development of new optical fiber sensor solutions. However, can fiber optic sensing address the application needs and provide an economical, effective and reliable bridge monitoring alternative? This and other questions are aimed to be answered by way of reviewing a number of real-life bridge installation practical lessons learned, challenges and successes.

Fiber Optic Sensors & Instruments

Optical fibers, because their small size and light-weight, have the capability to be embedded within concrete structures—prior to curing—without affecting its properties and be used as sensitive, but rugged, transducers to measure the internal state of stress and act as an effective on-line SHM devices. Fiber optic sensors have attractive features that make them very suitable and, in some cases, the only viable sensing solution. Some of the key attributes of fiber sensors are summarized in Table 1:

Table 1 Benefits of fiber optic sensors (FOS)
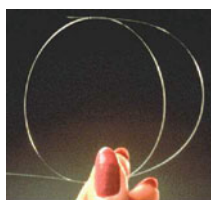
- *Galvanic isolation*
- *EMI immunity*
- *Intrinsically safe*
- *Passive: no need for electrical power*
- *Possibility of remote, multiplexed operation*
- *Small size and lightweight*
- *Integrated telemetry: fiber itself is a data link*
- *Wide bandwidth*
- *High sensitivity*

The basic principle behind FOS for SHM applications is that light sent through the fiber has its intensity, phase, wavelength or polarization altered by changes in the mechanical and thermal states of the surrounding host. Fiber optic strain and temperature sensors can also be surface-mounted onto concrete or steel surfaces and determine parameters of interest such as stress, strain, elongation, crack onset and growth, delamination and several others.

The Need for Structural Health Monitoring (SHM)

Since the condition of civil engineering works and infrastructure around the world is in a state of deterioration—due to aging of its materials, excessive use, overloading, weathering, lack of maintenance and proper inspection—it has become increasingly important in the last few years to determine the safety of a structure by the

non-destructive evaluation (NDE) of its strength and integrity. This as-assessment is essential for the repair, retrofit, rehabilitation, life extension or replacement of the structure in question. Furthermore, it is also frequently useful to develop means for the feedback and control of the state of health of a structure. In general, bridge owners must manage and ensure the safety of their structures even when their operation continues well beyond their design lifetime. Traditionally, most structures rely on strict maintenance procedures and visual inspections conducted every one to two years, but with very few or no permanently installed sensors. However, maintenance operations tend to be expensive; visual inspections can miss critical problems; and conventional electronic sensors can fail in harsh environments. When considering on-line SHM of bridge structures, there are really two key questions to address:

- *Is structural health monitoring (SHM) useful?*
- *When is it beneficial to use fiber optic sensors?*

Usefulness of SHM is typically more obvious for structures that have known problems. Selections of sensor type and placement are straightforward. Data analysis can be tailored to investigate a manageable set of hypotheses. But in a new structure—or in an older one that does not exhibit a particular problem—it is more difficult to justify the case for monitoring. Cost of adding a relatively comprehensive monitoring system to a new structure can add ½ to 1% to the total construction cost [1]. This cost would include the system hardware (instrumentation, sensors, cables, etc.) and installation into the structure. It does not include, however, the costs associated with data analysis.

Furthermore, sensing systems are very efficient in generating mountains of data. What to do with the vast amounts of data generated is, however, a tough challenge. Typically, engineers start with a mathematical model of the structure. This provides a base-line of comparison for the measured data and forms the guide for sensor placement on the structure. To date most data analyses have been performed by universities and research centers. Few mainstream civil engineering organizations (e.g., local departments of transportation) are well equipped, trained or funded to perform this type of analysis.

What is it worth to have the model, the data, and the answers? It is difficult to assign a monetary value for these endeavors. Certainly, if one avoids a catastrophic failure, the payback is clear. However other justifications are less tangible. For example, if more is learned about performance of a certain type of bridge over years or decades, then perhaps some design limits (i.e., costs) may be relaxed or useful-life standards increased. These have real value, but the payback is separated from the investment by generations.

For instance, Fig. 1 depicts a bridge fitted with a multi-sensor network—and video cameras—along its span. Measurements of strain, temperature, vibration, expansion, corrosion, and local weather conditions, are performed and collected through a collection of sensors interconnected by a common interrogation and data acquisition system. Having such capability renders the structure or building more "intelligent", whereby it is possible to know the condition and overall "state-of-affairs" of the bridge in question by examining in real-time and on-line the responses from individual sensors, as well as by facilitating the plotting of historical data—through
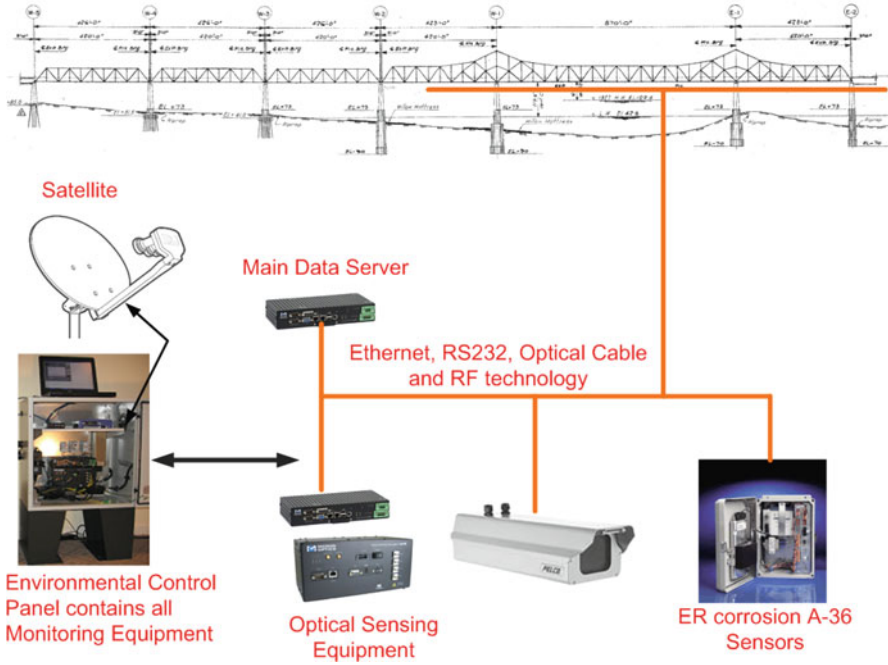
Fig. 1 Aspect of a bridge SHM configuration
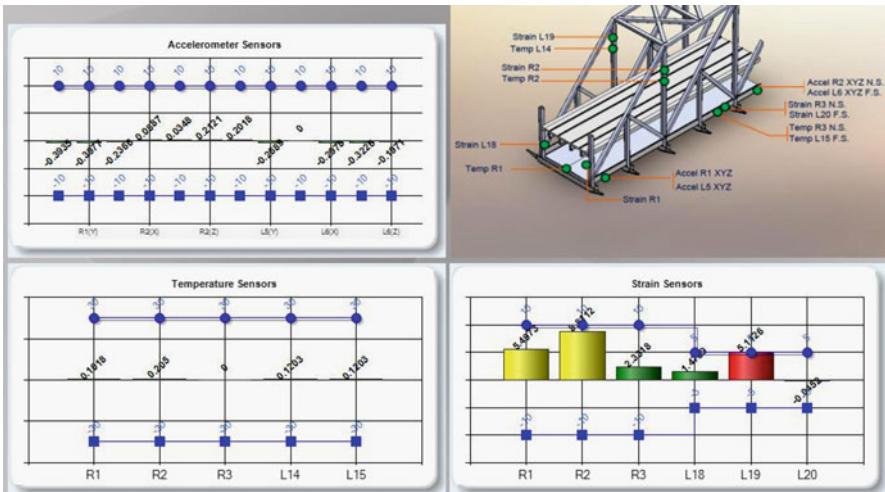
Fig. 2 Screen-shot image of IntelOptics® depicting the condition of a bridge and the readings of the various installed sensors

the use of dedicated graphical user interface (GUI) software coupled with storage databases—as depicted in Fig. 2, which shows the rendering of an instrumented bridge on top of which readings from individual in-stalled sensors can be monitored and accessed remotely, via the dedicated SHM managing software platform called IntelOptics®.

SHM Project Phases

There are three important phases to any SHM project: 1) *Pre-Installation*, 2) *Installation* and, 3) *Post-Installation*. Table 2 below provides a breakdown of the critical activities carried out within each phase. By far, the pre-installation is one of the most important, and where most care and attention must be paid. It is at this stage that the specific system's requirements and features; design and architecture; topology and communications; data analysis and storage; as well as expected project duration, scope and cost are defined and turned into a suitable SHM design.

To ensure a smooth running project and a successful operating SHM system, it is essential to maintain constant, continued and open discussions between all parties involved in the project but, primarily, between the customer/end-user and the system's designer/installer. Failure to do so, typically results in miscommunications that lead to project delays, cost overruns, erroneous selection of equipment, unrealistic expectations and an overall sense of dissatisfaction with the project, technology and SHM system. The converse is true—a well-defined, thoroughly explained and discussed project, with realistic expectations, timetables and well-defined objectives and expectations, leads to well-run and successful outcome SHM projects. Nevertheless, every SHM project is different and possesses its own set of challenges and technical hurdles.

Table 2 Phases of a SHM project

Pre-Installation	Installation	Post-Installation
• Project definition: scope & goals	• Laying of cables	• Final system test & re-programming
• Technical requirements & features	• Surface preparation	• Controlled testing
• SHM system design	• Sensor installation	• Initial system evaluation & trending
• Preliminary site visit & inspection	• Instrumentation installation	• Re-adjustment /programming
• Installation planning	• Data acquisition set-up & rogramming	• Repair & upgrades as needed
• Coordination with local authorities	• Initial test & system verifications	
• Securing of permits & insurance		
• Sensor integration & pre-assembly		
• Shipping, transportation & travel logistics		

Relevant Installation Issues and Considerations

A critical aspect of any SHM project—besides having good quality and reliable equipment—is the installation process. Better instruments and sensor packages have helped make installation easier and faster, but still about 50% of the cost of most FOS SHM systems lies in the installation alone. To mitigate some of these issues and possible cost overruns we recommend—based on our practical installation experience—to take the following actions.

Hence, start off with a sensible, flexible, and modular SHM system design that allows for sensors to be broken down into smaller sub-sets or installation sections. This will help facilitate the breakdown of the sensors' response for data processing and analysis, as well as to help compartmentalize any possible damage and the extent of impact of any sensor(s) malfunction. This also facilitates future system expansions, or replacement/upgrade of sensors.

Minimize the time required/spent on-site. This will help avoid prolonged bridge lane closures and traffic disruptions. Attempt to install sensors when the amount of construction activity—for a new bridge under construction—is minimal. This will avoid potential damage to the sensors and disruption to either working crew. In addition, it also helps have quieter background conditions to better define the zero-point operation for the sensors during their calibration.

Rely only on experienced personnel, familiar and trained with the use and handling of optical fibers and not afraid of working in heights, tight spaces, under harsh weather or in the presence of possible critters and rodents. Protect sensors and lead cables as much as possible and necessary. Cables needs to be properly laid out and, is possible and cost-effective, be protected by metallic conduit tubes and kept out of sight, to avoid potential vandalism and ensure a aesthetic, clean installation.

Conclusions

SHM systems have proven to be a useful tool for real time, on-line measurements of diverse mechanical and environmental parameters of a structure. Systems have been installed in a variety of different structures types. A common aspect of many SHM applications is the reliance on fiber optic sensors to perform measurements in ways that were not possible with other technologies. In general, commercial, off-the-shelf sensors, interrogation instruments, and installation methods are up to the task today. A growing number of installations around the world will drive continued improvement. Perhaps the biggest current challenge is to grow the number of available, qualified installers of fiber optic SHM systems.

Reference

[1] Doornink, J., et al, "Remote Health Monitoring of a High Per-formance Steel Bridge Using Fiber Optic Technology" http://www.ctre.iastate.edu/bec/index.cfm, Iowa State University, 2004.

Wireless Long-Term Monitoring of Asphalt Layer on a Motorway Bridge and Comparative Testing of Displacement

S.A. Bachmaier, A. Gordt, S. Jungmann and M. Krüger

Abstract Monitoring of civil structures is a growing application in nondestructive testing. Wireless systems supersede wired systems mainly by being easily deployable under various local structural conditions. The vast majority of today's existing structures are not equipped with monitoring systems by design. Wireless systems can still be installed as a retrofit. In the demonstration project described here, a 1350 m long motorway bridge over the Neckar River near Heilbronn, Baden-Württemberg, Germany was equipped with ambient and material temperature sensors as well as humidity sensors. The test setup is described in detail and interpretation of the data from initial measurements is provided. Furthermore, an assessment of the wireless monitoring system is presented, giving information about the packet drop rate, radio frequency calculations and wide-area network connectivity.

Keywords Asphalt layer • Distortion • Laser displacement measurements • Temperature monitoring • Wireless sensor network

System Description

Scope of Monitoring

On a motorway bridge over the river Necker near Heilbronn, Germany, in the past, the asphalt layer had to be replaced quite frequently. It is assumed that temperatures in the asphalt too high for its specification is the reason for the defects. The project's

S.A. Bachmaier (✉) • A. Gordt • S. Jungmann
Institute of Construction Materials, University of Stuttgart, Germany
e-mail: sebastian.bachmaier@iwb.uni-stuttgart.de

M. Krüger
Material Testing Institute, University of Stuttgart, Stuttgart, Germany
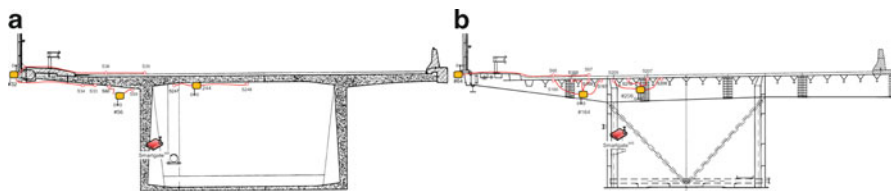
Fig. 1 (**a**) Cross section of concrete bridge (**b**) Cross section of steel bridge

intention is to monitor the temperature of construction elements and the environment for a period of 24 months. The bridge consists of a steel and a prestressed concrete section. Several sensors were installed in crosswise direction at each of the sections. Additionally, to link the temperature information with the actual asphalt degradation, lane grooves are measured at certain points in time with a laser displacement measurement system. The continuously collected monitoring data and the discrete reference data can be used to validate the hypothesis. The monitoring was carried out in the following ways:

1. Temperature measurement on prestressed concrete bridge (see Fig. 1a)

   - sensor in the transverse direction approximately every 1.0 m in the box girder and the cantilever area (8 temperature sensors in total, 2 of them including humidity sensors)
   - sensor on the edge of the truck lane in the pavement (2 temperature sensors)

2. Temperature measurement on steel bridge (see Fig. 1b)

   - sensor in the transverse direction approximately every 1.0 m in the box girder and the cantilever area (11 temperature sensors in total, 3 of them including humidity sensors)
   - sensor on the edge of the truck lane in the pavement (2 temperature sensors)

Wireless sensor network (WSN)

A wireless sensor network (WSN) measurement system was developed by the Institute of Construction Materials and the Material Testing Institute of the University of Stuttgart, together with TTI GmbH - TGU Smartmote, a university spin-off. The platform consists of a central processing board, a power board and sensor adaptation boards. These sensor adaptation boards are designed for a multitude of sensors and physical quantities. In addition to the hardware, operational software was designed. This comprises the node software, the data forwarder software on the WSN base station, the database connectivity and the data feature extraction and presentation. For a more thorough description of the system, refer to [1-3].
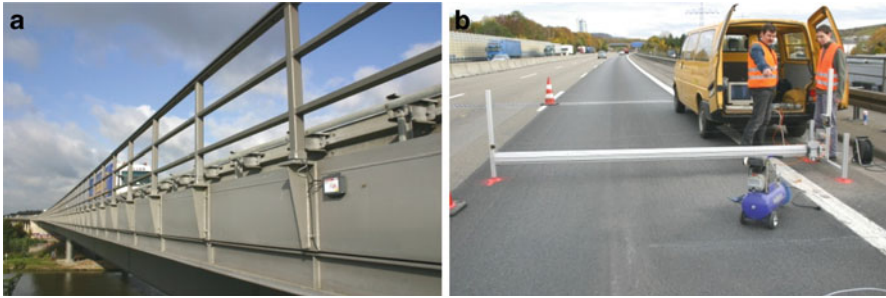
Fig. 2 (**a**) Installed wireless sensor node on the bridge (**b**) Lane groove measurements on a laser gantry

Installation of the WSN

Four temperature sensors were directly attached to the deck inside the box girder, another four sensors on the underside of the outer bracket. Additional two sensors were incorporated in a slot about 4 cm deep in the asphalt. Also an air temperature and humidity sensor was placed outside the bracket. These sensors are integrated into a wireless sensor node (air temperature and humidity) or attached to them (material temperature sensors). In most cases, two temperature sensors are connected to a wireless sensor node. Theoretically, the connection of up to four sensors is possible. Inside of the box girder, a base station was also installed. The base station continuously sends the measurement data via UMTS modem to the University of Stuttgart.

In Fig. 1, the two cross sections of both concrete and steel bridge are shown. Depicted are the base station, the sensor nodes and the sensors. Figure 2 a) shows one of the wireless sensors when installed on the bridge.

Measurement of the road surface profile

The measurement of the road surface profile was carried out using a laser distance measurement system. The laser slides on a rail from one side of the lane to the other and back again. The accuracy is about ± 0.5 mm relative to the height and about ± 2 mm relative to the worn track. The exact points of the first measurement were marked on the ground in order to use them for all following measurements.

The greatest challenge with the laser measurement were reflections from the sunlight. The brightness caused errors in the measurements, which had to be removed. See Fig. 2b) for the displacement measurement apparatus, which was operated from the van.

Measurement Results

Figures 3 and 4 show the lane grooves of the concrete bridge section and the steel bridge section, respectively. While the lane grooves for the concrete section are in the range of -8 mm to +20 mm, the steel section shows much higher grooves in the range of -20 mm to +50 mm. The clipping at 50 mm height results from the minimum displacement that the laser transducer is able to represent. The grooves on the steel bridge are much larger, most probably resulting from a higher temperature.

Figures 5 and 6 depict the temperate profile over four month in summer 2010. For the concrete bridge section, the maximum asphalt layer temperature occurred
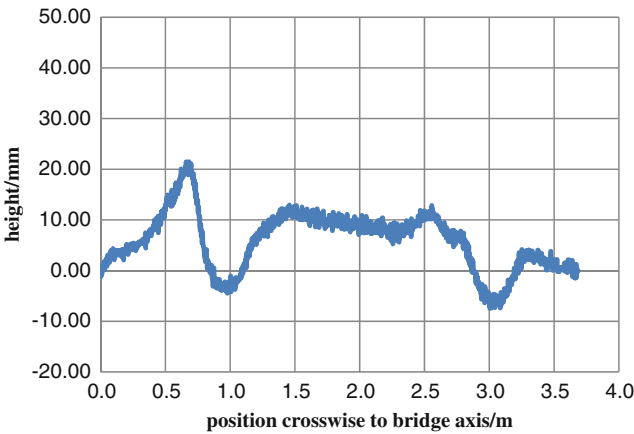
Fig. 3 Height profile of the concrete bridge section
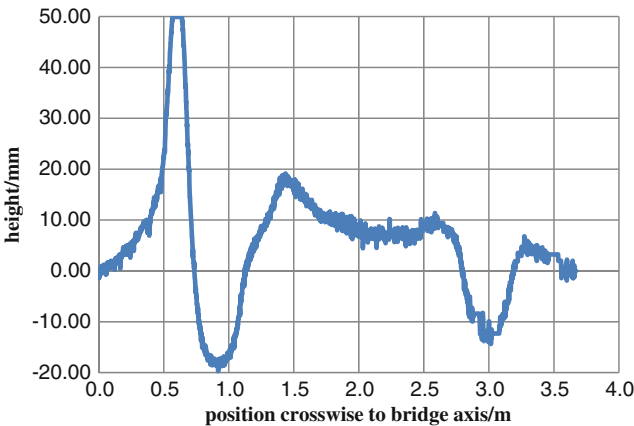
Fig. 4 Height profile of the steel bridge section
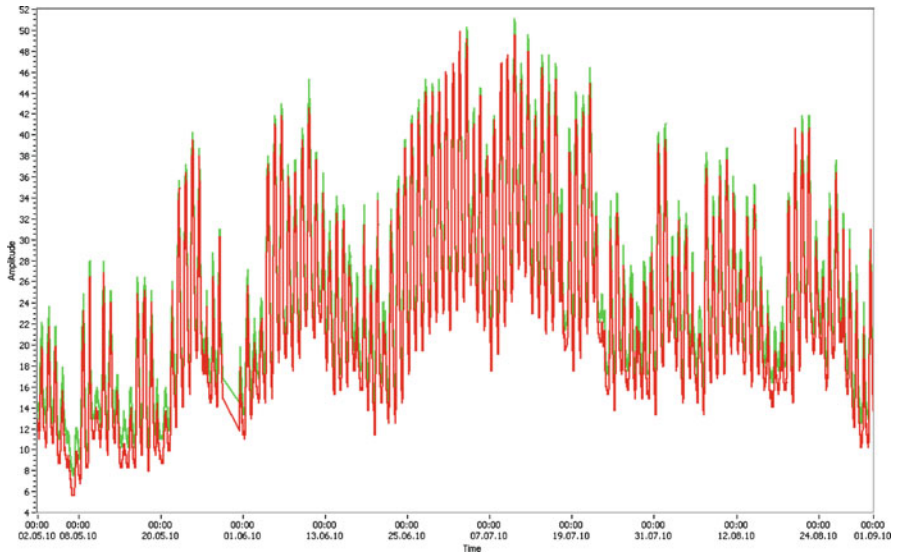
Fig. 5 Temperature profile of the concrete bridge section between 2010-05-01 and 2010-08-31. Green and red curve depict two separate sensors along the crosswise section with a distance of 2 m
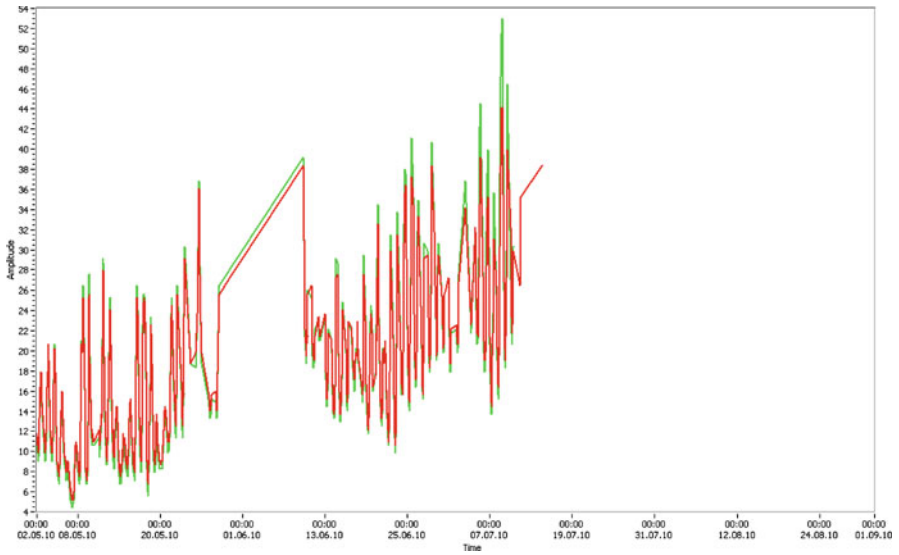
Fig. 6 Temperature profile of the steel bridge section between 2010-05-01 and 2010-08-31. Green and red curve depict two separate sensors along the crosswise section with a distance of 2 m

on 2010-07-10 with a peak temperature of 51 °C. On the steel bridge section, the maximum asphalt layer temperature occurred already on 2010-07-08 with a peak temperature of 53 °C. Unfortunately, after 2010-07-09, the sensors were removed during urgent maintenance work on the lane. The gap in measurement data beginning of June 2010 was due to transmission problems in the wireless sensor system. Reason was a mains power outage that is visible on both graphs, however, one of the base stations did not turn on again, when the mains was back on. For a more detailed description of the system failures and their analysis, refer to [3].

Conclusions

The expected outcome of the measurement campaign, that the higher temperature on the steel section of the bridge (due to the more light-weight construction) would justify the stronger development of lane grooves here, did not prove to be true. However, as far as the measurements show, the steel section does not show significantly higher absolute temperatures in summer. The day-night temperature span is a little larger, as the steel structure keeps less heat in its corpus and can cool down during night.

Due to the missing sensors from 2010-07-09 on, the evaluation cannot be continued as foreseen. However, further evaluations will have to be made, correlating the cumulative temperature-hours with the increase of the lane groove heights. This will be done also for the intermediate measurements of the lane profiles, which are not shown here. In addition, the temperatures of the girders and cantilevers will be taken into account.

References

[1] Bachmaier, S.A.; Krüger, M.; and Grosse, C.U. (2009): A Survey on Power Management for Long-Term Measurements using Wireless Sensor Networks. In: *4th International Conference on Structural Health Monitoring on Intelligent Infrastructure*. Zürich, Switzerland.

[2] Krüger, Markus; Grosse, Christian U.; Bachmaier, Sebastian A.; and Willeke, J. (2010): Wireless Monitoring of the Johanniskirche in Schwäbisch Gmünd. In: N. Banthia; A. Mufti (Ed.): *Conservation of Heritage Structures. 3rd International Workshop on Civil Structural Health Monitoring*. Vancouver: The University of British Columbia, S. 467–480.

[3] Bachmaier, Sebastian A. (2010): A Report on System and Radio Transmission Issues in a Star-Topology WSN. In: Reiner Kolla (Ed.): *9. Fachgespräch Sensornetze.* Würzburg, S. 63–66.

Eigenvector Normalization from Mass Perturbations: A Review

D. Bernal

Abstract Stochastic identification results are not sufficient to determine input-output relations because one constant for each identified mode is missing. Since the product of a mode and its constant is unique the constant can be absorbed into the modal scaling and it is in this context that the term eigenvector normalization is used in this paper. The seminal contribution in the normalization of operational modes is from Parloo et. al., whom, in a paper in 2002, noted that the required scaling can be computed from the derivative of the eigenvalues to known perturbations. This paper contains a review of the theoretical work that has been carried out on the perturbation strategy in the near decade that has elapsed since its introduction.

Keywords Eigenvector scaling • Modal models • Normalization • Operational modal analysis • Output-only identification • Sensitivities

Introduction

Results from operational modal analysis cannot be used to establish input-output relations because the information to properly scale the identified modes is unavailable. Since a number of applications in experimental dynamics and diagnostics are based on input-output maps, procedures to determine the proper modal scaling are of practical interest. The fundamental contribution in resolving the scaling issue is credited to Parloo et. al., [1], who showed that the information required is encoded in the derivatives of the eigenvalues with respect to known perturbations. The idea being, of course, that these derivatives can be estimated experimentally from changes in the eigenvalues obtained in two tests. Since perturbations of the mass are easiest to implement most of the work on the perturbation strategy has been restricted

D. Bernal (✉)
Civil and Environmental Engineering Department, Center for Digital Signal Processing, Northeastern University, Boston 02115
e-mail: bernal@neu.edu

to mass changes [1-5]. This paper focuses on contributions connected to algorithm development and does not, in particular, present a survey of experimental investigations or comparative studies.

Theoretical Preliminaries

The input-output relations of an arbitrarily damped, linear, time invariant system with N degrees of freedom can be expressed as a modal series in terms of complex eigenvalues λ and appropriately normalized complex eigenvectors, ψ as [6]

$$G(s) = \sum_{j=1}^{2N} \frac{\psi_j \, \psi_j^T}{s - \lambda_j} \tag{1}$$

For eq.1 to be valid the complex eigenvectors must be normalized such that

$$2\lambda_j \, \psi_j^T M \psi_j + \psi_j^T C \psi_j = 1 \tag{2}$$

where M and C $\in R^{NxN}$ are the mass and damping matrices [7]. Designating arbitrary normalized complex modes as φ one can write

$$\psi_j = \kappa_j \, \varphi_j \tag{3}$$

The objective of the mass perturbation strategy, when the complex mode model is selected, is to provide estimates of κ.

Normal Mode Model

In the special case where the damping distribution is (assumed) classical the relative phases in the eigenvectors are either zero or π and eq.1 can be written in terms of the modes of the undamped system as

$$G(s) = \sum_{j=1}^{N} \frac{\phi_j \, \phi_j^T}{s^2 + 2\omega_j \, \xi_j \, s + \omega_j^2} \tag{4}$$

where ω_j, ξ_j and ϕ_j are the undamped natural frequency, the fraction of critical damping, and the mass normalized eigenvector in the jth mode, respectively. The mass normalized modes satisfy

$$\phi_j^T M \phi_j = 1 \tag{5}$$

Expressing the mass normalized modes in terms of the arbitrarily normalized ones θ one has

$$f_j = \alpha_j \theta_j \tag{6}$$

and the objective of the mass perturbation strategy is to obtain estimates of α.

The Sensitivity Approach (Parloo et.al., 2002)

We present a derivation in the notation that is used throughout this paper and make the results explicit for both the complex mode and the normal mode model. We take the mass change as $\Delta M = \beta_0 M_1$, where β_0 is a scalar with units of mass, and M_1 is a distribution. When differentiating with respect to the magnitude of the perturbation the associated dummy variable is β.

<u>Complex Mode Model</u>

The polynomial eigenvalue problem is

$$\left[(M + \beta_0 M_1)\lambda^2 + C\lambda + K \right] \psi = 0 \tag{7}$$

Differentiating with respect to β, pre-multiplying by ψ^T and evaluating the result at $\beta=0$ one gets, after some simple algebra

$$(2\lambda \psi^T M \psi + \psi^T C \psi)\lambda^{'} + \psi^T M_1 \psi \lambda^2 = 0 \tag{8}$$

Substituting eq.2 into eq. 8 gives

$$\lambda^{'} = -\psi^T M_1 \psi \lambda^2 \tag{9}$$

from where it follows, adding the subscript j for specificity, that

$$\kappa_j^2 = \frac{-\lambda_j^{'}}{\varphi_j^T M_1 \varphi_j \, \lambda_j^2} \tag{10}$$

On the premise that only two tests are available the derivative has to be estimated with the forward difference and one has

$$\kappa_j^2 \cong \frac{\lambda_j - \overline{\lambda}_j}{\varphi_j^T \Delta M \varphi_j \, \lambda_j^2} \tag{11}$$

where $\overline{\lambda}$ is the eigenvalue in the perturbed condition.

Normal Mode Model

The undamped eigenvalue problem can be written as

$$K\phi_j = (M + \beta_0 M_1)\phi_j \gamma_j \tag{12}$$

where γ_j is the undamped eigenvalue. Differentiating with respect to β and evaluating at $\beta=0$ one gets

$$(K - M\gamma_j)\phi_j' = M\phi_j \gamma_j' + M_1\phi_j\gamma_j \tag{13}$$

Pre-multiplying by the transpose of the mode and recognizing that we've used the mass normalized mode gives

$$\gamma_j' = -\phi_j^T M_1 \phi_j \gamma_j \tag{14}$$

from where, substituting eq.6, one gets

$$\alpha_j^2 = \frac{-\gamma_j'}{\theta_j^T M_1 \theta_j \gamma_j} \tag{15}$$

On the premise that only two tests are available the derivative of the undamped eigenvalue has to be estimated with the forward difference and one has

$$\alpha_j^2 \cong \frac{(\gamma_j - \overline{\gamma}_j)}{\theta_j^T \Delta M \theta_j \gamma_j} \tag{16}$$

The Integration Approach (Parloo et.al., 2003)

To ensure accuracy in the finite difference estimate of the eigenvalue derivative the shift in the eigenvalue induced by the mass perturbation may need to be small because the relation between eigenvalue and perturbation amplitude is nonlinear. Small eigenvalue shifts, however, are random variables with large coefficients of variation and thus lead to large uncertainty on the estimated normalization constants. Parloo et.al., recognized this conflict and shortly after the appearance of [1] proposed an approach where the scaling constants are computed, not from the eigenvalue derivatives, but from the total changes in the eigenvalues. Here we designate the method proposed in [2] as the integration approach because the total eigenvalue changes are obtained by numerically integrating the eigenvalue vs mass perturbation relation. In the integration approach the formulation is nonlinear and the solution is obtained in an optimization context. It is opportune to note that, as is the case with all (general) formulations based on finite changes, the solution for the constants in the integration approach is modally coupled. To describe the algorithm let $\Delta\beta = \beta_0/q$ where q is an integer. By grouping the identified eigenvalues and eigenvectors in the

perturbed condition in the vector $\overline{\vartheta}$ and the matrix $\overline{\chi}$ and the corresponding quantities from the algorithm in $\overline{\vartheta}_A$ and $\overline{\chi}_A$ one can set a cost function that measures distance between the measurements and predictions, e.g.,

$$J = \left|(\overline{\vartheta} - \overline{\vartheta}_A)^T W_1 (\overline{\vartheta} - \overline{\vartheta}_A)\right| + \left|(\overline{\chi} - \overline{\chi}_A)^T W_2 (\overline{\chi} - \overline{\chi}_A)\right| \qquad (17)$$

where W_1 and W_2 are weighting matrices and it is understood that the estimated and measured eigenvectors should be normalized in some common fashion, e.g., to equal norm. The recursive approach is:

1) Select an estimate for the normalization constants for all the identified modes
2) Set j = 0
3) Compute the eigenvalue and the eigenvector derivatives for the assumed constants at $\beta = j\Delta\beta$ (expressions to be provided)
4) Let the eigenvalues and eigenvectors be expressed in a Taylor series about $\beta = j\Delta\beta$ and use the linear terms to estimate the eigenvalues and normalized eigenvectors at $\beta = (j+1)\Delta\beta$
5) Increase the counter, i.e., j = j+1
6) Repeat steps 3-5 until j = q.
7) Compute J from eq.17
8) Repeat from step #2 to minimize J.

While the integration approach incurs approximation from the fact that the update is done using a first order approximation this source of error can be made negligibly small by appropriate selection of the number of intervals q. Error from modal truncation, however, reflected in the fact that the eigenvector derivatives depend on all the modes, is a more important issue. In addition to the computational burden, which can be significant, another inconvenient feature of the integration approach is the fact that decisions have to be made regarding the weighting matrices W_1 and W_2.

Eigenvalue Derivatives

The derivatives of the eigenvalues in the complex and the normal mode model are given by eq. 9 and eq. 14.

Eigenvector Derivatives

For the sake of unity we designate the eigenvector derivative with respect to β as η_j and write it as

$$\eta_j = \Gamma Y j \qquad (18)$$

where Γ is a matrix that has all the appropriately normalized eigenvectors as its columns and $Yj = \{y_1 \quad . \quad y_k \quad .\}$. Taking r such that $r^T M_1$ is the diagonal of M_1 as a row vector one has [4,6]

Complex modes

$$y_k = \frac{\lambda_j^2}{(\lambda_k - \lambda_j)}(\psi_j^T M_1 \psi_k) \quad k \neq j \tag{19a}$$

$$y_k = -\psi_j^T M_1 \psi_j \lambda_j \quad k = j \tag{19b}$$

Normal modes

$$y_k = \frac{\gamma_j}{(\gamma_k - \gamma_j)}\phi_k^T M_1 \phi_j \quad k \neq j \tag{20a}$$

$$y_k = \frac{-\phi_k^T M_1 \phi_j}{2} \quad k = j \tag{20b}$$

Mode Invariance Approach (Brinker and Andersen 2004)

Consider the undamped eigenvalue problem in the original and the perturbed condition. Neglecting changes in the mode shapes due to the perturbation one finds that the scaling constant (for the normal mode model) is given by

$$\alpha_j^2 \cong \frac{(\gamma_j - \overline{\gamma}_j)}{\theta_j^T \Delta M \theta_j \overline{\gamma}_j} \tag{21}$$

Since the mode shapes do not change when the mass perturbation is proportional to the original mass one gathers that eq.21 tends to be most accurate when the mass perturbation is distributed. A comparison of eq.21 with eq.16 shows that the only difference is that in eq.21 the denominator contains the perturbed eigenvalue while the sensitivity approach uses the unperturbed one. Since γ and $\overline{\gamma}$ seldom differ by more than a few percent it follows that the two expressions usually provide similar results. The mode invariance scheme has only been developed for the normal mode model.

The Projection Approach (Bernal 2004)

The undamped eigenvalue problem in the perturbed condition, for mode j, is

$$K\overline{\theta}_j = (M + \Delta M)\overline{\theta}_j\overline{\gamma}_j \tag{22}$$

Expressing the perturbed mode on the basis of the unperturbed ones, namely, taking

$$\overline{\theta}_j = \theta_0 \Gamma j \tag{23}$$

where θ_0 is a matrix with all the identified unperturbed modes as its columns, and Γj is a vector. Substituting eq.23 into eq.22 one gets after some simple algebra

$$\alpha_k^2 = \frac{(\gamma_k - \overline{\gamma}_j)\Gamma j_k}{\theta_k^T \Delta M \overline{\theta}_j \overline{\gamma}_j} \tag{24}$$

where Γj_k is the kth entry of the Γj vector. Eq.24 shows that one can get as many estimates of the scaling constants as there are identified modes. Approximation in eq.24 comes from the fact that the exact value of Γj_k (i.e., the value that would be obtained from eq.23 if all the coordinates where measured and all the modes where identified) cannot generally be computed given the available information. In the real case measurements are limited and only a truncated modal space is available and the best estimate of the scaling constant is obtained when the constant for the kth mode is obtained using Γk_k (with this constant estimated from a least square solution of eq.23). As with the mode invariance method, only the normal mode model has been considered in the projection scheme.

The Receptance Method (Bernal 2011)

In the projection approach the number of sensors limits the number of modes that can be included in the projection (the columns in the θ_0 matrix) because otherwise the solution for Γj_k is not unique (we consider the over-determined case unique in the least square sense). The Receptance approach presented in [5] removes this limitation. A derivation of the Receptance scheme starts by noting that from eq.22 one can write

$$\left[K - M\overline{\gamma}_j\right]^{-1} \Delta M \overline{\theta}_j \overline{\gamma}_j = \overline{\theta}_j \tag{25}$$

and noting that the matrix in the parenthesis is the Receptance of the unperturbed system evaluated at $s = i\sqrt{\overline{\gamma}_j}$. Using the pole-residue form of the Receptance [6] one can write, therefore

$$\sum_{\ell=1}^{2N}\left(\frac{\phi_\ell \phi_\ell^T}{\gamma_\ell - \overline{\gamma}_\ell}\right)\Delta M\overline{\theta}_j\overline{\gamma}_j = \overline{\theta}_j \tag{26}$$

Substituting eq.6 into eq.26 gives

$$\sum_{\ell=1}^{2N}\theta_j\overline{\gamma}_j\left(\frac{\theta_\ell \Delta M\theta_\ell^T}{\gamma_\ell - \overline{\gamma}_\ell}\right)\alpha_\ell^2 = \overline{\theta}_j \tag{27}$$

One notes that eq.27 gives a projection of the perturbed mode on the original basis but, in contrast with the scheme in [4], the projection coefficients are given explicitly. When all the modes are identified eq.27 yields the exact solution independently of the number of measurements. Although approximation remains in the modally truncated case, the system of equations implicit in eq. 27 generally offer the best approximation to the scaling constants among the existing alternatives.

The Receptance Approach in the Complex Model (Bernal 2011)

The Receptance approach has been recently extended to the complex modal model in [8]. The derivation follows along the same lines as in the normal mode case and we do not present it in detail due to space constraints. The final expression, however, is

$$\sum_{\ell=1}^{n}\frac{\varphi_\ell(\varphi_\ell^T \Delta M\overline{\varphi}_j)\overline{\lambda}_j^2}{\lambda_\ell - \overline{\lambda}_j}k_\ell = \overline{\varphi}_j \tag{28}$$

where n is the number of identified complex modes (including conjugates). It is useful to note that the system of equations implicit in eq.28 can be written as

$$Q\kappa_I = vec(\overline{\Phi}) \tag{29}$$

where vec is the column stacking operator, $\overline{\Phi} = \begin{bmatrix}\overline{\varphi}_1 & . & \overline{\varphi}_n\end{bmatrix}$ $\kappa_I = \{\kappa_1 \quad \kappa_2 \quad . \quad \kappa_n\}$, and

$$Q = \begin{bmatrix}\Phi \chi_1 \\ \Phi \chi_2 \\ . \\ \Phi \chi_n\end{bmatrix} \tag{30}$$

with $\chi_j = diag(a_j^1, a_j^2, ... a_j^n)$ and

$$a_j^i = (\frac{\overline{\lambda}_j^2}{\lambda_i - \overline{\lambda}_j})\varphi_i^T \Delta M\overline{\varphi}_j \tag{31}$$

Concluding Remarks

Scaling constants for normalizing operational modes obtained from identification results are random variables. Given a set of probability distributions governing the eigenvalue and eigenvector entries the objective is to select a testing protocol and an analytical computation scheme such that practical constraints are satisfied and the error in the scaling constants is a variable with zero mean and a variance that is as small as possible. Given that there is no such thing as the "exact normalization" of a mode that is itself approximate (due to error in the identification) selection of error measures and criteria to compare the performance of the various alternatives has to be done with care. Formulation of guidelines for deciding between one algorithm and another requires that the problem be looked at in a probabilistic framework because variability of the identification is a critical component. Work in this direction is currently ongoing.

References

[1] Parloo, E., Verboven, P., Guillaume, P., and Van Overmeire, M., (2002). "Sensitivity-based operational mode shape normalization", *Mech. Syst. Signal Process*, 16, pp. 757–767.
[2] Parloo, E., Verboven, P., Cuillame, P., and Overmeire, M. V., (2003). "Iterative calculation of nonlinear changes by first-order approximations", *Proc. of the 20th Int. Modal Anal. Conf.*, Orlando FL., pp. 1084–1090.
[3] Brinker R., and Andersen P., (2004). "A way of getting scaled mode shapes in output-only modal testing", *Proc. 21st Int. Modal Anal. Conf.* – on CD.
[4] Bernal D., (2004). "Modal scaling from known mass perturbations", *J. Eng. Mech.*, ASCE, (130), 9, pp. 1083–1088.
[5] Bernal D., (2011)."A receptance based formulation for modal scaling using mass perturbations", *Mech. Syst. Signal Process*, 25(2) pp. 621–629.
[6] Heylen W., Lammens S., Sas P., (1997). Modal Analysis Theory and Testing, Departement Werktuigkunde, Katholieke Universiteit Leuven, Heverlee.
[7] Balmes E. (1997). "New results in the identification of normal modes from experimental complex modes", *Mech. Syst. Signal Process*, 11(2), pp. 229–243.
[8] Bernal D., (in review). "Complex eigenvector scaling from mass perturbations", *J. Eng. Mech.*, ASCE.

Health Monitoring of a Benchmark Structure Using Vibration Data

B. Gunes

Abstract Aging and deterioration of existing structures and the need for rapid assessment and evaluation of these structures for hazard mitigation has significantly expanded the research efforts in the field of structural health monitoring (SHM). SHM involves monitoring of a structure using periodically sampled measurements, extraction of damage sensitive features from these measurements, and assessment of the current health state/integrity of the system. The approach known as the Damage Locating Vector (DLV) technique is an SHM tool that interrogates changes in the flexibilities synthesized at sensor locations using the vibration data with respect to the location of damage. This paper presents the damage identification results of the Phase II Experimental Benchmark Structure of the IASC-ASCE Task Group on Structural Health Monitoring.

Keywords Damage assessment • DLV • Global methods • Localization • Vibration-based SHM

Introduction

Structural health monitoring (SHM) is the process of implementing a damage identification strategy for civil infrastructures. Damage identification problem involves detection, localization and assessment of the extent of damage in a structure so that its remaining life can be predicted and possibly extended. SHM encompasses both local and global methods of damage identification. The local methods include visual inspections and non-destructive evaluation tools such as acoustic emission, ultrasonic, magnetic particle inspection, radiography and eddy current. All these techniques, however, require apriori localization of the damaged zone and

B. Gunes (✉)
Civil Engineering Department, Atılım University
e-mail: bgunes@atilim.edu.tr

easy access to the portion of the structure under inspection. As an alternative that overcomes these limitations, global vibration based methods have been widely developed over the years [1, 2].

Most of the existing damage identification methods can be classified into two groups: model-based and non-model or feature-based methods. The model-based methods are essentially model updating procedures in which the mathematical model or the physical parameters of a structure is calibrated or updated using vibration measurements from the physical structure [3, 4]. Analytical sensitivities of response parameters to changes in physical properties are used to update modeling assumptions, physical sizing, elastic moduli, etc. The feature-based approaches detect structural changes by detecting damage features in the measured data without the need for an analytical model of the structure. The main task here is the extraction of damage features sensitive to structural changes so that damage can be identified from the measured vibration response of civil engineering structures. Natural frequency based metrics, mode shape based metrics, structural damping based metrics, modal strain energy based metrics, flexibility based methods and other matrix perturbation approaches, pattern recognition, neural networks and other statistical approaches, non-linear methods based on advanced time-variant transforms are the most commonly utilized features proposed in the literature for detecting damage in civil engineering structures. A critical review of the damage assessment methodologies based on the research and applications reported in the literature can be found in [5].

IASC-ASCE Phase 2 Experimental Benchmark Structure

The experimental benchmark problem is the 4-story, 2-bay by 2-bay steel-frame scale-model structure shown in Fig. 1. The structure is 2.5m × 2.5m in plan and is 3.6m tall. The nine vertical columns are bolted to a steel base frame, and the lower flanges of two of the base beams are encased in concrete, fixing the steel frame to the concrete slab. The members are hot-rolled, grade 300W steel which are specifically designed for this scale model test structure. The columns are B100x9 sections and the floor beams are S75x11 sections. In each bay the bracing system consists of two 12.7 mm (0.5 in) diameter threaded steel rods placed in parallel along the diagonal. One floor slab is placed in each bay per floor: four 1000 kg slabs at each of the first, second and third levels, four 750 kg slabs on the fourth floor. These masses are fixed to the structure using two channel sections to bolt each mass to the steel frame. The mass of each channel section is approximately 9.75kg for a total of 19.5 kg per mass for two channels. Fifteen accelerometers were placed throughout the frame to measure the responses of the test structure and on the base of the frame; 2 per floor measuring the north-south motion of the structure (along the strong axis), and 1 measuring the east-west motion of the structure (along the weak axis). A series of ambient and forced excitation including hammer and shaker tests were conducted on the structure with various damage scenarios as shown in Table 1. In the tests, damage is simulated by removing braces in the structure or by loosening the bolts at beam-column connections [6].

Fig. 1 (**a**) Benchmark structure, (**b**) beam-column connection, (**c**) a sample accelerometer

Table 1 Description of Test Cases

Case	Configuration
1	Fully braced configuration
2	All east side braces removed
3	Removed braces on all floors in one bay on southeast corner
4	Removed braces on 1st and 4th floors in one bay on southeast corner
5	Removed braces on 1st floor in one bay on southeast corner
6	Removed braces on all floors on east face, and 2nd floor braces on north face
7	All braces removed on all faces
8	Configuration 7 + loosened bolts on all floors at both ends of beam on east face, north side
9	Configuration 7 + loosened bolts on floors 1 and 2 at both ends of beam on east face, north side

Estimation of Modal Parameters

Stabilization/Consistency Diagram involves tracking of the modal parameters as a function of increasing model order to obtain the correct modal parameters. Figure 3 illustrates these diagrams for Tests 1 and 9. Once the diagram is prepared, the user is left with the task of separating the physical modes from the computational ones and choosing an estimate among several alternatives, that best represents a mode. The consistent-mode indicator function (CMI) can be utilized as a measure to select the better of two alternatives [7]. Using the Stabilization diagrams together with the CMI function, the identified modal parameters for the selected tests are shown in

Table 2 Modal properties of the braced structure: Healthy and damaged cases (Translation Dominated = TR, Torsion Dominated = TO and Strongly Coupled = SC)

	Braced Structure							
	Test 1 (undamaged case)				Test 4 (damaged case)			
No.	f (Hz)	zai(%)	CMI (%)	Mode	f (Hz)	zai (%)	CMI (%)	Mode
1	7.44	0.77	92	TR	7.25	0.85	89	TR
2	7.65	0.64	86	TR	7.56	0.65	97	TR
3	14.45	0.39	88	TO	13.93	0.24	76	TO
4	19.86	0.32	90	TR	19.66	0.36	77	TR
5	20.88	0.42	69	TR	19.93	0.59	80	TR
6	24.74	0.27	89	TR				
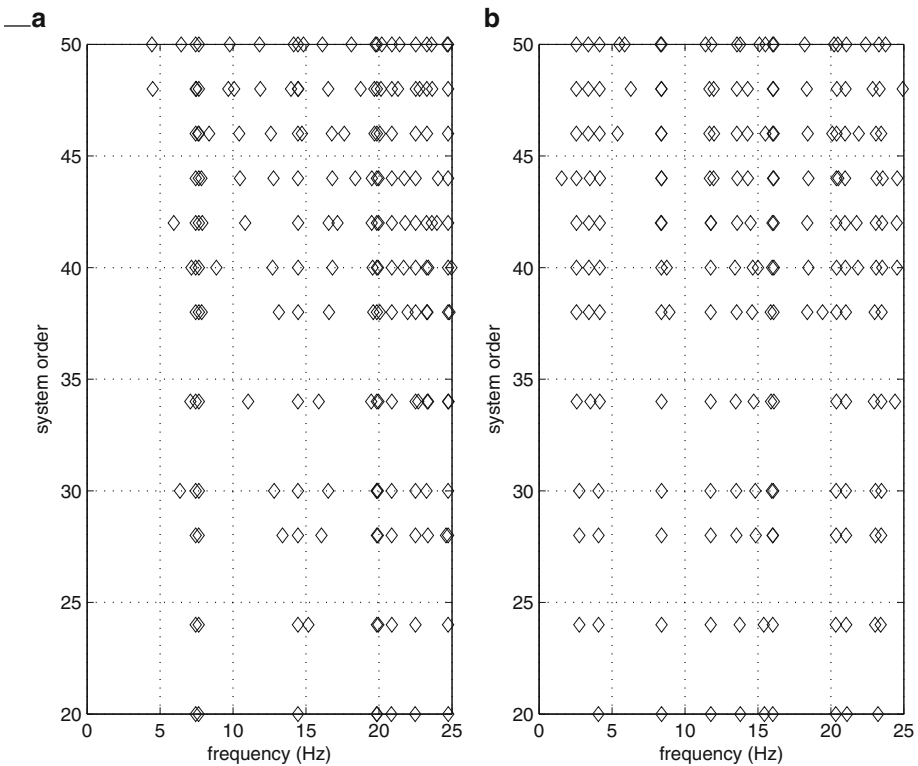
Fig. 2 Stability Diagram for the modal frequencies : (**a**) Test 1, (**b**) Test 9

Table 2. Note that both the fully braced test case (Test 1) and unbraced case (Test 7) are selected to represent the two healthy systems and Tests 4 and 9 are selected as the damage scenarios of these two structures, respectively. Eigensystem Realization Algorithm (ERA) was performed by computing several realizations with varying Hankel matrix size, forming a stabilization diagram as shown in Fig. 2,

Table 3 Modal properties of the unbraced structure: Healthy and damaged cases (Translation Dominated = TR, Torsion Dominated = TO and Strongly Coupled = SC)

| | *Unbraced Structure* | | | | | | | |
| | Test 7 (undamged case) | | | | Test 9 (damaged case) | | | |
No.	f(Hz)	ζ(%)	CMI (%)	Mode	f(Hz)	ζ(%)	CMI (%)	Mode
1	2.63	0.36	85	TO	2.57	0.53	98	TO
2	3.60	0.74	84	SC	3.39	0.90	86	SC
3	4.32	0.50	82	TR	4.16	0.36	99	TR
4	8.44	0.36	92	SC	8.38	0.36	100	SC
5	11.93	0.49	98	TR	11.66	0.39	93	TR
6	13.91	0.38	83	SC	13.58T	0.50	91	SC
7	16.15	0.32	91	TR	16.03	0.30	99	TR
8	21.58	0.37	73	TR	20.35	0.81	68	TR
9	23.57	0.66	74	TR	21.05	0.67	69	TR
					23.24	0.74	81	TR

and selecting the best-extracted modal parameters. The realization leading to a higher complex mode indicator function (CMI) is selected as the correct mode as shown in Tables 2 and 3.

Localization of Damage

Damage Locating Vector approach [8, 9] which is based on computing a set of vectors, DLVs that have the property of inducing stress fields whose magnitude is zero in the damaged elements, is utilized to localize damage. In this approach a weighted stress index (WSI) is computed using a statical model of the structure with a characterizing stress selected based on the type of the structure. The potentially damaged elements are identified as those having WSI<=1.0. It should be mentioned that DLVs are computed strictly from the data and the undamaged topology is required to compute the stress fields caused by the DLVs.

A 3-D 12-DOF shear building model is used to represent the undamaged model of the structure and the characterizing stress is selected as the story shears and the average of the end moments of the beams for the braced and the unbraced structure, respectively. The associated WSI indices of both cases computed for the frames in North-South and East-West directions are tabulated in Table 4.

As can be seen from the table, although the approach successfully localized the first and the second floor beams of the frames in the North-South direction as potentially damaged with WSI<1.0, for the unbraced frame; only the fourth floor of the North-South frame has a WSI less than 1 in the braced frame case. The first floor of the North-South frame, with a WSI=4.62, appears to be a 'false negative' localization. Approximation in the extraction of the flexibility coefficients and the discrepancy between the model used to compute the stress field given the DLVs and the real

Table 4 Weighted Stress Index for the braced and unbraced frame

Floor	WSI -Braced Frame (*case 4*) [removed braces on 1st and 4th floors]		WSI- Unbraced Frame (*case 9*) [loosened bolts on floors 1 and 2]	
	North-South	East-West	North-South	East-West
1	4.62	6.73	0.25	4.36
2	7.87	6.92	0.31	4.59
3	5.09	9.68	7.31	5.51
4	0.97	5.71	2.03	3.09

structure at the healthy state are the two main sources of errors that could lead to this 'false negative' identification. In this case however, one could speculate that it is the error in the estimation of the flexibility that has dominated since only one dominantly torsional mode was identified. Yet, still the fact that the DLV method provided a 'true' ranking of the elements for the potentially damaged set which can be a very useful feature in prioritization for the screening purposes.

References

[1] Sohn H., Farrar C.R., Hemez F.M., Shunk D.D., Stinemates D.W., and Nadler B.R. (2003) A review of structural health monitoring literature: 1996–2001, Los Alamos National Laboratory, USA.

[2] Chang, P. C., Flatau, A. and Liu, S. C. (2003) Review Paper: Health Monitoring of Civil Infrastructure. *Structural Health Monitoring*, 2(3); 257–267.

[3] Zimmerman DC, Kaouk M. (1992). Eigenstructure assignment approach for structural damage detection. *AIAA Journal*, 30(12), 1848–1855.

[4] Fritzen CP, Jennewein D, Kiefer T. (1998). Damage detection based on model updating methods. *Mechanical System Signal Process*, 12(1), 163–186.

[5] Gunes, B. and Gunes, O. (2010) From Structural Health Monitoring to Damage Assessment: A Critical Review, 9th International Congress on Advances in Civil Engineering, Trabzon, Turkey.

[6] Dyke, S. J., Bernal, D., Beck, J. and Ventura, C. (2004) Experimental Phase II of the Structural Health Monitoring Benchmark Problem. 16th Engineering Mechanical Conference.

[7] Pappa, R. (1994), *Eigensystem Realization Algorithm User's Guide for VAX/VMS Computers*, NASA TM 109066, 1994.

[8] Bernal, D. (2002) Load vectors for damage localization. *Journal of Engineering Mechanics*, 128(1), 7–14.

[9] Bernal, D. and Gunes, B (2004) A flexibility based approach for the localization and quantification of damage: A benchmark application. *Journal of Engineering Mechanics*, 130, 61–70.

Applying Alternative Identification Methods in Eccentric Mass Shaker Experiments

U. Karacadağlı and H. Luş

Abstract When eccentric mass shakers are used for forced vibration testing of actual structures, the Peak Picking Method is generally used for identifying modal parameters. Here we investigate the applicability of two time domain methods, namely the Eigensystem Realization Algorithm applied with Auto Regressive Exogeneous Models and the Covariance Driven Stochastic Subspace Method, and one frequency domain method, namely the Frequency Domain Decomposition Method, as alternatives to Peak Picking. To this end, a finite element model of a 3-storey building is prepared and forced vibration tests are simulated on this model based on the properties of the eccentric mass shaker present at the Boğaziçi University Structures Laboratory. Biases in modal parameter estimates are analyzed via Monte Carlo simulations and it is observed that identified mode frequencies and damping ratios fall within $\pm 3\%$ of the actual values, and that the identified mode vectors have MAC numbers higher than 0.95.

Keywords COV-SSI • Eccentric mass shaker • ERA • FDD • System identification

Introduction

System identification in structural engineering is the inverse problem of finding various properties of a system based on input-output or output measurements alone. Generally in experimental system identification the system is excited using some device that induces step, sinusoidal or random signals as to the system, and input-output signals are observed over a time interval. After the experiment, the first step is to choose an identification method and to determine the parameters of

U. Karacadağlı (✉) • H. Luş
Dept. of Civil Engineering, Boğaziçi University, Istanbul, Turkey
e-mail: karacadagli@gmail.com

the mathematical model. The model thus obtained may then be tested to see whether it is accurate or not. If it is not, with the feedback of the model, the procedure is repeated until the best fitted model is found. In structural system identification the desired set of parameters are generally the modal parameters.

Up until 1950s, much of system identification in engineering and control fields relied on Bode, Nyquist and Ziegler-Nichols charts or on step response analysis. Two seminal papers published in 1965 paved the way to two main identification techniques. The first one was the paper of Ho and Kalman [1] that gave birth to the development of subspace identification and the second one was the paper of Aström and Bohlin [2] that contributed to prediction error identification [3]. The solution of state-space realization problem was further improved by Akaike [4]. In the early nineties researchers found solutions to the problem of combining subspace identification and stochastic realization theory. Larimore [5], Van Overschee and de Moor [6] and Viberg [7] provided various algorithms for Stochastic-Subspace Identification (SSI).

System identification experiments can be classified in two main groups. The first one is forced vibration testing which is based on applying a controlled force to a structure, measuring the applied force if necessary and possible, measuring the response of the structure, and identifying system parameters according to the specified model. Forced vibration testing generally aims to estimate frequency response functions (FRFs) or impulse response functions which are the inverse Fourier transform of the frequency response functions. The second group is ambient vibration testing in which the response of the test structure to ambient effects is measured and this output data is used in identification. In this study, forced vibration tests via eccentric mass shakers are discussed. Eccentric mass shakers are machines that apply sinusoidal forces on structures via rotating masses. Typical eccentric mass shakers have one or two rotating masses whose eccentricity and configuration can be arranged to produce various force time histories.

System Identification Methods

ERA with ARX

Auto-Regressive models with eXogenous inputs (ARX) may be used to mathematically represent linear dynamical structural systems. An ARX model in time domain can be written as:

$$\sum_{k=0}^{p} \alpha_k \mathbf{y}(t_i + k) = \sum_{k=0}^{p} \beta_k \mathbf{u}(t_i + k) \tag{1}$$

where α and β are ARX coefficient matrices, $\mathbf{y}$ is the output, $\mathbf{u}$ is the input, and p is the ARX model order. This model implies that the output at the current time step can be written in terms of p previous outputs and p previous inputs and the current input. This is the prediction of current measurement from previous data and it is called forward-in-time prediction. By rearranging the coefficients and input-output data, one can obtain an overdetermined set of equations (if sufficient data exists) and the least-squares estimate for the coefficients of the ARX model can be derived. To make sure that the identified ARX model corresponds to a minimal realization, the Eigensystem Realization Algorithm (ERA) [8] may be employed. To this end, Markov parameters of the system are derived using the identified ARX model. ERA commences by constructing an initial Hankel matrix and finding its singular value decomposition as:

$$\mathbf{H}(0) = \begin{bmatrix} \mathbf{Y}_1 & \mathbf{Y}_2 & \cdots & \mathbf{Y}_h \\ \mathbf{Y}_2 & \mathbf{Y}_3 & \cdots & \mathbf{Y}_{h+1} \\ \vdots & \vdots & \vdots & \vdots \\ \mathbf{Y}_f & \mathbf{Y}_{f+1} & \cdots & \mathbf{Y}_{f+h-1} \end{bmatrix} = \left[\mathbf{U}_n \mathbf{S}_n^{1/2} \right] \left[\mathbf{S}_n^{1/2} \mathbf{V}_n^T \right] = \mathbf{O}_f \mathbf{C}_h \tag{2}$$

where $\mathbf{Y}_i$ is the i'th Markov parameter, n is the number of non-zero singular values and also the order of the state space model, $\mathbf{U}_n$ and $\mathbf{V}_n$ are the first n left and right singular vectors respectively, $\mathbf{S}_n$ is the $n \times n$ diagonal matrix of non-zero singular values, $\mathbf{O}$ and $\mathbf{C}$ are the observability and controllability matrices, h and f are the number of block rows and columns of Hankel matrix,respectively. All the coefficient matrices of the state space model can be retrieved from the observability and the controllability matrices. The success of the approach depends on determining the true "model order" of the system which is not a trivial problem with real life data since there are always noise and modeling errors leading to spurious "noise" modes in the identified model. To overcome this problem a stabilization diagram approach ([9]) is applied. The modes that consistently (according to chosen criteria) appear in various model orders are considered stable and are most likely to be physical modes.

Covariance driven stochastic subspace identification (COV-SSI)

COV-SSI algorithm [10] starts with calculation of output covariances defined as:

$$\mathbf{R}_i = E\left[\mathbf{y}(k+i)\mathbf{y}(k)^T \right] = \lim_{l \to \infty} \frac{1}{l} \sum_{k=0}^{l-1} \mathbf{y}(k+i)\mathbf{y}(k)^T \tag{3}$$

where $E[\bullet]$ is the expected value operator and $\mathbf{R}_i$ is the $m \times m$ output covariance matrix for a lag of i time steps. These covariance matrices are used to set up the following Toeplitz matrix and its singular value decomposition as:

$$\mathbf{T}_i = \begin{bmatrix} \mathbf{R}_i & \cdots & \mathbf{R}_1 \\ \vdots & \ddots & \vdots \\ \mathbf{R}_{2i-1} & \cdots & \mathbf{R}_i \end{bmatrix} = \begin{bmatrix} \mathbf{U}_n \mathbf{S}_n^{1/2} \end{bmatrix} \begin{bmatrix} \mathbf{S}_n^{1/2} \mathbf{V}_n^T \end{bmatrix} = \mathbf{O}_n \Gamma_n \tag{4}$$

Once the observability matrix is constructed, the output and the state transition matrices of the state space model may be obtained. Once again a stabilization – and - clustering approach is recommended to distinguish true system modes in an automated fashion ([11]).

Frequency domain decomposition (FDD)

Output only FDD is a combination of the peak picking method and the Complex Mode Indication Function (CMIF). Peak picking method is inaccurate especially when close modes are present and the CMIF method is inapplicable when input data set is not measurable. FDD is superior in that sense to both CMIF and the peak picking method. The CMIF is defined by Shih et al. [12] as the singular values of $[\mathbf{H}(i\omega)][\mathbf{H}(i\omega)]^T$ where $\mathbf{H}$ is the frequency response function matrix. In the CMIF method all singular values are plotted and in this plot the peaks of the highest singular values vector show modal frequencies. Since the spectrum of a white noise input will be constant, the output spectrum is given by:

$$\mathbf{G}_{yy}(i\omega) = \mathbf{H}(i\omega)\mathbf{G}_{xx}(i\omega)\mathbf{H}(i\omega)^T = K\mathbf{H}(i\omega)\mathbf{H}(i\omega)^T \tag{5}$$

where $\mathbf{G}_{yy}$ is the output spectrum, $\mathbf{G}_{xx}$ is the input spectrum, and K is a constant [13]. Then the SVD of the output spectral density matrix has peaks at the modal frequencies for the highest singular value vector and the first column of the left singular vector matrix corresponding to this peak gives the mode shape of the corresponding mode.

Data obtained from eccentric mass shakers

The identification methods discussed above require the applied input to be as white as possible. On the other hand in eccentric mass shaker experiments, a single sinusoidal wave is applied at a time to the system. To be able to use eccentric mass shaker test data with ERA and FDD, we use the fact a signal is white when it is stationary and contains equal energy from all frequency points of the spectrum. Since the

dynamical system tested is assumed to be linear and time invariant, superposition is also assumed to hold. Therefore once a sufficient number of sine waves are applied to the system and the inputs and responses are added up separately, a white – noise – like input and a corresponding output can be obtained. This idea is used for using ERA and FDD with eccentric mass shake data. To check whether sine-sweep testing can be done with eccentric mass shakers, a sine sweep experiment is simulated and the data obtained from the simulation is used with COV-SSI method.

Simulations and Results

To simulate eccentric mass shaker experiments, a 3 – story reinforced concrete building is modeled in SAP2000. In simulations, sine forces between 1 to 21 Hz with 0.1 Hz increments are applied at the roof and this force is placed at a point so as to be able to excite both translational and torsional modes. Acceleration measurements are taken from 4 points at each story level and contaminated with 5% root-mean-squared noise. These noisy measurements are then used to calculate translational and rotational accelerations of each story level. At the end all input and output data are added up to obtain white-noise like data sets. For COV-SSI, a sine sweep is applied at the top of the building, with a sweep interval of 1-21 Hz.

The results obtained with identification methods are summarized in Table 1. The abbreviation MAC in the table refers to Modal Assurance Criteria which is 1 when two vectors are the same and 0 when two vectors are orthogonal. It can be seen that per – cent error for identified modal parameters are lower than 5% (except the damping ratio of the first mode identified with COV-SSI) and MAC numbers are so close to 1 that they are interpreted as 1 for most of the modes except the second mode identified with COV-SSI and FDD. The damping ratios identified by FDD are not given in the table because the results of FDD were highly biased.

Table 1 System identification results

		Mode								
		1	2	3	4	5	6	7	8	9
Actual	Freq	2.98	3.40	4.07	9.67	11.51	15.04	16.89	21.35	30.32
	Damp	0.05	0.05	0.05	0.05	0.05	0.05	0.05	0.05	0.05
ERA	Freq	2.98	3.40	4.07	9.66	11.50	15.02	16.86	-	-
	Damp	0.05	0.05	0.05	0.05	0.05	0.05	0.05	-	-
	MAC	1.00	1.00	1.00	1.00	1.00	1.00	1.00	-	-
COV-SSI	Freq	3.00	3.25	4.07	9.66	-	-	-	-	-
	Damp	0.03	0.05	0.05	0.05	-	-	-	-	-
	MAC	1.00	0.21	1.00	1.00					
FDD	Freq	3.00	3.40	4.20	9.70	-	14.80	-	-	-
	MAC	1.00	0.71	0.99	1.00		0.99			

Conclusions

The analysis in this study showed that the proposed methodologies are satisfactory for real life applications of forced vibration tests with eccentric mass shakers. It was obvious that when both the input and the output are measured and ERA/ARX can be applied, modal parameters can be estimated better. On the other hand, COV-SSI and FDD are superior in the sense that they make it possible to identify the modal parameters when phase difference between the input and the output cannot be measured. Key factors effecting identification results are observed as the number inputs applied in different frequencies, especially at the frequencies close to mode frequencies and scanned frequency interval. Having close and coupled modes decreases the accuracy of results especially for output only identification methods used in this study.

Finally, the results of this study shows that with the methodology proposed here, ERA, COV-SSI and FDD can be used for system identification with eccentric mass shakers as alternatives to classical curve fitting methods.

References

[1] Ho, B. L. and R. E. Kalman, (1965), In: *Effective Construction of Linear State-Variable Models from Input/Output Data*, Proceedings of the 3rd Annual Allerton Conference on Circuit and System Theory, pp. 449–459, Illinois, USA.

[2] Aström, K. J. and T. Bohlin (1965), In: *Numerical Identification of Linear Dynamic Systems from Normal Operating Records*, Proceedings of the IFAC Symposium on Self-Adaptive System, pp. 127–136, Teddington, UK.

[3] Gevers, M. (2003), In: *A Personal View on the Development of System Identification*, Proceedings of the 13th IFAC Symposium on System Identification, pp. 773–784, Rotterdam, Netherlands.

[4] Akaike, H. (1974), *IEEE Transactions on Automatic Control*, vol. AC–19, no 6, pp. 667–674.

[5] Larimore, W. E. (1990), In: *Canonical Variate Analysis in Identification, Filtering and Adaptive Control*, Proceedings of the 29th IEEE Conference on Decision and Control, pp. 596–604, Honolulu, Hawaii.

[6] Van Overschee, P. and B. De Moor, (1993), *Automatica*, Vol. 29, No. 3, pp. 649–660.

[7] Viberg, M. (1995), *Automatica*, Vol. 31, No. 12, pp.1835–1853.

[8] Juang, J. N. and R. N. Pappa, (1985), *Journal of Guidance, Control, and Dynamics*, Vol. 8, No. 5, pp. 620–627.

[9] Magalhaes, F., A. Cunha and E. Caetano (2009), *Mechanical Systems and Signal Processing*, Vol. 23, pp. 316–329.

[10] Peeters, B. and G. De Roeck, (1999), *Mechanical Systems and Signal Processing*, Vol. 13, No. 6, pp. 855–878.

[11] Alıcıoğlu, B., H., Luş, (2008), *ASCE Journal of Structural Engineering*, Vol. 134, No. 6, 1016–1029, 2008.

[12] Shih, C. Y., Y. G. Tsuei, R. J. Allemang and D. L. Brown (1988), *Mechanical Systems and Signal Processing*, Vol. 2, No. 4, pp. 367–377.

[13] Brincker, R., L. Zhang and P. Andersen (2000), In: *Modal Identification from Ambient Responses using Frequency Domain Decomposition*, Proceedings of the 18th International Modal Analysis Conference, pp. 625–630, San Antonio, Texas.

Cost-Effective Dynamic Structural Health Monitoring with a Compact and Autonomous Wireless Sensor System

F. Bastianini, S. Sedigh, G. Pascale and G. Perri

Abstract Dynamic Structural Health Monitoring (D-SHM) in an attractive holistic approach to Non-Destructive Testing (NdT), based on the premise that damage influences the dynamic behaviour of a structure by altering its stiffness, mass or energy dissipation properties.

At present, the fact that the dynamic behaviour of a structure is severely affected by a variety of additional boundary and environmental conditions confines D-SHM to industrial applications where repeatability or environmental conditioning reduce the complexity of the problem, or where the technical and economical implications of costly and time-consuming test campaigns are not an issue.

In this work, the "Smartbrick" platform - an autonomous battery-operated wireless device purpose-built for environmental and structural monitoring - has been equipped with a vibration sensor that captures detailed acceleration data in response to natural occurrences such as small seismic or human-induced events. This enhancement makes the SmartBrick a D-SHM-ready platform with multi-year battery life, which allows a dramatic reduction in both equipment and installation costs, thus potentially expanding the practice of D-SHM to a considerably larger number of existing and new structures.

Keywords Battery-operated • D-SHM • Dynamic structural health monitoring • Smartbrick • Wireless sensor network • WSN

F. Bastianini (✉)
Sestosensor S.R.L., Bologna, Italy
e-mail: fbi@sestosensor.com

S. Sedigh
Missouri University of Science and Technology, Rolla (MO), USA

G. Pascale
University of Bologna, Bologna, Italy

G. Perri
Department of Public Works, Province of Bologna, Bologna, Italy

Introduction

Since the 19th century, a variety of techniques based on global interrogation of the dynamic behaviour of a structure have been proposed for the assessment of the health conditions and for the determination of structural damage, with potential applications to quality control, predictive maintenance, life cycle estimation and even disaster prevention [1]. Despite the increasing sophistication of modelling, computation, and data interpretation techniques [2], a number of practical issues confine the applicability of D-SHM methods to a limited number of specific cases. Although specialized data acquisition systems for temporary monitoring of vibrations have been proposed [1], most experimental studies [3] confirm that the severe influence of environmental conditions prevents D-SHM from being effectively carried out through periodic tests performed on a structure. Long-term, continuous, automated monitoring of vibration is claimed to be better-suited as an effective D-SHM method, as the data it yields is sufficiently large in volume to overcome ambient noise problems, and with time span and resolution sufficient for manifestation of seasonal dependencies of modal parameters on environmental conditions [4]. Unfortunately, continuous automated monitoring requires the permanent installation of sophisticated data acquisition systems with a large number of sensors (from ten to several hundred). The prohibitive cost of these systems limits their use to structures of major importance, such as large bridges [5].

The Smartbrick Data Acquisition Platform

Traditional "wired" SHM systems, such as automated monitoring systems used for recording vibration, typically carry cable installation costs that well exceed 50% of the total system investment [6]. With the aim of reducing these exorbitant installation costs, several research efforts in developing wireless networked devices for SHM (WSHM) have been carried out in the last decade [7]. With few exceptions, known wireless platforms feature a centralized design approach that requires some type of gateway-coordinator node with wired power and communication lines. The use of WSHM platforms monitoring historic structures is often hampered by aesthetic concerns, dimensions, or budget limitations that eliminate the possibility of using this type of wired node.

The "Smartbrick," an autonomous and self-contained WSHM device, has been proposed in response to the aforementioned shortcomings of existing WSHM platforms, and is especially well-suited to low sensor count applications [8].

The Smartbrick features multi-year battery life, and communicates using the GSM/GPRS mobile phone network, thus eliminating the need for cables and drastically reducing installation costs. The Smartbrick embeds sensors for temperature, inclinometers and acceleration. Pre-conditioned inputs for specific additional sensors are provided as well. The data collected, any alarms triggered and self-test information are automatically delivered to designated recipients through SMS

messages, email, and FTP file upload. Daemon applications and graphical interfaces resident on the servers provide an interactive user interface for data visualization through charts and diagrams.

Event-driven Data Acquisition for Dynamic Phenomena

In order to maximize battery life, the Smartbrick remains in deep sleep mode whenever possible, periodically switching to active mode for a brief time in order to read sensors that monitor slowly-changing phenomena and to send data. Such time-driven operation cannot capture structural vibrations induced by random environmental excitation. Hence, an event-driven operational mode and trigger system have been added to enable detection of acceleration peaks within the 2÷25 Hz frequency region. The trigger system developed has power consumption of less than 66 μW and has a negligible effect on the Smartbrick's battery life. Depending upon the options configured, data can be simultaneously acquired from up to eight different channels, with a total maximum sampling rate of 4100 S/s and memory depth of 64 k samples. The -3dB bandwidth of the sensor input is 0.1÷110 Hz for the embedded accelerometers and 2000 Hz for other channels.

The bench test confirmed that the sensitivity of the trigger system could reach and even exceed the design specification of 0.49 m/s^2 (50 mg) peak acceleration threshold in the 2÷25 Hz frequency band. The isotropy of the trigger with respect to the three coordinate directions is to be considered acceptable at the highest limit of sensitivity adjustment.

Field Testing Through Monitoring of a Historical Structure

Palazzo Malvezzi, a historical building dated to 1560 in Bologna (Italy), was selected as a case study for the validation of D-SHM using the Smartbrick. The building presents evolving crack damages in the northwest corner, due to the presence of a subsidence line across the foundation. Additional crack damages were found in the ceiling of a large vane conceived in origin as a ballroom. The room currently used as the Room of Council for the local Province Institution is connected with a balcony that was intended for hosting the orchestra through an oval opening located in the middle of the fresco-painted ceiling. Both the balcony and the vaulted ceiling are built on a framework featuring wooden elements. Crack damage was also observed on the structure.

Two Smartbrick devices were used to carry out D-SHM for the damaged areas. A first Smartbrick device was installed on the cracked floor of the room located at the northwest corner of the building ("Red Room"), providing a displacement gauge across the crack, bi-axial inclinometers, sensors for the surface and air temperature and tri-axial accelerometers for vibrations induced by human activity during normal use of the room for meeting and conferences. A second Smartbrick device was installed on the orchestra balcony, providing bi-axial inclinometers, tri-axial
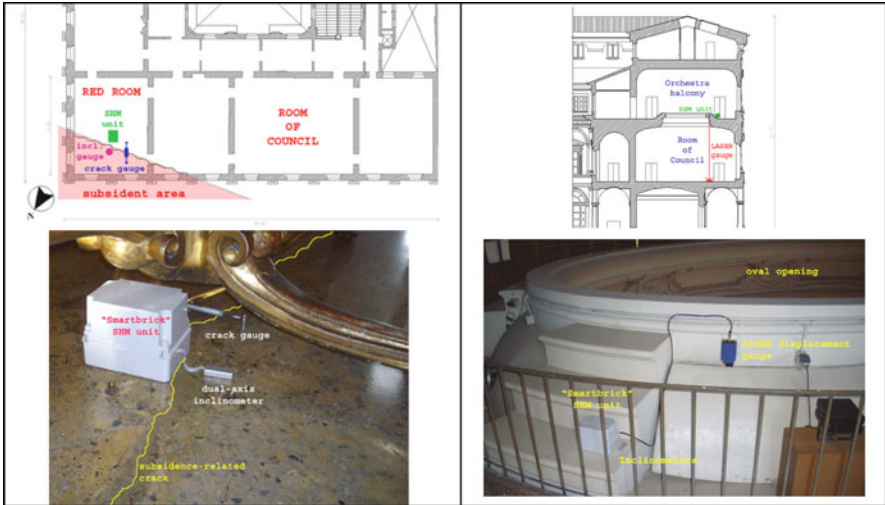
Fig. 1 *on the left*: survey and equipments in the northwest building corner (Red Room); *on the right*: vertical section and equipments in the Room of Council
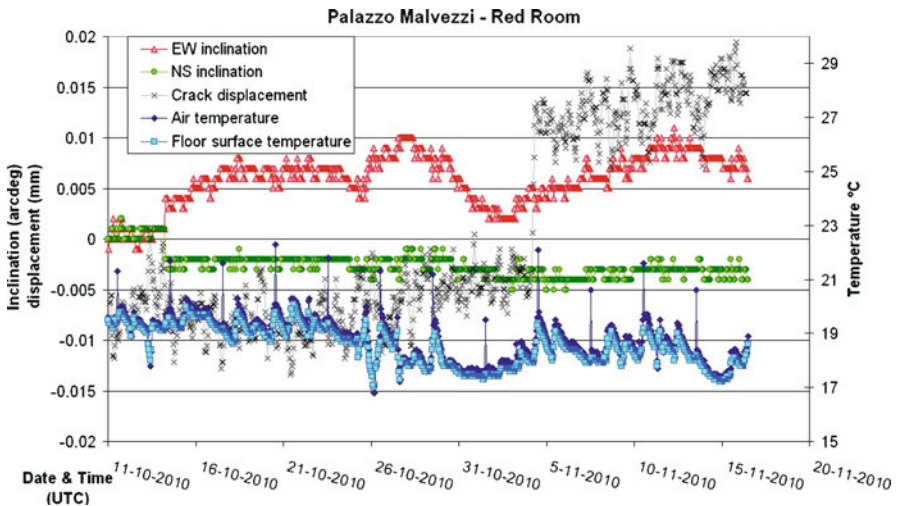
Fig. 2 Time history for monitoring data of the Red Room

accelerometers, sensors for the surface and air temperature and a LASER displacement gauge to evaluate the displacement of the balcony with respect to the floor of the Room of Council. Figure 1 depicts the installed devices.

Figures 2 and 3 summarize the data acquired by the two units. Although the time of observation is limited, some phenomena are observed: a +0.15mm change in the floor crack of the Red Room is observed while at the same time no notable
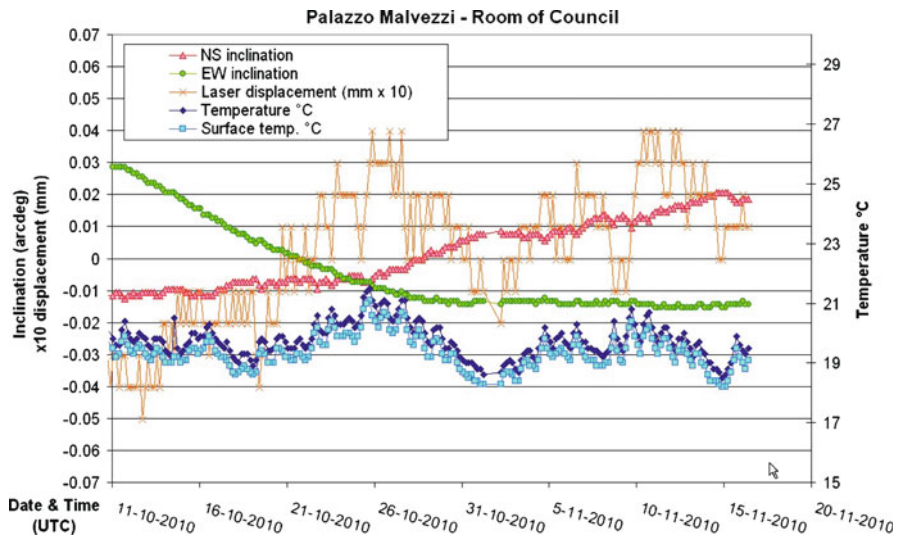
Fig. 3 Time history for monitoring data of the Room of Council
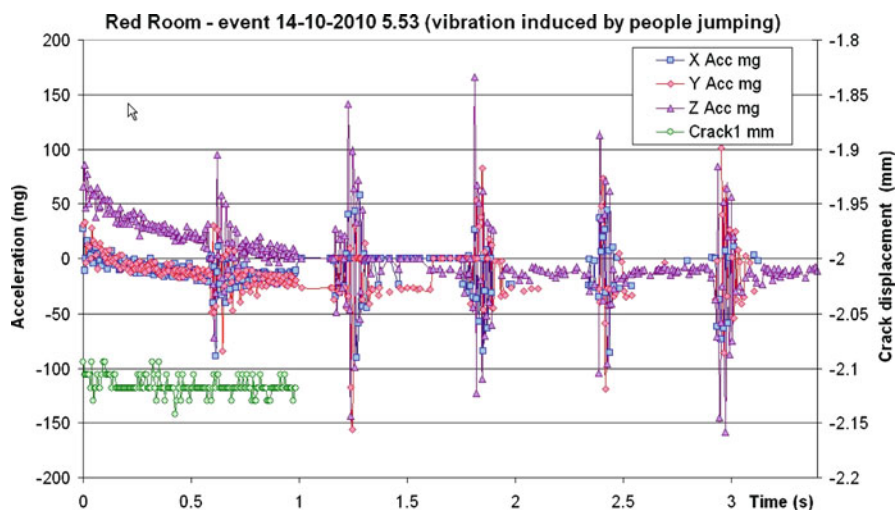
Fig. 4 Dynamic data acquisition triggered by human activity in the Red Room

change of inclination is reported. In the same period the orchestra balcony of the Room of Council exhibited a settlement involving both inclinations (0.04°) and distance (+0.5mm) of the oval opening edge from bottom room floor. This settlement is believed to be related to the seasonal change in air moisture content inducing distortions in the wooden frame of the structure and after this consideration a relative humidity gauge has been planned to be added to the installation.

Figure 4 reports a typical dynamic data acquisition event triggered by normal human activity where is observed that the correlation between the vibrations and the opening of the crack floor is not remarkable.

Conclusions

D-SHM enabled Smartbrick devices provide a novel and cost-effective data acquisition platform useful for a diverse array of structures. The platform proposed is particularly well-suited to monitoring of historical structures, where the goal is to utilize as few sensors as possible, and where the concurrent availability of data about environmental conditions, structural parameters, and vibrations is especially useful. Laboratory and field testing confirmed that the performance of the dynamic event trigger system developed meets and exceeds the technical requirements for capturing even light vibration events induced by the human activity typical for a building used for residential or commercial purposes.

References

[1] Wenzel H. and Pichler D. (2005), *Ambient Vibration Monitoring*, John Wiley & Sons, ISBN-13 978-0-470-02430-0.

[2] Salawu O. S. (1997), In: *Engineering Structures*, vol. 19, n. 9, pp. 718–723.

[3] Farrar C. R., Doebling S. W., Cornwell P. J. and Straser S. W. (1997), Proceedings of the 15th International Modal Analysis Conference, vol. 1, pp. 257–263.

[4] Rohrmann R. G., Said S., Schmid W. and Rücker W. F., (1999), Results of the automatic monitoring of the Westend bridge in Berlin, In: *BAM research report B*.

[5] Maeck J., (2003), Damage Assessment of Civil Engineering Structures by Vibration Monitoring. *PhD thesis*, Katholieke Universiteit Leuven, Leuven, Belgium, ISBN 90-5682-390–396.

[6] Straser E. G. and Kiremidjian A.S., (1998) A Modular, Wireless Damage Monitoring System for Structures, *Report No. 128*, John A., Blume Earthquake Engineering Centres Department of Civil and Environmental Engineering., Stanford University., Stanford, CA, USA.

[7] Lynch J. P. (2007), An Overview of Wireless Structural Health Monitoring for Civil Structures, Philosophical Transactions of the Royal Society of London. Series A, Mathematical and Physical Sciences, The Royal Society, London, vol. 365, n. 1851, pp. 345–372.

[8] Bastianini F., Sedigh S., and Harms T. (2009), Autonomous Structural Health Monitoring with the SmartBrick Platform. Proceedings of 12th International IEEE Conference on Intelligent Transportation Systems, St. Louis, MO (USA).

Preliminary Identification of Dynamic Characteristics of a Unique Building in Chile Following 27 February 2010 (Mᵂ=8.8) Earthquake

M. Çelebi, M. Sereci, R. Boroschek, R. Carreño and P. Bonelli

Abstract Following the 27 February 2010 ($M_w = 8.8$) Offshore Maule, Chile earthquake, a temporary, real-time data streaming array comprising 16 channels of accelerometers was deployed throughout a recently constructed 16 story tall building with three additional basement stories in Vina del Mar, Chile. This building was not damaged during the mainshock; however, it is similar in design to many other buildings with multiple shear walls that were damaged but did not collapse in Vina del Mar and other parts of Chile. The temporary array recorded low-amplitude response of the building from aftershocks. The recordings provided dynamic response characteristics of the cast-in-place reinforced concrete building. Available dynamic characteristics from mathematical modal analyses are compared to the observed responses. Distinct "major-axes" translational and torsional fundamental frequencies as well as frequencies of secondary modes are identified. Response data from each earthquake provide evidence of beating.

Keywords Core-shear wall building • Instrumentation • Modal analysis • Structural health monitoring

M. Çelebi (✉)
USGS, Menlo Park, CA, USA 94025
email: celebi@usgs.gov

M. Sereci
Digitexx Inc., Pasadena, CA, USA

R. Boroschek • R. Carreño
University of Chile, Santiago, Chile

P. Bonelli
UTFSM, Valparaiso, Chile

Introduction

During the reconnaissance mission organized by the Earthquake Engineering Research Institute to investigate the M_w8.8 Offshore Maule, Chile earthquake of 27 February 2010, a cooperative effort by the authors facilitated deployment of a temporary, real-time data streaming structural monitoring array comprising 16 channels of accelerometers distributed throughout an unoccupied 16-story tall building (with 3 additional basement stories) in Vina del Mar, Chile. The building was chosen to understand the dynamic characteristics of a core-shear wall building, which is a typical construction type in Chile. This type of construction, in general, performed well during both the M 7.8 1985 Valparaiso and the recent 27 February, 2010, Offshore Maule events. Modal analyses (including live loads) performed during the design/analyses processes have yielded the first 6 modal periods as 2.01, 1.532, 1.14, 0.47, 0.31 and 0.27 seconds. The first two correspond to the fundamental modes in the NS and EW directions respectively.

The Building

A picture of the building and a typical plan view showing the distribution of shear walls and column lines are shown in Fig. 1. Core shear walls are typically 35 cm thick, while the shear walls in the perimeter on the west and east edges are 30 cm
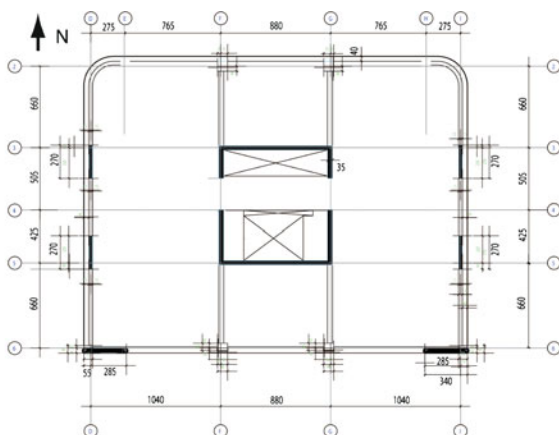
Fig. 1 *Left*: General picture of the building. *Right*: Typical plan view shows distribution of shear walls and columns as well as dimensions and the axes system

thick, and the two in the south edge are 40 cm thick. Columns located on the column line intersections that do not have shear walls are typically 80cm x 80cm in plan. Such a distribution of walls and columns with non-coincidental mass and rigidity centers naturally is expected to cause torsional behavior. Furthermore, the basement foundation is a 100 cm-thick mat without piles. The combination of lack of piles, a thick mat foundation, and a stiff structural system situated on a sub-foundation of approximately 100 m-thick alluvial material[1] make this building an ideal target to study rocking effects, if present.

Temporary Instrumentation and Data

Figure 2 shows temporary deployment of an array of 16 accelerometers. Several sets of earthquake response data have been recorded by the array. Quick analyses of the data for response characterisitics indicated similar and repeatable results. Hence, in this paper, only one set will be presented and discussed.
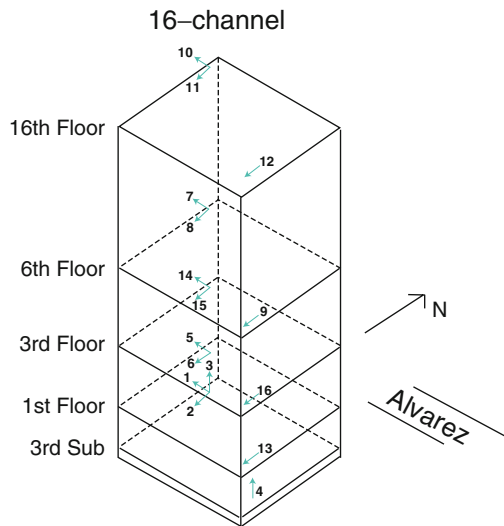
Fig. 2 Schematic of temporary deployment of accelerometers

---

[1] The site frequency has been computed to be approximately 1.5 Hz. Because of space limitations, computation of site frequency is not discussed in the paper.
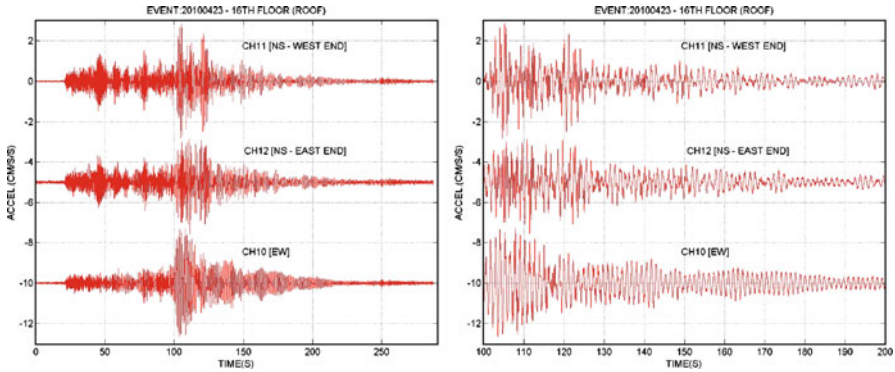
Fig. 3 Acceleration time histories recorded at the roof level of the building. *Left:* the complete record. *Right:* expanded portion of record windowed beteeen 100-200 to display possible beating and low-damping associated with the building at this level of shaking
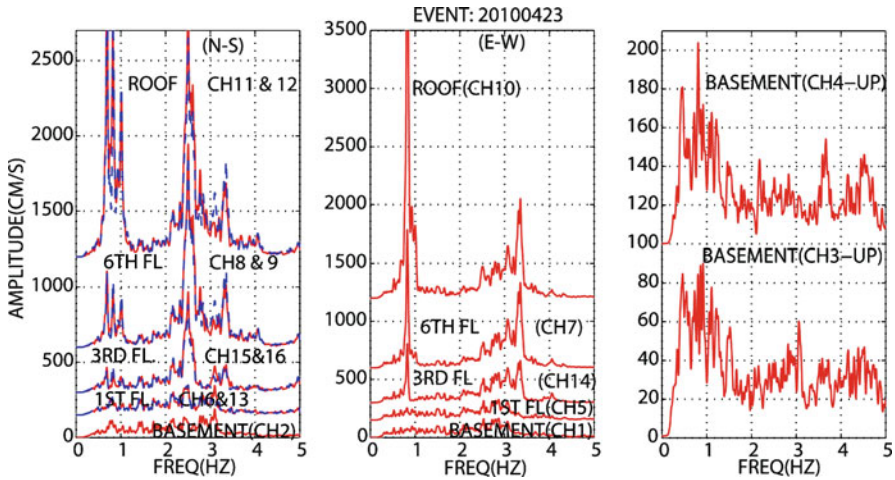
Fig. 4 Amplitude spectra computed from accelerations recorded from all channels of the array

Analyses of Data

Shown in Fig. 3 are acceleration time-histories of the response of the 16th floor [roof-level channels 10-12] of the building to an event that occurred at 06:03 AM local time on April 23, 2010 (M=5.9 located 65 km south of Concepcion and approximately 475 km south of Vina del Mar) To the right is an expanded 100-s interval of these records to better display the building behavior, which may include beating effects and low damping that most likely contributed to prolonged shaking. Amplitude spectra computed from the acceleration records are shown in Fig. 4.
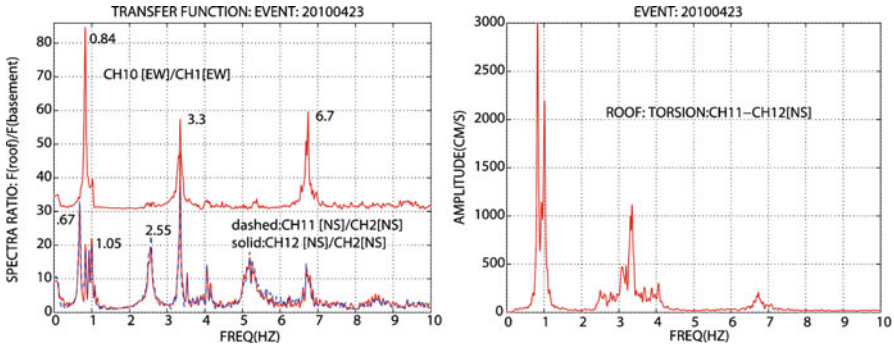
Fig. 5 *Left*: Transfer function of EW and NS records at the roof with respect to corresponding records in the basement. *Right*: Amplitude spectra of differential acceleration from parallel channels in the NS direction to assess torsional response. These plots are made for 0-10 Hz horizontal axes to observe higher mode frequencies as well

The spectra show predominant peaks at several frequencies in the NS, EW and vertical directions. Clearly, in the low frequency range of 1Hz or less (the expected range of the fundamental frequencies), several peaks are clearly identifiable (e.g. EW frequency [period] of 0.84Hz [1.2 s], and NS frequencies [periods] 0.67, 0.84 and 1.05 Hz [1.49s,1.2s and 0.95s]). These significant frequencies and those of higher modes are seen in the amplitude spectra as well as being clearly identifiable in the plot of transfer functions in Fig. 5a. In the EW direction, the transfer function, computed as the ratio of amplitude spectra of accelerations at the roof (CH10) to those in the basement (CH1), clearly indicates three distinct peaks at 0.84, 3.3 and 6.7 Hz (1.2, 0.3 and 0.15 s) corresponding to the first three modes. It is noted that these frequencies are identical to those obtained from amplitude spectrum for torsional response represented by the difference of the two parallel NS motions (e.g., CH11 & CH12) as shown in Fig. 5b. Thus, EW motions and torsional motions are coupled, and therefore the same frequencies appear in the transfer functions for the NS direction, as seen in Fig. 5a. TheNS transfer functions also exhibit two additional peaks at 0.67 and 1.05 Hz that do not appear in the spectra or transfer function for the EW direction; hence they are related only to the NS direction.

The challenge in identifying which one of the frequencies unique to the NS motions (0.67, 0.84 and 1.05 Hz) belong to what mode of vibration is made difficult by the fact that these frequencies are all in phase, as seen in Fig. 6 displaying cross-spectrum, phase and coherency between CH12 (NS) at the roof and CH9(NS) at 6th floor (and similarly for other combinations that are not presented herein). However, as seen in Fig. 7a, b, it is very likely that the frequency at 0.84 HZ is also the rocking frequency both for NS and EW directions, as identified by the auto-spectra, cross-spectra, phase angle and coherency plots for CH12(NS) and CH10 (EW), both at the roof, as compared to CH4 (UP) in the basement. This key
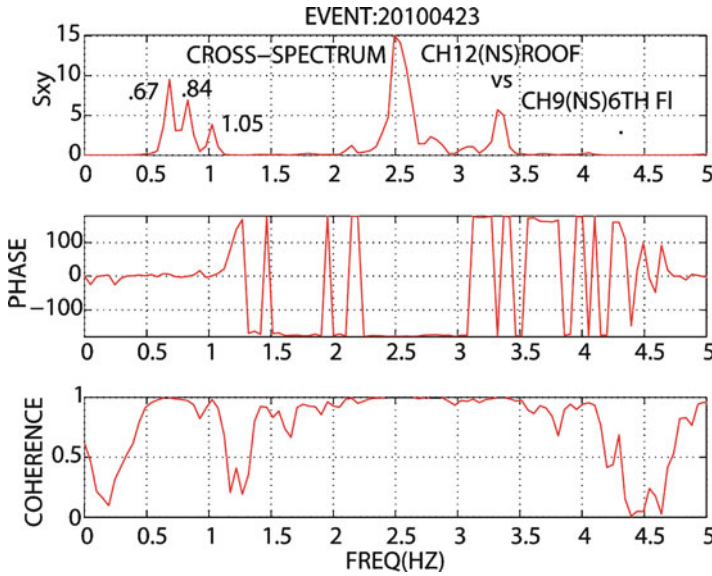
Fig. 6 Cross-spectrum, phase angle and coherency plots of acceleration recorded by CH12(NS) at the roof and CH9(NS) recorded at the 6th floor
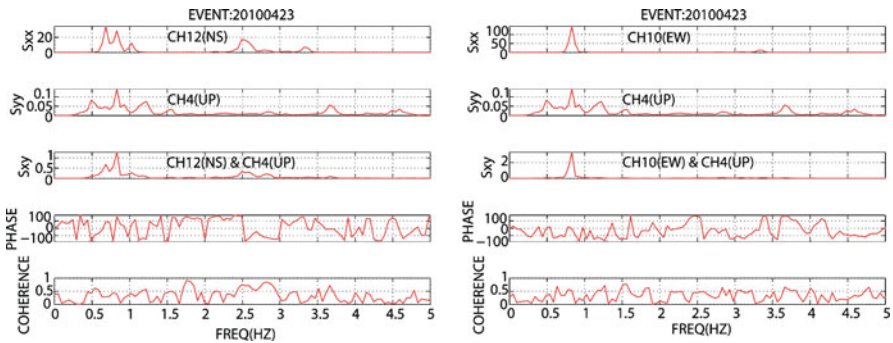
Fig. 7 Auto and Cross Spectra, Phase angles and coherency plots for vertical motion (CH4) in the basement paired with horizontal motions: *Left*: Ch12(NS) at the roof and *Right*: CH10(EW) at the roof

figure illuminates the close frequencies that are about 1 Hz or less. So, it is safely concluded that 0.84 Hz is one of the important frequencies – the translational fundamental frequency in the EW direction, the torsional fundamental frequency, and also the rocking frequency in the EW and NS directions.

Thus, in the EW direction the apparent frequency ($1/f^2_{apparent} = 1/f^2_{translational} + 1/f^2_{rocking}$) at 0.84 Hz is same as the rocking and translational frequency. In the NS direction, 1.05 Hz is the translational frequency and the apparent frequency is 0.67 Hz

computed also by the relationship: $1/f^2_{apparent}=1/f^2_{translational} + 1/f^2_{rocking}=1/1.05^2 +1/.84^2$ that leads to $f_{apparent} \sim 0.67$Hz which is consistently seen in the spectra and transfer functions.

An additional observation in the building response is the "beating effect". As observed in other structures [1,2], low-level damping and nearly identical (or close) translational and torsional frequencies in structural system causes coupling and beating effect with a period $T_b=2T_1T_2 /(T_1-T_2)$. During the beating effect, repetitively stored potential energy during the coupled translational and torsional deformations turns into repetitive vibrational energy. Thus, for this building, in the NS direction, with T1=1/1.05Hz=0.95s, and T2=1/.84Hz=1.2s, then, $T_b=2T_1T_2 /(T_1-T_2) = 2*.95*1.19 /(1.19-.95)=9.4$s which is close to the observed/recorded motions seen in Figure 3.

Conclusions

In the absence of widespread permanent accelerometer arrays in structures, which often is due to cost issues, an effective approach for non-destructive testing and extracting critical information on response characteristics is to deploy temporary arrays following large earthquakes to record significant aftershocks. This approach allows assessment of actual dynamic characteristics and significant modal behaviors that may not always be identified or accurately determined by mathematical models. In this preliminary study, the building exhibits frequencies attributable to translational, torsional, and rocking modes that are significantly different than those extracted from mathematical models. Furthermore, the beating effects are observed in the structure during the low-amplitude excitation generated by distant aftershocks almost two months after the main event. Assessment of critical damping ratios is left to future studies.

References

[1] Boroschek, R.L., and Mahin, S.A. (1991). Investigation of the Seismic Response of a Lightly-Damped Torsionally-coupled Building: University of California, Berkeley, Earthquake Engineering Research Center Report UCB/EERC-91/18, 291pp.
[2] Çelebi, M., (2004). Responses of a 14-Story (Anchorage, Alaska) Building to Far-Distance (Mw=7.9) Denali Fault (2002) and Near Distance Earthquakes in 2002, Earthquake Spectra, Journal of EERI, *Earthquake Spectra*, vol.20, no.3, pp. 693–706, August 2004.

Behaviour of Corrosion Damaged Reinforced Concrete Beams Strengthened Using CFRP Laminates

M. Tigeli, P. Moyo and H. Beushausen

Abstract This paper presents experimental results on the behaviour of corrosion damaged reinforced concrete beams repaired using a cementitious patch repair material and strengthened using carbon fibre reinforce polymer (CFRP) plates. Four RC beams (154 mm × 254 mm × 5000 mm long) were used. Three of the beams were subjected to different levels of accelerated corrosion (using an impressed anodic current and 5% NaCl solution) under sustained service loads while one beam acted as a control. The service load was estimated as 80% of cracking moment. The three corrosion-damaged beams were using a repair mortar; further, two of the patch-repaired beams were strengthened with carbon fibre reinforced polymer (CFRP) laminates. The effect of damage on the stiffness of the beams was inferred from natural frequencies, strain measurements and deflection measurements. The effect of patch repair and strengthening on corrosion damaged beams was deduced from the changes in their ultimate capacities. The results reveal that the stiffness and the ultimate capacity are improved by about 25% and 50% respectively when both patch repair and CFRP are applied on a damaged beam. Patch repair only, improved the stiffness by approximately 5% but did not improve the ultimate capacity.

Keywords CFRP strengthening • Patch repair • Corrosion damage • Damage assessment • Effectiveness of strengthening

Introduction

Over the years, the need for repair of RC structures has increased significantly, both for old and new structures. The main cause of structural damage in RC structures is corrosion of reinforcement. Therefore there is a need to understand the

M. Tigeli • P. Moyo (✉) • H. Beushausen
Department of Civil Engineering, Univesity of Cape Town, South Africa
e-mail: pilate.moyo@uct.ac.za

effects of corrosion damage on the structural properties of RC members such as stiffness and ultimate capacity in order to develop improved and effective repair strategies that will minimise the risk of further damage and structural failure both in the short and long term. Corrosion reduces the cross-sectional area of steel at the corrosion sites, leading to reduced stiffness and capacity of the structure to carry loading, which may result in structural failure if not detected and repaired or strengthened.

This study presents experimental results on the effectiveness of combined repair and strengthening of corrosion-damaged RC beams. Four RC beams were tested. All four beams were monitored for deflections during the accelerated corrosion period. The beam dynamic characteristics were assessed in the following states; undamaged, 10 % corroded, 15% corroded, exposed reinforcement, patch repaired and finally the CFRP strengthened state. The three corrosion-damaged beams were patch repaired using a cementitious repair mortar. Two of the beams were strengthened with CFRP laminates in addition to the repair. The effect of damage on the stiffness of the beams was inferred from strain measurements, deflections and dynamic properties (natural frequencies). The effect of patch repair and strengthening on corrosion damaged beams was deduced from the changes in their ultimate capacities.

Experimental Details

Specimen detail

The RC beam specimens had the following dimensions, 153 mm width, 254 mm depth and 5000 mm length. The reinforcing bars were placed symmetrical in the beam cross section; with the dimensions of the compression and tension reinforcement being 10 mm and 20 mm diameter respectively. Double-leg stirrups of 8 mm diameter mild steel were placed at 150 mm spacing centre to centre throughout the length of the beam. Figure 1 shows the reinforcement details of the beams used in the study.

Material properties

The beams were cast using ordinary Portland cement (OPC), with a w/b ratio of 0.45. 19 mm standard coarse aggregates were used. The average 28 day compressive strength of the concrete was 40 MPa, with a standard deviation of 2.8 MPa.
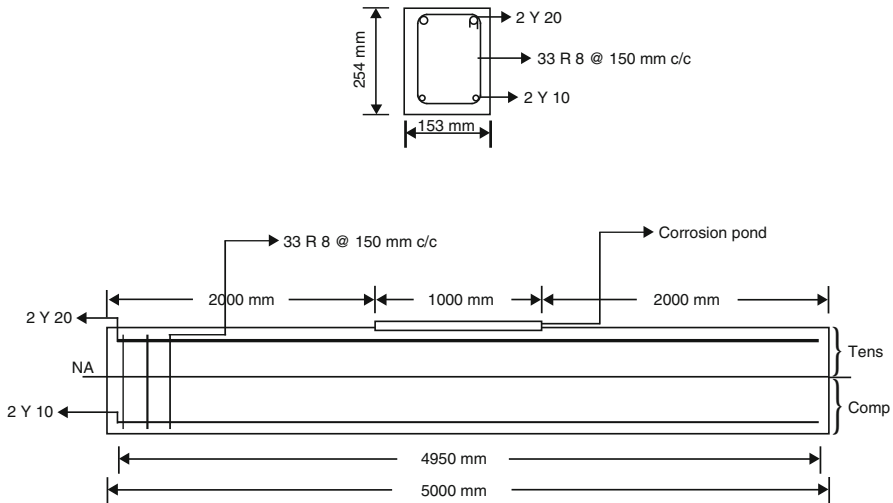
Fig. 1 Inverted beam reinforcement detail

Accelerated corrosion

Beams 2, 3, and 4 were provided with a PVC pond of dimensions 150, 1000 and 30 mm for corrosion located at the mid-span of the beam. A 5% NaCl solution was added into the pond and a 12 mm stainless steel bar of length 800 mm was immersed into the NaCl solution. To accelerate corrosion, the tensile steel bars and the stainless steel bar were connected to a power supply using electric copper wires. A silver brazing alloy with flux were used to connect the copper conductors to the ends of the tensile reinforcing steel bars and to the stainless steel bar. The connections between the wires and the steel bars or stainless steel bar were covered with shrink wrap to prevent moisture access.

The corrosion process consisted of 4-day wetting and 2-day drying cycles. For ease of monitoring, all corroded beam specimens were supplied with the same current intensity of 1000 $\mu A/cm^2$ which was divided equally between the two bars and the corrosion period was varied depending on the desired level of damage. The relationship between corrosion current density and the steel mass loss due to corrosion was determined using Faraday's law (Eq. 1):

$$I_{corr} = \Delta W F z \frac{D_{Fe}}{W_{Fe}} \tag{1}$$

Where I_{corr} is the current intensity ($\mu A/cm^2$), F is Faraday's constant (96 500 coulombs), ΔW is mass loss due to corrosion (g), W_{Fe} is the atomic mass of steel (55.8 g/mole), D_{Fe} is the density of steel (7.86 g/cm^3) and z is valence (2) from the oxidation reaction of steel.

Repair Process

Patch repair

The corrosion-damaged RC beams were prepared for repair by cutting-out the damaged concrete beyond the level of corroded steel, until sound concrete was reached. Damaged concrete was cut out with a grinder and broken out with a jack hammer to the level beyond the reinforcement to facilitate access to reinforcement when cleaning the corrosion products. The reinforcing bars were cleaned with a wire brush to remove the corrosion products before application of the patch repair mortars. Beams 2, 3 and 4 were patch repaired with a cementitious repair mortar.

Strengthening

The CFRP laminates (tesnile strength 4800MPa and Youngs modulus 230Gpa) were bonded on to the substrate using a special epoxy resin for the laminates. Before application of the CFRP laminates, the concrete surface was prepared by sandblasting the top concrete to expose aggregates and air blowing it to remove loose dust. The CFRP laminates were cleaned with a cleansing agent to remove excess dirt before application. The reason for using both the patch repair and CFRP laminates was to understand the combined effect of the two. In practice, they are usually used separate and they therefore fail to fully enhance the structure stiffness and capacity.

Beams 2 and 4, with 10% and 15% corrosion respectively, were patch repaired and strengthened with CFRP laminates. The CFRP laminates used were 50 mm in width, 1.2 mm thick and 4900 mm long. Each beam was strengthened with two laminates running parallel throughout the length of the beam on the tensile face. The CFRP laminates were anchored at the end with a 300 mm thick CFRP wrap. Both beams were strengthened on the tension side where the patch repair was applied.

Testing

Stiffness

Dynamic results

The modal characteristics used to infer stiffness were the natural frequencies. The frequencies were measured at the following stages; undamaged, 10 % corroded, 15% corroded, exposed reinforcement, patch repaired and finally the CFRP strengthened state. The fundamental natural frequencies for different beams are presented in Fig. 2 at undamaged, corroded, exposed reinforcement, patch repaired and CFRP strengthened referred to as stages 1, 2, 3, 4 and 5 respectively.
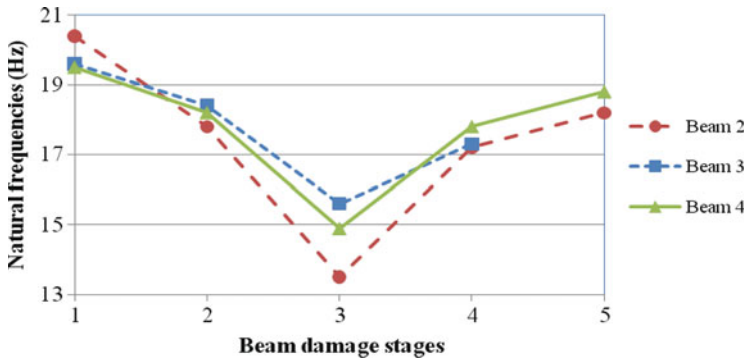
Fig. 2 Natural frequencies at different levels of corrosion-induced damage
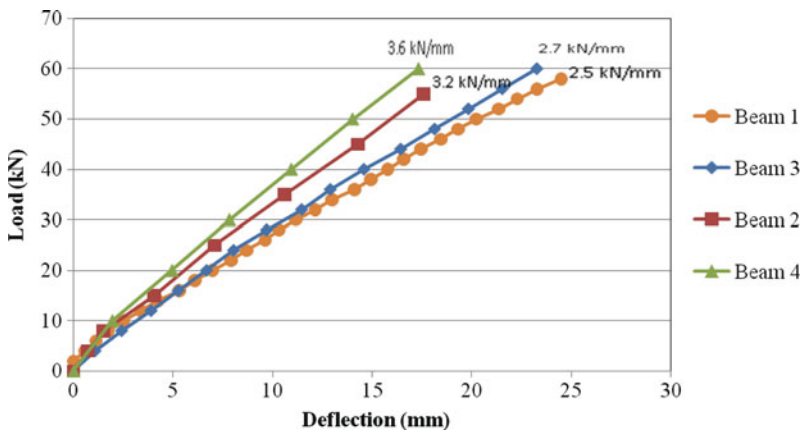
Fig. 3 Deflection measurements

The natural frequencies for the fundamental mode were used to analyse the effect of the changes in beam condition. The percentage change in the natural frequency was used as a damage indicator [1-2]. As observed from all the tested beams, there was an average decrease of 8 % in the natural frequency of the beam when it was corroded to 10% mass loss. The fundamental frequency increased to 9 % when the level of corrosion was increased to 15 %.

Deflections

The stiffness of the beams was inferred from deflection measurements measured when the beams were loaded to failure. For comparison, deflections presented in Fig. 3 are up to 60 kN loading as beams failed at different loadings. Beam 1 (control) had the least static stiffness of 2.5 kN/mm as it displayed the highest deflections,

followed by a Beam 3 (patch repaired) with stiffness of 2.7 kN/mm, Beams 2 and 4 with FRP strengthening presented the largest stiffness of 3.2 and 3.6 kN/mm respectively.

From the results presented, it can be observed that the application of both patch repair and CFRP strengthening improves the stiffness of the RC members by up to 50%. Patch repair on its own slightly improves the stiffness by less than 10 %. These results confirm to the work done by other researches [3], where the CFRP strengthened beams exhibited increased stiffness over the unstrengthened specimen.

Ultimate Capacity

All the beam specimens were tested for ultimate capacity. The failure loads for all beams are presented in Table 1. The results show that the Beam 3 (patch repaired) had the least capacity, followed by Beam 1 (control). Beams 2 and 4 with CFRP strengthening had the highest ultimate capacity. The 10% corroded beam with patch repair has a 5% reduction in ultimate capacity compared to the control beam. This proves that the reduction in area of steel plays a more significant role with regards to ultimate capacity than stiffness of members. The results demonstrate that CFRP carries a significant propotion of the load [3]. The ultimate capacity is dependent on the bond between CFRP and concrete as it will be observed from the failure mode that failure occurred when the laminates debonded. Once the laminates debond, the steel yields and failure takes place.

Conclusions

Patch repair and CFRP strengthening have a positive effect on the structural capabilities of improving the load carrying capacity of a flexural RC member, improving stiffness and protecting reinforcement from further corrosion damage. Application of patch repair and CFRP strengthening improves the stiffness of the beams by up to 30% while patch repair on its own improves the stiffness by less than 10%. Application of both CFRP and patch repair improves the ultimate capacity by up to 50%, while patch repair on its own fails to improve the ultimate capacity as it is dependent on steel reinforcement.

Table 1 Maximum failure load

Beam condition	Ultimate capacity (kN)
Beam 1: Undamaged	74
Beam 2: 10 % corroded + patch repair + CFRP	109
Beam 3: 10 % corroded + patch repair	70
Beam 4: 15 % corroded + patch repair + CFRP	110

References

[1] Baghiee N., Esfahani R.M. and Moslem K., (2008), Studies on damage and FRP strengthening of reinforced concrete beams by vibration monitoring, *Engineering Structures Journal*, vol 31, n 4, p 875–893.

[2] Dimarogonas, A.D., (1996), Vibration of cracked structures: A state of the art review, *Engineering Fracture Mechanics*, vol. 55, p. 831–857).

[3] Soudki A.K., Sherwood T. And Masoud S., (2003), *FRP Repair of Corrosion-Damaged Reinforced Concrete Beams*, Department of Civil Engineering, University of Waterloo.

Section 10
NDT and Evaluation of Historic Buildings and Monuments

Diagnosis of Historic Masonry Structures Using Non-Destructive Techniques

L. Binda, L. Cantini and C. Tedeschi

Abstract An accurate diagnosis of the state of conservation of historic structures is based on an extensive experimental investigation and on an appropriate structural analysis. A methodology of investigation to be applied to Cultural Heritage (C.H.) buildings is presented by the authors, based on a long experience in the field. The investigation steps are described, from the collection of historical documents and the visual inspection to: the geometrical and crack pattern survey, the detailed masonry section and quality description through on site mechanical and physical tests and use of Non Destructive (ND) techniques to the material characterisation and the structural monitoring.

Introduction

A correct preservation design of a historic structure should start from an accurate diagnosis of the state of damage based on: experimental on site and laboratory investigation, and on a structural analysis using the results of the investigation. These operations will deepen the knowledge of the building and help respecting its authenticity through an appropriate choice of intervention techniques.

Masonry structures in seismic areas were subjected to several earthquakes along their life, followed by partial reconstructions. They can also suffer for lack of maintenance, so that synergetic effects can cause their damage. Therefore a diagnosis on the state of conservation of the structure and on its vulnerability to future actions is needed and this should be based on the detection of damages and their causes and on a structural safety analysis.

L. Binda (✉) • L. Cantini • C. Tedeschi
DIS, Politecnico di Milano, Milan, Italy
e-mail: binda@stru.polimi.it

In order to fulfil these needs by overcoming the gap between our poor knowledge today and the complexity of these structures an experimental on site investigation is required and recommended also by Codes and Standards in several countries.

Non destructive techniques (NDTs) and/or Minor destructive Techniques (MDTs) can be helpful in detecting hidden features (wall texture, internal voids and flaws and characteristics of the wall section) which are so much important to define the structural behaviour under dead loads and environmental actions. Up to now most of the Non Destructive (ND) procedures can give only qualitative results. The application to masonry of the NDTs, although advanced, can be frustrating due to several factors, like the differences in masonry typologies and materials, the high non homogeneity of the materials, the difficulty of interpretation of the results of each single technique but also of harmonisation of the results. Furthermore, most of the NDTs come from other research fields and applications to more homogeneous materials (steel and concrete) and need a specific calibration.

A rather long experience of the authors has shown that several techniques have to be applied according to the needs of the building features. It is then important before choosing the appropriate NDTs to know which type of problem has to be solved, i.e. what it is necessary to find by NDT.

A description of the adopted methodology and a state of the art of the research in the fields will be introduced together with the last application of NDTs to the investigation of masonry structures.

Failed Repairs Due to Lack of Knowledge

The last 1977 Umbria and Marche, 2002 Molise, 2004 Garda lake and 2009 Abruzzo earthquake effects have shown that: a) for some building typologies and masonry morphologies the already applied structural models need to be adjusted to their real behaviour, b) the retrofitting techniques applied after the previous earthquakes (since 1979) still need improvement.

The interventions carried out in Italy, according to the previous seismic code indication were made in order to retrofit all the existing buildings (damaged and undamaged); they were assuming the safety criteria applied to new buildings. Historic masonry and masonry structures were considered too weak to bear future earthquakes, therefore they needed invasive interventions to respect the imposed safety coefficients.

The code suggested that these criteria could be attained for all the masonry buildings, especially for the weakest ones by:

a) substituting the original timber floors and roofs with reinforced concrete ones;
b) constructing r.c. tie beams in the wall thickness at every floor level and under the roof;
c) jacketing and/or injecting the walls in order to improve their shear strength.

As it is well known, the first two types of intervention are intended to improve the structural response of the building: type a) by ensuring "rigid floor" action, type b) by connecting load-bearing and shear walls in order to prevent out of plane failures. Even if experimental and analytical research has been carried out in the past decades on these techniques, nevertheless the effectiveness was always checked in terms of strength increasing rather than on compatibility with the original masonry [1].

The failures due to inadequate application of repair interventions are the most difficult to interpret. The questions to be answered are: what actually caused the failures and how did they develop and how serious were their consequences to the overall response of the building. The lack of knowledge on the original materials and structures was frequently the main cause of unsuccessful interventions. In this context a further problem has been found, that is the modality of intervention on the buildings repaired in the past with unsuccessful techniques.

Design for Structural Investigation and Diagnosis

Historic masonry buildings, whatever use is made of them at present or in the future, have to show structural stability. In fact the existing masonry buildings usually correspond to different typologies and to different behaviour of the structure: (i) isolated buildings, (ii) building in a row, (iii) complex buildings, (iv) towers, (v) palaces, (vi) churches, (vii) arenas [2]. The modelling of these structures can be very difficult. When the structure is a complex one, only linear elastic models are easily usable. Non-linear models are difficult to apply to complex geometries and to non homogeneous materials. Furthermore when the complexity of the structure is given by its evolution along the centuries starting from a simple volume to a more and more complex volume [2], then modelling has to take into account all the vulnerabilities and defects accumulated during the subsequent transformations.

No doubt that the failures mentioned in the previous Section could have been avoided if a better knowledge of the masonry texture and of the structure from its geometry to its modifications would have been available.

Figure 1 shows which type of investigation can be carried out through in situ and laboratory tests and which kind of parameters can constitute the input data for the structural analysis.

Once the detailed geometry and the damage survey has been carried out and mechanical parameters are obtained with on site tests and tests on materials, the structural analysis can be performed based on the investigation results and furthermore the diagnosis of the real state of the structure can be formulated. The designer should remember that every investigation has its cost; it is evident therefore that every single operation must be carefully designed and optimised to obtain the desired results.
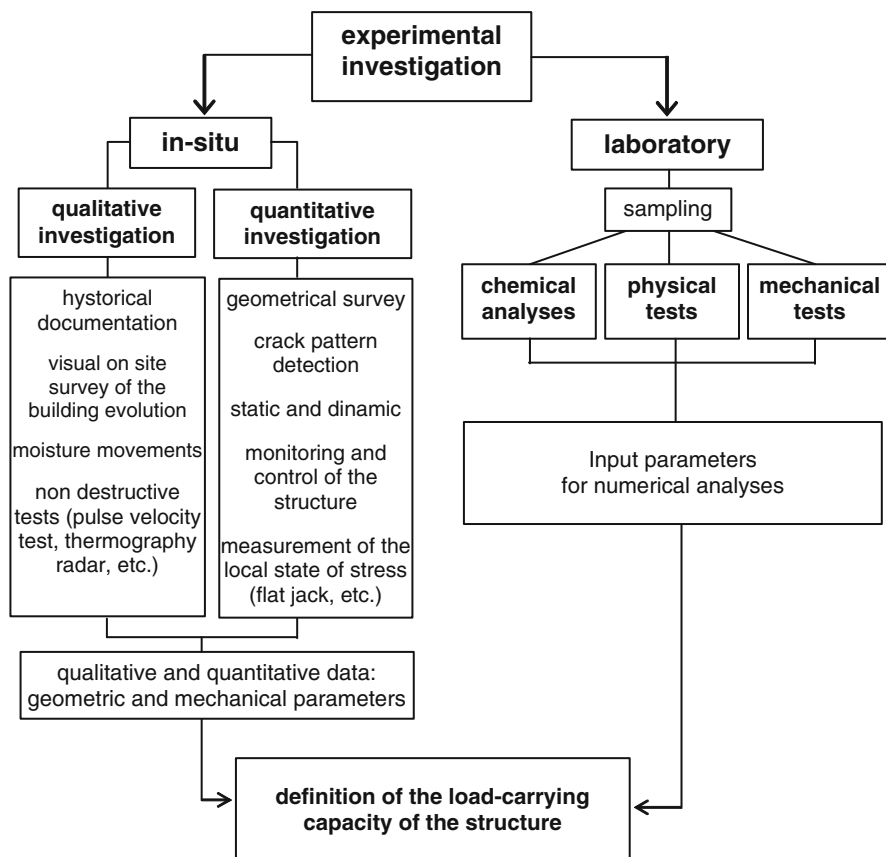
Fig. 1 Finalization of the experimental survey to the structural analysis

General Methodology and Procedures for Investigation

The necessity of establishing the building integrity or the load carrying capacity of a masonry building arises for several reasons including: (i) assessment of the safety coefficient of the structure (before or after an earthquake, or following accidental events like hurricanes, fire, etc.), (ii) change of use or extension of the building, (iii) assessment of the effectiveness of repair techniques applied to structures or materials, and (iv) long-term monitoring of material and structural performance.

The flow chart of Fig. 2 [2] schematically represents the needs to be fulfilled by the experimental investigation together with the techniques adequate to these needs and in the following the different steps of the investigation are illustrated.
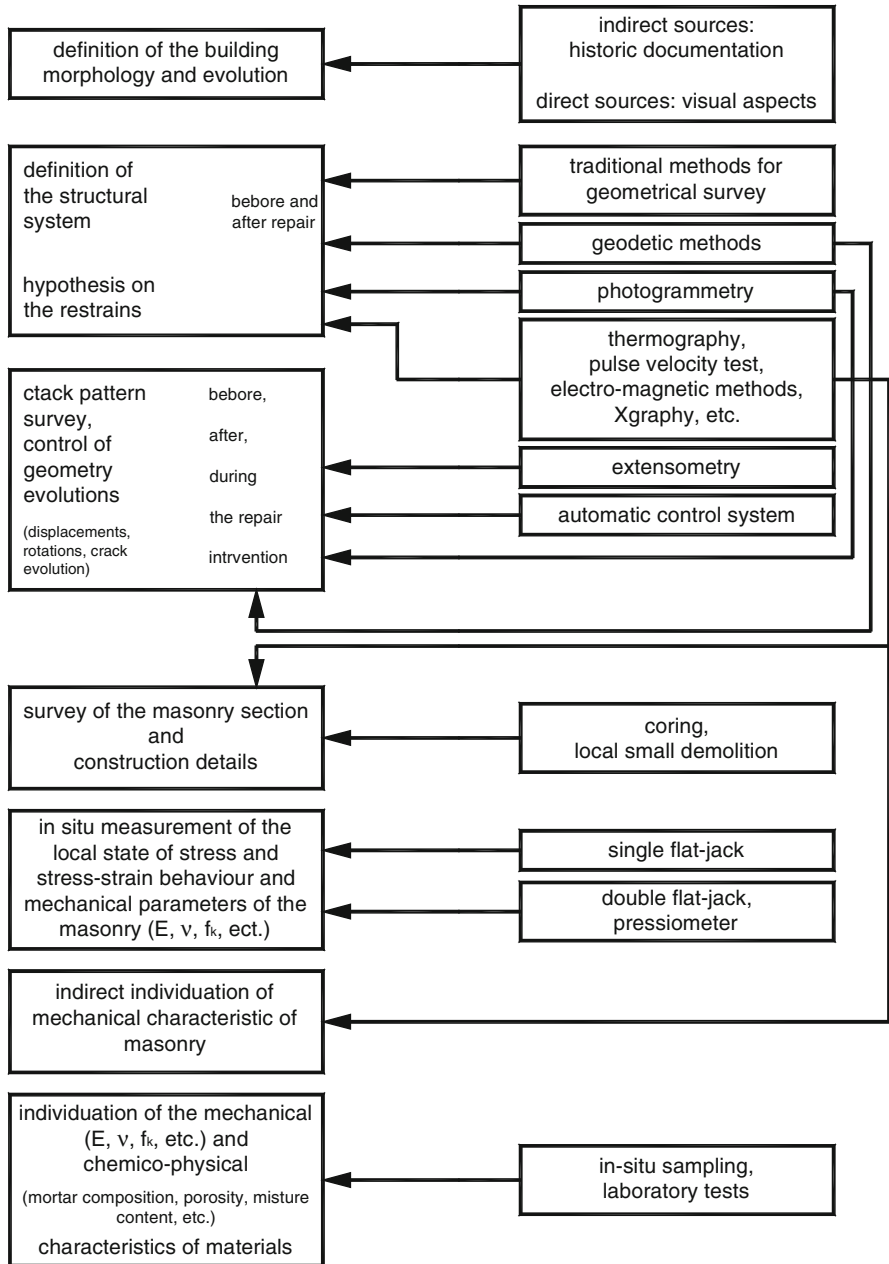
Fig. 2 Information required and correspondent investigation techniques

Building Evolution, Geometrical and Crack Pattern Survey and Monitoring

A preliminary in-situ visual survey is useful in order to: provide details on the geometry of the structure, identify the points where more accurate observations have to be concentrated. Following this survey a more refined investigation has to be carried out, identifying irregularities (vertical deviations, rotations, etc.). In the meantime the historical evolution of the structure has to be known in order to explain the signs of damage detected on the building (Fig. 3). Then a geometrical survey of the building has to be carried out. Often the geometrical details of the structure need a special refined survey. Traditional photogrammetry and use of laser scanner can be of great help in defining the geometry of vaults and arches.

Especially important is the survey and drawing of the crack patterns (Fig. 4). The interpretation of the crack pattern can be of great help in understanding the state of damage of the structure, its possible causes and the type of survey to be performed, provided that the evolution history of the building is already known [2]. The surveyed geometries are then given as input data to a structural calculation model.

Control of geometry evolution: structure control by static and dynamic monitoring

Where an important crack pattern is detected and its progressive growth is suspected due to soil settlements, temperature variations or to excessive loads, the measure of displacements in the structure as function of time has to be collected. The so called static monitoring systems can be installed on the structure in order to follow its evolution. They are frequently applied to important constructions, like bell towers or cathedrals (e.g. to the Pisa leaning Tower, to the Dome of the Florence Cathedral
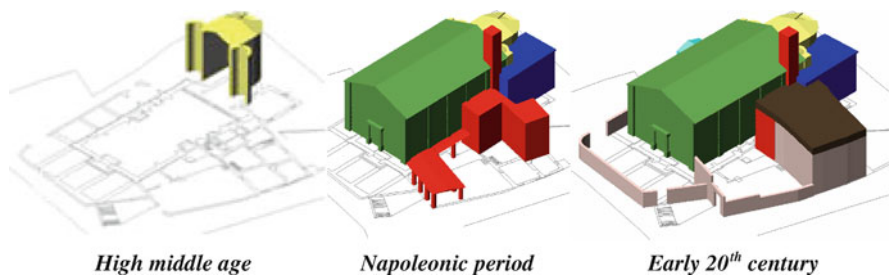
Fig. 3 Construction phases of the church of S. Michele at Sabbio Chiese
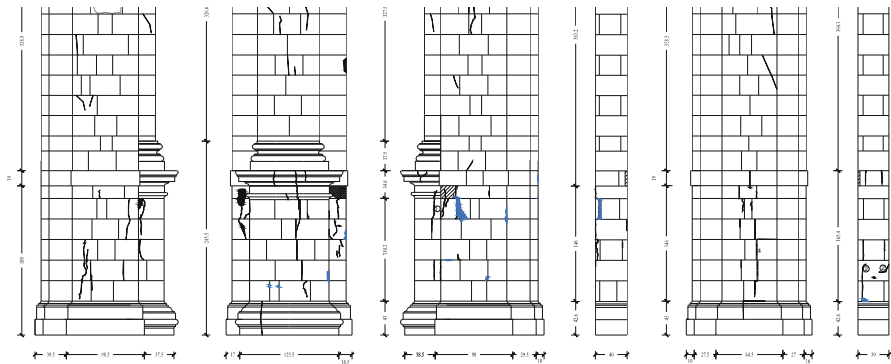
Fig. 4 Typical crack pattern of a pillar under heavy compressive stresses
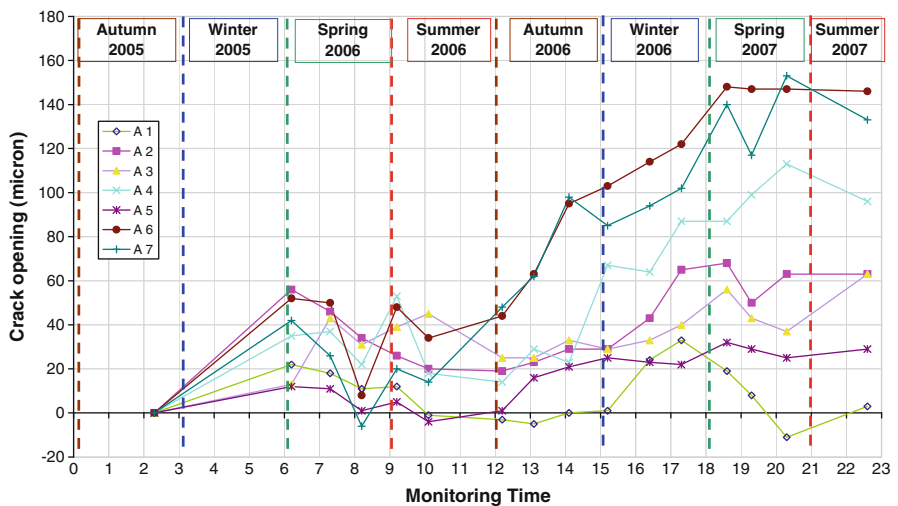
Fig. 5 Crack monitoring made with a removable extensometer

in Italy [1]) and the system may stay in place for years before a decision can be taken for repair or strengthening.

Very simple monitoring systems can be also applied to some of the most important cracks in masonry walls, where the opening of the cracks along the time can be measured by removable extensometers with high resolution. This simple system can give very important information to the designer on the evolution of the damage. Figure 5 shows the case of a cracks progression in the Basilica of St. Lorenzo in Cremona [3].

In-situ testing using dynamic methods can be considered a reliable non-destructive procedure to verify the structural behaviour and integrity of a building. The principal objective of the dynamic tests is to control the behaviour of the structure to vibration. The first test carried out can be seen also as the starting one of a periodical survey using vibration monitoring. Acceptance of vibration monitoring as an effective technique of diagnosis has been supported by different studies [4].

These tests are very important to detect eventual anomalies in the diagnostic phase and to calibrate efficient analytic models [4]. In this way it is possible to verify the effectiveness of the computational methods used in the analysis and control of the structure. The availability of an efficient numerical model allows for checking and predicting the structure behaviour to dynamic actions like, for example, strong winds effects and seismic actions.

The environmental excitation sources could be the wind, the traffic or the bell ringing in the particular case of towers [4]. The forced vibrations could be produced by local hammering systems or by the use of vibrodines. An accelerometer net is installed in chosen significant parts of the structure.

The dynamic tests allow detecting the frequencies, the modal shapes and the correspondent modal damping of a structure. These parameters are characteristics of the local and global behaviour of a structure.

Survey of the Masonry Section and Construction Details

Once the global geometry has been investigated, the complex structure of the wall must be known. The structural performance of a masonry wall can be understood provided the following factors are known: (i) the geometry; (ii) the characteristics of its masonry texture (single or multiple leaf walls, connection between the leaves, joints empty or filled with mortar), (iii) physical, chemical and mechanical characteristics of the components (bricks, stones, mortar); (iv) the characteristics of masonry as a composite material.

In the case of multiple leaf masonry, the masonry texture, which strongly influences the bearing capacity of the wall, often can not be easily identified (Fig. 6). The worst defect of these masonry walls is that they are not monolithic in the lateral direction.

Fig. 6 On site survey of stonework sections

Minor destructive techniques for masonry, sampling and coring

In order to understand the morphology of a masonry wall it is important a direct inspection. Sometimes it can be performed by removing few bricks or stones, surveying photographically and drawing the section of the wall. This can be more efficient than coring.

On-site Measurement of Mechanical Parameters: Flat Jack Test

The method was originally applied to determine the in-situ compression stress level of the masonry. The first applications of this technique on some historical monuments, clearly showed its great potential.

The determination of the stress under applied compression is based on the stress relaxation caused by a cut perpendicular to the wall surface; the stress release is determined by a partial closing of the cutting, i.e. the distance after the cutting is lower than before [5]. A thin flat-jack is placed inside the cut and the oil pressure into the jack is gradually increased to obtain the distance measured before the cut.

The displacements caused by the slot and the ones subsequently induced by the flat-jack are measured by a removable extensometer before, after the slot and during the tests. P_f corresponds to the pressure of the hydraulic system driving the displacements until equal to those read before the slot is executed. This value, multiplied by two known constants, gives the value of the stress in the masonry before the test.

The test has been also developed as double flat jack test to measure the stress-strain behaviour of the masonry under compression, by using two flat jacks.

Indirect Individuation of Geometrical and Mechanical Characteristics of Masonry: Non Destructive Tests

Many authors have mentioned the importance of evaluating existing masonry buildings by non-destructive investigation carried out in situ. NDTs can be used for several purposes: (i) detection of hidden structural elements, like floor structures, arches, pillars, etc., (ii) qualification of masonry and of masonry materials, (iii) mapping of non homogeneity of the materials used in the walls (e.g. use of different bricks in the history of the building), (iv) evaluation of the extent of mechanical damage in cracked structures, (v) detection of the presence of voids and flaws, (vi) evaluation of moisture content and capillary rise, (viii) detection of surface decay, and (viii) evaluation of mortar and brick or stone mechanical and physical properties.
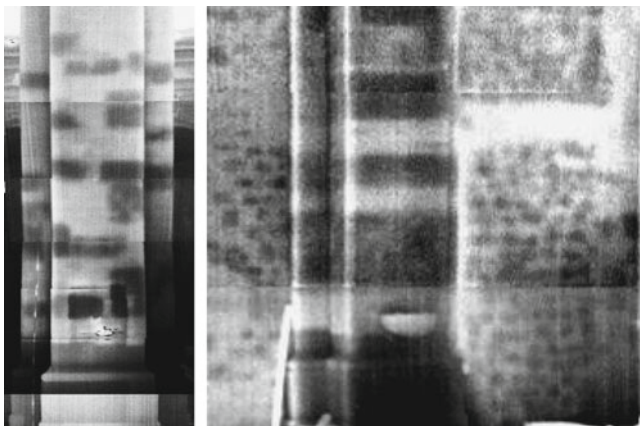
Fig. 7 IR thermography applied to a pillar and to a built-in pillar in a wall of the Church of St. Biagio (L'Aquila) to detect the hidden masonry texture

Thermovision applications

Thermovision is a NDT, which has been applied since several years to works of art and monumental buildings. The thermographic analysis is based on the thermal conductivity of a material and may be passive or active. The passive application analyses the radiation of a surface during thermal cycles due to natural phenomena (insulation and subsequent cooling). For the active application forced heating to the analyzed surfaces are applied.

A camera sensitive to infrared radiation collects the thermal radiation. In fact each material emits energy (electromagnetic radiation) in this field of radiation; the material is characterized by a thermal conductivity, that is the capacity of the material itself of transmitting heat, and its own specific heat. The result is a thermographic image in a colored scale. At each tone corresponds a temperature range. Usually the differences of temperatures are fraction of degree. Thermovision is particularly interesting for studies on frescoed walls [8-19]. Other applications can be: (i) survey of cavities, (ii) detection of inclusions of different materials, (iii) detection of water and heating systems, (iv) moisture presence. In the presence of moisture, the camera will find the coldest surface areas, where evaporation is taking place. In the diagnosis of old masonries, thermovision allows the analysis of the most superficial layers frequently hidden by renders (Fig. 7).

Sonic pulse velocity test

The testing methodology is based on the generation of sonic or ultrasonic impulses at a point of the structure. An elastic wave is generated by a percussion or by an
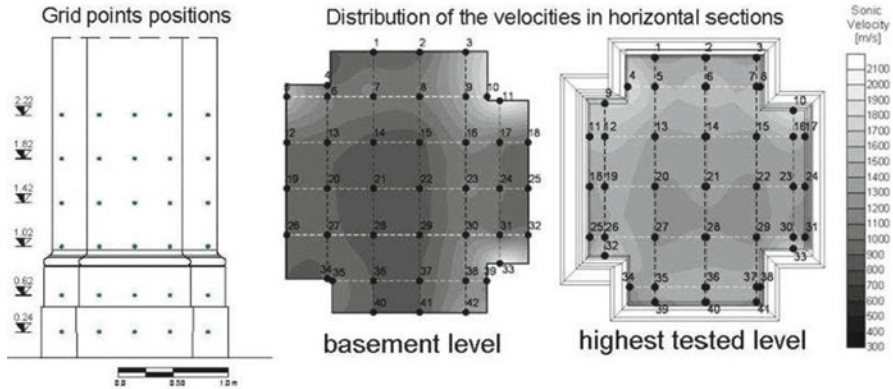
Fig. 8 Sonic tests on a pillar of the Church of St. Biagio, L'Aquila

electrodynamic or pneumatic device (transmitter) and collected through a receiver, usually an accelerometer, which can be placed in various positions.

The most used application to masonry walls consists generally in measuring the time the impulse takes to cover the distance between the transmitter and the receiver. The use of sonic tests for masonry structures has the following aims: (i) to qualify masonry through the morphology of the wall section; (ii) to detect the presence of voids and flaws and to find crack and damage patterns; (iii) to control the effectiveness of repair by injection technique which can change the physical characteristics of materials.

The limitation given by ultrasonic tests in the case of very inhomogeneous material made the sonic pulse velocity tests more appealing for masonry. Efforts have been made by the authors to correlate the sonic parameter to the mechanical characteristics of the material, but this correlation seems difficult [6].

The fundaments of wave propagation through solids allow recognising the theoretical capabilities and limitations of the technique. The velocity of a stress wave passing through a solid material is proportional to the density ρ, dynamic modulus E, and Poisson's ratio v of the material. Resolution in terms of the smallest recognisable features is related to the dominant wave-length (as determinate by the frequency) of the incident wave and also to the size of the tested element. As frequency increases, the rate of waveform attenuation also increases limiting the size of the wall section, which can be investigated. The optimal frequency is chosen considering attenuation and resolution requirements to obtain a reasonable combination of the two limiting parameters. In general it is preferable to use sonic pulse velocity with an input frequency of 3.5 kHz for stone and brick masonry. Figure 8 shows the results of sonic tests applied to the study of velocity distribution in two sections of a pillar damaged by the earthquake; the presence of low velocities indicates the presence of cracks and voids. The masonry texture is shown in Fig. 7.

| Radargram | Depth of the blocks | First layer stone blocks |
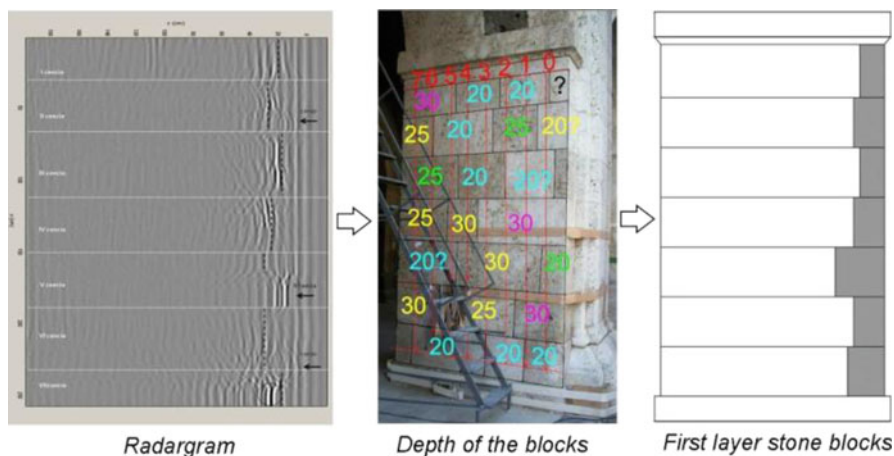
Fig. 9 Radargram achieved on a pillar of the Castle of L'Aquila and its relative interpretation to estimate the depth of the first layer of the stone blocks

It is important to stress that the pulse sonic velocity is characteristic of each masonry typology and it is impossible to generalize the values. The tests, then, have to be calibrated for the different types of masonry directly on site.

The application of RADAR

Among the techniques and procedures of investigation which have been proposed in these last years, radar seems from one hand to be most promising, from the other to need a great deal more of study and research [7]. Procedures to masonry can be the following: (i) to locate the position of large voids and inclusions of different materials, like steel, wood, etc.; (ii) to qualify the state of conservation or damage of the walls; (iii) to define the presence and the level of moisture; (iv) to detect the morphology of the wall section in multiple leaf stone and brick masonry structures (Fig. 9), (v) to detect the presence of cracks and flaws in a wall.

The method is based on the propagation of short electromagnetic impulses, which are transmitted into the building material using a dipole antenna. The impulses are reflected at interfaces between materials with different dielectric properties, i. e. at the surface and backside of walls, at detachments, voids, etc. When the transmitting and receiving antennas, which are often contained in the same housing, are moved along the surface of the object under investigation, radargrams (colour or grey scale intensity charts giving the position of the antenna against the travel time) are produced. Measuring the time range between the emission of the wave and the echo, and knowing the velocity of propagation in the media it is possible to know the depth of the obstacle in the wall. The presence of humidity and water highly

influences the results of radar tests. Therefore Radar tests need always a preliminary calibration in order to verify if the emitted signal is enough powerful to detect the opposite side of the wall and the wave speed.

The choice of the antenna frequency must be made on a site basis. During the test it is important to control the radar potentialities in relation to the frequency used.

One of the limits of the technique is the low readability of the results. In fact usually radar data are clearly readable only by experts. It is important to show results, as radargrams and graphics, which are significant to operators like architects and engineers [7].

Mechanical, Physical, Chemical Properties Through Laboratory Tests

If samples of the materials are needed for destructive tests they must be taken from the walls inflicting the lowest possible damage. The technique of sampling is very important, since samples must be as undamaged as possible in order to be representative of the material in situ. The aims of these tests are the followings: (i) to characterize the material from a chemical, physical and mechanical point of view, (ii) to detect its origin, (iii) to know its composition and content in order to use compatible materials for the repair, and (iv) to measure its decay and the durability to aggressive agents from new materials used for restoration.

Conclusions

A methodology for investigation on historic structures aimed to their preservation was outlined. Knowledge of the building details, materials and structural elements is essential in order to avoid past mistakes. Once the geometry, crack pattern, masonry wall morphology, hidden features, state of stress, stress-strain behaviour, materials properties and density variation are known, they can help in the collection of input data and calibration of mathematical models for the diagnosis of masonry structure.

NDTs and MDTs are efficient only if their application is carefully calibrated on the studied building. Nevertheless the interpretation of the results is a difficult task and should be accomplished in a multidisciplinary approach. Further research is needed on the complementarity of the techniques and on the development of appropriate software in order to obtain clear interpretations.

To this purpose it is important the production of guidelines for the correct application of investigation techniques to diagnosis problems of different classes of masonries. This is a task assumed by the authors and also by the members of a RILEM TC SAM, after a three years and more collaboration within European Projects.

References

[1] Modena C., Binda L. and Anzani A. (1997), Investigation for the design and control of the repair intervention on historical stone masonry wall. In: *7th Int. Conf. and Exhibition, Structural Faults and Repair 97*, Edinburgh, Vol. 3, p. 233.

[2] Binda, L. Saisi A. and Tiraboschi C. (2002), Investigation procedures for the diagnosis of historic masonries, In: *Structural Engineering Compendium I*, Elsevier, Oxford (UK), p. 321.

[3] Binda, L., Cardani, G., Gentile, C., Zanzi, L. and Massetti E. (2009), In: *Conf. Protection of Historical Buildings – PROHITECH* 2009, F.M. Mazzolani (Ed.), June 21–24 2009, Rome, Vol I., pp. 115–124.

[4] Gentile, C., Saisi A. and Binda L. (2002), Dynamic investigation of a historic masonry Bell Tower, In: *6th Int. Masonry Conf.*, London, 4th–6th Nov., p. 192.

[5] ASTM C1196-91 (1991), Standard test method for in situ compressive stress within solid unit masonry estimated using the flat-jack method, ASTM International, Philadelphia, ASTM.

[6] Binda, L., Anzani, A., Cantini, L., Cardani, G., Tedeschi, C. and Saisi, A. (2006), In: *1st Int. Conf. on Restoration of Heritage Masonry Structures*, 24-27/4/2006, Cairo, Egypt, pp. P10-1/ P10–10.

[7] Binda, L., Saisi, A. and Zanzi, L., (2008), In: *4-Day Int. Conf. Structural Faults & Repair*, Edinburgh, 10-12/6/2008, pp. 1–14.

Monitoring of Salt Content in Mineral Materials Using Wireless Sensor Networks

J. Frick, F. Lehmann, K. Menzel, H. Pakdel and M. Krüger

Abstract The recrystallization of salts due to changes in moisture content is one of the major damage mechanisms in historic materials like natural stones, bricks, plasters, and mortars. This paper presents a new development in the field of wireless monitoring the salt content in historic mineral materials. In this investigation ion selective potential sensors (electrodes) are used for monitoring salt displacement in time, influenced by changes in moisture content. Different kind of electrodes and electrode couplings are tested in laboratory, and in field measurements. For measuring the potential, low power data acquisition hardware was developed that is optimized for using it in wireless sensor networks. Data acquisition uses a competitive wireless sensor network system that is further developed in the SMooHS-Project (Smart Monitoring of Historic Structures, Collaborative Project in the 7th Framework Programme of the EU) to operate under harsh environments. First results of the laboratory and field test are presented, showing that long-term monitoring of salt content is feasible.

Keywords Ion selective electrodes • Material moisture • Mineral materials • Salts • Wireless monitoring • Desalination

Introduction

The in situ measurement of salts in historic building materials is a challenging task. Starting form experiences developed for the monitoring of chloride content in concrete [1, 2] a first ion selective electrode was chosen based on silver/silver chloride. Within the SMooHS-Project [3] a special low power node for potential measurements was developed to fit in a wireless sensor network system [4].

J. Frick (✉) • F. Lehmann • K. Menzel • H. Pakdel • M. Krüger
Materialprüfungsanstalt Universität Stuttgart, Germany
e-mail: Juergen.Frick@mpa.uni-stuttgart.de

Experimental

Different electrodes were developed and tested, starting from simple silver wires up to silver/silver chloride electrodes (Ag/AgCl). The latter one gave the best results and consists of a silver wire with electrochemically deposited AgCl and a final tip of AgCl on it. The measured potential is the difference between the potential of the ion selective silver/silver chloride electrode (Ag/AgCl) and the used saturated reference electrode. It can be written following Nernst's law [1]:

$$E_M = E^0_{Ag/AgCl} - \frac{RT}{F} \ln a_{Cl^-} - E_{Ref} \qquad with\ a_{Cl^-} = \gamma_{\pm}\ c_{Cl^-} \tag{1}$$

Here, $E^0_{Ag/AgCl}$ is the standard potential of the silver/silver chloride equilibrium reaction, R is the gas constant, F the Faraday constant, T the absolute Temperature [K], a_{Cl^-} the chloride activity, E_{Ref} the potential of the reference electrode, $\gamma_{\pm}$ the mean activity coefficients, and c_{Cl^-} the chloride concentration. The electrodes were tested in different solutions with varying Chloride content. The results are shown in Fig. 1. The concentration dependence follows the Nernst law (Eqn. 1) and is in good accuracy with the theoretical values. The mean activity coefficients $\gamma_{\pm}$ for NaCl and CaCl$_2$ solutions were taken from [5, 6] and the difference potential $E^0_{Ag/AgCl} - E_{Ref} = -18.9\ mV$ at 20 °C for a saturated calomel reference electrode from [2]. Two types of reference electrodes were used, saturated calomel and saturated Ag/AgCl electrodes (Schott Instruments 9801/85).

Small holes (Ø = 3 to 5 mm) were drilled in samples or walls to incorporate the electrodes. Different types of fixing materials were tested (gypsum, and mortars consisting of water based silica dispersions (Syton X30, Ludox HSA) with adapted filling materials). The developed wireless potential measurement node consists of
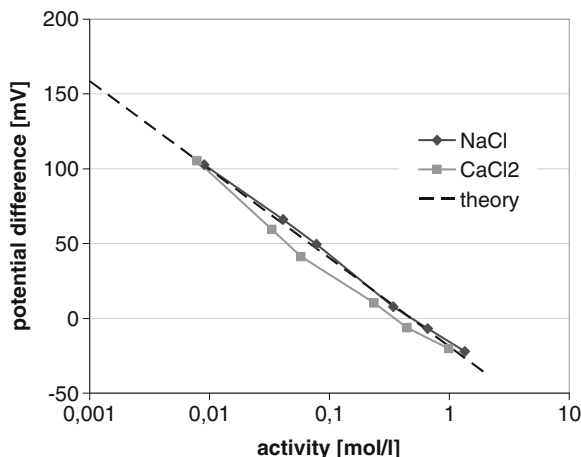
Fig. 1 Potential difference within different solutions. Reference electrode: Calomel

an electrometer with a scanner for eight channels. The input resistance is 100 GΩ. It transmits the data to a base station which is connected to the internet via GSM or a direct LAN connection. The data were stored in a SQL-database server. Due to the high input resistance special care was taken to the shielding. The latest version of the developed system was therefore equipped with triaxial cables. First measurements during development of the system and validation measurements were done with a multimeter Keithley model 2701/E with a multiplexer module model 7702 (Input resistance > 10 GΩ) with up to 40 channels.

Results

According to the situation in salt polluted mineral materials, three different experiments in laboratory and on site will be described. First a capillary suction experiment trying to detect capillary movement of salts in sandstone to simulate the situation in a wall with rising damp. Second a desalination process of the same sample after the capillary suction experiment. Desalination with different poultice materials is often used to reduce the salt content in salt polluted materials. The potential measurements allow it, in a non-destructive way to follow online the accumulation of salts in the poultice and to provide information on the optimal time to change the poultice. The third experiment was performed in a wall of the chapel in Schönbrunn castle in Vienna were a wall heating system was installed to avoid condensation on the wall.

The capillary suction experiment (solution 0.1 mol/l NaCl) was performed on a sample of Sander sandstone (4 x 4 x 15 cm^3) equipped with 6 Ag/AgCl electrodes. Figure 2 (left) shows the measured potential differences. The electrodes react on the
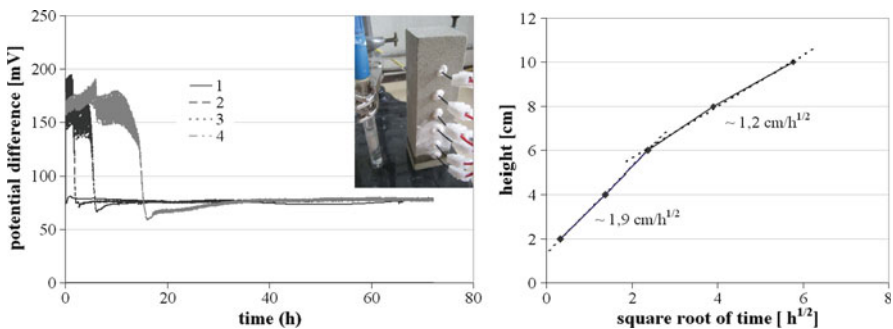
Fig. 2 Left: Capillary suction of Sander sandstone (4 x 4 x 15 cm^3) over time. Solution: NaCl 0.1 mol/l. Potential signals of the first 4 electrodes. Reference electrode: Calomel. The insert shows the experiment. Right: Arrival of solution (NaCl 0.1 mol/l) at electrodes over square root of time. Dashed: Interpolations of suction velocities of the two suction periods. The estimated values are given
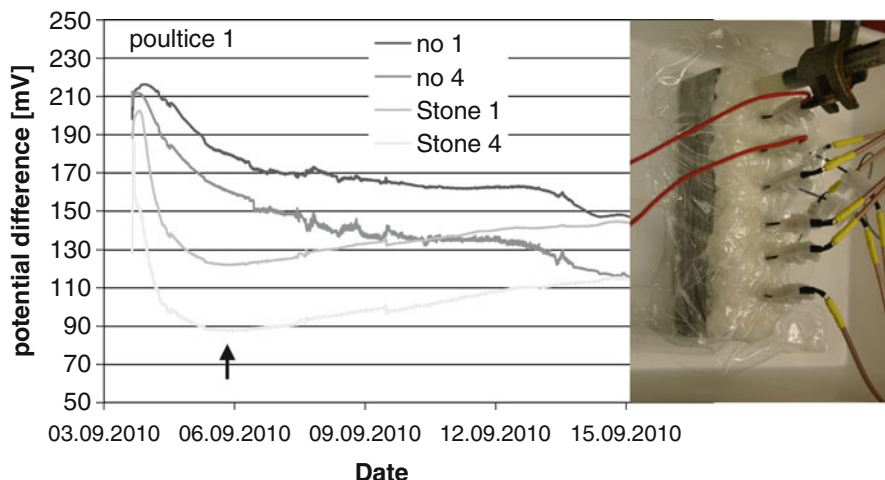
Fig. 3 Desalination of previous salinated Sander sandstone with poultices (Arbocel). Potential signals of two electrodes in the poultice and two in the stone. Reference electrode: Saturated Ag/AgCl. The insert shows the experiment

arrival of solution with a steep drop of potential followed by a rising to the final potential according to the salt content.

The arrival times follow a square root of time dependence in two periods (Fig. 2, right). The first one gives a suction velocity of 1.9 cm/h$^{1/2}$ and the second one of 1.2 cm/h$^{1/2}$. With porosity and density values from literature [7] a rough estimate gives reasonable values for the W-value of 2.7 and 1.6 kg/(m^{2}h$^{1/2}$). [8] give W-values parallel to sedimentation of 2.5 kg/(m^{2}h$^{1/2}$) and perpendicular of 3.3 kg/(m^{2}h$^{1/2}$) which are in good agreement to the first estimated value. According to the small size of sample the second value could be lowered by evaporation due to the open surface of the sample.

After drying of the previous salinated sample, desalination with two poultices (Arbocel) was performed. The poultices were mixed with demineralised water and putted on the sample (height: ~ 2 cm) and covered with a foil to prevent too fast drying. The installed electrodes in the stone and additional electrodes in the poultice (all Ag/AgCl) were used to measure the potential difference. The measured signals (Fig. 3) in the stone shows first a minimum after 2 days which corresponds to a dissolution of the crystallised salts in the stone. Then the potential rises until the end of the experiment which is due to the desalination process. The potential of poultice electrodes descends during the whole experiment due to the accumulation of salts. The final values of potentials are similar for corresponding electrodes in stone and poultice. The differences of the two positions are due to the previous suction with an accumulation of salts around electrode 4. The final height of solution was electrode 5.

A comparison is given of Chloride content from salt analyses of drill dust parallel to the electrodes (1.5 cm depth, Ø 3 mm) before and after desalination, and of the
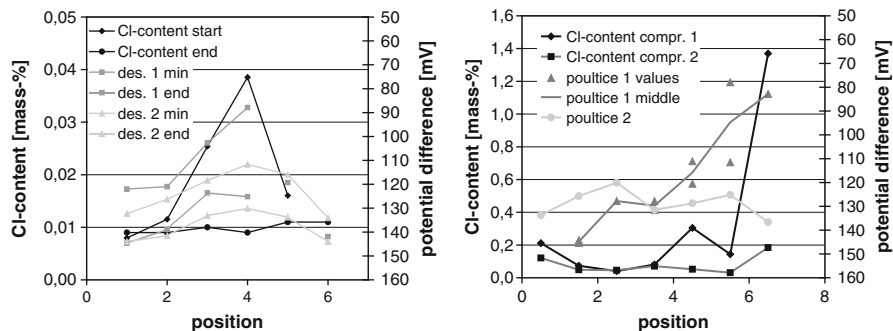
Fig. 4 Comparison of salt analyses of drill dust from the stone before and after desalination and of poultices with reciprocal potential values. Left: Stone values, the minimum and end values of potential are given. Right: Poultice values
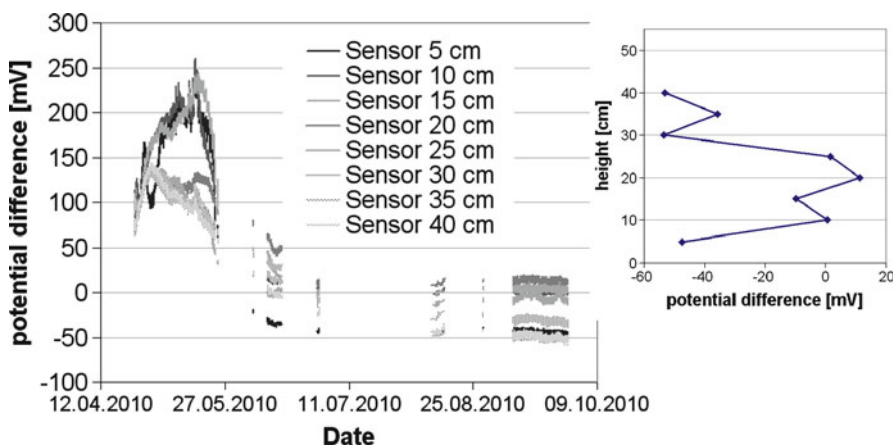
Fig. 5 Potential difference measurements in the chapel of Schönbrunn castle in Vienna in a wall plate of Adneter limestone after installation of a wall heating system. The Insert shows momentary values in the stable phase in September. Reference electrode: Calomel

poultices with the reciprocal potential (Fig. 4). The qualitative behaviour is comparable. The slight differences occur due to the different measurement conditions. The Chloride content is a middle value over a larger volume and the potential values are measurements at one point. Additional the analyses were taken after complete drying of stone and poultices.

A field test was performed at the chapel of Schönbrunn castle in Vienna. Eight electrodes were installed in a plate of Adneter limestone at a wall. The height was 5 to 40 cm above a wall heating system which was started at the same time. The energy provided from the system is 50 W per m. The system works since end of April 2010. Figure 5 shows the measured potential values.

After 2 to 3 months the system reaches stable conditions. The missing values in July and August are due to communication problems of the wireless system in that period. In September four electrodes show potentials of around -40 to -50 mV and four of around -10 to 10 mV. The temperature due to wall heating reaches 27.5 °C at 5 cm height and 21.9 °C at 50 cm height. Salt analyses of drill dust from electrode installation show a domination of Sulphates (Gypsum and Thenardite) with contents from 0.03 up to 7.23 mass-%, and some Chlorides from below 0,01 up to 0.07 mass-% in the efflorescence. Due to the salt mixture the potential values are only qualitative information. Additional salt analyses are foreseen in near future to give information of the stable phase.

Conclusions

The developed electrodes and electrometer show reasonable results and could be used to monitor the salt content in mineral materials. Further tests are needed to evaluate potential values in case of salt mixtures which are normal in historic buildings [9]. The desalination experiment shows the potential of the method for the development and optimisation of desalination procedures, and poultice materials. In this case the method could be used as non-destructive online monitoring tool on salt distributions.

References

[1] Angst, A.; Elsener, B.; Larsen, C.K.; Vennesland Ø. (2010) *J. Appl. Electrochem.*, vol. 40, pp. 561–573.
[2] Elsener, B.; Zimmermann, L.; Böhni, H. (2003) *Mater. Corros.*, vol. 54, pp. 440–446.
[3] Grosse, C.U.; Pascale, G.; Simon, S.; Krüger, M.; Troi, A.; Colla, C.; Rajčić, V; Lukomski, M. (2008) In: *Proceedings of In situ Monitoring of Monumental Surfaces – SMW08*, Florence 27th – 29th October 2008.
[4] Krüger, M.; Grosse, C.U.; Bachmaier, S.A.; Willeke, J. (2010) In: *Proceedings of the International Workshop on Preservation of Heritage Structures Using ACM and SHM. Proceedings of CSHM-3*, Canada, Ottawa-Gatineau.
[5] *Handbook of chemistry and physics* (2010–2011) 91st edn., CRC Press, Boca Raton, online version.
[6] Shreir, L.L.; Jarman, R.A.; Burstein, G.T. (1994) *Corrosion*, vol. 2, 3rd edn. Butterworth Heinemann, Oxford.
[7] Grimm, W.-D. (1990) *Bildatlas wichtiger Denkmalgesteine der Bundesrepublik Deutschland*, Arbeitshefte vol. 50, Bayerisches Landesamt für Denkmalpflege.

[8] Szilagyi, J. (1995) *Untersuchung petrophysikalischer Eigenschaften an Leitgesteinen der Denkmalpflege*, report within BMFT-project 7025B: *Verbesserung von Methoden zur Diagnose und Therapie von Tragstabilitätsschäden/schwächen kritischer Mauerwerks-Partien an Baudenkmälern, (*research contract Z/A-78, 1-10-1991) Technical University of Dresden – Professorship Applied Geology.

[9] Steiger, M. (2005) *Restoration of Buildings and Monuments – Bauinstand-setzung und Denkmalpflege*, vol. 11, no. 6, pp. 419–432.

Development and Application of Active Thermography for Monitoring of Deterioration Processes of Historic Structures

C. Maierhofer, R. Krankenhagen, M. Röllig, U. Kalisch and J. Meinhardt

Abstract As shown recently, the quantification of damage in historic masonry structures is possible by using active thermography. In this paper, a case study is presented concerning systematic studies of the determination of damage size and prognosis of damage increase inside a sandstone column by using different approaches of active thermography. Various heating sources as well as impulse and periodic heating have been compared. Reproducible investigations in regular time intervals for structural monitoring are possible.

Keywords Active thermography • Camera calibration • Historic structure • Monitoring • Sandstone

Introduction

Environmental influences like sun radiation, air pollution, moisture, freeze thaw alterations, vibration and settlements very often induce deterioration processes starting mainly at the surface of building structures. The temporal behaviour of these processes mainly depends on climatic and material parameters. For the prediction of structural performances and for the evaluation of protection measures, strategies for long term monitoring are urgently required. Thus, for early digital detection, spatial recording and quantification of damage at and close to the surface, innovative automated electronic methods have been evaluated and optimized in the frame of a national funded research project.

C. Maierhofer (✉) • R. Krankenhagen • M. Röllig
BAM Federal Institute for Materials Research and Testing, Berlin, Germany
e-mail: christiane.maierhofer@bam.de

U. Kalisch • J. Meinhardt
IDK Institute for Diagnosis and Conservation on Monuments in Saxony
and Saxony-Anhalt e. V., Halle, Germany

A measurement principle based on the combination of laser supported methods for recording the outer geometry and topology of building surfaces and for keeping geometrical changes (e. g. of cracks, bulging, deformation) and of active thermography for detecting defects in the near surface area, which cannot be seen directly (e. g. delaminations, voids, structure of masonry behind plaster, moisture at interfaces between plaster and masonry) is very well suited for monitoring. The combination of the geometric and thermographic data offers a more precise insight into the transport and deterioration processes taking part below the surface of historical structures [1]. On the one hand side, details which have been detected with active thermography can be related to small geometrical structures. This simplifies the interpretation of the finding. On the other side, marginal and long term geometrical modifications in the magnitude of submillimeters are perceived with active thermography, if the underlying processes have an influence on the thermal behaviour. In this case delaminations of layers or swelling and shrinkage due to different moisture contents can be identified.

In this contribution, one tool of this system is presented. Active thermography provides the detection and characterization of defects and inhomogeneities in building structures up to a depth of 10 cm. Different heat sources, the variation of heating duration and periodic heating reveals an adaption of this method to different testing problems. An application is presented demonstrating investigations of a column made of Lower Triassic sandstone.

Experimentals

The active approach of thermography investigation of historic masonry structures implies a direct heating. Common heating techniques are usually operating directly like step impulse and periodic heating [2]. The optimal heat source should generate a homogeneous heat flow without any delay along the whole surface area of the structure under investigation. In reality, these conditions can only be approximated. In several cases, radiation sources like flash lights, halogen lamps and infrared (IR) radiators have proven to be the most suitable sources by being fast and efficient and generating a homogeneous and moderate temperature increase at the surfaces of historical building materials. For uneven and/or inhomogeneous surfaces with varying emissivities and jutties, convective sources, e. g. fan heaters, should be applied [3].

Heating with a step impulse is visualised in Fig. 1. In Fig. 1a, the black line shows that the halogen lamps have been switched on for 60 s and a heat flow Q is introduced into the object for a duration time t. The related increase of surface temperature T as well as the cooling down is displayed in Fig. 1b, black line. Here, results of investigations on the sandstone column of the case study described below are shown as an example. For periodic heating (also known as lock-in thermography), the surface temperature is modulated with a step function or a sinus, e. g. by using halogen lamps, see Fig. 1 a, grey line. Thus, the surface background temperature is
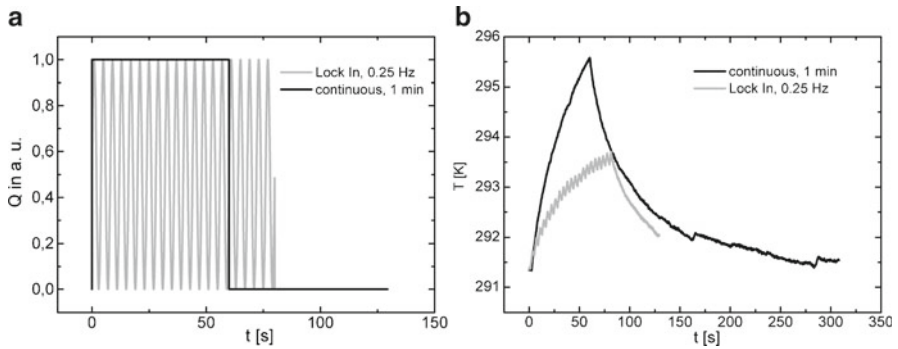
Fig. 1 (**a**) Heat flow Q in arbitrary units (a. u.) as a function of time for impulse heating for 1 min (black line) and periodic heating with a frequency of 0.25 Hz (grey line). (**b**) Average temperature T at the middle of the sandstone column (in the Magdeburg Cathedral of the case study described below) as a function of time during and after heating

increasing as shown in Fig. 1b, grey line. With periodic heating (on and off) for 80 s, only about half of the average temperature rise of impulse heating for 60 s was measured. The generated thermal waves are reflected at interfaces, where the thermal effusivity is changing abruptly. These reflections superimpose with the incident thermal waves and generate a specific temperature field at the surface. Intensity and phase of the temperature field vary with position and time and depend on depth and material properties of the reflector. This temperature field is recorded as a sequence of thermograms by the IR camera. Afterwards, the sequences, which are correlated to the frequency of the heat source, can be analyzed by Fast Fourier Transformation (FFT) [4].

In the case study presented below, a microbolometer IR camera (Variocam hr from Infratec) with a maximum frame rate of 50 Hz and an array size of 640 x 480 pixels was used. The lenses are exchangeable and a wide angle, standard or tele-photo lens can be mounted. As heating sources, a fan heater and two halogen lamps with a power of 500 W each were applied. In the following, only the results recorded by using the halogen lamps are presented.

Case study

The Protestant Cathedral Saint Mauritius and Saint Katharina in Magdeburg, Germany, is a Gothic monumental building with rich equipment. It was constructed from early 13th to the early 16th century and is the second largest cathedral in Germany after the Cologne Cathedral. The Bishop's corridor, constructed after 1232, is unusually wide and high [5]. Big windows correspond to the wide gothic vaults of the choir. Columns made of Lower Triassic sandstone run around the
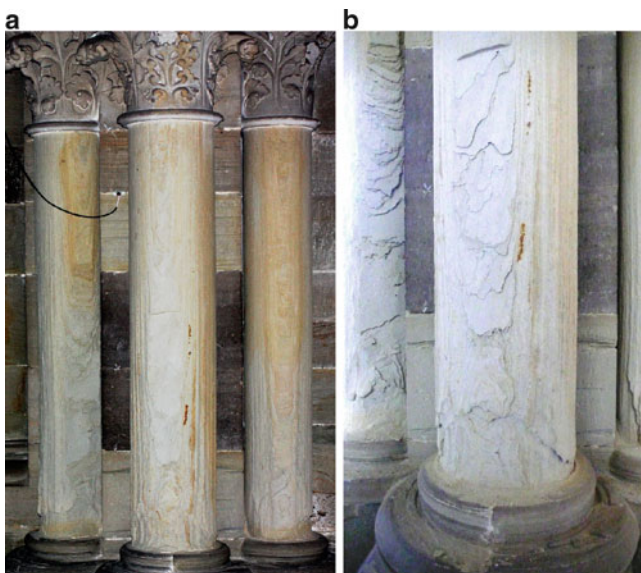
Fig. 2 (**a**) Octagon pillar with three sandstone columns in the bishops corridor. (**b**) Investigated sandstone column

octagon pillars, see Fig. 2 a. Several of these columns show large amounts of sand spreading and spalling due to environmental influences. One of these columns (see Fig. 2 b) has been an object of further research and thus has been selected for investigation with active thermography (and 3D laser scanner, see [1]). The heating was performed with impulse duration of 60 s as well as periodically with different frequencies of 0.25, 0.10 and 0.05 Hz for 10 to 20 periods by using two halogen lamps. During and after heating, the thermal images were recorded with a frame rate of up to 50 Hz with the above mentioned IR system. The distance of the two halogen lamps to the object surface was always 1.2 m, while the distance of the camera to the surface was 1.8 m. All investigations presented here were performed with the standard lens with a field of view of 30°x23°.

Results

The first measurement campaign was performed in June 2009 and was repeated in November 2009 and March 2010. The related thermograms recorded just after impulse heating of 60 s are shown in Fig. 3 a–c. The environmental parameters, the temperature of the surface before heating and the maximum temperature rise during heating are summarized in Table 1. Although the illumination with the halogen lamps could not be reproduced in an optimal way as shown in the thermograms in Fig. 3,
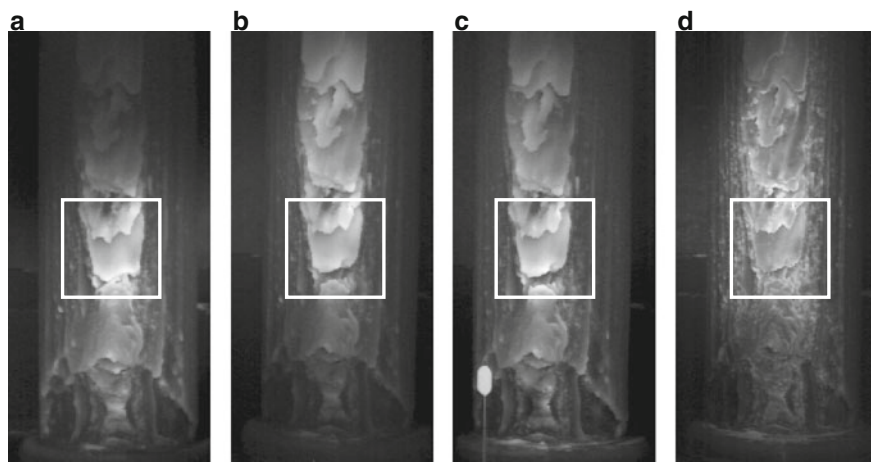
Fig. 3 (**a**) to (**c**) Thermograms of the sandstone column recorded directly after a heating time of 60 s using two halogen lamps. (**a**) June 2009, temperature range from 18.0 to 23.3 °C from black to white; (**b**) November 2009, from 10.6 to 18.0 °C; (**c**) March 2010, from 9.4 to 14.4 °C. (**d**) Amplitude image calculated from lock-in thermography at 0.05 Hz in November 2009

Table 1 Environmental conditions and maximum temperature rise at the surface of the sandstone column after 60 s heating with two halogen lamps at three different dates of investigation

	June 2009	November 2009	March 2010
Relative humidity	60%	62%	72%
Air temperature	19.0°C	13.5°C	10.0°C
Temperature on object surface (contact thermometer)	17.3°C	11.0°C	8.5°C
Maximum temperature rise directly after heating	5.9 K	7 K	5.9 K

and although the initial surface temperatures were different (maximum in June 2009, minimum in March 2010 after a cold winter), it is shown in Table 1 that the maximum temperature rise was more or less similar for all campaigns (from 5.9 to 7.0 K). By comparing the temperature distributions in the thermograms in figures 3 a to c, it becomes obvious that some significant loss of material occurred between June and November 2009 (see rectangulars). And it is also obvious, that this loss occurred at the position with the highest temperature (delamination) in Fig. 3a. Comparing Figs. 3b–c, only very small areas with additional loss of material can be detected, but again at the positions with the highest temperatures. Therefore, high temperatures reveal the positions where delaminations are present and where further loss of material is expected. In Fig. 3d, the amplitude image calculated from lock-in thermography with 0.05 Hz is shown. Here, the best contrast of the different layers is obtained. Based on the known geometrical data of lens and system set-up, a spatial resolution of 1.5 mm per pixel is calculated.

Conclusions

The aim of the presented research was the development and qualification of an efficient strategy for early detection, spatial recording and quantification of damage at and close to the surface. It has been shown that structural changes can be observed and predicted for longer periods by using active thermography. The analysis of thermograms with maximum thermal contrast after impulse heating enables the detection of detached layers while the analysis of data recorded with lock-in technique gives detailed information about the structural composition of the single layers. The loss of material can be recognised by means of varying shapes of the layers.

The thermograms show that the positions of heating sources and camera cannot be reproduced in detail for each time of data acquisition. Thus, an automated direct comparison and quantification of loss of material is only possible by mapping the thermal data to the 3D geometry. The 3D geometry can be captured very well by using a 3D laser scanner [1]. By the combination of both techniques, appropriate measures and repair can be applied at an early stage. Beyond that the effectiveness and sustainability of protective measures can be analyzed.

Further on, from the geometrical 3D model and the known position of the IR camera, the view angle of each surface point is known and enables the correction of angular dependent emissivities and thus temperature values. This is especially important for complex 3D structures like columns, sculptures, reliefs etc.

References

[1] Krankenhagen, R., Röllig, M., Maierhofer, C., Mecke, R., Schiller, M., Kalisch, U., Meinhardt, J., Hennen, C. (2010), Quantification of Damage Processes at Surfaces and Interfaces of Building Structures Using Optical Methods and Active Thermography, in: Proceedings of the 10th European Conference on Non-Destructive Testing, Moscow, http://www.ndt.net.

[2] Maldague, X. P. (2001), *Theory and Practice of Infrared Technology for Nondestructive Testing*, 1. edn, Wiley & Sons.

[3] Maierhofer, Ch., Arndt, R., Röllig, M., Rieck, C., Walther, A., Scheel, H., and Hillemeier, B. (2006), Application of impulse-thermography for non-destructive assessment of concrete structures, *Cement and Concrete Composites*, 28, pp. 393–401.

[4] Wu, D. and Busse, G. (1998), Lock-in thermography for nondestructive evaluation of materials, *Revue Generale de Thermique*, 37, pp. 693–703.

[5] Dehio, G. (2002), Der Bischofsgang des Magdeburger Domes, in: *Handbuch der deutschen Kunstdenkmäler*, Sachsen-Anhalt I, Deutscher Kunstverlag.

GPR Spectral Decomposition to Monitor Cracks in a Historic Building

L. Orlando

Abstract The paper deals with the ability of high-frequency multi-component GPR data to detect and monitor evolution of cracks over time. For this purpose, multi-component GPR data and advanced processing, based on spectral decomposition of GPR signal, are used. The study takes into account theoretical forward models and actual data acquired on the floor of an ancient building where cracks, with displacements from about 0.001 to 0.02 m and evolving during the time, are present. In-line and cross-line electric field components with x- and y-directed antennas were acquired. The 2x2 data matrix was collected along ten transects over five years. Time lapse analysis of spectral decomposition allows to overcome environmental influence on the data (as the coupling of the antenna-structure depending on the season in which the measurements were collected) and to discover and locate the zones affected by displacement variations which are not detectable by time slices.

Keywords Crack monitoring • GPR • Historical building • Multi component • Spectral decomposition • Theoretical modelling • Time lapse

Introduction

In this paper I address the problem of the detection and monitoring of cracks, affecting structures with instability problems, using high frequency ground penetrating radar (GPR). The ability to monitor small changes in the size of the cracks could be an useful tool for the control of underground movements, to use in the joint interpretation with extensometers, topographic survey and SAR (Synthetic Aperture Radar) [1,2,3,4] measurements.

L. Orlando (✉)
Department of DICEA, Sapienza University of Rome, Via Eudossiana 18, 00184, Rome, Italy
e-mail: Luciana.orlando@uniroma1.it

Many studies [5,6] pointed out both the ability of GPR technique to detect cracks and the difficulty to monitor their evolution over time [7]. The main problems in the monitoring of cracks are due to the influence of environmental variations on the GPR data, such as the antenna coupling and the amount, in repeated surveys, of scattered energy, which often do not allow a quantitative and/or a qualitative evaluation of displacement evolution over time. In this study, to by-pass these problems, I employ data collected in the same season over five years and an advanced processing based on the spectral decomposition (SD) of the signal [8]. The key of SD is to create a set of data cubes or maps, each corresponding to a different spectral frequency, which can reveal variation of frequency content. The concept behind spectral decomposition is that a reflection from cracks which changes feature in time can an amplitude spectra variation in narrow windows of frequency domain. To validate the use of SD forward models for simple and complex cracks reproducing the setting of the actual site are calculated.

The actual data were collected on the floor of an ancient building in which the damage occurs in the form of cracks [9] and stressed zones. This suggests that underground movements can be monitored by mapping the evolution of cracks and stressed zones during time using GPR frequency-lapse. The damage variations seem to have seasonal periods instead of a constant-over-time evolution.

Theoretical Model

In order to validate the ability of SD in cracks detection and monitoring, a forward model simulating an oblique displacement, filled by air, was calculated and mapped.

The modelling was performed using a Ricker wavelet with a 200 MHz peak frequency, and assigning to the host material a relative permittivity (ε_r) of 10, conductivity (σ) of 0.02 S/m and relative permeability (μ_r) of 1. The displacement is 0.03 m in size.

The theoretical model was calculated using a code based on a finite difference approximation algorithm on time domain FDTD, GprMax2D v.2.0 [10], which solves the Maxwell equation for electric and magnetic vector fields as a function of time and space. The problem is approached in a 2-dimensional space assuming that i) the media are homogeneous and isotropic; ii) the transmitter antenna is a linear source; iii) the constitutive parameters of media are frequency independent.

The spectral decomposition of models shows a decrease of spectral amplitude in correspondence of the crack. This result validates the utility of SD in the detection and evaluation of crack displacement.

Site Setting and Data Acquisition

The GPR surveys were performed on the floor of a building constructed at the end of the nineteenth century. The ~0.22 m thick floor has been restored and, starting from the bottom, it consists of ancient barrel vaults built with iron beams and bricks.

During the restoration phase the ancient bricks were joined and covered with a concrete layer which was reinforced with an iron net, above a concrete layer, including utilities is present. The floor is covered with tiles 0.015m thick. In a previous study [9] I found that the horizontal component of stress induces cracks with complex features on the floor because of the different rigidity of the floor layers. Cracks migrate laterally from the bottom to the top of the floor and are located in weakness zones as utilities, junction of tails, etc.

I investigated an area 10 x 1.2 m wide, with a multi-component (polarimetric) GPR system of IDS Corporation, equipped with 2 GHz bipolar antennas with dipoles placed in a rectangular arrangement [11,12]. The instrument allows acquisition of the electric field under four different configurations at the same time and location: parallel broadside y-directed antennas, parallel broadside x-directed antennas, perpendicular antennas with x-directed source and y-directed receiver, and perpendicular antennas with y-directed source and x-directed receiver. In this paper I analyze the two components acquired with parallel broadside y-directed antennas and with perpendicular antennas with y-directed source and x-directed receiver.

The data were collected several times over five years using the same scanning geometries and measurement settings. The main cracks on the tiles were mapped during each survey and referenced to the georadar surveys to aid interpretation of the GPR data. They do not show changes over time.

Profiles, about 10 m long and 0.10 m spaced, were acquired in continuous mode along the x-direction perpendicular to the main cracks and parallel to the long side of the investigated area. The electric field components were recorded with an in-line sampling interval of 0.02 m, total time window of 20 ns and time sampling of 0.014648 ns in each profile.

Data Processing and Analysis

The data were processed with a standard 2D scalar algorithm and with the spectral decomposition. The standard 2D processing includes time zero setting, spectral analysis and band pass filter (100-3200 MHz). The standard processed data were used to obtain vertical profiles, 3D cubes and time slices for both components.

Spectral decomposition (SD) consists in the calculation of a Fast Fourier Transform of the data to create a set of data cubes for each selected narrow frequency window [7]. I analyze only frequency slices referred to a 2ns window. The SD was applied to raw data taking into account a time window of 2ns which includes direct air wave and the near surface reflections. The data were first normalized to the maximum value of each data set and then corresponding spectra of each channel were compared.

Below I discuss the data of surveys 5 and 9 acquired in August 2006 and 2009, respectively.

Amplitude spectra (Fig. 1) of surveys 5 (a,b) and 9 (c,d), acquired with parallel broadside y-directed antennas (a, c) and perpendicular antennas with x-directed
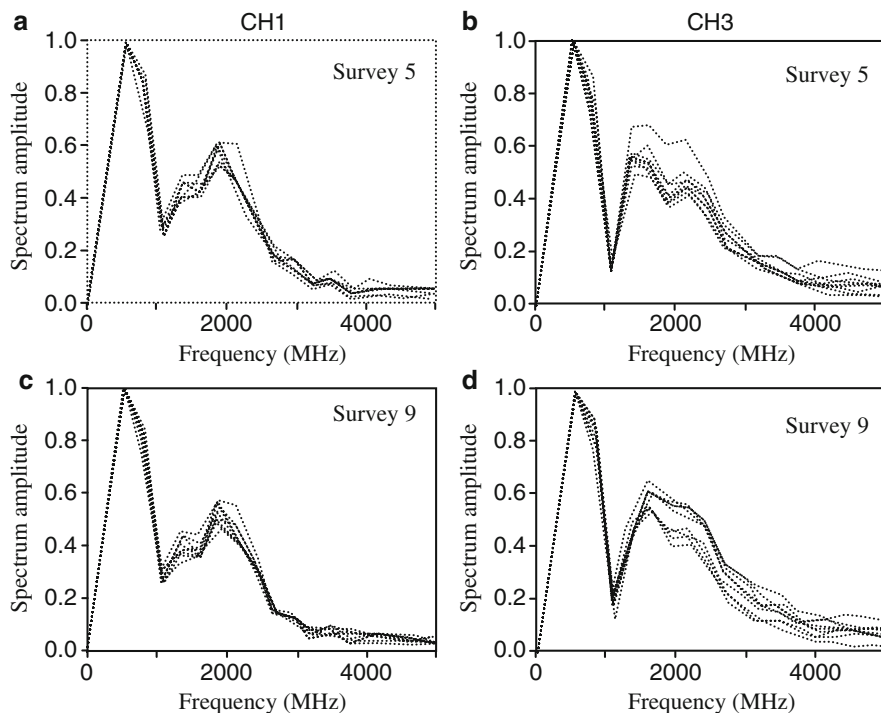
Fig. 1 Amplitude spectra of profiles of surveys 5 (**a**,**b**) and 9 (**c**,**d**), acquired with parallel broadside y-directed antennas (**a**,**c**) and perpendicular antennas with x-directed source (**c**,**d**)

source (c,d), show a decrease of amplitude spectra for band wide in the 1500-2600 MHz band over time of channel 1 (CH1) and an increase of amplitude spectra for band wide in the 2100-3200 MHZ band of cross-polarized channel 3 (CH3).

Taking into account the theoretical results, the spectral decomposition of the actual data related to a window of 2ns were calculated for step band wide of 260 MHz. In Fig. 2, the amplitude frequency lapses (1870-2130 MHZ) of in line (CH1) and cross line (CH3) data related to surveys 5 (a) and 9 (b) are compared. The data analysis shows variations of the amplitude spectum time in the zone indicated with the arrow. Spectum amplitude of channel 1 decreases and amplitude of channel 3 increases from survey 5 to survey 9. The variations of amplitude spectrum over the time are in agreement with the amplitude spectra of Fig. 1. SD, respect the simple amplitude spectra of profile, allows to locate the zone were the variation of frequency amplitude occurs over time. From the theory we know that the cross-polarized energy is generated by complex structures and therefore we have interpreted the zone indicated with arrow in Fig. 2 as a losing zone that has been exposed over time to stress.
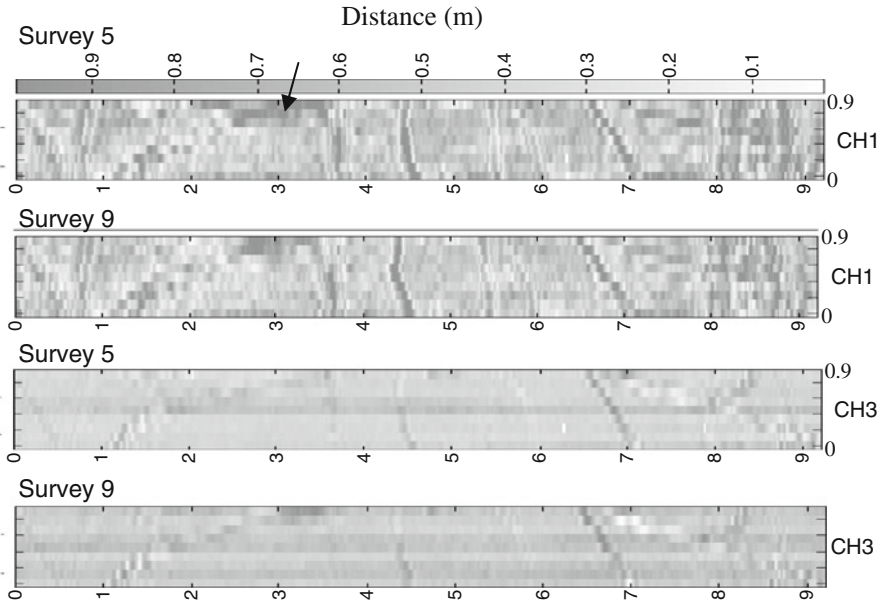
Fig. 2 Spectra lapse (frequency window 1870-2130MHz) of a window of 2 ns of in line (CH1) and cross line (CH3) data of survey 5 and 9

Conclusion

The study shows that 2 GHz multi-component GPR data are suitable for the reconstruction of the setting of a restored ancient floor in a building whose stability is affected by a landslide. In this study I demonstrate the ability of spectral decomposition to detect small changes in the crack size existing in the floor of the building. Amplitude spectra acquired with parallel broadside y-directed antennas and perpendicular antennas with x-directed source show a reverse trend over time of amplitude spectra for band wide in the 1500-2600 MHz band and allow to locate a loosening zone.

The actual data are validated by forward models which confirm a decrease of amplitude spectra of signal in correspondence of cracks.

References

[1] Pieraccini, M., Luzi, G., and Atzeni C., (2001), *Terrain mapping by ground-based interferometric radar*. IEEE Transactions on Geoscience and Remote Sensing, vol. 39, n.10, p. 2176–2181.
[2] Pieraccini, M., Mecatti, D., Noferini, L., Luzi, G., and Franchioni, G., and Atzeni, C., (2002), *SAR interferometry for detecting the effects of earthquakes on buildings*. NDT&E international, vol. 35, n. 8, p. 615–625.

[3] Pieraccini, M., Luzi G., Mecatti, D., Fratini, M., Noferini, L., Carissimi, L., Franchioni, G., and Atzeni, C., (2004), *Remote sensing of building structural displacements using a microwave interferometer with imaging capability*. NDT&E International, vol. 37, n. 7, p. 545–550.

[4] Tarchi, D., Rudolf, H., Pieraccini, M., and Atzeni, C., (2000), *Remote monitoring of buildings using a ground-based SAR: application to cultural heritage survey*. International Journal of Remote Sensing, vol. 21, n. 18, 3545–3551.

[5] Gross, R., Green, A., Horstmeyer, H., Holliger, K. and Baldwin, J., (2003), *3-D georadar images of an active fault: efficient data acquisition, processing and interpretation*. Subsurface Sensing Technologies and Applications, vol. 4, n. 1, p. 19–40.

[6] Marchesini, P. and Grasmueck, M., (2010), *Impact of spatial sampling and antenna polarization on 3D GPR fracture detection.* 13th Ground Penetrating Radar International Conference 21-24 June, Lecce Italy, p. 1–6.

[7] Orlando, L. and Slob, E., (2009), *Using multi-component GPR to monitor cracks in a historical building*. Journal of Applied Geophysics, vol. 67, p. 327–334.

[8] Partyka, G., Gridley, J., and Lopez, J., (1999), *Interpretational applications of spectral decomposition in reservoir characterization.* The Leading Edge, p. 353–360.

[9] Orlando, L. and Oliveti, E., (2008), *Multi-disciplinary approach for the instability analysis of a down-town site (Case Study)*. 70th EAGE Conference & Exhibition, Rome, Italy, 9–12 June 2008, p.1–4.

[10] Giannopoulos, A., (2003), *GprMax2D V 2.0 Electromagnetic simulator for Ground Probing Radar*. Software available at http://www.gprmax.org).

[11] Streich, R. and van der Kruk, J., (2007), *Accurate imaging of multicomponent GPR data based on exact radiation patterns*. IEEE Transactions on Geoscience and Remote Sensing, vol. 45, p. 93–103.

[12] van der Kruk, J., Wapenaar, C.P.A., Fokkema, J.T. and van den Berg, P.M., (2003), *Three-dimensional imaging of multicomponent ground-penetrating radar data*. Geophysics, vol. 68, n. 4, p. 1241–1254.

Using an Ultrasonic Echo Technique to Inspect the Structure of a Pumice Brick Vault in a Church

A. Hasenstab, G. Hilbert and K. Frühwald

Abstract Currently, the assessment of ultrasonic methods on pumice bricks is not a state-of-the-art technology. The vault of a neo-Gothic church made of pumice brick showed large cracks resulting from World War II and the structure of other areas was damaged. Normally, tasks like these are solved by visual inspection combined with drilling cores at a few measuring points. By this means, only the surface and just a few areas of the structure can be inspected. With ultrasonic echo it is possible to study the internal structure of the vault laminar. The investigations are non-destructive and have no effect on the monument.

The entire vault of the nave and aisles was examined, using the ultrasonic echo technique. The structural constitution differs even in one nave. The results show the need for quality control of the various restoration measures (some of which are only "cosmetic") by means of the ultrasonic echo technique. With the results, a detailed restoration concept and a priority list were developed in which the areas that need chemical strengthening (e. g. with silicic acid esters) are defined. By metering the application of the chemical strengthening agent to improve the structure, significant savings in material costs are possible.

In addition, the wooden roof structure was examined visually, tapped with a hammer, examined by an ultrasonic echo and drilling resistance technique and core samples taken. Areas with strong degradation caused by brown rot as well as other areas with active insect infestation were identified.

Keywords Inspection • NDT • Pumice bricks • Ultrasonic echo technique

A. Hasenstab
Ingenieurbüro Dr. Hasenstab, Augsburg, Germany

G. Hilbert
Remmers Fachplanung, Löningen, Germany

K. Frühwald (✉)
University of Applied Sciences Ostwestfalen-Lippe, Lemgo, Germany
e-mail: katja.fruehwald@hs-owl.de

Introduction

During the visual inspection of a damaged historic construction, the question often arises whether there is damage that is not visible on the surface. In the following paper, the inspection procedure for the St. Cornelius Church in Tönisvorst / Germany is shown (illustration 1 and 2). The inspected vault made of pumice brick is in the neo-Gothic style (1885-1903). Large cracks resulting from World War II were visible as well as structural damage in other areas. Normally, tasks like these are solved by visual inspection in conjunction with drilling cores taken from a few measuring points. With this approach, only the surface and a few areas of the structure can be inspected. And it was not clear whether the construction of the vault and the materials used in the different parts of the church were the same. The question was raised whether damaged areas with no visible cracks or other superficial damage could be detected with ultrasonic echo and, if so, whether the extent of structural damage around cracks could be determined.

Methods

The ultrasonic echo technique

The ultrasonic echo technique is based on the reflection of acoustic waves on material inhomogenities such as the back wall of the specimen or at any other interface. The signals received give indirect information about the condition of the structural unit or internal damage. Details on the ultrasonic echo technique, especially on timber, are given in [1-4].

Illustration 1 St. Cornelius Church in Tönisvorst / Germany
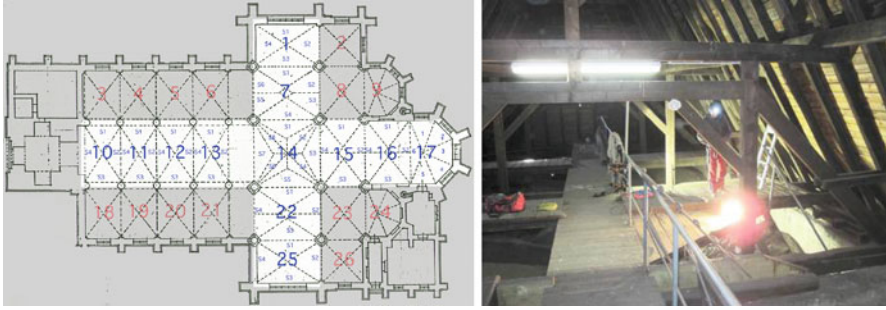
Illustration 2 Left: Plan of the church, inspected areas are highlighted, Right: View of the roof structure

transverse waves (also shear wave) spread perpendicularly to the direction of motion.
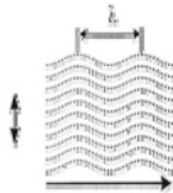
$$v_T = \sqrt{\frac{E}{\rho} \cdot \frac{1}{2 \cdot (1 + \mu)}}$$

E youngmodul
μ poisson ratio
ρ density

Illustration 3 Tansverse waves [6]

Currently, the assessment of ultrasonic methods on pumice brick is not state-of-the-art technology. The high content of air in the structure results in a high damping ratio for ultrasonic signals. This well known effect for longitudinal waves cannot be directly transferred to transverse waves. The analysis of the measurements is based on research work carried out by the Federal Institute for Materials Research and Testing (BAM) and the authors´ preliminary tests. With ultrasonic equipment optimized for concrete (density 2.0…2.6 g/cm³), measurements were carried out on mineral specimens with a density of approximately 1 g/cm³. The successful results on lightweight concrete (density 1.0…2.0 g/cm³) and porous concrete (e. g. Ytong, density 0.3…0.8 g/cm³) lead to the assumption that transverse waves (illustration 3) are transmitted through shear in the fine, coherent framework structure. Therefore, transverse waves were used for the measurements on pumice brick. The transverse wave transducers need no coupling agent, since they are coupled by point contact. The centre frequency was optimized at 55 kHz [5].

Tapping combined with visual inspection

Tapping the surface with a hammer is a common testing method for concrete bridges. In this case, tapping was used in addition to the ultrasonic measurements.

Measurements

For both testing methods – tapping and ultrasonic measurements – a direct contact to the surface of the vault is necessary. Because the condition of the vault was unknown, measurements on the top of the vault were carried out with safety ropes (illustration 4 left). First tapping of the surface with a hammer was used to check the measuring area. Damages close to the surface can be located by tapping, in this case no further measurements by ultrasound were necessary.

When measuring with ultrasonic echo, the measuring surface is very important. To compare which measuring surface of the vault (top or bottom) provides better results, some measurements were taken from both sides (illustration 5). In many areas, extended, laminar measurements from the bottom are not possible because of pews, sacral objects or an under floor heating system which makes the use of a cherry picker impossible. On the other hand, glass wool had been placed on the top of all vaults which had to be removed before measurements were carried out from the top.

In illustration 5 the results of ultrasonic measurements are shown. Illustration 5 left shows three different measurements ("parts") from the bottom: Part 1 and 3 show good results because the received signal energy was high which means that the structure was without damage. Part 2 is a damaged area: no signals can be received because of a crack (which did not extend to the surface). The indication of cracks is "indirect". Illustration 5 right shows the measurements from the top: Part 1 shows good results – intact structure without damage because the received signal energy was high. Part 2

Illustration 4 Left: Measurements on the top of the vault with safety ropes, glass wool was removed; Right: Measurements from the bottom taken while standing on a scaffold
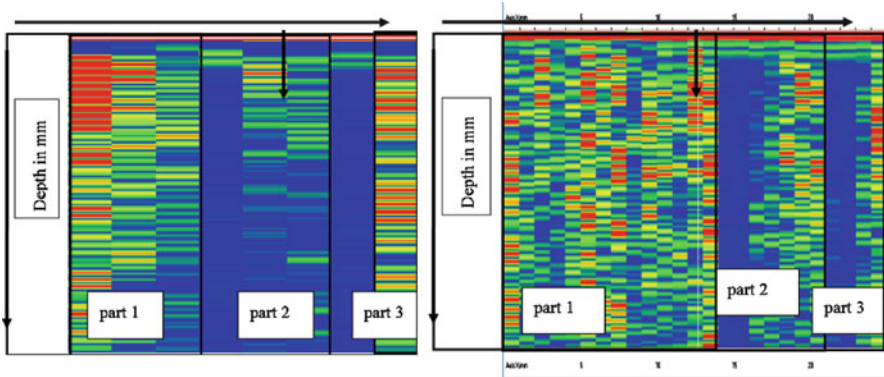
Illustration 5 Results of the ultrasonic echo measurements Left: measured from the bottom; part 1 and 3: structure without damage (the received signal energy was high); part 2: damaged area, no signals can be received because of a crack; Right: measured from the top; part 1: structure without damage; part 2: damaged area, no signals can be received because of a crack; part 3: damaged area, no signals can be received in the area around the crack which means that the area around the crack is also damaged
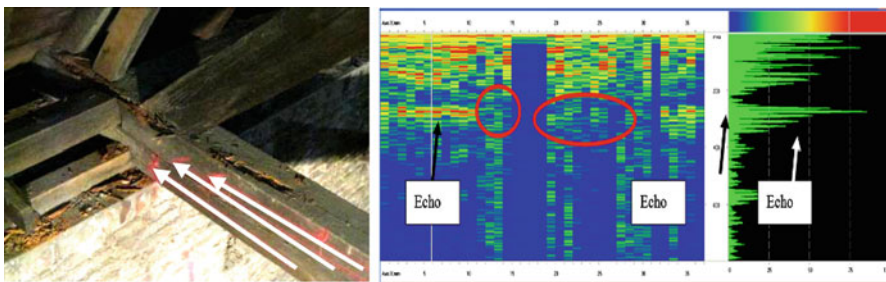
Illustration 6 Left: Heavily damaged roof structure exactly over a heaviliy damaged part of the vault (white arrows indicate the measuring lines). Right: Results of ultrasonic echo measurements of the marked beam: the first (left) part of the measurement was taken in the middle of the beam ("echo" = no damage), centre part along the top of the beam (circles = no "echo" = heavily damaged), third part (right) along the bottom of the beam ("echo" = no damage)

is a damaged area: no signals can be received because of a crack. Part 3 is a damaged area, no signals can be received from the area around the crack, which means that the area around the crack – which looks intact from the surface – is also damaged. So the extent of the damage around cracks can be located with ultrasonic echo.

While ultrasonic echo measurements were being carried out on the vaults, it was discovered that the wooden roof structure was damaged. Therefore, the wooden structure of the roof was examined visually, tapped with a hammer, examined using the ultrasonic echo and drill resistance technique and core samples taken. Large areas with heavy damage caused by brown rot were identified (particularly in some load-bearing nodes, see illustration 6, and the inferior purlin). Rotten areas were found

on the eaves, especially on the western side (= "weather side" with most of the rain and wind). Some areas with a heavily damaged vault were found directly under areas with a heavily damaged roof structure. Some of the rafters showed active insect infestation.

Conclusions

It was shown, that the ultrasonic echo measurements taken on vaults made of pumice brick can be taken from the top or the bottom of the vault. The measurements showed a different structure of the vault and different materials even in just one nave. Different bricks, different mortar between the bricks, different mortars on the surface and different materials to repair the cracks had been used. Large areas of the structure are damaged on the inside and it is not just areas close to the cracks that are damaged. In addition to the cracks apparently visible, cracks were also detected that were hidden below restoration work that had not always been properly carried out during the 70s. Many of these cracks are not visible from a distance. They can only be determined as insignificant or dangerous cracks by climbing close to the surface and testing them with ultrasonic echo. The restoration of the cracks with cement that was carried out after World War II was not successful because the modulus of elasticity between the pumice brick and the cement is very different. This resulted in new cracks close to the restored areas.

The results show the need for a quality control of the various restoration measures (some of which are only "cosmetic"), using the ultrasonic echo technique. With these results, a detailed restoration concept and a priority list were developed in which the areas in need of chemical strengthening (e. g. with silicic acid esters) are defined. By metering the application of the chemical strengthener to improve the structure significant savings in material costs are possible.

References

[1] Frühwald, K. and Hasenstab, A. (2009): Strength grading of hardwood with longitudinal ultrasonic waves and longitudinal vibration and locating defects in softwood and hardwood with low frequency ultrasonic echo technique, In: *Economic and Technical aspects on quality control for wood and wood products*, Proceedings of the Conference Cost Action E53, October 22–23, 2009, Lisbon

[2] Hasenstab, A. and Osterloh, K. (2009): Defects in wood non destructive locating with low frequency ultrasonic echo technique, In: Proceedings of the 7th International Symposium on Nondestructive Testing in Civil Engineering, 30.06.-03.07.2009, Nantes

[3] Hasenstab, A., Osterloh, K. and Krause, M. (2006): Testing of wooden construction elements with ultrasonic echo technique and X-Ray, In: Tagungsband der 9th European Conference on NDT, DGZfP (Ed.), BB 103–CD Th.2.4.1, September 25–29, 2006, Berlin

[4] Hasenstab, A., Krause, M., Rieck, C. and Hillemeier, B. (2003): Use of low Frequency ultrasound echo technique to determine cavities in wooden construction Composites, In: Proceedings

of the International Symposium Non-Destructive Testing in Civil Engineering (NDT-CE), DGZfP (Ed.), BB 85–CD, P51, 16.-19.09.2003, Berlin

[5] Shevaldykin, V., Samokrutov, A. and Kozlov, V. (2003): Ultrasonic Low-frequency short-pulse transducers with dry point contact. Development and Application, In: Proceedings of the International Symposium Non-Destructive Testing in Civil Engineering (NDT-CE), DGZfP (Ed.), BB 85-CD, V66, 16.-19.09.2003, Berlin

[6] Deutsche Gesellschaft für zerstörungsfreie Prüfung e. V. (DGZfP) (1999): Merkblatt für Ultraschell-Verfahren zur Zerstörungsfreien Prüfung mineralischer Baustoffe und Bauteile (B4), Deutsche Gesellschaft für zerstörungsfreie Prüfung e. V., Berlin

Acoustic Emission as a Non-Destructive Method for Tracing Damage: From Laboratory Testing to Monitoring Historic Structures

M. Strojecki, M. Łukomski, C. Colla and E. Gabrielli

Abstract Acoustic emission (AE) technique has recently become an important non-destructive tool to gain insight into the evolution of damage in materials. It is widely used as a laboratory method in material science and civil engineering. However, it has not been applied sufficiently in the field of cultural heritage, mainly due to the great variety of historic materials and limited knowledge about their physical properties. In comparison with other non-destructive techniques AE possesses some very important advantages – it is simple in application and does not require any external stimulation of the object.

In this paper a comparison of AE signals measured for different materials (stone samples, timber joist specimens) and different destructive and non-destructive processes, including mechanical tests, is presented. The proper evaluation of the results obtained in the laboratory can help to distinguish between AE signals related to material damaging and non-damaging processes. The presented work demonstrates the potential of AE as a practical tool to assess the risk of mechanical damage to historic building materials also at different moisture contents or in varying state of decay.

Keywords Acoustic emission • Material fracture • Monitoring • Non-destructive testing

M. Strojecki (✉) • M. Łukomski
Institute of Catalysis and Surface Chemistry, Polish Academy of Sciences,
ul. Niezapominajek 8, 30239 Kraków, Poland
e-mail: strojecki@o2.pl

C. Colla • E. Gabrielli
DISTART Dept., Engineering Faculty, Bologna University,
v.le Risorgimento 2, 40136 Bologna, Italy

Introduction

The care and protection of cultural heritage has, primarily, long been the task of conservators and curators. Many years of experience, intuition and great manual dexterity were the most important tools in their work. However, these skills have, in many cases, proved to be insufficient for making the right – scientifically justified – decisions concerning the best methods of preservation of historic buildings and artefacts [1,2].

In recent years there has been a better understanding of the need for preventive conservation techniques development based not only on experience and intuition, but primarily on an objective scientific basis. On the other hand, more and better cooperation between the conservation and scientific communities as well as the dynamic development of non-invasive techniques and measurement tools has made it possible to introduce and adapt them from the applied sciences to the field of cultural heritage protection.

AE considered as a laboratory method used in experiments with well-controlled conditions, when the influence of environmental noises can be controlled and minimized, has many obvious advantages, one of which is non-invasive character. However, the application of AE on site during long-term monitoring with difficult access and limited user maintenance is a major challenge. Nevertheless, the usefulness of AE as a reliable monitoring method has recently been confirmed also within the field of cultural heritage preservation. The method was successfully applied for the damage evolution assessment of large historic structures *i.e.* damaged historic buildings [3], bell towers [4,5] and cathedrals [6]. On the other hand, it was also used for objects of completely different sizes and kinds, *i.e.* for tracing the evolution of damage caused by climate-induced stress in wooden cultural objects [7,8].

Experimental

The results presented in the next section were obtained from two different types of materials, *i.e.* sandstone and wood. All of sandstone specimens, *i.e. sandstoneS2*, *sandstoneT4* and *sandstoneU4*, used in destructive compression tests were a historic material from near Stuttgart (Germany). The first was taken from the façade of a tenement house, while the second and third – consolidated and not consolidated, respectively, were collected from window frames (the same material as used for polychrome portals) of the Holy Cross Minster Schwäbisch Gmünd in Germany dated to around 1350. The consolidation was performed in 1980ies by the impregnation of the stone with silicic acid esters. Wooden specimens *poplar1* used in the destructive tension test as well as *spruce1* used in non-destructive friction test were sawn from a newly seasoned woods. The other two *i.e. spruce27B* and *spruce3* used in destructive compression and non-destructive 4-point bending test in elastic regime of wood were historic material (almost 100 years old) taken from the original beams of the roof construction of Palace Malvezzi dated 1560 in Bologna (Italy).

The AE experimental setup consisted of: a wideband differential AE sensor (*Phys. Acoust. Corp.*), an acoustic amplifier (*EA System*), a simultaneous-sampling analogue input card PCI-9812 (*Adlink Technology Inc.*) and a personal computer used for controlling the experiment as well as storing and post-processing the acquired data. AE signals in form of data sets were recorded within 128 or 64 ms time-windows for 1 MHz and 2 MHz sampling rate, respectively, while the duration of a typical AE event was of the order of hundreds of µs. The dead time between two consecutive data sets was found to be around 100 ms. Sets of row data recorded during whole test were next post-processed with the help of a computer program searching for individual AE events, extracting them and calculating the most important AE features *i.e.* amplitude, energy, duration and frequency distribution. Moreover, the program also calculated the frequency distributions averaged over any time-window length and visualised them graphically as a time-frequency coloured map, where the amplitude of each Fourier transformation is represented by a specific colour (see *Fig. 1*). The global frequency distribution averaged over all the Fourier transformations of each single AE event can also be calculated.

Results and discussion

Historic sandstone

The results of the first type of test, namely uniaxial compression performed on historic specimen *sandstone1* presented as a time-frequency map correlated with a stress-strain (s-s) curve as well as the cumulative energy (CE) and the hit rate (CH) are shown in *Fig. 1*.

As is depicted, the s-s curve is divided into three regions, *i.e.* elastic, plastic and post-failure. Within the elastic regime the stress increases linearly and low AE activity is observed (apart from the initial phase of the test when the specimen adapted to the UTM clamps). In the plastic region above 1.2 % of strain the AE activity increased rapidly reaching a maximum around 1.55 % of strain. The most interesting, from a monitoring point of view, are the strains above the elastic limit and below the value at which failure of the material begins. From this point both CE and CH change rapidly.

The analysis based on the comparison between frequency distributions calculated for AE signals from elastic and plastic regions can be used for choosing the best frequency range for tracing the micro-destruction progress. For the *sandstoneS2* specimen, there is a significant difference in frequency characteristics for signals measured within the elastic and the plastic region. In this case, the filtering out of all signals with frequency outside 500-600 kHz window allows the measuring mainly events connected with fracture. Almost all the AE events resulted from sample-to-clamps adaptation were removed making the transition between the elastic and plastic regions more distinct and accurate. Such analysis is illustrated in *Fig. 1*, where the comparison between CE and CH calculated for AE events recorded nearly
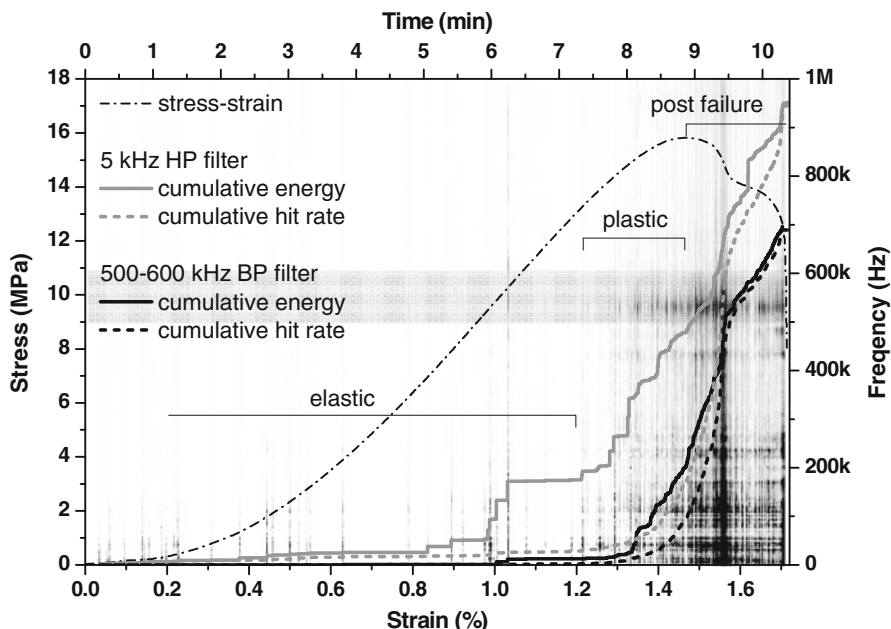
Fig. 1 Time-frequency map of *sandstoneS2* specimen correlated with stress-strain (dashed-dot) as well as cumulative energy (solid) and hit rate (dashed). Cumulative curves are calculated for AE events recorded with 5 kHz high-pass filter (grey) and digitally filtered in 500-600 kHz range (black)

without filtering (only 5 kHz high-pass filter was applied, grey lines) and with digital band-pass filter (black lines) is shown. Band-pass filtering also improved the correspondence between CE and CH curves.

In the case of historic sandstone from Schwäbisch Gmünd (both consolidated and not), the analysis of the frequency distribution was not so successful. The difference in frequency characteristic for the elastic and plastic regions is negligible and therefore the potential for discerning AE events related with destructive and non-destructive processes on the basis of frequency characteristic only is practically impossible.

Historic wood

From the comparison of frequency distributions presented in *Fig. 2a* it is evident that in mechanical tests on wood samples low-frequency AE signals (below 50 kHz) are dominant. However, AE signals related with the fracturing of wood have a high frequency content (*i.e.* above 100 kHz). Within this range, the frequency distribution is significantly different (more uniform) in the case of wood friction imitating a non-destructive process.
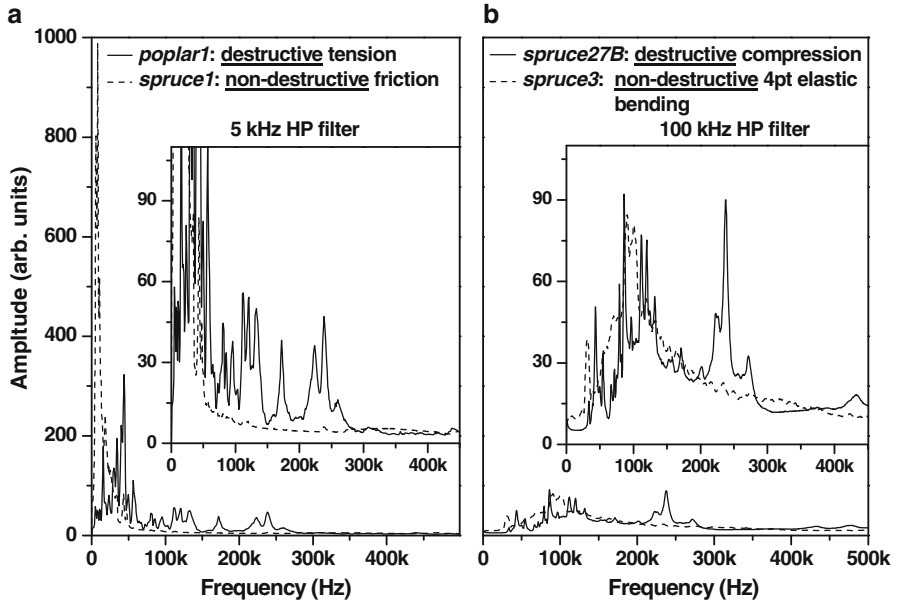
Fig. 2 Frequency distributions calculated for AE signals recorded during the destructive tension and compression (solid) as well as non-destructive friction and 4-point bending in the elastic regime of wood (dashed). High-pass (HP) frequency filter 5 kHz and 100 kHz was applied respectively. Curves are normalized to the same value of the cumulative energy

As is shown in *Fig. 2b*, it is even more pronounced when a high-pass frequency filter is applied (in this case it was 100 kHz). The 4-point bending in the elastic regime of wood, which is a non-destructive process, does not create events containing high frequencies. On the contrary, AE events related with destructive processes recorded during the compression test have a significant content of high frequencies (between 200 and 300 kHz). Therefore, it may be useful to apply band-pass frequency filtering for signals recorded from the wood specimen, especially when a high level of environmental low-frequency noise is expected. This may result in the significant increase of signal to noise ratio.

Conclusions

Different types of destructive (compression, tension) and non-destructive (friction, elastic 4-point bending) processes for two different types of materials - namely two sandstones from historic buildings as well as historic and new seasoned wood, were presented. A methodological approach of searching for the best and possibly the simplest micro-damage indicator based on frequency analysis was proposed.

At this point it should be noted that such an approach, focused on a high-frequency indicator of micro-damage, has one serious disadvantage. It requires using a relatively high sampling rate, *i.e.* at least two times greater than the searched frequency. It is connected with high power consumption and as a consequence it is unacceptable in the case of a long-term monitoring system based on battery power supply. The possible solution allowing to decrease power consumption of the monitoring system can be seen in *Fig. 1* – the cumulative energy is proportional to the cumulative hit rate, therefore it can be used as an indicator of micro-damage. Thus, in short, the measuring procedure can be as follows. After determining the proper frequency characteristics, adequate analogue frequency filters can be applied. Next, using an acceptably small sampling rate only the hit rate can be monitored. This makes AE monitoring very simple and robust. Therefore, to sum up one can say that there is potential that the AE method will be more widely introduced into the field of cultural heritage protection.

References

[1] G. Imkvist, *The chemistry of the Vasa* (2008), Doctoral diss., Dept. of Chemistry, SLU. *Acta Universitatis agriculturae Sueciae*, vol. 2008:57.
[2] K. Dardes and A. Rothe, *The Structural Conservation of Panel Paintings*: *Proc. Symp. at the J. Paul Getty Museum* (1998), Getty Conservation Institute.
[3] A. Carpinteri, G. Lacidogna, (2006), *Mater. Struct.*, vol. 39, pp. 161–167.
[4] A. Carpinteri, G. Lacidogna, (2007), *Eng. Struct.*, vol. 29, pp. 1569–1579.
[5] A. Anzani, L. Binda, A. Carpinteri, S. Invernizzi and G. Lacidogna, (2010), *J. Cult. Herit.*, (2010) vol. 11 n. 4 459–470.
[6] L.M. Suarez del Rio, V.G. Ruiz de Argandoña, L. Calleja, A. Rodriguez-Rey, C.M. Grossi-Sampedro, M. Montoto, (2010), In: *Materials, Technologies and Practice in Historic Heritage Structures*, part IV, pp. 351-365, M. Bostenaru Dan, R. Přikryl, Á. Török (Eds.), Springer.
[7] S. Jakieła, Ł. Bratasz, R. Kozłowski, (2007), *Stud. Conserv.*, vol. 52, p. 101.
[8] S. Jakieła, Ł. Bratasz, R. Kozłowski, (2008), *Wood Sci. Technol.*, vol. 42, n. 4, p. 269.

Thermographic Investigation of "leccese" Stone Masonry Structures

A. Largo and R. Angiuli

Abstract InfraRed Thermography (IRT) is a wireless, contactless and smart technique potentially suitable for the qualitative and/or quantitative buildings long-term monitoring. However, the monitoring of a particular object/defect in a masonry structure can succeed only if the thermographic survey is performed with a suitable experimental setup, defined after a specific laboratory calibration, leading to the proper definition of the operational parameters (active/passive approach, distances, time-windows, etc.). The aim of this document is to describe the advanced testing of "*leccese*" stone masonry samples, in order to evaluate the effectiveness of IR thermography to qualitatively detect defects and inhomogeneities (voids, irregular mortar joints, wooden and metallic inclusions) inside masonry textures or behind plaster layers, as well as evaluating the capacity of IR thermography to detect the beginning of material deterioration and its long term evolution. At the end of the experimental work the calibration of an infrared technique to be used for the NDT of historic structures was defined, by identifying the best set of operative parameters.

Keywords Masonry structures • Nondestructive evaluation • Infrared thermography • Conservation

Introduction

The aim of this document is to describe the advanced testing of "*leccese*" stone masonry samples, in order to evaluate the effectiveness of IR thermography to qualitatively detect defects and inhomogeneities inside masonry textures or behind plaster layers. The investigation was carried out in laboratory by considering two specimens, simulating a typical masonry structure of southern Italy, with enclosed

A. Largo (✉) • R. Angiuli
Consorzio CETMA, Brindisi, Italy
e-mail: alessandro.largo@cetma.it

defects and anomalies of different geometry and thermal characteristics. The first wall (W_1, single leaf masonry, plastered; reference, without defects) was built with a double thickness of lime plaster on the back side and two different types of plaster on the front side (lime plaster and cement plaster). The second wall (W_2, single leaf masonry, plastered; defected) was built with a series of defects behind the plaster, such as air bubbles, metallic and wooden inclusion, holes with different depth, etc.

The thermocamera employed was a ThermaCam SC2000 (a commercial micro-bolometric FLIR System, with a 320 x 256 Focal Plane Array) with the wide-angle 80° and the standard 24° lens; material emissivity was set to the value of 1.

The data analysis approach has foreseen to carry out a qualitative interpretation of thermograms: relative temperature variations and not absolute temperatures have been taken into account, as the real material emissivity has not been measured. The temperature scale visualised in each thermogram has been used to compare temperatures between areas in the same frame or between the same points in thermograms registered at different times. From this analysis it has followed the identification, location and extension of anomalies, which have then been evaluated. At the end of the experimental work the best set of operative parameters was identified. The work was carried out within the European Project SMOOHS "Smart Monitoring of Historic Structures" (http://www.smoohs.eu).

Laboratory Specimen and Apparatus

Two "*leccese*" stone wall specimens with dimensions of 1600x1500x250 mm³ were built as a minimum base for supporting the laboratory research activity.

Construction materials

Leccese stone. *Leccese* limestone is a calcareous stone dating back to the Miocene period (21 million years ago). Its unique compactness, colour and structure are due to its components, while its charm and geo-logical value are given by little bits of fossils.

Mortar and plaster. According to some ancient tenders of southern Italy private and public works, lime mortar is the main binder of "*leccese*" stone, "carparo" stone, tuff or heap of stones masonries. However, particular attention must be paid in the proportioning and manufacturing because traditional mortar has very few chances to bind these kinds of stone.

Manufacturing of laboratory specimens

Specimen 1 (W_1) was plastered with lime plaster on the back side (three plaster layers on the left side and two plaster layers on the right side) and with two different types of plaster on the front side (FASSA BORTOLO KS9 cement based on the left side

Table 1 Composition and thicknesses of plaster layers

	Lime paste [%]	"*Leccese*" stone powder [%]	Thickness [mm]
1st layer	35	65	10
2nd layer	50	50	5
3rd layer	75	25	5
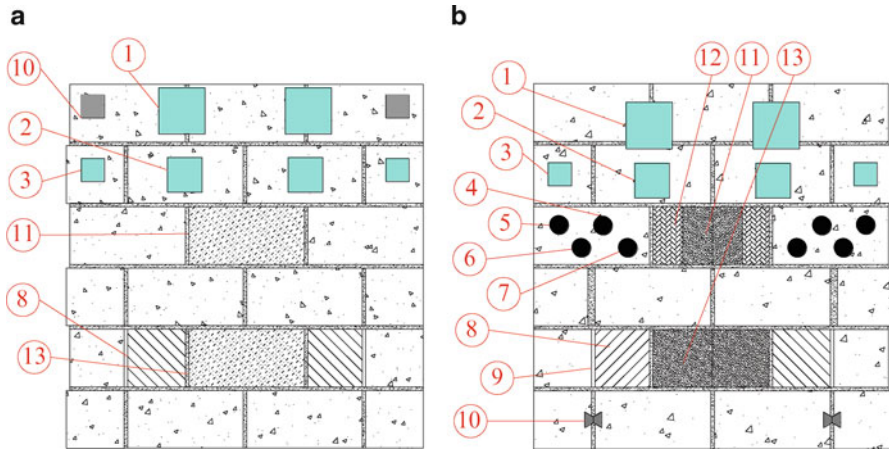
Fig. 1 W_2 with simulated defect: back side (**a**) and front side (**b**)
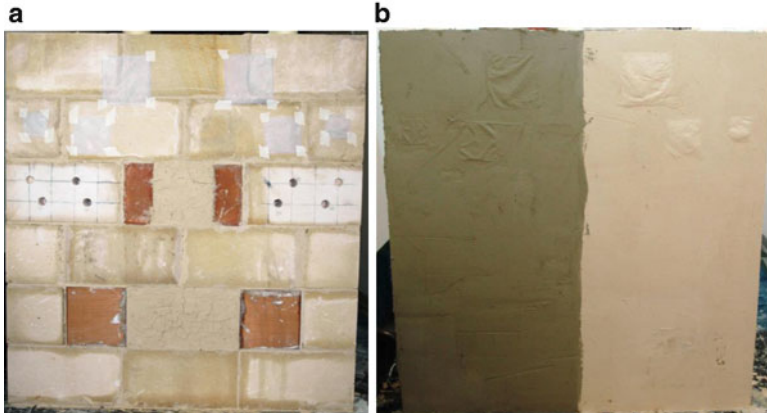
Fig. 2 W_2 with simulated defect before (**a**) and after plaster (**b**)

and lime based on the right side; thickness 10 mm). Mortar joints have thickness of approximately 1,5 cm and were made of 1/3 of lime paste and 2/3 of "*leccese*" stone powder. Composition and thicknesses of different plaster layers are reported in Table 1.

Specimen 2 (W_2) was built with the same block, mortar joints and plaster of W_1 with a series of defects behind the plaster, such as air bubbles, metallic and wooden insert, plaster filling and holes with different depth (Figs. 1 and 2). In detail:

1) plaster detachments (dim.: 10×10, 15×15 and 20×20 cm²), simulated by *Teflon* bags placed behind and between the plaster layers [defects n. 1-3];
2) dead holes (depth: 5, 10, 15 and 20 cm) with diameter of 80 mm [defects n. 4-7];
3) irregular mortar joints [defect n. 9] and metallic inclusion [defect n. 10];
4) wooden inclusion (dim. 25×25×25 cm³) [defect n. 8]
5) different type of brick material (dim. 25×12.5×4.5 cm³) [defect n. 12]
6) bricks of different thickness (blocks with thickness equal to 12.5 cm, instead of 25.0 cm; air gap filled with mortar) [defects n. 11, 13]

Experimental Program

The experimental program aimed at evaluating the effectiveness of IR thermography to qualitatively detect defects and inhomogeneities inside masonry textures or behind plaster layers, as well as evaluating the capacity of IR thermography to detect the beginning of material deterioration and its long term evolution. All the tests (reference and defected wall) were performed with an active approach in reflection mode with both heating system and camera positioned on the same side with respect to the specimen. At this purpose, a support for four infrared lamps, each one with a power 1300 W, was used; this scheme was chosen in order to ensure a uniform heating of the widest possible investigated area.

Test on Specimen W_1

W_1 was tested for the calibration of the experimental setup in order to assure a uniform heating of the surfaces to be inspected and to understand the heat propagation phenomena. Some preliminary tests have been performed on both sides of the wall, in order to define the best experimental setting for the heating apparatus and the test set-up (Fig. 3). On the back side, according to the infrared survey pointed out that the masonry texture becomes fully visible after about 20 minutes of heating (acquisition rate of 10 minutes).
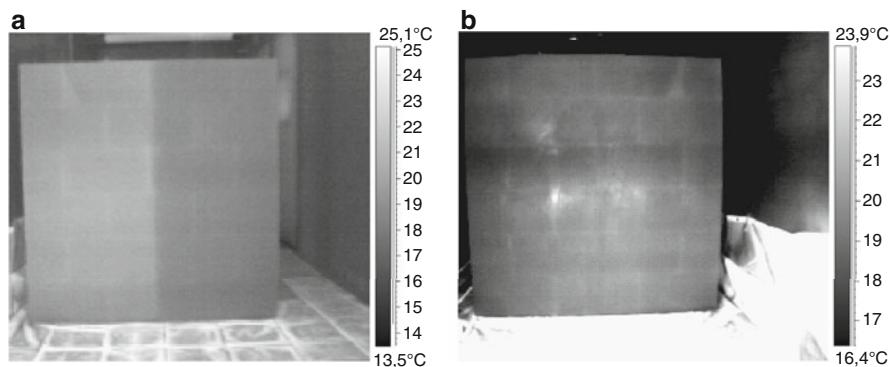
Fig. 3 W_1 reference wall: front side (**a**) and back side (**b**)
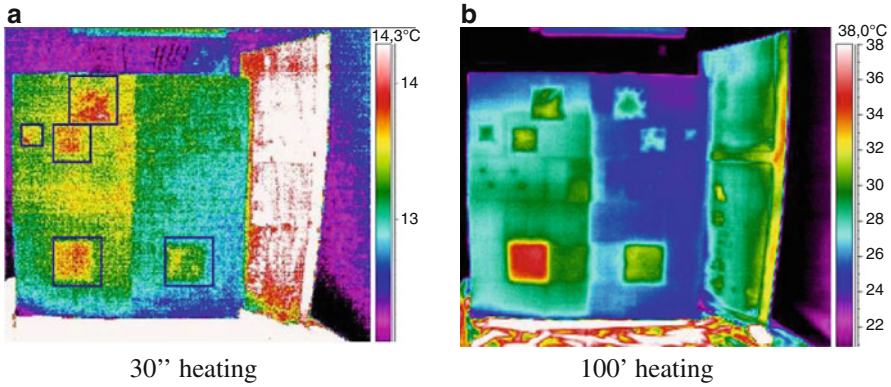
Fig. 4 W$_2$ front side with different heating time

On the front side, on the contrary, the masonry texture becomes fully visible after 8 minutes of heating on the left side (cement plaster) and after about 18 minutes on the right side (lime plaster). The infrared lamps were placed at about 2 metres from the specimen.

Test on specimen W$_2$

Based on the results obtained on W$_1$, W$_2$ was tested for the calibration of the experimental thermographic procedure able to identify hidden defects behind the plaster (many parameters were investigated: IR lamps – wall distance, number of turned-on lamps, horizontal and vertical inclination of each lamp, heating time, etc.), in order to define the best set of experimental operative parameters allowing the best visibility for each defect and define a reliable post processing procedure. Sequences of thermal images were recorded at a time interval of 120'' and 30'', during both heating and cooling transient up to room temperature. Heating time ranged from 60' up to 100', depending on the IR lamps – specimen distance and the depth of the defects behind the plaster.

Specimen W$_2$ front side. In Fig. 4, two thermal images of the specimen W$_2$, recorded during the heating transient after 30'' and 100', respectively, are shown. In 3b all the defects, with the exception of n. 9 and 10 are strongly visible. The experimental survey evidenced that it is not necessary to heat for more than 100', because afterwards it is not possible to highlight any significant increase in the thermal contrast.

In order to define the best set of experimental operative parameters, the following data were recorded and/or investigated for each defect:

1) T_0: starting temperature (during heating or cooling);
2) *best visibility*: time at which the difference between the temperature of the defected and a sound area next to the defect is maximized (i.e. time at which the thermal contrast between any inspected area and a sound reference region in maximized);

3) ΔT_1 and ΔT_2: respectively, deviation between the starting temperature (T_0) and the temperature at which each defect start to be visible (ΔT_1) and reach the best visibility (ΔT_2);
4) *measured dimension* and *error*: size of the defect measured according to the post-processing procedure and difference from the real defected area.

Conclusion

This document described the advanced testing of "*leccese*" stone masonry samples in order to evaluate the effectiveness of IR thermography to qualitatively detect defects and inhomogeneities inside masonry textures or behind plaster layers. Experimental studies gave promising results and lead to the following conclusions:

1) Defects under cement plaster need a shorter heating time to become visible, in comparison with defects under lime plaster; moreover, defects n. 1, 2, 3 and 8 on the left side remain visible longer than on the right side;
2) The error made in the estimation of the defected area has a minor deviation when measured on the left side of the wall (cement plaster);
3) During the cooling transient, the best visibility is reached immediately after the switching off of the heating apparatus;
4) On both sides, the defect n. 8 is still detectable after almost 5 hours after the switching off of the heating apparatus;
5) On the right side, under the same conditions, almost all the defects reach the best visibility after a time longer than on the left side;
6) After 21 minutes the warming of the specimen is no longer necessary for the detection of the defects;
7) In most cases defects are detectable just with a ΔT_1 of 2 or 3 degrees. These small differences in temperature are very important in cultural heritage diagnosing when the damage of the works to be inspected must be prevented.

References

[1] X.P.V. Maldague; "Theory and Practice of Infrared Technology for Non-destructive Testing"; A Wiley-Interscience Publication, John Wiley & Sons Inc.; Newyork. 2001.
[2] J.G. Sun, "Analysis of quantitative measurement of defects by pulsed thermal imaging", Review of QNDE, D.O. Thompson and D.E. Chimenti Eds., 21 (2002) 572–576.
[3] Largo A., Corvaglia P. and Colla C. "Thermography investigations of Roman archaeological masonry", On Site Assessment of Concrete, Masonry and Timber Structures (SACOMATIS), Como, Settembre 2008.
[4] Largo A., Corvaglia P. and e Manni O. "Stato dell'innovazione del metodo termografico nelle sue applicazioni civili e dei beni culturali", Giornale dell'ingegnere ed. speciale: "I controlli non distruttivi" (settore industriale e civile), n. 4 – Marzo 2010.

Non Invasive Measurements of Moisture in Full-Scale Stone and Brick Masonry Models After Simulated Flooding: Effectiveness of GPR

G. Cardani, L. Cantini, S. Munda, L. Zanzi and L. Binda

Abstract Within the framework of a European Commission project entitled Cultural HEritage against Flood (CHEF), a research was carried out in Milan on full-scale stone and brick masonry models by means of a simulated flood to investigate the effects of floods on historic and masonry buildings. The objective was to evaluate the post-flood moisture content and the drying process through non-destructive or minor-destructive techniques. Several non-destructive testing (NDT) were applied (thermography, sonic tests, radar) and were compared with the powder drilling test. Thermography and radar tests were the most useful; the attention is here more concentrated on radar tests which revealed interesting results. A high frequency GPR system was used to perform measurements on selected points of the models at selected intervals during the drying period. Radar velocity, radar amplitude in transmission and in reflection mode, radar waveform distortion and spectra were analyzed as a function of time after flooding and were compared to moisture content assessed by the powder drilling method. Measurements of radar velocity and radar waveform distortion were found meaningful and in agreement with the expected drying process.

Keywords Masonry • Minor-destructive • NDT • Powder drilling • Radar • Sonic • Thermography

Introduction

An experimental research started on site within the framework of a European Commission project entitled Cultural HEritage against Flood (CHEF) on the effects of floods on cultural heritage. A simulation of flood was performed in Milan on some full-scale masonry models, especially built for research, exposed

G. Cardani (✉) • L. Cantini • S. Munda • L. Zanzi • L. Binda
DIS, Politecnico di Milano, Milano, Italy
e-mail: cardani@stru.polimi.it

to the environmental agents of the city. The masonry materials used for the full scale models were largely investigated in the past [1] and subjected to decay caused by the crystallization of sodium sulphate coming from the ground. Some of the walls were also treated with surface treatments used as consolidant or water repellent and their durability was studied [1]. These walls can actually simulate the state of naturally contaminated walls before a possible flood and represent a situation for which the main parameters are known and can be controlled. Several NDTs were applied as: thermography, sonic tests, radar tests and compared with powder drilling tests [2] as proposed by standards for the detection of moisture in masonry walls. Here, the attention will be more concentrated on radar tests. Previous works on masonry already presented good results where radar velocity is used as moisture indicator [3, 4]. In the paper, radar velocity, radar amplitude in transmission and in reflection mode, radar waveform distortion and radar spectra were analyzed as a function of. time after flooding and compared to moisture content assessed by the powder drilling method.

Full-scale Models and Flood Simulation

Three full-scale physical models were built in 1990 in stone and brick masonry in a polluted area of Milan; they are one-floor buildings with the principal facades divided into modular orthogonal panels exposed South and West (Fig. 1a). The walls of the models are made with sandstone blocks or with soft-mud facing bricks. The models are 3.8 m high on the front side (38 and 30 cm thick the brick and stone masonry walls respectively) and 3.4 m on the rear side. Prior to construction, the subsoil was coated with a layer of bentonite in order to assure the capillary rise of water into the masonry (Fig. 1b, c).

A flood simulation was carried out on a portion of four different walls. First the subsoil was fed by water for about a month and then a tank with additional water was sealed to each panel for a period of 4 days. The walls used for these tests were: 1) Stone masonry panels: untreated (A4) and treated by a surface coating of epoxy resin (A1) and 2) Brick masonry panels: untreated (B4) and treated as A1 (B1). The tests were performed with models in dry conditions (or better natural conditions as a function of the environment), immediately after the flood simulation and after
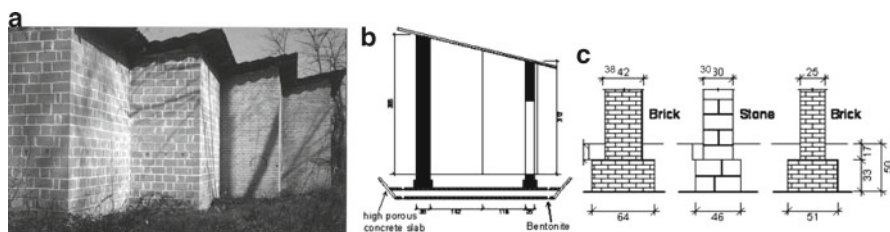
Fig. 1 (**a**) View of some full-scale masonry walls: sandstone on the left and brick on the right, (**b**) cross section of one model and (**c**) Details of the facade walls

regular periods of time during the drying process. The investigation survey [5, 6] consisted in: a) passive thermography, comparing the wet and the dry areas of each masonry panel; b) Radar in the wet and dry areas of each panel with an antenna frequency of 2GHz; c) Sonic pulse velocity tests (3.5kHz) performed in direct transmission, on a selected area across the evaporation line; d) Powder drilling test carried out to verify the moisture content and distribution, at 2 different heights (30cm and 120cm, wet and dry area respectively) in 4 different depth intervals in order to monitor the whole cross section of each masonry panel.

Radar Velocity and Calibration with Powder Drilling Tests

The average velocity of the radar wave through the cross section of the masonry was estimated from the travel time of the reflection generated by the opposite side of the wall. Figs. 2 and 3 show the results for the A1 stone wall and the B1 brick wall respectively. Similar plots were obtained for the A4 and B4 walls. According to the velocity results, the flood simulation did not affect the stone wall above the level of the tank indicating the absence of capillary rise effects while some variations of the velocity were observed on one of the brick walls (B1) up to a couple of measurement

Fig. 2 Stone masonry. Average velocity measurements at 12 selected positions (see left). The dashed box shows the water tank position
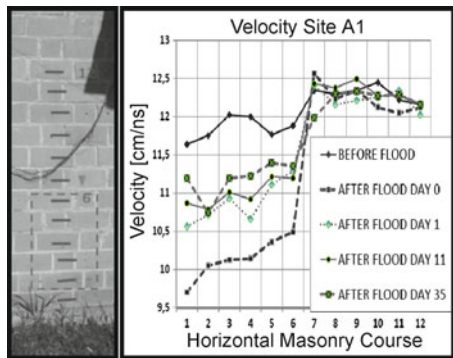
Fig. 3 Brick masonry. Average velocity measurements at 14 selected positions (see left). The dashed box shows the water tank position
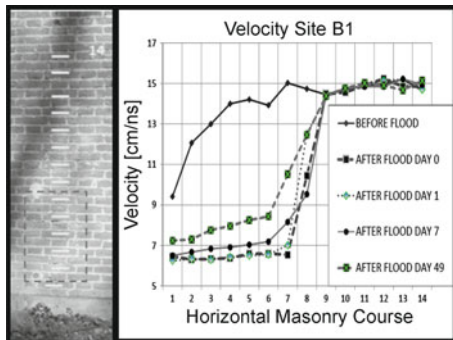
Fig. 4 Radar velocity vs. moisture from the powder drilling method
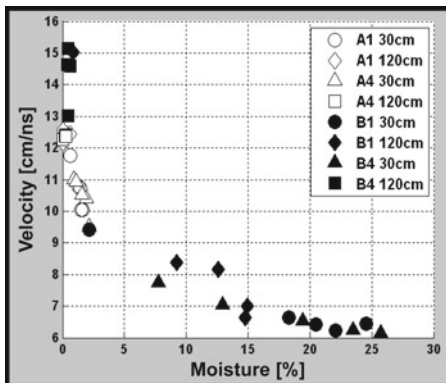
points, i.e., about 20cm, above the tank perimeter. Where the wall was not interested by the flood simulation the radar velocity is quite stable with oscillations lower than 0.5cm/ns. Before flooding, unlike stone masonry, the brick masonry velocity is progressively decreasing moving the measuring point closer to the soil. This indicates a remarkable moisture gradient in the lower part of the brick wall due to capillary rise from the soil. In the stone masonry, the flooding effect is observed as a velocity decrease of about 2cm/ns. After one day from tank removal the velocity is already 1cm/ns higher indicating a fast drying process occurring during the first hours. During the following weeks, the drying process is progressing at a lower rate. After 35 days the velocity is still 0.5cm/ns lower than the velocity before flooding indicating that although the experiments were performed in the summer season it takes a lot of time to return to the original situation. During the drying process a different behaviour between the odd and the even stone courses can also be observed due to the different orientation of the stones in the measuring points. The even courses show a slower drying process because the velocity is measured by crossing two stones put as stretchers rather than one. It means that the mortar is keeping a significant amount of moisture and its drying process is slower than the stone one put as headers.

In the brick masonry, the flooding produces a more remarkable effect: the velocity after the tank removal is 6.5cm/ns vs. a velocity before flooding ranging between 9.5 and 14cm/ns as a function of the course distance from soil. After 1 day no velocity variations are observed indicating a slower drying process compared to the stone walls. After 7 days the velocity increase is still minimal and after 7 weeks the velocity range in the flooded portion of the masonry is still much lower than the range observed before flooding. The different behaviour observed in the stone and in the brick masonries is explained by the strong difference in porosity between this type of stone and the bricks. The higher porosity of the bricks determines the higher velocity variations and the longer drying process observed with these experiments.

The drying process was also monitored at few selected positions by measuring the moisture level with the powder drilling method. Two positions for each tested wall were chosen, one in the lower part of the flooded area at 30cm from the soil and one above the tank position at 120cm from the soil. Figure 4 shows the radar velocity as a

function of the moisture level assessed with the powder drilling method (average value measured through the wall section). The plot combines stone and brick data to show the remarkable difference of the moisture levels measured in the two materials. The general behaviour in Fig. 4 shows a velocity that rapidly decreases as moisture increases within the 0-2.5% range. Then, it changes significantly and the curve tends to bend towards a quasi-horizontal asymptote for moisture levels that are reached only in the brick masonry structure (up to 26%). Stone and brick data are surprisingly aligned along a common trend curve but in general different trend curves can be expected from different materials depending on the respective permittivities. Figure 4 seems to indicate that the radar velocity method is not sensitive enough to discriminate moisture levels in the 0-1% range. For higher moisture levels the method looks quite consistent but it is difficult to derive a quantitative conclusion about its accuracy because the powder drilling method could also be affected by intrinsic measuring errors.

Radar Wave Distortion

Other methods were explored to obtain moisture indications from the radar data. Amplitudes of reflected events, either the opposite side reflection or the surface reflection measured by keeping the antenna at a constant distance from the wall surface, were analyzed versus drying time and moisture levels. Although the emitted radar intensity was accurately calibrated at the beginning of each measuring session, the data looks poorly consistent and unreliable. A more promising method seems to be the analysis of the radar wave distortion produced by the different combination of the air wave with the surface wave travelling in the material with different velocity depending on moisture. Before flooding, the radar wave consists of a constructive combination of the air-wave and the surface wave travelling in the material between the TX and RX antennas. After flooding, the surface wave velocity decreases dramatically because of the higher permittivity of the moist material. As a result the two waves tend to separate and the A-scan looks very different with a lower amplitude excursion spanning over a longer time window. To compare these observations with the moisture measured by the powder drilling method, the time delay of the last negative significant oscillation belonging to the near-surface radar wave has been plotted on a graph as in Fig. 5. The figure illustrates all the data measured on the B1 and B4 walls at 30 and 120 cm from the soil. The result is encouraging since a rather consistent trend can be observed. The accuracy is probably lower compared to the average velocity method but again, for a quantitative and rigorous analysis of the accuracy of the method, laboratory tests are necessary.

Likely, a more robust parameter can be defined in order to increase the reliability of the method. A similar analysis was also performed on the radar wave recorded on the stone walls. As expected no significant distortions of the radar wave were observed because of the restricted range of permittivity variations induced by the low moisture levels. Longer TX-RX separations are needed to observe waveform distortions within the permittivity range measured on the stone walls. Thus, the

Fig. 5 Time indicator of radar wave distortion vs. moisture from the powder drilling method
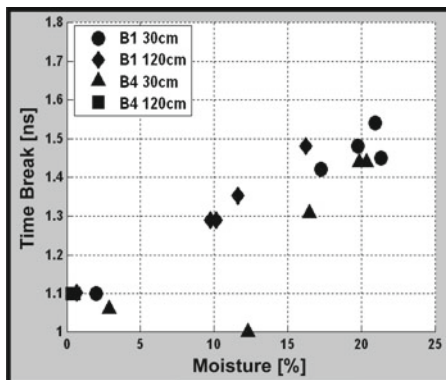
optimization of the radar hardware for this kind of measurements is another option that is still to be explored before deriving conclusive estimates about the sensitivity and the accuracy of the method.

Conclusions

Different radar parameters were measured on full scale stone and brick masonry models before and after a flood simulation. The average radar velocity through the wall cross section is the most robust indicator of the moisture level and can be calibrated on-site at few selected positions by using the powder drilling method. The amplitudes of the reflected events, despite an accurate calibration of emitted radar intensity, looks poorly consistent with moisture data. A more promising method seems to be the analysis of the radar wave distortion produced by the different combination of the air wave with the surface wave travelling in the material with different velocity depending on moisture. The preliminary results are encouraging and the method is still to be optimized. If successful, this method would be very interesting because the measurement is expected to be influenced only by the near-surface portion of the masonry. Thus, by performing this test on both sides of the wall and by combining the results with the average velocity method, moisture variations through the wall cross section could be observed.

References

[1] Binda L., Rocca P., Squarcina T. (1996), Deterioration of masonry surfaces and of surface treatments: experimental result on full scale models, *The Masonry Society Journal*, vol. 14, n. 2, pp. 25–36.
[2] RILEM Recommendation MS93/15 (1993), Improvement of the drilling method for the determination in building materials.

[3] Forde M.C., McCavitt N., Binda L., Colla C. (1993), *Identification of moisture capillarity in masonry using digital impulse radar*, 5th Int. Conf. on Structural Faults and Repair, Edinburgh, pp. 397–403.

[4] Maierhofer C., Wostmann J., Trela C., Rollig M. (2008), *Investigation of moisture content and distribution with radar and active thermography*, Int. Rilem Conf. SACOMATIS 2008, Varenna, Italy, pp. 411–420.

[5] Cardani G., Cantini L., Munda S., Tiraboschi C., Binda L. (2010), *The effects of floods on masonry walls: ND techniques to evaluate the drying rate*, 3rd Euromediterranean Symposium on Advances in Geomaterials and Structures, Djerba, Tunisy, pp. 523–528.

[6] Binda L., Cardani G., Zanzi L. (2010), Nondestructive Testing Evaluation of Drying Process in Flooded Full-Scale Masonry Walls, *Journal of Performance of Constructed Facilities*, vol. 24, no.5, 2010, ASCE, USA, pp. 473–483.

Damp and Salt Rising in Damaged Masonry Structures: Numerical Modelling and NDT Monitoring

C. Colla, L. Molari, E. Gabrielli and S. de Miranda

Abstract Existing research on structural deterioration of historic structures generally concentrated on direct mechanical causes of deterioration rather than on physical-chemical effects of aggressive agents on the mechanical parameters of masonry and their interaction. The research presented herein studies deterioration of masonry in a unified environmental framework which accounts for both the mechanical and the physical-chemical effects and their coupling. Numerical models and experiments have considered various cases including mechanically damaged and undamaged masonry walls with moisture capillary rise from foundations, with and without salt inclusions at different concentrations. Examples from on-going work are shown.

Keywords Coupled model • Masonry • Moisture rising • NDT techniques • Salts rising

Introduction

Centuries of masonry construction in the majority of Countries have left a wide historical building-stock inheritance whose correct preservation and use has become a priority. The causes of structural deterioration can be subdivided into two main groups: physical-chemical and mechanical aspects. Regarding masonry, greater attention has been drawn to direct mechanical degradation causes while less attention has been devoted to physical-chemical effects and to their interaction with the mechanical parameters. Due to recent severing of environmental conditions, the environmental decay cannot be disregarded, as it causes a slow deterioration in the mechanical properties. Considering interaction between environment and construction materials, the presence of water has a pre-eminent role. The water rise in masonry is a decay promoter not only for the freezing-thaw cycles; but also for the consequences of capillary rise and crystallization of penetrating substances (salts).

C. Colla (✉) • L. Molari • E. Gabrielli • S. de Miranda
DICAM Dept., Engineering Faculty, Bologna University, Bologna, Italy
e-mail: camilla.colla@mail.ing.unibo.it

Background

Moisture capillary rise is one of the main causes of environmental decay in masonry: this phenomenon affects the propagation of penetrating substances in the material and creates tension because of freezing-thaw cycles or, in presence of salt ions, due to their crystallization and chemical reactions. When water is close to small cavities such as pores in bricks, stones or mortar, it rises spontaneously driven by a pressure, function of the superficial water tension, of capillary tube radius and of the contact angle between water drops and material surface. The water rise continues until capillary pressure equals hydrostatic pressure. Moisture capillary rise, which theoretically could rise up to about 15 m height, in most real cases reaches 2-3 m or less because of water evaporation. In fact, capillary rise needs time: if initially its speed is of about 2 cm/hour, later it is much slower and the phenomenon kinetic is close to zero after few years if water suction is constant. Water evaporation through the surfaces affects the residual moisture content in the wall, which is also affected by the masonry type and the microclimate (wind, temperature, humidity…). Moisture in masonry varies, for same heights, with wall thickness and tends to be lower from the surface with greater evaporation but, in the lower part of wall, moisture content can reach 20-30%.

The practical consequences of moisture capillary rise in masonry are many and all negative. I.e., the water transport brings to salt deposits formation on the external surfaces (efflorescence, aesthetically disturbing whitish deposits) or just beneath it (sub-efflorescence, when the water evaporation is so fast that salt deposition and crystallization happens inside the masonry). All hydro soluble salts that are present in the ground, in the foundations or in the masonry itself undergo in time the same upwards journey, accumulating in the highest and cortical part of the masonry. Because of salts presence, some chemical reactions can take place if sulphates are included. These are particularly dangerous for the stability of mortars and plasters. In presence of moisture, the growth of vegetable micro organisms is favoured (mould, moss, fungi, lichens), with serious consequences on the aesthetic of masonry. Also alkali-aggregate reaction can take place in moist masonries, in the long time. These phenomena will not be discussed here; neither will the consequences of freezing-thaw cycles. Instead, sulphates react chemically generating ettringite and thaumasite [1] but also mirabilyte and/or thenardite according to moisture and temperature conditions. Because salt crystallization can imply a considerable volume increase, tensions in the materials accumulate in the salt deposit areas until bulging and detachment of flakes or material break up happens. This causes a real damage to masonry.

Objectives

This work's aim, in the frame of the 7th FP European project SMooHS, is to study the masonry deterioration in a unified environmental framework, which accounts for both mechanical and physical-chemical parts of the problem and their coupling.

Masonry physical models replicating historic panels have been built in the laboratory and numerical models by F.E. technique have been developed for various experimental cases including mechanically damaged and undamaged masonry walls with moisture capillary rise from foundations, with and without salt inclusions at different concentrations. Examples from ongoing work will be shown.

Test Object

Experiments and analyses have been carried out on a masonry model built in the laboratory by means of solid clay bricks (dimensions 250 x 120 x 55 mm³) and hydraulic lime mortar. The panel measures 1.16 x 0.25 x 1.3 m³ and it is made of 20 masonry courses (Fig. 1a). The panel has been studied both in as-built conditions and after a semi-diagonal compression test, which has caused mechanical damage and a severe crack pattern (Fig. 1c). Water and brine of sodium chloride have been considered as diffusive agents during moisture capillary in both experimental and numerical study cases. Material properties are summarized in Table 1 [2]. The salt considered in the study herein reported is sodium chloride (2160 Kg/m³) at 0.05% brine concentration.
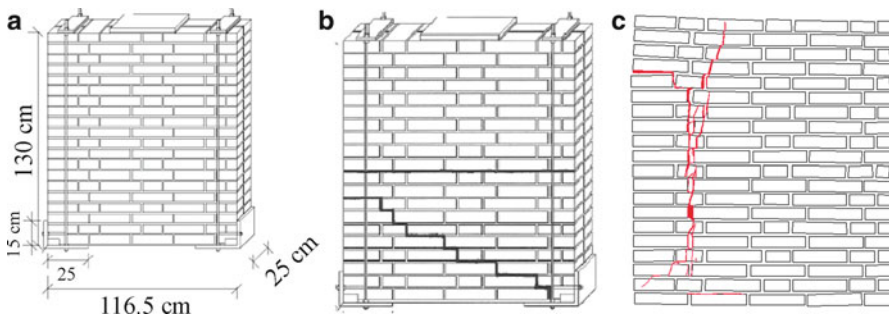
Fig. 1 (**a**) Masonry wall before damage, (**b**) panel with a simulated initial pattern of damage, (**c**) real crack pattern [3] on the wall, after a diagonal compression test

Table 1 Mortar and brick parameters used in the numerical simulations [2]

	Bricks	Mortar
Mass (Kg/m³)	1757	1800
E (N/mm2)	3840	981
ν	0.2	0.2
μ (water vapour diffusion resistance factor)	8	12

Numerical Simulations

As mentioned above, the diffusion of aggressive agents such as ions of salts dissolved in water is one of the main causes of environmental decay. For this reason, a model which takes into account the diffusion of water and heat as well as the diffusion of penetrating substances has been developed considering also the coupling between these processes. The evaporation phenomenon cannot be neglected because it affects directly the water rise and it primes the salt crystallization.

The masonry model has been studied as a porous, isotropous, 2-dimensional medium, and diffusive processes have been represented in the mid-plane of the wall but differential equations governing moisture, heat and aggressive flow account, for example, for evaporation flow orthogonal to the mid-plane. The coupling between these equations is in the diffusive coefficients, similarly to what reported in [4] and [5] for the case of concrete.

Two are the tests simulated:

Diffusion of salts at 0.05% in undamaged masonry wall: the input values of diffusion coefficients have been initially based on [6-7] but modified for porous media. The simulation of the diffusive problem has been carried out by F.E. analysis using Strauss7 and 2-D (plate) 4-node elements of 5-mm side (Fig. 2a). The simulation results are shown visualizing a salt (sodium chloride) concentration (g/mm^3) map in the lower 10 masonry courses of the wall after 18 days (Fig. 2b).

Diffusion of salts at 0.05% in cracked masonry wall: the above simulation has been repeated for a similar wall with hypothetical crack pattern (Fig. 1b). Cracks are localised in mortar joints and the damaging parameter is equal to 0.5 (Fig. 2c, d).
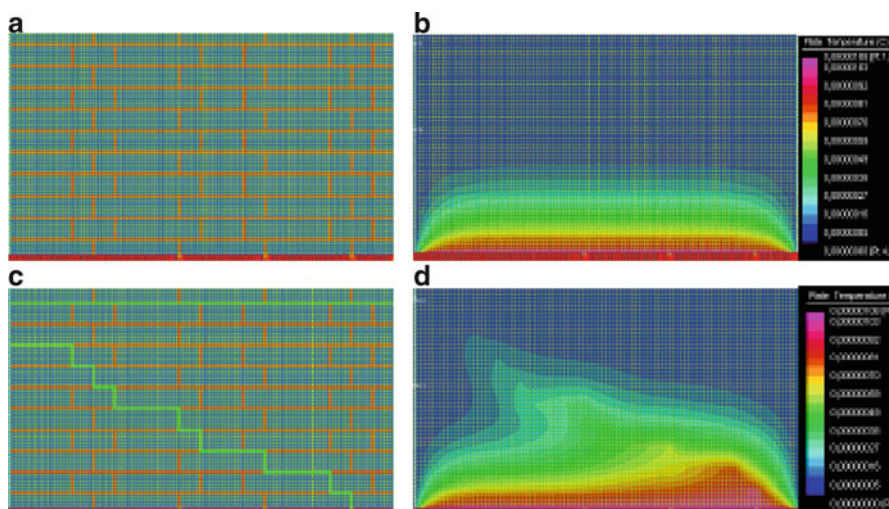
Fig. 2 (**a**) Masonry model, first 10 courses, undamaged, (**b**) map of salt concentration at 18 days, (**c**) cracked model, d) salt concentration at 18 days [8]

Experimental Work

A moisture capillary rise experiment has been carried out on the really cracked masonry panel (Fig. 1c) placed in a water basin. The height of water rising in the wall has been monitored by visual inspection, photographic documentation and infrared (IR) thermography. During the experiment, the base of the wall has been constantly kept in contact with 15-20 mm deep fresh water, while main environmental parameters have been measured (moisture and temperature of the air, temperature of the water and superficial temperature of the specimen). A Flir B250 thermocamera mounted on a tripod has been used in a passive mode for repeatedly acquiring thermograms both of the whole specimen and a close-up of its lower part. Instants of data acquisition have been denser in the first minutes and hours from the beginning of the experiment and have become sparser towards the end of it. A metrical reading of moisture rise from the wall bottom has been taken at selected points on the front and rear side of the specimen: in particular at mid point of wall width, over the crack and, symmetrically, on the right hand side of wall. As expected, the presence of mechanical damage has influenced the moisture capillary rise in the wall, that is, especially in the first phases of the test, the height of water rise has been faster at the crack, on the left of the wall front side (Fig. 3a, c). Also the mortar head joints have been a favourite path for the water, in comparison with the bricks at the same masonry courses. In general, the level of water rise has shown to be very uneven on the outer surfaces of the wall.

Unexpectedly, two points have been highlighted by IR monitoring: the first is that inspection of moisture level is more easily readable by IR than by visual or photographic inspection (Fig. 3b). This is especially true when the colour of moist material does not differ significantly from dry material. The difference between dry and moist material is shown in the thermograms by the slight difference in surface temperature between the 2 areas, as the moist, lower region will result cooler due to water evaporation. In the thermogram of Fig. 3c, the lower temperatures are shown in light blue, green and yellow tones. The second aspect is that moisture capillary rise has revealed a second area of mechanical damage on the right hand side of the wall. This decay had not been noticed during previous crack pattern survey. At a closer look with a magnifying glass, damage has been observed located at mortar joint/brick interfaces, including bed joints and it is due to shear stress during the mechanical test.
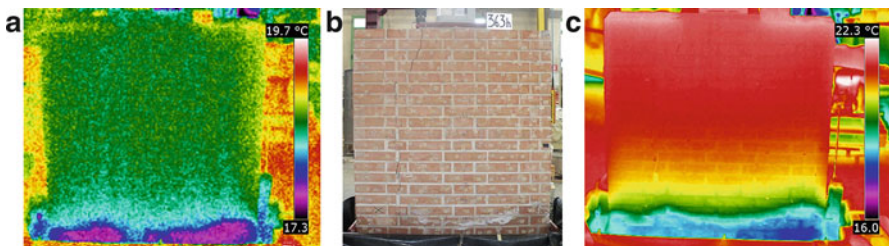
Fig. 3 (**a**) IR thermogram (T=17.3°-19.7°C) after 2 days, (**b**) photo of wall after13 days, (**c**) IR thermogram (T=16°-22.3°C) after 13 days

Conclusions

Given the diffusion and relevance of masonry constructions, and the deterioration attack they are undergoing from environmental causes, their study and conservation is of primary and topical importance. The present work reports about an ongoing research and preliminary results from modelling and experiments. Environmental decay in masonry walls has been discussed both in sound and mechanically damaged conditions. The focus has been put on moisture capillary rise as diffusion vehicle for penetrating substances such as salt in the materials, and its crystallization as a mean for provoking additional damage. The study of these phenomena aims at understanding and reproducing how environmental factors and their coupling affect the health state of masonry, and at foreseeing its damage evolution in time.

On a masonry panel built in the laboratory and simulating historic masonry, mechanical and non-destructive tests have been conducted, such as experimental moisture capillary rise monitoring by IR thermography of the flawed panel. At the same time, various studies have been performed by F.E. modelling. Water evaporation has a paramount role on both capillary rise rate in masonry and salt crystallization. The coupling between moisture and salt diffusion has been observed. It has also been seen how the presence of a crack pattern in the masonry panel affects considerably the speed of moisture rise and the distribution of salts, showing that where masonry suffers greater mechanical damage, higher salt concentrations and thus a higher risk may occur.

References

[1] Collepardi M., Coppola L., (1996), Il ruolo dell'umidita' nel degrado dei materiali nelle murature, *Il Nuovo Cantiere*, vol. 6, pp. 44–51, June 1996.
[2] Colla C., (2009), D5.2 Report on laboratory and on-site activity, EU funded research project report, Project N°212939, University of Bologna, pp. 235.
[3] Ciantelli C. (2010), *Diagnostica delle murature storiche con prove soniche: sperimentazione in laboratorio*, Undergraduate degree thesis, Faculty of Math., Physical and Natural Sciences, Bologna University, Bologna, Italy, 203 pages.
[4] Saetta A., Scotta R., Vitaliani R. (1993), Analysis of cloride diffusion into partially saturated concrete, *ACI Materials. Journal*, 90, 441–451.
[5] Bazant Z. P., Najjar L.J., (1972), non linear water diffusion in non saturated concrete, *Materials and Structures*, RILEM, vol. 5, No. 25, 3–20.
[6] Gerard B., Laborderie C., (1998), Coupled diffusion-damage modelling and the implications on failure due to strain localisation, *International Journal of Solids and Structures*, vol. 35, no. 31–32, 4107–4120.
[7] Colombo P., Colleselli F., (2004), Elementi di geotecnica, Zanichelli, pp. 480.
[8] Fiocchi M., (2010), *Modellazione del degrado ambientale di strutture in muratura*, Undergraduate degree thesis, Faculty of Engineering, Bologna University, Bologna, Italy, 148 pp.

Simulation and Test Procedures to correlate Structural Damage with Moisture and Salts Migration in Masonry

C. Colla, P. Baldracchi, A. Troi, F. Ubertini and R. Carli

Abstract In historic masonry structures – focus of the 7FP European project SMOOHS – the monitoring and effects of environmental agents in walls and of structural problems is being investigated in a joint perspective. Numerical simulations and experimental work aim to correlate the decay effects of moisture and salt transport in masonry, with structural damage. To better address the problem, a cross-feeding collaboration is set up between numerical and experimental studies. Initial experimental data obtained in the lab on masonry materials become the main input data for hygro-thermal simulations of behaviour of masonry specimens in aggressive environment, that is solutions of sodium sulphate (Na_2SO_4). Simulation output helps to improve the experimental accelerated ageing procedures. Later, the salt damage process development in these specimens and their reduced structural capacity will be mechanically evaluated. A function relating these parameters will couple hygro-thermal and structural simulations to predict a structural damage index for historical buildings.

Keywords Historical masonry • Hygrothermal analysis • Laboratory test • Salt migration • Structural damage index

Introduction and objectives

Historical masonry structures, as an important part of our world's cultural heritage, need to be preserved and protected for next generations. Environmental phenomena are between the main causes of structural damages and the role of water is of key

C. Colla • F. Ubertini • R. Carli
DICAM Department, Engineering Faculty, University of Bologna, Bologna, Italy

P. Baldracchi (✉) • A. Troi
EURAC – Institute for Renewable Energy, Bolzano, Italy
e-mail: paolo.baldracchi@eurac.edu
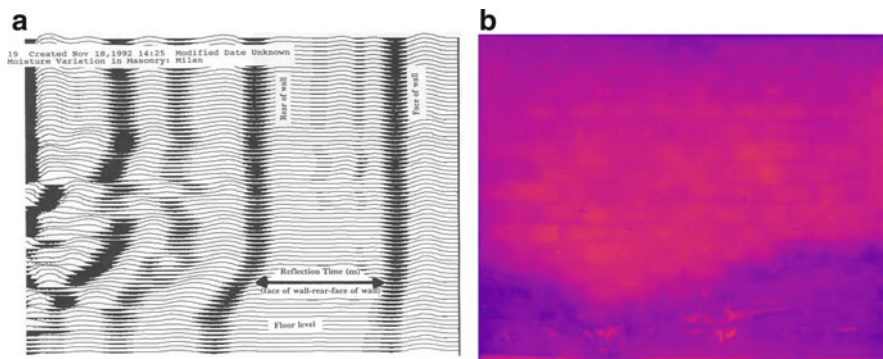
Fig. 1 (**a**) Vertical survey line on masonry, with level of water capillary rise [6]; (**b**) IR thermography on a masonry wall showing capillary rise level on surfaces

importance in various deterioration mechanisms [1]. For this reason, in recent years, many studies have been carried out to understand the mechanism of degradation processes due to moisture and salts migration in porous materials [2-7]. Nonetheless, a clear correlation between moisture and salt migration in historical masonry walls and structural damage that can be used as a decay index has not been established. NDT testing, such as GPR radar, IR-thermography, sonic, ultrasonic and impact-echo test, have so far been recognized as a main tool for structural diagnosis as they can give detailed information on the inner characteristics of the elements and on their health conditions. As an example, it is possible to determine on masonry walls the level of water capillary rise by means of NDT techniques, such as GPR radar; moreover, the effects of degradation phenomena on surfaces, due to environment, can be assessed by IR thermography (Fig. 1). So, the use of NDT on historical masonry structures should be greatly recommended, although it is necessary to better evaluate and enhance their capacity to detect the beginning of material and structural deterioration and its evolution over longer periods.

Within the 3-year 7th FP EU Project SMooHS, Smart Monitoring of Historic Structures (2008-2011), numerical simulations and lab tests are being jointly carried out to establish a correlation between moisture and salt migration in historical masonry walls, and structural damage. Several masonry specimens of different dimensions have been built using bricks and lime mortar as it would be found in historical buildings selected as case studies in the SMooHS project. These specimens are undergoing different types of ageing from wetting and drying, through capillary rise or full immersion in bath. Moisture solutions also vary from tap water to different salt concentrations. Drying phases of the specimens have been foreseen in open-air ventilation or forced in an oven.

Salt attack by sodium sulphate has been chosen in this study because of its destructive nature. It is responsible for significant damage in porous materials due to volume increasing and high hydration pressure generated during phase changes [4]

and especially during mirabilite crystallization [7]. Repeated cycles of crystallization/hydration within walls can lead to internal stress and, thus, to micro-cracking and loss of strength in the materials. Numerical investigation of the maximization of thenardite/mirabilite crystallization in masonry, and their phase changes, can guarantee the damaging phenomena to best address the experimental procedure. The main aim of this work is to assess the salt related damage progress in masonry, comparing data obtained both from numerical simulation and lab tests. This should allow to draw a function relating structural parameters with moisture and salt content of the studied masonry specimens, which will be useful to couple hygrothermal and structural simulations in order to predict a structural damage index for historical buildings. The paper's approach is to determine the experiments layout with the help of simulations as well as the experiments implementation. These are described and preliminary results are discussed.

Experimental Work I

Masonry specimens of dimensions 250x185x120 mm^3, that is 3-brick columns with 2 mortar joints, have been built in the lab using solid clay bricks (250x120x55 mm^3) and natural hydraulic lime mortar (10mm thick joints). Among the physical parameters affecting the hygro-thermal characteristics of the materials only the density (brick 1790 kg/m^3, mortar 1900 kg/m^3) and the porosity (23.2 Vol-% for the bricks and 20.6 for the mortar) have been determined experimentally. This reduced amount of measured hygro-thermal material parameters has caused problems to initial simulations as the necessary input information could not be satisfactorily selected from assumed similar materials in the SW database. In turn, this has caused preliminary simulation analyses to provide unrealistic water, respectively brine, uptake timings in the considered materials. Thus, experiments of moisture capillary rise from the base (saturated Na_2SO_4 solution), and absorption by full immersion have been conducted in controlled air moisture and temperature conditions, according to the norms [8-9], both on brick units and small masonry assemblies. The obtained data from this 2 extreme cases have served for feeding the simulations with sufficiently accurate assumptions on material properties, as well as the right order of magnitude for material viscosity.

Meanwhile, the design of the accelerated ageing test procedure for the masonry samples has started considering different hypotheses of several cycles of soaking and drying phases, that is soaking by full immersion in a 10% brine concentration of sodium sulphate and subsequent forced drying in a climatic chamber with controlled environmental parameters, to extend the damaging crystallization phase changes between thenardite and mirabilite. This design phase has considered mainly logistic and time issues together with proper temperature and relative humidity values.

Simulations

Numerical simulations of moisture and salt migration in small masonry samples have been carried out using the software Delphin (v.5.6). Mono-dimensional analyses have been performed in order to predict the time distribution of moisture and salt concentration (sodium sulphate Na_2SO_4 and its phases) in the masonry assemblies and to select the most efficient wetting and drying cycles, replicable in laboratory, that maximize the crystallization of the two main phases of sodium sulphate: thenardite (Na_2SO_4) and mirabilite ($Na_2SO_4 \cdot 10H_2O$). Also 2-D analyses have been carried out, but only to simulate moisture migration since salt migration is not jet implemented in the software for 2-D problems. The same geometry of the masonry samples built in the lab has been introduced into the software simulations.

In the very preliminary numerical analyses, the unknown hygrothermal parameters of the construction materials -clay bricks and lime mortar- had been chosen from suitable values in the SW database. As reported above, facing unsatisfactory output, the modelling has been improved by feeding it with data from water and brine uptake experiments. The simulations will be further improved by adding measured hygrothermal properties of the materials as soon as available.

The simulations have been conducted considering different boundary conditions, replicable in laboratory:

1. Water contact to simulate a bath of the specimens in tap water
2. Solution contact to simulate a bath of the specimens in 10% brine
3. Ambient conditions defining a constant temperature (20°C) and RH (50%)
4. Oven conditions defining a variable T (20°-60°C) and RH (20%-75%).

The initial conditions of the samples have been set to: T 20ºC, RH 50%, salt mass density of each phase equal to zero. Starting from these input, the sample has been simulated immersed in a sodium sulphate solution and then dried in a climatic chamber, to force the salt crystallization and hydration.

In the phase diagram for sodium sulphate (Fig. 2a), it is possible to observe that (i) at T>32.4°C with decreasing RH always thenardite crystallises from a solution, whilst (ii) at lower temperatures the salt crystallises according to RH and T values. Changing T and RH can cause hydration of thenardite to mirabilite and vice versa. Within the boundary conditions described, various cycles have been simulated, varying the T and RH in the oven, the time duration of each wetting/drying phase and taking into account the feasibility of these tests in the specific laboratory. It has been found that keeping a low RH (20%) in the oven the sample dries out too fast inducing much more thenardite than mirabilite crystallization, while, with a higher RH (50% to 75%), the sample dries out slowly and crystallization occurs only after temperature decrease, with a similar amount of thenardite and mirabilite. Thus, to maximize mirabilite crystallization, the experimental design proposal reported in the following "Experimental II" paragraph, appears effective.

The results (Fig. 2b) show that thenardite crystallization occurs mainly during the last period of drying in the oven when the temperature is high (more than 32.4 °C) and the RH is below the equilibrium line 1 of Fig. 2a. Mirabilite crystallization starts
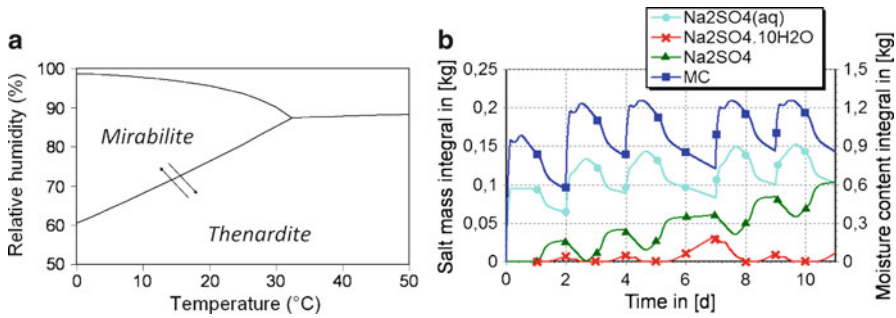
Fig. 2 (**a**) Sodium sulphate phase diagram [10]; (**b**) Simulation results showing salt and moisture content (MC) as an integral curve of 5 accelerated ageing cycles

when the temperature decreases towards ambient temperature (20° C). The longer the time period at ambient condition, the higher the amount of mirabilite crystallization. Simulations show also that crystallization occurs only within the exterior layer of the sample that is: mirabilite within 5 mm from the sample edge and thenardite within 1 mm (only surface efflorescence).

Experimental Work II

After the design phase and the numerical checking, the accelerated ageing by salt crystallization has started to be replicated on the masonry samples. Laboratory ageing tests are being conducted on the 1st set of masonry samples (3-brick columns) following the optimum timing and environmental conditions of wetting/drying cycles verified by numerical simulations. In this first part of the experiments, the cycles are being repeated 20 times in order to reach the maximum damage degree. Photographic documentation and visual inspections have been performed every 2 cycles, to monitor the damage progress.

Every cycle consists of the following steps:

– 3 hours of immersion in sodium sulphate solution;
– 8 hours of drying in climatic chamber, with T up to 60°C (this low value avoids dilatation damage in masonry) and RH decreasing to 50%;
– 18 hours in climatic chamber at constant temperature (60°C) and relative humidity (50%);
– 8 hours in climatic chamber, at constant humidity (50%) and decreasing temperature until 20°C plus 8 more hours of rest in the climatic chamber.

From the visual inspection, salt crystallization on the specimens surface (efflorescences) is evident already after very few cycles with exfoliation and cracks in the bricks (Fig. 3) whilst the mortar joints experience loss of material with progressive erosion. In later cycles, beginning of detachment between mortar and bricks has occurred at selected interfaces, for a limited specimens number.
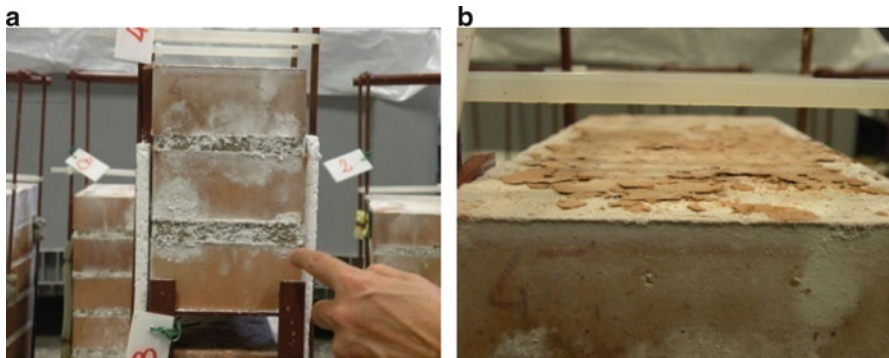
Fig. 3 Results of visual inspection of a masonry specimen during accelerated ageing cycles: (**a**) after 5 cycles, (**b**) detail of efflorescence and exfoliation

Discussion and Conclusions

Numerical simulations of salt and moisture transport in masonry have been used to verify the design of the experimental setup and the most effective wetting/drying cycles for accelerated ageing. Comparison of preliminary simulations and water/solution uptake experiments has shown sufficiently accurate modelling for the sake of setup definition. Ageing test has accordingly started in the laboratory. The simulation model will be further enhanced and material hygro-thermal characteristics need to be measured and implemented; 2-D salt migration simulations will be performed as soon as the model will be implemented by SW developer. At the end of experimental ageing cycles on the masonry samples, damage development due to salt crystallization will be mechanically evaluated to establish a correlation between salt migration and structural damage. This will then be implemented in a coupled model for hygrothermal and structural modelling.

References

[1] Collepardi, M., (1990), Degradation and restoration of masonry walls of historical buildings, *Mater. Struct.*, 23 (134), pp. 81–102.
[2] Binda, L., Baronio, G., (1998), Crystallization test by total immersion of specimens, *Mater. Struct.*, 31, pp.10–15.
[3] Theoulakis, P., Moropoulou, A., (1999), Salt crystal growth as weathering mechanism of porous stone on historic masonry, *J. porous Mater.*, 6, pp. 345–358.
[4] Rodriguez-Navarro, C. et al., (2000), How does sodium sulfate crystallize? *Cem. and Concrete Res.*, 30, pp. 1527–1534.

[5] Lubelli, B.et al. (2004), The role of salt in the occurrence of different damage mechanisms and decay patterns on brick masonry, *Constr. Build. Mater.*, 18, 119–124.

[6] Binda, L., Colla, C. et al. (1994), Identification of moisture capillarity in masonry using digital impulse radar, *J. Constr. & Build. Mater.*, vol.8, No.2, pp. 101–107.

[7] Steiger, M. et al. (2008), Crystallization of sodium sulphate phases in porous materials: The phase-diagram Na_2SO_4-H_2O and the generation of stress, *Geochimica et Cosmochimica*, Acta 72, pp. 4291–4306.

[8] UNI EN 15801:2010, Conservation of cultural property, Test methods-Determination of water absorption by capillarity, February 2010, pp.14.

[9] UNI EN 1925:2000, Natural stone test methods – Determination of water absorption coefficient by capillarity, December, 2000, pp.16.

[10] An expert chemical model for determining the environmental conditions needed to prevent salt damage in porous materials, Final Report – Project ENV4-CT95-0135 (1996–2000)

Wireless Monitoring of Moisture Content in Mineral Materials by Electrical Impedance Measurements

F. Lehmann, J. Frick, M. Krüger and K. Menzel

Abstract Changes in the moisture content and the resulting recrystallisation of the entrained salts is one of the major damage causes in historic materials like natural stones, tiles, plasters and mortars. This paper presents a new development in wireless monitoring of the moisture content in historic mineral materials. In this ongoing research, electrical impedance measurements are carried out to monitor the changes in the measured electrical conductivity of materials, as affected by both the total moisture content and the salt concentration. A measurement system consisting of a pair of electrodes, a sensor board and a low power data acquisition hardware was developed which was optimised for use in wireless sensor networks. Initial results of the laboratory validation tests are presented in the paper.

Keywords Impedance measurements • Mineral materials • Moisture • Salt • Wireless monitoring

Introduction

Within the frame of the European SMooHS project [1], an adaptable wireless sensor system with a multitude of different sensors for monitoring historic structures and buildings is being developed. One sensor module was developed to measure changes in the complex impedance of mineral materials. This value is dependent on both the moisture content and the salt concentration - two properties that are very important in the assessment of structural cultural possessions. By continuously observing the impedance at one or more points of an object, it is anticipated to detect water, and with it salt intrusions into the material, before it can lead to damage.

In a first series of laboratory measurements, the developed sensor element was, amongst others, cross-checked against a proven reference system with respect to

F. Lehmann (✉) • J. Frick • M. Krüger • K. Menzel
Materialprüfungsanstalt Universität Stuttgart, Germany
e-mail: frank.lehmann@mpa.uni-stuttgart.de

its accuracy and reliable measurement range. Furthermore, three different coupling agents were evaluated concerning their response behaviour upon changes in the material and their applicability to natural stone.

Electrical Impedance Measurements on Mineral Materials

The electrical impedance Z of a material is a measure for its opposition to an electric current. Mathematically, it is a vector addition of the material's resistance R and reactance X. The former describes the opposition of the material against the flow of an electric current, while the latter describes the opposition of the material against a change in the frequency f of the applied alternating current. In the case of a direct current, i.e. without any change in the current over time ($f = 0$), the impedance becomes the material's resistance.

$$Z = R - i \cdot X \tag{1}$$

$$= |Z| \cdot e^{i\varphi} \tag{2}$$

where the magnitude $|Z| = \sqrt{R^2 + X^2}$ and the phase angle $\varphi = \arctan\left(\dfrac{X}{R}\right)$.

When passing a current from an electrode into an electrolyte, a change in the type of conduction takes place. While in the metal the current can be described as drift of free electrons, in the electrolyte it is a shifting of ions. At the interface between the two states, an electrical double layer is formed, which is due to the effort of the electrons to pass over into the electrolyte at the cathode (reduction) and to the oxidation of the ions at the anode. In the reverse conclusion this means, that a measurement of the resistance between two electrodes - which implies the application of a current, i.e. an external potential - always includes the potential of the phase boundary [2]. In the case of a two-point impedance measurement system, this problem of the electrode polarisation can be reduced by increasing the measurement frequency, which yields a reduction of the polarisation reactance (decrease of X). On the other hand, a frequency too high would result in a corruption of the measurement results due to a disproportionally high current via the measurement cell itself, compared to the current through the material. This is especially true in the case of a low material conductivity [3]. The frequency range in complex impedance measurements on mineral materials therefore has to be carefully optimised.

Electrical Impedance Measurements using SmartMote^WS Nodes

To capture electrical impedance data in mineral materials, an impedance meter for the use with SmartMote^WS sensor nodes (see Fig. 1) in a wireless sensor network was developed [4]. It consists of two electrodes which are to be embedded in the material

Fig. 1 SmartMote^WS node with electrical impedance measurement board

Fig. 2 Measurement electrodes
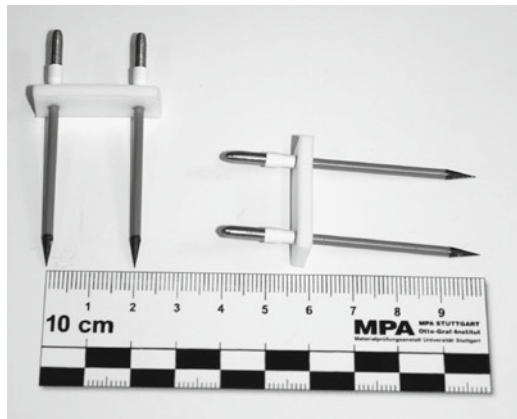
to be tested and an attached measurement board. The impedance measurement is conducted by an Analog Devices AD5933 network analyzer chip [5] which is capable of measuring in a frequency range from 10 Hz to 100 kHz and an impedance range from 1 kΩ to 10 MΩ. Due to the sensor node's small dimensions, autonomous power supply and wireless data transmission, it can easily be installed on objects and structures without impairing the sight.

Standard timber moisture measurement pins are currently used as electrodes (Fig. 2). The steel pins are coated with a non-conductive material except for a conical tip and a connection end. To ensure the pin position in the material, they are connected with a piece of PTFE. A minimal invasive intrusion into the structure with a small drill is required for their placement. They can then be glued into the structure to assure a good and lasting connection between the material and the electrodes. In preliminary laboratory tests, an electrode distance of 20 mm was chosen. While a greater distance yields a higher impedance, which might be out of the measurement range, a smaller distance might focus too much on local effects.

Measurement Accuracy and Range

To be able to exploit the entire impedance range of the measurement chip, different internal gain resistors have to be used. They control both the upper and lower limit of the measurement range, with the value of the gain resistor being the smallest measurable resistance. To find adequate gain resistors and to evaluate the system's effective range, a set of ohmic resistors between 10 Ω and 22 GΩ was measured. Their real resistivities were determined using a commercially available multimeter. As a reference, the set was also recorded using a Schlumberger 1260 impedance/gain-phase analyzer. Figure 3 shows the measurement deviation of the wireless impedance meter with different gain resistors in comparison to the Schlumberger 1260 reference system. The impedance meter measurements were each 1-point calibrated with a resistor according to the actual gain resistance. This results in relatively large discrepancies between the measured and the actual resistance values. Note, that the chip's stated impedance range only starts at 1 kΩ. In the test, a frequency sweep from 10 Hz to 100 kHz was carried out. Corresponding to the theory, no or only little reactance was measured. The results show the average value of the determined impedance, which here corresponds to the resistance.

The values for the impedance within the admissible ranges show accuracy with a maximum deviation from the actual impedance of 0.18. As expected, high impedances are not measurable with small gain resistors, although a range of 3 decades can be covered. To further increase the measurement accuracy, the system's 1-point calibration can be extended to a 2- or multi-point calibration. Figure 4 shows the same measurements as Fig. 3, but with each measurement calibrated at the neighbouring full decade. Consequently, the accuracy of the measurements is greatly increased. This is not surprising, as a further refinement of the calibration
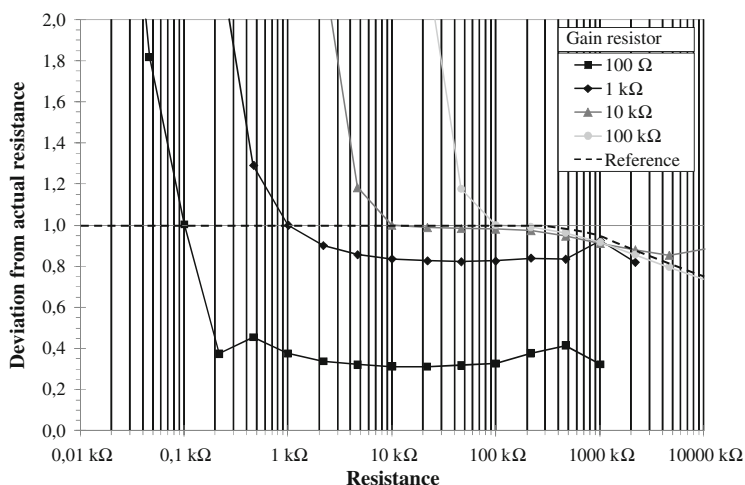
Fig. 3 Measurement deviation from actual resistance. 1-point calibration
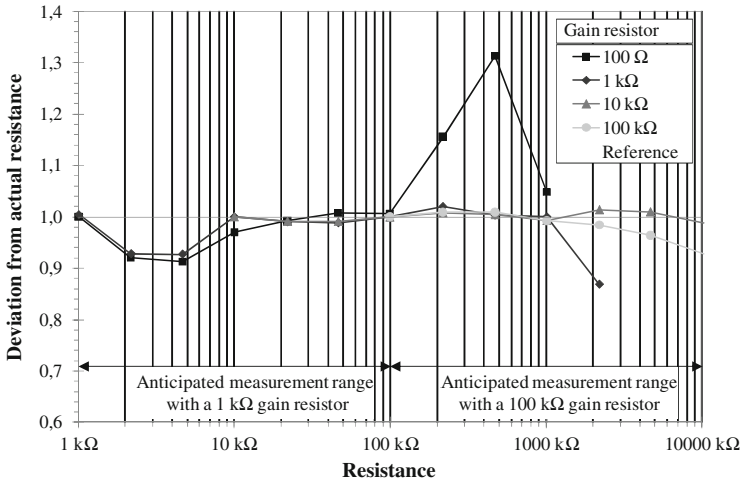
Fig. 4 Measurement deviation from actual resistance. Calibration at each full decade

steps would eventually lead to a straight line. However, two important findings can be derived:

- Especially the impedance range close to the gain resistor requires a fine step size in the calibration. The smaller the gain resistor, the more calibration points have to be recorded.
- Given a good calibration, only two different gain resistors are needed to cover the entire measurement range, e.g. a 1 kΩ and a 100 kΩ gain resistor for the impedance ranges from 1 to 100 kΩ and 100 kΩ to 10 MΩ respectively. This is very important in terms of measurement duration and thus battery life of the sensor nodes.

Generally, a very high accuracy in the measurements can be achieved. This holds especially true for the fact, that the system is originally designed to measure changes in the impedance, not absolute values only.

Electrode Coupling

To find a suitable adhesive for the electrodes, several different glue types were tested in the laboratory, amongst others dispersed white lime hydrate, silica stone glue and silicic acetate bonded stone injection compound. Figure 5 shows the development of the impedance at 1 kHz for three different electrode adhesives, when a water front propagates into an accordingly equipped sandstone. The time of the addition of water is marked in the graph with a vertical line. This event is recognised almost immediately by the embedded temperature sensor. After one hour, two of the electrode pairs
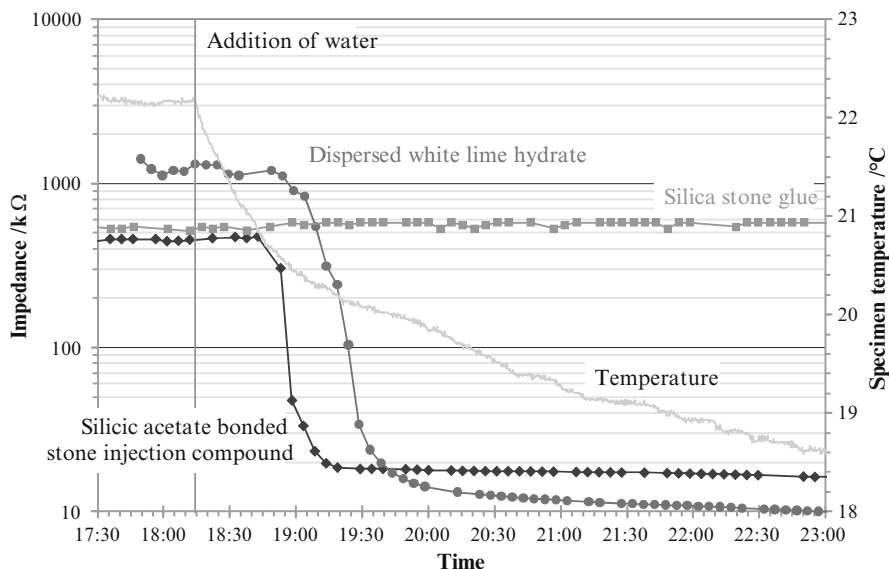
Fig. 5 Development of electrical impedance for different coupling adhesives

indicate the arrival of the water front. The impedance then declines while the water front passes the measurement area and approaches a constant value when the sandstone is fully saturated. It is apparent, that the silicic acetate compound shows a much more agile behaviour than the dispersed white lime hydrate. This is most probable due to the difference in permeability of the two materials.

The difference in the absolute values is believed to be a result of the difference in the coupling strength and thus in the electric conductivity. While the silicic acetate compound allows a compact installation of the electrodes in the surrounding material, the dispersed white lime hydrate leads to a rather loose connection, which results in a higher impedance in the beginning. When the water surrounds the electrodes due to capillary forces, the conductivity is higher compared to a dense adhesive contact, leading to a lower final impedance. In the case of the silica stone glue, no change is noticed over the entire measurement period. This is due to the hydrophobic character of the glue as long as it is not fully dried out. The electrodes were glued into the sandstone approximately 24 h prior to the testing.

Conclusion and Outlook

The presented wireless impedance meter has proven its value in initial laboratory measurements. When calibrated sufficiently, preferably using a 2- or multi-point calibration, it shows a very high accuracy.

While in presented tests, standard timber moisture measurement steel pins were used as embedded electrodes, currently other materials are investigated for their suitability. This includes platinised and iridium oxide coated titanium electrodes, as well as gold- and rhodium-plated steel electrodes. It is believed that these materials might show a more favourable behaviour in the measurements with respect to the electrical double layer. More research is also needed to investigate the optimal electrode coupling. So far, the electrodes were directly glued into the material, which calls for a minimal invasive intrusion. Especially in the case of valuable historic monuments, even this is often undesirable. Therefore, a further focus lies on non-invasive and reversible electrode surface coupling. To study in-situ effects on the measurement system, a device is now installed at the Holy Cross Minster in Schwäbisch Gmünd, Germany.

References

[1] SMooHS - *Smart Monitoring of Historic Structures*. European Commission (EU). Seventh Framework Programme - ENVIRONMENT. Project reference: 212939. URL: http://www.smoohs.eu. 18. January 2011.

[2] Hamann, C.H., Hamnett, A., Vielstich, W.: *Electrochemistry*. Wiley-VCH, Weinheim, 2007.

[3] Fafilek, G.: *Leitfähigkeit. Wahlübung zur Elektrochemie.* Institut für Chemische Technologien und Analytik, TU Wien, 2009.

[4] URL: http://www.shm.uni-stuttgart.de. 18. January 2011.

[5] URL: http://www.analog.com/static/imported-files/data_sheets/AD5933.pdf. 18. January 2011.

Determination of Mechanical Properties of Natural Stone and Brick Elements in Masonry Heritage Buildings

A.M. Grămescu, S. Gelmambet, M. Drăgoi and B.D. Pericleanu

Abstract The paper presents the results of investigation and documentary research conducted by the authors upon the constituent material of stone and brick masonry structures located in Dobrudja county. It's important to mention that in Dobrudja are encountered a great number of heritage buildings belonging to 18th – 19th century that have a stone and brick masonry structure resistance. For these reasons the main objective of the study is to determine the mechanical properties of materials which structure is made of. In order to achieve this objective the authors have determined the mechanical characteristics of brick and stone elements in masonry with nondestructive methods for various heritage buildings in Dobrudja area. To verify and validate the results obtained by nondestructive methods, those results were compared with the ones obtained by applying destructive methods in the laboratory of the Faculty of Civil Engineering, "Ovidius" University of Constanta. The results have been summarized and constitute the beginning of a database of mechanical characteristics. The obtained results offer a valuable amount of information in establishing measures for interventions in restoration.

Keywords Heritage buildings • Mansonry • Mechanical properties • Stone

Introduction

In the research program a series of studies and researches on mechanical properties of masonry were conducted for a series of heritage buildings from Dobrudja area (Constanta County, City of Constanta and Tulcea County) - buildings which according with National List of Historical Monuments are classified as historical monuments or are located in areas of historic preservation or constructions with

A.M. Grămescu • S. Gelmambet • M. Drăgoi (✉) • B.D. Pericleanu
"Ovidius" University of Constanta, Constanta, Romania
e-mail: dragoi.mihaela@gmail.com
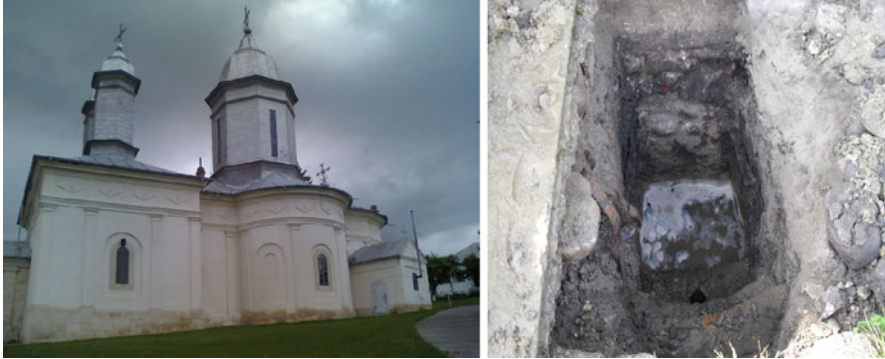
Fig. 1 Church of Ratesti Monastery, 1887

Fig. 2 Traditional house, 1780

Fig. 3 Dara church, 1650

architecture or materials and technologies of great historical importance for the communities which they belong to. Limestones (with compressive strenght ranging from 12-55 MPa) and sandstones are the most well known of sedimentary stones, being the most widely used in construction.

After their selection and processing in order to meet current code requirements for nondestructive and destructive testing it remained a total number of 10 specimens of stone and 16 specimens of brick. The first specimens were taken from the infrastructure of two orthodox religious buildings classified as class A in our national list of historical monuments (Figs. 1 and 3), the next specimens were taken from interior and exterior walls of buildings dating from 1780, 1887 and 1920 - buildings located in historical sites or historic preservation areas (Fig. 2). The research was conducted both in the laboratory and in situ.

Results Presentation

Nondestructive tests were performed in situ, before taking each specimen from the established location. Two methods were applied: superficial hardness method (Schmidt hammer method - R^I) and ultrasonic pulse method (R^{II}). The measurement dates and results were summarized in Table 1 for stone elements and Table 2 for brick elements.

For each specimen we determined the average kick index (N) and, using the calculated coefficient determined experimentally both in situ and in laboratory tests (C_t), the compression strength was determined in column 8 of Tables 1 and 2. The specimens were also subjected to destructive tests and the data was summarize in columns 4, 5 and 6 of the Tables 1 and 2. A comparison of results obtained by the two methods – nondestructive (Schmidt hammer method) and destructive - is presented in Figs. 4 and 5.

After applying the ultrasonic pulse method, the longitudinal wave propagation velocity through the specimens was measured, the duration of this spread also and, using the experimental data from situ and laboratory analysis the compressive strength on each specimen was established. The data are summarized in Table 1 for stone elements and Table 2 for brick elements in column no. 9. In Figs. 6 and 7a comparasion has been made between the values of compressive strength determined by

Table 1 Summary of findings for stone elements

No. of sample	year	N	A [m²]	F [kN]	R destructive [MPa]	C_t	R^I nondestructive [MPa]	R^{II} nondestructive [MPa]
1	1650	17,5	0,011	164	15,37	0,9	15,75	15,44
2	1887	49	0,008	116	14,33	0,3	14,70	14,01
3	1887	30,5	0,004	92	22,45	0,8	24,40	19,46
4	1887	53	0,011	298	27,81	0,6	31,80	27,91
5	1650	36	0,015	200	12,83	0,4	14,40	12,86
6	1887	37,5	0,010	238	23,33	0,7	26,25	23,15
7	1920	57	0,009	292	31,29	0,6	34,20	30,14
8	1920	42	0,009	149	15,07	0,4	16,80	15,9
9	1780	48	0,004	119	31,85	0,7	33,60	31,77
10	1780	54	0,003	14	5,17	0,1	5,40	5,24

Table 2 Summary of findings for brick elements

No. of sample	year	N	A [mm²]	F [kN]	R destructive [MPa]	C$_t$	R^I nondestructive [MPa]	R^{II} nondestructive [MPa]
1	1780	23,5	0,020	288	14,32	1,3	17,87	15,63
2	1780	23	0,020	298	14,62	1,3	18,46	13,22
3	1780	21,5	0,026	554	20,79	1,3	18,98	20,58
4	1650	35	0,010	214,5	21,20	0,8	17,76	20,77
5	1887	28	0,017	286	16,86	1,1	18,59	11,45
6	1887	17	0,014	134,2	9,76	1,1	10,67	11,67
7	1887	16	0,010	86	8,13	1,1	9,02	8,97
8	1887	21	0,014	164	12,01	1,1	13,75	8,48
9	1887	23,5	0,011	132	12,19	1,1	13,2	9,8
10	1887	31	0,005	52	9,90	1,1	11,66	12,08
11	1887	25	0,023	114,7	5,03	1,1	5,83	11,15
12	1920	23	0,014	106	7,66	0,6	4,56	4,63
13	1920	23	0,017	126,2	7,54	0,6	4,56	8,46
14	1920	26	0,012	99	7,99	0,6	4,92	7,85
15	1920	25	0,008	48,2	5,88	0,6	3,18	11,46
16	1920	26	0,017	162	9,22	0,6	6	8,73

Fig. 4 Comparative analysis of the results (nondestructive – destructive methods) for stone elements
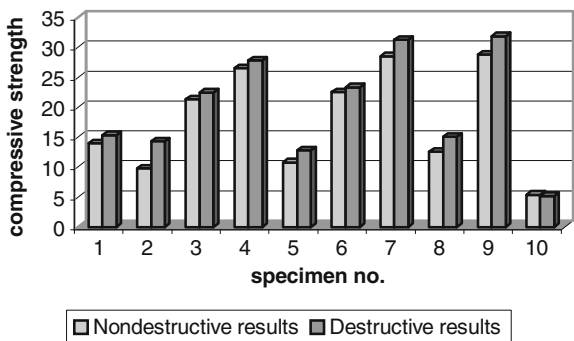
Fig. 5 Comparative analysis of the results (nondestructive – destructive methods) for brick elements
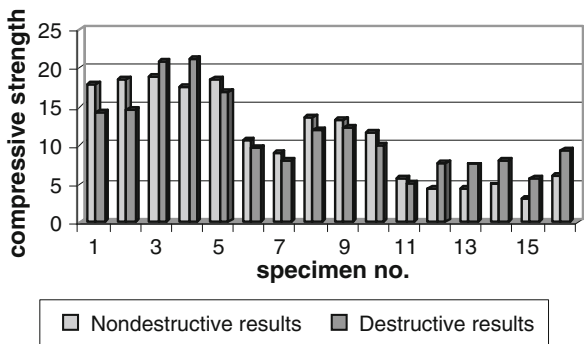
Fig. 6 Comparative analysis of the results (nondestructive and destructive methods) for stone elements
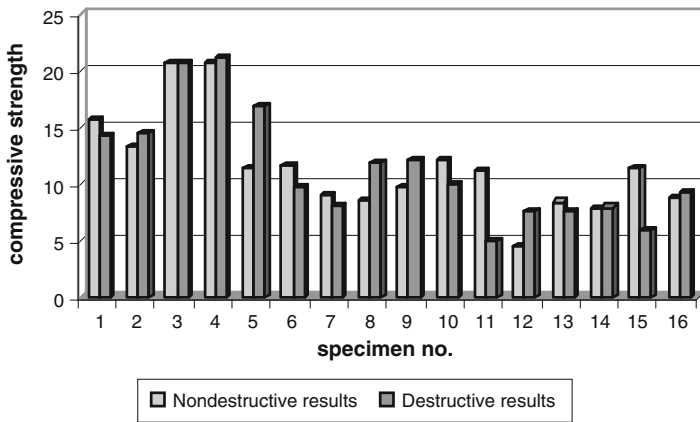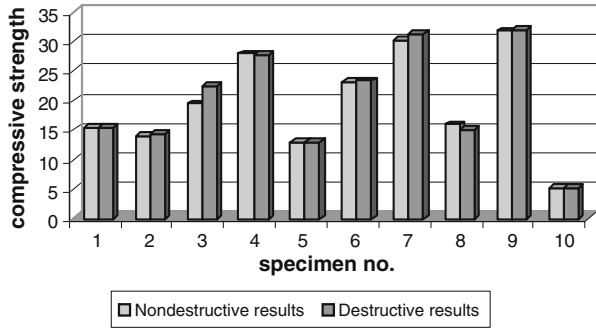
Fig. 7 Comparative analysis of the results (nondestructive - destructive methods) for brick elements

ultrasonic pulse method and the compressive strength values determined on destructive tests.

The results from nondestructive testing show an average compressive strength of 11.18 MPa (superficial hardness method) and 11.55 MPa (ultrasonic pulse method) compared to an average strength of 11.45 MPa obtained after the destructive tests.

Conclusions

The findings of the research conducted are expected to constitute the beginning of a valuable database both by its applicability at assessing the strength and stability of historic buildings and in clarifying technical details of the history of construction in the area of reference. The mechanical properties obtained by nondestructive methods can be used in numerical simulations of the structure, thus resulting in a response

much closer to their real behavior. Studying the results, large differences between specimens values can be observed due to:

– for bricks: their age, the brick manufacturing process, the existing state of degradation of building;
– for stone: its age, state of degradation of existing building.

The specimens from buildings which have been well preserved over time have obtained better results of compressive strength.

Another interesting aspect is observed by comparing the results obtained on the constructions from Dobrudja County and Buzau County. Note in this case that the compressive strength of bricks from Dobrogea County ($R_{c\ average}$ ~ 9,5MPa) is much weaker than those from Buzau County ($R_{c\ average}$ ~ 18MPa). It can be observed that the values obtained for Buzau brick compared to the ones used in Dobrudja are much better (~ 50%). The data from the specimens considered will provide the first steps of a very interesting and useful database in order to conclude on the intervention solutions for assuring the strength and stability of heritage buildings that fit the parameters presented.

Future research directions aim to increase the database, to determine physical characteristics of the constituent material, and also to determin the masonry resistance considering the influence of mortar, time and execution technology.

References

[1] Gramescu Ana Maria, Barbu Daniela A.M.: *Repairing and strengthening the constructions*, AGIR Publishing House, Bucharest, 2008.
[2] Stanescu Gheorghe: *Dobrudja: history in pictures*, North Star Publishing House Constanta, 2008.

Mobile UV-VIS Absorption Spectrometry Investigations in the "Alexander-Sarcophagus" in Istanbul

H. Piening

Abstract For several years, UV-VIS-spectrometry has been employed to identify colorants used in the polychromy of diverse art objects such as paintings, textiles and ancient sculptures. UV-VIS-spectrometry is a non-destructive method used to identify colorants (pigments and dyestuffs). The surface to be examined is briefly illuminated by white light. Part of the white light is absorbed and part is reflected. The reflected light is detected and split by a spectrometer. Achromatic materials can also be identified if the spectral range is adjusted to the visible light in the near UV and the near infrared region. The spectra can be compared with those in specially created data libraries. The combination of high efficient optical equipment such as light source, fibre optics and diode-array detector together with the mathematical preparation of the spectra enables us to identify successfully nearly 90% of the colorants without taking samples. The various technical options for this analytical method and the results obtained by examining the Alexander-sarcophagus owned by the Archaeological Museum of Istanbul will be illustrated. It was possible to identify more than 24 colorants.

Keywords Ancient sculptures • Non-destructive • Polycromy • UV-VIS-spectrometry

The Method

Many ancient buildings and sculptures still show unmistakable traces of their former polychromy. Even now, little attention is paid to these remnants of their original splendidly colourful appearance, either because the traces of colour seem impossible to interpret, or because it would be irresponsible to take samples for the purpose of investigation.

H. Piening (✉)
Bavarian Palace Administration, Laboratory for Archaeometry, Munich, Germany
e-mail: heinrich.piening@bsv.bayern.de

To identify pigments and other colorants used for that polychromy, non-destructive methods of analysis should be applied. However, because of the way that the equipment is constructed, methods such as X-ray fluorescence analysis or Raman spectroscopy can be used only to a very limited extent at the location of the work of art and do not produce usable results for every kind of colorant. Mobile UV-VIS absorption spectrometry offers an alternative.

In the field of analyzing colorants used on works of art, this method has been employed for almost twenty years to identify historic colorants in book illuminations [1]. For over ten years it has been used by the Bayerische Schlösserverwaltung (Bavarian Palace Administration) to identify colorants in every context (paintings, wall paintings, textile dyes, wood stains and polychrome wood).

UV-VIS absorption spectrometry is a purely physical procedure in which white (polychromatic) light is directed onto the area to be examined. The size of the area from which readings are taken is 1.5 mm². Part of the light is absorbed by the surface, the rest is reflected. The reflected part of the light exhibits different characteristics for each colouring agent. The method makes use of the extended wavelength region [2] between 300 and 1100 nm, since almost all colorants are optically active within this region. Specific interactions take place between electromagnetic radiation and the physical and chemical structure of the colorant [3]. The interactions are multi-layered and produce unambiguous characteristic spectra. These "optical fingerprints" can be compared using mathematical criteria, though a mathematical similarity is not necessarily to be equated with a spectral similarity [4]. The important thing here is to have sufficient verified material for comparison.

Application

In practice, a high-resolution diode array spectrometer is used. The light source (halogen bulb or high-pressure xenon lamp) provides the necessary excitation energy, which is directed onto the surface under examination by a fibre-optic light guide. The reflected light also passes to the spectrometer by means of a light guide. The diode row of the spectrometer delivers the information received to the measurement computer (Fig. 1). To measure the absorptions of a colorant, a reference spectrum of the light source is stored using a white reflectance standard (Spectralon™). The spectrum is represented as the relationship between the wavelength (x-axis) and the dimensionless intensity (y-axis).

The colorants are identified by matching the measured spectrum against verified data in existing data libraries. These data libraries are not on the market and were developed by the author. More than 6000 spectres of identified material in different contexts are helpful for the identification of unknown material. By means of appropriate search algorithms mathematical similarities are identified and presented in a hit list which is then verified by the analyst. The analyst decides on the basis of experience what further procedures should be undertaken.
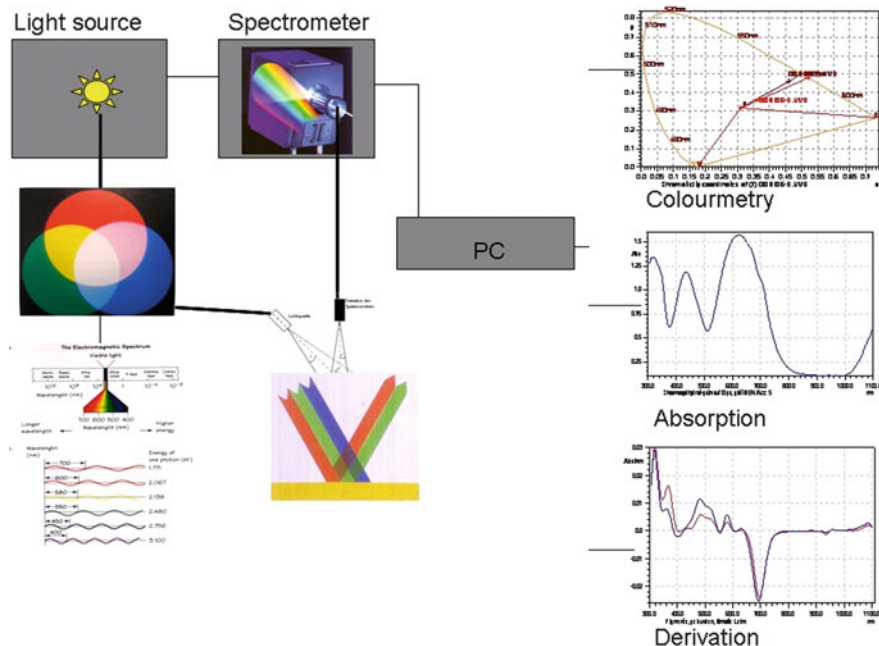
Fig. 1 Schematic representation of the measuring system. The white light source has a broad spectral range for the excitation. The light is directed to the examination area and a part of the light is absorbed. The reflected light is split in the spectrometer. The presentation of the data varies according to the intended use

By mathematical processing the spectra mixtures of colours can be recognized. Here the first derivative helps in the recognition of mixtures of colorants, since each component produces separate inflexion points in the spectrum [5]. In addition, colorimetric data can be generated from a measurement. They do provide information about the colour impression of the colorant. The chromaticity system (CIE 1931, X, Y, Z) [6] and the dominant wavelength are of assistance in arriving at a conclusion.

Procedural Method as Applied to the Object

At the location, the spectrometer is calibrated to the standards. Depending on the conditions of the surroundings, the measurements are usually taken with a hand-held light guide using a measuring angle of approximately 45° to 0°. +/− 15° will not affect the quality of the spectrum. For the measurements a measuring duration is 30–150 ms, and a mean spectrum based on at least five ore more measurements is automatically calculated and stored.

Results: The Colorants of the "Alexander-Sarcophagus" in Istanbul

During the last five years, more than 60 ancient objects of art were examined and over 3000 scans were taken. More than 80 % of the data were interpreted up to now. These results give an essential overview of the used colorants and fundamental information for a scientific reconstruction. The results of the coproduction of scientific findings and analytical based reconstruction are shown at the travelling exhibition "Gods in Colour" and the latest results were just published by Vinzenz Brinkmann, Oliver Primavesi and Max Hollein [7].

The Alexander-Sarcophagus at the Archaeological Museum of Istanbul is definitely one of the most impressive relics of antique sculptures. The sarcophagus was excavated in 1887 at the royal necropolis of Sidon. The marble sarcophagus was made c. 320 B.C. for king Abdalonymos, a friend of Alexander the Great. Being in an excellent state of preservation, it still gives an impressive idea of its former magnificence. The polychrome paint work which survives in many places forms an important part of the sarcophagus' appearance.

In February 2006, official permission was granted to examine the sarcophagus and to take photogrammetric measurements. To identify the colorants, UV-VIS-absorption spectrometry was used [8] (Fig 2). Based on the examination of the sarcophagus in situ and the evaluation of the results, some particularities could be observed:

The colorants were chosen very carefully, thus emphasizing certain parts of the sculptural work. There are several details which were partly sculptured and partly painted onto the surface. To accentuate lower laying areas of the relief, outlines of the same colour were used. These lines were applied first thus enhancing the depth of colour and the three-dimensional appearance of the sculptural work. They were probably not applied by the painter as they would have enhanced rather than covered traces of the stone working.

The painting was executed with great delicacy and subtlety, as can be seen on eyes, bridles, armour and clothes. Since mixtures of pigments could not be detected so far we can assume that the colorants were used unmixed. The pigments are very clean, without residues of minerals which generally are often found after grinding minerals. This indicates a high technological standard of pigment preparation in the ancient world. Different colours were placed side by side, only rarely on top of each other. In fact, outlines and shadows were detailed by using various and finely graded nuances of the same pigment. The remains of paint appear dense and poorly bound. Unfortunately the identification of the binding media was not possible up to now as it would require material samples.

Two blue pigments were detected, which only differ slightly in their visual appearance. One pigment is Egyptian blue (Fig 3, a), a synthetic calcium-copper-silicate, produced and used in Egypt since antiquity. The second pigment can not be clearly identified. There are indications, however, that the pigment could be smalt, a finely ground cobalt glass. The red part of the colour palette is represented by the colorants minium, pure red iron oxide pigments, red ochre in different variants and

Fig. 2 Taking measurements at the Alexander-sarcophagus, Archaeological Museum Istanbul

a

b

Alexander-Sa.Langseite 8 Pferd Auge blau
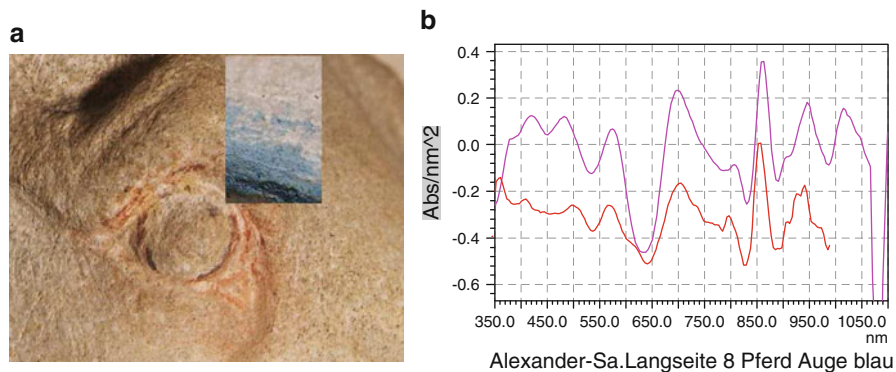
Fig. 3 (**a**) Right eye of the horse of Alexander the Great, detail of the measuring point. (**b**) Spectrum of blue part of the horse eye, —— Egyptian blue, data library, Piening, 2nd derivation

madder lake. The bright iron oxide red and the madder lake are of particular importance in this case. Madder lake is produced by a chemical reaction of an extract of madder roots (*Rubia tinctorum* L., *Rubia peregrina* L.) - which is used for dyeing textiles – and alum (potassium-aluminium-sulphate). Depending of the preparation of the plant extract, the colours vary between reddish brown and bright red or even pink. Different types of yellow ochre could be identified. These colours show nuances between almost white yellow and gold or red ochre. Ochre pigments can be differentiated according to their source and quality of preparation. Two different

a

b

Subtracted Data: SCHLA92.paw, violet ./.marble
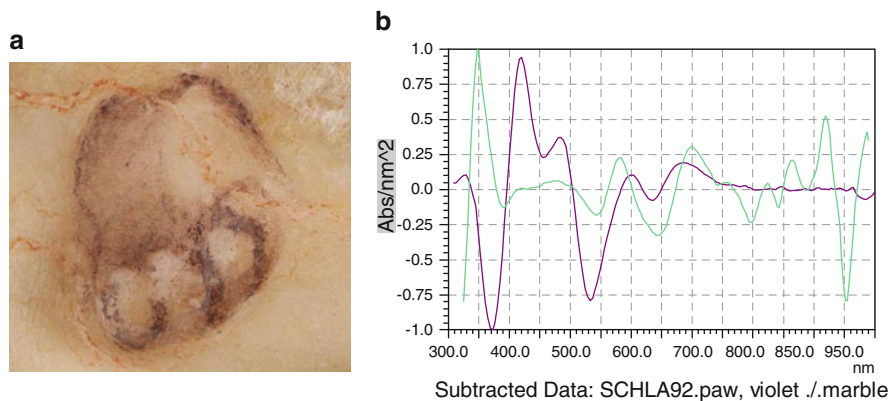
Fig. 4 Painted paw of the saddle cloth, horse of Alexander the Great *Fig. 4a:*— Spectrum of painted paw; — purple of Tyros (6`6 Dibromindigo), collection Schweppe, data library Piening, 2nd derivation

types of green pigments were used. One variant seems to be a green umbra, an iron-manganese pigment. An intensive bluish green can be identified as Egyptian green. Egyptian green was produced in a similar process to Egyptian blue. The violet colorants are quite surprising. One type of violet is a colour-intensive hematite. A second violet variant can be identified as madder lake. The third colorant is an organic dyestuff, which has a strong similarity to antique purple (!). This dyestuff was used very sparingly on the Alexander sarcophagus and only on military insignia (Fig 4, a). This corresponds to the army tradition of purple military insignia, either dyed or painted onto armour.

The colorants identified so far demonstrate the very high technological standard of preparing pigments and dyestuffs, and also the skills of the painters. The results obtained lead to a better understanding of antique polychrome sculpture. It would also allow a close reconstruction of the lost splendour. The data collected from the "Alexander-sarcophagus" are not yet completely evaluated. However, interesting results are to be expected, especially if compared to findings concerning other antique sculptures.

Conclusions

UV-VIS absorption spectrometry is a calorimetrical method which can reliably be used for field research. The different kinds of substrates do not affect the results significantly. Nearly 90% of pigments and dyes used on art objects can be identified with this non-destructive method by using intelligent analytical software and a comprehensive data base.

References

[1] Fuchs, Robert. (1990), Oltrogge, Doris: Das Auge des Restaurators und das Auge des Naturwissenschaftlers. Zeitschrift für Kunsttechnologie und Konservierung. 4.1 1990, pp. 90–106.

[2] The region of the spectrum visible to the human eye is that between 380 und 780 nm.

[3] Nassau, K. (1998) The fifteen causes of colour, in: Colour for Science, Art and Technology, Amsterdam, Lausanne, New York 1998, pp.123–168.

[4] Piening, Heinrich (2007): Mobile UV-VIS-Absorptionsspektroskopie- Einsatzmöglichkeiten zur zerstörungsfreien Materialanalytik in der Konservierung und Restaurierung von Kunst und Kulturgut, Dresden 2007, p. 68 ff.

[5] Ebel, Siegfried (1995):. Algorithmen zum direkten Spektrenvergleich, in: Würzburger Skripte zur Ananlytik, Validierung spektrometrische Analyseverfahren, Würzburg 1995, p. 34.

[6] Fischer, Ernst Peter; Silvestri, Narciso; Stromer, Klaus (1998): Farbsysteme in Kunst und Wissenschaft, Cologne 1998, pp. 121–125.

[7] Brinkmann, Vinzenz; Primavesi, Oliver; Hollein, Max (Ed.) (2010): Circumlitio – The Polychromy of the Antique and Mediaeval Sculpture, Frankfurt a.M. 2010

[8] UV-VIS-Spectrometer TIDAS T-Spec 3, J&M Analytik AG, Essingen, Germany

Structural Monitoring and Investigation Campaign in the Church of St. Giuseppe dei Minimi in L'Aquila, After the 6th of April 2009 Earthquake

F. Casarin, M. Dalla Benetta, C. Modena, F. da Porto, M.R. Valluzzi, L. Cantini, C. Tedeschi and P. Condoleo

Abstract The oratory of St. Giuseppe dei Minimi in L'Aquila, Italy, sustained serious damage after the seismic events of April 2009. The earthquake caused out-of-plane overturning of the façade, with wide cracks on both lateral walls. Such rotation caused the "sinking" in the crack of one of the pillars of the belfry, which did not collapse, but remained in a very dangerous situation. After the initial stabilisation measures, carried out during the months following the seismic event, field investigations were carried out by the authors in spring-summer 2010, to guide the final strengthening intervention, supervised by the Italian Ministry of Culture. The investigation campaign involved intensive use of non and minor destructive techniques, such as thermography, radar, sonic tests, core sampling, single and double flat jack tests and chemical analysis on sampled materials. Moreover, the overall dynamic characteristics of the church were extracted from vibrations measured in the upper areas of the building, using output only techniques. Finally, a structural monitoring system was installed in the church (involving also the adjacent St. Biagio church), to monitor the damage progression and to evaluate the effectiveness of strengthening applications.

Keywords Cultural heritage buildings • Earthquake • Masonry • NDT • Structural monitoring

F. Casarin (✉) • M.D. Benetta • C. Modena • F. da Porto • M.R. Valluzzi
Department of Structural and Transportation Eng., University of Padua, Italy
e-mail: casarin@dic.unipd.it

L. Cantini • C. Tedeschi • P. Condoleo
Department of Structural Engineering, Polytechnic of Milan, Italy

Background

The oratory of St. Giuseppe dei Minimi in L'Aquila, Italy, reported serious damage, as many other churches of the city, after the seismic events of the April 2009, although the overall performance of the church was quite satisfactory as it survived the earthquake (magnitude 5.8 on the Richter scale). The first construction of the oratory dates back to 1646, when a part of the previous St. Biagio church was given to the brotherhood of the Suffragio, which decided to build a new, small church, however maintaining some features of the ancient one, such as the two lancet windows and the thirteenth century portal in the facade on via Roio. The church was opened in 1649, but construction works continued up to 1701. After only 2 years, the earthquake of 1703 induced severe damage on the church. Finally, in 1770 the building was sold to the brotherhood of S. Giuseppe dei Minimi.

Reported damage pattern

The façade of the oratory of St. Giuseppe dei Minimi was subjected, due to the seismic forces, to an overturning mechanism towards the outside, as indicated by the wide cracks on the two side walls, close to the corners (Fig. 1). Quite likely, the presence in the S-W corner of the overhanging belfry structure worsened the situation, since a massive pillar of the belfry acted as a wedge for the crack below. Few other damage mechanisms were detected, such as shear damage in the façade and in the back wall of the apse.

Fig. 1 Wide cracks on both sides of the façade, indicating the detachment of this last from the rest of the building

Field Investigations

After the initial comprehension of the dynamics which led to the observed damage pattern (e.g. by using the kinematic mechanisms approach based on limit analysis), the investigation campaign started, involving a wide use of non and minor destructive techniques, such as thermography, radar, sonic tests, to identify the masonry texture and to evaluate its homogeneity, at different depths, core drilling tests, to detect the inner composition of the walls, single and double flat jack tests to estimate the local state of stress and the stress-strain behaviour of selected masonry elements, and laboratory analysis on sampled materials. Moreover, the overall dynamic characteristics of the church were detected by using output only techniques (ambient vibrations), measuring the vibrations in the upper areas of the building. Tests were applied to the vertical load bearing elements (pillars, walls), in order to proceed with consistent bases in the following structural assessment phase, and finally strengthening and conservation design.

Tests application and results

Results emerged from the tests applied on the structures of the St. Giuseppe dei Minimi oratory proposed useful information on the constituting masonry typology, analyzed both via non destructive and minor destructive techniques. The layout of the applied techniques is reported in Fig. 2.

Sonic tests [1] – diffusedly applied on the perimeter walls of the building, and in one of the four irregular cross section massive pillars sustaining the vault of the central hall of the oratory – gave qualitative/quantitative information on the characteristics of the resisting masonry elements. From the analysis of results, it emerged the possible presence of internal voids and/or irregularities in positions SO5, a remarkable masonry heterogeneity in positions SO1, SO3 and SO4, and a fairly good masonry "composition" in position SO2 (Figure 3). From the sonic tests carried out, an overall average sonic velocity value of about 1010 m/s emerged, on 164 analyzed sonic paths.

Termography [2] was applied to the apse and side walls, showing different masonry arrangements: in general the masonry typology corresponds to irregularly shaped stone blocks disposed in fairly regular horizontal courses. Pilasters are on the contrary composed by a more regular masonry typology, namely squared stone blocks alternated with regular layers of brickwork masonry.

Radar tests [3] confirmed what emerged with the other testing methodologies, and by direct visual inspection (core samples extraction and video endoscope): inner composition in relatively irregular stone masonry, sometimes brickwork masonry facing, "solid" composition throughout the thickness (absence of loose infill).
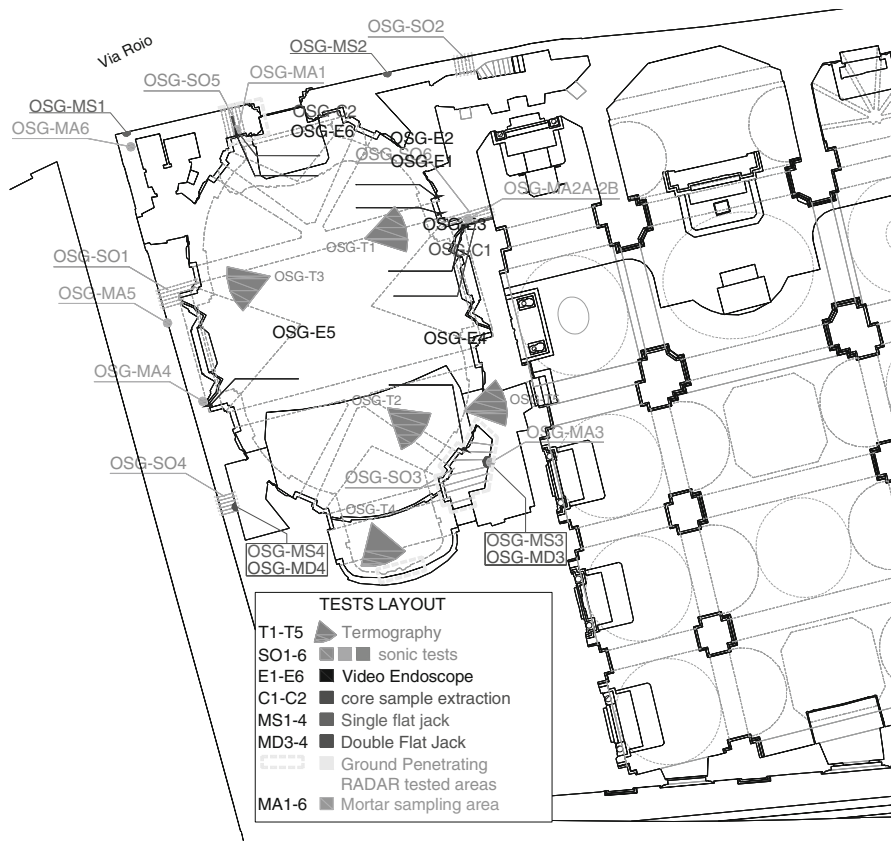
Fig. 2 Tests layout, experimental activities
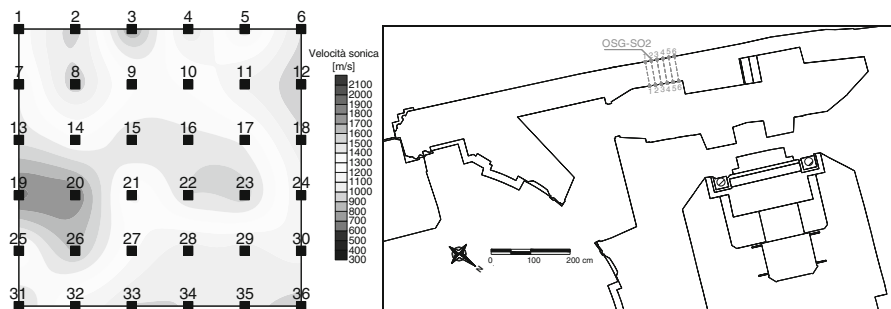
Fig. 3 Sonic test results representation: velocity values mapping, test OSG SO2
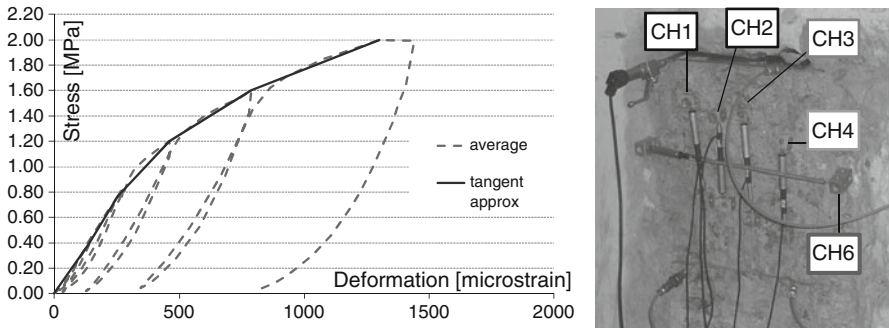
Fig. 4 Double Flat Jack – stress-strain relationship, average values on the vertical displacement transducers, test OSG MD3
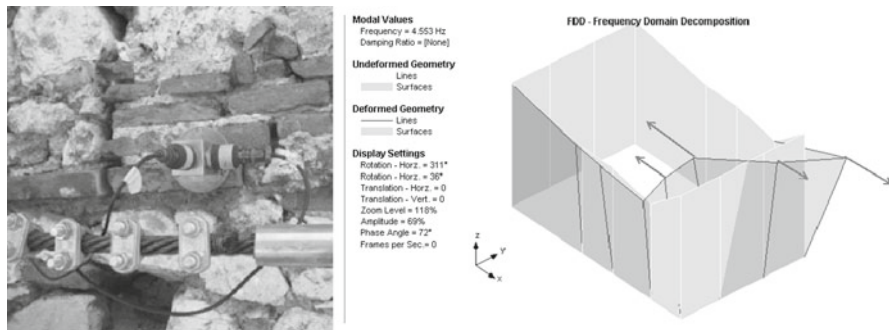
Fig. 5 Dynamic identification tests: acceleration transducers and mode shapes

Although demonstrated a certain presence of irregularities in the masonry composition through ND methodologies, flat jack tests [4,5] indicated fairly good mechanical characteristics of masonry, since medium-high compressive stress values were attained still masonry stiffness being not substantially decreased (Fig. 4). During test MD3, Young's modulus values were approximately between 3000 N/mm² (stress range 0,00-1,00 N/mm²) and 1000 N/mm² (stress range 1,00-2,00 N/mm²), while they were quite constant around 2000 N/mm² throughout test MD4 (max attained stress value equal to 1,50 N/mm²).

It also emerged a very high stress concentration at the base of the façade (as expected because of the remarkable out of plumb), especially in the S-East corner, where values of local compressive stress of 4,5 N/mm² were measured.

The dynamic behavior of the building was finally assessed via operational modal analysis procedures [6]. Six mode shapes clearly emerged (two in transverse direction and four related to the behavior of the façade, Fig. 5). The aim of the dynamic identification was to define the global dynamic response of the building in the
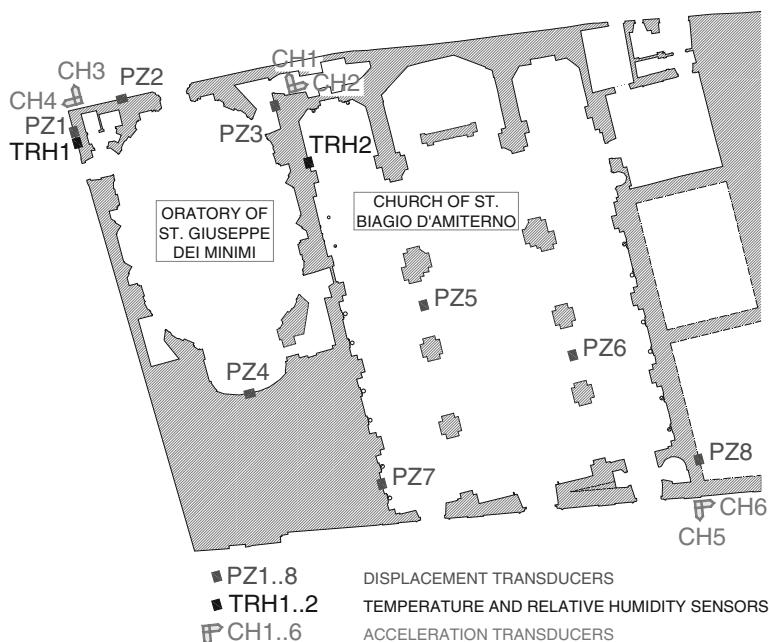
Fig. 6 Static and dynamic monitoring system layout

present-day or "damaged" state, in order both to calibrate reference behavioral models and to appraise the effects induced by the strengthening intervention which should start in spring-summer 2011. In fact, a dynamic and static monitoring system installed in the church in November 2010 (involving also the adjacent St. Biagio church), is continuously assessing the conditions of the buildings by evaluating static and dynamic parameters (cracks monitored via displacement transducers, vibrations via accelerometers, Fig. 6), and this will propose interesting information on the progression or stability of the assessed damage pattern, with reference to the already carried out stabilisation actions (e.g. hooping of the façade) and the foreseen strengthening interventions.

Conclusions

The investigation techniques applied on the oratory aimed at the attainment of a higher degree of knowledge about the structure and its constitutive elements, in order to proceed with the seismic evaluation of the building and the strengthening application in a more informed fashion. Minor destructive tests, quantitatively determined the masonry mechanical properties used for the successive structural analysis, and were complemented by other non-destructive tests

describing in a qualitative/quantitative manner the characteristics of individual structural elements.

Monitoring is being more and more considered, in conservation of cultural heritage buildings, as a key activity in order to increase the knowledge on the structural behaviour of monuments and therefore to have a deeper insight into their structural condition that allows optimization of the strengthening intervention, if needed, and prevention of intrusive repair works unless justified through quantitative evaluation [7,8].

References

[1] RILEM Recommendation TC 127-MS (1996). *MS.D.1 Measurement of mechanical pulse velocity for masonry*, (published in Materials and Structures, Vol. 29, October 1996 pp. 463–466).

[2] Maldague, X. (2001). 'Infrared technology for non-destructive testing', John Wiley and Sons, Inc. (Ed.), ISBN 0-471-18190-0.

[3] ASTM D6432-99 (2005). Standard guide for using the surface ground penetrating radar method for subsurface investigation

[4] RILEM Recommendation MDT.D.4 (2004). *In-situ stress tests based on the flat-jack*, (published in Materials and Structures, Vol. 37, N. 7, 491–496, DOI: 10.1007/BF02481588).

[5] RILEM Recommendation MDT.D.5 (2004). *In-situ stress-strain behaviour tests based on the flat-jack*, (published in Materials and Structures, Vol. 37, N. 7, 497–5001, DOI: 10.1007/BF02481589).

[6] Brincker, R., Zhang, L., and Andersen P. (2000). *Modal Identification from Ambient Responses using Frequency Domain Decomposition*. Proceedings 18th International Modal Analysis Conference, San Antonio, TX

[7] Casarin F., Valluzzi M.R., da Porto F., Modena C. (2008). *Structural monitoring for the evaluation of the dynamic response of historical monuments*, SACoMaTiS 2008, eds. L. Binda, M. di Prisco, R. Felicetti, ISBN 978-2-35158-061-5, p. 787–796, Publisher RILEM Publications SARL

[8] *Guidelines for evaluation and mitigation of seismic risk to cultural heritage with reference to technical constructions regulation* (2006). Ministry for Cultural Heritage and Activities, General Direction of Architectural Heritage and Landscape – Dept. of Civil Protection Agency (Italy)

Investigation Methodology Applied to the Structure of the Church of St. Biagio in L'Aquila

L. Cantini, P. Condoleo, S. Munda, C. Tedeschi, C. Tiraboschi, F. Casarin, E. Simonato and L. Binda

Abstract After the earthquake that stroke the city of L'Aquila during the night of April 6th 2009, many historical buildings at the city centre were severly damaged. Nevertheless many others survived the seismic event with only local damages, showing a good mechanical behaviour against vertical and horizontal actions. In order to continue preserving these buildings, a careful investigation is necessary before applying any repair technique, new or traditional to understand the past design practices for building durable and safe structures. In order to understand the structural behaviour of the church of St. Biagio in L'aquila, an extensive diagnostic investigation based on non-destructive and minor destructive techniques was carried out by the authors. The paper describes mainly the applied methodology which can produce some guidelines to be followed in the future study of other Cultural Heritage (C. H.) buildings hit by the earthquake.

Introduction

The buildings that survived the earthquake, that stroke L'Aquila during the night of April 6th 2009, are the evidence of appropriate construction techniques already known at their location even centuries ago which gave them adequate performance against the effects of time and several earthquakes. Investigation techniques can

---

L. Cantini (✉) • P. Condoleo • S. Munda • C. Tedeschi • C. Tiraboschi • L. Binda
Dept. of Structural Engineering, Politecnico di Milano, Milano, Italy
e-mail: cantini@stru.polimi.it

F. Casarin • E. Simonato
Dept. of Structural and Transportation Engineering, Università degli studi di Padova, Padua, Italy
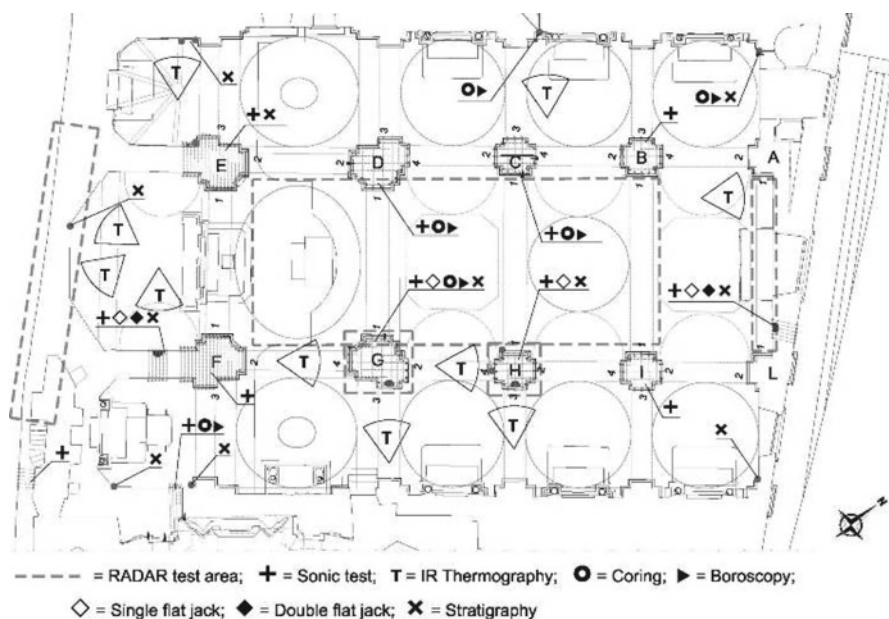
Fig. 1 Localization of the tests carried out in St. Biagio Church

evaluate the characteristics of these buildings revealing their state of conservation. The authors have experienced a diagnostic activity on the ancient church of St. Biagio in the centre of L'Aquila, nearby the Cathedral. The church main damage was the collapse of the tympanum on top of the facade; other damages concerned part of the central nave timber vault, the shallow domes of the lateral naves and some cracking of the pillars and of the apses. The rest of the structures resisted to the earthquake: in fact the central and lateral naves, the apses with their vaults and the roof are still standing. The survival of this building under the seismic actions demonstrates that traditional buildings can stand heavy events according to the mechanical characteristics of their structures.

In order to identify and understand the behaviour of the building system of the church of St. Biagio, an extensive diagnostic investigation based on non-destructive and minor destructive techniques (Fig. 1) was applied [1]. The paper describes mainly the applied methodology together with a short report on the numerous results for lack of space.

Methodology of Investigation for the Assessment of Structural Damages

Performing a contained amount of non destructive tests, extended just to the most significant areas of the load bearing walls of the church, the authors provided the basic information to develop the final conservation design of the church.

This methodology is based on four level of knowledge: i) study of the historical evolution of the building structure from the origin to today, ii) interpretation of the damage mechanisms occurred to the different structural elements by surveying the crack pattern present on masonry walls, vaults and timber structures; iii) detection of the morphology of the different masonry sections, by performing thermographic, radar and sonic tests, and core drilling tests; iv) measure of the state of stress and of the mechanical characteristics of the load bearing walls, applying single flat jack tests, and double flat jack tests; v) chemical analysis on mortars. This paper provides the description of the techniques used to qualify the structure of the Church of St. Biagio, their potentialities and their limits, the problem solved by each ND technique or by the complementary use of more ND techniques. The collected data and information were used to carry out a first dynamic analysis of the structure.

The aim of the research was also to implement a methodology useful for the estimation of the damage that must be known to calibrate a design on a building stroke by an earthquake.

Damage Survey and Emergency Actions After the Event

The mostly affected area of St. Biagio was the façade, where the out-of-plane collapse of the upper part, the overall overturning mechanism were noticed (Fig. 2a). A 1980's "strengthening" intervention, consisting in the substitution of the original timber roof with a heavier and stiffer r.c. structure, may have worsened the earthquake effects on masonry elements. Other reported damages are the collapse of portions of the timber vaults of the main nave, cracks in the domes of the aisles, at the base of the pillars due to out of plane actions, and at the keystones of the transverse arches.

Provisional interventions – rapidly carried out after the seismic event by specialized teams of fire brigades – given the low probability of damage progression, considered the moderate reported overall damage level, aimed at the protection

Fig. 2 Collapse of the upper part of the façade (**a**), design (**b**) and realization of the intervention (**c**)

of the church by closing the breach in the wall through the application of a waterproof nylon sheet connected to a wooden beams frame solidly fixed to the church (Fig. 2b, c).

Geometrical and Crack Pattern Survey and Damage Interpretation

Cracks are the evidence of the response of the building provided to contrast the movements produced by the seismic event. Their developments must be studied to interpret the actions that stroke the building. The interpretation of the crack pattern allows one to understand the collapse mechanisms of the structure, as well as the damage in the other parts. Moreover, the crack pattern was visually surveyed to highlight the presence of discontinuities in the different structures. After the survey, the crack pattern was correlated to the mechanisms reported in a template proposed by the Ministry of Cultural Heritage [2].

In the present case, the most relevant seismic action acted in the longitudinal direction of the church, and determined the damage of the walls of the central nave and of the façade. By the several in situ observations, the interpretation of the state of damage of the church allows to recognize also the low transversal intensity of the seismic action, which effects were probably fade out due to the presence of the adjacent buildings, while the longitudinal walls cracks were surveyed next to the arches (Fig. 3), spanning between the pilasters of the lateral naves. This information was correlated to those regarding the historical development of the complex: in the baroque age, the church was rebuilt and restyled. The diagnostic tests confirmed the presence of an external brickwork leaf detached from the inner lateral walls by 7 cm (see Fig. 5).
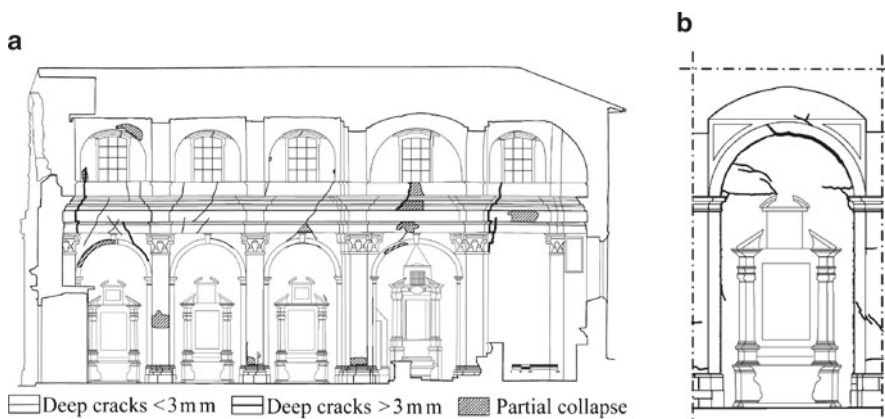
Fig. 3 Section of the central nave (**a**); detail of the cracks of the lateral nave (**b**)

State of Damage and Masonry Quality

An extensive use of non destructive and minor destructive tests was proposed to study in depth some characteristic of the masonry elements church and the extension of their damages.

Thermovision. Active thermographic tests were carried out on the following representative areas: the internal side of the main façade, the apses, and the pillars and the lateral walls. The thermograms revealed the masonry texture of the investigated structures, and permitted to identify hidden structures (such as filled up windows or doors) and discontinuities. Thermography provided also information to verify the historical evolution of the church: the presence of heterogenic masonry textures and various materials (stones bricks) indicated structures belonging to different ages and different ways to conceive the building technique to apply.

Direct sonic tests. The velocity of propagation of sonic waves is strongly influenced by the density and the connections between the elements forming the structures. The results indicated that pillars which do not present an extended crack pattern are characterized by high velocities, while the pillars with a large concentration of cracks present much lower velocities. Sonic velocity is a parameter that provides a first indication to identify the damaged areas on which the investigation campaign can be developed.

RADAR tests. GPR tests were performed on masonry structures to identify the morphology of the section of walls and pillars. The method is based on the dielectric properties of the materials and this property is strongly influenced by the moisture content. Therefore Radar tests provided indications concerning the areas affected by this problem. Moreover, an extended application was carried out on the floor of the central nave to detect the presence of ancient structures and the foundations under the pillars.

Inspections. Supported by the results coming from the previously mentioned techniques, the positions of boroscopy and videoboroscopy tests were set on specific areas of walls, parasters and pillars, in order to verify the presence of irregularities and the stratigraphy of the structures (see Fig. 4a). Inspections were carried out in
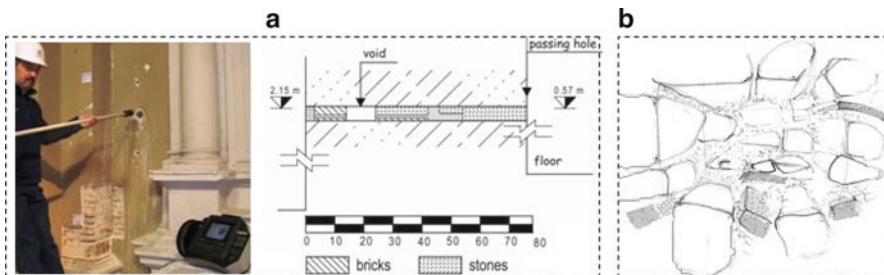
Fig. 4 Interpretation of video-boroscopy (**a**) and inspection of the section (**b**)

order to verify the information coming from other non destructive techniques: providing qualitative results, these techniques can present some uncertainties for the interpretation of their data. Placing limited inspections in the supposed most representative areas of the investigated structures, a final control of the efficiency of the applied techniques is available. Figure 4b shows an inspection revealing the presence of stone block and bricks in the same texture, as suggested by the thermographic tests performed before.

Single and double flat jack. The local values of the compressive stress and stress-strain behaviour in strategic points were provided respectively by single flat jack and double flat jack tests. The identification of concentration of stress on walls and pillars and information concerning their deformability are parameters of great importance for the safety design of the building.

Dynamic Analysis and Monitoring. The dynamic behavior of the building was finally assessed via operational modal analysis procedures [3]. Several mode shapes and related frequencies clearly emerged. Interesting results emerged from the data collection also in adjacent buildings, where different frequencies and mode shapes were detected, observation related to hammering and dynamic interactions between structures in aggregate.

Conclusion

The methodology developed by the authors [1] through many years of experience was applied to the St. Biagio church with success. The high number of inspections and ND tests carried out on site was useful to suggest the designers a careful intervention respectful of the building authenticity. The developed methodology paved the way for use of some NDT as sonic tests and thermography in similar future investigations.

Due to lack of space it is impossible to detail the complementary use of NDTs and MDTs. Nevertheless some general comments are possible:

– geometrical and crack pattern survey allowed to outline the mechanism of damage and to interpret them for the structural analysis and for emergency actions;
– the complementary of NDTs and MDTs allowed to: survey the masonry texture and sections (thermovision, radar, sampling and coring), the masonry quality (sonic, flat jack, radar, sampling and material characterization) in detail.

References

[1] Binda, L., and Maierhofer, C. (2007), "On site assessment of historic masonry structures", In: *Masonry International Journal of British Society*, vol. 20, N. 3, pp. 91–150.

[2] Ordinanza P.C.M. 3431/2005, "Modello per la valutazione della vulnerabilità sismica delle chiese", Annex C, In: *Linee guida per l'applicazione al patrimonio culturale della normativa tecnica di cui all'Ordinanza P.C.M. 3274/2003*, Department of Civil Protection and Ministry of Cultural Heritage, 2005.

[3] Brincker, R., Zhang, L., and Andersen P. (2000), "Modal Identification from Ambient Responses using Frequency Domain Decomposition", In: *Proceedings 18th International Modal Analysis Conference*, San Antonio, TX.

Use of Thermovision for the Survey of a Timber Vault in Torino

L. Cantini, C. Tedeschi, C. Tiraboschi and L. Binda

Abstract In order to study the building technology of an old 19th century timber vault in the Palace of the Academy of Sciences in Torino, authors performed several diagnostic tests to detect the construction technique and the damages to this structure. The vault has the peculiarity of being a timber structure, made with a specific technology that is not easily visible from intrados and extrados. For this reason the interpretation of its mechanical behaviour must be based on the knowledge of its construction technology. The non destructive technique that provided the most interesting information was IR thermography. This technique provided valuable data about the timbering used to build the shell of the vault and enabled correct execution of other minor destructive tests, such as light sampling and stratigraphic investigation on the painted plaster.

Keywords Building techniques • Detachments • Thermographic test • Timber vault • Stratigraphic investigation

Introduction

The vault of the Academy of Science in Turin (Figs. 1a, b) was damaged by wastewater coming from a broken pipe in the fire protection system [1]. As a result, staining on the stucco-work of the intrados of the vault appeared. After the removal of the damaged water pipe, the vault had to be repaired. In order to determine the extent of the damage, the authors were asked to detect the presence of water and the consequent damages to the structure using non destructive tests in order to avoid spoiling the painted vault. The vault had the peculiarity to be a timber structure [2], made by a specific technology that is not easily visible from intrados and extrados.

L. Cantini (✉) • C. Tedeschi • C. Tiraboschi • L. Binda
Dept. of Structural Engineering, Politecnico di Milano, Milano, Italy
e-mail: cantini@stru.polimi.it

Fig. 1 View of the Assembly Room (**a**); digital straightening image of the intrados of the vault (courtesy of professor M. Chiorino from Politecnico di Torino) (**b**); execution of the test by the IR camera on the intrados of the vault (**c**)

For this reason the interpretation of its mechanical behaviour must be based on the knowledge of its construction technology. The non-destructive technique that provided the most interesting information was IR thermography (Fig. 1c).

IR thermography is a non destructive technique that can provide a characterization of the superficial layers of a construction element without a direct contact between the testing device and the observed area. The technique is based on the recording of the superficial distribution of temperatures by a thermographic camera that is designed to observe the infrared radiation emitted from materials. In this case, authors explored using passive and active thermography, and obtained significant results that helped to characterize the position of the wooden elements forming the structure. Active thermography was useful to detect the presence of detachments between the rendering and the real structure and even to evaluate the crack pattern present on the intrados of the vault. The results could be interpreted also with the use of light sampling and stratigraphic investigation on the painted plaster. This research represents an opportunity to calibrate the potentiality of the thermographic test in characterizing a typology of an original timber vault.

Field Tests

The activities of the authors, for the study of the vault of the Assembly Room, were part of a larger investigation campaign coordinated by members of the Academy of Science and the designer responsible for the safety project of the vault. Different research teams took care of various aspects concerning the vault: the geometric characteristics of its structure; the state of conservation of the wooden elements; the structural safety of the timber system; the damages of the stucco-work covering the intrados; the control of the mechanical behaviour of the vault by finite element model.

The authors studied in depth the features of the structure of the vault. A complementary use of different diagnostic techniques was proposed: thermovision, to identify the elements forming the timber vaults and to detect damages; stratigraphic survey, to study the layers of the plaster on the intrados of the vault; boroscopy, to observe the section in the timber vault; dynamic tests, to determine the tensile stress in tie-rods elements. Timber experts were in the meantime detecting the state of conservation of the timber elements. Thermovision was supposed to be a promising application in order to detect the correct position of the wooden frame composing the shell of the structure. The knowledge of the lay-out of each frame was necessary to perform, in the most significant position, minor destructive tests on the structure: boroscopy to detect the depth of the section and stratigraphic analysis to observe the different layers applied on the wooden shell of the vault in order to identify the technology used to connect the different elements.

Thermography was carried out by an IR camera, Avio TVS 500E model, 320x240 Dpi, Vanadium Oxide microbolometer sensor type. When active thermography was applied, the heating system consisted of an infrared lamp, with a heat output of about 1.5 kW. For the detection of the presence of detached areas of the stuccowork, it was thought to use active IR thermography. After heating the surface of the intrados for about 40 minutes by the IR lamp, detached parts should provide a higher distribution of temperatures due to the presence of air between the detached layers of plaster and the support [3, 4]. For the same reason, even the presence of passing through cracks should result more evident if air can penetrate deep in the section of the vault. Finally, for the identification of the structural elements of the wooden frame, passive thermography was supposed to work correctly: performing the tests at the end of April, it was possible to work in a very good condition in order to have two different thermal gradients at the extrados and at the intrados of the vault [5, 6]. This condition permitted to observe by the IR camera a consistent increasing of the temperature emitted from the surfaces of the vault during the day. Thank to the different thermal conductivity and heating capacity of the materials forming the vault, each single element was clearly recognizable by a specific range of temperatures.

Detection of the Construction Technique

The study of the building system of the timber vault was requested in order to identify the elements that compose the structure. The technology of this architectonic typology is not very well known, due to the fact that the construction methodology was influenced by local building traditions: for this reason each timber vault presents peculiar characteristics. Generic interpretation of its properties are available in manuals describing traditional buildings techniques (see Fig. 2a), but specific details of the frame can be realized following different models and rules.

The geometry of the vault of the Assembly Room presents a pavilion shape, with a very low profile forming a flat central area. The structure is leaning on masonry walls on three sides, while it is supported by a coated timber beam on the fourth side
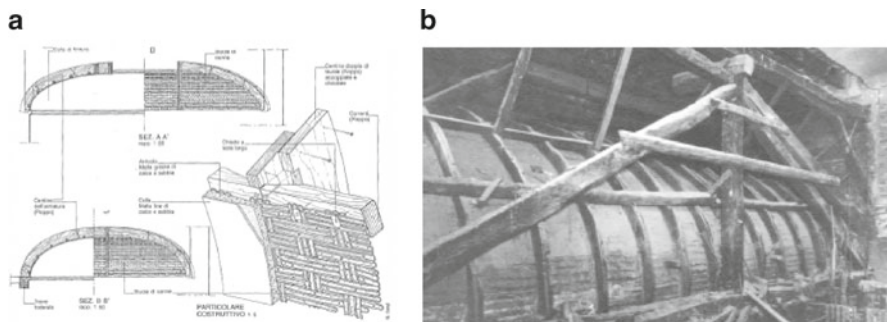
Fig. 2 Detail of the representation of a wooden vault (**a**) (taken from "Manuale del recupero del comune di Città di Castello", p.101, DEI, Roma, 2003); view of the extrados of the vault of the Assembly Room of the Academy of Science (**b**)
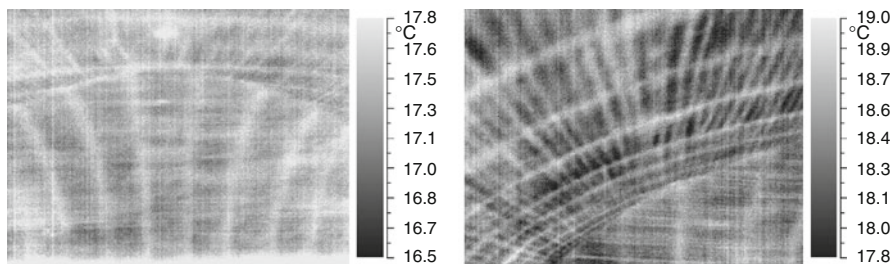
Fig. 3 Two thermograms of the intrados of the vault showing the timbering

(Fig. 2b). The curved shell is built up by a series of ribs made by simple poplar planks, coupled by split-level joints and hobnailed. On the lower part of the ribs, wooden strips are inserted. In many cases, as suggested by several technical manuals [7, 8], a mat formed by plaited canes used to be fixed to the timbering. This caning could be covered by a layer of plaster, in order to protect the wooden elements from pests. The caning itself could be present on both sides of the timbering. In this case a short layer of caning was visible only at the basement of the extrados of the vault. The rest of the structure at this side showed a sequence of strips alternate to mortar and peaces of bricks, used as filling material between the wooden strips. The intrados of the vault is totally covered by painted plaster and for this reason it was not possible to identify the presence of the caning on this side.

Thermovision was assumed to be the correct technique to study: a) the position of the main timber structures b) the system of the horizontal wooden planks; c) the information concerning the connections between the main elements. Thank to a scaffolding designed to access the intrados of the vault, thermographic tests were carried on observing the whole surface of the structure maintaining a correct perpendicular framing with it. The results (see Fig. 3) showed that caning was not present at this side of the vault, except for an area along the basement. The intrados of
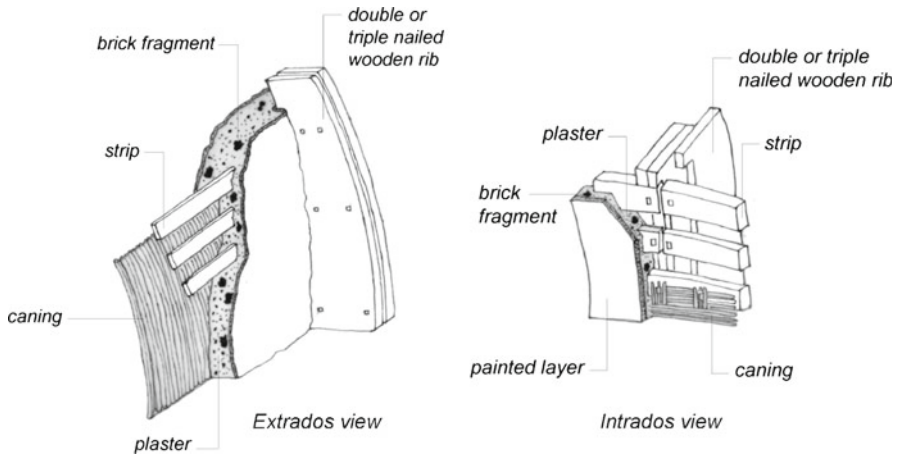
Fig. 4 3D models of the building technology of the timber vault

the vault results to be formed by painted plaster placed on the shell made by the wooden strips and the mortar filling.

As said before, this result was obtained in a very favourable condition, working in a confined environment that accumulated warmth from the extrados side to the opposite one: this transmission of heat from one side to another permitted to recognize very clearly the peculiar temperature that characterized each single element of the vault: wooden strips presented a temperature of about 18.4°C; mortar filling between the strips had a characteristic temperature close to 18.2°C; the presence of the main ribs provided a superficial temperature on the extrados of about 18.7°C. Figure 4 shows two 3D models of the building system of the section of the vault, obtained by the results coming from IR thermovision and other tests.

Interpretation of the Crack Pattern and Detection of Detachments

The vault presents an extended crack pattern that was surveyed trying to classify each crack: usually dangerous cracks cross the whole section of the structure, but in this case the extrados of the vault was not clearly visible in order to verify the presence of cracks with the same development of the one surveyed on the opposite side. Active IR thermography permitted the detection of the passing through cracks indicating the presence of higher temperatures due to the air contained in those passing through cracks (see Fig. 5a). The crack pattern is clearly due to movements of the supporting timber structure which has to be repaired.
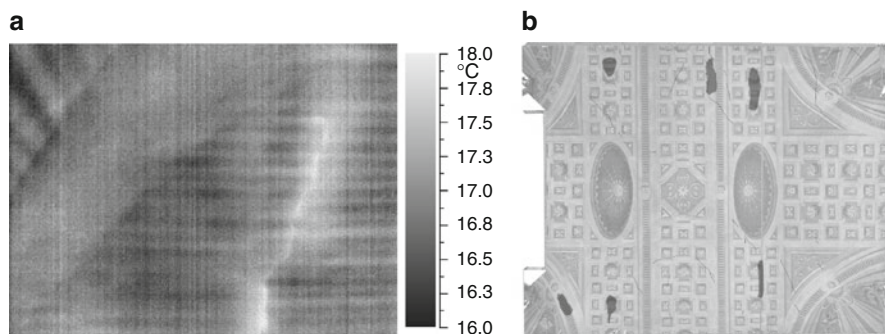
Fig. 5 Thermogram revealing the presence of a passing through crack (**a**) and localization of the detected detachments (**b**)

Conclusions

The results of the survey will be the bases for the definition of the model which is going to be used for the structural analysis of the vault. Its layout could not be based simply on typological classifications coming from manuals, but the peculiar features of the structure had to be studied in depth. IR Thermography supported the tests applied to reach different level of knowledge of the timber vault: the characteristics of the hidden elements forming the frame of the shell completed the information achieved by the geometrical survey; the detection of the crossing cracks drove the designer to a correct interpretation of the crack pattern of the vault; the identification of the detached areas of the stucco-work was useful to define the point of the structure on which other tests to verify the state of conservation of the vault could be performed.

References

[1] Binda, L., Cantini, L. (2010), *Applicazioni di indagini termografiche per lo studio di strutture storiche*, graduation thesis, third year students Cogliati F. A. and Soresi D., Faculty of Architecture, Politecnico di Milano.
[2] A.A.V.V. (1988), *Tra Società e Scienza. 200 anni di storia dell'Accademia delle Scienze di Torino*, Umberto Allemandi & Co (Ed.)., Torino.
[3] Saisi, A., Lualdi, M., Binda L. (2007), *Non-destructive testing techniques applied for diagnostic investigation: Syracuse cathedral in Sicily, Italy*, In: International Journal of Architectural Heritage: Conservation, Analysis and Restauration, n. 4.
[4] Rosina, E., Spodek, J. (2003), *Using infrared thermography to historic wood framed buildings in north America*, APT Bullettin, n. 34.
[6] Arndt, R., Maierhofer, Ch., Rolling, M. (2006), *Quantitative Pulse-Phase Thermography for Masonry and Concrete Structures*, in Proceedings of the 9th European Conference on NDT, Berlin, September 25–29, 2006.
[7] Giovanetti, F. (1993), *Manuale del recupero del comune di Città di Castello*, DEI (ed.), Roma.
[8] Breymann, G. A. (2003), *Archi volte e cupole*, Dedalo Librerie (ed.), Roma.

Wireless Monitoring of Heritage Structures –Selected Case Studies

S.A. Bachmaier and M. Krüger

Abstract Monitoring of cultural heritage structures is an application area for Wireless Sensor Networks (WSNs) which is implemented in the project "Smart Monitoring of Historic Structures (SMooHS)", funded by the European Commission within the 7th Framework Programme. The project aims at the development of a WSN system especially designed for use on real structures to enable smart interpretation of acquired data and comparison of results with those obtained from established laboratory tests in an effort to evaluate the usefulness of the WSN system. While the development of the WSN system is still ongoing by the partners, many sensor types are already supported. This paper presents WSN implementations on the Holy Cross Minster in Schwäbisch Gmünd, Germany, Schönbrunn Castle Chapel in Vienna, Austria, archaic houses in Hebron, Palestine, and Bode Museum in Berlin, Germany. The system design, including hardware and software, sensor types and their characteristics, and their adaptation to the system is described. System setup is described for each case study and results of initial measurements are shown, including smart automatic interpretation mechanisms. An assessment of the wireless monitoring system concludes the paper, stating research needs and future work.

Keywords Case studies • Environmental sensing • Historic buildings • Long-term monitoring • Wireless sensor network

S.A. Bachmaier (✉)
Institute of Construction Materials, University of Stuttgart, Germany
e-mail: sebastian.bachmaier@iwb.uni-stuttgart.de

M. Krüger
Material Testing Institute, University of Stuttgart, Stuttgart, Germany

System Description: Hardware and Software

Need for monitoring cultural heritage structures

The Wireless Sensor Network presented here was designed especially for the application in outdoor environments, while at the same time keeping in mind the demands of historic objects as defined within the SMooHS project [1, 2]. These demands include specific types of sensors derived from the problems tackled most often when dealing with movable and immovable cultural heritage. Weathering processes arise from environmental conditions; hence, it is mandatory to be able to monitor these. Air temperature and air humidity can be measured easily, while wall temperature and wall moisture already conflict with the necessity of the method to be non-destructive. Humidity issues arise either from capillary suction of ground moisture or by condensation of air humidity. To keep track of the air masses that carry the moisture, airflow sensors can be use. Inclination sensors can be used to detect faltering walls even earlier than with other methods. These and many other requirements lead to the WSN as presented in the following.

System development

Base system. The basic functionality common to all sensor nodes, e.g. communication, data processing etc., is integrated into the so-called processor board. This processor board allows the interfacing of different sensor adaptation boards. In addition to the processor board there is a power supply module, capable of powering the sensor node by battery or by alternative concepts. With the implemented Lithium Thionyl Chloride Battery (Li-SOCl2), which has very low nominal self-discharge rate (less than 1%/year), the lifetime of the system could be tens of years if only power consumption is considered.

Sensor adaption boards. Most sensors differ in their way of how to read out data, so for each sensor a sensor adaptation board has to be present in the system, allowing the proprietary sensor interface to communicate with the standardized base system. Fig. 1a) shows small adaptation for the connection of two airflow sensors, while Fig. 1b) shows an electrometer board, which is larger than the tiny standard board layout, however allowing to measure eight channels with extremely high input impedance of up to 1 GΩ. As can be seen for the electrometer, it is also easy to integrate non-standard designs in the system, when required. Currently, four further sensor boards are available: i) a signal conditioning board for interfacing piezo- and PVDF-sensors for acoustic emission and dynamic analysis; ii) a multi-sensor signal conditioning board for strain gauges, displacement transducers and pressure cells in combination with temperature/humidity and vibration measurements; iii) an inclination sensor board; iv) an impedance converter system for electrochemical analysis and impedance spectroscopy.
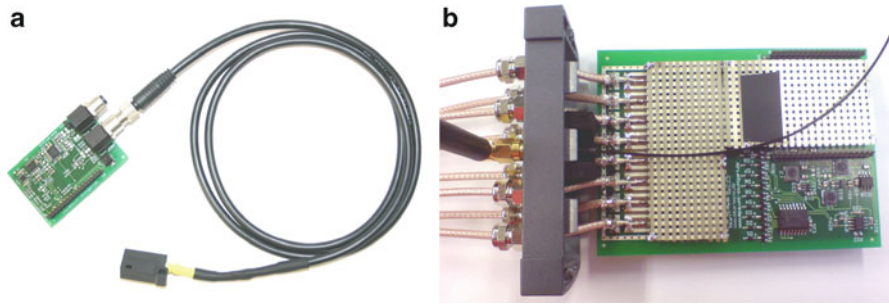
Fig. 1 a) Sensor adaptation board for airflow sensor (also depicted with a small cable for easier mounting) **b**) Sensor adaptation board for electrometer sensor, with an eight-channel multiplexer
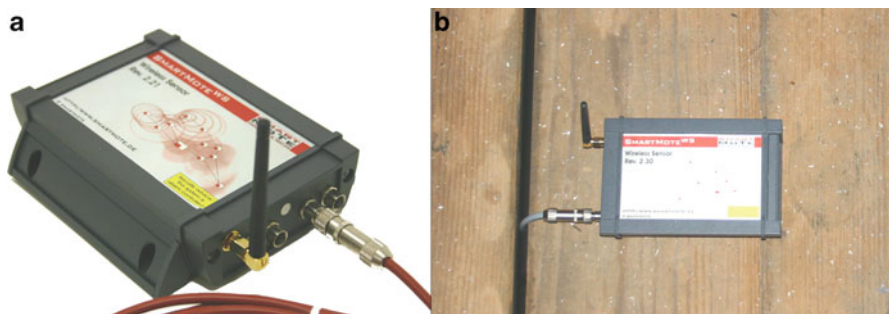
Fig. 2 a) Wireless sensor node, readily assembled. **b**) Wireless sensor node, deployed

Software. The node is operated by customized embedded software that was programmed in-house. Application software resides upon a boot loader that handles communication and provides other base functionality. Software is configurable over-the-air and, when necessary, both boot loader or application software can be updated over-the-air. Transmission is done by a routing-free direct-path communication with acknowledgements. This ensures a reliable communication with minimum energy costs. Drawback is a limited range, and for larger deployments either several base stations are required or a multi-hop protocol has to be used. Application software is specific to the measurement task at hand and can also provide data preprocessing if desired.

Housing. Fig. 2a) depicts a completely assembled and housed wireless node. In this casing, the sensor node is water and dust protected (IP65) and could work in a temperature range of -20 °C – +80 °C. Fig. 2b) shows the same node when it was deployed on a ceiling of church nave, measuring temperature and humidity on two points, one directly at the node and the other about 1 m below the ceiling with an external sensor hanging down through a gap in the wooden planks.

Case Studies on Historic Buildings

Holy Cross Minster, Schwäbisch Gmünd

The Holy Cross Minster is a late gothic hall church built from the 14th to 16th century. The church is richly furnished with sculptures as in the five, partly as polychromy, and many gargoyles and pinnacles. Deterioration of the portals originates mainly from the swellable claybound sandstone, the freezing and thawing cycles, humidity input from above and agitations by door closing. These problems were tackled by installing an electrometer sensor node, measuring the effect of desalination packages that were applied to the salinated parts of the portal. Details of the observations made and related graphs can be found in [4]. Vibrations on the wooden frame on the south portal are monitored by a three-axial accelerometer. See Fig. 3 for an example curve of an event. Events are evaluated for the rate they occur as well as for maximum signal strength and for peak signal frequency. Table 1 shows these statistics for the 2010-09-30.
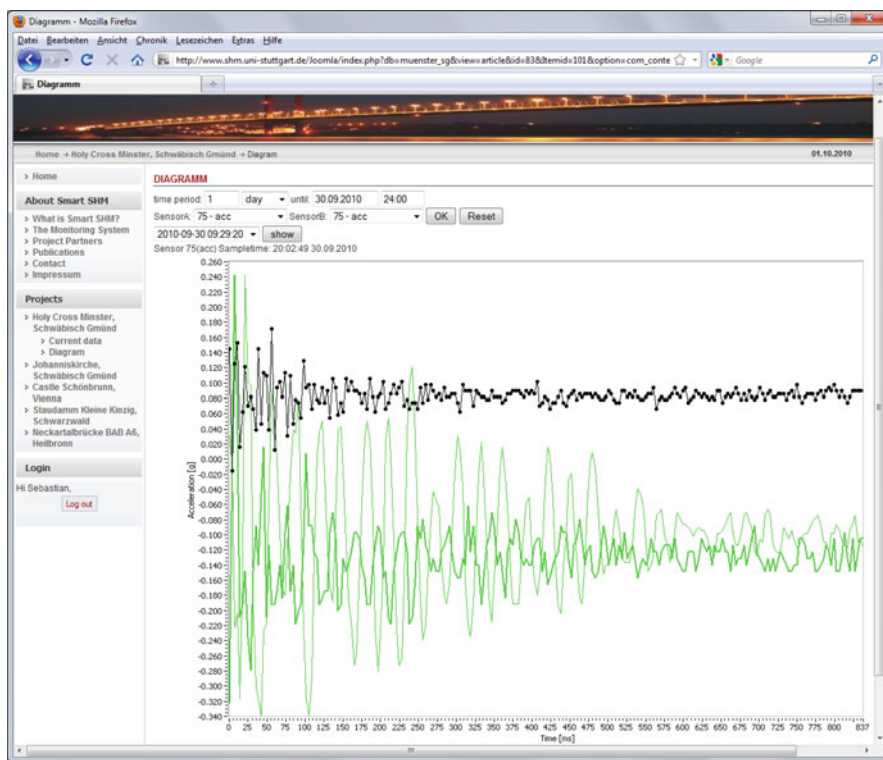
Fig. 3 View of closing door event, wirelessly recorded by acceleration sensor, as presented on the University of Stuttgart SHM website [3]

Table 1 Acceleration statistic on the south choir portal

Events	Max. acceleration (pp)	Mean peak frequency
152	0.8 g	34.3 Hz

Schönbrunn Castle Chapel, Vienna

The Chapel is situated in a northwestern corner of the Castle and in this way exposed to wind and rain, which normally comes from western directions in Austria. Problems arise from the humidity rising in the wall, which attack the marble decorations. Therefore, the actual condition with respect to temperature, airflow, air humidity and wall humidity is monitored in the chapel.

Bode Museum, Berlin

In Bode Museum, Berlin, the list of surveys includes monitoring of air temperature and humidity again, as well as contact temperature of the walls. Additionally, to have a good input for the Computational Fluid Dynamics (CFD) simulation that is performed by the European Academy Bolzano (EURAC), airflow sensors are installed on three passages. With all this input, the indoor climate will be calculated, to see differences between climatized and non-climatized areas of the museum and issues related to that. In addition, light sensors will be installed, that track both visible light and ultra-violet (UV) radiation, which is both considered harmful to pictures and historic objects. With a sufficiently short measurement interval, an energy profile can be erected, that gives the lux·h/year or W·h/year of harmful radiation.

Results and Outlook

The usability of WSN in cultural heritage monitoring is proved by the test cases shown and others that had to be skipped. Data fusion and automatic data interpretation is still work in progress. Raw data can be accessed via the access webpage [3] and is open to everyone for certain test cases. The variety of sensors used in the context of the presented test cases shows the easy integration of sensor types into the existing WSN framework.

With respect to system reliability and security, certain efforts are necessary. While for scalar sensor types, a certain degree of loss rate can be tolerated for time series this is not always tolerable. However, this depends on the exact sensor and the exact demand. Results of the system and radio transmission stability for some test cases that were equipped with the same system can be found at [5]. It was found that

from the theoretical point of view, a simple star topology is supposed to lead to no problems for its simplicity, however, in practical applications problems may arise.

References

[1] Pamplona, M. and Simon, S. (2010). *7th Framework Programme: SMooHS.*, D2.1 Real Problems apparent at cultural heritage and monitoring demands and deficits, Report, p. 9.
[2] SMooHS (2010). http://www.smoohs.eu, date of last access: 2010-10-01
[3] Smart Structural Health Monitoring (2010). http://www.shm.uni-stuttgart.de, date of last access: 2010-10-01
[4] Institute of Construction Materials (2010). http://www.iwb.uni-stuttgart.de, date of last access: 2010-10-01
[5] Bachmaier, S. (2010). In: *Proceedings of Fachgespräch Sensornetze*, A Report on System and Radio Transmission Issues in a Star-Topology WSN, Würzburg

Section 11
NDT Planning, Practice, Reliability, Codes and Standards

Differences in International Strategy for the NDT of Concrete

M.C. Forde

Abstract Clients worldwide face increasing pressure to obtain best value for money from NDT surveys. Yet this gives rise to the dilemma of whether a high quality survey and analysis is being undertaken. ACI 228 Committee provides documentation on the available NDT test methods, but stops short of giving advice on the interpretation of data. RILEM TC Committee on the NDT of Concrete does give advice – but the Committee has a fixed term of operation.

This paper discusses progress towards international standards of NDT of concrete and makes specific comments on differences in international practice. Finally, examples of best international practice in NDT will be highlighted. The American Concrete Institute (ACI) is identified as a leader in translation from research to practice.

Keywords Concrete • Data interpretation • International standards • Methods • NDT • Practice

Introduction

Worldwide there is increasing pressure to obtain best value for money from NDT surveys. Yet this gives rise to the dilemma of whether a high quality survey and analysis is being undertaken. ACI 228 [1] Committee provides documentation on the available NDT test methods, but stops short of giving advice on the interpretation of data. RILEM TC Committee on the NDT of Concrete does give advice – but the Committee has a fixed term of operation.

The aim of most Civil Engineering NDT is to achieve the highest quality of visual imaging of the relevant internal features of a structure. Medical ultrasonics and NMR have provided excellent images and so has aircraft ultrasonic imaging of

M.C. Forde (✉)
University of Edinburgh
e-mail: m.forde@ed.ac.uk

metallic structures. In the Civil Engineering NDT community, concrete has seen more developments than masonry, perhaps because the material is more widely used and there are more problems with aging concrete structures.

Structure of the Industry Internationally

The structure of the civil engineering NDT industry is less mature than that of the aerospace and Medical Industries. One of the reasons that the civil engineering NDT industry is less mature is that civil engineering projects are one off or bespoke and most civil engineering infrastructures perform satisfactorily for the first 30 years with little maintenance. This means that there is not the opportunity for systematic and straightforward training for repetitive surveys as in say aero engine inspection.

The overall result of fragmentation in the industry is that there are many small operators with limited skills and yet they attempt to offer a whole range of services. Sometimes these small operators will promote a specific NDT technique to the exclusion of a better technique. Being a very small operator means lower overheads, but means that these operators do not have the resources to discuss complicated issues with like minded colleagues. The client clearly faces a dilemma.

The Informed Client

It has become clear that there is an urgent need for "Informed Clients". Simply specifying a "Comprehensive NDT Inspection" is no longer good enough. Some critical aspects of surveys are highlighted below. Universities need to incorporate NDT into their curriculums.

Measuring & Delivering NDT Research Impact

In the UK, university research is measured by a combination of peer assessment reviews and evaluation of metrics: RAE'2008 and next REF 2014 (Research Excellence Framework). A key feature of REF 2014 is that Research Impact will be measured.

Thus a key issue to be discussed is how to channel international research publications into engineering practice. Quality peer reviewed papers in ISI rated journals are vital in order to archive good NDT research – but industry will rarely make use of this data.

The way forward is to incorporate research innovation into international codes of practice and standards and thus into industry. Unless NDT research is adopted by industry, little has been achieved. Typical international codes of practice and standards include:

- ACI Technical Report 228.2R-98 (1998) [1]
- ASTM C 597

- Concrete Society TR48 (1997) [2]
- BS & EU test standards BS 1881 #201; BS 1881 #203 (206); ISO/DIS 8047
- Highways Agency (UK) BA86/06 (2006) [3]
- Rilem TC 207-INR "Interpretation of NDT results and assessment of RC structures"

ACI: Although slow to evolve, due to consensus voting, and inevitably conservative – ACI has the advantage of a standing committee system that meets twice per year at the ACI Conventions.

ASTM & British Standards: standardize one off test procedures with limited discussion.

Concrete Society (UK): publishes one off reports

Highways Agency: no standing committee.

Rilem: detailed reports after a 5-year fixed term committee life. No formal continuation of committees and limited dissemination outside the Rilem membership.

Examples of ACI "Impact"

There are 3 outstanding examples of ACI Impact in developing and promoting methods for the NDT of concrete structures:

(1) Ground Penetrating Radar GPR. This technology evolved from geophysics. ACI 228.2R-98 has played a major role in disseminating many areas of innovations in interpretation. Examples of international research which have impacted GPR practice include the significance of antenna centre frequency.
(2) Impact Echo (I-E) is a spectacular success in terms of translation from university research at Cornell University and NIST - to industrial practice. An example of international collaboration and research which has impacted on IE practice includes the significance of impactor frequency.
(3) Impulse response, marketed as s'Mash, is an industry driven innovation in NDT testing of structures. This technique enables a large area of concrete to be tested relatively rapidly compared to impact echo. The technique is considered to be appropriate for comparative analyses rather than absolute measurement. Essentially, the test mobilises bending modes in a slab like surface and thus areas of higher mobility will indicate honeycombing within the concrete or a void beneath the concrete member – depending upon the response characteristics.

Comments will be focused on GPR, I-E, ultrasonics and tomographic imaging below.

Ground Penetrating Radar (GPR)

Continuing the theme of the "Informed Client" – a critical area relates to the significance of antenna centre frequency.

Table 1 GPR resolution and minimum detection depth (Zmin)

Material	ε_r	Frequency in air (MHz)	Frequency in material (MHz)	Velocity (mm/ns)	Wavelength (mm)	Resolution (mm)	Z_{min} (mm)
Dry Concrete	6	1,500	1,050	123	117	59	39
Damp Concrete	10	1,500	1,050	95	90	45	30
Dry Concrete	6	900	630	123	195	98	65
Damp Concrete	10	900	630	95	151	76	50
Dry Concrete	6	500	350	123	351	176	117
Damp Concrete	10	500	350	95	271	136	90
Dry Concrete	6	100	70	123	1757	879	586
Damp Concrete	9	100	70	95	1357	679	452

Where ε_r = relative dielectric constant

The radar pulse is reflected at interfaces where there is a change in the di-electric properties of layers. The shallowest depth that can be detected is one-third of the wavelength, λ, [4]. Table 1 summarizes the resolution and minimum depth (Zmin) that can be detected for different centre frequencies and concrete conditions. Resolution refers to the smallest target that is detectable. These numbers are based upon the assumptions that resolution is based upon $\lambda/2$ and the minimum detectable depth is $\lambda/3$. Calculations assume that the centre frequency in air of a dipole radar antenna signal reduces by approximately 30% when brought into contact with concrete [5].

Impact Echo

The ACI 228 Document has addressed and updated Impact Echo work in line with developments arising since the original work of [6] and later work of [7] was published. Impact echo testing is well known and illustrated below:

The contact time of the impactor determines the minimum depth and lateral dimension of the flaw that can be detected. These factors are as follows:

- Using spherical impactors, the contact time (assuming no local crushing of the concrete) is approx a linear function of the ball diameter tc (in μs) ≈ 4.3 D where D is the impactor diameter in millimeters Fig. 1a.
- The maximum useable frequency contained in the impact is approximately the inverse of the contact time (fmax $\approx 1/tc$).
- The smallest flaw depth (or plate thickness) that can be measured for a given wave speed and impact duration equates to half the wavelength ($\lambda/2$) associated with the resonant thickness frequency [7, 8, 9] Fig. 1b.
- The minimum lateral dimension of a flaw that can be detected, regardless of depth, equals the wavelength associated with the maximum useable frequency [7].

Thus the minimum lateral dimension of flaw that can be detected is affected both by the contact time and flaw depth. See Sansalone and Streett [7] for additional information.
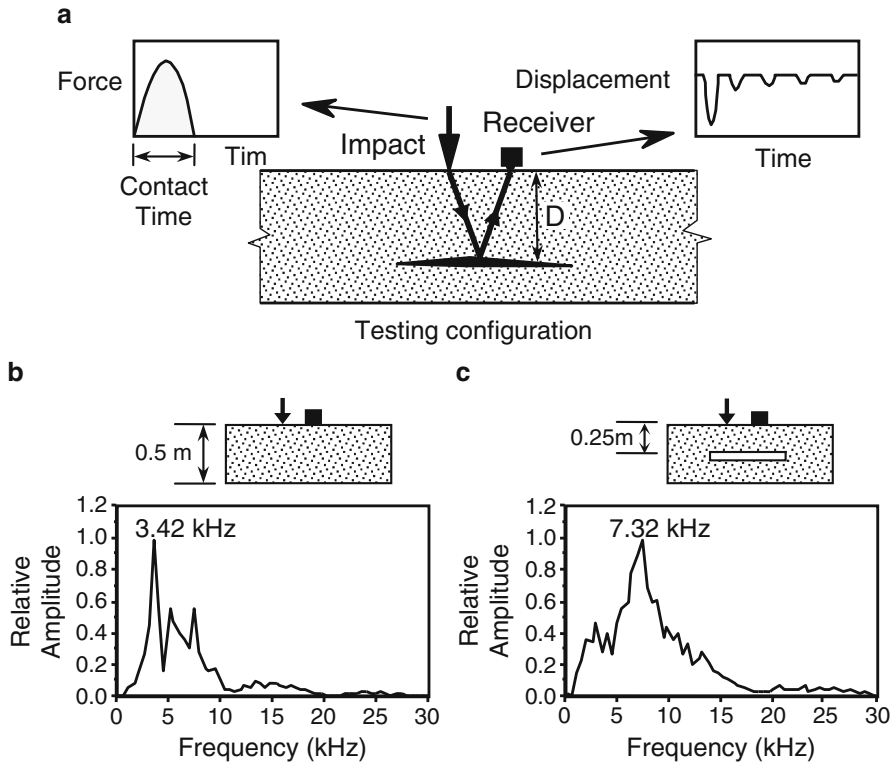
Fig. 1 Impact Echo Test

Table 2 Minimum depth & flaw size related to Impactor diameter

Sphere diameter (mm)	Contact time t_c (µs)	Maximum useful frequency = $1/t_c$ (kHz)	Minimum-depth of flaw that can be detected (mm)	Minimum lateral dimension of flaw that can be detected (mm)
5	22	47	43	86
6.5	28	36	56	112
8	34	29	69	138
9.5	41	24	82	163
11	47	21	95	189
12.5	54	19	108	215

Assuming a P-wave speed through concrete of 4,000 m/s, Table 2 gives the minimum depth and lateral dimension of a flaw that can be detected for typical sizes of spherical impactors. The values in Table 2 are based on a maximum useful frequency equal to the inverse of the contact time. Sansalone and Streett [7], suggest a maximum useable frequency of 1.25 times this value. However Table 2 provides a

more conservative estimate of detectable flaw depth or size, to account for some inelastic behavior during impact - that is the surface of the concrete crumbles slightly upon impact.

Shear Wave Ultrasonics & Tomography

Other areas of innovation relate to sonic and ultrasonic tomography.

Low cost ultrasonic tomography has been used successfully to identify voiding in metallic ducts in post-tensioned concrete bridge beams - Fig. 2 and 3 [10]. The system used was hand operated and used 56 kHz ultrasonic transducers for both transmission and reception.

By using a fuzzy logic tomographic software program, areas of very low velocity can be identified – as seen in Fig. 4 below.

A new approach to ultrasonic inspection, the "MIRA" system, involves the use of shear waves and multi-transducers with dry contacts and tomographic imaging using SAFT techniques Figs. 5 and 6. This is an exciting new approach which should see wider applications in the next decade.

Other Key NDT Developments not Supported by ACI

ACI 228 is a consensus led document that focuses on existing site proved technology, rather than "research in progress". One can sense the tensions and arguments that can emerge about lack of innovation in ACI documents. Areas where ACI 228 has not adopted innovative technology includes a number of areas.

Data Fusion – Robotics

BAM has focused on issues related to data fusion, particularly with respect to concrete structures – fusing impact echo, shear wave ultrasonics and GPR. In order to achieve credible data fusion precision, robotic locational precision is required for readings. Hand operated systems did not give sufficient locational precision [11]. A substantial reference to the BAM NDT Toolbox is available on the internet [12].

Whole Structure Dynamic Testing – Modal Analysis

Whole structure dynamic testing has proved difficult, but more effective on metallic than concrete structures. Gentile [13] has given an excellent example of such an investigation on a concrete arch bridge; Aktan has reported on metallic and other structures [14]. ACI define whole structure dynamic testing as monitoring and not site proven.

a) Complete coverage   b) Surface and side coverage   c) Side coverage only
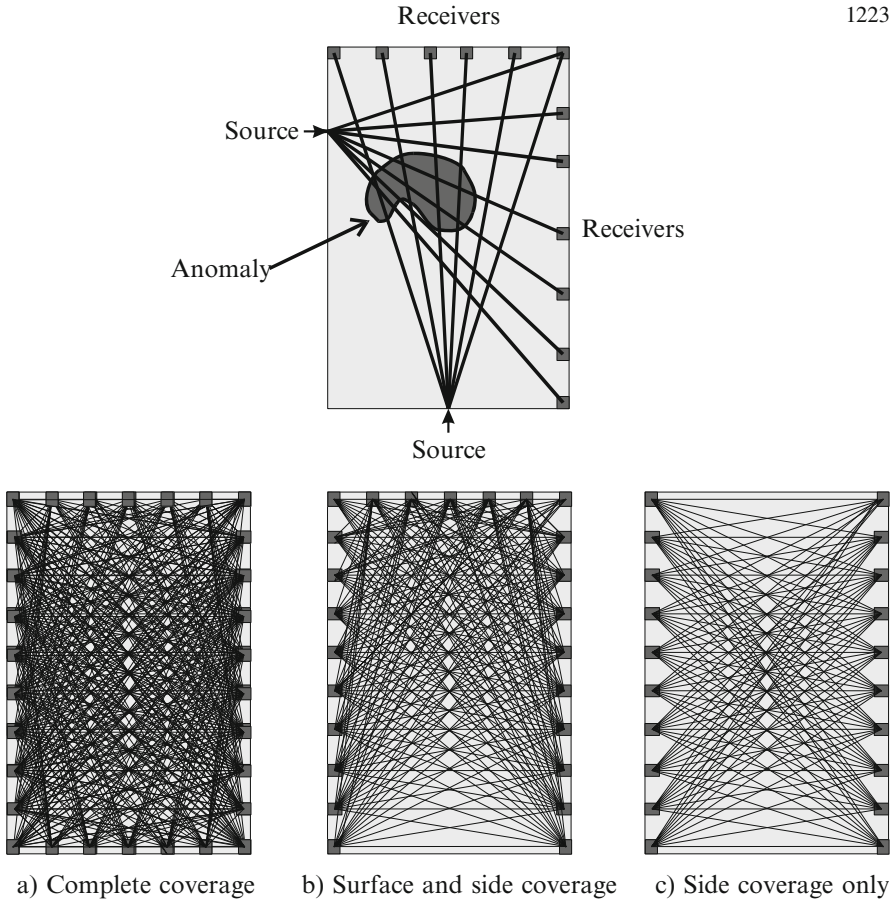
Fig. 2 Tomographic ray paths

Note: The voids are formed by an air gap or a polystyrene
box-out
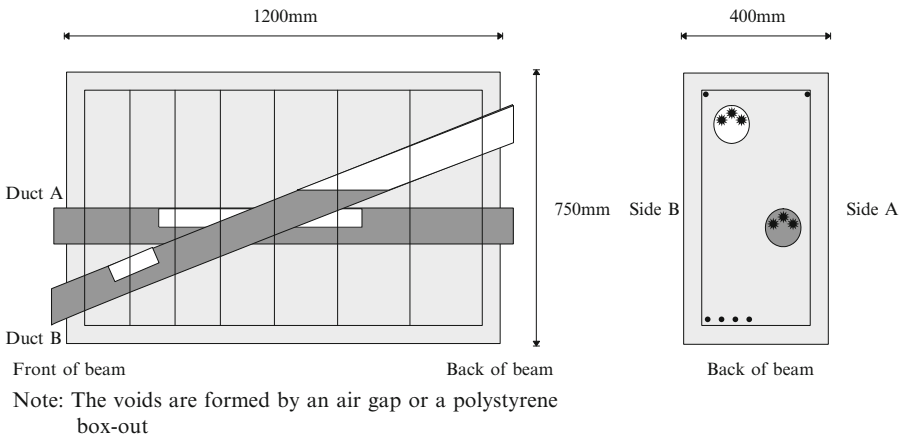
Fig. 3 Stanger model with included defects shown
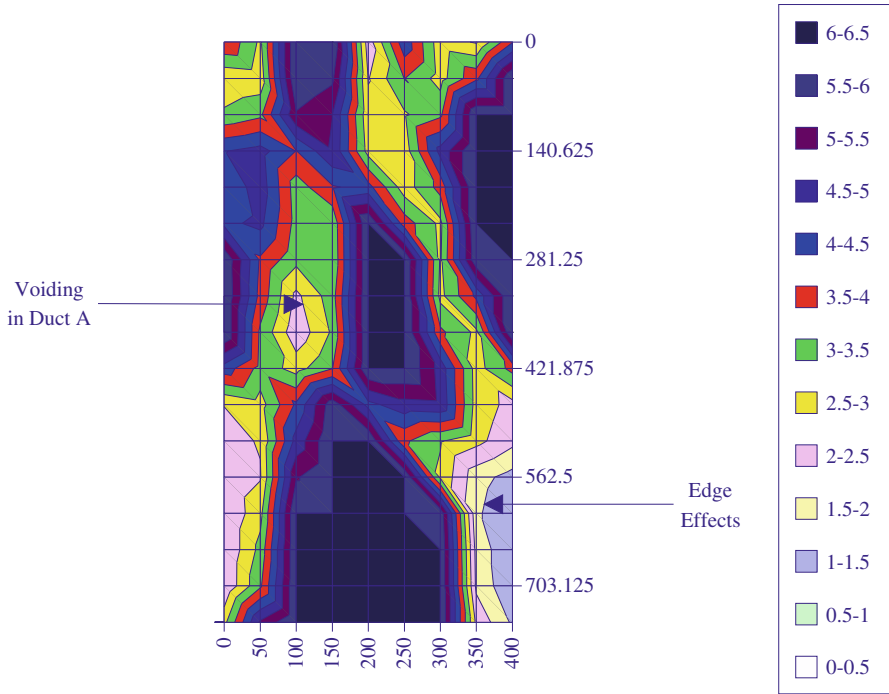
Fig. 4 2-D tomographic interpretation of the ultrasonic tests on this beam [10]
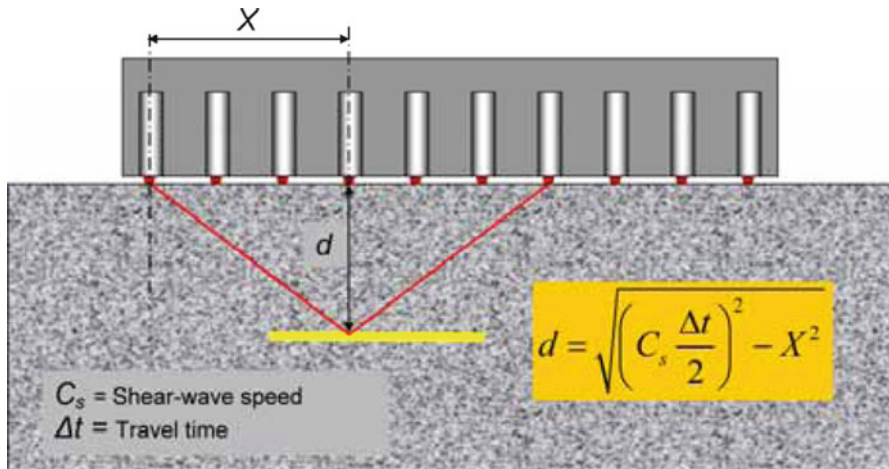
Fig. 5 Principles of MIRA ultrasonic tomography (Germann Instruments)
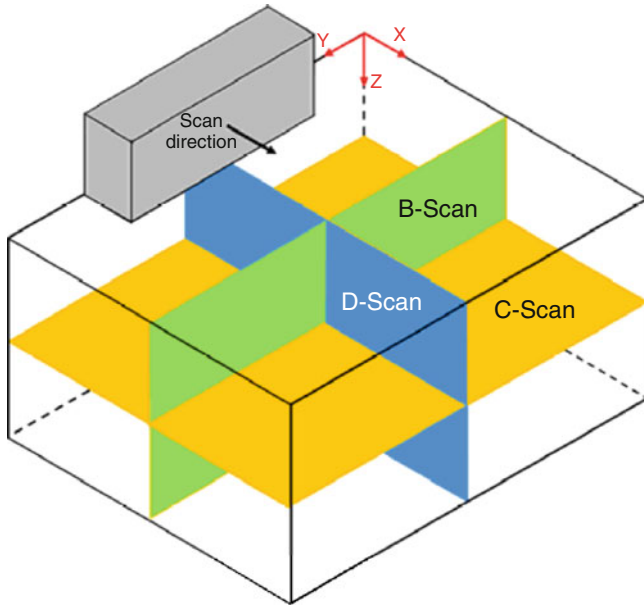
Fig. 6 Example of tomographic slice (Courtesy of Germann Instruments)

Acoustic Emission (AE)

Acoustic emission (AE), where Japan is a world leader in research and practice, has proved increasingly successful on concrete beams and bridges [15, 16]. The ACI 228 debate again revolves around whether AE is monitoring or NDT.

Role of Independent Manufacturers

Small to medium enterprises (SMEs) are key to driving innovation into international industry.

In the GPR sector one has seen a change from complex difficult to use general purpose GPR systems that require a graduate level of skill to operate – to the development of specific technical solutions sharply focused on industrial applications. A good example has been the low cost high frequency GPR systems used to detect reinforcing bars in concrete floor slabs. These systems are often purchased by plumbers to enable detection of post-tensioned cables when drilling to install en-suite bathrooms in conversions.

Conclusions

(1) Translation from academic to industry impact is critical if NDT is to move forward.
(2) Impact can be achieved by harnessing ACI, Rilem, ASTM and so on.
(3) Innovation comes from both researchers in universities and research institutes - plus critically SMEs.
(4) The role of the informed Client is crucial.

References

[1] ACI Technical Report 228.2R-98 (1998) *Nondestructive Test Methods for Evaluation of Concrete in Structures*, ACI, Farmington Hills, MI, USA, p. 62.
[2] Concrete Society Technical Report TR48 (1997), *Guidance on Radar Testing of Concrete Structures*, The Concrete Society, Slough, UK, p 88.
[3] BA86/06 (2006) *Bridge Advice Note: Advice Notes on the Non-Destructive Testing of Highway Structures*, The Highways Agency, London, http://www.standardsforhighwyas.co.uk, 247 pages.
[4] McCann, DM & Forde, M.C., (2001) Review of NDT Methods in the Assessment of Concrete and Masonry Structures, *NDT&E International*, Elsevier Science, Vol. 34, pp. 71–84.
[5] Padaratz, I.J., Hardy, M.S.A. & Forde, M.C. (1997) Coupling effects of radar antennae on concrete, *Proc 4th Int Conf: NDT-CE*, University of Liverpool, 8-11 April 1997, Vol 1, 237–245
[6] Sansalone, M & Carino, NJ (1986) *Impact-Echo: A Method for Flaw Detection in Concrete Using Transient Stress Waves*, NBSIR 86-3452, National Bureau of Standards, Gaithersburg, Maryland, Sept., 222 pp.
[7] Sansalone M.J. & Streett W.B. (1997) *Impact-echo*, Bullbrier Press, Ithaca, NY.
[8] Martin, J. & Forde, M.C. (1995) Influence of concrete properties on impulse hammer spectrum and compression wave velocity, *J. Construction & Building Materials*, 1995, Vol. 9, No. 4, 245–255
[9] Martin, J, Hardy, M.S.A., Usmani, A.S. & Forde, M.C. (1998) Accuracy of NDE in bridge assessment, *Engineering Structures*, Vol 20, No. 11, 979–984.
[10] Martin, J, Broughton, K.J., Giannopoulos, Hardy, M.S.A. & Forde, M.C. (2001) Ultrasonic Tomography of Grouted Duct P-T R.C. Bridge Beams, *NDT&E International*, Elsevier Science, 2001, 34, 107–113.
[11] Niederleithinger, E., Helmerich, R., Streicher, D., Stoppel, M., Wiggenhauser, H. (2006) Automated non-destructive investigation of railway bridge condition, *Proc. 11th Int. Conf. Structural Faults & Repair-2006*, Assembly Rooms, Edinburgh, 13-15 June 2006, Engineering Technics Press, CD-Rom, ISBN 0-947644-59-8.
[12] http://www.bam.de/ZfPbau-kompendium.htm.
[13] Gentile, C (2006) Dynamic characteristics of an historic arch bridge, *Proc. 11th Int. Conf. Structural Faults & Repair-2006*, Assembly Rooms, Edinburgh, 13–15 June 2006, Engineering Technics Press, CD-Rom, ISBN 0-947644-59-8.

[14] Naghavi, R. & Aktan, A.E., (2003) Nonlinear Behavior of Existing Heavy-Class Steel Truss Bridges, *Journal of Structural Engineering*, Vol. 129, No. 8, August, 2003.

[15] Ohtsu, M. & Watanabe, H. (2001) Quantitative Damage Estimation of Concrete by Acoustic Emission, *Construction and Building Materials*, Vol. 15, Nos. 5–6, 217–224.

[16] Shigeishi, M., Colombo, S., Broughton, K.J., Rutledge, H., Batchelor, A.J., & Forde, M.C. (2001). Acoustic emission to assess and monitor the integrity of bridges, *Construction and Building Materials*, Elsevier Science, Vol 15, No. 1, 2001, 35–49

NDT Planning for Fatigue Sensitive Structures Under Uncertainty

D.M. Frangopol and S. Kim

Abstract Timely maintenance actions on deteriorating structures depend on the quality of the non-destructive testing (NDT) method. Damage detection with less delay can lead to less maintenance delay. The efforts to detect existing fatigue cracks and predict fatigue crack propagation reliably will contribute to reduce the damage detection delay, and furthermore to establish optimum maintenance and management strategies of fatigue sensitive structures. In this paper, a probabilistic approach for optimum NDT planning for deteriorating structures subjected to fatigue is presented. The optimum NDT plan is obtained by minimizing the expected damage detection delay. Uncertainties associated with fatigue damage occurrence / propagation and quality of the NDT are considered to formulate the damage detection delay. Effects of number and/or quality of the NDT on optimum planning are studied. The approach presented is illustrated using a realistic example of a fatigue sensitive structure.

Keywords Detection delay • Fatigue • Optimization • Propagation • Quality of inspection

Introduction

NDT of steel structures including bridges, offshore structures and naval ships is essential to assess the structural integrity, and to predict the remaining lifetime. Steel structures are usually inspected by NDT at uniform or non-uniform time intervals, in order to detect damage with less delay and take appropriate maintenance actions. Generally, maintenance actions depend on the quality of NDT method. During the last decades, there have been important efforts to detect existing fatigue cracks and predict fatigue

D.M. Frangopol (✉) • S. Kim
Department of Civil and Environmental Engineering, ATLSS Engineering Research Center,
Lehigh University, Bethlehem, PA 18015, USA
e-mail: dan.frangopol@lehigh.edu

crack propagation reliably. It has been expected that these efforts will contribute to reduce the damage detection delay, and furthermore to establish more realistic maintenance and management strategies for fatigue sensitive structures.

In this paper, uncertainties associated with fatigue crack damage occurrence / propagation and damage detection are studied, and finally optimum NDT planning to minimize damage detection delay is presented. The formulation of expected damage detection delay considers these uncertainties. The optimum NDT planning is a solution of an optimization problem by minimizing the expected damage detection delay. Effects of number and/or quality of NDT on optimum planning are studied. The approach presented in this paper is applied to a ship hull structure.

NDT for Fatigue Crack Detection Under Uncertainty

Fatigue sensitive steel structures including bridges, offshore and naval structures can continuously deteriorate under various loadings [1]. Initial fatigue cracks may be pre-existing from fabrication. Under repetitive loads, the initial cracks can be propagated into macro-cracks which may lead to failure, or unserviceability of a structure.

Crack growth model

In order to predict the crack length due to fatigue, Paris' equation [2] has been used [3, 4]. The ratio of the crack length increment *da* to stress cycle increment *dN* is described as [2]

$$da \, / \, dN = C \left(\Delta K \right)^{m} \qquad for \, \Delta K > \Delta K_{thr} \tag{1}$$

where a = crack length; N = number of cycles; ΔK = stress intensity factor; and ΔK_{thr} = threshold of stress intensity factor. C and m are material parameters. The stress intensity factor ΔK is [5]

$$\Delta K = S \cdot Y(a) \sqrt{\pi a} \tag{2}$$

where S = stress range, and $Y(a)$ = geometry function. Based on Eqns. (1) and (2), crack size associated with a prescribed time, and time for crack to reach a specific size can be predicted.

NDT to detect fatigue crack

Development of NDT techniques to improve the accuracy and efficiency has been performed during the last two decades. These NDT techniques can be categorized into global and local techniques [6]. The local NDT technique can be used to detect and measure local damage in a structural component. The global NDT techniques

Fig. 1 Relation between probability of detection and fatigue damage intensity
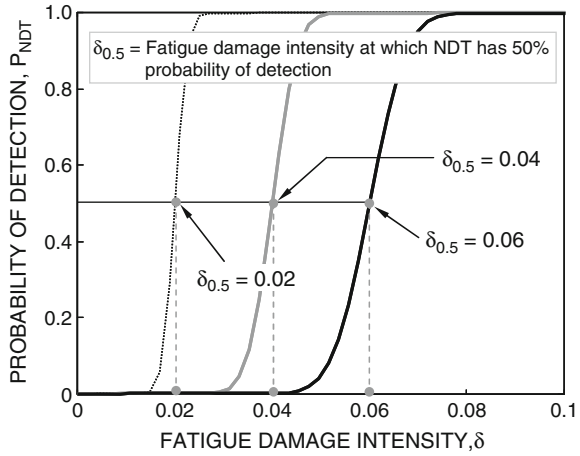
focus on an entire structural system. The following NDT techniques are commonly used to detect fatigue crack in steel structures: visual inspection, liquid penetrant testing, magnetic particle testing, radio graphic testing, ultrasonic testing, and acoustic emission testing [1]. The local NDT technique is applied to detect, verify, and quantify crack damage in a steel structure, after the location associated with possible fatigue crack damage is identified by the global NDT technique.

Probability of fatigue damage detection

The probability of detection for a given crack length can represent the quality of NDT method. The relation between probability of detection and fatigue crack length is expressed by a detectability function. This function has the following representative forms: (a) shifted exponential distribution, (b) logistic curve, and (c) normal cumulative distribution function (CDF). Figure 1, using the normal CDF as detectability function [7], shows the relation between the probability of detection P_{NDT} and the fatigue damage intensity δ for $\delta_{0.5} = 0.02$, 0.04 and 0.06. $\delta_{0.5}$ is defined in Fig. 1. The fatigue damage intensity δ is expressed as $(a - a_{min}) / (a_{max} - a_{min})$, where a_{min} and a_{max} are the minimum and maximum crack sizes. The value of δ ranges from zero (i.e., no damage) to one (i.e., full damage). In Fig. 1, it is evident that the NDT associated with smaller $\delta_{0.5}$ leads to higher probability of detection for a given fatigue damage intensity δ. In this study, $\delta_{0.5}$ is used to represent the quality of NDT.

Optimum NDT Planning

Timely maintenance actions can be achieved through damage detection with less delay as mentioned previously. For this reason, the minimization of the damage detection delay is the objective of optimum NDT planning in this study.

Expected damage detection delay

Considering uncertainties associated with damage occurrence / propagation and NDT, the expected damage detection delay $E(t_{delay})$ for the *n*-time application of the same NDT, is formulated as [8]

$$E\left(t_{delay}\right) = \sum_{i=1}^{n+1}\left[\left\{\int_{t_{NDt,i-1}}^{t_{NDT,i}} E\left(t_{delay}\right)_i \cdot f_T\left(t\right)\right\} dt\right] \tag{3}$$

where $f_T(t)$ = PDF of damage occurrence time *t*; $t_{NDT,i}$ = *i*th NDT; and $E(t_{delay})_i$ = expected damage detection delay when $t_{NDT,i-1} \leq t \leq t_{NDT,i}$. $E(t_{delay})_i$ is formulated using an event tree model. For example, if a NDT is applied three times to detect damage, there are four cases of $E(t_{delay})_i$ according to damage occurrence time *t* as: $t_s \leq t \leq t_{NDT,1}$ (case 1); $t_{NDT,1} \leq t \leq t_{NDT,2}$ (case 2); $t_{NDT,2} \leq t \leq t_{NDT,3}$ (case 3); and $t_{NDT,3} \leq t \leq t_e$ (case 4), where t_s and t_e are the lower and upper bounds of damage occurrence time *t*. For case 3, $E(t_{delay})_3$ is expressed as

$$E\left(t_{delay}\right)_3 = \left(t_{NDT,3} - t\right) \times P_{NDT,3} + \left(t_{NDT,e} - t\right) \times \left(1 - P_{NDT,3}\right) \tag{4}$$

where $P_{NDT,3}$ = probability of detection associated with the third application of the NDT.

Application

The proposed approach is applied to a naval ship hull structure. As shown in Fig. 2, the joint between longitudinal plate and bottom plate of a ship hull structure is treated as the critical location. The sea water waves can induce repeated loading, under which the fatigue crack in the bottom plate can initiate and propagate in the transverse direction as shown in Fig. 2.

NDT planning is a solution of an optimization problem to minimize the expected damage detection delay $E(t_{delay})$ as follows [8]

$$\text{Find} \qquad \mathbf{t_{NDT}} = \left\{t_{NDT,1}, t_{NDT,2}, ..., t_{NDT,n}\right\} \tag{5}$$

$$\text{to minimize} \qquad E\left(t_{delay}\right) \tag{6}$$

$$\text{such that} \qquad t_{NDT,i} - t_{NDT,i-1} \geq 1\text{year} \tag{7}$$

$$\text{given} \qquad n, \delta_{0.5} \text{ and } f_T\left(t\right) \tag{8}$$

where $\mathbf{t_{NDT}}$ = vector consisting of *n* design variables of NDT times. The number of applications of the NDT *n*, $\delta_{0.5}$, and $f_T(t)$ are given as indicated in Eqn. (8).

a

Ȼ of mid section

b

DETAIL

Longitudinal plate

Bottom plate

Loading and unloading in a longitudinal direction

Cracks

Crack length *a*

DETAIL
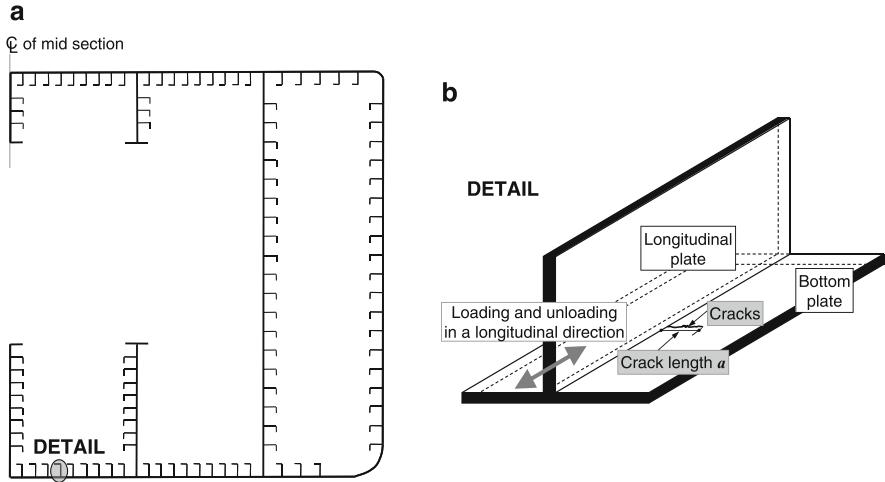
Fig. 2 Schematic representation of (**a**) cross sectional view; and (**b**) the assumed critical location for fatigue (adapted from [8])

The relation between the minimum expected damage detection delay $E(t_{delay})$ and number of applications of the NDT *n* is presented in Fig. 3a. Each point of this figure is the solution of the optimization problem. When *n* = 3, the optimum NDT plans associated with $\delta_{0.5}$ = 0.02, 0.04 and 0.06 are illustrated in Fig. 3b. If three applications of NDT with $\delta_{0.5}$ = 0.02 are used to detect fatigue damage, the NDT has to be performed at 8.95, 11.46 and 15.02 years. The associated expected damage detection delay is 4.98 years (see Fig. 3a).

Conclusions

This paper presents a probabilistic approach for optimum NDT planning. The optimum NDT plan is a solution of an optimization problem to minimize the expected damage detection delay considering the uncertainties associated with damage occurrence and propagation, and quality of the NDT. Effects of number applications and quality of NDT method on optimum planning are studied.

Fig. 3 (**a**) Relation between minimum $E(t_{delay})$ and number of NDTs n; and (**b**) optimum NDT plan when $n = 3$

a

MINIMUM EXPECTED FATIGUE DAMAGE DETECTION DELAY

$\delta_{0.5}$ = Fatigue damage intensity at which NDT has 50% probability of detection

$\delta_{0.5} = 0.06$

$\delta_{0.5} = 0.04$

$\delta_{0.5} = 0.02$

NUMBER OF NON-DESTRUCTIVE TESTINGS, n

b

Number of NDTs $n = 3$

$t_{NDT,1} = 11.78$ $t_{NDT,2} = 14.44$ $t_{NDT,3} = 18.41$

$t_{NDT,1} = 10.67$ $t_{NDT,2} = 13.28$ $t_{NDT,3} = 17.10$

$t_{NDT,1} = 8.95$ $t_{NDT,2} = 11.46$ $t_{NDT,3} = 15.02$

$\delta_{0.5}$

TIME (YEARS)
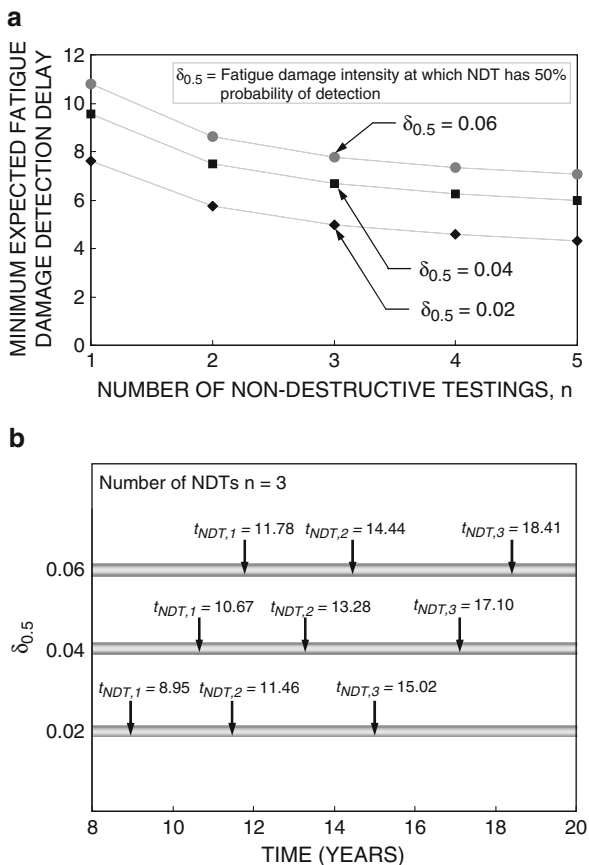
References

[1] Fisher, J.W., Kulak, G.L., and Smith, I.F. (1998). *A fatigue primer for structural engineers.* National Steel Bridge Alliance.

[2] Paris, P.C., and Erdogan, F.A. (1963). *J. Basic Eng.* TRANS. ASME, 85(Series D), pp. 528–534.

[3] Schijve, J. (2003). *Int. J. Fatigue*, Elsevier, vol. 25, n. 8, pp. 679–702.

[4] Mohanty, J.R., Verma, B.B., and Ray, P.K. (2009). *Int. J. Fatigue*, Elsevier, vol. 31, n. 3, pp. 418–424.

[5] Irwin, G.R. (1958). *"The Crack-extension-force for a crack at a free surface boundary."* NRL report 5120.

[6] Fu. G. (2004). *Non-destructive testing for steel highway bridges.* NDT Methods Applied to Fatigue Reliability Assessment of Structures, J. Mohammadi (Ed.), ASCE, pp. 23–31.

[7] Frangopol, D.M., Lin, K.Y., and Estes, A.C. (1997). *J. Struct. Eng.*, ASCE, vol. 123, n. 10, pp. 1390–1401.

[8] Kim, S. and Frangopol, D.M. (2011). *Int. J. Fatigue*, Elsevier, vol. 33, n. 3, pp. 448–459.

A Proposal for Reliability Improvement of Non-Destructive Evaluation Technology for Concrete

T. Kamada, M. Iwanami, T. Shiotani, Y. Oshima and S. Uchida

Abstract The subcommittee of the JSCE (Japan Society of Civil Engineers) concrete committee for the improvement of the reliability of non-destructive evaluation technology for concrete chaired by Professor Toshiro Kamada of Osaka University (Committee 339 below) has discussed measures for the improvement of the reliability of non-destructive evaluation technology from two perspectives: education, and standards and specifications. This paper describes the roles that standards and specifications play in terms of improving the reliability of these technologies. Moreover, a pattern of reliability based on the client-engineer correlation is identified. As a result, it was found that the reliability of non-destructive evaluation can be enhanced to some extent by identifying the scope of application and standardizing the method of non-destructive testing. For ultimate improvement of reliability, the pattern of reliability itself should be changed through technical innovation for non-destructive testing or the enlightenment of the client.

Keywords Concrete • Non-destructive evaluation • Reliability improvement • Satisfaction • Standards and specifications

---

T. Kamada (✉)
Osaka University, Osaka, Japan
email: kamada@civil.eng.osaka-u.ac.jp

M. Iwanami
Port and Airport Research Institute, Kanagawa, Japan

T. Shiotani • Y. Oshima
Kyoto University, Kyoto, Japan

S. Uchida
Saga University, Saga, Japan

Introduction

Ideal situations of the education and certification of personnel as well as the validation of NDT methods are shown in some international standards such as ISO 9712 (qualification and certification of personnel involved in non-destructive testing), DIN EN 473(Non-destructive testing - Qualification and certification of NDT personnel - General principles), and so on. Against the background, the subcommittee of JSCE (Japan Society of Civil Engineers) concrete committee for improvement the reliability of non-destructive evaluation technology for concrete chaired by Professor Toshiro Kamada of Osaka University (Committee 339 below) has discussed the measures for improvement the reliability of non-destructive evaluation technology, especially focusing on concrete field, from two perspectives: education, and standards and specifications. This paper describes the roles that standards and specifications play for improvement the reliability. Moreover, a pattern of reliability based on the client-engineer correlation is identified.

Pattern of Reliability

A pattern of reliability was assumed. The reliability of non-destructive testing greatly depends on the satisfaction of the client with small variations of test results and other points. In the case of a low level of demand of the client, satisfaction is achieved even if the test results are not fully accurate or inadequate. Even if highly accurate results with small variations are obtained, the level of satisfaction is low (not as good as expected) as compared with the demand exceeding the results. Thus, one of the reasons for the loss of reliability of non-destructive testing of concrete is the gap between the excessively high expectations of the client and the technical level available. If the engineer is not sufficiently skilled and uses the method outside the designated scope of application or follows a wrong procedure or makes a wrong interpretation of results, the test results vary greatly. The variations deteriorate the reliability of results although some are caused by the technical level available or the variations of concrete materials. Variations of results are, however, relatively evaluated. Variations may sometimes pose no problems in the case where the demand for the accuracy or validity of results is low. When crack widths are required with a margin of error of plus or minus 10 cm, for example, a variation of 1 cm is not a problem. In the case where a margin of error of 1 mm is allowed, a variation of 1 cm is considered unreliable. In this study, therefore, "high level of satisfaction" is regarded as the "reliable state".

   Figure 1 shows a pattern of reliability created between the client and engineer. Specific demand that the client presents to the engineer arises from the needs at a higher level. For example, in the case where there is a need to evaluate the soundness of a structure in terms of compressive strength, a demand is presented for knowing the compressive strength with a certain level of accuracy. The engineer,
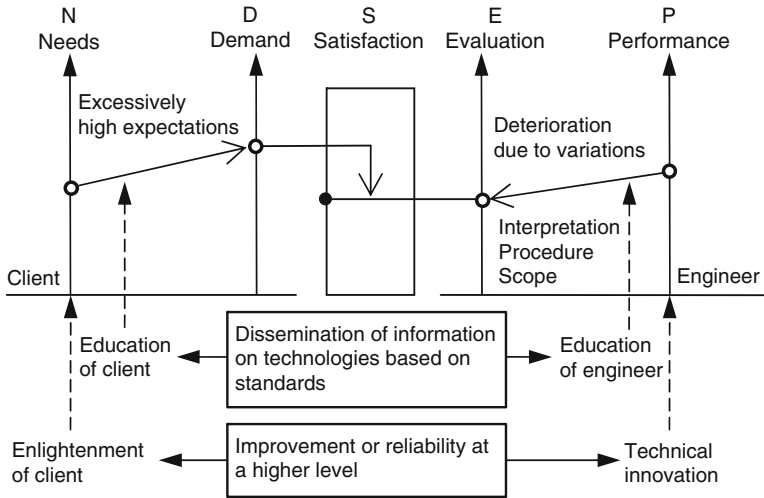
Fig. 1 Pattern of reliability

receiving the demand from the client, selects and implements a non-destructive testing method. Then, the capacity of estimating compressive strength (level of P) varies according to the non-destructive testing method selected by the engineer. Even if an appropriate non-destructive testing method is selected, measurements vary greatly according to the skill of the engineer or engineer's interpretation of an appropriate procedure or scope of application of the method. The final results of non-destructive testing are therefore evaluated based on their accuracy or variations. Evaluated here are not the quantitative results of non-destructive testing but the qualitative results. When estimating the crack depth by a non-destructive testing method for example, the results may vary for technical reasons and further variations may occur according to the skill of the engineer. The qualitative reliability of the results are evaluated as the results of non-destructive testing. Finally, the satisfaction of the client is determined based on the balance between the evaluation of and the demand for test results.

The terms used in Fig. 1 are defined below.

Needs (N)

Needs are the basic desire of the client and basically do not change. In the case where the client irrationaly demands compressive strength or other parameter for the purpose of evaluating the soundness of the structure, the needs may be changed by suggesting another appropriate parameter. It is assumed here that needs may be replaced through the "enlightenment of the client".

Demand (D)

Demand is an expectation arising from the needs of the client. Demand may sometimes be represented by a specific figure related to accuracy or other parameter. In numerous cases, reliability is deteriorated as the client has a great expectation without understanding the technical level or the scope of application of the non-destructive testing. Then, the excessively high expectation may be optimized by presenting standards to the client or educating the client on standards.

Performance (P)

This is the performance of a non-destructive testing method, which is enhanced only through technical innovation. It cannot be improved by standardization of non-destructive testing or education of the engineer.

Evaluation (E)

This is the result of evaluation of non-destructive test results. Evaluation is made not of the test results but of the reliability of test results. The results of non-destructive testing generally vary according to the performance of the equipment or the skill of the engineer. The highest performance provided by a non-destructive testing method is rarely achieved and reliability is deteriorated to some extent. The result of evaluation can, however, be reinforced by reducing variations through the education of the engineer or standardization of the testing method.

Satisfaction (S)

This refers to the satisfaction of the client, and is determined based on the balance between the evaluation E obtained by the non-destructive testing and the demand D of the client. The balance determines the level of reliability.

Based on the above definitions, satisfaction (reliability) can be improved by several methods. The first method involves the enhancement of performance (P) (Fig. 2). Technical innovation enhances performance. Performance can be improved solely through technical innovation such as the enhancement of equipment performance and the discovery of new principles. Even with no enhancement of equipment performance, the performance of non-destructive testing can be improved by reinforcing the skills of engineers and standardizing methods and providing uniform interpretations of test results (Fig. 3). The results of non-destructive testing vary according to the skill of the engineer. Minimizing the amplitude of variations,
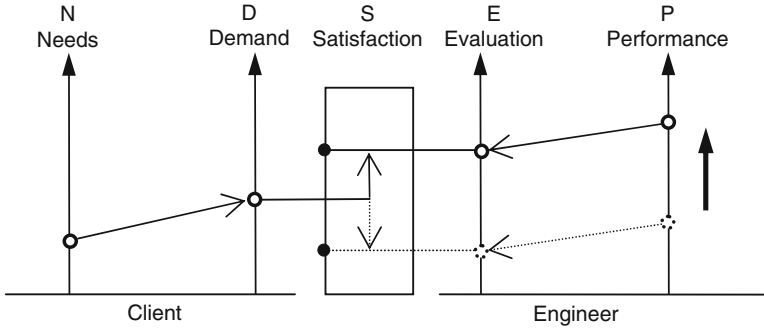
Fig. 2 Performance enhancement through technical innovation
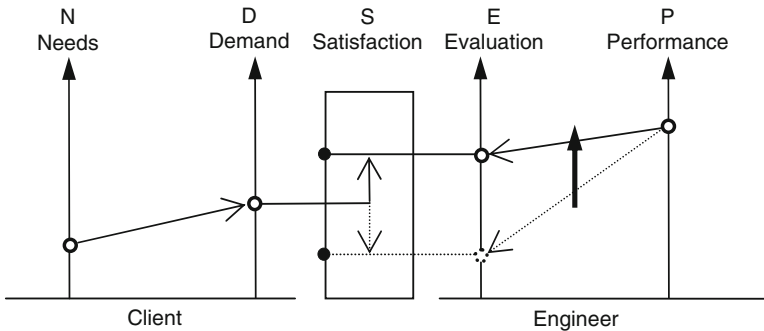
Fig. 3 Enhancement of evaluation by reducing variations

making evaluations properly and improvement measurement accuracy are expected to improve the performance of non-destructive testing. Identifying the appropriate technical level may help modify excessively high demand of the client (Fig. 4). The needs of the client can be changed through enlightenment by the engineer (Fig. 5). For example, replacing the needs for compressive strength for the purpose of determining soundness with the needs for another parameter may enable the suggestion of a higher-level non-destructive testing method fit for the parameter. The above discussions show that standards and specifications serve as a basis for disseminating information on appropriate technical levels to the client and as a means of standardizing procedures and interpretations and of optimizing the scope of application for the engineer. Organizing standards and specifications and educating clients and engineers on standards and making them familiar with standards are expected to improve the reliability of non-destructive testing.

The above discussions suggest that identifying the scope of application and standardizing methods and providing uniform interpretations of test results for non-destructive testing enable the reduction of excessively high expectations of the client and of the variations of test results according to the skill of the engineer.

Fig. 4 Reduction of expectations by disseminating information on technical levels to the client

Fig. 5 Replacement of needs through enlightenment

Closing Remark

Committee 339 examined the role that standards and specifications play to improve the reliability of non-destructive testing. As a result, it was found that the reliability of non-destructive testing can be enhanced to some extent by identifying the scope of application and standardizing the method of non-destructive testing. For ultimate improvement of reliability, the pattern of reliability itself should be changed through technical innovation for non-destructive testing or the enlightenment of the client.

Data Fusion to Improve the Concrete Diagnosis

V. Garnier, M.A. Ploix and D. Breysse

Abstract Numerous non-destructive testing (NDT) methods are used for concrete structures to obtain relevant data about material properties and damage states for reliable condition assessment. Whether the objective is to determine physical properties such as the porosity and the water saturation rate, or mechanical properties such as the elastic modulus or the compressive strength, sensitivity of NDT techniques to many characteristics of the material and its environment is a commonly encountered problem. Thus, accurate and reliable information is often difficult to extract due to the high level of uncertainty involved. Complementary use of different NDT methods for coherent combination of information obtained from each method is a sensible strategy to improve evaluation. The data fusion methodology presented in this paper makes use of the complementary data obtained from different non-destructive or destructive techniques to improve diagnosis reliability. In the case of imprecise and uncertain data, an assessment can still be made with a quantitative measure of the uncertainty involved. The methodology is based on the possibility theory and allows the selection of the best combination of data and techniques to evaluate the material. Applications of the methodology are presented and the results are discussed. Results show good agreement between estimations by data fusion and measured values. Also shown by the results is that the selection of complementary techniques is essential for a better estimation of indicators and improved diagnosis.

Keywords Compressive strength • Data fusion • Diagnosis • Quality

---

V. Garnier (✉) • M.A. Ploix
Laboratory of Mechanics and Acoustics - LCND team - Aix Marseille University,
13625, Aix en Provence, Cedex 01, France
e-mail: vincent.garnier@univ-amu.fr

M.A. Ploix
Laboratoire de Caractérisation Non Destructive, Université de la Méditerranée,
13625, Aix en Provence, Cedex 01, France

D. Breysse
12M, Université de Bordeaux 1, 33405, Talence, Cedex, France

Introduction

Non Destructive Testing gives information on the mechanical properties or pathologic states of concretes by the experimental measurements inversion. A lot of parameters influence the results of these evaluations. The regression laws between the NDT measures and the concrete characteristics are often uncertain. A solution to improve the diagnosis is to combine the information produced by the different techniques. We propose to use data fusion to combine the measurements in order to help for the decision and to increase its reliability.

The more commonly used methods for data fusion are based on classification (like Dempster-Shafer theory) in particular for the image fusion: X-ray and ultrasounds in welds [1-2], infrared thermography and eddy currents in carbon reinforced composite [3], radar waves and ultrasounds on reinforced concrete for image reconstruction [4], medical imagery in the brain [5], and infrared thermography images in nuclear applications [6]. Moreover data fusion has been already used for assessing civil engineering components [3] [4] [7-8]. Its classical use is to analyze two or more images that are compared and processed together. That increases contrast, decreases noise and makes defects clearer.

Data Fusion

Data fusion using the possibility theory has been chosen in the French project SENSO [9] because it allows combining heterogeneous information more or less precise and reliable, to provide global quantitative information with increased quality [10-12]. This theory based on fuzzy sets is more appropriate for this quantitative estimation problem than the usual methods of classification. Moreover the adopted way of data fusion is a translation of human logic, with notions of possibility, credibility… contrary to statistical methods based on probability.

The process consists in three steps: Data modeling - Fusion process - Decision.

Data modelsling

The distribution of possibilities $\pi(u)$ for a NDT measurement is supposed to be trapezoidal around a mean value. It is plotted on the vertical axis on Fig. 1.

To determine only one indicator like porosity, modulus or strength, we have to extend this distribution by the correlation curve between the observable (result of ultrasonic, resistivity or radar… measurement) and the researched indicator.

In this case, for a simple calculation, we work with linear regression, in blue. If we combine three pieces of information $\pi 1$ $\pi 2$ *and* $\pi 3$, we get different possible configurations as presented in Fig. 2.

Fig. 1 Extension of the possibilities distribution for an observable on the indicator (strength for example)
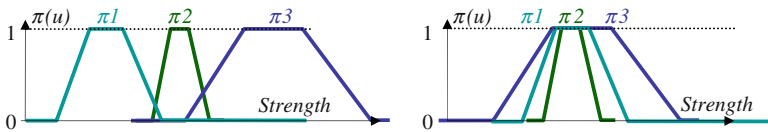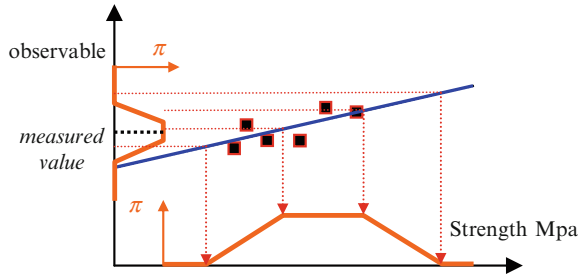
Fig. 2 Results of two measures obtained by three techniques
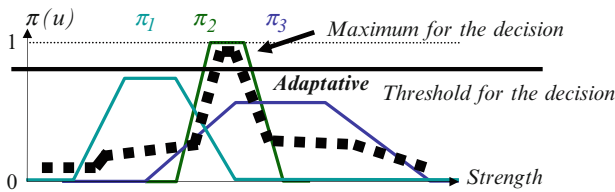
Fig. 3 Solution (dotted line) of data fusion including the techniques reliability

In the first figure, the concordance between the different results is bad. The indicator values proposed by each method are really different.

In the second, the concordance is good.

Fusion process

For typical experimental results given in Fig. 3, we introduce the reliability of each technique by an index issued from the laboratory measurements.

It can be defined by an expert regarding his confidence in the techniques or by statistical experimental analysis [13]. It varies from 0 to 1 and it modulates the maximum value of the possibilities distribution. We use an operator developed by Delmotte [14] to calculate the data fusion (dotted line in Fig. 3). It adapts itself depending on the concordance.

Decision

The distribution of the possibilities for the three merged measurements generally shows a solution that is extracted from the maximum value or from a distribution over a threshold decided by the expert as shown in Fig. 3.

The height and the width of the distribution are criteria of the quality of the result after the fusion. The higher the maximum, the better the quality of the solution. The narrower the peak, the better the solution.

Application

In this example, the data comes from Italian bridges on which Rebound Hammer *R*, Ultrasonic Velocity *Vus* and Pull-Out force *F* measurements have been realized at many locations on several piers and beams. Thirteen cores for different locations give the compressive strength f_c by destructive testing. The regression laws, the determination coefficient R² and the standard deviation Sd are determined for each observable.

$$Vus = 15.635.f_c + 3909 \qquad R^2 = 0.503 \qquad Sd = 94(m/s)$$

$$R = 0.1794.f_c + 38.45 \qquad R^2 = 0.416 \qquad Sd = 1.72$$

$$F = 0.577.f_c + 12.54 \qquad R^2 = 0.612 \qquad Sd = 2.7kN$$

We implement these relations and coefficients in a module specially developed [13]. We test the different measurement sets and combine them to extract the concrete strength after fusion by the maximum of the possibilities distribution. The R² coefficients are bad. They are by hypothesis the index of each observable.

The Table 1 presents the strength obtained by the fusion of the experimental NDT values, the destructive measured ones and the shift between the two values. RV is the relative variation Δ strength / measured strength. The shifts between the results obtained by fusion and measurements are very low for more than half of the results with a relative variation coefficient RV smaller than 10 %.

On the first line Fig. 4 shows the possibilities distributions of the three observables for two points 6 and 5. The second line plots the results after the fusion process. For point 6 we get the best estimation regarding the merged and experimental values. The concordance is very good and the solution is unique. The shift is 0.

It is important to remark that the maximum value of the merged solution is more important than the maximum of the measurements distributions. So the fusion reinforces the information and gives more confidence in the results.

Table 1 Merged, measured and shift strength for the 13 points of the bridge

Point	Strength (N/mm²)		Δ Strength	RV
	Fusion	Measurement	(N/mm²)	%
1	28,7	29,3	0,6	0,02
2	49,4	35,1	14,3	0,41
3	51,2	46,6	5,6	0,10
4	34,5	43,3	8,8	0,20
5	20,4	35,7	15,3	0,43
6	27,9	27,8	0,1	0,00
7	39,9	41,4	1,5	0,04
8	16,8	25,1	8,3	0,33
9	36,4	24,9	11,5	0,46
10	66,9	63,8	3,1	0,05
11	23,4	32,4	9,0	0,28
12	33,4	33,0	0,4	0,01
13	34,5	32,8	1,7	0,05
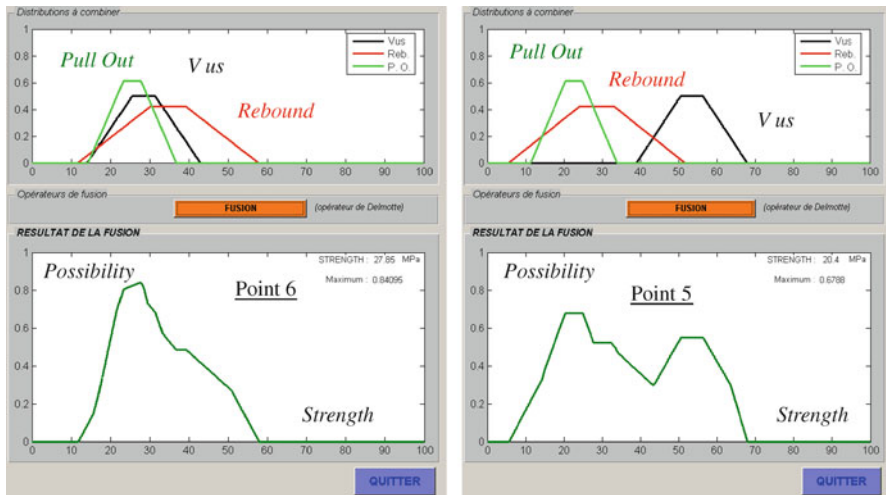
Fig. 4 Possibilities distributions for point 6 (RV=0) and 5 (RV=0.43)

On the other hand, the bad predictions generally present a characteristic possibilities distribution like the one proposed for point 5 (RV=0.43). The concordance between the three distributions is very bad. The result of the fusion is not good and two maximums are possible. This double solution informs on the bad fusion that is generally issued from bad initial measurement data or by regression laws. It is very easy to reject the results from these calculations. The points that do not present good results show this type of distribution. We can say without doubt that the confidence in the solution is very low.

Conclusions

In the case of bad regression laws, inversing the direct problem is not possible. The data combination can generate conflicts. The data fusion is able to give a solution to the problem of conflict between the information given by different techniques of measurement. The result of fusion can, in the case of a bad concordance, lead us to reject the NDT evaluation. Proposing a solution is always possible, but we can have a critical opinion of the results.

On the other hand, if there is no conflict, the result is reinforced by the different measures. We have applied this principle to the strength evaluation on a set of current concretes with three different measures. The prevision of the strength is possible in a lot of cases with a small uncertainty. This is an important improvement in the determination of the concrete strength and allows proposing an index of confidence to give a quantitative solution of the evaluation quality.

References

[1] Dromigny-Badin A., Rossato S. & Zhu.M., (1997), *Traitement du Signa,l* vol.14, p 499–510
[2] Kaftandjian V., Zhu Y.M., Dupuis O. & Babot D., (2005), IEEE *Transactions on Instrumentation and Measurement*, p 1968–1977
[3] Gros X.E., Bousigue J. & Takahashi K., (1999), *NDT&E International*, vol. 32, p 283–292
[4] Kohl C. & Streicher D., (2006), *Cement & Concrete Composites*, vol. 28, p 402–413
[5] Bloch I., (1996), *Pattern Recognition Letters*, vol 17, p 905–919
[6] Moysan J., Durcher A., Gueudre C. & Corneloup G., (2007), *NDT&E International,* vol. 40, p 478–485
[7] Horn D., (2006), Proceedings, *European Congress of Non Destructive Testing* Berlin,
[8] Maierhoffer C., Zacher G., Kohl C. & Wostmann J., (2008), *Journal of Nondestructive Evaluation*, vol. 27, p 47–57
[9] Lmdc-Senso, (2009) *Stratégie d'évaluation non destructive pour la surveillance des ouvrages en béton*, final report, 274 p.
[10] Zadeh L.A., (1999), *Fuzzy Sets and Systems*, vol. 100 Suppl. p 9–34
[11] Bouchon-Meunier B., Marsala C., (2003), *Logique Floue, Principes, Aide à la Décision*, Hermes – Lavoisier
[12] Bloch I., (2003) *Fusion d'informations en traitement du signal et des images*, Hermes – Lavoisier
[13] Ploix M.A., Garnier V., Breysse D. & Moysan J., (2011), *NDE data fusion to improve the evaluation of concrete structures, NDT&E International*, vol. 44 , p 442–448
[14] Delmotte F., (2000), *Traitement du Signal*, vol. 17, p 299–311

Approach for the Life-Cycle Management of Structures Including Durability Analysis, SHM and Maintenance Planning

P. Furtner and R. Veit-Egerer

Abstract A tailor-made model was developed, which utilizes state-of-the-art information from literature as well as VCE's experience gained in the course of performing bridge monitoring and bridge inspection worldwide. Probabilistic methods are used for the service life calculations of the whole structure as well as for individual structural members. The reason is to cover occurring uncertainties which have to be also implemented into the established maintenance plan in terms of lower & upper bounds of life expectancy. The starting point of the bridge's service life – in terms of the safety level – is according to the initial over design and depends on the applied design code and certain safety considerations in the course of the static calculations. This paper presents a custom model developed for service life prediction of bridge structures based on the state-of-the-art information from the literature and VCE's worldwide experience in bridge monitoring and inspection. The developed model was implemented in an urban highway extension project with more than 100 existing and new bridges.

Keywords Condition assessment • Lifetime assessment • Maintenance optimization • Service life calculation • Structural health monitoring

Introduction

The A15 highway is the main connection of the Rotterdam seaport with the industrial area in the Netherlands. At present the A15 suffers from considerable accessibility and safety problems. A major upgrade and extension project has been planned to increase the number of traffic lanes and to switch to a safer and more efficient road design.

P. Furtner (✉) • R. Veit-Egerer
VCE – Vienna Consulting Engineers, Austria
e-mail: furtner@vce.at

The project is implemented by means of a PPP (=Private-Public-Partnership) model, where the design, execution, maintenance, operation and financing are placed into the hands of a market party (contractor) for more than 25 years including a construction time of 5 years. The payments to the contractor are conditional on compliance with and verification of the road availability.

As the payment of the contractor is dependent on the availability and the traffic impediment, a well elaborated maintenance concept is of major interest. A Management Information System (MIS) shall be developed and implemented for the optimisation of the condition assessment and the maintenance planning of all engineering structures as well as the road pavement over the whole availability period. This MIS shall collect and analyse all relevant data from visual inspection, structural health monitoring, maintenance measures and the traffic management system. The results will be interpreted and lead to an as-precise-as possible maintenance planning. A continuously working, dynamic updating procedure for the maintenance plan shall be implemented.

Applied Methodologies

With the introduction of lifecycle aspects it became even more important to create a time depending deterioration model represented by a condition index. Numerous models have been already developed that describe the transition of a variety of
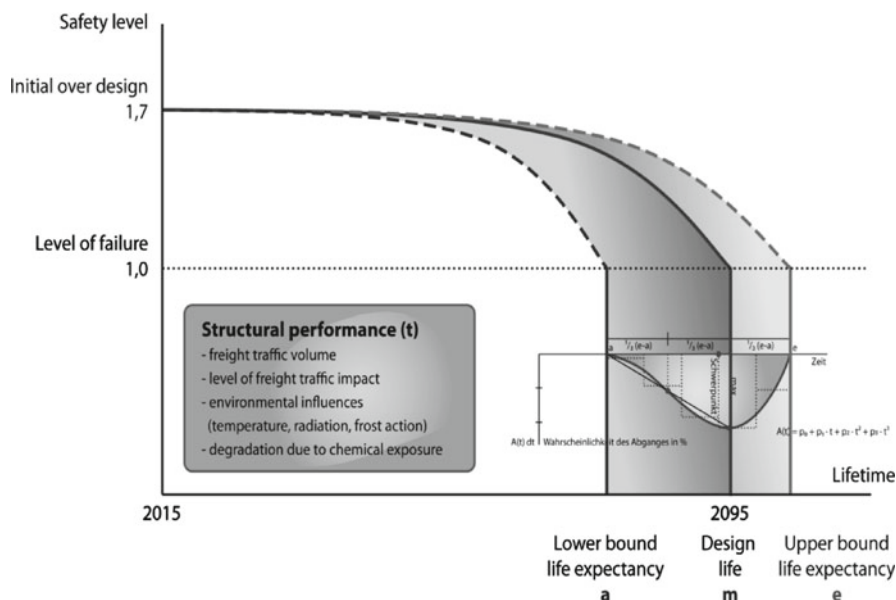
Fig. 1 Expected (analytical) lifetime of new structures

condition states which are mainly based on a linear deterioration where the deterioration rate can be expressed in terms of condition rating loss per year. Actually most of the existing Bridge Management Systems (BMS) use the Markov chain approach to model condition deterioration.

The determination/estimation of the design life of new structures

A tailor-made model was developed, which utilizes state-of-the-art information from literature (European, American & Asian) as well as VCE's experience gained in the course of performing bridge monitoring and bridge inspection worldwide. This knowledge has been incorporated into the assessment procedure that is briefly described in the following.

Probabilistic methods are used for the service life calculations of the individual items. The reason is to cover occurring uncertainties which have to be also implemented into the established maintenance plan in terms of lower & upper bounds of life expectancy.

The starting point of the bridge's service life – in terms of the safety level – is according to the initial over-design and depends on the applied design code and certain safety considerations in the course of the static calculations. To estimate the range of lifetime in the first step, statistic analyses using probability density functions are applied – covering the operational lifetime depending on the following parameters:

– cross section design
– static system
– material
– year of construction

Exemplified for the primary load bearing structure:

$$Average\ design\ life = a' + 0.6^* (e' - a') \tag{1}$$

where

$$a' = a \cdot k_1 \cdot k_2 \cdot k_3 \cdot k_4 \ \text{....adapted lower bound life expectancy} \tag{2}$$

$$e' = e \cdot k_1 \cdot k_2 \cdot k_3 \cdot k_4 \ \text{....adapted upper bound life expectancy} \tag{3}$$

a=45 years……lower bound life expectancy
e= 120 years….upper bound life expectancy
k_1, k_2, k_3, k_4 ….factors for influence parameters (see also Table 1)

To guarantee these stated ranges of theoretical design life of new structures the following aspects have to be considered:

– concrete cover
– concrete quality (concrete grade)
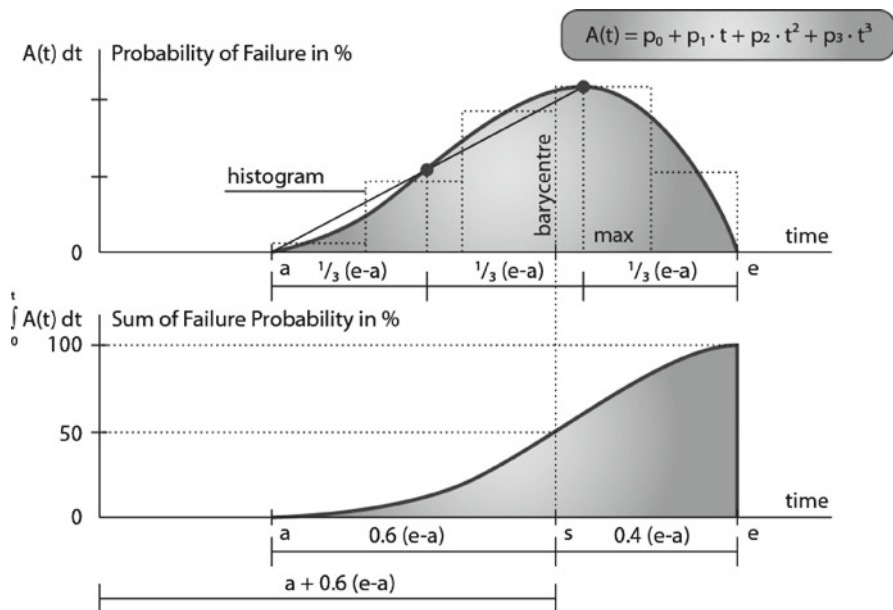
Fig. 2 Failure probability and sum of the failure probability

Table 1 Parameters which influence the lifetime of a bridge

Year of construction	k_1	Static system	k_3
<1970	0.667	Vault	1.2
1971-1985	0.9	Frames and arches	1.05
>1986	1	Girder/beam, slab, other	1
Cross section design	k_2	Material	k_4
Solid cross section	1.05	Stone	1.2
Box girder	1	Concrete and reinforced concrete	1.1
T-beam, composite section etc.	0.95	Prestressed concrete, steel-concrete composite	1
Corrugated profile	0.8	Wood	0.8

– environmental influences
– regular maintenance
– bridge monitoring

To address the deterioration process properly, the following sources of impact affecting the Structural Performance (t) are to be considered in detail:

– freight traffic volume
– level of freight traffic impact

– environmental influences (temperature, radiation, frost action)
– degradation due to chemical exposure

For demonstration purposes, a well established approach (suggested by A. Miyamoto (Japan) and D. Frangopol (USA)) [1,2] is described briefly, which covers all the major sources of deterioration impact. For the present demands these suggestions will necessarily have to be broadened and refined due to each of the listed major issues.

The task of chloride induced corrosion – covered by the CUR Guideline "Sustainability of constructional concrete in relation to chloride-initiated reinforcement corrosion" is to be highlighted in the current project.

Soundness (vertical axis) $h_n(t)$ - initial consideration (NEW Structures):

$$h_n(t) = b_n - a_n(t - t_n)c \tag{4}$$

Where:

t: is the year of service life ending
n: the number of times a remedial action was taken by year t (Index)
a_n: the slope of the deterioration curve at the time the nth remedial action has been taken
b_n: the soundness of the existing bridge at the time the nth remedial action has been taken, which changes according to the effectiveness of the remedial action taken
c: is the power exponent of the deterioration equation

Updating consideration (Existing structures):
The parameters a and b are updated every time repair or strengthening is carried out by using the following equations:

$$b_n = h_n(t_n) = h_n - 1(t_n) + R^* \rho \tag{5}$$

$$R = (h_n - 1(t_n - 1) - h_n - 1(t_n)) \tag{6}$$

$$a_n = a_n^* \eta_n \tag{7}$$

Where:

ρ: parameter for reducing soundness recovery
a_0: the slope of the initial deterioration curve
η: parameter for increasing the rate of deterioration.

The determination/estimation of the design life of existing structures

Basically the same methodology and the same sources of impact are utilized for primary load bearing members as well as for secondary load bearing members.

What makes the difference for the analysis itself is the fact that design assumptions are replaced as well as possible by everything, supporting a deeper understanding of the previous lifeline of the investigated structure:

– initial static calculation
– schedule of maintenance and rehabilitation measures
– loading history (historical traffic data)
– material tests (chloride penetration, carbonatisation, material strength, …)
– historical data about environmental exposure
– judgement / rating from bridge inspections
– performed monitoring campaigns

Each of these variables can strongly affect the current maintenance condition and determine the offset between the initial safety level in the year of construction and the present date of judgment.

The continuative progression is applied in a similar way to the new structure – but of course depends on the former impact. The use of the established maintenance condition matrix supports the individual determination of the current remaining structural resistance and the present risk level by means of a comprehensive weighting function.

Conclusions

In times of shrinking budgets at public authorities big infrastructure projects are put into the hands of private bodies in form of PPP models for a long period. As the payments to the private contractor depend on the availability of the infrastructure, either directly by tolls or indirectly by periodic payments from the authorities, a well elaborated maintenance concept is of major interest for the contractor. Appropriate condition assessment and condition monitoring of the infrastrucutre as well as life-cycle analysis and prediction are the basic tools for maintencance planning. The tools of structural health monitoring are perfectly suited for this purpose.

References

[1] Bondini, F. and Frangopol, D.M., 2008. Life-Cycle Civil Engineering. CRC Press Taylor & Frances Group, London. ISBN: 978-0-415-46857-2 (hbk).
[2] Cruz, P.J.S, Frangopol, D.M., and Neves, L.C., eds. 2006. Bridge Maintenance, Safety, Management, Life-Cycle Performance and Cost. Taylor & Fracis, London. ISBN: 0415403154.
[3] Wenzel, H., 2008. Health Monitoring of Bridges, J. Wiley and Sons Ltd, ISBN0470031735; Chichester England.
[4] Frangopol, D.M., Kong, J.S., and Gharaibeh, E.S. 2001. Reliability-based life-cycle management of highway bridges. Journal of Computing in Civil Engineering, Vol. 15, Issue 1, pp. 27–34.

A New Crane System for Remote Inspection and NDT

R. Drewello, N. Wetter, B. Beckett and N. Beckett

Abstract For non-destructive investigation of structures and materials, a crane system was developed to enable easy access and implementation of different non-destructive methods, such as high-resolution photography and detailed 3D scanning of surfaces. The crane was specifically designed for remote inspection and documentation of cultural assets. It was constructed from the world's smallest crane base that allows access through standard doorways. The crane is self-propelled by a non-abrasive caterpillar drive and has a small turning circle. The hydraulic outriggers ensure a level and secure ground base. A newly constructed telescopic mast mounted on the crane's original arm enables compactness in retracted state and the ability to reach an extension length of up to 22 meters. With the help of an extra mast, which is driven by an electric motor, the mast can be extended and retract by remote control. A high-resolution camera with a flash unit can be installed on the 3D head placed at the front of the crane. The head is controlled from the ground and can be placed in a variety of positions. The camera is operated remotely and features a live-image view on the ground based computer that allows easy positioning in front of the object. Examples from initial applications are provided in the paper.

Keywords Crane • High resolution • Monitoring • Non-destructive analysis • Scanning

R. Drewello (✉) • N. Wetter
Building Preservation Science, University of Bamberg, Germany
email: rainer.drewello@uni-bamberg.de

B. Beckett • N. Beckett
Beckett&Beckett Photography and Conservation, Germany

Inspection Needs

In the field of restoration and conservation of cultural assets, such as listed buildings, the first important task is the documentation and damage assessment. Due to the extremely rare and usually fragile areas, non-contact survey and analyses techniques are particularly important. This, however, requires good access to the areas to be recorded. If, for example, a wall surface requires recording for the planning of preservation measures and is located at a great height then a fixed scaffold is required for access. Fixed scaffolding needs anchoring points which may damage the fabric of the building, thus scaffolding is not suitable for this type of investigation. The aim of the project was to develop a crane system that allows a non-contact survey at heights of more than 20 meters. Especially important are the dimensions of the system to ensure, that the crane passes through standard doorways, has good manouverability and therefore can be used easily and safely for historic interiors.

The Crane System

As a base module, a mini-crane "carrier" produced in Japan was selected. The crane is motorized and self-propelled by a petrol engine or an electricical supply. Two levers control the movement for the body of the crane itself. The crane arm can be operated via remote control. To ensure high stability, four hydraulic outriggers for stabilisation are extended. The carrier weighs one ton, this is necessary for its stability. The small dimensions (1.87 m (L) x 0.59 m (W) x 1:29 m (H)) allows to move through a standard door or passage. For indoor use, a specially designed electric motor with a hydraulic pump system was constructed to replace the petrol engine. The original crane arm was removed and a newly developed telescopic arm attached. The hydraulic controll that originally operated the rotating and tilting can still be used for the telescopic boom.

The company Frick Gerätebau from Seligenstadt, Germany together with the Chair of Engineering of the Friedrich-Alexander University Erlangen-Nuremberg developed, a telescopic mast specifically for this carrier. This arm, which is capable to reach a length up to 24 meters is made of aluminum hollow profiles and can be extended and retracted with an electric motor. A supporting boom with a grip system moves and stops each element separately they are then secured with bolts. The supporting boom moves the single elements to a pre-programmed length. A control box with builtin touch screen operates the boom arm. A further remote control can move the 3D camera head that is mounted on the top of the crane giving a full range of motion. The camera head is free to rotate, tilt on its axis and provides space for a high-resolution camera or further equipment as required. With a payload of 30kg it can easily hold a professional camera and flash system. The flash unit is also controlled from the ground and is synchronized with the camera. For the tests a Hasselblad digital camera is used and

Fig. 1 The Crane system with the steering unit in transportation state

Fig. 2 The partly extended crane system, with the camera and flash illumination during the experimental phase in an industrial hall to test the range and safety of the system

controlled via a Laptop with the option of live-view. Cable management is an important task. The large amount of cabling connected to the control of the individual components of the crane are fixed together on removable metal hooks that can quickly be removed.

Initial Tests

The test phase was started in an old factory building, were the complete system could be tested and minor adaptions have been made (Image 2). The camera is simply controlled from the ground and the telescopic boom can be remotely positioned. The flash system provides suitable illumination, even for the larger areas that require

Image 3 Assembled 3D
head with flash illumination
and camera attached

Image 4 Image taken during
the tests in the industrial hall.
The image, at a height of
approximatly 20 meter,
shows the details of the
historic iron construction

documentation; the flash can be also controlled via laptop (Image 3) The high resolution images provide the required information which is needed for documentation and further processing (Image 4).

Due to the high resolution of the camera, it is possible to see damages, such as corrosion, blistering and flaking of the paint layers.

In the near future the system will be used within the research project "Bamberg Cathedral Digital" that includes a complete surveying and documentation of one of the most famous buildings in the World Heritage Site of Bamberg. The task will be carried out using a combination of surveying techniques (photogrammetry, 3D laser scanning and rectified photography). The crane system has to support the high resolution recording in the upper areas of the main and side aisle walls inside the building.

The high resolution images will be rectified creating an accurate record of the masonry work for a damage assessment at a scale of 1:20. Due to the existing under floor heating system, the payload of the floor is limited. This restricts the use of other lifting devices that are normally in use. Therefore, the crane system has a unique opportunity for recording the Cathedrals highly decorative interior.

References

[1] Beckett N, Schick B, Findlater P (2006): *Imaging architectural sites for conservation*, in: MacDonald L(edit), Oxford, 384–386

[2] Beckett B, Beckett N, Drewello R (2008): *Monitoring of historic surfaces in high definition – From a research project to a Small and Medium-sized Enterprise (SME)*, CHRESP Conference, Ljubljana, Slovenia

Integration of NDT in Rapid Screening of Concrete Structures

S. Sundar Kumar, B.H. Bharatkumar, G. Ramesh and T.S. Krishnamoorthy

Abstract Ageing of infrastructures is a major concern for the civil engineering community world over. Buildings, bridges, and every other structure are expected to serve for the designed life provided periodic inspection and proper maintenance is done. However maintenance is a word seldom associated with civil infrastructure. Non Destructive Testing (NDT) has gained relevance in this context as more and more infrastructure are getting aged and replacement of a existing structure with a new one is not feasible every time and within a short span of time. Testing, evaluation of the existing condition and retrofitting of the structures will extend the service life and hence give the authorities time to think about future course of action. This paper intends to provide a scheme to evaluate the existing condition of any concrete structure and suggests 'points' based evaluation. The scheme consists of standard NDT techniques both field and laboratory tests that are generally employed individually and their results analyzed separately. The formulated scheme has been employed on two existing buildings and its applicability demonstrated.

Keywords Carbonation • Chemical analysis • Condition level • Nondestructive testing • Ultrasonic pulse velocity

Introduction

Condition assessment of the civil engineering structures has become a necessity with large number of the concrete structures crossing the intended life span. Moreover lack of maintenance has further contributed to the problem, since it has led to degradation of relatively new structures also. Non Destructive Testing

S. Sundar Kumar (✉) • B.H. Bharatkumar • G. Ramesh • T.S. Krishnamoorthy
CSIR - Structural Engineering Research Centre, (Council of Scientific and Industrial Research),
CSIR Madras Complex, Taramani, Chennai 600 113, India
email: ssk@serc.res.in

(NDT) gains a lot of relevance due to the fact that, it is the only way in which the present condition of an existing structure can be accessed scientifically and the extent of damage/deterioration quantified. Many tests have been developed over the years to determine various characteristics of the materials, which serve as a basis to further evaluate and arrive upon the existing condition of the structure. Basically NDT can be classified into three categories, one in which the behaviour of the structure is monitored by intentionally loading it to a certain level, core compressive strength, pull out tests etc to determine the existing strength of structure. Next category of tests which can be classified as indirect method of strength assessment are essentially chemicals analysis such as pH, chloride, sulphate estimation in the concrete samples. Level of these substances in the concrete gives us an indication about the quality which in turn can be correlated with the strength. The third category is in a true sense non destructive evaluation, tests such as ultrasonic pulse velocity (UPV), rebound hammer (RH) give us an idea about the integrity and surface characteristics which are reliable indications about the quality of the existing concrete.

The tests involved here are well established with good reliability. However the interpretation of the results is still to a large extend dependent on the person who conducts these results. Quantification of the level of damage from tests results needs standardization. This is available for most of the individual tests through standards and codes. However standardization of the damage level is necessary. In this paper we have tried to present a scheme where in a single number can indicate the damage level. This would be helpful in estimating the seriousness of the situation.

Scheme for Evaluating the Condition of Concrete

The proposed scheme consists basically of two stages of evaluation. The first stage, being 'Visual Inspection' wherein visible signs of deterioration such as cracks, spalling, honeycomb, leaching etc are look for. Documenting the location of the signs of deterioration in the structure is the most important aspect at this stage. The second stage consists of a series of tests that are commonly used in concrete evaluation. The tests recommended are Core Test [2], Carbonation Test [2], Concrete Cover determination, UPV Test [2] [4], Rebound Hammer Test [2] [5], Half Cell Potential [2][3], Chemical Analysis [2] (pH, Chlorides, Sulphates). The decision regarding tests to be conducted shall be decided based on the observations from the visual inspection. Once completed, based on the results of the tests, points shall be awarded as per Table 1. Further a Damage Index shall be arrived by summing up the individual scores from each test results and normalizing it with the number of tests conducted. Visual Inspection shall also be considered as a test in the quantification process. It is necessary that at least a minimum of four tests need to be conducted for the final damage index to remain relevant. Hence, Damage Index = $\sum$ Individual Test Scores/ Number of Test Conducted. Finally based on the Damage Index damage level of the structure may be arrived upon as per Table 2.

Table 1 Scoring Scheme Based on Test Results

Criteria		Score					
		10	8	6	4	2	0
Visual Inspection	Cracks	Nil	Minor	Minor	Medium	Large	Large
	Spalling	Nil	Nil	Minor	Minor	Medium	Heavy
Reinforcement Corrosion		Nil	<5%	5-10%	10-20%	20-30%	>30%
No. of Points having half cell potential values < -300 mV		Nil	<5%	5-15%	15-30%	30-50%	>50%
No. of Points having UPV values < 3 km/sec		Nil	<5%	5-10%	10-25%	25-40%	>40%
Avg. Rebound Hammer value		>45	40-45	30-40	20-30	10-20	<10
Chloride content (kg/m3) & pH of concrete powder	Cl	<0.6	<0.6	<0.6	>0.6	>0.6	>0.6
	pH	>12	11.5-12	10-11.5	10-11.5	9-10	<9

Table 2 Damage Level Classification of the Structures

Damage Index	Level	Structure Condition	Remarks
10.0 – 9.0	0	Good	No visible damage but greater part in the initiation period
9.0 – 7.5	1	Minor Damage	Minor visible damage, if left unattended may lead to loss in structural integrity.
7.5 – 6.0	2	Moderate Damage	Moderated visible damage, loss in structural integrity initiated, needs to be attended as soon as possible.
6.0 – 4.0	3	Severe Damage	Severe damage visible, falling parts may be dangerous but the loss of serviceability and safety of the structure are minimal, needs to attended at the earliest
4.0 – 2.0	4	Heavy Damage (Reduced safety	Loss of serviceability and reduced safety of the structure, immediate action has to be taken.
2.0 – 0.0	5	Heavy Damage/ Collapse	Repair or rehabilitation may not be possible/ viable. Demolition may be thought upon for safety of nearby structures and public.

Case Studies

Two building structures, an unfinished residential apartment complex and a chemical manufacturing factory were investigated for their health status with the proposed method to arrive at the damage level.

Fig. 1 UPV Test in Progress

Fig. 2 Half Cell Potential being recorded

Case study 1 (residential building unfinished for 15 years)

The structure under consideration here is a residential complex which was constructed more than 15 years ago, but was left unfinished; it has now been decided to complete the remaining work. The investigations were carried out on two framed buildings. The first building consisted of 24 and the second one 16 apartments. Minor cracks were found at few locations but there were no signs of spalling during the visual inspection. Based on the preliminary survey, eight apartments in the first building and four apartments in the second building were identified for carrying out the NDT investigations. In each apartment, three columns and three beams were identified and investigated. UPV and half cell potential were taken at select locations. Concrete powder samples were collected to determine the pH and the chloride content. Concrete cores were extracted to determine the compressive strength of the concrete. Figures 1 and 2 shows the NDT (UPV and Half

Table 3 Damage Level Classification for the Residential Building

Results	Score
Minor crack and No spalling	8
UPV(<3.0 km/sec is <5% points)	8
Half cell potential (<-300 mV is 5 – 15 % points)	6
Cl is > 0.6 kg/m^3 and pH is 10-11.5	4
Damage Index = (8+8+6+4)/4 = 6.5	Damage Level = 2 (Moderate Damage)

Table 4 Damage Level Classification for the Chemical Factory Building

Results	Score
Larger cracks and medium spalling	2
UPV(<3.0 km/sec is 10-15% points)	4
Average Rebound Hammer Value 20-30	4
Cl is > 0.6 kg/m^3 and pH is 10-11.5	4
Damage Index = (2+4+4+4)/4 = 3.5	Damage Level = 4 (Heavy Damage/ Reduced Safety)

cell Potential) in progress. The results obtained from the field investigations were analyzed and the final score arrived at are given in Table 3. Based on the test results and evaluation scheme the structure falls under the category 'moderate damage', which essentially indicated that structural deterioration has been initiated and hence proper measures have to be taken before finishing the remaining works in the building so that the occupants are safe and the structure is able to perform well during its service life.

Case study 2 (chemical factory)

The second building assessed with the scheme is a chemical factory engaged in the manufacture of agro and non-agro chemicals. Visual inspection revealed that the condition of the concrete elements were quite bad due to poor maintenance and exposure to aggressive chemical environment. The columns in the ground floor showed extensive cracking and spalling, exposing the steel reinforcement bars. These bars had undergone severe corrosion. Most of the columns in the first floor were found to be in a fairly good condition during the visual examination. The RC beams at many locations had undergone extensive cracking. Most of the beams exhibited spalling of concrete leading to exposure of corroded reinforcement. The columns and beams in the first floor area were found to be in a fairly good condition. It was decided to conduct UPV test, Schmidt (Rebound) Hammer Test, compression test on concrete core, concrete powder samples to determine Chlorides, Sulphates and pH on the select beams and columns.

Table 4 lists the scores obtained by the building. It was found that the average UPV values for the RC columns and beams in the ground floor were below 3.5 km/sec.

The rebound hammer values in these columns were also in the range of 20-30, indicating that the quality of concrete near surface layer is also not satisfactory. The minimum UPV values in as much as 24 ground floor columns were less than 3.5 km/sec and in 14 columns, the values were less than 3 km/sec. It was found that the chloride content of the samples was in the range of 1.06 - 7.6 kg/m^3 for the columns in the ground floor which is rather high when compared with the permissible value of 0.6 kg/m^3 specified in the Indian standard [1]. The pH of the concrete sample was around 10 thus indicating availability of sufficient alkalinity though a reduction has been initiated. The damage index was 3.5 which brought the building under heavy damage/reduced safety category.

Concluding Remarks

A simple method to integrate the available standard non destructive tests such as UPV test and Rebound hammer tests along with chemical analysis to arrive at the existing condition of a structure has been proposed. The evaluating scheme proposed here is kept simple so that persons with minimal knowledge in civil engineering can follow it will the help of codes of practices. The scoring scheme is based on the value generally recommended by the Indian standards, these values can suitably modified when the methods is being adopted in other places. Two cases studies have been stated where the above method of screening was used to arrive at the condition of the structures.

References

[1] Indian Standard IS 456 (2000). *Plain and Reinforced Concrete – Code of Practice, Fourth Revision*, Bureau of Indian Standards, New Delhi.
[2] Bungey J. H. and Millard S. G.(1996). *Testing of Concrete in Structures*, third edition, Blackie Academic & Professional.
[3] Srinivasan P. (1996). *Corrosion of Reinforcement in Concrete Structures – Electrochemical Aspects and Site Testing*, Proc. of Advanced Course on Damage Assessment of Distressed Concrete Structures, Structural Engineering Research Centre, Chennai, India, pp DAR: 05 (1–28).
[4] Indian Standard IS 13311_1 (1992). *Non Destructive Testing of Concrete- Methods of Test, Part 1 Ultrasonic Pulse Velocity*, Bureau of Indian Standards, New Delhi.
[5] Indian Standard IS 13311_2 (1992). *Non Destructive Testing of Concrete- Methods of Test, Part 2, Rebound Hammer*, Bureau of Indian Standards, New Delhi.

Author Index

Subject Index